ΕΘΝΙΚΟ ΜΕΤΣΟΒΙΟ ΠΟΛΥΤΕΧΝΕΙΟ
ΣΧΟΛΗ ΠΟΛΙΤΙΚΩΝ ΜΗΧΑΝΙΚΩΝ
ΕΡΓΑΣΤΗΡΙΟ ΕΔΑΦΟΜΗΧΑΝΙΚΗΣ

NATIONAL TECHNICAL UNIVERSITY
SCHOOL OF CIVIL ENGINEERING
SOIL MECHANICS LABORATORY

Experimental Study of the Anisotropic Flow Deformation and Critical State of Sand

DOCTORAL THESIS

Panayiotis K. Triantafyllos

Civil Engineer, M.Sc.

Athens, July 2020

Εθνικο Μετσοβιο Πολυτεχνειο
Σχολη Πολιτικων Μηχανικων
Εργαστηριο Εδαφομηχανικης

Πειραματική Διερεύνηση των Ανισότροπων Χαρακτηριστικών Παραμόρφωσης κατά την Αστοχία και της Κρίσιμης Κατάστασης Άμμου

ΔΙΔΑΚΤΟΡΙΚΗ ΔΙΑΤΡΙΒΗ

Παναγιώτης Κ. Τριαντάφυλλος

Πολιτικός Μηχανικός, Μ.Δ.Ε.

Συμβουλευτική Επιτροπή : Βασιλική Ν. Γεωργιάννου
Γεώργιος Δ. Μπουκοβάλας
Γεώργιος Γκαζέτας

Εγκρίθηκε από την επταμελή εξεταστική επιτροπή την 27η Ιουλίου 2020.

Βασιλική Ν. Γεωργιάννου, Καθηγήτρια Ε.Μ.Π.

Γεώργιος Δ. Μπουκοβάλας, Καθηγητής Ε.Μ.Π.

Γεώργιος Γκαζέτας, Ομότιμος Καθηγητής Ε.Μ.Π.

Ιωάννης Φ. Δαφαλιάς, Καθηγητής University of California, Davis, U.S.A.

Αχιλλέας Γ. Παπαδημητρίου, Αναπληρωτής Καθηγητής Ε.Μ.Π.

Μιχαήλ Ι. Καββαδάς, Καθηγητής Ε.Μ.Π.

Νικόλαος Γερόλυμος, Αναπληρωτής Καθηγητής Ε.Μ.Π.

Αθήνα, Ιούλιος 2020

....

Παναγιώτης Κ. Τριαντάφυλλος

Διδάκτωρ Πολιτικός Μηχανικός Ε.Μ.Π.

DEDICATION

To my family and loved ones

七転び八起き

ACKNOWLEDGEMENTS

Every end is a peculiar event, incongruent in duration with what precedes or follows it yet a real milestone for both, and as the long-awaited moment signaling the completion of the present study is nearing, I feel the need to sincerely thank all those who contributed to this effort.

First off, I would like to express my deep gratitude to Professor Vasiliki Georgiannou for her continuous encouragement and guidance which vitally assisted in the completion of this thesis. I appreciate her extremely valuable comments and criticisms on the manuscript, and her overall support as the supervisor of the thesis. I feel sincerely grateful for the time she spent and the effort she patiently made while working with me.

I also wish to gratefully thank Professor Yannis Dafalias for being a true mentor who offered me invaluable support, encouragement and inspiration throughout my studies and especially when they have been needed most. Among the innumerable things that I have learned from him is that the investigation of the meaning of words is the prerequisite for learning (as stated by Antisthenes, the ancient Greek cynic philosopher: *ἀρχὴ σοφίας ἡ τῶν ὀνομάτων ἐπίσκεψις*).

Very special thanks are due to Professor George Bouckovalas and Professor George Gazetas, members of the doctoral committee, for reading and commenting on the manuscript, and offering their assistance and advice. Professor Achilleas Papadimitriou deserves special acknowledgement for his generous support and inspired ideas that gave the solution to many problems faced in this study. The help and advice of Professor Evangelos Sapountzakis and Professor Vlasis Koumousis, with whom I have cooperated during my postgraduate studies in the National Technical University of Athens, is also gratefully acknowledged.

The experience of working with Dr Ioannis-Orestis Georgopoulos and learning from him was deeply influential and life changing thus I owe him the most special acknowledgements. The time we spent together upgrading the hollow cylinder apparatus was the best part of this study in retrospect.

I wish to sincerely thank Mr Stelios Tsentidis who used his technical skills to help me with experimentation, especially during my first steps in the laboratory. Dr Maria Konstadinou also helped me with my first experiments in the hollow cylinder apparatus and I wish to thank her for that.

Many friends and colleagues have helped me and contributed to this study. Thanks are due to Kostas Papanikolopoulos, Nikos Bozikis, Chara Prassa, Alexandros Petalas, George Belokas, Sotiris Alevizos, Manolis Vairaktaris, Alexandros Theocharis, Eleni Pavlopoulou and Stelios Chaviaras. I would also like to thank the personnel of the Department of Geotechnical Engineering for the accommodation and services they offered me.

Last but not least, I wish to express my deepest gratitude to my family and my loved ones for their support, love and patience all these years. Very warm thanks are due to my mother, Asimenia, my father, Kimon, and my brother, Pantelis. Heartfelt thanks are due to Leonidas, Despina and Roubini.

Palaio Faliro, Athens — Panayiotis K. Triantafyllos

27/7/2020

This research was co-financed by the EU (European Social Fund) and Greek national funds through the Operational Programme "Education and Lifelong Learning" of the National Strategic Reference Framework-Research Funding Programme: Thales - Investing in Knowledge Society through the European Social Fund.

This research has received funding from the European Research Council under the European Union's Seventh Framework Programme FP7-ERC-IDEAS Advanced Grant Agreement n° 290963 with acronym SOMEF.

This research has received funding from the General Secretariat for Research and Technology of Greece (Matching Funds Program) under the project titled SOFI – SOil Fabric Investigation with Grant No 67108800.

ΠΕΙΡΑΜΑΤΙΚΗ ΔΙΕΡΕΥΝΗΣΗ ΤΩΝ ΑΝΙΣΟΤΡΟΠΩΝ ΧΑΡΑΚΤΗΡΙΣΤΙΚΩΝ ΠΑΡΑΜΟΡΦΩΣΗΣ ΚΑΤΑ ΤΗΝ ΑΣΤΟΧΙΑ ΚΑΙ ΤΗΣ ΚΡΙΣΙΜΗΣ ΚΑΤΑΣΤΑΣΗΣ ΑΜΜΟΥ

Διδακτορική Διατριβή

του

Παναγιώτη Κ. Τριαντάφυλλου

ΕΚΤΕΝΗΣ ΣΥΝΟΨΗ

Αντικείμενο και στόχοι διδακτορικής διατριβής

Στην παρούσα διδακτορική διατριβή διερευνήθηκε πειραματικά η μηχανική συμπεριφορά άμμου υπό συνθήκες τριαξονικής και γενικευμένης φόρτισης. Συγκεκριμένα, διερευνήθηκε η ανισότροπη συμπεριφορά της άμμου M31 σε συνθήκες μονότονης ρευστοποίησης (flow deformation) καθώς και στην κρίσιμη κατάσταση (critical state). Οι πειραματικές δοκιμές εκτελέστηκαν στη συσκευή στρεπτικής διάτμησης κοίλου κυλινδρικού δοκιμίου και σε δύο συσκευές τριαξονικής φόρτισης του Εργαστηρίου Εδαφομηχανικής, του Εθνικού Μετσόβιου Πολυτεχνείου.

Ο πρώτος στόχος που τέθηκε ήταν η μελέτη της Κρίσιμης Κατάστασης (ΚΚ) της άμμου και ο προσδιορισμός των αντίστοιχων μηχανικών παραμέτρων υπό συνθήκες τριαξονικής φόρτισης. Ο δεύτερος στόχος αφορούσε την εξέταση της επίδρασης της εγγενούς ανισοτροπίας (inherent anisotropy) (Casagrande and Carrillo 1944) και της ιστορίας φόρτισης (loading history) στα μηχανικά χαρακτηριστικά της άμμου υπό συνθήκες μονότονης ρευστοποίησης (flow deformation) (Ishihara 1993) και γενικευμένης αστοχίας. Κατά τη μονότονη ρευστοποίηση το εδαφικό δοκίμιο υπόκειται σε μη-συγκεντρωμένη παραμόρφωση (diffuse deformation) ενώ η συμπεριφορά του συστήματος δοκίμιο – συσκευή φόρτισης είναι οιονεί ασταθής (Daouadji et al. 2011). Τα πειραματικά αποτελέσματα κρίθηκαν κατάλληλα να χρησιμοποιηθούν για την επαλήθευση ή διάψευση των προβλέψεων ορισμένων προσομοιωμάτων, καταστρωμένων στα πλαίσια της Θεωρίας Διακλάδωσης (Bifurcation Theory), σχετικά με την ασταθή συμπεριφορά των γεωϋλικών (Darve and Laouafa 2000, Darve et al. 2004, Prunier et al. 2009). Τέλος, τέθηκε ως στόχος να εκτελεστεί σε φυσικές συνθήκες το «πείραμα σκέψης» που επινοήθηκε από τον καθηγητή Δαφαλιά (Dafalias 2016) και αφορά την επιβολή στροφής των κυρίων αξόνων τάσεως στην ΚΚ, διατηρώντας σταθερές τις ενεργές κύριες τιμές τάσεως. Αυτό το πείραμα, το οποίο είχε προσομοιωθεί προγενέστερα από τους Theocharis et al. (2017, 2019) με χρήση της Μεθόδου Διακριτών Στοιχείων (Discrete Element Method), έχει ως σκοπό να αναδείξει την επίδραση της ανισότροπης εσωτερικής δομής (fabric) (Brewer 1964, Oda 1972) στη μηχανική συμπεριφορά άμμου στην ΚΚ και να αποδείξει την αναγκαιότητα αναθεώρησης της κλασσικής Θεωρίας Κρίσιμης Κατάστασης (ΘΚΚ) (Roscoe et al. 1958, Schofield and Wroth 1968), όπως προτάθηκε από τους Li and Dafalias (2012) οι οποίοι εισήγαγαν τη Θεωρία Ανισοτροπικής Κρίσιμης Κατάστασης (ΘΑΚΚ).

Η ΘΚΚ διατυπώνει ότι τα κοκκώδη υλικά που υποβάλλονται σε φόρτιση φτάνουν στην κρίσιμη και σταθερή κατάσταση (critical and steady state) ύστερα από εκτεταμένη παραμόρφωση. Η κατάσταση αυτή αντιστοιχεί στο παρατηρούμενο φαινόμενο διαρκούς διατμητικής παραμόρφωσης του κοκκώδους υλικού υπό σταθερό όγκο και σταθερές τάσεις (αποκλίνουσα και ισοτροπική). Η αξία της ΘΚΚ έγκειται στο γεγονός ότι η αναφορά στην τελική κατάσταση (ultimate state) μέσω κάποιας καταστατικής παραμέτρου αποτελεί την πεμπτουσία της αποτελεσματικής περιγραφής και προσομοίωσης της ελαστοπλαστικής συμπεριφοράς των κοκκωδών υλικών (Wroth and Basset 1965, Been and Jefferies 1985, Triantafyllos et al. 2020b). Στα πλαίσια της ΘΚΚ διατυπώνονται δύο ικανές και αναγκαίες συνθήκες για την επίτευξη και διατήρηση της κρίσιμης κατάστασης σύμφωνα με τις οποίες ο αποκλίνων λόγος τάσεων (deviatoric stress ratio, $\eta_c = (q / p')_c = M$) είναι μία σταθερά του υλικού και ο δείκτης πόρων (void ratio, e_c) είναι μία μοναδική συνάρτηση της ισοτροπικής τάσης (isotropic stress, p')· σημειώνεται ότι q είναι η αποκλίνουσα τάση και ότι ο κάτω δείκτης c σημαίνει «στην κρίσιμη κατάσταση».

Μία από τις υποθέσεις της ΘΚΚ είναι ότι το εδαφικό υλικό στερείται ανισότροπης εσωτερικής δομής λόγω της έντονης αναμόχλευσης που υπόκειται για να φτάσει στην ΚΚ (Schofield and Wroth 1968). Διατυπώνεται, επίσης, ότι το εδαφικό υλικό φτάνει στην ΚΚ και παραμορφώνεται διαρκώς υπό σταθερό όγκο όταν και μόνο όταν τηρούνται οι εξής συνθήκες: $q = Mp'$ και $v = \Gamma - \lambda \ln p'$ (Schofield and Wroth 1968); όπου v είναι ο ειδικός όγκος του εδαφικού υλικού και M, Γ και λ είναι σταθερές του εδαφικού υλικού. Είναι προφανές ότι η εσωτερική δομή στην ΚΚ θεωρείται πρακτικά ισότροπη και για αυτόν τον λόγο οι ικανές και αναγκαίες συνθήκες για την επίτευξη και διατήρηση της ΚΚ περιλαμβάνουν μόνο βαθμωτά μεγέθη (scalar quantities). Αντιθέτως, σύγχρονες μελέτες έχουν δείξει ότι η εσωτερική δομή στην ΚΚ είναι εντόνως ανισότροπη και προσανατολισμένη προς την κατεύθυνση της φόρτισης στην οποία υποβλήθηκε το κοκκώδες υλικό μέχρι να φτάσει στην ΚΚ (Thornton 2000, Masson and Martinez 2001, Zhang and Thornton 2007, Li and Li 2009, Fu and Dafalias 2011, Wiebicke et al. 2017, Theocharis et al. 2017 and 2019). Επομένως, η ανισότροπη εσωτερική δομή επηρεάζει σημαντικά τη μηχανική συμπεριφορά των κοκκωδών υλικών σε κάθε κατάσταση συμπεριλαμβανομένης και της κρίσιμης κατάστασης.

Το «πείραμα σκέψης» που περιγράφηκε προηγουμένως (Dafalias 2016) στοχεύει στο να διερευνηθεί εάν το εδαφικό υλικό που βρίσκεται στην ΚΚ, όταν ικανοποιούνται ταυτόχρονα οι δύο διατυπωμένες ικανές και αναγκαίες συνθήκες, παραμείνει στην ΚΚ καθώς εκκινείται η στροφή των κύριων αξόνων τάσεως, διατηρώντας σταθερές τις ενεργές κύριες τιμές τάσεως. Στην περίπτωση που ο δείκτης πόρων του εδαφικού υλικού μεταβληθεί, όπως έχει προγενέστερα δειχθεί στην αριθμητική προσομοίωση του πειράματος από τους Theocharis et al. (2017, 2019), τότε αυτό εγκαταλείπει την ΚΚ και οι δύο διατυπωμένες συνθήκες είναι αναγκαίες αλλά όχι ικανές για τη διατήρηση της ΚΚ. Οι Li and Dafalias (2012) πρότειναν την αναθεώρηση της ΘΚΚ με την προσθήκη μίας τρίτης συνθήκης η οποία απαιτεί μία νέα παράμετρος ανισότροπης δομής (fabric anisotropy variable) να λάβει την κρίσιμη τιμή της ταυτόχρονα με τον αποκλίνοντα λόγο τάσεων και τον δείκτη πόρων ώστε να επιτευχθεί και να διατηρηθεί η ΚΚ. Η νέα παράμετρος λαμβάνει την κρίσιμη τιμή της όταν ο τανυστής δομής (Satake 1978, Oda et al. 1985) προσανατολιστεί με την κατεύθυνση φόρτισης και ταυτόχρονα αποκτήσει την κρίσιμη, κατά μέγεθος (norm), τιμή του. Επομένως, η χρήση της νέας παραμέτρου εξηγεί γιατί το εδαφικό υλικό εγκαταλείπει την ΚΚ όταν εκκινείται η στροφή των κύριων αξόνων τάσεως παρόλο που δεν παραβιάζονται αρχικώς οι δύο συνθήκες της κλασσικής ΘΚΚ, ενώ η προσθήκη της τρίτης συνθήκης καθιστά τη θεωρία πλήρη στην αναθεωρημένη της μορφή (ΘΑΚΚ).

Αναβάθμιση και τροποποίηση των συσκευών φόρτισης

Για την επίτευξη των στόχων που τέθηκαν στην παρούσα διδακτορική διατριβή εκτελέστηκαν, αρχικώς, εργασίες που αφορούσαν την τροποποίηση και αναβάθμιση των συσκευών τριαξονικής φόρτισης και στρεπτικής διάτμησης. Κινητά μέρη σχεδιάστηκαν, κατασκευάστηκαν και προσαρτήθηκαν στις συσκευές φόρτισης με σκοπό την επιβολή συνοριακών συνθηκών που αποτρέπουν την εκδήλωση ανεπιθύμητων διακλαδισμένων μορφών παραμόρφωσης (bifurcated deformation modes; Vardoulakis and Sulem 1995). Η συσκευή υψηλών πιέσεων τροποποιήθηκε ώστε να εκτελεστούν δοκιμές σε αρχική μέση ενεργό τάση έως και 6 MPa με σκοπό την καθυστέρηση της ανάπτυξης των ζωνών συγκεντρωμένης παραμόρφωσης (strain-localisation zones) στα πυκνότερα δοκίμια άμμου (Desrues and Hammad 1989). Η συσκευή στρεπτικής διάτμησης αναβαθμίστηκε ώστε να καταστεί δυνατός ο ανεξάρτητος έλεγχος των πιέσεων περίσφιγξης μέσα και έξω από το κοίλο κυλινδρικό δοκίμιο (Hight et al. 1983). Επίσης, ο έλεγχος τύπου «κλειστού βρόχου» (closed-loop control) όλων των συνοριακών φορτίων που δρουν στο κοίλο κυλινδρικό δοκίμιο επετεύχθη με χρήση ενός νέου λογισμικού σε προγραμματιστικό περιβάλλον LabVIEW το οποίο αλληλεπιδρά με τα συστήματα σέρβο-ελέγχου της συσκευής στρεπτικής διάτμησης. Η αναβάθμιση αυτή επέτρεψε την εκτέλεση τασικών οδεύσεων γενικευμένης φόρτισης, κατάλληλων για τη διερεύνηση της επίδρασης της εγγενούς ανισοτροπίας και της ιστορίας φόρτισης στη μηχανική συμπεριφορά της άμμου.

Πειραματικά αποτελέσματα, μέρος I: Κρίσιμη Κατάσταση άμμου

Για τη μελέτη της κρίσιμης κατάστασης της άμμου M31, με τα φυσικά χαρακτηριστικά που αναγράφονται στον Πίνακα 3, παρασκευάστηκαν δοκίμια με τη μέθοδο απόθεσης σε νερό, τα οποία στερεοποιήθηκαν ισότροπα (άμμος IC) σε μέση ενεργό τάση, p'_{in}, κυμαινόμενη από 100 έως 6000 kPa· σημειώνεται ότι ο δείκτης *in* σημαίνει «στην αρχική κατάσταση». Έπειτα, τα δοκίμια υποβλήθηκαν σε μονοτονική τριαξονική συμπίεση υπό συνθήκες ελεύθερης ή εμποδιζόμενης στράγγισης· οι δοκιμές αυτές ανήκουν στην κατηγορία A (A-series tests). Τα Σχήματα 1a και b δείχνουν τις ενεργές τασικές οδεύσεις (effective stress paths) στο $q - p'$ επίπεδο και τις καμπύλες αποκλίνουσας τάσης – παραμόρφωσης ($q - \varepsilon_q$), αντιστοίχως, από τις δοκιμές ελεύθερης στράγγισης, ενώ τα Σχήματα 1c και d δείχνουν τα ίδια διαγράμματα από τις δοκιμές εμποδιζόμενης στράγγισης. Τα πειραματικά αποτελέσματα υποδεικνύουν την ύπαρξη μίας μοναδικής γραμμής στον $p' - e - q$ χώρο στην οποία καταλήγουν οι οδεύσεις φόρτισης (loading paths) όταν ο ρυθμός των τάσεων και των πλαστικών ογκομετρικών παραμορφώσεων της άμμου μηδενίζεται πρακτικώς ύστερα από εκτεταμένη παραμόρφωση (Roscoe et al. 1958, Been et al. 1991, Verdugo and Ishihara 1996, Triantafyllos et al. 2020b). Η Γραμμή Κρίσιμης Κατάστασης (ΓΚΚ) προσδιορίστηκε ανεξαρτήτως της αρχικής τιμής του δείκτη πόρων και της μέσης ενεργού τάσης και ανεξαρτήτως του τύπου της όδευσης φόρτισης (ελεύθερης ή εμποδιζόμενης στράγγισης), όπως φαίνεται στα Σχήματα 2a και b τα οποία απεικονίζουν την προβολή της ΓΚΚ στα $q - p'$ και $e - p'$ επίπεδα. Ο Πίνακας 4 δίνει τις παραμέτρους κρίσιμης κατάστασης της άμμου M31 σύμφωνα με την εξίσωση που πρότειναν οι Li and Wang (1998).

Η προβολή της ΓΚΚ στο $e - p'$ καταστατικό επίπεδο χρησιμοποιήθηκε για να προσδιοριστεί η καταστατική παράμετρος, $\psi = e - e_c(p')$, των Been and Jefferies (1985) σε κάθε στάδιο της φόρτισης. Η παράμετρος αυτή εκφράζει τη διαφορά της τρέχουσας τιμής του δείκτη πόρων, e, από την τιμή του δείκτη πόρων στην ΚΚ για την τρέχουσα τιμή της ισοτροπικής τάσης, $e_c(p')$. Τα πειραματικά αποτελέσματα υποδεικνύουν μία σαφή εξάρτηση της μηχανικής συμπεριφοράς της άμμου από την καταστατική παράμετρο, ψ (Manzari and Dafalias 1997, Li and Dafalias 2000). Η εξέλιξη των παραμέτρων η και ε_{vol} (ή $\Delta u \,/\, p'_{in}$) βρέθηκε καλά συσχετισμένη με την εξέλιξη της καταστατικής παραμέτρου, ψ· όπου $\eta = q \,/\, p'$ είναι ο αποκλίνων λόγος τάσεων, ε_{vol} είναι η ογκομετρική παραμόρφωση και $\Delta u \,/\, p'_{in}$ είναι η υπερπίεση του ύδατος πόρων κανονικοποιημένη ως προς τη μέση ενεργό τάση στο τέλος της ισότροπης στερεοποίησης. Για παράδειγμα, ο αποκλίνων λόγος τάσεων, η_{pt}, στο σημείο αλλαγής φάσης (phase transformation point) (Ishihara et al. 1975) αυξάνεται ενώ ο αποκλίνων λόγος τάσεων, η_p, και η απόλυτος τιμή του λόγου διαστολικότητας, $D_p = (\mathrm{d}\varepsilon_{vol}^p \,/\, \mathrm{d}\varepsilon_q^p)_p$, στην κατάσταση κορυφαίας αστοχίας (peak failure) μειώνονται όταν η καταστατική παράμετρος, ψ, γίνεται λιγότερο αρνητική, όπως φαίνεται στο Σχήμα 3· σημειώνεται ότι ο άνω δείκτης p στον ορισμό του D σημαίνει «πλαστικός» και ότι στη συγκεκριμένη εργασία χρησιμοποιήθηκαν οι ελαστοπλαστικές παραμορφώσεις για τον προσδιορισμό του D, ενώ ο κάτω δείκτης p σημαίνει «στην κατάσταση κορυφαίας αστοχίας» που αντιστοιχεί στη μεγιστοποίηση του λόγου τάσεων η. Επίσης, η σχέση λόγου τάσεων – διαστολικότητας, η – D, είναι διαφορετική για πυκνή και χαλαρή άμμο, δηλαδή εξαρτάται από την καταστατική παράμετρο, ψ, όπως φαίνεται στο Σχήμα 4.

Πειραματικά αποτελέσματα, μέρος ΙΙ: Μηχανικά χαρακτηριστικά άμμου υπό συνθήκες μονότονης ρευστοποίησης και γενικευμένης αστοχίας

Για τη μελέτη της μηχανικής συμπεριφοράς της άμμου παρασκευάστηκαν χαλαρά δοκίμια με τη μέθοδο απόθεσης σε νερό, τα οποία στερεοποιήθηκαν ισότροπα (άμμος IC) σε μέση ενεργό τάση, p'_c = 200 kPa (ή 100 kPa ή 300 kPa). Έπειτα, τα δοκίμια υποβλήθηκαν σε μονοτονική φόρτιση εμποδιζόμενης στράγγισης υπό σταθερή μέση ολική τάση, p, και σταθερή παράμετρο ενδιάμεσης κύριας τάσης, $b = (\sigma'_2 - \sigma'_3) / (\sigma'_1 - \sigma'_3) = 0.5$, διατηρώντας τον προσανατολισμό του άξονα της μέγιστης κύριας τάσης, σ'_1, σταθερό σε διάφορες κατευθύνσεις ως προς την κατακόρυφο, μετρούμενες με τη γωνία α (ή $\alpha_{\sigma'1}$) (βλ. Σχήμα 5)· οι δοκιμές αυτές ανήκουν στην κατηγορία Α (A-series tests). Σημειώνεται ότι κατά την απόθεση της άμμου υπό την επίδραση της βαρύτητας δημιουργούνται οριζόντια επίπεδα διαστρωμάτωσης (bedding planes) πάνω στα οποία προσανατολίζονται επιλεκτικά οι μεγάλοι άξονες των μη σφαιρικών κόκκων σχηματίζοντας μία εγγενώς ανισότροπη εσωτερική δομή (inherently anisotropic fabric) (Arthur and Menzies 1972, Oda 1972). Επομένως, όταν αλλάζει ο προσανατολισμός του άξονα της μέγιστης κύριας τάσης ως προς τα οριζόντια επίπεδα διαστρωμάτωσης μεταβάλλονται τα μηχανικά χαρακτηριστικά της άμμου. Αξίζει, όμως, να επισημανθεί ότι ανισότροπη εσωτερική δομή παράγεται όχι μόνο εξαιτίας του επιλεκτικού προσανατολισμού των μεγάλων αξόνων των μη σφαιρικών κόκκων αλλά και εξαιτίας του επιλεκτικού προσανατολισμού των κάθετων διανυσμάτων διεπαφής (contact normal vectors) των κόκκων (σφαιρικών ή μη) και των μεγάλων αξόνων των κενών μεταξύ των κόκκων. Τα τρία αυτά στοιχεία εσωτερικής δομής εξελίσσονται κατά τη φόρτιση των κοκκωδών υλικών με διαφορετικούς ρυθμούς (Oda et al. 1985, Wang et al. 2017).

Η χαλαρή άμμος επέδειξε εντόνως ανισότροπα μηχανικά χαρακτηριστικά στις δοκιμές φόρτισης εμποδιζόμενης στράγγισης κατά τις οποίες οι τιμές των α, b και p παραμέτρων διατηρήθηκαν σταθερές (δοκιμές ακτινικής φόρτισης) (radial loading tests). Τα Σχήματα 6a και b δείχνουν τις ενεργές τασικές οδεύσεις στο $q_d - p'$ επίπεδο και τις καμπύλες οκταεδρικών διατμητικών τάσεων – παραμορφώσεων ($\tau_{oct} - \gamma_{oct}$), αντιστοίχως· σημειώνεται ότι q_d είναι η διαφορά τάσεων $\sigma'_1 - \sigma'_3$, η οποία ισούται με την αποκλίνουσα τάση, q, όταν b = 0 ή 1. Στα διαγράμματα παρατηρείται η τυπική συμπεριφορά παροδικής μονότονης ρευστοποίησης (limited flow deformation) (Nakata et al. 1998) για τη χαλαρή κορεσμένη άμμο η οποία εκδηλώνεται με την πτώση της αντοχής, q_d, μετά το σημείο παροδικού μεγίστου (transient-peak state) και με ταυτόχρονη συσσώρευση μονότονης διατμητικής παραμόρφωσης και υπερπίεσης του ύδατος πόρων (Vaid and Chern 1983). Η πτώση της αντοχής, q_d, οφείλεται στην ανάπτυξη της υπερπίεσης του ύδατος πόρων (Sassitharan et al. 1993) ενώ ο αποκλίνων λόγος τάσεων, $\eta = q / p'$, αυξάνεται, δηλαδή το αμμώδες υλικό κρατύνεται με ταυτόχρονη μείωση των ενεργών τάσεων (Lade et al. 1988). Λόγω των παραμέτρων ελέγχου (control parameters) που επιλέχθηκαν η μείωση της αντοχής οδηγεί σε αστάθεια (instability) με στοιχεία δυναμικής απόκρισης (Castro 1969, Chu and Leong 2001) και διακλάδωση (bifurcation) της συμπεριφοράς του συστήματος συσκευή φόρτισης – δοκίμιο μέχρι το σημείο αλλαγής φάσης πέραν του οποίου ανακτάται η αντοχή, ο έλεγχος των παραμέτρων φόρτισης και η ευστάθεια (Triantafyllos et al. 2020a).

Η συμπεριφορά της άμμου γίνεται, εν γένει, περισσότερο συστολική όταν ο σ'_1-άξονας απομακρύνεται από την κατακόρυφο με αποτέλεσμα η αντοχή, q_d, στο σημείο παροδικού μεγίστου και στο σημείο αλλαγής φάσης να μειώνεται με τη γωνία α· επίσης, η κανονικοποιημένη υπερπίεση του ύδατος πόρων, $\Delta u / p'_{in}$, και η οκταεδρική διατμητική παραμόρφωση, γ_{oct}, στο σημείο αλλαγής φάσης αυξάνονται όταν αυξάνεται η γωνία α. Στην κατάσταση κορυφαίας αστοχίας η τιμή του λόγου τάσεων, sin φ_p (ο δείκτης p σημαίνει «στην κατάσταση κορυφαίας αστοχίας» που αντιστοιχεί στη μεγιστοποίηση των λόγων τάσεων sin φ και η), μειώνεται, εν γένει, με την αύξηση της γωνίας α. Μολαταύτα, η περισσότερο ασθενής απόκριση παρατηρείται όταν η γωνία α λαμβάνει τιμές μεταξύ 60° και 75°, διότι τότε ένα από τα επίπεδα στα οποία ο λόγος της διατμητικής προς την ορθή τάση γίνεται μέγιστος (maximum stress obliquity planes – επίπεδα οιονεί αστοχίας) τείνει να προσανατολιστεί με το οριζόντιο επίπεδο διαστρωμάτωσης. Επομένως, η εγγενής ανισοτροπία επηρεάζει τα μηχανικά χαρακτηριστικά της άμμου στο σημείο παροδικού μέγιστου αντοχής, στο σημείο αλλαγής φάσης και στην κατάσταση κορυφαίας αστοχίας.

Τα σημεία παροδικού μεγίστου αντοχής στις δοκιμές ακτινικής φόρτισης εμποδιζόμενης στράγγισης ταυτίζονται πρακτικώς με τα σημεία εκκίνησης της αστάθειας (instability points) και σε αυτά αντιστοιχεί ένας λόγος τάσεων, sin φ_{ip} (ο δείκτης ip σημαίνει «στο σημείο αστάθειας»), ο οποίος μειώνεται με την αύξηση της γωνίας α. Ενώνοντας, επομένως, τα σημεία παροδικού μεγίστου αντοχής με την αρχή των αξόνων στον $q_d - p'$ χώρο τάσεων προκύπτουν γραμμές με διαφορετική κλίση ανάλογα με την τιμή της γωνίας α, οι οποίες ουσιαστικά αποτελούν τις Γραμμές Αστάθειας (Instability Lines) κατά τον ορισμό του Lade (1993). Στην παρούσα διδακτορική διατριβή ορίστηκε η Επιφάνεια Αστάθειας (Instability Surface, IS) στον $Y - X$ χώρο τάσεων, όπου $Y = 2\tau_{z\theta} / (\sigma'_{zz} + \sigma'_{\theta\theta})$ και $X = (\sigma'_{zz} - \sigma'_{\theta\theta}) / (\sigma'_{zz} + \sigma'_{\theta\theta})$, η οποία διέρχεται από τα σημεία αστάθειας και αποτελεί τη γενίκευση της έννοιας της γραμμής αστάθειας του Lade (Triantafyllos et al. 2020a). Στη συνέχεια, εξετάστηκε αν η εκκίνηση της μονότονης ρευστοποίησης υπό συνθήκες φόρτισης εμποδιζόμενης στράγγισης που περιλαμβάνουν συνεχή στροφή των κύριων αξόνων τάσεως μπορεί να συσχετιστεί με τη διάσχιση της Επιφάνειας Αστάθειας (ΕΑ) ή κάποιας εναλλακτικής επιφάνειας όπως η Τοπική Οριακή Επιφάνεια (Local Boundary Surface) που ορίστηκε από τους Symes et al. (1984) και Shibuya et al. (1987, 2003a, 2003b).

Επεξηγήσεις σχετικά με τον προσδιορισμό των σημείων αστάθειας, των γραμμών αστάθειας και της επιφάνειας αστάθειας δίνονται στα Σχήματα 7a και b τα οποία δείχνουν τις τασικές οδεύσεις στο q_d – *p'* και *Y* – *X* επίπεδο, αντιστοίχως, από τρεις δοκιμές μονοτονικής φόρτισης εμποδιζόμενης στράγγισης με διαφορετικές τιμές της γωνίας κατεύθυνσης της μέγιστης κύριας τάσεως, *α*, και κοινές τιμές των *b* και *p* παραμέτρων. Στο Σχήμα 7a επισημαίνονται τα σημεία αστάθειας (συμπαγείς κύκλοι) και οι γραμμές αστάθειας (διακεκομμένες γραμμές) ενώ οι ίδιες οι τασικές οδεύσεις (συμπαγείς γραμμές) αποτελούν την προβολή ενός τμήματος της Τοπικής Οριακής Επιφάνειας από τον q_d – *p'* – *a* – *b* (= 0.5) χώρο στο q_d – *p'* επίπεδο. Στο Σχήμα 7b απεικονίζονται στο *Y* – *X* εκτροπικό επίπεδο οι τασικές οδεύσεις από τις ίδιες δοκιμές φόρτισης εμποδιζόμενης στράγγισης και ένα τμήμα της επιφάνειας αστάθειας, όπως αυτό προσδιορίζεται ενώνοντας τα τρία σημεία αστάθειας.

Στο Σχήμα 8 προσδιορίζονται γεωμετρικά οι κύριες κατευθύνσεις τάσεως και παραμορφώσεως στα *Y* – *X* και Y_s – X_s εκτροπικά επίπεδα, όπου $Y_s = 2\tau_{z\theta}$ και $X_s = \sigma'_{zz} - \sigma'_{\theta\theta}$, τα οποία χρησιμοποιούνται κατά κόρον στην παρούσα διδακτορική διατριβή, ενώ στον Πίνακα 1 δίνονται οι αλγεβρικοί τύποι για τον υπολογισμό των γωνιών κύριας κατεύθυνσης τάσεως και παραμορφώσεως καθώς και των ρυθμών αυτών. Η τασική όδευση που απεικονίζεται στα *Y* – *X* και Y_s – X_s επίπεδα του Σχήματος 8 αφορά στροφή των κυρίων αξόνων τάσεως και η κύρια κατεύθυνση τάσεως, προσαυξητικής τάσεως και προσαυξητικής παραμορφώσεως υποδεικνύεται με την υπέρθεση των μοναδιαίων διανυσμάτων, **σ**, d**σ** και d**ε**, αντιστοίχως, στο τρέχον τασικό σημείο. Σημειώνεται ότι οι τανυστές αντιμετωπίζονται στο εξής ως διανύσματα χάριν ευκολίας του γεωμετρικού προσδιορισμού των κύριων κατευθύνσεων.

Η γωνία που σχηματίζουν τα διανύσματα **σ**, d**σ** και d**ε** με τον οριζόντιο άξονα (*X* ή *Xs*) είναι ίση με $2\alpha_{\sigma'1}$, $2\alpha_{d\sigma'1}$ και $2\alpha_{d\varepsilon1}$, αντιστοίχως, ενώ η γωνία που σχηματίζει το διάνυσμα d**s** με τον X_s-άξονα δεν ισούται κατ' ανάγκη με $2\alpha_{d\sigma'1}$. Με βάση τη σύμβαση που υιοθετήθηκε η γωνία $\alpha_{\sigma'1}$ μεταβάλλεται από την τιμή 0^o στην τιμή $+45^o$ στην τιμή $\pm 90^o$ στην τιμή -45^o και πάλι στην τιμή 0^o όταν το διάνυσμα **σ** στρέφεται αντίθετα από την φορά κίνησης των δεικτών του ρολογιού, δείχνοντας προς τα θετικά του X_s-άξονα όταν $\alpha_{\sigma'1} = 0^o$ και προς τα θετικά του Y_s-άξονα όταν $\alpha_{\sigma'1} = +45^o$· η ίδια σύμβαση χρησιμοποιείται για τις γωνίες $\alpha_{d\sigma'1}$ και $\alpha_{d\varepsilon1}$. Εναλλακτικά, η γωνία $\alpha^*_{\sigma'1}$ (ή $\alpha^*_{d\sigma'1}$ ή $\alpha^*_{d\varepsilon1}$) μεταβάλλεται από την τιμή 0^o στην τιμή $+45^o$ στην τιμή $+90^o$ στην τιμή $+135^o$ και τέλος στην τιμή $+180^o$ / 0^o όταν το διάνυσμα **σ** (ή d**σ** ή d**ε**) στρέφεται αντίθετα από την φορά κίνησης των δεικτών του ρολογιού ξεκινώντας από τον X_s-άξονα. Η δεύτερη σύμβαση χρησιμοποιείται για τον προσδιορισμό της γωνίας μη ομοαξονικότητας (non-coaxiality angle), $\xi = \alpha^*_{d\varepsilon1} - \alpha^*_{\sigma'1}$, η οποία υποδεικνύει την απόκλιση της κύριας κατεύθυνσης της προσαυξητικής παραμορφώσεως από την κύρια κατεύθυνση τάσεως. Σημειώνεται ότι στην παρούσα εργασία χρησιμοποιήθηκαν οι ελαστοπλαστικές παραμορφώσεις για τον προσδιορισμό του ξ με την παραδοχή ότι οι ορθές παραμορφώσεις $\varepsilon_{\theta\theta}$ και ε_{rr} είναι ίσες.

Το Σχήμα 9 δείχνει την επιφάνεια αστάθειας, IS, της χαλαρής άμμου και τα περιγράμματα ίσων τιμών γ_{oct} και Δu / p'_{in} κατά τη συστολική φάση απόκρισης στο Y – X επίπεδο, όπως προσδιορίστηκαν από τα δεδομένα των δοκιμών ακτινικής φόρτισης εμποδιζόμενης στράγγισης. Η επιφάνεια αστάθειας και τα περιγράμματα είναι ελλείψεις (ή τμήματα ελλείψεων) συμμετρικές ως προς τον X-άξονα, των οποίων ο μικρός άξονας είναι παράλληλος προς τον Y-άξονα σε θέση με X > 0. Επομένως, η εκκίνηση της αστάθειας και η ανάπτυξη μίας δεδομένης τιμής της παραμέτρου Δu / p'_{in} ή γ_{oct} αντιστοιχεί σε μικρότερο λόγο τάσεων, sin φ, όταν η γωνία α ($\alpha_{\sigma'1}$) αυξάνεται, υποδεικνύοντας την επίδραση της εγγενούς ανισοτροπίας στην παραμορφωσιμότητα της άμμου. Η επιφάνεια αστάθειας και το περίγραμμα Δu / p'_{in} = 0.60 είναι «ανοικτά» στο ένα άκρο διότι η άμμος αναπτύσσει Δu / p'_{in} < 0.60 και παραμένει ευσταθής όταν η κατεύθυνση του σ'_1-άξονα είναι κοντά στην κατακόρυφο. Στο Σχήμα 9 απεικονίζονται, επίσης, και τα διανύσματα d$\boldsymbol{\varepsilon}$ στα σημεία αστάθειας τα οποία αποκλίνουν από την κατεύθυνση της κύριας τάσης (ακτινική κατεύθυνση) και κλίνουν προς την κατεύθυνση του Y-άξονα. Δεδομένου ότι η κύρια κατεύθυνση προσαυξητικής παραμόρφωσης $\alpha_{d\varepsilon1}$ = ±45° ($\alpha^*_{d\varepsilon1}$ = +45° ή +135°) αντιστοιχεί σε παραμόρφωση τύπου απλής διάτμησης (simple-shear deformation mode) συνάγεται ότι η ύπαρξη οριζόντιων επιπέδων διαστρωμάτωσης πιθανώς να προάγει την παραμόρφωση αυτού του τύπου λόγω της κινηματικής διευκόλυνσης της ολίσθησης στα επίπεδα διαστρωμάτωσης (Miura et al. 1986, Triantafyllos et al. 2020a).

Για τη μελέτη της επίδρασης της ιστορίας στερεοποίησης και φόρτισης στη μηχανική συμπεριφορά της άμμου παρασκευάστηκαν χαλαρά δοκίμια με τη μέθοδο απόθεσης σε νερό, τα οποία στερεοποιήθηκαν ανισότροπα (άμμος AC) σε μέση ενεργό τάση, p'_c = 200 kPa (ή 100 kPa), και σε διάφορους λόγους τάσεων στερεοποίησης, K_c = σ'_{3c} / σ'_{1c} (ο δείκτης c σημαίνει «στην κατάσταση στερεοποίησης»), μέχρι την τιμή K_c = 0.40 που αντιστοιχεί πρακτικά σε συνθήκες K_o-στερεοποίησης για τη χαλαρή άμμο. Στη δεύτερη φάση στερεοποίησης μεταβλήθηκε η τιμή της παραμέτρου b από 0 σε 0.5 και της τάσεως p' από p'_c σε p'_{in} (> p'_c) και στη συνέχεια επιβλήθηκε μονοτονική φόρτιση εμποδιζόμενης στράγγισης με στροφή των κύριων αξόνων τάσεως και σταθερές p και b (= 0.5) παραμέτρους. Στις δοκιμές τύπου B (B-series tests) η αποκλίνουσα τάση, q, αυξάνεται μονότονα ενώ ταυτόχρονα στρέφονται οι κύριοι άξονες τάσεως. Στις δοκιμές τύπου C (C-series tests) η αποκλίνουσα τάση, q, διατηρείται σταθερή ενώ στρέφονται οι κύριοι άξονες τάσεως προκαλώντας την ανάπτυξη υπερπίεσης του ύδατος πόρων και, επομένως, την αύξηση του αποκλίνοντος λόγου τάσεων, η = q / p', καθώς οι ενεργές τάσεις αποφορτίζονται ισότροπα (dσ'_1 = dσ'_2 = dσ'_3 = -du < 0) (Symes et al. 1984, Nakata et al. 1998, Sivathayalan and Vaid 2002, Yang et al. 2007, Triantafyllos et al. 2020a). Αξίζει να σημειωθεί ότι στις δοκιμές τύπου B η γωνία της κύριας κατεύθυνσης τάσης, $\alpha_{\sigma'1}$, δεν μπορεί να μεταβληθεί πέραν της τιμής +45° δεδομένου ότι η γωνία της κύριας κατεύθυνσης προσαυξητικής τάσης, $\alpha_{d\sigma'1}$, είναι σταθερή και ίση με +45° (υπό ευσταθείς συνθήκες), ενώ στις δοκιμές τύπου C είναι δυνατόν να εκτελεστούν πολλαπλοί κύκλοι μονότονης στροφής των κύριων αξόνων τάσεως.

Τα Σχήματα 10a και b δείχνουν τις τασικές οδεύσεις στο $q_d – p'$ και $Y – X$ επίπεδο, αντιστοίχως, από τις δοκιμές τύπου B και C* (C* είναι οι δοκιμές τύπου C κατά τις οποίες η αστάθεια προκλήθηκε κατά το πρώτο μισό του πρώτου κύκλου στροφής των κύριων αξόνων τάσεως). Στο Σχήμα 10a οι διακεκομμένες ευθείες γραμμές που διέρχονται από την αρχή των αξόνων είναι οι γραμμές αστάθειας του Lade για τη χαλαρή ισότροπα στερεοποιημένη άμμο όπως προσδιορίστηκαν στις δοκιμές τύπου A. Η τιμή της γωνίας $\alpha_{\sigma'1}$ υποδεικνύεται με ετικέτες σε ορισμένα τασικά σημεία (κοίλοι κύκλοι) συμπεριλαμβανομένων των σημείων αστάθειας (συμπαγείς κύκλοι). Η διακεκομμένη καμπύλη γραμμή αποτελεί μία εκτίμηση της τασικής όδευσης C2 κατά την ασταθή φάση απόκρισης, για την οποία τα καταγεγραμμένα δεδομένα είναι ανεπαρκή λόγω χρήσης χαμηλής συχνότητας καταγραφής σε αυτήν τη δοκιμή. Στο Σχήμα 10b απεικονίζονται η επιφάνεια αστάθειας για $Y \geq 0$ και τα σημεία αστάθειας, ενώ τα μοναδιαία διανύσματα $\mathrm{d}\boldsymbol{\varepsilon}$ υποδεικνύουν την κύρια κατεύθυνση της προσαυξητικής παραμόρφωσης στα σημεία αστάθειας.

Τα αποτελέσματα που παρουσιάζονται στα Σχήματα 10a και b και η ανάλυση των παραμορφώσεων υποδεικνύουν ότι στις δοκιμές τύπου B η ανάπτυξη μίας συγκεκριμένης τιμής παραμόρφωσης, γ_{oct}, και η πρόκληση αστάθειας απαιτεί μικρότερη αύξηση της γωνίας $\Delta\alpha_{\sigma'1}$ και της τάσης, q_d, όταν η τιμή του K_c μειώνεται· η παράμετρος $\Delta\alpha_{\sigma'1}$ εκφράζει τη μονότονη αύξηση της γωνίας της κύριας κατεύθυνσης τάσεως. Τα αποτελέσματα αυτά υποδηλώνουν την τρωτότητα της χαλαρής AC άμμου έναντι ρευστοποίησης που προκαλείται από μικρές διαταραχές στο μέγεθος και την κατεύθυνση των κύριων τάσεων όταν η στατική διατμητική τάση είναι υψηλή, για παράδειγμα σε συνθήκες K_o-στερεοποίησης (Sivathayalan and Vaid 2002, Georgiannou and Konstadinou 2014, Georgiannou et al. 2018, Triantafyllos et al. 2020a). Από την άλλη πλευρά, όταν η στατική διατμητική τάση είναι μικρή η γωνία $\alpha_{\sigma'1}$ στο σημείο αστάθειας μεγαλώνει και η αντοχή, q_d, στο σημείο αστάθειας και στο σημείο αλλαγής φάσης μικραίνει. Σημειώνεται ότι η ανισότροπη στερεοποίηση ενισχύει την ανισοτροπία που δημιουργείται κατά την απόθεση της άμμου (Hu et al. 2010) και αυτή η αλλαγή εντοπίζεται μακροσκοπικά στη διόγκωση της Τοπικής Οριακής Επιφάνειας γύρω από το σημείο στερεοποίησης στον $q_d – p' – a$ χώρο (Shibuya et al. 2003b). Επομένως, οι τασικές οδεύσεις από τις δοκιμές τύπου B αποτελούν ίχνη πάνω σε διαφορετικές Τοπικές Οριακές Επιφάνειας ανάλογα με την τιμή του λόγου K_c. Παρομοίως, στις δοκιμές τύπου C η ανάπτυξη συγκεκριμένης τιμής παραμόρφωσης, γ_{oct}, και η πρόκληση αστάθειας απαιτεί μικρότερη αύξηση της γωνίας $\Delta\alpha_{\sigma'1}$ όταν η τιμή του K_c μειώνεται. Επίσης, για μία δεδομένη τιμή του λόγου K_c η μονότονη στροφή $\Delta\alpha_{\sigma'1}$ μέχρι την εκκίνηση της αστάθειας είναι μεγαλύτερη στις δοκιμές τύπου C σε σύγκριση με τις δοκιμές τύπου B.

Το Σχήμα 10b δείχνει ότι στις δοκιμές φόρτισης τύπου B και C*, στις οποίες επιβάλλεται στροφή των κύριων αξόνων τάσεως, η αστάθεια της χαλαρής AC άμμου συμβαίνει όταν η τασική όδευση διασχίζει την επιφάνεια αστάθειας, IS, που έχει οριστεί από τις δοκιμές ακτινικής φόρτισης σε χαλαρή IC άμμο. Αυτά τα αποτελέσματα υποδεικνύουν ότι η γωνία διατμητικής αντίστασης, φ, στο σημείο αστάθειας εξαρτάται μόνο από την τιμή της γωνίας της κύριας κατεύθυνσης τάσεως, $\alpha_{\sigma'1}$, ενώ είναι ανεξάρτητη από τον λόγο τάσεων στερεοποίησης, K_c, και την ιστορία φόρτισης που προηγείται της κινητοποιήσεως της κατάστασης ($\alpha_{\sigma'1}$, φ), επιβεβαιώνοντας τα ευρήματα των Nakata et al. (1998), Sivathayalan and Vaid (2002). Το Σχήμα 11a δείχνει τις τασικές οδεύσεις και τα σημεία αστάθειας στο $Y – X$ επίπεδο από τις δοκιμές τύπου A, B και C* σε χαλαρή άμμο στερεοποιημένη σε μέση ενεργό τάση p'_c = 200 kPa, ενώ το Σχήμα 11b δείχνει τα σημεία αστάθειας από τις ίδιες δοκιμές στο $\varphi – \alpha_{\sigma'1}$ επίπεδο. Παρόμοια συμπεριφορά άμμου παρατηρήθηκε σε δοκιμές φόρτισης τύπου A και B με μέση ενεργό τάση στερεοποίησης p'_c = 100 kPa, δηλαδή η αστάθεια συνέβη όταν η τασική όδευση διέσχισε την επιφάνεια αστάθειας, IS. Μολαταύτα, θα πρέπει να σημειωθεί ότι όλες οι τασικές οδεύσεις στο Σχήμα 11a διασχίζουν την επιφάνεια αστάθειας υπό μία μεγάλη γωνία. Θεωρητικά, το έργο δευτέρας τάξεως, d^2W (Hill 1958), πρέπει αναγκαστικά να μηδενιστεί για να συμβεί αστάθεια και επειδή αυτή η ποσότητα εξαρτάται από την κατεύθυνση προσαυξητικής τάσης και την ιστορία φόρτισης (Darve et al. 1995) είναι πιθανόν η ευστάθεια να διατηρηθεί εάν η επιφάνεια αστάθειας διασχισθεί υπό διαφορετικές κατευθύνσεις.

Αξίζει να σημειωθεί ότι ορισμένες από τις τασικές οδεύσεις στο $Y – X$ επίπεδο του Σχήματος 11a παρουσιάζουν ένα διακριτό χαρακτηριστικό μετά το σημείο αστάθειας που υποδεικνύει ότι συμβαίνει στροφή των κύριων αξόνων τάσεως είτε προς την κατεύθυνση $\alpha_{\sigma'1} = 0^o$ είτε προς την κατεύθυνση $\alpha_{\sigma'1} = 90^o$ διότι η τάση Y_s αποφορτίζεται μη αναλογικά ως προς την τάση X_s. Αυτή η αυθόρμητη (ανεξέλεγκτη) συμπεριφορά, η οποία παρατηρείται και στις δοκιμές ακτινικής φόρτισης, αποτελεί ένα τυπικό παράδειγμα διακλάδωσης αφού η τασική όδευση ακολουθεί μία απρόβλεπτη, μη μοναδική πορεία που εξαρτάται από τις ατέλειες του συστήματος συσκευή φόρτισης – δοκίμιο (Chu and Leong 2001, Desrues and Georgopoulos 2006). Οι Triantafyllos et al. (2020a) πρότειναν ότι η εγγενής ανισοτροπία, μεταξύ άλλων παραγόντων, επηρεάζει τη διακλάδωση της συμπεριφοράς του συστήματος δεδομένου ότι τα χαρακτηριστικά διακλάδωσης είναι περισσότερο ευδιάκριτα όταν η αστάθεια συμβαίνει σε συνδυασμούς τάσεων με $22.5^o \leq \alpha_{\sigma'1} \leq 35^o$ ή με $60^o \leq \alpha_{\sigma'1} \leq 75^o$, δηλαδή είτε όταν ένα από τα επίπεδα οιονεί αστοχίας τείνει να προσανατολιστεί με το οριζόντιο επίπεδο διαστρωμάτωσης ή όταν η ολίσθηση στο οριζόντιο επίπεδο είναι ο κυρίαρχος μηχανισμός παραμόρφωσης (δηλ. όταν $\alpha_{d\varepsilon 1} = +45^o$, βλ. και Σχήμα 10b). Επίσης, παρατηρήθηκε ότι οι τασικές οδεύσεις μετά τη διακλάδωση ακολουθούν παρόμοιες διαδρομές ανεξαρτήτως της προηγούμενης ιστορίας φόρτισης (π.χ. βλ. τις τασικές οδεύσεις A4, A6, B1, B4, C1) και αυτή η συμπεριφορά συνδέεται συχνά με την κίνηση του σημείου τάσεων πάνω σε κάποια οριακή επιφάνεια που περιγράφει την καταστατική συμπεριφορά του αμμώδους υλικού (Roscoe et al. 1958, Symes et al. 1984).

Τα Σχήματα 12a και b δείχνουν τις τασικές οδεύσεις στο $q_d – p'$ και $Y – X$ επίπεδο, αντιστοίχως, από τις δοκιμές τύπου C, στις οποίες η αστάθεια συνέβη μετά την ολοκλήρωση του πρώτου κύκλου στροφής των κυρίων αξόνων τάσεως. Αυτό επετεύχθη επιλέγοντας υψηλότερες τιμές του λόγου τάσεων στερεοποίησης, K_c, οι οποίες, ωστόσο, αντιστοιχούν σε στατική τάση, q_d, μεγαλύτερη από την ελάχιστη αντοχή της ισότροπα στερεοποιημένης άμμου για $α_{σ'1} \geq 45^o$. Δεδομένου ότι ο ρυθμός ανάπτυξης της υπερπίεσης του ύδατος πόρων υπό ευσταθείς συνθήκες μειώνεται μετά τον πρώτο κύκλο στροφής των κυρίων αξόνων τάσεως (Ishihara and Towhata 1983, Nakata et al. 1998, Yang et al. 2007) η τασική όδευση από τις δοκιμές τύπου C διασχίζει την επιφάνεια αστάθειας υπό μικρή γωνία. Όπως φαίνεται στο Σχήμα 12b η ευστάθεια διατηρείται όταν η επιφάνεια αστάθειας διασχίζεται υπό μικρή γωνία (σχεδόν εφαπτομενικά) ενώ, όπως θα δειχτεί στη συνέχεια, χάνεται όταν η τασική όδευση στο q_d – p' επίπεδο διατέμνει τον φθίνοντα κλάδο της Τοπικής Οριακής Επιφάνειας με φορά προς τα έξω.

Οι ετικέτες που επισυνάπτονται στους κοίλους κύκλους στο Σχήμα 12a υποδεικνύουν την τιμή της γωνίας $α_{σ'1}$ στις αντίστοιχες τασικές καταστάσεις, ενώ οι ετικέτες που επισυνάπτονται στους συμπαγείς ρόμβους υποδεικνύουν την τιμή της γωνίας $α_{σ'1}$ στα σημεία αστάθειας. Στην περίπτωση της τασικής όδευσης C6, ο συμπαγής ρόμβος υποδεικνύει την κατάσταση στην οποία η άμμος αστοχεί στην κορυφαία τιμή q_d / p' (ή q / p') και χάνεται ο έλεγχος του προγράμματος φόρτισης (loss of controllability) (Nova 1994), ενώ η δυναμική αστάθεια που οδηγεί στην παροδική μονότονη ρευστοποίηση (flow instability) συμβαίνει σε μία άλλη κατάσταση κορυφαίας αστοχίας που υποδεικνύεται με ένα τετράγωνο το οποίο έχει ένα σύμβολο x στο κέντρο του· ουσιαστικά, η άμμος ρευστοποιείται αφού προηγουμένως έχει επιβληθεί στροφή των κυρίων αξόνων τάσεως πάνω στην επιφάνεια κορυφαίας αστοχίας.

Η καμπύλη που προσαρμόζεται στους συμπαγείς ρόμβους (σημεία αστάθειας) στο Y – X επίπεδο του Σχήματος 12b ονομάζεται η εξελιγμένη επιφάνεια αστοχίας (evolved instability surface) και είναι ένα τμήμα έλλειψης (με τον κύριο άξονά της να ταυτίζεται με τον X-άξονα και τον δευτερεύοντα άξονα της να είναι παράλληλος στον Y-άξονα σε θέση με $X > 0$) που βρίσκεται μεταξύ της αρχικής επιφάνειας αστάθειας (initial instability surface) και της επιφάνειας κορυφαίας αστοχίας. Τονίζεται ότι είναι δυνατόν να οριστούν διαφορετικές επιφάνειες αστάθειας που αντιστοιχούν σε διαφορετικές ιστορίες φόρτισης και στερούνται εγγενούς αξίας (Darve et al. 1995). Μολαταύτα, η χρησιμότητα αυτών των νοητικών κατασκευασμάτων έγκειται στο γεγονός ότι επισημαίνουν την εξάρτηση της συνθήκης εκκίνησης της αστάθειας από την ιστορία τάσεων – παραμορφώσεων. Επίσης, υποδεικνύουν ότι η συμπεριφορά της άμμου κατά τη φάση της παροδικής μονότονης ρευστοποίησης επηρεάζεται από την εγγύτητα του σημείου αστάθειας προς την επιφάνεια κορυφαίας αστοχίας, πιθανώς εξ αιτίας της εξελισσόμενης ανισοτροπίας (evolving / induced anisotropy).

Η επίδραση της ιστορίας τάσεων στη συνθήκη αστάθειας χαλαρής άμμου επισημαίνεται στο Σχήμα 13 το οποίο δείχνει τη γωνία διατμητικής αντίστασης, $φ$, σε συνάρτηση με τη γωνία κύριας κατεύθυνσης τάσεως, $α_{σ'1}$, στα σημεία αστάθειας και κορυφαίας αστοχίας. Τα σημεία αστάθειας στις δοκιμές τύπου A συμβολίζονται με συμπαγείς (ή κοίλους) κύκλους, στις δοκιμές τύπου B ή C* (C1-2) με συμπαγή τετράγωνα και στις δοκιμές τύπου C (C3-6) με συμπαγείς ρόμβους (ή με το τετράγωνο που έχει το σύμβολο x στο κέντρο του). Τα σημεία κορυφαίας αστοχίας στις δοκιμές όλων των τύπων απεικονίζονται με τα σύμβολα x. Το Σχήμα 13 επίσης δείχνει την αρχική επιφάνεια αστάθειας, την εξελιγμένη επιφάνεια αστάθειας, την επιφάνεια κορυφαίας αστοχίας και την όδευση εξέλιξης των συνδυασμών ($\alpha_{\sigma'1}$, φ) στη δοκιμή C6. Είναι προφανές ότι η τιμή της γωνίας φ_{ip} στο σημείο αστάθειας δεν είναι αποκλειστική συνάρτηση της γωνίας $\alpha_{\sigma'1}$ αλλά εξαρτάται, επίσης, και από την ιστορία φόρτισης. Για παράδειγμα, η γωνία φ_{ip} είναι ίση με 20.0^o, 25.6^o ή 39.1^o στις δοκιμές A13, C3 και C6, αντιστοίχως, ενώ η γωνία $\alpha_{\sigma'1}$ είναι περίπου ίση με 60^o. Επίσης, η όδευση εξέλιξης των συνδυασμών ($\alpha_{\sigma'1}$, φ) στη δοκιμή C6 διασχίζει ευσταθώς την αρχική επιφάνεια αστάθειας και φτάνει στην επιφάνεια κορυφαίας αστοχίας, πάνω στην οποία κινείται προτού προκληθεί η ασταθής μονότονη ρευστοποίηση. Σημειώνεται ότι το σχήμα της επιφάνειας κορυφαίας αστοχίας υποδεικνύει την επίδραση της εγγενούς ανισοτροπίας στα χαρακτηριστικά αστοχίας.

Η επίδραση της ιστορίας παραμορφώσεων στη συνθήκη αστάθειας και στη συμπεριφορά χαλαρής άμμου κατά τη μονότονη ρευστοποίηση επισημαίνεται στο Σχήμα 14 το οποίο δείχνει την τιμή της κανονικοποιημένης υπερπίεσης του ύδατος πόρων, Δu / p'_{in}, σε συνάρτηση με τη γωνία κατεύθυνσης της κύριας τάσεως, $\alpha_{\sigma'1}$, στα σημεία αστάθειας και αλλαγής φάσης που παρατηρήθηκαν στις δοκιμές τύπου A και C (C3-6)· σε αυτό το σχήμα θεωρείται ότι $\alpha_{pt} \equiv \alpha_{ip}$. Με σκοπό να διαχωριστεί η πλαστική συστολή που συμβαίνει ασταθώς κατά τη μονότονη ρευστοποίηση από αυτήν που συμβαίνει πριν την εκκίνηση της αστάθειας (Borja 2006) και να ποσοτικοποιηθεί έμμεσα η πρώτη ορίστηκε η παράμετρος μονότονης ρευστοποίησης (flow parameter) $U_I = (u_{pt} - u_{ip}) / p'_{in}$. Προσομοιώσεις φόρτισης κοκκωδών υλικών με τη μέθοδο διακριτών στοιχείων (DEM) έχουν δείξει ότι η αποφόρτιση των τάσεων p' και q κατά την ισόχωρη μονοτονική ρευστοποίηση συνδέεται με τη μείωση του αριθμού των σημείων διεπαφής των κόκκων και την αποδυνάμωση των φορτισμένων δομών κόκκων (force chains) (Gong et al. 2012, Guo and Zhao 2013), Η παράμετρος U_I ενδέχεται να εκφράζει μακροσκοπικά αυτήν την αποδόμηση, η οποία εξαρτάται από την ιστορία τάσεων – παραμορφώσεων όπως θα δειχτεί στη συνέχεια.

Το Σχήμα 14 δείχνει ότι στις δοκιμές τύπου A ο λόγος $(\Delta u / p'_{in})_{\mathrm{ip}}$ είναι πρακτικά σταθερός και ίσος με 0.30, ανεξαρτήτως της τιμής της γωνίας $\alpha_{\sigma'1}$, ενώ ο λόγος $(\Delta u / p'_{in})_{\mathrm{pt}}$ είναι ίσος με 0.44 όταν $\alpha_{\sigma'1}$ = 10^o, έπειτα αυξάνεται σε 0.90 – 0.91 όταν η γωνία $\alpha_{\sigma'1}$ λαμβάνει τιμές στο εύρος 60^o – 75^o και τελικά μειώνεται ελαφρώς στην τιμή 0.83 όταν $\alpha_{\sigma'1}$ = 90^o. Αντιθέτως, στις δοκιμές τύπου C (C3-6) ο λόγος $(\Delta u / p'_{in})_{\mathrm{ip}}$ είναι ίσος με 0.68 – 0.69 όταν η γωνία $\alpha_{\sigma'1}$ κυμαίνεται μεταξύ 57.4^o και 64.4^o και μειώνεται σε 0.55 όταν η γωνία $\alpha_{\sigma'1}$ κυμαίνεται μεταξύ 79.6^o και 90.0^o, ενώ ο λόγος $(\Delta u / p'_{in})_{\mathrm{pt}}$ είναι ίσος με 0.85 όταν η γωνία $\alpha_{\sigma'1}$ κυμαίνεται μεταξύ 57.4^o και 90.0^o. Ένα σημαντικό συμπέρασμα είναι ότι η τιμή του λόγου $(\Delta u / p'_{in})_{\mathrm{pt}}$ δεν επηρεάζεται πρακτικώς από την ιστορία φόρτισης (όταν $K_c \geq 0.64$) και εξαρτάται μόνο από την τιμή α_{pt}, ενώ η τιμή της παραμέτρου $U_I = (u_{pt} - u_{ip}) / p'_{in}$ μειώνεται δραστικά στις δοκιμές C3 έως C6. Παρόμοια αποτελέσματα που αφορούν την εξάρτηση του λόγου $(\Delta u / p'_{in})_{\mathrm{pt}}$ από την τιμή της γωνίας α_{pt}, η οποία πιθανώς οφείλεται στην εγγενή ανισοτροπία της άμμου, έχουν αναφερθεί από τους Yoshimine et al. (1998), Yoshimine and Ishihara (1998). Σημειώνεται ότι χαμηλότερες τιμές της παραμέτρου U_I αντιστοιχούν σε υψηλότερες τιμές της παραμέτρου sin φ_{ip} (στις δοκιμές τύπου C), υποδεικνύοντας ότι η συμπεριφορά της άμμου κατά τη μονότονη ρευστοποίηση γίνεται λιγότερο συστολική σε μία δεδομένη κύρια κατεύθυνση τάσεως, $\alpha_{\sigma'1}$, όταν η ρευστοποίηση προκαλείται πιο κοντά στην επιφάνεια κορυφαίας αστοχίας, πιθανώς λόγω της εξελισσόμενης ανισοτροπίας.

Τα Σχήματα 15a και b δείχνουν την τασική όδευση στο q_d – p' και Y – X επίπεδο, αντιστοίχως, από τη δοκιμή C3 χρησιμοποιώντας τους ίδιους συμβολισμούς με αυτούς στο Σχήμα 12. Στο Σχήμα 15a απεικονίζονται, επίσης, οι τασικές οδεύσεις από τις δοκιμές A8 και A13 με σκοπό να αποτυπωθεί η τοπική οριακή επιφάνεια (LBS) της ισότροπα στερεοποιημένης χαλαρής άμμου για $\alpha_{\sigma'1}$ = 45° και 60°. Η τασική όδευση C3 διασχίζει την αρχική επιφάνεια αστάθειας (initial IS) στο σημείο 1 με $\alpha_{\sigma'1}$ = 45° και φ = 22.1° κατά τη διάρκεια του πέμπτου κύκλου φόρτισης, μολαταύτα, η ευστάθεια διατηρείται μέχρι το σημείο όπου ο φθίνων κλάδος της τοπικής οριακής επιφάνειας διατέμνεται μέσα στον ίδιο κύκλο φόρτισης στο σημείο 2 με $\alpha_{\sigma'1}$ = 57.4° και φ = 25.6°. Σημειώνεται ότι η αρχική επιφάνεια αστάθειας διασχίζεται υπό μία μικρή γωνία ενώ η τοπική οριακή επιφάνεια διατέμνεται με φορά προς τα έξω. Επίσης, το ένα από τα επίπεδα οιονεί αστοχίας σχηματίζει γωνία 11° με το οριζόντιο επίπεδο διαστρωμάτωσης στο σημείο 1, ενώ ταυτίζεται με αυτό στο σημείο 2. Αυτά τα αποτελέσματα υποδεικνύουν ότι το σημείο αστάθειας υπό συνθήκες φόρτισης εμποδιζόμενης στράγγισης με συνεχή στροφή των κυρίων αξόνων τάσεως «προσελκύεται» σε συνδυασμούς ($\alpha_{\sigma'1}$, φ) που αντιστοιχούν σε δυσμενείς κινηματικές συνθήκες παραμόρφωσης.

Οι τιμές των παραμέτρων $(\Delta u\ /\ p'_{in})_{\rm pt}$ και $U_I = (u_{pt} - u_{ip})\ /\ p'_{in}$ στη δοκιμή C3 είναι 0.86 και 0.18, αντιστοίχως. Όταν συγκριθούν με τις αντίστοιχες τιμές στη δοκιμή A11, οι οποίες είναι 0.70 και 0.39, μπορεί να συναχθεί ότι το χαλαρότερο δοκίμιο C3 (e = 0.721), το οποίο ρευστοποιήθηκε στην κύρια κατεύθυνση τάσεως α_{ip} = 57.4°, είναι λιγότερο συστολικό κατά τη φάση της μονότονης ρευστοποίησης από το πυκνότερο δοκίμιο A11 (e = 0.699), το οποίο ρευστοποιήθηκε στην κύρια κατεύθυνση τάσεως α_{ip} = 49.5°. Το ίδιο συμπέρασμα συνάγεται και από τη σύγκριση των τιμών της διατμητικής παραμόρφωσης, γ_{oct}, στο σημείο αλλαγής φάσης στις δοκιμές C3 και A11, που είναι 3.9% και 3.5%, αντιστοίχως. Προφανώς, η ιστορία τάσεων - παραμορφώσεων που προηγείται της έναρξης της μονότονης ρευστοποίησης επηρεάζει την μεταγενέστερη συμπεριφορά παρόλο που η τιμή του λόγου $(\Delta u\ /\ p'_{in})_{\rm pt}$ εξαρτάται μόνο από τις παραμέτρους α_{pt} και e (βλ. Σχήμα 14).

Τα ζεύγη σημείων 3 – 4 και 5 – 6 στο Σχήμα 15b υποδεικνύουν την έναρξη και λήξη δύο έντονων γεγονότων ανάπτυξης συγκεντρωμένων παραμορφώσεων τα οποία συνέβησαν σε μεγάλες παραμορφώσεις (σε ονομαστική παραμόρφωση $\gamma_{oct} \approx$ 16% και 18%, αντιστοίχως) και έγιναν αντιληπτά μέσω οπτικής παρατήρησης και ερμηνείας του τρόπου ανάπτυξης των ονομαστικών τάσεων και παραμορφώσεων· ασθενής συγκέντρωση των παραμορφώσεων, με μη ανιχνεύσιμη επίδραση στα μετρούμενα μεγέθη στα σύνορα του δοκιμίου, παρατηρήθηκε για πρώτη φορά στο σημείο H (γ_{oct}

= 8.2%) όταν η αντοχή της άμμου επανακτήθηκε υπό συνθήκες πλαστικής διαστολής μετά το σημείο αλλαγής φάσης. Οι ονομαστικές τιμές των $\alpha_{\sigma'1}$ και φ υποδεικνύουν ότι το ένα από τα επίπεδα οιονεί αστοχίας σχηματίζει γωνία 11° με το οριζόντιο επίπεδο διαστρωμάτωσης στα σημεία 3 και 4, ενώ ταυτίζεται με αυτά στα σημεία 5 και 6. Επομένως, τα σημεία ασταθούς διακλάδωσης με συγκέντρωση των παραμορφώσεων ενδέχεται να «προσελκύονται» σε συνδυασμούς ($\alpha_{\sigma'1}$, φ) που αντιστοιχούν σε δυσμενείς κινηματικές συνθήκες παραμόρφωσης, όπως ακριβώς και τα σημεία ασταθούς διακλάδωσης χωρίς συγκέντρωση των παραμορφώσεων. Όπως είναι αναμενόμενο, η ασταθής διακλάδωση χωρίς συγκέντρωση παραμορφώσεων προηγείται εκείνης με συγκέντρωση παραμορφώσεων κατά την εξέλιξη της μονότονης φόρτισης (Desrues and Viggiani 2004, Nicot and Darve 2011, Lü et al. 2018).

Τα μοναδιαία διανύσματα, d**ε**, στο Σχήμα 15b υποδεικνύουν ότι η κύρια κατεύθυνση της προσαυξητικής παραμόρφωσης βρίσκεται μεταξύ των κύριων κατευθύνσεων της τάσης (διάνυσμα **σ**) και της προσαυξητικής τάσης (διάνυσμα d**σ**) υστερώντας πίσω από τη δεύτερη. Σημειώνεται ότι το διάνυσμα d**σ** είναι κάθετο προς το διάνυσμα **σ** και δεν έχει αναγκαστικά την ίδια κατεύθυνση με το διάνυσμα d**s**. Η ανάλυση των δεδομένων δείχνει ότι η γωνία μη ομοαξονικότητας, $\xi = \alpha^*_{d\varepsilon 1} - \alpha^*_{\sigma'1}$, φθίνει με την αύξηση της γωνίας διατμητικής αντίστασης, φ, καθώς ο ένας κύκλος στροφής των κυρίων αξόνων τάσεως διαδέχεται τον άλλον, όμως επηρεάζεται και από την αλλαγή του προσανατολισμού του σ'_1-άξονα ως προς την κατακόρυφο μέσα σε κάθε κύκλο· το Σχήμα 19 που παρουσιάζεται στη συνέχεια συνοψίζει τα χαρακτηριστικά μη ομοαξονικότητας της άμμου στη δοκιμή C3 καθώς και στις άλλες δοκιμές τύπου B και C. Η μη ομοαξονική συμπεριφορά αλλάζει απότομα στο σημείο αστάθειας μη συγκεντρωμένης παραμόρφωσης (σημείο 2) όπου παρατηρείται ο μηδενισμός της γωνίας ξ καθώς η όδευση ακολουθεί την ακτινική κατεύθυνση κατά τη μονότονη ρευστοποίηση (d**ε** = **σ** = -d**σ**), διότι οι τάσεις Y_s και X_s αποφορτίζονται αναλογικά σε αυτήν τη δοκιμή· υπό αυτές τις συνθήκες ελαχιστοποιείται το κανονικοποιημένο έργο δευτέρας τάξεως, d^2W_{norm} (Πίνακας 1). Μετά την κορυφαία αστοχία της άμμου η τασική όδευση κινείται πάνω στην επιφάνεια αστοχίας ενώ η άμμος παραμορφώνεται υπό πρακτικά σταθερό αποκλίνοντα λόγο τάσεων, η, σταθερή μέση ενεργό τάση, p', και σταθερή γωνία μη ομοαξονικότητας, ξ.

Η σταθερή κατάσταση στην οποία εισέρχεται τελικώς η άμμος μετά την αστοχία δεν αντιστοιχεί στην κρίσιμη κατάσταση, καθώς η τιμή e είναι χαμηλότερη της $e_c(p')$, ενώ διακόπτεται από την εκκίνηση ασταθειών συγκεντρωμένης παραμόρφωσης στα σημεία 3 και 5 (Triantafyllos et al. 2020a). Στα σημεία αυτά η γωνία ξ αυξάνεται απότομα καθώς η κύρια κατεύθυνση προσαυξητικής παραμόρφωσης διακλαδίζεται προς την τιμή $\alpha_{d\varepsilon 1}$ = -45° ($\alpha^*_{d\varepsilon 1}$ = 135°) που αντιστοιχεί σε παραμόρφωση τύπου απλής διάτμησης, η οποία συγκεντρώνεται στο κάτω μισό μέρος του δοκιμίου. Μολαταύτα, οι ομοαξονικές συνθήκες παραμόρφωσης αποκαθίστανται στο τέλος των γεγονότων αστάθειας συγκεντρωμένης παραμόρφωσης, δηλαδή στα σημεία 4 και 6 (Roscoe 1970, Vardoulakis et al. 1978, Zhang and Thornton 2007). Παρομοίως, τα γεγονότα αστάθειας συγκεντρωμένης παραμόρφωσης αποτυπώνονται και στη μετρούμενη (εξωτερικώς) πίεση του ύδατος πόρων η οποία στο αρχικό στάδιο αυξάνεται απότομα, υποδηλώνοντας την ανάπτυξη πλαστικής συστολής μέσα στη ζώνη συγκεντρωμένων παραμορφώσεων πιθανώς λόγω της έντονης μη ομοαξονικότητας, ενώ στο τελικό στάδιο μειώνεται, επειδή η άμμος παραμορφώνεται προς την κρίσιμη κατάσταση (Desrues et al. 1996, Vardoulakis and Georgopoulos 2005).

Τα Σχήματα 16a και b δείχνουν την τασική όδευση στο $q_d - p'$ και $Y - X$ επίπεδο, αντιστοίχως, από τη δοκιμή C6 χρησιμοποιώντας τους ίδιους συμβολισμούς με αυτούς στο Σχήμα 12. Η τασική όδευση κινείται από την κατάσταση στερεοποίησης (σημείο 1 με η = 0.38) στην κατάσταση κορυφαίας αστοχίας (σημείο 3 με η = 1.23) υπό ευσταθείς συνθήκες ενώ οι ενεργές κύριες τάσεις αποφορτίζονται ισότροπα ($d\sigma'_1 = d\sigma'_2 = d\sigma'_3 = -du < 0$), λόγω της ανεξέλεγκτης ανάπτυξης της πίεσης του ύδατος πόρων. Αυτά τα ευρήματα είναι πρωτότυπα διότι, σύμφωνα με σύγχρονα προσομοιώματα καταστρωμένα στα πλαίσια της Θεωρίας Διακλάδωσης, η κατεύθυνση ισότροπης αποφόρτισης περιλαμβάνεται στο σύνολο των ασταθών κατευθύνσεων της χαλαρής άμμου ακόμα και σε χαμηλές τιμές του αποκλίνοντος λόγου τάσεων, μακριά από την κορυφαία αστοχία (Darve and Laouafa 2000, Darve et al. 2004, Sibille at al. 2007, Prunier et al. 2009). Σημειώνεται ότι η αρχική επιφάνεια αστάθειας διατέμνεται σε διαφορετικά σημεία είτε εφαπτομενικά (π.χ. στο σημείο 2) είτε υπό μικρή γωνία, ενώ η τασική όδευση κινείται συνεχώς κάτω από την τοπική οριακή επιφάνεια μέχρι να φτάσει στη γραμμή κορυφαίας αστοχίας, στο σημείο 3. Σε αυτό το σημείο η τιμή της στατικής τάσης q_d είναι μικρότερη από την ελάχιστη αντοχή της άμμου που αντιστοιχεί στην τρέχουσα τιμή της γωνίας $\alpha_{\sigma'1}$ (= 30.2°) και ως εκ τούτου δεν προκαλείται μονότονη ρευστοποίηση (Poulos et al. 1985).

Στο σημείο 3 (γ_{oct} = 1.7%) η πίεση του ύδατος πόρων αρχίζει να μειώνεται ελαφρώς υποδεικνύοντας ότι συμβαίνει ήπια πλαστική διαστολή η οποία οδηγεί σε χαλάρωση (softening) υπό συνθήκες μη συγκεντρωμένης παραμόρφωσης διότι το τασικό σημείο κινείται υποχρεωτικά στην επιφάνεια κορυφαίας αστοχίας, της οποίας το σχήμα επηρεάζεται από την εγγενή ανισοτροπία της άμμου (βλ. Σχήμα 13 και την αναφορά Symes et al. 1984). Ταυτόχρονα, η τάση q_d αρχίζει να μειώνεται εν μέρει λόγω των τάσεων που αναπτύσσονται στις μεμβράνες που περιβάλλουν το δοκίμιο και εν μέρει λόγω της απόκρισης της άμμου (διότι το τασικό σημείο οφείλει να παραμείνει πάνω στην τοπική οριακή επιφάνεια που κατέρχεται) και, επομένως, ο έλεγχος του προγράμματος φόρτισης χάνεται. Η απώλεια του ελέγχου του προγράμματος φόρτισης υπό οιονεί στατικές συνθήκες υποδηλώνει την εκκίνηση μίας αστάθειας μη συγκεντρωμένης παραμόρφωσης η οποία αντιστοιχεί σε αυξανόμενες ενεργές κύριες τάσεις ($d\sigma'_1$, $d\sigma'_2$, $d\sigma'_3 \geq 0$) και μειούμενο αποκλίνοντα λόγο τάσεων ($d\eta < 0$), χωρίς την πρόκληση μονότονης ρευστοποίησης, επιβεβαιώνοντας για πρώτη φορά με φυσικό πείραμα τις προβλέψεις των προσομοιωμάτων του Darve (Darve and Laouafa 2000, Darve et al. 2004, Sibille at al. 2007, Prunier et al. 2009). Έπειτα, η πίεση του ύδατος πόρων αρχίζει να αυξάνεται ξανά και στο σημείο 4 προκαλείται δυναμική αστάθεια που οδηγεί σε μονότονη ρευστοποίηση.

Στο σημείο 4 η γωνία $\alpha_{\sigma'1}$ είναι 64.4°, η γωνία φ είναι 39.1° και η παραμόρφωση γ_{oct} ≈ 6.6% (η ακριβής τιμή του γ_{oct} είναι άγνωστη διότι το όργανο μέτρησης της γωνίας στρέψης βγήκε εκτός ορίων λειτουργίας ακριβώς πριν από το σημείο 4). Από μία φαινομενολογική σκοπιά η μονότονη ρευστοποίηση συνέβη όταν κατά τη στροφή των κυρίων αξόνων τάσεως η τοπική οριακή επιφάνεια βρέθηκε κάτω από το τασικό σημείο και η ελάχιστη αντοχή της άμμου έγινε μικρότερη από την τρέχουσα τιμή της στατικής διατμητικής τάσης (βλ. Σχήμα 16a). Από μία μικροσκοπική σκοπιά η μονότονη ρευστοποίηση συνέβη όταν ένα από τα επίπεδα οιονεί αστοχίας έγινε οριζόντιο, υποδεικνύοντας ότι οι ασταθείς διακλαδώσεις υπό φόρτιση εμποδιζόμενης στράγγισης με στροφή των κυρίων αξόνων τάσεως συμβαίνουν επιλεκτικά σε τασικούς συνδυασμούς που αντιστοιχούν σε δυσμενείς κινηματικές συνθήκες παραμόρφωσης, δηλαδή σε ολίσθηση / διάτμηση πάνω στα επίπεδα διαστρωμάτωσης της άμμου.

Όσον αφορά την παραμόρφωση της άμμου στη δοκιμή C6 πριν την εκκίνηση της αστάθειας μονότονης ρευστοποίησης παρατηρήθηκαν παρόμοια χαρακτηριστικά μη ομοαξονικότητας όπως αυτά στη δοκιμή C3. Συγκεκριμένα, η γωνία μη ομοαξονικότητας, ξ, μειώνεται με την αύξηση του φ, όμως, μέσα στον κύκλο φόρτισης υπάρχει η περιοχή του $\alpha_{\sigma'1}$ από -45° έως -22.5°, που αντιστοιχεί σε αποφόρτιση της τάσεως $\tau_{z\theta}$, στην οποία το ξ λαμβάνει υψηλές τιμές, που μειώνονται και αυτές με την αύξηση της γωνίας φ. Αυτή η συμπεριφορά διερευνήθηκε περεταίρω για να εξακριβωθεί εάν σχετίζεται με τη σύζευξη των ελαστικών και πλαστικών χαρακτηριστικών παραμόρφωσης της άμμου (elastic – plastic coupling) (Tatsuoka and Ishihara 1974, Hueckel 1976, Dafalias 1977). Η άμμος παραμορφώνεται μετά το σημείο 3 σε μία σταθερή κατάσταση που χαρακτηρίζεται από μικρές αλλαγές στον αποκλίνοντα λόγο τάσεων, η, στη μέση ενεργό τάση, p', και στη γωνία μη ομοαξονικότητας, ξ, η οποία, όμως, διακόπτεται από την εκκίνηση της αστάθειας μονότονης ρευστοποίησης στο σημείο 4. Το Σχήμα 19 που παρουσιάζεται στη συνέχεια συνοψίζει τα χαρακτηριστικά μη ομοαξονικότητας της άμμου στη δοκιμή C3 καθώς και στις άλλες δοκιμές τύπου B και C.

Η τασική όδευση D1 με τα χαρακτηριστικά που φαίνονται στο Σχήμα 17 είναι κατάλληλη να χρησιμοποιηθεί για να επιβεβαιωθεί, πρώτον, ότι η κατεύθυνση διάτμησης της αρχικής επιφάνειας αστάθειας στο Y – X επίπεδο και της τοπικής οριακής επιφάνειας στο q_d – p' επίπεδο επηρεάζει τη συνθήκη αστάθειας της χαλαρής άμμου και, δεύτερον, ότι η αποφόρτιση της μη διαγώνιας συνιστώσας, $\tau_{z\theta}$, του τανυστή τάσεως επηρεάζει τη μη ομοαξονική συμπεριφορά της άμμου σε ένα φαινόμενο ελαστικής – πλαστικής σύζευξης. Η μονότονη στροφή των κύριων αξόνων τάσεως πραγματοποιείται στη δοκιμή D1 με συχνότητα $f = 10^{-3}$ Hz ενώ η μέση ολική τάση, p, διατηρείται πρακτικώς σταθερή, η παράμετρος ενδιάμεσης κύριας τάσης, b, ταλαντώνεται μεταξύ της τιμής 0.40, όταν $\alpha_{\sigma'1}$ = ±90°, και της τιμής 0.52, όταν $\alpha_{\sigma'1}$ = 0°, και οι τάσεις q και q_d μεταβάλλονται περιοδικά με τρόπο που εξασφαλίζει την αποφόρτισή τους όταν η γωνία $α_{σ'1}$ μεταβάλλεται από -35° σε 0° ή από 35° σε 90°, δηλαδή στις περιοχές αποφόρτισης της τάσεως $τ_{zθ}$. Σημειώνεται ότι οι τάσεις q και q_d αποφορτίζονται εντόνως και ελεγχόμενα όταν η γωνία $α_{σ'1}$ μεταβάλλεται από 45° σε 90°, δηλαδή στην περιοχή που συνέβησαν οι αστάθειες στις δοκιμές C3 έως C6 (βλ. Σχήμα 12). Επίσης, παρατηρείται ότι η μικρή μεταβολή του b δεν αναμένεται να μεταβάλλει την τοπική οριακή επιφάνεια της χαλαρής άμμου, ειδικά στην περιοχή «εφελκυσμού» (Lam and Tatsuoka 1988, Shibuya et al. 2003a).

Τα Σχήματα 18a και b δείχνουν την τασική όδευση στο $q_d – p'$ και $Y – X$ επίπεδο, αντιστοίχως, από τη δοκιμή D1 χρησιμοποιώντας τους ίδιους συμβολισμούς με αυτούς στο Σχήμα 12. Τα πειραματικά αποτελέσματα υποδεικνύουν ότι ο μερικός έλεγχος της κατεύθυνσης προσαυξητικής τάσης στο $Y – X$ επίπεδο μέσω της ελεγχόμενης αποφόρτισης της αποκλίνουσας τάσεως, q, καθυστερεί την εκκίνηση της ασταθούς μονότονης ρευστοποίησης. Συγκεκριμένα, όταν η αρχική επιφάνεια αστάθειας και η τοπική οριακή επιφάνεια διατέμνονται σχεδόν ταυτόχρονα στη γειτονιά του σημείου 1, η κατεύθυνση διάτμησης είναι εφαπτόμενη στην πρώτη επιφάνεια και προσανατολισμένη προς το εσωτερικό της δεύτερης, επομένως, δεν προκαλείται αστάθεια. Έπειτα, η τασική όδευση συνεχίζει να κινείται πάνω στην αρχική επιφάνεια αστάθειας και κάτω από την τοπική οριακή επιφάνεια διότι η ελεγχόμενη αποφόρτιση της τάσης q περιορίζει τον ρυθμό ανάπτυξης της υπερπίεσης του ύδατος πόρων.

Είναι ενδιαφέρον να συγκριθούν τα αποτελέσματα από τις δοκιμές D1 και C3 στις οποίες η τασική όδευση διατέμνει την αρχική επιφάνεια αστάθειας περίπου στο ίδιο σημείο στο $Y – X$ επίπεδο. Σε αντίθεση με τη δοκιμή C3, στη δοκιμή D1 η ασταθής μονότονη ρευστοποίηση προκαλείται στο σημείο 2, μακριά από το σημείο 1, όταν ο φθίνων κλάδος της τοπικής οριακής επιφάνειας διατέμνεται με φορά προς τα έξω. Σημειώνεται ότι τα σημεία αστάθειας στις δοκιμές D1 και C3 βρίσκονται κοντά στον $σ'_1 – σ'_2 – σ'_3$ χώρο τάσεων και ότι η όδευση ακολουθεί στα σημεία αυτά την κατεύθυνση ισότροπης αποφόρτισης, όμως οι τιμές της γωνίας $α_{ip}$ είναι διαφορετικές· επίσης, τα σημεία αστάθειας ανήκουν στην ίδια εξελιγμένη επιφάνεια αστάθειας. Η σύγκριση της απόκρισης της άμμου στις δοκιμές D1 και A17 αναδεικνύει την επίδραση της ιστορίας φόρτισης στην παροδική μονότονη ρευστοποίηση: η τιμή των παραμέτρων $(Δu / p'_{in})_{pt}$, $U_I = (u_{pt} – u_{ip}) / p'_{in}$ και $γ_{oct,pt}$ είναι 0.90, 0.23 και 3.3%, και 0.91, 0.59 και 4.5%, αντιστοίχως, υποδεικνύοντας ότι το δοκίμιο D1, με e = 0.738 και $α_{ip}$ = -85.5°, συμπεριφέρεται λιγότερο συστολικά από το δοκίμιο A17, με e = 0.727 και $α_{ip}$ = 79.1°, κατά την παροδική μονότονη ρευστοποίηση λόγω της διαφορετικής ιστορίας τάσεων – παραμορφώσεων.

Η παραμόρφωση της άμμου στη δοκιμή D1 είναι μη ομοαξονική με χαρακτηριστικά παρόμοια εκείνων της άμμου στις δοκιμές C3 και C6 (βλ. Σχήμα 19b στη συνέχεια). Η γωνία $ξ$ μειώνεται, εν γένει, με τη γωνία $φ$, μηδενίζεται απότομα στο σημείο αστάθειας (σημείο 2) και γίνεται αναπάντεχα μικρή στο σημείο 1, διότι η ολίσθηση πάνω στο οριζόντιο επίπεδο διαστρωμάτωσης που είχε ενεργοποιηθεί προγενέστερα εμμένει. Η διαφορά της απόκρισης της άμμου στη δοκιμή D1 σε σύγκριση με τις δοκιμές C3 και C6 έγκειται στο γεγονός ότι η γωνία ξ είναι ιδιαίτερα υψηλή και στις δύο περιοχές αποφόρτισης της τάσης $\tau_{z\theta}$, δηλαδή όταν η γωνία $\alpha_{\sigma'1}$ μεταβάλλεται από -35^o σε 0^o ή από 45^o σε 90^o. Δεδομένου ότι η αποφόρτιση της αποκλίνουσας τάσης, q, οδηγεί στη μείωση του αποκλίνοντος λόγου τάσεων, η, μολονότι η πίεση του ύδατος πόρων, u, αυξάνεται, τα ελαστικά χαρακτηριστικά της άμμου είναι περισσότερο τονισμένα στις φάσεις ταυτόχρονης αποφόρτισης των τάσεων q και $\tau_{z\theta}$. Καθώς ο αριθμός των κύκλων φόρτισης αυξάνεται ο $\tau_{z\theta} - \gamma_{z\theta}$ βρόχος υστέρησης επιδεικνύει μειούμενα μέτρα αποφόρτισης, πιθανώς λόγω των πλαστικών μεταβολών στην εσωτερική δομή που επήλθαν κατά τη φόρτιση, υποδεικνύοντας ότι η εξάρτηση της γωνίας ξ από τη γωνία φ στις φάσεις αποφόρτισης είναι ένα φαινόμενο σύζευξης των ελαστικών και πλαστικών χαρακτηριστικών παραμόρφωσης της άμμου.

Τα Σχήματα 19a και b δείχνουν τη σχέση μεταξύ των γωνιών ξ και φ υπό ευσταθείς συνθήκες στις δοκιμές τύπου C (C1 έως C6) και B, αντιστοίχως, ενώ στο δεύτερο σχήμα συμπεριλαμβάνονται και τα αποτελέσματα από τη δοκιμή D1. Η άμμος στις δοκιμές τύπου C στερεοποιήθηκε ανισότροπα σε μέση ενεργό τάση p'_c = 200 kPa και σε λόγο τάσεων K_c = 0.48 – 0.75, και τα χαλαρά δοκίμια (e = 0.704 – 0731) υποβλήθηκαν σε στροφή των κύριων αξόνων τάσεως διατηρώντας την αποκλίνουσα τάση, q, σταθερή. Σε αυτές τις δοκιμές η γωνία του διανύσματος d**σ** με το διάνυσμα **σ** στον $Y_s - X_s$ χώρο (βλ. Σχήμα 8a) παραμένει σταθερή στις 90^o όσο διατηρείται η ευστάθεια του συστήματος. Η άμμος στις δοκιμές B1, B2 και B3 στερεοποιήθηκε ανισότροπα σε μέση ενεργό τάση p'_c = 200 kPa και σε λόγο τάσεων K_c = 0.80, 0.50 και 0.40, αντιστοίχως, ενώ στη δοκιμή B7 η άμμος στερεοποιήθηκε σε μέση ενεργό τάση p'_c = 100 kPa και σε λόγο τάσεων K_c = 0.40. Τα χαλαρά δοκίμια (e = 0.711 – 0.728) υποβλήθηκαν σε στροφή των κύριων αξόνων τάσεως διατηρώντας την κατεύθυνση του διανύσματος d**σ** σταθερή στις $\alpha_{d\sigma'1}$ = +45^o και αυξάνοντας μονότονα την αποκλίνουσα τάση, q. Στις δοκιμές τύπου B η γωνία μεταξύ των διανυσμάτων d**σ** και **σ** μειώνεται ξεκινώντας από την τιμή 90^o.

Δύο διακριτές καμπύλες, οι οποίες επισημαίνονται με το γράμμα L ή U, απεικονίζουν τη σχέση μεταξύ του ξ και του φ στις δοκιμές τύπου C, ανεξαρτήτως της τιμής του K_c (με εξαίρεση την τιμή K_c = 0.48, στη δοκιμή C1, που θα συζητηθεί στη συνέχεια), του e και του αριθμού των προηγούμενων κύκλων φόρτισης. Η L-καμπύλη, που αντιστοιχεί σε τασικές καταστάσεις με το $\alpha_{\sigma'1}$ εκτός της περιοχής (-45^o , -22.5^o), δείχνει ότι η γωνία ξ μειώνεται μη γραμμικά με τη γωνία φ και τείνει να γίνει σταθερή για $\varphi \geq 35^o$, δηλαδή όταν η άμμος αστοχεί. Η σταθεροποίηση του ξ με το φ σχετίζεται με την επίτευξη της σταθερής κατάστασης χωρίς τάση για μεταβολή του όγκου, όπως παρατηρήθηκε στη δοκιμή C3, ή με τάση για ήπια πλαστική διαστολή, όπως παρατηρήθηκε στις δοκιμές C1 και C6· μολαταύτα, η σταθερή κατάσταση διακόπτεται από την εκκίνηση ασταθειών μη συγκεντρωμένης ή συγκεντρωμένης παραμόρφωσης. Σημειώνεται ότι προσομοιώσεις της στροφής των κύριων αξόνων τάσεως υπό συνθήκες ελεύθερης στράγγισης και σταθερές ενεργές κύριες τιμές τάσεως με χρήση της Μεθόδου Διακριτών Στοιχείων (Discrete Element Method) έχουν δείξει ότι τα κοκκώδη υλικά εισέρχονται τελικώς σε σταθερή κατάσταση με παρόμοια χαρακτηριστικά (Tong et al. 2014, Li et al. 2016, Theocharis et al. 2019). Αντίθετα, η U-καμπύλη, που αντιστοιχεί σε τασικές καταστάσεις με το $\alpha_{\sigma'1}$ εντός της περιοχής (-45° , -22.5°), δείχνει ότι το ξ μειώνεται μη γραμμικά με το φ χωρίς σημάδια σταθεροποίησης, ενώ λαμβάνει σημαντικά μεγαλύτερες τιμές από αυτές που αντιστοιχούν στην L-καμπύλη για $\varphi \leq 25°$. Παρόμοια αποτελέσματα από δοκιμές στροφής των κυρίων αξόνων τάσεως διατηρώντας σταθερές τις ενεργές κύριες τιμές τάσεως έχουν αναφερθεί από τους Tong et al. (2010).

Το Σχήμα 19b δείχνει ότι η σχέση μεταξύ του ξ και του φ στη δοκιμή D1 περιγράφεται από τις ίδιες καμπύλες (L και U) με αυτές στις δοκιμές τύπου C, με μόνη διαφορά το ότι η γωνία ξ είναι ιδιαίτερα υψηλή και στις δύο περιοχές αποφόρτισης της τάσης $\tau_{z\theta}$. Αντιθέτως, στις δοκιμές τύπου B διαφορετικές καμπύλες περιγράφουν τη σχέση του ξ με το φ πριν την κορυφαία αστοχία, με τη γωνία ξ να αυξάνεται για δεδομένη τιμή του φ (ή του η) όταν ο λόγος K_c μειώνεται· μολαταύτα, η εξελισσόμενη τιμή της γωνίας $\alpha_{\sigma'1}$ που αναγράφεται στις ετικέτες πρέπει και αυτή να ληφθεί υπόψη. Η τιμή της μέσης ενεργού τάσης p'_c στις δοκιμές B3 (200 kPa) και B7 (100 kPa) με $K_c = 0.40$ και $e = 0.727 – 0.728$ φαίνεται να μην επηρεάζει την τιμή του ξ πριν την αστοχία. Μετά την αστοχία η τιμή του p'_c έχει μεγαλύτερη επίδραση στη γωνία φ από ότι στη γωνία ξ, ενώ η τιμή του K_c έχει μικρή επίδραση στη γωνία ξ, με τα σημεία (φ , ξ) να βρίσκονται κοντά στην L-καμπύλη που ορίστηκε στις δοκιμές τύπου C. Μολαταύτα, η σταθερή κατάσταση δεν επιτυγχάνεται μετά την αστοχία στις δοκιμές τύπου B διότι συμβαίνει έντονη πλαστική διαστολή και το ξ μειώνεται, ενώ ο ρυθμός στροφής των κύριων αξόνων τάσεως μειώνεται και αυτός, καθώς η κύρια κατεύθυνση τάσεως $\alpha_{\sigma'1} = +45°$ προσεγγίζεται με σταθερή κατεύθυνση προσαυξητικής τάσεως $\alpha_{d\sigma'1} = +45°$.

Αξίζει να σημειωθεί ότι η γωνία ξ πριν την κορυφαία αστοχία στις δοκιμές B3 και B7 είναι μεγαλύτερη από αυτήν που παρατηρείται στη δοκιμή C6 για παρόμοια τιμή των γωνιών φ και $\alpha_{\sigma'1}$, παρά το γεγονός ότι ο ρυθμός στροφής των κύριων αξόνων τάσεως είναι μικρότερος στις πρώτες δοκιμές (βλ. τα σημεία σύγκρισης P, P1 και P2). Στις δοκιμές B3 και B7 ο λόγος τάσεων στερεοποίησης K_c είναι 0.40 (και αντιστοιχεί πρακτικά σε συνθήκες K_o-στερεοποίησης) ενώ στη δοκιμή C6 είναι 0.64. Επιπροσθέτως, η σύγκριση μεταξύ των τιμών του ξ αφορά καταστάσεις στροφής των κύριων αξόνων τάσεως που έπονται της ανισότροπης στερεοποίησης με $\alpha_{\sigma'1} = 0°$ στην περίπτωση των δοκιμών B3 και B7, ενώ στην περίπτωση της δοκιμής C6 έχει ήδη προηγηθεί ένας κύκλος φόρτισης. Αντιθέτως, στη δοκιμή C1 με $K_c = 0.48$ η τιμή του ξ στην αρχική φάση φόρτισης μετά την ανισότροπη στερεοποίηση είναι υψηλότερη από αυτήν που αντιστοιχεί στην L-καμπύλη και υψηλότερη από τις τιμές που παρατηρήθηκαν στις δοκιμές B3 και B7. Σημειώνεται, επίσης, ότι η διατμητική παραμόρφωση, ε_q, που αναπτύσσεται στη φάση της ανισότροπης στερεοποίησης μειώνεται στις δοκιμές B3, B7, C1 και C6 κατά τη σειρά αναγραφής και ότι η ανισότροπη στερεοποίηση περιλαμβάνει μία φάση προ-διάτμησης κατά την οποία ο λόγος η αυξάνεται υπό σταθερή τάση p'.

Τα δεδομένα από τις δοκιμές B3, B7, C1 και C6 υποδεικνύουν ότι η συμπεριφορά της άμμου γίνεται εντόνως μη ομοαξονική όταν οι κύριοι άξονες τάσεως στραφούν ύστερα από μία διαδικασία διάτμησης και παραμόρφωσης με σταθερή κύρια κατεύθυνση τάσεως. Υποδεικνύουν, επίσης, ότι ο ρυθμός στροφής των κύριων αξόνων τάσεως έχει τότε δευτερεύουσα επίδραση στη μη ομοαξονικότητα της άμμου σε σύγκριση με την ένταση της προ-διάτμησης. Επομένως, η πλαστική συστολή λόγω της έντονης μη ομοαξονικότητας σε αυτήν την περίπτωση ενδέχεται να δρα ως αποσταθεροποιητικός παράγοντας και να συσχετίζεται με την τρωτότητα των ανισότροπα στερεοποιημένων άμμων έναντι ρευστοποίησης όταν η στατική διατμητική τάση είναι υψηλή (βλ. Σχήμα 10), όπως για παράδειγμα στην περίπτωση των K_o-στερεοποιημένων εδαφών ή στην περίπτωση εδαφικών πρανών. Συγκεκριμένα, μία μικρή τασική διαταραχή η οποία περιλαμβάνει στροφή των κύριων αξόνων τάσεως (π.χ. η αλλαγή της γεωμετρίας μίας πλαγιάς στο πεδίο) προκαλεί έντονη μη ομοαξονικότητα και πλαστική συστολή που οδηγεί στην αστάθεια μη συγκεντρωμένης παραμόρφωσης με τρόπο ανάλογο ως προς αυτόν που περιγράφηκε από τον καθηγητή Βαρδουλάκη (Vardoulakis et al. 1978, Vardoulakis and Graf 1985, Vardoulakis and Georgopoulos 2005) για την περίπτωση της αστάθειας συγκεντρωμένης παραμόρφωσης.

Πειραματικά αποτελέσματα, μέρος ΙΙΙ: Πρέπει η Θεωρία Κρίσιμης Κατάστασης να αναθεωρηθεί ώστε να περιλαμβάνει την επίδραση της ανισότροπης εσωτερικής δομής;

Για τη διερεύνηση της επίδρασης της ανισότροπης εσωτερικής δομής της άμμου στην κρίσιμη κατάσταση παρασκευάστηκαν χαλαρά δοκίμια τα οποία υποβλήθηκαν σε μονοτονική φόρτιση εμποδιζόμενης στράγγισης με σταθερή κύρια κατεύθυνση τάσεως (ακτινική φόρτιση). Η μονοτονική φόρτιση εμποδιζόμενης στράγγισης τερματίστηκε στις διάφορες δοκιμές σε τασικές καταστάσεις μετά την κορυφαία αστοχία και όσο το δυνατόν πλησιέστερα στην κρίσιμη κατάσταση. Έπειτα, οι συνθήκες στράγγισης άλλαξαν με σπουδή ώστε να μην προκληθεί μεταβολή στις ενεργές τάσεις τη στιγμή της αλλαγής και να εξασφαλιστεί στην επόμενη φάση στροφής των κύριων αξόνων (ΚΑ) τάσεως ο έλεγχος των ενεργών κύριων τιμών (ΚΤ) τάσεως και η ελεύθερη στράγγιση του δοκιμίου. Η στροφή των ΚΑ τάσεως εκτελέστηκε διατηρώντας σταθερές τις ενεργές ΚΤ τάσεως σύμφωνα με το «πείραμα σκέψης» του καθηγητή Δαφαλιά (Dafalias 2016). Εκτελέστηκε, επίσης, στροφή των ΚΑ τάσεως με σταθερές ενεργές ΚΤ τάσεως μετά την ανισότροπη στερεοποίηση της άμμου, χωρίς να προηγηθεί φόρτιση.

Τα Σχήματα 20a και b δείχνουν την όδευση τάσεων και παραμορφώσεων, αντιστοίχως, από τη δοκιμή PAR1 στο εκτροπικό επίπεδο τάσεων και παραμορφώσεων, αντιστοίχως. Το δοκίμιο σε αυτήν τη δοκιμή στερεοποιήθηκε ανισότροπα σε η = 1.01 (K_c = 0.40, που αντιστοιχεί πρακτικά σε συνθήκες K_o-στερεοποίησης) και p'_c = 100 kPa και υποβλήθηκε σε έναν πλήρη κύκλο στροφής των κύριων αξόνων τάσεως με σταθερές τιμές p' = 100 kPa, η = 1.01 και b = 0, χωρίς να προηγηθεί φόρτιση. Το Σχήμα 20a δείχνει ότι η παραμόρφωση της άμμου είναι εντόνως μη ομοαξονική αφού η κύρια κατεύθυνση της προσαυξητικής παραμόρφωσης (διάνυσμα d**ε**) βρίσκεται μεταξύ των κύριων κατευθύνσεων της τάσης (διάνυσμα **σ**) και της προσαυξητικής τάσης (διάνυσμα d**σ**) υστερώντας πίσω από τη δεύτερη. Η όδευση παραμορφώσεως στο Σχήμα 20b υποδεικνύει ότι η πλαστική παραμορφωσιμότητα της άμμου επηρεάζεται έντονα από την εγγενή και εξελισσόμενη ανισοτροπία της εσωτερικής δομής: Το θετικό και αρνητικό μέγιστο του X_ε είναι 0.08% και -1.06%, αντιστοίχως, με το αρνητικό μέγιστο να αναπτύσσεται μετά την κατάσταση που αντιστοιχεί σε $\alpha_{\sigma'1}$ = 90°, ενώ το θετικό και αρνητικό μέγιστο του Y_ε είναι 0.93% και -1.14%, αντιστοίχως. Η επίδραση της εγγενούς ανισοτροπίας υποδηλώνεται από το γεγονός ότι το ακτινικό διάνυσμα στο τέλος του κύκλου φόρτισης (το οποίο δείχνει την παραμένουσα παραμόρφωση) έχει προσανατολισμό $\alpha^*_{d\varepsilon1}$ = 135° και το κέντρο της ανοικτής ελλειπτικής τροχιάς παραμορφώσεων βρίσκεται σε θέση με $X_\varepsilon < 0$.

Το Σχήμα 21a δείχνει την εξέλιξη των μεγεθών ε_{vol}, σ'_1, σ'_2 και σ'_3 με τη γωνία $\alpha^*_{\sigma'1}$ ενώ το Σχήμα 21b δείχνει την εξέλιξη των γωνιών $\alpha^*_{d\varepsilon1}$ και $\alpha^*_{d\sigma'1}$ με τη γωνία $\alpha^*_{\sigma'1}$. Οι διακεκομμένες γραμμές στο Σχήμα 21b αντιστοιχούν στη συνθήκη ομοαξονικής παραμόρφωσης, $\alpha^*_{d\varepsilon1} = \alpha^*_{\sigma'1}$, και οι ετικέτες N απαριθμούν το πλήθος των ολοκληρωμένων κύκλων στροφής των ΚΑ τάσεως. Όπως φαίνεται στο Σχήμα 21a, κατά τη διάρκεια του πρώτου κύκλου στροφής των ΚΑ τάσεως συσσωρεύεται προοδευτικά συστολική ογκομετρική παραμόρφωση παρά το γεγονός ότι οι ενεργές ΚΤ τάσεως διατηρούνται πρακτικώς σταθερές. Η κλίση $d\varepsilon_{vol} / d\alpha^*_{\sigma'1}$ είναι πολύ μικρή όταν η γωνία $\alpha^*_{\sigma'1}$ αυξάνεται από 0° σε 22.5°, έπειτα αυξάνεται και λαμβάνει τη μέγιστη τιμή της όταν $\alpha^*_{\sigma'1}$ = 114° ($\alpha_{\sigma'1}$ = -66°), όπως υποδεικνύεται με τη διακεκομμένη εφαπτόμενη γραμμή, και τελικά μειώνεται μετά από αυτό το σημείο. Το Σχήμα 21b δείχνει ότι η γωνία μη ομοαξονικότητας, $\xi = \alpha^*_{d\varepsilon1} - \alpha^*_{\sigma'1}$, μεταβάλλεται μέσα στον κύκλο φόρτισης, όντας περίπου ίση με 11.5° όταν $\alpha^*_{\sigma'1}$ = 33.5° ($\alpha^*_{d\varepsilon1}$ = 45°), δηλαδή όταν η παραμόρφωση του δοκιμίου αντιστοιχεί σε οιονεί απλή διάτμηση ($d\varepsilon_{zz} = 0$, $d\varepsilon_{\theta\theta} = d\varepsilon_{rr} \rightarrow 0^+$, $d\varepsilon_{z\theta} \neq 0$), και μειώνεται ραγδαία καθώς η γωνία $\alpha^*_{\sigma'1}$ αυξάνεται από 33.5° σε 45° διότι ο μηχανισμός ολίσθησης στα επίπεδα διαστρωμάτωσης εμμένει. Η μέγιστη γωνία ξ = 21° παρατηρείται για $\alpha^*_{\sigma'1}$ = 114° ($\alpha_{d\varepsilon1}$ = 135°) όταν ο ρυθμός $d\varepsilon_{vol} / d\alpha^*_{\sigma'1}$ γίνεται ταυτόχρονα μέγιστος και το δοκίμιο παραμορφώνεται σε οιονεί απλή διάτμηση. Παρατηρείται, επίσης, ότι η γωνία ξ αυξάνεται όταν η τάση $\tau_{z\theta}$ αποφορτίζεται.

Το Σχήμα 22 δείχνει τα αποτελέσματα από τη δοκιμή PAR3: Το Σχήμα 22a δείχνει την τασική όδευση στο $q - p'$ επίπεδο, το Σχήμα 22b δείχνει την εξέλιξη των μεγεθών η, ε_{vol} (αριστερός κατακόρυφος άξονας) και $\Delta u / p'_{in}$ (δεξιός κατακόρυφος άξονας) με την παραμόρφωση ε_q, το Σχήμα 22c δείχνει την τασική όδευση στο $Y_s - X_s$ επίπεδο και το Σχήμα 22d δείχνει την όδευση παραμορφώσεως στο $Y_\varepsilon - X_\varepsilon$ επίπεδο. Το δοκίμιο σε αυτήν τη δοκιμή στερεοποιήθηκε ισότροπα σε μέση ενεργό τάση p'_c = 100 kPa και υποβλήθηκε σε μονοτονική ακτινική φόρτιση εμποδιζόμενης στράγγισης με b = 0.5 και $\alpha_{\sigma'1}$ = 15°. Η μονοτονική ακτινική φόρτιση τερματίστηκε στην τασική κατάσταση μετά την κορυφαία αστοχία με p' = 343 kPa, η =1.05 και ε_q = 7.6%, ενώ η άμμος διαστελλόταν πλαστικά υπό ομοαξονικές συνθήκες παραμόρφωσης και χωρίς εμφανή στον γυμνό οφθαλμό σημάδια συγκεντρωμένης παραμόρφωσης. Στη συνέχεια, εκτελέστηκε στροφή των ΚΑ τάσεως υπό στραγγιζόμενες συνθήκες και διατηρώντας σταθερές τις ενεργές ΚΤ τάσεως. Το Σχήμα 23a δείχνει την εξέλιξη των μεγεθών ε_{vol}, σ'_1, σ'_2 και σ'_3 με τη γωνία $\alpha^*_{\sigma'1}$ κατά τη φάση της στροφής των ΚΑ τάσεως, ενώ το Σχήμα 23b δείχνει την εξέλιξη των γωνιών $\alpha^*_{d\varepsilon 1}$ και $\alpha^*_{d\sigma'1}$ με τη γωνία $\alpha^*_{\sigma'1}$ κατά τη διάρκεια και των δύο φάσεων.

Τα δεδομένα που παρουσιάζονται στα Σχήματα 22 και 23 υποδεικνύουν ότι η παραμόρφωση της άμμου κατά την ακτινική φόρτιση είναι αρχικά μη ομοαξονική όμως γίνεται σταδιακά ομοαξονική στη φάση της πλαστικής διαστολής και χαλάρωσης μετά την κορυφαία αστοχία. Έπειτα, η παραμόρφωση γίνεται ακαριαία μη ομοαξονική και η άμμος αρχίζει να συστέλλεται πλαστικά ακριβώς τη στιγμή που αρχίζει η στροφή των ΚΑ τάσεως με σταθερές τις ενεργές ΚΤ τάσεως. Οι τιμές των μεγεθών $d\varepsilon_{vol}$ / $d\varepsilon_q$ και ξ τη στιγμή εκείνη είναι 0.47 και 27.8^o, αντιστοίχως, καθώς όμως η γωνία $\alpha_{\sigma'1}$ μεταβάλλεται από 15.0^o σε 42.3^o ο λόγος $d\varepsilon_{vol}$ / $d\alpha_{\sigma'1}$ παραμένει πρακτικά σταθερός ενώ η γωνία ξ μειώνεται ραγδαία. Η ανάλυση των δεδομένων υποδεικνύει ότι η άμμος στη δοκιμή PAR3 βρίσκεται κοντά στην κρίσιμη κατάσταση όταν εκκινείται η στροφή των κύριων αξόνων τάσεως και, παρά το γεγονός ότι προηγουμένως παρατηρείται πλαστική διαστολή υπό ομοαξονικές συνθήκες παραμόρφωσης, τη στιγμή εκκίνησης η συμπεριφορά της άμμου γίνεται ακαριαία συστολική και εντόνως μη ομοαξονική.

Το Σχήμα 24 παρουσιάζει τα αποτελέσματα από τις δοκιμές PAR2 και PAR4 μαζί με αυτά από τη δοκιμή PAR3. Συγκεκριμένα, το Σχήμα 24a δείχνει την εξέλιξη των μεγεθών η (αριστερός κατακόρυφος άξονας) και ε_{vol} (δεξιός κατακόρυφος άξονας) με την παραμόρφωση ε_q, το Σχήμα 24b δείχνει την εξέλιξη των μεγεθών ε_{vol} (αριστερός κατακόρυφος άξονας) και ξ (δεξιός κατακόρυφος άξονας) με τη γωνία $\alpha_{\sigma'1}$, το Σχήμα 24c δείχνει τις οδεύσεις παραμόρφωσης στο $Y_\varepsilon - X_\varepsilon$ επίπεδο και το Σχήμα 24d δείχνει την εξέλιξη του συνδυασμού (p' , e) στο καταστατικό επίπεδο μαζί με τη γραμμή κρίσιμης κατάστασης, η οποία θεωρείται μοναδική ανεξαρτήτως του τύπου φόρτισης (Li and Dafalias 2012, Salvatore et al. 2017, Zhou et al. 2017). Στις δοκιμές PAR2-4 η άμμος στερεοποιήθηκε ισότροπα σε μέση ενεργό τάση p'_c = 100 kPa ή 200 kPa, έπειτα υποβλήθηκε σε μονοτονική φόρτιση εμποδιζόμενης στράγγισης με b = 0.5 και $\alpha_{\sigma'1}$ = 15^o και ύστερα σε στροφή των ΚΑ τάσεως με σταθερές τις ενεργές ΚΤ τάσεως, υπό συνθήκες ελεύθερης στράγγισης. Το Σχήμα 24b δείχνει μόνο τα αποτελέσματα από τη φάση στροφής των ΚΑ τάσεως, ενώ τα υπόλοιπα σχήματα και από τις δύο φάσεις. Οι συνθήκες κατά την εκκίνηση της στροφής των ΚΑ τάσεως στις δοκιμές τύπου PAR παρουσιάζονται στον Πίνακα 5. Είναι σημαντικό να σημειωθεί ότι στη δοκιμή PAR4 η εκκίνηση της στροφής των ΚΑ τάσεως έγινε σε μικρότερη διατμητική παραμόρφωση, ε_q, από ότι στη δοκιμή PAR3, ενώ στη δοκιμή PAR2 έγινε σε μεγαλύτερη. Επίσης, σημειώνεται ότι στη δοκιμή PAR2 υπήρχαν εμφανείς ζώνες συγκεντρωμένης παραμόρφωσης στο δοκίμιο όταν ξεκίνησε η στροφή των ΚΑ τάσεως.

Τα αποτελέσματα στο Σχήμα 24 δείχνουν καθαρά ότι η άμμος επιδεικνύει έντονη μη ομοαξονικότητα και πλαστική συστολή όταν η μονοτονική φόρτιση με σταθερούς ΚΑ τάσεως διακοπεί στη φάση της χαλάρωσης από μία συνεχή στροφή των ΚΑ τάσεως με σταθερές ενεργές ΚΤ τάσεως. Μάλιστα, η ένταση της μη ομοαξονικότητας και της συσχετισμένης πλαστικής συστολής γίνεται μεγαλύτερη όταν η προηγούμενη διατμητική διαδικασία (προ-διάτμηση) είναι εντονότερη σε όρους συσσώρευσης διατμητικής παραμόρφωσης. Συγκεκριμένα, κατά την εκκίνηση της στροφής των ΚΑ τάσεως στις δοκιμές PAR4, PAR3 και PAR2 η διατμητική παραμόρφωση, ε_q, είναι 4.7%, 7.6% και 12.4%, αντιστοίχως, η γωνία ξ είναι 25.9^o, 27.8^o και 32.5^o, αντιστοίχως, και ο λόγος dε_{vol} / dε_q είναι 0.10, 0.47 και 0.97, αντιστοίχως. Καθώς, όμως, η στροφή των ΚΑ τάσεως συνεχίζεται η γωνία μη ομοαξονικότητας, ξ, φθίνει ραγδαίως και η εξέλιξη του ξ με το $\alpha_{\sigma'1}$ γίνεται κοινή στις τρεις δοκιμές ανεξάρτητα από την ιστορία φόρτισης, ενώ ο λόγος διαστολικότητας, dε_{vol} / dε_q, παραμένει διαφορετικός. Το «πείραμα σκέψης» του καθηγητή Δαφαλιά (Dafalias 2016) είναι η οριακή περίπτωση της ακολουθίας των πειραμάτων που παρουσιάζονται εδώ και δεδομένου ότι τα παρατηρούμενα χαρακτηριστικά μη ομοαξονικότητας και πλαστικής συστολής γίνονται σταδιακά εντονότερα καθώς προσεγγίζεται η κρίσιμη κατάσταση συνάγεται ότι τα πειραματικά αποτελέσματα της παρούσας εργασίας επαληθεύουν τον ισχυρισμό ότι η Θεωρία Ανισοτροπικής Κρίσιμης Κατάστασης που προτάθηκε από τους Li and Dafalias (2012) αποτελεί μία αναγκαία αναθεώρηση της κλασσικής Θεωρίας Κρίσιμης Κατάστασης.

Αξίζει να σημειωθεί ότι τα πειραματικά αποτελέσματα είναι πρωτότυπα διότι υποδεικνύουν ότι η επίδραση της προ-διάτμησης στην ένταση της μη ομοαξονικότητας και πλαστικής συστολής κατά τη μεταγενέστερη στροφή των ΚΑ τάσεως είναι σημαντικότερη από την επίδραση των παραμέτρων η, p’, b και e. Για παράδειγμα, σύμφωνα με τους Tong et al. (2010), το μέγεθος της συστολικής ογκομετρικής παραμόρφωσης, ε_{vol}, που συσσωρεύεται κατά τη στροφή των ΚΑ τάσεως με σταθερές ενεργές ΚΤ τάσεως αυξάνεται όταν κάθε μία από τις παραμέτρους η, p’, b και e αυξάνεται. Μολαταύτα, η άμμος στη δοκιμή PAR4 συστέλλεται λιγότερο από ότι η άμμος στη δοκιμή PAR3 παρόλο που η τιμή των παραμέτρων η και p’ είναι μεγαλύτερη στην πρώτη δοκιμή, ενώ η τιμή των παραμέτρων b και e είναι πρακτικά η ίδια (βλ. Πίνακα 5).

Επίσης, σύμφωνα με τους Miura et al. (1986), Gutierrez et al. (1991), Li and Yu (2010) και Tong et al. (2010, 2014) το μέγεθος της γωνίας μη ομοαξονικότητας, ξ, μειώνεται όταν η στροφή των ΚΑ τάσεως εκτελείται σε μεγαλύτερο η, σε μεγαλύτερο b και σε μεγαλύτερο e. Μολαταύτα, όπως φαίνεται στο Σχήμα 25 το οποίο απεικονίζει την εξέλιξη του ξ με το $\alpha^*_{\sigma'1}$ στις δοκιμές PAR1-4, η γωνία ξ στη δοκιμή PAR4 είναι μεγαλύτερη από αυτήν στη δοκιμή PAR1 παρόλο που στην πρώτη δοκιμή η τιμή των παραμέτρων η, b και e είναι μεγαλύτερη. Το παρατηρούμενο φαινόμενο μετά την αλλαγή της κατεύθυνσης των ΚΑ τάσεως είναι, όμως, παροδικό και η δέσμη των σημείων από τις δοκιμές PAR2-4 φαίνεται να κινείται προς τα σημεία από τη δοκιμή PAR1 καθώς η στροφή των ΚΑ τάσεως εξελίσσεται. Τέλος, τονίζεται ότι το παροδικό αυτό φαινόμενο παρατηρείται και στην περίπτωση που η προ-διάτμηση επιβάλλεται κατά την ανισότροπη στερεοποίηση της άμμου με υψηλή στατική διατμητική τάση (για παράδειγμα, σε συνθήκες K_o-στερεοποίησης), όπως εδείχθη στις δοκιμές αστράγγιστης φόρτισης τύπου Β και C (βλ. Σχήμα 19b). Η πρωτοτυπία σε αυτήν την περίπτωση έγκειται στο γεγονός ότι η επίδραση της προ-διάτμησης στην ένταση της μη ομοαξονικότητας είναι σημαντικότερη από την επίδραση του ρυθμού στροφής των κύριων αξόνων τάσεως που έχει επισημανθεί από τους Gutierrez et al. (1991).

Συμπεράσματα

Στην παρούσα διδακτορική διατριβή διερευνήθηκε πειραματικά η μηχανική συμπεριφορά της άμμου M31 υπό συνθήκες τριαξονικής και γενικευμένης φόρτισης. Συγκεκριμένα μελετήθηκε η επίδραση της ανισοτροπίας της άμμου στη μονότονη ρευστοποίηση, στη γενικευμένη αστοχία και στην κρίσιμη κατάσταση. Τα δοκίμια της άμμου παρασκευάστηκαν με τη μέθοδο απόθεσης σε νερό και στερεοποιήθηκαν σε μεγάλο εύρος τάσεων $p'_c = (\sigma'_{1c} + \sigma'_{2c} + \sigma'_{3c}) / 3$ και λόγου τάσεων $K_c = \sigma'_{3c} / \sigma'_{1c}$. Η μονοτονική ή ανακυκλική φόρτιση των δοκιμίων πραγματοποιήθηκε με σταθερούς ή στρεφόμενους κύριους άξονες (ΚΑ) τάσεως και με δύο διαφορετικές τιμές της παραμέτρου ενδιάμεσης κύριας τάσης, $b = (\sigma'_2 - \sigma'_3) / (\sigma'_1 - \sigma'_3)$. Οι πειραματικές δοκιμές εκτελέστηκαν στη συσκευή στρεπτικής διάτμησης κοίλου κυλινδρικού δοκιμίου και σε δύο συσκευές τριαξονικής φόρτισης του Εργαστηρίου Εδαφομηχανικής, του Εθνικού Μετσόβιου Πολυτεχνείου. Όλες οι συσκευές τροποποιήθηκαν ή αναβαθμίστηκαν για τις ανάγκες της παρούσας εργασίας.

Για τον προσδιορισμό των χαρακτηριστικών κρίσιμης κατάστασης της άμμου εκτελέστηκαν δοκιμές μονοτονικής τριαξονικής συμπίεσης υπό συνθήκες ελεύθερης και εμποδιζόμενης στράγγισης σε δοκίμια άμμου στερεοποιημένα ισότροπα σε μέση ενεργό τάση, p'_c, από 100 kPa έως 6000 kPa. Προσδιορίστηκε μία μοναδική γραμμή κρίσιμης κατάστασης στον $p' - e - q$ χώρο, ανεξάρτητη των αρχικών συνθηκών και του τύπου της όδευσης φόρτισης (ελεύθερης ή εμποδιζόμενης στράγγισης). Η συμπεριφορά της άμμου καθ' όλη τη διάρκεια της φόρτισης μέχρι την κρίσιμη κατάσταση μπορεί να συσχετιστεί με την εξέλιξη της καταστατικής παραμέτρου, ψ, των Been and Jefferies (1985). Για παράδειγμα, ο αποκλίνων λόγος τάσεων, η, στο σημείο αλλαγής φάσης αυξάνεται ενώ ο αποκλίνων λόγος τάσεων, η, και η απόλυτος τιμή του λόγου διαστολικότητας, D, στην κατάσταση κορυφαίας αστοχίας μειώνονται όταν η καταστατική παράμετρος, ψ, γίνεται λιγότερο αρνητική. Επίσης, η σχέση λόγου τάσεων – διαστολικότητας, $\eta - D$, είναι διαφορετική για χαλαρή και πυκνή άμμο.

Για τη μελέτη της μηχανικής συμπεριφοράς της άμμου παρασκευάστηκαν χαλαρά δοκίμια τα οποία στερεοποιήθηκαν ισότροπα (άμμος IC) σε μέση ενεργό τάση, $p'_c =$ 200 kPa (ή 100 kPa ή 300 kPa). Έπειτα, τα δοκίμια υποβλήθηκαν σε μονοτονική φόρτιση εμποδιζόμενης στράγγισης με σταθερή μέση ολική τάση, *p*, και σταθερή παράμετρο ενδιάμεσης κύριας τάσης, b = 0.5, διατηρώντας τον προσανατολισμό του άξονα της μέγιστης κύριας τάσης, σ'_1, σταθερό σε διάφορες κατευθύνσεις ως προς την κατακόρυφο, μετρούμενες με τη γωνία $\alpha_{\sigma'1}$ (ή α) (ακτινική φόρτιση). Δοκιμές εκτελέστηκαν για τιμές της γωνίας $\alpha_{\sigma'1}$ από 0^o έως 90^o και για b = 0.5. Η χαλαρή άμμος επέδειξε τυπική συμπεριφορά παροδικής μονότονης ρευστοποίησης (limited flow deformation) με πτώση της αντοχής, *q*, μετά το σημείο παροδικού μεγίστου, λόγω της αύξησης της πίεσης του ύδατος πόρων, και ανάκτηση της αντοχής μετά το σημείο αλλαγής φάσης. Στη φάση της παροδικής μονότονης ρευστοποίησης η απόκριση του συστήματος δοκίμιο – συσκευή φόρτισης γίνεται ασταθής λόγω των επιλεγμένων παραμέτρων ελέγχου, ενώ το δοκίμιο δεν εμφανίζει σημάδια συγκεντρωμένης παραμόρφωσης.

Η συμπεριφορά της άμμου στις δοκιμές ακτινικής φόρτισης (δοκιμές τύπου Α) γίνεται, εν γένει, περισσότερο συστολική όταν ο σ'_1-άξονας απομακρύνεται από την κατακόρυφο με αποτέλεσμα η αντοχή, *q*, στο σημείο παροδικού μεγίστου και στο σημείο αλλαγής φάσης να μειώνεται με τη γωνία $\alpha_{\sigma'1}$· επίσης, η κανονικοποιημένη υπερπίεση του ύδατος πόρων, Δu / p'_{in}, και η οκταεδρική διατμητική παραμόρφωση, γ_{oct}, στο σημείο αλλαγής φάσης αυξάνονται όταν αυξάνεται η γωνία $\alpha_{\sigma'1}$. Στην κατάσταση κορυφαίας αστοχίας η τιμή του λόγου τάσεων, sin φ, μειώνεται, εν γένει, με την αύξηση της γωνίας $\alpha_{\sigma'1}$. Μολαταύτα, η περισσότερο ασθενής απόκριση παρατηρείται όταν η γωνία $\alpha_{\sigma'1}$ λαμβάνει τιμές μεταξύ 60^o και 75^o, διότι τότε ένα από τα επίπεδα οιονεί αστοχίας (maximum stress obliquity planes) τείνει να προσανατολιστεί με το οριζόντιο επίπεδο διαστρωμάτωσης. Επομένως, η εγγενής ανισοτροπία επηρεάζει τα μηχανικά χαρακτηριστικά της άμμου στο σημείο παροδικού μεγίστου αντοχής, στο σημείο αλλαγής φάσης και στην κατάσταση κορυφαίας αστοχίας.

Τα σημεία παροδικού μεγίστου στις δοκιμές ακτινικής φόρτισης ταυτίζονται πρακτικά με τα σημεία στα οποία προκαλείται η αστάθεια μη συγκεντρωμένης παραμόρφωσης και εκκινείται η φάση της μονότονης ρευστοποίησης. Τα σημεία αυτά ορίζουν στο Y – X επίπεδο τάσεων την Επιφάνεια Αστάθειας (IS) η οποία αποτελεί τη γενίκευση της Γραμμής Αστάθειας του Lade (Lade 1993) αφού υποδεικνύει τους συνδυασμούς ($\alpha_{\sigma'1}$, φ) στους οποίους προκαλείται η αστάθεια υπό συνθήκες γενικευμένης ακτινικής φόρτισης. Παρατηρήθηκε ότι η αστάθεια προκαλείται σε μικρότερο λόγο τάσεων sin φ όταν η γωνία $\alpha_{\sigma'1}$ γίνεται μεγαλύτερη. Παρομοίως, μία δεδομένη τιμή της παραμόρφωσης, γ_{oct}, ή της κανονικοποιημένης υπερπίεσης του ύδατος πόρων, Δu / p'_{in}, στη συστολική φάση απόκρισης αναπτύσσεται σε μικρότερο λόγο τάσεων sin φ όταν η γωνία α γίνεται μεγαλύτερη. Τα δεδομένα αυτά υποδεικνύουν ότι η εγγενής ανισοτροπία επηρεάζει την παραμορφωσιμότητα και τη συνθήκη ρευστοποίησης της άμμου.

Για τη μελέτη της επίδρασης της ιστορίας στερεοποίησης και φόρτισης στη μηχανική συμπεριφορά της άμμου παρασκευάστηκαν χαλαρά δοκίμια με τη μέθοδο απόθεσης σε νερό, τα οποία στερεοποιήθηκαν ανισότροπα (άμμος AC) σε μέση ενεργό τάση,

p'_c = 200 kPa (ή 100 kPa), και σε διάφορους λόγους τάσεων στερεοποίησης, K_c (= 0.40 – 0.80). Στη δεύτερη φάση στερεοποίησης μεταβλήθηκε η τιμή της παραμέτρου b από 0 σε 0.5 και της τάσεως p' από p'_c σε p'_{in} (> p'_c) και στη συνέχεια επιβλήθηκε μονοτονική φόρτιση εμποδιζόμενης στράγγισης με στροφή των ΚΑ τάσεως και σταθερές p και b (= 0.5) παραμέτρους. Στις δοκιμές τύπου B η αποκλίνουσα τάση, q, αυξάνεται μονότονα ενώ ταυτόχρονα στρέφονται οι ΚΑ τάσεως. Στις δοκιμές τύπου C η αποκλίνουσα τάση, q, διατηρείται σταθερή ενώ στρέφονται οι ΚΑ τάσεως προκαλώντας την ανάπτυξη υπερπίεσης του ύδατος πόρων και, επομένως, την αύξηση του αποκλίνοντος λόγου τάσεων, $\eta = q \ / \ p'$, καθώς οι ενεργές τάσεις αποφορτίζονται ισότροπα ($d\sigma'_1 = d\sigma'_2 = d\sigma'_3 = -du < 0$). Στη δοκιμή D1 η αποκλίνουσα τάση, q, μεταβάλλεται περιοδικά ενώ στρέφονται οι ΚΑ τάσεως με πρακτικά σταθερές p και b (= 0.40 – 0.52) παραμέτρους.

Η αστάθεια στις δοκιμές τύπου B προκαλείται μετά από μία μικρή αύξηση της αποκλίνουσας τάσης και στροφή των ΚΑ τάσεως όταν ο λόγος K_c είναι μικρός, υποδηλώνοντας την τρωτότητα της ανισότροπα στερεοποιημένης άμμου έναντι ρευστοποίησης όταν η στατική διατμητική τάση είναι μεγάλη, όπως για παράδειγμα σε συνθήκες K_o-στερεοποίησης. Η στροφή των ΚΑ τάσεως υπό σταθερή αποκλίνουσα τάση στις δοκιμές τύπου C επιφέρει πλαστική συστολή, αστάθεια, παροδική μονότονη ρευστοποίηση και τελικά αστοχία της χαλαρής άμμου για τις τιμές του K_c που εξετάστηκαν σε αυτήν την εργασία. Για μία δεδομένη τιμή του K_c η στροφή των ΚΑ τάσεως μέχρι την εκκίνηση της αστάθειας είναι μεγαλύτερη στις δοκιμές τύπου C σε σύγκριση με τις δοκιμές τύπου B. Παρατηρήθηκε, επίσης, ότι η αστάθεια προκαλείται όταν η τασική όδευση από τις δοκιμές τύπου B και C διατέμνει την επιφάνεια αστάθειας που ορίστηκε στις δοκιμές τύπου A υπό μία μεγάλη γωνία. Αντιθέτως, δεν προκαλείται αστάθεια όταν η διάτμηση γίνεται υπό μικρή γωνία ή εφαπτομενικά.

Και στους δύο τύπους δοκιμών η παραμόρφωση της άμμου κατά τη στροφή των ΚΑ τάσεως είναι μη ομοαξονική, με τη γωνία μη ομοαξονικότητας, ξ, να μειώνεται, εν γένει, καθώς αυξάνεται ο λόγος τάσεων sin φ (ή η). Στις δοκιμές τύπου C και στη δοκιμή D1 παρατηρήθηκαν διακριτά μοτίβα μη ομοαξονικής συμπεριφοράς αντιστοιχούντα στη φόρτιση και αποφόρτιση της μη διαγώνιας συνιστώσας, $\tau_{z\theta}$, του τανυστή τάσεως. Τα μοτίβα αυτά ήταν κοινά σε όλες τις δοκιμές, ανεξαρτήτως της τιμής του K_c και του αριθμού των κύκλων στροφής των ΚΑ τάσεως, με εξαίρεση την αρχική φάση στροφής μετά από την ανισότροπη στερεοποίηση σε χαμηλό K_c. Στην περίπτωση της φόρτισης, η γωνία ξ μειώνεται μη γραμμικά με τη γωνία φ, ενώ μετά την αστοχία της άμμου η γωνία ξ σταθεροποιείται καθώς η άμμος παραμορφώνεται στην σταθερή κατάσταση· μολαταύτα, η σταθερή κατάσταση διακόπτεται από την πρόκληση ασταθειών συγκεντρωμένης ή μη παραμόρφωσης. Στην περίπτωση της αποφόρτισης, η γωνία ξ είναι ιδιαίτερα υψηλή και μειώνεται μη γραμμικά με τη γωνία φ, χωρίς να δείχνει σημάδια σταθεροποίησης, πιθανώς λόγω της σύζευξης των ελαστικών και πλαστικών χαρακτηριστικών παραμόρφωσης (elastic – plastic coupling). Στις δοκιμές τύπου B παρατηρήθηκαν διακριτά μοτίβα εξάρτησης του ξ

από το φ πριν την κορυφαία αστοχία ανάλογα με την τιμή του K_c, ενώ μετά την κορυφαία αστοχία η συμπεριφορά είναι παρόμοια για όλες τις τιμές του K_c χωρίς, όμως, να παρατηρείται η σταθερή κατάσταση.

Στις δοκιμές τύπου B και C στις οποίες η άμμος στερεοποιήθηκε σε πολύ χαμηλό K_c παρατηρήθηκε έντονη μη ομοαξονικότητα και πλαστική συστολή κατά τη στροφή των ΚΑ τάσεως που ακολούθησε αμέσως μετά την ανισότροπη στερεοποίηση. Η επίδραση της προ-διάτμησης στην ένταση της μη ομοαξονικότητας αποδείχθηκε σημαντικότερη από την επίδραση του ρυθμού στροφής των κύριων αξόνων τάσεως που έχει επισημανθεί από τους Gutierrez et al. (1991). Το φαινόμενο αυτό δικαιολογεί, ίσως, την τρωτότητα των ανισότροπα στερεοποιημένων άμμων έναντι ρευστοποίησης, σε συνθήκες στροφής των ΚΑ τάσεως, όταν η στατική διατμητική τάση είναι υψηλή. Συγκεκριμένα, μία μικρή τασική διαταραχή που περιλαμβάνει στροφή των ΚΑ τάσεως (π.χ. η αλλαγή της γεωμετρίας μίας πλαγιάς) επιφέρει έντονη μη ομοαξονικότητα και πλαστική συστολή λόγω της προ-διάτμησης με αποτέλεσμα να προκαλείται αστάθεια μη συγκεντρωμένης παραμόρφωσης, με τρόπο ανάλογο προς αυτόν που περιγράφηκε από τον καθηγητή Βαρδουλάκη για την περίπτωση της αστάθειας συγκεντρωμένης παραμόρφωσης (Vardoulakis et al. 1978, Vardoulakis and Graf 1985, Vardoulakis and Georgopoulos 2005).

Τα αποτελέσματα από τις δοκιμές τύπου C υποδεικνύουν ότι οι συνδυασμοί φ και $\alpha_{\sigma'1}$ στο σημείο εκκίνησης της μονότονης ρευστοποίησης (σημείο αστάθειας) δεν είναι μοναδικοί, παρόλο που κάτι τέτοιο διατυπώνεται σε παρελθοντικές έρευνες (Nakata et al. 1998, Sivathayalan and Vaid 2002). Η συνθήκη εκκίνησης και τα χαρακτηριστικά παραμόρφωσης της μονότονης παροδικής ρευστοποίησης εξαρτώνται από την ιστορία τάσεων – παραμορφώσεων, συμπεριλαμβανομένης της επίδρασης του λόγου τάσεων στερεοποίησης, K_c, και της κατεύθυνσης της προσαυξητικής τάσεως. Η εξάρτηση αυτή είναι θεωρητικώς αναμενόμενη αφού το έργο δευτέρας τάξεως, d^2W, το οποίο πρέπει να μηδενιστεί για να προκληθεί η αστάθεια, είναι μία κατευθυντική ποσότητα που εξαρτάται από την ιστορία φόρτισης (Daouadji et al. 2011). Επίσης, διαπιστώθηκε ότι η εκκίνηση αμφοτέρων των ασταθειών μη συγκεντρωμένης και συγκεντρωμένης παραμόρφωσης κατά τη μονότονη φόρτιση εμποδιζόμενης στράγγισης με στροφή των ΚΑ τάσεως συμβαίνει επιλεκτικά σε τασικές καταστάσεις που αντιστοιχούν σε δυσμενείς κινηματικές συνθήκες παραμόρφωσης, δηλαδή σε διάτμηση ή / και ολίσθηση στα οριζόντια επίπεδα διαστρωμάτωσης· επιβεβαιώθηκε, μάλιστα, ότι η αστάθεια μη συγκεντρωμένης παραμόρφωσης συμβαίνει πριν την αστάθεια συγκεντρωμένης παραμόρφωσης. Τα δεδομένα αυτά υποδεικνύουν την επίδραση της εγγενούς ανισοτροπίας και της ιστορίας φόρτισης στην ασταθή συμπεριφορά της άμμου.

Τα αποτελέσματα αυτής της εργασίας υποδεικνύουν ότι η τασική κατάσταση της χαλαρής άμμου που υποβάλλεται σε στροφή των ΚΑ τάσεως υπό συνθήκες εμποδιζόμενης στράγγισης και με σταθερή αποκλίνουσα τάση μπορεί να μεταβληθεί κατά την κατεύθυνση ισότροπης αποφόρτισης ($d\sigma'_1 = d\sigma'_2 = d\sigma'_3 < 0$) από το σημείο ανισότροπης στερεοποίησης έως την κατάσταση κορυφαίας αστοχίας χωρίς να προκληθεί αστάθεια μη συγκεντρωμένης παραμόρφωσης (μονότονη ρευστοποίηση). Αυτά τα ευρήματα είναι πρωτότυπα διότι, σύμφωνα με σύγχρονα προσομοιώματα καταστρωμένα στα πλαίσια της Θεωρίας Διακλάδωσης, η κατεύθυνση ισότροπης αποφόρτισης περιλαμβάνεται στο σύνολο των ασταθών κατευθύνσεων της χαλαρής άμμου ακόμα και σε χαμηλές τιμές του αποκλίνοντος λόγου τάσεων, μακριά από την κορυφαία αστοχία (Darve and Laouafa 2000, Darve et al. 2004, Sibille at al. 2007, Prunier et al. 2009). Στη συνέχεια, εδείχθη ότι μία οιονεί στατική αστάθεια μη συγκεντρωμένης παραμόρφωσης μπορεί να προκληθεί υπό αυξανόμενες ενεργές τάσεις και μειούμενο αποκλίνοντα λόγο τάσεων, ακολουθούμενη από μία δυναμική αστάθεια μη συγκεντρωμένης παραμόρφωσης (μονότονη ρευστοποίηση) υπό μειούμενες ενεργές τάσεις και αποκλίνοντα λόγο τάσεων. Η πρωτοτυπία εδώ έγκειται στο γεγονός ότι επιβεβαιώνονται για πρώτη φορά με φυσικό πείραμα οι προβλέψεις των προσομοιωμάτων του Darve σχετικά με τη δυνατότητα πρόκλησης αστάθειας σε κατεύθυνση που αντιστοιχεί σε αυξανόμενες ενεργές τάσεις (Darve and Laouafa 2000, Darve et al. 2004, Sibille at al. 2007, Prunier et al. 2009).

Για τη διερεύνηση της επίδρασης της ανισότροπης εσωτερικής δομής της άμμου στην κρίσιμη κατάσταση παρασκευάστηκαν χαλαρά δοκίμια τα οποία υποβλήθηκαν, πρώτα, σε μονοτονική φόρτιση εμποδιζόμενης στράγγισης με σταθερή κύρια κατεύθυνση τάσεως (ακτινική φόρτιση) και, έπειτα, σε στροφή των ΚΑ τάσεως με σταθερές ενεργές ΚΤ τάσεως όσο το δυνατόν πλησιέστερα στην κρίσιμη κατάσταση. Παρατηρήθηκε ότι η άμμος επιδεικνύει έντονη μη ομοαξονικότητα και συστέλλεται πλαστικά όταν η φόρτιση με σταθερούς ΚΑ τάσεως διακόπτεται από μία συνεχή στροφή των ΚΑ τάσεως. Η ένταση της μη ομοαξονικότητας και της συσχετισμένης πλαστικής συστολής γίνεται μεγαλύτερη όταν η προηγούμενη διατμητική διαδικασία (προ-διάτμηση) είναι εντονότερη σε όρους συσσώρευσης διατμητικής παραμόρφωσης. Τα αποτελέσματα είναι πρωτότυπα διότι υποδεικνύουν ότι η επίδραση της προ-διάτμησης στη συμπεριφορά της άμμου είναι σημαντικότερη από αυτήν των παραμέτρων η, p', b και e που έχει επισημανθεί σε παρελθοντικές έρευνες (Miura et al. 1986, Li and Yu 2010, Tong et al. 2010 and 2014), όμως η επίδραση αυτή είναι παροδική και φθίνει καθώς συνεχίζεται η στροφή των ΚΑ τάσεως.

Συγκεκριμένα, εδείχθη ότι η άμμος συμπεριφέρεται εντόνως μη ομοαξονικά και συστέλλεται αμέσως όταν εκκινείται η στροφή των ΚΑ τάσεως με σταθερές τις ενεργές ΚΤ τάσεως πολύ κοντά στην κρίσιμη κατάσταση, μολονότι στην προηγούμενη φάση ακτινικής φόρτισης διαστελλόταν πλαστικά στην κατάσταση αστοχίας υπό ομοαξονικές συνθήκες παραμόρφωσης· μάλιστα, το φαινόμενο γίνεται προοδευτικά εντονότερο καθώς προσεγγίζεται η κρίσιμη κατάσταση. Το «πείραμα σκέψης» του καθηγητή Δαφαλιά (Dafalias 2016) είναι η οριακή περίπτωση της ακολουθίας των δοκιμών που εκτελέστηκαν στην παρούσα εργασία, επομένως, τα πειραματικά αποτελέσματα που παρουσιάζονται επαληθεύουν τον ισχυρισμό ότι η Θεωρία Ανισοτροπικής Κρίσιμης Κατάστασης που προτάθηκε από τους Li and Dafalias (2012) αποτελεί μία αναγκαία αναθεώρηση της κλασσικής Θεωρίας Κρίσιμης Κατάστασης.

Τα αποτελέσματα της παρούσας διδακτορικής διατριβής προσφέρουν νέα γνώση και συμβάλλουν στη βαθύτερη κατανόηση της επίδρασης της ανισοτροπίας και της ιστορίας φόρτισης στη μηχανική συμπεριφορά της άμμου. Η διαδικασία απόθεσης και η ιστορία φόρτισης επηρεάζουν τον σχηματισμό και την εξέλιξη της εσωτερικής δομής και αυτή η διαδικασία στο μικροσκοπικό επίπεδο καθορίζει εν τέλει τη μακροσκοπική μηχανική συμπεριφορά της άμμου σε κάθε κατάσταση, συμπεριλαμβανομένης της κρίσιμης. Αναδεικνύεται, επομένως, η αναγκαιότητα ανάπτυξης προσομοιωμάτων που δύνανται να προσομοιώσουν την επίδραση της εσωτερικής δομής στη μηχανική συμπεριφορά της άμμου υπό γενικευμένες και σύνθετες συνθήκες φόρτισης, όπως αυτές που επιβλήθηκαν στην παρούσα εργασία. Ως μελλοντικός στόχος έρευνας τίθεται η εφαρμογή τεχνικών πειραματικής μέτρησης του τανυστή δομής κοκκωδών υλικών μέσω φυσικών ιδιοτήτων όπως η ηλεκτρική αγωγιμότητα και η ταχύτητα διάδοσης των μηχανικών κυμάτων. Επίσης, ένα ελκυστικό αντικείμενο για μελλοντική έρευνα αφορά τη διερεύνηση της μηχανικής συμπεριφοράς άμμου υπό συνθήκες πραγματικής τριαξονικής φόρτισης.

Βιβλιογραφία

Arthur JRF, Menzies BK (1972) Inherent anisotropy in a sand. Géotechnique 22 (1), 115–129

Been K, Jefferies MG (1985) A state parameter for sands. Géotechnique 35 (2), 99–112

Been K, Jefferies MG, Hachey J (1991) The critical state of sands. Géotechnique 41 (3), 365–381

Borja RI (2006) Condition for liquefaction instability in fluid-saturated granular soils. Acta Geotechnica 2006; 1:211-224

Brewer R (1964) Fabric and mineral analysis of soils. John Wiley and Sons, Inc. pp. 129-158

Casagrande A, Carillo N (1944) Shear failure of anisotropic materials. Proc. Boston Soc. Civ. Engrs, 31, 74-87

Castro G (1969) Liquefaction of sands. Harvard Soil Mechanics Series No. 81, Harvard University, Cambridge, Mass

Chu J, Leong WK (2001) Pre-failure strain softening and pre-failure instability of sand: a comparative study. Géotechnique 51 (4), 311–321

Dafalias YF (1977) Elasto-plastic coupling within a thermodynamic strain space formulation of plasticity. Int. J. Non-Linear Mech., Vol. 12, pp. 327-337

Dafalias YF (2016) Must critical state theory be revisited to include fabric effects? Acta Geotechnica (2016) 11:479, DOI 10.1007/s11440-016-0441-0

Daouadji A, Darve F, Al Gali H, Hicher PY, Laouafa F, Lignon S, Nicot F, Nova R, Pinheiro M, Prunier F, Sibille L, Wan R (2011) Diffuse failure in geomaterials: Experiments, theory and modelling. Int. J. Numer. Anal. Meth. Geomech. (2011), 35(16), 1731-1773

Darve F, Flavigny M, Meghachou M (1995) Constitutive modelling and instabilities of soil behaviour. Computers and Geotechnics 17 (1995), 203-224

Darve F, Laouafa F (2000) Instabilities in granular materials and application to landslides. Mech. Cohes-Frict. Mater., 2000; 5:627-652

Darve F, Servant G, Laouafa F, Khoa HDV (2004) Failure in geomaterials: continuous and discrete analysis. Comput. Methods Appl. Mech. Engrg. 193 (2004), 3057-3085

Desrues J, Hammad W (1989) Shear banding dependency on mean stress level in sand. Numerical Methods for Localization and Bifurcation of Granular Bodies, International Workshop, Gdańsk-Sobieszewo, September 25-30, 1989

Desrues J, Chambon R, Mokni M, Mazerolle F (1996) Void ratio inside shear bands in triaxial sand specimens studied by computed tomography. Géotechnique 46 (3), 529-546

Desrues J, Viggiani G (2004) Strain localization in sand: an overview of the experimental results obtained in Grenoble using stereophotogrammetry. International Journal for Numerical and Analytical Methods in Geomechanics, 2004, 28: 279-321

Desrues J, Georgopoulos I-O (2006) An investigation of diffuse failure modes in undrained triaxial tests on loose sand. Soils and Foundations, Vol.46, No.5, 585-594

Fu P, Dafalias YF (2011) Fabric evolution within shear bands of granular materials and its relation to critical state theory. International Journal for Numerical and Analytical Methods in Geomechanics, 2011, 35: 1918-1948

Georgiannou VN, Konstadinou M (2014) Torsional shear behavior of anisotropically consolidated sands. J. Geotech. Geoenviron. Eng., ASCE 140 (2), ISSN: 1090-0241/04013017(14)

Georgiannou VN, Konstadinou M, Triantafyllos PK (2018) Sand behavior under stress states involving principal stress rotation. Journal of Geotechnical and Geoenvironmental Engineering, 2018, 144(6): 04018028

Gong G, Thornton C, Chan AHC (2012) DEM simulations of undrained triaxial behavior of granular material. Journal of Engineering Mechanics, Vol. 138, No 6, 560-566

Guo N, Zhao J (2013) The signature of shear-induced anisotropy in granular media. Computers and Geotechnics, 47, 1-15

Gutierrez M, Ishihara K, Towhata I (1991) Flow theory for sand during rotation of principal stress direction. Soils and Foundations, Vol.31, No.4, pp. 121-132

Hight DW, Gens A, Symes MJ (1983) The development of a new hollow cylinder apparatus for investigating the effects of principal stress rotation in soils. Géotechnique 33, No. 4, 355-383

Hill R (1958) A general theory of uniqueness and stability in elastic-plastic solids. Journal of the Mechanics and Physics of Solids (1958); 6:239-249

Hu M, O'Sullivan C, Jardine RR, Jiang M (2010) Stress-induced anisotropy in sand under cyclic loading. Granular Matter, 12: 469-476

Hueckel T (1976) Coupling of elastic and plastic deformation of bulk solids. Mechanica 11:227–235

Ishihara K, Tatsuoka F, Yasuda S (1975) Undrained deformation and liquefaction of sand under cyclic stresses. Soils and Foundations, Vol.15, No.1, 29-44

Ishihara K, Towhata I (1983) Sand response to cyclic rotation of principal stress directions as induced by wave loads. Soils and Foundations, Vol.23, No.4, 11-26

Ishihara K (1993) Liquefaction and flow failure during earthquake. Géotechnique, Vol. 43, No. 3, pp.351-415

Lade PV, Nelson RB, Ito YM (1988) Instability of granular materials with nonassociated flow. Journal of Engineering Mechanics, Vol. 114, No. 12, 2173-2191

Lade PV (1993) Initiation of static instability in the submarine Nerlerk berm. Canadian Geotechnical Journal 30: 895-904

Lam WK, Tatsuoka F (1988) Effects of initial anisotropic fabric and σ_2 on strength and deformation characteristics of sand. Soils and Foundations, Vol.28, No.1, pp. 89-106

Li XS, Wang Y (1998) Linear representation of steady-state line for sand. J. Geotech. Geoenviron. Eng., 124(12), 1215-1217

Li XS, Dafalias YF (2000) Dilatancy for cohesionless soils. Géotechnique 50, No. 4, 449-460

Li X, Li XS (2009) Micro-macro quantification of the internal structure of granular materials. J. Eng. Mech., 135(7), 641-656

Li X, Yu H-S (2010) Numerical investigation of granular material behaviour under rotational shear. Géotechnique 60, No. 5, 381-394

Li XS, Dafalias YF (2012) Anisotropic critical state theory: role of fabric. Journal of Engineering Mechanics, Vol. 138, No. 3, 263-275

Li X, Yang D, Yu H-S (2016) Macro deformation and micro structure of 3D granular assemblies subjected to rotation of principal stress axes. Granular Matter (2016) 18:53, DOI: 10.1007/s10035-016-0632-2

Lü X, Huang M, Qian J (2018) Influences of loading direction and intermediate principal stress ratio on the initiation of strain localization in cross-anisotropic sand. Acta Geotech., 13: 619-633, 2018

Manzari MT, Dafalias YF (1997) A critical state two-surface plasticity model for sands. Géotechnique 47, No. 2, 255-272

Masson S, Martinez J (2001) Micromechanical analysis of the shear behavior of a granular material. J. Eng. Mech., 127(10), 1007-1016

Miura K, Miura S, Toki S (1986) Deformation behavior of anisotropic dense sand under principal stress axes rotation. Soils and Foundations, Vol.26, No.1, 36-52

Nakata Y, Hyodo M, Murata H, Yasufuku N (1998) Flow deformation of sands subjected to principal stress rotation. Soils and Foundations, Vol.38, No.2, 115-128

Nicot F, Darve F (2011) Diffuse and localized failure modes: Two competing mechanisms. International Journal for Numerical and Analytical Methods in Geomechanics, Vol. 35, 586-601

Nova R (1994) Controllability of the incremental response of soil specimens subjected to arbitrary loading programmes. Journal of the Mechanical Behavior of Materials, 5(2):193-201

Oda M (1972) Initial fabrics and their relations to mechanical properties of granular material. Soils and Foundations, Vol.12, No.1, 18-36

Oda M, Nemat-Nasser S, Konishi J (1985) Stress-induced anisotropy in granular masses. Soils and Foundations, Vol.25, No.3, 85-97

Poulos SJ, Castro G, France JW (1985) Liquefaction evaluation procedure. Journal of Geotechnical Engineering, ASCE, Vol.111, No.6, pp. 772-792

Prunier F, Nicot F, Darve F, Laouafa F, Lignon S (2009) Three-dimensional multiscale bifurcation analysis of granular media. Journal of Engineering Mechanics, Vol. 135, No. 6, 493-509

Roscoe KH, Schofield AN, Wroth CP (1958) On the yielding of soils. Géotechnique 8 (1), 22–53

Roscoe KH (1970) The influence of strains in soil mechanics. Tenth Rankine Lectrure, Géotechnique 20, No. 2, 129-17

Salvatore E, Mondoni G, Ando E, Albano M, Viggiani G (2017) Determination of the critical state of granular materials with triaxial tests. Soils Found. (2017), https://doi.org/10.1016/j.sandf.2017.08.005

Sasitharan S, Robertson PK, Sego DC, Morgenstern NR (1993) Collapse behavior of sand. Can. Geotech. J. 30, 569-577

Satake M (1978) Constitution of mechanics of granular materials through graph representation. Theoretical and Applied Mechanics 26, University of Tokyo Press, pp. 257-266

Schofield AN, Wroth CP (1968) Critical state soil mechanics. McGraw-Hill, London

Shibuya S, Hight DW (1987) A bounding surface of granular materials. Soils and Foundations, Vol.27, No.4, 123-136

Shibuya S, Hight DW, Jardine RJ (2003a) Four-dimensional local boundary surfaces of an isotropically consolidated loose sand. Soils and Foundations, Vol.43, No.2, 89-103

Shibuya S, Hight DW, Jardine RJ (2003b) Local boundary surfaces of a loose sand dependent on consolidation path. Soils and Foundations, Vol.43, No.3, 85-93

Sibille L, Nicot F, Donzé FV, Darve F (2007) Material instability in granular assemblies from fundamentally different models. Int. J. Numer. Anal. Meth. Geomech., 2007; 31:457–481

Sivathayalan S, Vaid YP (2002) Influence of generalized initial state and principal stress rotation on the undrained response of sands. Canadian Geotechnical Journal, 39 (1): 63 – 76

Symes MJ, Gens A, Hight DW (1984) Undrained anisotropy and principal stress rotation in saturated sand. Géotechnique 34, No. 1, 11-27

Tatsuoka F, Ishihara K (1974) Drained deformation of sand under cyclic stresses reversing direction. Soils and Foundations, Vol.14, No.3, pp. 51-65

Theocharis AI, Vairaktaris E, Dafalias YF, Papadimitriou AG (2017) Proof of incompleteness of Critical State Theory in granular mechanics and its remedy. Journal of Engineering Mechanics, Vol. 143 (2), 1-12

Theocharis AI, Vairaktaris E, Dafalias YF, Papadimitriou AG (2019) Necessary and sufficient conditions for reaching and maintaining critical state. International Journal for Numerical and Analytical Methods in Geomechanics, 43: 2041-2045

Thornton C (2000) Numerical simulations of deviatoric shear deformation of granular media. Géotechnique 50, No. 1, 43-53

Tong Z, Zhang J, Yu Y, Ga Zhang (2010) Drained deformation behavior of anisotropic sands during cyclic rotation of principal stress axes. Journal of Geotechnical and Geoenvironmental Engineering, Vol. 136, No.11, pp. 1509-1518

Tong Z, Fu P, Dafalias YF, Yao Y (2014) Discrete element method analysis of non-coaxial flow under rotational shear. Int. J. Numer. Anal. Meth. Geomech., 2014; 38:1519–1540

Triantafyllos PK, Georgiannou VN, Dafalias YF, Georgopoulos I-O (2020a) New findings on the evolution of the instability surface of loose sand. Acta Geotechnica, https://doi.org/10.1007/s11440-019-00887-7

Triantafyllos PK, Georgiannou VN, Pavlopoulou EM, Dafalias YF (2020b) Strength and dilatancy of sand before and after stabilisation with colloidal-silica gel. Géotechnique (under review)

Tsomokos A (2005) Experimental study of the behaviour of a soil element under monotonic and cyclic torsional shear. PhD Thesis, National Technical University of Athens

Vaid YP, Chern JC (1983) Effect of static shear on resistance to liquefaction. Soils and Foundations, Vol.23, No.1, pp. 47-60

Vardoulakis I, Goldscheider M, Gudehus G (1978) Formation of shear bands in sand bodies as a bifurcation problem. International Journal for Numerical and Analytical Methods in Geomechanics, 1978, 2: 99-128

Vardoulakis I, Graf B (1985) Calibrations of constitutive models for granular materials using data from biaxial experiments. Géotechnique 35, No. 3, 299-317

Vardoulakis I, Sulem J (1995) Bifurcation analysis in geomechanics. Chapman and Hall, 1995

Vardoulakis I, Georgopoulos I-O (2005) The "stress-dilatancy" hypothesis revisited: shear-banding related instabilities. Soils and Foundations, Vol.45, No.2, pp. 61-76

Verdugo R, Ishihara K (1996) The steady state of sandy soils. Soils and Foundations, Vol.36, No.2, pp. 81-91

Wang R, Fu P, Zhang J-M, Dafalias YF (2017) Evolution of various fabric tensors for granular media toward the critical state. J. Eng. Mech., 2017, 143(10): 04017117

Wiebicke M, Andò E, Salvatore E, Viggiani G, Herle I (2017) Experimental measurement of granular fabric and its evolution under shearing. Powders and Grains (2017), EPJ Web of Conferences. 140. 02020. 10.1051/epjconf/201714002020.

Wroth CP, Basset RH (1965) A stress-strain relationship for the shearing behaviour of a sand. Géotechnique 15, No. 1, 32-56

Yang ZX, Li XS, Yang J (2007) Undrained anisotropy and rotational shear in granular soil. Géotechnique 57, No. 4, 371-384

Yoshimine M, Ishihara K, Vargas W (1998): Effects of principal stress direction and intermediate principal stress on undrained shear behavior of sand. Soils and Foundations, Vol. 38, No. 3, 179-188

Yoshimine M, Ishihara K (1998) Flow potential of sand during liquefaction. Soils and Foundations, Vol. 38, No. 3, 189-198

Zhang L, Thornton C (2007) A numerical examination of the direct shear test. Géotechnique 57, No. 4, 343-354

Zhou W, Liu J, Ma G, Chang X (2017) Three-dimensional DEM investigation of critical state and dilatancy behaviors of granular materials. Acta Geotechnica (2017) 12:527-540

Πίνακες

Πίνακας 1 Κατάλογος των συμβόλων και των εξισώσεων που χρησιμοποιήθηκαν για τον υπολογισμό των μέσων τάσεων, παραμορφώσεων και άλλων παραμέτρων στις δοκιμές στρεπτικής διάτμησης

Table 1 List of symbols and equations used to calculate the average stresses, strains and other parameters in torsional-shear tests

Direction HC	**Stress**	**Strain**
Vertical	$\sigma_{zz} = \frac{F}{\pi\left(r_o^2 - r_i^2\right)} + \frac{p_o r_o^2 - p_i r_i^2}{r_o^2 - r_i^2}$	$\varepsilon_{zz} = -\frac{v_H}{H}$
Circumferential	$\sigma_{\theta\theta} = \frac{p_o r_o - p_i r_i}{r_o - r_i}$	$\varepsilon_{\theta\theta} = \frac{(\varepsilon_{vol} - \varepsilon_{zz})}{2}$ **or** $\varepsilon_{\theta\theta} = \varepsilon_{vol} - \varepsilon_{zz}$
Radial	$\sigma_{rr} = \frac{p_o r_o + p_i r_i}{r_o + r_i}$	$\varepsilon_{rr} = \frac{(\varepsilon_{vol} - \varepsilon_{zz})}{2}$ **or** $\varepsilon_{rr} = 0$
Rotational	$\tau_{z\theta} = \frac{3T}{2\pi(r_o^3 - r_i^3)}$	$\gamma_{z\theta} = 2\varepsilon_{z\theta} = \frac{2\theta\left(r_o^3 - r_i^3\right)}{3H(r_o^2 - r_i^2)}$
Principal	**Stress**	**Strain**
Major	$\sigma_1 = \frac{\sigma_{zz} + \sigma_{\theta\theta}}{2} +$	$\varepsilon_1 = \frac{\varepsilon_{zz} + \varepsilon_{\theta\theta}}{2} +$

	$+\sqrt{\left(\frac{\sigma_{zz}-\sigma_{\theta\theta}}{2}\right)^2+\tau_{z\theta}^2}$	$+\sqrt{\left(\frac{\varepsilon_{zz}-\varepsilon_{\theta\theta}}{2}\right)^2+\varepsilon_{z\theta}^2}$
Intermediate	$\sigma_2=\sigma_{rr}$	$\varepsilon_2=\varepsilon_{rr}$
Minor	$\sigma_3=\frac{\sigma_{zz}+\sigma_{\theta\theta}}{2}-$ $-\sqrt{\left(\frac{\sigma_{zz}-\sigma_{\theta\theta}}{2}\right)^2+\tau_{z\theta}^2}$	$\varepsilon_3=\frac{\varepsilon_{zz}+\varepsilon_{\theta\theta}}{2}-$ $-\sqrt{\left(\frac{\varepsilon_{zz}-\varepsilon_{\theta\theta}}{2}\right)^2+\varepsilon_{z\theta}^2}$
Invariant	**Stress**	**Strain**
	$q=(\frac{1}{2}\{(\sigma_1-\sigma_2)^2+$ $+(\sigma_2-\sigma_3)^2+(\sigma_3-\sigma_1)^2\})^{1/2}$	$\gamma=(\frac{2}{9}\{(\varepsilon_1-\varepsilon_2)^2+$ $+(\varepsilon_2-\varepsilon_3)^2+(\varepsilon_3-\varepsilon_1)^2\})^{1/2}$
	$p'=\frac{\sigma_1'+\sigma_2'+\sigma_3'}{3}=$ $=\frac{\sigma_1+\sigma_2+\sigma_3}{3}-u$	$\varepsilon_{vol}=\varepsilon_1+\varepsilon_2+\varepsilon_3\ (=\frac{-\Delta V}{V})$
	$\tau_{oct}=\frac{1}{3}(\{(\sigma_1-\sigma_2)^2+$ $+(\sigma_2-\sigma_3)^2+(\sigma_3-\sigma_1)^2\})^{1/2}$	$\gamma_{oct}=\frac{2}{3}(\{(\varepsilon_1-\varepsilon_2)^2+$ $+(\varepsilon_2-\varepsilon_3)^2+(\varepsilon_3-\varepsilon_1)^2\})^{1/2}$
Parameters	**Stress**	**Strain**
Difference	$q_d=\sigma_1-\sigma_3$	
	$X=\frac{\sigma_{zz}'-\sigma_{\theta\theta}'}{\sigma_{zz}'+\sigma_{\theta\theta}'},\ X_s=\sigma_{zz}'-\sigma_{\theta\theta}'$	$X_\varepsilon=\frac{\varepsilon_{zz}-\varepsilon_{\theta\theta}}{2}$
	$Y=\frac{2\tau_{z\theta}}{\sigma_{zz}'+\sigma_{\theta\theta}'},\ Y_s=2\tau_{z\theta}$	$Y_\varepsilon=\varepsilon_{z\theta}$
Direction of major principal stress/strain	$\alpha\equiv\alpha_{\sigma'1}=0.5\cdot\tan^{-1}\frac{Y}{X}=$ $=0.5\cdot\tan^{-1}\frac{Y_s}{X_s}$	$\alpha_{\varepsilon1}=0.5\cdot\tan^{-1}\frac{Y_\varepsilon}{X_\varepsilon}$

Direction of major principal incremental stress/strain	$\alpha_{d\sigma'1} = 0.5 \cdot \tan^{-1} \frac{dY_s}{dX_s}$	$\alpha_{d\varepsilon 1} = 0.5 \cdot \tan^{-1} \frac{dY_\varepsilon}{dX_\varepsilon}$
Ratio	$b = \frac{\sigma_2^{'} - \sigma_3^{'}}{\sigma_1^{'} - \sigma_3^{'}}$	
Ratio	$\sin\varphi = \frac{\sigma_1^{'} - \sigma_3^{'}}{\sigma_1^{'} + \sigma_3^{'}}$	
Ratio	$\eta = \frac{q}{p^{'}}$	
Ratio	$K_c = \frac{\sigma_{3c}^{'}}{\sigma_{1c}^{'}}$	
Second-order work	$d^2W = (d\sigma_{zz} - d\sigma_{\theta\theta})(\frac{d\varepsilon_{zz} - d\varepsilon_{\theta\theta}}{2}) + 2d\tau_{z\theta}d\varepsilon_{z\theta}$, for isochoric conditions under b=0.5	
Normalised second-order work	$d^2W_{norm} = d^2W / \left[\sqrt{(d\sigma_{zz} - d\sigma_{\theta\theta})^2 + (2d\tau_{z\theta})^2} \cdot \sqrt{(\frac{d\varepsilon_{zz} - d\varepsilon_{\theta\theta}}{2})^2 + (d\varepsilon_{z\theta})^2} \right]$, for isochoric conditions under b=0.5	
Angle between the σ'₁-axis and the planes of max(τ/σₙ')	$\theta_{1,2} = \pm(45° - \varphi_{mob} / 2)$	

Πίνακας 2 Κατάλογος των βασικών συμβόλων και συντομογραφιών

Table 2 Notations and abbreviations

α material constant used in the relationship of the critical state line in the $e - (p'/p_a)^\alpha$ plane

ε_1 major principal strain

ε_2 intermediate principal strain

ε_3 minor principal strain

ε_q deviatoric strain, $\varepsilon_q = 2^{1/2}/3[(\varepsilon_1 - \varepsilon_2)^2 + (\varepsilon_2 - \varepsilon_3)^2 + (\varepsilon_3 - \varepsilon_1)^2]^{1/2}$

ε_{vol} volumetric strain, $\varepsilon_{vol} = \varepsilon_1 + \varepsilon_2 + \varepsilon_3$

η deviatoric stress ratio, $\eta = q/p'$

λ slope of the critical state line in the $e - (p'/p_a)^\alpha$ plane

ξ non-coaxiality angle, $\xi = \alpha_{d\varepsilon 1} - \alpha_{\sigma' 1}$

σ'_1 major principal effective stress

σ'_2 intermediate principal effective stress

σ'_3 minor principal effective stress

φ angle of shearing resistance (degrees)

φ_c angle of shearing resistance at the critical state (degrees)

ψ state parameter of Been and Jefferies, $\psi = e - e_c(p')$

ACST anisotropic critical state theory

B Skempton's pore-pressure coefficient

c cohesion

CSL critical state line in the $p' - e - q$ space

CST critical state theory

D dilatancy ratio, $D = d\varepsilon^p_{vol} / d\varepsilon^p_q$ (the superscript p stands for plastic)

e void ratio, $e = V_v / V_s$

$e_c(p')$ void ratio at the critical state at mean effective stress p'

e_Γ material constant indicating the intercept of the critical state line in the $e - (p'/p_a)^\alpha$ plane with the $p' = 0$ axis

HCA hollow cylinder apparatus

IP instability point

IS instability surface

M deviatoric stress ratio, q / p', at the critical state

PA principal axes

PTP phase-transformation point

PV principal values

p' mean effective stress, $p' = (\sigma'_1 + \sigma'_2 + \sigma'_3) / 3$

p_a atmospheric pressure at zero elevation (101 kPa)

q deviatoric stress, $q = [1/2 \{(\sigma'_1 - \sigma'_2)^2 + (\sigma'_2 - \sigma'_3)^2 + (\sigma'_3 - \sigma'_1)^2\}]^{1/2}$

u pore-water pressure in excess of atmospheric pressure

V_s volume of sand particles

V_v volume of voids

Πίνακας 3 Φυσικά χαρακτηριστικά της άμμου M31

Table 3 Physical characteristics of M31 Sand

Specific gravity, G_s (-):	2.66
Minimum void ratio, e_{min} (-):	0.50
Maximum void ratio, e_{max} (-):	0.80
Grain size D_{10} (mm):	0.214
Grain size D_{30} (mm):	0.258
Grain size D_{50} (mm):	0.310
Grain size D_{60} (mm):	0.339
Coefficient of uniformity, C_u (-):	1.58
Coefficient of curvature, C_h (-):	0.92

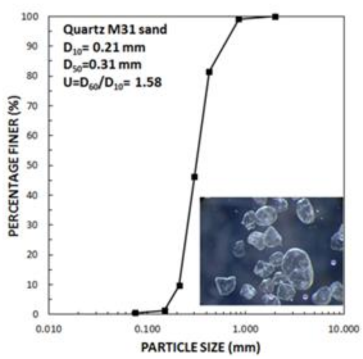

D_p is the grain size (diameter) corresponding to p% finer in the grain size distribution curve. The coefficient of uniformity is $C_u = D_{60} / D_{10}$ while the coefficient of curvature is $C_h = (D_{30})^2 / (D_{60} * D_{10})$

Πίνακας 4 Παράμετροι κρίσιμης κατάστασης της άμμου M31

Table 4 Critical-state parameters of M31 Sand

$e_c(p') = e_\Gamma - \lambda(p'/p_a)^\alpha$, p_a=101 kPa and $\eta_c = (q / p')_c = M$				
	e_Γ	**λ**	**α**	**M (for b = 0)**
M31 Sand	0.7682	0.0112	0.70	1.24

Πίνακας 5 Συνθήκες κατά την έναρξη της στροφής των κύριων αξόνων τάσεως στις δοκιμές τύπου PAR

Table 5 Conditions at the initiation of stress rotation in PAR-series tests

Test	**η (-)**	**p' (kPa)**	**b (-)**	**α (°)**	**ε_q (%)**	**e (-)**	**ψ (-)**	**Pre-shearing**
PAR1	1.01	100	0	0	0.78	0.693	-0.064	AC
PAR2	1.02	507	0.5	15	12.4	0.726	-0.008	RL
PAR3	1.05	343	0.5	15	7.6	0.744	0.003	RL
PAR4	1.12	402	0.5	15	4.7	0.733	-0.006	RL

Σχήματα

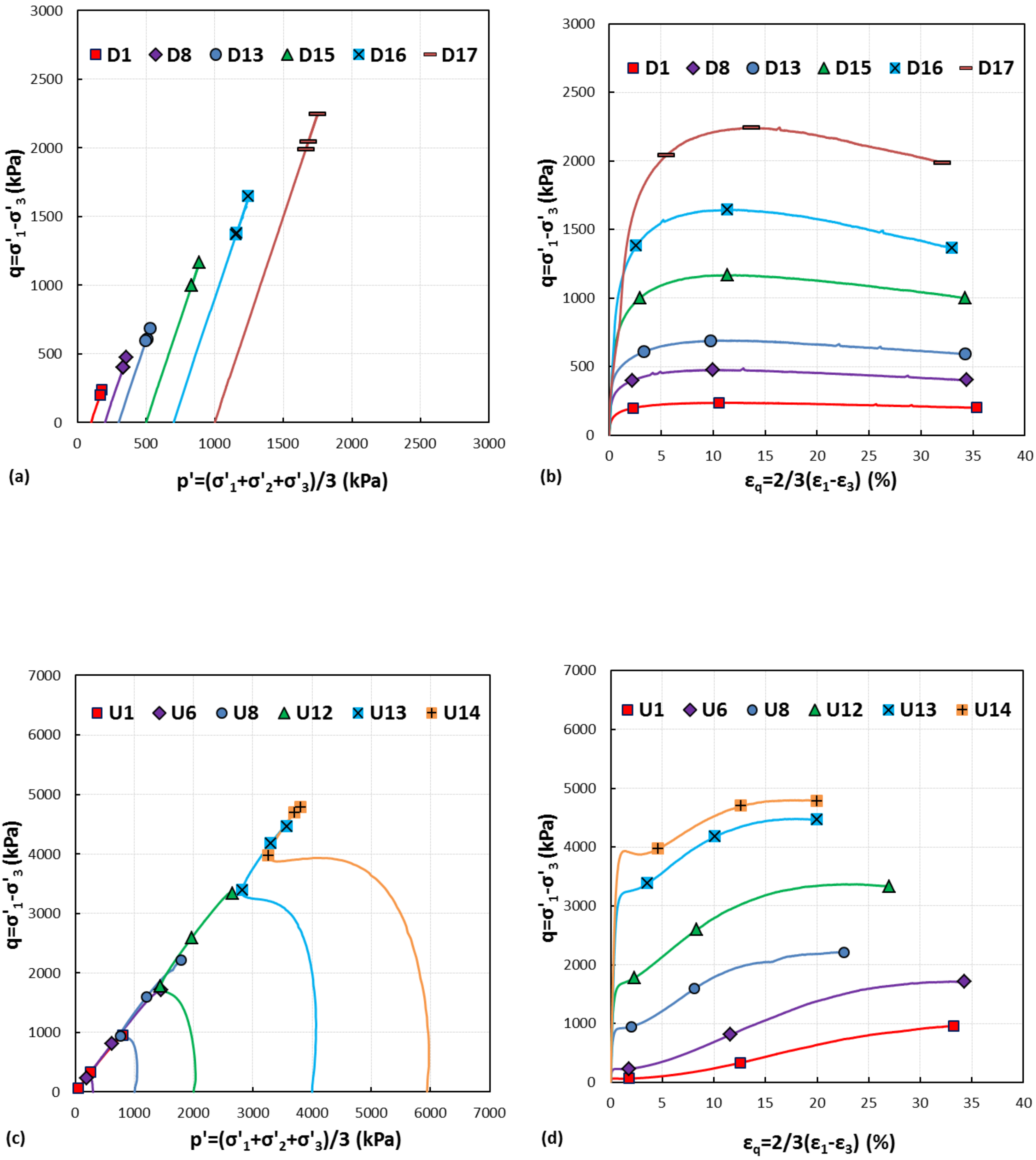

Σχ. 1 Απόκριση ισότροπα στερεοποιημένης άμμου σε μονοτονική τριαξονική συμπίεση υπό στραγγιζόμενες (**a** & **b**) και αστράγγιστες (**c** & **d**) συνθήκες. **a** & **b** Ενεργές τασικές οδεύσεις στο $q - p'$ επίπεδο. **c** & **d** Καμπύλες αποκλίνουσας τάσης – παραμόρφωσης ($q - \varepsilon_q$)

Fig. 1 Response of IC sand to monotonic triaxial compression under drained (**a** & **b**) and undrained (**c** & **d**) conditions. **a** & **b** Effective stress paths in the $q - p'$ plane. **c** & **d** Deviatoric stress – strain curves ($q - \varepsilon_q$)

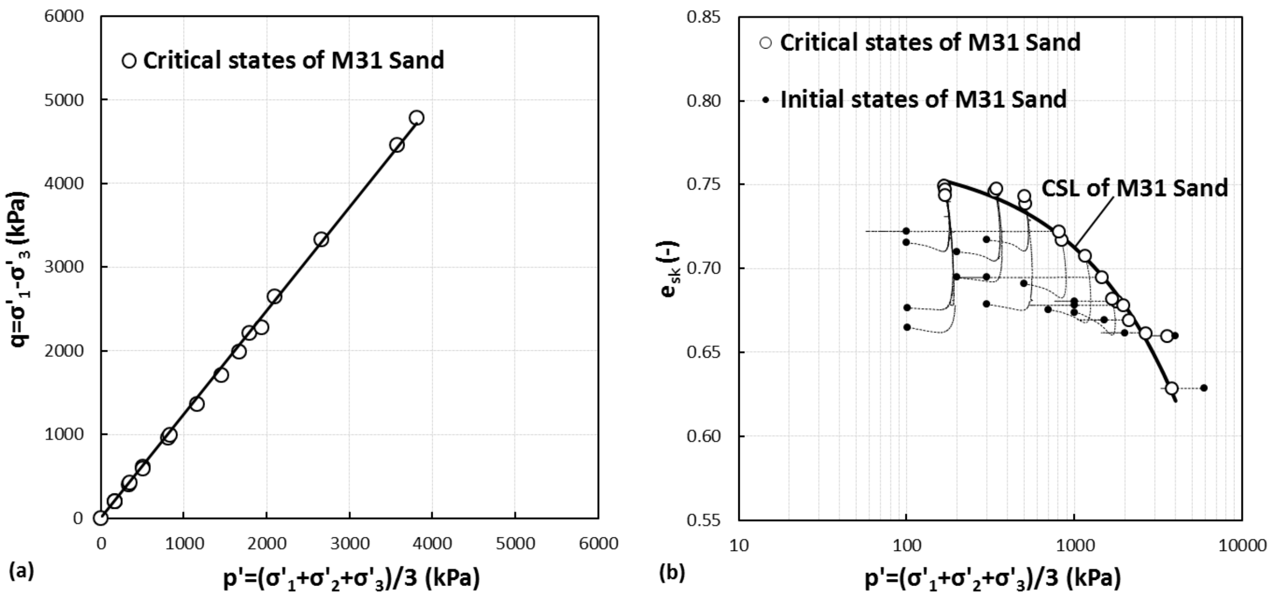

Σχ. 2 Προβολή της Γραμμής Κρίσιμης Κατάστασης της άμμου M31 στο $q - p'$ επίπεδο τάσεων (**a**) και στο $e - p'$ καταστατικό επίπεδο (**b**)

Fig. 2 Projection of the Critical State Line of M31 Sand in the $q - p'$ stress plane (**a**) and in the $e - p'$ state diagram (**b**)

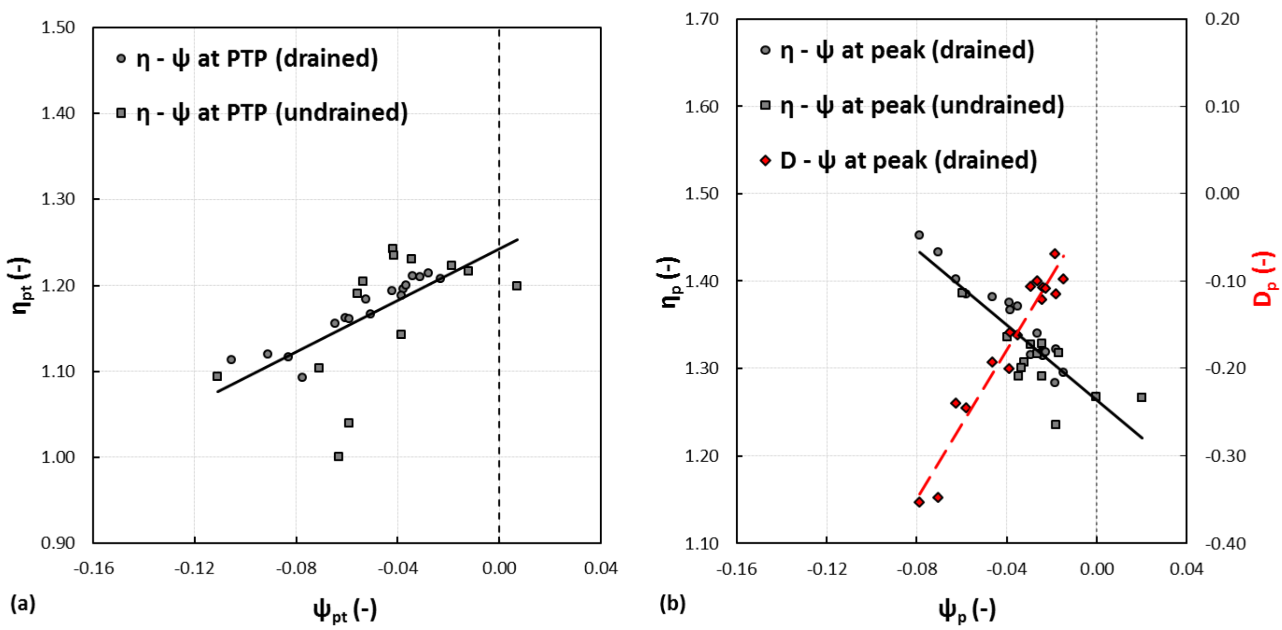

Σχ. 3 Λόγος τάσεων, η, σε συνάρτηση με την καταστατική παράμετρο, ψ, στο σημείο αλλαγής φάσης (**a**) και λόγος τάσεων, η, και λόγος διαστολικότητας, D, σε συνάρτηση με την καταστατική παράμετρο, ψ, στην κατάσταση κορυφαίας αστοχίας (**b**)

Fig. 3 Stress ratio, η, against the state parameter, ψ, at phase transformation point (**a**) and stress ratio, η, and dilatancy ratio, D, against the state parameter, ψ, at peak failure state (**b**)

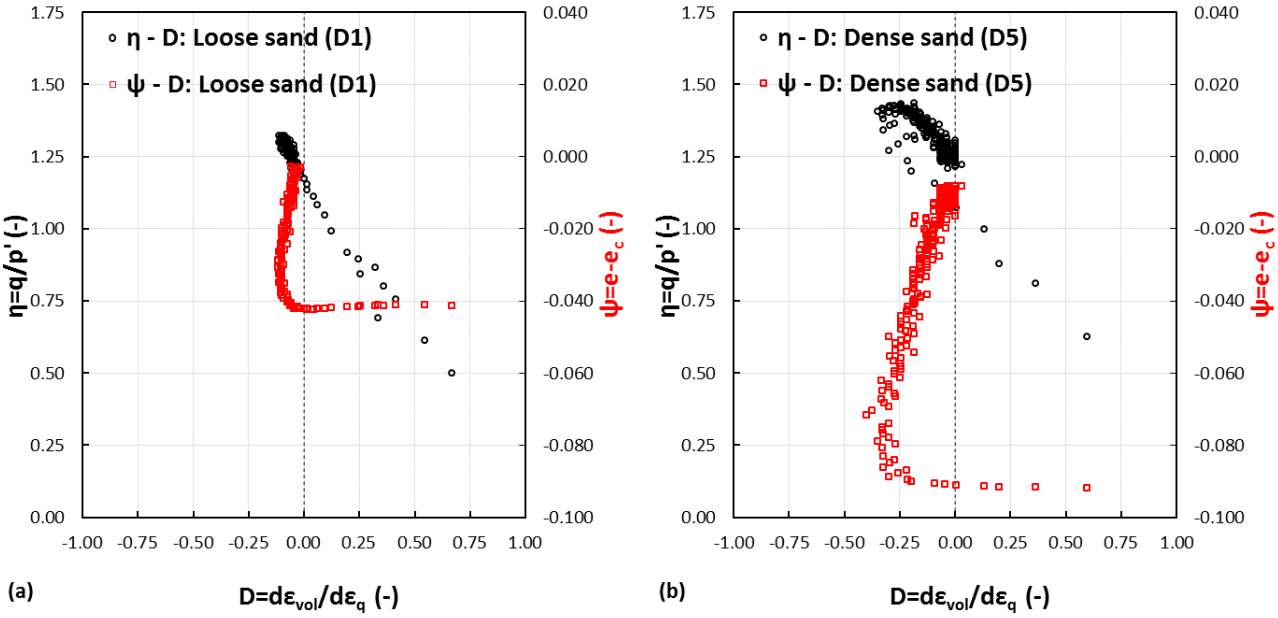

Σχ. 4 Σχέση λόγου τάσεων – διαστολικότητας, $\eta - D$, και εξέλιξη της καταστατικής παραμέτρου, ψ, σε συνάρτηση με τον λόγο διαστολικότητας, D, για χαλαρή (**a**) και πυκνή άμμο (**b**)

Fig. 4 Stress – dilatancy relationship, $\eta - D$, and evolution of state parameter, ψ, with the dilatancy ratio, D, for loose (**a**) and dense sand (**b**)

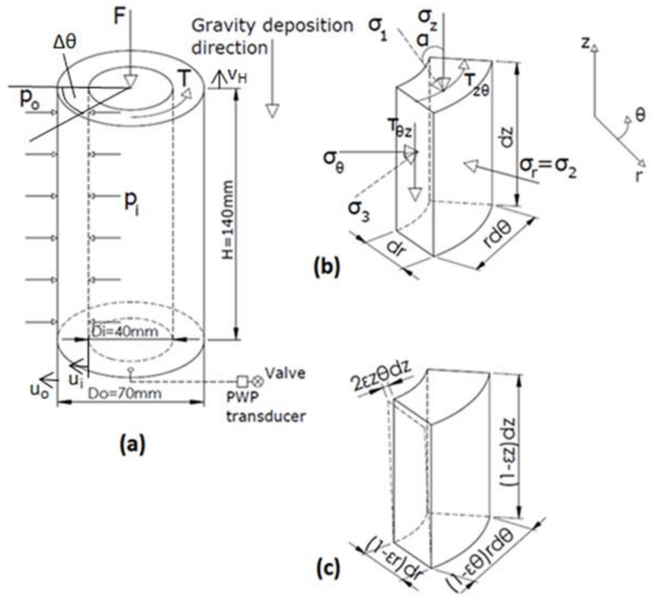

Σχ. 5 a Κοίλο κυλινδρικό δοκίμιο και επιβαλλόμενα συνοριακά φορτία. **b** Συνιστώσες τάσεως στο μη παραμορφωμένο εδαφικό στοιχείο. **c** Συνιστώσες παραμορφώσεως αντιστοιχούσες σε συνδυασμό πολύ-αξονικής και στρεπτικής παραμόρφωσης

Fig. 5 a Hollow cylindrical specimen and applied boundary loads. **b** Stress components on the undeformed soil element. **c** Strain components associated with the combined multiaxial and torsional deformation

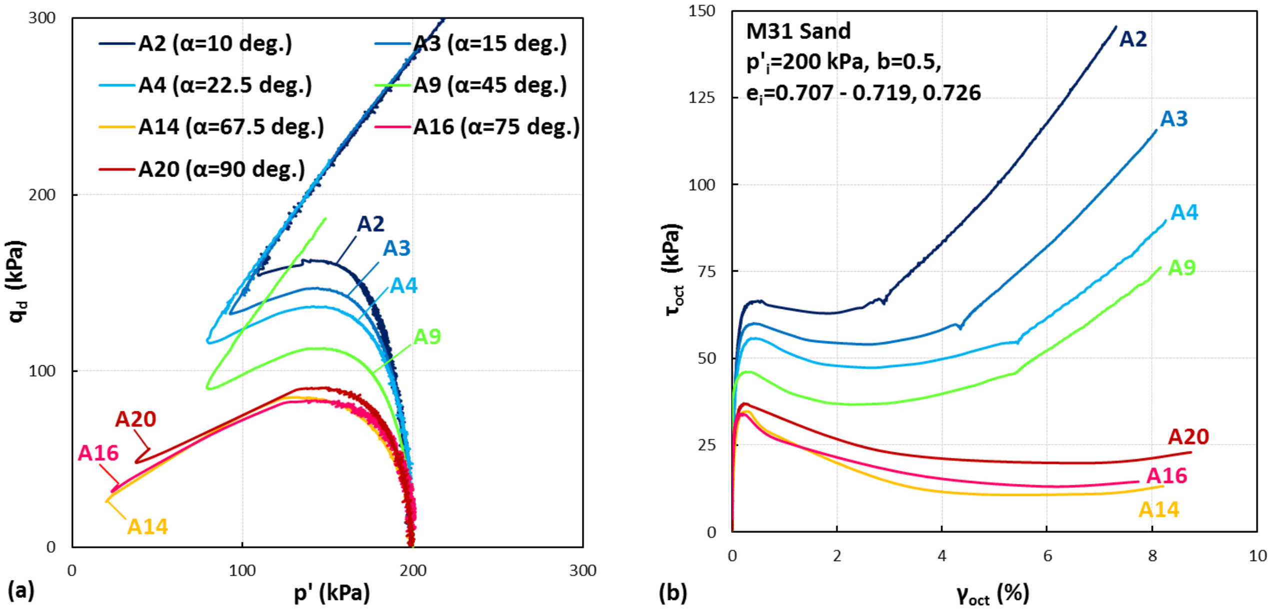

Σχ. 6 Απόκριση χαλαρής ισότροπα στερεοποιημένης άμμου σε μονοτονική φόρτιση εμποδιζόμενης στράγγισης με σταθερές *α*, *b* και *p* παραμέτρους **a** Ενεργές τασικές οδεύσεις στο $q_d - p'$ επίπεδο. **b** Καμπύλες οκταεδρικής διατμητικής τάσης – παραμόρφωσης ($\tau_{oct} - \gamma_{oct}$)

Fig. 6 Response of loose IC sand to monotonic undrained loading with constant *α*, *b* and *p* parameters **a** Effective stress paths in the $q_d - p'$ plane. **b** Octahedral shear stress – strain curves ($\tau_{oct} - \gamma_{oct}$)

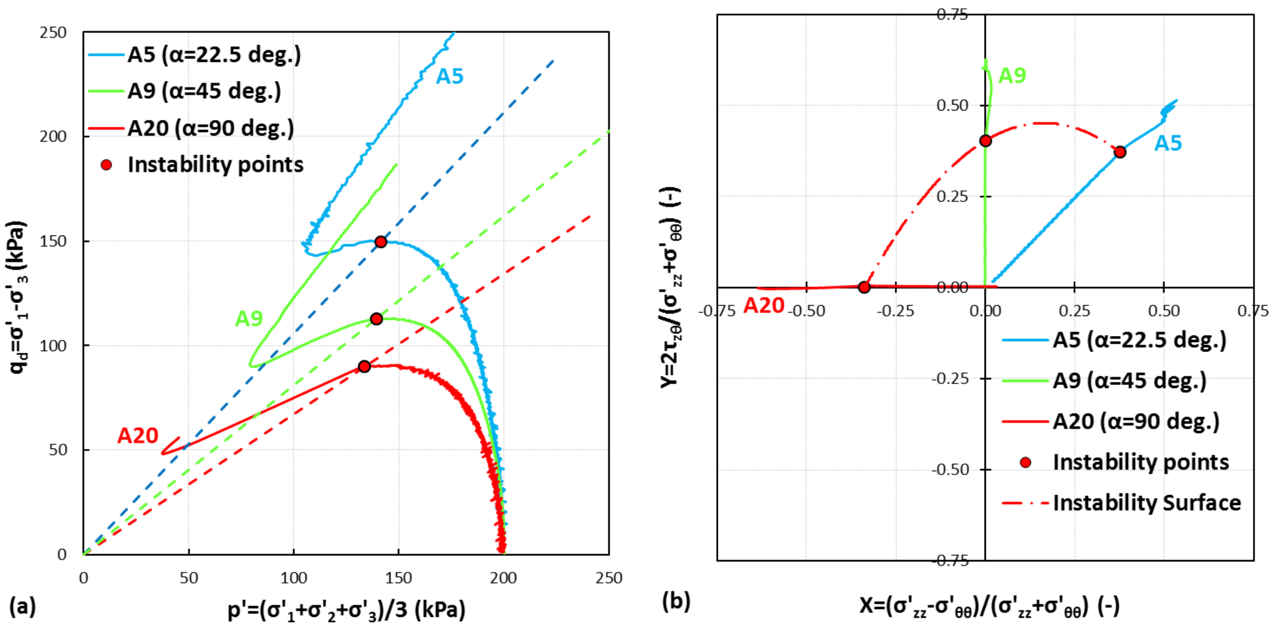

Σχ. 7 Ορισμός της Τοπικής Οριακής Επιφάνειας, των Γραμμών Αστάθειας και της Επιφάνειας Αστάθειας της χαλαρής ισότροπα στερεοποιημένης άμμου με τη βοήθεια των τασικών οδεύσεων **a** στο $q_d - p'$ επίπεδο και **b** στο $Y - X$ επίπεδο

Fig. 7 Definition of the Local Boundary Surface (Symes et al. 1984, Sibuya and Hight 1987), Instability Lines (Lade 1993) and Instability Surface (Triantafyllos et al. 2020a) of loose isotropically consolidated sand by means of stress paths **a** in the $q_d - p'$ plane and **b** in the $Y - X$ plane

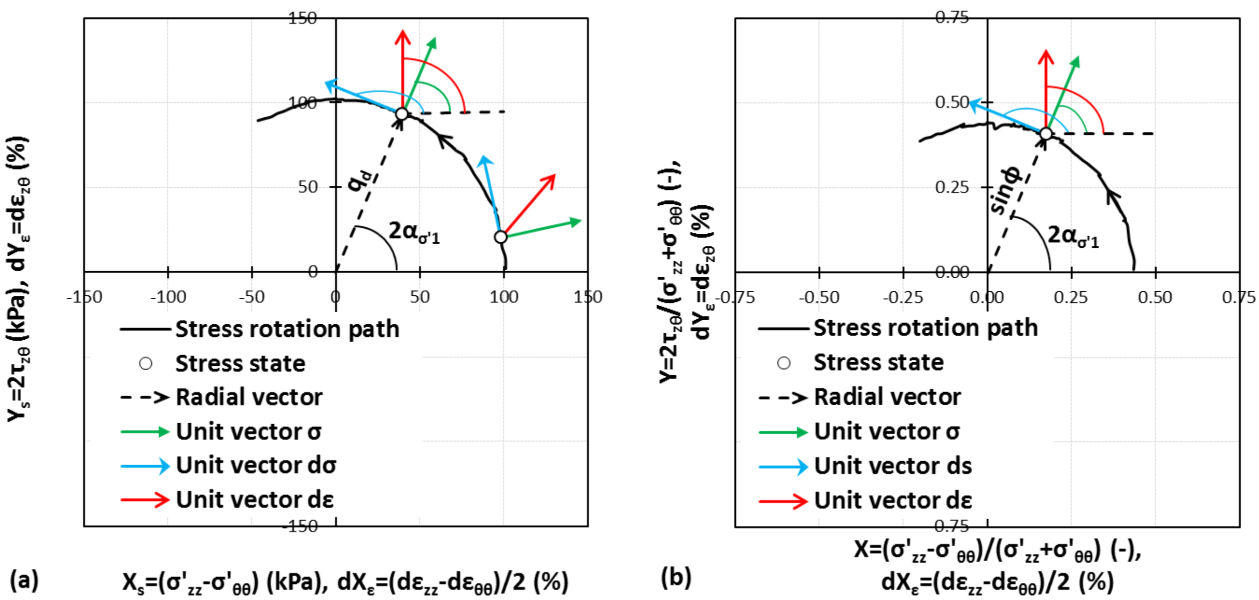

Σχ. 8 Τασική όδευση που σχετίζεται με στροφή των κύριων αξόνων τάσεως και κύριες κατευθύνσεις τάσεως, **σ**, προσαυξητικής τάσεως, d**σ**, και προσαυξητικής παραμορφώσεως, dε: **a** στο $Y_s - X_s$ επίπεδο και **b** στο $Y - X$ επίπεδο

Fig. 8 Stress path associated with rotation of the stress principal axes and principal directions of stress, **σ**, incremental stress, d**σ**, and incremental strain, dε: **a** in the $Y_s - X_s$ plane and **b** in the $Y - X$ plane

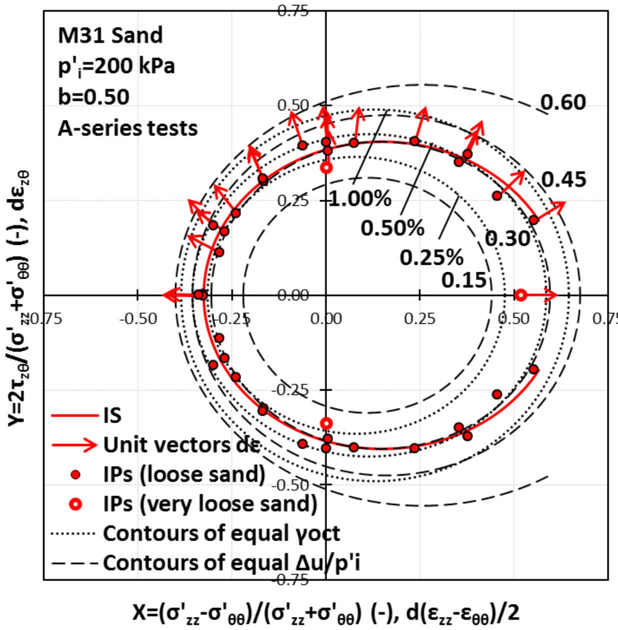

Σχ. 9 Επιφάνεια αστάθειας της χαλαρής ισότροπα στερεοποιημένης άμμου και περιγράμματα ίσων τιμών γ_{oct} και $\Delta u / p'_{in}$ κατά τη συστολική φάση απόκρισης στο $Y - X$ επίπεδο

Fig. 9 Instability surface (IS) of loose isotropically consolidated sand and contours of equal γ_{oct} and $\Delta u / p'_{in}$ during the contractive phase of response in the $Y - X$ plane

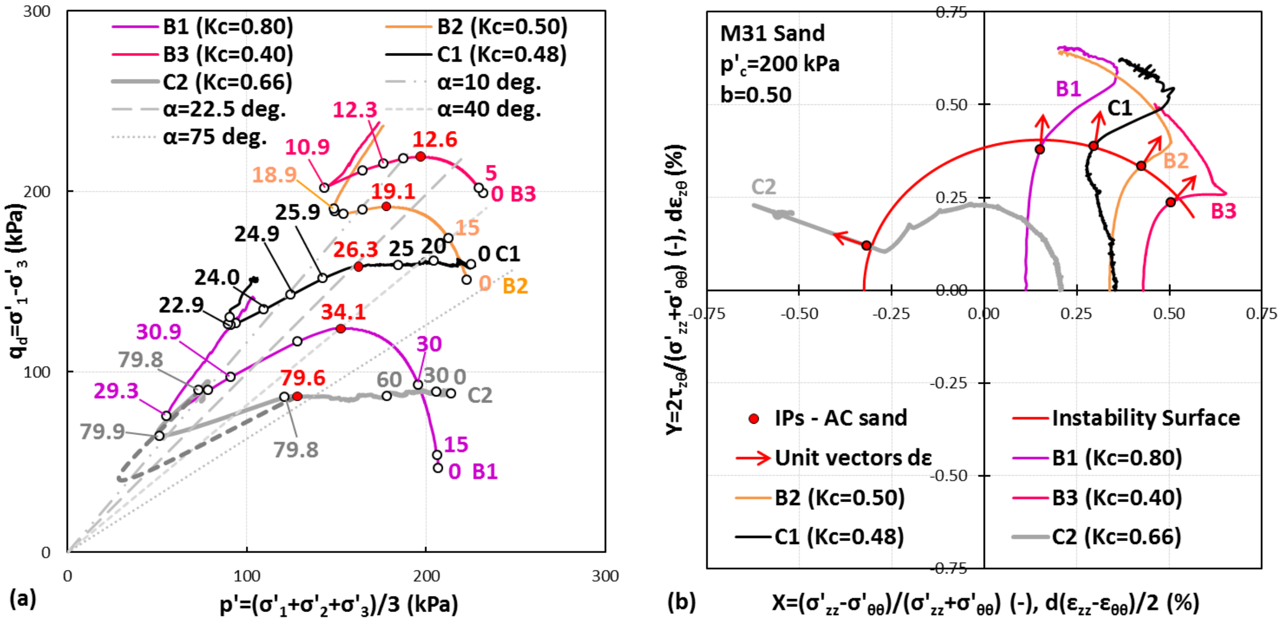

Σχ. 10 Απόκριση χαλαρής ανισότροπα στερεοποιημένης άμμου σε μονοτονική φόρτιση εμποδιζόμενης στράγγισης με στροφή των κύριων αξόνων τάσεως και σταθερές *b* και *p* παραμέτρους. **a** Ενεργές τασικές οδεύσεις στο $q_d - p'$ επίπεδο. **b** Τασικές οδεύσεις στο $Y - X$ επίπεδο

Fig. 10 Response of loose AC sand to monotonic undrained loading with rotating stress principal axes and constant *b* and *p* parameters. **a** Effective stress paths in the $q_d - p'$ plane. **b** Stress paths in the $Y - X$ plane

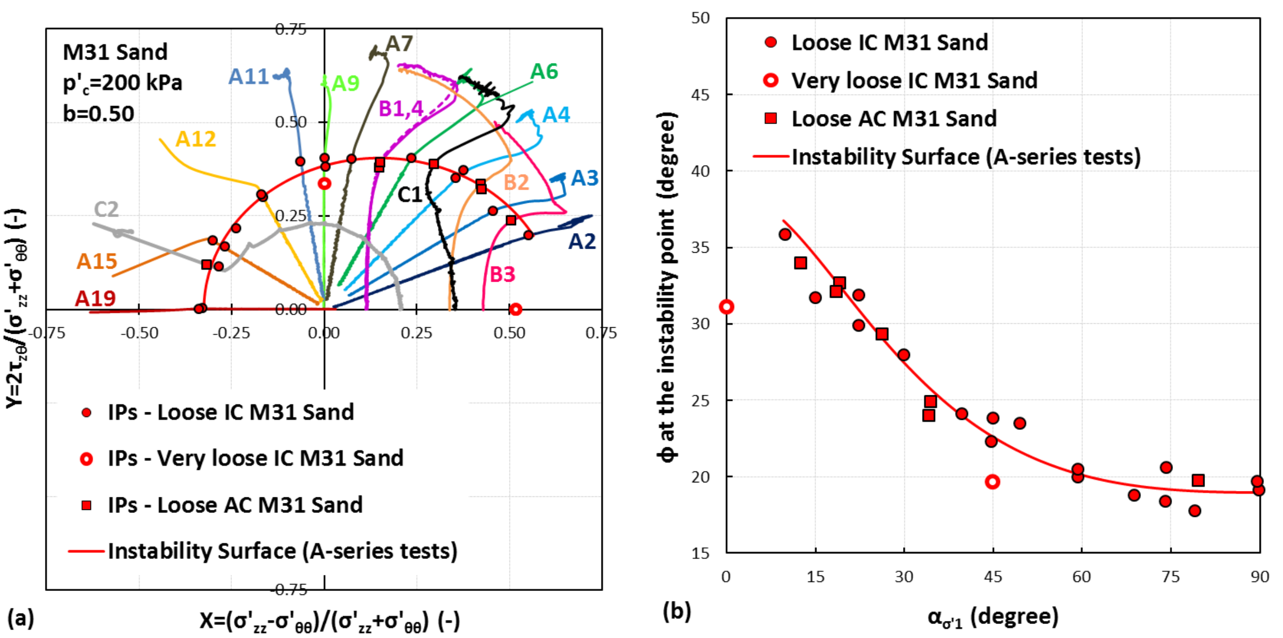

Σχ. 11 Σημεία αστάθειας χαλαρής άμμου για διαφορετικές ιστορίες στερεοποίησης και αστράγγιστης φόρτισης. **a** Σημεία αστάθειας και τασικές οδεύσεις στο $Y - X$ επίπεδο. **b** Σημεία αστάθειας στο $\varphi - \alpha_{\sigma'1}$ επίπεδο

Fig. 11 Instability points of loose sand for different histories of consolidation and undrained loading. **a** Instability points and stress paths in the $Y - X$ plane. **b** Instability points in the $\varphi - \alpha_{\sigma'1}$ plane

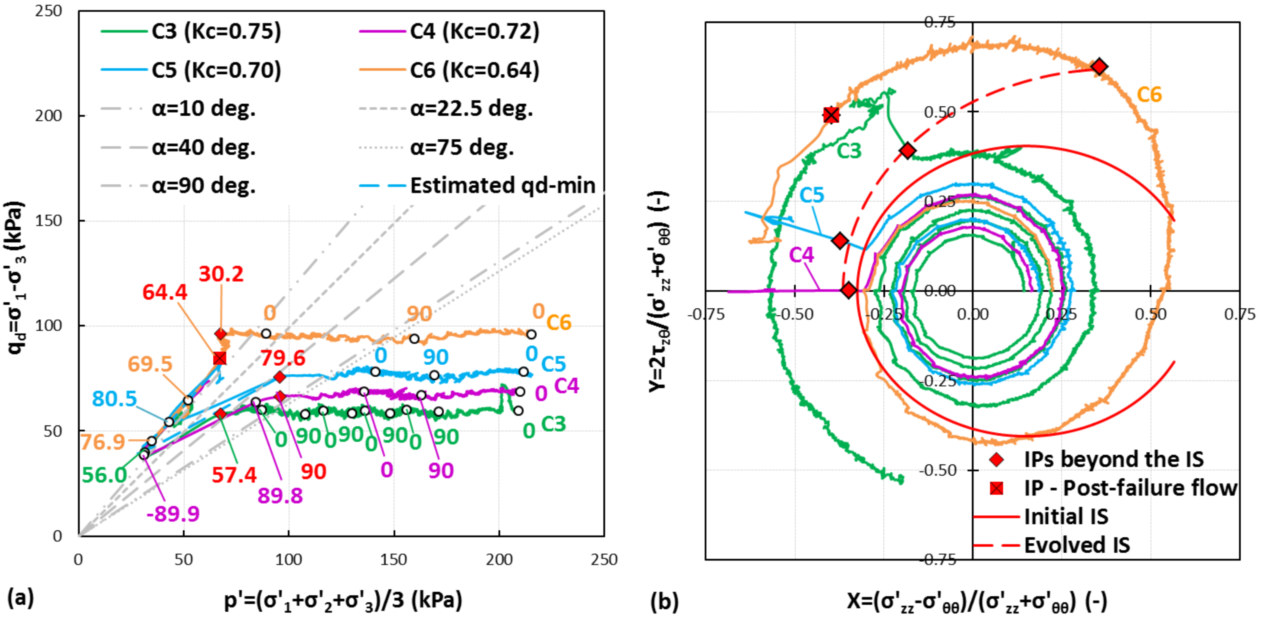

Σχ. 12 Απόκριση χαλαρής ανισότροπα στερεοποιημένης άμμου σε μονοτονική φόρτιση εμποδιζόμενης στράγγισης με στροφή των κύριων αξόνων τάσεως και σταθερές q, p και b παραμέτρους. **a** Ενεργές τασικές οδεύσεις στο $q_d - p'$ επίπεδο. **b** Τασικές οδεύσεις στο $Y - X$ επίπεδο

Fig. 12 Response of loose AC sand to monotonic undrained loading with rotating stress principal axes and constant q, p and b parameters. **a** Effective stress paths in the $q_d - p'$ plane. **b** Stress paths in the $Y - X$ plane

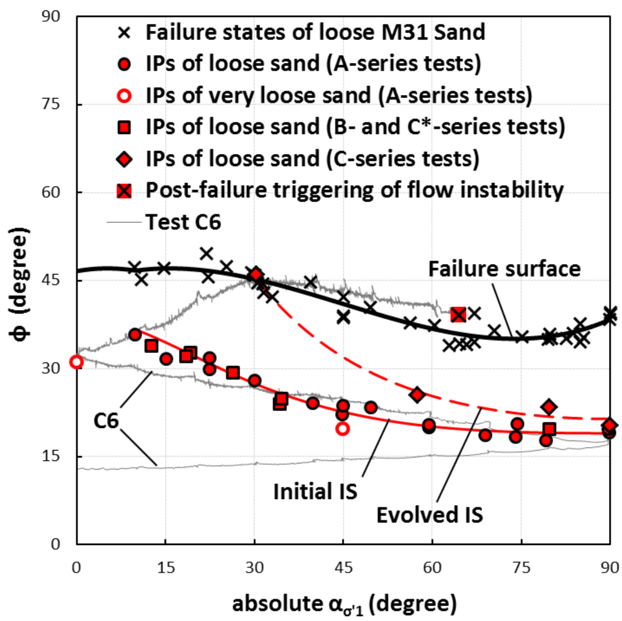

Σχ. 13 Επίδραση της ιστορίας τάσεων στη συνθήκη αστάθειας χαλαρής άμμου: γωνία διατμητικής αντίστασης, φ, σε συνάρτηση με τη γωνία κύριας κατεύθυνσης τάσεως, $\alpha_{\sigma'1}$, στα σημεία αστάθειας και κορυφαίας αστοχίας

Fig. 13 Stress history effects on the flow instability condition of loose sand: mobilised angle of shearing resistance, φ, against the principal stress direction angle, $\alpha_{\sigma'1}$, at the instability and peak-failure states

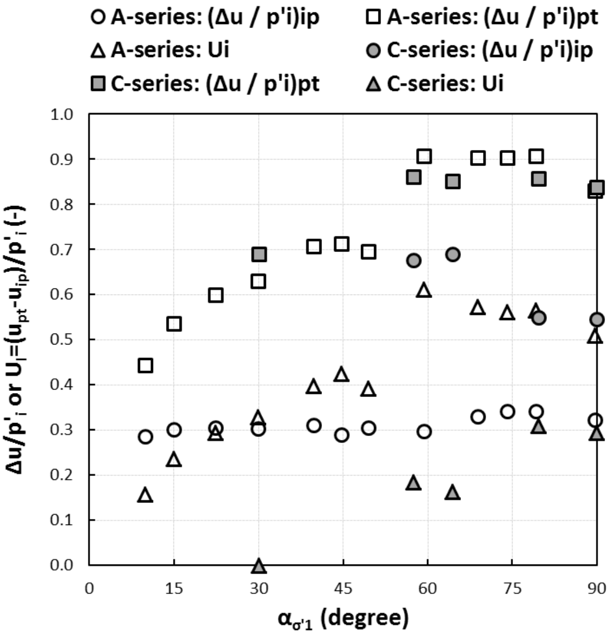

Σχ. 14 Επίδραση της ιστορίας παραμορφώσεων στη συνθήκη αστάθειας και στη συμπεριφορά της χαλαρής άμμου κατά τη μονότονη ρευστοποίηση: κανονικοποιημένη υπερπίεση του ύδατος πόρων, Δu / p'_{in}, και παράμετρος μονότονης ρευστοποίησης, U_I, σε συνάρτηση με τη γωνία κύριας κατεύθυνσης τάσεως, $\alpha_{\sigma'1}$, στα σημεία αστάθειας και αλλαγής φάσης

Fig. 14 Strain history effects on the triggering condition and deformation pattern of flow of loose sand: normalised excess pore-water pressure, Δu / p'_{in}, and flow parameter, U_I, against the principal stress direction angle, $\alpha_{\sigma'1}$, at the instability and phase-transformation points

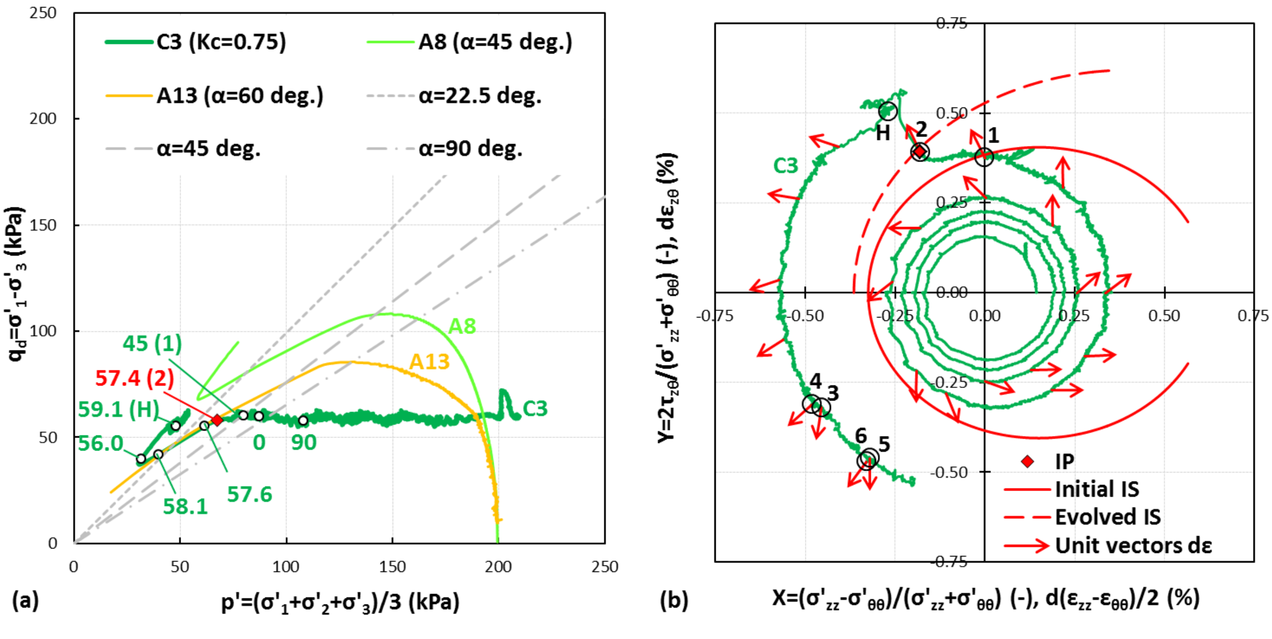

Σχ. 15 Τασική όδευση της δοκιμής C3: **a** στο $q_d - p'$ επίπεδο και **b** στο $Y - X$ επίπεδο

Fig. 15 Stress path of test C3: **a** in the $q_d - p'$ plane and **b** in the $Y - X$ plane

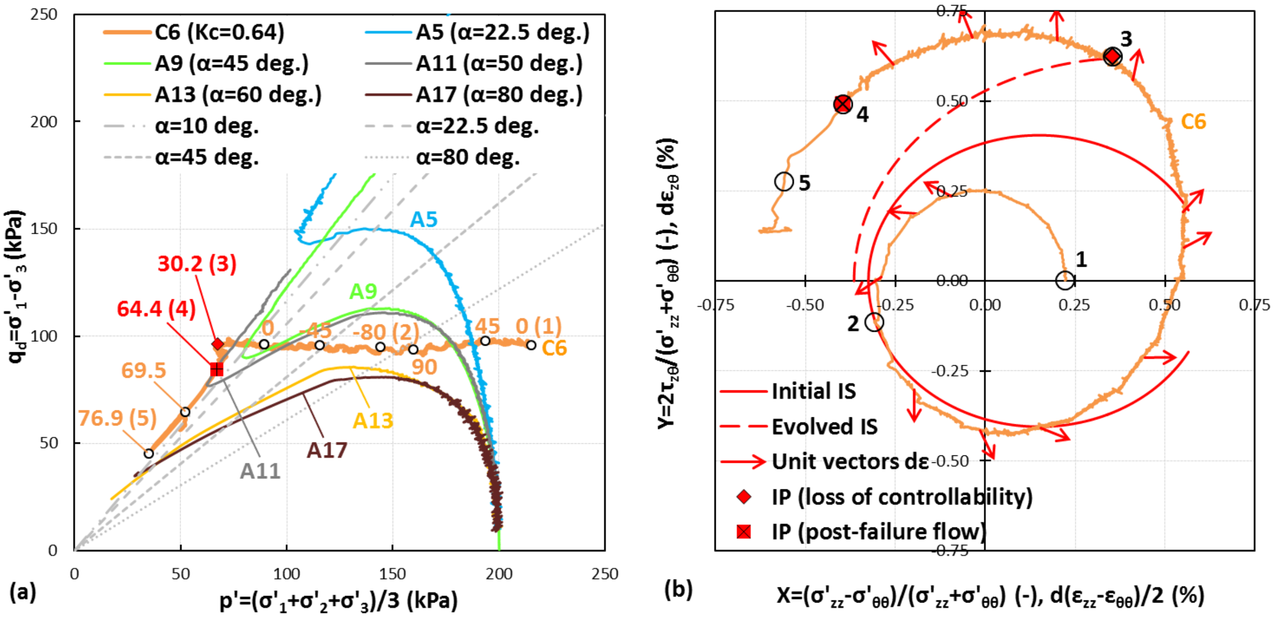

Σχ. 16 Τασική όδευση της δοκιμή C6: **a** στο $q_d - p'$ επίπεδο και **b** στο $Y - X$ επίπεδο

Fig. 16 Stress path of test C6: **a** in the $q_d - p'$ plane and **b** in the $Y - X$ plane

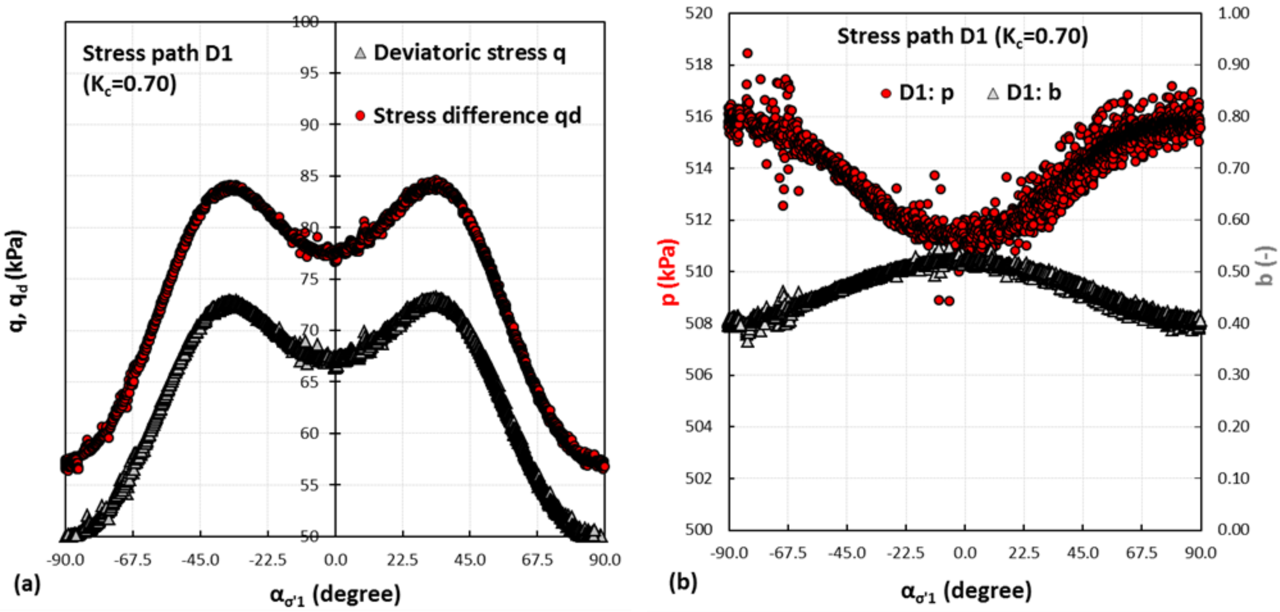

Σχ. 17 Χαρακτηριστικά της τασικής όδευσης D1. **a** Περιοδική μεταβολή των τάσεων q και q_d με τη γωνία $\alpha_{\sigma'1}$. **b** Περιοδική μεταβολή της τάσης p και της παραμέτρου b με τη γωνία $\alpha_{\sigma'1}$

Fig. 17 Characteristics of the stress path D1. **a** Periodic change of q and q_d with $\alpha_{\sigma'1}$. **b** Periodic change of p and b with $\alpha_{\sigma'1}$

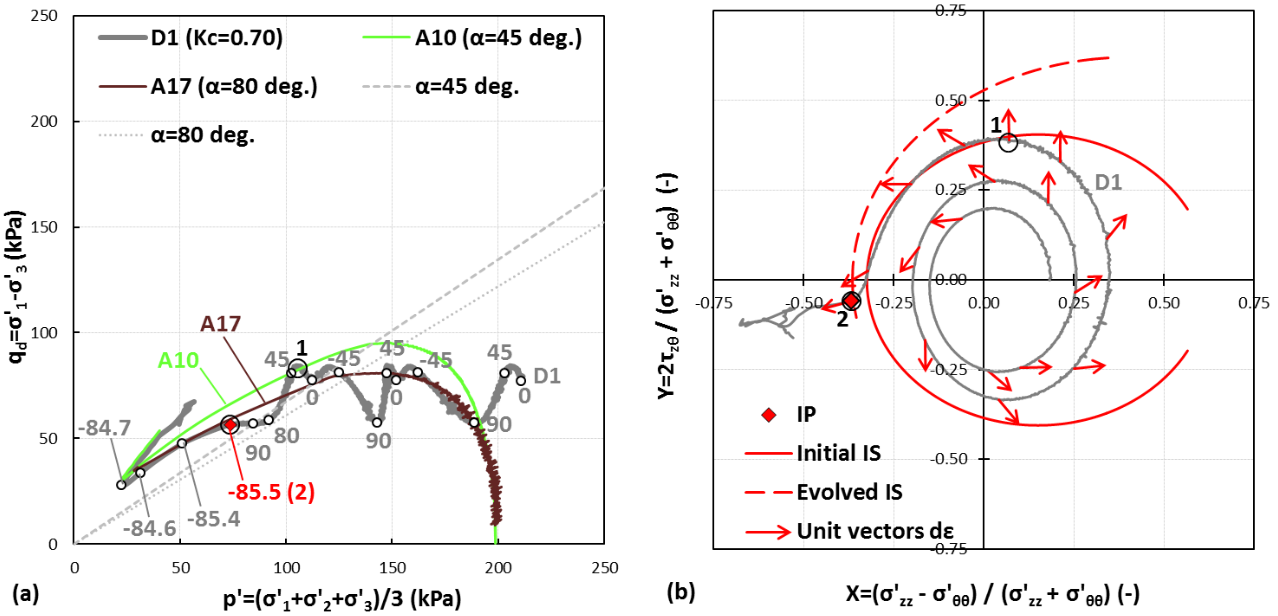

Σχ. 18 Τασική όδευση της δοκιμή D1: **a** στο $q_d - p'$ επίπεδο και **b** στο $Y - X$ επίπεδο

Fig. 18 Stress path of test D1: **a** in the $q_d - p'$ plane and **b** in the $Y - X$ plane

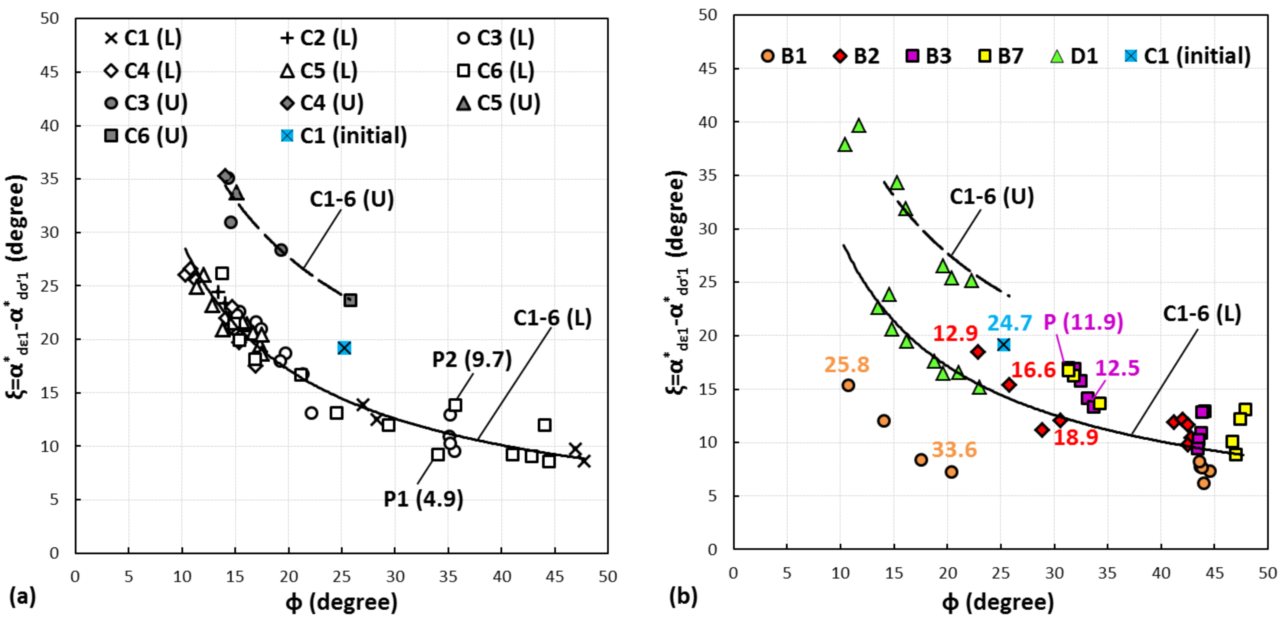

Σχ. 19 Επίδραση της ιστορίας τάσεων – παραμορφώσεων στη μη ομοαξονική συμπεριφορά της άμμου υπό φόρτιση εμποδιζόμενης στράγγισης με στροφή των κύριων αξόνων τάσεως. **a** Σχέση μεταξύ των γωνιών ξ και φ στις δοκιμές τύπου C. **b** Σχέση μεταξύ των γωνιών ξ και φ στις δοκιμές τύπου B και στη δοκιμή D1

Fig. 19 Stress – strain history effects on the non-coaxiality of sand under undrained loading with rotation of the stress principal axes. **a** Relationship between the angles ξ and φ in the C-series tests. **b** Relationship between the angles ξ and φ in the B-series tests and in test D1

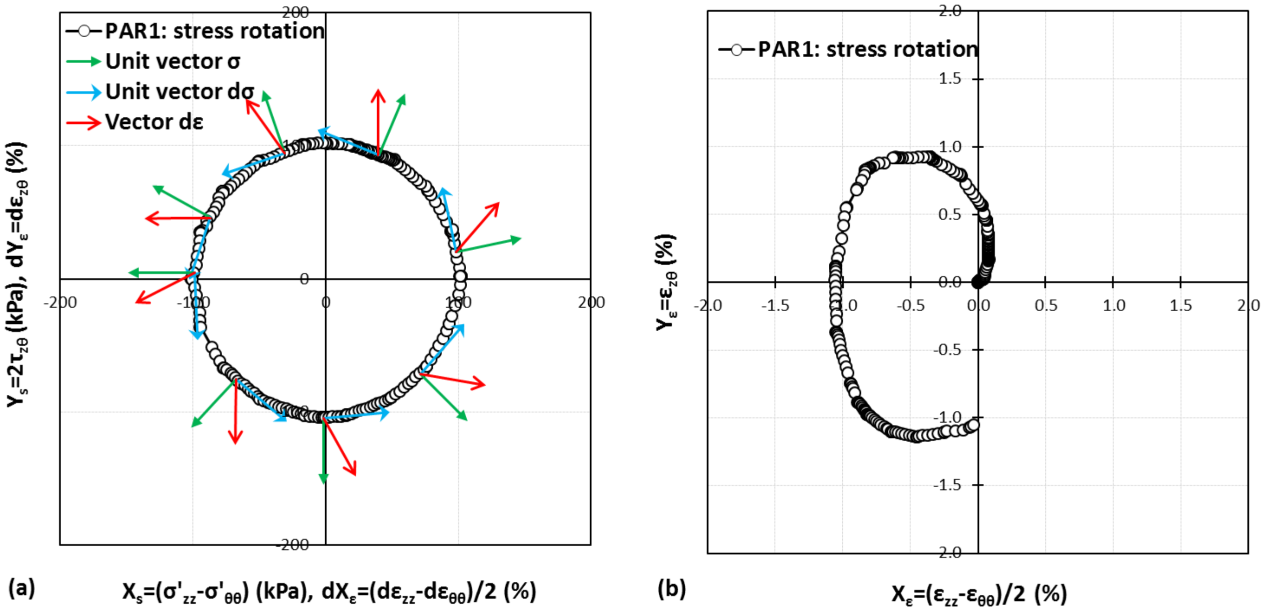

Fig. 20 Στροφή των κύριων αξόνων τάσεως με σταθερές τις ενεργές κύριες τιμές τάσεως στη δοκιμή PAR1 με η = 1.01, b = 0 και p' = 100 kPa. **a** Τασική όδευση στο $Y_s - X_s$ επίπεδο. **b** Όδευση παραμορφώσεως στο $Y_\varepsilon - X_\varepsilon$ επίπεδο

Fig. 20 Rotation of the stress principal axes at constant effective stress principal values in test PAR1 at η = 1.01, b = 0 and p' = 100 kPa. **a** Stress path in the $Y_s - X_s$ plane. **b** Strain path in the $Y_\varepsilon - X_\varepsilon$ plane

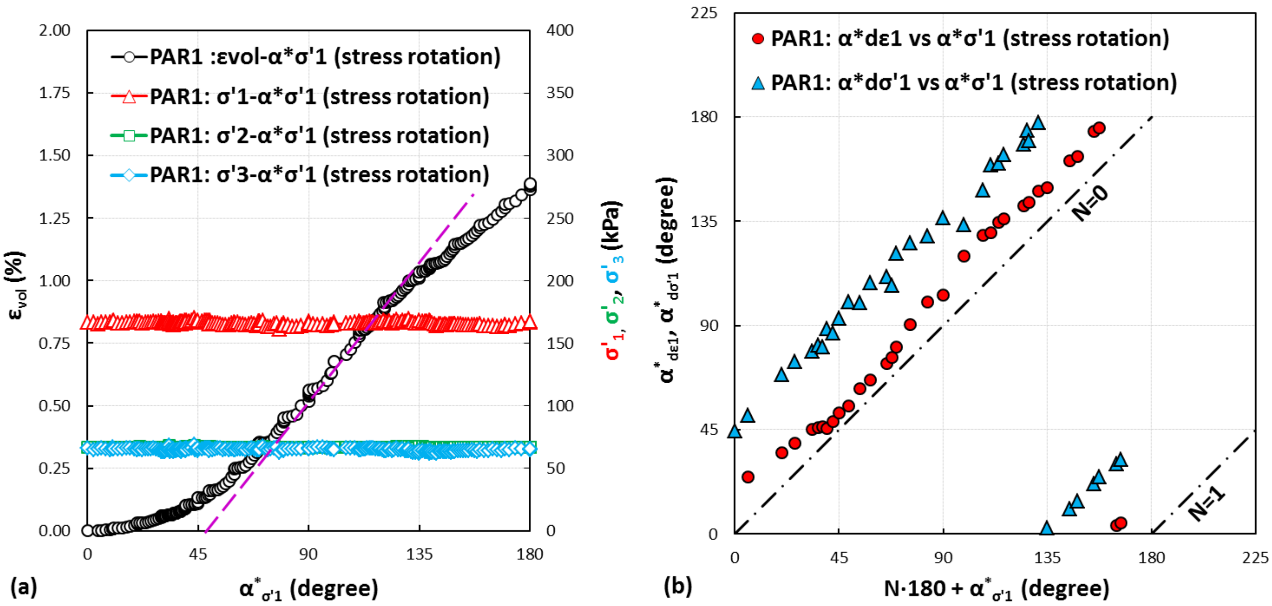

Fig. 21 Στροφή των κύριων αξόνων τάσεως με σταθερές τις ενεργές κύριες τιμές τάσεως στη δοκιμή PAR1 με η = 1.01, b = 0 και p' = 100 kPa. **a** Εξέλιξη των μεγεθών ε_{vol}, σ'_1, σ'_2 και σ'_3 με τη γωνία $\alpha^*_{\sigma'1}$. **b** Εξέλιξη των μεγεθών $\alpha^*_{d\varepsilon1}$ και $\alpha^*_{d\sigma'1}$ με τη γωνία $\alpha^*_{\sigma'1}$

Fig. 21 Rotation of the stress principal axes at constant effective stress principal values in test PAR1 at η = 1.01, b = 0 and p' = 100 kPa. **a** Evolution of ε_{vol}, σ'_1, σ'_2 and σ'_3 with $\alpha^*_{\sigma'1}$. **b** Evolution of $\alpha^*_{d\varepsilon1}$ και $\alpha^*_{d\sigma'1}$ with $\alpha^*_{\sigma'1}$

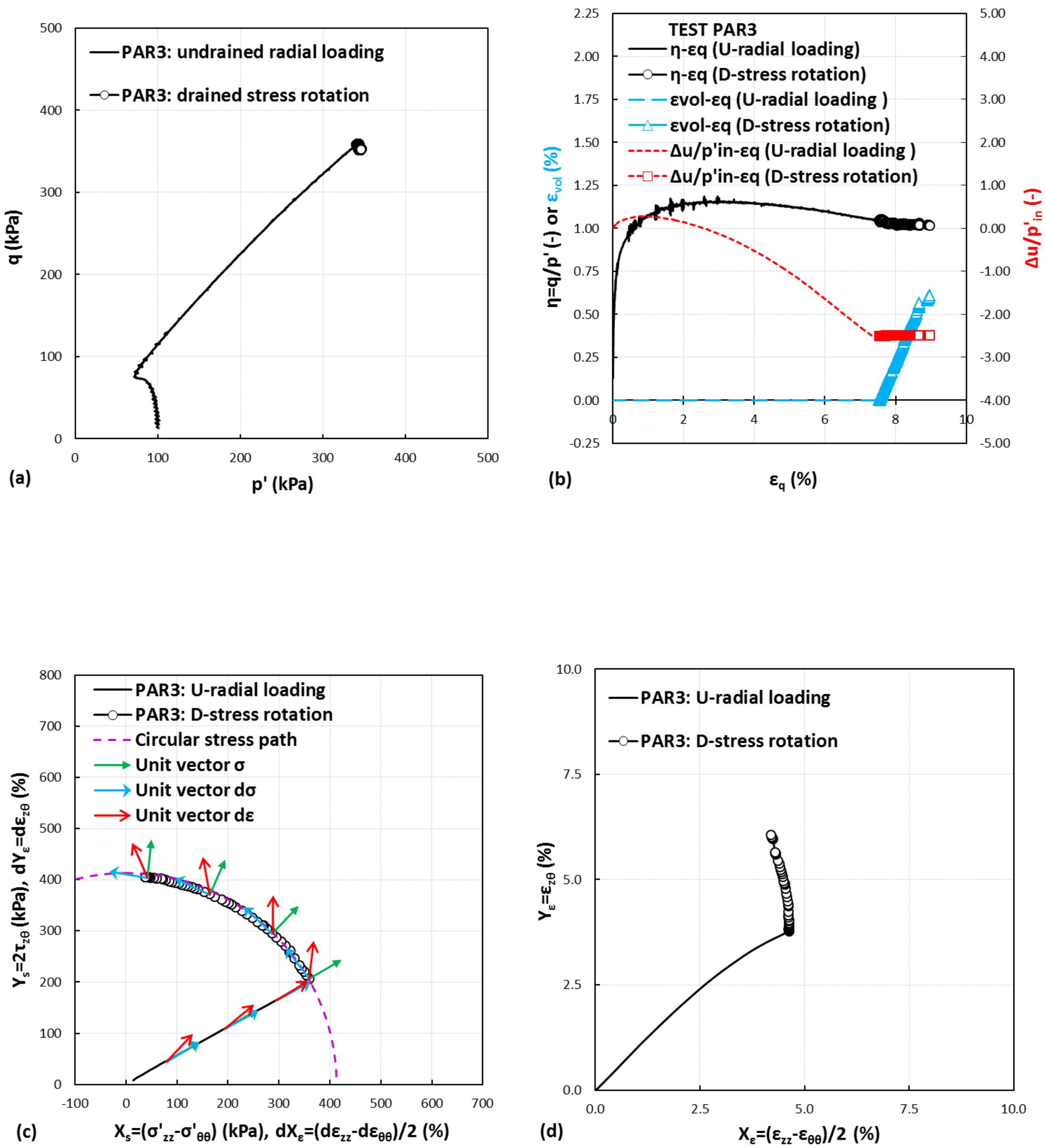

Fig. 22 Στροφή των κύριων αξόνων τάσεως με σταθερές τις ενεργές κύριες τιμές τάσεως στη δοκιμή PAR3 με η = 1.05, b = 0.5 και p' = 343 kPa. **a** Τασική όδευση στο $q - p'$ επίπεδο. **b** Εξέλιξη των μεγεθών η, ε_{vol} και Δu / p'_i με την παραμόρφωση ε_q. **c** Τασική όδευση στο $Y_s - X_s$ επίπεδο. **d** Όδευση παραμορφώσεως στο $Y_\varepsilon - X_\varepsilon$ επίπεδο

Fig. 22 Rotation of the stress principal axes at constant effective stress principal values in test PAR3 at η = 1.05, b = 0.5 and p' = 343 kPa. **a** Stress path in the $q - p'$ plane. **b** Evolution of η, ε_{vol} and Δu / p'_i with ε_q. **c** Stress path in the $Y_s - X_s$ plane. **d** Strain path in the $Y_\varepsilon - X_\varepsilon$ plane

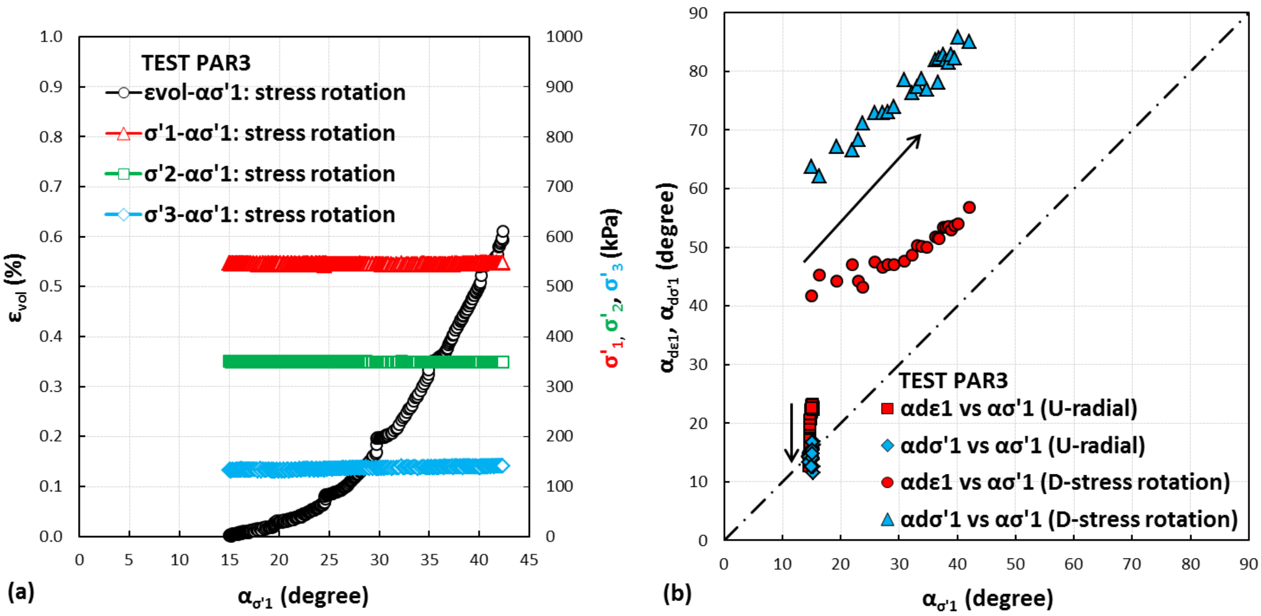

Fig. 23 Στροφή των κύριων αξόνων τάσεως με σταθερές τις ενεργές κύριες τιμές τάσεως στη δοκιμή PAR3 με η = 1.05, b = 0.5 και p' = 343 kPa. **a** Εξέλιξη των μεγεθών ε_{vol}, σ'_1, σ'_2 και σ'_3 με τη γωνία $\alpha^*_{\sigma'1}$. **b** Εξέλιξη των μεγεθών $\alpha^*_{d\varepsilon1}$ και $\alpha^*_{d\sigma'1}$ με τη γωνία $\alpha^*_{\sigma'1}$

Fig. 23 Rotation of the stress principal axes at constant effective stress principal values in test PAR3 at η = 1.05, b = 0.5 and p' = 343 kPa. **a** Evolution of ε_{vol}, σ'_1, σ'_2 and σ'_3 with $\alpha^*_{\sigma'1}$. **b** Evolution of $\alpha^*_{d\varepsilon1}$ και $\alpha^*_{d\sigma'1}$ with $\alpha^*_{\sigma'1}$

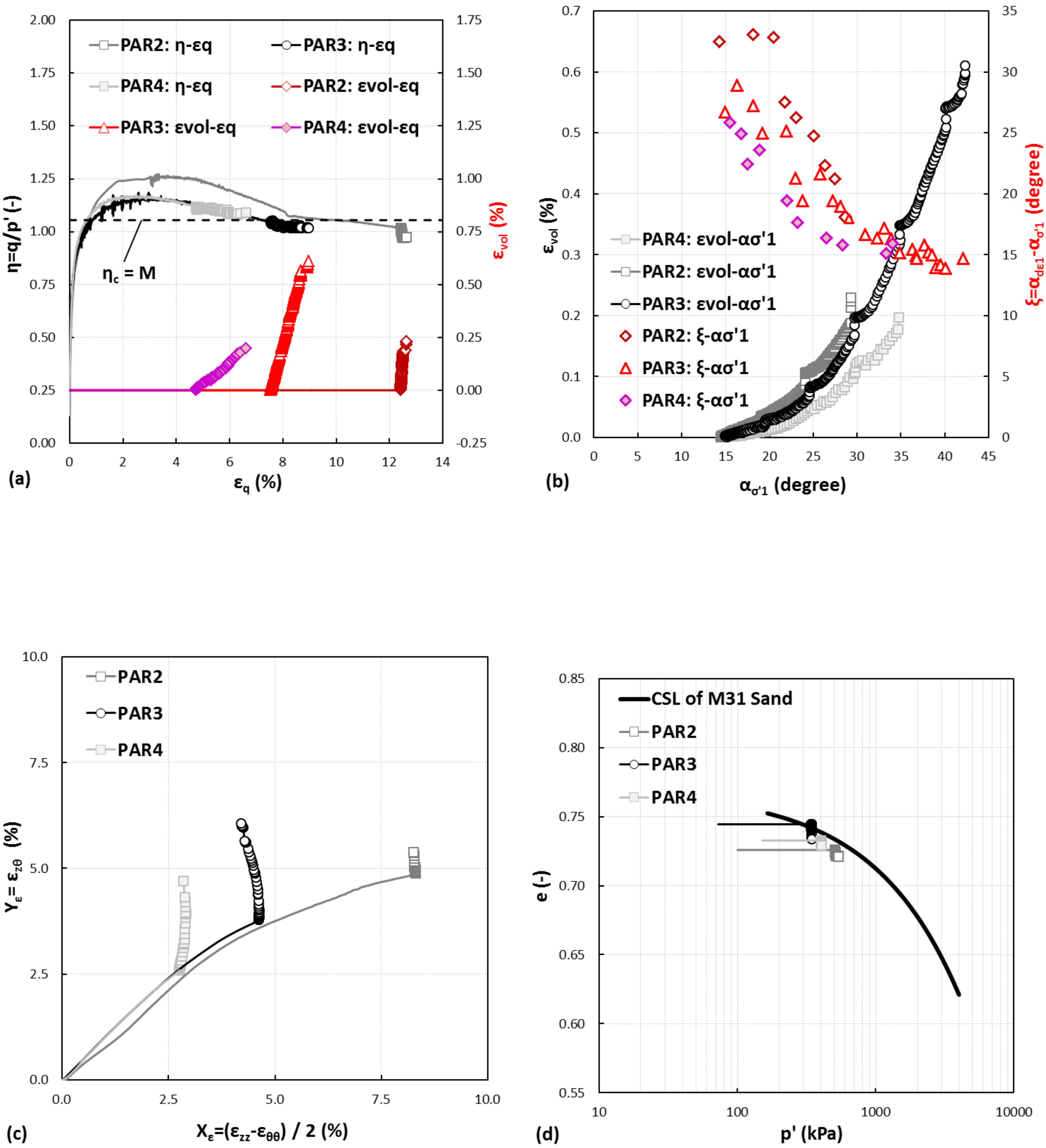

Σχ. 24 Επίδραση της ιστορίας τάσεων – παραμορφώσεων, πλησιάζοντας την κρίσιμη κατάσταση, στη διαστολικότητα και μη ομοαξονικότητα της άμμου κατά τη στροφή των κύριων αξόνων τάσεως. **a** Εξέλιξη των μεγεθών η και ε_{vol} με την παραμόρφωση ε_q. **b** Εξέλιξη των μεγεθών ε_{vol} και ξ με τη γωνία $\alpha_{\sigma'1}$. **c** Οδεύσεις παραμορφώσεως στο $Y_\varepsilon - X_\varepsilon$ επίπεδο. **d** Εξέλιξη της κατάστασης της άμμου στο $e - p'$ επίπεδο

Fig. 24 Stress – strain history effects, nearing critical state, on the dilatancy and non-coaxiality of sand during rotation of the stress principal axes. **a** Evolution of η and ε_{vol} with ε_q. **b** Evolution of ε_{vol} and ξ with $\alpha_{\sigma'1}$. **c** Strain paths in the $Y_\varepsilon - X_\varepsilon$ plane. **d** Evolution of the state of sand in the $e - p'$ plane

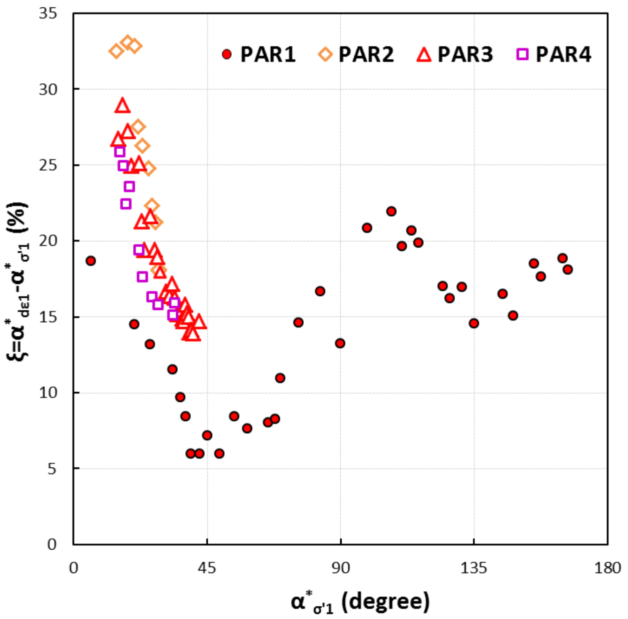

Σχ. 25 Επίδραση της ιστορίας τάσεων – παραμορφώσεων στη μη ομοαξονικότητα της άμμου κατά τη στροφή των κύριων αξόνων τάσεως με σταθερές ενεργές κύριες τιμές τάσεως: Εξέλιξη της γωνίας ξ με τη γωνία $\alpha^{*}_{\sigma'1}$

Σχ. 25 Stress – strain history effects on the non-coaxiality of sand under rotation of the stress principal axes at constant effective stress principal values: Evolution of the angle ξ with angle $\alpha^{*}_{\sigma'1}$

EXPERIMENTAL STUDY OF THE ANISOTROPIC FLOW DEFORMATION AND CRITICAL STATE OF SAND

Doctoral Thesis

by

Panayiotis K. Triantafyllos

EXTENDED ABSTRACT

This thesis investigates experimentally the mechanical behaviour of sand under triaxial and generalised loading. The anisotropic flow deformation and critical state of M31 Sand were investigated using the hollow cylinder apparatus and two triaxial apparatuses of the National Technical University of Athens, all of which were either updated or modified for the needs of the present study. Monotonic and cyclic loading was imposed on water pluviated sand specimens under a broad range of consolidation effective stresses, $p'_c = (\sigma'_{1c} + \sigma'_{2c} + \sigma'_{3c}) / 3$, and stress ratios, $K_c = \sigma'_{3c} / \sigma'_{1c}$, with fixed or rotating stress principal axes (PA) and with two different values of the intermediate principal stress parameter, $b = (\sigma'_2 - \sigma'_3) / (\sigma'_1 - \sigma'_3)$.

The results of monotonic triaxial compression tests indicate the existence of a unique critical state line in the $p' - e - q$ space for M31 Sand, irrespective of the initial value of void ratio and mean effective stress and drainage conditions. The state parameter, ψ, proposed by Been and Jefferies (1985) normalises the strength and dilatancy characteristics of sand while the stress – dilatancy relationship depends on state. The results of monotonic undrained loading tests at different fixed directions of the σ'_1-axis with respect to the vertical, measured by the angle $\alpha_{\sigma'1}$, and with constant p and b = 0.5 showed that the inherent anisotropy affects the strength and deformability of isotropically consolidated loose sand at the instability point, phase transformation point and peak-failure state. The response of sand becomes, in general, more contractive and less stiff when the angle $\alpha_{\sigma'1}$ increases yet the weakest response is observed when one of the maximum stress obliquity planes tends to align at failure with the horizontal bedding plane. The same amount of shear strain or normalised excess pore-water pressure is accumulated in the contractive phase of response at a lower deviatoric stress ratio when $\alpha_{\sigma'1}$ is higher. Moreover, flow instability is triggered at a lower deviatoric stress ratio when $\alpha_{\sigma'1}$ is higher. Despite the fixity of the stress PA the deformation of sand is (weakly) non-coaxial up to the peak-failure state,

becoming coaxial only after intense dilative straining post-peak, while the principal direction of incremental stain is biased towards $\alpha_{d\varepsilon 1}$ = +45º, possibly because sliding occurs more easily along the horizontal bedding plane.

Undrained loading tests were conducted on anisotropically consolidated loose sand with monotonically rotating stress PA at constant p and b = 0.5 and with either monotonically increasing, constant or cyclically changing deviatoric stress, q, in order to investigate the effect of consolidation and loading history on the mechanical behaviour of sand. It was found that the combinations of $\varphi = \sin^{-1} [(\sigma'_1 - \sigma'_3) / (\sigma'_1 + \sigma'_3)]$ and $\alpha_{\sigma'1}$ at the triggering of flow instability are not unique, albeit being stated differently in previous studies (Nakata et al. 1998, Sivathayalan and Vaid 2002). On the contrary, the triggering condition and deformation pattern of flow depend on the stress - strain history, including the effect of K_c and incremental stress direction; a new flow parameter indicates this dependence. It was also shown that a small stress disturbance involving rotation of the stress PA can trigger flow when the sand is consolidated at low K_c, e.g. under K_o-conditions. For higher values of K_c the rotation of the stress PA at constant q may still induce plastic contraction, flow instability and failure of sand. Apart from the effects of stress - strain history on bifurcation the inherent anisotropy also plays an important role since the triggering of both diffuse and localised instabilities occurs preferably at stress states corresponding to unfavourable deformation kinematics, i.e. to shearing and sliding along the horizontal bedding plane.

The rotation of the stress PA is associated with strong non-coaxiality that persists past the state of peak failure. Distinct non-coaxiality patterns and elastic - plastic coupling, associated with the unloading of the non-diagonal component of the stress tensor, were observed during the first cycles of stress rotation, at low deviatoric stress ratio, when the deviatoric stress was kept constant. The non-coaxiality angle, ξ, decreases with the deviatoric stress ratio in both non-coaxiality patterns, though, the sand ultimately deforms in a steady state corresponding to a stabilised angle of non-coaxiality, mean effective stress and deviatoric stress ratio, only to be arrested by the triggering of diffuse or localised instabilities. These non-coaxiality patterns are, in general, independent of the value of K_c and the number of the previous stress rotation cycles and are also observed in the case that the deviatoric stress changes periodically. On the other hand, distinct non-coaxiality patterns are observed before peak failure depending on the value of K_c when the rate of stress rotation decreases as the deviatoric stress increases, though, the differences become less pronounced past the peak-failure state. Interestingly, stronger non-coaxiality corresponds to a lower K_c and the effect of pre-shearing on non-coaxiality appears to be more important than the effect of the rate of stress rotation, which has been previously pointed out by Gutierrez et al. (1991).

Among the novel findings of this study are those indicating that the stress state of loose sand subjected to undrained principal stress rotation at constant deviatoric stress may move along the direction of isotropic stress unloading from the consolidation state to the failure state without triggering flow. This behaviour is a contrast to the predictions of recent models developed within the framework of Bifurcation Theory which indicate that the direction of isotropic unloading belongs to the set of unstable directions of loose sand even at low deviatoric stress ratio, away from the peak failure state (Darve and Laouafa 2000, Darve et al. 2004, Sibille at al. 2007, Prunier et al. 2009). Once the failure surface has been reached it was shown that a quasi-static diffuse instability can be triggered under increasing effective stresses and decreasing stress ratio, followed by a dynamic diffuse instability under decreasing stresses and stress ratio. Consequently, the experimental results verify for the first time the predictions of the numerical analyses by Darve that instability may occur under increasing effective stresses and decreasing stress ratio (Darve and Laouafa 2000, Darve et al. 2004, Sibille at al. 2007, Prunier et al. 2009).

This study shows that sand exhibits strong non-coaxiality and contracts whenever the loading with fixed stress PA is interrupted by a continuous rotation of the stress PA. The degree of non-coaxiality and associated contractancy becomes higher when the previous shearing becomes more intense in terms of shear strain accumulation. The novel findings reported herein indicate that the influence of pre-shearing on sand's behaviour is more important than the influence of the degree of stress rotation and the level of η, p', e and b, reported in previous studies (Miura et al. 1986, Gutierrez et al. 1991, Li and Yu 2010, Tong et al. 2010 and 2014), but diminishes gradually as the stress rotation continues. Specifically, it is shown that sand exhibits strong non-coaxiality and contracts immediately upon initiating the rotation of the stress PA at constant effective stress principal values (PV) very close to critical state despite the fact that it was previously dilating on the failure surface in a coaxial deformation mode, under radial loading; the phenomenon becomes increasingly intense as critical state is approached. Dafalias's (2016) thought experiment is the limiting case of the sequence of experiments performed herein thus the presented experimental evidence is supporting the claim that the Anisotropic Critical State Theory by Li and Dafalias (2012) constitutes a necessary revision of the classical Critical State Theory.

Accordingly, the effect of pre-shearing on the non-coaxiality and contractancy of highly-stressed sand is also apparent when undrained loading is imposed after anisotropic consolidation. In this case, a small stress disturbance involving rotation of the stress PA induces strong non-coaxiality and the associated plastic contraction triggers flow instability. This situation is the diffuse analogue of the mechanism in the incipient shear band described by Vardoulakis (Vardoulakis et al. 1978, Vardoulakis and Graf 1985, Vardoulakis and Georgopoulos 2005) and may explain the vulnerability of sands to spontaneous liquefaction, in stress-rotation conditions, when the static shear stress is high.

The results of this thesis offer new knowledge and contribute towards the deeper understanding of the effects of anisotropy and loading history on the mechanical behaviour of sand. The deposition process and loading history influence the formation and evolution of fabric and this microscopic process controls the macroscopic mechanical behaviour of sand at every state, including the critical one. Consequently, the necessity is highlighted to develop models that can simulate the effects of fabric on the mechanical behaviour of sand under generalised and complex loading conditions, similar to those imposed in the present study. The future research will be directed towards the application of techniques for measuring the fabric tensor of granular media by means of physical properties like the electrical conductivity and the mechanical wave velocity. Likewise, the investigation of the mechanical behaviour of sand under true triaxial loading conditions is an attractive subject for future research.

TABLE OF CONTENTS

CHAPTER 1: INTRODUCTION

1.1 NECESSITY AND SCOPE OF THE THESIS

Understanding the behaviour of soil is an essential prerequisite for protecting both the built environment and human life since the majority of human-made structures interact with soil masses in plenty of different ways, rendering them exposed to the catastrophic phenomena associated with the failure of soils. Liquefaction of soils is such a catastrophic phenomenon that has caused severe damage to built environment and loss of human lives in the past, while it remains a challenging issue for academic research over time.

Although liquefaction is frequently triggered by strong seismic events, as for example the 1925 Santa Barbara earthquake, the 1964 Niigata earthquake and the 1995 Kobe earthquake, to name a few, flow deformation of soil slopes has been reportedly induced by small stress disturbances under quasi-static conditions (Ishihara 1993, Lade 1993). From the viewpoint of soil mechanics, it is noteworthy the fact that the stress state at the triggering of liquefaction is frequently located inside the plastic limit surface and at this state there may exist a diversity of incremental stress or strain directions along which unstable flow deformation can be induced (Lade et al. 1988, Chu et al. 1993). On top of this the corresponding kinematic field can be diffuse, showing no obvious signs of strain localisation (Castro 1969, Lade et al. 1988, Chu et al. 1993, Desrues and Georgopoulos 2006).

Albeit unambiguously fascinating these mechanical peculiarities that characterise the non-associated soil materials may also become quite unsettling as soon as it is realised that the application of the conventional plastic limit analysis in engineering problems, such as the stability of slopes, may in some cases fail to predict the triggering of flow instability (Lade 1993, Darve and Laouafa 2000). Furthermore, the consideration of the triggering of localised instabilities in the hardening regime does not remedy the problem since flow deformation frequently manifests itself in chaotic patterns preceding the formation of a distinct failure surface (Nicot and Darve 2011). In an attempt to remedy this problem some researchers developed models within the framework of Bifurcation Theory (Vardoulakis and Sulem 1995) that rely upon the second-order work criterion (Hill 1958) in order to determine the conditions that trigger diffuse instabilities (Darve et al. 1995, Darve et al. 2004, Nicot et al. 2007, Prunier et al. 2009, Daouadji et al. 2011, Lü et al. 2018).

From the bifurcation analysis perspective diffuse instabilities initiate at points with perturbed physical properties or concentrated stress from which they spread in all directions through the surrounding soil volume, ergo a localised failure mechanism is physically absent. On a theoretical basis the triggering of instability in the homogeneous system requires that the stress state is located inside the bifurcation domain, the incremental stress (or strain) direction belongs in the set of unstable directions along which the second-order work becomes non-positive and the control parameters of the loading programme are proper, in the sense that they allow the instability to occur (Daouadji et al. 2011). In other words, at a given stress state the necessary condition for instability is the non-positive sign of the second-order work which is a directional quantity that depends on the previous stress - strain history.

Having these theoretical considerations as point of departure the present study embarks upon the experimental investigation of the effects of the stress - strain history and direction of incremental stress on the flow-instability condition of sand. The aim is to perform undrained loading tests on both isotropically and anisotropically consolidated sand with either fixed or rotating stress principal axes (PA), at constant $p = (\sigma_1 + \sigma_2 + \sigma_3) / 3$ and $b = (\sigma'_2 - \sigma'_3) / (\sigma'_1 - \sigma'_3) = 0.5$. The loading programme includes rotation of the stress principal axes with either monotonically increasing, constant or periodically changing deviatoric stress, simulating a variety of loading situations occurring in situ, hence the data set that is going to be collected can be scarcely found in the literature (Symes et al. 1984, Shibuya and Hight 1987, Nakata et al. 1998, Sivathayalan and Vaid 2002, Shibuya et al. 2003a and b, Yang et al. 2007).

Another research topic in the present study concerns the effects of fabric (Brewer 1964, Oda 1972) on the mechanical behaviour of sand. The gravity deposited sand exhibits different mechanical properties when subjected to loading with the stress major principal axis orientated at different angles with respect to the direction of deposition (Oda et al. 1978, Tatsuoka 1986, Miura et al. 1986, Shibuya and Hight 1987, Yoshimine et al. 1998, Nakata et al. 1998, Uthayakumar and Vaid 1998, Lade et al. 2014). The anisotropy in the mechanical properties of sand is attributed to the directional characteristics of fabric in the microscopic level, i.e. the preferred orientation of the long axes of particles or voids and the preferred orientation of contact normals, which can be described using a fabric tensor (Oda 1972, Satake 1978, Oda et al. 1985). The anisotropy formed during the process of deposition under the action of gravity is termed the inherent anisotropy (Cassagrande and Carillo 1948).

Physical and numerical studies have shown that the anisotropy of fabric of granular materials resembling sands evolves in response to the applied stresses after deposition and this phenomenon is known as the stress-induced anisotropy (Oda et al. 1985, Rothenburg and Bathurst 1989), though the different characteristics of fabric evolve under a different rate (Wang et al. 2017). Specifically, the internal structure has been found to rotate following the rotation of the stress PA (Oda and Konishi 1974, Li and Yu 2010), while in the case that the latter are kept fixed during loading coaxiality between the principal directions of fabric and stress is achieved ultimately (Li and Yu 2009). The magnitude of fabric anisotropy, defined as the difference or the ratio between the major and minor principal values of the fabric tensor, also evolves as the level of the deviatoric stress ratio increases during loading with fixed or rotating stress PA.

Dafalias (2016) pointed out that the premise of the classical Critical State Theory (CST) (Roscoe et al. 1958, Schofield and Wroth 1968) concerning the isotropy of fabric at critical state, which is supposedly the result of the intense remoulding needed to reach such a state, does not comply with the results of recent studies indicating the existence of a strongly anisotropic fabric at critical state, coaxial in direction with the stress (Thornton 2000, Masson and Martinez 2001, Zhang and Thornton 2007, Li and Yu 2009, Li and Li 2009, Fu and Dafalias 2011, Wiebicke et al. 2017, Theocharis et al. 2017 and 2019). According to the CST, the phenomenon during which a granular material keeps deforming in continuing shearing, under constant volume and stress, is termed the critical state (CS) and the analytical conditions stated to be necessary and sufficient for reaching and maintaining CS are given by: $\eta = q\ /\ p' = \eta_c = M$ and $e = e_c = e_c(p')$, where $\eta_c = M$ is the value of the deviatoric stress ratio at CS, which is a material constant, and $e_c = e_c(p')$ is the value of the void ratio at CS, which is a unique function of p'.

Dafalias (2016) conceived a thought experiment that may prove that the CST is incomplete because it does not take into account the role of fabric anisotropy: a soil specimen is first loaded monotonically with fixed stress PA until it reaches CS and afterwards the stress PA are rotated while keeping the effective stress principal values (PV) constant. The question raised then is whether the specimen will remain at CS or not while shearing continues with rotating directions of stress and strain rate at fixed effective stress PV. The fixity of the effective stress PV means that p' and q remain constant thus the critical void ratio, e_c, at the corresponding p' also remains constant, while the current value of void ratio, e, at the instant that the rotation of the stress PA is initiated is equal to e_c. Consequently, if the two analytical conditions presented above are indeed necessary and sufficient for reaching and maintaining CS the specimen should remain at CS because these conditions remain valid during the stress PA rotation. On the contrary, if the CS is abandoned then the two analytical conditions are necessary but not sufficient for maintaining CS, unless the fixity of the directions of stress and strain rate relative to the specimen's axes is tacitly assumed at CS (Theocharis et al. 2019), and the CST is incomplete.

Theocharis et al. (2017, 2019) performed numerical simulations of this experiment using the Discrete Element Method (DEM) and showed that the granular material contracts immediately upon initiating the rotation of the stress PA at CS while keeping the effective stress PV constant. These results showed that the two analytical conditions presented above are necessary but not sufficient for maintaining CS and proved the incompleteness of the CST. As a means to remedy this incompleteness Li and Dafalias (2012) proposed the Anisotropic Critical State Theory (ACST) which introduces a third analytical condition at CS that is satisfied when an evolving fabric tensor becomes aligned with the loading direction and attains its critical value normwise. The three analytical conditions in the new theory become both necessary and sufficient for reaching and maintaining CS.

The present study sets out with the aim to perform physically the thought experiment proposed by Dafalias (2016) and simulated by Theocharis et al. (2017, 2019) in order to investigate the effects of fabric anisotropy on the critical state behaviour of sand. Achieving this aim means that unique experimental data of great value will be acquired proving physically that the Anisotropic Critical State Theory by Li and Dafalias (2012) constitutes a necessary revision of the classical Critical State Theory.

1.2 ORGANISATION OF THE THESIS

This thesis consists of eight chapters and one Appendix. **Chapter 2** presents an extended review of past literature on aspects concerning the fabric of sands. The way is discussed in which the microscopic aspects related to fabric affect the strength and deformation frictional characteristics of sand, placing emphasis on the dilatancy mechanism. It is shown that the behaviour of sands depends on the combination of mean effective stress and void ratio but is also directional dependent meaning that it is highly affected by the direction of loading with respect to the specimen's axes. An effort is made to correlate the anisotropy in sands' behaviour with the anisotropy in fabric characteristics and present the techniques used to quantify these characteristics. Finally, it is shown that the localisation of strain results in specific localised patterns of anisotropy and inhomogeneity of void ratio. The detailed presentation of fabric aspects reported in literature is justified since it aids the interpretation of the results of the present study.

Chapter 3 discusses the concept of critical state of soils and other granular materials and presents the experimental results that led to the foundation of the Critical State Theory (CST) by Roscoe et al. (1958) and Schofield and Wroth (1968). The critical state can be used as a reference state for describing and simulating the mechanical behaviour of sands, especially their dilatancy. Then, the effects of fabric anisotropy on dilatancy and critical state are discussed and the question is raised concerning the necessity of revisiting the classical CST to include these fabric anisotropy effects, as proposed by Li and Dafalias (2012) who introduced the Anisotropic Critical State Theory (ACST). This study aims at giving an answer to this question.

Chapter 4 discusses the concept of flow deformation of sands which is a catastrophic liquefaction phenomenon. Aspects such as the effects of state, anisotropy and principal stress rotation on the flow behaviour of sands are discussed in the light shed by previous experimental studies. This chapter also presents the results of numerical studies that use the principles of Bifurcation Theory in order to predict the triggering of flow instability. Some predictions of the numerical models are viewed through a critical prism in the present study.

Chapter 5 presents the capabilities of the hollow cylinder apparatus (HCA) of the National Technical University of Athens before and after the upgrade accomplished for the needs of the present study. The relationships used to calculate the average stresses and strains in torsional-shear testing are derived and the limitations that the inevitable non-uniformities of stress and strain impose are discussed. This chapter also presents the physical characteristics of the material tested (M31 Sand) and describes the specimen preparation method.

Chapter 6 presents the results of the drained and undrained triaxial compression tests performed in this study for determining the critical state characteristics of M31 Sand. Using the unique critical state line that was determined the dependence of strength and dilatancy characteristics of sand on the state parameter proposed by Been and Jefferies (1985) was verified. Then, an attempt was made to perform loading tests in the HCA in accordance with the requirements of the thought experiment proposed by Dafalias (2016). The dilatancy and non-coaxiality of sand were also investigated under generalised loading conditions with either fixed or rotating stress PA.

Chapter 7 presents the results of the undrained generalised loading tests performed in this study for investigating the effects of inherent anisotropy and stress - strain history on the flow deformation of sand. Isotropically and anisotropically consolidated sand specimens were subjected to loading with either constant or rotating stress PA and with constant p and b = 0.5. The deviatoric stress ratio was increased monotonically, kept constant or changed periodically in the course of principal stress rotation. The experimental results obtained were used to verify or falsify some of the predictions of numerical models developed within the framework of Bifurcation Theory.

Chapter 8 presents the summary and conclusions of the thesis. Finally, the directions towards which future research will be oriented are discussed.

The **Appendix** at the end of the thesis presents the articles in which the results of this this study were published.

1.3 SYMBOLS AND ABBREVIATIONS

The symbols and abbreviations used in this study are presented in the tables of the Extended Abstract, Chapter 6 and Chapter 7.

1.4 BIBLIOGRAPHY

Been K, Jefferies MG (1985) A state parameter for sands. Géotechnique 35 (2), 99–112

Brewer R (1964) Fabric and mineral analysis of soils. John Wiley and Sons, USA

Casagrande A, Carillo N (1944) Shear failure of anisotropic materials. Proc. Boston Soc. Civ. Engrs, 31, 74-87

Castro G (1969) Liquefaction of sands. Harvard Soil Mechanics Series No. 81, Harvard University, Cambridge

Chu J, Lo S-CR, Lee IK (1993) Instability of granular soils under strain path testing. Journal of Geotechnical Engineering, Vo. 119, No. 5, pp. 874-892

Dafalias YF (2016) Must critical state theory be revisited to include fabric effects? Acta Geotechnica (2016) 11:479, DOI 10.1007/s11440-016-0441-0

Daouadji A, Darve F, Al Gali H, Hicher PY, Laouafa F, Lignon S, Nicot F, Nova R, Pinheiro M, Prunier F, Sibille L, Wan R (2011) Diffuse failure in geomaterials: Experiments, theory and modelling. Int. J. Numer. Anal. Meth. Geomech. (2011), 35(16), 1731-1773

Darve F, Flavigny M, Meghachou M (1995) Constitutive modelling and instabilities of soil behaviour. Computers and Geotechnics 17 (1995), 203-224

Darve F, Laouafa F (2000): Instabilities in granular materials and application to landslides. Mech. Cohes-Frict. Mater., 2000; 5:627-652

Darve F, Servant G, Laouafa F, Khoa HDV (2004) Failure in geomaterials: continuous and discrete analysis. Comput. Methods Appl. Mech. Engrg. 193 (2004), 3057-3085

Desrues J, Georgopoulos I-O (2006) An investigation of diffuse failure modes in undrained triaxial tests on loose sand. Soils and Foundations, Vol.46, No.5, 585-594

Fu P, Dafalias YF (2011) Fabric evolution within shear bands of granular materials and its relation to critical state theory. International Journal for Numerical and Analytical Methods in Geomechanics, 2011, 35: 1918-1948

Hill R (1958) A general theory of uniqueness and stability in elastic-plastic solids. Journal of the Mechanics and Physics of Solids (1958); 6:239-249

Ishihara K (1993) Liquefaction and flow failure during earthquake. Géotechnique, Vol. 43, No. 3, pp.351-415

Lade PV, Nelson RB, Ito YM (1988) Instability of granular materials with nonassociated flow. Journal of Engineering Mechanics, Vol. 114, No. 12, 2173-2191

Lade PV (1993) Initiation of static instability in the submarine Nerlerk berm. Canadian Geotechnical Journal 30: 895-904

Lade PV, Rodriguez NM, Van Dyck EJ (2014) Effects of principal stress directions on 3D failure conditions in cross-anisotropic sand. Journal of Geotechnical and Geoenvironmental Engineering, 2014, 140(2): 04013001

Li X, Li XS (2009) Micro-macro quantification of the internal structure of granular materials. J. Eng. Mech., 135(7), 641-656

Li X, Yu H-S (2010) Numerical investigation of granular material behaviour under rotational shear. Géotechnique 60, No. 5, 381-394

Li XS, Dafalias YF (2012) Anisotropic critical state theory: role of fabric. Journal of Engineering Mechanics, Vol. 138, No. 3, 263-275

Lü X, Huang M, Qian J (2018) Influences of loading direction and intermediate principal stress ratio on the initiation of strain localization in cross-anisotropic sand. Acta Geotech., 13: 619-633, 2018

Masson S, Martinez J (2001) Micromechanical analysis of the shear behavior of a granular material. J. Eng. Mech., 127(10), 1007-1016

Miura K, Miura S, Toki S (1986) Deformation behavior of anisotropic dense sand under principal stress axes rotation. Soils and Foundations, Vol.26, No.1, 36-52

Nakata Y, Hyodo M, Murata H, Yasufuku N (1998) Flow deformation of sands subjected to principal stress rotation. Soils and Foundations, Vol.38, No.2, 115-128

Nicot F, Darve F, Dat Vu Khoa H (2007) Bifurcation and second-order work in geomaterials. Int. J. Numer. Anal. Meth. Geomech., 2007; 31:1007-1032

Nicot F, Darve F (2011) Diffuse and localized failure modes: Two competing mechanisms. International Journal for Numerical and Analytical Methods in Geomechanics, Vol. 35, 586-601

Oda M (1972) Initial fabrics and their relations to mechanical properties of granular material. Soils and Foundations, Vol.12, No.1, 18-36

Oda M, Konishi J (1974) Microscopic deformation mechanism of granular material in simple shear. Soils and Foundations, Vol.14, No.4, 26-38

Oda M, Koishikawa I, Higuchi T (1978) Experimental study of anisotropic shear strength of sand by plane strain test. Soils and Foundations, Vol.18, No.1, 25-38

Oda M, Nemat-Nasser S, Konishi J (1985) Stress-induced anisotropy in granular masses. Soils and Foundations, Vol.25, No.3, 85-97

Prunier F, Nicot F, Darve F, Laouafa F, Lignon S (2009) Three-dimensional multiscale bifurcation analysis of granular media. Journal of Engineering Mechanics, Vol. 135, No. 6, 493-509

Roscoe KH, Schofield AN, Wroth CP (1958) On the yielding of soils. Géotechnique 8 (1), 22–53

Rothenburg L, Bathurst RJ (1989) Analytical study of induced anisotropy in idealized granular materials. Géotechnique 39, No. 4, 601-614

Satake M (1978) Constitution of mechanics of granular materials through graph representation. Theoretical and Applied Mechanics 26, University of Tokyo Press, pp. 257-266

Schofield AN, Wroth CP (1968) Critical state soil mechanics. McGraw-Hill, London

Shibuya S, Hight DW (1987) A bounding surface of granular materials. Soils and Foundations, Vol.27, No.4, 123-136

Shibuya S, Hight DW, Jardine RJ (2003a) Four-dimensional local boundary surfaces of an isotropically consolidated loose sand. Soils and Foundations, Vol.43, No.2, 89-103

Shibuya S, Hight DW, Jardine RJ (2003b) Local boundary surfaces of a loose sand dependent on consolidation path. Soils and Foundations, Vol.43, No.3, 85-93

Sivathayalan S, Vaid YP (2002) Influence of generalized initial state and principal stress rotation on the undrained response of sands. Canadian Geotechnical Journal, 39 (1): 63 – 76

Symes MJ, Gens A, Hight DW (1984) Undrained anisotropy and principal stress rotation in saturated sand. Géotechnique 34, No. 1, 11-27

Tatsuoka F, Sakamoto M, Kawamura T, Fukushima S (1986) Strength and deformation characteristics of sand in plane strain compression at extremely low pressures. Soils and Foundations, Vol.26, No.1, pp. 65-85

Theocharis AI, Vairaktaris E, Dafalias YF, Papadimitriou AG (2017) Proof of incompleteness of Critical State Theory in granular mechanics and its remedy. Journal of Engineering Mechanics, Vol. 143 (2), 1-12

Theocharis AI, Vairaktaris E, Dafalias YF, Papadimitriou AG (2019) Necessary and sufficient conditions for reaching and maintaining critical state. International Journal for Numerical and Analytical Methods in Geomechanics, 43: 2041-2045

Thornton C (2000) Numerical simulations of deviatoric shear deformation of granular media. Géotechnique 50, No. 1, 43-53

Uthayakumar M, Vaid YP (1998) Static liquefaction of sands under multiaxial loading. Canadian Geotechnical Journal 35, pp. 273-283

Wang R, Fu P, Zhang J-M, Dafalias YF (2017) Evolution of various fabric tensors for granular media toward the critical state. J. Eng. Mech., 2017, 143(10): 04017117

Wiebicke M, Andò E, Salvatore E, Viggiani G, Herle I (2017) Experimental measurement of granular fabric and its evolution under shearing. Powders and Grains (2017), EPJ Web of Conferences. 140. 02020. 10.1051/epjconf/201714002020.

Yang ZX, Li XS, Yang J (2007) Undrained anisotropy and rotational shear in granular soil. Géotechnique 57, No. 4, 371-384

Yoshimine M, Ishihara K, Vargas W (1998) Effects of principal stress direction and intermediate principal stress on undrained shear behavior of sand. Soils and Foundations, Vol. 38, No. 3, 179-188

Zhang L, Thornton C (2007) A numerical examination of the direct shear test. Géotechnique 57, No. 4, 343-354

CHAPTER 2: FABRIC OF SANDS

2.1 INTRODUCTION

Sands are granular soil materials deposited in the field mainly under the action of gravity. The geometrical arrangement of sand grains described with the term *fabric* (Brewer 1964, Oda 1972a) is characterised by the density of packing as well as the orientational distribution of contact normal vectors and particles. Although sands are frequently treated as continuum media in the field of Soil Mechanics the effects of the particulate nature and fabric of sands on their mechanical behaviour cannot be overlooked.

The present chapter presents an extended review of past literature on aspects concerning the fabric of sands. The way in which the microscopic aspects related to fabric affect the strength and deformation characteristics of sand is discussed, placing emphasis on the dilatancy mechanism. It is shown that the behaviour of sands depends on the combination of mean effective stress and void ratio but is also directional dependent meaning that it is highly affected by the direction of loading with respect to the specimen's axes. An effort is made to correlate the anisotropy in sands' behaviour with the anisotropy in fabric characteristics and present the techniques used to quantify these characteristics. Finally, it is shown that the localisation of strain results in specific localised patterns of anisotropy and inhomogeneity of void ratio. The detailed presentation of fabric aspects reported in literature is justified since it aids the interpretation of the results of the present study.

2.2 EFFECTS OF THE NON-DIRECTIONAL CHARACTERISTICS OF FABRIC AND GRAIN PROPERTIES ON THE FRICTIONAL BEHAVIOUR OF SANDS

Sand grains that lack bonding are packed together under the action of gravity and remain at static equilibrium via the normal and shear forces that act at interparticle contact points. Figure 2.1 shows the interaction of two grains at their contact point. It is noted that there exists always a contact surface between grains, instead of a geometrical point, otherwise the stress (i.e. the force over surface) becomes infinite; nevertheless, the term *contact point* is used hereinafter. The normal and shear force are related by the well-known *law of friction,* introduced by Leonardo da Vinci circa

1493 (Hutchings 2016), which states that "the force of friction acting between two sliding surfaces is proportional to the load pressing the surfaces together".

Since the frictional phenomenon of slippage occurs at the intergranular contacts when the sand deforms it is apparent that the greater normal force makes slippage difficult to occur and increases the sand's stiffness and strength (Towhata 2008). If the two grains are not sliding then the *obliquity* of the direction of the resultant contact force (i.e. the vector sum of normal force and friction) with respect to the vertical defines the mobilised friction angle which is lower than the intergranular friction angle (Horn and Deere 1962).

The simple and fundamental direct-shear test offers insight into the frictional, confining-stress-dependent mechanism that controls sand's stiffness and strength. A schematic diagram of the direct shear apparatus is shown in Fig. 2.2. A prismatic specimen is formed by pouring sand into the space between two rigid containers. A normal effective stress, σ'_n, is applied along the vertical direction and confinement of sand is achieved. Afterwards, a horizontal displacement of the container induces shear distortion of sand and the mobilised shear force, T, is monitored. The shear stress, τ, is calculated as the ratio of shear force over the current area of the cross-section of the specimen, and plotted against shear displacement, as shown in Fig. 2.3. The stress σ'_n is maintained constant throughout shearing in the case described here. Figure 2.3a shows that if different sand specimens with the same relative density, D_r, are sheared under drained conditions at different normal effective stresses, σ'_n, the peak shear stress τ_p increases with σ'_n; these results indicate the frictional characteristics of sand at peak state. Moreover, the initial slope of the stress-displacement curve (which is non-linear) indicates that the stiffness of sand, also, increases with confining stress. The failure of sand occurs on the horizontal plane and Coulomb's criterion states:

$$\tau_p = tan\,\varphi \cdot \sigma_n^{'} \tag{2.1}$$

The term $tan\varphi$ is the friction coefficient and φ is the angle of internal friction.

It is apparent that there exists no unique value of shear strength of sand, in terms of peak shear stress. However, if Eq. 2.1 is rearranged to yield the ratio of mobilised shear stress over the constant effective stress then the following equation is formed:

$$tan\,\varphi_{mob} = \frac{\tau}{\sigma_n^{'}} \tag{2.2}$$

The term φ_{mob} is the *mobilised friction angle*. Failure of sand occurs when the stress ratio of Eq. 2.2 reaches its maximum value. For the drained shear loading described previously this condition concurs with the maximum shear stress condition, but this is not always the case. Consequently, it can be stated that regarding failure sand is a *stress-ratio-dependent* material. The mobilised stress ratio plays an important role in all aspects of the mechanical behaviour of sand, as will be shown in the following.

The failure stress ratio, *tan* φ or *tan* φ_p, for a given relative density of sand is less sensitive to the effective confining stress than the peak shear stress, t_p; in general, it increases considerably at extremely low stresses (5 kPa - 50 kPa; Tatsuoka et al. 1986b) and decreases considerably at extremely high stresses (> 1 MPa; Yamamuro and Lade 1996). The mobilised friction angle, before and after peak failure, can be divided into various components (Terzaghi et al. 1996, Sadrekarimi and Olson 2011) according to the equation:

$$\varphi_{mob} = \varphi_\mu + \varphi_g = \varphi_\mu + \varphi_d + \varphi_p \tag{2.3}$$

The *interparticle friction angle*, φ_μ, depends on the constituent minerals of grains and the surface roughness in the microscopic scale; this component of shearing resistance is purely frictional. The angle φ_g expresses the *geometrical interference* (or *interlocking*) that mobilises shearing resistance by means of particle relative movement and interaction, i.e. by *dilation* or *particle climbing* (φ_d) and by *particle rearrangement* and *damage* (φ_p) (Lupini et al. 1981, Sadrekarimi and Olson 2011). Owing to the important contribution of dilation and constant-volume remoulding mechanisms to shearing resistance, some engineers prefer the term *mobilised angle of shearing resistance* to describe φ_{mob}.

Each of the components of φ_{mob} contributes to shearing resistance to a different degree depending on whether the sand is at pre- or post-failure state. The degree of contribution depends, also, on the void ratio, e, of sand and on the effective confining stress. For example, at dense packing and low stresses, the dilation mechanism prevails, while at high stresses dilation is suppressed and breakage of grains dominates. Sture et al. (1998) reported values of φ_{mob} in the range of 46.7° to 70° and dilation angles in the range of 30° to 31° for sand subjected to drained triaxial compression under extremely low confining stress, in the range of 0.05 kPa to 1.3 kPa. The tests were performed in a space shuttle during space missions. Anastasopoulos et al. (2010) also reported values of φ_{mob} higher than 50° in direct-shear tests under normal stresses lower than 10 kPa.

Dense sand at a given effective confining stress demonstrates higher peak shear stress, τ_p, and peak stress ratio, $(\tau/\sigma'_n)_p$, than loose sand, as can be seen in Fig. 2.3b. However, at large shear displacements, both sands reach a common *ultimate strength*, τ_{ult}, which increases with confining stress. The void ratio, e, is a non-directional characterictic of fabric which indicates how densely the grains are packed. When e is low the grains are closely packed and the average number of contact points per grain, called the *coordination number*, is large (Oda 1977). This means that the skeleton structure is stable, since each grain is well supported by the neighbouring grains, and also each grain has to climb over the adjacent grains in order to move, resulting in a high dilation angle, φ_d. It is apparent that the variation in the value of the fabric characteristic e can explain the different peak strengths and stress ratios of loose and dense sand, at the same confining stress.

Regarding the ultimate state of sand, Casagrande (1936 and 1938) observed that when loose and dense sand specimens are sheared under drained triaxial conditions at the same confining stress they ultimately reach a common void ratio. Loose sand contracts and reaches the *critical void ratio*, e_c, while dense sand initially contracts and then dilates until it reaches the same void ratio e_c, which is unique at a given effective confining stress. This behaviour is presented in Fig. 2.4 that shows the stress - strain and stress - void ratio curves for loose and dense sand sheared at the same confining stress. It is noted that the sand continues to accumulate shear deformation under constant volume and stresses (shear and normal) at the ultimate state. Figures 2.3a and b show that different ultimate shear strengths are mobilised at different confining stresses, indicating the frictional characteristics of sand at ultimate states; the different values of ultimate void ratio may also justify the different ultimate strengths. If the critical void ratio is defined for different values of the effective confining stress then the *critical void ratio* (CVR) *line* can be drawn in the $e - \sigma'_c$ state plane, where σ'_c is the effective confining stress. The CVR line is shown in Fig. 2.5a in linear scale and in Fig. 2.5b in semi-logarithmic scale.

Casagrande (1936 and 1938) performed only drained triaxial compression tests because the instrumentation required to measure the pore-water pressure changes was not available at that time; yet, he had the ingenuity to predict that if loose sand is subjected to undrained loading the tendency to contract would squeeze the incompressible water and impose a pressure increase inside the water-saturated sand pores. This would result in a decrease of the effective confining stress, since the compressive load is partly removed from the interparticle contact surfaces and applied on the pore water, under overall constant void ratio. The state point (σ'_c , e) of loose sand would travel horizontally until the ultimate state is reached at the effective stress corresponding to the specific critical void ratio. The path of the state point can be seen in Fig. 2.5 for both loose and dense sand, subjected to drained or undrained loading. The prediction of Casagrande was verified later (Penman 1953, Castro 1969, Poulos 1981, Been et al. 1991, Verdugo and Ishihara 1996) and nowadays the change in the state of sand when loaded under undrained conditions towards the ultimate state is common knowledge.

The ultimate state of sand was thoroughly investigated by Verdugo and Ishihara (1996) who performed drained and undrained triaxial compression tests on very loose, loose, medium loose and medium dense specimens, consolidated to mean effective stress varying in a very broad range (0.1 - 3 MPa). The conventional triaxial apparatus and the applied stress state (axisymmetric) are shown in Fig. 2.6. However, Verdugo and Ishihara (1996) used a more sophisticated triaxial apparatus with enlarged lubricated end platens to avoid strain non-uniformities and shear banding (see Section 2.9). They observed that the sand ultimately keeps deforming in continuing shearing, under constant deviatoric stress, q (= $\sigma'_1 - \sigma'_3$), constant mean effective stress, p' (= $\{\sigma'_1 + \sigma'_2 + \sigma'_3\}$ / 3), and constant volume, in the case of drained loading, or constant pore-water pressure, in the case of undrained loading.

The results from the study by Verdugo and Ishihara (1996) are in perfect agreement with the observations made by Casagrande (1936 and 1938) concerning the ultimate state of sand, termed the *ultimate steady state* or *steady state* or *critical state* by other researchers (Roscoe et al. 1958, Schofield and Wroth 1968, Been et al. 1991). Specifically, it was found that the combinations $(p', e)_{ss}$ at steady state in triaxial compression form a unique line, called the *ultimate steady state line* (USSL) or *critical void ratio line* (CVRL) or *critical state line* (CSL), irrespective of the initial combinations $(p', e)_{in}$. Consequently, the existence of a unique fabric in terms of void ratio at the ultimate state was verified.

Figure 2.7a shows the stress - strain curves from tests on medium dense sand consolidated to 0.1 MPa, 1 MPa, 2 MPa and 3 MPa and subjected to undrained triaxial compression (Verdugo and Ishihara 1996). The corresponding effective stress paths are presented in Fig. 2.7b. The void ratio at the beginning of shearing (initial void ratio) is common for all specimens. It can be seen that at large axial strain (ε_{ax} > 20%) all specimens mobilise a common ultimate strength, q_{ult}, irrespective of the initial effective stress. This deviatoric stress would have remained constant if shearing had continued, however, unloading was performed. During unloading all stress -strain curves are coincident. The effective stress paths in Fig. 2.7b demonstrate that all medium dense specimens are contractive in the initial phase of shearing and dilative afterwards, until the ultimate state is reached in which there exists no volume-change tendency. The initial response becomes more contractive as the initial confining stress increases. The response of sand changes from contractive to dilative at the *phase transformation point* (Ishihara et al. 1975), which can be identified as an "elbow point" on the stress-path curve. All the sand specimens reach the ultimate state at a common stress, p'_{ult}, since they have the same void ratio, and the stress paths from all tests coincide during unloading indicating that a common fabric was developed at large deformations.

Figures 2.8a and b present the stress - strain curves and the effective stress paths from tests on medium loose sand consolidated to 0.1 MPa, 1 MPa, 2 MPa and 3 MPa and subjected to undrained triaxial compression, while Figs 2.9a and b display the results from similar tests on loose sand (Verdugo and Ishihara 1996). All medium loose specimens reach the ultimate steady state at large deformation at common stresses q_{ult} and p'_{ult}, irrespective of the initial confining stress. Both ultimate stress values are lower than the respective ones from tests on medium dense sand. Loose sand demonstrates even lower steady-state strength and ultimate mean effective stress. It is important to note that in the case that loose sand is sheared at high mean effective stress (1 MPa and 2 MPa) it remains contractive until the ultimate state is reached. On the other hand, the medium loose sand sheared at p'_o = 2 MPa or 3 MPa is very contractive, yet, it exhibits phase transformation before it reaches the ultimate state.

Figure 2.10 shows the *steady state line* (SSL) or *ultimate steady state line* (USSL) obtained from undrained triaxial compression tests on sand specimens at various initial states (Verdugo and Ishihara 1996). The steady state line of this sand (Toyoura sand) is curved in semi-logarithmic scale and straight in linear or exponential scale (Verdugo and Ishihara 1996, Li and Wang 1998). Sand specimens with an initial state to the right and above the SSL demonstrate contractive behaviour until reaching the ultimate state while those with an initial state to the left and below demonstrate dilative behaviour. However, some medium loose specimens located initially to the right of the SSL exhibit phase transformation and dilative response before the ultimate state is reached.

It is very important to recognise that whether the sand's response is contractive or dilative depends both on the void ratio and the mean effective stress. Dense sand demonstrates contractive response if the mean effective stress is very high, and vice versa, loose sand demonstrates dilative response if the mean effective stress is very low. Specifically, the distance of the current point (p' , e) from the respective ultimate point at the same stress (p' , e_c) was defined as the *state parameter* $\psi = e - e_c(p')$ by Been and Jefferies (1985) and it was shown that ψ is well correlated with the mechanical characteristics of sand; detailed discussion on this subject will be presented in Chapter 3. At the current point of discussion, it is highlighted that specimens consolidated to 0.1 MPa and to 3 MPa (that is a ratio of consolidation stresses equal to 30) and having the same void ratio reach the same ultimate state (p' , e_c) when subjected to undrained compression. This is strong experimental evidence indicating the existence of a unique ultimate combination of mean effective stress and void ratio, irrespective of the initial state of sand.

At the ultimate state a higher mean effective stress corresponds to a lower void ratio and a higher strength. Figure 2.11 shows the ultimate stress states in the q / 2 - p' space from all undrained triaxial compression tests performed by Verdugo and Ishihara (1996). It is apparent that the ultimate states form a straight line that passes through the origin, called the *ultimate strength envelope*. Using the M symbol to denote the unique value of the stress ratio, $\eta = q / p'$, at the ultimate state then the following equation holds in triaxial conditions (Schofield and Wroth 1958):

$$sin\,\varphi_{ult} = \frac{3 \cdot M}{6 + M} \tag{2.4}$$

The term φ_{ult} is the ultimate angle of shearing resistance, while $sin\,\varphi_{ult} = [\ (\sigma'_1 - \sigma'_3) / (\sigma'_1 + \sigma'_3)\ ]_{ult}$. It is important to note that in the study by Verdugo and Ishihara (1996) the term "ultimate stress ratio" represents the stress ratio at the *ultimate material state*. Similarly, Li (1997), Li et al. (1999) and Li and Dafalias (2000) pointed out that "the failure surface characterised by an ultimate deviatoric stress ratio does not necessarily represent the ultimate material state (which is in fact the critical state), unless the void ratio also reaches a critical value".

From Eq. 2.4 it is apparent that a unique angle of shearing resistance is mobilised at ultimate steady state. Since at steady state the sand keeps deforming in continuing shearing at constant stress and volume (or constant pore-water pressure) the dilatancy contribution is zero. The ultimate angle of shearing resistance is suggested to be an *intrinsic material property*, yet, for most sands the value of φ_{ult} is greater than the interparticle friction angle, φ_{μ}. The friction angle φ_{μ} is influenced by the roughness and mineralogy of grains (Skinner 1969, Negussey et al. 1988, Sadrekarimi and Olson 2011), while the angle of shearing resistance φ_{ult} depends also on the particle shape (Guo and Su 2007) that affects the constant-volume remoulding mechanism (Rowe 1962).

Koerner (1970) reported that angularity can increase the ultimate angle of shearing resistance of a single-mineral soil by as much as 8°. Certainly, the angularity increases the angle of shearing resistance prior to the ultimate state as well, since it causes an interlocked fabric and provides extra restraint to particle rolling that enhances dilatancy (Guo and Su 2007, Tsomokos and Georgiannou 2010, Sadrekarimi and Olson 2011). It is noted that Taylor (1948) used the term “interlocking” to describe the effect of dilatancy, while Guo and Su (2007) suggested that interlocking may exist at the peak state, as a supplementary mechanism to dilatancy, but not at the ultimate state. Moreover, Penman (1953) reported a slight decrease in the measured residual angle of shearing resistance of silt subjected to drained triaxial compression when the initial void ratio increased (see also Been et al. 1991); Penman (1953) suggested that a mechanism different than Taylor’s interlocking, which is suppressed at the ultimate state, might justify this finding.

Verdugo and Ishihara (1996) reported that the ultimate behaviour of sand subjected to drained triaxial compression (TC) loading can be described within the steady state framework proposed for undrained TC loading. Figures 2.12a and b present the stress - strain and deviatoric stress - void ratio curves, respectively, for Toyoura sand with various initial void ratios e_o, consolidated to stress p'_o = 0.1 MPa and subjected to drained TC. The comparison of the stress - strain curves indicates that the initial stiffness of sand (i.e. the initial slope of the stress - strain curve) decreases with e_o. For axial strains $\varepsilon_{ax} \leq 20\%$, the same amount of ε_{ax} corresponds to a lower deviatoric stress when e_o is higher. However, at axial strains $\varepsilon_{ax} > 20\%$ all stress - strain curves merge into a single one. This indicates that a unique ultimate strength, q_{ult}, is mobilised irrespective of the initial void ratio. The deviatoric stress - void ratio curve indicates a similar behaviour: a unique strength and void ratio are exhibited at ultimate state, irrespective of e_o. When the sand is consolidated to stress p'_o = 0.5 MPa the behaviour is qualitatively the same (see Figs 2.13a and b), yet, the ultimate strength is higher and the void ratio is lower. These results clearly show that the sand reaches a steady state of deformation when sheared under drained conditions.

Verdugo and Ishihara (1996) found that the steady states of Toyoura sand are unique, irrespective of the stress - path history. Figure 2.14 illustrates this concept since a unique steady state line in the e - p' plane captures well all the ultimate states of Toyoura sand, irrespective of the drainage conditions and initial state $(p', e)_o$. Similar conclusions were drawn by Been et al. (1991) who subjected Erksak and Toyoura sand to both triaxial compression and extension loading. However, a detailed discussion on the ultimate states of sand subjected to different modes of shearing (i.e. compression, extension etc.) will be presented in Chapter 3. The uniqueness of the ultimate stress ratio $(q / p')_{ult}$ is also evidenced here. Figure 2.15 shows the mobilised stress ratio, q / p', against the axial strain, ε_{ax}, for Toyoura sand subjected to drained triaxial compression. Figures 2.15a and b refer to sand with various initial void ratios e_o, consolidated to stresses p'_o = 0.1 MPa and 0.5 MPa, respectively. It is apparent that a unique stress ratio q / p' is mobilised at the ultimate state, irrespective of the initial void ratio and confining stress, and its value M is the same as the one mobilised ultimately under undrained loading conditions. Consequently, it can be inferred that there exists a unique line in the q - p' - e space that consists of the ultimate states of sand subjected to triaxial compression loading (Roscoe et al. 1958, Schofield and Wroth 1968).

2.3 EFFECTS OF THE NON-DIRECTIONAL CHARACTERISTICS OF FABRIC ON THE STIFFNESS OF SANDS

Deformation of sands is generally irreversible. The stress - strain curve is non-linear, even at very small strain, and unloading does not fully erase previously accumulated strain. The strain range at which linear elastic deformation occurs is $\varepsilon < 0.001\%$ or $\varepsilon < 10^{-5}$ (Iwasaki et al. 1978, Jardine et al. 1984, Burland 1989, Shibuya et al. 1992, Jiang et al. 1997). Moreover, the reversible part of strain is in most cases negligible in comparison with the irreversible part (Barden et al. 1969, Tatsuoka 1976). The particulate nature of sands accounts for this inelastic mechanism of deformation. If a load is applied to an assembly of grains then the ratio of shear over normal force at some contacts inevitably reaches the limiting value $\tan \varphi_{\mu}$ and sliding occurs. Some grains roll and override other grains, while others lose contact and fall into the void space. It is apparent that these patterns of deformation at the microscopic scale are irreversible and this is reflected in the deformational behaviour of sand at the macroscopic scale.

The stiffness moduli of sand are highly affected by the irreversible deformation. The definition of various stiffness moduli of sand subjected to monotonic triaxial compression is presented in Fig. 2.16 on a non-linear stress - strain curve. The initial slope of the curve at very small strain ($< 10^{-5}$) is the *elastic Young's modulus* E_{max}. The slope of the tangent line at point A, corresponding to strain ε_A, is the *tangent Young's modulus* E_{tan} at that point, while the slope of the line connecting point A with the origin O is the *secant Young's modulus* E_{sec}. If a small amplitude cyclic stress is induced at one point of the stress - strain curve via unloading and reloading then the *equivalent Young's modulus* E_{eq} is defined as the slope of the narrow stress loop formed. If the stress amplitude is small enough to produce strain $\Delta\varepsilon < 10^{-5}$ then linear elastic unloading and reloading is performed and the loop becomes a line with slope equal to the elastic modulus. This modulus is affected by the stress history and the current stress state and stress ratio (Yu and Richart 1984, Jiang et al. 1997, Hoque and Tatsuoka 1998) so it can be different than the initial modulus E_{max}.

Figures 2.17a and b present the elastic and inelastic deformation characteristics of two granular geomaterials subjected to drained compression under plane-strain and triaxial conditions, respectively, in the tests performed by Shibuya et al. (1992). The axial strain is measured externally (i.e. outside the cell environment) using proximity transducers, which capture the response at moderate strains plotted on the lower horizontal axes, while it is also measured internally (i.e. inside the cell environment) by means of very sensitive *local displacement transducers* (LDT) (Goto et al. 1991), which capture the response at small strains plotted on the upper horizontal axes. The LDTs are placed on the specimen, as can be seen in Figure 2.18, and provide accurate measurement of small strains ($\sim 10^{-6}$), free of bedding and compliance error. Figure 2.17a displays the results from monotonic plane strain compression (PSC) test on sand and from one small stress amplitude unloading - reloading cycle. Figure 2.17b displays the results from monotonic triaxial compression (TC) test on gravel and from three small stress amplitude unloading - reloading cycles. It is noted that the modulus E in PSC, defined as the local slope, is related to Young's modulus E in TC, but these moduli are not the same.

It is apparent in Fig. 2.17 that the tangent and secant moduli of both granular materials decrease as the axial strain increases since the non-linear stress - strain curves are concave downward. It can be suggested that as the deviatoric stress, q, increases monotonically, so does the stress ratio, q / p', hence at the grain scale more and more contacts become unstable and slide because the ratio F_S / F_N (see Fig. 2.1) reaches the limit value $\tan \varphi_\mu$. The soil yields and strain is accumulated, while the stiffness decreases due to the damage induced to fabric. Moreover, it can be seen that yielding of soil occurs at strain higher than 0.001%, while at lower strain the response is linear elastic with modulus E_{max}. The unloading and reloading by a small amount of stress occur along a line or a narrow loop with slope approximately equal to the initial slope E_{max}. During unloading a smaller amount of strain than the one induced during virgin loading is erased. This strain is mainly related to the elastic rebound of grains, while some extremely small sliding may still occur (Shibuya et al. 1992). Reloading by the same small amount of stress does not induce irreversible strain (at least not a significant amount) and the same sloped line is followed. The grain contacts are more stable during this re-increase in stress ratio due to the memory of the previous loading and straining at the same stress ratio.

The discussion on the degradation of elastoplastic stiffness presented previously implied that the monotonic increase in stress ratio induces strain and decreases the tangent modulus (Vardoulakis 1980). However, it should be noted that if large stress amplitude cycles are imposed and the stress ratio changes repeatedly between $+\eta$ and $-\eta$ under drained conditions then the induced inelastic strain amplitude, after the stabilisation of the hysteresis loop, is the predominant factor that controls the degradation of elastoplastic stiffness, excluding the densification effects (Iwasaki et al.

1978, Tatsuoka et al. 1979, Seed et al. 1986, Vucetic and Dobry 1991). The characteristic degradation curve of elastoplastic modulus with strain amplitude is presented in Fig. 2.19. It can be seen that the ratio G / G_o (where G is the elastoplastic shear modulus at strain amplitude γ, further discussed later, and $G_o \equiv G_{max}$ is the elastic shear modulus at $\gamma_o = 10^{-6}$) decreases as the strain amplitude increases. Higher strain amplitude is induced by higher cyclic stress amplitude and, thus, higher extreme stress ratio, η. Moreover, it can be seen that the degradation of G / G_o is less significant when the effective confining stress is higher. This is because the “soil discreteness” is limited under high confinement (Towhata 2008). Lastly, it is observed that most sands exhibit similar G / G_o degradation curves irrespective of the differences in testing conditions.

The effect of strain amplitude on the degradation of stiffness is always apparent and predominant, irrespective of the initial shear stress and stress ratio or past cyclic stress history and over-consolidation history (Tatsuoka et al. 1979). This type of modulus strain dependence is at least as important as the dependence on confining stress and in many applications can even be more important (Houlsby et al. 2005; Roscoe 1970, Vardoulakis 1980, Cubrinovski and Ishihara 1998, Michaelides et al. 1998). Nevertheless, the effect of void ratio and confining stress on the elastic and elastoplastic moduli is discussed next.

The dependence of the elastoplastic moduli on the void ratio, e, is considered first. It is apparent in Figs 2.12a and 2.13a that the tangent and secant elastoplastic moduli at a given strain and confining stress level increases when the void ratio decreases. Dense sands are stiff and deform less under a given shear stress increment because the closely packed grains are mutually well supported and move only if the fabric is unlocked by means of dilative processes. Elastoplastic moduli depend, also, on the level of effective confining stress for a given strain level and void ratio, as can be seen in Figs 2.7a, 2.8a and 2.9a. Inelastic deformation is related to a frictional sliding mechanism, among other mechanisms such as dilatancy, so the confining stress dependence is justified. However, the dilatancy contribution is suppressed gradually as the confining stress increases.

On the other hand, the justification of the dependence of the elastic moduli on void ratio and confining stress needs a more scholastic interpretation. The reason is that the mechanism of irreversible frictional sliding and the coupled (via dilatancy) irreversible volume change, resulting from grains overriding other grains, is inert during elastic deformation. To begin with, we present the classic relationship that highlights this dependence (Hardin and Richart 1963):

$$G_{max} = 2630 \cdot \frac{(2.17 - e)^2}{1 + e} \cdot (p')^{0.5} \quad (p' \text{ and } G_{max} \text{ in lb/in}^2) \qquad (2.5a)$$

for rounded sands ($0.3 < e < 0.8$), or:

$$G_{max} = 1230 \cdot \frac{(2.97 - e)^2}{1 + e} \cdot (p')^{0.5} \quad (p' \text{ and } G_{max} \text{ in lb/in}^2) \tag{2.5b}$$

for angular sands (0.6 < e < 1.3). The term G_{max} is the elastic shear modulus (i.e. the slope dτ / dγ at very low γ, where τ and γ are the shear stress and shear strain in simple shear or torsional shear mode), e is the void ratio and p' is the mean effective stress. If S.I. units are used (i.e. kN/m^2 are used instead of lb/ m^2) then the angularity parameters 2630 and 1230 are substituted by 700 and 330, respectively (Richart et al. 1970). Affifi and Richart (1973) studied the time dependence of G_{max} and reported that the length of time the confining pressure is applied on certain soil materials may introduce important changes in G_{max} depending on the value of mean grain dimension D_{50}. Nevertheless, the stiffness of sands is not significantly affected.

According to Eq. 2.5, the elastic modulus of sand decreases with void ratio and increases with mean effective stress. Higher void ratio means looser packing and less grain contact points in a given volume of stressed sand. When a small increment of stress causes elastic deformation we can imagine that the induced increment of strain is higher if the grain contact points are fewer, because the load increment is applied on fewer points. This means that the excess *intergranular stress* is higher. Consequently, the elastic modulus is lower when void ratio is higher, and vice versa.

On the other hand, if the same small increment of stress is applied on sand having the same void ratio but subjected to higher effective confining stress then the elastic modulus is higher. In order to understand why this happens, we recall that a single point stressed contact between two solids cannot physically exist (Hertz 1882). Johnson (2003) suggests that "under the action of the slightest load the solids deform in the vicinity of their point of first contact so that they touch over an area which is finite, though small compared with the dimensions of the two solids". Figures 2.20a and b display the *interference fringes* at the contact of two equal cylindrical lenses, with their axes inclined at 45°, before and after the loading of contact, respectively. It is now reasonable to suggest that the grain contact surfaces are broader when the sand is confined under a higher effective stress. Consequently, the increment of load that causes elastic deformation induces less increment of strain because this load is applied on a broader surface at grain contacts and the excess intergranular stress is lower. This means that the elastic modulus of sand is higher under higher effective confining stress.

2.4 EFFECTS OF THE NON-DIRECTIONAL CHARACTERISTICS OF FABRIC ON THE DILATANCY OF SANDS

Sands subjected to shear deformation undergo irreversible volume changes. Loose sands contract and decrease in volume, while dense sands dilate and increase in volume. If the total volume changes of water saturated sands are restricted via imposing undrained conditions of shear deformation (i.e. blocking the drainage of pore water) then an increase in pore-water pressure is observed under contractive response, while a decrease in pore-water pressure is observed under dilative response. The change in pore-water pressure corresponds to the occurrence of plastic volumetric strain albeit the zero condition on total volumetric strain; in this case, the plastic volumetric strain is equal in magnitude with the elastic one but of different sign hence the total volumetric strain is zero.

The *dilatancy* of granular materials, which is the coupling between the plastic incremental shear and volumetric strains, was first described scientifically by Reynolds in 1885. It can be stated that the dilatancy of sands is due to their particulate nature: particle movements during deformation and failure of sands are not necessarily in the direction of the applied shear stress (Rowe 1962). On the contrary, solid steel can deform in shear isochorically (before the growth of plastic holes) because the "sea of negative electrons", as described by Feynman et al. (1964), holds the dislocated positive ions together "like some kind of glue". However, solidifying metals exhibit dilative behaviour, as reported by Gourlay and Dahle (2007), in a pattern similar to the one exhibited by granular materials. The plastic incremental volumetric strain of a granular material is related to the plastic incremental shear strain via the *dilatancy ratio*, which is a function of the mobilised stress ratio; the latter function is called the *stress - dilatancy relationship*.

Taylor (1948) proposed a stress - dilatancy theory based on energy considerations and experimental results from direct shear tests on sand. Figure 2.21 presents the idealisation of the kinematics and statics of the shear zone of sand (shear band) that dilates under shear distortion in plane strain mode. The reference to the positive axes in Fig. 2.21 provides the convention of positive stress and displacement. Following Taylor's energy considerations, the incremental work done by the external shear and normal force per unit area of the shear plane is:

$$\delta W = \tau \cdot \delta u_h - \sigma' \cdot \delta u_v \tag{2.6}$$

where τ and σ' are the shear and normal effective stress acting on the shear planes, and u_h and u_v are the relative 2D-displacements of the shear zone boundaries in the horizontal and vertical direction, respectively (see Fig. 2.21). Equation 2.6 can be rewritten in terms of rate of work done by the stresses:

$$\frac{\delta W}{\delta u_h} = \sigma' \cdot \left(tan\,\varphi_s - tan\,\psi_s \right) \tag{2.7}$$

where φ_s is the mobilised Coulomb friction angle, and ψ_s is the mobilised dilatancy angle, while the two mobilised stress ratios, $tan\ \varphi_s$ and $tan\ \psi_s$, are functions of the loading history parameter u_h (Vardoulakis and Georgopoulos 2005), that is:

$$tan\,\varphi_s = \frac{\tau}{\sigma'},\ tan\,\varphi_s = f_s(u_h) \tag{2.8a}$$

and:

$$tan\psi_s = \frac{\delta u_v}{\delta u_h},\ tan\psi_s = d_s(u_h) \tag{2.8b}$$

Granular materials are frequently assumed to be purely dissipative media. This means that the grains are rigid enough and the elastic deformations are minimal hence the elastic energy stored is practically negligible and the work done by internal forces is almost completely dissipated, that is:

$$\delta W \approx \delta D \tag{2.9}$$

where δD is the dissipated energy in heat production, acoustic emission, grain crushing and grain attrition. It is noted that on the basis of the 2nd Law of Thermodynamics (Fermi 1936) this assumption yields that the first-order incremental work is positive, $\delta W > 0$, which in turn results in the condition that the mobilised dilatancy angle is always lower than the mobilised friction angle (i.e. $\delta W > 0 \Rightarrow \psi_s < \varphi_s$) (Vardoulakis and Sulem 1995, Vardoulakis and Georgopoulos 2005). Moreover, Vardoulakis (1980) stated that the breakdown of the normality rule in sands and the consequent *non-associative flow rule* (Schofield and Wroth 1968) also result in the inequality $\psi_s < \varphi_s$. However, Vardoulakis and Graf (1985) reported novel experimental results indicating that inside the shear band it can exist a short-lived transient phase of post-failure deformation during which the normality rule approximately holds (i.e. $\psi_s \approx \varphi_s$).

The stress - dilatancy theory proposed by Taylor assumes that the energy dissipation rate is constant and independent of the hardening parameter $tan\ \varphi_s$:

$$\frac{\delta D}{\delta u_h} = \sigma' \cdot tan\varphi_{eq},\ \varphi_{eq} = const. \tag{2.10}$$

According to Eq. 2.10, the sand dissipates energy in the same way as a purely-frictional Coulomb material that deforms at constant volume with a constant friction angle, as can be seen in Fig. 2.22. Many authors assumed that the mobilised friction angle, φ_{eq}, of the equivalent (in energy dissipation aspects) purely-frictional solid should be taken as the friction angle at the ultimate state of sand, φ_{ult}, or at the phase transformation point, φ_{cv}, because at these states the sand deforms at constant volume with a constant friction angle. Some authors (Rowe 1962, de Josselin de Jong 1976) have proposed that the parameter φ_{eq} is a true angle of friction and considered it to be the interparticle friction angle, φ_μ. However, Skinner's (1969) and Koerner's (1970) physical experiments and Calvetti's et al. (2003) numerical experiments (Discrete Element Method simulations) do not verify this hypothesis.

Vardoulakis and Georgopoulos (2005) derived the following equation from Eqs 2.6, 2.9 and 2.10:

$$tan\varphi_s - tan\psi_s = tan\varphi_{eq} \tag{2.11a}$$

or

$$tan\varphi_s = tan\varphi_{eq} + tan\psi_s \tag{2.11b}$$

Equation 2.11b indicates that the shear strength of sands is attributed both to frictional resistance and to resistance due to the geometrical interference of grains. Notice that Eq. 2.11b, which is obtained based on energy considerations, is similar to Eq. 2.3, both indicating that non-frictional mechanisms, such as dilatancy, contribute to the shearing resistance of sands. Vardoulakis and Georgopoulos (2005) also used Eqs 2.8a and b to re-write Eq. 2.11b in the form:

$$d_s = f_s - f_{eq} \tag{2.12a}$$

in which they have considered the equivalent stress ratio function:

$$f_{eq} = tan\varphi_{eq} \tag{2.12b}$$

Equation 2.12a states that the dilatancy ratio is a function of the mobilised stress ratio and becomes zero when the latter becomes equal to the intrinsic equivalent stress ratio. Consequently, Eq. 2.12a is a stress - dilatancy relationship.

Gutierrez and Ishihara (2000) modified the stress – dilatancy relationship of sand in order to take into account the effects of non-coaxiality on the stress – dilatancy and energy dissipation mechanisms. Non-coaxiality is the non-coincidence of the principal directions of stress and plastic incremental strain. This behaviour is in contrast to the notion of coaxiality in plasticity (St. Vénant 1870) or in isotropic linear elasticity (Ishihara and Towhata 1983) and is reminiscent of the non-coaxiality observed in anisotropic linear elasticity (Vaniello 1996, Raftoyiannis 2007). Particularly, sands exhibit strong non-coaxiality when subjected to loading with rotating stress principal axes and weak non-coaxiality when subjected to loading with fixed stress principal axes, non-coincident with the principal axes of fabric (see Section 2.5), yet the degree of non-coaxiality diminishes as the sand is sheared to failure (Symes et al. 1984, Wong and Arthur 1985, Miura et al. 1986, Gutierrez and Ishihara 1991).

The modified Taylor – Gutierrez – Ishihara stress - dilatancy rule is:

$$\frac{d\varepsilon_v^p}{\left|d\varepsilon_q^p\right|} = \eta_c - c \cdot \frac{q}{p'} \tag{2.13}$$

where the dilatancy ratio under triaxial loading is:

$$D = \frac{d\varepsilon_v^p}{\left|d\varepsilon_q^p\right|} \tag{2.14}$$

The term $d\varepsilon_v^p$ is the plastic (irreversible) incremental volumetric strain and $d\varepsilon_q^p$ is the plastic incremental deviatoric strain. The dilatancy ratio, *D*, defines the direction of plastic flow in the *q* ($d\varepsilon_q^p$) - *p'* ($d\varepsilon_v^p$) space (Schofield and Wroth 1968). The parameter $\eta_c = (q\ /\ p')_c$ represents the stress ratio *q / p'* at which dilatancy is zero either at the ultimate or at the phase-transformation state (Gutierrez and Ishihara 2000). The non-coaxiality parameter *c* which multiplies the mobilised stress ratio *q / p'* varies with the stress ratio level and direction of incremental stress, and is introduced to account for the non-coaxiality effects on the stress - dilatancy relationship of sands. It is noted that the right parts of Eqs 2.12a and 2.14 differ in sign due to the different conventions for positive quantities used. Figures 23a and b present the stress - dilatancy plots from loading tests with both fixed and rotating stress principal axes; in the latter case, principal stress rotation was performed at fixed effective stress principal values. The results in the first figure are not corrected for non-coaxiality while the results in the second are. It can be seen that a practically unique stress – dilatancy relationship may describe the behaviour of sand under loading with both fixed and rotating stress principal axes after the correction for non-coaxiality is applied.

Vardoulakis and Georgopoulos (2005) pointed out that Taylor's stress - dilatancy formulation holds only for coaxial deformation. In the case that non-coaxial deformation is developed smoothly, Vardoulakis and Georgopoulos (2005) suggested that the modified relationship proposed by Gutierrez and Ishihara (2000) should be applied to account for non-coaxiality effects. However, if during a deformation process an abrupt rotation of the principal stress directions is induced, as in the case of an incipient shear band, then the modified dilatancy rule collapses. Gutierrez and Vardoulakis (2007) reported that significant differences are observed in the stress - dilatancy response of dilative sand subjected to triaxial loading before and after the occurrence of shear band bifurcation. These differences were attributed to the strong non-coaxiality occurring due to the sudden rotation of the stress principal axes in the incipient shear band (Vardoulakis et al. 1978). Figure 2.24a and b show the stress - dilatancy plots, before and after bifurcation, of the sheared sand at *p'* = 40 kPa and 120 kPa, respectively. It is apparent that the stress - dilatancy path follows different routes pre- and post-peak.

Many authors proposed various models to describe the stress - dilatancy relationship of sands after Taylor's theory was published. Newland and Allely (1957) proposed a model for the deformation mechanism of sand which is based on geometrical consideration of the spatial arrangement of grain particles, instead of applying energy considerations. The fundamental assumptions of their theory are shown in Fig. 2.25. The spherical particles under the arbitrary geometrical packing displayed in Fig. 2.25a represent the sand grains. The sliding of particles is the only deformation mechanism considered and occurs along the direction of the tangent at the contact point between adjacent particles. Even though different directions of particle sliding are physically manifested, a unique inclination of the sliding planes is considered, in order to aid the algebraic calculations. The direction of the sliding planes is different than the direction of the planes along which the shear stress τ is applied, as can be seen in Fig. 2.25c. The angle θ between the two families of planes justifies the dilatancy mechanism, while the evolution of this angle justifies the peak and the residual strength of sand in terms of peak (θ = max) and zero (θ = 0) dilatancy rates. Under these assumptions the theory suggests:

$$\frac{\tau_{max}}{\sigma_n^{'}} = tan(\varphi_\mu + \theta_{max}) \tag{2.15a}$$

$$\left(\frac{\delta v}{\delta \Delta}\right)_{max} = tan\,\theta_{max} \tag{2.15b}$$

$$\frac{\tau_r}{\sigma_n^{'}} = tan\,\varphi_\mu \tag{2.15.c}$$

where the term φ_μ is the interparticle friction angle, θ_{max} is the maximum angle between the planes of sliding and planes of shearing, τ and σ'_n are the shear and normal stress acting on the plane of shearing, and $(\delta v / \delta \Delta)_{max}$ is the maximum ratio of volume expansion to shear displacement. The residual strength τ_r is mobilised when "particles rise up on top of each other and individual values of θ become equal to zero", while the maximum strength is mobilised when the value of θ is maximum (i.e. the dilatancy rate is maximum).

Rowe (1962) studied the stress - dilatancy relationship for regular and irregular packings of uniform rigid rods and spheres. Two different regular packings of rods are shown in Fig. 2.26, while an assembly of spheres before and after being compressed to failure is shown in Fig. 2.27. Rowe (1962) considered only the mechanism of sliding between the rods or spheres in his study. For the two different packings, shown in Fig. 2.26, subjected to two-dimensional compression loading, he found that there exists a unique energy ratio:

$$-\frac{\sigma_1^{'} \cdot \dot{\varepsilon}_1}{\sigma_2^{'} \cdot \dot{\varepsilon}_2} = \frac{\sigma_1^{'}}{\sigma_2^{'}\left(1 + \dfrac{d\dot{V}}{V \cdot \dot{\varepsilon}_1}\right)} = \frac{tan(\varphi_\mu + \beta)}{tan\,\beta} \tag{2.16a}$$

$$D = 1 + \frac{d\dot{V}}{V \cdot \dot{\varepsilon}_1} \tag{2.16b}$$

where the term on the left is the ratio of the work done per unit volume by the active stress σ'_1, to the work done by the passive stress σ_2', the intermediate term is the energy ratio manipulated algebraically, the term φ_μ is the interparticle friction angle and the term β is the deviation of the tangent at the contact points from the direction of σ'_1 (Fig. 2.26). Notice that compressive stress and strain are taken as positive, while when the stress is in the same direction with strain rate (incremental strain) the work done is positive and the stress is termed "active". The dot above the symbols indicates the rate of the symbolised quantity. Obviously, the ratio D is a dilatancy quantity. Rowe (1962) hypothesised that Nature is efficient so the rate of internal work done $\dot{E}$ (i.e. the term on the left side of Eq. 2.16a) should be minimum. The algebraic relationships for a minimum to occur are $\mathrm{d}\dot{E}\ /\ \mathrm{d}\beta = 0$ and $\mathrm{d}^2\dot{E}\ /\ \mathrm{d}\beta^2 > 0$ and yield $\beta = 45° - \varphi_\mu / 2$, consequently the following stress - dilatancy relationship is produced:

$$\dot{E} = \frac{\sigma_1^{'}}{\sigma_2^{'}\left(1+\dfrac{d\dot{V}}{V\cdot\dot{\varepsilon}_1}\right)} = tan^2(45° + \varphi_\mu / 2) \tag{2.17}$$

The stress - dilatancy relationship given by Eq. 2.17 was produced adopting the minimum energy rate principle. De Josselin de Jong (1976) obtained the same result by considering the same model as Rowe (1962) but applying the friction laws only. It is important to note that the energy rate minimisation makes the stress ratio $R = \sigma'_1 / \sigma'_2$ uniquely related to dilatancy ratio D, and independent of the particle packing, described by the angle β, and void ratio, e (Li and Dafalias 2000). However, Li and Dafalias (2000) showed that the stress ratio R and dilatancy ratio D are indeed uniquely related for a given packing of rods, as indicated by the equilibrium at rod contacts in packing A or B in Fig. 2.26, yet the value of R (or D) is volume dependent. The dependence $D = D(e)$ or $D(\beta)$ (since $e = e(\beta)$) "is due to the equilibrium and kinematic microscopic constraints imposed by the given packing". Figure 2.28 shows that for a given stress ratio $\eta = (\sigma'_1 - \sigma'_2) / (\sigma'_1 + \sigma'_2)$ the dilatancy D depends not only on η but also on e and β.

The recognition of the factors that affect dilatancy is the key to understanding the behaviour of sands and modelling it within a unified framework. The stress - dilatancy relationships proposed by Taylor (1948) and Rowe (1962) suggest that dilatancy is a unique function of the stress ratio. This consideration contradicts the experimental evidence and makes the unified modelling of sand behaviour difficult (Li and Dafalias 2000). For example, Fig. 2.29 shows that Toyoura sand (tested by Verdugo and Ishihara 1996) may be contractive or dilative at the same stress ratio η. The observed difference in the dilatancy behaviour is due to the difference in the material state, expressed by means of the state parameter, ψ, proposed by Been and Jefferies (1985).

Li and Dafalias (2000) pointed out that one more paradox arises if the dilatancy is considered as a unique function of stress ratio. Let us consider a medium-to-dense sand subjected to undrained triaxial compression. As loading proceeds and the stress ratio increases the sand response changes from contractive to dilative at the phase transformation state (Ishihara et al. 1975), corresponding to stress ratio $\eta = M^d$. Afterwards, the material reaches the failure envelope, which is the peak stress ratio line in the q - p' space, and continues to exhibit dilative response; for many sands the failure stress ratio η_f is equal to the critical stress ratio M though the failure state is not identical to the critical state (the latter being the ultimate material state) because the void ratio is not critical (i.e. $\eta_f = M$ but $e \neq e_c$; Penman 1953, Roscoe et al. 1958, Li 1997). Consequently, the effective stress path in the q - p' space travels to the right along the failure envelope with slope $\eta_f = M$ still the dilation tendency ceases only when the ultimate material state is reached. In fact, the dilatancy is gradually exhausted during the constant-η phase that is termed *dilative shear failure* (Li 1997). It is obvious that if the dilatancy is considered a unique function of stress ratio (and of some intrinsic material properties) then an inexhaustible dilatancy would be related to the constant-η phase. However, this behaviour is not supported by experimental evidence.

Moreover, the dilatancy of sand is zero at both the phase transformation and critical state. If $D = D(\eta\ ,\ \varphi_\mu)$, as proposed by Taylor (1948) and Rowe (1962), then M^d should be equal to M and because M is an intrinsic material property so should also be M^d. According to Li and Dafalias (2000), this means that the phase transformation is intrinsic and the stress ratio M^d is independent of e and p', while the response of sand should change from contractive to dilative whenever the stress ratio reaches the value M^d (or M). However, it has been observed that when e is very high or p' is very high (or both) the sand does not exhibit phase transformation. More importantly, experimental results indicate that as the sand becomes denser (due to the combined effects of e and p') phase transformation is realised at a lower stress ratio. This behaviour is evidenced in Fig. 2.30 which shows the results from the loading tests on Toyoura sand performed by Verdugo and Ishihara (1996).

On the other hand, an opposite argument is stated in the literature. According to Vaid and his colleagues, the constant-volume friction angle, φ_{cv}, is indeed an intrinsic material property and so the stress ratio η_{cv} is unique; η_{cv} is related to $\sin\varphi_{cv}$ in triaxial compression conditions via the relationship (see also Eq. 2.4) (Negussey et al. 1988, Uthayakumar and Vaid 1998):

$$\eta_{cv} = \frac{6 \cdot \sin\varphi_{cv}}{(3 - \sin\varphi_{cv})} \tag{2.18}$$

The uniqueness of stress ratio η_{cv} indicates that all constant-volume states, either transient or steady, should have stress points in the q - p' space that lie on the same constant-η line (see also Wood 1990). This concept is visualised in Fig. 2.31 which shows the phase-transformation state, the steady state reached after fully contractive deformation and the steady state reached after dilative deformation all lying on the same line. However, experimental data reported by various researchers indicate that the phase-transformation line has not a unique slope (Verdugo and Ishihara 1996, Nakata et al. 1998, Zdravkovic and Jardine 2001, Georgiannou et al. 2018).

The state-dependent dilatancy of sands was modelled by Manzari and Dafalias (1997), Li et al. (1999), Li and Dafalias (2000) and other researchers. Cubrinovski and Ishihara (1998) also proposed a stress - dilatancy relationship that depends on the material state via the implicit dependence of the introduced *dilatancy parameter* μ (the evolving μ is used instead of the fixed M or η_c in Eq. 2.13) on the plastic shear strain, while this strain is linked to the evolution of state (e , p') through the stress - strain model. However, even though the strain-dependent behaviour of sand is well acknowledged (see Section 2.3), the strain is not a direct state parameter so this formulation may become problematic (see also Li 1997). On the other hand, Wan and Guo (1998) modified Rowe's stress - dilatancy relationship to incorporate the density dependence using the critical void ratio as a reference.

Presented in summary, Dafalias (Manzari and Dafalias 1997, Li and Dafalias 2000) models take into account that the phase-transformation line is moving as the state of sand changes. The current state of sand is described by the state parameter $\psi = e - e_c(p')$, introduced by Been and Jefferies (1985). The state parameter, ψ, measures the distance of the current void ratio, e, of sand subjected to mean effective stress, p', from the respective critical void ratio, e_c, at the same stress p', as can be seen in Fig. 2.32. The virtual *phase-transformation stress ratio* or *dilatancy stress ratio*, M^d, is given by the relationships:

$$M^d = M + k \cdot \psi \qquad (2.19a)$$

according to Manzari and Dafalias (1997), or:

$$M^d = M \cdot e^{m \cdot \psi} \qquad (2.19b)$$

according to Li and Dafalias (2000). In the above relationships, the term M is the critical stress ratio $(q \ / \ p')_{cs}$ in triaxial mode of loading (being different in compression compared to extension mode), the terms k and m are positive modelling parameters, the term ψ is the state parameter and e is the base of the natural logarithm. It is noted that the critical stress ratio is Lode-angle-dependent and in the general mode of loading is obtained from the values M_c and M_e corresponding to triaxial compression and extension, respectively, as described by Wang et al. (1990) and Manzari and Dafalias (1997).

The dilatancy function, $D = \mathrm{d}\varepsilon_v{}^p / \left|\mathrm{d}\varepsilon_q{}^p\right|$, is given by the relationship:

$$D = \frac{D_o}{M} \cdot \left(M \cdot e^{m \cdot \psi} - \eta \right) \qquad (2.20)$$

where ψ is the state parameter, D_o and m are positive modelling parameters, M is the critical stress ratio and η is the mobilised stress ratio $q \ / \ p'$. It is apparent from Eq. 2.20 that "the dilatancy D depends on the difference of the current stress ratio η from a reference stress ratio $Me^{m\psi}$, which is similar to the stress - dilatancy theory proposed by other researchers (Rowe 1962, Schofield and Wroth 1958, Roscoe and Burland 1968) but with the reference stress ratio varying with ψ instead of being fixed" (Li and Dafalias 2000). It is noted that phase transformation occurs when the mobilised stress ratio, η, becomes equal to the virtual dilatancy stress ratio, M^d.

Up to this point of presentation, only the non-directional characteristics of the fabric of sands, measured by the void ratio e, were taken into consideration. In the next section, the directional characteristics of fabric are introduced and methods for measuring these characteristics are presented. The strength, deformability, dilatancy and ultimate state of sands are considered under a revised framework in order to take into account the *fabric anisotropy*.

2.5 FABRIC ANISOTROPY

Sands are particulate materials consisting of discrete grains of various shapes put together in the field or in the laboratory mainly under the action of gravity. The geometrical arrangement of sand grains described with the term *fabric* (Oda 1972a, Brewer 1964) is characterised by the density of packing as well as the orientational distribution of contact normal and particle directions. Fabric anisotropy results from the shape and packing of the deposited grains and can be described quantitatively in the microscopic scale. Anisotropy in the microscopic scale accounts for the anisotropic mechanical behaviour of sands observed macroscopically hence it is very important to study the former in order to understand the latter.

Kjellman (1936) was possibly the first to notice that when the gravity-deposited sand is subjected to isotropic compression it exhibits anisotropic deformability. He observed that the vertical normal strain (i.e. the normal strain along the direction of deposition) is lower than the horizontal normal strains, which are practically equal. Ladd et al. (1977) reported that specimens of natural undisturbed sand subjected to isotropic compression demonstrated a ratio of volumetric to axial strain equal to 5.8 and, thus, a ratio of horizontal to vertical compressibility equal to around 2.4 (Gazetas 1981). For isotropic materials subjected to isotropic compression, the three normal strains are expected to be identical. Sands formed in the field or in the laboratory by means of gravity deposition are *cross-anisotropic (*or *transversely isotropic) materials*; they exhibit a vertical axis of rotational symmetry and horizontal planes of isotropy. Nowadays, the simple procedure of hydrostatic compression is used in order to characterise macroscopically the initial cross-anisotropic characteristics of fabric by means of deviation of the direction of incremental strain from the hydrostatic axis (Lade and Abelev 2005).

An even more extreme example of shear deformation of an anisotropic geomaterial subjected to isotropic compression was reported by Allirot at al. (1977). These researchers studied a soft stratified rock with cross-anisotropic fabric. They formed cylindrical specimens with the axis of the cylinder oriented at various angles θ with respect to the normal to the strata, as shown in Fig. 2.33. The specimens were subjected to many cycles of isotropic loading and unloading at elevated pressures; the pressure was increased in each cycle, reaching a maximum value of 1000 bars (1 bar = 0.987 atm) during the last cycle, and the anisotropic plastic deformation was observed. The specimens characterised by an angle $0° < \theta < 90°$ deformed into elliptic inclined cylinders. The specimen with $\theta = 0°$ remained a right cylinder with circular cross-section, while the one with $\theta = 90°$ remained a right prism but with elliptic cross-section. All the deformed specimens are shown in Fig. 2.34a, while the cross-sections before and after deformation of the specimens with $\theta = 0°$ and 90° are shown in Figs 2.34b and c, respectively. Similar distortional patterns of deformation of specimens with inclined axis of rotational symmetry subjected to triaxial or plane-strain compression along the vertical direction were reported by Boehler and Sawczuk (1977) and Oda et al. (1978).

The aforementioned examples highlight the anisotropic deformation of geomaterials under hydrostatic or deviatoric loading. These results indicate that the fabric of geomaterials formed by means of mere deposition in the laboratory or sedimentation and lithification in the field is anisotropic. From a microscopic point of view, there are some fabric-related directional quantities that give a measure of anisotropy. These quantities, as well as the techniques used to measure them in the case of sands, are discussed next.

A. *The orientational distribution of contact normal vectors gives a measure of fabric anisotropy*. The grains of sand deposited under the action of gravity have more contact surfaces with normals oriented along the direction of deposition (Oda 1972a). The contact normal orientation is the direction of the normal vector, N_i, to the tangential contact plane between two grains; in fact, there exist two opposite normal vectors at a given contact, each "attached" to a different grain. Figure 2.35b shows a grain (G1) with four contact surfaces characterised by the contact normals N_i. The contact normals N_i can be determined by measuring two direction angles α and β with respect to three fixed reference axes in the physical space, as can be seen in Fig. 2.36. The angular frequency distribution of the contact normals or probability density of the contact normals, $E(\alpha,\beta)$, can thus be determined as a function of α and β. This distribution provides, after tensor-calculus manipulations (Satake 1978, Oda et al. 1985), the *intensity of anisotropy*, i.e. the ratio of the major to the minor principal component of the contact-normal tensor, and the *preferred orientation* of the contact normals, i.e. the direction along which the major principal component of the contact-normal tensor is observed. In order to detect the contact points in a sand mass and determine the contact-normal directions, Oda (1972a and b) impregnated a low-viscosity polyester resin into the pores of the sand specimens without disturbing the depositional fabric. After a curing period, the resin turned into a hard vitreous matrix that kept steadily the sand grains in their depositional configuration. The stabilised sand was cut with a diamond saw and polished in order to prepare *thin sections* that were studied by means of a *petrographic microscope*. Thin sections were cut along vertical, horizontal and inclined planes, as can be seen in Fig. 2.37. The inclined planes were cut at 45° above the horizontal plane. The directions of contact normals were, then, determined by means of visual inspection.

B. *The orientational distribution of non-spherical grains gives a measure of fabric anisotropy.* The long axes of non-spherical grains tend to align with the horizontal planes, called the *bedding planes*, when sand is deposited under the action of gravity. The directions of the long axes of the grains (L-axes) with respect to the reference fixed horizontal axis (X-axis) can be determined in order to quantify fabric anisotropy. The angle θ between the L-axis and the X-axis is shown in Fig. 2.38 for a natural grain captured on a thin section; a parallelogram is used to enclose the grain in order to determine the apparent dimensions of the long and short axes. The ratio of the length of the long axis to the length of the short axis, called *aspect ratio*, affects the intensity of anisotropy (Oda 1978), as will be shown next. If regular shaped elements (e.g. oval prismatic elements) are used in physical or numerical experiments then the exact shape and orientation of each element can be described by means of a second-order tensor (Oda et al. 1985). Oda (1972a) presented the orientational distributions of the long axes of sand grains in the form of *frequency histograms*.

C. *The orientational distribution of elongated voids gives a measure of fabric anisotropy.* The volume occupied by grains inside a sand mass is complementary to the volume occupied by voids, thus, anisotropy is associated not only with the shape (and packing) of grains but also with the shape of voids. The process B described previously can be applied with some modifications (Oda et al. 1985) in order to determine the relative dimensions of the principal axes of the voids and the directions of the long axes of the voids. The orientational distribution of elongated voids can, then, be used to describe and quantify the anisotropy of fabric by means of a second-order fabric tensor.

Figure 2.39 shows the results reported by Oda (1972a) in the form of frequency histograms of the orientation angles θ of the apparent long axes of sand grains in a vertical (V), an inclined (at 45° above the horizontal plane) and a horizontal (H) thin section. The thin sections were cut from specimens formed by pouring sand into a cylindrical mould, tapping the side walls to achieve densification and impregnating the sand pores with the stabilising resin; the angles θ were measured on the thin sections by means of microscope inspection. It can be seen that in the case of vertical and incline sections there exists an almost unimodal frequency distribution with a peak value indicating a preferred orientation at around θ=0°. On the other hand, the frequency distribution in the horizontal section does not show any preferred orientation of the apparent long axes. Consequently, the grains tend to align their long axes along the horizontal bedding planes perpendicular to the direction of gravity deposition. On the horizontal planes though, the grains are randomly oriented meaning that the sand exhibits *transverse isotropy*.

The transverse isotropy of sand makes the function that gives the probability density of the contact normals $E(\alpha,\beta)$ degenerate to $E = E(\beta)$, meaning that the distribution of the contact normals depends only on the polar angle β and not on the azimuth angle α shown in Fig. 2.36. This function is plotted in Fig. 2.40 for the same sand for which the histograms are presented in Fig. 2.39 (Oda 1972a). The angles β are measured on the thin sections by means of microscope inspection. The dashed horizontal line in the plot corresponds to the isotropic fabric with no preferred orientation of the contact normals. It is obvious that the sand's fabric is anisotropic in the sense that the contact normals are highly concentrated at around $\beta = 0°$, close to the vertical direction of gravity deposition.

Figure 2.41 shows a cubic volume of a gravity deposited sand with elongated grains and distinct bedding planes, called sand A; the frequency histograms and probability density function of sand A are shown in Figs 2.39 and 2.40, respectively, indicating the anisotropy of fabric in terms of particles and contact normals orientation. A cubic volume of a gravity deposited sand with rounded grains, called sand D, is also presented in Fig. 2.41 for comparison. Sand D cannot exhibit anisotropy in terms of preferred orientation of the long axes of grains because the grain shape is nearly spherical. Still, the fabric of sand D is anisotropic in terms of orientational distribution of the contact normals and elongated voids. For example, Graton and Fraser (1935) showed that when identical spheres are put into a random packing most of the interparticle contact planes have small-angle dips. Moreover, Kallstenius and Bergau (1961) found that the density of gravity deposited spheres is different in vertical than in horizontal sections, and identified chain-like sphere structures (see also Oda 1972a). Li (2006) and Li and Dafalias (2012) reported that the packing anisotropy of identical rods with circular cross-section affects dilatancy. These observations justify why granular materials with nearly spherical grain shape can exhibit strongly anisotropic behaviour (Arthur and Dunstan 1969 and 1970, Arthur and Menzies 1972, Shibuya and Hight 1987).

Casagrande and Carillo (1944) distinguished the *inherent anisotropy* of granular materials, which is the result of the deposition process and grain shape characteristics, from the *induced anisotropy*, which evolves due to straining in response to the applied stresses. However, many researchers argue that the deposition is, actually, a specific stress - strain history and propose the term *depositional anisotropy* instead of the term *inherent anisotropy*. In general, whenever a granular material is subjected to a deviatoric load the fabric characteristics evolve in order to sustain this load as efficiently as possible. The deviatoric stress, q, is given by the relationship:

$$q = \sqrt{\frac{1}{2}\left\{\left(\sigma_1 - \sigma_2\right)^2 + (\sigma_2 - \sigma_3)^2 + (\sigma_3 - \sigma_1)^2\right\}} \tag{2.21}$$

where σ_1, σ_2, σ_3 are the principal values of stress. Note that only stress differences are participating in the equation thus the total or the effective stresses (Terzaghi 1925) can be used interchangeably. The deviatoric stress, q, given by Eq. 2.21 is an *invariant quantity* regardless of the orientation of the coordination system used. If axisymmetric stress conditions are applied, that is $\sigma'_2 = \sigma'_3 \neq \sigma'_1$ or $\sigma'_2 = \sigma'_1 \neq \sigma'_3$, the invariant quantity q takes the simpler form:

$$q = \sigma_1 - \sigma_3 \tag{2.22}$$

The maximum deviatoric stress that can be sustained when a cross-anisotropic sand is subjected to drained loading depends not only on the value of mean effective stress p' but also on the direction of the σ'_1-axis with respect to the direction of the normal to the bedding planes. This is a typical example of strength anisotropy of sands.

Oda et al. (1978) investigated the effect of inherent anisotropy on the strength, stiffness and dilatancy characteristics of gravity deposited sand subjected to drained triaxial and plane strain compression (TC and PSC in abbreviation). The direction of the σ_1-axis was fixed and vertical in both types of testing, while the bedding planes of the specimens were inclined at various angles δ with respect to the vertical plane. This practically means that the bedding planes were horizontal when δ = 90° and vertical when δ = 0°. The techniques used to form specimens with non-horizontal bedding planes are presented in Fig. 2.42, for both types of testing. The sand was poured into a tilted container, forming horizontal bedding planes. The longitudinal axis of the container made an angle δ with the horizontal. Afterwards, the saturated sand was frozen, rotated until the tilted container became vertical and trimmed to the dimensions which fitted the apparatus used. The frozen specimens were covered with a rubber membrane and placed inside the cell of the apparatus. A low suction was applied during the period of thawing. Afterwards, the specimens were consolidated isotropically and subjected to monotonic drained PSC or TC.

Figures 2.43a and b show the stress - strain and volumetric behaviour of Toyoura sand specimens with inclined bedding planes subjected to drained PSC and TC, respectively (Oda et al. 1978). The influence of fabric anisotropy on the mechanical behaviour of sand is immediately recognised. The peak strength at failure, q_p, and the concurrent peak dilatancy ratio, $(d\varepsilon_{vol} / d\varepsilon_1)_p$, increase with the angle δ, for both PSC and TC loading tests, though at higher strain a common ultimate strength is mobilised, possibly due to the erasure of the initial fabric and evolution of a new fabric common to all specimens. The tangent and secant shear moduli, also, increase with δ, though the initial slope seems to be independent of δ. Figure 2.43a shows that, in the case of PSC tests, the specimens with δ = 24° and 30° exhibit the minimum values of peak strength. This is because when δ = 15° - 30° the direction of the σ'_1-axis makes an angle of 60° - 75° with the normal to the bedding planes and one of the *planes of maximum stress obliquity* (i.e. the planes on which the stress ratio τ / σ'_n is maximum) coincides or almost coincides with the bedding planes (see also Matsuoka 1974, Matsuoka and Ishizaki 1981, Tatsuoka et al. 1986b, Miura et al. 1986, Nakata et al. 1998, Lade et al. 2014).

Figure 2.43 shows that the peak strength is more sensitive to δ in PSC than in TC tests, which means that the effect of anisotropy on strength is more profound under plane strain conditions (Oda et al. 1978). Moreover, the peak state is reached at smaller strain and the peak strength is higher for a given δ in PSC than in TC tests, at least for the case with $\sigma'_3 = 2.0$ kgf/cm^2 shown in Figs 2.43a and b. The peak dilatancy ratio is higher under PSC than TC loading though this ratio is mobilised at lower strain and decreases quickly in the post-peak regime, resulting in a lower ultimate dilation (see also Cornforth 1964). These observations may indicate that the constraint $\varepsilon_2 \equiv 0$ provides lateral support and enhances the fabric interlocking resulting in a beneficial effect on strength (Tatsuoka et al 1986b, Shibuya and Hight 1987, Zdravkovic and Jardine 2000 and 2001; O'Sullivan et al. 2013). Moreover, the interlocking slows down the evolution of fabric up to the failure state and this may be the reason why the initial fabric anisotropy has more profound effect on the peak strength in the case of PSC tests. Nevertheless, the fabric is unlocked after the peak state, possibly due to shear banding (Vardoulakis et al. 1978, Vardoulakis 1980), and evolves more quickly as the sand is sheared towards the ultimate state.

In the study by Oda et al. (1978), the effect of inherent anisotropy on the mechanical behaviour of sand was highlighted, yet, it was also suggested that the initial properties of fabric evolve due to the imposed stress-strain history. Oda (1972b) had already measured one directional property of sand fabric as it evolved during deformation under drained TC loading. This property was the ratio S_z / S_x of the summation of projected areas of grain contact surfaces on the vertical YZ-plane (S_z) to the summation of projected areas of grain contact surfaces on the horizontal XY-plane (S_x). The methodology used to determine the *fabric index* S_z / S_x is presented in Fig. 2.44a. The projected areas of grain contact surfaces were measured on thin sections cut from resin-stabilised sand using a petrographic microscope; the stabilisation and inspection techniques used were the same as the ones described previously. Two vertical (V) and two horizontal (H) thin sections are shown in Fig. 2.44b. The first pair of thin sections corresponds to specimen T-2 which was loaded until the stress ratio, σ'_1 / σ'_3, and the axial strain, ε_a, reached the values 2.65 and 0.37%, respectively. Afterwards, the axial load was removed and the specimen, which had pores saturated with water-resin solution, was left to cure under suction until it became hard enough to be treated and cut. The second pair of thin sections corresponds to specimen T-6 which was loaded until the values $\sigma'_1 / \sigma'_3 = 4.09$ and $\varepsilon_a = 5.18\%$ were reached and then it was unloaded, left to cure and treated.

Oda (1972b) interpreted the experimental results and measurements of the fabric property S_z / S_x and reported a finding with great importance for the comprehension of sand behaviour. He stated that the mobilised stress ratio, σ'_1 / σ'_3, and dilatancy ratio, $d\varepsilon_{vol} / d\varepsilon_1$, depend on the current value of the evolving fabric property, S_z / S_x, in the way described by the following equations:

$$\frac{\sigma_1'}{\sigma_3'} = k_1 \cdot \frac{S_z}{S_x} + k_2 \tag{2.23a}$$

$$\frac{d\varepsilon_{vol}}{d\varepsilon_1} = k_3 \cdot \frac{S_z}{S_x} + k_4 \tag{2.23b}$$

The terms k_1 to k_4 are material constants which Oda (1972b) suggested to be independent of fabric and grain shape. Despite the dependence of the stress and dilatancy ratio on S_z / S_x, Oda (1972b) stated that the stress - dilatancy relationship is actually independent of S_z / S_x (see also Tatsuoka 1976) and can be given by the following equation:

$$\frac{\sigma_1'}{\sigma_3'} = k_5 \cdot \frac{d\varepsilon_{vol}}{d\varepsilon_1} + k_6 \tag{2.24}$$

The stress - dilatancy relationship expressed by Eq. 2.24 was found to fit well, with a unique set of parameters k_5 and k_6, the data corresponding to pre-failure and failure states from loading tests on specimens with inclined bedding planes at various angles with respect to the major principal axis of stress, formed using two quartz sands and different compaction methods (Oda 1972b). The tested specimens had different initial void ratios and were consolidated to different initial effective confining stresses (σ'_{3c} = 0.5 - 3.0 kgf/cm^2). Consequently, the constants k_5 and k_6 are independent of the current value of the fabric property S_z / S_x and are determined for each granular material without being related to fabric. It was suggested that only the type of mineral (or, alternatively, the intergranular friction angle, φ_μ) affects these constants and not the grain shape (see also Rowe 1962). The stress - dilatancy plots of the two quartz sands are shown in Fig. 2.45. However, it is important to note that recent physical and numerical experiments showed the dependence of stress – dilatancy behaviour on both the state and anisotropy of sand (Verdugo and Ishihara 1996, Yoshimine et al. 1998, Wan et al. 2010, Huang et al. 2014) which was successfully simulated by state-of-the-art constitutive models (Manzari and Dafalias 1997, Li and Dafalias 2000, Li and Dafalias 2002, Dafalias and Manzari 2004, Dafalias et al. 2004, Li and Dafalias 2012).

Oda et al. (1974b, 1982, 1985) investigated the stress-induced anisotropy of granular assemblies consisted of photoelastic rods with circular or oval cross sections. The photoelastic rods were placed by hand in tilted containers, as shown in Fig. 2.46, in order to form assemblies with inclined initial bedding planes. The bedding planes inclination angle, θ, is measured from the horizontal X_1-axis in these studies, meaning that horizontal bedding planes correspond to θ = 0°, while vertical ones correspond to θ = 90°. The granular assemblies were subjected to bi-axial compression or simple-shear loading and photoelastic pictures were taken at various states in the course of deformation. In this way, the fabric properties of the granular assemblies were monitored during the successive phases of monotonic loading and straining, without the need to follow the previously used methodology (Oda 1972b) of unloading different specimens and stabilising them with resin, in order to inspect the fabric at one state at a time. Figure 2.47 shows the photoelastic pictures of an assembly of oval-shaped rods, with horizontal initial bedding planes, subjected to biaxial compression. The pictures are taken at various states, namely the initial, the pre-failure, the failure and the post-failure state.

Oda et al. (1985) used second-order tensors (Satake 1978) in order to describe the fabric anisotropy associated with contact normals, particles shape and voids shape. Specifically, the fabric tensor $\mathbf{N_{ij}}$ describes the orientational distribution of contact normals. If N_1 and N_2 are the major and minor principal components of $\mathbf{N_{ij}}$ then the ratio N_1 / N_2 is an index showing the intensity of anisotropy due to the different density of contact normals along the different directions. The preferred orientation of contact normals is defined by the inclination angle α, which shows the direction along which the maximum value, N_1, is observed. In the same way, the fabric tensor $\mathbf{S_{ij}}$ describes the orientational distribution of rod particles with non-circular cross sections. If S_1 and S_2 are the major and minor principal components of $\mathbf{S_{ij}}$ then the ratio S_1 / S_2 is an index showing the intensity of anisotropy due to the different density of particles' long axes along the different directions. The preferred orientation of the particles' long axes is defined by the inclination angle β, which shows the direction along which the maximum value, S_1, is observed. Lastly, the fabric tensor $\mathbf{V_{ij}}$ describes the orientational distribution of elongated voids. The ratio of the major and minor principal values, V_1 / V_2, is an index showing the intensity of anisotropy due to the different density of voids' long axes along the different directions. The preferred orientation of the voids' long axes is defined by the inclination angle γ, which shows the direction along which the maximum value, V_1, is observed. The inclination angles α, β and γ are measured with respect to the horizontal reference X_1-axis.

Figure 2.48 shows the evolution of the anisotropy indices N_1 / N_2, S_1 / S_2 and V_1 / V_2, inclination angles α, β and γ, stress ratio, σ'_1 / σ'_2, and volumetric strain, ε_{vol}, with increasing axial strain, ε_a. The results shown are from bi-axial compression tests on three different assemblies consisted of two different types of oval-shaped rods (Oda et al. 1985). The oval I rod has an aspect ratio equal to 1.1, so the particle has an almost circular cross section, while the oval II rod has an aspect ratio equal to 1.4, showing an elongated shape of cross section. Figure 2.48 shows that the anisotropy index N_1 / N_2 follows always the same evolution trend as the stress ratio σ'_1 / σ'_2, increasing pre-peak, attaining the maximum value at failure and then decreasing post-peak. High but different values of the index N_1 / N_2 are mobilised at failure depending on the type of oval rods and the value of θ, for example N_1 / N_2 > 30 in the case of oval II rods assembly with θ = 0°, N_1 / N_2 > 3.5 in the case of oval II rods assembly with θ = 60° and N_1 / $N_2 \approx 7$ in the case of oval I rods assembly with θ = 0°.

Figure 2.48 also shows that the preferred orientation of contact normals remains fixed when θ = 0°, irrespective of the type of oval rods, since the inclination angle α shows a constant value of around 90° (Oda et al. 1985). This means that when the σ'_1-axis is normal to the bedding planes the major principal direction of the fabric tensor $\mathbf{N_{ij}}$ remains fixed as the assembly is compressed and only the fabric intensity changes. On the other hand, in the case of oval II rods assembly with θ = 60° the inclination angle α has an initial value of around 130° and changes gradually in the course of deformation towards the value of 90°. This means that the major principal direction of the fabric tensor $\mathbf{N_{ij}}$ rotates because the density of the contact normals builds up along the direction of the σ'_1-axis which is initially different than the principal direction of the fabric tensor $\mathbf{N_{ij}}$.

Oda et al. (1985) drew two important conclusions regarding the evolution of the fabric tensor $\mathbf{N_{ij}}$. The first is that the strain hardening process of a granular assembly (i.e. the increase in stress ratio with shear strain) is closely related to the appearance of new contacts along the direction of the σ'_1-axis and elimination of existing contacts along the direction of the σ'_2-axis. This mechanism results in increasing fabric anisotropy intensity associated with the formation of column-like structures of particles bearing the compressive load along the direction of the σ'_1-axis (see Fig. 2.47c). These structures will be called *force bearing chains* or *force chains* hereinafter. After the peak state (failure state) is reached, the force chains begin to buckle and collapse leading to *strain softening* (i.e. to a decrease in stress ratio with shear strain). Oda et al. (1985) stated that the structural collapse leads to a “diffuse distribution” of contact normals at the ultimate state, as indicated by the rapid decrease in the index N_1 / N_2 post-peak (see Fig. 2.48). However, the fabric at the ultimate state is definitely anisotropic as has been recently shown by physical and numerical micromechanical studies (Thornton 2000, Fu and Dafalias 2011b, Li and Dafalias 2012, Zhao and Guo 2013, Wiebicke et al. 2017). The second conclusion drawn by Oda et al. (1985) is that the major principal direction of the fabric tensor $\mathbf{N_{ij}}$ rotates in order to become coincident with the fixed major principal direction of the stress tensor. Consequently, the contact normal fabric tensor evolves norm-wise and direction-wise during loading with fixed stress principal axes.

Oda and Konishi (1974a) pointed out that the major principal direction of the contact normal fabric tensor rotates towards the major principal direction of the stress tensor also in the case that the latter rotates as well. They performed 2D simple-shear loading tests using photoelastic cylinders of different radii, which were packed randomly in dense and loose assemblies with horizontal bedding planes. Figure 2.49a shows the results from these tests in terms of the shear force and volumetric strain plotted against shear distortion. The direction angle, β, was defined as the angle between the normal to the contact of two adjacent cylinders and the reference Z-axis shown in Fig. 2.49b. The evolution of β at each contact was monitored using successive photoelastic pictures taken during loading and the evolving orientational distribution of contact normals was then determined as shown in Figs 2.49 c and d for the cases a dense and a loose assembly of cylinders, respectively. It is apparent that the predominant orientation of contact normals changes from 0° towards 45° in order to align with the rotating σ'_1-axis during the simple shear loading (Roscoe et al. 1967, Roscoe 1970). It can be also inferred that as the shear force increases new contact normals appear near the direction of the $\sigma'1$-axis and existing contact normals vanish near the direction of the $\sigma'2$-axis. Consequently, the contact normal fabric tensor evolves norm-wise and direction-wise under the concurrent increase in shear stress and rotation of the stress principal axes.

Oda et al. (1985) showed that the fabric tensors related to particles and voids orientation also evolve in the course of deformation though at a different rate than that corresponding to the contact normals fabric tensor. With reference to Figs 2.46, 2.47, 2.48 the evolution of the fabric tensor related to particles orientation is discussed next. It is apparent that the fabric anisotropy intensity is higher in the case of particles with elongated shape of cross section (e.g. oval II rods). The oval I rods have almost circular cross sections so the anisotropy index S_1 / S_2 expressing the ratio of the principal values of the fabric tensor $\mathbf{S_{ij}}$ does not exceed 1.1 and is omitted in Fig. 2.48c. In the case of oval II rods assembly with θ = 0° (Fig. 2.48a) the preferred orientation of the long axes of particles is initially at an angle of β = 0° to the horizontal and increases slightly at post-failure states. Accordingly, the anisotropy index S_1 / S_2 has an initial value of approximately 1.3 and drops to 1.2 at the ultimate state. In the case of oval II rods assembly with θ = 60° (Fig. 2.48b), the direction angle β is initially equal to 60° and decreases slightly with vertical strain, while the anisotropy index S_1 / S_2 is initially equal to 1.3 and drops to 1.1 at the ultimate state. It is important to notice that the direction angle β and the anisotropy index S_1 / S_2 remain approximately constant until the failure state is reached. This means that the particles orientation evolves very slowly and can be thought of as a fabric characteristic that endures during shearing up to the failure state, justifying the observed effects of the inherent anisotropy on the strength and dilatancy of granular materials.

Oda et al. (1985) observed that the initial shape of voids is almost circular in all assemblies tested, as can be seen in Figs 2.48a, b and c which show that the value of the anisotropy index V_1 / V_2 expressing the ratio of the principal values of the fabric tensor $\mathbf{V_{ij}}$ is around 1.1. However, the shape of voids becomes elongated in the course of deformation since the anisotropy index V_1 / V_2 increases and reaches its maximum value of around 1.5 at large strains related to post-failure states, and afterwards begins to decrease. It is interesting to notice that the voids become slender and simultaneously their growing long axis rotates in order to align with the direction of the σ'_1-axis. Figure 2.50 illustrates in successive photoelastic pictures the evolution mechanism that makes the smaller voids connect with each other to form elongated voids that exist between the column-like structures of particles that support the compressive load. Oda et al. (1985) suggested that the slender voids are prone to collapse upon stress reversal or lateral loading and this microscopic mechanism associated to stress-induced anisotropy may justify the macroscopically observed contractive behaviour of sands under such loading conditions (Ishihara et al. 1975, Goldscheider 1975, Yamada and Ishihara 1981, Vaid and Chern 1983, Papadimitriou et al. 2001, Dafalias and Manzari 2004a).

Up to this point, the directional fabric characteristics that are the source of anisotropy of granular materials have been presented and the physical techniques used to measure these evolving characteristics have been discussed. Apart from physical techniques, there are also *numerical techniqu*es which allow the measurement of the directional fabric characteristics, as well as a number of other properties at the micro scale. The most popular of these techniques is the *Discrete Element Method (DEM)*, introduced by Cundall and Strack (1979).

The basic idea of DEM is that the mechanical behaviour of an assembly of discs, spheres or otherwise shaped elements can be described by applying the fundamental laws of Mechanics. A small number of mechanical parameters, such as the intergranular friction angle, φ_μ, and the normal and shear stiffnesses at the grain contact points, k_n and k_s, respectively, are used in the force - displacement law (Hooke's law), Coulomb's friction law and Newton's Laws of Mechanics in order to define the position, velocity and acceleration of the discrete elements, as well as their interaction (Cundall and Strack 1979). As stated by Cundall and Strack (1979), "the interaction of particles is monitored contact by contact and the motion of the particles modelled particle by particle".

DEM simulations offer the advantage of scholastic monitoring and direct measurement of the fabric properties, at any state during loading. Complex stress and strain histories can be applied under various boundary conditions, manipulated skillfully. Specimens can be formed to have the desired initial fabric characteristics (anisotropic or isotropic, homogeneous or intentionally inhomogeneous etc.), while identical specimens can be tested multiple times. Moreover, local measurements of strain or void ratio are easily acquired when performing DEM simulations, for example inside the shear band or in an arbitrary domain inside the specimen (Fu and Dafalias 2011a). Despite the small number of elements that is usually used due to computational limitations it has been shown that many aspects of the macroscopic behaviour of granular materials can be simulated efficiently using DEM, while concurrently insight is gained into the mechanisms governing the microscopic behaviour. Selected results from DEM studies will be presented next, without investigating the details in the numerical techniques used.

2.6 EFFECTS OF THE DIRECTIONAL CHARACTERISTICS OF FABRIC AND GRAIN PROPERTIES ON THE FRICTIONAL BEHAVIOUR OF SANDS

Coulomb's failure criterion for granular materials describes the condition for *shear failure on a plane*. The maximum value of shear stress τ_p that a non-cohesive granular material can mobilise on a plane, for a given normal stress σ'_n acting on this plane, is given by Eq. 2.1; that is: $\tau_p = \tan\varphi \ \sigma'_n$, where φ is the material's angle of shearing resistance. This relation is the well-known Coulomb's shear failure criterion. The strength characteristics of granular materials are frequently determined experimentally by means of triaxial and plane strain compression tests under drained conditions. In both testing procedures, the minor principal effective stress σ'_3 is held constant while σ'_1 increases, due to the imposed increments of displacement or force, until it reaches the maximum value σ'_{1p} at failure; note that the material fails when stress ratio $\eta = q / p'$ or $\sin \varphi_b = (\sigma'_1 - \sigma'_3) / (\sigma'_1 + \sigma'_3)$ becomes maximum. In this case, Mohr's failure criterion suggests:

$$\sin\varphi = \frac{\sigma'_{1p} - \sigma'_3}{\sigma'_{1p} + \sigma'_3} \tag{2.25}$$

Notice that Coulomb's criterion, expressed by Eq. 2.1, is a shear plane based formulation of failure condition, while Mohr's criterion, expressed by Eq. 2.25, is a principal stress space based formulation (Fu and Dafalias 2011a, Tong et al. 2014). Nevertheless, it is common in soil mechanics practice to convert the one criterion into the other and use the so-called Mohr - Coulomb failure criterion. The graphical representation of the Mohr - Coulomb criterion is shown in Fig. 2.51c. The Mohr's circle expands, as σ'_1 increases, until it touches the failure line which is a boundary to the admissible stress states. Note that both stress ratios tan φ and sin φ can be determined using the Mohr's circle shown in Fig. 2.51c. The material is assumed to fail on the plane of maximum stress obliquity, along which the maximum ratio τ / σ'_n is mobilised. The slope of the failure line is $(\tau / \sigma'_n)_{max}$ or tan φ; the shear and normal stresses acting on the failure plane are given by the coordinates of the point at which the circle touches the failure line (point a in Fig. 2.51c).

Let us consider the case in which the material tested exhibits fabric anisotropy. The *tilting angle*, δ, is defined as the angle between the bedding plane of the granular material and the plane on which the principal stress σ'_1 acts, as shown in Fig. 2.51a. The tilting angle δ is substantially the same as the angle θ defined in Fig. 2.46, ranging between 0° and 90°. As has been already presented, if a granular material with tilted bedding planes is subjected to drained plane strain compression the failure stress ratio (or the failure major principal stress σ'_{1p}) is strongly dependent on δ (see Fig. 2.43a). Consequently, in many studies the angle of shearing resistance is suggested to be a function of δ and is expressed by reorganising Eq. 2.25 to yield:

$$\varphi(\delta) = \sin^{-1}\left(\frac{\sigma'_{1p}(\delta) - \sigma'_3}{\sigma'_{1p}(\delta) + \sigma'_3}\right) \tag{2.26}$$

However, Fu and Dafalias (2011a) pointed out that the applicability of Eq. 2.26 to anisotropic materials needs careful consideration because some noteworthy assumptions are implied. Specifically, it is assumed that along *any* potential failure plane the maximum feasible shear stress, τ_p, is proportional to the normal effective stress, σ'_n, via the relation $\tau_p = \tan\varphi\ \sigma'_n$, where the angle of shearing resistance, φ, depends on δ; φ does not depend, though, on the inclination of the *actual* failure plane with respect to the bedding plane. Secondly, it is assumed that failure occurs when the mobilised stress ratio τ / σ'_n becomes equal to tan φ *in any plane*.

Concerning these assumptions, Fu and Dafalias (2011a) stated that "for materials with anisotropic strength characteristics, shear strength is apparently dependent on the orientation of the potential shear plane with respect to the bedding plane, but such shear plane does not have to coincide with the plane of maximum stress obliquity" (see also Roscoe 1970, Vardoulakis et al. 1978, Vardoulakis 1980); note that the terms *shear plane* and *failure plane* are used interchangeably. For example, in Fig. 2.51b the maximum stress obliquity plane (a - a) is displayed together with two other potential failure planes (b - b and c - c). Failure actually occurs on the plane along which the mobilised stress ratio τ / σ'_n first reaches the maximum feasible stress ratio τ_p / σ'_n which in fact depends on the orientation of the potential failure plane with respect to the bedding plane. Consequently, a – a plane is not necessarily the failure plane even though on this plane the mobilised stress ratio τ / σ'_n is higher than that corresponding to the other planes. This is because the maximum feasible stress ratio τ_p / σ'_n (i.e. the strength in terms of stress ratio) on a - a plane may be greater than that on the other planes in a higher extend (Fu and Dafalias 2011a).

Fu and Dafalias (2011a) described the orientation of the bedding plane with respect to the failure plane by means of the *inclination angle*, ψ (or ψ_b), which is the angle that the failure plane should rotate in the direction of shear (clockwise or counterclockwise) in order to coincide with the bedding plane. The inclination angle ψ has values in the range between 0° and 180°; Figure 2.52 shows how the inclination angle ψ is defined and highlights its usage in geotechnical analysis and design. For example, in the analysis of foundation bearing capacity (Fig. 2.52a) and slope stability (Fig. 2.52b) problems the failure plane is known or assumed and the normal effective stresses acting along it can be approximately calculated based on the current conditions (though, the previous stress - strain history also influences these stresses, as indicated by Tavenas et al. 1980), while the principal stresses in the soil body are typically unknown. Consequently, a failure criterion based on ψ instead of δ is preferable. Moreover, Tatsuoka et al. (1990) reported two types of shear bands in laboratory testing, namely the A-type and B-type shear bands shown in Fig. 2.51d, which cannot be distinguished if the failure criterion is formulated in principal stress space; this means that it cannot be predicted whether the failure plane (shear band) in a triaxial or plane strain compression test points upwards of downwards from left to right. Finally, Desrues et al. (1985) stated that localisation of strain (shear banding) occurs rather inevitably at large strains thus the deformation of sand masses bifurcates ultimately into the plane strain mode, irrespective of the initial boundary conditions, justifying the usage of a shear plane based failure criterion.

Fu and Dafalias (2011a) performed 2D DEM simulations of direct shear and biaxial compression loading on assemblies of ellipse-shaped particles. The fabrication of the master pack from which the various specimens were "trimmed out" was carried out by pluviating the particles under gravity and achieving a strong bias in the orientation of the long axes of particles. The master pack was homogeneous in terms of void ratio distribution and exhibited strong fabric anisotropy since most of the long axes of particles were aligned parallel to the horizontal. The results of the numerical fabrication process are shown in Fig. 2.53. Afterwards, the master pack was rotated counterclockwise by an angle ψ and a specimen appropriate for direct shear testing at this value of ψ was trimmed out in a horizontal direction, as can be seen in Fig. 2.54.

Numerous direct shear tests were performed by Fu and Dafalias (2011a) at various inclination angles ψ under two different normal effective stresses σ'_n. Selected results are shown in Fig. 2.55 in the form of plots of the mobilised stress ratio τ / σ'_n and volumetric strain ε_v versus the horizontal relative displacement of the two virtual loading walls (Fig. 2.54b). The fundamental behavioural patterns of granular materials were reproduced in the 2D DEM simulations: the peak value of the stress ratio, τ_p / σ'_n, was found to depend on ψ, while the ultimate value was not; higher value of τ_p / σ'_n was associated with higher peak dilatancy rate and higher ultimate dilation; after the peak state was reached, a softening behaviour was occasionally evidenced towards the ultimate state. The response in terms of evolution of the stress ratio with shear distortion for a given inclination angle ψ was the same for the two different normal effective stresses. It is worthy to note that the maximum value of τ_p / σ'_n is exhibited when ψ = 115°, instead of 90°, while the minimum value of τ_p / σ'_n is exhibited when ψ = 60°, instead of 0°.

Figure 2.56 shows the variation of the peak stress ratio τ_p / σ'_n with the inclination angle ψ in linear and polar coordinates system reported by Fu and Dafalias (2011a). Strong anisotropy in the strength characteristics is evidenced, with the maximum and minimum values of τ_p / σ'_n corresponding to ψ = 115° and ψ = 60°, respectively. Similar findings were reported earlier by Mahmood and Mitchell (1974) and Guo (2008), who used modified direct shear apparatuses to test physical granular materials with tilted bedding planes. Mahmood and Mitchell (1974) tested specimens with ψ = 0° and ψ = 90°, and found that the latter exhibited much higher shear strength than the former. Guo (2008) performed direct shear tests on specimens with ψ varying between 0° and 90°, and found a minimum of strength at ψ between 30° and 45°, depending on the type of sand tested, void ratio and stress level. The maximum strength was always exhibited at ψ = 90°. Guo (2008) did not perform tests at ψ > 90°, presumably due to the false hypothesis that the strength variation with ψ is symmetrical about the vertical axis of ψ = 90° (Tong et al. 2014). However, the distribution tan $\varphi_p(\psi)$, shown in Fig. 2.56, is neither symmetrical nor anti-symmetrical about a vertical axis, though it is periodic with the prime period of π (i.e. 180°) (Tong et al. 2014).

The distribution of peak stress ratio with ψ, shown in Fig. 2.56, indicates that a shear failure criterion for granular materials with inherent fabric anisotropy can be formulated in the following equation:

$$\frac{\tau_{\mathrm{p}}}{\sigma'_{\mathrm{n}}} = tan\left[\varphi(\psi)\right]$$
(2.27)

Equation 2.27 states that "there exists a unique association of the failure stress ratio acting on a shear failure plane, with the inclination angle ψ of the original bedding plane with respect to the shear plane" (Fu and Dafalias 2011a). In this way, the failure criterion accounts for the kinematics of the failure mechanism instead of considering only the stresses in the principal stress space; this is achieved by comparing the mobilised stress ratio τ / σ'_n and the maximum feasible stress ratio τ_p / σ'_n on each kinematically viable failure plane.

Fu and Dafalias (2011a) checked the peak strength prediction in accordance to Eq. 2.27, which was based on numerical simulations of direct shear loading, against the results from numerical simulations of biaxial compression loading. The specimen preparation method, consolidation and shearing process in the biaxial compression tests are shown in Fig. 2.57. Note that the tilting angles δ of the specimens tested varied between 0° and 90° due to the symmetry of biaxial stress conditions, as can be seen in Fig. 2.57a. The variation of the peak stress ratio σ'_{1p} / σ'_3 with the tilting angle δ is shown in Fig. 2.58: the results from the biaxial compression tests are in good agreement with the predictions based on the results from direct shear tests. The peak stress ratio firstly decreases and then increases slightly with δ, exhibiting a minimum at δ = 60°. It should be noticed that the minimum strength is exhibited at the same value of ψ = 60° and δ = 60° (Fig. 2.56 and 2.58) in the simulations of direct shear and biaxial compression loading, respectively, only by coincidence. Different mechanisms are responsible for the minimum strength in each case. For example, in the case of biaxial compression loading the maximum stress obliquity plane coincides with the bedding plane when δ = 60°, resulting in low strength because sliding occurs more easily along the bedding plane (Matsuoka 1974, Matsuoka and Ishizaki 1981, Tatsuoka et al. 1986b, Miura et al. 1986, Nakata et al. 1998, Lade et al. 2014).

The results from the simulation of biaxial compression loading on the specimen with a tilting angle of δ = 30° are shown in Fig. 2.59 (Fu and Dafalias 2011a). Specifically, Fig. 2.59a shows the calculated mobilised stress ratio τ / σ'_n on all potential failure planes for two values of σ'_1 / σ'_3, together with the predicted peak stress ratio τ_p / σ'_n at the same potential failure planes, determined using Eq. 2.27 fitted to the results from direct shear tests. The loci of equal mobilised stress ratio are plotted against ψ and β, the latter of which is the angle between the horizontal and the potential failure plane, called the *shear plane angle*. The graphical definition of angle β is shown in Fig. 2.60, while Eq. 2.28 gives the relation between δ, β and ψ:

$$\psi = \left\{\begin{matrix} \delta - \beta & if\, 0<\beta<\delta \\ 180° + \delta - \beta & if\, \delta<\beta<90° \\ \beta - \delta & if\, 90°<\beta<180° \end{matrix}\right\} \tag{2.28}$$

As can be seen in Fig. 2.59a, failure is *predicted* to occur at $\sigma'_1 / \sigma'_3 = 3.97$ along the shear plane with β = 113°, which is close but not identical to one of the maximum stress obliquity planes. The corresponding inclination angle of the bedding plane is ψ = 83° (reported by mistake equal to 73° in the original text by Fu and Dafalias 2011a). Moreover, the plane with β = 58° is on the verge of failure, since the mobilised stress ratio is $\tau / \sigma'_n = 0.98\ \tau_p / \sigma'_n$. The plane with β = 58° is thus termed the secondary failure plane, with the primary being the one with β = 113°. It is noted that the secondary failure plane is close but not identical to the second maximum stress obliquity plane. The predictions are in very good agreement with the results from the biaxial compression test, as the material actually failed at $\sigma'_1 / \sigma'_3 = 3.84$, which is only 3% lower than the predicted value of 3.97; moreover, the inclination of the primary and secondary failure plane observed in the biaxial compression test (Figs 2.59b to e) agrees remarkably well with the predicted value in each case. The simulation also showed that the secondary failure plane dominates the localisation pattern at large strains, a phenomenon observed in physical experiments and reported by Desrues et al. (1996) and Desrues and Viggiani (2004).

The failure criterion proposed by Fu and Dafalias (2011a), which was based on 2D DEM simulations of direct shear tests, predicts accurately the failure stress ratio and orientation of the failure planes of a granular material with inclined bedding planes, subjected to virtual biaxial compression. However, the success of the criterion and DEM simulation techniques was far more than that. Tong et al. (2014) performed physical direct shear tests on two sands and one blend of glass beads and validated the DEM predictions concerning the variation of peak stress ratio in the full range of bedding plane orientations with respect to the failure plane. Specifically, the DEM prediction that the peak stress ratio is attained for ψ beyond 90°, a fact that is somewhat counterintuitive and not reported in literature at the time of predicting, was verified by the physical direct shear tests carried out subsequently. This event is called an *A-class prediction*.

For the sake of History of Science, we note that possibly the most famous A-class prediction was made by Albert Einstein in 1915 when he published his work on *General Relativity*. General Theory of Relativity (GTR) is the geometric theory of gravitation which generalises Newton's law of Universal Gravitation (Isaac Newton 1687) and states that gravity is a *geometric property* of space and time. GTR predicted that a beam of light is bent when it passes next to an object with big mass due to the *curvature* induced in the spacetime by that mass. The prediction was verified at the eclipse of 1919 by Eddington (Hobson et al. 2006). Regarding Soil Mechanics, another famous A-class prediction was made by Vardoulakis et al. (1978), a few years after Roscoe's historical lecture (Roscoe 1970; Tenth Rankine Lecture); Vardoulakis et al. (1978) predicted theoretically and verified experimentally the effect of non-coaxiality on the inclination angle of shear band and showed that Coulomb's and Roscoe's solutions are actually two extreme cases depending on the degree of non-coaxiality (see also Arthur et al 1977b, Vardoulakis 1980). It is noted that one of the aims of the present study is to validate the prediction made by Dafalias (2016) which states that the sand will contract plastically if the stress principal axes are rotated at critical state while keeping the effective stress principal values constant.

The results from the physical direct shear tests performed by Tong et al. (2014) are shown in Figs 2.62 to 2.67. Tong et al. (2014) investigated the behaviour of Fujian sand, mica sand and a blend of glass beads. The scanning electron microscope images of the grains as well as the gradation curves of the materials are presented in Fig. 2.61. The influence of the bedding plane inclination angle ψ_b on peak friction angle φ_p for all the granular materials tested is shown in Fig. 2.62. The variation of φ_p with ψ_b for the 2D virtual material used in the DEM simulations of direct shear tests performed by Fu and Dafalias (2011a) is also shown, for qualitative comparison. It is apparent that the novel findings of the latter authors are verified physically since the maximum φ_p is exhibited for ψ_b beyond 90° in all cases expect of glass beads. The actual values of ψ_b corresponding to maximum and minimum φ_p depend mainly on the shape, surface texture and angularity of the material grains. However, both the natural materials and artificial material exhibited ψ_b - φ_p curves that have an ascending segment followed by a steeply-descending segment. The strongly anisotropic characteristics of the packing of almost spherical glass beads, which demonstrated a difference between the maximum and minimum φ_p equal to 6°, are notable (Fig. 2.62d).

Figure 2.63 shows the stress ratio τ / σ'_n and vertical displacement δ_v plotted against the horizontal displacement δ_h for mica sand sheared at σ'_n = 150 kPa (Tong et al. 2014); it is noted that the relative vertical and horizontal displacements of the two shear boxes are related to the volumetric and shear strain, respectively, hence the slope dδ_v / dδ_h is a measure of dilatancy (see Eq. 2.8b). It is apparent that the bedding plane inclination angle ψ_b affects significantly the evolution of the stress and dilatancy ratio until the peak state is reached. The maximum peak stress ratio for mica sand is exhibited for ψ_b = 120° and the concurrent peak rate of dilation demonstrates a maximum value as well. Mica sand is not at the ultimate material state when shearing is terminated at δ_h = 7.2 mm. However, the stress ratio curves show a trend to converge into a unique line, irrespective of the initial bedding plane inclination angle. This trend indicates that the behaviour of sand at ultimate state is governed by the intrinsic characteristics of the material, while the initial fabric characteristics have been altered dramatically (see also Sadrekarimi and Olson 2011 and 2012).

Figure 2.64 shows the τ / σ'_n - δ_h and δ_v - δ_h curves for Fujian sand sheared at σ'_n = 300 kPa (Tong et al. 2014). The behaviour of Fujian sand is qualitatively similar to the behaviour of mica sand, yet, some differences are apparent due to the different physical and morphological characteristics of their grains. The peak stress ratio in the case of Fujian sand is reached at lower δ_h than in the case of mica sand; however, in both cases the influence of the bedding plane inclination angle ψ_b on the displacement δ_h corresponding to peak state is minimal. Tong et al. (2014) suggested that this behavioural pattern is due to the variation of the thickness of shear band, which is a function of the mean grain dimension d_{50} (Roscoe 1970, Mühlhaus and Vardoulakis 1987, Oda et al. 1998, Oda and Kazama 1998). Higher value of d_{50} means wider shear band and, consequently, larger shear displacement is required to reach the peak state. It is also apparent that the mobilised peak stress ratio depends on ψ_b, while the ultimate stress ratio does not. However, in some tests, the severe distortion of specimen at large displacements and, possibly, the tilting of the loading plate lead to an increase in stress ratio and decrease in volume. Fujian sand exhibits the maximum peak stress ratio for $\psi_b = 105°$, while it exhibits two local minimums of τ / σ'_n for $\psi_b =$ 30° and 150°; the peak dilatancy rate and ultimate dilation are, also, maximum for ψ_b = 105°.

Figure 2.65 shows the τ / σ'_n - δ_h and δ_v - δ_h curves for the glass beads blend sheared at σ'_n = 150 kPa (Tong et al. 2014). Despite the high sphericity of glass beads, this granular assembly exhibits strong anisotropy. The peak stress ratio, peak dilatancy rate and ultimate dilation depend on ψ_b; the difference between maximum and minimum φ_p is 6°. The blend of glass beads exhibits the maximum peak stress ratio for $\psi_b = 90°$, while it exhibits two local minimums of τ / σ'_n for $\psi_b = 15°$ - 30° and $\psi_b =$ 165°; the peak dilatancy rate and ultimate dilation are, also, maximum for $\psi_b = 90°$. The peak state is reached at $\delta_h < 1$ mm because the value of d_{50} is low, hence, the thickness of shear band is small. Moreover, the grain interlocking is weak because the grains have smooth surface and spherical shape, thus, the dilatancy rate reaches quickly its peak value.

Figure 2.66 shows the value of φ_p - φ_p^{min} plotted against ψ_b in a polar coordinates system for the three sands tested by Tong et al. (2014), in order to highlight the influence of particle sphericity, roughness and angularity on the direction dependent component of φ_p. The radial coordinate is φ_p - φ_p^{min}, while the angular coordinate is ψ_b. An interesting conclusion drawn by Tong et al. (2014) is that “the particle shape but not surface texture determines the degree of dependency of shear strength on loading direction”. The flaky shape of the grains of mica sand corresponds to a high value of the difference φ_p - φ_p^{min}, equal to almost 10°, while the more spherical shape of the grains of Fujian sand and glass beads corresponds to a lower value of around 5°, irrespective of the different degree of surface roughness and angularity that characterises the latter two materials. On the other hand, Tong et al. (2014) pointed out that the surface texture does affect the absolute value of peak and ultimate shear strength, as can be seen in Figs 2.63, 2.64 and 2.65.

The mobilised friction angle and dilatancy angle are quantitatively related by the equation proposed by Bolton (1986):

$$\varphi_{\mathrm{p}} = \varphi_{\mathrm{r}} + 0.8 \cdot \psi_{\mathrm{d}}^{max} \tag{2.29a}$$

where φ_p is the peak friction angle, φ_r is the residual friction angle at ultimate state and ψ_d^{max} is the maximum angle of dilation, calculated from the results of drained plane strain compression tests using the following equation:

$$\psi_{\mathrm{d}}^{max} = arcsin\frac{\dot{\varepsilon}_1 + \dot{\varepsilon}_3}{\dot{\varepsilon}_1 - \dot{\varepsilon}_3} \tag{2.29b}$$

where $\dot{\varepsilon}_1$ and $\dot{\varepsilon}_3$ are the major and minor principal strain rates, which correspond to the increments of vertical and horizontal strain, respectively. Notice that Eq. 2.29b can be applied, also, with a minus sign in the numerator of the fraction, in accordance with the convention for the positive strain rates used. Tong et al. (2014) found that Eq. 2.29a is valid qualitatively when direct shear tests are performed on specimens with different bedding plane inclination angles ψ_b. Specifically, they found that the maximum dilation angle ψ_d^{max} and the angle difference φ_p - φ_r show similar variation trends with ψ_b, as can be seen in Fig. 2.67.

2.7 EFFECTS OF THE DIRECTIONAL CHARACTERISTICS OF FABRIC ON THE STIFFNESS OF SANDS

The dependence of elastic stiffness moduli on void ratio, e, and mean effective stress, p', has already been discussed in Section 2.3 and microscopic mechanisms that may explain this dependence have been presented. In the present section, the effects of fabric anisotropy on the elastic stiffness moduli are discussed. It can be reasonably suggested that both inherent and induced fabric anisotropy affect these moduli. For example, gravity deposited sand demonstrates a fabric with the contact normals oriented more densely, in the statistical sense, along the vertical direction and more sparsely along the horizontal. This means that the vertical Young's modulus, E_v, is higher than the horizontal Young's modulus, E_h, even under isotropic stress conditions, because the small increment of macroscopic stress dσ' is distributed as increment of intergranular stress at more contacts when the direction of dσ' is vertical. Moreover, if sand is loaded to attain an anisotropic stress state by increasing σ_v', let it be σ'_v / $\sigma'_h > 1$, then the initial fabric is altered as new contact normals appear in the vertical direction and existing contacts disappear in the horizontal (Oda 1972b). Consequently, the stress-induced anisotropy, which is related to the condition $\sigma'_v / \sigma'_h > 1$, causes the ratio E_v / E_h to increase further. Some of the experimental techniques used to measure the ratio E_v / E_h are discussed next.

Jiang et al. (1997) and Hoque and Tatsuoka (1998) tested various granular materials in a specially designed triaxial apparatus, equipped with sophisticated instrumentation for measuring local strains of very small values (< 0.001%), in order to measure the horizontal and vertical elastic moduli. This instrumentation included *linear variable displacement transducers* (LVDTs) located outside the triaxial cell, vertical and horizontal *gap sensors* (GSs) located on the cap and the side surfaces of the specimen, and vertical and horizontal *local displacement transducers* (LDTs) (Goto et al. 1991) located on the four side surfaces of the prismatic specimen. The instrumentation and prismatic specimen are shown in Fig. 2.68. Jiang et al. (1997) performed small amplitude stress cycles (drained) on Chiba gravel material, by means of applying cyclic stress increments either in the vertical direction ($\pm d\sigma'_v \neq 0$ and $d\sigma'_h = 0$) or in the horizontal direction ($\pm\, d\sigma'_h \neq 0$ and $d\sigma'_v = 0$). Five stress cycles were performed at various isotropic and anisotropic stress states shown as circles with a cross in the centre in Fig. 2.69. At each stress state, the gravel material was aged for around 30 minutes or more. One triaxial compression (TC) test was, also, performed at constant σ'_h = 29 kPa by increasing σ'_v until the failure state was reached. During the TC loading process small amplitude stress cycles were performed at various intermediate stress states, without allowing ageing to occur.

The definitions of the elastic moduli and Poisson's ratios in the studies by Jiang et al. (1997) and Hoque and Tatsuoka (1998) are based on the assumption of cross-anisotropic material, with a vertical axis of rotational symmetry. The Young's modulus E_v and Poisson's ratio ν_{vh} are acquired by small cyclic stress increments along the vertical direction as follows:

$$E_v = \left(\frac{d\sigma_v^{'}}{d\varepsilon_v}\right)_{d\sigma_h^{'}=0} \tag{2.30a}$$

$$\nu_{vh} = -\left(\frac{d\varepsilon_h}{d\varepsilon_v}\right)_{d\sigma_h^{'}=0} \tag{2.30b}$$

The lateral strain of an elastic cross-anisotropic material subjected to simultaneous changes $d\sigma'_v$ and $d\sigma'_h$ is given by the following equation:

$$d\varepsilon_h = \left(\frac{1}{E_h}\right)\cdot d\sigma_h^{'} - \left(\frac{\nu_{hh}}{E_h}\right)\cdot d\sigma_h^{'} - \left(\frac{\nu_{vh}}{E_v}\right)\cdot d\sigma_v^{'} \tag{2.31}$$

In the case of lateral stress cycles the condition $d\sigma'_v = 0$ holds so the following equations are obtained:

$$E_h = F_h \cdot \left(1 - \nu_{hh}\right) \tag{2.32a}$$

$$F_h = \left(\frac{d\sigma_h^{'}}{d\varepsilon_h}\right)_{d\sigma_v^{'}=0} \tag{2.32b}$$

where ν_{hh} is the Poisson's ratio that expresses the expansion along one horizontal direction when a normal stress increment causes contraction along the other horizontal direction; notice that the independent control of σ'_v and σ'_h along the two horizontal directions is required to apply simultaneously the conditions of $d\sigma'_h \neq 0$ and $d\sigma'_v = 0$. However, the stresses σ'_v and σ'_h along the two horizontal directions can be controlled independently in the true triaxial or hollow cylinder apparatus but not in the triaxial apparatus used by Jiang et al. (1997). On the other hand, the square prismatic triaxial specimen used by Jiang et al. (1997) (Fig. 2.68) has numerous advantages that can be found only partly in the case of true triaxial or hollow cylinder apparatus (Hight et al. 1983, Zdravkovic and Jardine 1997). For example, the compliance and bedding errors, as well as the membrane penetration errors, are fully eliminated when local instrumentation is set up in the way shown in Fig. 2.68. Lacking the capability of controlling independently the two horizontal stresses, the terms v_{hh}, v_{hv} and E_h are calculated unavoidably based on assumptions (see Jiang et al. 1997 and Hoque and Tatsuoka 1998). Nevertheless, the terms F_h and μ_{hv} are determined by linear regression of data from the five small amplitude stress cycles, as shown in Fig. 2.70, where μ_{hv} is given by the equations:

$$\mu_{hv} := -\left(\frac{d\varepsilon_v}{d\varepsilon_h}\right)_{d\sigma_v'=0} \tag{2.33a}$$

$$\mu_{hv} = \frac{2v_{hv}}{(1-v_{hh})} \tag{2.33b}$$

Figure 2.70 shows that the material response is approximately linear elastic when the single-amplitude strain is ε_{SA} < 0.001% (Jiang et al. 1997). The measurement of extremely small displacements dictates the necessity to eliminate the compliance and bedding errors, as well as membrane penetration errors. Figure 2.71 shows the σ'_v - ε_v and σ'_h - ε_h response curves when the material is subjected to isotropic loading - unloading that induces strain of the order of magnitude 0.1%. The solid lines represent the two response curves produced by the most accurate measurements provided by the LDTs; stiffer response is evidenced along the vertical direction due to the inherent anisotropy of fabric. The broken line representing the σ'_v - ε_v curve is determined from the GS measurements, which suffer from bedding error that causes overestimation of strain, while the dotted / broken line representing the σ'_v - ε_v curve is determined from the external LVDT measurements, which suffer from both bedding and compliance errors that cause significant overestimation of strain. The dotted line representing the σ'_h - ε_h curve is determined from the GS measurements, which suffer from the penetration of membrane that supports the taped plate of the gap sensor into the voids of the coarse grain material. It is obvious that testing prismatic square triaxial specimens with horizontal LDTs (Fig. 2.68) mounted on the vertical boundaries of the prism is an advantageous technique concerning the accuracy in the determination of small strains.

Figure 2.72 shows the Young's moduli E_v, F_h and E_h and Poisson's ratio v_{vh} at isotropic stress states (Jiang et al. 1997). The value v_{hh} = 0.24 is assumed in order to determine E_h as a function of the measured F_h (Eq. 2.32a). The normalising factor proposed by Hardin and Richart (1963), f(e) = (2.17 - e)^2 / (1 + e), is used to make the results from tests on specimens with different void ratios comparable. Two types of results are shown: the first corresponds to (small amplitude) stress cycles performed at isotropic stress states before any stress cycles are performed at anisotropic stress states, while the second type corresponds to stress cycles performed at isotropic stress states after similar stress cycles are performed at anisotropic stress states. It is apparent that both moduli E_v and E_h are stress dependent, having values proportional to $\sigma'_v{}^{0.52} = \sigma'_h{}^{0.52} = p'^{\,0.52}$ (see also Eq. 2.5), while v_{vh} is independent of mean effective stress; both the stiffness moduli and Poisson's ratio are independent of the previous stress history applied at anisotropic states. The most important result is that the ratio E_v / E_h is around 2.2 indicating the significant effect of inherent anisotropy on the small-strain stiffness of gravel.

Figure 2.73 shows the plot of E_v / f(e) against σ'_v, for the values of E_v acquired by means of small amplitude stress cycles at isotropic and anisotropic stress states, imposed after a short period of ageing (Jiang et al. 1997). The black line displays the average trend in the variation of E_v when the stress cycles are performed at isotropic stress states, while the various hollow symbols correspond to the results when the stress cycles are performed at anisotropic stress states. Moreover, the values of E_v acquired when the stress cycles are performed at anisotropic states during TC loading, without previous ageing, are indicated by black solid squares. Similarly, the plot of E_h / f(e) against σ'_h is displayed at isotropic stress states, with the average trend shown by a broken line, and at anisotropic stress states, with the results indicated by hollow symbols; ageing was not allowed in both cases. It is apparent that the modulus E_v measured after ageing at each stress state is proportional to $\sigma'_v{}^{0.50}$ and independent of σ'_h, while the modulus E_h is proportional to $\sigma'_h{}^{0.50}$ and independent of σ'_v. This means that the ratio E_v / E_h increases in proportion to $(\sigma'_v / \sigma'_h)^{0.50}$, as can be seen in Fig. 2.74, indicating the effect of stress-induced anisotropy.

Another important observation in Fig. 2.73 is that the value of E_v acquired at anisotropic stress states without any previous ageing is similar to the value acquired at the same states after ageing when $\sigma'_v / \sigma'_h < 2$ (and $\sigma'_v < 100$ kPa; see also Fig. 2.69). However, as the stress ratio σ'_v / σ'_h increases while the gravel is sheared towards failure, the value of E_v acquired without ageing at a given $\sigma'_v > 100$ kPa is lower than the value acquired at the same σ'_v (but different σ'_h) after ageing (see black solid squares at states with high σ'_v in Fig. 2.73). Jiang et al. (1997) suggested that "this behaviour is due to the damage induced to fabric by shear deformation and recovery from the damage by ageing".

2.8 EFFECTS OF THE DIRECTIONAL CHARACTERISTICS OF FABRIC ON THE DILATANCY OF SANDS

Although the direction of loading with respect to the normal to the bedding plane has been acknowledged as a factor affecting the dilatancy ratio, $D := d\varepsilon_v^p / d\varepsilon_q^p$, of cross anisotropic sands (Oda 1972b, Tatsuoka 1976) it has been the consensus for many years that the stress – dilatancy relationship does not depend strongly on fabric anisotropy (Taylor 1948, Rowe 1962, Schofield and Wroth 1968, Roscoe and Burland 1968: for clays, Oda 1972b, Tatsuoka 1976, Nova and Wood 1979, Wood 1990, Gutierrez et al. 1993, Wood et al. 1994, Gutierrez and Ishihara 2000, Gutierrez and Vardoulakis 2007). Few past studies have indicated that the stress – dilatancy relationship indeed depends on fabric anisotropy (Tatsuoka et al. 1986b, Lam and

Tatsuoka 1988), a fact that has been well documented by recent studies (Li and Dafalias 2002, Dafalias and Manzari 2004, Dafalias et al. 2004, Wan et al. 2010, Li and Dafalias 2012). A detailed discussion on this subject is presented in Chapter 3.

2.9 STRAIN LOCALISATION EFFECTS ON THE EVOLUTION OF FABRIC INHOMOGENEITY AND ANISOTROPY

The ideal loading test on a soil specimen involves a uniform deformation field attained by means of uniform stressing of a homogeneous material. However, the fabric of soils is not perfectly homogeneous while inevitable stress and strain non-uniformities develop during testing due to boundary conditions effects. Refinements in the boundary conditions and achievement of practically homogeneous fabric cannot, in fact, prevent the development of non-uniform strain fields which means that the loss of homogeneity may occur spontaneously in granular materials (Vardoulakis 1979, Vardoulakis 1983, Hettler and Vardoulakis 1984, Papamichos and Vardoulakis 1995); in this case, strains begin to concentrate at subliminal imperfections causing failure that spreads to other soil elements progressively while the existence of stronger imperfections can only intensify this tendency. A characteristic example is that of a triaxial compression test on a cylindrical soil specimen using enlarged and lubricated end platens (Bishop and Green 1965, Drescher and Vardoulakis 1982): although the deformation is practically uniform at low strains the specimen barrels or bulges at higher strains and zones of localised shear strain (*shear bands*) may appear ultimately, at very high strains.

As far as the deformation of the specimen remains diffuse (non-localised) and homogeneous the global behaviour of the specimen under stable conditions can be considered representative of the elemental (constitutive) behaviour of the soil material since the different elements inside the soil mass deform in the same way; the global behaviour is observed by means of the measurement of displacements, volume changes, pressures and forces at the boundaries of the specimen. On the other hand, after the occurrence of strain localisation the global behaviour becomes nominal because the local behaviour inside the shear band is different than that outside the shear band and the measured mechanical quantities at the specimen's boundaries do not represent either (Casagrande and Watson 1938, Roscoe 1970, Vardoulakis et al. 1978, Vardoulakis and Sulem 1995, Desrues et al. 1996, Georgiannou and Burland 2006, Fu and Dafalias 2011a and b). The shear bands, which are also called *failure surfaces* or *rupture surfaces* of *shear surfaces* of *slip surfaces*, are formed in physical and numerical experiments as well as in the field (see Figs 2.27, 2.52 and 2.59) though there have been reported cases in which soils fail in a seemingly diffuse mode (Castro 1969, Lade et al. 1988, Chu et al. 1992, Desrues and Georgopoulos 2006, Nicot and Darve 2011, Jiang et al. 2017, Wang et al. 2017).

Figure 2.27 shows the sole shear plane which was formed in an assembly of uniform rigid spheres subjected to triaxial compression (under vacuum confinement) by Rowe (1962). On the other hand, Fig. 2.59 shows the progressive formation of many parallel and conjugate (i.e. approximately symmetrical about the vertical σ'_1-axis) shear planes in the DEM simulation of biaxial compression of a granular material performed by Fu and Dafalias (2011a). The zones of concentrated strain that correspond to the shear planes are identified in this study as areas of increased particle rotation because at the shear band boundaries the gradient of particle rotation is particularly high (Oda et al. 1982, Mühlhaus and Vardoulakis 1987, Oda and Kazama 1998, Oda et al. 1998, Hall et al. 2010a). A similar phenomenon is observed at the interface of soil layers with different stiffnesses penetrated by a pile when a seismic event occurs, i.e. strain and stress is induced kinematically, due to the increased curvature, at the layers' interface (Kavvadas and Gazetas 1993). In other studies, the zones of shear strain localisation are recognised also as zones of intense dilation (Desrues et al. 1996, Fu and Dafalias 2011b). Apparently, the shear bands in granular materials can be viewed as zones of intense evolution of the directional and non-directional characteristics of fabric.

Figure 2.75 illustrates the concept of failure and shear banding in soil materials. According to Coulomb's failure criterion (Eq. 2.1), the soil fails when the stress ratio τ / σ'_n along the maximum stress obliquity plane reaches the peak value tan φ, where φ is the angle of shearing resistance. The maximum stress obliquity plane makes an angle of $\theta_C = 45° + \varphi / 2$ with the direction of the minor principal stress σ_3. Coulomb's theory states that the shear band is formed along the direction θ_C when the peak failure state is reached. However, it is frequently suggested that the narrow shear band is distinct in dense sands only, while in loose sands a diffuse distribution of parallel and conjugate shear planes develops. The inclination of shear band has been extensively investigated in the literature, for example, Fu and Dafalias (2011a) showed that the shear band does not necessarily coincide with the plane of maximum stress obliquity due to the effects of the inherent anisotropy on the shear strength of granular materials, as discussed previously in Section 2.6.

Roscoe (1970) was among the first to state that the inclination of the shear band should be related to the plastic flow rule of the granular material (Vardoulakis et al. 1978); Roscoe (1970) assumed that St. Venant's (1870) rule of coaxiality between the principal directions of stress and plastic strain rate is valid at failure under simple shear loading and proposed a solution for the shear band inclination angle, θ_R, with respect to the direction of the σ_3-axis given by the following equation:

$$\theta_R = 45° + v / 2 \tag{2.34}$$

where the term v is the angle of dilatancy (at failure), which defines the direction of plastic flow (see Section 2.4). The dilatancy angle is given by the following equation (Hansen 1958) that corresponds to biaxial conditions (see also Eq. 2.29b):

$$sin\,v = \frac{\dot{\varepsilon}_1^{pl} + \dot{\varepsilon}_2^{pl}}{\dot{\varepsilon}_1^{pl} - \dot{\varepsilon}_2^{pl}} \tag{2.35}$$

where $\dot{\varepsilon}_1^{pl}$ and $\dot{\varepsilon}_2^{pl}$ are the rates of the principal plastic strains. In the case of simple shear loading the ratio of the rate of the plastic normal strain along the vertical direction over the rate of the plastic shear strain corresponding to the distortion of the specimen's boundaries is equal to sin *v*. Roscoe's equation (Eq. 2.34) indicates that the rupture surfaces in sand masses coincide with *zero-extension lines*. This statement was based on experimental evidence from simple shear tests performed at Cambridge (Roscoe et al. 1967, Cole 1967); the application of radiograph techniques in simple shear tests (Coumoulos 1968) revealed horizontal dark bands of concentrated shear strain and validated Roscoe's suggestion. Two superimposed radiographs of dense sand with embedded lead shots subjected to simple shear loading are shown in Fig. 2.76. It is noted, though, that the horizontal direction corresponds perforce to a zero-extension line in simple shear testing.

Vardoulakis et al. (1978) carried out a bifurcation analysis of the results from drained biaxial compression tests on both dense and loose sand. A specially designed biaxial apparatus was used in order to impose boundary conditions that allow the occurrence of the bifurcation modes shown in Fig. 2.77. The specimen is seated on a bottom plate which, in turn, is placed on a roller bearing, while the cap plate is either clamped or hinged at the loading piston, as shown in Fig. 2.78. The roller bearing allows the free relative movement of the two parts of the specimen after the formation of the shear band while the measurement of the dilatancy angle inside the shear band can be achieved using a hodograph. Vardoulakis et al. (1978) reported that shear banding occurred spontaneously (out of subliminal imperfections, under uniform strains) at peak failure, for both dense and loose sand, and an almost plane failure surface was formed. Vardoulakis et al. (1978) showed that Coulomb's solution for the inclination angle of shear band with respect to the σ_3-axis (i.e. $\theta_C = 45° + \varphi / 2$) constitutes an upper bound corresponding to non-rotating principal stress axes. On the other hand, Roscoe's solution (i.e. $\theta_R = 45° + v / 2$, see Eq. 2.34) constitutes a lower bound corresponding to co-rotating principal axes of stress and strain rate during failure. Vardoulakis et al. (1978) stated that both solutions can be correct theoretically and experimentally, while intermediate inclination angles are also possible.

Vardoulakis (1980) studied the spontaneous occurrence of shear banding in the biaxial (plane-strain) compression test on dry sand and reported that due to fail of the normality rule the localisation of strain always occurs in the hardening regime (i.e. pre-peak). Desrues et al. (1985) used the *stereophotogrammetric method* and verified this observation, while Oda et al. (1978) reported that no shear band was observed at peak failure of dense Toyoura sand (D_r = 90%) in plane-strain compression, though, parallel shear bands were formed in the post-peak regime. Tatsuoka et al. (1990) used the *laser-speckle technique* (Yamaguchi 1981) and observed that shear bands can be formed in the pre-peak regime when sand is subjected to plane-strain compression, while the development of these bands become intense in the post-peak regime. Finno et al. (1997) used the stereophotogrammetric method and observed that the stress state at the onset of strain localisation under plane-strain compression is very close, yet, precedes the peak state.Vardoulakis (1980) stated that “the theoretical solution of the shear band inclination is a geometrical mean of the classical Coulomb and Roscoe solutions”, which was also verified experimentally by Arthur et al. (1977b). The equation for the shear band inclination angle with respect to the σ_3-axis proposed by Arthur et al. (1977b) and Vardoulakis (1980) is:

$$\theta_{A-V} = 45^\circ + \frac{1}{2}(\varphi_p / 2 + v_p / 2) \tag{2.36}$$

where φ_p and v_p is the angle of shearing resistance and dilatancy angle at peak, respectively.

Finno et al. (1997) performed drained and undrained plane-strain compression tests on loose sand and monitored the evolution of strains both globally and locally using the stereophotogrammetric method. They found that shear banding occurs in loose sand at an inclination angle between the Arthur - Vardoulakis’ and Coulomb’s solutions. They also noticed that the local normal strain parallel to the shear band is essentially zero, verifying Roscoe’s observation. Tatsuoka et al. (1990) suggested that for inherently anisotropic sands the Arthur - Vardoulakis’ solution cannot be exclusively used in any mode of loading (simple shear, torsional shear, plane-strain compression); in these cases Coulomb’s, Roscoe’s and Arthur - Vardoulakis’ solutions are feasible, while the bedding plane orientation with respect to the zero extension direction is an important factor that influences the shear band inclination. On the other hand, Fu and Dafalias (2011a) suggested that the bedding plane orientation with respect to the kinematically viable shear planes is an important factor that determines the shear band inclination.

Mühlhaus and Vardoulakis (1987) incorporated the principles of Cosserat’s Theory into the framework of Bifurcation Theory and made predictions about the shear band inclination and evolution of its thickness. In short, Cosserat’s (or micro-polar) continuum theory is an extension of the classical continuum theories that includes the couple stresses, defined as torque per unit area, together with the classical stresses, defined as force per unit area. Cosserat’s theory describes the non-classical behaviour of materials, which have at least one important length scale derived from the microstructure, when localised deformation occurs, for example, in the case of shear banding. Both the theoretical predictions of Mühlhaus and Vardoulakis (1987) and the hypothesis of Roscoe (1970) concerning the shear band thickness in granular materials were verified experimentally. Mühlhaus and Vardoulakis (1987) reported that the shear band thickness is a small multiple of the mean grain dimension d_{50} ($\approx 16d_{50}$). Roscoe (1970) had already suggested a value of around $10d_{50}$, while Oda and Kazama (1998) reported a value of $7d_{50}$ to $8d_{50}$, and Finno et al. (1997) measured a value ranging from $10d_{50}$ to $25d_{50}$. It is important to notice that the couple stresses affect the development of the micro-fabric of shear bands (Oda 1993), and that the importance of particle rotations inside the shear bands (Oda and Kazama 1998, Fu and Dafalias 2011b) justifies the use of micro-polar models (Bardet and Prubet 1992, Vardoulakis and Sulem 1995).

The study by Mühlhaus and Vardoulakis (1987) pointed out that the microstructure of granular materials should be taken into consideration when shear banding is modelled. The constitutive equations, in this case, should include a physical property with the dimension of length (e.g. the length d_{50}); otherwise, for continuum materials without microstructure only the first gradient of deformation is used to describe straining and, hence, the thickness of shear band cannot be predicted because the formulation of the problem does not include a physical property with the dimension of length. Han and Vardoulakis (1991) introduced a second distinct length scale which is derived from the intrinsic permeability k of sand that governs fluid flow inside the saturated pores; this formulation eases the mathematical modelling of water-saturated porous materials with strain-rate sensitivity. According to the aforementioned studies, it is questioned whether in the small-scale physical models a material with scaled-down grain dimension with respect to the prototype material (e.g. powder used instead of sand) should be used or not. Mühlhaus and Vardoulakis (1987) suggested that the effect of microstructure can be described in numerical studies by a finite element method incorporating Cosserat's principles (see also Vardoulakis 1989, Vardoulakis and Aifantis 1989, Vardoulakis and Aifantis 1991).

The relation between the mean grain size d_{50} and the inclination angle of shear band has been reported in past experimental studies. Arthur and Dunstan (1982) performed plane strain tests on sand with isotropic initial fabric, attained by deposition along the direction of σ_2, and reported that the shear band inclination angle increased from Roscoe's value θ_R to Coulomb's value θ_C as the particle size decreased, or equivalently as the specimen size in relation to the constituent particles increased. Tatsuoka et al. (1990) and Mokni (1992) reported a similar behaviour. On the other hand, Viggiani et al. (2001) performed drained plane-strain compression tests on blends of a single-origin sand having different gradations and sizes of mean grain, and reported that these factors cannot be related to the orientation of the shear band in a simple and direct way.

What happens inside the shear bands is a fundamental question in Soil Mechanics and Geotechnics, and the answers we seek are both qualitative and quantitative. As a matter of fact, failure of geomaterials is frequently manifested in a localised mode of straining. Desrues and Viggiani (2004) stated that "the phenomenon of shear banding has quite a practical relevance, as stability and deformation characteristics of earth structures are often controlled by the soil behaviour within the shear bands". Moreover, many elastoplastic constitutive models use a unique reference state, the so-called Critical State, in order to simulate the behaviour of geomaterials under various stress and strain conditions. The critical state of sands is reached after intense monotonic straining; consequently, it is possible that it can be reached only inside the shear band, especially in the case of dense sands (Vardoulakis 1977). For these reasons, it is essential to investigate the sand response inside the shear band.

Some qualitative hypotheses regarding the sand behaviour inside the shear band have been reported throughout the years. Casagrande and Watson (1938) suggested that after the localisation of strain in a sand specimen, the expansive volume change measured globally takes place in the shear band only, thus, the evolution of the void ratio in that domain is expected to be very substantial. Roscoe (1970) presented the superimposed radiograph images shown in Fig. 2.76 and suggested that "the dark band represents the rupture surface, in which the sand has dilated to the critical state". Vardoulakis (1977) stated that "for an overcritically dense sand the critical state cannot be reached following an overall homogeneous deformation. The critical state can only be reached inside the shear bands".

Desrues et al. (1985) performed loading tests on dry dense sand using the true triaxial apparatus and the biaxial apparatus; the main goal of their study was to investigate qualitatively and quantitatively the strain localisation patterns of dense sand. The biaxial apparatus was specially designed so photographs could be taken during the deformation of the specimen and the stereophotogrammetric method could be applied. The stereophotogrammetric method, firstly used in Grenoble by Beynet and Trampczynkski (1977) who studied qualitatively the displacement fields in continuum media, was developed further by Desrues and Duthilleul (1984) to obtain quantitative results concerning the strain fields in sand specimens. Moreover, the cubic and parallelepipedic specimens tested in the true triaxial apparatus were stabilised and investigated post-mortem using the gamma-ray absorption method, apart from being observed with the naked eye.

Desrues et al. (1985) performed plane strain tests ($\varepsilon_2 \equiv 0$) in the true triaxial apparatus with constant σ'_3 and $d\varepsilon_1 > 0$ (compression) or $d\varepsilon_1 < 0$ (extension), as shown in Fig. 2.79. It is noted that the plane of biaxial shearing is defined by the vertical σ_1-axis and the horizontal σ_3-axis and that the vertical strain, ε_1, is not necessarily the major principal strain (the principal stresses and strains are unordered). Moreover, it is important to note that six rigid boundary platens were used to impose strain-controlled loading and localisation of strain actually occurred, in contrast to the established belief up to that day that shear banding is prevented under these conditions (e.g. Lade 1982). The localised deformation patterns in the stabilised, dyed specimens are visible to the naked eye in Fig. 2.80. It can be inferred that shear bands begin at the corner points, which are strong singularities of non-smooth topology, then propagate until they reach a rigid boundary on which they are reflected (Figs 2.79 and 2.80). Moreover, Desrues et al. (1985) observed that the specimens which were loaded first in compression and then in extension showed two shear bands which "developed successively in a quite independent way", as can be seen in Fig. 2.79.

The local sand density, ρ, inside the shear bands of the parallelepipedic specimen shown in Fig. 2.80 (Photo 1) was measured by Desrues et al. (1985) using the gamma-ray absorption technique. The results shown in Fig. 2.81 indicate the density distribution along the αβ-line that crosses the shear band before and after testing. It can be seen that the density inside the shear bands decreased dramatically while the density outside the shear bands remained practically constant. Desrues et al. (1985) reported that the volumetric strain inside the shear bands was as high as $\Delta V / V = 5$ - 7%, verifying previous conjectures that the shear bands are areas of strong dilation. Mooney et al. (1998) tested sand in plane strain compression and used the technique of stereophotogrammetry to verify that high incremental volumetric strains occur inside the shear band, yet, the dilatancy ratio drops slightly just after its formation at peak failure, because the local incremental shear strains are accordingly high.

On the other hand, Vardoulakis and Goldscheider (1981), Vardoulakis and Graf (1985), Han and Drescher (1993) and Vardoulakis and Georgopoulos (2005) reported that the dilatancy in the incipient shear band is at first negative (contractancy) and then turns to positive, even in the case of dense sand. The results indicating the initial contractancy inside the incipient shear band are shown in Fig. 2.82. The contractancy of sand was attributed to the non-coaxiality resulting from the rotation of the principal direction of stress and incremental strain as the simple-shear mechanism takes over (Vardoulakis and Graf 1985, Vardoulakis and Georgopoulos 2005 and Gutierrez and Vardoulakis 2007). An attenuating dynamic oscillation in the regime of positive dilatancy (see Fig. 2.82) was also reported by Vardoulakis and Goldscheider (1981), Vardoulakis and Graf (1985) and Vardoulakis and Georgopoulos (2005), indicating "a sequence of collapsing and restructuring of the granular microstructure" and "material growth of the shear band".

Desrues et al. (1985) performed axisymmetric compression tests, with $\sigma_2 = \sigma_3 < \sigma_1$ in a stress-controlled mode or with $\varepsilon_2 = \varepsilon_3 < \varepsilon_1$ in a strain-controlled mode, and axisymmetric extension tests, with $\sigma_2 = \sigma_3 > \sigma_1$ in a stress-controlled mode or with $\varepsilon_2 = \varepsilon_3 > \varepsilon_1$ in a strain-controlled mode, in the true triaxial apparatus, as shown in Fig. 2.83; it is recalled that the principal stresses and strains are unordered. The schematic patterns of the localised deformation are also displayed in Fig. 2.83. Desrues et al. (1985) reported the occurrence of two different plain deformation mechanisms: the simple mechanism occurring in stress-controlled tests and the double mechanism occurring in both stress- and strain-controlled tests. In spite of the imposed axisymmetric stress conditions the deformation kinematics switch suddenly to the plane-strain mode when the simple mechanism of shear banding is triggered. This situation is illustrated in Fig. 2.84 where can be seen that the specimen stops deforming along the ε_2-axis while it keeps deforming along the directions of the other two axes; concurrently, the globally measured strength and dilatancy rate decrease.

Desrues et al. (1985) observed that the plane deformation mechanism can occur simultaneously along the two directions of equal stress or strain. Figure 2.83 shows schematically the double mechanism observed in axisymmetric compression and extension tests, while Photo 2 in Fig. 2.80 shows this specific strain localisation pattern developed in a specimen subjected to axisymmetric compression. In Photo 2, a cross is evidenced on the upper face of the specimen and reflected shear bands can be seen on each lateral side. Desrues et al. (1985) stated that when the double mechanism occurs, “the overall kinematics can remain axisymmetric as though no localization takes place inside the sample”. Desrues et al. (1996) and Desrues and Viggiani (2004) showed that a similar axisymmetric mechanism of localised deformation can be formed in cylindrical sand specimens subjected to axisymmetric loading and, as a consequence, the localisation of strain may remain concealed to the naked eye. The detection of strain localisation becomes even more difficult in the case of loose sand due to the small change in the void ratio inside the zones of strain localisation and the relatively increased width of these zones (Tatsuoka et al. 1986b, Desrues and Viggiani 2004).

Desrues et al. (1985) performed plane-strain compression tests in a specially designed biaxial apparatus and investigated the initiation and propagation of the shear band, as well as the evolution of the void ratio and shear distortion ($d\gamma = (d\varepsilon_1 - d\varepsilon_3) / 2$) inside the shear band. The technique of stereophotogrammetry was used to analyse the photographs taken along the direction of the ε_2-axis ($\varepsilon_2 = 0$), as can be seen in Fig. 2.85a. The tests were performed in a strain-controlled mode. Figure 2.85b shows the typical axial load – axial displacement curve and volumetric strain – axial displacement curve. The numbers on the former curve indicate the serial numbers of the photographs. It can be seen that the successive photographs 3, 4 provide information about the response just before the peak state. The deformation characteristics during the 3-4 stage are shown in Fig. 2.86; the contours of equal axial displacement are displayed in Fig. 2.86a, the contours of equal lateral displacement are displayed in Fig. 2.86b, the contours of equal shear distortion are displayed in Fig. 2.86c and the contours of equal volume change are displayed in Fig. 2.86d. It is noted that these contours offer quantitative information about the deformation field.

The results in Fig. 2.86 indicate that during the 3-4 stage the deformation field is non-homogeneous, since the contours in Fig. 2.86a (Fig. 2.86b) are not parallel horizontal (vertical) lines. The contours are distorted showing a dense configuration in the middle of the specimen, along an inclined direction, which indicates a high displacement gradient. The concentrated shear distortion in two parallel diagonal zones in the middle of the specimen, shown in Fig. 2.86c, indicates that shear banding occurred during the 3-4 stage just before the peak state (Vardoulakis 1980). The fact that the two parallel shear bands were initiated in the central part of the specimen and not at the corners was explained by Desrues et al. (1985) as a result of progressive accumulation of strains in this part in previous stages possibly due to a random perturbation. Artificial perturbations were, also, induced in other experiments and validated the conclusion drawn by Vardoulakis and Graf (1982) that “the location of the first localisation is very sensitive to the imperfections of the test”. However, Desrues et al. (1985) suggested that intense deformation heterogeneities are observed at the corners of the cubic and parallelepipedic specimens tested in the true triaxial apparatus even before the triggering of localisation.

The mechanism of shear band propagation during a biaxial compression test can be monitored during the post-peak deformation increments 4-5 and 5-6 by analysing the equal shear distortion contours, shown in Figs 2.87a and b, respectively. The two parallel shear bands propagate independently in the same direction, without converging, and the upper one bisects the specimen when it reaches the upper boundary. Desrues et al. (1985) also captured the shear band reflection on the rigid boundary (upper or lower platen) in other tests. For example, Fig. 2.88 shows the equal shear distortion contours in a different test just before and after the propagating shear band reaches the rigid boundary. It is noted that these results prove the potentiality of shear band reflection since the propagation of the shear band is monitored step by step. On the other hand, if the strain localisation patterns are observed and analysed only at the final state (see Fig 2.80) then it cannot be stated with certainty whether a single shear band was reflected at the rigid boundary or two different shear bands were initiated at the same point of the rigid boundary and propagated along different directions.

The results from the gamma-ray investigation of the specimen post-mortem (i.e. after the termination of the test), shown in Fig. 2.81, revealed that significant dilation occurred inside the shear band, while the volume outside the shear band changed only slightly. The loosening of the soil inside the shear band is an "essential damaging factor" that may justify the post-failure strain softening, since the coordination number decreases and the mutual support of the grains is weakened (Oda 1977). Desrues et al. (1985) also observed the local dilation in situ using the technique of stereophotogrammetry. The square symbols shown in Fig. 2.86d display the quantitative information concerning the change of volume obtained by stereophotogrammetric analysis; these symbols have size proportional to the local volumetric strain increment during the 3-4 stage, just before the peak state. The volumetric strain increment is higher than 0.03 inside the incipient shear band, while outside is almost zero. However, Desrues et al. (1985) observed that the local dilatancy ratio $d\varepsilon_{vol}$ / $d\gamma$ attenuated inside the shear band soon after its formation. These findings support the notion that the critical void ratio is attained inside the shear band while the void ratio of sand outside the shear band remains almost unaltered (Casagrande and Watson 1938, Roscoe 1970, Vardoulakis 1977).

On the other hand, Mooney et al. (1998) reported that the local dilatancy rate attenuates slowly inside the shear band yet the ultimate void ratio is not uniquely related to mean effective stress. Drescher and Vardoulakis (1982) pointed out that the true material softening inside the shear band is very slow, while Goldscheider and Vardoulakis (1980) measured the post-failure softening characteristics inside the shear band in the biaxial test. Moreover, Fu and Dafalias (2011b) performed DEM simulations of direct shear and biaxial compression tests to investigate the fabric evolution inside the shear band and found that the material attains a unique ultimate void ratio that depends only on the mean effective stress, irrespective of the initial fabric characteristics and boundary conditions. However, Fu and Dafalias (2011b) reported that the ultimate state of the tested virtual material is reached only at shear strains as high as 300 - 350%.

Desrues and his colleagues used Computed Tomography (CT) (Desrues 1984, Colliat-Dangus et al. 1988, Desrues et al. 1991, Desrues et al. 1996) in order to monitor the evolution of void ratio of sand specimens during triaxial testing. In computed tomography an X-ray scanner is used to acquire “cross-sectional images of the attenuation of an X-ray beam through a body”. In soil testing this is achieved by rotating and translating the X-ray source and detector around and along the soil specimen’s axis. The details of the procedure, which produces a radiographic density map of slices of a body, are shown in Fig. 2.89. The radiographic density, expressed in modified Hounsfield units (MHU), is linearly correlated to the mass density of a material with homogeneous chemical composition. Desrues at al. (1996) calibrated the radiographic density against the mass density of carefully prepared homogeneous sand specimens having various densities. The calibration of the CT measurements on Hostun sand is shown in Fig. 2.90.

A typical density profile along a line that crosses the shear band and the density map of a cross section of a dense specimen are shown in Fig. 2.91. Desrues et al. (1996) observed that “this profile appears more as a round trench with a smooth transition to the neighbouring soil mass (rather) than a sharp cut with homogeneous density inside”. Desrues at al. (1996) suggested that the observed density profile can be interpreted in different ways: first, it is probable that the spatial resolution of the computed tomography apparatus is responsible for obtaining such a profile, second, the true density profile in shear bands may actually be a smooth curve and, third, it is also probable that, so close to the grain scale, only an average measure over the shear band has a physical meaning at the continuum level. Moreover, Oda et al. (1998) examined the X-ray photographs of thin plates cut from resin-stabilised specimens and observed that large voids appear periodically along the shear band. These observations indicate that the shear bands are heterogeneous, a fact that was verified in the DEM simulations performed by Fu and Dafalias (2011b). The inception of the idea that shear bands are heterogeneous is rather attributed to Dr. G. Mandl who reported some microscopic observations in a seminar back in 1974. In 1974, Vardoulakis commented on Mandl’s experiments and reported that “the shear band consists of three parallel layers with different deformation patterns” (Vardoulakis and Sulem 1995). On the other hand, Roscoe (1970) reported that the results from the simple shear tests performed by Stroud (1970), who used a regular pattern of embedded lead shots in order to determine the local strains by means of displacement gradient calculations, indicate that the strains inside the shear band are uniform.

Desrues et al. (1996) performed drained triaxial compression tests on dense and loose cylindrical sand specimens and analysed the deformation using computed tomography. The specimens were loaded, unloaded and placed in the X-ray apparatus in order to be scanned; afterwards, the specimens were reloaded and the procedure was repeated at different strain levels. A fixed initial mean effective stress was imposed in all tests. The boundary conditions involved lubricated and non-lubricated end platens, as well as long and short specimens with initial height to diameter ratio h_o / d_o equal to 1.9 and 1.0, respectively. Desrues et al. (1996) tested both homogeneous specimens and specimens with slight perturbations and found that strain localisation can develop in different complex patterns depending on the test conditions.

Figure 2.92 shows the trace of the shear band in Specimen rfdt4 (dense specimen with h_o / d_o = 196 / 101 mm / mm and non-lubricated ends), at global axial strain ε_a = 13%, in a section perpendicular to the specimen's axis, located 72 mm above the bottom platen initially, and in a second section containing the specimen's axis. Figure 2.93 shows the evolution of stress ratio and global void ratio with global axial strain during test rfdt4. A single shear band appeared in the post-peak regime at global axial strain ε_a = 7% and remained the sole localisation zone throughout shearing at higher strains; the shear band was not perfectly planar. It is noted that these results verify that strain softening precedes the localisation of strain in triaxial compression loading (Drescher and Vardoulakis 1982, Lade and Prabucki 1995). The dilation of dense sand stopped suddenly at ε_a = 7% and the global void ratio curve reached a plateau, which as will be shown next lacks physical relevance. It can be seen that the stress ratio curve exhibits a narrow peak and a steeply descending branch.

A different localisation pattern was observed in Specimen hfdt1 (dense specimen with h_o / d_o = 100 / 100 mm / mm and non-lubricated ends) which was tested under extreme end restraint due to the lack of lubrication and squat shape (see Bishop and Green 1965). Figure 2.94 shows two computed tomography images at different cross-sections of Specimen hfdt1, the first (Fig. 2.94a) located near the upper platen (80 mm from the bottom platen) and the second (Fig. 2.94b) located at middle height (50 mm from the bottom platen) between the two platens; both images correspond to global axial strain ε_a = 13%. A complex localisation pattern is revealed, consisting of a rigid cone attached to the upper platen with its tip pointing downwards (see also Deman 1975, Drescher and Vardoulakis 1982). The cone is delimited by a surface of large dilation, shown as a dark circle of decreasing diameter when the cross-section is located nearer to the bottom platen. The sand outside the rigid cone also exhibits severe localisation patterns in the form of dilation surfaces with approximately straight traces on the cross-section planes.

On the other hand, the use of squat specimens and lubricated end platens (Vardoulakis 1979, Drescher and Vardoulakis 1982, Hettler, and Vardoulakis 1984) postpones the onset of localisation. For example, in test rfdt8 (on a dense specimen with h_o / d_o = 100 / 100 mm / mm, lubricated ends and an embedded soft perturbation) the density field was still non-localised at ε_a = 19%. However, the computed tomography images at ε_a = 27%, shown in Fig. 2.95, indicate the existence of complex localisation patterns. Figure 2.96 shows the illustration of the void ratio field in a tomogram across the axis of specimen rfdt8. In the tomogram can be seen that the shear bands do not pass through the artificial imperfection that is embedded in the specimen's axis (see the dark disc in the middle of the image). Figure 2.97 shows the evolution of the stress ratio and global void ratio with global axial strain during test rfdt8. It can be seen that a significant decline in strength (strain softening) occurs before the onset of localisation in the triaxial compression test, for example up to ε_a = 19%. However, the studies by Deman (1975) and Drescher and Vardoulakis (1982) show that even in the case of testing with lubricated end platens an amount of strain softening is attributed to bulging at large strains, while the true material softening develops very slowly (see also Mooney et al. 1998). Consequently, the apparent strain softening just after the peak state in triaxial compression loading is not necessarily associated with strain localisation yet it may be affected to some degree by other types of deformation heterogeneities.

The comparison of the response of a dense squat specimen under loading with lubricated end platens (Specimen rfdt8) with the response of a dense slender specimen under loading with non-lubricated end platens (Specimen rfdt4) highlights the effects of slenderness and end restraint on the global behaviour and strain localisation of sand specimens. The peak in the stress ratio – axial strain curve from the test on Specimen rfdt8 (Fig. 2.97) is flat and corresponds to a large global axial strain, while the dilation rate attenuates slowly after localisation. On the other hand, the peak in the stress ratio – axial strain curve from the test on Specimen rfdt4 (Fig. 2.93) is narrow and corresponds to a small global axial strain, while the dilation rate diminishes rapidly after localisation. The residual stress ratio is practically the same for the two specimens however the final global void ratio is not, even though the initial mean effective stress is common. Moreover, there is no obvious correlation between the stabilisation of void ratio and mobilisation of the peak stress ratio in both tests.

From the results presented by Desrues et al. (1996) and discussed previously it can be inferred that the global measurements at large strains may provide erroneous information about the critical void ratio of sand, especially in the case of dense specimens subjected to loading with non-lubricated end platens. In the case of loose specimens, the ultimate global void ratio is more representative of the void ratio at critical state, as will be shown next, since the localised zones are wider, less distinct and the difference between the void ratio inside and outside them is not so important. For example, the computed tomography image of Specimen rflt2 (loose specimen with h_o / d_o = 100 / 100 mm / mm and lubricated ends) at ε_a = 42%, shown in Fig. 2.98, reveals only faint localisation patterns. An investigation of shear banding in loose sand subjected to undrained plane strain compression was, also, carried out by Finno et al. (1997) and Mooney et al. (1997) using the technique of stereophotogrammetry.

Desrues et al. (1996) compared the computed tomography images of Specimens rfdt4, hfdt1, rfdt8 and rfdt8 shown in Figs 2.92, 2.94, 2.95 and 2.96, correspondingly, and drawn some interesting conclusions. Specimen hfdt1 (dense specimen with h_o / d_o = 100 / 100 mm / mm and non-lubricated ends) exhibited a complex and axisymmetric pattern of severe localisation (Fig. 2.94). This is because multiple localisation mechanisms are favoured in lieu of a single localisation mechanism that breaks the initial symmetry due to the extreme end restraint. On the other hand, Specimen rfdt4 (dense specimen with h_o / d_o = 196 / 101 mm / mm and non-lubricated ends) exhibited a single localisation mechanism because the "globally biased initial density distribution" acted as a symmetry-breaking imperfection. Other symmetry-breaking factors are the bad centring of the specimen, non-symmetrically placed artificial perturbations and non-parallel end platens. However, the symmetrically placed soft perturbation inside Specimen rfdt8 did not break the symmetry and the shear bands did not pass through it.

A spectacular localisation pattern, which was proved to be somewhat generic, was exhibited in Specimen rfdt8 (dense specimen with h_o / d_o = 100 / 100 mm / mm, lubricated ends and an embedded soft perturbation). Figure 2.99 shows a density profile of this specimen reconstructed from a set of six computed tomography slice images (see Fig. 2.95) placed next to each other. Two structures are apparent as traces on the plane parallel to the specimen's axis, the first with the shape of an inverted V and the second with the shape of a parabola oriented towards the lower platen. The geometrical interpretation given by Desrues et al. (1996) is shown in Fig. 2.100. A cone structure with its side surface being the region of intense dilation is centred on the specimen's axis, having "its tip outside the specimen and its contour matching exactly the specimen's bottom section". A set of inclined "plane strain mechanisms associated in pairs" also exists; each pair creates a structure which resembles a triangular roof enclosing a gable of relatively intact sand material, at least up to the point where the cone surface is reached. The top line of this roof-like structure is a diameter of the specimen's top section. The angle of the cone is approximately the same with the angles between the two planes forming each roof-like structure. This means that the conjugate shear surfaces have the same dip angle with respect to the horizontal top plane.

It is noted that the complex localisation pattern in the cylindrical specimen, presented in Figs 2.95, 2.99 and 2.100, can be seen as the generalisation of the double plane-strain mechanism arrested by Desrues et al. (1985) when they tested cubic specimens in the true triaxial apparatus (Fig. 2.80). In the latter case, the two plane strain mechanisms took place simultaneously in such a way that the overall axisymmetry was preserved; these two mechanisms were found to be particularly sensitive to the geometry of the specimen and apparatus (e.g. they were initiated at the corner singularities). On the other hand, in cylindrical specimens with "perfect" boundary conditions and initial density homogeneity there is no constraint that would favour a particular mechanism. In this case, Desrues et al. (1996) suggested that the complete development of a given mechanism is a matter of global organisation of the deformation over the specimen. However, imperfections such as bad centring of the specimen, non-parallel end platens and asymmetrically embedded perturbations can induce one single and predominant localisation mechanism.

Desrues at al. (1996) measured both the global and local void ratio inside the strain-localisation zones. Figure 2.101 presents the evolution of these two void ratios with global axial strain for the various tests performed at σ'_3 = 60 kPa. The "global" measurement is averaged over the cross-section of the specimen, while the "local" is averaged over the strain-localisation zone. The results discussed next were obtained from tests on dense and loose specimens of Hostun RF sand.

Figure 2.101 indicates that the dense specimens with lubricated ends (Specimens rfdt3, rfdt6, rfdt7 and rfdt8) exhibit a similar pattern of evolution of the global void ratio: the sand is dilative up to an axial strain of around 20% whereupon dilation is arrested and a common void ratio plateau is reached. On the other hand, the dense and slender specimen with non-lubricated ends (Specimen rfdt4) behaves differently showing an initial rapid dilation that is exhausted quickly at around ε_a = 7%; when dilation is arrested in test rfdt4 a plateau that differs from the one observed in the aforementioned tests is reached. In all cases, the local void ratio curves diverge from the global ones when localisation occurs; the slope of the former curves is steeper compared with the slope of the latter still one should consider that both sets of curves are plotted against global axial strain. The most remarkable finding is that all dense specimens attain a common ultimate void ratio that is considerably higher than the various ultimate global void ratios, proving than the latter lack physical relevance. Furthermore, it can be seen that the local and global void ratio curves of loose specimens (rflt1 and rflt2) do not differ much, when being discernible; both curves converge towards the same ultimate plateau, which is identical to the plateau of the local void ratio curves of dense specimens. This intriguing finding indicates that a critical void ratio exists inside the shear band in the drained tests with a common effective confining stress σ'_3 = 60 kPa; similar results were reported earlier by Coumoulos (1968) and Stroud (1970) (see also Roscoe 1970 and Fu and Dafalias 2011b).

Oda and his colleagues (Oda 1993, Oda and Kazama 1998, Oda et al. 1998) studied the evolution of the microstructure of shear bands and the way that strain localisation is related to the induced anisotropy and dilatancy of dense sands. Oda et al. (1998) suggested that the anisotropy induced in the strain-hardening regime is an absolutely necessary condition to generate the shear band structure. If a well-developed anisotropy does not exist then a distinct shear band cannot be formed, as in the case of very loose sand (see for example Fig. 2.98). It is well documented that the failure of dense sand under drained plane strain compression is associated with localisation near the peak state, followed by intense softening and strong, yet attenuating, dilation. Oda and Kazama (1998) suggested that this behaviour is attributed to the buckling of column-like grain structures inside the shear band. These structures are gradually formed along the direction of the major principal stress during hardening (see also Section 2.5) as the fabric is reorganised to carry the compressive load more efficiently. When these columns buckle, large voids are formed between them inside the growing shear band, as shown in Fig. 2.103, resulting in ultimate local void ratio higher than the maximum void ratio e_{max} determined by standard procedures. Consequently, this microstructure evolution model justifies the extensive dilation inside the shear band and growth of the shear band thickness. Moreover, it justifies the strain softening behaviour since the buckled columns lose the ability to carry load.

Experimental evidence of the existence of large voids between buckled grain columns inside the shear band is shown in Fig. 2.102. Figures 2.102a and b show an assembly of photoelastic rods at the peak and residual state, respectively, in plane strain compression (Oda et al. 1982). Moreover, Fig. 2.102c displays the microscope image of a thin section of stabilised Toyoura sand showing a periodic appearance of large voids (marked with the letters a-e) along the shear band (delimited by the lines 0-1). The geometrical interpretation of the microstructure evolution model proposed by Oda and Kazama (1998) is shown in Fig. 2.103 (see also Fig. 2.50). It can be inferred that the particles comprising the buckled column undergo an important amount of rotation. In a previous study, Oda et al. (1982) found that particle rolling rather than particle sliding is the major mechanism of micro-deformation in an assembly of rods, while this mechanism is also important in the case of natural sands (Mühlhaus and Vardoulakis 1987, Vardoulakis and Sulem 1995). Moreover, Oda and Kazama (1998) observed that the particle orientation changes abruptly at the shear band boundaries and that particle rotation inside the shear band occurs, on average, in parallel to the corresponding macroscopic rotation in the continuum sense (Fig. 2.103b). Consequently, the particle rolling that is related to grain-column buckling seems to be associated with the extensive dilation inside the shear band.

The X-ray computed tomography (CT) was developed further throughout the years to improve the spatial resolution. Oda et al. (2004) reported that the conventional X-ray CT does not provide spatial resolution high enough to generate an image in which the individual grains and voids can be distinguished. On the other hand, the development of microfocus X-ray CT (or X-ray μCT) allows the generation of images in which each grain can be clearly distinguished from the others, even if its size is of the order of magnitude of tens of micrometres. The basic principle of X-ray μCT is that a decelerating charged particle produces electromagnetic radiation (James Clerk Maxwell 1865). X-ray radiation is artificially generated when electrons that are firstly accelerated under high voltage (of the order of hundreds of kV) collide against a heavy metal (tungsten) target and reduce speed. Oda et al. (2004) reported that this heavy metal target should be small enough to minimise the scattering areas on the X-ray detector (image intensifier); in a microfocus X-ray apparatus the target is about 5 μm in size. Figure 2.104 shows schematically the difference between conventional and microfocus X-ray CT. Oda et al. (2004) verified the findings reported by Oda and

Kazama (1998) and Oda et al. (1998) using the X-ray μCT, as can be seen in the images shown in Fig. 2.105.

Microfocus X-ray CT is used by many researchers around the world (Viggiani et al. 2004, Lenoir et al. 2007, Hall et al. 2010a, Hasan and Alshibli 2010 and 2012, Andò et al. 2012a) and is considered a powerful and promising tool for the investigation of the microstructure of granular materials. When combined with mathematical processes such as Digital Image Correlation (DIC) (Hall et al. 2010b), Volumetric Digital Image Correlation (V-DIC) (Lenoir et al. 2007, Hall et al. 2010a), Particle Image Velocimetry (PIV) (White et al. 2003) and ID-Track (Andò et al. 2012a and b), the so-called full-field measurements (Viggiani and Hall 2008) are obtained and the kinematics of individual grains are observed. This means that displacements and rotations in three dimensions are monitored continuously for each individual grain in a specimen, either being inside or outside the shear band. Consequently, the evolution of fabric of natural granular materials is observed in situ and valuable microscopic information is obtained (Andò et al. 2013, Wiebicke et al. 2017).

2.10 SOPHISTICATED TESTING APPARATUSES FOR INVESTIGATING THE INFLUENCE OF FABRIC ANISOTROPY ON THE MECHANICAL BEHAVIOUR OF SANDS

As has been discussed in the previous sections, fabric anisotropy has a strong effect on the mechanical behaviour of sands. However, conventional testing apparatuses do not possess the qualities needed for investigating the fabric anisotropy effects. For example, in the triaxial apparatus (Fig. 2.6), two of the three controlled normal stresses are obligingly equal to each other (i.e. $\sigma_x \equiv \sigma_y$, where the xy-plane is the horizontal plane and the z-axis is the vertical axis of the specimen). In the triaxial compression (TC) test, the vertical stress (σ_z) is increased under constant horizontal stresses, thus, $\sigma_z = \sigma_1$ and $\sigma_x = \sigma_2 = \sigma_y = \sigma_3$; note that $\sigma_1 \geq \sigma_2 \geq \sigma_3$ are the ordered principal stresses. In the triaxial extension (TE) test, the vertical stress (σ_z) is decreased (unloading) under constant horizontal stresses, thus, $\sigma_z = \sigma_3$ and $\sigma_x = \sigma_1 = \sigma_y = \sigma_2$. The specimens tested in the triaxial apparatus have typically a cross-anisotropic fabric with horizontal bedding planes. This means that the σ_1-axis is either normal (in TC) or parallel (TE) to the bedding planes, while the σ_2-axis is always parallel to the bedding planes. Moreover, the change in the direction of the σ_1-axis from normal to parallel to the bedding planes is necessarily associated with a change in the value of the intermediate principal stress parameter, $b = (\sigma_2 - \sigma_3) / (\sigma_1 - \sigma_3)$ (Bishop 1966; see also Habib 1953), from 0 to 1. These constraints, which are also imposed in the plane strain (biaxial) apparatus, pose limitations to the investigation of sand anisotropy.

There is always the choice of preparing specimens with inclined bedding planes in order to be tested in the triaxial or plane strain apparatus (see Section 2.5 and Fig.

2.42). Nevertheless, if the principal axes of stress do not coincide with the principal axes of fabric, parasitic strains and / or stresses may develop in the specimens (see Fig. 2.34). Moreover, even if this problem is overcome, for example by using the stereophotogrammetry or laser-speckle technique to measure the non-uniform deformation field, there is a serious limitation of the conventional apparatuses that cannot be overcome: the principal directions of stress remain fixed or change with a 90° jump during homogeneous testing. Consequently, a continuous rotation of the principal axes of stress, which occurs frequently in situ, cannot be applied during homogeneous testing. The soil behaviour under principal stress rotation has been investigated using other apparatuses, as will be presented in the next chapters of this study (Broms and Casbarian 1965, Roscoe et al. 1967, Ishihara and Li 1972, Arthur et al. 1977a, Tatsuoka et al. 1982, Ishihara and Towhata 1983, Hight et al. 1983, Symes et al. 1984, Miura et al. 1986, Tatsuoka et al. 1986a, Nakata et al. 1998, Georgiannou et al. 2018).

The true triaxial apparatus, shown in Fig. 2.106, is appropriate for testing cubical or parallelepipedic soil specimens under the independent control of the three principal stresses. The value of the intermediate principal stress parameter, *b*, can be changed continuously from 0, corresponding to triaxial compression with $\sigma_1 > \sigma_2 = \sigma_3$, to 1, corresponding to triaxial extension with $\sigma_1 = \sigma_2 > \sigma_3$; accordingly, the Lode angle θ (Lode 1926) can be fully controlled in the true triaxial apparatus, as shown in Fig. 2.107. Figure 2.107 shows the octahedral plane which is perpendicular to the diagonal of the principal stress space; every stress state P (σ_1 , σ_2 , σ_3) in the principal stress space can be depicted on a octahedral plane. The distance of the octahedral plane from the origin of the principal stress space is related to the mean effective stress, the distance of the stress point from the origin of the octahedral plane is related to the deviatoric stress and the angular coordinate of the stress point is related to the Lode angle. In the case that a soil specimen with cross-anisotropic fabric is tested and the material axes coincide with the principal axes of stress (i.e. the bedding planes are either horizontal or vertical) each of the three principal stresses can act either normal or parallel to the bedding planes, allowing the investigation of aspects related to fabric anisotropy together with the effects of the stress system on soil's behaviour.

Yamada and Ishihara (1979) performed monotonic true triaxial tests on saturated cross-anisotropic sand. Drained loading was imposed using flexible membrane boundaries under constant mean effective stress. Most of the specimens had horizontal bedding planes, while some specimens were rotated by 90° about the horizontal x-axis after the sand had been deposited along the vertical z-axis. The principal axes of stress and the bedding planes of a regular (non-rotated) specimen are shown in Fig. 2.108; the stress condition at point P and the performed radial stress paths on the octahedral plane (corresponding to constant Lode angle, θ, and intermediate principal stress parameter, *b*) are also shown in Fig. 2.108.

Figures 2.109a and b show the plot of the principal strains against the stress ratio in the compression ZC-test (with $\sigma_z = \sigma_1$ and $\sigma_x = \sigma_3 = \sigma_y = \sigma_2$ and $b = 0$ and $\theta = 0°$) and in the compression YC-test (with $\sigma_y = \sigma_1$ and $\sigma_x = \sigma_3 = \sigma_z = \sigma_2$ and $b = 0$ and $\theta = 120°$), respectively; both tests were performed on regular specimens (with horizontal bedding planes). The results from the ZC-test indicate that the horizontal strains ε_x and ε_y are essentially equal due to the isotropy of fabric on the horizontal planes and symmetric stress conditions about the z-axis (i.e. $\sigma_x = \sigma_y$). On the other hand, the strains ε_x and ε_z are not equal in the YC-test, despite the fact that $\sigma_x = \sigma_z$, due to fabric anisotropy. It can be also seen that the expansive strain ε_z in the YC-test is larger than the respective expansive strain ε_y in the ZC-test. This means that the specimen expands more easily along the direction of deposition than along the direction perpendicular to the direction of deposition. Conversely, the compressive strain ε_z in the ZC-test is lower than the respective compressive strain ε_y in the YC-test, indicating that the specimen contracts less easily along the direction of deposition than along the direction perpendicular to the direction of deposition.

The hollow cylinder torsional shear apparatus (HCA) is the most sophisticated device for investigating the effects of anisotropy and principal stress rotation on the mechanical behaviour of soils. A hollow specimen is subjected to different pressures inside and outside, while a vertical normal load and a torque load are applied on the specimen's horizontal boundaries. In the HCA, the magnitude of the three principal stresses and the direction of the major principal stress with respect to the vertical, measured by angle α or $\alpha_{\sigma'1}$, can be controlled independently. It is noticed that the angle α can be changed continuously from 0° to 90°, a capability that is not provided by the conventional triaxial, true triaxial or simple shear apparatus. The continuous rotation of the stress principal axes can be imposed under changing or constant principal stresses and under the control of the b-parameter. Moreover, in contrast to the simple shear apparatus, the application of the shear stress $\tau_{z\theta}$ results in the automatic development of the complementary shear stress, $\tau_{\theta z}$, while there is no restriction on the zero-extension directions (Hight et al. 1983). Figure 2.110 shows the HCA, the boundary pressures and loads, and the internal stresses in a soil element.

Yoshimine et al. (1998) performed an extensive series of monotonic undrained torsional shear tests on saturated sand under different combinations of α and b. Figure 2.111 shows some indicative results from tests at different α and common $b = 0.5$ and from tests at different b and common $\alpha = 45°$. It can be seen that the behaviour of sand becomes more contractive and less stiff when α increases under fixed b or when b increases under fixed α. These results indicate the influence of fabric anisotropy and stress system on the mechanical behaviour of sand, which should be taken into consideration in the geotechnical design and analysis. The tests in the present study are performed in a hollow cylinder apparatus in order to investigate the behaviour of sand under loading with both fixed and rotating stress principal axes.

2.11 SUMMARY

Sands are granular materials that are deposited in the field mainly under the action of gravity and as such they exhibit frictional mechanical characteristics, as well as the property of dilatancy. This is because the sand masses equilibrate by means of the normal and shear stresses acting at the intergranular contacts, thus, the mechanical behaviour of sands is particularly sensitive to density and effective confinement, while the direction of deformation does not necessarily coincide with the direction of shearing due to micromechanical constraints. Moreover, sands exhibit anisotropic mechanical characteristics because the grain arrangements formed under gravity deposition exhibit different geometrical properties along the different directions. For example, the contact normals are densely oriented along the vertical direction of deposition, while the long axes of non-spherical grains are preferentially aligned with the horizontal bedding planes. The statistical distribution of the orientations of the contact normals and long axes of grains (or voids) can be described mathematically by means of a second-order tensor, called the fabric tensor, which provides a measure of fabric anisotropy. The fabric anisotropy attributed to gravity deposition is called the inherent anisotropy and affects the strength, stiffness and dilatancy of sands.

Under the application of external loads the internal fabric is reorganised in order to sustain these loads more efficiently. The mechanism of fabric reorganisation is called the (stress-) induced anisotropy. For example, as the granular material is subjected to deviatoric loading the increase in the stress ratio σ'_1 / σ'_3 causes new grain contacts to form along the direction of the σ'_1-axis and existing grain contacts to vanish along the direction of the σ'_3-axis, which means that the fabric anisotropy intensity increases in response to the increase in stress ratio. In the case that the principal directions of stress rotate during shearing the principal directions of fabric follow suit, which means that the fabric anisotropy evolves not only in terms of intensity but also in terms of orientation; the principal directions of fabric also rotate in order to align with the fixed principal directions of stress when the initial fabric axes are inclined with respect to the stress axes. However, the grains orientations evolve more slowly than the contact normals or voids orientation during shearing, yet, inside the zones of strain localisation considerable re-alignment of grains accrues from the intense remoulding.

The plastic incremental shear strain of sands is generally coupled to the plastic incremental volumetric strain and this fundamental property shared by all granular materials is called dilatancy. Many researchers proposed, in the past, theories and models that rely upon micromechanics in order to explain the dilatancy of sands. According to these theories, the dilatancy ratio, defined as the plastic incremental volumetric strain over the plastic incremental shear strain, is correlated with the current value of the deviatoric stress ratio and the intergranular friction characteristics of the material; the mathematical description of this dependence is called the stress – dilatancy relationship. However, recent micromechanical studies have shown that both the dilatancy ratio and the stress – dilatancy relationship depend, additionally, on the material state, determined as the current combination of void ratio and mean effective stress with reference to an ultimate material state (critical state), as well as on the state of fabric anisotropy.

The critical state of granular materials is frequently attained inside the zones of strain localisation and the intense remoulding of fabric inside these zones is associated with considerable changes in the non-directional and directional characteristics of fabric. The next chapter presents the classical Critical State Theory by Roscoe et al. (1958) and Schofield and Wroth (1968) and the the Anisotropic Critical State Theory, proposed recently by Li and Dafalias (2012) as a revision that takes into account the fabric effects at critical state.

2.12 BIBLIOGRAPHY

Affifi SS, Richart FE Jr (1973) Stress-history effects on shear modulus of soils. Soils and Foundations, Vol.13, No.1, 77-95

Allirot D, Boehler JP, Sawczuk A (1977) Irreversible deformations of an anisotropic rock under hydrostatic pressure. Int. J. Rock Mech. Min. Sci. & Geomech. Abstr., Vol. 14, pp. 77-83

Anastasopoulos I, Georgarakos T, Georgiannou V, Drosos V, Kourkoulis R (2010) Seismic performance of bar-mat reinforced-soil retaining wall: Shaking table testing versus numerical analysis with modified kinematic hardening constitutive model. Soil Dynamics and Earthquake Engineering, Vol. 30, pp. 1089-1105

Andò E, Hall SA, Viggiani G, Desrues J, Besuelle P (2012a) Grain-scale experimental investigation of localised deformation in sand: a discrete particle tracking approach. Acta Geotech., 7, No. 1, 1-13

Andò E, Hall SA, Viggiani G, Desrues J, Besuelle P (2012b) Experimental micromechanics: grain-scale observation of sand deformation. Geotech. Lett. 2, No. 3, 107-112

Andò E, Viggiani G, Hall SA, Desrues J (2013) Experimental micromechanics of granular media studied by x-ray tomography: recent results and challenges. Geotech. Lett. 3, No. 3, 142-146

Arthur JRF, Dunstan T (1969) Radiography measurements of particle packing. Nature, Lond. 223, 5205, 464-468

Arthur JRF, Dunstan T (1970) Radiological techniques developed to describe particle packing. Jnl Powder Tech. 3, 195-207

Arthur JRF, Menzies BK (1972) Inherent anisotropy in a sand. Géotechnique 22 (1), 115–129

Arthur JRF, Chua KS, Dunstan T (1977a) Induced anisotropy in a sand. Géotechnique 27 (1), 13-30

Arthur JRF, Dunstan T, Al-Ani QAJL, Assadi A (1977b) Plastic deformation and failure in granular media. Géotechnique 27 (1), 53-74

Arthur JRF, Dunstan T (1982) Rupture layers in granular media. Proc. IUTAM Symp. on Deformation and Failure of Granular Material, Delft, pp. 453-458

Barden L, Khayatt AJ, Wightman A (1969) Elastic and slip components of the deformation of sand. Canadian Geotechnical Journal, Vol. 6, pp.227-240

Bardet JP, Prubet J (1992) Shear-band analysis in idealized granular material. Journal of Engineering Mechanics, Vol. 118, No. 2, 397-415

Barnes GE (1995) Soil mechanics: principles and practice. Macmillan Press LTD, London 1995

Been K, Jefferies MG (1985) A state parameter for sands. Géotechnique 35 (2), 99–112

Been K, Jefferies MG, Hachey J (1991) The critical state of sands. Géotechnique 41 (3), 365–381

Beynet JM, Trampczynski W (1977) Application de la stereophotogrammetrie a la mesure des deplacements et a I'etude de l'ecoulement des materiaux. Mater. Constr. 10, 281-288

Bishop AW, Bjerrum L (1960) The Relevance of the triaxial test to the solution of stability problems. ASCE Conf. on Strength of Cohesive soils, pp 437 - 501

Bishop AW, Green GE (1965) The influence of end restraint on the compression strength of a cohesionless soil. Géotechnique 15 (3), 243–266

Bishop AW (1966) The strength of soils as engineering materials. Géotechnique 16 (2), 91–130

Boehler JP, Sawczuk A (1977) On yielding of oriented soils. Acta Mechanica 27, 185-206

Bolton MD (1986) The strength and dilatancy of sands. Géotechnique 36 (1), 65–78

Brewer R (1964) Fabric and mineral analysis of soils. John Wiley and Sons, Inc. pp. 129-158

Broms BB, Casbarian AO (1965) Effects of rotation of the principal stress axes and of the intermediate principal stresses on the shear strength. Proc. 6th International Conference on Soil Mechanics and Foundation Engineering, Vol. 1, pp. 18-23

Burland JB (1989) Ninth Laurits Bjerrum Memorial Lecture: “Small is beautiful”: the stiffness of soils at small strains. Canadian Geotechnical Journal 26, 499-516

Calvetti F, Viggiani G, Tamagnini C (2003) A numerical investigation of the incremental behavior of granular soils. Revista Italiana di Geotechnica, 37, 5-23

Casagrande A (1936) Characteristics of cohesionless soils affecting the stability of slopes and earthfills. Journal of the Boston Society of Civil Engineering, January, 13-32

Casagrande A, Watson JD (1938) Compaction tests and critical density investigations of cohesionless materials for Franklin Falls Dam, Merrimack Valley flood control. Corps of Engineers, U.S. Army Engineering Office, p. BII-7

Casagrande A, Carillo N (1944) Shear failure of anisotropic materials. Proc. Boston Soc. Civ. Engrs, 31, 74-87

Castro G (1969) Liquefaction of sands. Harvard Soil Mechanics Series No. 81, Harvard University, Cambridge, Mass

Chu J, Lo S-CR, Lee IK (1992) Strain-softening behavior of granular soil in strain-path testing. Journal of Geotechnical Engineering, Vo. 118, No. 2, pp. 191-208

Cole ERL (1967) The behaviour of soils in the simple shear apparatus. Ph.D. thesis, University of Cambridge

Cornforth DH (1964) Some experiments on the influence of strain conditions on the strength of sand. Géotechnique 14, 143–167

Colliat-Dangus JL, Desrues J, Foray P (1988) Triaxial testing of granular soil under elevated cell pressure. In Advanced triaxial testing for soil and rocks (edited by R.T. Donaghe, R.C. Chaney and M.L. Silver), STP977, pp. 290-310. Philadelphia: American Society for Testing and Materials

Coumoulos DG (1968) A radiographic study of soils. Ph.D. thesis, University of Cambridge

Cubrinovski M, Ishihara K (1998) Modelling of sand behaviour based on state concept. Soils and Foundations, Vol.38, No. 3, 115-127

Cundall PA, Strack ODL (1979) A discrete numerical model for granular assemblies. Géotechnique 29 (1), 47–65

Dafalias YF, Manzari MT (2004) A simple plasticity sand model accounting for fabric change effects. J. Eng. Mech., 130(6), 622-634

Dafalias YF, Papadimitriou AG, Li XS (2004) Sand plasticity model accounting for inherent fabric anisotropy. J. Eng. Mech., 130(11), 1319-1333

De Josselin de Jong (1976) Rowe’s stress-dilatancy relation based on friction. Géotechnique 26 (3), 527–534

Deman F (1975) Achsensymetrische spannungs-und verformunysfelder in trockenem sand. Dissertation, Universität Karlsruhe, Veröffentlichungen IBF, No. 62

Desrues J (1984) Localisation de la deformation plastique dans le matérieux granulaires. These d’etat, Université de Grenoble

Desrues J, Duthilleul B (1984) Mesure du champ de deformation d’un objet plan par la methode stereophotogrammetrique de faux relief. J. Met. theor. appl. 3(1) 79-103

Desrues J, Lanier J, Stutz P (1985) Localization of the deformation in tests on sand sample. Engineering Fracture Mechanics, Vol. 21, No. 4, pp. 909-921

Desrues J, Mokni M, Mazerolle F (1991) Tomodensitométrie et localisation dans les sables. Deformation of soils and displacement of structures. Proc.10th Eur. Conf. Soil Mech., Florence, 61-64

Desrues J, Chambon R, Mokni M, Mazerolle F (1996) Void ratio inside shear bands in triaxial sand specimens studied by computed tomography. Géotechnique 46 (3), 529-546

Desrues J, Viggiani G (2004) Strain localization in sand: an overview of the experimental results obtained in Grenoble using stereophotogrammetry. International Journal for Numerical and Analytical Methods in Geomechanics, 2004, 28: 279-321

Desrues J, Georgopoulos I-O (2006) An investigation of diffuse failure modes in undrained triaxial tests on loose sand. Soils and Foundations, Vol.46, No.5, 585-594

Drescher A, Vardoulakis I (1982) Geometric softening in triaxial tests on granular materials. Géotechnique 32 (4), 291-303

Einstein A (1915a) Grundgedanken der allgemeinen Relativitätstheorie und Anwendung dieser Theorie in der Astronomie. Preussische Akademie der Wissenschaften, Sitzungsberichte, 1915 (part 1), 315

Einstein A (1915b) Zur allgemeinen Relativitätstheorie. Preussische Akademie der Wissenschaften, Sitzungsberichte, 1915 (part 2), 778–786, 799–801

Einstein A (1915c) Erklärung der Perihelbewegung des Merkur aus der allgemeinen Relativitätstheorie. Preussische Akademie der Wissenschaften, Sitzungsberichte, 1915 (part 2), 831–839

Einstein A (1915d) Feldgleichungen der Gravitation. Preussische Akademie der Wissenschaften, Sitzungsberichte, 1915 (part 2), 844–847

Fermi E (1936) Thermodynamics. Dover Publications, Inc., New Work

Feynman RP, Leighton RB, Sands M (1964) The Feynman lectures on Physics: mainly electromagnetism and matter. Addison-Wesley publishing company

Finno RJ, Harris WW, Mooney MA, Viggiani G (1997) Shear bands in plane strain compression of loose sand. Géotechnique 47 (1), 149–165

Fu P, Dafalias YF (2011a) Study of anisotropic shear strength of granular materials using DEM simulation. International Journal for Numerical and Analytical Methods in Geomechanics, 2011, 35: 1098-1126

Fu P, Dafalias YF (2011b) Fabric evolution within shear bands of granular materials and its relation to critical state theory. International Journal for Numerical and Analytical Methods in Geomechanics, 2011, 35: 1918-1948

Gazetas G (1981) Deformational soil anisotropy: experimental and mathematical modeling. Report, Publication No. 8102, Case Institue of Technology, Case Western University of technology

Georgiannou VN, Burland JB (2006) A laboratory study of slip surface formation in an intact natural stiff clay. Géotechnique 56 (8), 551–559

Georgiannou VN, Konstadinou M, Triantafyllos PK (2018) Sand behavior under stress states involving principal stress rotation. Journal of Geotechnical and Geoenvironmental Engineering, 2018, 144(6): 04018028

Goldscheider M (1975) Dilatanzverhalten von sand bei geknickten verformungswegen. Mech. Res. Com., 2, 143-188

Goldscheider M, Vardoulakis I (1980) Remarques à Loi rhéologique incrémentale de sols. By F. Darve, M. Boulon and R. Chambon. J. Méc. 19, 203-208

Goto S, Tatsuoka F, Shibuya S, Kim Y-S, Sato T (1991) A simple gauge for local small strain measurements in the laboratory. Soils and Foundations, Vol.31, No.1, pp. 169-180

Gourlay CM, Dahle AK (2007) Dilatant shear bands in solidifying metals. Nature, Vol. 445, doi: 10.1038/nature05426

Graton LC, Fraser HJ (1935) Systematic packing of spheres with particular relation to porosity and permeability. J. of Geology, 43, 785-909

Guo P, Su X (2007) Shear strength, interparticle locking, and dilatancy of granular materials. Canadian Geotechnical Journal 44, 579-591

Guo PJ (2008) Modified direct shear test for anisotropic strength of sand. J. Geotech. Geoenviron. Eng. 134(9):1311-1318

Gutierrez M, Ishihara K, Towhata I (1991) Flow theory for sand during rotation of principal stress direction. Soils and Foundations, Vol.31, No.4, pp. 121-132

Gutierrez M, Ishihara K, Towhata I (1993) Model for the deformation of sand during rotation of principal stress directions. Soils and Foundations, Vol.33, No.3, pp. 105-117

Gutierrez M, Ishihara K (2000) Non-coaxiality and energy dissipation in granular materials. Soils and Foundations, Vol.40, No.2, 49-60

Gutierrez M, Vardoulakis I (2007) Energy dissipation and post-bifurcation behaviour of granular soils. International Journal for Numerical and Analytical Methods in Geomechanics, 31:435-455

Habib P (1953) Influence de la variation de la contrainte moyenne sur la resistance au cisaillement des sols. Proceedings of the 3rd International Conference on Soil Mechanics and Foundation Engineering, Zurich, Switzerland, Vol. 1, pp. 131-136

Hall SA, Bornert M, Desrues J, Pannier Y, Lenoir N, Viggiani G, Bésuelle P (2010a) Discrete and continuum analysis of localised deformation in sand using X-ray and μCT and volumetric digital image correlation. Géotechnique 60 (5), 315-322

Hall SA, Wood DM, Ibraim E, Viggiani G (2010b) Localised deformation patterning in 2D granular materials revealed by digital image correlation. Granular Matter (2010) 12: 1-14

Han C, Vardoulakis I (1991) Plane-strain compression experiments on water-saturated fine-grained sand. Géotechnique 41 (1), 49-78

Han C, Drescher A (1993) Shear bands in biaxial tests on dry coarse sand. Soils and Foundations, Vol.33, No.1, 118-132

Hansen B (1958) Line ruptures regarded as narrow rupture zones. Basic equations based on kinematic considerations. Proc. Conf. Earth Pressure Probl., Brussels 1, 39-48

Hardin BO, Richart FE Jr (1963) Elastic wave velocities in granular soils. Journal of Soil Mechanics and Foundations Division, ASCE, Vol. 89, No. SM1, pp. 33-65

Hasan A, Alshibli KA (2010) Experimental assessment of 3-D particle-to-particle interaction within sheared sand using synchrotron microtomography. Géotechnique 60 (5), 369-379

Hasan A, Alshibli KA (2012) Three dimensional fabric evolution of sheared sand. Granular Matter (2012) 14: 469-482

Hertz HR (1882) Über die berührung fester elastischer Körper (On the contact of rigid elastic solids). In: Miscellaneous Papers. Jones and Schott, Editors, J. reine und angewandte Mathematik 92, Macmillan, London (1896), p. 156

Hettler A, Vardoulakis I (1984) Behaviour of dry sand tested in a large triaxial apparatus. Géotechnique 34 (2), 183-198

Hight DW, Gens A, Symes MJ (1983) The development of a new hollow cylinder apparatus for investigating the effects of principal stress rotation in soils. Géotechnique 33, No. 4, 355-383

Hobson MP, Efstathiou GP, Lasenby AN (2006) General Relativity: an introduction for physicists. Cambridge University Press, 2006

Hoque E, Tatsuoka F (1998) Anisotropy in elastic deformation of granular materials. Soils and Foundations, Vol.38, No.1, pp. 163-179

Horn HM, Deere DU (1962) Frictional characteristics of minerals. Géotechnique 12, No. 4, 319-335

Houlsby GT, Amorosi A, Rojas E (2005) Elastic moduli of soils dependent on pressure: a hyperelastic formulation. Géotechnique 55, No. 5, 383-392

Huang X, O’Sullivan C, Hanley KJ, Kwok CY (2014) Discrete-element method analysis of the state parameter. Géotechnique 64, No. 12, 954-965

Hutchings IM (2016) Leonardo da Vinci’s studies of friction. Wear, http://dx.doi.org/10.1016/j.wear.2016.04.019

Ishihara K, Li S-I (1972) Liquefaction of saturated sand in triaxial torsion shear test. Soils and Foundations, Vol.12, No.2, 19-39

Ishihara K, Tatsuoka F, Yasuda S (1975) Undrained deformation and liquefaction of sand under cyclic stresses. Soils and Foundations, Vol.15, No.1, 29-44

Ishihara K, Towhata I (1983) Sand response to cyclic rotation of principal stress directions as induced by wave loads. Soils and Foundations, Vol.23, No.4, 11-26

Iwasaki T, Tatsuoka F, Takagi W (1978) Shear moduli of sands under cyclic torsional shear loading. Soils and Foundations, Vol.18, No.1, pp. 39-56

Jardine RJ, Symes MJ, Burland JB (1984) The measurement of the soil stiffness in the triaxial apparatus. Géotechnique, Vol. 34, No. 3, pp.323-340

Jiang G-L, Tatsuoka F, Flora A, Koseki J (1997) Inherent and stress-state-induced anisotropy in very small strain stiffness of a sandy gravel. Géotechnique 47, No. 3, 509-521

Jiang M, Zhang A, Fu C (2017) 3D DEM simulations of drained triaxial tests on inherently anisotropic granulates. European Journal of Environmental and Civil Engineering, DOI: 10.1080/19648189.2017.1385541

Johnson KL (2003) Contact mechanics. Cambridge University Press 2003 (First Edition 1985)

Kallstenius T, Bergau W (1961) Research on the texture of granular masses. Proc. Fifth Inter. Conf. Soil Mech. Found. Engng., 1, 158-165

Kavvadas M, Gazetas G (1993) Kinematic seismic response and bending of the free-head piles in layered soil. Géotechnique 43, No. 2, 207-222

Kjellman W (1936) Report on an apparatus for consummate investigation of the mechanical properties of soils. Proc. 1st Int. Conf. Soil Mech., Vol.2, pp.16-20

Koerner RM (1970) Behaviour of single mineral soils in triaxial shear. J. Soil Mech. Found. Div. ASCE 96, No. SM4, 1373-1390

Kramer SL (1996) Geotechnical Earthquake Engineering. Prentice Hall, New Jersey

Ladd CL, Foot R, Ishihara K, Schlosser F, Poulos H (1977) Stress-deformation and strength characteristics. IX Int. Conf. Soil Mech. Fdn. Engrg., Tokyo, 421-494

Lade PV (1982) Localization effects in triaxial tests on sand. In Proc. IUTAM Conf. on Deformation and Failure of Granular Media, Delft, pp. 461-471

Lade PV, Nelson RB, Ito YM (1988) Instability of granular materials with nonassociated flow. Journal of Engineering Mechanics, Vol. 114, No. 12, 2173-2191

Lade PV, Prabucki MJ (1995) Softening and preshearing effects in sand. Soils and Foundations, Vol.35, No.4, 93-104

Lade PV, Abelev AV (2005) Characterization of cross-anisotropic soil deposits from isotropic compression tests. Soils and Foundations, Vol.45, No.5, 89-102

Lade PV (2007) Modeling failure in cross-anisotropic frictional materials. International Journal of Solids and Structures 44 (2007), 5146-5162

Lade PV, Rodriguez NM, Van Dyck EJ (2014) Effects of principal stress directions on 3D failure conditions in cross-anisotropic sand. Journal of Geotechnical and Geoenvironmental Engineering, 2014, 140(2): 04013001

Lade PV (2016) Triaxial testing of soils. Wiley Blackwell (2016)

Lam WK, Tatsuoka F (1988) Effects of initial anisotropic fabric and σ_2 on strength and deformation characteristics of sand. Soils and Foundations, Vol.28, No.1, pp. 89-106

Lenoir N, Bornert M, Desrues J, Bésuelle P, Viggiani G (2007) Volumetric digital image correlation applied to X-ray microtomography images from triaxial compression tests on argillaceous rock. Strain (2007), 43, 193-205

Li X (2006) Micro-scale investigation on the quasi-static behavior of granular material. Ph.D. Thesis, Hong-Kong Univ. of Science & Technology, Kong Kong

Li XS (1997) Modeling of dilative shear failure. J. Geotech. Geoenviron. Eng., 123(7), 609-616

Li XS, Wang Y (1998) Linear representation of steady-state line for sand. J. Geotech. Geoenviron. Eng., 124(12), 1215-1217

Li XS, Dafalias YF, Wang Z-L (1999) State-dependent dilatancy in critical constitutive modelling of sand. Can. Geotech. J. 36, 599-611

Li XS, Dafalias YF (2000) Dilatancy for cohesionless soils. Géotechnique 50, No. 4, 449-460

Li XS, Dafalias YF (2002) Constitutive modelling of inherently anisotropic sand behaviour. J. Geotech. Geoenviron. Eng., 128(10), 868-880

Li XS, Dafalias YF (2012) Anisotropic critical state theory: role of fabric. Journal of Engineering Mechanics, Vol. 138, No. 3, 263-275

Lode W (1926) Versuche über den einfluss der mittleren hauptspannung auf das fliessen der metalle. Eisen, Kupfer und Nickel, Zeitschrift für Physik, 36, 913 – 939

Lupini JF, Skinner AE, Vaughan PR (1981) The drained residual strength of cohesive soils. Géotechnique 31, No. 2, 181-313

Mahmood A, Mitchell JK (1974) Fabric-property relationships in fine granular materials. Clays Miner. 22(5-6):397-408

Manzari MT, Dafalias YF (1997) A critical state two-surface plasticity model for sands. Géotechnique 47, No. 2, 255-272

Matsuoka H (1974) Stress-strain relationship of sands based on the mobilized plane. Soils and Foundations, Vol.14, No.2, pp. 47-61

Matsuoka H, Ishizaki H (1981) Deformation and strength of anisotropic soil. Proc., 10th ICSMFE, Stockholm, Vol. 1, pp. 699-702

Maxwell JC (1865) A dynamical theory of the electromagnetic field. Philosophical transactions of the Royal Society of London 155, 459-512

Michaelides O, Bouckovalas G, Gazetas G (1998) Non-linear soil properties and impedances for axially vibrating pile elements. Soils and Foundations, Vol.38, No.3, 129-142

Miura K, Miura S, Toki S (1986) Deformation behavior of anisotropic dense sand under principal stress axes rotation. Soils and Foundations, Vol.26, No.1, 36-52

Mokni M (1992) Relations entre d'eformations en masse et déformations localisées dans les matériaux granulaires. Thèse de Doctorat de l'Université J. Fourier, Grenoble, France

Mooney MA, Viggiani G, Finno RJ (1997) Undrained shear band deformation in granular media. J. Eng. Mech. 1997.123:577-585

Mooney MA, Finno RJ, Viggiani GM (1998) A unique critical state for sand? J. Geotech. Geoenviron. Eng. 1998.124:1100-1108

Mühlhaus H-B, Vardoulakis I (1987) The thickness of shear bands in granular materials. Géotechnique 37, No. 3, 271-283

Nakata Y, Hyodo M, Murata H, Yasufuku N (1998) Flow deformation of sands subjected to principal stress rotation. Soils and Foundations, Vol.38, No.2, 115-128

Negussey N, Wijewickreme WKD, Vaid YP (1988) Constant volume friction angle of granular materials. Canadian Geotechnical Journal 25, 50-55

Newland PL, Allely BH (1957) Volume changes in drained triaxial tests on granular materials. Géotechnique 7, No. 1, 17-34

Newton Isaac (1687) Philosophiæ Naturalis Principia Mathematica. Imprimatur S. Pepys, Reg. Soc. Præses

Nicot F, Darve F (2011) Diffuse and localized failure modes: Two competing mechanisms. International Journal for Numerical and Analytical Methods in Geomechanics, Vol. 35, 586-601

Nova R, Wood DM (1979) A constitutive model for sand in triaxial compression. International Journal for Numerical and Analytical Methods in Geomechanics, Vol. 3, 255-278 (1979)

Oda M (1972 a) Initial fabrics and their relations to mechanical properties of granular material. Soils and Foundations, Vol.12, No.1, 18-36

Oda M (1972 b) The mechanism of fabric changes during compressional deformation of sand. Soils and Foundations, Vol.12, No.2, 1-18

Oda M, Konishi J (1974a) Microscopic deformation mechanism of granular material in simple shear. Soils and Foundations, Vol.14, No.4, 26-38

Oda M, Konishi J (1974b) Rotation of principal stresses in granular material during simple shear. Soils and Foundations, Vol.14, No.4, 39-53

Oda M (1977) Co-ordination number and its relation to shear strength of granular material. Soils and Foundations, Vol.17, No.2, 29-42

Oda M, Koishikawa I, Higuchi T (1978) Experimental study of anisotropic shear strength of sand by plane strain test. Soils and Foundations, Vol.18, No.1, 25-38

Oda M, Konishi J, Nemat-Nasser S (1982) Experimental micromechanical evaluation of strength of granular materials: effects of particle rolling. Mechanics of Materials 1 (1982), 269-283

Oda M, Nemat-Nasser S, Konishi J (1985) Stress-induced anisotropy in granular masses. Soils and Foundations, Vol.25, No.3, 85-97

Oda M (1993) Micro-fabric and couple stress in shear bands of granular materials. Powders and Grains 93, (ed. Thornton), 161-166, Balkemma, Rotterdam

Oda M, Kazama H, Konishi J (1998) Effects of induced anisotropy on the development of shear bands in granular materials. Mechanics of Materials 28 (1998) 103-111

Oda M, Kazama H (1998) Microstructure of shear bands and its relation to the mechanisms of dilatancy and failure of dense granular soils. Géotechnique 48, No. 4, 465-481

Oda M, Takemura T, Takahashi M (2004) Microstructure in shear band observed by microfocus X-ray computed tomography. Géotechnique 54, No. 8, 539-542

O'Sullivan C, Wadee MA, Hanley KJ, Barreto D (2013) Use of DEM and elastic stability analysis to explain the influence of the intermediate principal stress on shear strength. Géotechnique 63, No. 15, 1298-1309

Papadimitriou AG, Bouckovalas GD, Dafalias YF (2001) Plasticity model for sand under small and large cyclic strains. Journal of Geotechnical and Geoenvironmental Engineering, Vol.127, No.11, pp. 973-983

Papamichos E, Vardoulakis I (1995) Shear band formation in sand according to non-coaxial plasticity model. Géotechnique 45, No. 4, 649-661

Penman ADM (1953) Shear characteristics of a saturated silt, measured in triaxial compression. Géotechnique 3, 312-328

Poulos SJ (1981) The steady state of deformation. Journal of the Geotechnical Engineering Division, ASCE, Vol. 107, pp. 553-562

Raftoyiannis IG (2007) Composite materials structures. (notes in Greek)

Reades DW, Green GE (1976) Independent stress control and triaxial extension tests on sand. Géotechnique **26**(4), 551 – 576

Richart FE Jr, Hall JR Jr, Woods RD (1970) Vibrations of soils and foundations. Prentice-Hall, Inc., 1970

Roscoe KH, Schofield AN, Wroth CP (1958) On the yielding of soils. Géotechnique 8 (1), 22–53

Roscoe KH, Basset RH, Cole ERL (1967) Principal axes observed during simple shear of a sand. Proc. Geotech. Conf., Oslo, pp. 231-237

Roscoe KH, Burland JB (1968) On the generalized stress-strain behaviour of "wet" clay. In Engineering plasticity. Edited by J. Heyman and F.A. Leckie. Cambridge University Press, London, UK. pp.535-609

Roscoe KH (1970) The influence of strains in soil mechanics. Tenth Rankine Lectrure, Géotechnique 20, No. 2, 129-170

Rowe PW (1962) The stress-dilatancy relation for static equilibrium of an assembly of particles in contact. Proc. R. Soc. Lond. A 1962 269, 500-527

Sadrekarimi A, Olson SM (2011) Critical state friction angle of sands. Géotechnique 61 (9), 771–783

Sadrekarimi A, Olson SM (2012) Effect of sample-preparation method on critical-state behavior of sands. Geotechnical Testing Journal, Vol. 35, No. 4

Satake M (1978) Constitution of mechanics of granular materials through graph representation. Theoretical and Applied Mechanics 26, University of Tokyo Press, pp. 257-266

Schofield AN, Wroth CP (1968) Critical state soil mechanics. McGraw-Hill, London

Seed HB, Wong RT, Idriss IM, Tokimatsu K (1986) Moduli and damping factors for dynamic analysis of cohesionless soils. Journal of Geotechnical engineering, Vol. 112, No.11, 1016-1032

Shibuya S, Hight DW (1987) A bounding surface of granular materials. Soils and Foundations, Vol.27, No.4, 123-136

Shibuya S, Tatsuoka F, Teachavorasinskun S, Kong XJ, Abe F, Kim Y-S, Park C-S (1992) Elastic deformation properties of geomaterials. Soils and Foundations, Vol.32, No.3, 26-46

Skinner AE (1969) A note on the influence of interparticle friction on the shearing strength of a random assembly of spherical particles. Géotechnique 19, No. 1, 150-157

St Vénant B (1870) Mémoire sur l'éstablissment des équations différentielles des mouvements intérieurs á leur premier état. C.R. Acad. Sci. Paris, 70, 473-480 (1870)

Stroud MA (1970) The behaviour of sand at low stress levels in the simple shear apparatus. Ph.D. thesis, University of Cambridge

Sture S, Costes NC, Batiste SN, Lankton MR, Alshibli KA, Jeremic B, Swanson RA, Frank M (1998) Mechanics of granular materials at very low effective stresses. J. Aerospace Engng ASCE 11, No 3, 67-72

Symes MJ, Gens A, Hight DW (1984) Undrained anisotropy and principal stress rotation in saturated sand. Géotechnique 34, No. 1, 11-27

Tatsuoka F (1976) Stress-dilatancy relations of anisotropic sands in three dimensional stress condition. Soils and Foundations, Vol.16, No.2, pp. 1-18

Tatsuoka F, Iwasaki T, Fukushima S, Sudo H (1979) Stress conditions and stress histories affecting shear modulus and damping of sand under cyclic loading. Soils and Foundations, Vol.19, No.2, pp. 29-43

Tatsuoka F, Muramatsu M, Sasaki T (1982) Cyclic undrained stress-strain behavior of dense sands by torsional simple shear test. Soils and Foundations, Vol.22, No.2, pp. 55-70

Tatsuoka F, Sonoda S, Hara K, Fukushima S, Pradhan TBS (1986a) Failure and deformation of sand in torsional shear. Soils and Foundations, Vol.26, No.4, pp. 79-97

Tatsuoka F, Sakamoto M, Kawamura T, Fukushima S (1986b) Strength and deformation characteristics of sand in plane strain compression at extremely low pressures. Soils and Foundations, Vol.26, No.1, pp. 65-85

Tatsuoka F, Nakamura S, Huang C-C (1990) Strength anisotropy and shear band direction in plane strain tests of sand. Soils and Foundations, Vol.30, No.1, pp. 35-54

Tavenas F, Trak B, Leroueil S (1980) Remarks on the validity of stability analysis. Can. Geotech. J. 1980; 17: 61-73

Taylor DW (1948) Fundamentals of Soil Mechanics. John Wiley, 1948

Terzaghi K (1925) Erdbaumechanik auf Bodenphysikalischer Grundlage. Leipzig u. Wien, F. Deuticke, 1925

Terzaghi K, Peck RB, Mesri G (1996) Soil mechanics in engineering practice. 3rd edn. London: Wiley

Thornton C (2000) Numerical simulations of deviatoric shear deformation of granular media. Géotechnique 50, No. 1, 43-53

Tong Z, Fu P, Zhou S, Dafalias YF (2014) Experimental investigation of shear strength of sands with inherent fabric anisotropy. Acta Geotechnica, DOI 10.1007/s11440-014-0303-6

Towhata I (2008) Geotechnical earthquake engineering. Springer 2008

Tsomokos A, Georgiannou VN (2010) Effect of grain shape and angularity on the undrained response of fine sands. Canadian Geotechnical Journal 47 (5), pp. 539-551

Uthayakumar M, Vaid YP (1998) Static liquefaction of sands under multiaxial loading. Canadian Geotechnical Journal 35, pp. 273-283

Vaid YP, Chern JC (1983) Effect of static shear on resistance to liquefaction. Soils and Foundations, Vol.23, No.1, pp. 47-60

Vaniello M (1996) Coaxiality of strain and stress in anisotropic linear elasticity. Journal of Elasticity, 42: 283-289, 1996

Vardoulakis I (1977) Sherfugenbildung in Sandkorpern als Verzweigungsproblem. Veröffenthichungen des Instituts für Boden- und Felsmechanik, Universität Karlsruhe, Heft 70

Vardoulakis I, Goldscheider M, Gudehus G (1978) Formation of shear bands in sand bodies as a bifurcation problem. International Journal for Numerical and Analytical Methods in Geomechanics, 1978, 2: 99-128

Vardoulakis I (1979) Bifurcation analysis of the triaxial test on sand samples. Acta Mechanica 32, 35-54 (1979)

Vardoulakis I (1980) Shear band inclination and shear modulus of sand in biaxial tests. International Journal for Numerical and Analytical Methods in Geomechanics, 4: 103-119 (1980)

Vardoulakis I, Goldsheider M (1981) Biaxial apparatus for testing shear bands in soils. Proc. 10th ICSMFE, Stockholm, Vol. 4, pp. 819-824

Vardoulakis I, Graf B (1982) Imperfection sensitivity of the biaxial test on dry sand. Proc. IUTAM Conf. Deformation and failure of granular materials, Delft, pp. 485-491, Rotterdam, Balkema

Vardoulakis I (1983) Rigid granular plasticity model and bifurcation in the triaxial test. Acta Mech. 49, 251-272

Vardoulakis I, Graf B (1985) Calibrations of constitutive models for granular materials using data from biaxial experiments. Géotechnique 35, No. 3, 299-317

Vardoulakis I (1989) Shear banding and liquefaction in granular materials on the basis of a Cosserat continuum theory. Ingenieur-Archiv 59, 106-113

Vardoulakis I, Aifantis EC (1989) Gradient dependent dilatancy and its implications in shear banding and liquefaction. Ingenieur-Archiv 59, 197-208

Vardoulakis I, Aifantis EC (1991) A gradient flow-theory of plasticity for granular materials. Acta Mechanica 87, 197-217

Vardoulakis I, Sulem J (1995) Bifurcation analysis in geomechanics. Chapman and Hall, 1995

Vardoulakis I, Georgopoulos I-O (2005) The “stress-dilatancy” hypothesis revisited: shear-banding related instabilities. Soils and Foundations, Vol.45, No.2, pp. 61-76

Verdugo R, Ishihara K (1996) The steady state of sandy soils. Soils and Foundations, Vol.36, No.2, pp. 81-91

Viggiani G, Küntz M, Desrues J (2001) An experimental investigation of the relationships between grain size distribution and shear banding in sand. P.A.Vermeer et al. (Eds.): LNP 568, pp. 111–127, 2001. Springer-Verlag Berlin Heidelberg 2001

Viggiani G, Lenoir N, Bésuelle P, di Michiel M, Marello S, Desrues J, Kretzschmer, M (2004) X-ray microtomography for studying localized deformation in fine-grained geomaterials under triaxial compression. C.R. Mecanique 332 (2004), 819-826

Viggiani G, Hall SA (2008) Full-field measurements, a new tool for laboratory experimental geomechanics. Deformational Characteristics of Geomaterials, Burns, Mayne and Santamarina (Eds.)

Vucetic M, Dobry R (1991) Effect of soil plasticity on cyclic response. Journal of Geotechnical Engineering, Vol. 117, No.1, 89-107

Wan RG, Guo RG (1998) A simple constitutive model for granular soils: modified stress-dilatancy approach. Comput. Geotech. 22, No 2, 109-133

Wan R, Nicot F, Darve F (2010) Micromechanical formulation of stress-dilatancy as a flow rule in plasticity of granular materials. Journal of Engineering Mechanics, 136, 589-598

Wang Z-L, Dafalias YF, Shen C-K (1990) Bounding surface hypoplasticity model for sand. Journal of Engineering Mechanics, Vol. 116, No. 5, 983-1001

Wang R, Fu P, Zhang J-M, Dafalias YF (2017) Evolution of various fabric tensors for granular media toward the critical state. J. Eng. Mech., 2017, 143(10): 04017117

White DJ, Take WA, Bolton MD (2003) Soil deformation measurement using particle image velocimetry (PIV) and photogrammetry. Géotechnique 53, No. 7, 619-631

Wiebicke M, Andò E, Salvatore E, Viggiani G, Herle I (2017) Experimental measurement of granular fabric and its evolution under shearing. Powders and Grains (2017), EPJ Web of Conferences 140, 02020 (2017)

Wong RKS, Arthur JRF (1985) Induced and inherent anisotropy in sand. Géotechnique 35, No. 4, 471-481

Wood DM (1990) Soil behaviour and Critical State soil mechanics. Cambridge University Press, 1990

Wood DM, Belkheier K, Liu DF (1994) Strain softening and state parameter for sand modelling. Géotechnique 44, No. 2, 335-339

Yamada Y, Ishihara K (1979) Anisotropic deformation characteristics of sand under three dimensional stress conditions. Soils and Foundations, Vol. 19, No. 2, 79-94

Yamada Y, Ishihara K (1981) Undrained deformation characteristics of loose sand under three-dimensional stress conditions. Soils and Foundations, Vol. 21, No. 1, 97-107

Yamaguchi I (1981) Speckle displacement and decorrelation in the diffraction and image fields for small object deformation. Opt. Acta, 28-10, pp. 1359-1376

Yamamuro JA, Lade P (1996) Drained sand behavior in axisymmetric tests at high pressures. Journal of Geotechnical Engineering, Vol. 122 (2), pp. 109-119

Yoshimine M, Ishihara K, Vargas W (1998) Effects of principal stress direction and intermediate principal stress on undrained shear behavior of sand. Soils and Foundations, Vol. 38, No. 3, 179-188

Yu P, Richart FE Jr (1984) Stress ratio effects on shear modulus of dry sands. Journal of Geotechnical Engineering, Vol. 110, No. 3, 331-345

Zdravkovic L, Jardine RJ (1997) Some anisotropic stiffness characteristics of a silt under general stress conditions. Géotechnique 47, No. 3, 407-437

Zdravkovic L, Jardine RJ (2000) Undrained anisotropy of Ko-consolidated silt. Canadian Geotechnical Journal 37: 178-200

Zdravkovic L, Jardine RJ (2001) The effect on anisotropy of rotating the principal stress axes during consolidation. Géotechnique 51, No. 1, 69-83

Zhao J, Guo N (2013) Unique critical state characteristics in granular media considering fabric anisotropy. Géotechnique 63, No. 8, 695-704

2.13 FIGURES

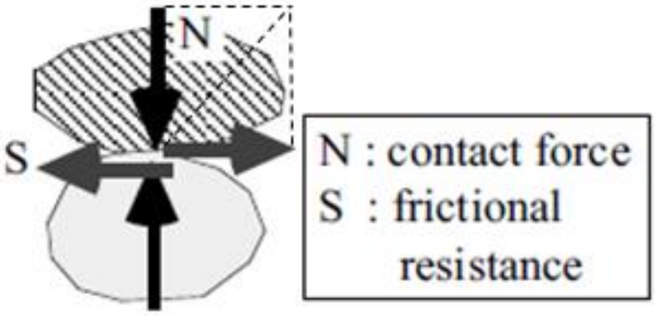

Fig. 2.1 Interaction between two grains via normal and shear force at the interparticle contact (after Towhata 2008)

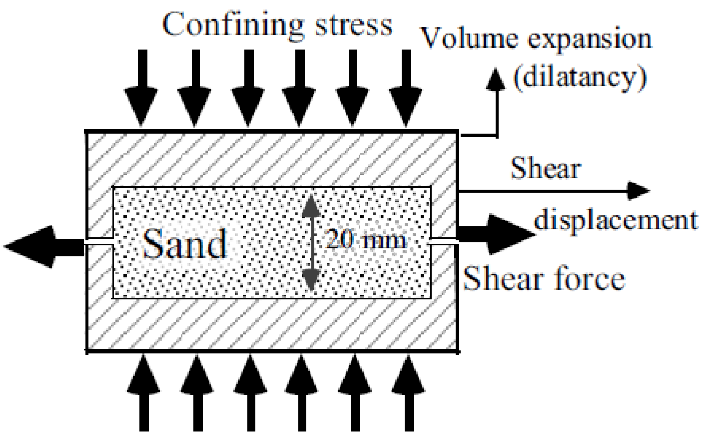

Fig. 2.2 The direct-shear apparatus (after Towhata 2008)

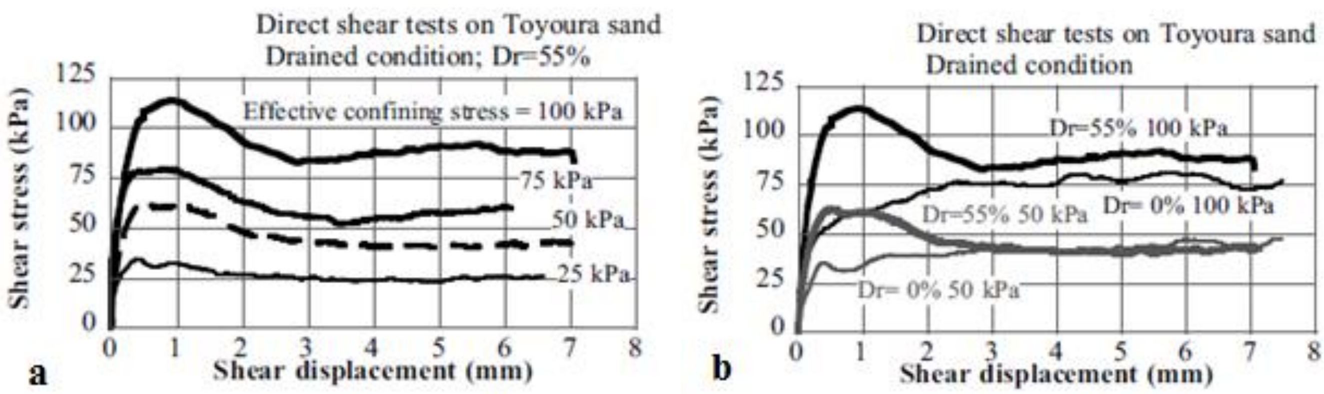

Fig. 2.3 Shear stress - displacement curves of sand subjected to direct-shear loading. **a** Influence of confining stress on drained stress - strain behaviour of sand. **b** Influence of relative density of sand on drained stress - strain behaviour of sand (after Towhata 2008)

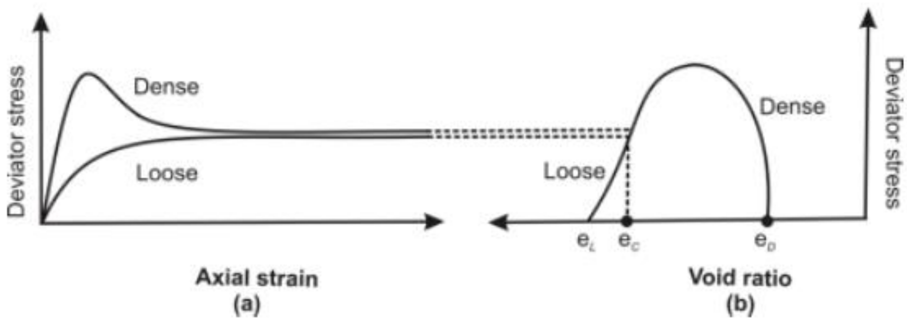

Fig. 2.4 The concept of critical void ratio of dense and loose sand loaded under drained conditions at the same confining stress (Casagrande 1936). **a** Stress - strain curves. **b** Stress - void ratio curves

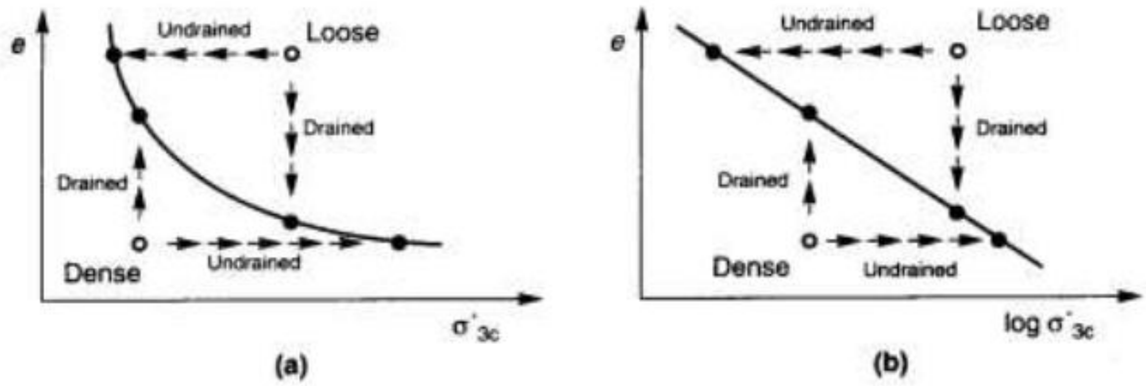

Fig. 2.5 Critical void ratio (CVR) line in the $e - \sigma'_{3c}$ plane (Casagrande 1936). **a** CVR line in linear scale. **b** CVR line in semi-logarithmic scale (after Kramer 1996)

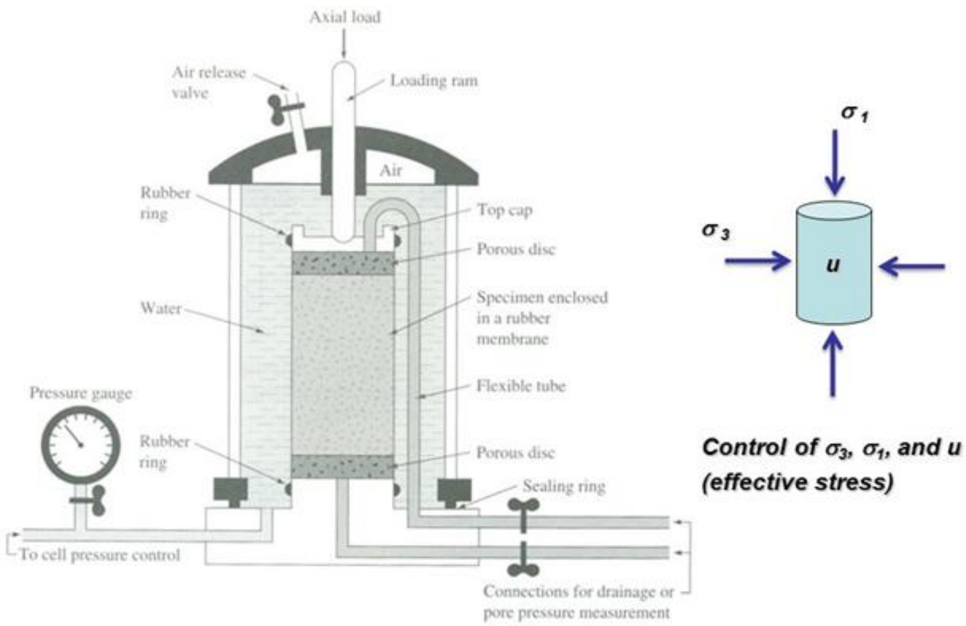

Fig. 2.6 The triaxial apparatus for axisymmetric loading of cylinders (after Bishop and Bjerrum 1960)

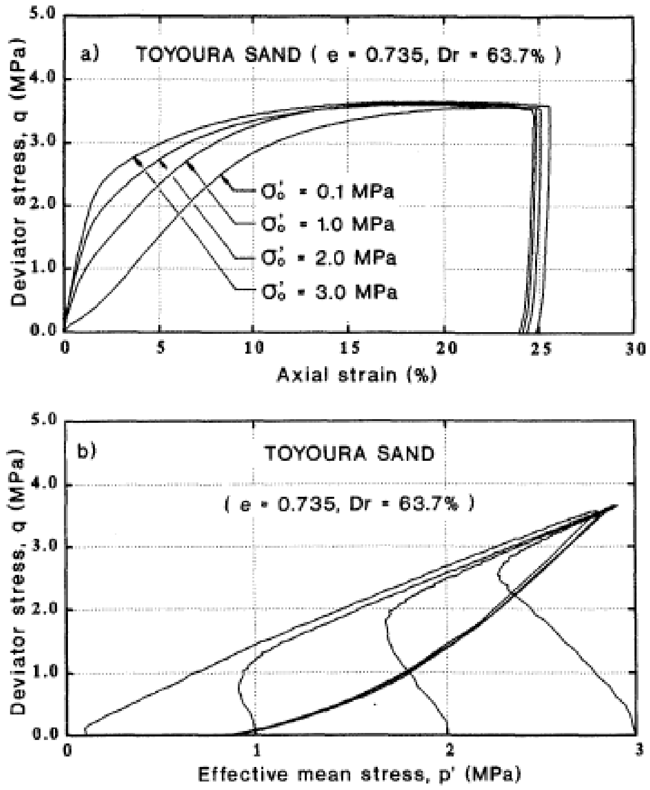

Fig. 2.7 Monotonic undrained triaxial compression tests on medium dense sand, consolidated to different mean effective stresses. **a** Stress - strain curves. **b** Effective stress paths (after Verdugo and Ishihara 1996)

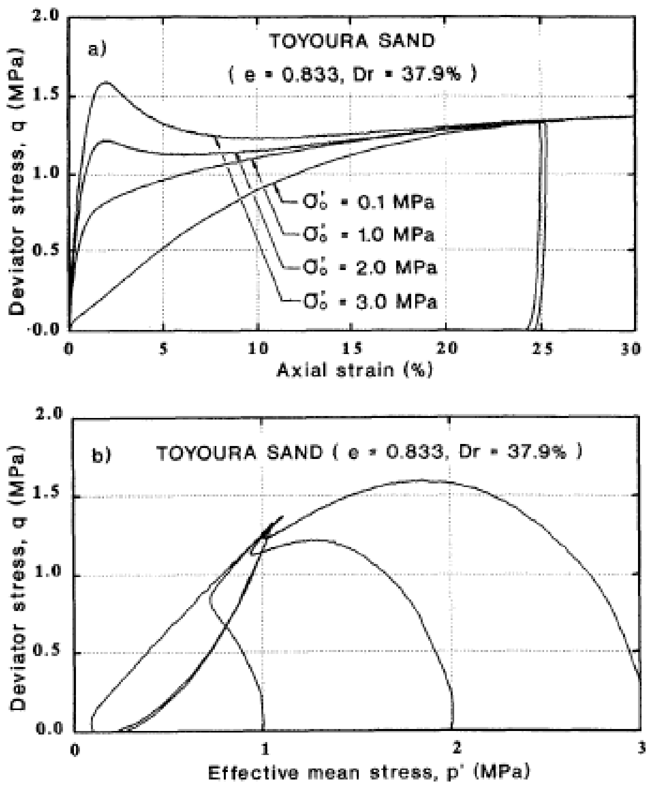

Fig. 2.8 Monotonic undrained triaxial compression tests on medium loose sand, consolidated to different mean effective stresses. **a** Stress - strain curves. **b** Effective stress paths (after Verdugo and Ishihara 1996)

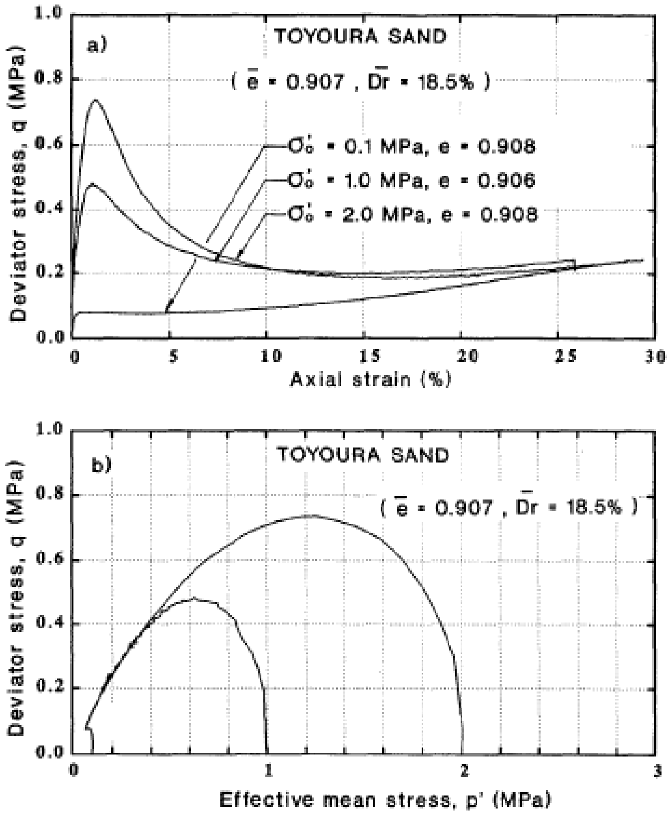

Fig. 2.9 Monotonic undrained triaxial compression tests on loose sand, consolidated to different mean effective stresses. **a** Stress - strain curves. **b** Effective stress paths (after Verdugo and Ishihara 1996)

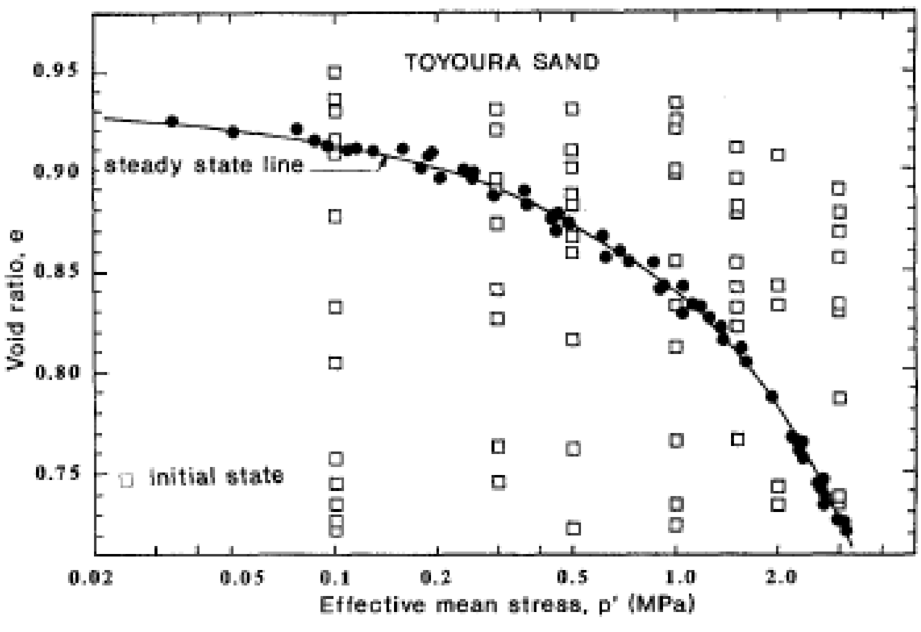

Fig. 2.10 The steady state line in the *e* - *p'* plane obtained from undrained triaxial compression tests on sand specimens under different initial states (after Verdugo and Ishihara 1996)

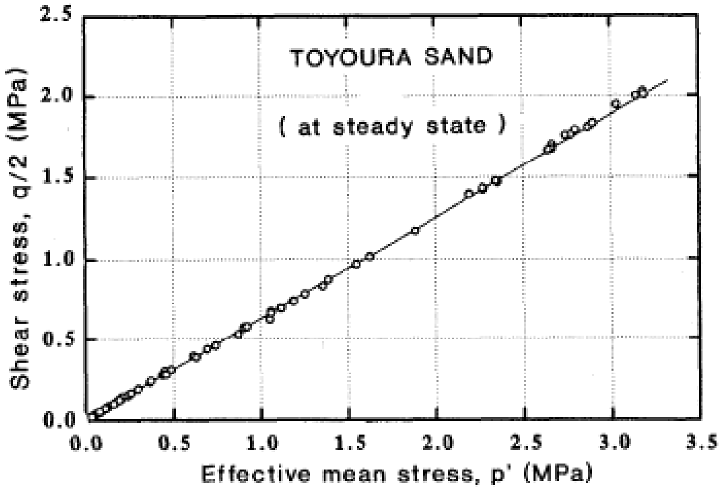

Fig. 2.11 The steady state strength envelope in the *q* / 2 - *p'* plane obtained from undrained triaxial compression tests on sand specimens under different initial states (after Verdugo and Ishihara 1996)

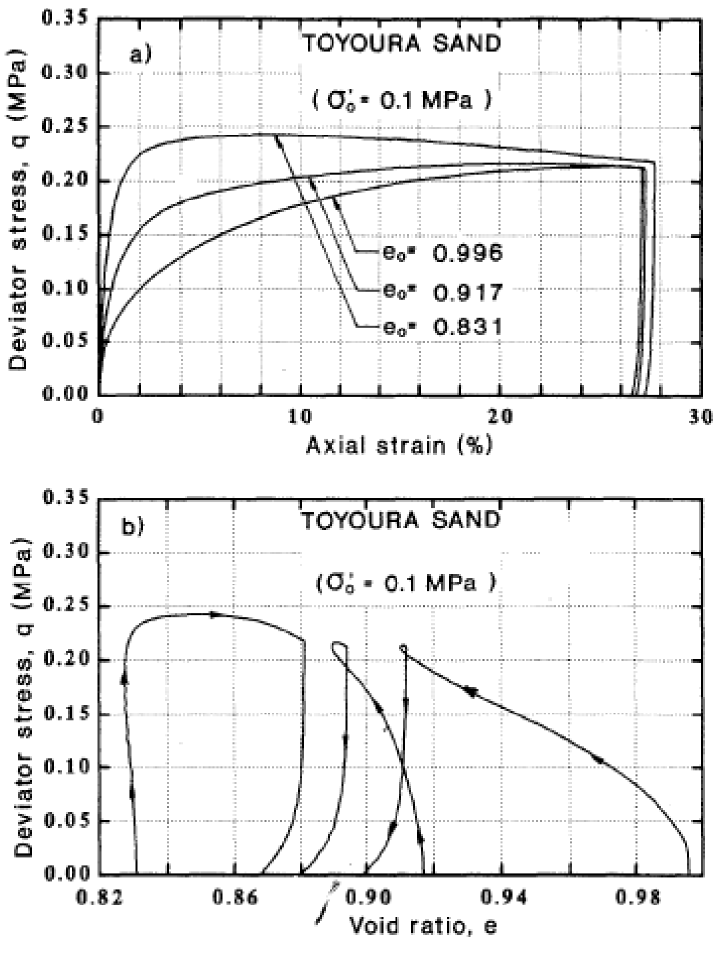

Fig. 2.12 Monotonic drained triaxial compression tests on very loose, loose and medium loose sand, consolidated to stress $p'_o = 0.1$ MPa. **a** Stress - strain curves. **b** Deviatoric stress - void ratio curves (after Verdugo and Ishihara 1996)

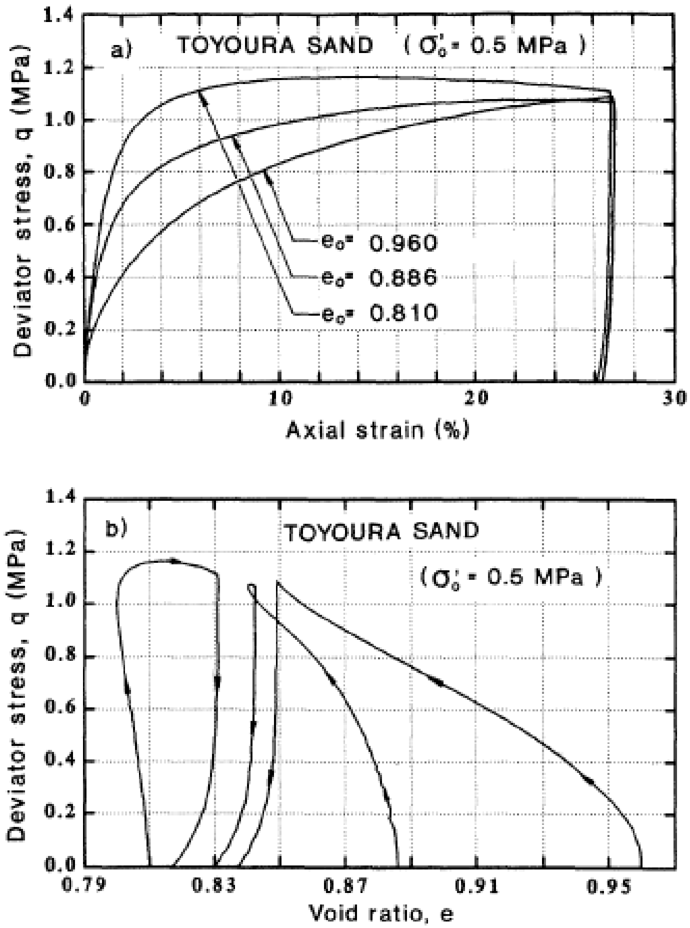

Fig. 2.13 Monotonic drained triaxial compression tests on very loose, loose and medium loose sand, consolidated to stress $p'_o = 0.5$ MPa. **a** Stress - strain curves. **b** Deviatoric stress - void ratio curves (after Verdugo and Ishihara 1996)

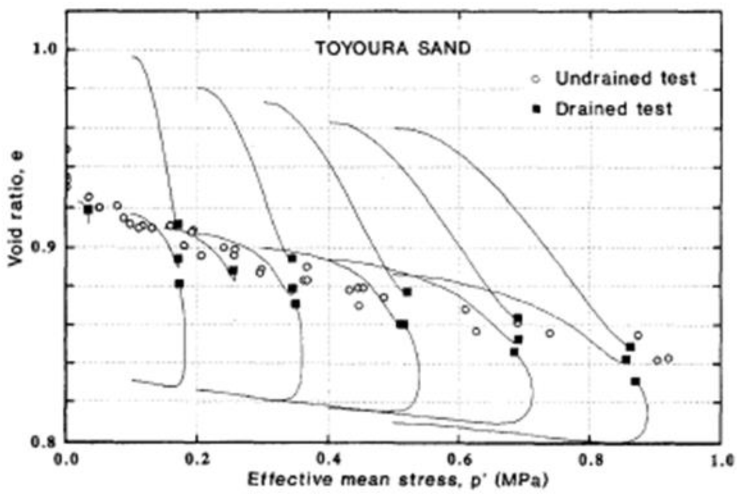

Fig. 2.14 Ultimate states in the *e* - *p'* plane of sand subjected to triaxial compression under both drained and undrained conditions (after Verdugo and Ishihara 1996)

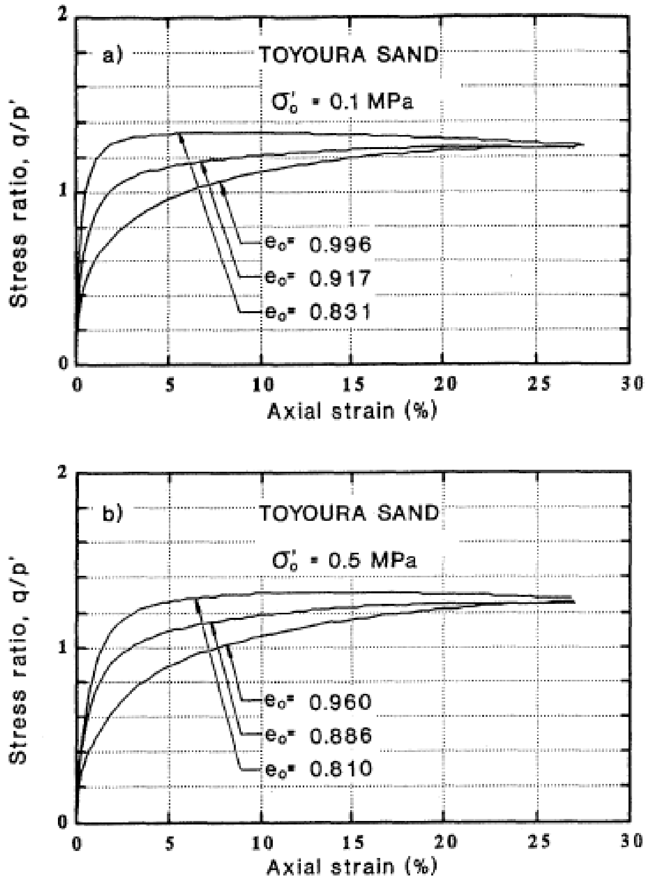

Fig. 2.15 Mobilised stress ratio of sand subjected to drained triaxial compression versus axial strain. **a** p'_o = 0.1 MPa. **b** p'_o =0.5 MPa (after Verdugo and Ishihara 1996)

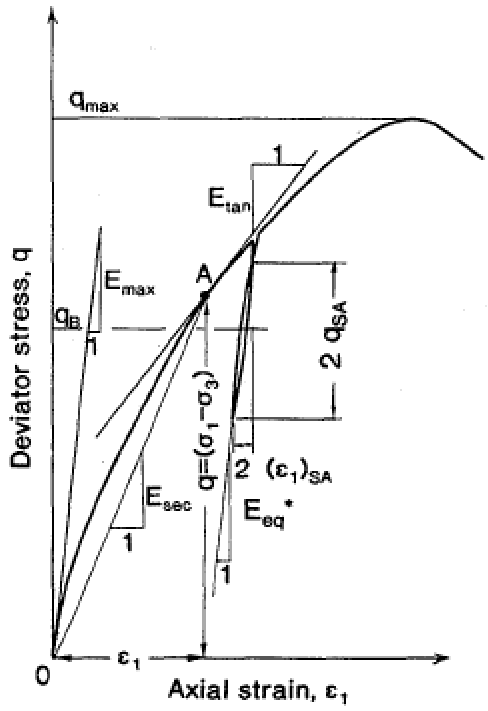

Fig. 16 Definition of stiffness moduli of a soil material subjected to monotonic triaxial compression (after Shibuya et al. 1992)

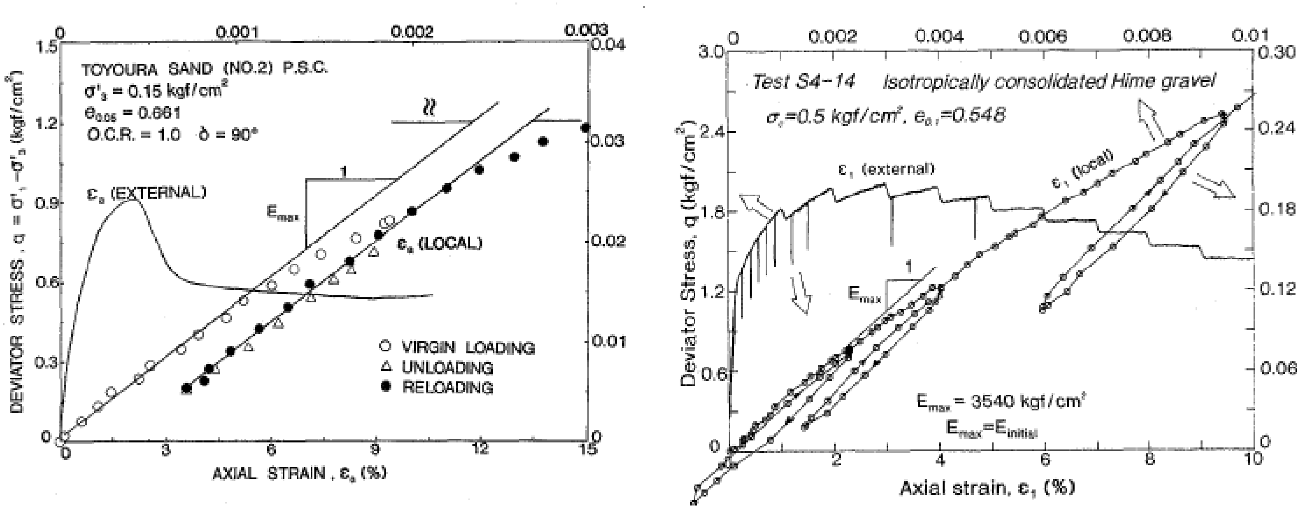

Fig. 2.17 Elastic and inelastic deformation characteristics of two granular geomaterials subjected to compression. **a** Sand subjected to drained plane strain compression. **b** Gravel subjected to drained triaxial compression (after Shibuya et al. 1992)

Fig. 2.18 Local displacement transducers (LDTs) placed directly on a sand specimen with the shape of a rectangular prism prepared for triaxial testing (after Towhata 2008)

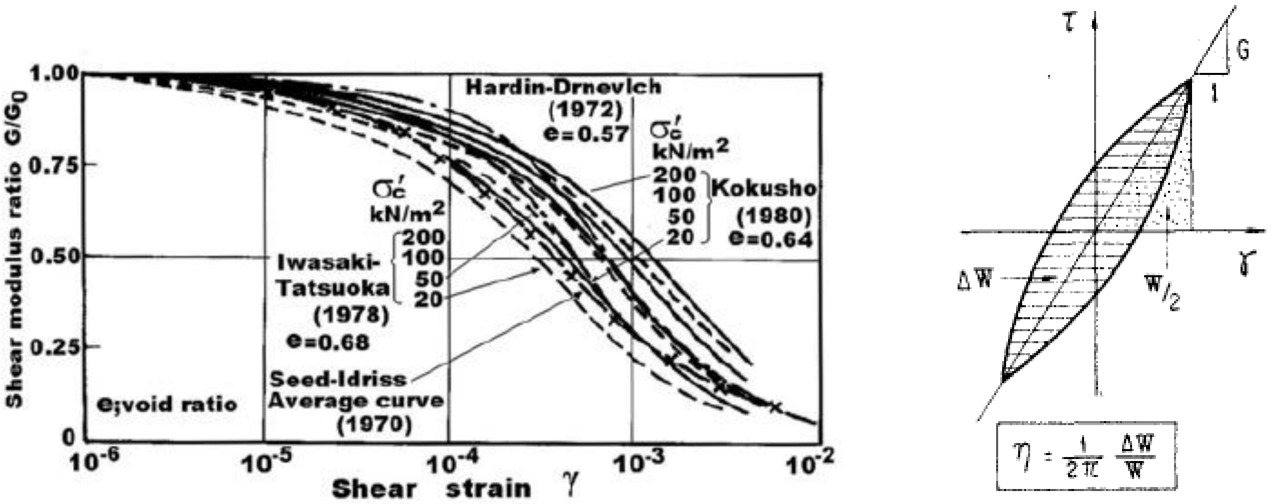

Fig. 2.19 Left: Degradation curves of elastoplastic shear modulus with strain amplitude for sands subjected to cyclic loading at various stress amplitudes (after Towhata 2008 and Kokusho 1987). **Right**: Definition of elastoplastic shear modulus *G* after stabilisation of the hysteresis loop (after Iwasaki et al. 1978)

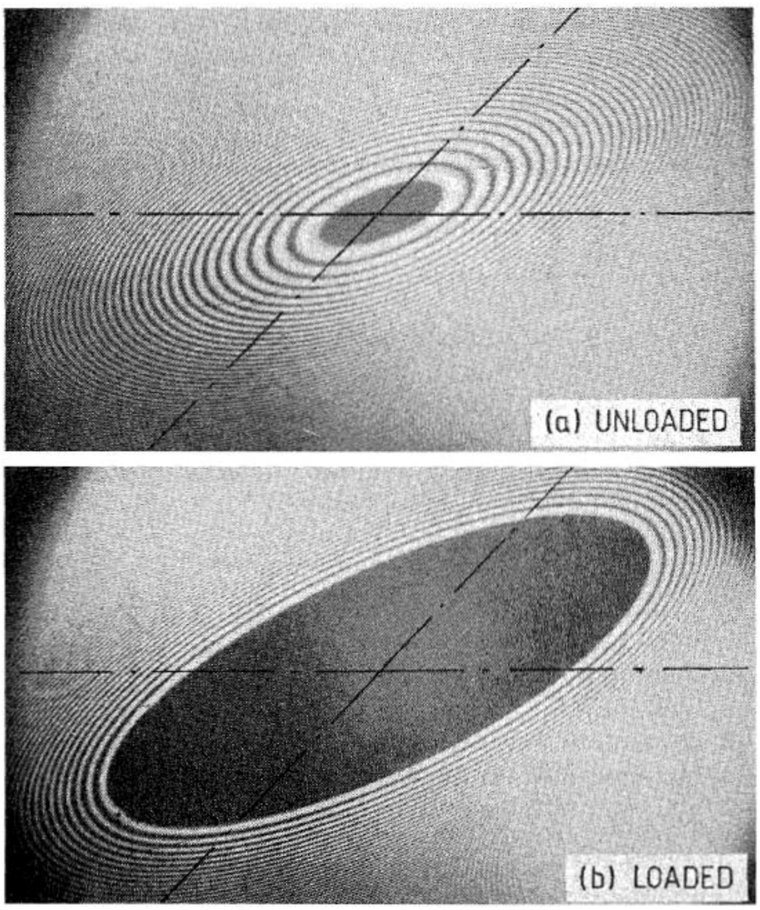

Fig. 2.20 The contact surface of two equal cylindrical lenses with their axes inclined at 45° visualised by the interference fringes. **a** Unloaded contact. **b** Loaded contact (after Johnson 2003)

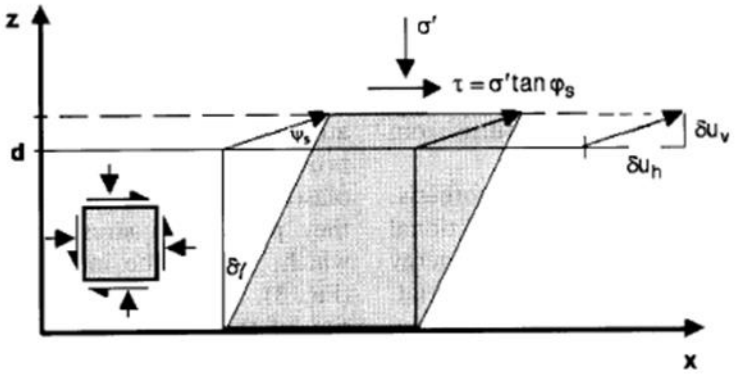

Fig. 2.21 Idealisation of the kinematics and statics of the shear zone (shear band) of sand that dilates under shear distortion in plane-strain mode (after Vardoulakis and Georgopoulos 2005)

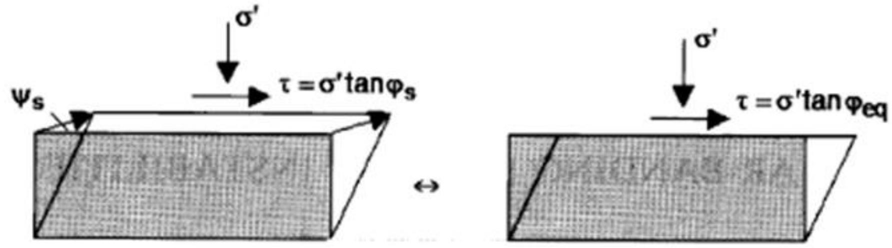

Fig. 2.22 Stress, deformation and energy dissipation in direct shear mode of loading of: **a** a granular material with frictional - dilatant characteristics and **b** an equivalent purely-frictional solid that dissipates energy in constant rate according to Taylor's theory (after Vardoulakis and Georgopoulos 2005**)**

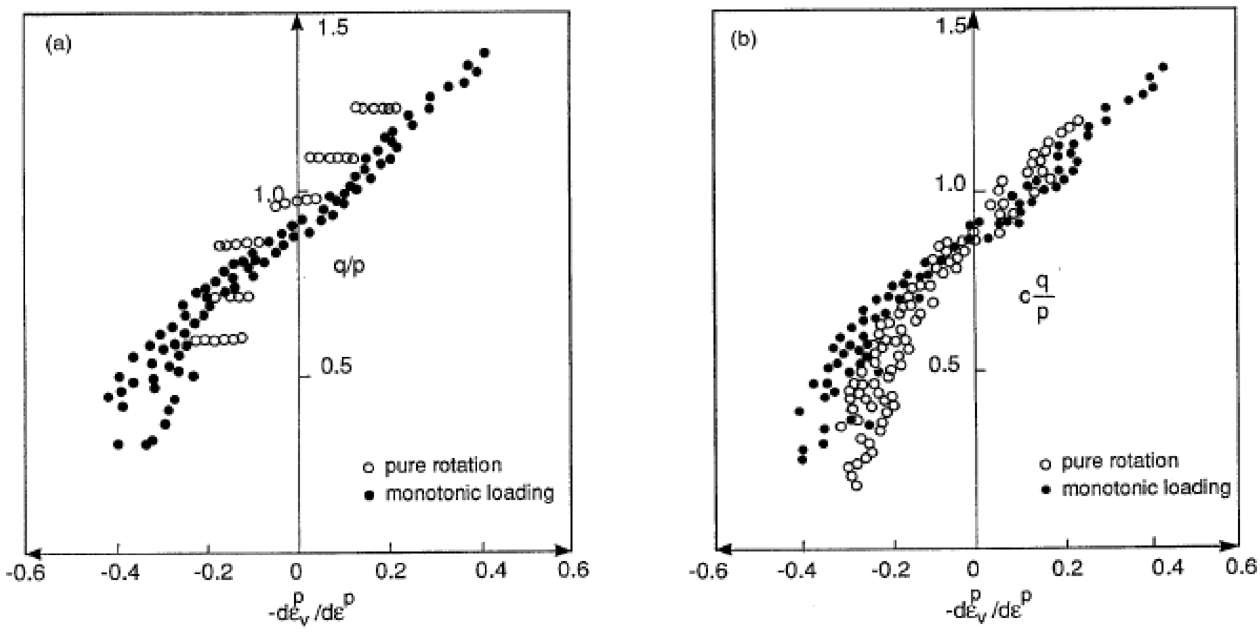

Fig. 2.23 Comparison of stress - dilatancy plots from loading tests with both fixed and rotating stress principal axes; principal stress rotation is performed while keeping the effective stress principal values constant. **a** Stress - dilatancy relationship without correction for non-coaxiality. **b** Stress - dilatancy relationship with correction for non-coaxiality (after Gutierrez and Ishihara 2000)

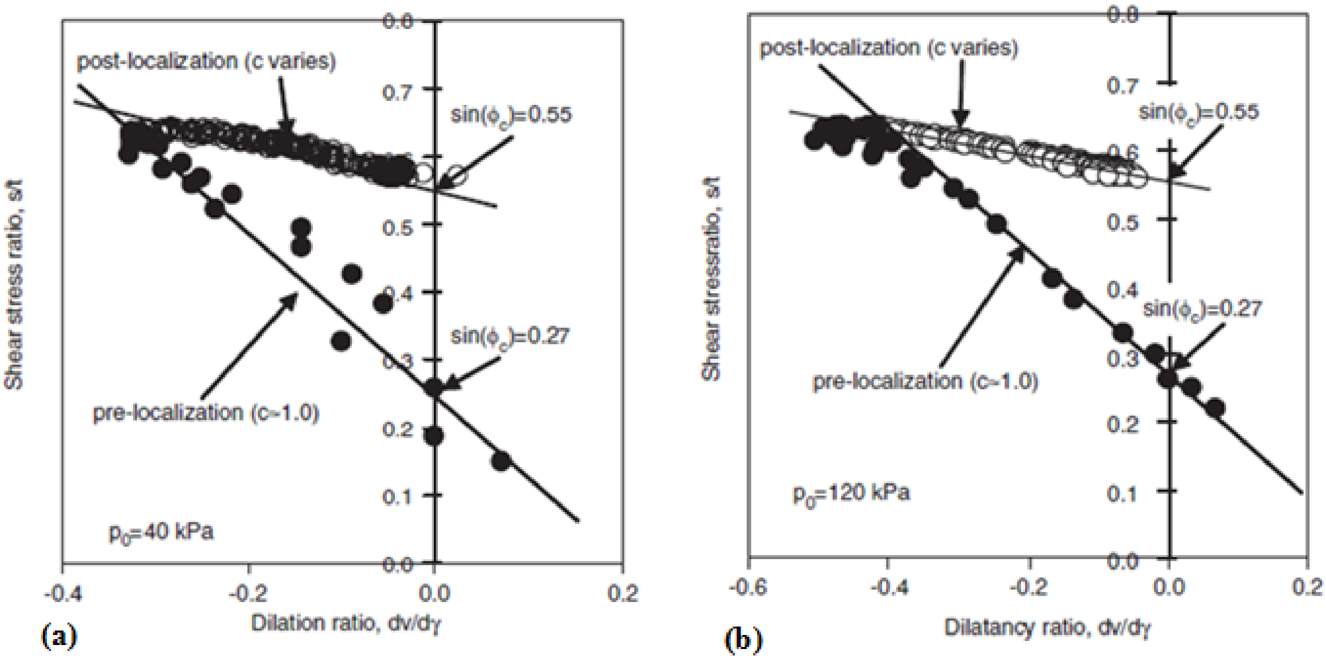

Fig. 2.24 Stress - dilatancy plots prior to and after the shear-band bifurcation for dilatant sand subjected to triaxial compression at: **a** *p'* = 40 kPa and **b** *p'* = 120 kPa (after Gutierrez and Vardoulakis 2007)

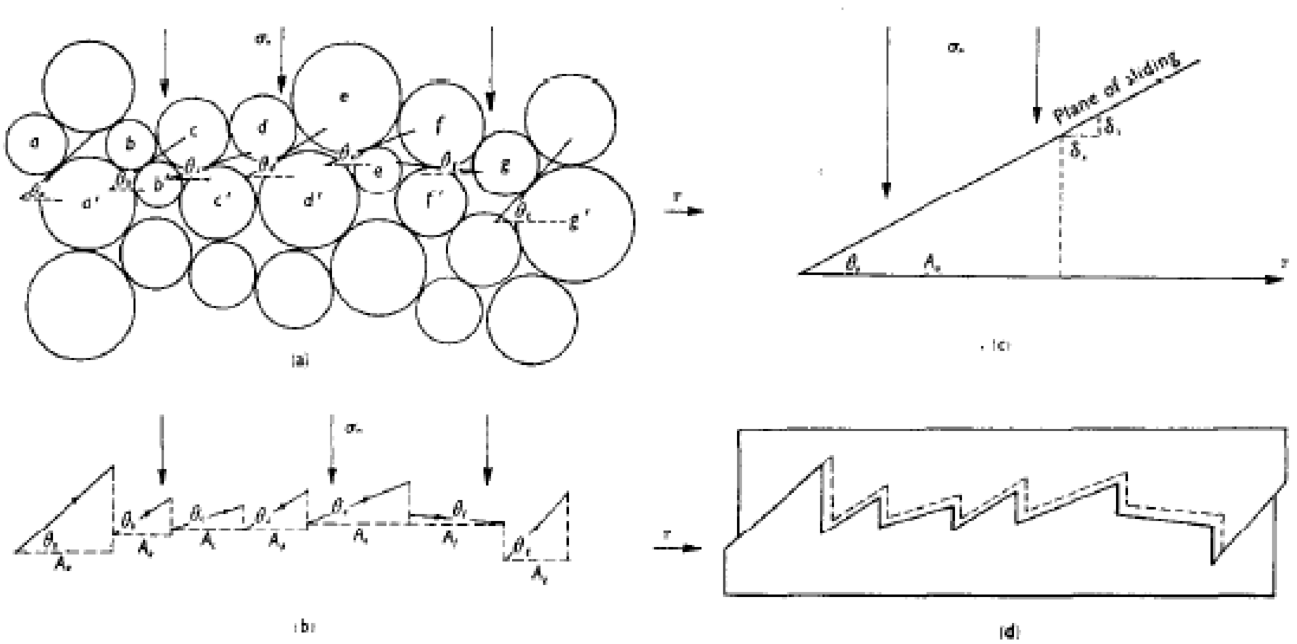

Fig. 2.25 The basic assumptions of the deformation model for sands proposed by Newland and Allely (1957). **a** Geometrical packing of spherical particles representing grains. **b** Sliding of adjacent particles along the direction of the tangent at contact points. **c** Non-coincidence of the directions of the plane of sliding and the plane of shearing. **d** Equivalent mechanism of sliding between two blocks along the serrated contact surface (after Newland and Allely 1957)

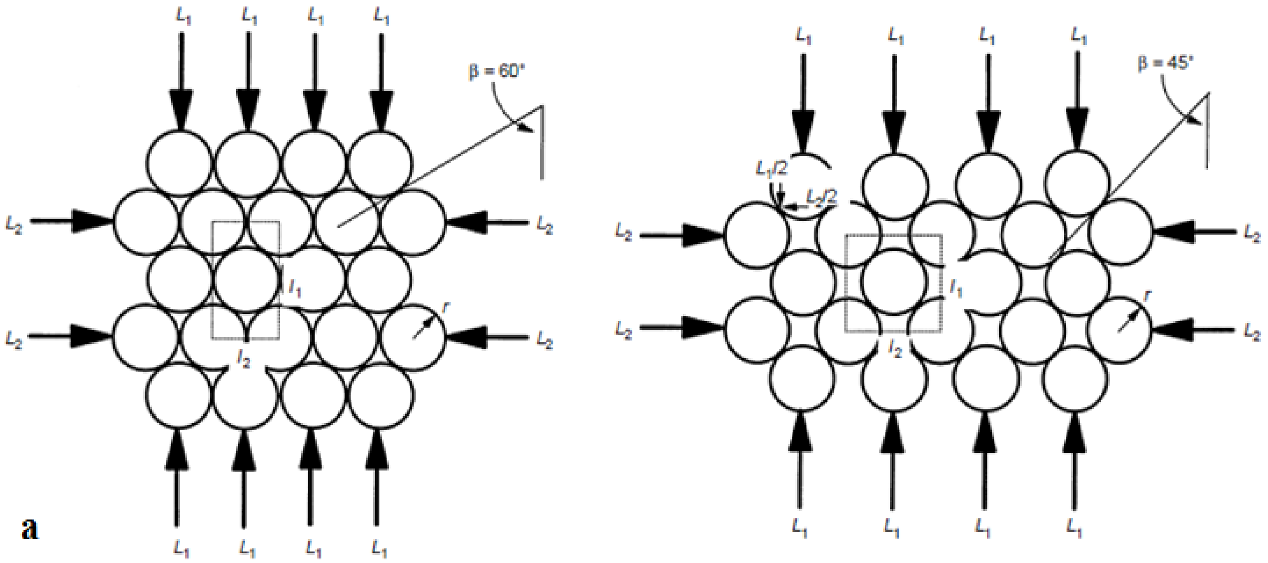

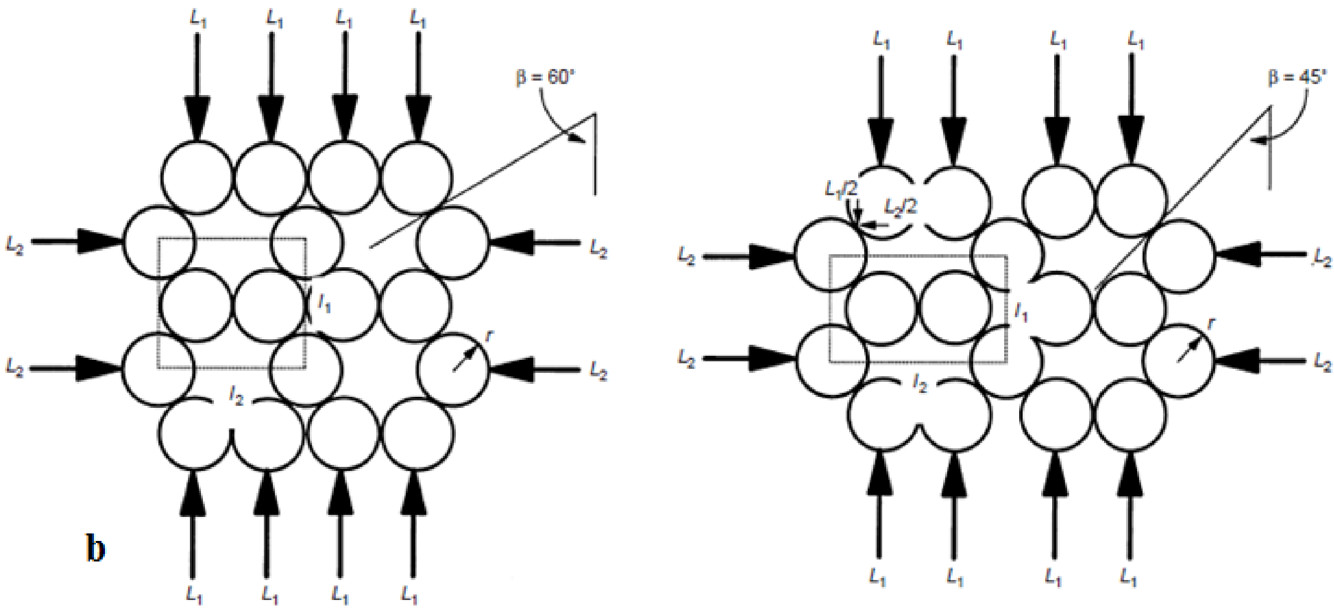

Fig. 2.26 Two different regular packings of uniform cylindrical rods, in dense and loose state, subjected to loading in order to study the stress - dilatancy relationship. **a** Dense (left) and loose (right) packing A. **b** Loose (left) and dense (right) packing B (after Li and Dafalias 2000)

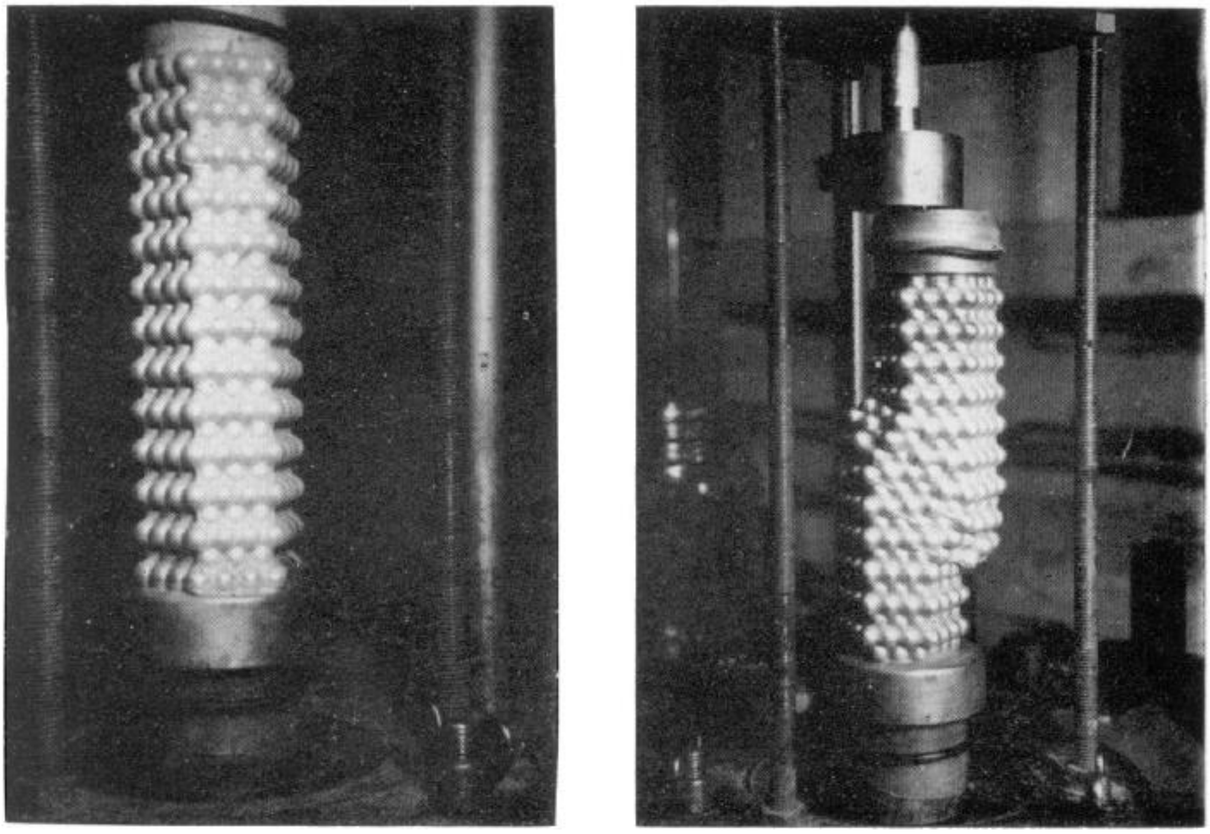

Fig. 2.27 Assembly of uniform rigid spheres subjected to compression: **a** before the formation of shear zone, **b** after the formation of shear zone (after Rowe 1962)

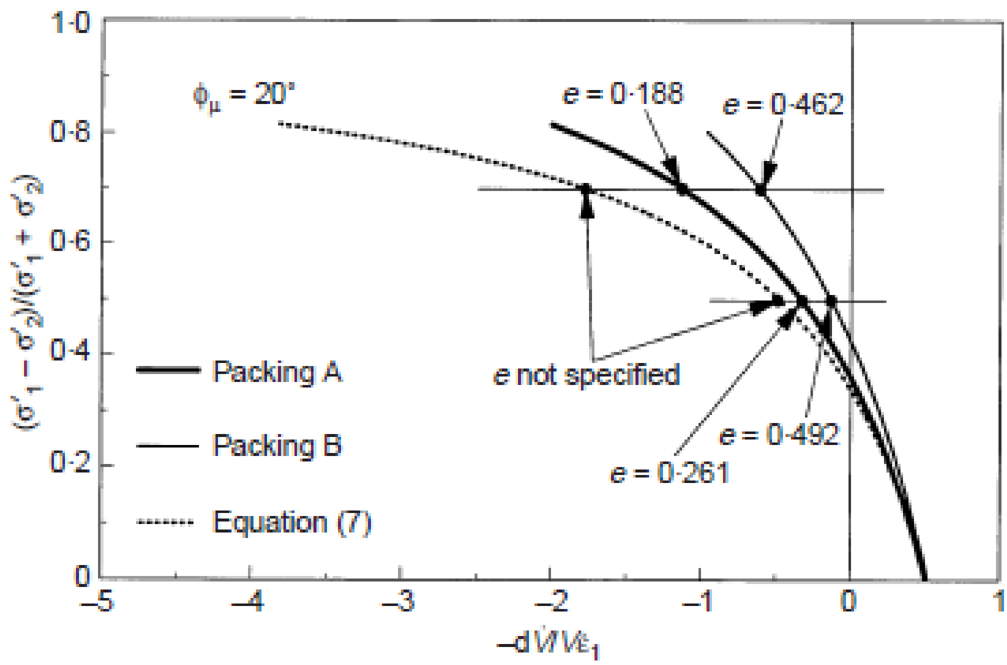

Fig. 2.28 Influence of the kinematic constraints at rod contacts on the stress - dilatancy relationship. Note that Equation 7 that produces the dotted curve shown in this figure corresponds to Equation 2.17 of the present study (after Li and Dafalias 2000)

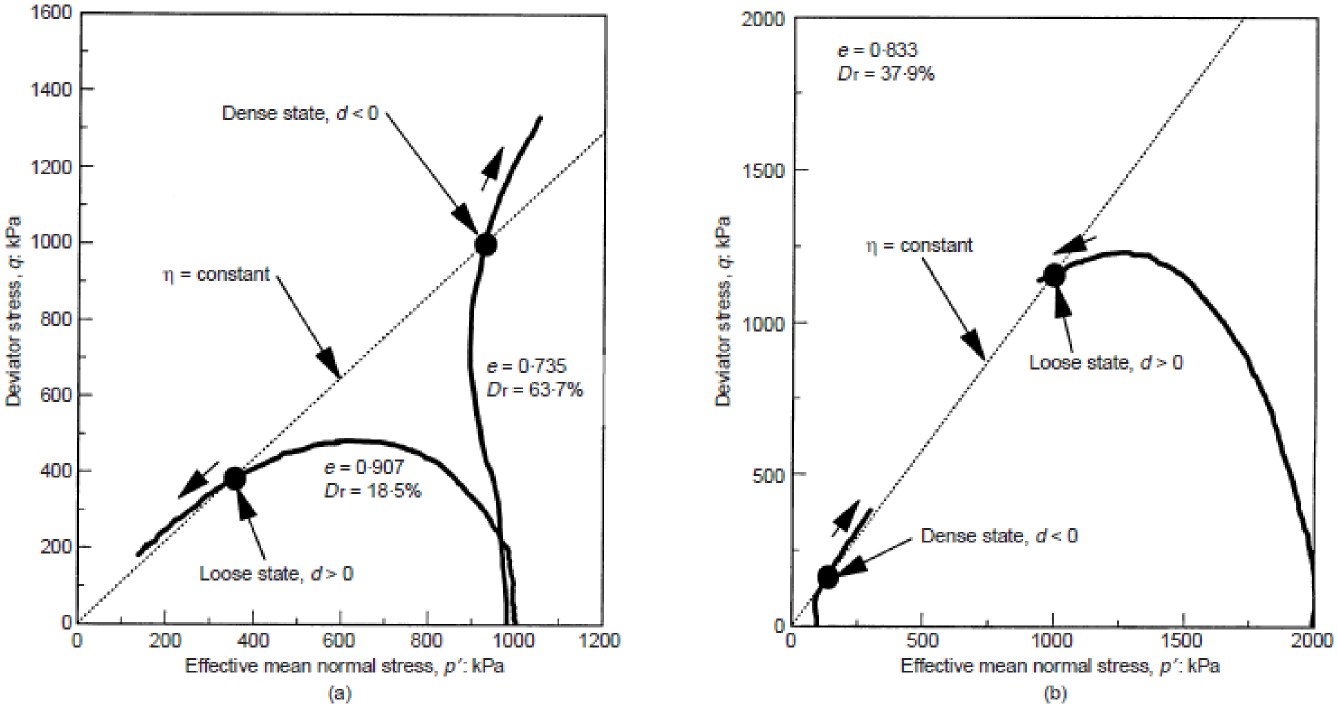

Fig. 2.29 Undrained response of sand under triaxial compression at initial states corresponding to: **a** the same effective confining stress but different void ratios, **b** the same void ratio but different effective confining stresses (after Li and Dafalias 2000; data from Verdugo and Ishihara 1996)

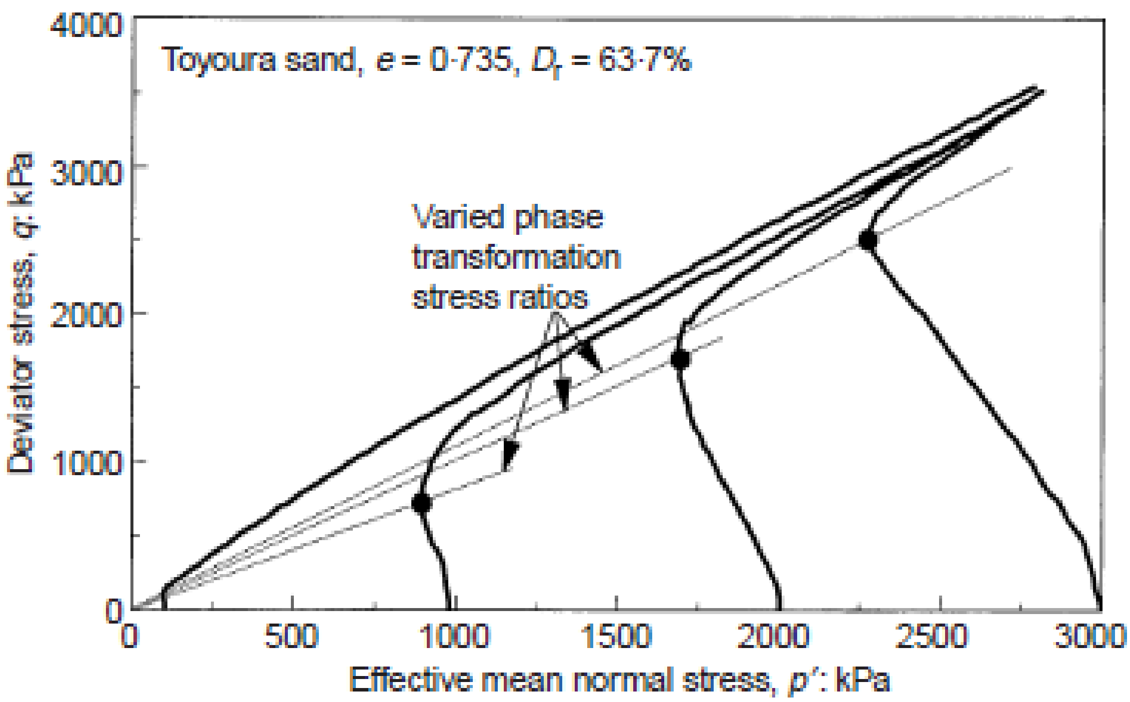

Fig. 2.30 The dependence of the stress ratio at phase transformation on the state of sand (after Li and Dafalias 2000; data from Verdugo and Ishihara 1996)

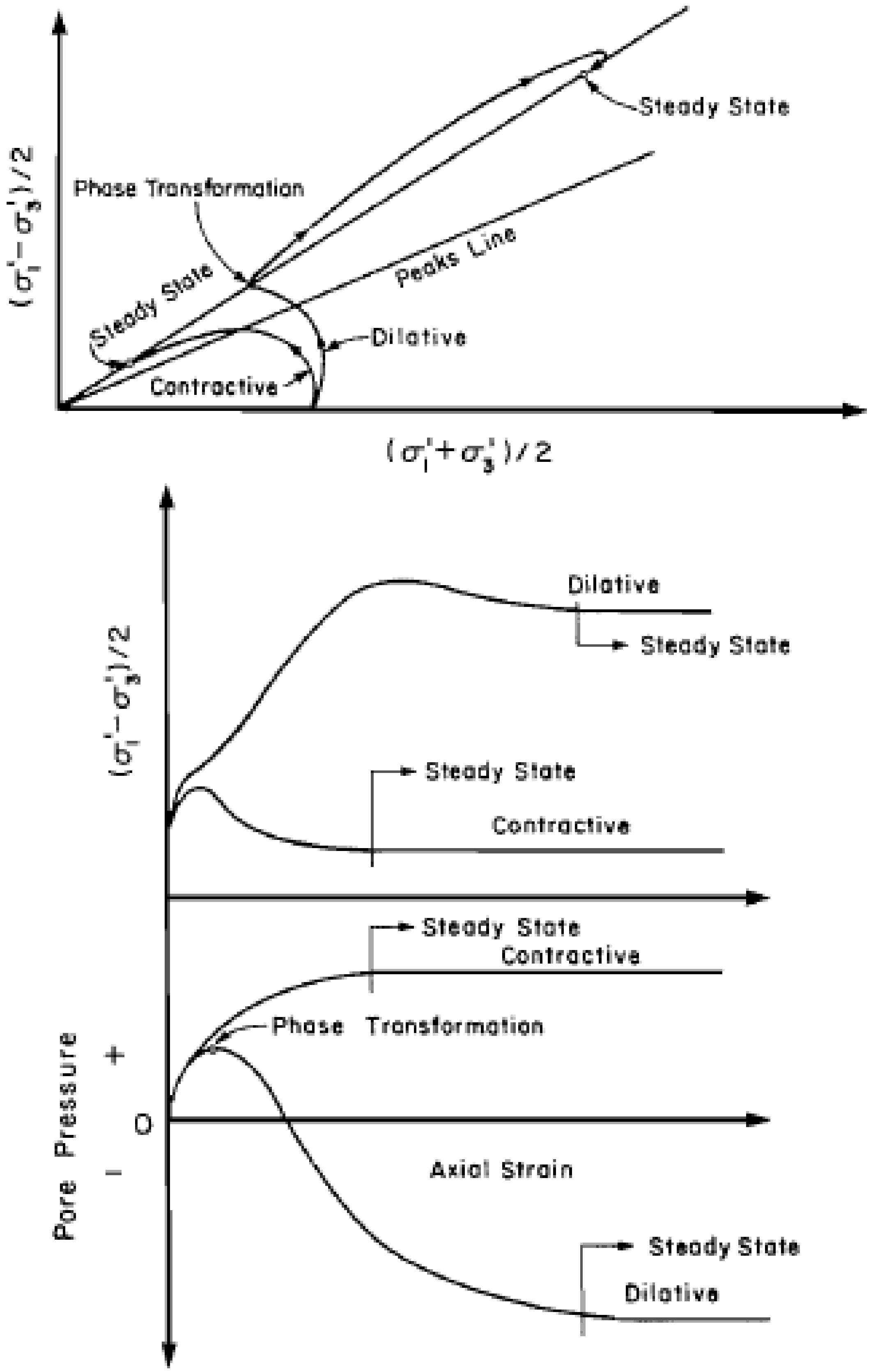

Fig. 2.31 States of zero dilatancy of sand subjected to undrained loading (after Negussey et al. 1988)

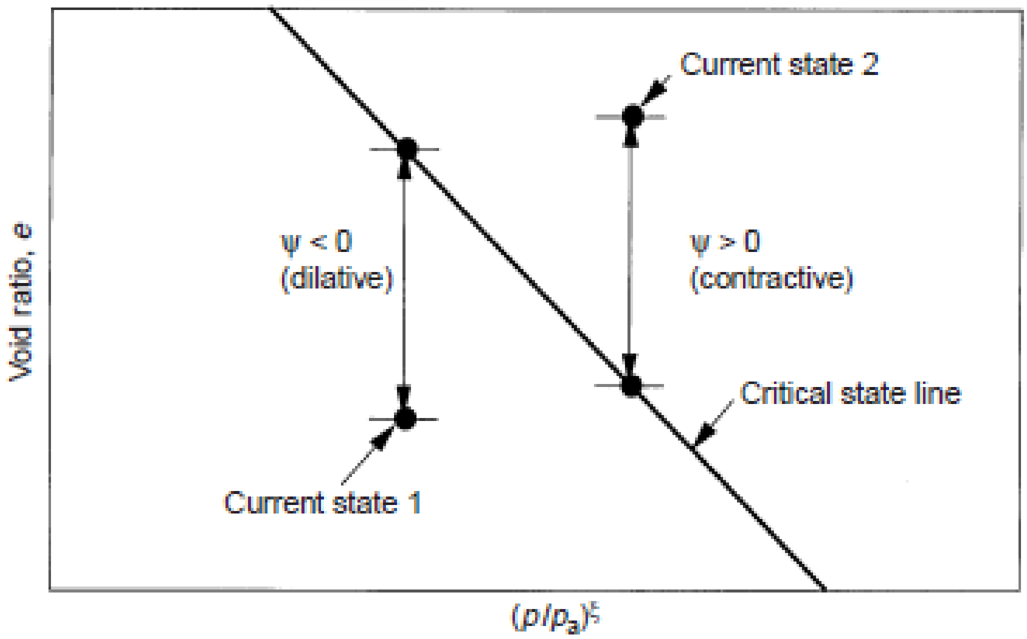

Fig. 2.32 The state parameter $\psi = e - e_c(p')$ of sand being denser than critical (1) and looser than critical (2) (after Li and Dafalias 2000)

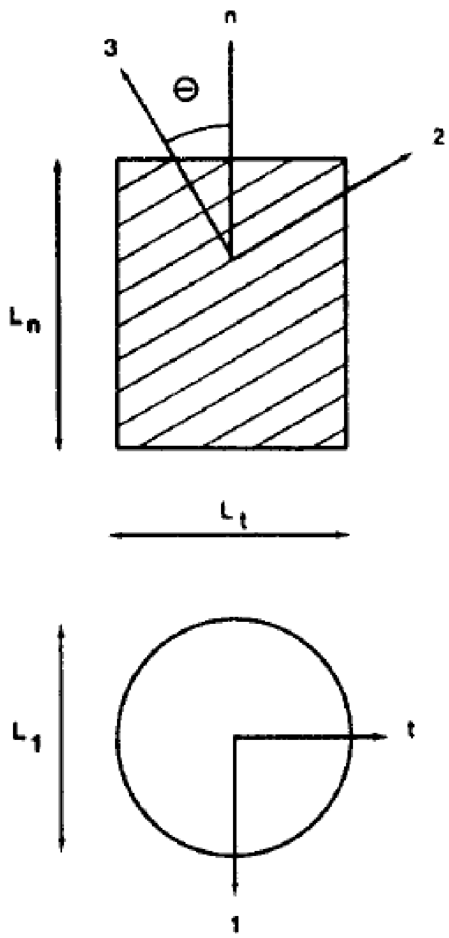

Fig. 2.33 Cylindrical test specimen of stratified soft rock formed with the cylinder axis at an angle θ with respect to the normal to the strata (after Allirot et al. 1977)

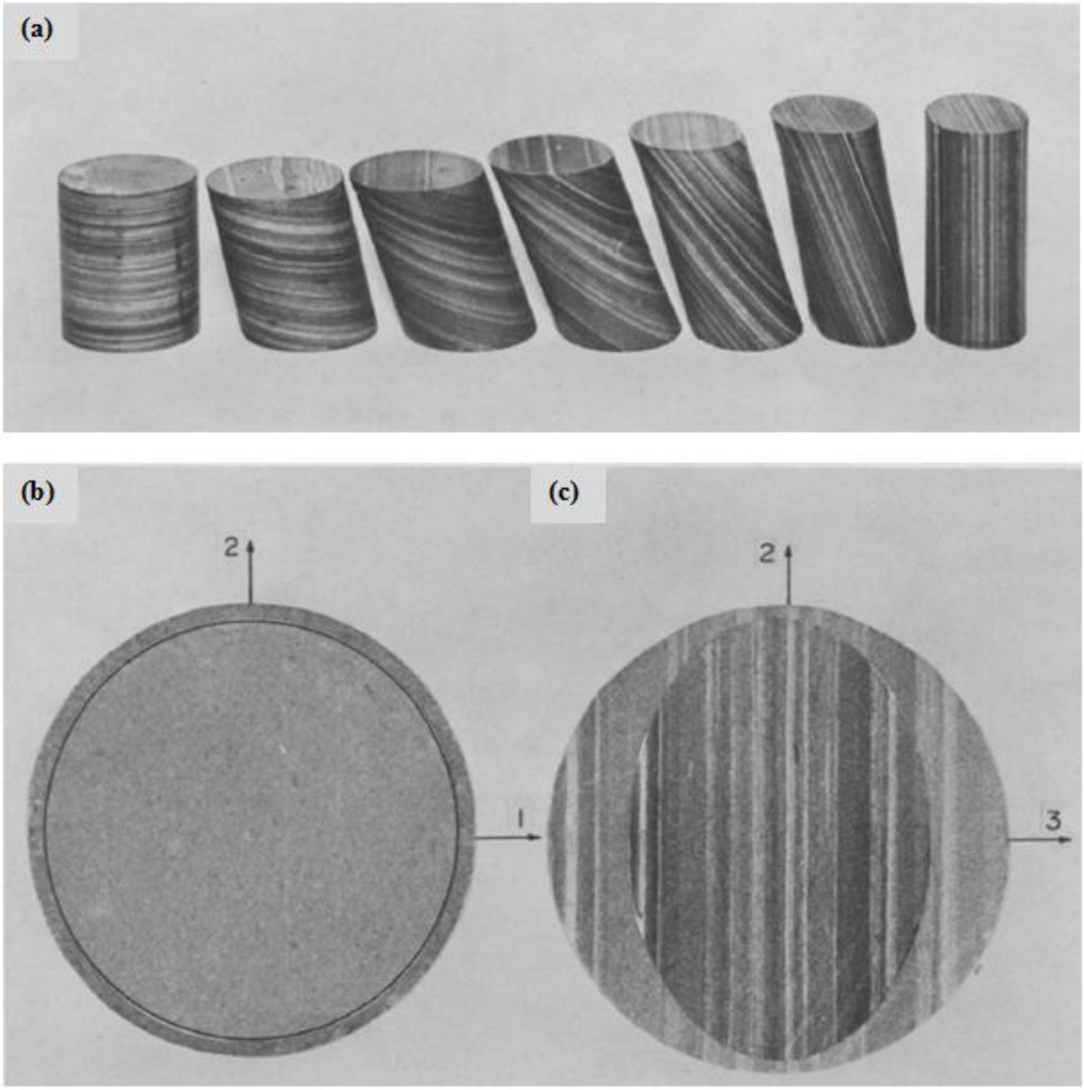

Fig. 2.34a Deformed cylindrical specimens of stratified soft rock, with a variety of angles θ between the cylinder axis and the normal to the strata, subjected to many high-pressure isotropic loading - unloading cycles. **b** The specimen with θ = 0° before and after deformation. **c** The specimen with θ = 90° before and after deformation (after Allirot et al. 1977)

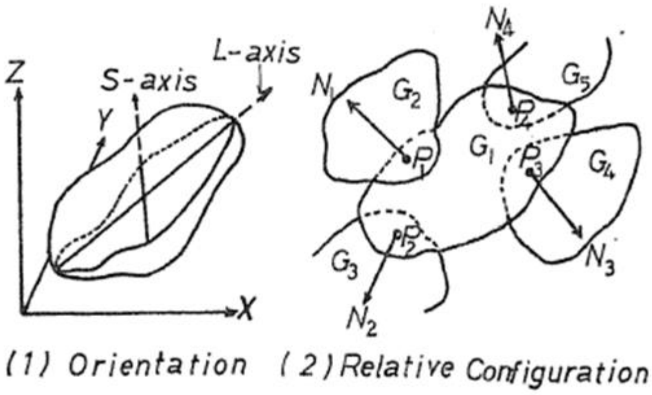

Fig. 2.35 Definition of particle and contact normal orientation. **1** The orientation of the long axis of grains. **2** The orientation of the normal vector to the tangent plane at the contact point between two grains (after Oda 1972a)

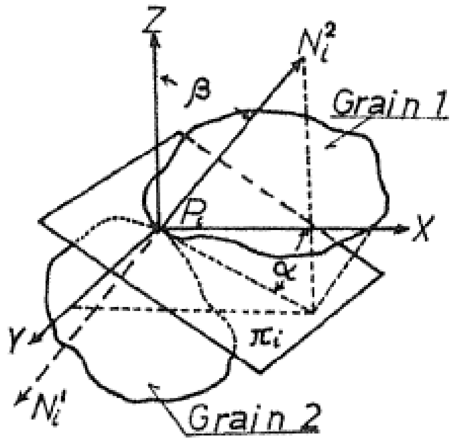

Fig. 2.36 Determination of the contact normal direction by means of the direction angles α and β (after Oda 1972a)

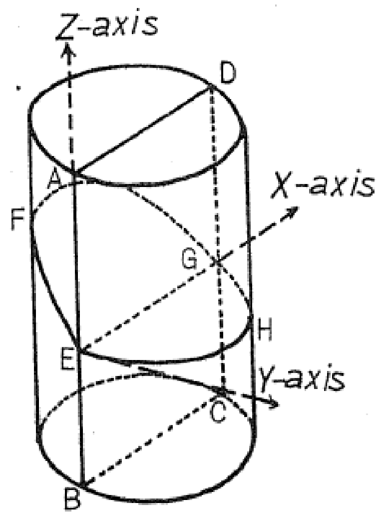

Fig. 2.37 Preparation of thin sections along vertical, horizontal and inclined planes by cutting a resin-stabilised cylindrical specimen of sand (after Oda 1972a)

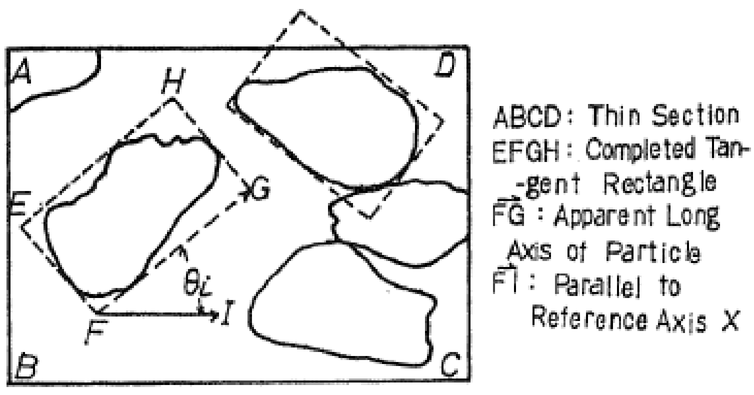

Fig. 2.38 Determination of the direction of the apparent long axis of a grain on a thin section (after Oda 1972a)

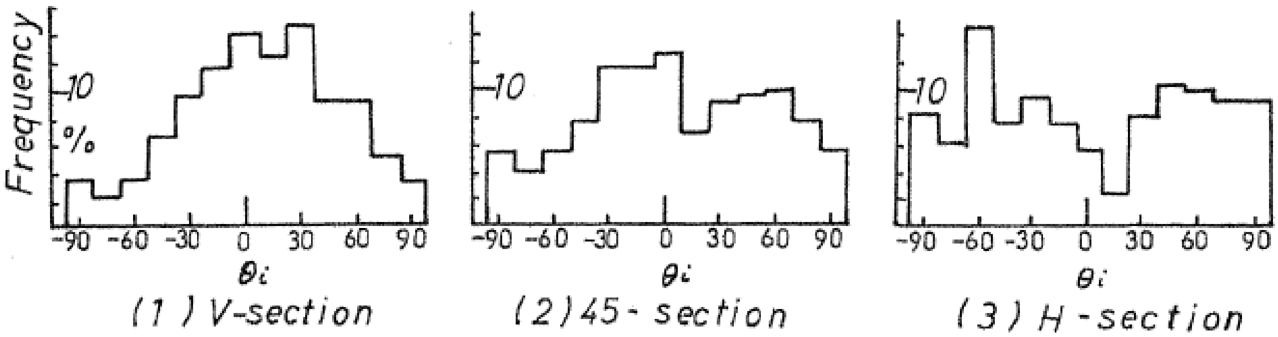

Fig. 2.39 Frequency histograms of the orientation angle θ of the apparent long axis of grains in various thin sections cut from a stabilised sand specimen. **1** Vertical section. **2** Section inclined at 45° above the horizontal plane. **3** Horizontal section (after Oda 1972a)

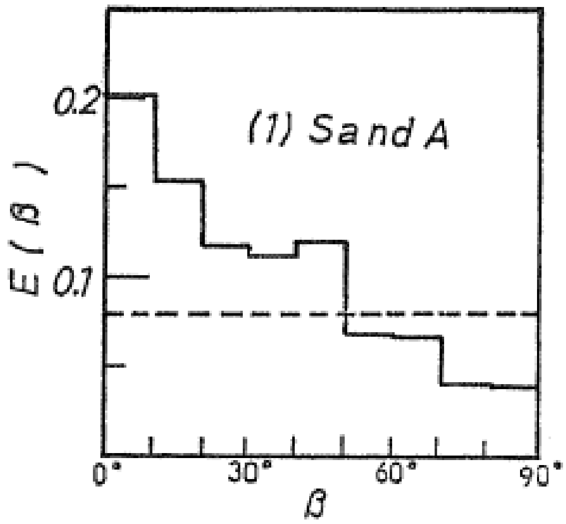

Fig. 2.40 Probability density of contact normals as a function of the direction angle β. The dashed line represents the uniform distribution of contact normals corresponding to isotropic fabric (after Oda 1972a)

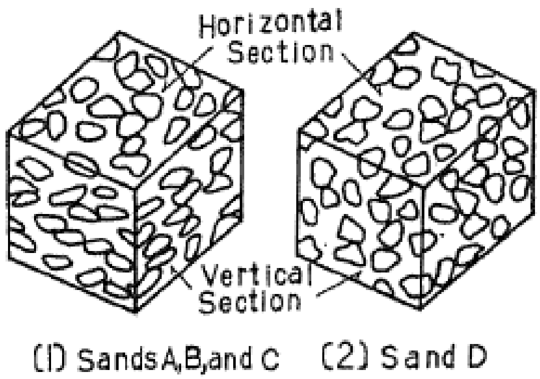

Fig. 2.41 **1** A cubic volume of sand A consisted of elongated grains. **2** A cubic volume of sand D consisted of round grains (after Oda 1972a)

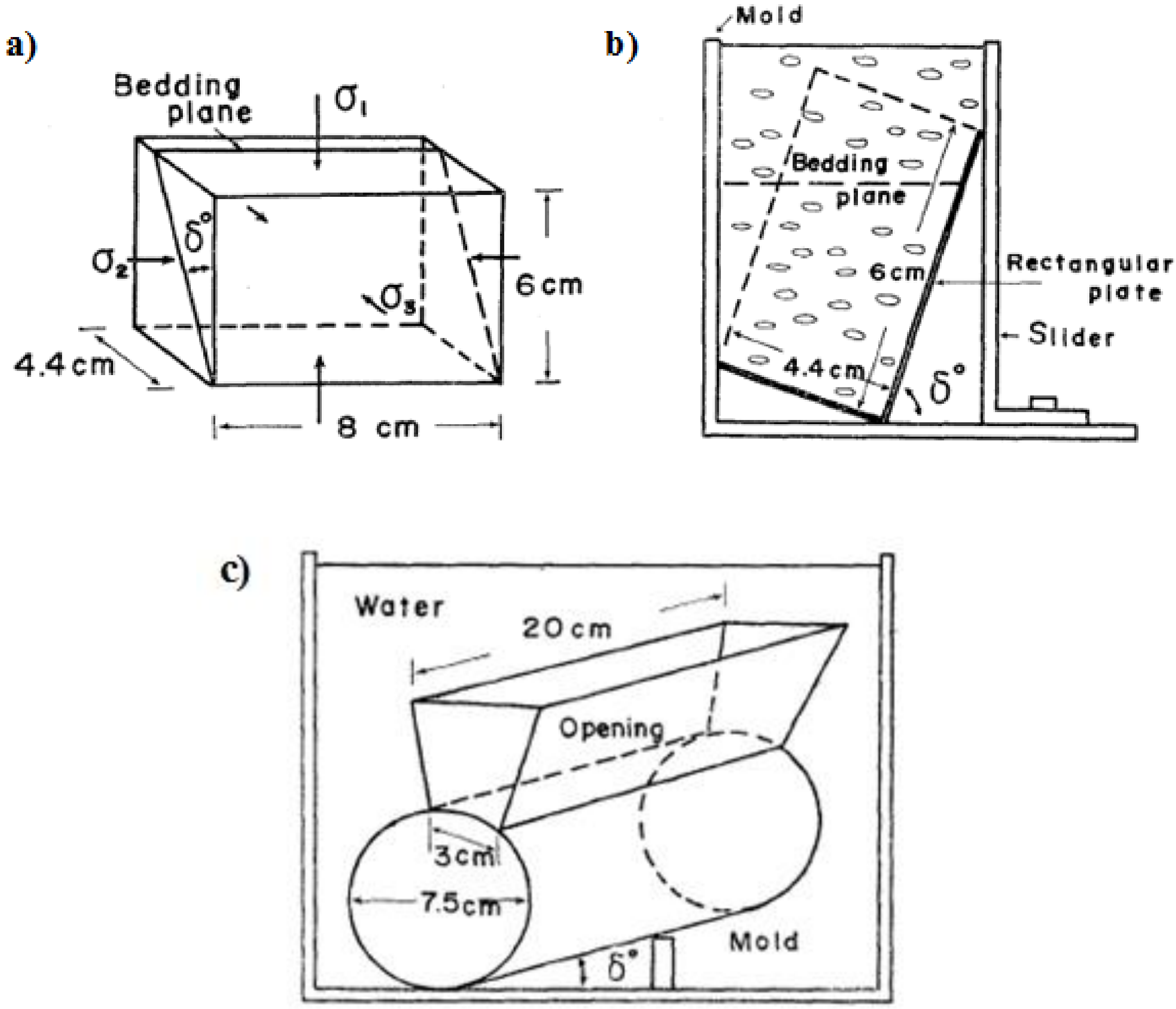

Fig. 2.42 Experimental techniques used to form specimens with inclined bedding planes. **a** The bedding plane direction with respect to the vertical plane. **b** The tilted container used to form specimens with inclined bedding planes for plane strain compression tests. **c** The titled container used to form specimens with inclined bedding planes for triaxial compression tests (after Oda et al. 1978)

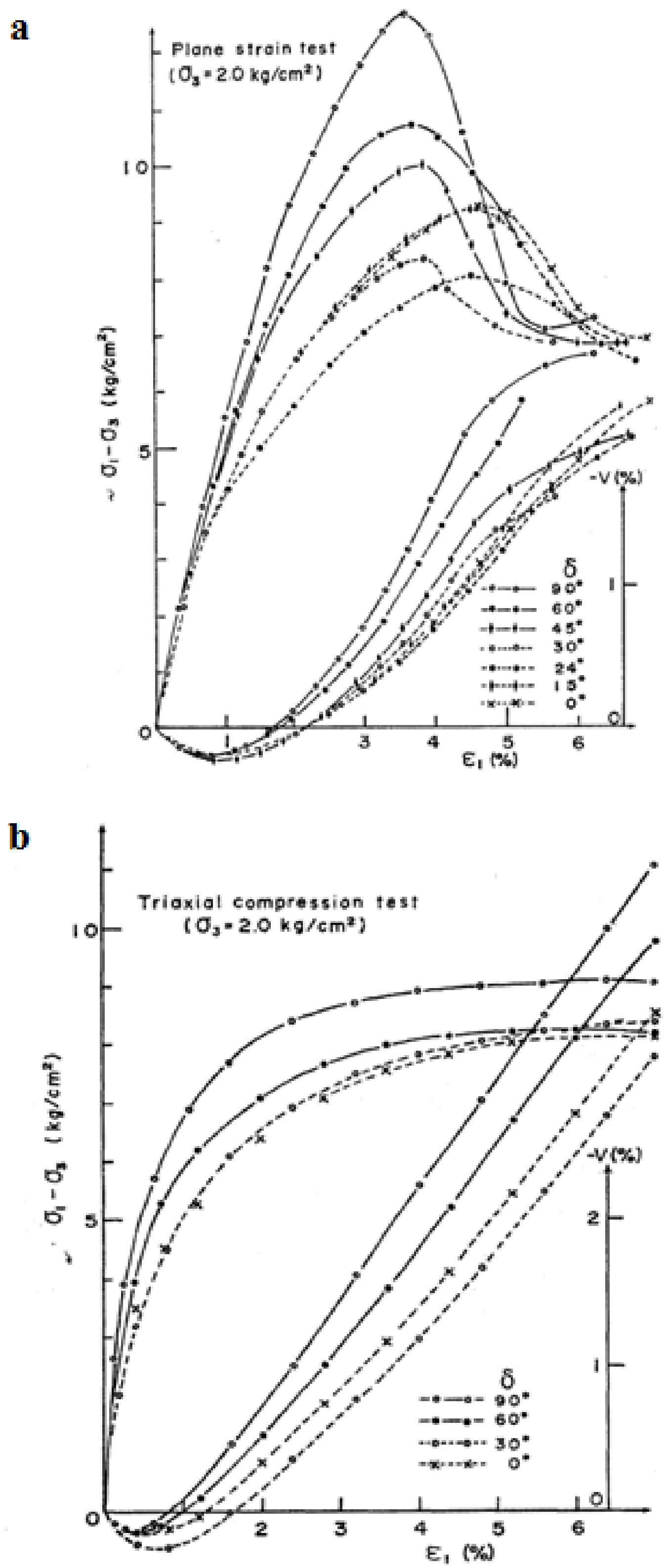

Fig. 2.43 Influence of fabric anisotropy on the strength, stiffness and dilatancy characteristics of Toyoura sand. **a** Stress - strain and volumetric behaviour of sand specimens with inclined bedding planes subjected to plane strain compression **b** Stress - strain and volumetric behaviour of sand specimens with inclined bedding planes subjected to triaxial compression. Note that *v* stands for volumetric strain $-\varepsilon_{vol}$ (after Oda et al. 1978)

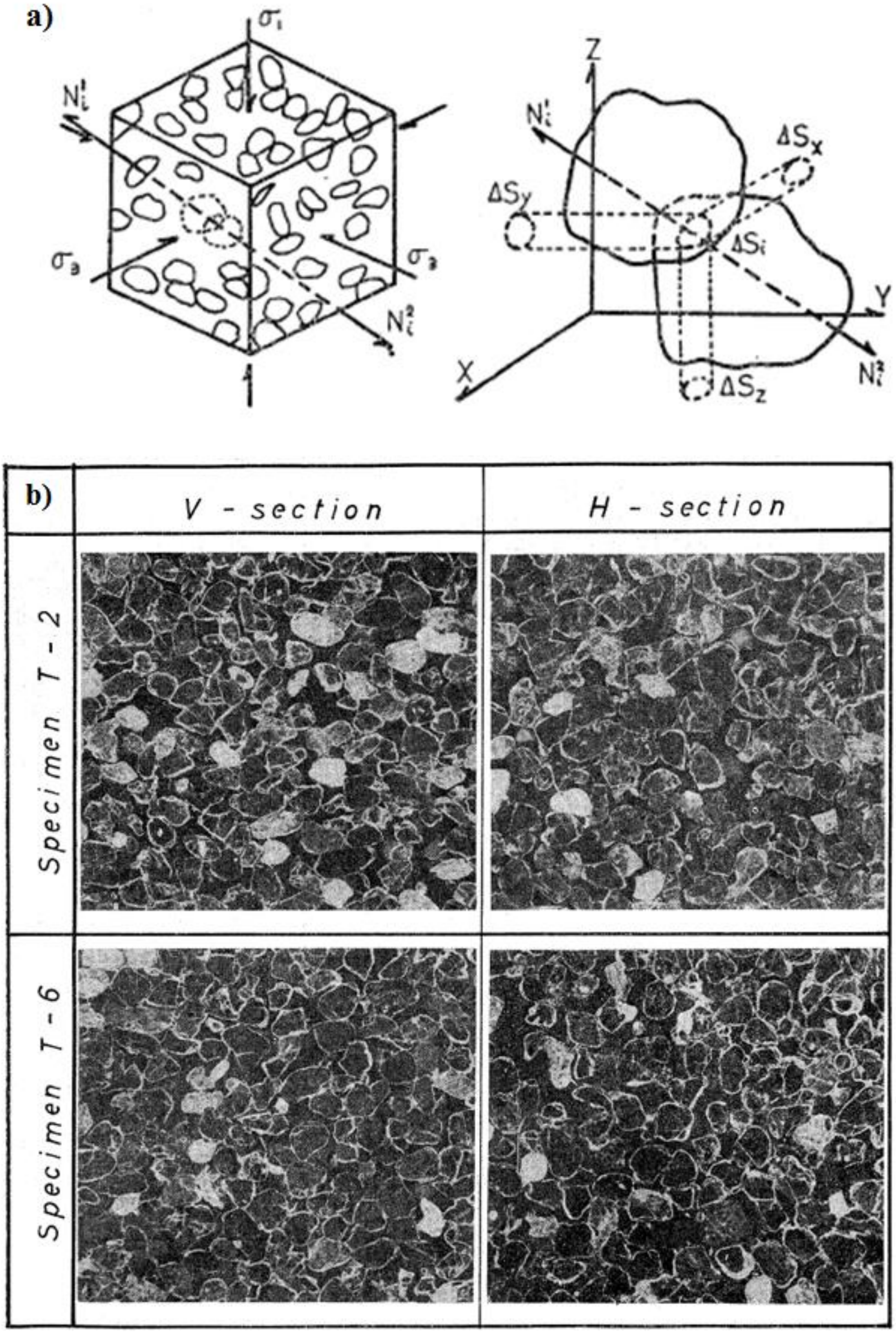

Fig. 2.44 Determination of the fabric index S_z / S_x of sand. **a** Projected grain contact areas. **b** Two pairs of thin sections cut from two specimens that were compressed until different values of stress ratio and strain were reached (after Oda 1972b)

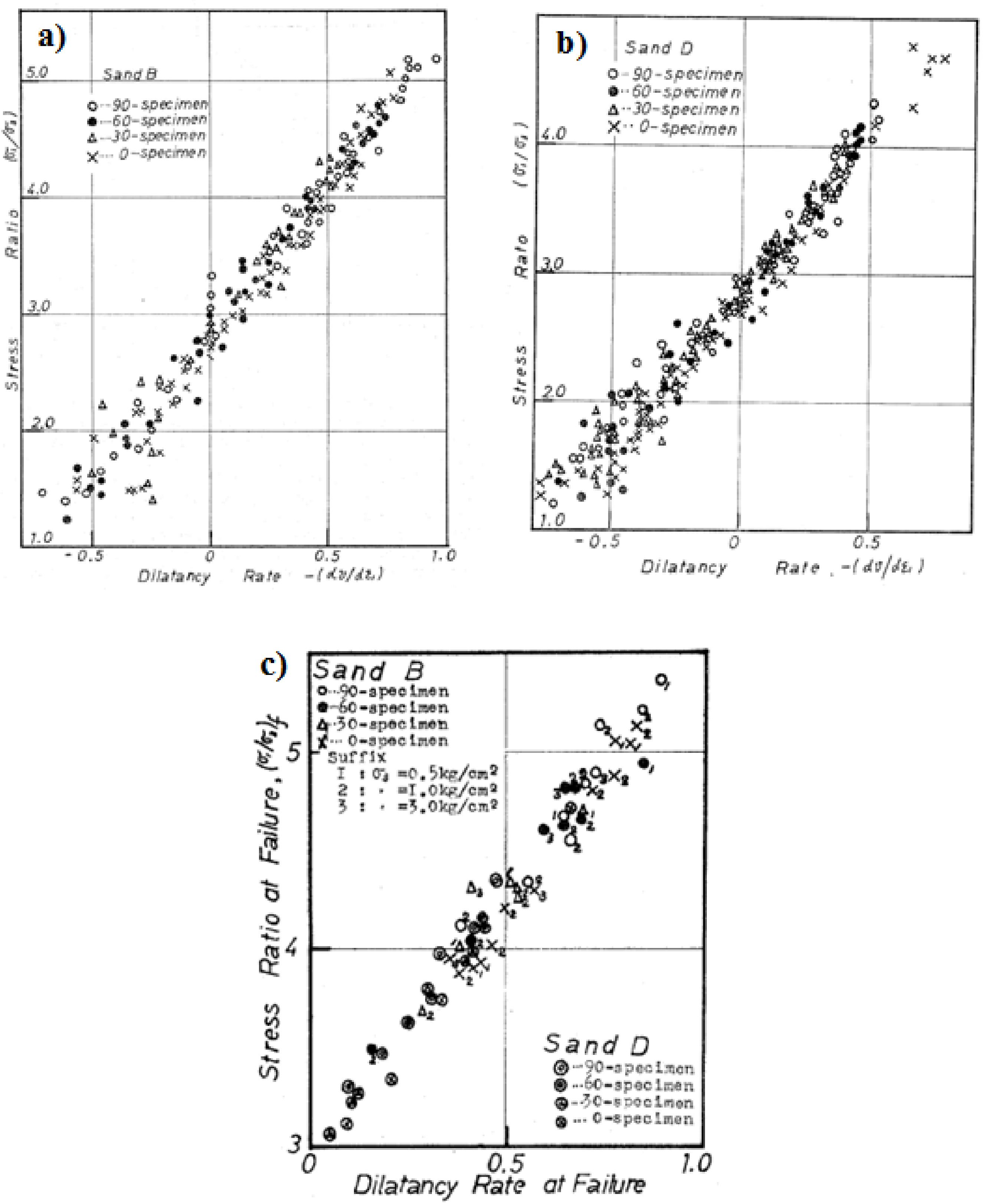

Fig. 2.45 Stress - dilatancy plots for two quartz sands subjected to drained triaxial compression. **a** Pre-failure states of sand B. **b** Pre-failure states of sand D. **c** Failure states of sands B and D (after Oda 1972b)

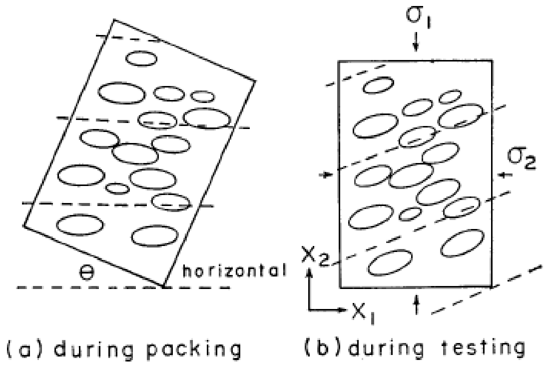

Fig. 2.46 Definition of the bedding plane angle θ with respect to the reference X_1 and X_2 axes (after Oda et al. 1985)

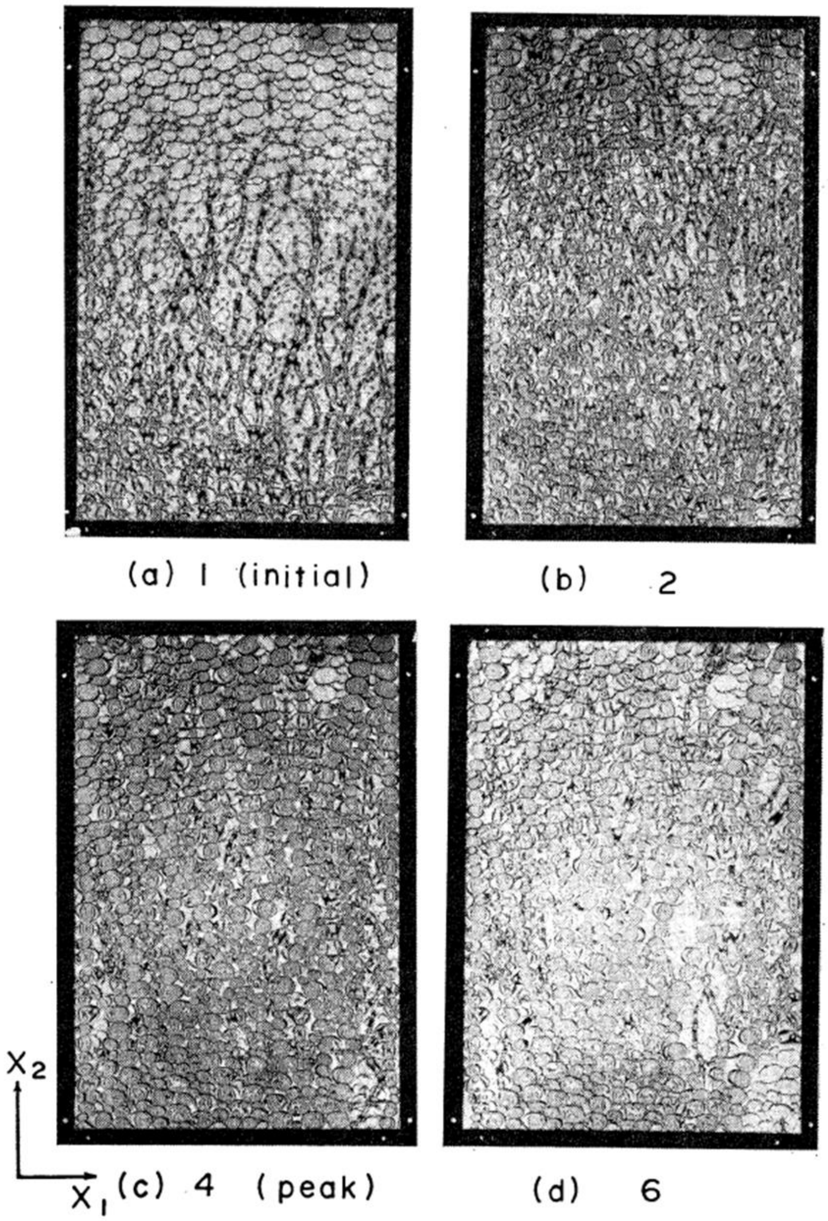

Fig. 2.47 Photoelastic pictures of an assembly of oval-shaped rods subjected to biaxial compression. **a** Initial state. **b** Pre-failure state. **c** Failure state. **d** Post-failure state. Note that the major principal stress σ_1 is oriented along the vertical X_2-direction (after Oda et al. 1985)

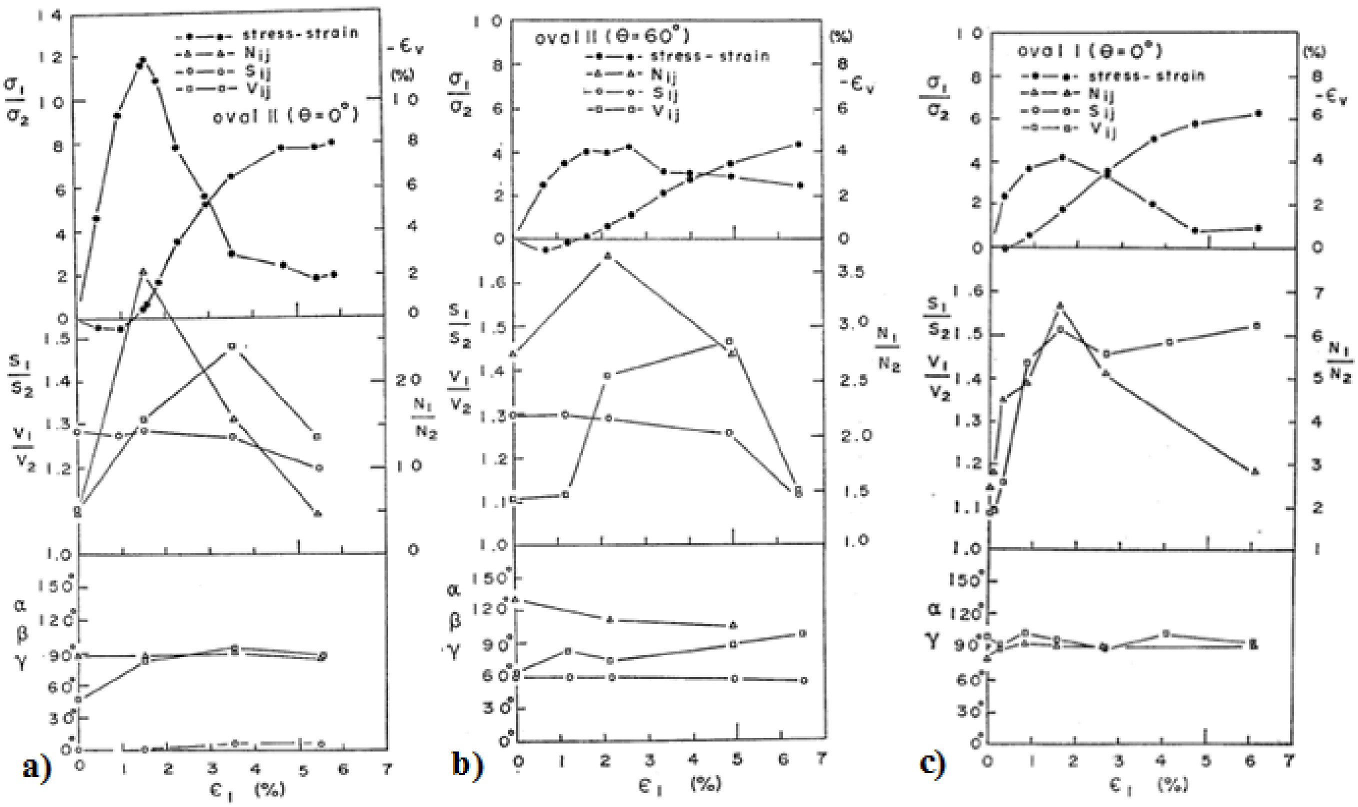

Fig. 2.48 Evolution of fabric of three different granular assemblies consisted of oval-shaped rods during biaxial compression. **a** Oval II (θ = 0°). **b** Oval II (θ = 60°). **c** Oval I (θ = 0°). Note that oval I rods have aspect ratio equal to 1.1 while oval II rods have aspect ratio equal to 1.4 (after Oda et al. 1985)

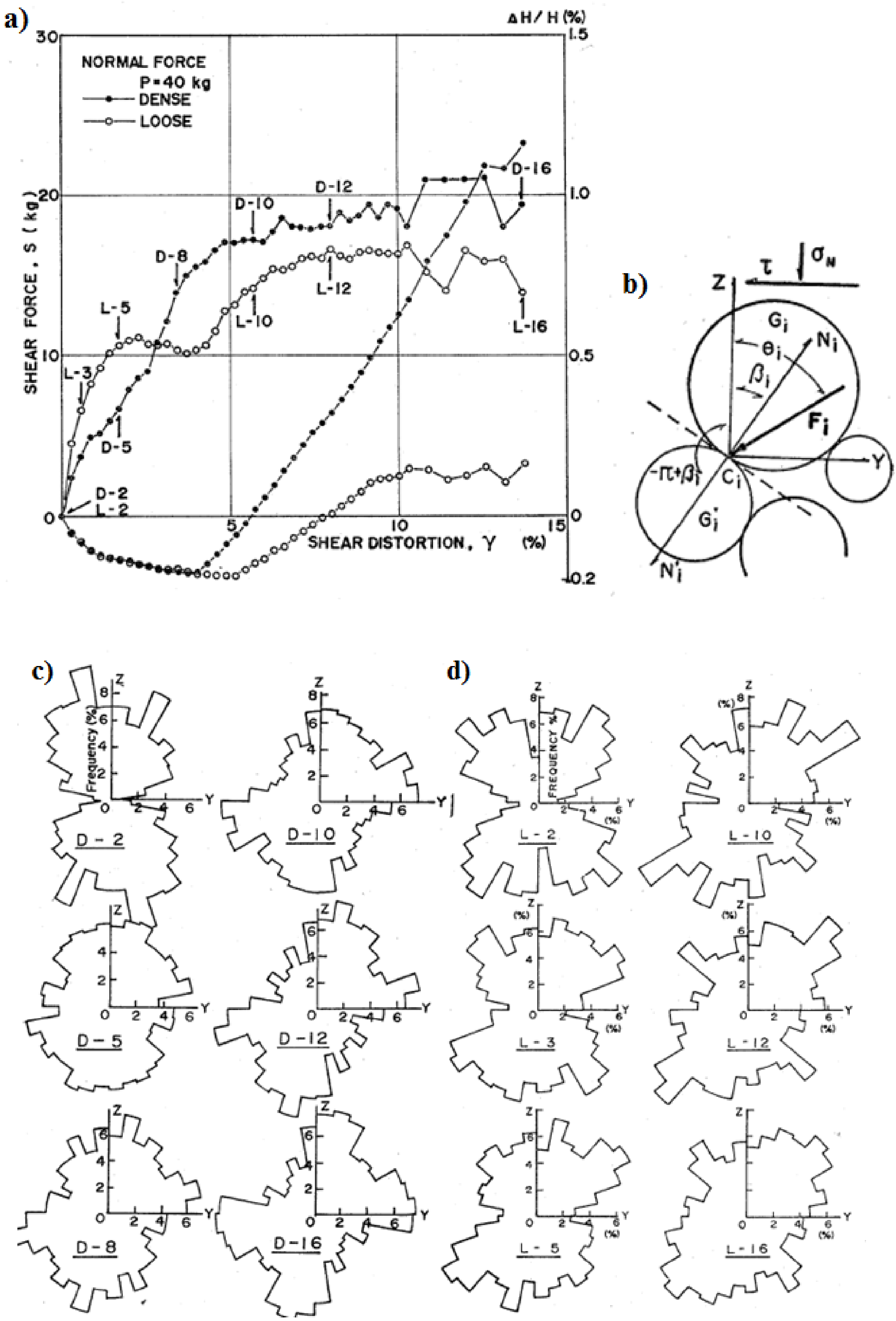

Fig. 2.49 Simple shear loading of assemblies of photoelastic rods. **a** Stress and volumetric strain plotted against shear distortion. **b** The direction angle β of the contact normal with respect to the reference axes. **c** Evolution of the orientational distribution of contact normals of a dense assembly. **d** Evolution of the orientational distribution of contact normals of a loose assembly (after Oda and Konishi 1974)

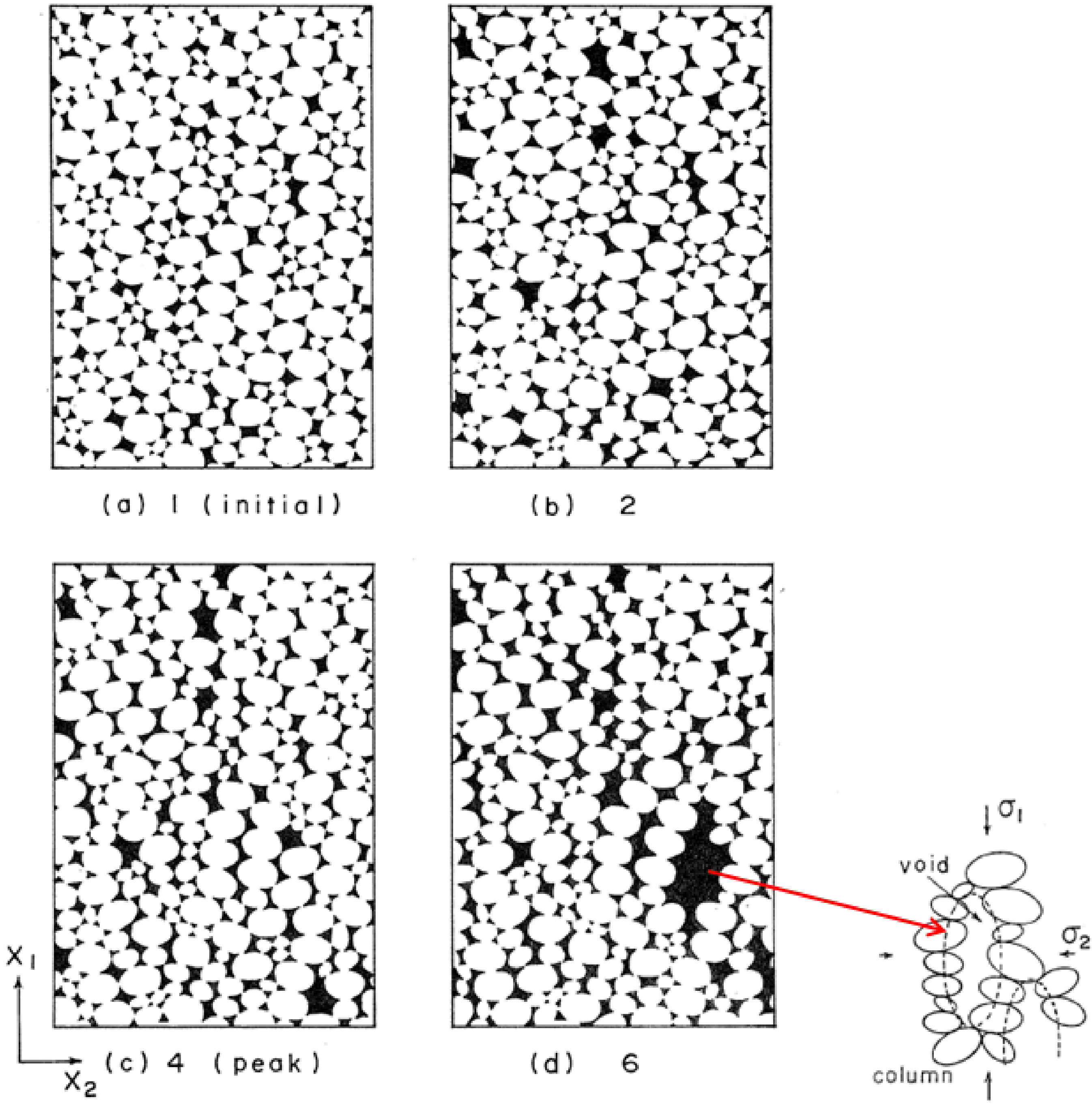

Fig. 2.50 Mechanism of evolution of the voids shape during biaxial compression of an assembly of oval-shaped photoelastic rods (type II with $\theta = 0°$). **a** Initial state. **b** Pre-failure state. **c** Failure state. **d** Post-failure state. Note that the major principal stress σ_1 is oriented along the vertical X_2-direction; X_2 is wrongly displayed in this figure (after Oda et al. 1985)

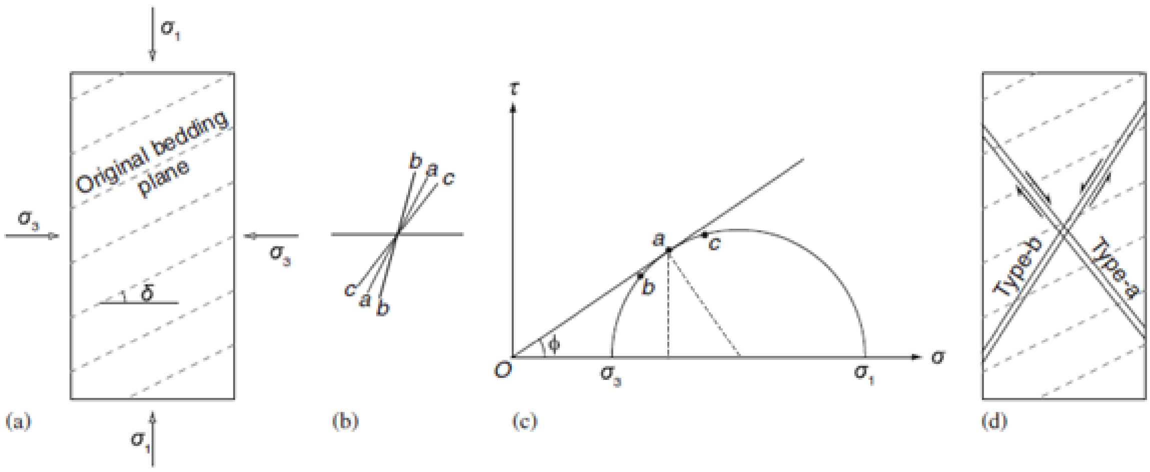

Fig. 2.51 Biaxial compression of a specimen with inclined to the horizontal bedding planes. **a** Boundary stress conditions and definition of the tilting angle, δ, of bedding plane. **b** Orientations of three potential failure planes. **c** The state of stress on each of the three potential failure planes illustrated by means of a Mohr's circle. **d** Two types of failure planes (after Fu and Dafalias 2011a)

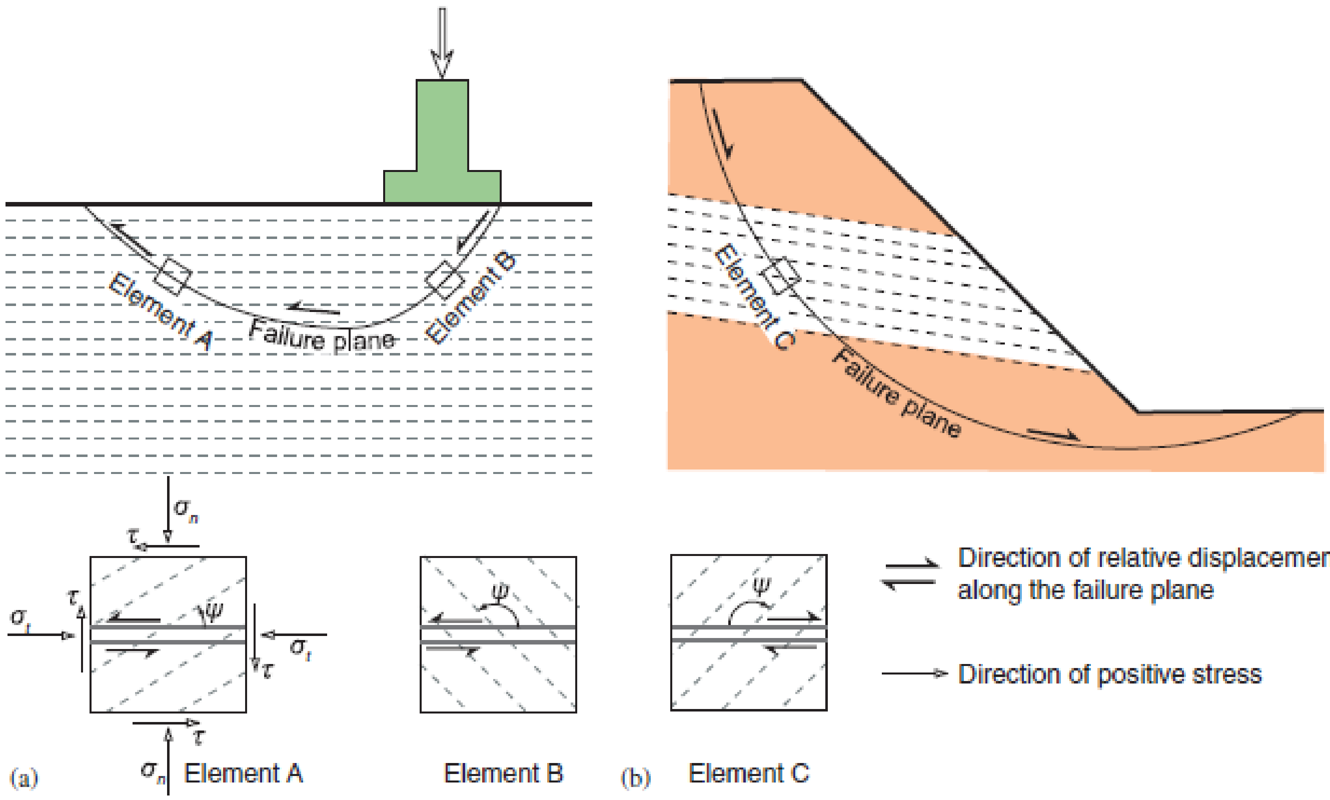

Fig. 2.52 Failure planes in inherently anisotropic soil masses; the definition of the bedding plane inclination angle ψ. **a** Failure plane assumed in a shallow foundation problem. **b** Failure plane assumed in a slope stability problem (after Fu and Dafalias 2011a)

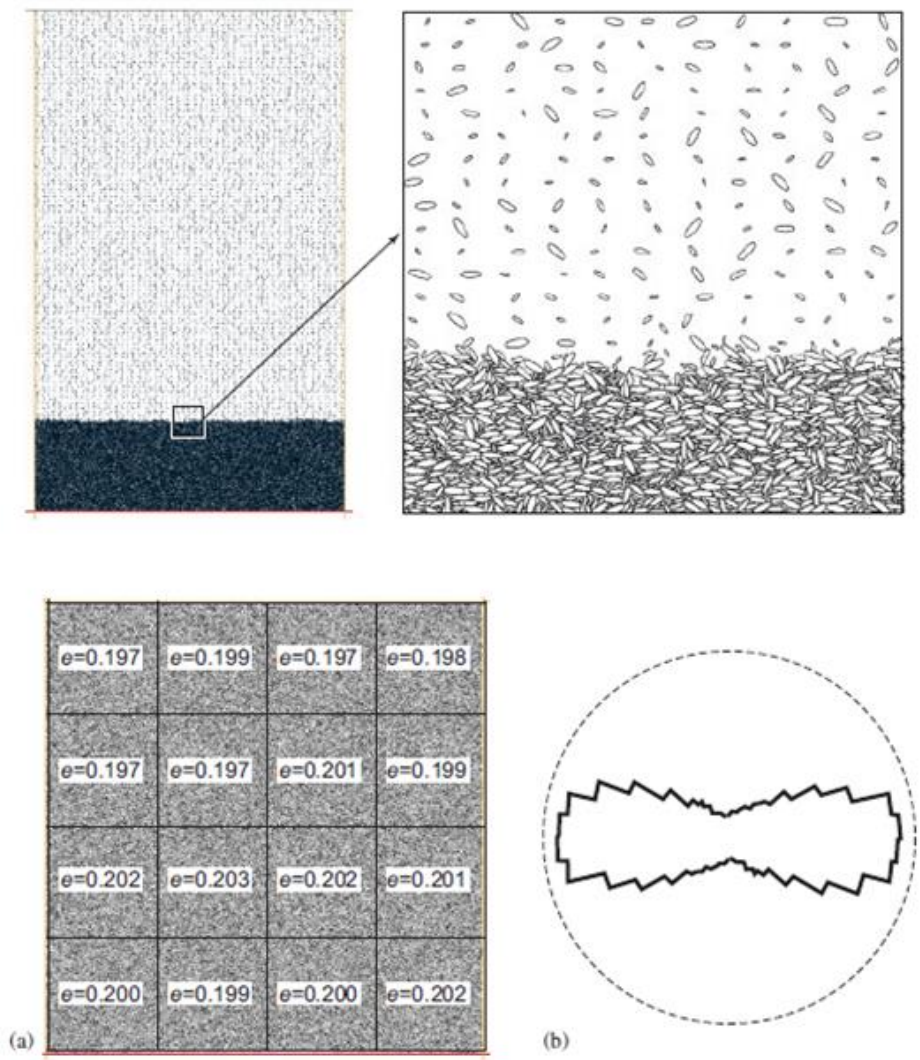

Fig. 2.53 Fabrication process of the master pack from which homogeneous and anisotropic virtual specimens are "trimmed out". **Up:** Particle pluviation under gravity. **a** Homogeneous distribution of void ratio inside the master pack. **b** Orientational distribution of particles' long axes (after Fu and Dafalias 2011a)

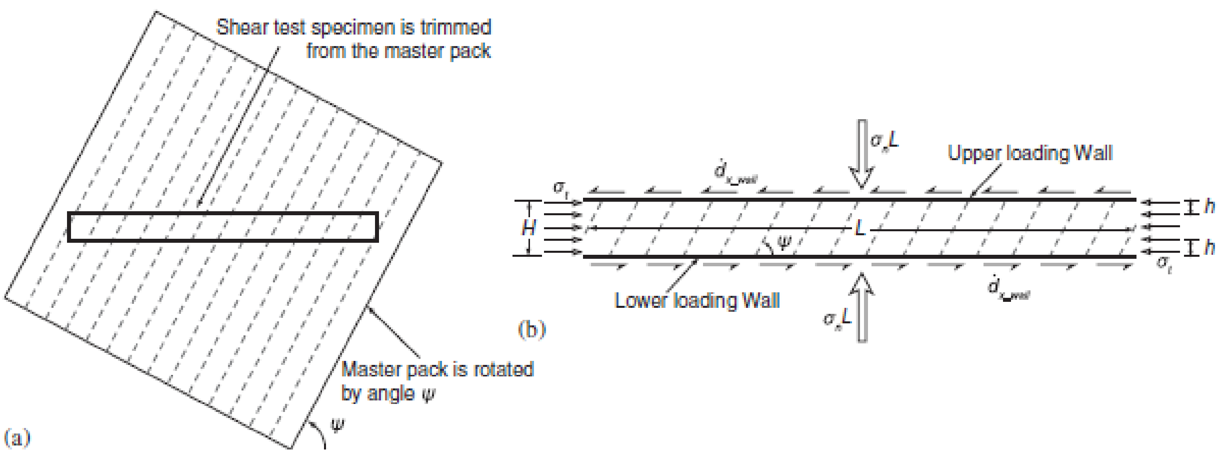

Fig. 2.54 a Fabrication of a specimen for direct shear testing by trimming it out of the rotated master pack. **b** Boundary conditions applied in the direct shear test (after Fu and Dafalias 2011a)

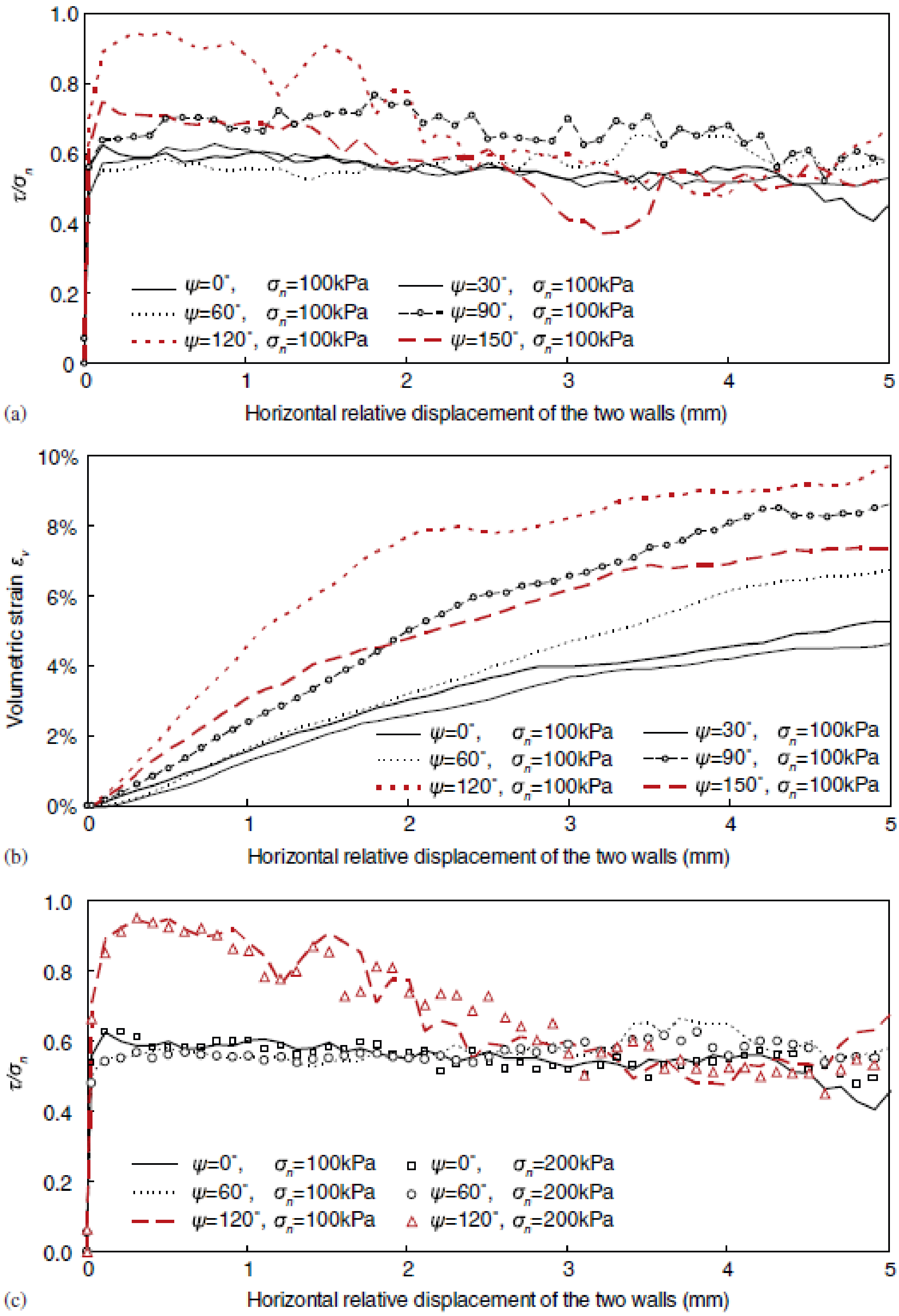

Fig. 2.55 Simulations of direct shear loading performed with the 2D discrete element method. **a** Mobilised stress ratio versus horizontal displacement at σ'_n = 100 kPa. **b** Volumetric strain versus horizontal displacement at σ'_n = 100 kPa. **c** Comparison of the evolution of stress ratio for the two different levels of σ'_n (after Fu and Dafalias 2011a)

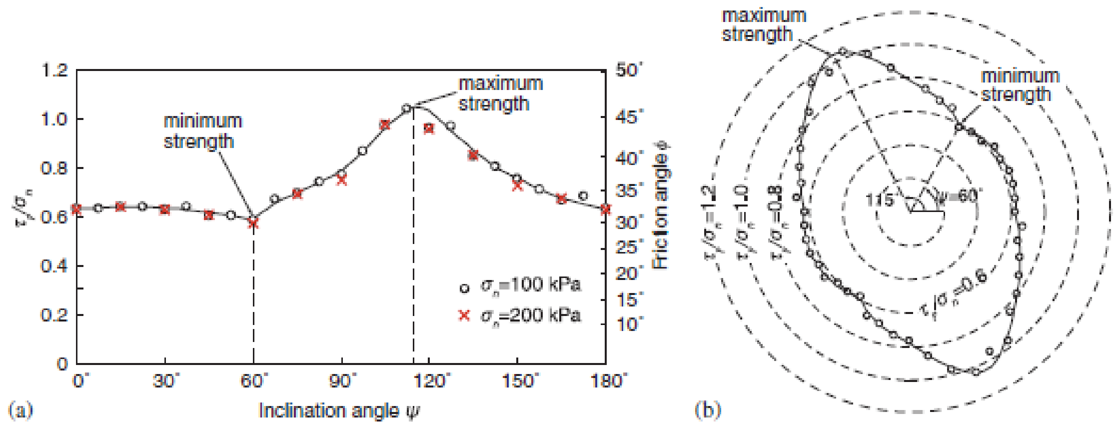

Fig. 2.56 Variation of the peak stress ratio with the inclination angle in 2D DEM simulations of direct shear loading: **a** in linear coordinates system, **b** in polar coordinates system (after Fu and Dafalias 2011a)

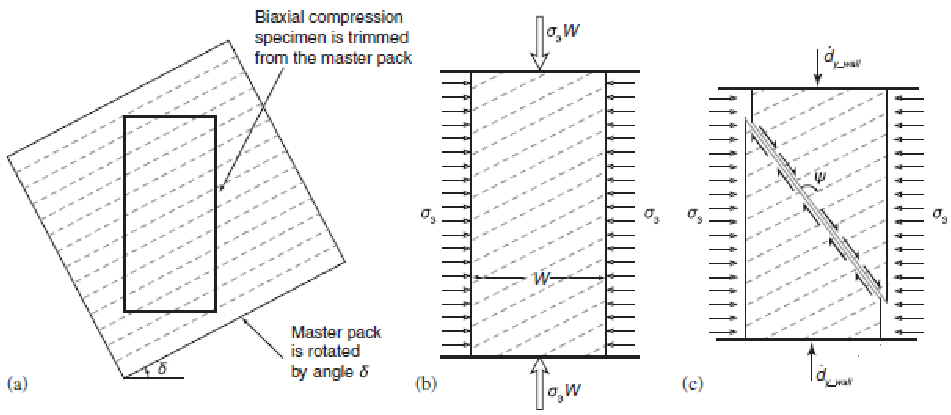

Fig. 2.57 Preparation, consolidation and biaxial compression loading of a specimen with tilted initial bedding planes using 2D DEM simulations. **a** Trimming the specimen out of the master pack. **b** Consolidating the specimen. **c** Loading the specimen (after Fu and Dafalias 2011a)

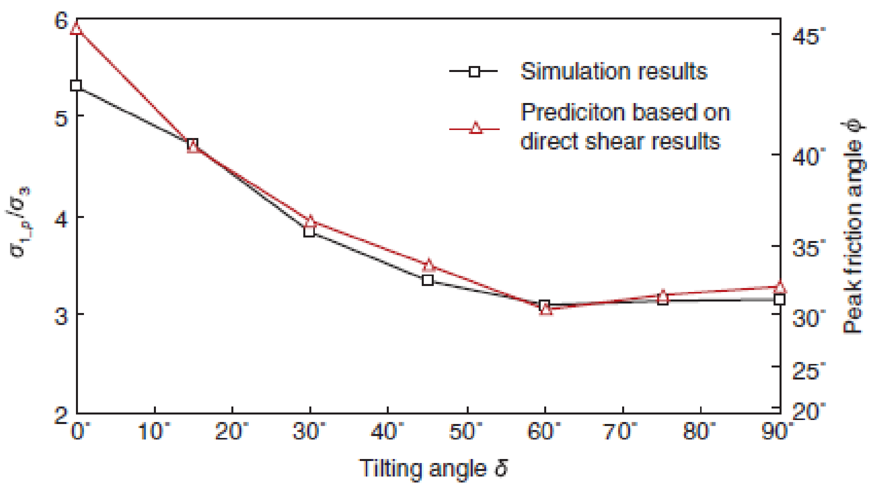

Fig. 2.58 Variation of the peak stress ratio with the tilting angle in 2D DEM simulations of biaxial compression loading (after Fu and Dafalias 2011a)

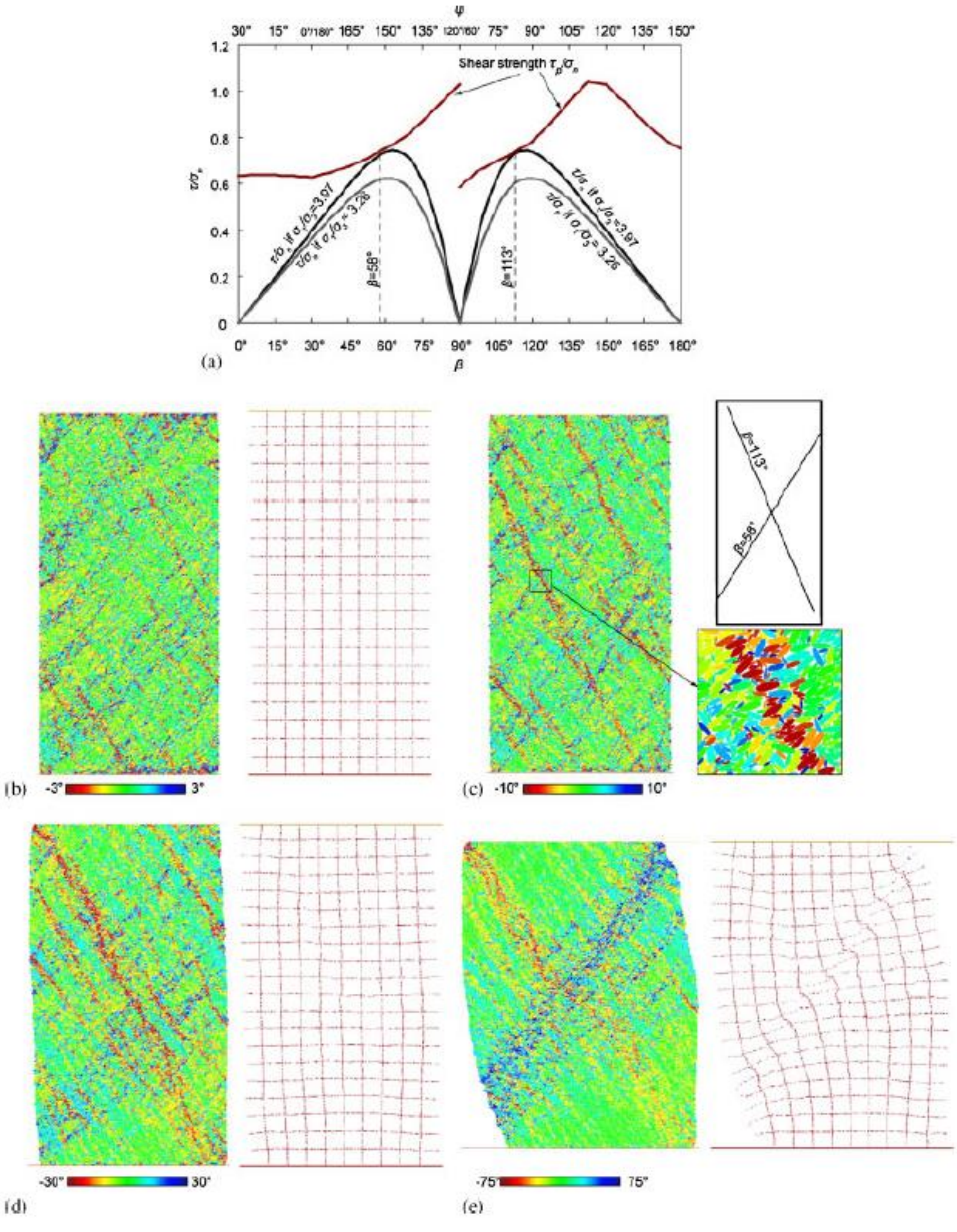

Fig. 2.59 The evolution of stress and deformation during a DEM simulation of biaxial compression loading on a specimen with δ = 30°. **a** Mobilised stress ratio τ / σ'_n on all potential failure planes, corresponding to two values of σ'_1 / σ'_3. **b** through **e** Contours of equal angle of rotation of individual particles and overall deformation at different axial strain levels (after Fu and Dafalias 2011a)

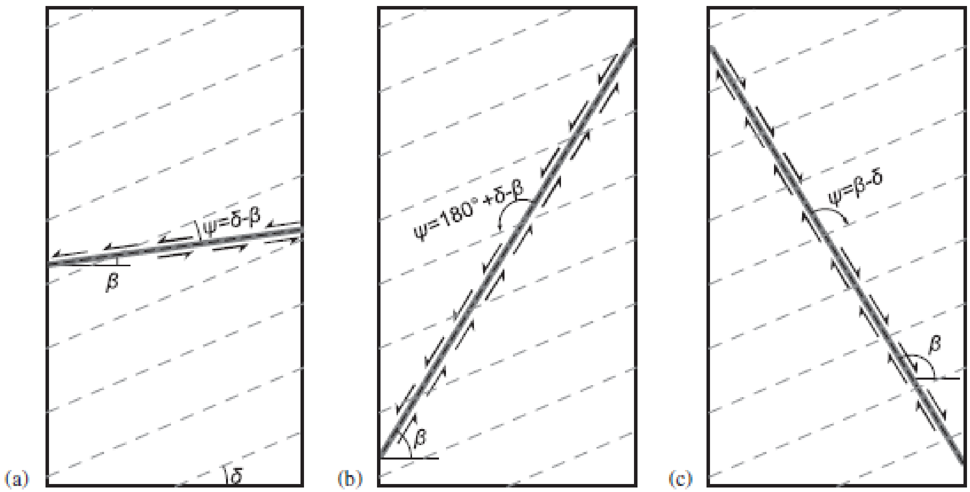

Fig. 2.60 Types of potential shear planes and the corresponding relationship between the bedding plane tilting angle, δ, the shear plane angle, β, and the bedding plane inclination angle, ψ (after Fu and Dafalias 2011a)

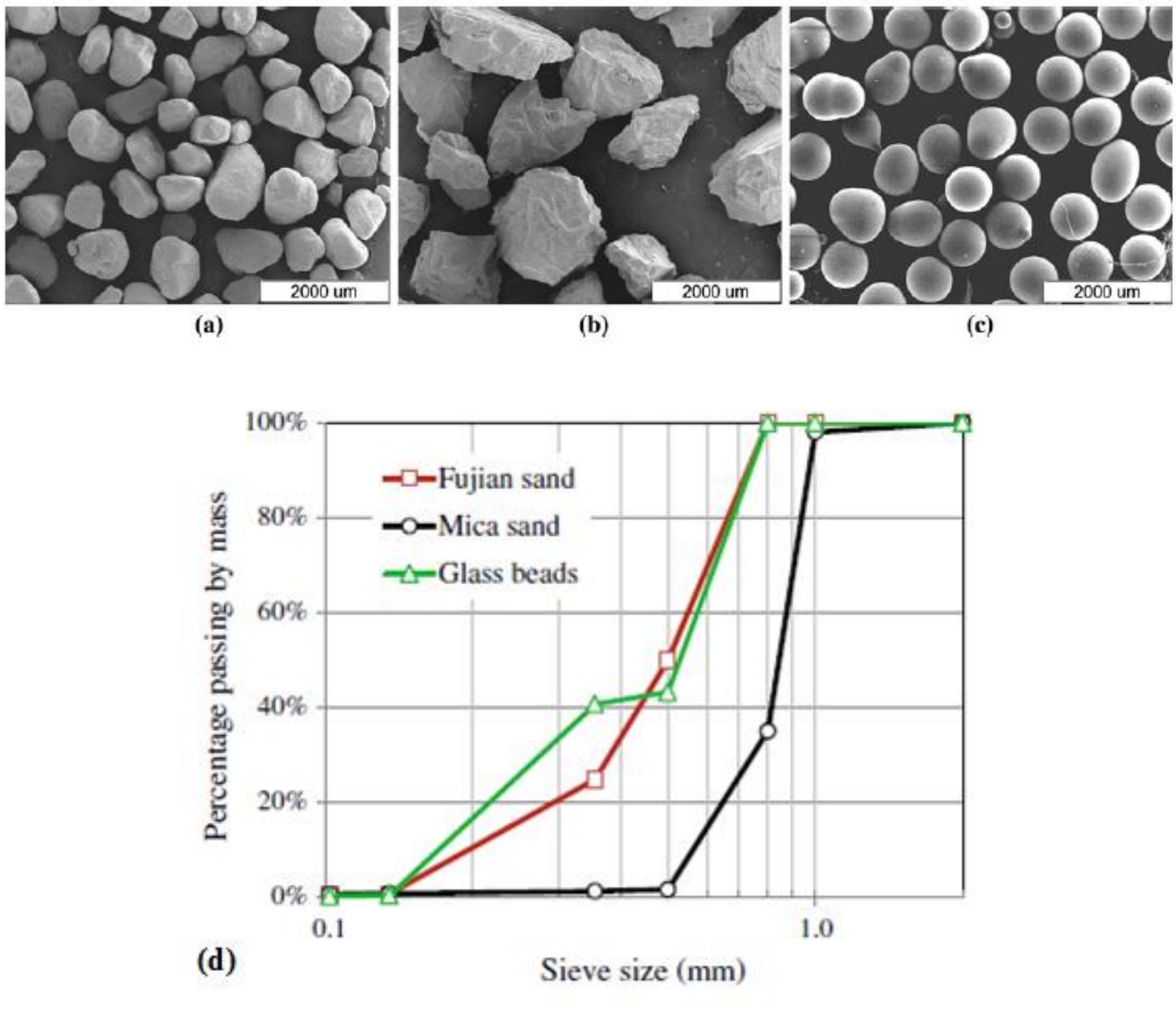

Fig. 2.61 Scanning electron microscope images of: **a** Fujian sand grains, **b** mica sand grains, **c** glass beads. It is noted that only one of the sizes of the glass beads used to form the blend is shown. **d** Gradation curves of the materials tested (after Tong et al. 2014)

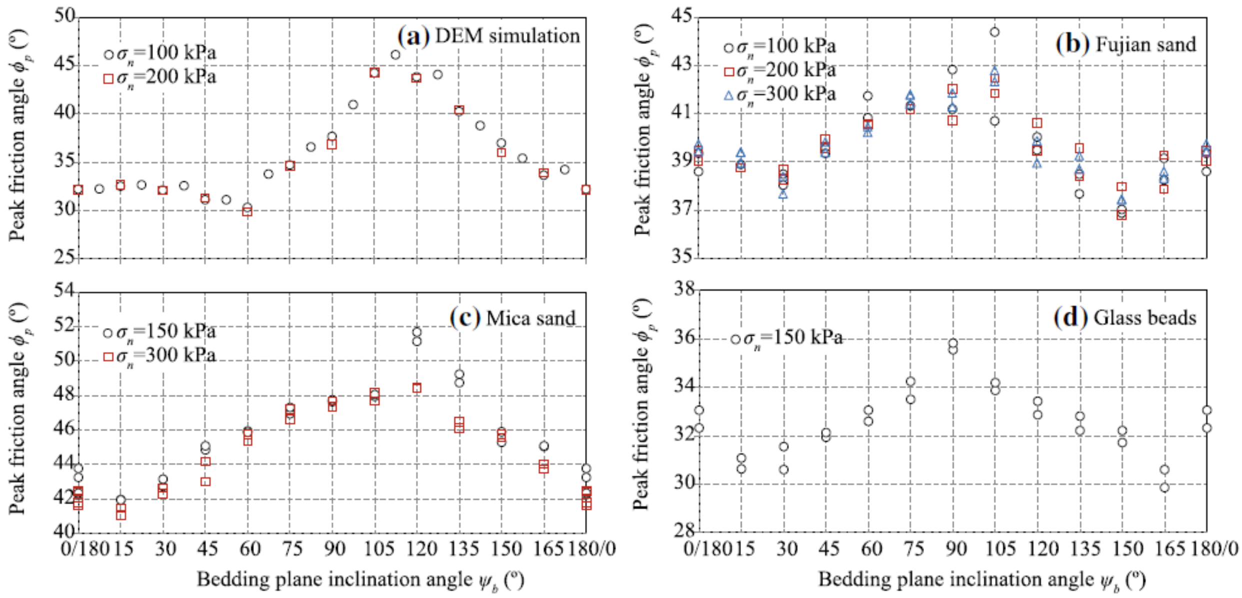

Fig. 2.62 Influence of the bedding plane inclination angle, ψ_b, on peak friction angle, φ_p, for all the granular materials tested by Tong et al. (2014) and Fu and Dafalias (2011a). Results from: **a** DEM simulations of direct shear tests on ellipse shaped 2D elements, **b** direct shear tests on Fujian sand, **c** direct shear tests on Mica sand, **d** direct shear tests on glass beads (after Tong et al. 2014)

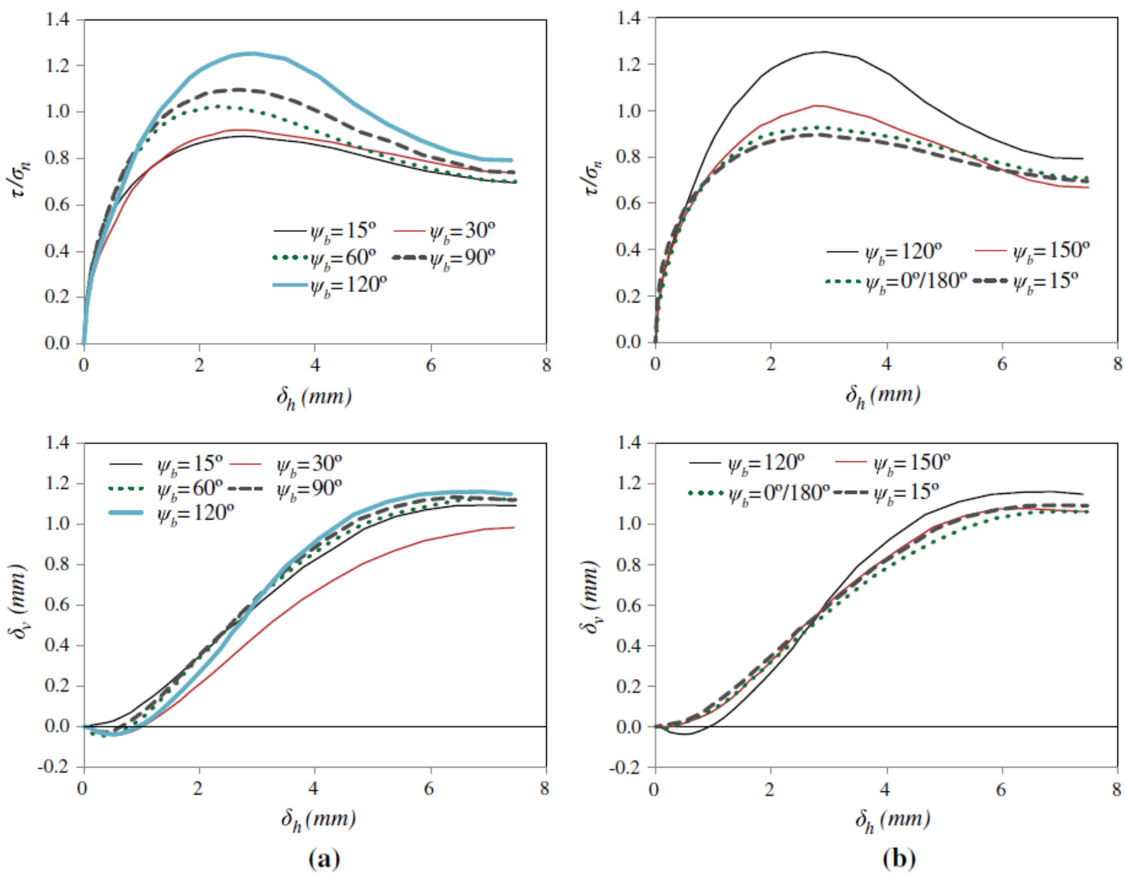

Fig. 2.63 Stress ratio τ / σ'_n and vertical displacement δ_v plotted against horizontal displacement δ_h in direct shear tests of mica sand at σ'_n = 150 kPa. **a** Curves corresponding to the ascending segment of the ψ_b - φ_p curve. **b** Curves corresponding to the descending segment of the ψ_b - φ_p curve (after Tong et al. 2014)

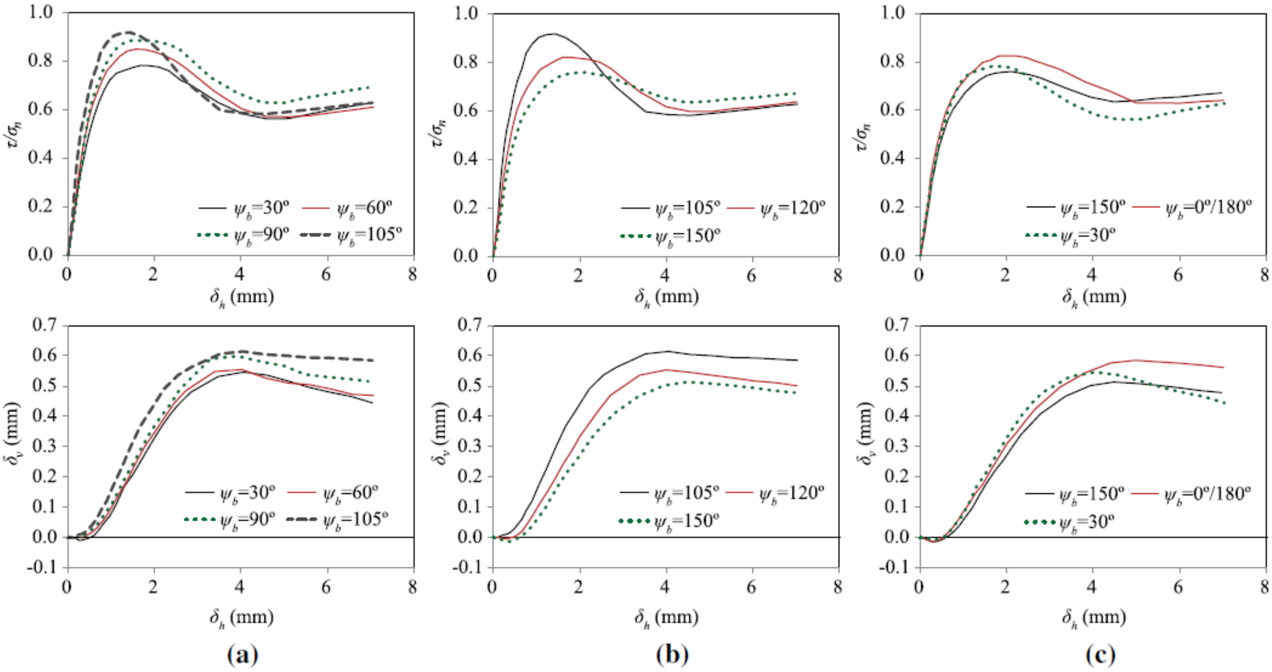

Fig. 2.64 Stress ratio τ / σ'_n and vertical displacement δ_v plotted against horizontal displacement δ_h in direct shear tests of Fujian sand at σ'_n = 300 kPa. **a** Curves corresponding to the ascending segment of the ψ_b - φ_p curve. **b** Curves corresponding to the descending segment of the ψ_b - φ_p curve. **c** Curves corresponding to the transitional segment of the ψ_b - φ_p curve between the two local minimums of φ_p (after Tong et al. 2014)

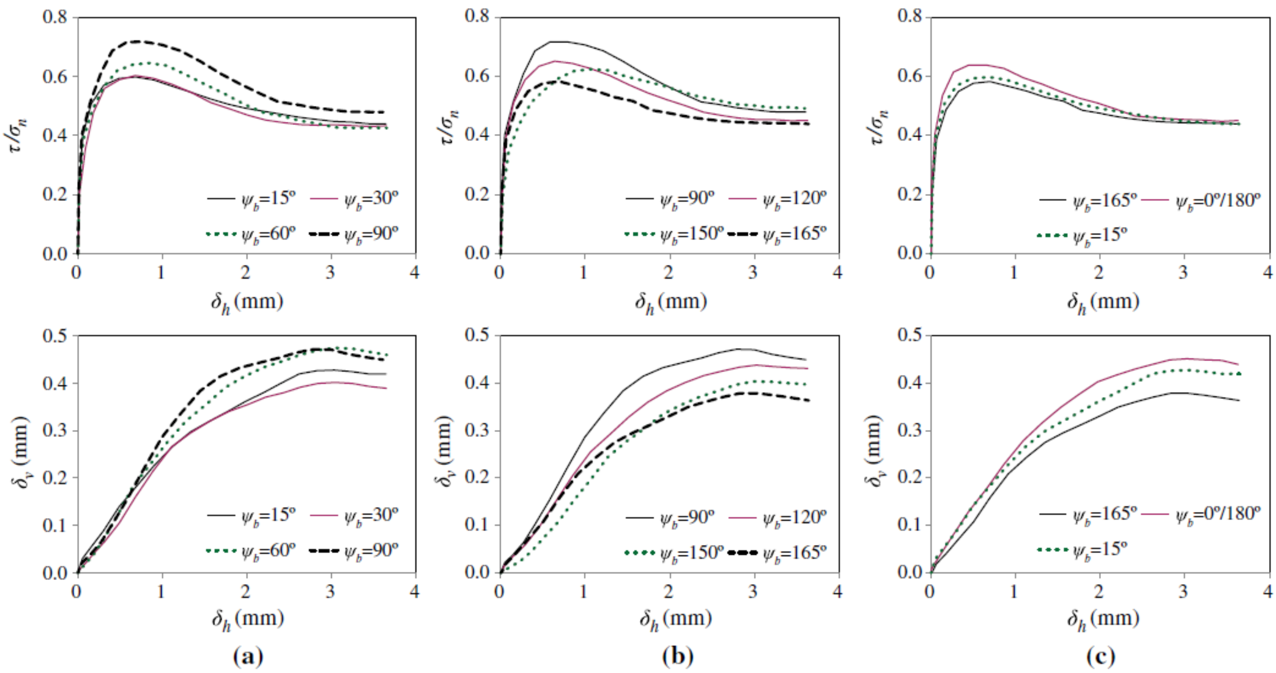

Fig. 2.65 Stress ratio τ / σ'_n and vertical displacement δ_v plotted against horizontal displacement δ_h in direct shear tests of glass beads at σ'_n = 150 kPa. **a** Curves corresponding to the ascending segment of the ψ_b - φ_p curve. **b** Curves corresponding to the descending segment of the ψ_b - φ_p curve. **c** Curves corresponding to the transitional segment of the ψ_b - φ_p curve between the two local minimums of φ_p (after Tong et al. 2014)

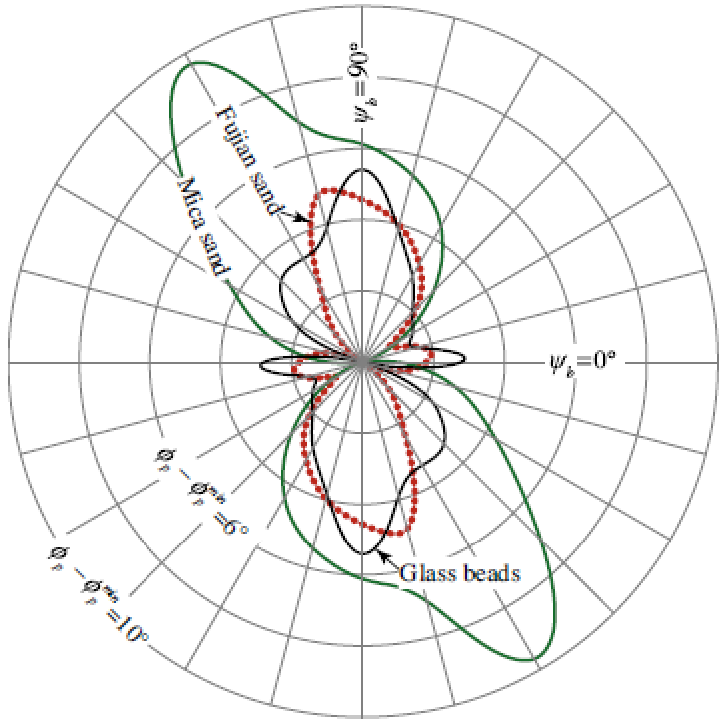

Fig. 2.66 The value of the angle difference φ_p - φ_p^{min} plotted against ψ_b in a polar coordinates system for three sands with different grain characteristics (after Tong et al. 2014)

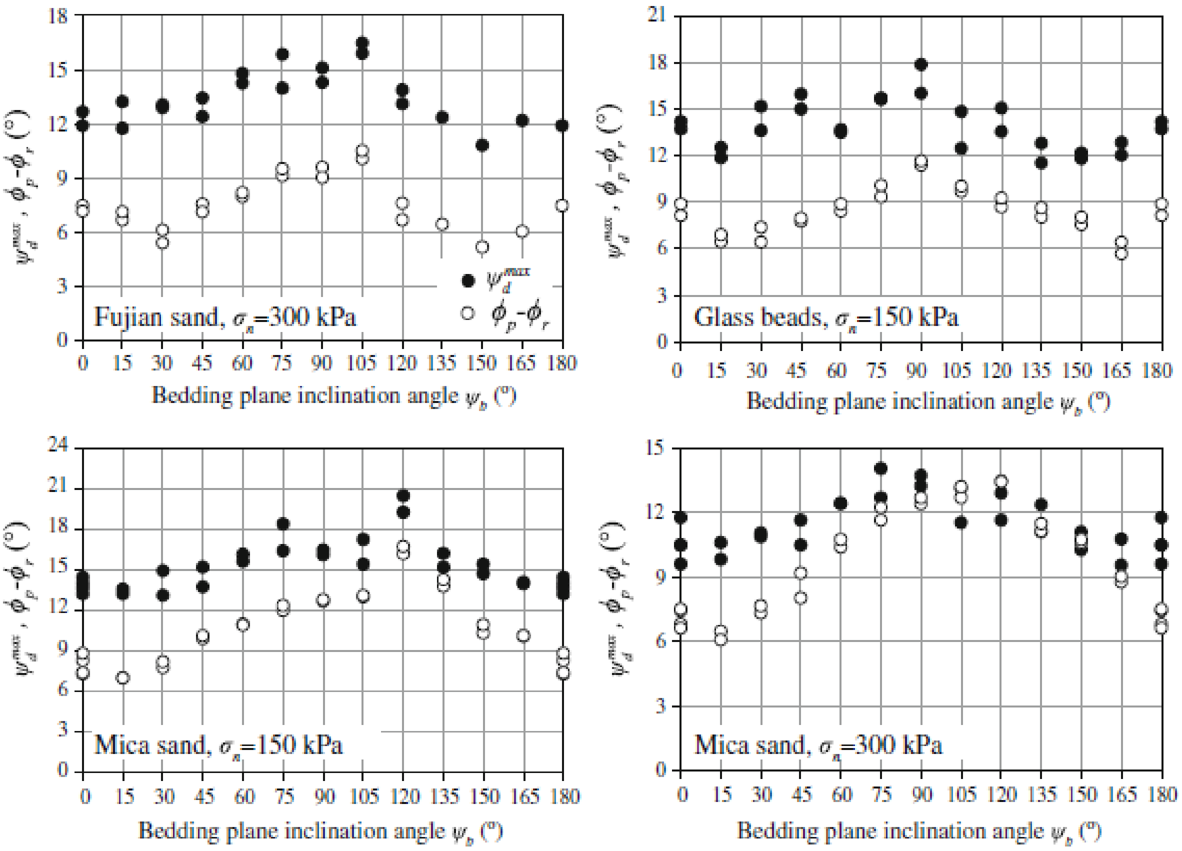

Fig. 2.67 Peak dilation angle ψ_d^{max} and angle difference φ_p - φ_r plotted against the bedding plane inclination angle ψ_b (after Tong et al. 2014)

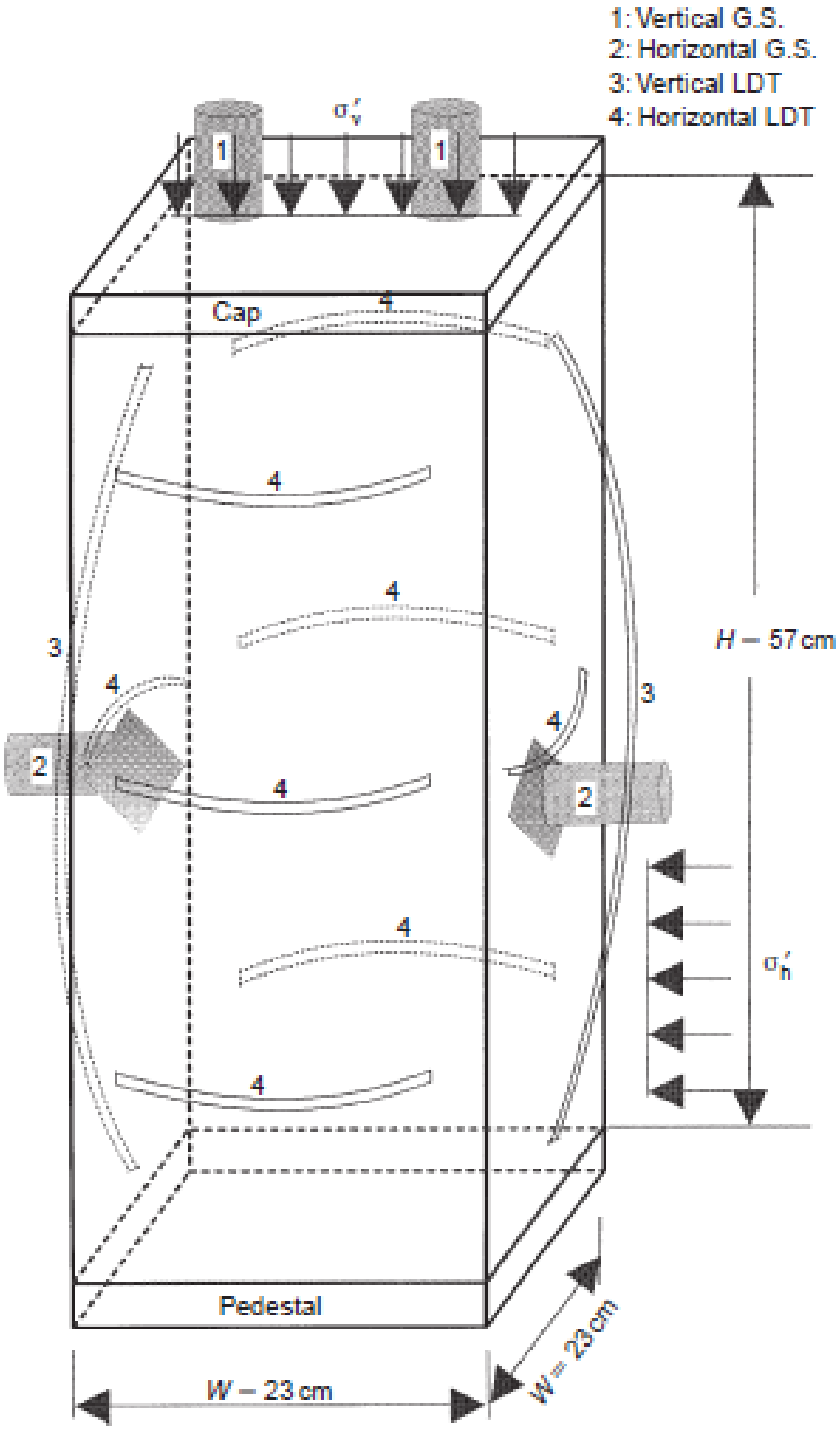

Fig. 2.68 Square prismatic triaxial specimen and instrumentation for measuring small strains (after Jiang et al. 1997)

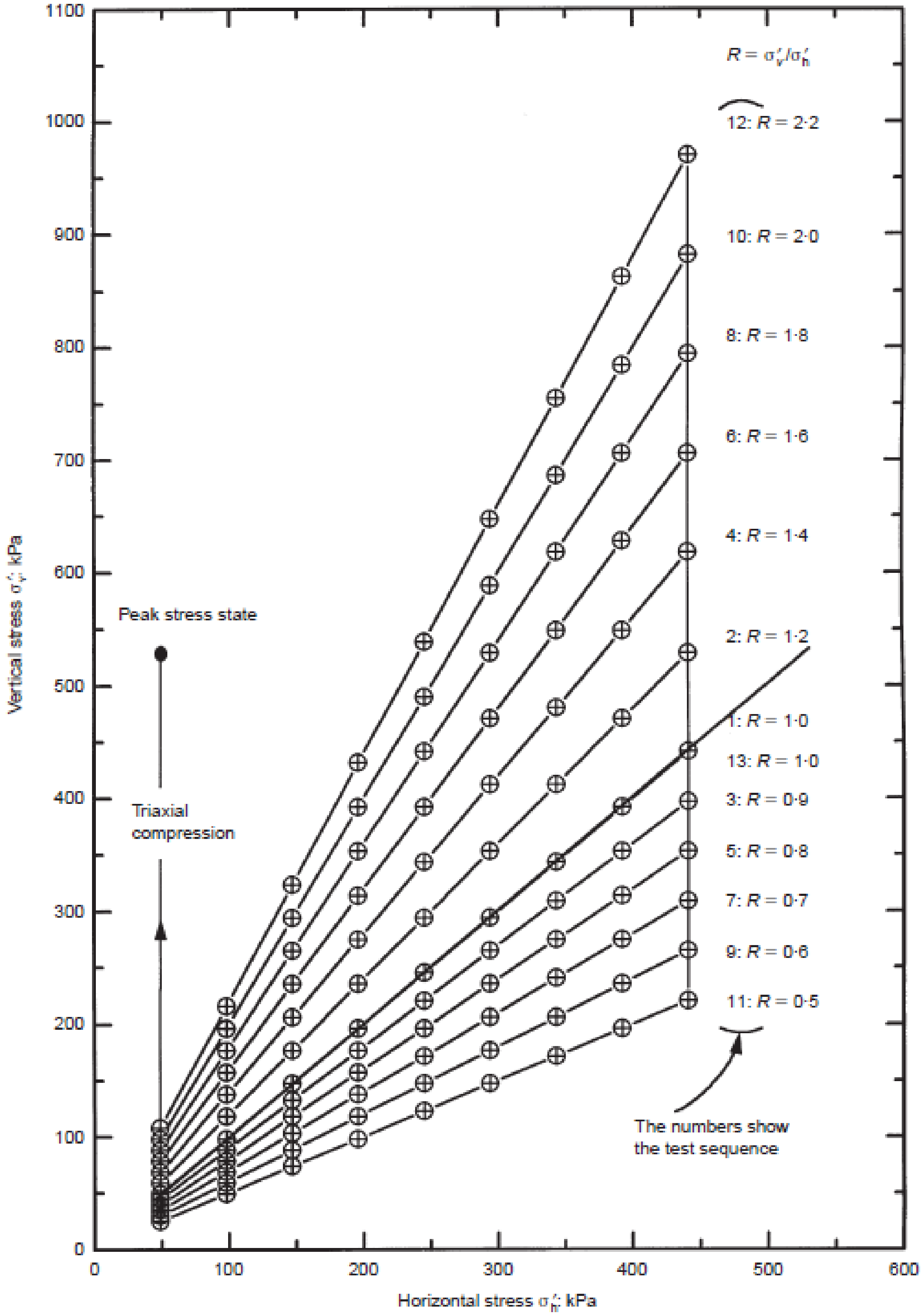

Fig. 2.69 Stress states at which small amplitude stress cycles were performed (after Jiang et al. 1997)

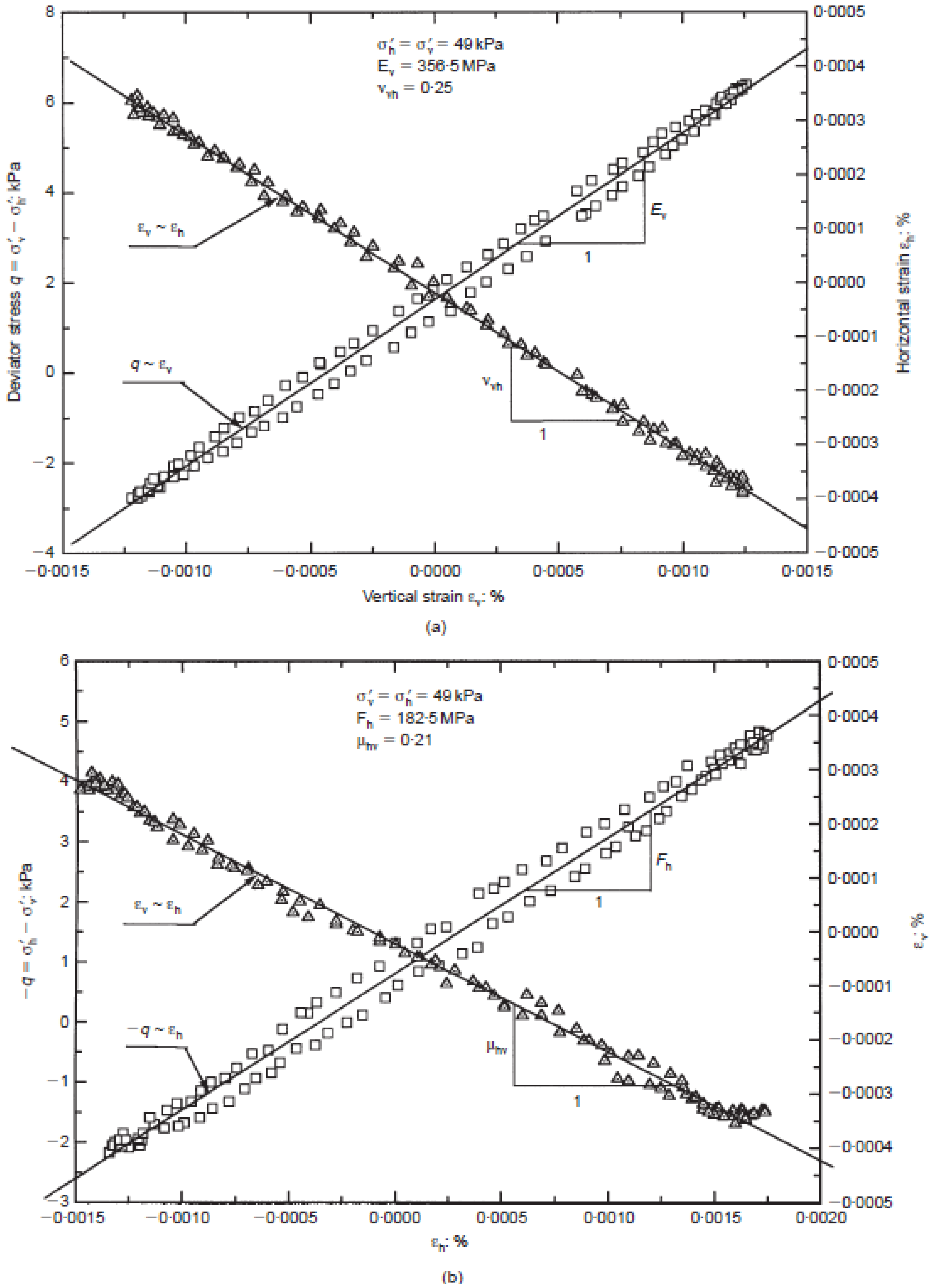

Fig. 2.70 Small amplitude stress cycles performed at isotropic stress state in order to determine the elastic moduli and Poisson's ratios of Chiba gravel. **a** Small amplitude stress cycles along the vertical direction. **b** Small amplitude stress cycles along the horizontal direction (after Jiang et al. 1997)

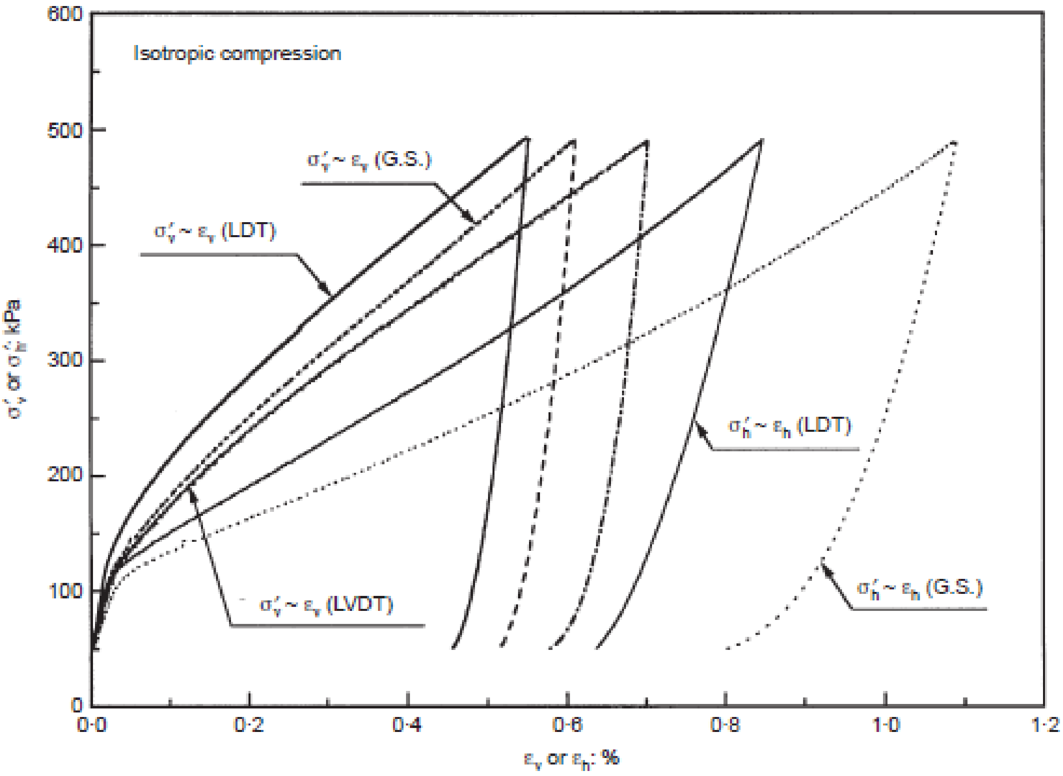

Fig. 2.71 Measurement of the strains of gravel material under isotropic loading – unloading using different instrumentation (after Jiang et al. 1997)

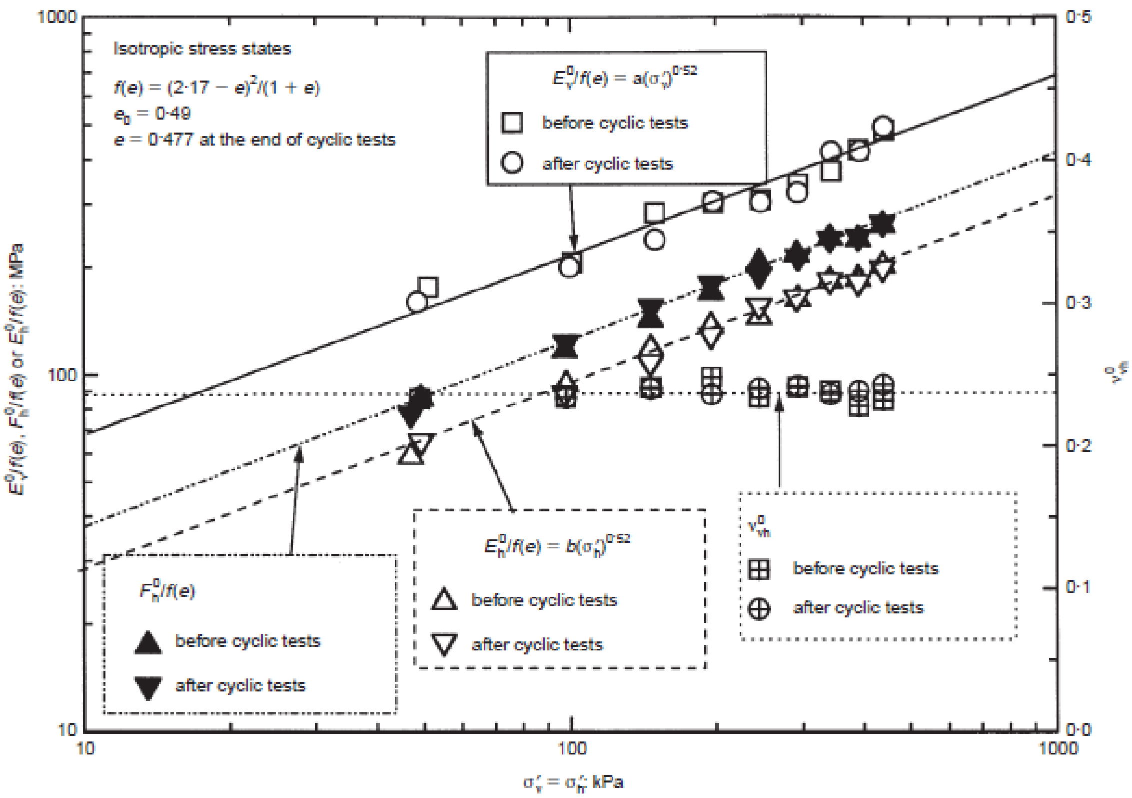

Fig. 2.72 Young's moduli E_v, F_h and E_h and Poisson's ratio ν_{vh} at isotropic stress states. Note that the value $\nu_{hh} = 0.24$ was assumed in order to determine E_h as a function of the measured F_h (after Jiang et al. 1997)

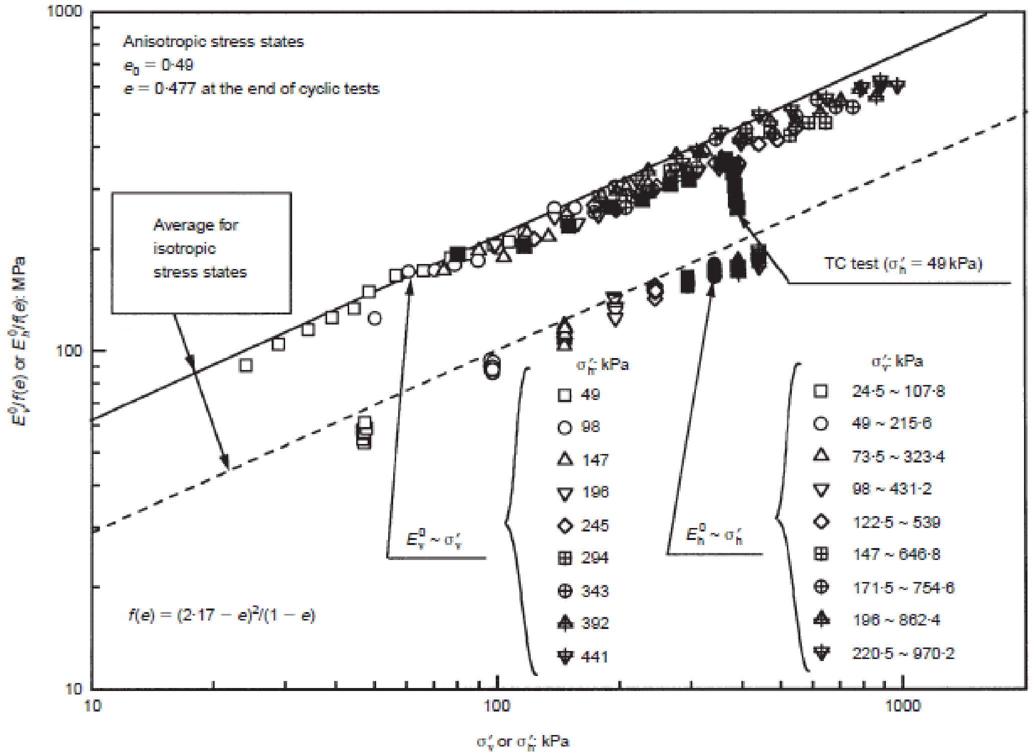

Fig. 2.73 Plot of Young's moduli E_v and E_h versus σ'_v and σ'_h, respectively, at isotropic and anisotropic stress states after ageing. The value of E_v determined at anisotropic stress states during TC loading corresponds to small amplitude stress cycles imposed without previous ageing. Note that the value $\nu_{hh} = 0.24$ was assumed in order to determine E_h as a function of the measured F_h (after Jiang et al. 1997)

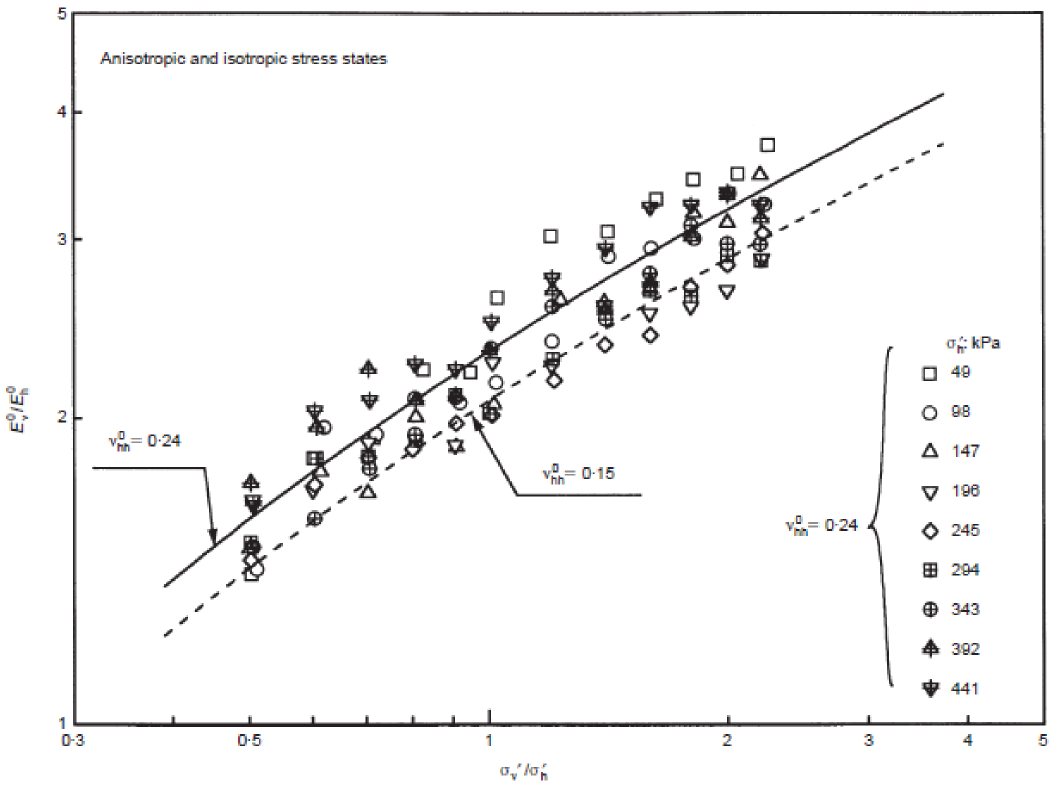

Fig. 2.74 Ratio E_v / E_h of the two moduli plotted against the stress ratio σ'_v / σ'_h (after Jiang et al. 1997)

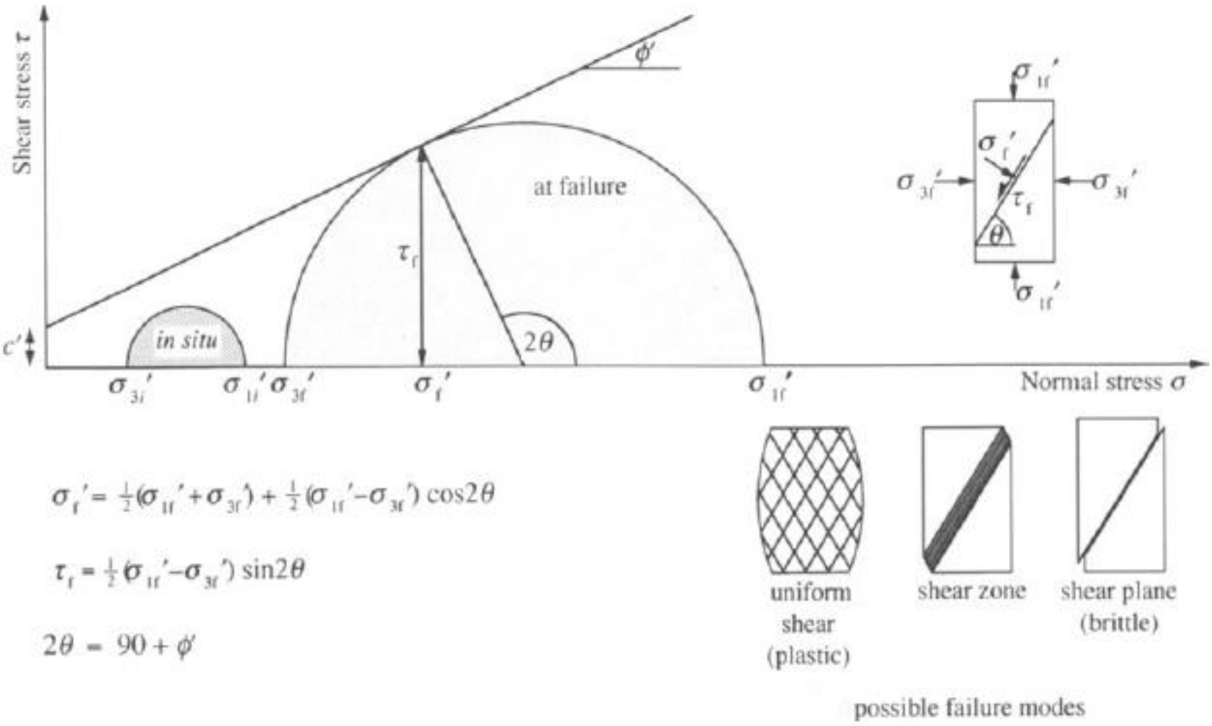

Fig. 2.75 Diffuse and localised failure of soils (after Barnes 1995)

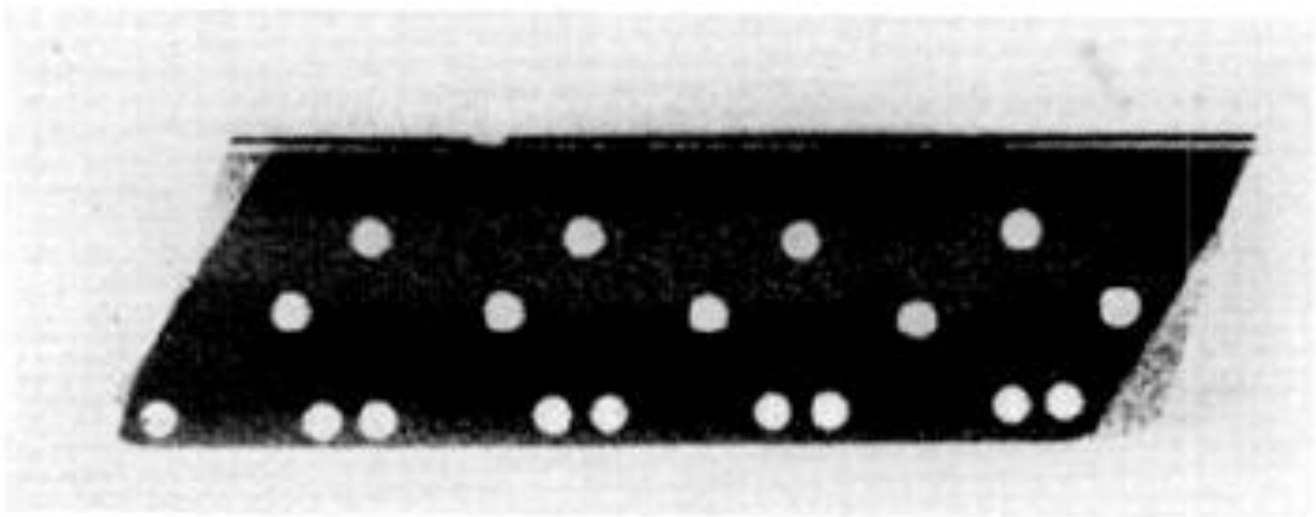

Fig. 2.76 Two superimposed radiographs of dense sand with embedded lead shots subjected to simple shear loading. The radiographs correspond to a shear strain increment at post-peak conditions. Notice that the black rupture zone between the bottom and middle row of shots is the shear band along a line of zero-extension (after Roscoe 1970)

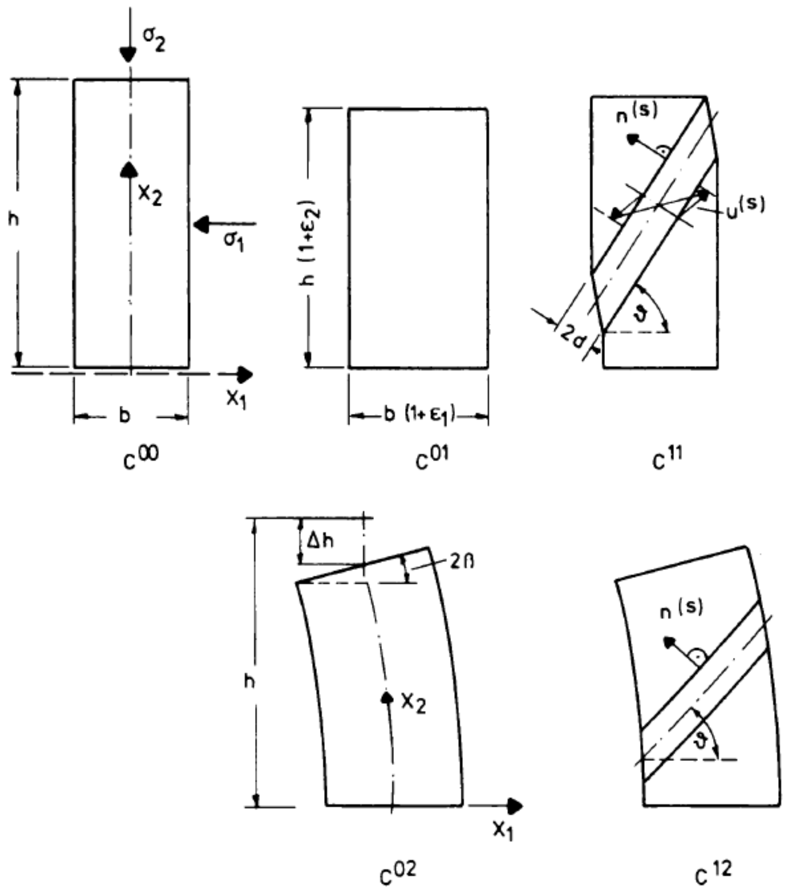

Fig. 2.77 Bifurcation to different modes of deformation in biaxial testing (after Vardoulakis et al. 1978)

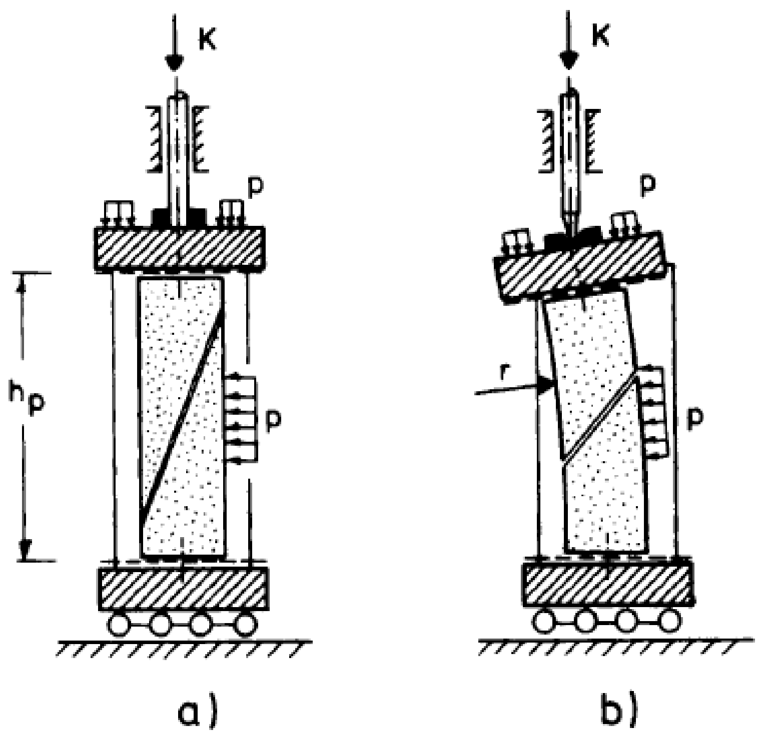

Fig. 2.78 Boundary conditions and loading systems in biaxial tests: **a** system for mode C^{11}, **b** system for mode C^{12}. The modes C^{11} and C^{12} are shown in Fig.2.77 (after Vardoulakis et al. 1978)

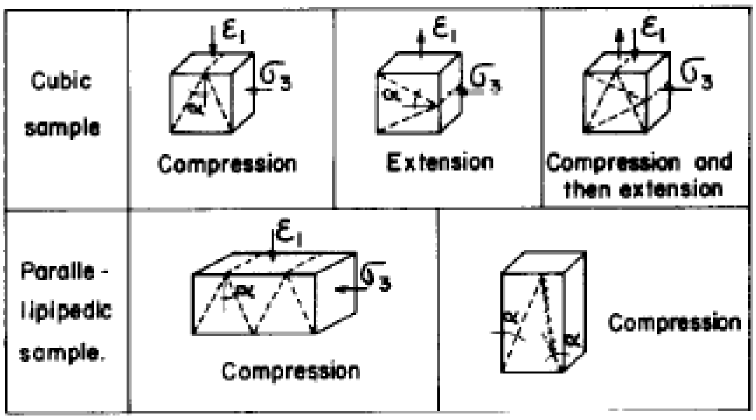

Fig. 2.79 Schematic illustration of the strain localisation patterns of cubic and parallelepipedic specimens subjected to plane strain loading in the true triaxial apparatus (after Desrues et al. 1985)

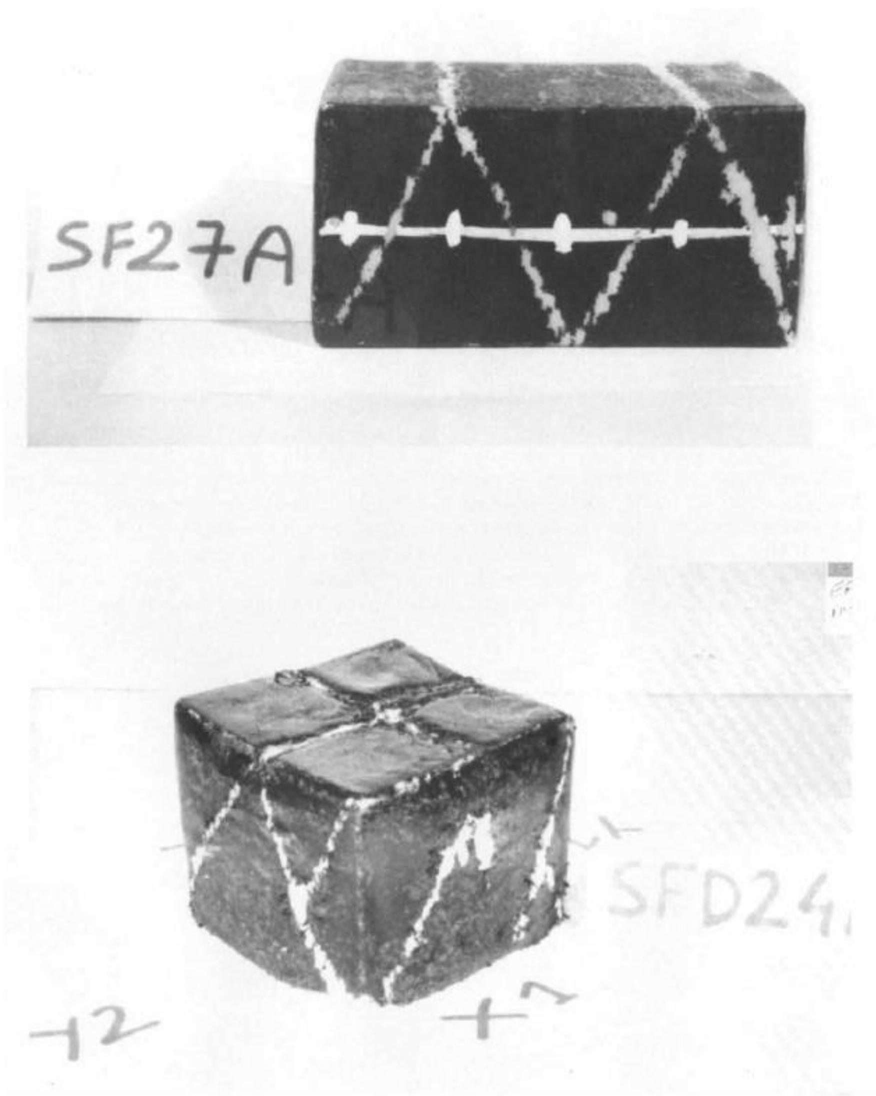

Fig. 2.80 Localised deformation of stabilised, dyed specimens subjected to plane strain loading in the true triaxial apparatus. **Photo 1** Multiple reflections of a propagating shear band on the rigid boundaries of a parallelepipedic specimen. **Photo 2** Reflection of shear bands on the rigid boundaries of a cubic specimen (after Desrues et al. 1985)

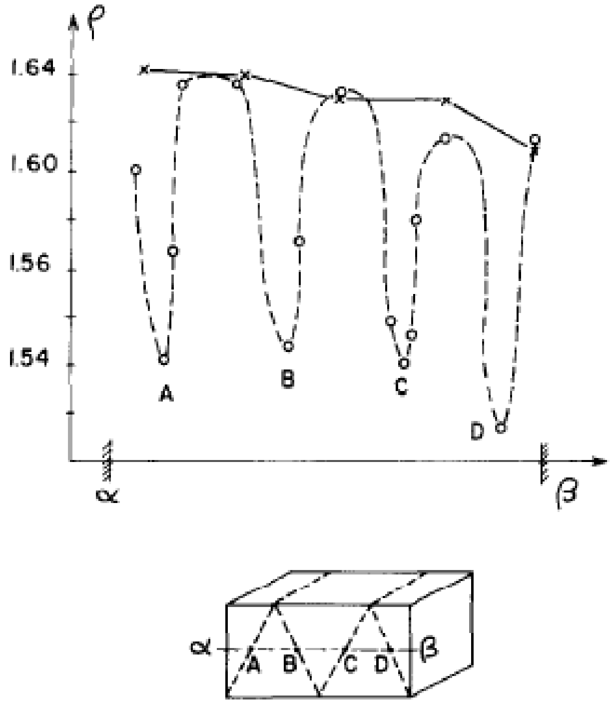

Fig. 2.81 Density distribution of a sand specimen along the αβ-line that crosses the shear bands, determined using the gamma-ray absorption technique. The line connecting the x-symbols in the figure represents the initial density distribution, while the line connecting the circle symbols represents the final density distribution after shear banding (after Desrues et al. 1985)

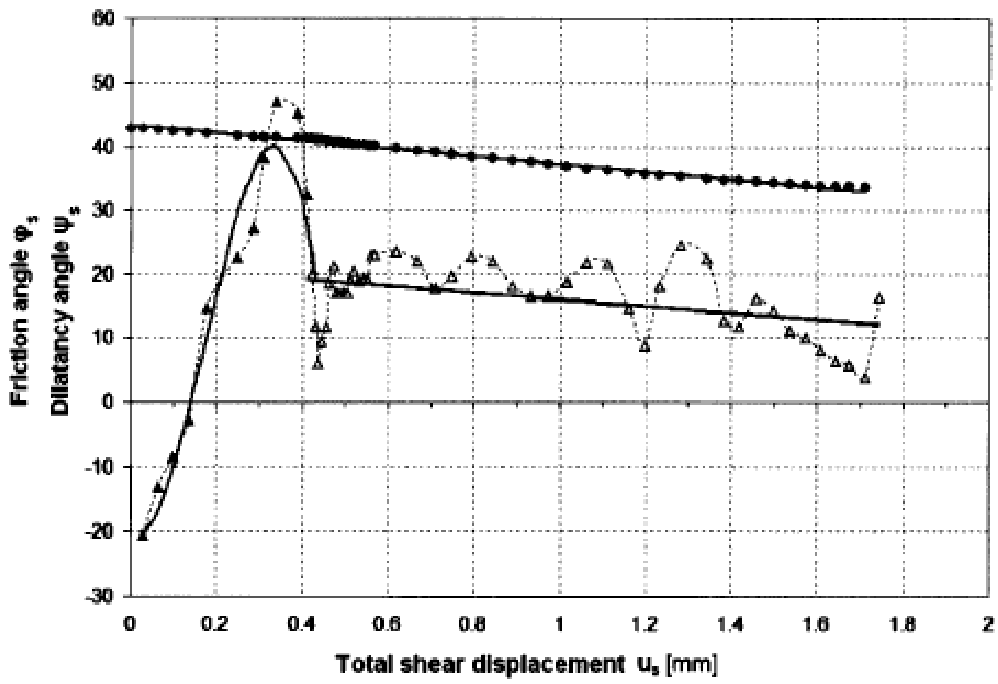

Fig. 2.82 Post-failure evolution of the friction angle, φ_s, and dilatancy angle, ψ_s, with the shear displacement inside the shear band. The solid lines correspond to averaging; the circles and triangles correspond to the experimentally determined values of φ_s and ψ_s, respectively (after Vardoulakis and Georgopoulos 2005; results from the BSE-5 test, after Vardoulakis and Graf 1985)

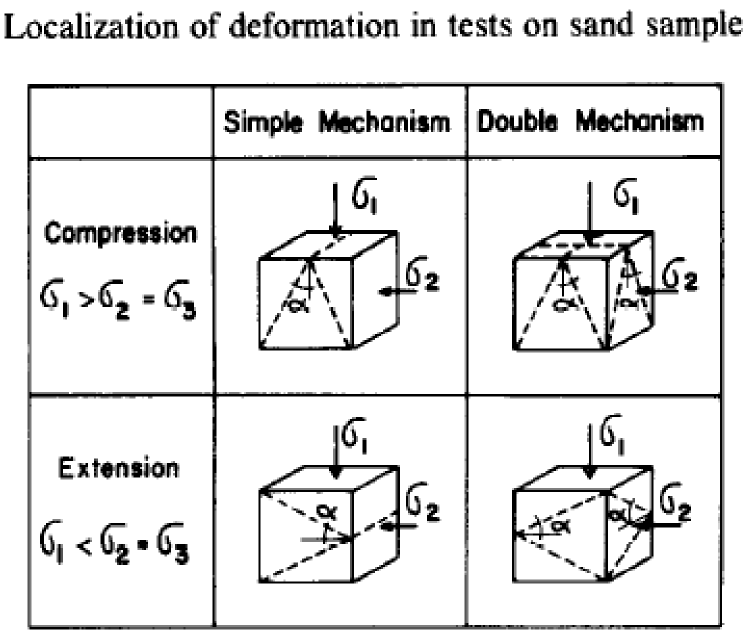

Fig. 2.83 Schematic illustration of the strain localisation patterns of cubic and parallelepipedic specimens subjected to axisymmetric loading in the true triaxial apparatus (after Desrues et al. 1985)

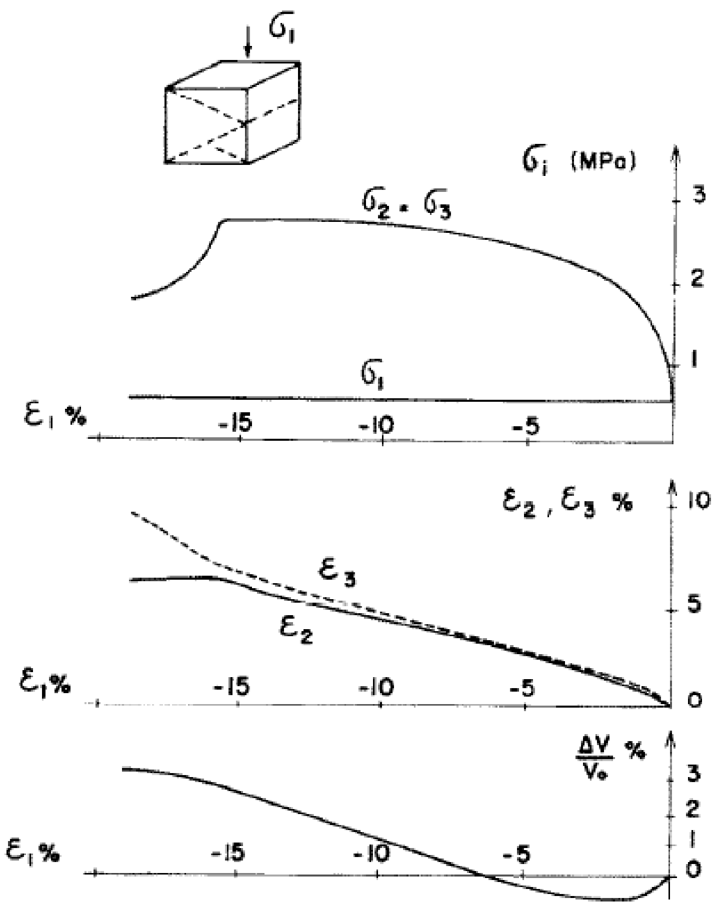

Fig. 2.84 Global stresses and strains (normal and volumetric) plotted against the vertical strain in an axisymmetric stress-controlled extension test. It is noted that $\sigma_2 = \sigma_3 > \sigma_1$ (after Desrues et al. 1985)

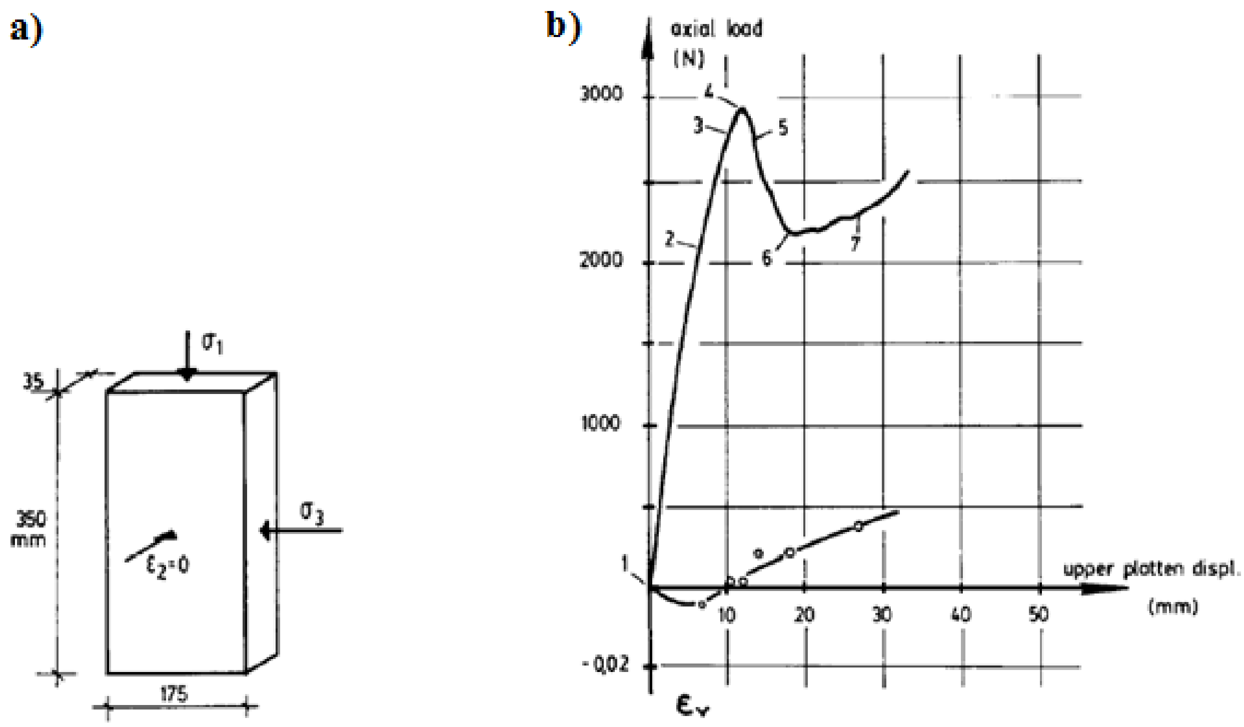

Fig. 2.85 Plane strain compression test in the biaxial apparatus. **a** Specimen dimensions and boundary conditions. **b** Load - displacement and volumetric strain - displacement curves. The numbers on the former curve indicate the serial numbers of photographs (after Desrues et al. 1985)

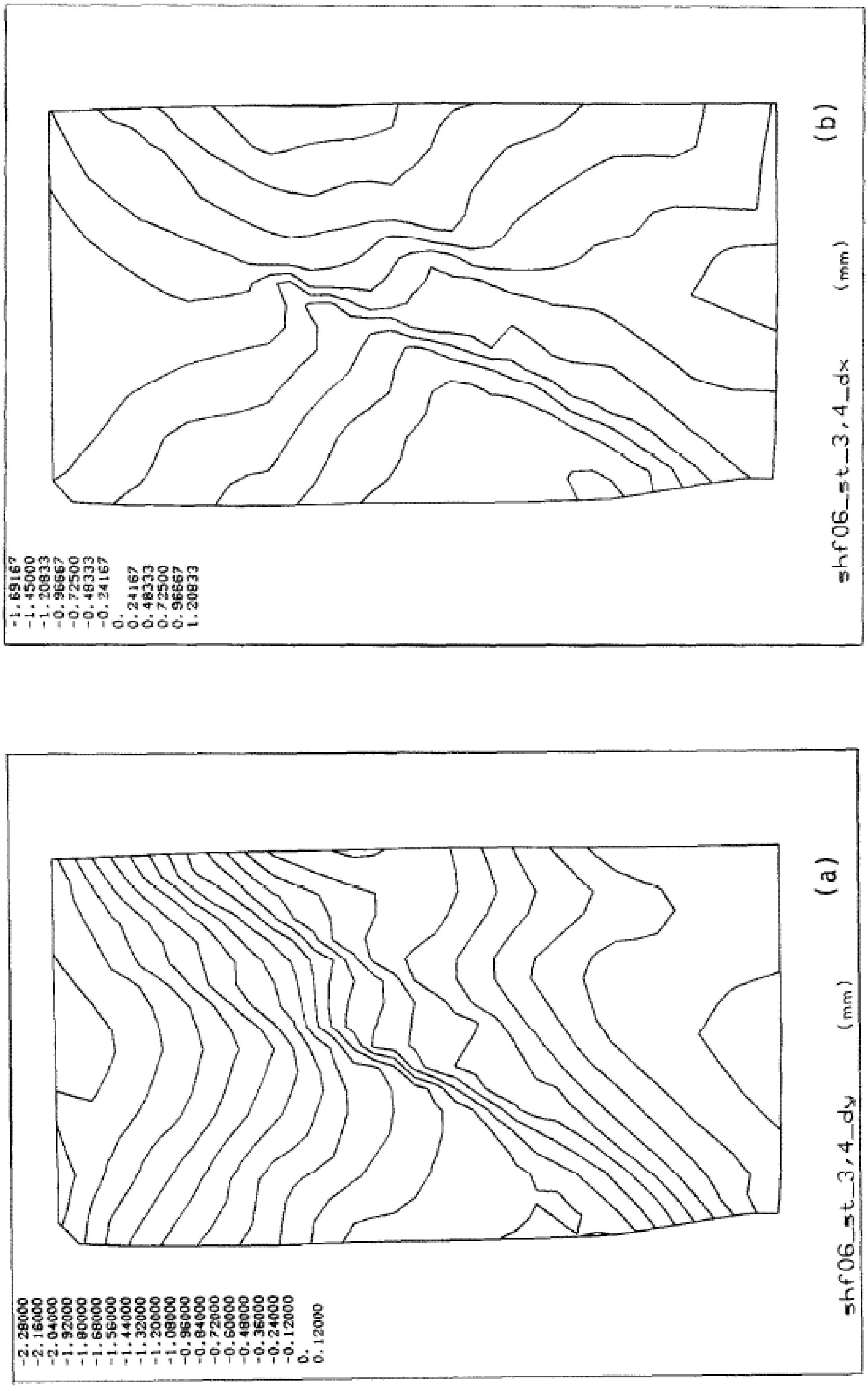

Fig. 2.86 Formation of the shear band in the pre-peak regime (increment 3-4). **a** Contours of equal axial displacement. **b** Contours of equal lateral displacement (**c** and **d** on next page) (after Desrues et al. 1985)

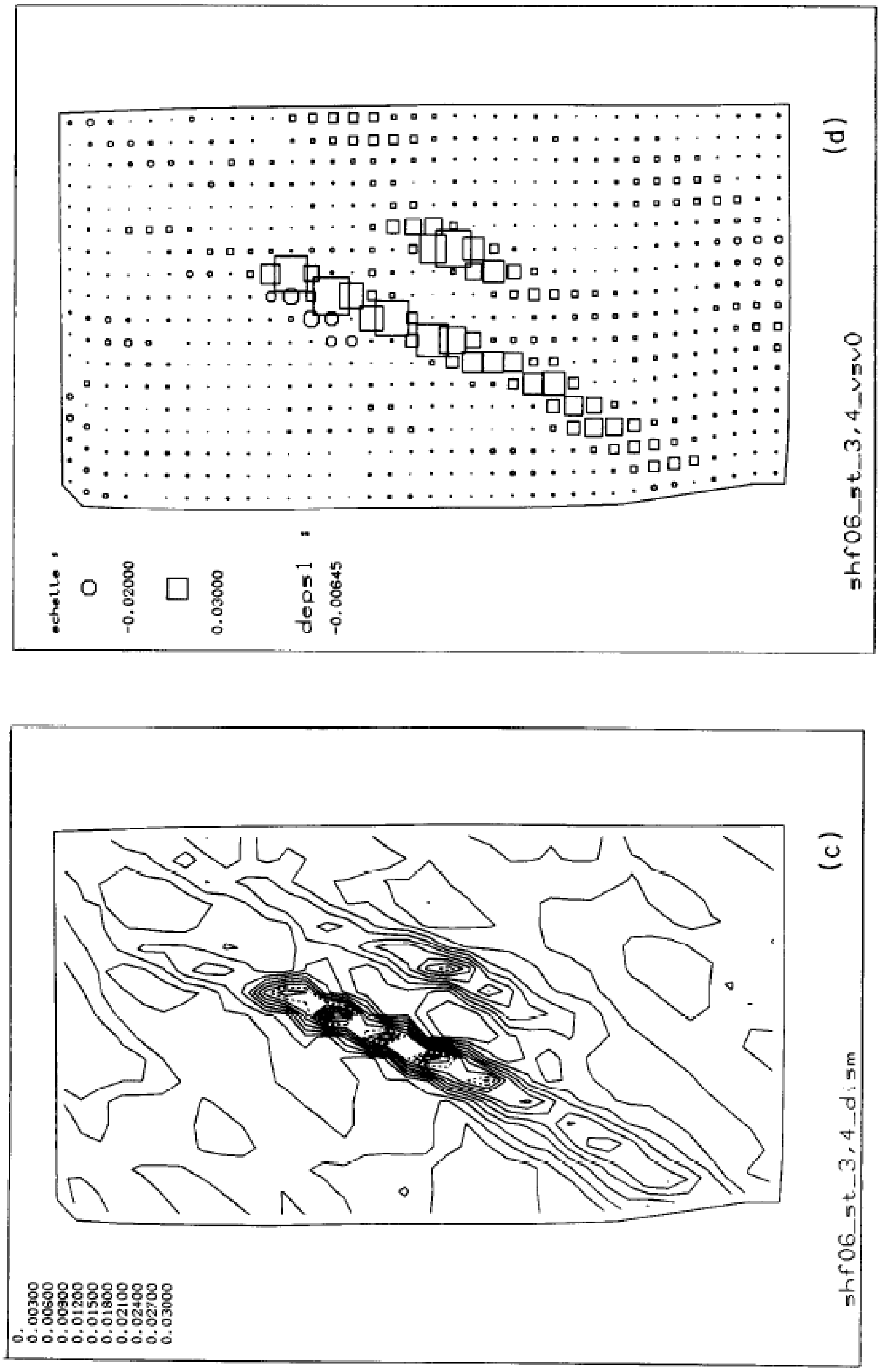

Fig. 2.86 Formation of the shear band in the pre-peak regime (increment 3-4). **c** Contours of equal incremental shear distortion dγ = (dε_1 - dε_2) / 2. **d** Local incremental volumetric strain indicated using square symbols with size proportional to the incremental strain magnitude (**a** and **b** on previous page) (after Desrues et al. 1985)

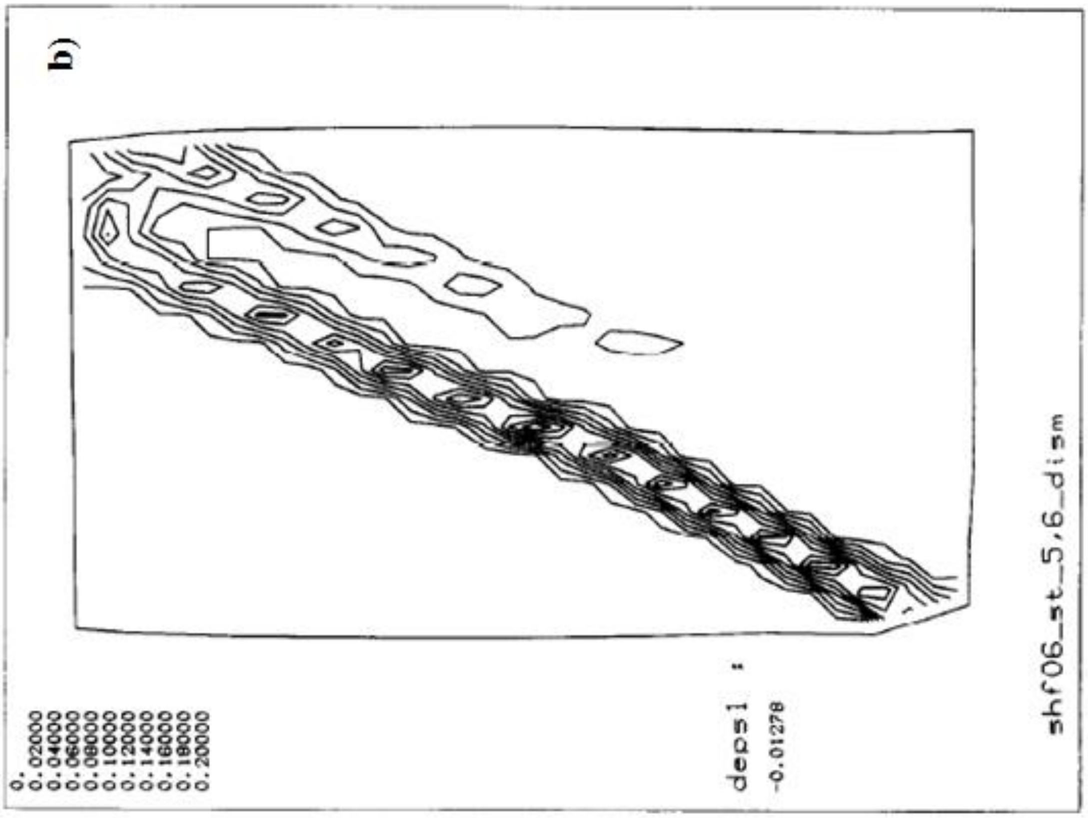

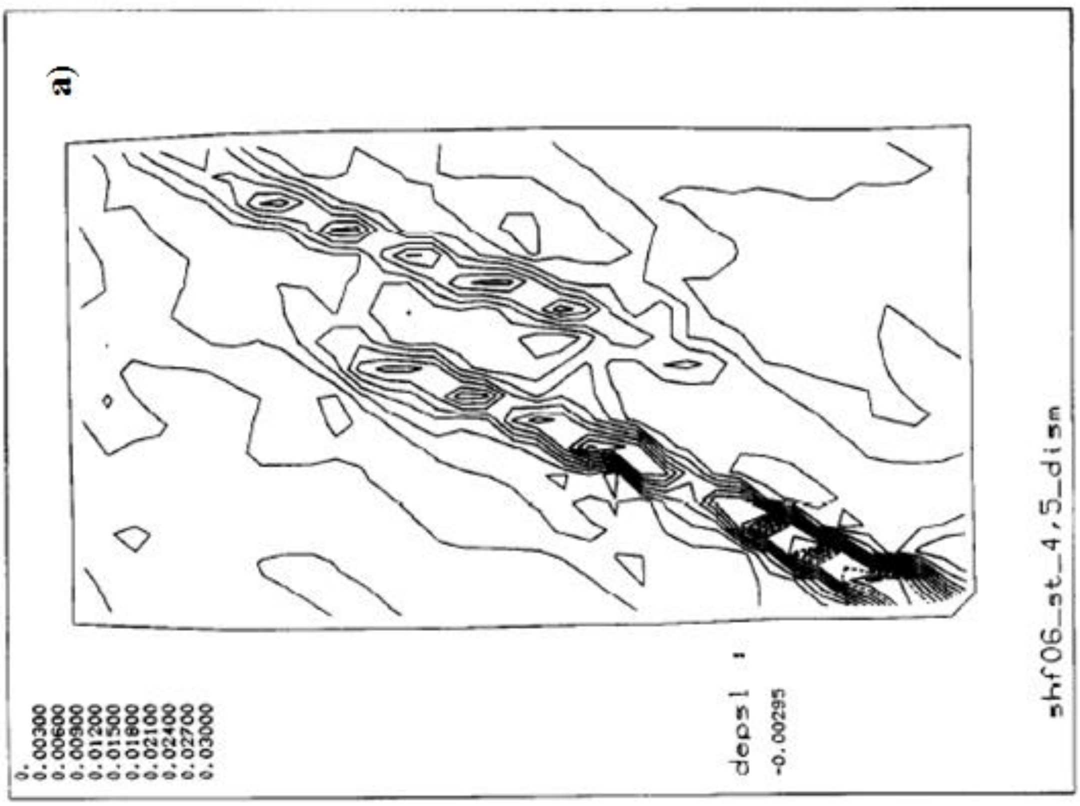

Fig. 2.87 Contours of equal incremental shear distortion indicating the propagation of the shear band: **a** during the post-peak increment 4-5, **b** during the post-peak increment 5-6 (after Desrues et al. 1985)

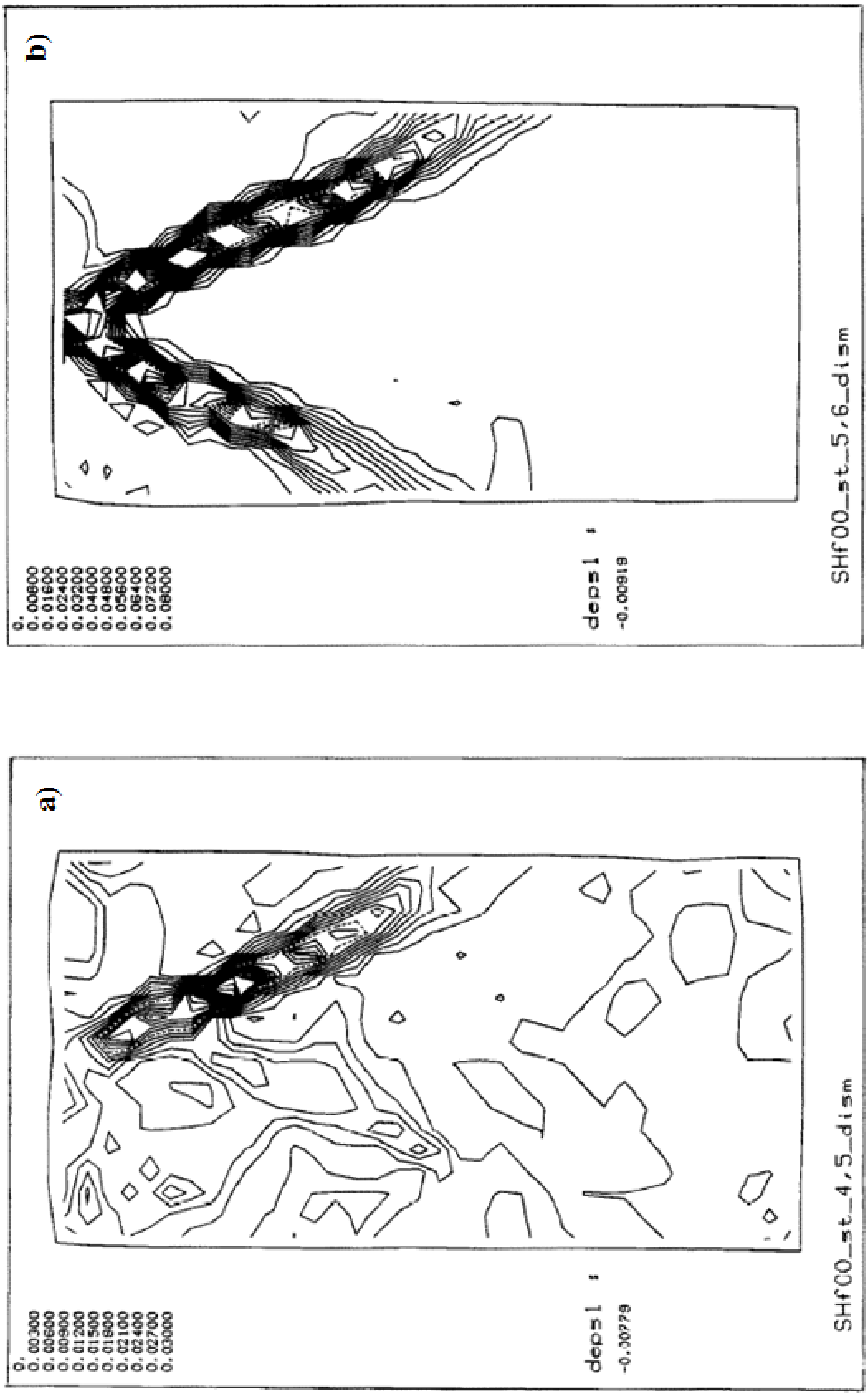

Fig. 2.88 Experimental evidence proving the reflection of a propagating shear band on a rigid boundary: **a** contours of equal incremental shear distortion during the increment 4-5, **b** contours of equal incremental shear distortion during increment 5-6 (after Desrues et al. 1985)

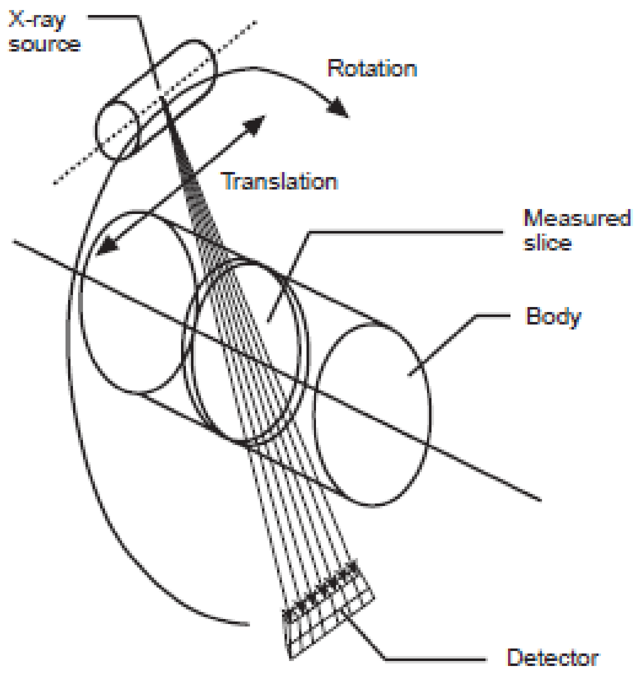

Fig. 2.89 "Computed tomography is based on the recording of a set of attenuation profiles of a collimated X-ray beam through a body: each profile is obtained by translation of the beam, and the set of profiles, by rotation of the beam direction in a plane perpendicular to the axis of the measurement field, and the procedure results in a radiographic density map of a slice of the body, whose thickness depends on the width of the beam" (figure and caption after Desrues et al. 1996)

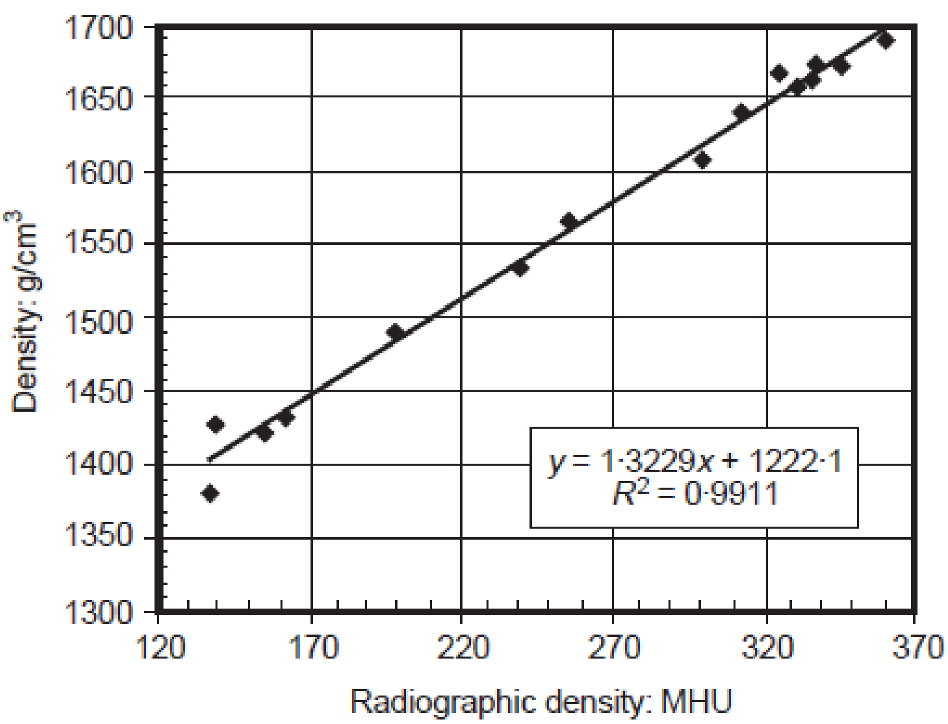

Fig. 2.90 Calibration of Hostun sand's mass density against radiographic density. The mass density is the total mass over the specimen volume, while the radiographic density is acquired by the average over the specimen (after Desrues et al. 1996)

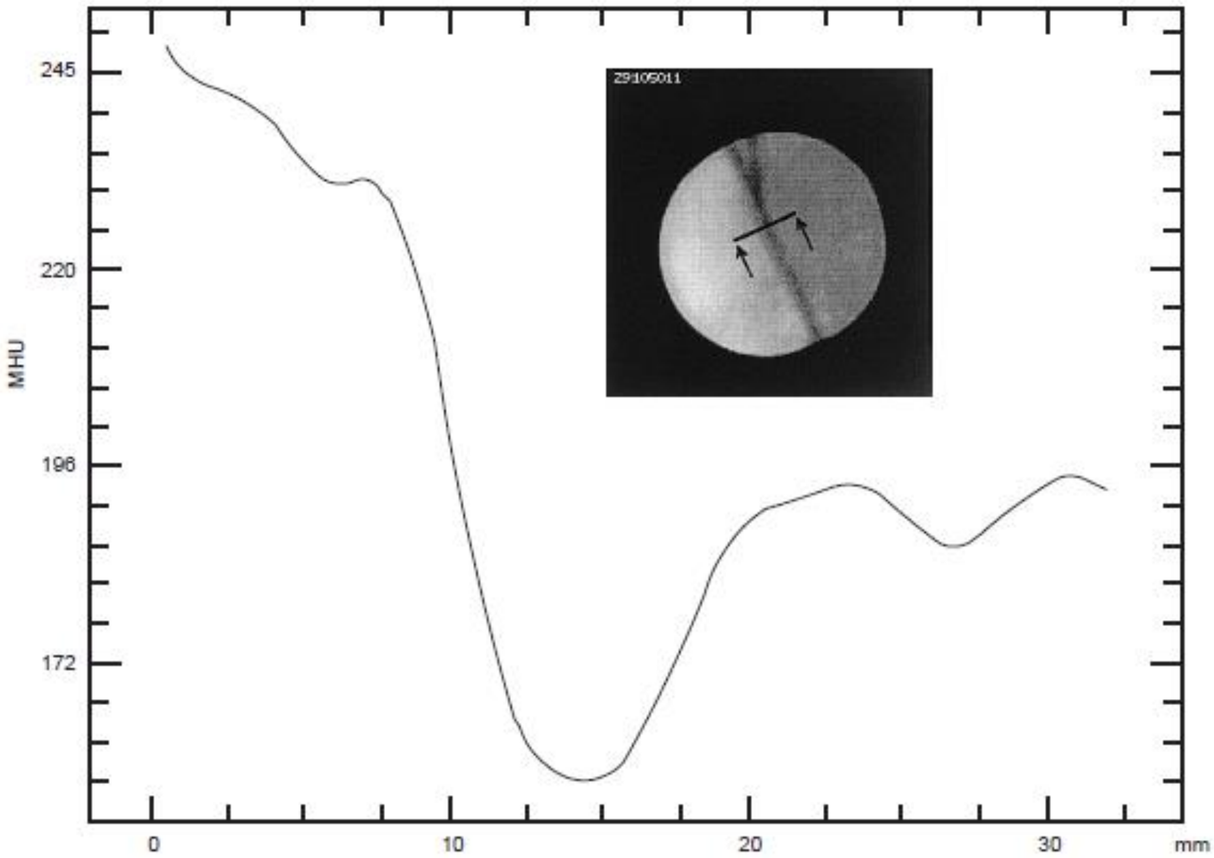

Fig. 2.91 Density profile along a line that crosses the shear band and density map of a cross section of a dense sand specimen. The line along which the density profile is displayed is indicated on the density map (after Desrues et al. 1996)

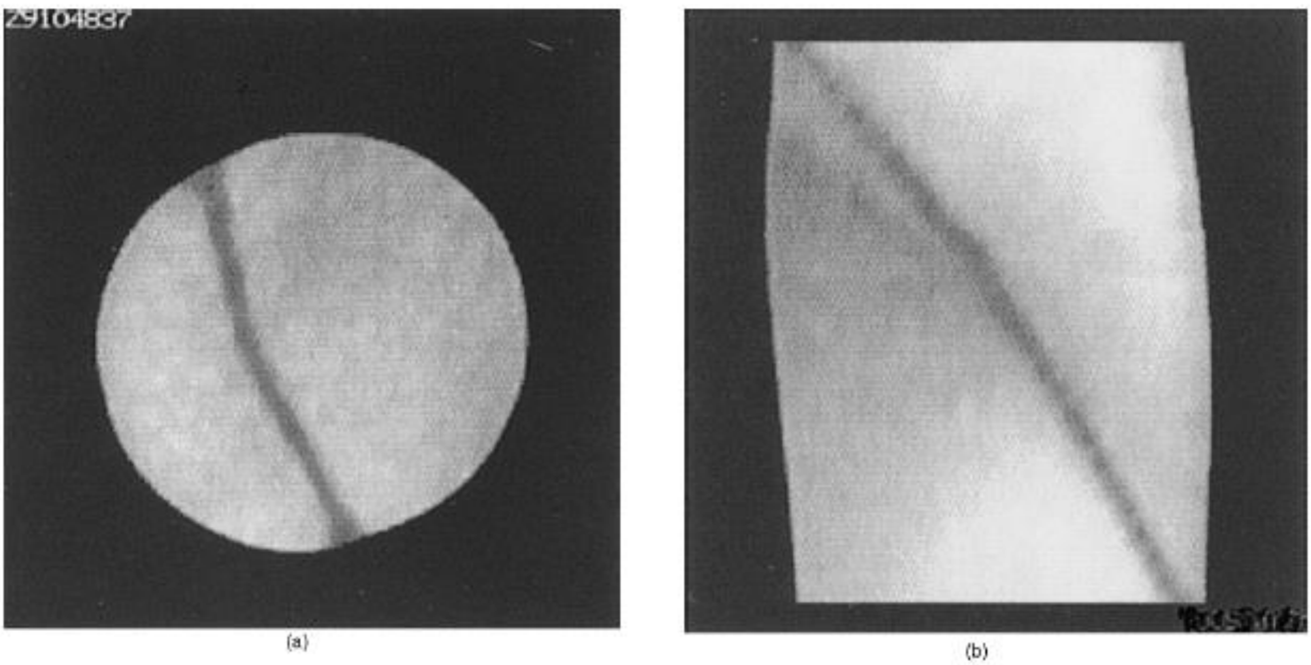

Fig. 2.92 The trace of the shear band in Specimen rfdt4 (dense specimen with h_o / d_o = 196 / 101 mm / mm and non-lubricated ends), at global axial strain ε_a = 13%, in a section: **a** perpendicular to the specimen's axis, located 72 mm above the bottom platen initially, **b** containing the specimen's axis (after Desrues et al. 1996)

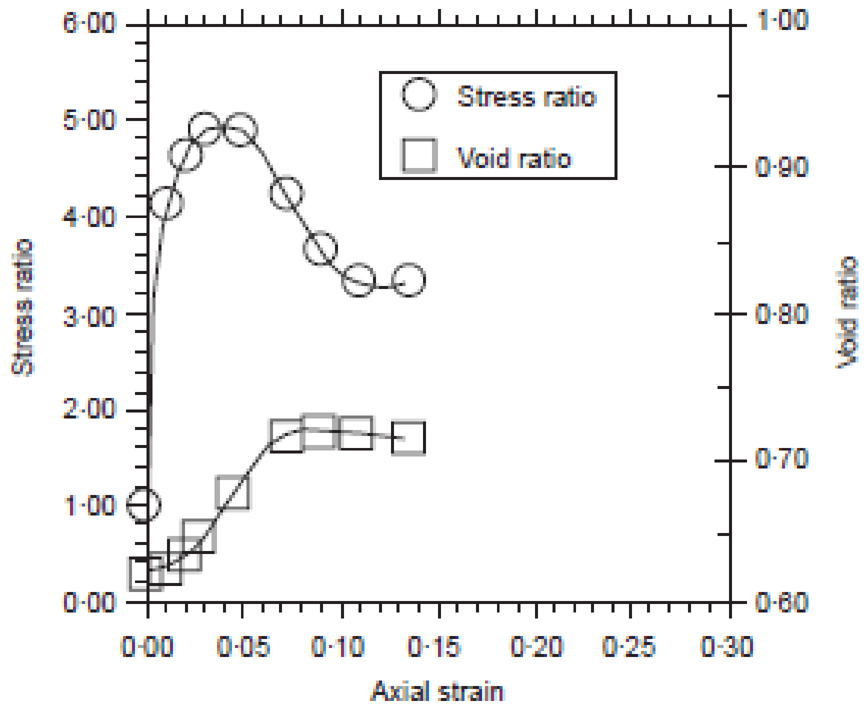

Fig. 2.93 Evolution of the stress ratio and global void ratio with global axial strain in test rfdt4 (on a dense specimen with h_o / d_o = 196 / 101 mm / mm and non-lubricated ends) (after Desrues et al. 1996)

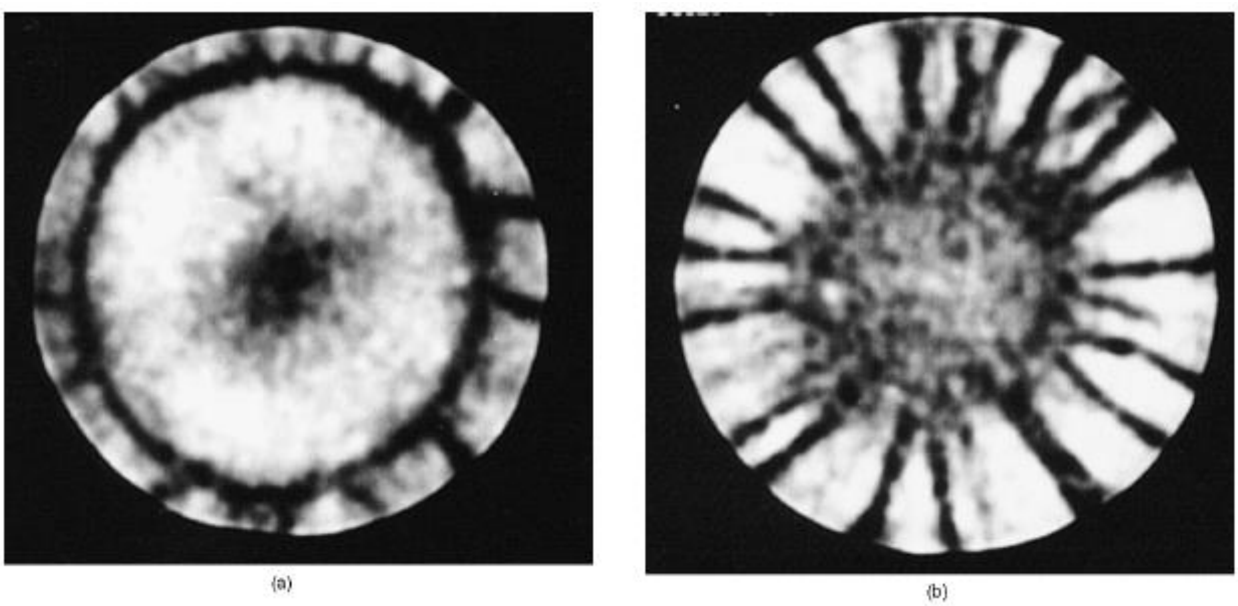

Fig. 2.94 Two computed tomography images at different cross-sections of Specimen hfdt1 (dense specimen with h_o / d_o = 100 / 100 mm / mm and non-lubricated ends) showing complex localisation patterns. Cross-section: **a** near the upper platen (80 mm from the bottom platen) and **b** at middle height (50 mm from the bottom platen) between the two platens at axial strain ε_a = 13% (after Desrues et al. 1996)

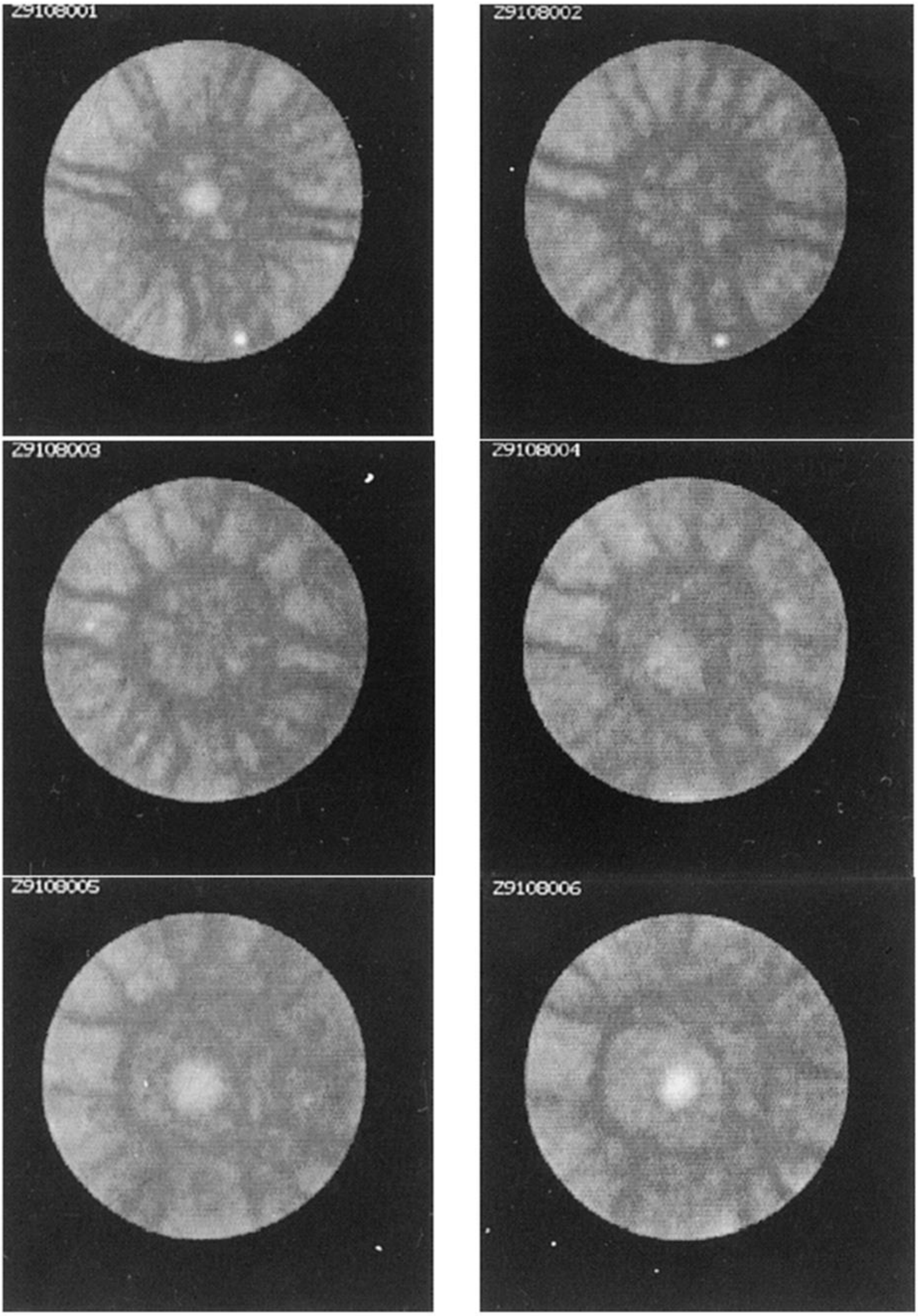

Fig. 2.95 Six computed tomography images at different cross-sections of Specimen rfdt8 (dense specimen with h_o / d_o = 100 / 100 mm / mm, lubricated ends and an embedded soft perturbation) revealing complex localisation patterns. Cross-sections located at: **1** 4 mm, **2** 8 mm, **3** 12 mm, **4** 16 mm, **5** 20 mm, **6** 24 mm from the top platen (after Desrues et al. 1996)

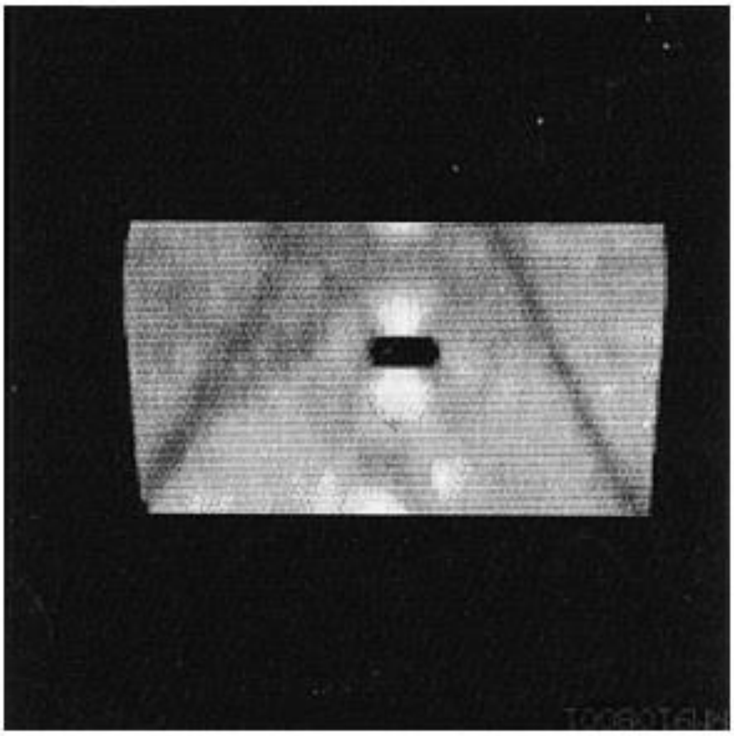

Fig. 2.96 Illustration of the void ratio field in a tomogram across the axis of Specimen rfdt8 (dense specimen with h_o / d_o = 100 / 100 mm / mm, lubricated ends and an embedded soft perturbation). It is noticed that the shear bands do not pass through the artificial perturbation that is embedded in the specimen's axis, shown as a dark disc in the middle of the image (after Desrues et al. 1996)

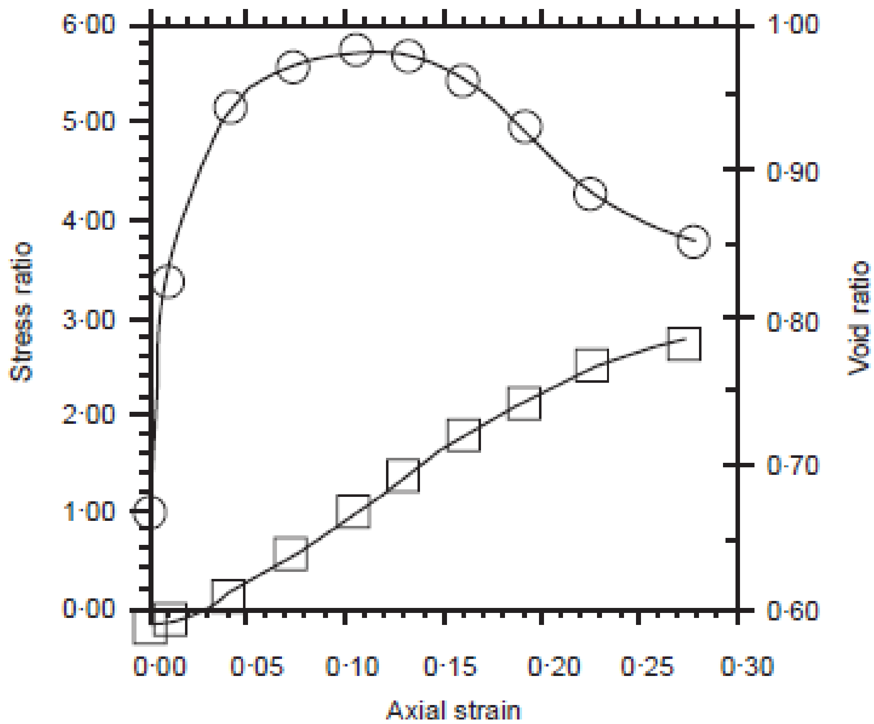

Fig. 2.97 Evolution of the stress ratio and void ratio with global axial strain in test rfdt8 (on a dense specimen with h_o / d_o = 100 / 100 mm / mm, lubricated ends and an embedded soft perturbation) (after Desrues et al. 1996)

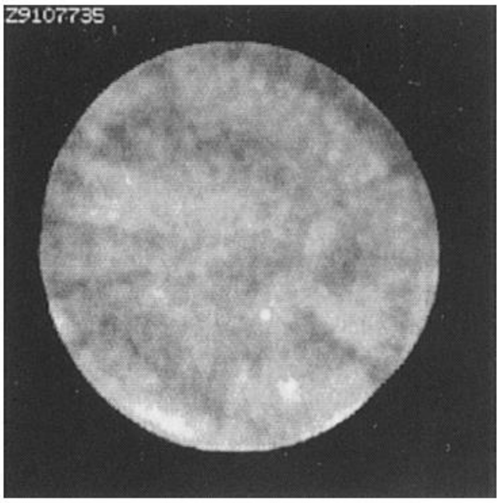

Fig. 2.98 Patterns of weak localisation in Specimen rflt2 at $\varepsilon_a = 42\%$ (loose specimen with $h_o / d_o = 100 / 100$ mm / mm and lubricated ends) (after Desrues et al. 1996)

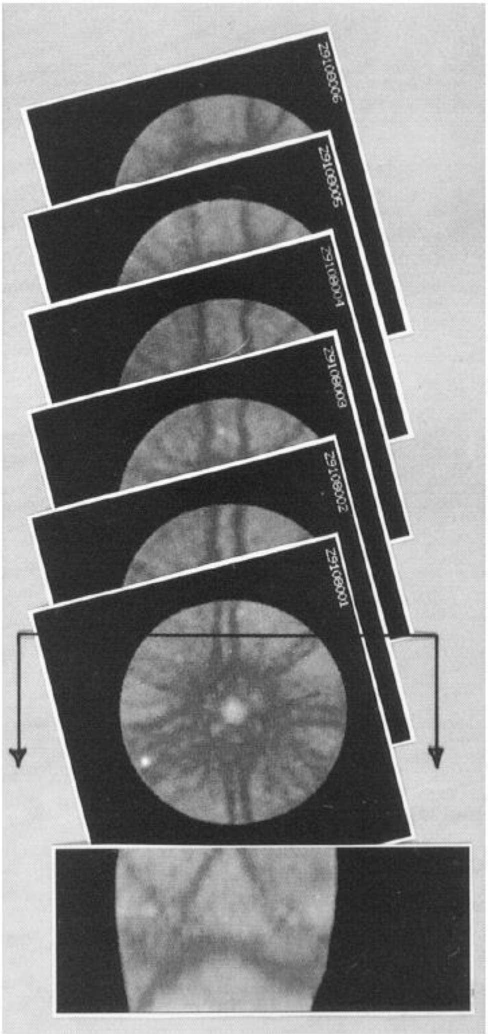

Fig. 2.99 "Localisation patterns in Specimen rfdt8: reconstruction of the density of the specimen on a plane parallel to the axis, and perpendicular to a pair of localization planes (bottom picture shows the inverted V produced by the two associated planes intersecting on the top platen; the trace of the cone appears as a parabola oriented towards the lower platen)" (caption and figure after Desrues et al. 1996)

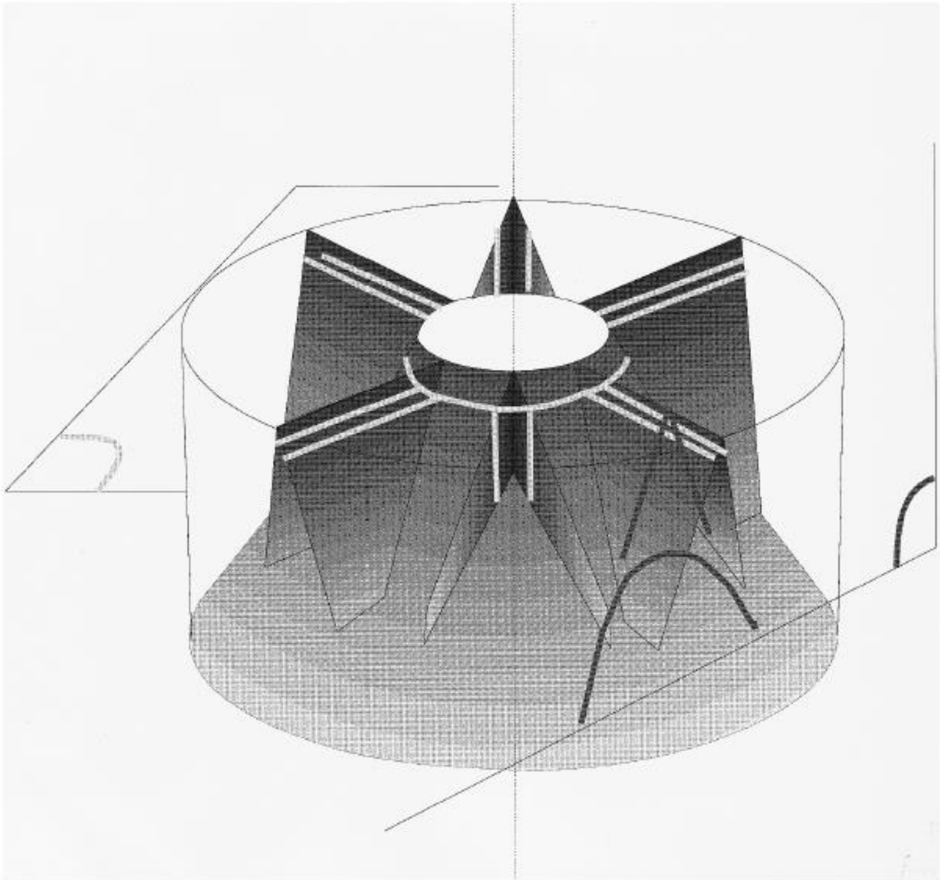

Fig. 2.100 Geometrical interpretation of the generic localisation patterns observed in Specimen rfdt8 (after Desrues et al. 1996)

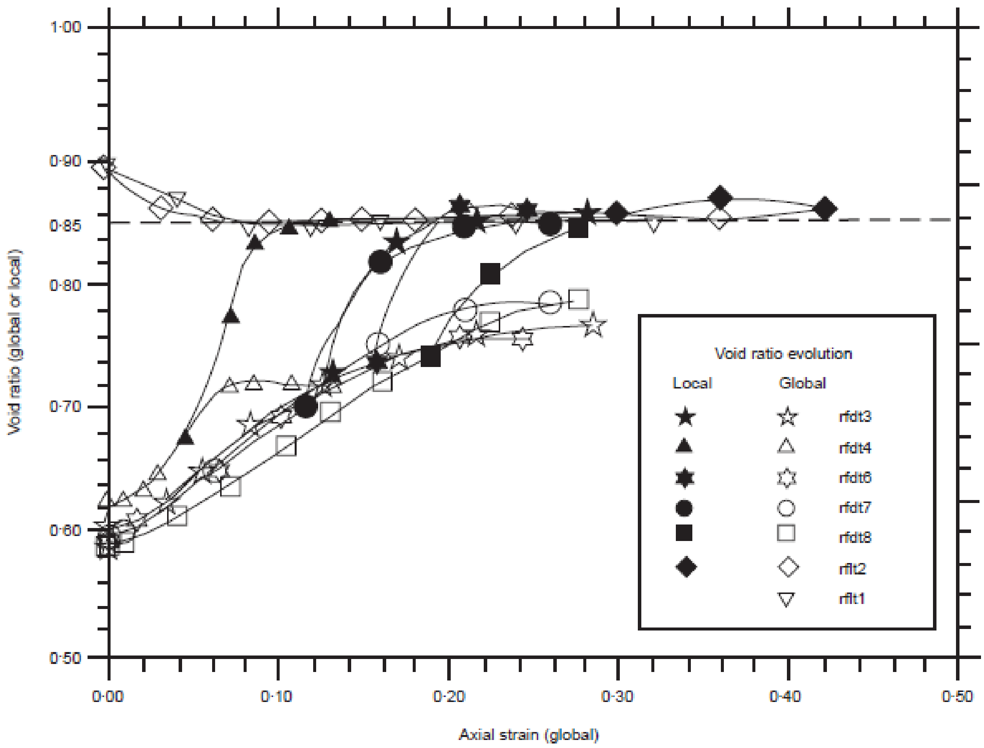

Fig. 2.101 Evolution of the global and local void ratio with global axial strain of loose and dense Hostun RF sand specimens subjected to triaxial compression under $\sigma'_3 = 60$ kPa (after Desrues et al. 1996)

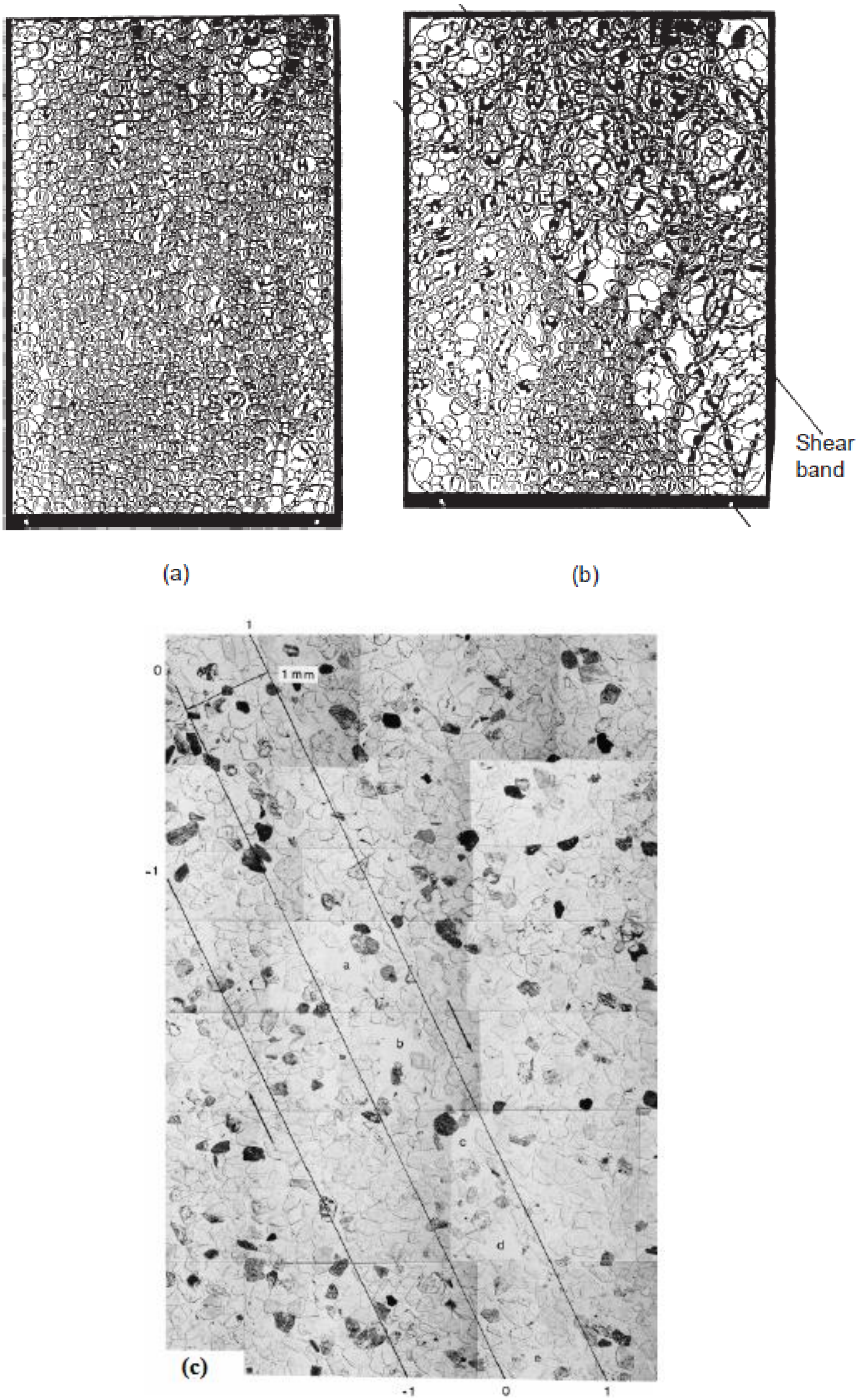

Fig. 2.102 Shear band microstructure exhibiting large voids between buckled grain columns: **a** photoelastic picture of a compressed rod assembly at peak stress state, **b** photoelastic picture of a compressed rod assembly at residual state, **c** microscope image of a thin section of stabilised Toyoura sand showing a periodic appearance of large voids (marked with the letters a-e) along the shear band (delimited by the lines 0-0 and 1-1) (after Oda and Kazama 1998; pictures **a** and **b** after Oda et al. 1982)

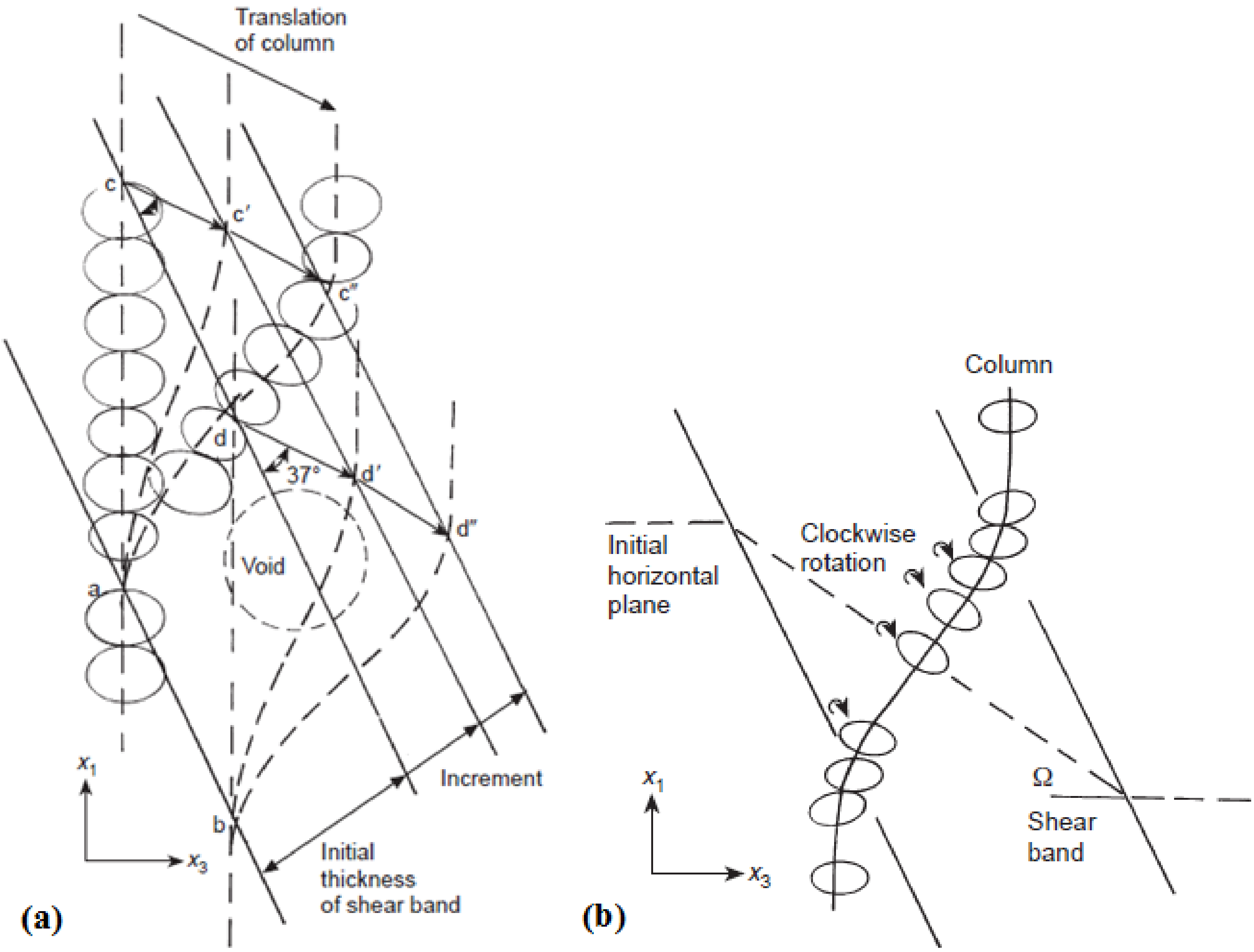

Fig. 2.103 Schematic illustration of the kinematics of grains and grain columns inside the shear band: **a** development of large voids between the buckled grain columns, **b** particle rotation in parallel with the corresponding rotation in the continuum sense (after Oda and Kazama 1998)

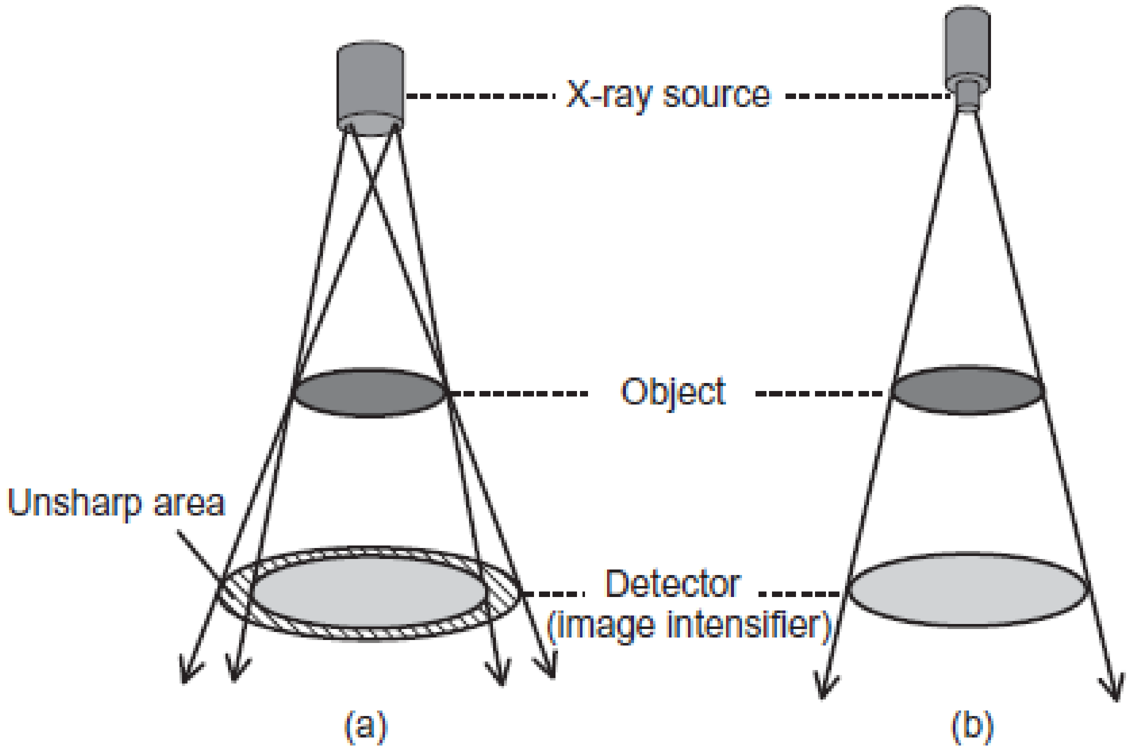

Fig. 2.104 Illustration of the difference between conventional and microfocus X-ray computed tomography. **a** Conventional X-ray apparatus. **b** Microfocus X-ray apparatus. Note that the size of the X-ray source affects drastically the spatial resolution (after Oda et al. 2004)

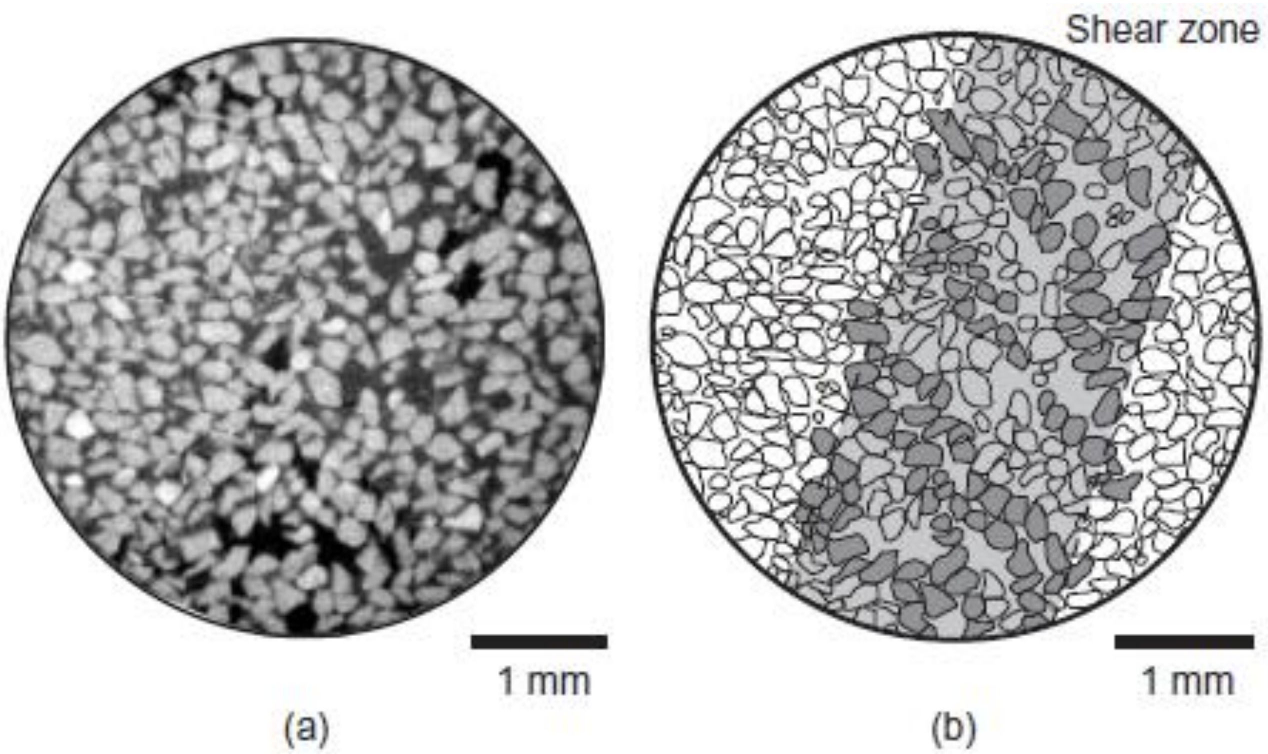

Fig. 2.105 Microstructure of sand in a shear band. **a** Image produced by X-ray μCT. **b** A sketch that shows schematically the column-like grain structures inside the shear band and the large voids developed between them (after Oda et al. 2004)

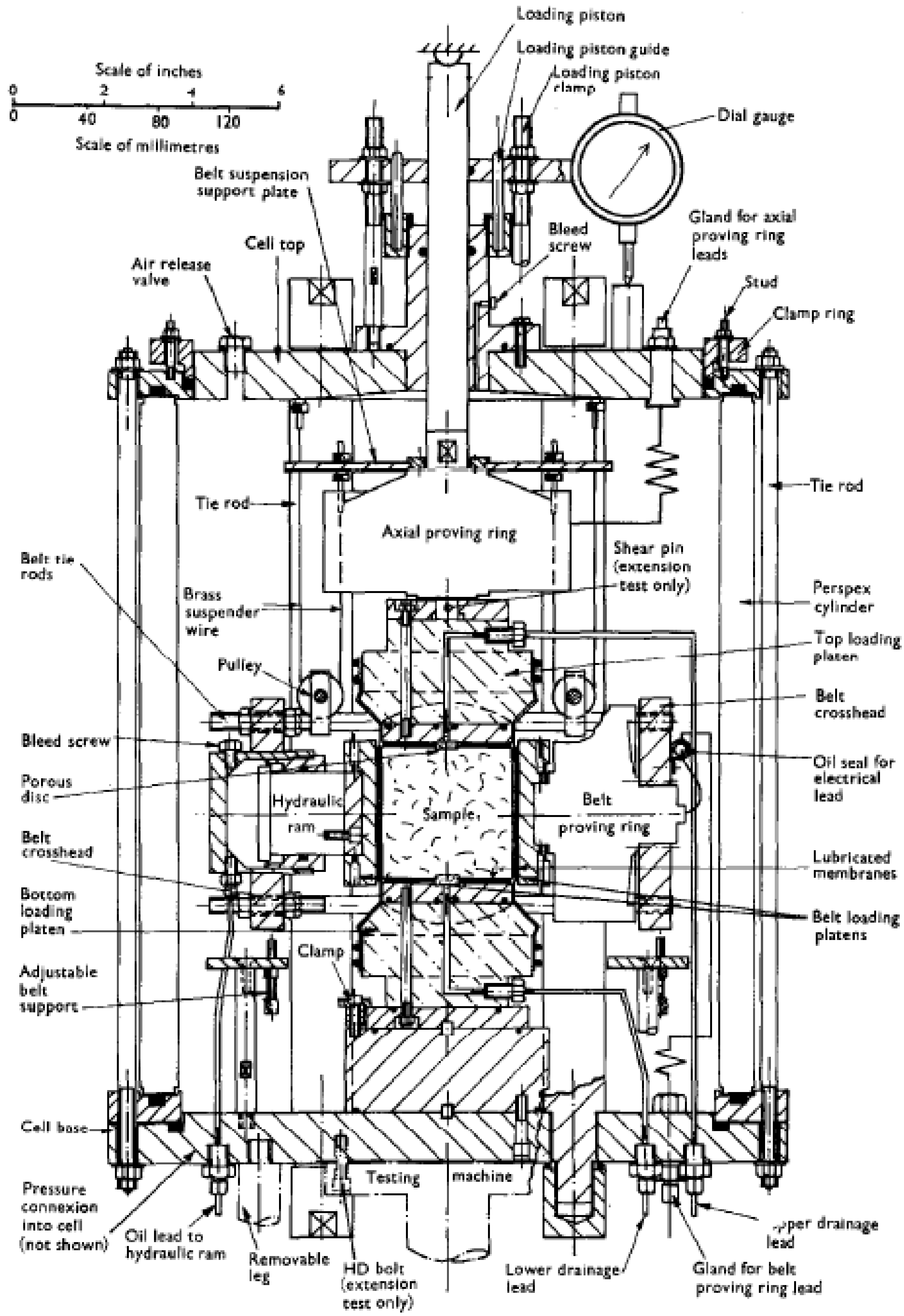

Fig. 2.106 The true triaxial apparatus for testing cubic / parallelepipedic specimens under the independent control of the three principal stresses (after Reades and Green 1976)

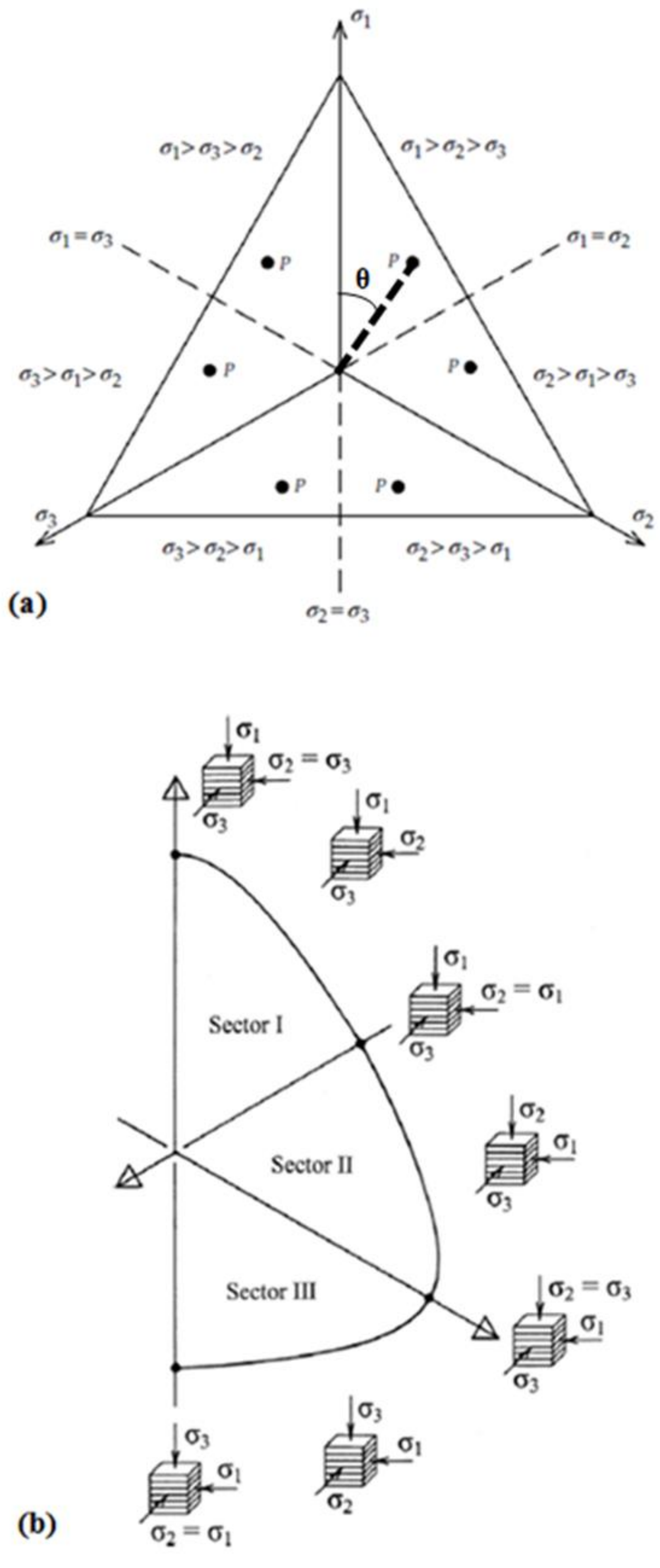

Fig. 2.107 True triaxial loading of cross-anisotropic sand: **a** stress - state point P located in each of the six sectors of the octahedral plane. The Lode angle θ indicates the direction of shear stress on the octahedral plane. **b** Schematic illustration of the direction of the stress principal axes with respect to the horizontal bedding planes. Note that the stress principal axes coincide with the material axes (after Lade 2007 and 2016)

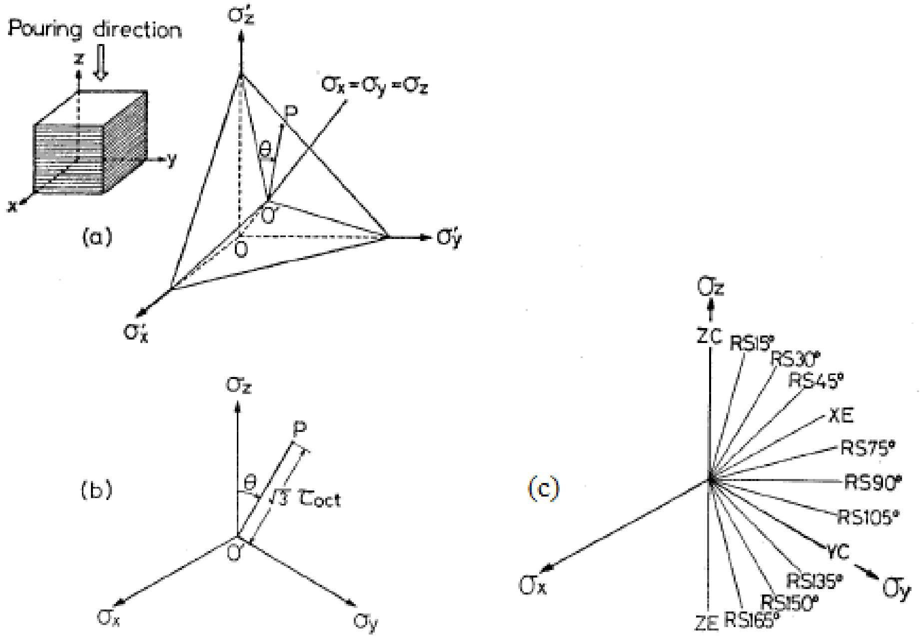

Fig. 2.108 a Stress - state point P of a specimen with horizontal bedding planes in the principal stress space. **b** Stress representations on the octahedral plane. **c** Radial stress paths on the octahedral plane (after Yamada and Ishihara 1979)

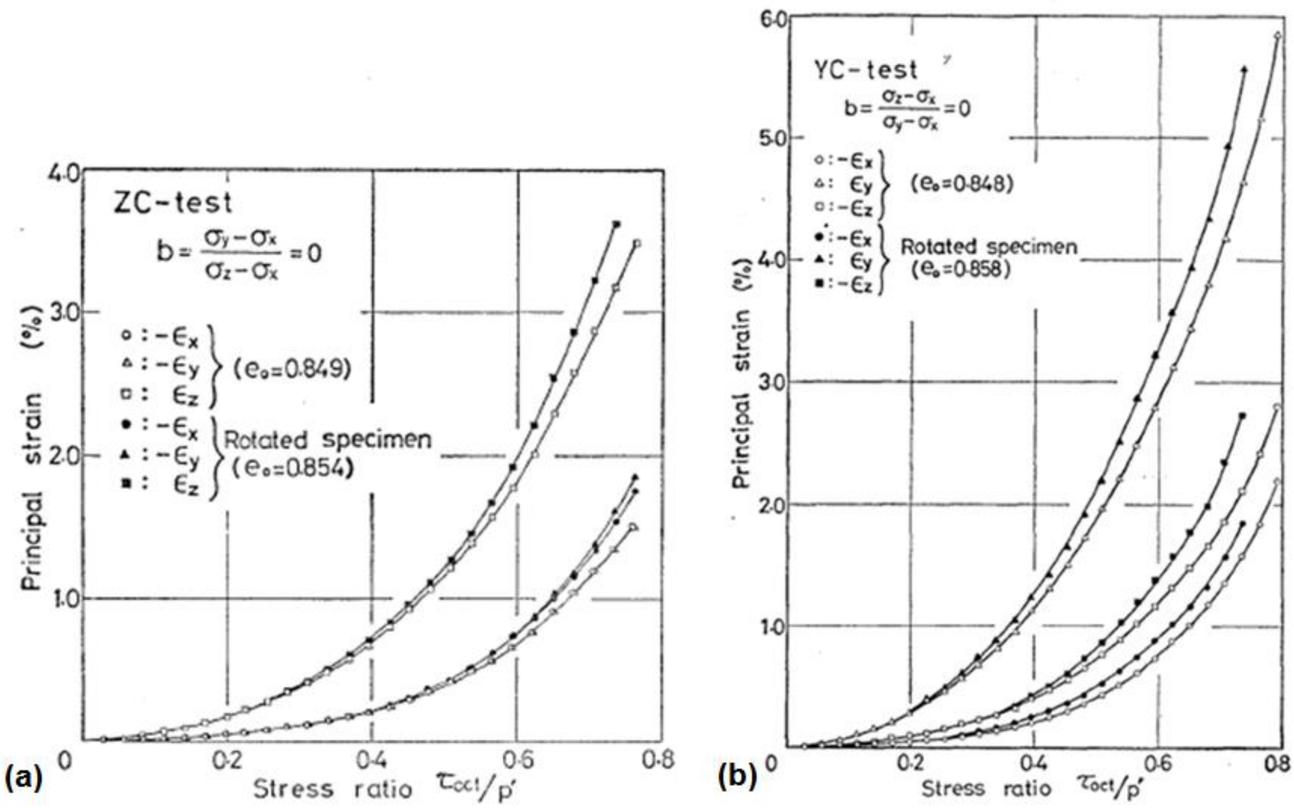

Fig. 2.109 Principal normal strains versus stress ratio: **a** in compression ZC-test with $\sigma_z = \sigma_1$, $\sigma_x = \sigma_3 = \sigma_y = \sigma_2$, b = 0 and θ = 0°, **b** in compression YC-test with $\sigma_y = \sigma_1$, $\sigma_x = \sigma_2 = \sigma_z = \sigma_2$, b = 0 and θ = 120° (after Yamada and Ishihara 1979)

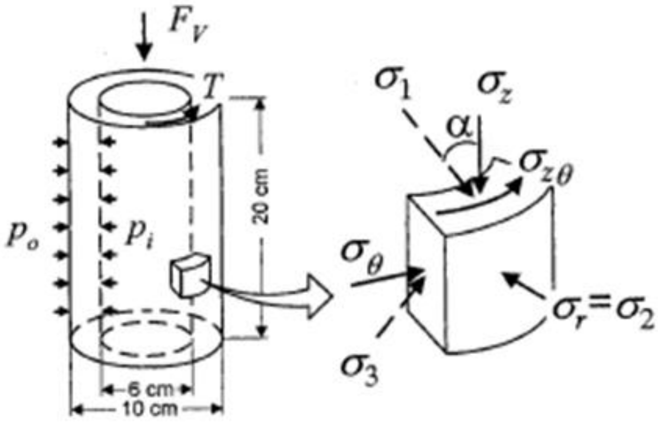

Fig. 2.110 The hollow cylinder torsional shear apparatus for testing specimens under the independent control of the magnitude of the three principal stresses and direction of the major principal stress with respect to the vertical (photo after Towhata 2008; figure after Yoshimine et al. 1998a)

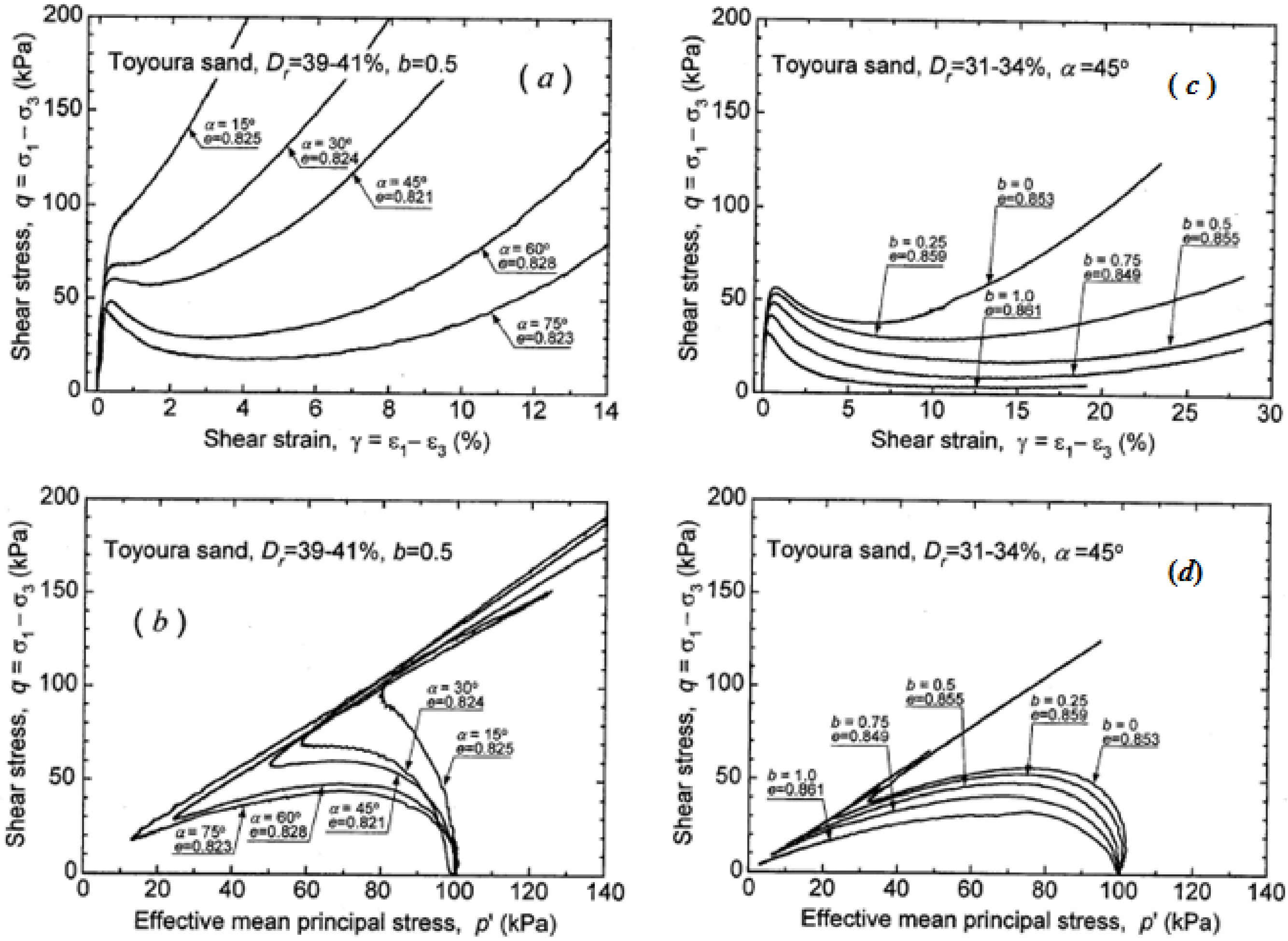

Fig. 2.111 Influence of the principal stress direction, indicated by the angle α, on the undrained behaviour of gravity deposited sand: **a** stress - strain curves, **b** effective stress paths. Influence of the intermediate principal stress parameter, b, on the undrained behaviour of gravity deposited sand: **c** stress - strain curves, **d** effective stress paths (after Yoshimine et al. 1998a)

CHAPTER 3: CRITICAL STATE OF SANDS

3.1 INTRODUCTION

Critical state (CS) of a granular material is the observed physical phenomenon of shear deformation at constant stress and volume under continuing shearing. The CS can be used as a reference state for understanding and modelling the elastoplastic behaviour of granular materials within the *Critical State Soil Mechanics* (CSSM) framework. The constitutive models developed within the CSSM traditionally treat the granular materials as elastoplastic continuum media exhibiting the property of dilatancy. However, recent studies have shown that the microstructure (fabric) affects the mechanical behaviour of granular materials and proposed the incorporation of fabric-related quantities into the CSSM framework and constitutive models.

The present chapter presents the experimental evidence that supports the concept of CS of granular materials and especially of sands, while it also discusses the points of criticism. It is shown that the dilatancy of sands can be correlated to a state parameter that is determined with reference to the ultimate state (CS). It is also shown that the dilatancy is highly affected by the anisotropy of fabric which evolves as the sand is sheared towards the CS. The *Anisotropic Critical State Theory* (ACST) introduced by Li and Dafalias (2012) proposes a revision of the classical *Critical State Theory* (CST) (Roscoe et al. 1958, Schofield and Wroth 1968) in order to "render the theory complete by incorporating in its premises the role of fabric". This chapter presents the way in which the fabric effects are considered in the new ACST and describes the thought experiment conceived by Dafalias (2016) in order to prove that the ACST is a necessary enhancement of the classical CST.

3.2 THE CONCEPT OF CRITICAL STATE OF COHESIVE AND NON-COHESIVE SOILS

Roscoe et al. (1958) established the concept of critical state (CS) of cohesive and non-cohesive soils. Regarding the behaviour of clays, they found that there exists a *State Boundary Surface* (SBS) in the q - p' - e space that separates the possible from the impossible states of clay sheared under drained or undrained conditions. The SBS comprises two other surfaces, namely the *Hvorslev surface* and the *Roscoe surface*, which meet at the *Critical State Line* (CSL), as can be seen in Fig. 3.1; the CSL consists of the ultimate states of clay reached under monotonic loading. In the article by Roscoe et al. (1958) the term *Critical Voids Ratio Line* (CVR Line) was used, as will be discussed later. The Hvorslev surface (Hvoslev 1937) is a *ruled surface* of parallel straight lines that limits the states of *overconsolidated clay* (OC) in the q - p' - e space (Roscoe et al. 1958, Atkinson and Bransby 1978). The stress path of an overconsolidated clay specimen progresses almost vertically in stress space until it reaches the Hvorslev surface, where the material fails. Afterwards, it traverses the Hvorslev surface until it reaches the CSL. On the other hand, the stress paths of tests on *normally-consolidated clay specimens* (NC) form the curved portion of the SBS that links the *Normal Consolidation Line* (NCL) with the CSL, namely the Roscoe surface. Consequently, the stress path of a NC clay specimen moves from the NCL towards the CSL, traversing the Roscoe surface. NC clay fails when the critical state is reached. The clay, either NC or OC, deforms continuously in shear under constant mean effective stress, deviator stress and volume (or pore-water pressure) as far as it remains in critical state.

The stress path of an undrained test remains on a constant-e plane in the q - p' - e space, while the respective stress path of a drained test crosses an infinite number of constant-e planes as it moves towards the critical state line. The two types of stress path become directly comparable if the stresses are scaled by division by the *equivalent mean effective stress* p'_e (Atkinson and Bransby 1978). p'_e is the stress that corresponds to the current void ratio e via the equation of the normal consolidation line, irrespective of the current stress p'. It is noticed that in the case of clays, each void ratio is uniquely related to a mean effective stress on the locus of the iso-NCL when the material is subjected to virgin isotropic consolidation up to this stress. Figure 3.2 shows the drained and undrained stress paths of triaxial tests on NC and OC clay specimens in the dimensionless stress space q / p'_e - p' / p'_e. Alternatively, a boundary energy correction was applied by Roscoe et al. (1958) in the case of drained tests in order to obtain a drained SBS which can be compared with the undrained SBS; this correction will be discussed next.

The stress paths of the NC specimens shown in Fig. 3.2 progress from the iso-NCL (point N) towards the CSL (point C) traversing across the Roscoe surface, which is unique for both drained and undrained tests. Moreover, the Roscoe surface in the dimensionless stress space is unique irrespective of the initial mean effective stress and void ratio of the different specimens tested. The straight line TC in Fig. 3.2 represents the Hvorslev surface that is the locus of *failure points* of OC specimens. Hvorslev (1937) found that the peak strength of OC specimen is a function of the mean effective stress and void ratio of the specimen *at failure*. It is noted that the Hvorslev surface was originally defined based on fully-drained tests on saturated clays in the shear box. However, the experimental results of Parry (1960) indicate that the Hvorslev surface captures the failure states of OC specimens in both drained and undrained triaxial tests (see Atkinson and Bransby 1978). The paths of heavily overconsolidated specimens shown in Fig. 3.2 do not reach the CSL due to strain localisation; it can be suggested that the localisation behaviour of heavily overconsolidated clay is somewhat similar to that of dense sand.

Roscoe et al. (1958) investigated the validity of the concept of *Critical Voids Ratio Line* (CVR Line) for clays and sands. The existence of the CVR line was firstly indicated by Casagrande (1936 and 1938), who observed that when loose and dense sand specimens are sheared under drained triaxial conditions at the same confining stress they reach a common ultimate void ratio at large strain. Loose sand contracts and reaches the critical void ratio, e_c, while dense sand initially contracts and then dilates until it reaches the same void ratio e_c, which is unique for a given effective confining stress (see Section 2.2). Taylor (1948) suggested that if two sand specimens with the same void ratio are subjected to undrained (constant-*e*) loading at different initial mean effective stresses then they undergo such a pore-water pressure build up that they reach the critical state at the same ultimate effective stress corresponding to this specific void ratio (see also Been et al. 1991, Verdugo and Ishihara 1996). Roscoe et al. (1958) were the first to validate Casagrande's suggestions for both sands and clays; more importantly, they showed that the CVR definitions become more explicit if the concept of loading paths in the q - p' - e space is used together with the concept of the state boundary surface (or yield surface).

Roscoe et al. (1958) analysed the results from the triaxial tests on Weald Clay specimens performed at Imperial College, London, by Gilbert (1954) and epitomised by Henkel (1956). Figure 3.3 shows the state boundary surface (SBS), the normal consolidation line (NCL) and the critical voids ratio line (CVR line) for Weald Clay together with two undrained and two drained loading paths. A three-dimensional view in the q - p' - w space is displayed. The undrained loading paths PRQ (η = 1; η is the *overconsolidation ratio*, here) and P''Q (η = 8) remain on the constant-*w* plane (w = 20.7%), while the drained loading paths PR'Q (η = 1) and P''R''Q'' (η = 8) begin from the plane with $w \approx$ 20.7% and afterwards the former shows contraction while the latter dilation towards the critical void ratio. The critical void ratio is different in the case of the two drained tests because the mean effective stress is different. The loading of specimen with η = 8 was terminated before reaching the critical state, while shear banding inhibited the progression of the loading paths of specimens with η > 8 (not shown in Fig. 3.3) towards the CVR line. It is noted that the water content, *w*, is the ratio of water mass over solids mass, the specific gravity of soil particles, G_s, is the ratio of solids density over water density and the relation between *w* and *e* is: (w / 100)% = e / G_s, so *w* and *e* can be used interchangeably.

Figure 3.4 shows in detail the undrained loading paths of triaxial tests on Weald Clay in a constant water content (w = 20.7%) section in the q - p' - w space. It is noted that the stress paths of specimens with slightly different initial water content can be properly compared in the q / p'_e - p' / p'_e space (Atkinson and Bransby 1978). It can be seen that the loading paths progress towards the SBS and then traverse the SBS towards the CVR Line at point Q. The path of the NC specimen (consolidated to initial stress p' = 60 lb. / sq.in. = 413.7 kPa) follows the curved route PRQ on the

Roscoe surface, turns to the left and progresses towards Q. On the other hand, the paths of the heavily overconsolidated specimens (η > 8) move upwards, turn to the right and become tangential to the Hvorslev surface VUQ, as they progress towards Q. It is noted that the *extension cut-off line*, which corresponds to zero effective radial stress under triaxial compression and limits the Hvorslev surface at low p' / p'_e (Wood 1990), is shown in Fig. 3.2 but not in Figs 3.3 and 3.4. The heavily overconsolidated specimens with η > 8 do not reach the CVR line due to strain localisation.

Roscoe et al. (1958) analysed also the results from drained triaxial tests on specimens of Weald Clay, performed by Gilbert (1954). They investigated if the drained loading paths climb up and traverse the same SBS as the undrained paths, and if they terminate at the same CVR line. The drained loading paths become comparable with the undrained when a *boundary energy correction* is applied to account for the stress - dilatancy effect on the boundary work done by or against the cell pressure σ_3 (see also Taylor 1948, Penman 1953, Bishop 1954). The corrected deviatoric stress, q, is acquired if the quantity $\sigma_3\, d\varepsilon_{vol} / d\varepsilon_1$ is subtracted algebraically from the applied stress difference (σ_1 - σ_3); the correction factor is taken negative when the specimen contracts, thus, the corrected q is higher than the applied (σ_1 - σ_3) in this case. Figures 3.5 and 3.6 show the projections of the drained loading paths of NC (η = 1) and OC (η = 8) Weald Clay, respectively, on the q - p', w - p' and w - q planes. Both the applied stress path and the loading path after the boundary energy correction are shown. The normal consolidation curve is also indicated with a broken-dotted line, while the undrained state boundary surface is indicated with a broken line. The state points projected on the w - p', q - p' and w - q planes have the indices “1”, “2” and “3”, respectively.

It is apparent in Fig. 3.5 that the corrected drained loading path of NC specimen essentially coincides with the undrained SBS (in the Roscoe surface section) and terminates at the CVR line. A minor discrepancy is due to the difference in the initial water content value in the drained and undrained tests and due to the mild contraction still evidenced when the drained test was terminated at point Q’ (Roscoe et al. 1958). Consequently, Q’ is very close to point X’ that lies near the CVR line determined by undrained tests. On the other hand, the loading path of OC specimen (η = 8) shown in Fig. 3.6 stops at point Q’’ away from the CVR because the test was terminated just after failure while the specimen was still expanding (Roscoe et al. 1958). However, Roscoe et al. (1958) stated that “had the test been continued the loading path could be expected to become tangential to X’’Y’’ and end at X’’, when the sample would have reached an ultimate state”. It is noted that the curved line X’’Y’’ lies on the Hvorslev surface and X’’ lies on the CVR line obtained from undrained tests. Based on these observations, Roscoe et al. (1958) suggested that the drained and undrained state boundary surfaces coincide and that the ultimate points of drained tests confirm the same CVR line that applied to the undrained tests.

The unique critical voids ratio line (or critical state line) of Weald Clay in the *q - p' - w* space is described by the three projections on the reference planes shown in Fig. 3.7. The ultimate-state points from 25 drained tests with $\eta \leq 8$ (well-conditioned tests on uniformly deformed specimens) are projected on the three reference planes together with the CVR line obtained from undrained tests. The isotropic NCL in the *w - p'* plane is also displayed in Fig. 3.7b. It is noted that if a semi-logarithmic scale (i.e. *w* - ln*p'*) is used then the NCL is parallel to the CVR line and lies on the "wet" side of the latter. The common slope of the two lines is usually represented by the Greek letter λ, while the slope of the *swelling line* in the case of isotropic unloading is represented by the Greek letter κ. The agreement between the ultimate state points in the *q - p' - w* space obtained from both drained and undrained tests on NC and OC Weald Clay specimens is obvious. Roscoe et al. (1958) reported that the critical state concept was also verified experimentally for Supreme Kaolin, Wiener Tegel, Kleinbelt Ton, London Clay and the clays tested by Haefeli (1951).

Roscoe et al. (1958) investigated whether the critical state concept can be applied to non-cohesive granular materials as well. They suggested that in the case of sands, silts and other non-cohesive granular materials some considerable difficulties exist and impede the collection of reliable information at large strains; this information is needed to check the validity of the critical state concept. Specifically, the difficulties are related to the high *dilatancy potential* that non-cohesive granular materials typically exhibit; large strains are required to exhaust this dilatancy potential and reach the ultimate phase of continuous shear deformation at constant stress and volume, while strain localisation frequently occurs under severe deformation (see Section 2.9). Moreover, in the case of undrained tests, the suppressed dilation due to the constant volume condition imposed by the "incompressibility" of water (see Section 2.2) induces a considerable decrease in pore-water pressure. Liberation of air phase may occur due to *de-saturation* or *cavitation* as the pore-water pressure decreases (Penman 1953). Consequently, the constant volume condition is violated and the resulting volume changes cannot be measured by conventional means. Even if the global volume changes are indeed measured (using the technique suggested by Roscoe et al. 1958 and Head 1998), localisation of volumetric strain is expected to occur in the areas of *vapour nucleation.*

Nevertheless, it should be noticed that whether or not the critical state concept is valid for non-cohesive granular materials is not a matter of strain localisation and non-homogeneities that occur during testing. Instead, there are some important differences in the behaviour of cohesive and non-cohesive materials that should be considered. For example, if a non-cohesive material is compressed isotropically to a given mean effective stress, *p'*, then the void ratio attained after consolidation is not uniquely related to *p'* but depends on the *deposition void ratio*. This means that the concept of uniqueness of the NCL is not valid for non-cohesive materials. The consolidation lines initiated at different deposition void ratios are parallel between each other when plotted in semi-logarithmic scale. If usual consolidation stresses (i.e., not extremely high) are applied these lines lie to the "dry" side of the CSL and have a less steep slope. Consequently, it is not possible to group the tests into families according to an initial overconsolidation ratio (Roscoe et al. 1958). However, if an elevated consolidation stress is applied then all consolidation lines converge into a unique line which is parallel to the CSL and lies on the "wet" side of the latter (Vesic and Clough 1968, Luzzani and Coop 2002). This compressibility pattern is shown in Fig. 3.8 for three different sands.

It is apparent from the relative position of the consolidation and critical state line in Fig. 3.8 that loose and dense sand may be regarded as lightly and heavily overconsolidated material, respectively, unless a very high consolidation stress is applied, in which case the very loose sand can be regarded as a normally consolidated material. It is also apparent that the concept of uniqueness of the NCL is valid for sands at extremely high stresses (see, also, the Granta Gravel model in Schofield and Wroth 1968; Atkinson and Bransby 1978). Some researchers adopted this concept and proposed a unified modelling of the behaviour of clays and sands within the critical state framework (Crouch et al. 1994). However, other researchers highlighted that the *grain crushing* due to consolidation and shearing at elevated stresses changes the gradation of sand in such a way that a *new material* is formed with different mechanical behaviour and different critical state characteristics (Luzzani and Coop 2002, Wood and Maeda 2008, Bandini and Coop 2011, Vilhar et al. 2013, Ghafghazi et al. 2014, Ciantia 2019). Li and Dafalias (2000) thus stated that "the well-established framework for clay modelling should not be directly transplanted to sand without a careful examination".

Another important difference between the behaviour of sands and clays is that when (medium-to-dense) sand is subjected to undrained triaxial compression the stress ratio $\eta = q \,/\, p'$ may reach a value equal to M (i.e. the critical stress ratio) during plastic loading and remain constant without the sand being in critical state; *finite shear strain* is accumulated while the sand is experiencing *dilative shear failure* and the stress path moves along the $\eta = M$ line (Li 1997, Li and Dafalias 2000). Li (1997) suggested that the dilative shear failure is a combination of *neutral loading* (i.e. constant-η loading) and *perfect plasticity* under which the material has a well-defined stress - strain relationship. This stress - strain relationship is not related to the material's plastic modulus, though, it pertains to the direction of plastic flow (see Section 2.4), which can be described by a *dilatancy parameter*. The concept of dilative shear failure of sands is illustrated in Fig. 3.9 where it is highlighted that the direction of plastic flow changes under constant-η loading until the critical state is reached. This behaviour implies that "dilatancy is not only a function of stress state but also a function of internal material state, and in particular of the proximity of the material state to the critical state" (Li et al. 1999; see also Section 2.4).

Roscoe et al. (1958) stated that the triaxial tests on Braehead Silt performed by Penman (1953) provided the first experimental evidence that the CVR concept, introduced by Casagrande and developed by Hvorslev, may also be valid in the case of cohesionless media. Figure 3.10 shows the undrained SBS and CVR line for Braehead Silt in the q - p' - e space. The undrained loading path GHIQ of a triaxial compression test on loose silt is shown to climb up to the SBS in the section of the Hvorslev surface. The Hvorslev surface appears to be a ruled surface formed by straight lines of *varying slopes* that pass through the e-axis. Consequently, the SBS of this silt does not exhibit a *cohesion intercept* as does the SBS of the OC clay. It is noted that loose silt behaves like an overconsolidated material at usual levels of mean effective stress (i.e. not extremely high), as has been indicated earlier. The projection of the undrained loading path GHIQ on the q - p' plane is shown in Fig. 3.11. The characteristics of dilative shear failure are apparent since the undrained loading path moves for the most part on a constant-η line ($\eta = q / p'$). The slope of the constant-η line depends on the void ratio; Figure 3.12 demonstrates this dependence. It can be inferred that the dilative shear failure of silt or sand occurs along the line with slope M, as suggested by Li (1997) and Li and Dafalias (2000).

The ultimate point Q of an undrained loading path (see Figs 3.10 and 3.11) can be defined uniquely by its coordinates (p'_Q , q_Q) or by the parameters ($-\Delta u_Q$, q_Q); Δu_Q is the ultimate excess pore-water pressure which is negative under usual levels of mean effective stress, unless the silt is at extremely loose state. However, it is noted that extremely loose fabric of sands or silts is only achieved in the laboratory by using the *moist tamping* specimen preparation technique that creates a *honeycomb-like* skeleton structure (Casagrande 1975). A void ratio higher than the one achieved by the processes of water or dry pluviation or some other standardised procedure, $e > e_{max}$, can be obtained by moist tamping, while even if the fabric is compacted to a denser state it still remains collapsible and significantly contractive. Thus, some researchers state that the response of moist-tamped specimens does not represent the real behaviour of in-situ pluviated deposits of sand or silt (Vaid and Sivathayalan 2000). Penman (1953) did not use moist tamping and this is the reason why the SBS for Braehead Silt is well-defined only on the “dry” side of the CVR line (Fig. 3.10); moreover, the CVR line was defined with considerable scatter due to the vapour liberation caused by the decrease in pore-water pressure, as can be seen in Penman’s graphs displaying the ultimate points ($-\Delta u_Q$, e_c) and (q_Q , e_c), where e_c is the consolidation void ratio. The two graphs are shown in Fig. 3.13 while the CVR line is shown in Fig. 3.10.

Roscoe et al. (1958) investigated if the drained triaxial compression tests on Braehead Silt performed by Penman (1953) define a drained SBS and CVR line that coincide with the respective SBS and CVR line for the undrained tests. They applied the boundary energy correction described above and not the one suggested by Penman (i.e. the boundary work per unit of volume is defined as $\sigma_3\ d\varepsilon_{vol}$ and not as $p\ d\varepsilon_{vol}$, based on the suggestions made by Bishop 1954 concerning the work-conjugate stress - strain quantities). Figure 3.14 shows the projection on the e - q plane of the drained loading paths of two specimens consolidated to mean effective stress p' = 30 lb. / sq.in. (= 206.7 kPa). The CVR line obtained from undrained tests is also shown with a broken-dotted line. Moreover, the displayed XY broken line represents the intersection of the stress plane under drained conditions (common to both specimens, with a slope Δq / $\Delta p'$ = 3 / 1) with the undrained SBS; X is the intersection point of the XY line and the undrained CVR line. It is noted that both tested specimens had initial states on the "dry" side of the CVR line and remained on this side as they approached the CVR line. However, the one specimen was looser than the other even though both were relatively dense and behaved like overconsolidated materials.

Roscoe et al. (1958) suggested that if the SBS and CVR concepts are valid in the case of silts then the applied stress paths and loading paths (after the boundary energy correction) shown in Fig. 3.14 should become tangential to XY and *end at X*. However, there is an apparent discrepancy and it can be inferred that the corresponding error becomes more significant when the initial density of the specimen increases. The reason for this discrepancy is mainly the development of non-homogeneous deformation due to strain localisation, while loading with non-lubricated end platens results in further deformation non-uniformities (Bishop and Henkel 1957). Roscoe et al. (1958) made a meaningful statement that motivated extensive research up to this day; they suggested that if the true values of the (p' , e , q) combinations had been obtained inside the localisation zone where the *actual* deformation occurs, the loading paths would have ended at X. The inception of this idea dates back to the work by Casagrande and Watson (1938) (see Section 2.9). It is apparent that the concept of uniqueness of the CVR line for sands and silts can be verified only if the measurement of the local void ratio inside the shear band is feasible (Coumoulos 1968, Roscoe 1970, Vardoulakis 1977, Desrues et al. 1996, Mooney et al. 1998, Fu and Dafalias 2011).

Roscoe (1953) developed the *simple shear apparatus* in order to overcome the limitations of the triaxial apparatus in imposing large strains uniformly. However, the problem of strain localisation remained unsolved, as evidenced in the results of the tests performed by Cole (1967). The use of the simple shear apparatus in combination with the γ-rays technique developed by Coumoulos (1968) provided the means to measure the local void ratio changes inside the shear band. It is noted that Coumoulos (1968) measured only the local volumetric strain and not the local shear strain (Roscoe 1970). On the other hand, Stroud (1970) embedded a regular pattern of lead shots inside the dense specimens tested in the simple shear apparatus and managed to measure the local volumetric and shear strains.

Other researchers also studied the fabric characteristics inside the shear band in order to determine the critical state of granular materials. Desrues et al. (1985) measured the local void ratio inside the shear band *post-mortem*, by using the γ-ray technique on stabilised sand specimens after testing; they also monitored the evolution of the void ratio and shear strain inside the zones of localisation *in-situ* using the stereophotogrammetric technique. Desrues et al. (1996) used the technique of X-ray computed tomography and acquired quantitative information about the evolution of void ratio inside the shear band. Oda and Kazama (1998) inspected with a microscope the shear band region of resin-stabilised specimens after testing; they determined the local void ratio using the *scanning line* method. A similar post-mortem inspection of resin-stabilised specimens was carried out by Oda et al. (2004) using the microfocus X-ray computed-tomography technique. Mooney et al. (1998) applied a non-invasive analysis technique, based on stereophotogrammetry, to measure the strains (both shear and volumetric) inside the shear band in plane strain compression tests. Recently, Fu and Dafalias (2011) performed DEM simulations to study the evolution of fabric inside the shear bands and made continuous measurements of the void ratio (and other fabric characteristics) in the local scale using specimens with a variety of initial fabrics.

Figure 3.15 shows the results of simple shear tests on dense and loose sand performed by Cole (1967). In these tests, the global volumetric strain and the average shear strain were determined based on the measured boundary displacements. The measurements made by Coumoulos (1968) are also shown in Fig. 3.15b as plots of the local void ratio versus the average shear strain. It can be seen that both the dense and loose specimen reach a common critical void ratio, determined by local measurements, when sheared under the same vertical stress. However, if the void ratio is measured only globally then the void ratio reached ultimately in the case of dense specimen is not relevant to the actual critical void ratio (see also Desrues et al. 1996 and Fig. 2.101). Stroud (1970) also verified the uniqueness of the CVR at a given vertical stress in simple shear testing. However, Mooney et al. (1998) suggested that although a unique critical stress state exists for a given confining stress, a unique relationship between void ratio and confining stress at the critical state there exists not. On the other hand, the DEM simulations performed by Fu and Dafalias (2011) verified the existence of a unique CVR line, irrespective of the initial fabric of the specimens tested, while they noticed that reaching critical state requires the development of very large strains.

Roscoe et al. (1958) performed simple shear tests on sands and other granular materials such as glass beads and steel balls. The steel balls exhibited a favourable behaviour in the sense that it was feasible to form a very loose initial fabric on the "wet" side of the CVR line and there was no risk of particle crushing. Fully drained simple shear tests were performed by increasing the shear stress τ on the horizontal plane under constant vertical stress σ'_v, hence, the stress principal axes rotated (Roscoe et al. 1967). In the following, the symbol τ_i means that the shear stress τ has been corrected for boundary energy. The advantages of the simple shear apparatus allowed the collection of valuable information that verified the concept of the SBS and CVR line for the granular materials tested, as discussed next.

Figure 3.16 shows the evolution of the void ratio of steel ball assemblies with the horizontal displacement of the simple shear apparatus, for the tests performed by Roscoe et al. (1958) at fixed and constant (during shearing) vertical stress σ'_v = 20 lb. / sq.in. (= 137.8 kPa). It is apparent that a unique critical void ratio exists for the given vertical stress, irrespective of the initial void ratio of each assembly. Figure 3.17a shows the corresponding applied stress paths and the corrected loading paths projected on the e - τ plane; it can be seen that all loading paths end at the same point Q. Moreover, the loading paths have a common boundary XY line corresponding to the straight line τ_i = 5.2 lb. / sq.in. (= 35.8 kPa), which is the intersection of the σ'_v = 20 lb. / sq.in. (= 137.8 kPa) plane with the drained SBS. It can be inferred from the results in Fig. 3.17a and Fig. 3.14 that a more consistent behaviour with the one exhibited by clays is evidenced for the steel balls than for the Braehead Silt. Steel ball assemblies having various initial void ratios were sheared at different vertical stresses σ'_v and the tests results indicate that a unique ultimate point $(e, \tau_i)_{ult}$ corresponds to each stress σ'_v. Consequently, a unique CVR line is defined in the τ_i - σ'_v - e space; the projections of the CVR line on the t_i - σ'_v and e - σ'_v planes are shown in Figs 3.17b and c, respectively, for assemblies made of steel balls and glass beads.

Figure 3.18 shows the characteristic consolidation curves and the projection of the CVR line of the steel ball material on the e - σ'_v plane in linear and semi-logarithmic scale. The curve ABC represents the loosest possible states on the "wet" side of the CVR line; the densest possible states on the "dry" side are obtained by loading along the line A''B''C'' and unloading to an OC state such as D''. It can be seen that the CVR line of steel ball material is straight in semi-logarithmic scale though for many sand materials it has been reported that the CVR line is curved or bi-linear (e.g., Verdugo and Ishihara 1996, Li and Wang 1998; Been et al. 1991). The consolidation curves of the steel ball material are similar to the overconsolidation curves of clay still they do not converge into a unique NCL for the stresses applied. Figure 3.18 also shows the projection on the e - σ'_v plane of two loading paths beginning from a state C on the "wet" side of the CVR line and from a state D'' on the "dry" side. The first steel ball assembly contracts until the loading path reaches the CVR line at E, while the second steel ball assembly dilates until the loading path reaches the CVR line at E''.

Figure 3.19 shows the drained SBS in the τ_i - σ'_v - e space for steel balls subjected to simple shear loading. The data presented are from thirty nine tests performed at various σ'_v by Roscoe et al. (1958). Two drained loading paths are also shown, namely the loading path PQ beginning from a state looser than critical and the loading path P'R'Q' beginning from a state denser than critical. The loading path PQ rises almost vertically and then traverses the SBS up to the ultimate Q point on the CVR line, while the specimen accumulates contractive volumetric strain. On the other hand, the loading path P'R'Q' moves towards the R' point, while the specimen contracts, and then traverses the SBS, while the specimen dilates, until it reaches the CVR line at Q'. It can be seen that the SBS is an inclined plane that passes through the e-axis (i.e. there exists no cohesion intercept). It is also obvious that the SBS captures the loading paths that approach either from the "wet" or the "dry" side of the CVR line and leads them to the CVR line. However, Atkinson and Bransby (1978) reported that "the drained SBS surface for sand, defined in the Hvorslev section (i.e. defined from loading paths of specimens denser than critical), should be considered only as a boundary to the state of sand since there is no guarantee that other possible loading paths (e.g. undrained paths) will necessarily coincide with the drained SBS".

The concept of uniqueness of the CVR line in the *e* - *p'* plane was verified for various sands subjected to triaxial compression in recent years (Wood 1990, Been et al. 1991, Verdugo and Ishihara 1996). It is noted that some researchers suggested that different CVR lines exist for the same sand depending on whether it undergoes unstable deformation during flow liquefaction or deforms stably (see Chapter 4), because in the first case a "flow" structure is developed (Castro 1969, Casagrande 1975, Poulos 1981, Alarcon-Guzman et al. 1988); however, this suggestion was revised later and it was stated that the rate of straining does not affect the position of the CVR line (Poulos et al. 1985, Castro et al. 1985, Poulos 1988). Moreover, it should be noticed that the CVR line has been related to steady states (Castro 1969, Poulos 1981, Alarcon-Guzman et al. 1988, Vaid et al. 1990) or critical states (Been et al. 1991) though not all the cases of steady state correspond also to critical state (Verdugo and Ishihara 1996, Li and Dafalias 2012). On the other hand, the projection of the CVR line on the *q* - *p'* plane, which is characterised by the critical stress ratio $\eta_{cr} = (q / p')_{cr} \equiv M$, depends at least on the *mode of loading* (Lode-angle dependence), while the dependence of M on other factors has been reported by Penman (1953) and Been et al. (1991).

Been et al. (1991) reported that the critical and steady state lines in the *e* - *p'* plane for Erksak Sand were found to be identical and independent of the stress path (drained or undrained), mode of loading (triaxial compression or extension), sample preparation method (wet pluviation or moist compaction), initial density of sand (denser or looser than critical) and type of loading (load- or strain-controlled). It is important to notice that only the ultimate states of continuous shear deformation under constant stress and volume (or pore-water pressure) were selected as steady / critical states in their study. Been et al. (1991) also reported that the critical state friction angle, φ_{cs}, measured in compression and extension tests at mean effective stress, p'_{cs}, lower than 1 MPa, decreases with increasing void ratio (see also Penman 1953). On the other hand, Vaid et al. (1990) reported that "while a single steady state line (in the *e* - *p'* plane) emerges for compression loading, extension loading yields several lines, each characteristic to a given deposition void ratio". However, in the article by Vaid et al. (1990) the quasi-steady state observed in undrained tests (Alarcon-Guzman et al. 1988) is considered to be a true ultimate steady state (see also Castro 1969, Vaid and Chern 1985). Yoshimine and Ishihara (1998) showed that the quasi-steady state frequently coincides with the phase-transformation point but does not necessarily coincide with the ultimate steady state.

Verdugo (1992) found that the phase-transformation line (PTL) in the *e* - *p'* plane is not unique in triaxial compression but its position depends both on the deposition void ratio, e_{20}, and consolidation mean effective stress, p'_c, while the ultimate steady state line is unique (see also Verdugo and Ishihara 1996). Yoshimine and Ishihara (1998) and Yoshimine et al. (1998) verified and generalised the findings of Verdugo (1992);

they pointed out that the position of the PTL in the *e - p'* space depends on e_{20} and p'_c in triaxial compression (TC), triaxial extension (TE) and simple shear (SS) mode of loading, while a different PTL corresponds to each mode for a given p'_c. It is important to notice that Yoshimine and Ishihara (1998) determined experimentally many PTLs for different p'_c in TE and SS loading though *the ultimate steady state was not reached in these modes*. However, if the SSL is assumed to constitute an upper limit to the distribution of quasi-steady state lines then it may be inferred that different ultimate SS lines correspond to different modes of loading (see also Riemer and Seed 1997).

On the other hand, Li and Dafalias (2012) and Dafalias and Li (2013) stated that "a thermodynamic consideration of the critical state in conjunction with Gibbs' condition of equilibrium can provide proof of uniqueness of the critical state line in the *e - p'* space in regards to various modes of shearing"; the concept of uniqueness of the critical state line in the *e - p'* plane irrespective of the shearing mode (triaxial compression or extension) was recently verified by X-ray micro-tomography studies (Salvatore et al. 2017). Moreover, Fu and Dafalias (2011) performed DEM simulations and found that the void ratio at the ultimate / critical state depends on the mean effective stress; a unique CSL in the *e - p'* space was confirmed irrespective of the initial bedding plane orientation in regards to the shear direction. Another important finding of Fu and Dafalias (2011) is that the fabric of granular materials at critical state is anisotropic. Li and Dafalias (2012) suggested that the classical Critical State Theory should be revisited in order to incorporate in its premises the role of fabric, as discussed next.

3.3 ANISOTROPIC CRITICAL STATE THEORY

The Critical State Soil Mechanics (CSSM) was established as a general theoretical framework for modelling the elastoplastic behaviour of soils and other granular materials with the property of dilatancy (Roscoe et al. 1958, Scofield and Wroth 1968). The Cam-clay model describes the behaviour of a conceptual material (i.e. the Cam-clay) that resembles the behaviour of real soil materials, using the CSSM principles. The original Cam-clay stress - dilatancy relationship (Roscoe and Schofield 1963) is derived based on thermodynamic consideration of the dissipated power and is given by the following equation:

$$D = M - \eta$$
(3.1)

where $D := \mathrm{d}\varepsilon_v^p / \left|\mathrm{d}\varepsilon_q^p\right|$ is the dilatancy ratio, M is the critical stress ratio (which is a material constant) and η is the mobilised stress ratio $q\ /\ p'$. The modified Cam-clay stress - dilatancy relationship (Roscoe and Burland 1968) is given by:

$$D = (M^2 - \eta^2) / 2\eta \tag{3.2}$$

using the same symbolisms as in Eq. 3.1.

The relationships given by Eqs 3.1 and 3.2 imply that the dilatancy ratio, D, is dependent only on the current value of the stress ratio, η, and the material constant M. On the other hand, Manzari and Dafalias (1997) proposed a stress - dilatancy relationship that takes into account the dependence on state (see Section 2.4); the concept of state-dependent dilatancy was later adopted by other researchers (Cubrinovski and Ishihara 1998, Wan and Guo 1998, Li et al. 1999, Li and Dafalias 2000) and reflects the consensus that the efficient modelling of the elastoplastic behaviour of granular materials requires the reference to the ultimate state (Wroth and Basset 1965). According to Li and Dafalias (2000), the stress - dilatancy relationship in triaxial loading is given by the following equation:

$$D = \frac{D_o}{M} \cdot \left(M \cdot e^{m \cdot \psi} - \eta \right) \tag{3.3}$$

where ψ is the state parameter proposed by Been and Jefferies (1985), D_o and m are positive modelling parameters, M is the (Lode-angle dependent) critical stress ratio and η is the mobilised stress ratio.

According to Eq. 3.3, the dilatancy ratio of sand depends on the difference of the current stress ratio η from a *moving* reference stress ratio $M^d = M\ e^{m\psi}$, where M^d is the *dilatancy stress ratio* that corresponds to the slope of the phase-transformation line in the q - p' plane at the moment that η becomes equal to $M^d \neq M$ ($\psi \neq 0$) and the dilatancy ratio becomes momentarily $D = 0$. The stress ratio M^d is moving while the state parameter ψ changes in a way that when the sand is at critical state the following relationships hold simultaneously: $\psi = 0$ and $\eta = M^d = M$ hence the dilatancy ratio becomes again $D = 0$. Obviously, the transient state of zero dilatancy that corresponds to the phase-transformation point (Ishihara et al. 1975) does not necessarily occur when $\eta = M$, a fact that is verified by experiments (Verdugo and Ishihara 1996). Moreover, the dilative shear failure (Li 1997) during which the dilatancy is gradually exhausted while the sand is sheared under constant $\eta = M$ towards the critical state can be modelled efficiently (see Figs 3.9 and 3.11).

Apart from the stress ratio, η, and the state parameter, ψ, other factors that affect the dilatancy of sands are the orientation of the major principal stress axis with respect to the deposition direction, measured by the angle α, and the intermediate principal stress parameter, $b = (\sigma'_2 - \sigma'_3) / (\sigma'_1 - \sigma'_3)$. Vaid and Chern (1985) pointed out that sand of a given initial state combination (e , p') may exhibit dilative response to undrained triaxial compression ($\alpha = 0°$ and $b = 0$) and contractive response to undrained triaxial extension ($\alpha = 90°$ and $b = 1$). This behaviour is verified in many other studies (Vaid et al. 1990, Riemer and Seed 1997, Yoshimine and Ishihara 1998). Figure 3.20 shows the results of loading tests with various fixed values of α and b

performed by Yoshimine et al. (1998) in the hollow cylinder apparatus. It can be seen that the undrained response of sand to generalised loading depends strongly on α and b. Consequently, the dilatancy functions in Eqs 3.1 to 3.3 should be modified to account for this type of dependence.

Manzari and Dafalias (1997) generalised the dilatancy function given by Eq. 3.3 in a multiaxial stress space in order to account for the effect of the loading mode; however, the effects of fabric on dilatancy were not modelled. Li and Dafalias (2002) proposed a critical state compatible constitutive framework that incorporates the effect of the inherent anisotropy on dilatancy. They introduced a scalar-valued *anisotropic state variable* A that is properly defined based on the fabric and stress tensors. The CSL in the e - p' plane is not unique but depends on A, thus, the (state-dependent) dilatancy also depends on A; this dependence is the result of the characteristics of inherent anisotropy that are not erased during shearing. According to Li and Dafalias (2002), "the survival of fabric anisotropy at the critical state is expected to mainly be associated with the preferred orientation of the sand particles", justifying the non-uniqueness of the CSL. The concept of fabric-dependent CSLs was adopted in other studies as well (Dafalias et al. 2004, Li and Dafalias 2004, Papadimitriou et al. 2005, Yang et al. 2008).

However, the uniqueness of the CSL in the e - p' plane is a fundamental premise of the critical state theory, while this concept is supported by the findings of recent studies (Fu and Dafalias 2011, Li and Dafalias 2012, Dafalias and Li 2013, Li and Dafalias 2015, Salvatore et al. 2017, Zhao and Guo 2013, Zhou et al. 2017). Dafalias (2016) pointed out that the state and fabric dependent dilatancy of soils can be modelled efficiently within the CCSM framework without relying on multiple CSLs if the evolution of fabric is taken into account. For example, Li and Dafalias (2012) proposed a general constitutive framework which incorporates a second-order *fabric tensor* **F**, a scalar-valued *Fabric Anisotropy Variable A* (which is different than the variable A introduced by Li and Dafalias 2002), a moving *Dilatancy State Line (DSL)*, which is the reference line for the *Dilatancy State Parameter (DSP)* ζ, and a unique *Critical State Line (CSL)* in the e - p' space, which is the reference line for the *State Parameter (SP)* ψ. Each of the above conceptual artefacts used in the constitutive framework proposed by Li and Dafalias (2012) is presented next.

The deviatoric second-order fabric tensor **F** describes quantitatively the orientational distribution of contact normal vectors, non-spherical grains or void vectors (Oda 1972a, Satake 1978, Oda et al. 1985, Li and Li 2009, Fu and Dafalias 2011, Li and Dafalias 2012); bold letters are used hereinafter to symbolise tensorial quantities. It is noted that **F** should be considered as a *per unit volume measure* to be consistent with thermodynamic energy dissipation requirements (Li and Dafalias 2015, Dafalias 2016). The following relationship holds:

$$\mathbf{F} = \mathrm{F} \cdot \mathbf{n}_{\mathrm{F}} \tag{3.4}$$

where $F \geq 0$ is the norm and $\mathbf{n}_F$ is the unit-norm deviatoric tensor-valued direction of $\mathbf{F}$. The norm F is normalised with respect to its value at critical state, which is Lode angle dependent, in such way that as the sand is sheared towards critical state the norm F evolves to attain its critical value $F_c = 1$ (Li and Dafalias 2012, Dafalias 2016). The direction of $\mathbf{F}$ also evolves to align with the unit-norm deviatoric tensor-valued loading direction $\mathbf{n}$ (i.e. $\mathbf{n}_{Fc} = \mathbf{n}$), which is defined along the deviatoric plastic-strain rate indicating the direction of plastic flow; obviously, the condition $\mathbf{n}_F = \mathbf{n}$ may hold in specific occasions prior to critical state and, then, the fabric evolves towards its critical value only norm-wise. The direction $\mathbf{n}$ is related to the stress tensor direction in some but not in all cases (Li and Dafalias 2012, Dafalias 2016).

The fabric anisotropy variable A is introduced to model the effect of non-coaxiality of the fabric-tensor and loading directions together with the effect of the evolution of the fabric-tensor norm F; the FAV A is given by the relationship (Li and Dafalias 2012):

$$\mathrm{A} = \mathbf{F} : \mathbf{n} = \mathrm{F}\mathbf{n}_{\mathrm{F}} : \mathbf{n} = \mathrm{FN} \tag{3.5}$$

where $\mathrm{N} = \mathbf{n}_{\mathrm{F}} : \mathbf{n}$ is a scalar measure of the relative orientation of $\mathbf{F}$ and $\mathbf{n}$ as produced by the trace of the product of the two tensor-valued directions. It is noted that at critical state $F = F_c = 1$ and $\mathbf{n}_{\mathbf{F}} = \mathbf{n}_{Fc} = \mathbf{n}$ hence $N = N_c = \mathbf{n}_{\mathbf{Fc}} : \mathbf{n} = \mathbf{n} : \mathbf{n} = 1$ and $A = A_c = 1$. Consequently, as the critical state is approached the fabric tensor evolves towards its critical value norm-wise and direction-wise; the evolution of $\mathbf{F}$ is described by the separate evolution of the two scalar quantities F and N towards their critical unit values that leads to the condition A = 1. At this point it is highlighted that $A = A_c = 1$ is the new analytical condition at critical state introduced within the Anisotropic Critical State Theory (ACST) but more details will be given in the following.

Li and Dafalias (2012) simulated the experimental results of Yoshimine et al. (1998) using a model that was developed within the ACST framework; the undrained response of sand to monotonic loading in compression (b = 0) and extension (b = 1) mode was simulated quite satisfactory, as can be seen in Fig. 3.21. The loading in compression mode was performed with the σ_1-axis inclined at angles α = 0°, 15°, 30° and 45° with respect to the vertical, while the loading in extension mode was performed at α = 60°, 75° and 90°. The initial fabric of sand was cross-anisotropic with a vertical axis of rotational symmetry. Figure 3.22 shows the results of the simulations extended to a very high level of shear strain in order to attain a critical state; the vertical line indicates the strain at which the physical experiments were terminated. The results of a conventional triaxial compression test (α = 0° and b = 0) on very loose sand (e = 0.900) are also included in Fig. 3.22.

Figure 3.22a shows the evolution of the ratio q / M with shear strain, where M is the Lode angle dependent critical stress ratio $(q / p')_{cs}$ corresponding either to b = 0 or to b = 1. Figures 3.22b and c show the evolution of the FAV A and fabric-tensor norm F with shear strain, respectively. It is apparent that a common value of q / M is reached at very large strains in all tests despite the significantly different previous responses;

this is because the critical state is reached at the same ultimate mean effective stress since all specimens have the same void ratio. On the other hand, the very loose specimen suffers a complete liquefaction with $p' = q = 0$ and remains in this state without evolving towards the critical state. The FAV A and fabric-tensor norm F reach the unit value at critical state in all tests yet their evolution is quite different in earlier stages. It can be seen that the fabric is far enough from its critical state when the physical experiments are terminated. It is important to notice that the shortest route to the critical state is in the compression mode when the direction of σ_1 is initially collinear to the direction of the major principal component of the contact normal fabric tensor (or, alternatively, σ_1 is normal to the bedding plane), and remains that way throughout shearing.

The results shown in Figs 3.4, 3.15, 3.17 and 3.20 - 3.22 indicate that the dilatancy of granular materials depends both on state and fabric. Based on the micromechanical model proposed by Rowe (1962) and the energy dissipation considerations adopted within the Critical State Theory (CST) (Schofield and Wroth 1968), the dilatancy depends on the difference between the mobilised stress ratio and a fixed reference stress ratio, which is a material property. However, recent models propose that the reference stress ratio changes when the state parameter, ψ, changes, i.e. when the distance of the current point in the e - p' plane changes with respect to the reference CSL (Manzari and Dafalias 1997, Li and Dafalias 2000). Since within the ACST the concept of multiple CSLs in the e - p' plane is abandoned, an alternative ingenious idea is adopted to account for the effects of fabric on dilatancy. A new reference line is introduced in the e - p' plane, i.e. the Dilatancy State Line (DSL), which moves as the FAV A changes, and the distance of the current state point (e , p') from the DSL now affects dilatancy (Li and Dafalias 2012). The DSL is shown in Fig. 3.23 together with the unique CSL; the geometric meaning of the state parameter, ψ, and dilatancy state parameter, ζ, is also illustrated. In fact, the DSL exists in the e - p' - A space and relates the *dilatancy void ratio*, e_d, to e, p' and A by means of the function $e_d = e_d(e , p' , A)$, which gives $e_d(e , p' , 1) = e_c(p')$ thus one expects the condition $e_d = e_c = e$ at critical state in Fig. 3.23 (e_c is the critical void ratio for the given p'). It is obvious that the DSL coincides with the CSL when A = 1, while the value of FAV A determines the location of the DSL in the e - p' plane as it evolves towards the CSL.

The DSL plays the role of the CSL when A $\neq$ 1 in the sense that it specifies whether the sand is contractive or dilative, depending on the difference of the current void ratio, e, from the dilatancy void ratio, e_d, which is the dilatancy state parameter, ζ (Li and Dafalias 2012), given by:

$$\zeta = e - e_d \tag{3.6}$$

The sand exhibits contractive behaviour when $\zeta > 0$, dilative when $\zeta < 0$ and no-volume-change tendency when $\zeta = 0$; in the latter case the sand is either in a transient state of zero dilatancy (e.g. at phase transformation or in a quasi-steady state) or in an ultimate steady state / critical state. When A = 1 it is $e_d = e_c$ (= e) and hence $\zeta = \psi$ (= 0). Equation 3.6 can be re-written in the following form (see also Fig. 3.21):

$$\zeta = e - e_d = (e - e_c) - (e_d - e_c) = \psi - \psi_A \tag{3.7}$$

where the quantity $\psi_A = e_d - e_c$ is called the *Anisotropy Parameter* (AP) (Li and Dafalias 2012). The AP is used to determine the location of the points (e_d , p') on the DSL by means of a constant-p' translation of each critical point (e_c , p') on the CSL to the position ($e_c + \psi_A$, p'). Obviously, if the position of the CSL is known then the analytical expression of the function $e_d = e_d(e , p' , \mathrm{A})$ or $\psi_A = \psi_A(e , p' , \mathrm{A})$ is needed to define the position of the DSL. Li and Dafalias (2012) proposed the relations:

$$\psi_A = \psi_A(e, p', \mathrm{A}) = e_A(e, p')(\mathrm{A} - 1) \tag{3.8a}$$

$$e_d = e_c + \psi_A = e_c(p') + e_A(e, p')(\mathrm{A} - 1) \tag{3.8b}$$

$$\zeta = \psi - \psi_A = e - e_c(p') - e_A(e, p')(\mathrm{A} - 1) \tag{3.8c}$$

where in a first approximation it can be assumed that $e_A(e , p') = e_A$, i.e. e_A is a material constant independent of e and p'. In this case, the CSL is translated in parallel by an amount of $e_A \cdot (\mathrm{A} - 1)$, which depends only on A. In any case, the DSP ζ measures the distance of the current value of both non-directional (e) and directional characteristics (A) of fabric from their critical state values for a given p'.

Li and Dafalias (2012) proposed that the dilatancy function within the ACST, which takes into account the dependence on state and fabric, can be given by the following equation in triaxial loading conditions:

$$D = \frac{D_o}{M} \cdot \left(M \cdot e^{m \cdot \zeta} - \eta \right) \tag{3.9}$$

where ζ is the DSP used instead of ψ (see Eq. 3.3), D_o and m are positive modelling parameters, M is the Lode angle dependent critical stress ratio and η is the mobilised stress ratio.

Having modified the dilatancy function to account for the effects of state and fabric, Li and Dafalias (2012) queried whether the classical Critical State Theory is complete or not since it does not include in its premises the role of (anisotropic) fabric. A granular material is at critical state when it keeps deforming in continuing shearing at constant stress and volume. The critical state phenomenon under general stress conditions is expressed analytically by (Li and Dafalias 2012):

$$\dot{\mathrm{p}}' = 0,\ \dot{\mathbf{s}} = \mathbf{0},\ \dot{\varepsilon}_{\mathrm{v}} = 0 \text{ but } \dot{\mathbf{e}} \neq \mathbf{0} \tag{3.10}$$

where p' is the mean effective stress, $\mathbf{s}$ is the deviatoric part of the stress tensor, ε_v is the volumetric strain, $\mathbf{e}$ is the deviatoric part of the strain tensor and the superposed dot indicates the rate. The analytical expression of the CS phenomenon under triaxial stress conditions is given by:

$$\dot{p}' = 0,\ \dot{q} = 0,\ \dot{\varepsilon}_v = 0 \text{ but } \dot{\varepsilon}_q \neq 0 \tag{3.11}$$

where $q = \sigma_1 - \sigma_3$ and $\varepsilon_q = 2/3\ (\varepsilon_1 - \varepsilon_3)$. The classical Critical State Theory by Roscoe et al. (1958) and Schofield and Wroth (1968) introduces two analytical conditions that are stated to be necessary and sufficient for reaching and maintaining CS, given by:

$$\eta = \eta_c = \left(\frac{q}{p'}\right)_c = M \tag{3.12a}$$

$$e = e_c = e_c(p') \tag{3.12b}$$

where M is the Lode angle dependent critical stress ratio and $e_c = e_c(p')$ is the critical void ratio corresponding to mean effective stress p'. In general mode of loading the invariant that corresponds to the triaxial deviatoric stress, q, is $\sqrt{(3/2)\mathbf{s}:\mathbf{s}}$, while the Lode angle dependent critical stress ratio is obtained as described by Wang et al. (1990) and Manzari and Dafalias (1997).

The analytical conditions in Eqs 3.12a and b dictate requirements only for the critical value of the non-directional fabric characteristic (i.e. the void ratio, e) and the ratio of the stress invariants (i.e. the stress ratio q/p'), while no reference is made to the non-directional characteristics of fabric. Li and Dafalias (2012) suggested that since the behaviour of sands before the critical state is highly affected by fabric anisotropy (Oda et al. 1978, Lam and Tatsuoka 1988, Tatsuoka et al. 1990, Yoshimine et al. 1998, Nakata et al. 1998, Uthayakumar and Vaid 1998) it is reasonable to suggest that the same holds true at critical state; this suggestion is supported by recent physical and numerical micromechanical studies that indicate the existence of a strongly anisotropic fabric at critical state (Oda 1972b, Oda et al. 1985, Thornton 2000, Masson and Martinez 2001, Li and Li 2009, Fu and Dafalias 2011, Wiebicke et al. 2017). Consequently, Li and Dafalias (2012) proposed that the analytical conditions of Eqs 3.12a and b should be enhanced to account for the fabric effects at critical state as follows:

$$\eta = \eta_c = \left(\frac{q}{p'}\right)_c = M \tag{3.13a}$$

$$e = e_c = e_c(p') \tag{3.13b}$$

$$\mathrm{A} = \mathrm{A}_c = 1 \tag{3.13c}$$

where the third condition states that the FAV A should reach its critical state value together with the stress ratio and void ratio in order to reach and maintain a CS. According to Eq. 3.5, this means that the fabric tensor **F** should reach its critical state value norm-wise and direction-wise; notice that the direction of **F** becomes collinear to the loading direction **n** at critical state hence a sudden change of **n** while the sand is at critical state immediately leads to abandonment of this state. This may happen if *reverse loading* or *rotational shear* (Wang et al. 1990) is imposed while the sand is at critical state.

Dafalias (2016) conceived a thought experiment to prove that the classical CST is incomplete and that the ACST proposed by Li and Dafalias (2012) is a necessary revision that renders the theory complete. The thought experiment stated that if a sand is brought to a critical state by means of monotonic loading with fixed stress principal axes in regard to the specimen axes and afterwards the stress principal axes are rotated at constant effective stress principal values then, according to the CST, the sand should not undergo plastic volumetric changes but should remain at CS instead, since the analytically expressed requirements of critical values for the stress and void ratio are not violated. If plastic volumetric changes indeed occur then the analytical conditions of CST are necessary but not sufficient for maintaining CS, unless tacitly assumed that the "fixity of stress and strain rate directions in regard to the sample is considered at CS". Theocharis et al. (2017, 2019) realised this thought experiment by means of Discrete Element Method (DEM) simulations of this loading process and confirmed numerically the one of the two outcomes hypothesised by Dafalias (2016), namely that the granular material contracted immediately upon initiating the rotation of the stress principal axes at CS. The authors showed that the use of the fabric-related quantity (i.e. the FAV A) involved in the new analytical condition at CS according to ACST can explain the observed dilatancy patterns. One of the aims of the present study is to perform Dafalias' (2016) thought experiment in the hollow cylinder apparatus.

3.4 SUMMARY

The Critical State Soil Mechanics (CSSM) framework was established by Roscoe et al. (1958) and Schofield and Wroth (1968) in order to accommodate constitutive models that treat soils as elastoplastic continuum materials with the property of dilatancy. The critical state concept is valid for sands though not by direct transplantation of all notions that are valid for clays. However, the first models of the stress - dilatancy behaviour proposed within the framework of CSSM overlooked the dependence on state and fabric. A revision of the stress - dilatancy relationship was proposed by Manzari and Dafalias (1997) and Li and Dafalias (2000) to model the dependence of dilatancy on state, while further revisions were proposed to model the effects of fabric anisotropy on dilatancy (Li and Dafalias 2002, Li and Dafalias 2004, Dafalias et al. 2004, Li and Dafalias 2012).

Li and Dafalias (2012) introduced the Anisotropic Critical State Theory which is a theoretical framework that accommodates advanced critical state-based constitutive models that take into account the effects of state and anisotropic fabric on dilatancy and other mechanical properties of granular materials. Li and Dafalias (2012) proved the uniqueness of the critical state line in the *e* - *p'* plane by means of thermodynamic considerations and enhanced “the requirements of critical values for the stress and void ratio of the classical Critical State Theory by an additional requirement of critical value for an appropriate measure of fabric-anisotropy”. Dafalias (2016) conceived a thought experiment to prove that the classical CST is incomplete, since it does not include in its premises the role of (anisotropic) fabric. Dafalias (2016) stated that the thought experiment will show whether the ACST introduced by Li and Dafalias (2012) is a necessary revision of or a convenient supplement to the classical CST. Theocharis et al. (2017, 2019) performed Discrete Element Method simulations of Dafalias' (2016) thought experiment and proved the necessity of revising the classical CST, while they showed that the Fabric Anisotropy Variable A introduced by Li and Dafalias (2012) facilitates the efficient modelling of the dilatancy of granular materials under complex loading conditions. However, the performance of Dafalias' (2016) thought experiment by physical means remains a challenging open research topic.

3.5 BIBLIOGRAPHY

Alarcon-Guzman A, Leonards GA, Chameau JL (1988) Undrained monotonic and cyclic strength of sands. Journal of Geotechnical Engineering, Vol. 114, No.10, pp. 1089-1109

Atkinson JH, Bransby PL (1978) The mechanics of soils: an introduction to critical state mechanics. McGraw-Hill Book Company (UK) Limited

Bandini V, Coop MR (2011) The influence of particle breakage on the location of the critical state line of sands. Soils and Foundations, Vol. 51, No. 4, 591-600

Been K, Jefferies MG (1985) A state parameter for sands. Géotechnique 35 (2), 99–112

Been K, Jefferies MG, Hachey J (1991) The critical state of sands. Géotechnique 41 (3), 365–381

Bishop AW (1954) Correspondence on “Shear characteristics of a saturated silt measured in triaxial compression,” by A.D.M. Penman, Géotechnique 4, 43–44

Bishop AW, Henkel DJ (1957) The measurement of soil properties in the triaxial test. London: Edward Arnold (publishers) LTD

Casagrande A (1936) Characteristics of cohesionless soils affecting the stability of slopes and earthfills. Journal of the Boston Society of Civil Engineering, January, 13-32

Casagrande A, Watson JD (1938) Compaction tests and critical density investigations of cohesionless materials for Franklin Falls Dam, Merrimack Valley flood control. Corps of Engineers, U.S. Army Engineering Office, p. BII-7

Casagrande A (1975) Liquefaction and cyclic deformation of sands: a critical review. Pierce Hall Cambridge, Massachusetts January 1976

Castro G (1969) Liquefaction of sands. Harvard Soil Mechanics Series No. 81, Harvard University, Cambridge, Mass

Castro G, Poulos SJ, Leathers FD (1985) Re-examination of slide of lower San Fernando dam. J. Geotech. Engrg., ASCE, 111(9), 1093-1107

Ciantia MO, Arroyo M, O’Sullivan C, Gens A, Liu T (2019) Grading evolution and critical state in a discrete numerical model of Fontainebleau sand. Géotechnique 69 (1), 1–25, https://doi.org/10.1680/jgeot.17.P.023

Cole ERL (1967) The behaviour of soils in the simple shear apparatus. Ph.D. thesis, University of Cambridge

Coumoulos DG (1968) A radiographic study of soils. Ph.D. thesis, University of Cambridge

Crouch RS, Wolf JP, Dafalias YF (1994) Unified critical-state bounding-surface plasticity model for soil. Journal of Engineering Mechanics, Vol. 120, No. 11, 2251-2270

Cubrinovski M, Ishihara K (1998) Modelling of sand behaviour based on state concept. Soils and Foundations, Vol.38, No. 3, 115-127

Dafalias YF, Papadimitriou AG, Li XS (2004) Sand plasticity model accounting for inherent fabric anisotropy. J. Eng. Mech., 130(11), 1319-1333

Dafalias Y, Li XS (2013) Revisiting the paradigm of critical state soil mechanics: fabric effects. Q. Yang et al. (Eds): Constitutive Modeling of Geomaterials, SSGG, pp. 13-26, Springer-Verlag Berlin Heidelberg 2013

Dafalias YF (2016) Must critical state theory be revisited to include fabric effects? Acta Geotechnica (2016) 11:479, DOI 10.1007/s11440-016-0441-0

Desrues J, Lanier J, Stutz P (1985) Localization of the deformation in tests on sand sample. Engineering Fracture Mechanics, Vol. 21, No. 4, pp. 909-921

Desrues J, Chambon R, Mokni M, Mazerolle F (1996) Void ratio inside shear bands in triaxial sand specimens studied by computed tomography. Géotechnique 46 (3), 529-546

Fu P, Dafalias YF (2011) Fabric evolution within shear bands of granular materials and its relation to critical state theory. International Journal for Numerical and Analytical Methods in Geomechanics, 2011, 35: 1918-1948

Ghafghazi M, Shuttle DA, DeJong JT (2014) Particle breakage and the critical state of sand. Soils and Foundations, Vol. 54, No.3, 451-461

Gilbert GD (1954) Shear strength properties of Weald Clay. Ph.D. Thesis, London

Haefeli R (1951) Investigations and measurement of the shear strengths of saturated cohesive soils. Géotechnique 2, 186-208

Head KH (1998) Manual of soil laboratory testing. Volume 3: effective stress tests. John Wiley and Sons Ltd, Second edition 1998, First edition 1992 by Pentech Press Limited

Henkel DJ (1956) The effect of overconsolidation on the behaviour of clays during shear. Géotechnique 6, 139-150

Huang X, Hanley KJ, O'Sullivan C, Kwok CY, Wadee MA (2014) DEM analysis of the influence of the intermediate stress ratio on the critical-state behaviour of granular materials. Granular Matter (2014) 16:641-655

Hvorslev MJ (1937) über die Festigkeitseigenschaften gestörter bindiger Böden" ("On the physical properties of remoulded cohesive soils"). Ingeniorvidenskabelige Skrifter. A. No. 45. 159 pp.

Ishihara K, Tatsuoka F, Yasuda S (1975) Undrained deformation and liquefaction of sand under cyclic stresses. Soils and Foundations, Vol.15, No.1, 29-44

Lam WK, Tatsuoka F (1988) Effects of initial anisotropic fabric and σ_2 on strength and deformation characteristics of sand. Soils and Foundations, Vol.28, No.1, pp. 89-106

Li XS (1997) Modeling of dilative shear failure. J. Geotech. Geoenviron. Eng., 123(7), 609-616

Li XS, Wang Y (1998) Linear representation of steady-state line for sand. J. Geotech. Geoenviron. Eng., 124(12), 1215-1217

Li XS, Dafalias YF, Wang Z-L (1999) State-dependent dilatancy in critical constitutive modelling of sand. Can. Geotech. J. 36, 599-611

Li XS, Dafalias YF (2000) Dilatancy for cohesionless soils. Géotechnique 50, No. 4, 449-460

Li XS, Dafalias YF (2002) Constitutive modelling of inherently anisotropic sand behaviour. J. Geotech. Geoenviron. Eng., 128(10), 868-880

Li XS, Dafalias YF (2004) A constitutive framework for anisotropic sand including non-proportional loading. Géotechnique 54, No. 1, 41-55

Li X, Li XS (2009) Micro-macro quantification of the internal structure of granular materials. J. Eng. Mech., 135(7), 641-656

Li XS, Dafalias YF (2012) Anisotropic critical state theory: role of fabric. Journal of Engineering Mechanics, Vol. 138, No. 3, 263-275

Li XS, Dafalias YF (2015) Dissipation consistent fabric tensor definition from DEM to continuum for granular media. Journal of the Mechanics and Physics of Solids 78 (2015) 141-153

Luzzani L, Coop MR (2002) On the relationship between particle breakage and the critical state of sands. Soils and Foundations, Vol.42, No.2, pp. 71-82

Manzari MT, Dafalias YF (1997) A critical state two-surface plasticity model for sands. Géotechnique 47, No. 2, 255-272

Masson S, Martinez J (2001) Micromechanical analysis of the shear behavior of a granular material. J. Eng. Mech., 127(10), 1007-1016

Mooney MA, Finno RJ, Viggiani GM (1998) A unique critical state for sand? J. Geotech. Geoenviron. Eng. 1998.124:1100-1108

Nakata Y, Hyodo M, Murata H, Yasufuku N (1998) Flow deformation of sands subjected to principal stress rotation. Soils and Foundations, Vol.38, No.2, 115-128

Oda M (1972a) Initial fabrics and their relations to mechanical properties of granular material. Soils and Foundations, Vol.12, No.1, 18-36

Oda M (1972b) The mechanism of fabric changes during compressional deformation of sand. Soils and Foundations, Vol.12, No.2, 1-18

Oda M, Koishikawa I, Higuchi T (1978) Experimental study of anisotropic shear strength of sand by plane strain test. Soils and Foundations, Vol.18, No.1, 25-38

Oda M, Nemat-Nasser S, Konishi J (1985) Stress-induced anisotropy in granular masses. Soils and Foundations, Vol.25, No.3, 85-97

Oda M, Kazama H, Konishi J (1998) Effects of induced anisotropy on the development of shear bands in granular materials. Mechanics of Materials 28 (1998) 103-111

Oda M, Kazama H (1998) Microstructure of shear bands and its relation to the mechanisms of dilatancy and failure of dense granular soils. Géotechnique 48, No. 4, 465-481

Oda M, Takemura T, Takahashi M (2004) Microstructure in shear band observed by microfocus X-ray computed tomography. Géotechnique 54, No. 8, 539-542

Papadimitriou A, Dafalias Y, Yoshimine M (2005) Plasticity modelling of the effect of sample preparation method on sand response. Soils and Foundations, Vol.45, No.2, 109-123

Parry RHG (1960) Triaxial compression and extension tests on remoulded saturated clay. Géotechnique 10, 166-180

Penman ADM (1953) Shear characteristics of a saturated silt, measured in triaxial compression. Géotechnique 3, 312-328

Poulos SJ (1981) The steady state of deformation. Journal of Geotechnical Engineering Division, ASCE, Vol. 107, pp. 553-562

Poulos SJ, Castro G, France JW (1985) Liquefaction evaluation procedure. Journal of Geotechnical Engineering, ASCE, Vol.111, No.6, pp. 772-792

Poulos SJ, Castro G, France JW (1988) Closure to discussion: Liquefaction evaluation procedure. Journal of Geotechnical Engineering, ASCE, Vol.114, No.2, pp. 251-259

Riemer MF, Seed RB (1997) Factors affecting apparent position of steady state line. Journal of Geotechnical and Geoenvironmental Engineering, Vol. 123 (3), pp. 281-288

Roscoe KH (1953) An apparatus for the application of simple shear to soil samples. Proc. 3rd Int. Conf. Soil Mech., 1: 186-191

Roscoe KH, Schofield AN, Wroth CP (1958) On the yielding of soils. Géotechnique 8 (1), 22–53

Roscoe KH, Schofield AN (1963) Mechanical behaviour of an idealized “wet” clay. Proc. Eur. Conf. Soil Mech. Found. Engng., Wiesbaden 1, 47-54

Roscoe KH, Basset RH, Cole ERL (1967) Principal axes observed during simple shear of a sand. Proc. Geotech. Conf., Oslo, pp. 231-237

Roscoe KH, Burland JB (1968) On the generalized stress-strain behaviour of “wet” clay. In Engineering plasticity. Edited by J. Heyman and F.A. Leckie. Cambridge University Press, London, UK. pp.535-609

Roscoe KH (1970) The influence of strains in soil mechanics. Tenth Rankine Lectrure, Géotechnique 20, No. 2, 129-170

Rowe PW (1962) The stress-dilatancy relation for static equilibrium of an assembly of particles in contact. Proc. R. Soc. Lond. A 1962 269, 500-527

Salvatore E, Mondoni G, Ando E, Albano M, Viggiani G (2017) Determination of the critical state of granular materials with triaxial tests. Soils Found. (2017), https://doi.org/10.1016/j.sandf.2017.08.005

Satake M (1978) Constitution of mechanics of granular materials through graph representation. Theoretical and Applied Mechanics 26, University of Tokyo Press, pp. 257-266

Schofield AN, Wroth CP (1968) Critical state soil mechanics. McGraw-Hill, London

Stroud MA (1970) The behaviour of sand at low stress levels in the simple shear apparatus. Ph.D. thesis, University of Cambridge

Tatsuoka F, Nakamura S, Huang C-C (1990) Strength anisotropy and shear band direction in plane strain tests of sand. Soils and Foundations, Vol.30, No.1, pp. 35-54

Taylor DW (1948) Fundamentals of Soil Mechanics. John Wiley, 1948

Theocharis AI, Vairaktaris E, Dafalias YF, Papadimitriou AG (2017) Proof of incompleteness of Critical State Theory in granular mechanics and its remedy. Journal of Engineering Mechanics, Vol. 143 (2), 1-12

Theocharis AI, Vairaktaris E, Dafalias YF, Papadimitriou AG (2019) Necessary and sufficient conditions for reaching and maintaining critical state. International Journal for Numerical and Analytical Methods in Geomechanics, 43: 2041-2045

Thornton C (2000) Numerical simulations of deviatoric shear deformation of granular media. Géotechnique 50, No. 1, 43-53

Uthayakumar M, Vaid YP (1998) Static liquefaction of sands under multiaxial loading. Canadian Geotechnical Journal 35, pp. 273-283

Vaid YP, Chern JC (1985) Cyclic and monotonic undrained response of saturated sands. *In* Advances in the Art of Testing Soils Under Cyclic Loading Conditions, Proceedings of the ASCE Convention, Detroit, pp. 171–176

Vaid YP, Chung EKF, Kuebris RH (1990) Stress path and steady state. Canadian Geotechnical Journal 27, pp. 1-7

Vaid YP, Sivathayalan S (2000) Fundamental factors affecting liquefaction susceptibility of sands. Canadian Geotechnical Journal 37, pp. 592-606

Vardoulakis I (1977) Sherfugenbildung in Sandkorpern als Verzweigungsproblem. Veröffenthichungen des Instituts für Boden- und Felsmechanik, Universität Karlsruhe, Heft 70

Verdugo R (1992) Characterization of sandy soil behaviour under large deformation. Ph.D. thesis, University of Tokyo

Verdugo R, Ishihara K (1996) The steady state of sandy soils. Soils and Foundations, Vol.36, No.2, pp. 81-91

Vesic AS, Clough GW (1968) Behaviour of granular materials under high stresses. Proc. Am. Soc. Civil Engrs, 94, SM3, 661-688

Vilhar G, Jovičić V, Coop MR (2013) The role of particle breakage in the mechanics of a non-plastic silty sand. Soils and Foundations, Vol. 51, No. 1, 91-104

Wan RG, Guo RG (1998) A simple constitutive model for granular soils: modified stress-dilatancy approach. Comput. Geotech. 22, No 2, 109-133

Wang Z-L, Dafalias YF, Shen C-K (1990) Bounding surface hypoplasticity model for sand. Journal of Engineering Mechanics, Vol. 116, No. 5, 983-1001

Wiebicke M, Andò E, Salvatore E, Viggiani G, Herle I (2017) Experimental measurement of granular fabric and its evolution under shearing Powders and Grains (2017), EPJ Web of Conferences. 140. 02020. 10.1051/epjconf/201714002020

Wood DM (1990) Soil behaviour and Critical State soil mechanics. Cambridge University Press, 1990

Wood DM, Maeda K (2008) Changing grading of soil: effect on critical states. Acta Geotechnica (2008), 3: 3-14

Wroth CP, Basset RH (1965) A stress-strain relationship for the shearing behaviour of a sand. Géotechnique 15, No. 1, 32-56

Yang ZX, Li XS, Yang J (2008) Quantifying and modelling fabric anisotropy of granular soils. Géotechnique 58, No. 4, 237-248

Yoshimine M, Ishihara K, Vargas W (1998) Effects of principal stress direction and intermediate principal stress on undrained shear behavior of sand. Soils and Foundations, Vol. 38, No. 3, 179-188

Yoshimine M, Ishihara K (1998) Flow potential of sand during liquefaction. Soils and Foundations, Vol. 38, No. 3, 189-198

Zhao J, Guo N (2013) Unique critical state characteristics in granular media considering fabric anisotropy. Géotechnique 63, No. 8, 695-704

Zhou W, Liu J, Ma G, Chang X (2017) Three-dimensional DEM investigation of critical state and dilatancy behaviors of granular materials. Acta Geotechnica (2017) 12:527-540

3.6 FIGURES

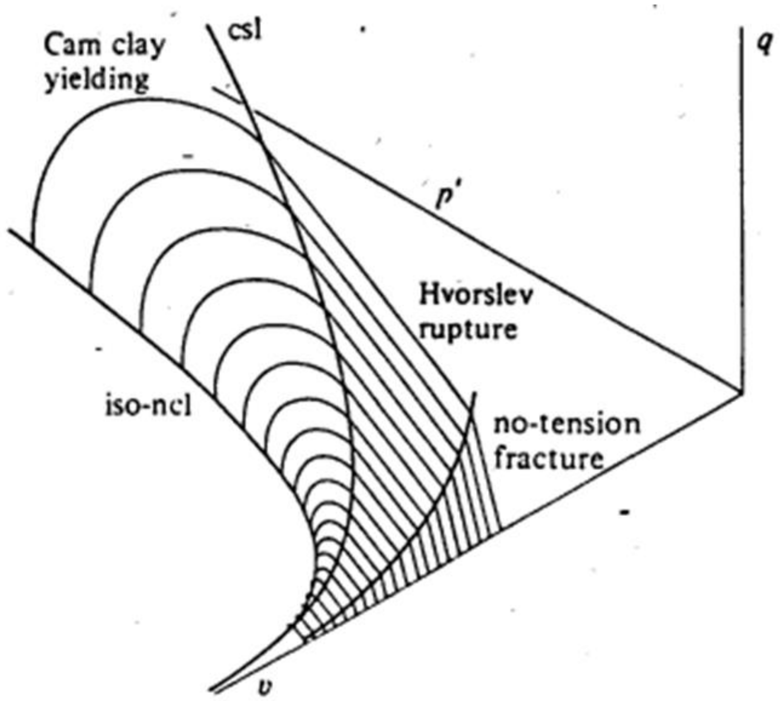

Fig. 3.1 The complete State Boundary Surface (SBS) in the q - p' - v space comprising the Hvoslev surface and Roscoe surface, with the intersection of the two surfaces being the Critical State Line (CSL). Note that the specific volume is $v = 1 + e$, where e is the void ratio. The locus shown in the figure with the name "Cam clay yielding" is actually the Roscoe surface that links the normal consolidation line (ncl) with the critical state line (csl) (after Wood 1990)

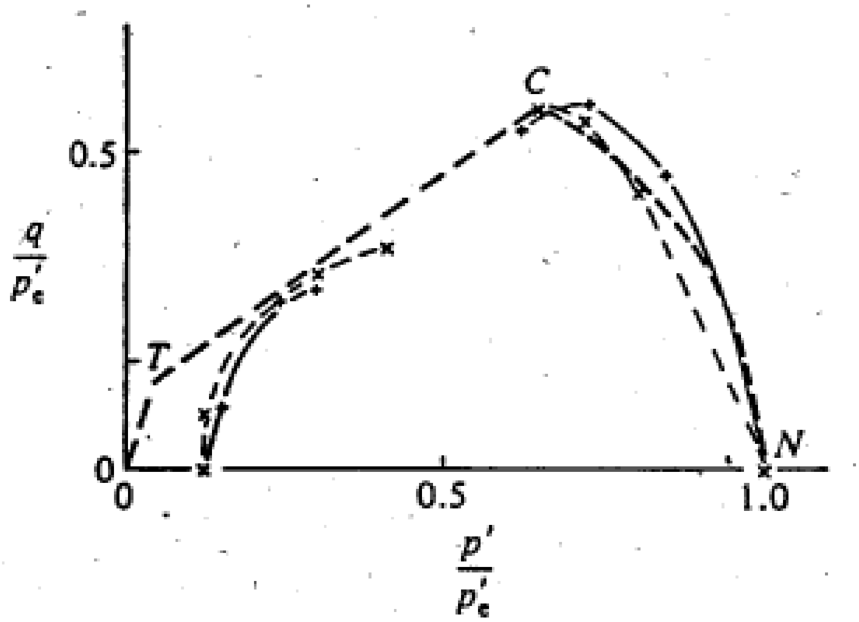

Fig. 3.2 Drained and undrained stress paths of triaxial tests on normally- and over-consolidated clay specimens in the dimensionless stress space q / p'_e - p' / p'_e. The cross symbols correspond to drained stress paths while the x-symbols correspond to undrained. The line OT with slope 3:1 is the no-extension limit corresponding to zero radial effective stress (figure after Wood 1990; data after Bishop and Henkel 1957)

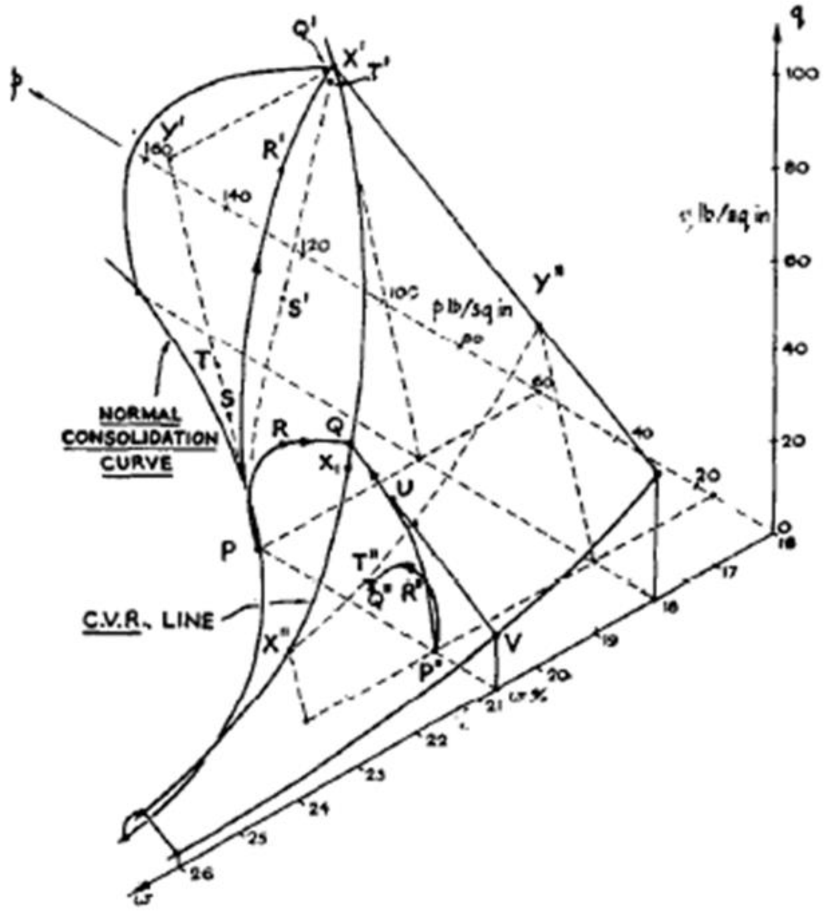

Fig. 3.3 The State Boundary Surface, Normal Consolidation Line and Critical Voids Ratio Line in the *q* - *p'* - *w* space for Weald Clay (figure after Roscoe et al. 1958; data after Gilbert 1954, Henkel 1956)

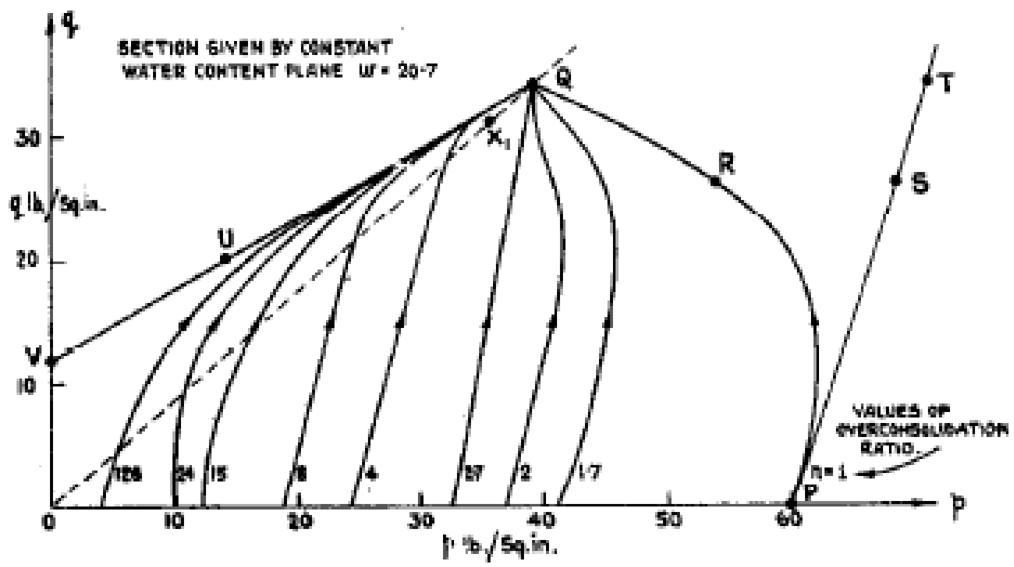

Fig. 3.4 Undrained loading paths of triaxial tests on Weald Clay on the section corresponding to constant water content w = 20.7% (w / 100% = e / G_s). The Hvorslev surface VUQ is not limited in this figure by the no-extension line. It is noted that the symbol η stands, here, for the overconsolidation ratio which varies from 1 to 24, according to Henkel (figure after Roscoe et al. 1958; data after Gilbert 1954, Henkel 1956)

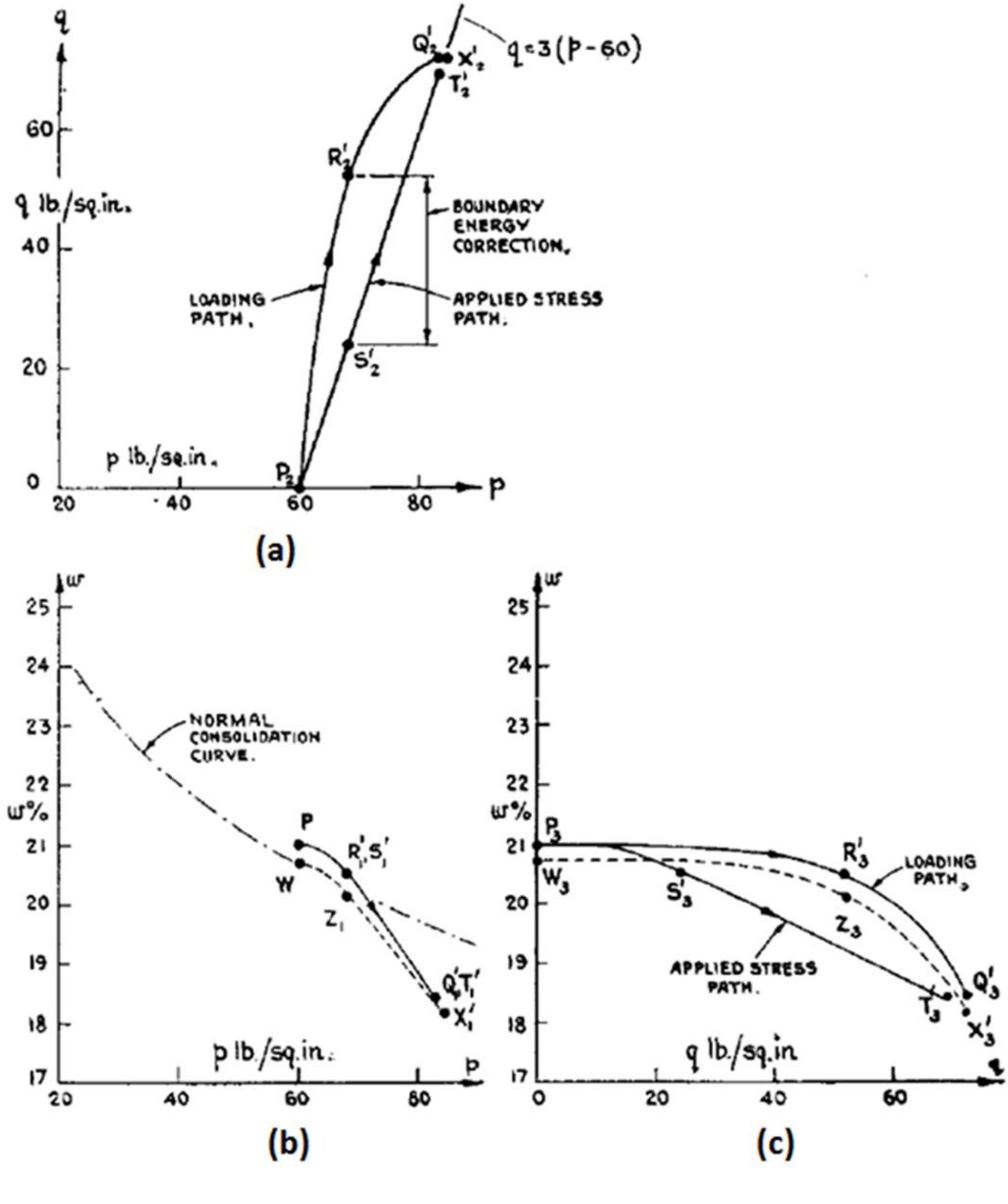

Fig. 3.5 Drained loading path of a triaxial test on normally-consolidated (η = 1) Weald Clay. **a** Projection on the *q* - *p'* plane. **b** Projection on the *w* - *p'* plane. **c** Projection on the *w* - *q* plane (figure after Roscoe et al. 1958; data after Gilbert 1954, Henkel 1956)

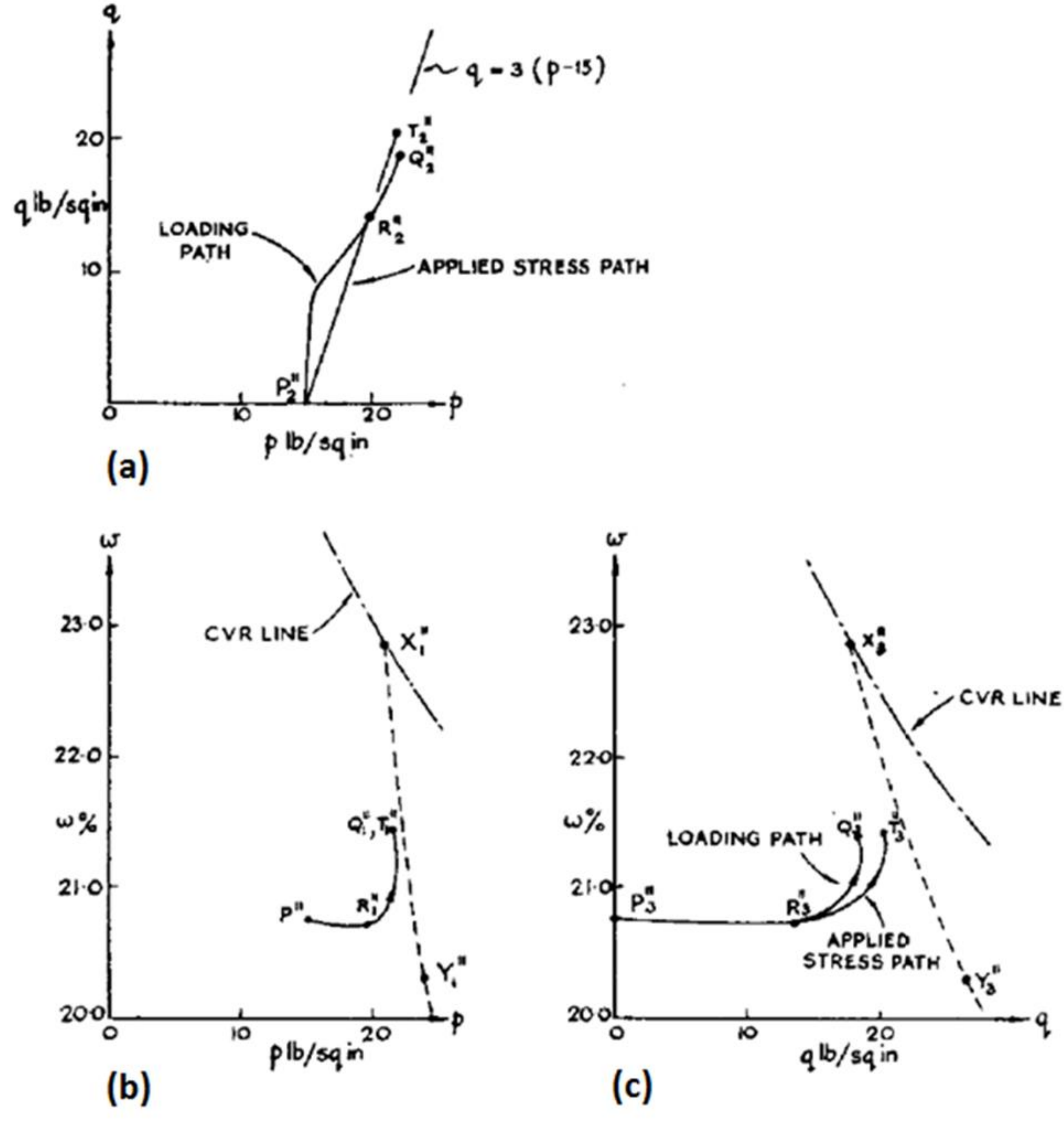

Fig. 3.6 Drained loading path of a triaxial test on overconsolidated (η = 8) Weald Clay. **a** Projection on the *q* - *p'* plane. **b** Projection on the *w* - *p'* plane. **c** Projection on the *w* - *q* plane (figure after Roscoe et al. 1958; data after Gilbert 1954, Henkel 1956)

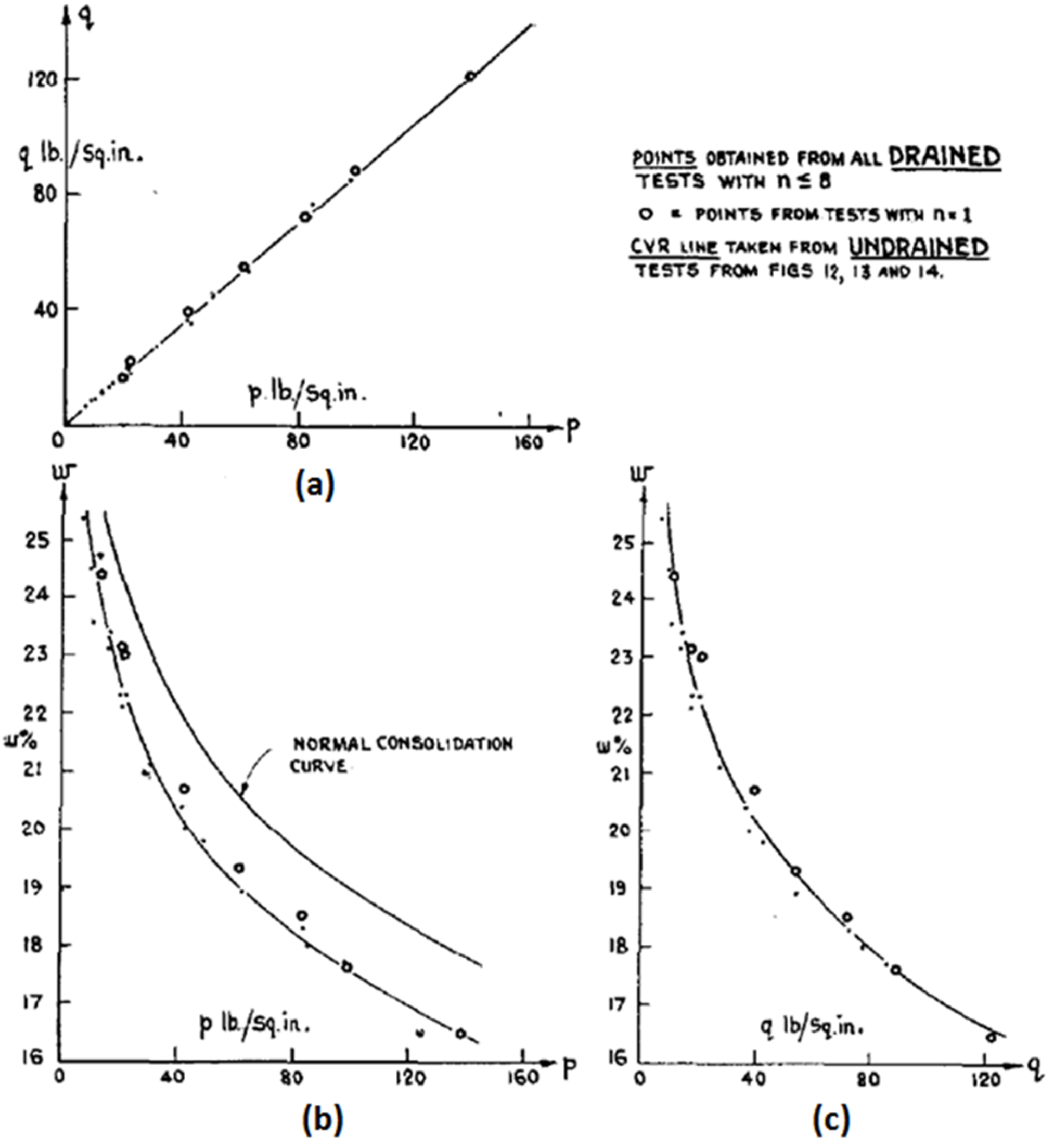

Fig. 3.7 Ultimate states of drained triaxial tests on Weald Clay (25 tests with $\eta \leq 8$) plotted together with the CVR line determined from the results of undrained tests. Projection: **a** on the q - p' plane, **b** on the w - p' plane, **c** on the w - q plane (figure after Roscoe et al. 1958; data after Gilbert 1954, Henkel 1956)

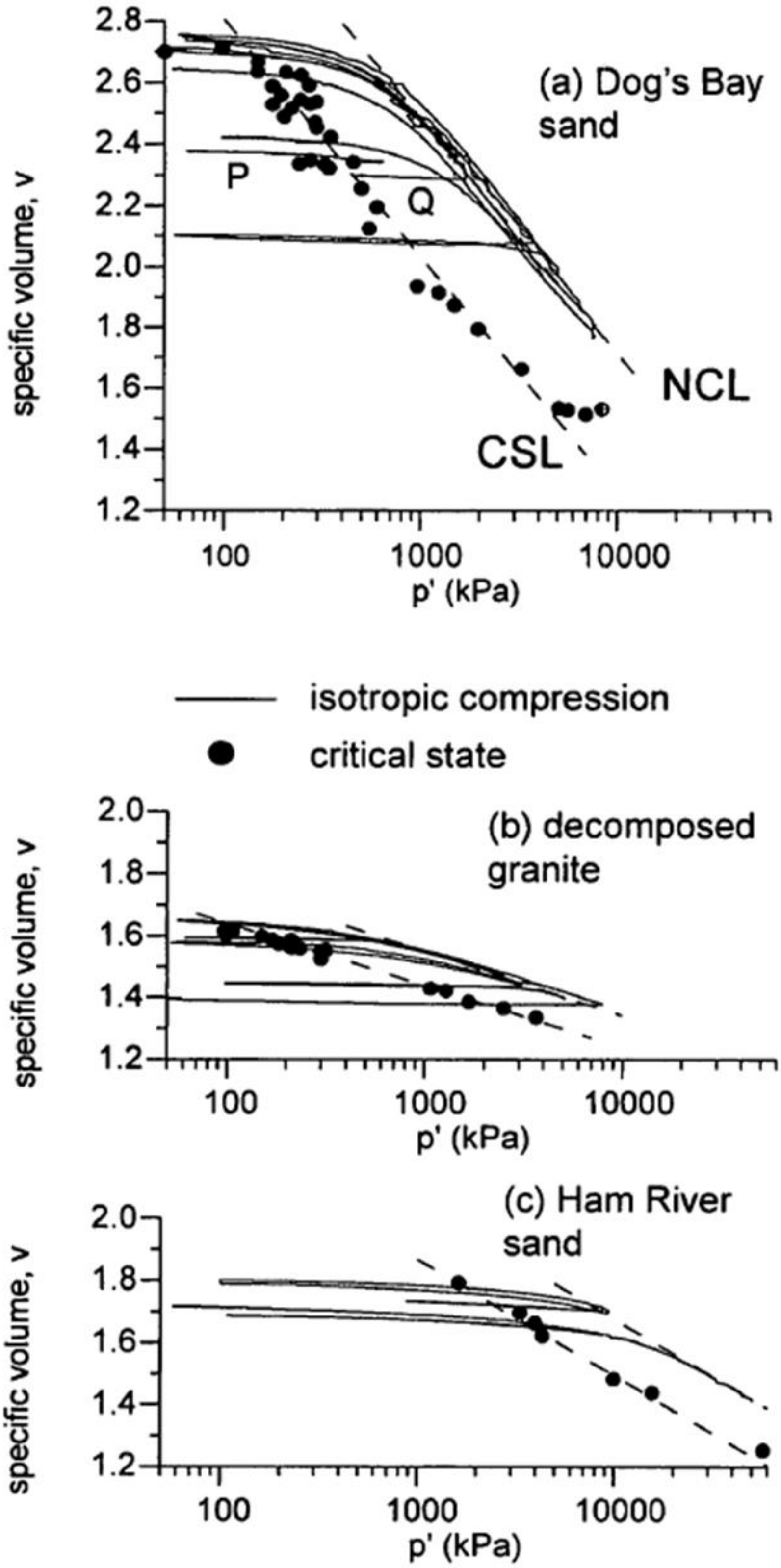

Fig. 3.8 Isotropic compression lines at elevated mean effective stress and critical state lines for three sands (after Luzzani and Coop 2002)

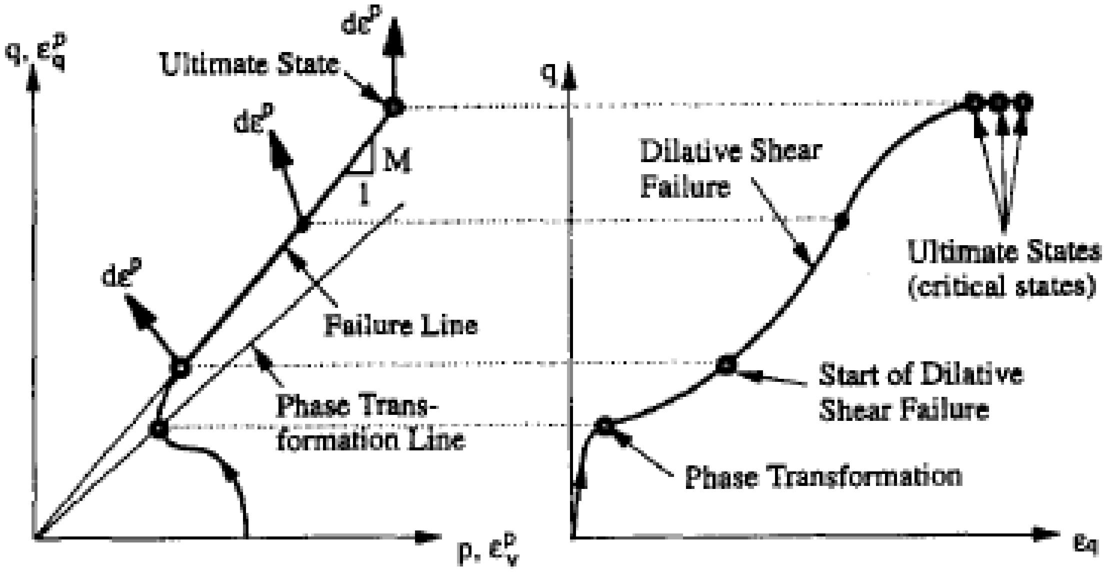

Fig. 3.9 The concept of dilative shear failure of sand (after Li 1997)

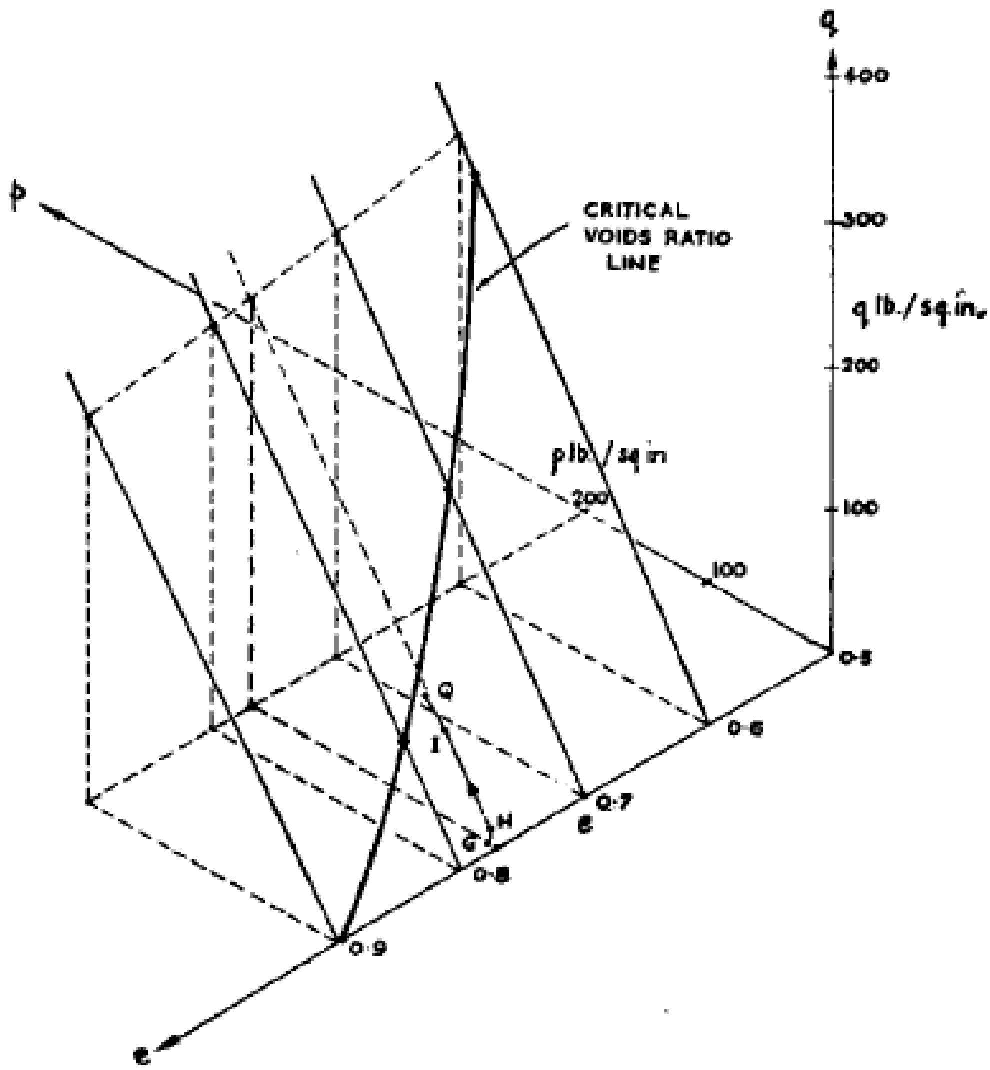

Fig. 3.10 The undrained State Boundary Surface and CVR line for Braehead Silt (figure after Roscoe et al. 1958; data after Penman 1953)

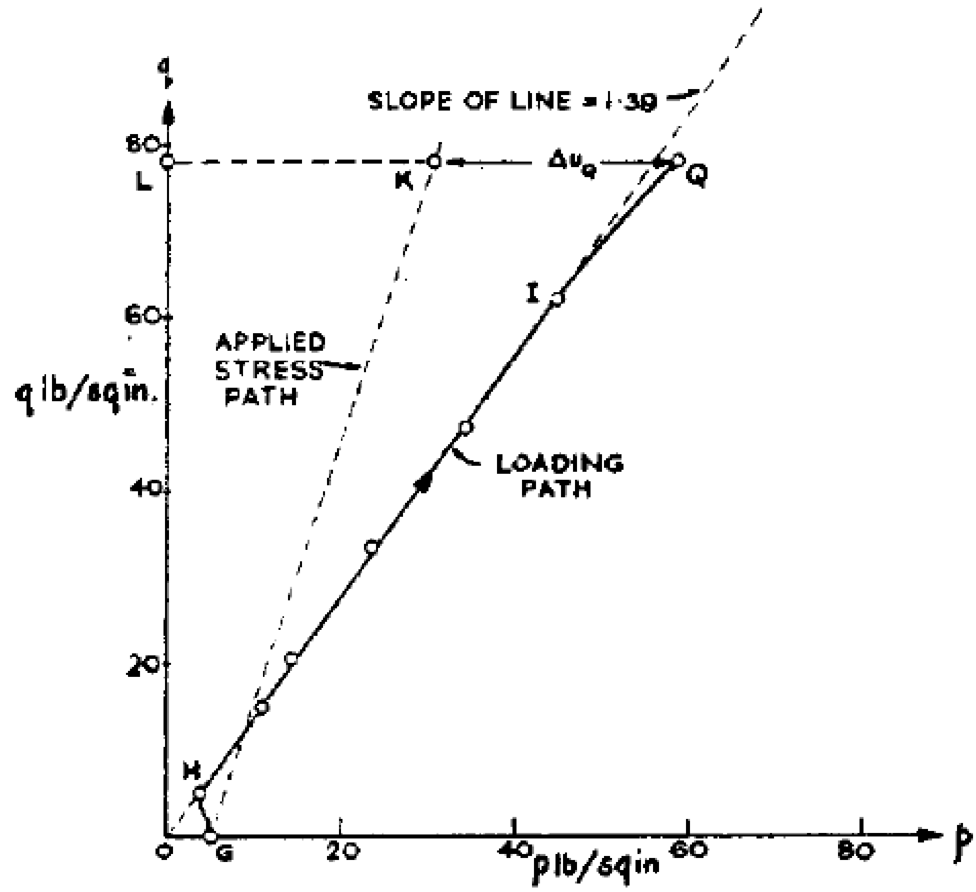

Fig. 3.11 Projection of the undrained loading path on the *q* - *p’* plane for Braehead Silt (figure after Roscoe et al. 1958; data after Penman 1953)

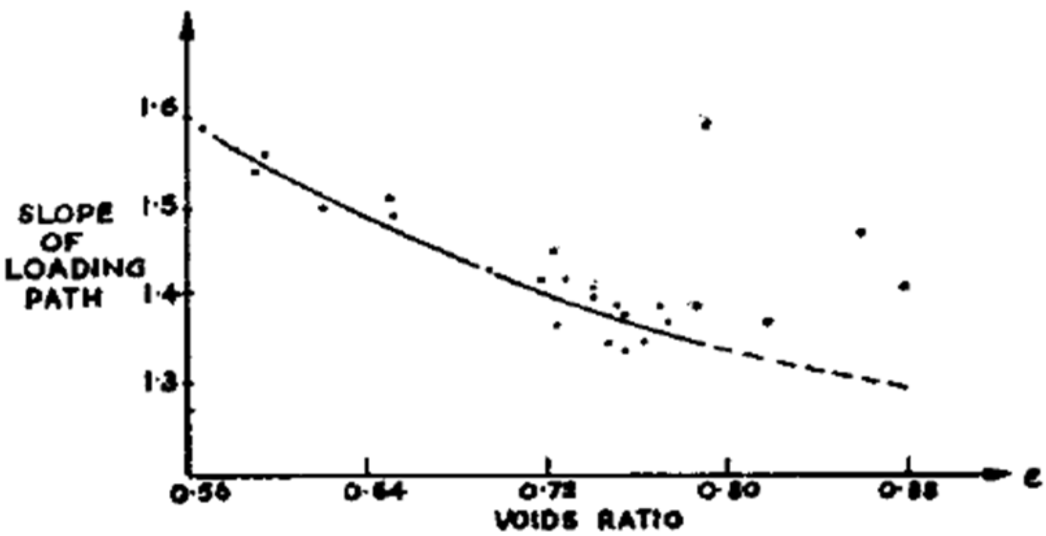

Fig. 3.12 Slope of the undrained SBS as a function of void ratio for Braehead Silt (figure after Roscoe et al. 1958; data after Penman 1953)

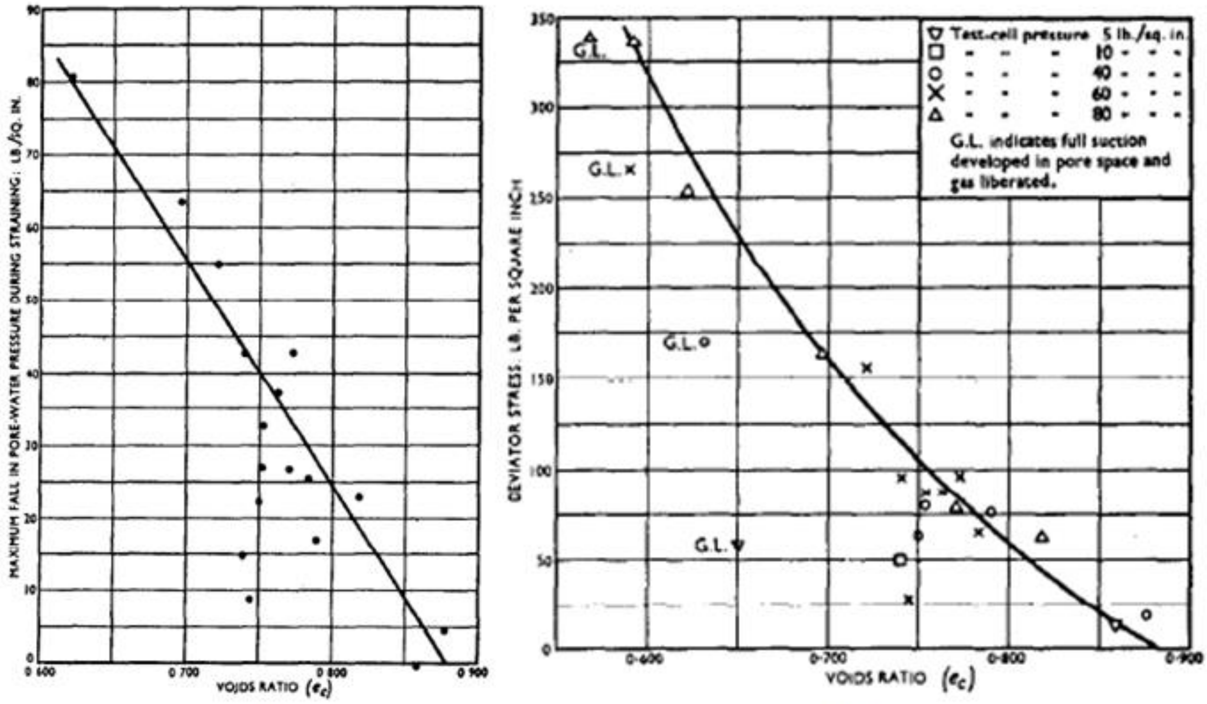

(a) (b)

Fig. 3.13 The CVR line determined from the results of undrained compression tests on Braehead Silt. **a** Ultimate excess pore-water pressure (-Δu_Q) versus consolidation void ratio for specimens consolidated to mean effective stress p' = 5 lb. / sq.in.(= 34.5 kPa). **b** Ultimate deviatoric stress versus consolidation void ratio for specimens consolidated to different effective stresses (after Penman 1953)

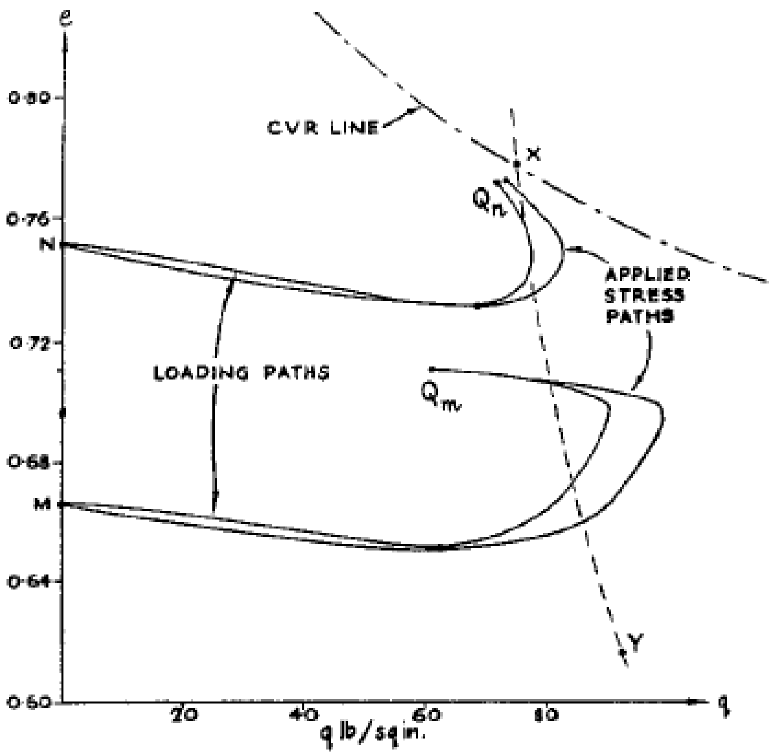

Fig. 3.14 Drained triaxial compression paths on Braehead Silt (figure after Roscoe et al. 1958; data after Penman 1953)

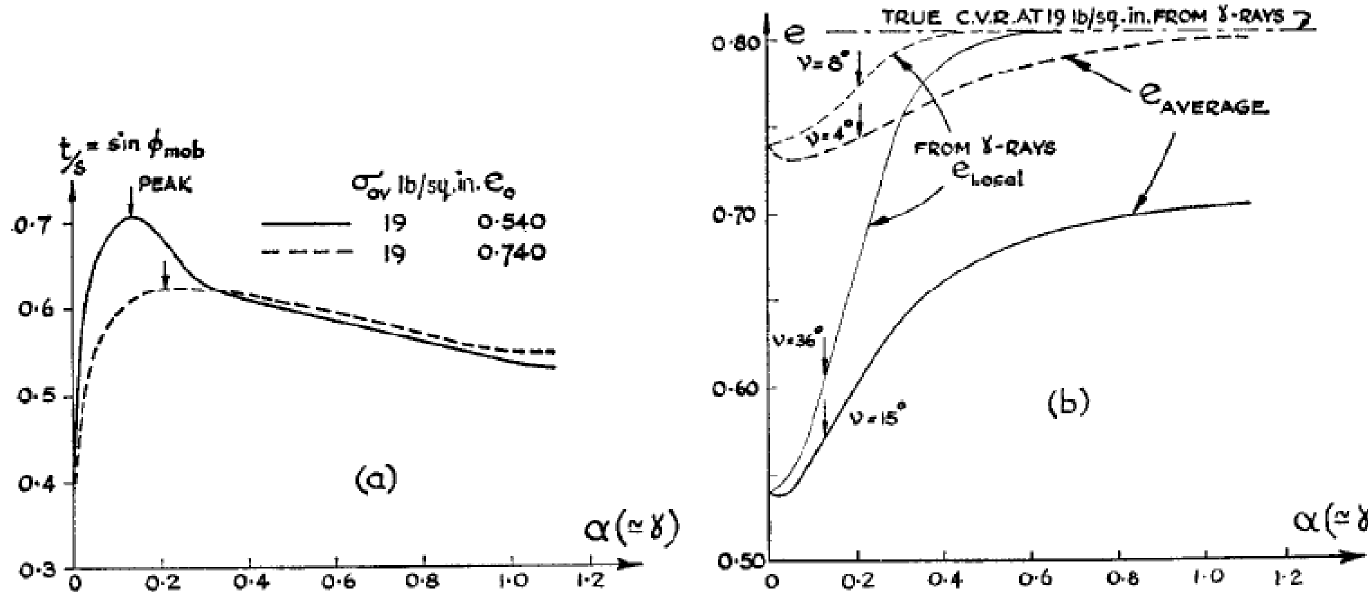

Fig. 3.15 Dense (full line) and loose (dashed line) sand tested in the simple shear apparatus under constant vertical stress equal to 19 lb. / sq.in. (= 130.9 kPa). **a** Stress ratio plotted against average shear strain. **b** Global and local void ratio plotted against average shear strain. It is noted that the average shear strain is determined from the boundary displacements while the local void ratio is measured using γ-rays (figure after Roscoe 1970; data after Cole 1967 and Coumoulos 1968)

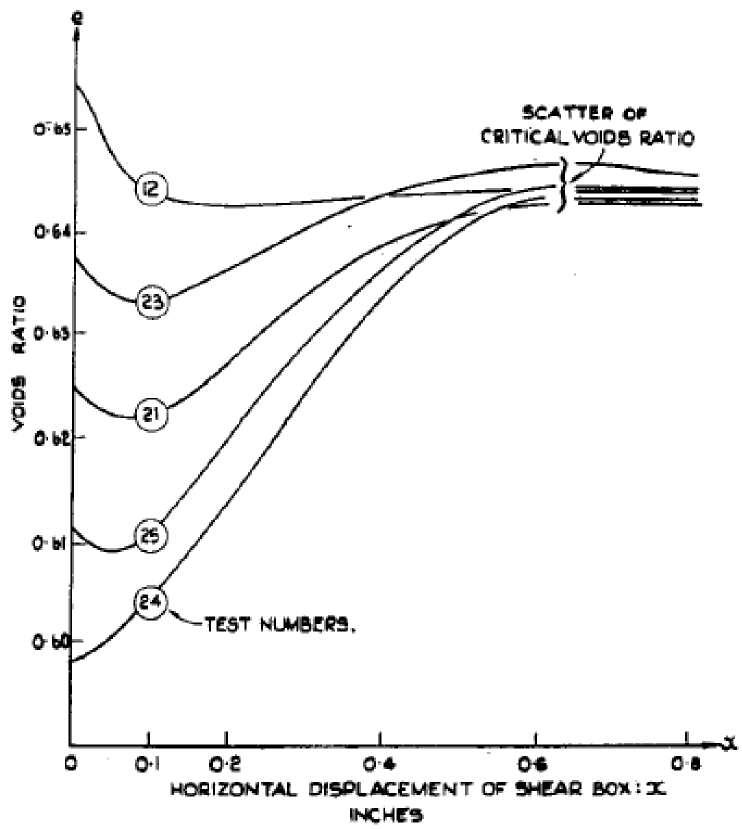

Fig. 3.16 Evolution of the void ratio of steel ball assemblies with horizontal displacement for drained tests in the simple shear apparatus. All tests were performed at fixed and constant vertical stress σ'_v = 20 lb. / sq.in. (= 137.8 kPa) (after Roscoe et al. 1958)

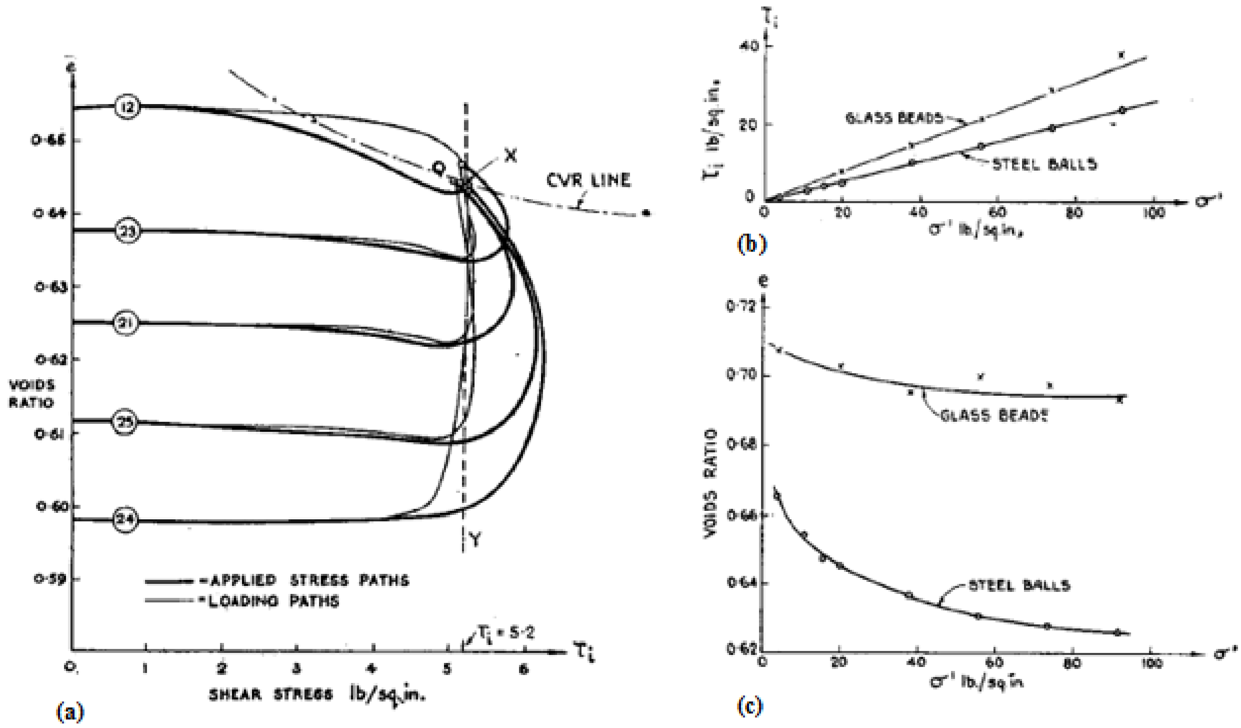

Fig. 3.17 a Applied stress paths and corrected loading paths of drained simple shear tests performed at fixed and constant vertical stress σ'_v = 20 lb. / sq.in. (= 137.8 kPa). **b** Projections of the CVR line on the reference planes for steel balls and glass beads (after Roscoe et al. 1958)

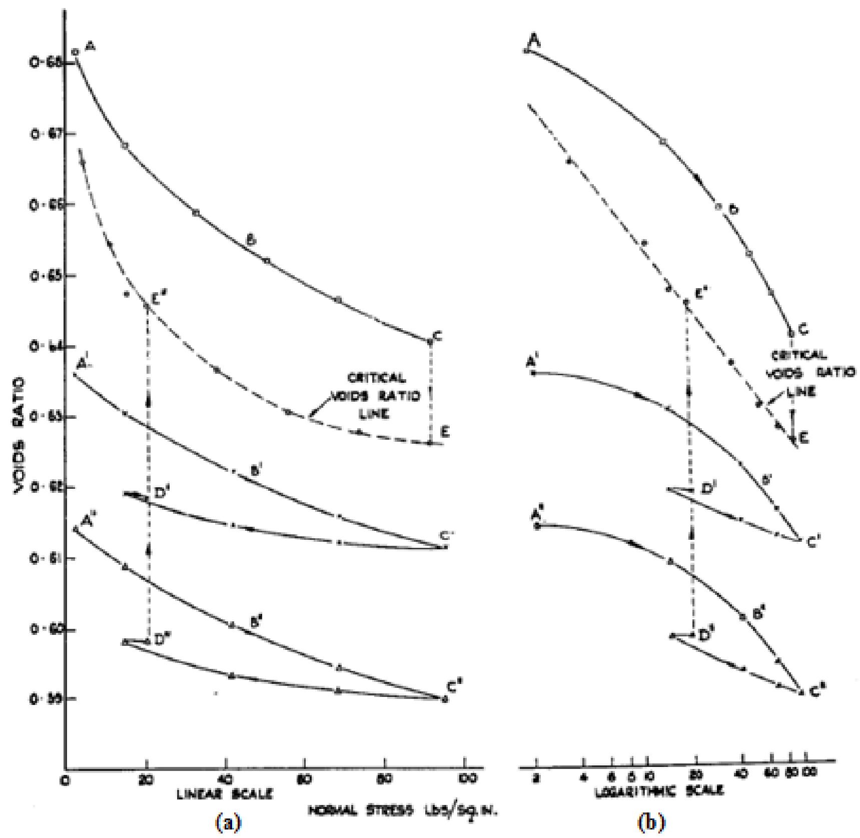

Fig. 3.18 Characteristic consolidation curves and projection of the CVR line for tests on steel balls: **a** in linear scale, **b** in semi-logarithmic scale (after Roscoe et al. 1958)

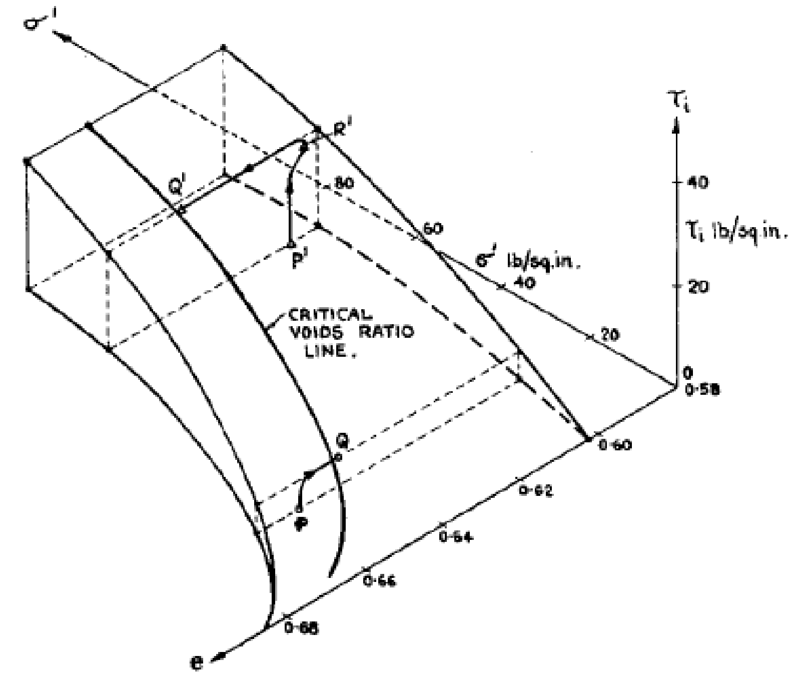

Fig. 3.19 Drained State Boundary Surface for steel balls subjected to simple shear loading (after Roscoe et al. 1958)

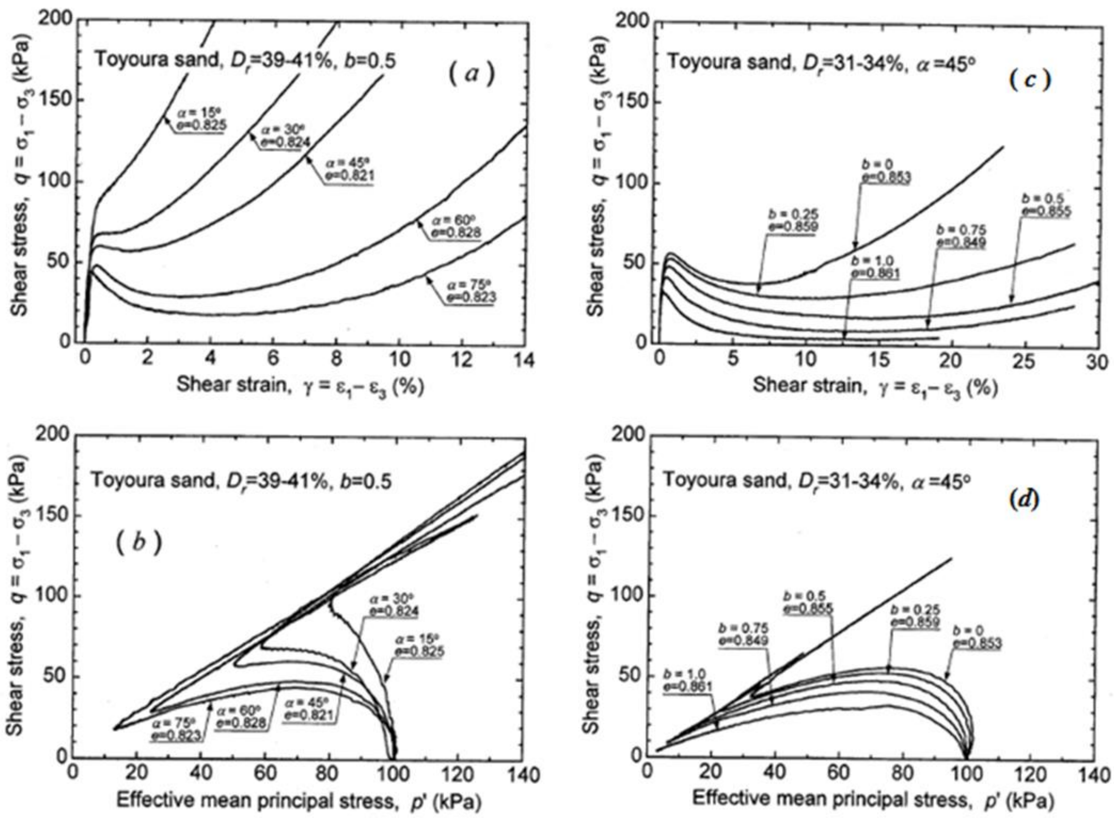

Fig. 3.20 Influence of the principal stress direction angle, α, on the undrained behaviour of gravity deposited sand: **a** stress - strain curves, **b** effective stress paths. Influence of the intermediate principal stress parameter, b, on the undrained behaviour of gravity deposited sand: **c** stress - strain curves, **d** effective stress paths (after Yoshimine et al. 1998)

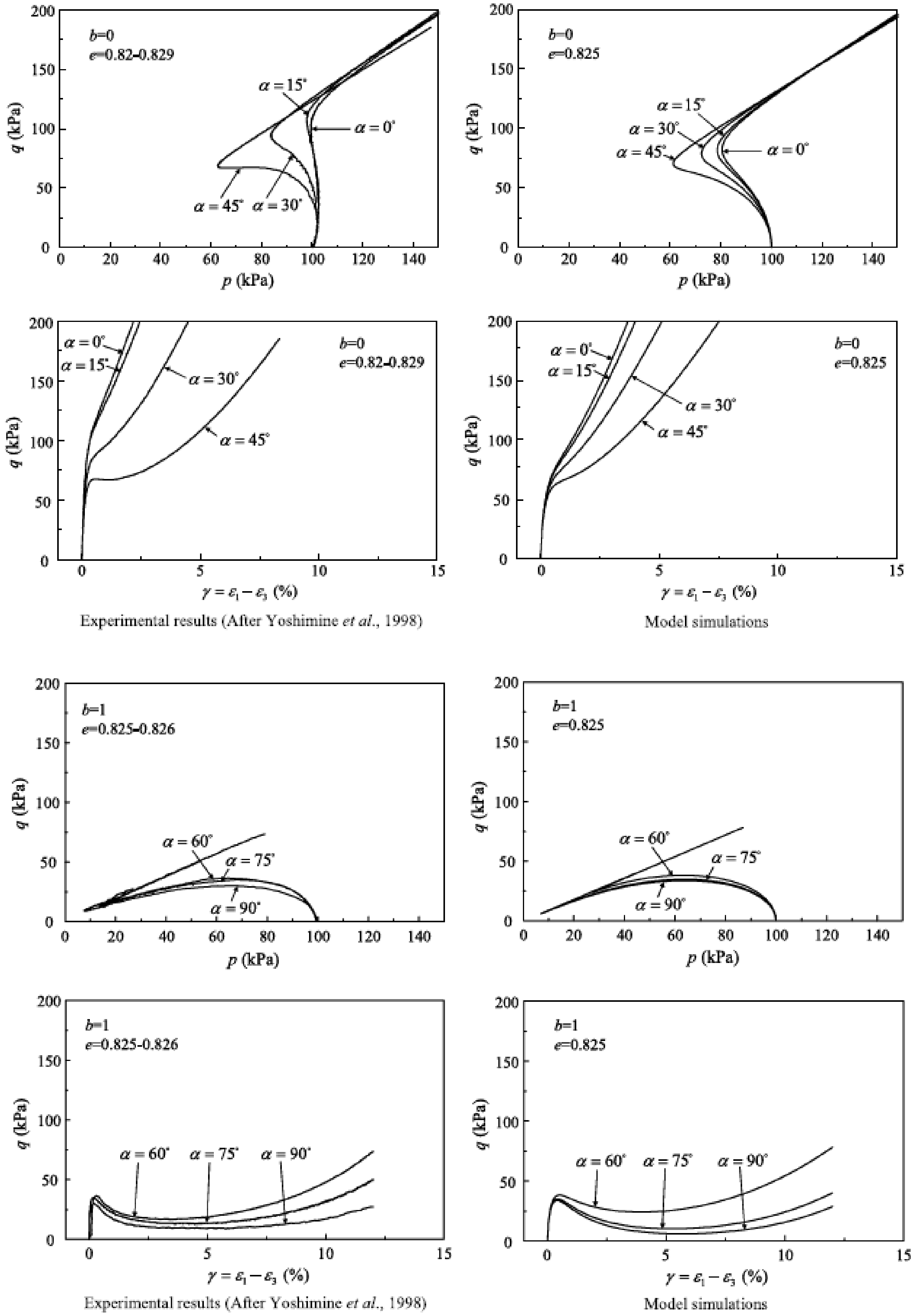

Fig. 3.21 Comparison of the experimental results of Yoshimine et al. (1998) and model simulations of Li and Dafalias (2012) in compression (b = 0) and extension (b = 1) loading at different principal stress direction angles, α (after Yoshimine et al. 1998 and Li and Dafalias 2012)

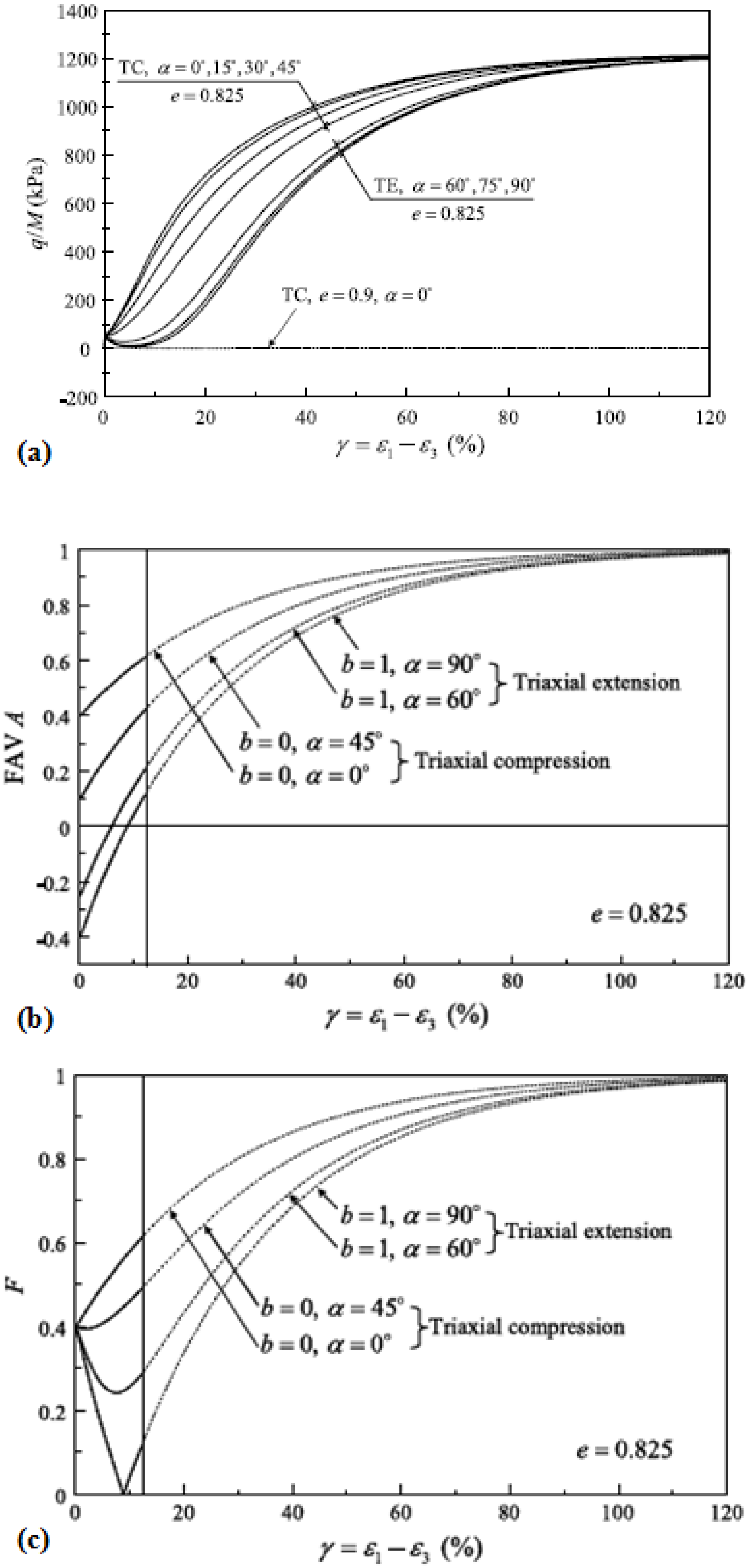

Fig. 3.22 Evolution of q / M, A and F with shear strain, γ, in the simulations of monotonic undrained loading with fixed values of α and b (after Li and Dafalias 2012)

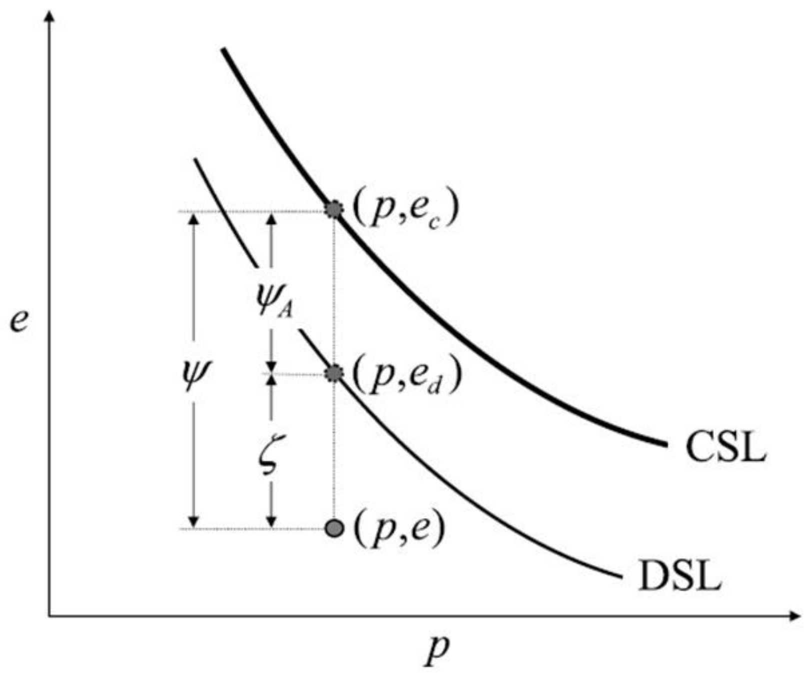

Fig. 3.23 The unique critical state line (CSL) and moving dilatancy state line (DSL) in the *e* - *p'* plane that are used as reference lines to determine the state parameter, ψ, and the dilatancy state parameter, ζ, respectively, in accordance with the Anisotropic Critical State Theory (after Li and Dafalias 2012)

CHAPTER 4: FLOW DEFORMATION OF SANDS

4.1 INTRODUCTION

Flow deformation of sands is a catastrophic *liquefaction phenomenon* that occurs in the field when the shear strength decreases, due to pore-water pressure build up, below the stress level that is required for static equilibrium. The decrease in strength inevitably results in large soil deformation that is driven by the static shear stress imposed by gravity. Loose saturated sands in sloping ground or under the foundations of structures are particularly vulnerable to flow, which can be triggered under monotonic or cyclic undrained loading, or even under undrained loading with constant deviatoric stress. The catastrophic nature of flow deformation and the fact that this phenomenon can be triggered by small stress disturbances occurring in the field motivate further research on this topic.

The present chapter presents the findings of past experimental studies concerning the undrained behaviour and flow deformation of saturated sands. It is shown that the state and fabric anisotropy influence the response of sands to undrained loading and determine whether a flow or non-flow behaviour is exhibited. Moreover, it is shown that sands are particularly prone to flow when subjected to loading involving rotation of the stress principal axes, a situation met frequently in situ. This chapter also presents the findings of numerical and theoretical studies that investigate the flow deformation phenomenon within the frameworks of Stability and Bifurcation Theory and Critical State Theory in order to aid the interpretation of the experimental results of the present study.

4.2 UNDRAINED BEHAVIOUR AND FLOW DEFORMATION OF SANDS UNDER MONOTONIC LOADING

Castro (1969) studied the liquefaction of loose saturated sands by means of stress-controlled (load-controlled) monotonic and cyclic undrained triaxial tests. In monotonic tests, a dead weight increment was applied in each loading step. The results of a typical monotonic test are shown in Fig. 4.1. It can be seen that the deviatoric stress increases until a *peak point* is reached at an axial strain of about 0.5%. At the peak point, any attempt to impose a further axial stress increment results in a sudden increase in the pore-water pressure and axial strain, with a simultaneous unloading of the deviatoric stress. Consequently, the sand response becomes *unstable* no matter how small the target stress increment is, due to the particular control parameters (Nova 1994) used in the experiment. It is noted that the stress unloading occurs *spontaneously* without reversing the loading direction hence it corresponds to a decrease in strength. The excess pore-water pressure reaches a value almost equal to the initial effective confining stress, thus, the deviatoric stress decreases to a minimum level that corresponds to the new effective confining stress. The axial strain increases from 0.5% to 20% in just 0.7 seconds, while it took 14 minutes to reach the value of 0.5% under stable stepwise loading. After the mobilisation of the *minimum strength*, the sand deforms continuously in shear under constant stresses (deviatoric and effective isotropic) and pore-water pressure. This behaviour is often called the *flow deformation* of sands in literature.

The experimental results of Castro (1969) were used to verify two earlier hypotheses of Casagrande (Casagrande 1936, Casagrande and Watson 1938). The first concerns the existence of a *critical void ratio* that corresponds to a given effective confining stress at the ultimate state reached after the sand is sheared extensively; this concept is the basic idea of the Critical State Theory (see Chapter 3). The second concerns the development of a *flow structure* of loose liquefied sands when unstable high-rate deformation is exhibited under undrained loading. Casagrande postulated that at the onset of liquefaction the structure of loose sands changes abruptly into a “minimum resistance flow structure” that is different from the “normal structure” developed in the case of drained loading or undrained loading of dense material, in which the rate of deformation is low because the behaviour of sand is dilative and stable. This may be justified by the fact that Castro (1969) determined different *Critical Void Ratio* (CVR) lines (see Chapter 2 and 3) corresponding to stable response (drained or undrained) or unstable response; similar findings were reported by Alarcon-Guzman et al. (1988).

Castro (1969) distinguished three characteristic monotonic undrained behaviours of sand specimens consolidated isotropically to the same effective confining stress, each corresponding to a different density. Figure 4.2 shows that very loose sand (curves “a”) is highly contractive and behaves unstably. The deviatoric stress decreases suddenly after the mobilisation of the *peak strength*, q_p, as a result of the pore-water pressure build up that causes the effective confining stress to drop almost to zero. The shear deformation increases continuously under constant stresses and pore-water pressure after the *minimum undrained strength*, q_{min}, is mobilised. This type of behaviour (flow deformation) was later termed the *steady state of deformation* by Poulos (1981), who also stated that, at steady state, the deformation velocity is constant. However, Fu and Dafalias (2011) and Li and Dafalias (2012) suggested that the true ultimate steady state (i.e. the critical state) of granular materials is attained only after extensive shear deformation that cannot be achieved in physical testing without violating deformation homogeneity.

On the other hand, Castro (1969) reported that dense sand (curves “c” in Fig. 4.2) behaves stably since the deviatoric stress increases continuously with shear strain as far as the dilatancy is not exhausted (Verdugo and Ishihara 1996, Li 1997). The pore-water pressure increases initially and then decreases, indicating a tendency for contraction which soon turns into dilation at the phase transformation point (Ishihara et al. 1975). At very large deformation (not shown in Fig. 4.2) the dilatancy is exhausted and dense (saturated) sand reaches the *ultimate steady state* at which it keeps deforming in continuing shearing under constant stresses and pore-water pressure (Verdugo and Ishihara 1996, Yoshimine and Ishihara 1998). The ultimate steady state is actually the critical state (Roscoe et al. 1958, Schofield and Wroth 1968).

Lastly, Catsro (1969) observed that medium-dense sand (curves "b" in Fig. 4.2) exhibits a behaviour intermediate between those of loose and dense sand which becomes only temporarily unstable. The stress - strain curve demonstrates a *transient peak strength* (Bishop 1971), q_p, followed by unstable stress unloading towards the *minimum undrained strength*, q_{min}. The sand undergoes *limited flow deformation* under constant stresses and pore-water pressure at the state of minimum undrained strength; this behaviour was later termed the *quasi-steady state* by Alarcon-Guzman et al. (1988). The limited flow deformation, or quasi-steady state, is terminated since phase transformation occurs and strength is regained due to the decrease in pore-water pressure and increase in effective confining stress. It is noted that the minimum-q point may or may not coincide with the phase-transformation point (Vardoulakis and Sulem 1995, Finno et al. 1996). At very large deformation the medium-dense sand reaches the *ultimate steady state* when the dilatancy is exhausted (Verdugo and Ishihara 1996). Figure 4.3 shows the characteristic types of monotonic undrained behaviour of sand according to Yoshimine and Ishihara (1998) in order to clarify the use of terminology. It is important to notice that the various "steady" states defined by different researchers do not always correspond to the true ultimate material state (critical state) (Li and Dafalias 2012).

Castro (1969) found that flow deformation is triggered also in the case of anisotropically consolidated (AC) sand subjected to monotonic loading and of isotropically consolidated (IC) sand subjected to cyclic loading. Figures 4.4 and 4.5 show the evolution of deviatoric stress and excess pore-water pressure with axial strain as well as the effective stress paths (ESPs) for these two cases of triaxial loading. Castro (1969) also performed monotonic drained loading tests under strain-controlled conditions to check whether or not the CVR line obtained from these tests coincides with the one obtained from the undrained tests in which dynamic flow liquefaction was observed. Figure 4.6 shows the stress - strain and void ratio - strain curves for two loose and one dense specimen subjected to drained loading.

Castro (1969) figured out that two different CVR lines exist for the same sand, as shown in Fig. 4.7, depending on whether dynamic flow liquefaction occurs or not. The e_F-line (the letter F stands for flow) corresponds to the combinations (σ'_3 , e) that are mobilised at steady-state (flow liquefaction) or quasi-steady state (limited flow liquefaction) in monotonic undrained loading tests of both IC and AC sand specimens.

The steady states of IC sand specimens that exhibited flow liquefaction in cyclic undrained loading tests are also included. On the other hand, the e_S-line corresponds to the combinations (σ'_3 , e) that are mobilised ultimately in monotonic drained tests (in which sand behaves stably and does not liquefy) when the shear deformation increases continuously under constant stresses and void ratio. It is noted that only the ultimate states of loose specimens subjected to drained loading are included in Fig. 4.7 because dense specimens undergo severe strain localisation and thus the global measurements of the boundary load and displacement and of the volume change do not represent the soil element behaviour (see also Desrues et al. 1996). Castro (1969) suggested that the ultimate points (σ'_3 , e) in the monotonic undrained loading tests on dilative (dense) sand specimens would have reached the e_S-line if larger strains had been allowed to develop (see, for example, the square symbols in Fig. 4.7 with the arrows showing the evolution of state at the end of testing).

Castro (1969) interpreted the existence of two different CVR lines as the consequence of the existence of two different structures of sand, as suggested earlier by Casagrande (Casagrande 1936, Casagrande and Watson 1938). The “normal structure” corresponds to stable slow-rate deformation under drained or dilative undrained response, while the “flow structure” corresponds to unstable high-rate deformation of liquefied sand. Similar results were reported by Alarcon-Guzman et al. (1988) who suggested that a *structural collapse* occurs when the unstable flow deformation of sand is triggered. Casagrande urged Castro to perform strain-controlled undrained loading tests on loose sand in order to check if the deformation rate has an effect on the minimum undrained strength, q_{min}, and position of the CVR line (Casagrande 1975). The results of tests with slow and high deformation rate are compared in Fig. 4.8.

Figure 4.8 shows that the CVR line in the e - σ'_3 plane corresponding to slow-rate undrained deformation (E_{sc}-line) differs from the one corresponding to high-rate undrained deformation (F-line). The effective confining stress σ'_3 during flow, for a given void ratio, is about 2.5 times higher in the former case meaning that the strength q_{min} decreases when the strain rate increases. Casagrande (1975) reported that the slow strain rate “causes locally groups of sand grains to lose temporarily their flow structure” hence the strength q_{min} increases. It is noted that during Castro’s (1969) load-controlled tests the strain rate was about 20,000 times faster than the one developed during strain-controlled tests. If one compares the relative position of the e_s-line in Fig. 4.7 with the E_{sc}-line in Fig. 4.8 it can be found that the *residual strength*, q_{ult}, of loose sand subjected to drained loading is even higher than the minimum strength, q_{min}, of loose sand subjected to undrained strain-controlled loading. According to Casagrande (1975), this is because a flow structure cannot develop under drained deformation.

However, other researchers performed loading tests on sands and drawn different conclusions concerning the effect of strain rate on the minimum strength, q_{min}, and position of the CVR line. Poulos et al. (1988) reported that a series of triaxial tests on a narrow graded, fine, angular, quartz sand showed the existence of a unique CVR line; both load- and strain-controlled tests were performed and the strain rate during the steady-state deformation was four orders of magnitude higher in the former tests than in the latter tests. Been et al. (1991) performed triaxial loading tests on medium-to-fine quartz Erksak sand with sub-rounded grains and found that the CVR line is not affected by the strain rate; the strain rate at steady state was 4% / h and about 300,000% / h in strain-controlled and load-controlled tests, respectively. Yamamuro and Lade (1993) found that the strain rate affects the response of coarse Cambria sand to high-pressure undrained triaxial compression; specifically, they found that the effective stress ratio at the peak point (i.e. the point of peak strength, q_p) is not affected by the strain rate though the peak strength, q_p, increases with strain rate. After the peak point, the ESPs converge to a single curve indicating that the minimum strength, q_{min}, does not depend on strain rate. On the other hand, Yamamuro and Lade (1998) performed undrained triaxial compression tests on silty sand at usual confining pressure and different rates of strain. They found that both the peak and minimum strengths increase with strain rate. They also reported that the steady state line is not unique even in the case that a constant strain rate is applied.

Poulos et al. (1985) proposed a procedure for evaluating the *liquefaction susceptibility* of soil masses subjected to static shear stress as, for example, in the case of sloping ground, embankments and foundations of structures. The procedure is in fact a *stability analysis* that compares the static shear stress required for equilibrium, termed the *driving shear stress*, with the *minimum undrained strength*, q_{min}, that corresponds to the steady state or quasi-steady state. It is noted that the quasi-steady state strength is conservatively used in the analysis instead of the much higher ultimate steady state strength (see, for example, Fig. 4.3) because the latter is mobilised at very large deformation and only if the negative excess pore-water pressure (due to plastic dilation) is not dissipated; these conditions, however, are irrelevant to the stability analysis of soil masses in the field (Ishihara 1993, Verdugo and Ishihara 1996, Riemer and Seed 1997, Yoshimine and Ishihara 1998, Sivathayalan and Vaid 2002). The key feature of the liquefaction analysis is the determination of the minimum undrained strength, q_{min}, of soil which corresponds to the in-situ void ratio by means of the *Steady State Line* (SSL) (Poulos 1981). According to Castro (1969) and Poulos et al. (1985), the minimum undrained strength, q_{min}, is a function *only* of the void ratio.

On the other hand, Konrad (1990a and b) found that the minimum undrained strength, q_{min}, depends on the *initial state* of sand, i.e. on the initial combination of void ratio and mean effective stress; similar findings were reported by Riemer and Seed (1997). The dependence of q_{min} on the effective consolidation stress means that the SSL is non-unique since the deviatoric stress is related to the mean effective stress via the frictional condition at steady state (see Chapter 2), which in turn is related to the initial void ratio via the SSL. Figure 4.9 shows the ESPs and stress - strain curves of monotonic undrained compression tests on sand performed by Riemer and Seed (1997). The isotropically consolidated sand specimens have the same void ratio but different effective consolidation stress. It is apparent that the minimum undrained strength, q_{min}, increases with effective consolidation stress. This means that the quasi-steady state points in the *e* - *p'* plane are not unique for a given void ratio, as can be seen in Fig. 4.10. However, if the true ultimate material states, attained after extensive deformation, are plotted in the state diagram then a *unique ultimate steady state line* (USSL) (Verdugo and Ishihara 1996) or *critical state line* (CSL) (Been et al. 1991, Li and Dafalias 2012) can be defined (see also Chapters 2 and 3).

Another problem with the liquefaction analysis proposed by Poulos et al. (1985) is that the minimum undrained strength, q_{min}, is not a unique function of the void ratio, instead it depends strongly on the direction of the major principal stress, σ_1, with respect to the bedding planes of cross-anisotropic sands; q_{min}, depends also on the mode of loading. The strength anisotropy has significant consequences since in real loading situations the direction of the σ_1-axis with respect to the bedding planes varies along the potential failure surface (along which flow deformation may be triggered, as suggested by Finno et al. 1996). Moreover, the σ_1-axis may rotate during construction and operation of structures that are supported by, or support, the potentially liquefiable soil (Ishihara and Li 1972, Bjerrum 1973, Goldscheider 1975, Ishihara and Towhata 1983, Zdravkovic et al. 2002). Examples of these loading situations are presented in Fig. 4.11. Vaid et al. (1990) reported that the minimum undrained strength, q_{min}, of loose sand is considerably lower in triaxial extension than in compression when all the other factors (i.e. the effective consolidation stress and void ratio) are the same. Figure 4.12 illustrates the dependence of q_{min} on the mode of triaxial loading (compression or extension) which has been also reported by Bishop (1971), Tatsuoka and Ishihara (1973), Hanzawa (1980) and Miura and Toki (1982). Moreover, Symes et al. (1984, 1985) and Shibuya and Hight (1987) found that the minimum undrained strength, q_{min}, under generalised (non-triaxial) loading conditions decreases gradually when the direction of the σ_1-axis tends to align with the horizontal bedding planes.

Considering the stress path dependence of the minimum undrained strength, q_{min}, some researchers suggested that there exist different steady state lines (SSLs) in the *e* - *p'* plane for different modes of loading. For example, Vaid et al. (1990) found that the SSL is unique in the triaxial compression mode though in the triaxial extension mode different SSLs correspond to different deposition void ratios, as shown in Fig. 4.13. It is noted, though, that Vaid et al. (1990) treated the steady states and quasi-steady states in the state diagram interchangeably. Riemer and Seed (1997) also reported that the locus of the quasi-steady states in the *e* - *p'* plane for loose sand is not unique instead it depends on the mode of loading, as shown in Fig. 4.14. However, other authors suggest that if the true ultimate material states, and not the quasi-steady states, are used to determine the critical state line in the *e* - *p'* plane, the locus obtained is indeed unique (Been et al. 1991, Verdugo and Ishihara 1996, Li and Dafalias 2012, Zhao and Guo 2013, Salvatore et al. 2017, Zhou et al. 2017).

Yoshimine and Ishihara (1998) treated the quasi-steady states as a special case of phase transformation points that do not correspond to ultimate material states. They found that in the case of undrained triaxial compression (TC) the position of the phase transformation line (PTL) in the e - p' plane depends both on the deposition void ratio, e_{20}, and the effective consolidation stress, p'_c. This dependence is illustrated in Fig. 4.15 which shows the phase transformation lines for different values of e_{20} and p'_c; it can be inferred that the quasi-steady state is exhibited in triaxial compression only if the phase transformation line is very close to the ultimate steady state line (USSL), for sand deposited in the loosest state. The same dependence applies in the case of undrained triaxial extension (TE) though many quasi-steady state lines are determined corresponding to different values of e_{20}, as can be seen in Fig. 4.16. The ultimate material states are not reached in the triaxial extension mode but it is assumed that the ultimate steady state line is the upper limit of the quasi-steady state lines. Figure 4.17 shows the different phase transformation lines and the assumed ultimate steady state line in the case of simple shear (SS) loading. It can be seen that the characteristic lines in simple shear mode are located between the respective lines corresponding to triaxial compression and triaxial extension. Consequently, the behaviour of sand is the most dilative under triaxial compression loading the less dilative under triaxial extension loading while it is intermediate under simple shear loading.

Yoshimine et al. (1998) investigated the monotonic undrained behaviour of sand using the hollow cylinder apparatus (HCA). In the HCA the angle α, expressing the direction of the major principal stress, σ_1, with respect to the vertical direction, and the intermediate principal stress parameter, $b = (\sigma'_2 - \sigma'_3) / (\sigma'_1 - \sigma'_3)$, can be controlled independently. By varying the (fixed in each test) angle α at constant b, the direction of the σ_1-axis relative to the horizontal bedding planes (of the gravity deposited sand) changes and thus the effects of fabric anisotropy on the mechanical behaviour of sand can be investigated in a given mode of loading. On the other hand, by varying the (fixed in each test) parameter b at constant α, the effects of the mode of loading on the mechanical behaviour of sand can be investigated while the stress principal axes (PA) are kept fixed at any orientation with respect to the bedding planes.

The stress paths and stress - strain curves of the loading tests performed by Yoshimine et al. (1998) are shown in Fig. 4.18. It is apparent that sand of a given initial state (p' , e) becomes more contractive and prone to flow when the fixed (in each test) angle α increases, for a given value of b, or when the fixed (in each test) parameter b increases, for a given value of α. The dilative behaviour of sand may turn into contractive as these two parameters change. Specifically, the transient-peak undrained strength, q_p, and the minimum undrained strength, q_{min}, decrease gradually when α increases from 15° to 75° (for the fixed value of b = 0.50), while the shear strain and excess pore-water pressure accumulated at the phase transformation point increase with α (see also Ishihara 1993). It is striking to observe that the deviatoric stress q at shear strain γ = 3% is about 8 times larger when α = 15° than when α = 75°. In the former case, the sand is strongly dilative and shows a continuous increase in q, while in the latter the sand is contractive and exhibits a decrease in strength and limited flow deformation up to the phase transformation point. Similar observations can be made for the response of sand to undrained loading with fixed α and varying b though the differences are not so pronounced.

The behavioural patterns of sand shown in Fig. 4.18 have been also reported by other researchers (Nakata et al. 1998, Uthayakumar and Vaid 1998, Shibuya et al. 2003a) yet the response to loading with α = 90° is not always the weakest and the response to loading with b = 0 (or 1) is not always the strongest. For example, the resistance to loading with 60° < α < 75° is particularly weak since one of the planes of maximum stress obliquity tends to align with the horizontal bedding plane at failure, facilitating the sliding mechanism, as shown in Fig. 4.19 (Matsuoka 1974, Oda et al. 1978, Matsuoka and Ishizaki 1981, Tatsuoka et al. 1986, Miura et al. 1986, Nakata et al. 1998, Lade et al. 2014). Moreover, the resistance to loading with b = 0.25 - 0.50 is particularly strong because conditions of quasi plane strain deformation are achieved for these values of b (Cornforth 1964, Tatsuoka et al. 1986, Shibuya and Hight 1987, Yoshimine et al. 1999, Zdravkovic and Jardine 2000 and 2001, O'Sullivan et al. 2013).

Ishihara (1993), Yoshimine and Ishihara (1998) and Yoshimine et al. (1998) introduced the *flow potential* parameter to quantify the susceptibility of saturated sands to flow liquefaction. The flow potential, u_f, of sand is defined as the maximum normalised excess pore-water pressure developed under monotonic undrained loading. The flow potential corresponds to the value of the normalised excess pore-water pressure ratio at the phase transformation point (PTP) and is given by:

$$u_f = \left(1 - \frac{p'_{PT}}{p'_c}\right) \cdot 100\ (\%) \tag{4.1}$$

where p'_{pt} and p'_c are the mean effective stress at the phase transformation point and end of consolidation, respectively. A higher u_f means that the sand is more susceptible to flow liquefaction, with the value of u_f = 100% corresponding to static liquefaction. The flow potential is affected by the physical characteristics and gradation of sand, as well as by the initial state, inherent anisotropy and mode of loading. If different sand specimens are prepared using the same method (e.g. the dry deposition method) and tested with the same α and b then u_f varies only with the initial state. On the other hand, if the preparation method and initial state is the same for all specimens then u_f varies with α and b.

Figure 4.20 shows the contours of equal u_f in the e - p'_c plane for dry-deposited Toyoura sand in different modes of loading. These contours are produced based on the results of triaxial compression (TC), triaxial extension (TE) and simple shear (SS) tests performed by Yoshimine and Ishihara (1998). It can be seen that sand of a given initial state is characterised by the highest u_f in TE, followed by the second highest u_f

in SS and finally by the lowest u_f in TC. Moreover, in a given mode of loading, u_f increases as the sand becomes looser. Figure 4.21 shows the flow potential surfaces in the α - b - u_f space corresponding to a given initial state (p'_c , e_c) of dry-deposited Toyoura sand. These surfaces are produced based on the results of the loading tests with fixed α and b performed by Yoshimine et al. (1998) in the HCA. It is apparent that sand of a given initial state is characterised by a higher u_f when α is higher, for a given b, or when b is higher, for a given α. Moreover, for a given combination of α and b, u_f increases if the sand density decreases. These findings clearly show that the undrained behaviour and flow susceptibility of sands are highly influenced by the initial state, inherent anisotropy and mode of loading.

Nakata et al. (1998) investigated the undrained behaviour and flow deformation of sand with varying relative density under generalised loading. The tests were performed in the HCA and included loading with both fixed and rotating stress principal axes (PA); only the results of the former loading tests are discussed here, while the results of the latter are presented in Section 4.4. Nakata et al. (1998) showed that sand consolidated isotropically to mean effective stress p'_c may or may not exhibit flow behaviour and loss of strength depending on the void ratio, e, or the relative density D_r = [(e – e_{max}) / (e_{max} – e_{min})] 100%. This means that the flow deformation and loss of strength becomes less intense as the density of sand increases until this type of behaviour is completely eliminated above a specific density level. In the case that flow behaviour (full flow or limited flow) is exhibited, Nakata et al. (1998) suggested that there exists a *critical stress ratio* (CSR), $\eta = q / p'$ or $\sin \varphi = (\sigma'_1 - \sigma'_3) / (\sigma'_1 + \sigma'_3)$, the mobilisation of which signals the triggering of flow. The concept of CSR was earlier presented by Vaid and Chern (1983 and 1985) as a criterion for predicting phenomenologically the triggering of flow under both monotonic and cyclic triaxial loading (see Section 4.3), while Lade (Lade et al. 1988, Lade 1992) introduced the *instability line* (IL) in stress space (see Section 4.5), the slope of which is the CSR.

Nakata et al. (1998) investigated also the effect of the orientation of the major principal stress, σ_1, with respect to the vertical (normal to the bedding plane) on the flow triggering condition, in conjunction with the effect of relative density. They performed monotonic undrained loading tests with fixed b = 0.5 and p'_c = 100 kPa, and with fixed α that varied, in general, from 15° to 75° with an increment of 15°. The loading was imposed by increasing the deviatoric stress, q (= $[1/2\ \{(\sigma_1 - \sigma_2)^2 + (\sigma_2 - \sigma_3)^2 + (\sigma_3 - \sigma_1)^2\}]^{1/2}$), under constant mean total stress, p. Nakata et al. (1998) found that the CSR of loose sand decreases with α in such a way that a hyperbolic curve can be determined in the φ - α plane, indicating the combinations of φ and α at the triggering of flow; it was found that loose sand flows for all values of α examined. In the case that medium-dense sand flows, the CSR also decreases with α, while for a given α it is higher than that of loose sand. However, there exists a limiting condition for medium-dense sand, as the angle α decreases, in which the CSR becomes equal to the phase transformation ratio and no flow is observed for this or for a lower α.

Figure 4.22 shows the effective stress paths (ESPs) and stress - strain curves of the monotonic undrained tests performed by Nakata et al. (1998) on sand specimens with a relative density, D_r, of around 90%, 60% or 30%. It can be seen that dense sand with D_r = 90% shows a strongly dilative behaviour with continuously increasing q (*non-flow deformation*) for all principal stress direction angles, α, yet the behaviour is stiffer and more dilative for lower values of α. Medium-dense sand with D_r = 60% shows a dilative behaviour for α = 15° and 30° (in the latter case the transient-peak point vanishes and becomes a phase-transformation point at the limit), while for α from 45° to 75° *limited flow deformation* (quasi-steady state) is exhibited. The accumulated shear strain during the limited flow deformation increases with α (see also Ishihara 1993). On the other hand, loose sand with D_r = 30% exhibits loss of strength and flow deformation for all principal stress direction angles, α. For α = 15°, limited flow deformation is observed, while for α = 30°, *full flow deformation* without phase transformation (steady state) is evidenced, at least for the shear strains reached during testing. For the values of α from 45° to 75°, *static liquefaction* occurs with approximately zero p' and q.

Poulos (1981) and Poulos et al. (1985) suggested that the inherent anisotropy of sand is completely erased at steady state because the skeleton structure has been severely remoulded. However, Nakata et al. (1998) found that different steady states are obtained under loading at different principal stress direction angles, α, as can be seen in Figs 4.22e and f. According to Nakata et al. (1998), this may occur because some features of the initial fabric endure up to the steady state or because the evolving fabric characteristics are affected by the stress history that precedes the mobilisation of the steady state. It should be noticed, though, that the various "steady" states reported in the literature are not necessarily critical states. For example, the flow deformation at zero or nearly zero mean effective stress termed "the steady state deformation" by Poulos (1981), and observed also by Nakata et al. (1998), is not a critical state unless the state point (p', e) lies indeed on the critical state line in the e - p' plane and the anisotropy of fabric has attained its critical value as well (Yoshimine and Ishihara 1998, Fu and Dafalias 2011, Li and Dafalias 2012, Zhao and Guo 2013, Theocharis et al. 2017 and 2019). Consequently, the non-uniqueness of "steady" state reported by Nakata et al. (1998) is not an unexpected result.

Nakata et al. (1998) found that the value of the deviatoric stress, q, and excess pore-water pressure, Δu, at the phase transformation point and transient peak state depend on α, as shown in Fig. 4.23. It is apparent that both q_{PT} and q_{CSR} decrease with α, while in some limiting situations the two stresses coincide; note that the subscripts PT and CSR mean "at the phase transformation point" and "at the transient peak state", respectively. In the case that phase transformation is observed, q_{PT} decreases with α, while for a given α, q_{PT} is lower for sand with D_r = 60% than for sand with D_r = 90%. The excess pore-water pressure Δu_{PT} increases with α which means that the mean effective stress, p'_{PT}, decreases with α; for a given α, Δu_{PT} is higher for sand with D_r = 60% than for sand with D_r = 90%. On the other hand, the excess pore-water pressure

Δu_{CSR} is practically unique and equal to 30 kPa, irrespective of the value of α and D_r. Similar results were reported by Ishihara (1993) who found that the value of p'_{CSR} / p'_i in monotonic undrained triaxial compression is unique (= 0.61), irrespective of the initial value of p' and e.

Nakata et al. (1998) investigated the effect of D_r and α on the mobilised friction angle, φ, at the phase transformation point (PT), transient-peak state (CSR), steady state (SS) and peak-failure state (P); the peak-failure state is the state of maximum stress ratio, $\eta = q / p'$ or $\sin \varphi = (\sigma'_1 - \sigma'_3) / (\sigma'_1 + \sigma'_3)$. Figure 4.24 shows the variation of φ_{PT}, φ_{CSR}, φ_{SS} and φ_P with α, for the three levels of D_r. It can be seen that for a given α, φ_{CSR} and φ_P increase with D_r, while φ_{PT} decrease with D_r. On the other hand, for a given relative density (D_r = 90% or 60%), φ_P and φ_{PT} decrease with α, become minimum at $\alpha = 60°$ and then increase slightly at $\alpha = 75°$. The minimum at $\alpha = 60°$ is associated with the alignment of one of the maximum stress obliquity planes with the horizontal bedding plane. In the case of loose or medium-dense sand (D_r = 30% or 60%, respectively), φ_{CSR} decreases hyperbolically with α.

In the studies by Yoshimine et al. (1998) and Nakata et al. (1998), the results of which has been presented in the previous paragraphs, the anisotropic behaviour of sand was investigated by means of monotonic undrained loading tests on isotropically consolidated specimens at various fixed principal stress direction angles, α. On the other hand, Sivathayalan and Vaid (2002) performed monotonic undrained loading tests on water pluviated loose specimens that were brought to various *generalised initial stress states*, characterised by the parameters p'_c or σ'_{mc} (fixed at 200 kPa in all tests), b_c (= 0, 0.4 or 0.5), $K_c = \sigma'_{1c} / \sigma'_{3c}$ (≥ 1) and α_c (= 0° - 90°). The specimens were first consolidated isotropically to mean effective stress p'_c = 200 kPa and then subjected to drained pre-shearing under constant p', b and α, until the target value of K_c was reached. The generalised pre-shearing is expected to alter to some degree the fabric anisotropy developed due to the process of deposition through water under the action of gravity; this has been reported to be also the case when conventional anisotropic consolidation is performed (Zdravkovic and Jardine 2001, Shibuya et al. 2003b). Sivathayalan and Vaid (2002) imposed undrained loading by increasing the deviatoric stress under constant α_c, p_c (mean total stress) and b_c, using water-saturated loading pistons in order to sustain the stability throughout testing.

Figure 4.25 shows the stress - strain curves and the ESPs of monotonic loading tests performed by Sivathayalan and Vaid (2002) on identical loose sand specimens brought to initial stress states with the same p'_c, b_c and K_c (= $\sigma'_{1c} / \sigma'_{3c}$) but different α_c. The parameters p, b and α were kept constant during loading and the only variable from test to test was the principal stress direction angle, α. The results in Fig. 4.25 show that the behaviour of sand is anisotropic, being more contractive and prone to flow when α is higher. The transient-peak strength and minimum undrained strength decrease with α, while the excess pore-water pressure and shear strain accumulated at the state of minimum undrained strength increases with α. These results indicate that some of the features of depositional fabric anisotropy are not altered during pre-shearing.

Figure 4.26 shows the stress - strain curves and the ESPs of monotonic loading tests performed by Sivathayalan and Vaid (2002) on identical loose sand specimens brought to initial stress states with the same p'_c, b_c and α_c but different K_c. For each value of α_c (= 0°, 30°, 60° and 90°) the values of K_c = 1.00, 1.25, 1.50 and 2.00 were attained during pre-shearing and the subsequent loading was performed by keeping α, b and p constant. It can be seen that for a given K_c (= σ'_{1c} / σ'_{3c}) the sand becomes more contractive and prone to flow when α increases, as has been already shown in Fig. 4.25 for the case of K_c = 1.50. For a given α, the increase in K_c results in a rise of the effective stress path in the q - p' plane and increase of the transient-peak strength and minimum undrained strength; notice that in the plots, the stress difference $q_d = \sigma_1 - \sigma_3$ is used instead of the deviatoric stress q (= $[1/2\ \{(\sigma_1 - \sigma_2)^2 + (\sigma_2 - \sigma_3)^2 + (\sigma_3 - \sigma_1)^2\}]^{1/2}$). These results indicate that some of the features of the depositional fabric anisotropy are altered during pre-shearing. It is noted that the void ratio after consolidation and pre-shearing is approximately the same for all specimens, despite the different values of the static shear stress.

Sivathayalan and Vaid (2002) investigated the conditions that trigger flow of loose saturated sand subjected to generalised loading. Figure 4.27 shows the critical stress ratio (CSR) lines in the t - s' plane (where $t = (\sigma'_1 - \sigma'_3) / 2$ and $s' = (\sigma'_1 + \sigma'_3) / 2$) drawn to fit the data points that correspond to the transient-peak states observed in the tests the results of which are presented in Fig. 4.26. The slope of the CSR-line equals $t / s' = \sin \varphi_{CSR}$ and becomes less steep when α increases, indicating that flow is triggered at a lower stress ratio when the σ_1-axis tends to align with the horizontal bedding plane. Figure 4.27 shows that the mobilised friction angle, φ_{CSR}, at the onset of flow decreases hyperbolically with α, as has been earlier reported by Nakata et al. (1998; see Figs 4.24b and c). The results presented indicate that the CSR depends only on the principal stress direction angle, α, and not on $K_c = \sigma'_{1c} / \sigma'_{3c}$. However, Kato et al. (2001) performed monotonic undrained triaxial compression tests (α = 0° and b = 0) on IC and AC sand specimens of the same void ratio and showed that the stress ratio, q / p', at the transient-peak point (i.e. the CSR) is independent of $K_c^* = \sigma'_{3c} / \sigma'_{1c}$ (≤ 1) only if $K_c^* \geq 0.5$, otherwise it is somewhat higher for sands with $K_c^* < 0.5$ than with $K_c^* \geq 0.5$.

Sivathayalan and Vaid (2002) modified Bishop's (1971) *brittleness index* I_B in order to describe more efficiently the susceptibility of anisotropically consolidated loose sand to flow deformation. Bishop's (1971) brittleness index is defined as:

$$I_B = \frac{S_{peak} - S_{min}}{S_{peak}} \tag{4.2}$$

where S_{peak} and S_{min} are the (transient) peak strength and minimum undrained strength (e.g. $S \equiv (\sigma_1 - \sigma_3) / 2$), respectively, of loose sand subjected to monotonic undrained loading. The modified brittleness index is defined as:

$$I_{\bar{B}} = \frac{S_{peak} - S_{min}}{S_{peak} - S_{static}} \tag{4.3}$$

where S_{static} is the static shear stress (i.e. the initial shear stress), while the other symbols are the same as in Eq. 4.2. The modified brittleness index normalises the drop of strength past the triggering of flow with respect to the stress increment needed to trigger flow, thus, it describes more efficiently the effect of K_c on the susceptibility of AC sands to flow. A higher brittleness index (conventional or modified) means higher susceptibility of sand to flow.

Figure 4.28 shows that both the conventional and the modified brittleness index increase with α, indicating that sand becomes more susceptible to flow when α is higher. However, the conventional brittleness index is practically constant with K_c (= $\sigma'_{1c} / \sigma'_{3c}$), while the modified brittleness index increases with K_c, especially when α is higher. Values of the modified brittleness index higher than unity mean that sand is potentially unstable since $S_{min} < S_{static}$ (see also Poulos et al. 1985) and, thus, flow deformation may be triggered by a small increment of shear stress or by some other undrained perturbation. Castro (1969) indicated that sands subjected to high levels of static shear stress are particularly vulnerable to spontaneous flow liquefaction triggered by a small stress disturbance (see Fig. 4.4), a fact also pointed out by Lade (1993), Sivathayalan and Da Ha (2011), Georgiannou and Konstantinou (2014), Georgiannou et al. (2018). Consequently, the modified brittleness index describes successfully the observed vulnerability of highly stressed sands to spontaneous flow liquefaction.

Sivathayalan and Vaid (2002) investigated the effect of K_c (= $\sigma'_{1c} / \sigma'_{3c}$) and α on the minimum undrained strength mobilised at quasi-steady state or steady state. Figure 4.29 shows the variation of $q_{d,min} / 2$ (or $S_{QSS/SS}$) with K_c and α. For a given K_c, the minimum undrained strength decreases with α, while for a given α, the minimum undrained strength increases with K_c, even though the strength loss is more severe, as indicated by the modified brittleness index. This is possibly because the drained pre-shearing at high K_c and inclined σ_1-axis with respect to the vertical alters the depositional fabric anisotropy and makes the sand more resistant to the subsequent loading at the same principal stress direction. Similar results are reported by Zdravkovic and Jardine (2001) and Shibuya et al. (2003b). However, if the minimum undrained strength is normalised with respect to the major principal stress then it becomes independent of K_c and dependent only on e and α (e is the void ratio); this is shown in Fig. 4.30. Georgiannou et al. (2018) applied a similar normalisation of the transient-peak strength and found that it becomes independent of p'_c, K_c and, interestingly, of the value of α; this is shown in Fig. 4.31 which presents the results of monotonic undrained loading tests under both fixed and rotating stress principal axes.

Symes et al. (1984) interpreted the results of monotonic undrained loading tests on medium-loose sand under both fixed and cyclically rotating directions stress principal axes within a unified framework based on the concept of *Local Boundary Surface* (LBS). They showed that the set of the effective stress paths of monotonic undrained loading tests on IC sand at various fixed α (= 0°, 22.5° and 45°) defines a surface in the q - p' - α space (for a given value of the void ratio, e, and b = 0.5) with specific properties. This locus of stress states, shown in Fig. 4.32, was initially called the *State Boundary Surface* (SBS) and later renamed the *Local Boundary Surface* (LBS) (Zdravkovic and Jardine 2000, Shibuya et al. 2003a and b; see also Tatsuoka 1972, Gens 1985). The LBS was postulated to be a boundary to the admissible stress states under undrained loading with fixed or rotating stress principal axes. If an effective stress path (ESP) probes the LBS pointing outwards then the pore-water pressure increases and the deviatoric stress evolves in such a way that the ESP moves obligingly along the LBS, without progressing beyond it; this situation is termed a *loading interference* with the LBS.

Since the ESPs of undrained loading tests on contractive sand exhibit a transient-peak state and a subsequent decrease in strength, the same feature is evidenced in the LBS. A *peak line* connects all the transient-peak states, corresponding to different values of α, and beyond this line the LBS exhibits a descending *post-peak branch*. The decrease in q (q is plotted on the vertical axis) is halted at the phase transformation points beyond which strength is regained; note that different phase transformation points correspond to different values of α. Consequently, the *contractant region* of the LBS is divided into the *pre-peak branch* and the *post-peak branch*. A loading interference with the peak line or the post-peak branch of the LBS results in flow instability under stress-controlled undrained conditions; the instability is manifested as a decrease in strength and runaway deformation. During the unstable flow, the ESP progresses on the post-peak branch of the LBS. However, if the probing direction is changed to point inwards in relation to the LBS then stability is regained and this situation is called *unloading interference* with the LBS (Symes et al. 1984, Shibuya and Hight 1987). The LBS also includes a *dilatant region* which comprises the failure lines for the different values of α, as can be seen in Fig. 4.32.

Shibuya and Hight (1987) performed similar loading tests with those of Symes et al. (1984) though they covered the full range of principal stress direction angles, α (= 0°, 15°, 30°, 45°, 60° and 90°). The intermediate principal stress parameter, b, was kept constant and fixed at 0.5 in all tests, while the mean total stress was kept constant at 600 kPa. The LBS of loose IC sand defined by Shibuya and Hight (1987) in the q - p' - α space is shown in Fig. 4.33. The shape of the LBS expresses phenomenologically the fabric anisotropy of sand developed due to gravity deposition and preserved under isotropic consolidation, termed the *initial anisotropy*. However, the initial anisotropy is altered gradually as the sand is loaded towards peak failure and beyond (Oda et al.

1985) and the induced alterations cannot be monitored macroscopically when the LBS is determined. Shibuya et al. (2003a) defined the LBS of loose IC sand in the four-dimensional q - p' - α - b space by performing monotonic undrained loading tests with various combinations of α (= 0°, 15°, 30°, 45°, 60° or 90°) and b (= 0, 0.5 or 1). The 4-D LBS is shown in Fig. 4.34 as a family of superimposed 3-D surfaces in the q - p' - α space, with the innermost corresponding to b = 1 and the outermost to b = 0.

Shibuya et al. (2003b) showed that the LBS of anisotropically consolidated sand differs from that of the isotropically consolidated sand, possibly because the depositional fabric anisotropy is intensified by anisotropic consolidation, while it is attenuated by isotropic consolidation. The LBSs of loose IC and AC sand for b = 0.3 are shown in Figs 4.35 and 4.36. Figures 4.35 and 4.36 show that in the case of sand subjected to anisotropic consolidation at $K_c = \sigma'_{3c} / \sigma'_{1c} = 0.5$, α_c = 0° and b_c = 0 the LBS (for b = 0.3) expands in the q - p' - α space in the region of $0° \leq \alpha \leq 15°$, i.e. around the consolidation stress state C_A. This is possibly due to the intensification of the depositional fabric anisotropy by anisotropic consolidation. As a result, the response of sand to the subsequent loading with the direction of the σ_1-axis being inclined at an angle $0° \leq \alpha \leq 15°$ to the vertical is very stiff. On the other hand, the ESPs of AC and IC sand coincide in the post-peak regime when $\alpha \geq 30°$ indicating that the consolidation-induced anisotropy becomes less influential away from the consolidation stress state C_A in the q - p' - α space.

4.3 UNDRAINED BEHAVIOUR AND FLOW DEFORMATION OF SANDS UNDER CYCLIC LOADING

Flow deformation of sands is manifested as the accumulation of *unidirectional* shear strain while the strength decreases to a minimum level and the stress ratio increases, without involving *reversal of the loading direction*. Therefore, flow is a situation different than *cyclic mobility*, as can be seen in Fig. 4.37. Nevertheless, flow deformation can be triggered both under monotonic and cyclic loading (i.e. both under monotonic and cyclic change of the deviatoric stress, q). The conditions under cyclic loading that trigger flow have been investigated in the past and a correlation between the monotonic and cyclic undrained behaviour of sands has been found to exist. In most cases, it is postulated that there exists a locus in the q - p' plane determined in monotonic undrained loading tests, such as a line or a surface, the crossing of which by the effective stress path (ESP) of a cyclic undrained loading test triggers flow.

Vaid and Chern (1983 and 1985) performed monotonic undrained triaxial loading tests on loose sand and found that flow deformation is triggered when a unique *Critical Stress Ratio* (CSR) is mobilised. They also found that the mobilisation of the same CSR during cyclic undrained triaxial loading triggers flow, irrespective of the consolidation stress ratio $K_c = \sigma'_1 / \sigma'_3$ and cyclic stress level τ_{cy} / σ'_{3c} (where τ_{cy} is the single-amplitude cyclic shear stress). The effective stress paths in the t - s' plane (where $t = (\sigma'_1 - \sigma'_3) / 2$ and $s' = (\sigma'_1 + \sigma'_3) / 2$) of cyclic undrained loading tests on loose IC and AC sand specimens are shown in Fig. 4.38. The broken line passing through the origin of the stress space is the CSR-line, while the solid line is the failure envelope. It is apparent that flow is triggered at a stress ratio considerably lower than the ratio corresponding to failure. It can be also seen that the flow deformation is terminated when the pore-water pressure begins to decrease, due to plastic dilation, and strength is regained as the mean effective stress increases; this behaviour under cyclic undrained loading is reminiscent of the *limited flow liquefaction* occurring under monotonic undrained loading (Castro 1969, Nakata et al. 1998).

Figure 4.38 shows that the reversal of the loading direction past the phase-transformation point induces severe plastic contraction that may lead to a transient condition of approximately zero effective stress, called *initial liquefaction* (Seed and Lee 1966). This peculiar case of development of considerable plastic volumetric strains during the deliberate unloading of stress and stress ratio was also reported by Ishihara et al. (1975) who introduced the concept of *phase transformation*. According to Ishihara et al. (1975), the phase transformation line indicates the stress ratio threshold beyond which stress unloading induces instability and liquefaction, as can be seen in Fig. 4.39. Notice that the term "instability" was used by Ishihara et al. (1975) but it does not refer to the case of flow instability. The role of the CSR and phase transformation ratio in the triggering of instability (of the flow type or not) during cyclic loading was also pointed out by other researchers (Konrad 1993, Georgiannou et al. 2008, Georgiannou 2011, Konstantinou and Georgiannou 2013 and 2014).

Symes et al. (1984), Shibuya and Hight (1987) and Shibuya et al. (2003a and b) showed that the *Local Boundary Surface* (LBS) (in the q - p' - α or q - p' - α - b space) defined by means of a set of effective stress paths (ESPs) of monotonic undrained loading tests forms a boundary to the admissible stress states under any type of undrained loading (monotonic or cyclic) of sand specimens with the same consolidation history and void ratio. They also showed that flow instability is triggered when the peak line or the post-peak regime of the LBS (see Section 4.2) is probed with an outwards direction; this situation, which is called a *loading interference* with the LBS, implies that the triggering of instability depends on the loading direction. Specifically, Symes et al. (1984), Shibuya and Hight (1987) and Shibuya et al. (2003a and b) showed that flow instability is triggered in cyclic undrained triaxial compression - extension tests when the LBS is probed in the post-peak regime with an outwards direction, while the same holds true in tests in which the direction of the stress principal axes is rotated cyclically under undrained conditions and constant deviatoric stress, as discussed further in Section 4.4. Figure 4.40 shows the ESP of a cyclic undrained triaxial compression - extension test. It is apparent that the ESPs of monotonic undrained triaxial compression (broken line M7) and extension (broken line M16) tests bound the stress space in which the ESP of the cyclic undrained test can move, while flow instability is triggered when the latter probes the descending branch of the former with an outwards direction.

Similar results were reported by Alarcon-Guzman et al. (1988) who performed monotonic and cyclic undrained torsional-shear tests on IC sand; the apparatus used could accommodate both solid and hollow cylinder specimens and the loading tests were performed under stress-controlled conditions. Figure 4.41 shows the ESPs of cyclic and monotonic undrained loading tests. It can be seen that the ESP of the monotonic test forms a boundary to the stress space in which the ESP of the cyclic test can move, while any effort to move beyond the descending branch of this boundary is halted by the triggering of flow. It is also apparent that the CSR-line determined in the monotonic test can be crossed stably under stress-controlled cyclic loading.

Other researchers verified the findings of Alarcon-Guzman et al. (1988) by performing undrained tests on anisotropically consolidated or pre-sheared sands, or mixtures of sands with finer materials (clayey sands or silty sands). Georgiannou et al. (1991) reported that “the effective stress paths for the normally consolidated soils (author’s note: clayey sands) loaded monotonically in triaxial compression and extension are shown to form a bounding envelope which determines the pattern of behaviour under cyclic loading”. Georgiannou et al. (1991) showed that the same envelope also bounds the stress space in which the ESPs for the overconsolidated soils can move. Figures 4.42 and 4.43 show the effective stress paths and stress - strain curves of the undrained tests performed by Georgiannou et al. (1991). Ishihara et al. (1991) reported similar results for sands subjected to triaxial loading, shown in Fig. 4.44, while Yamamuro and Covert (2001) presented similar results for silty sands subjected to triaxial loading, shown in Fig. 4.45. On the other hand, Hyodo et al. (1994) showed that the triggering of flow of sands subjected to cyclic undrained triaxial loading occurs when the ESP reaches either the CSR-line or the post-peak regime of the ESP of the monotonic undrained test, depending on the initial static shear stress.

4.4 UNDRAINED BEHAVIOUR AND FLOW DEFORMATION OF SANDS UNDER LOADING INVOLVING ROTATION OF THE STRESS PRINCIPAL AXES

The loading of soils in the field frequently involves rotation of the stress principal axes (PA), with some characteristic examples being the occurrence of seismic events, the action of waves on the seabed, the construction of earth dams and embankments, the movement of vehicles and the formation of shear zones (Broms and Casbarian 1965, Peacock and Seed 1968, Ishihara and Li 1972, Bjerrum 1973, Goldscheider 1975, Arthur et al. 1980 and 1981, Ishihara 1983, Hight 1983, Vardoulakis and Graf 1985, Gutierrez et al. 1991, Zdravkovic and Jardine 2001, Vardoulakis and

Georgopoulos 2005, Gutierrez and Vardoulakis 2007). The continuous rotation of the stress PA results in the accumulation of contractive volumetric strains, under drained conditions, or excess pore-water pressure, under undrained conditions, even if the deviatoric stress q (= $[1/2\ \{(\sigma_1 - \sigma_2)^2 + (\sigma_2 - \sigma_3)^2 + (\sigma_3 - \sigma_1)^2\}]^{1/2}$) or stress difference t (= $(\sigma_1$ - $\sigma_3)$ / 2) is kept constant (Ishihara and Towhata 1983, Symes et al. 1984, Towhata and Ishihara 1985, Miura et al. 1986, Nakata et al. 1998, Sivathayalan and Vaid 2002, Yang et al. 2007, Tong et al. 2010). Moreover, it has been shown that flow deformation can be triggered under undrained conditions when the stress PA rotate at constant q in a similar way as when q changes cyclically (Symes et al. 1984).

Ishihara (1983), Ishihara and Towhata (1983) and Towhata and Ishihara (1985) showed analytically that the propagation of waves at the surface of sea induces a *continuous monotonic rotation* of the stress PA in soil elements at the seabed, while the stress difference $t = (\sigma_1 - \sigma_3) / 2$ remains constant. This can be realised by considering that the shear stress acting on the horizontal plane τ_{vh} (or $\tau_{z\theta}$ in cylindrical coordinates) and the stress difference between the vertical normal stress and horizontal normal stress $(\sigma_v - \sigma_h) / 2$ (or $(\sigma_{zz} - \sigma_{\theta\theta}) / 2$ in cylindrical coordinates), change cyclically with a phase difference of π / 2 rad and, thus, the vectorial sum of the two has a magnitude equal to the constant t. Ishihara and Towhata (1983) also performed tests in the hollow cylinder apparatus (HCA) in order to simulate this specific loading situation. The applied loads at the boundaries of the hollow cylinder specimen and the developed average stresses are shown in Fig. 4.46. The principal stresses are given as functions of the stresses that act on the horizontal and vertical planes by the following equations:

$$\sigma_1 = \frac{(\sigma_{zz} + \sigma_{\theta\theta})}{2} + \sqrt{(\frac{\sigma_{zz} - \sigma_{\theta\theta}}{2})^2 + \tau_{z\theta}{}^2} \tag{4.4a}$$

$$\sigma_2 = \sigma_{rr}$$

(4.4b)

$$\sigma_3 = \frac{(\sigma_{zz} + \sigma_{\theta\theta})}{2} - \sqrt{(\frac{\sigma_{zz} - \sigma_{\theta\theta}}{2})^2 + \tau_{z\theta}{}^2} \tag{4.4c}$$

The stress difference t is then equal to:

$$t = \sqrt{(\frac{\sigma_{zz} - \sigma_{\theta\theta}}{2})^2 + \tau_{z\theta}{}^2} \tag{4.4d}$$

The angle α between the σ_1-axis and the vertical is given by the following equation (note that Ishihara and Towhata (1983) use the symbol β):

$$tan\,2\alpha = \frac{2\tau_{z\theta}}{\sigma_{zz} - \sigma_{\theta\theta}} \tag{4.4e}$$

In the tests performed by Ishihara and Towhata (1983) the inner cell pressure and outer cell pressure are equal to each other (i.e. $p_i = p_o$) thus the following relationships hold:

$$\sigma_{\theta\theta} = \sigma_{rr} = p_o = p_i \tag{4.5a}$$

$$b = sin^2 \alpha \tag{4.5b}$$

Ishihara and Towhata (1983) showed that the continuous monotonic rotation of the stress PA at constant t induces cumulative plastic volumetric strain since the pore-water pressure increases cycle after cycle of stress rotation. The stress path in the $\tau_{z\theta}$ - $(\sigma_{zz} - \sigma_{\theta\theta}) / 2$ plane of the principal stress rotation tests is shown in Fig. 4.47, while the results of the tests are shown in Fig. 4.48. The sand specimen was consolidated isotropically to mean effective stress p'_c = 294 kPa (point O) and then a stress difference of $(\sigma_{zz} - \sigma_{\theta\theta}) / 2$ = 56.9 kPa was applied under undrained conditions. A small amount of excess pore-water pressure (25 kPa) was generated during this triaxial compression phase as indicated by the stress point moving from O to A in Fig. 4.48a. Afterwards, the stress difference t was kept constant at 56.9 kPa while the two shear stresses $\tau_{z\theta}$ and $(\sigma_{zz} - \sigma_{\theta\theta}) / 2$ were changed cyclically, causing a continuous monotonic rotation of the σ_1 and σ_3 axes. It can be seen that the mean effective stress decreased from 269 kPa (point A) to 80 kPa (point A_2) during the two cycles of stress rotation as a result of plastic contraction. Finally, the sand was unloaded from the triaxial stress state A_2 to the stress state O' and further plastic contraction was induced causing initial liquefaction (Ishihara et al. 1975, Seed and Lee 1966).

The cause of plastic contraction under the condition of constant t may be the monotonic rotation of the stress PA or the cyclic changes in the out-of-plane stress differences $(\sigma_1 - \sigma_2)$ and $(\sigma_2 - \sigma_3)$ that inevitably occur when the parameters b and α are not controlled independently (i.e. when $p_i = p_o$). Ishihara and Towhata (1983 and 1985) suggested that the plastic contraction occurs mainly due to the rotation of the stress PA. Their suggestion was later verified by Symes et al. (1984), Miura et al. (1986), Nakata et al. (1998), Sivathayalan and Vaid (2002), Yang et al. (2007) and Tong et al. (2010) who performed undrained or drained stress rotation tests while keeping the magnitude of the total principal stresses σ_1, σ_2 and σ_3 constant, and observed the accumulation of plastic contraction cycle after cycle of stress rotation. This behaviour is of tremendous importance since it cannot be predicted by the classical elastoplasticity theory, as highlighted by Ishihara and Towhata (1983), Vardoulakis and Graf (1985), Wang et al. (1990), Gutierrez et al. (1993), Vardoulakis and Georgopoulos (2005), Gutierrez and Vardoulakis (2007) and Li and Dafalias (2004 and 2012) who proposed new elastoplastic constitutive models (and a new theory) to remedy this deficiency.

It is important to notice that the rotation of the stress PA may induce plastic contraction of sand irrespective of the current orientation of the stress PA and the direction of rotation with respect to the bedding planes. This was pointed out by

Towhata and Ishihara (1985) who found that the liquefaction resistance of IC sand subjected to cyclic torsional-shear loading is higher than that of sand subjected to cyclic loading with a simultaneous cyclic rotation of the stress PA. In the former case, the direction of the σ_1-axis is kept fixed at $\alpha_{\sigma 1} = \pm 45°$ (disadvantageous orientations) and a jump of 90° occurs when the cyclic stress becomes momentarily zero (i.e. at the isotropic stress state), while in the latter, the σ_1-axis continuously rotates between $\alpha_{\sigma 1} = +45°$ and $\alpha_{\sigma 1} = -45°$(advantageous orientations). Moreover, Symes et al. (1984) showed that the cyclic rotation of the stress PA under undrained conditions at constant q induces cumulative plastic contraction of loose sand, irrespective of whether the σ_1-axis rotates towards the bedding planes or towards the normal to the bedding planes, while Sivathayalan and Vaid (2002) observed the same behaviour under monotonic rotation of the stress PA at constant q.

Symes et al. (1984) verified the findings and postulations of Ishihara and Towhata (1983), i.e. they showed that the rotation of the stress PA at constant $t = (\sigma_1 - \sigma_3) / 2$ and b induces cumulative plastic contraction. Symes et al. (1984) performed undrained stress-controlled tests in which the stress PA rotate a) monotonically from $\alpha = 0°$ to 45°, b) monotonically from $\alpha = 45°$ to 0° and c) cyclically from $\alpha = 0°$ to 24.5° and then back to $\alpha = 0°$ for four cycles. Symes et al. (1984) interpreted the results of the stress rotation tests using the concept of the Local Boundary Surface (LBS) determined in the monotonic undrained tests with fixed stress PA. Figure 4.49a shows the ESPs in the t - p' plane of the monotonic undrained tests at constant α (= 0°, 24.5° and 45° in tests A0, A2 and A4, respectively) and b (= 0.5), while Fig. 4.49b shows the corresponding stress - strain curves. The ESPs of the monotonic undrained tests at constant α form the LBS in the t - p' - α space (for $b = 0.5$) shown in Figs 4.49c and d. Figure 4.50 shows the ESP of the test R3 in which the stress PA were rotated cyclically under undrained conditions at constant t and b. Figure 4.51 shows the plot of t versus γ_{oct} (octahedral shear strain) for the test R3, while Fig. 4.52 shows the projection of the ESP R3 and LBS on the α - p' plane, with the latter displayed as a set of contours of constant t. Finally, Fig. 4.53 shows the effective stress path R3 and failure surface in the t / p' - α plane and Fig. 4.54 shows the stress - strain curve during the three stages of loading in test R3, together with the corresponding curves of tests A0 and A4.

The ESP of test R3 is divided into three stages starting from point J1 and ending at point M (Fig. 4.50). During the first stage, four cycles of principal stress rotation from $\alpha = 0°$ to 24.5° and back to 0° are performed under constant t (route J1 to J5), during the second, monotonic principal stress rotation from $\alpha = 0°$ to 45° is performed under constant t (route J5 to K5) and during the third, the stress difference t is increased to failure under the condition of $\alpha = 45°$ (route K5 to M). Point J1 ($t = 61$ kPa, $\alpha = 0°$) is reached after subjecting the IC sand specimen to multiaxial compression with $\alpha = 0°$ and $b = 0.5$ until the value of $t = 61$ kPa is imposed. The part A - J1 (A is the isotropic stress state at the end of consolidation) of the ESP R3 coincides with the first part of the ESP A0 indicating the very good repeatability of the test results. The basic characteristic of the ESP R3 is that it progresses parallel to the *p'*-axis towards lower values of *p'* due to the plastic contraction induced by the rotation of the stress PA at constant σ_1, σ_2 and σ_3. It is noted that as the mean effective stress, *p'*, decreases the effective stress ratio, *t* / *p'*, increases thus further plastic strains are induced by this loading process.

The rotation of the σ_1-axis in test R3 is initiated at point J1 and lasts for four cycles, identified by the following sequences of letters J1-K1-J2, J2-K2-J3, J3-K3-J4 and J4-K4-J5 (Fig. 4.50). During the first half of the first stress rotation cycle (J1-K1), the ESP R3 remains on the pre-peak regime of the contractant region of the LBS (because a *loading interference* with the LBS occurs since the stress state is on the LBS and the stress probe direction points outwards; see Section 4.2). A considerable amount of excess pore-water pressure is generated in order the ESP to remain on the LBS (Fig. 4.50b) or, conversely, it is generated because the ESP traverses the LBS. Past the point K1, the ESP progresses below the LBS and, hence, substantially lower excess pore-water pressure is generated during the second and third stress rotation cycles. Nevertheless, the excess pore-water pressure is accumulated progressively, irrespective of the direction of stress rotation, i.e. irrespective of whether the stress rotation occurs from 0° to 24.5° or from 24.5° to 0°. These findings support the suggestion that the effects of stress rotation on the undrained behaviour of sand are more profound than the effects of the inherent anisotropy (Towhata and Ishihara 1985).

During the first half of the fourth stress rotation cycle (J4-K4) in test R3, the rate of pore-water pressure generation increases and the ESP progresses more quickly to the left in the *t* - *p'* space. This occurs because the ESP approaches the LBS which is moving towards lower values of *t* in the *t* - *p'* plane as the angle α increases. The ESP reaches the pots-peak regime of the LBS at point K4 with an outwards stress probe direction in the *t* - *p'* - α space (Figs 4.50a and b) and flow deformation is triggered. Flow is manifested as a sharp increase in the rate of accumulation of excess pore-water pressure and shear strain (Figs 4.51 and 4.52) that is about to cause an *unstable stress unloading* along the descending branch of the LBS (Fig. 4.50). Nevertheless, stability is regained since the direction of the σ_1-axis rotates from 24.5° to 0° (K4-J5) and, thus, an *unloading interference* with the LBS occurs at K4 and the ESP retreats to stress states below the rising LBS (Fig. 4.50). It is noted that the loss and regaining of stability in the vicinity of point K4 indicates that the triggering of instability depends on the loading direction (see Chapter 4.5). The increase in pore-water pressure and shear strain during the phase K4-J5 is still relatively large (Figs 4.52 and 4.54) because the ESP progresses in the vicinity of the failure surface (Fig. 4.53).

The next stage of the test R3 (Stage 2) involves a monotonic stress rotation from α = 0° to 45° while keeping the value of *t* constant. The part J5-L-K5 of the ESP corresponds to this stage (Figs 4.52 and 4.53). It can be seen that from point J5 to point L a positive increase in pore-water pressure results in an increase in the effective stress ratio *t* / *p'* and brings the stress state on the dilatant region of the LBS, i.e. on the failure surface. As the stress rotation from lower to higher values of α continues past the point L on the failure surface, t decreases mildly and a negative change in the pore-water pressure is generated because the stress state should obligingly remain on the LBS (Figs 4.50, 4.52 and 4.53). It can be seen that despite the negative pore-water pressure generation from point L to point K5, a large amount of shear strain is developed because stress rotation occurs on the failure surface (Fig. 4.54). At the time that the stress rotation is terminated at point K5 (α = 45°), the stress state is quite close to that attained in the loading test A4 (Figs 4.52 and 4.53), while the same holds true for the stress - strain point (Fig. 4.54). During the subsequent stage (Stage 3), the stress difference t is increased and the sand undergoes a dilative shear failure (Li 1997), while the ESP and stress - strain curve of test R3 is quite similar to those of test A4 (Figs 4.50a and 4.54).

Shibuya and Hight (1987) followed the line of thought of Symes et al. (1984) and determined the LBS of IC sand in the t - p' - α space for the full range of α (from 0° to 90°) under the condition of b = 0.5. They showed that the cyclic rotation of the direction of the σ_1-axis from α = 0° to 90° and back to 0° under undrained conditions at constant t and b (i.e. at constant σ_1, σ_2 and σ_3) induces cumulative plastic contraction and accumulation of excess pore-water pressure, irrespective of the direction of rotation. They also showed that flow deformation is triggered when the ESP of the undrained stress rotation test reaches the post-peak regime of the LBS with an outwards stress probe direction. Shibuya and Hight (1987) also imposed monotonic rotation of the direction of the σ_1-axis at constant t and b and showed that the ESP progresses to the left in the t - p' plane due to the plastic contraction of sand and accumulation of excess pore-water pressure; at the instant when the peak-line of the LBS is probed with an outwards direction, flow deformation is triggered.

Shibuya et al. (2003a) determined the LBS of IC sand in the t - p' - α - b space for the full range of α (from 0° to 90°) and b (from 0 to 1). The LBS was then used to interpret the results of tests imposing cyclic changes of α and b under undrained conditions, while keeping the stress difference t constant. Shibuya et al. (2003a) also performed tests in which a monotonic change in α is imposed at constant b and t, and tests in which a monotonic change in α is imposed under constant b and monotonically changing t (increasing or decreasing). Moreover, Shibuya et al. (2003b) determined the LBS of AC sand in the t - p' - α - b space and performed principal stress rotation tests. The LBS was found to be an efficient conceptual artefact that can be used to interpret the undrained behaviour of sand and triggering of flow under principal stress rotation.

Nakata et al. (1998) investigated the flow deformation of sands subjected to undrained principal stress rotation. They proposed a flow-triggering condition different than the one suggested by Symes et al. (1984), Shibuya and Hight (1983) and Shibuya et al. (2003a and b), based on the mobilisation of the Critical Stress Ratio (CSR) (Vaid and Chern 1983 and 1985), which is the effective stress ratio (η or sin φ) at the contractive state of peak q in monotonic undrained loading tests. Firstly, they showed that the behaviour of IC sand under monotonic undrained loading at constant b and p depends strongly on the fixed value of α and relative density, D_r, of the specimen. Loose sand exhibits a decrease in q past a contractive peak state (flow deformation), irrespective of the value of α, while dense sand exhibits a continuously increasing q (non-flow deformation), due to plastic dilation, irrespective of α. Medium-dense sand shows continuous increase in q (non-flow deformation) at lower values of α ($\leq 30°$) and decrease in q followed by phase transformation and increase in q (limited-flow deformation) at higher values of α ($> 30°$). Nakata et al. (1998) showed that, in the case of loose sand, the mobilised friction angle, φ_{CSR}, at the onset of flow decreases hyperbolically with α, possibly due to the effect of the inherent anisotropy (Fig. 4.24c). In the case of medium-dense sand, a similar trend is observed in the range of α that corresponds to limited-flow deformation (Fig. 4.24b).

Nakata et al. (1998) also performed undrained principal stress rotation tests on AC sand and investigated the flow triggering condition. They found that the continuous monotonic rotation of the stress PA at constant σ_1, σ_2 and σ_3 induces cumulative plastic contraction, as indicated by the continuous increase in the excess pore-water pressure, irrespective of the relative density of sand. However, whether flow deformation occurs or not depends on the value of relative density and level of deviatoric stress during stress rotation. Figures 4.55a, b and c show the cyclic change of the total normal stresses, σ_{zz}, $\sigma_{\theta\theta}$ and σ_{rr}, and torsional shear stress, $\tau_{z\theta}$, within each cycle of stress rotation in the test on the dense specimen D30, while Figs 4.55d and e show the evolution of excess pore-water pressure and strains, respectively; the characteristics of the specimen D30 after consolidation are: D_r = 95.7%, p' = 100 kPa, q = 52.0 kPa, α = 0° and b = 0.5. Figure 4.56a shows the effective stress paths in the q - p' plane of all stress rotation tests on dense specimens including the specimen D30.

Figures 4.55d and e show that despite the high value of the relative density of specimen D30 the pore-water pressure increases steadily during the first four stress rotation cycles, while fluctuation and reversing of the sign of the rate of pore-water pressure evolution is observed within each cycle; the net increase in the pore-water pressure during the first cycle is the greatest. After the completion of the fourth stress rotation cycle, a (non-flow) steady state is attained, during which the excess pore-water pressure oscillates around the value Δu = 55 kPa (= 0.55 p'_c). This steady state occurs on the failure surface (i.e. on the peak-η lines; see Fig. 4.56a) and has the characteristics of *cyclic mobility* (Nakata et al. 1998) and *shakedown* of the pore-water pressure generation (Tong et al. 2014b). It is noted that a negative change of pore-water pressure is generated during the first half of each cycle, i.e. from α = 0° to α = 90°, and a positive change during the second half, i.e. from α = 90° to α = 0°; however, only positive change of the pore-water pressure is observed during the first stress rotation cycle. A similar pattern of alterations between dilation and contraction was observed by Tong et al. (2014b) in the DEM simulations of drained principal stress rotation tests.

The evolution of the excess pore-water pressure and strains during the principal stress rotation test on the medium-dense specimen M20 is shown in Figs 4.55f and g, while the ESP in the *q* - *p'* plane is shown in Fig. 4.56b; the characteristics of the specimen M20 after consolidation are: D_r = 61.7%, *p'* = 100 kPa, *q* = 34.6 kPa, α = 0° and *b* = 0.5. It can be seen that during the first stress rotation cycle in test M20, the pore-water pressure increases continuously. During the second stress rotation cycle, the ESP crosses the critical stress ratio (CSR) line determined in the monotonic loading test on IC sand and flow deformation is triggered; note that different CSR-lines are determined for different values of α in the monotonic loading tests. Flow is manifested as a sudden increase in the rate of accumulation of excess pore-water pressure and strains. Flow is terminated when the phase transformation line in the *q* - *p'* plane determined in monotonic loading tests is reached. Consequently, *limited flow* is exhibited though no sign of stress unloading (strength decrease) is apparent.

Figures 4.55h and i show the evolution of excess pore-water pressure and strains during the principal stress rotation test on the loose specimen L10, while Fig. 4.56c shows the ESP in the *q* - *p'* plane; the characteristics of the specimen L10 after consolidation are: D_r = 35.5%, *p'* = 100 kPa, *q* = 17.3 kPa, α = 0° and *b* = 0.5. It can be seen that during the first eleven stress rotation cycles in test L10, the pore-water pressure increases progressively, with the greatest increase observed during the first cycle. The fluctuations of pore-water pressure do not occur (or are hardly discernible) in this test, instead in the first half of each stress rotation cycle the pore-water pressure remains approximately constant. During the twelfth cycle, the ESP crosses the CSR-line determined in the monotonic loading tests and flow deformation is triggered. Flow is manifested as a sudden increase in the rate of accumulation of excess pore-water pressure and strains, while a spontaneous stress unloading (loss of strength) is also evidenced. It is noted that phase transformation does not occur in this test and the increase in pore-water pressure during flow reduces the mean effective stress to zero.

Figure 4.57 shows the results of the stress rotation test on the dense specimen D30 in terms of α - *p'*, η - α and γ - α plots ($\gamma = [2/9\ \{(\varepsilon_1 - \varepsilon_2)^2 + (\varepsilon_2 - \varepsilon_3)^2 + (\varepsilon_3 - \varepsilon_1)^2\}]^{1/2}$). Figure 4.57a shows that the mean effective stress decreases progressively cycle after cycle due to the accumulation of excess pore-water pressure; the greatest decrease occurs during the first stress rotation cycle. Figure 4.57b shows that the stress ratio, η, increases progressively cycle after cycle due to the accumulation of excess pore-water pressure and decrease in *p'* at constant *q*. However, fluctuation of η is observed due to fluctuation of pore-water pressure. The fluctuation becomes more intense during the fourth and fifth stress rotation cycles when the η - α curve follows closely the shape of the failure surface. Figure 4.57c shows that during the first three stress-rotation cycles the accumulated shear strain is small (0.3%), while a considerable increase in γ occurs during the fourth and fifth stress rotation cycles. This is because the ESP crosses the phase transformation line and approaches the failure surface.

Figure 4.58 shows the α - *p'*, η - α and γ - α plots for the medium-dense specimens M20 and M50. In the case of specimen M20, a large decrease in *p'* and increase in η

occurs during the first cycle of stress rotation. Afterwards, the combination of η_{CSR} and α is mobilised at around α = 60° during the second stress rotation cycle and flow deformation is triggered. A sudden increase in the rate of accumulation of excess pore-water pressure and shear strain is observed though the rapid increase is restrained when the combination of η_{PT} and α is mobilised. Past the phase transformation point, the mean effective stress continues to decrease while the effective stress ratio increases because excess pore-water pressure is still accumulating; the shear strain is also accumulating with a high rate. On the other hand, the specimen in test M50 does not exhibit flow behaviour although the sustained deviatoric stress during stress rotation is higher than the one applied in test M20. It can be seen that the stress state of sand in test M50 crosses stably the phase transformation line and reaches the failure line at around α = 40°. The stress ratio η increases initially and then decreases as the stress state moves on the failure surface. The shear strain increases continuously with a high rate though no signs of flow deformation are evidenced in the pattern of straining.

Figure 4.59 shows the α - p', η - α and γ - α plots for the loose specimens L05, L10 and L50. In the case of specimen L10, a large decrease in p' occurs during the first cycle of stress rotation, while during the subsequent cycles, p' decreases continuously with a decreasing rate. During the twelfth cycle of stress rotation, the stress state moves on the locus of critical combinations of η_{CSR} and α, and flow deformation is suddenly triggered at around α = 90°. Notice that the loss of stability occurs at the point where the generation of excess pore-water pressure becomes more intense, indicating the dependence of the instability condition on the loading direction. The shear strain at the triggering of instability in test L10 is very small (< 0.25%). On the other hand, during the subsequent flow the shear strain γ increases to a value in excess of 8% as the specimen liquefies. In the case of specimen L05, the sustained deviatoric stress during stress rotation is too small to cause a considerable increase in u and γ, even after as many as twenty cycles. On the other hand, the sustained deviatoric stress in test L50 is very high, still only limited-flow deformation is exhibited with a small sudden increase in u and γ.

Nakata et al. (1998) interpreted the results of the undrained tests with fixed and rotating stress PA and suggested that “flow deformation occurs when the effective stress state of the sample attains the critical stress ratio”. According to their findings, the mobilised stress ratio η_{CSR} at the onset of flow depends only on the principal stress direction angle α, for a given relative density of sand, and does not depend on the consolidation stress ratio, $K_c = \sigma'_3 / \sigma'_1$, or the stress history that precedes the mobilisation of the state (α , η_{CSR}). This means that the mobilisation of the critical combination (α , η_{CSR}) determined in undrained loading tests with fixed α and b is a sufficient condition for flow instability under undrained conditions involving rotation of the stress PA at constant q. However, this postulation is challenged in this study both theoretically and experimentally.

Sivathayalan and Vaid (2002) investigated the behaviour of loose sand subjected to undrained loading with both fixed and rotating stress PA. The results of the loading tests with fixed α have been already presented in Section 4.2 and, thus, only the results of the stress rotation tests are presented next. It is recalled that Sivathayalan and Vaid (2002) subjected the sand to drained pre-shearing in order to study the influence of generalised initial stress state on the undrained behaviour of sand. According to Sivathayalan and Vaid (2002), the term "initial stress state" encompasses a) the mean effective stress p'_c, b) the static shear stress $(\sigma_{1c} - \sigma_{3c})$ / 2 or, alternatively, the effective stress ratio $K_c = \sigma'_{1c} / \sigma'_{3c}$, c) the value of the intermediate principal stress parameter $b_c = (\sigma_{2c} - \sigma_{3c}) / (\sigma_{1c} - \sigma_{3c})$, d) the value of the inclination angle of the σ_1-axis with respect to the vertical α_c, e) the void ratio e_c and f) the directional characteristics of fabric, quantified microscopically with the techniques presented in Chapter 2 (Section 2.5). It is noted that the subscript letter "c" is used to indicate that the value of the parameter refers to the initial state.

Figure 4.60 shows the results of monotonic undrained loading tests on loose sand with axisymmetric initial stress state (b = 0 and α = 0°) and different levels of initial shear stress (K_c = 1.0, 1.5, 2.0 and 2.0). In these tests, the stress difference σ_d (= σ_1 - σ_3) is increased by $\Delta\sigma_d$, under constant p and b = 0, while the direction of the σ_1-axis is simultaneously rotated by $\Delta\alpha$, in such way that the ratio $\Delta\alpha / \Delta\sigma_{dn}$ (where $\sigma_{dn} = \sigma_d / p'_c$) remains constant and equal to 1.75. It can be seen that a transient-peak state is exhibited for all values of K_c and stress unloading occurs until the phase transformation point is reached. However, a lower increase in σ_d and α is required to trigger flow when K_c is higher. Sivatahayalan and Vaid (2002) reported that the transient-peak state and phase-transformation point are attained at approximately the same value of α (i.e. $\alpha_p \approx \alpha_{PT}$) which decreases with K_c, as shown in Fig. 4.60c; this means that the stress PA remain practically fixed during the limited flow. They also suggested that the value of K_c and stress-rotation history affect the value of the minimum undrained strength q_{min}, as shown in Fig. 4.60b.

Sivathayalan and Vaid (2002) performed monotonic undrained loading tests on loose sand with anisotropic axisymmetric initial stress state (K_c = 2.00, b = 0 and α = 0°). In these tests p and b are kept constant while a different degree of principal stress rotation is imposed. The dimensionless parameter $\Delta\alpha / \Delta\sigma_{dn}$, which expresses the degree of principal stress rotation, is equal to $\Delta\alpha / \Delta\sigma_{dn}$ = 0.70, 1.75, 3.50 and ∞, as shown in Fig. 4.61; $\Delta\alpha / \Delta\sigma_{dn}$ = 0 means that the stress difference is increased without any stress rotation, while $\Delta\alpha / \Delta\sigma_{dn} = \infty$ means that the stress rotation is imposed without any change in the stress difference. It is noted that in the case of $\Delta\alpha / \Delta\sigma_{dn}$ = ∞, the the σ_1 and σ_3 axes are rotated while the magnitude of σ_1, σ_2 and σ_3 is kept fixed. It can be seen that stress unloading and limited-flow deformation is exhibited for all values of $\Delta\alpha / \Delta\sigma_{dn}$, yet the response of sand becomes weaker when the degree of stress rotation increases, i.e. when the ratio $\Delta\alpha / \Delta\sigma_{dn}$ increases (Fig. 4.61). The value of α_p ($\approx \alpha_{PT}$) increases when $\Delta\alpha / \Delta\sigma_{dn}$ increases, while the transient-peak strength, q_p, and minimum undrained strength, q_{min}, decrease when $\Delta\alpha / \Delta\sigma_{dn}$ increases. In the case of $\Delta\alpha$ / $\Delta\sigma_{dn} = \infty$, plastic contraction is initially induced due to the mere rotation of the stress PA, hence, the pore-water pressure increases. However, the effective stress ratio increases as the pore-water pressure increases and the mean effective stress decreases inducing further plastic shear and volumetric strains. It is noted that the increase in $\eta = q / p'$ occurs simultaneously with the rotation of the σ_1-axis away from the vertical. In the course of loading, a stress state is reached at which the (constant) deviatoric stress cannot be further sustained and decreases spontaneously as the sand flows. Afterwards, phase transformation occurs, the sand begins to dilate plastically and the strength is regained as the mean effective stress increases due to the decrease in pore-water pressure.

Figure 4.62 shows the response of sand to principal stress rotation at constant σ_d ($\Delta\alpha$ / $\Delta\sigma_{dn} = \infty$) and different initial stress states. The initial stress states are characterised by the same $p'_c = 200$ kPa, $b_c = 0.5$, $K_c = 2.00$ but different $\alpha_c = 0°$, 45° and 90°. The case with $p'_c = 200$ kPa, $b_c = 0.5$, $K_c = 1.50$ and $\alpha_c = 45°$ is also investigated. It can be seen that different types of flow behaviour are exhibited depending on the value of α_c. Limited-flow deformation with a mild loss of strength is exhibited when $\alpha_c = 0°$, while full-flow deformation with considerable loss of strength occurs when $\alpha_c = 45°$ and 90°. The undrained strength mobilised at quasi-steady state at around $\alpha = 25°$, in the case of $\alpha_c = 0°$, is much higher than the one mobilised at steady-state at around $\alpha = 79°$, in the cases of $\alpha_c = 45°$ and 90°. On the other hand, in the case of $K_c = 1.50$ and $\alpha_c = 45°$, stress rotation by 45° causes only 40 kPa of excess pore-water pressure without any loss of strength or flow, indicating that the value of static shear stress influences the deformation mechanism during stress rotation. It is noted that a small difference in the value of minimum undrained strength, $\sigma_{d,min}$, is evidenced in the cases of $\alpha_c = 45°$ and 90°, despite the fact that the value of α at steady state is exactly the same. This may indicate the effects of stress-history or generalised pre-shearing on $\sigma_{d,min}$. It is also noted that a positive change of pore-water pressure is induced during stress rotation under constant σ_d, irrespective of whether the σ_1-axis rotates towards the vertical or horizontal direction. In the case of $\alpha_c = 90°$, the σ_1-axis rotates towards the vertical direction causing the minimum strength to rise, thus, flow is triggered solely due to the increase in effective stress ratio.

Figure 4.63a shows the effective stress states at the onset of stress unloading and flow in stress-rotation tests. The two lines through the origin bound the stress states at which stress unloading and flow is triggered in the tests with fixed stress PA (constant α). It is noted that the tests with fixed stress PA were performed under the condition of $b = 0.4$, while the tests with rotating stress PA under the condition of $b = 0$ or 0.5. Figure 4.63b shows the variation of the mobilised friction angle, φ_{CSR}, at the onset of stress unloading with the principal stress direction angle, α, for the tests with rotating (hollow rhombuses) or fixed (solid line) stress PA. It can be seen that φ_{CSR} decreases hyperbolically with α, possibly due to the effect of the inherent anisotropy. It can be also seen that stress unloading is triggered when the unique combination of α and φ_{CSR} is mobilised, irrespective of the value of K_c, initial stress state and stress history that precedes the mobilisation of this combination (the scatter may be due to the different values of *b*). The findings of Sivathayalan and Vaid (2002) are in good agreement with those of Nakata et al. (1998) yet the conclusions of these researchers are questioned in the present study.

4.5 INVESTIGATION OF THE FLOW BEHAVIOUR OF SANDS WITHIN THE FRAMEWORK OF STABILITY AND BIFURCATION THEORY

Flow deformation of sand masses in the field is actually an unstable behaviour (Casagrande 1975, Alarcon-Guzman et al. 1988, Ishihara 1993), with a characteristic example being the flow failure of slopes. Regarding laboratory testing, instability occurs if proper *control parameters* are chosen, corresponding to a *mixed loading programme* (Vardoulakis 1986, Darve and Laouafa 2000, Daouadji et al. 2011, Nicot et al. 2011), i.e. in the case of stress- or load-controlled testing with uncontrollable generation of excess pore-water pressure (Castro 1969, Vaid and Chern 1983, Symes et al. 1984, Lade et al. 1988, Chu et al. 1993, Chu and Leong 2001). Under these conditions, the deformation mode bifurcates (Nicot et al. 2007, Daouadji et al. 2011) when instability is triggered, hence, the principles of *Stability* and *Bifurcation Theory* can be applied to determine the flow-instability condition (Hill 1958, Vardoulakis and Sulem 1995, Darve et al. 1995a). Failure along distinct shear zones is also a bifurcated unstable behaviour that may appear together with the flow mechanism in real slopes (Nicot and Darve 2011) so it will be discussed briefly here. The definitions of stability / instability and bifurcation are given next.

Lyapunov's (1907) definition of stability can be applied to continuum mechanics in accordance with the following formalism (Darve and Laouafa 2000, Daouadji et al. 2011):

"A mechanical stress - strain state (for a given rate-independent material after a given stress - strain history) is called stable if any "small" change of any admissible loading d*l* leads to a "small" change of the response d*r*".

More formally:

$$\forall \varepsilon > 0\ \exists \eta = \eta(\varepsilon) > 0 \text{ such that } \|\mathrm{d}l\|_\alpha < \eta \Rightarrow \|\mathrm{d}r\|_\alpha < \varepsilon \qquad (4.6)$$

where $\|\cdot\|_\alpha$ denotes the considered norm in the associated normed space (e.g. in $\mathbf{R}^n$, the Euclidean norm $\|\cdot\|_2$ is used). Defining *failure* as the mobilisation of the peak stress ratio (since sands are stress-ratio dependent materials), it can be suggested that, in general, failure states are unstable because a small or no change in stress induces large strain (Darve et al. 1995a and 2004, Daouadji et al. 2011). Moreover, the state of peak strength, *q*, and post-peak states attained in a stress- or load-controlled undrained triaxial test on a loose saturated sand specimen are also unstable for the same reason (Darve and Laouafa 2000). Stress - strain states of sand elements inside the shear band are accordingly unstable (Drescher and Vardoulakis 1982, Finno et al. 1996, Mooney et al. 1998, Vardoulakis and Georgopoulos 2005).

Lyapunov's (1907) definition of stability is fundamental yet *Hill's sufficient condition for stability* (Hill 1958) is a useful concept for investigating instabilities in geomaterials (Darve et al. 1995a and 2004, Vardoulakis and Sulem 1995). The latter condition states that "a stress - strain state is stable if, *for all* ($\mathrm{d}\overline{\overline{\sigma}}$, $\mathrm{d}\overline{\overline{\varepsilon}}$) or ($\mathrm{d}\underset{\sim}{\sigma}$, $\mathrm{d}\underset{\sim}{\varepsilon}$) linked by the constitutive relation, the *second-order work* is strictly positive":

$$\mathrm{d}^2W = \mathrm{d}\overline{\overline{\sigma}} : \mathrm{d}\overline{\overline{\varepsilon}} > 0 \tag{4.7a}$$

$$\mathrm{d}^2W = \mathrm{d}\underset{\sim}{\sigma}\mathrm{d}\underset{\sim}{\varepsilon} > 0 \tag{4.7b}$$

where d^2W is the second-order work, $\mathrm{d}\overline{\overline{\sigma}}$ and $\mathrm{d}\overline{\overline{\varepsilon}}$ are the incremental stress and strain (or, strictly, the rates of stress and strain), respectively, in tensorial form, while $\mathrm{d}\underset{\sim}{\sigma}$ and $\mathrm{d}\underset{\sim}{\varepsilon}$ are the incremental stress and strain, respectively, in vectorial representation of the symmetrical second-order tensor (Nicot et al. 2007, Prunier et al. 2009, Nicot and Darve 2011). The incremental constitutive relation for rate independent materials is (Darve et al. 1995):

$$\mathrm{d}\underset{\sim}{\varepsilon} = \underset{\sim}{M}_{\underset{\sim}{h}}(\underset{\sim}{u})\mathrm{d}\underset{\sim}{\sigma} \tag{4.8}$$

where $\underset{\sim}{M}$ is the constitutive matrix which, in the case of *non-associative* granular materials, is non-symmetrical and depends on the previous stress - strain history and the current state (characterised by the memory parameters and state variables $\underset{\sim}{h}$). The constitutive models which use a nonlinear operator *M* are called incrementally non-linear, while the constitutive models which use a linear operator M are called incrementally linear (Darve et al. 1995a and b). The constitutive matrix is a function of the direction $\underset{\sim}{u}$ of the incremental stress given by the following equation:

$$\underset{\sim}{u} = \mathrm{d}\underset{\sim}{\sigma} / \left\|\mathrm{d}\underset{\sim}{\sigma}\right\| \tag{4.9}$$

It is important to note that the condition expressed by Eq. 4.7 is *sufficient only* for stability (when *flutter instabilities* are excluded; Bigoni 2000 and 2012), meaning that stability may be sustained in some cases when this condition is violated (Lade et al. 1987, Darve and Laouafa 2000, Daouadji et al. 2011). A characteristic example is the deformation-controlled undrained axisymmetric compression test on loose saturated sand in which the control programme, $\mathrm{d}\varepsilon_1$ = positive constant, $\mathrm{d}\varepsilon_2 = \mathrm{d}\varepsilon_3$ and $\mathrm{d}\varepsilon_1 + 2\mathrm{d}\varepsilon_3 = 0$, can be sustained beyond the peak-*q* point and only small changes in the response parameters are observed for small changes in the control parameters. As shown in Fig.

4.64, the second-order work (expressed by $d^2W = dq\ d\varepsilon_1$ in the case of undrained axisymmetric compression perpendicular to the bedding planes of the specimen) vanishes at the peak-q point and becomes negative in the post-peak regime. On the other hand, the *necessary condition* for instability is the vanishing of the second-order work:

$$d^2W = d\underset{\sim}{\sigma} d\underset{\sim}{\varepsilon} \leq 0 \tag{4.10}$$

Taking into consideration the condition given by Eq. 4.10, it can be stated that in the case of contractive sand subjected to undrained axisymmetric compression (Fig. 4.3f), the peak-q states, post-peak-q states and peak-η states are potentially unstable. In the case of dilative sand exhibiting *dilative shear failure* under undrained axisymmetric compression (Fig.4.3d and Fig. 3.9), the second-order work is positive (Lade et al. 1988, Li 1997, Li et al. 1999) and any small change of the control parameters causes a small change of the response parameters, irrespective of the type of the control parameters. However, the second-order work may become non-positive and large deformations may be induced by small stress changes if another stress direction is probed at a failure state (Darve et al. 2004). On the other hand, the stress - strain states of the soil elements inside the shear band are potentially unstable according to Eq. 4.10 (Drescher and Vardoulakis 1982, Finno et al. 1996, Mooney et al. 1998, Nicot and Darve 2011).

It has been demonstrated that flow deformation and shear banding of sands are unstable behaviours; it will be shown next that a bifurcation of the deformation mode occurs when these instabilities are triggered. Bifurcation can be defined as the *loss of uniquenes*s of the response of a mechanical system: there exist more than one response paths from a given state (*bifurcation point*) for the same loading path, meaning that “the system may follow different bifurcated branches, departing from the fundamental response path” (Nicot and Darve 2011; Darve et al. 2004). The loss of uniqueness is observed in both physical and numerical experiments (Darve et al. 1995a, Desrues and Georgopoulos 2006), while the non-unique bifurcated branches are highly affected by the *perturbations* and *imperfections* in the system (Vardoulakis and Graf 1982, Desrues et al. 1985 and 1996, Vardoulakis and Sulem 1995, Ikeda et al. 2008, Daouadji et al. 2011). Bifurcation can be also defined as “the sudden change in the nature of the response of the system under continuous evolution of the internal variables (or loading parameters)” (Nicot and Darve 2011). A particular case of bifurcation occurs under stationary loading parameters: “the system evolves toward another mechanical state from an equilibrium configuration, with no change in the control parameters” (Nicot et al. 2007; Sibille et al. 2008).

It can be now justified that bifurcation occurs when flow deformation is triggered in situ or in laboratory testing. A characteristic example is the *spontaneous liquefaction* of soil masses in the field. Terzaghi and Peck (1948) used the term “spontaneous liquefaction” to describe the unstable behaviour of loose deposits of sands that suddenly flow much like a viscous fluid, as a result of minor disturbances (Ishihara

1993). Eckersley (1990) reported that a model slope (1 m in height), consisted of cocking coals placed inside a tank, suddenly collapsed and flowed as the water table was raised slowly. Darve et al. (2004) applied a numerical discrete method to study the kinematic patterns of a slope consisted of rods that was placed inside a rotating box. They observed that surficial grain avalanches appeared, under a chaotic pattern of the displacement field, as the rotation angle of the box increased. Sibille et al. (2008) performed DEM simulations of axisymmetric loading on loose and dense specimens. Firstly, the specimens were subjected to drained compression until the target equilibrium state was reached. Then, a perturbation was induced and the evolution towards another mechanical state was monitored. In some cases, even the slightest perturbation resulted in a dynamic response and collapse of the specimen. The physical experiments of Castro (1969), Symes et al. (1984), Alarcon-Guzman et al. (1988), Lade et al. (1988), Chu et al. (1993), Chu and Leong (2001) and Desrues and Georgopoulos (2006) also showed that the response of loose sand to undrained loading may suddenly become dynamic and non-unique when diffuse flow deformation is triggered.

In all the aforementioned cases, a common behavioural pattern is evidenced: the transition from a (quasi-)static to a dynamic response with a burst of kinetic energy (Darve et al. 2004, Daouadji et al. 2011, Nicot and Darve 2015). Thus, a bifurcation of the deformation mode occurs either as the control parameters change monotonically or remain stationary; in the latter case the kinetic energy is developed spontaneously (i.e. without any change in the control parameters) and the *sustainability* of the equilibrium state is lost (Nicot et al. 2007). If no strain localisation is observed then a *continuous bifurcation* occurs. On the contrary, in the case of shear banding, the strain mode bifurcates from a diffuse one to a strictly discontinuous one, thus a *discontinuous bifurcation* occurs (Darve et al. 2004). It is noted that both straining patterns (diffuse and localised) may coexist in large-scale problems or in the field (Nicot and Darve 2011), while in laboratory testing, dynamic flow deformation may occur inside the shear band (Eckersley 1990, Finno et al. 1996, Vardoulakis and Georgopoulos 2005), while diffuse modes of deformation typically precede the localised ones (Desrues and Vigiani 2004, Nicot and Darve 2011, Lü et al. 2018).

Flow deformation and shear banding are bifurcated potentially unstable behaviours thus the principles of Stability and Bifurcation Theory can be applied to determine the triggering condition of these phenomena. It should be emphasised that using the appropriate criterion for flow instability and shear banding is of tremendous importance in Geotechnical Analysis and Design. For example, the Stability Analysis of slopes has been traditionally based on the plastic limit analysis (Duncan 1996). Since the homogeneous plastic limit condition indicates the unrealistic situation of failing when the slope angle equals the material's peak friction angle, an alternative analysis procedure has been proposed. It is hypothesised that the soil fails along a *slip surface* the shape of which is in general a priori assumed; the slip surface is a discontinuity between a rigid sliding mass and a rigid stable base (Tavenas et al. 1980). The *critical slip surface* that corresponds to the minimum *Factor of Safety* (FS) should be determined, where FS is given by the following equation (Poulos et al. 1985):

$$\mathrm{FS} = \frac{\text{shear strength of the soil}}{\text{shear stress required for equilibrium}} \tag{4.11}$$

Loose saturated deposits of sand are collapsible and thus susceptible to the strength drop induced by the excess pore-water pressure build up (Eckersley 1990, Sasitharan et al. 1993, Skopek et al. 1994, Anderson and Riemer 1995), hence, the minimum undrained strength (q_{min}) should be used in Eq. 4.11. According to Poulos et al. (1985), when FS is less than one, the soil mass is in *unstable equilibrium* and a perturbation (static or dynamic) may trigger liquefaction. Conversely, when FS is higher than 1, the soil is in *stable equilibrium*.

There are some pitfalls and shortcomings regarding the classical stability analysis procedure presented above. Both terms of the ratio in Eq. 4.11 depend on the current state and previous stress - strain history of each soil element along the potential slip surface. The equilibrium shear stress in the denominator is influenced by the normal stress distribution which depends on the stress - strain history that precedes the formation (“incremental genesis”) and loading of the slope. Tavenas et al. (1980) compared the normal stress along a potential slip surface of an excavated slope determined by means of photo-elasticity (and also confirmed by numerical methods) with the one obtained by considering the slope geometry alone and not the loading history. They showed that the normal stress in the latter case was seriously overestimated along the upper part of the slip surface while it was seriously underestimated along the lower part of the slip surface. Duncan (1996) and Laouafa and Darve (2002) considered two slopes with the same geometry and boundary conditions but different stress - strain histories. The first slope was formed by means of an excavation process while the second was an embankment. Excavation causes negative excess pore-water pressure thus the long-term stress conditions are crucial concerning stability, while in the case of an embankment the reverse is true. In both cases the current state depends not only on the geometry but also on the previous stress - strain history. It is obvious that a stability analysis that does not consider the stress - strain history cannot estimate realistically the current state of the soil elements and, consequently, the safety factor.

The uncertainties regarding the value of the numerator of the ratio in Eq. 4.11 are even more serious. The conventional stability analysis is frequently based on the classical Steady State Theory (Poulos et al. 1985) within which the minimum undrained strength of soil is deemed to be a unique function of the in-situ void ratio. As already discussed in Section 4.2, the minimum undrained strength, q_{min}, depends also on the effective consolidation stress, the direction of the σ_1-axis with respect to the bedding planes of the soil and the mode of loading. Sivathayalan and Vaid (2002) and Shibuya et al. (2003b) showed that the shear stress level during anisotropic consolidation also affects the value of q_{min} exhibited during the subsequent loading. Zdravkovic and Jardine (2001) showed that the consolidation of soils with inclined stress PA with respect to the bedding planes also affects the minimum undrained strength, q_{min}, while Sivathayalan and Vaid (2002) reported that the generalised pre-shearing of sands has, similarly, an effect on q_{min}.

Darve and Laouafa (2000) and Laouafa and Darve (2002) noticed that the conventional stability analysis does not take into account the velocity and strain (at the material point or global level) or the time evolution of stress, strain and other physical quantities. Since the triggering of instability in the field is associated with bifurcation of the deformation mode, the outbursts of kinetic energy and evolution of strain in time should not be overlooked (see for example Darve et al. 2004). More importantly, Darve (Darve and Laouafa 2000, Laouafa and Darve 2002, Darve et al. 2004) highlighted that the stability analysis that relies exclusively on the plastic limit condition is inherently problematic. This is the case even if a sophisticated analysis is run, for example one that uses the Finite Element Method (FEM), and the stress - strain history is taken into consideration. The inaccuracy lies in the fact that a large number of catastrophic unstable bifurcations of the response of geomaterials may occur before the plastic limit is reached and before the triggering of strain localisation.

Vardoulakis (1980) treated the localisation of the deformation of dry dense sand in biaxial (plane strain) testing as a bifurcation problem. The theoretical analysis and experimental results presented by Vardoulakis (1980) indicate that, due to the non-associative characteristics of sands, localisation may occur in the hardening regime, i.e. before the plastic limit (failure) condition is satisfied. This finding was later verified by Desrues et al. (1985) using the stereophotogrammetric method. Hettler and Vardoulakis (1984) tested dry dense sand in a properly designed large triaxial apparatus accommodating squat specimens with a slenderness ratio $\kappa = H / D$ (H is the initial height and D is the initial diameter of the cylindrical specimen) equal to 0.36 or 0.59. They used enlarged and lubricated end platens, yet, they found that in the case of more slender specimens (κ = 0.59) the deformation bifurcated to an inhomogeneous diffuse bulging mode before reaching the limiting state. Lade et al. (1988) showed that contractive sand specimens subjected to undrained triaxial loading in a stress- or load-controlled mode may become unstable strictly inside the plastic limit surface and deform without any obvious signs of strain localisation.

The non-associativity of sands, which dictates that the *yield surface* does not coincide with the *plastic potential surface*, is the reason why the stability can be lost inside the plastic limit surface. Figure 4.65 shows the set of yield surfaces of a non-associative isotropic granular material in the Rendulic plane (i.e. the bisector plane in the principal stress space containing the triaxial stress states), while Fig. 4.66 shows the yield surface and plastic potential surface in the same plane. As can be seen in the latter figure, a wedge is formed between the two surfaces. The shaded wedge in Fig. 4.66 is located within a larger region bounded by the lines that correspond to constant stress ratio σ'_1 / σ'_3 and constant stress difference (σ'_1 - σ'_3), and the loading directions inside this wedge are associated with decreasing effective stresses. Lade et al. (1987, 1988 and 1989) observed that sand subjected to a stress probe inside this particular wedge undergoes plastic straining and is potentially unstable since Inequality 4.7b is not satisfied. For example, the effective stress path of an undrained compression test on loose or medium loose sand may progress along the directions included inside the shaded wedge and, in this case, instability can be triggered if the control parameters are proper. Figure 4.67 shows the effective stress paths in the Rendulic plane of undrained compression tests on sand specimens with different relative density.

Lade et al. (1988) stated that the *region of potential instability* in the Rendulic plane "is located at and above the solid points indicating the maximum stress differences" obtained from monotonic undrained triaxial tests on saturated contractive sand, as shown in Fig. 4.68. Lade (1992 and 1993) defined the *instability line* (IL) in the q - p' plane as "the line connecting the tops of a series of effective stress paths from undrained tests on loose soils" (see Fig. 4.69). He suggested that this line provides the lower boundary of the region of potential instability. Many researchers reported that instability is triggered at stress states on or beyond Lade's IL, for a considerable number of monotonic and cyclic, undrained and drained loading histories (Vaid and Chern 1983, Sassitharan et al. 1993, Lade 1994, Hyodo et al. 1994, Nakata et al. 1998, Sivathayalan and Vaid 2002, Leong and Chu 2002, Chu et al. 2003, Georgiannou et al. 2008). However, according to other researchers instability may also be triggered at stress states below the IL (Nova 1989, Chu et al. 1992 and 1993, Darve et al. 1995a, Laouafa and Darve 2002, Daouadji et al. 2011).

Darve et al. (1995a) and Laouafa and Darve (2002) suggested that Lade's IL lacks intrinsic value since it is determined for a particular triaxial loading history (i.e. undrained compression), while different lines can be determined for different triaxial loading histories (i.e. partially drained compression4). Moreover, the IL is not the true lower boundary of the region of potential instability (bifurcation domain) (Nova 1989, Darve et al. 2004, Sibille et al. 2007, Prunier et al. 2009, Daouadji et al. 2011). The true lower boundary of the bifurcation domain comprises the states at which the determinant of the symmetric part of the constitutive matrix is vanishing in one unique first unstable stress direction. The determinant under consideration is inherently a directional quantity, while the vanishing of it, is closely related to the vanishing of the second-order work d^2W (Darve et al. 2004, Nicot and Darve 2011), as will be shown next. Consequently, the lower boundary of the bifurcation domain can be established if a directional analysis is carried out in the way proposed by Gudehus (1979). It is noted that the lower boundary of the bifurcation domain is more or less *intrinsic* for a given material (the relative density and mean effective stress still influence the shape and position of this locus; Laouafa and Darve 2002, Prunier et al. 2009), as the plastic condition is in at first approximation.

The numerical and physical techniques used to identify unstable stress states and determine the bifurcation domain of a granular material are presented next, while the role of the second-order work d^2W (Hill 1958) in the search of unstable stress states is highlighted using general constitutive formulations (i.e. without referring to a particular constitutive model). Firstly, it is shown that the second-order work is a directional quantity in the stress (or strain) space that depends not only on the current state but also on the previous stress - strain history. Substituting the expression for $\mathrm{d}\underset{\sim}{\varepsilon}$ (given by Eq. 4.8) in Eq. 4.10 the following equation is derived:

$$\mathrm{d}^2W = {}^{\mathrm{t}}\,\mathrm{d}\underset{\sim}{\sigma}\underset{\sim}{M}\left(\underset{\sim}{u}\right)\mathrm{d}\underset{\sim}{\sigma} \qquad (4.12)$$

where the superscript "t" denotes the transpose of the vector. Substitution of $\mathrm{d}\underset{\sim}{\sigma}$ (given by Eq. 4.9) in Eq.4.12 yields:

$$\mathrm{d}^2W = \left\|\mathrm{d}\underset{\sim}{\sigma}\right\|^2 \; {}^{\mathrm{t}}\underset{\sim}{u}\underset{\sim}{M}\left(\underset{\sim}{u}\right)\underset{\sim}{u} \qquad (4.13)$$

It is obvious that d^2W depends on both the current state and previous stress - strain history since the constitutive matrix $\underset{\sim}{M}$ exhibits this kind of dependence. Moreover, the value of d^2W depends on the direction $\underset{\sim}{u}$ of the incremental stress at a given stress - strain state, reached after a given stress - strain history, albeit d^2W being a scalar quantity.

The directional dependence of the second-order work means that d^2W at a given stress state may be positive along some incremental stress directions and negative or nil along other incremental stress directions; in the latter case, the stress state is deemed to be potentially unstable because there exist directions along which Inequality 4.10 holds. The sign of d^2W is, in general, a function of $\underset{\sim}{u}$ but not of $\left\|\mathrm{d}\underset{\sim}{\sigma}\right\|$, unless a strongly non-linear behaviour is exhibited for finite $\left\|\mathrm{d}\underset{\sim}{\sigma}\right\|$ (Sibille et al. 2007 and 2008). It should be noticed that similar results are obtained if the unstable directions are determined using strain probes (with direction given by the unit vector, $\underset{\sim}{v} = \mathrm{d}\underset{\sim}{\varepsilon} / \left\|\mathrm{d}\underset{\sim}{\varepsilon}\right\|$) in the strain space. Furthermore, the directional character of d^2W is generic for rate-independent granular materials since no particular constitutive model is considered so far.

The second-order work can be expressed in normalised form as the scalar product of the two unit vectors $\underset{\sim}{u} = \mathrm{d}\underset{\sim}{\sigma} / \left\|\mathrm{d}\underset{\sim}{\sigma}\right\|$ and $\underset{\sim}{v} = \mathrm{d}\underset{\sim}{\varepsilon} / \left\|\mathrm{d}\underset{\sim}{\varepsilon}\right\|$:

$$\mathrm{d}^2W_{norm} = \frac{\mathrm{d}\underset{\sim}{\sigma}\mathrm{d}\underset{\sim}{\varepsilon}}{\left\|\mathrm{d}\underset{\sim}{\sigma}\right\|\left\|\mathrm{d}\underset{\sim}{\varepsilon}\right\|} \qquad (4.14)$$

Obviously, d^2W_{norm} is the cosine of the angle θ between the vectors $\mathrm{d}\underset{\sim}{\sigma}$ and $\mathrm{d}\underset{\sim}{\varepsilon}$, thus, its value varies in the range [-1 , 1]. In the case of axisymmetric loading and under the condition of coaxiality between the stress rate and strain rate tensors the following equations give the value of cos θ:

$$\cos\theta = \frac{\mathrm{d}^2W}{\sqrt{\mathrm{d}\sigma_1^2 + 2\mathrm{d}\sigma_3^2}\sqrt{\mathrm{d}\varepsilon_1^2 + 2\mathrm{d}\varepsilon_3^2}} \tag{4.15a}$$

$$\cos\theta = \frac{\mathrm{d}^2W}{\sqrt{\mathrm{d}q^2 + \mathrm{d}p^2}\sqrt{\mathrm{d}\varepsilon_q^2 + \mathrm{d}\varepsilon_v^2}} \tag{4.15b}$$

where ($\mathrm{d}\sigma_1$, $\sqrt{2}\mathrm{d}\sigma_3$) and ($\mathrm{d}\varepsilon_1$, $\sqrt{2}\mathrm{d}\varepsilon_3$) are the vectors of stress rate and strain rate in the Rendulic plane with norms $\|\mathrm{d}\underset{\sim}{\sigma}\| = \sqrt{\mathrm{d}\sigma_1^2 + 2\mathrm{d}\sigma_3^2}$ and $\|\mathrm{d}\underset{\sim}{\varepsilon}\| = \sqrt{\mathrm{d}\varepsilon_1^2 + 2d\varepsilon_1^2}$, respectively (Sibille et al. 2007). The corresponding vectors in the q - p plane are ($\mathrm{d}q$, $\mathrm{d}p$) and ($\mathrm{d}\varepsilon_q$, $\mathrm{d}\varepsilon_v$), while the respective norms are $\sqrt{\mathrm{d}q^2 + \mathrm{d}p^2}$ and $\sqrt{\mathrm{d}\varepsilon_q^2 + \mathrm{d}\varepsilon_v^2}$ (Lade and Pradel 1990); note that all normal stresses are effective and the work-conjugate pair of deviatoric stress and strain is $q = \sigma_1 - \sigma_3$ and $\varepsilon_q = 2/3\ (\varepsilon_1 - \varepsilon_3)$.

Given the fact that the sign of d^2W depends on the direction of the incremental stress, the detection of potentially unstable stress states requires the performance of a directional analysis. Specifically, at a given stress state reached after a given stress - strain history, stress probes $\mathrm{d}\underset{\sim}{\sigma}$ of equal and sufficiently small norm are applied along different directions in the stress space and the strain response $\mathrm{d}\underset{\sim}{\varepsilon}$ is monitored. Gudehus (1979) introduced this type of directional analysis in order to obtain the so-called strain response envelope. As can be seen in Fig. 4.70, the applied stress probe $\mathrm{d}\underset{\sim}{\sigma}$ in the Rendulic plane forms an angle α with the $\sqrt{2}\mathrm{d}\sigma_3$-axis, while the response vector $\mathrm{d}\underset{\sim}{\varepsilon}$ forms an angle β with the $\sqrt{2}\mathrm{d}\varepsilon_3$-axis. The difference between the angles α and β gives the angle θ which appears in the Eq. 4.15a. If the value of cos θ is negative or nil then the stress state is reputed to be potentially unstable.

Figure 4.71 shows the results of a numerical directional analysis under axisymmetric conditions performed by Darve and Laouafa (2000). In the simulation of the behaviour of Hostun Sand the material was first subjected to isotropic compression to different effective confining stresses, σ'_3, and then to drained triaxial compression until the stress state at the target $\eta = q\ /\ p'$ was attained. Afterwards, the stress probe analysis described previously was performed and the normalised second-order work d^2W_{norm} was determined along various directions of incremental stress. Figure 4.71 shows the circular diagrams of d^2W_{norm} for dense and loose Hostun Sand and for two different values of η for each density. These diagram illustrates the dependence of d^2W_{norm} on α (α is the angle between the vector $\mathrm{d}\underset{\sim}{\sigma}$ and the horizontal $\sqrt{2}\mathrm{d}\sigma_3$-axis in the Rendulic plane). In order to facilitate the presentation of the results, an arbitrary constant value c is added to the polar value of d^2W_{norm} so (Sibille et al. 2007):

$$\forall\alpha :\ \mathrm{d}^2W_{norm}(\alpha) + c \geq 0 \tag{4.16}$$

The circle in the diagrams in Fig. 4.71 corresponds to $d^2W_{norm} = 0$, while inside the circle d^2W_{norm} is negative and outside the circle d^2W_{norm} is positive.

Figure 4.71 shows that, for a given relative density, the increase in η induces a decrease in d^2W_{norm} along the directions included in the south-west quadrant of the Rendulic plane of incremental stress (i.e. along the directions with $d\sigma_1 < 0$ and $\sqrt{2}d\sigma_3 < 0$). d^2W_{norm} vanishes along one first unstable direction of incremental stress in this quadrant. The stress ratio η at which d^2W_{norm} vanishes firstly is lower when the sand is looser. Consequently, the experimental results of Lade (Lade et al. 1988, 1989, 1990a and 1990b) that showed instabilities in undrained loading tests on loose contractive sand along loading directions corresponding to decreasing effective stresses were verified numerically by Darve, who also exposed instabilities of dense dilating sand under drained loading conditions, as will be shown next. It is noted that only two points on the response strain envelope shown in Fig. 4.70 correspond to isochoric deformation, hence, the stress probing along the directions shown in Fig. 4.71 induces contractive, dilative or isochoric deformation.

In the case that stress probes are imposed at a higher stress ratio than the one corresponding to the vanishing of d^2W_{norm} along one first unique direction of incremental stress, a set of unstable directions of incremental stress is obtained along which d^2W_{norm} is either nil or negative. These directions form a cone with its apex at the stress state from which the stress probes are initiated. d^2W_{norm} is nil along the incremental stress directions at the boundaries of the cone, while d^2W_{norm} is negative along the incremental stress direction inside the cone. Figure 4.72 shows the *cones of unstable stress directions* or *instability cones* in the Rendulic stress plane, for dense and loose Hostun Sand, obtained by means of a numerical directional analysis (Darve et al. 2004). The cones for loose sand are broader than for dense sand, when the stress state is the same. At low stress ratio a cone containing stress directions along which $\sqrt{2}\, d\sigma'_3 \leq 0$ and $d\sigma'_1 < 0$ is formed, the opening of which broadens for both loose and dense sand as the stress ratio increases, while at higher stress ratio a second cone appears containing stress directions along which $\sqrt{2}\, d\sigma'_3 > 0$ and $d\sigma'_1 \geq 0$. A physical loading programme that corresponds to this peculiar situation has been unknown so far (Darve et al. 2004, Sibille et al. 2007).

The stress states, at which one first unstable incremental stress direction is detected, yielding a line as a degenerate case of instability cone, form the so-called *lower boundary of the Bifurcation Domain*. This limit line is closer to the hydrostatic axis when the sand is looser, in the same way as the failure envelope (which is the upper limit of the Bifurcation Domain) is less steep when the sand is looser. The lower boundary of the Bifurcation Domain is strictly related to the vanishing of the determinant of the symmetric part of the constitutive matrix in one unique first unstable stress direction; the vanishing of this determinant is further related to the vanishing of the second-order work (Darve et al. 2004, Nicot et al. 2011). Consequently, a large domain exists in the stress space comprising the stress states at which unstable bifurcations can be triggered, leading to catastrophic events before the plastic limit condition is satisfied. The non-associative characteristics of sands are the reason why the Bifurcation Domain exists. The Geotechnical Analysis and Design should take into consideration that failure-like catastrophic events may be triggered before the failure condition that corresponds to the mobilisation of the peak stress ratio is satisfied. Flow deformation of sands is only one particular case of unstable bifurcation that can be investigated within the framework of Stability and Bifurcation Theory.

The results presented in Figs 4.71 and 4.72 were obtained using the incrementally non-linear constitutive model of Darve for modelling the macroscopic behaviour of Hostun Sand in axisymmetric loading mode. On the other hand, Sibille et al. (2007 and 2008) investigated the behaviour of a granular material subjected to axisymmetric stress probing by means of Discrete Element Method (DEM) simulations and verified the existence of a large bifurcation domain in stress space and cones of unstable stress directions inside it. Figures 4.73 and 4.74 show the circular diagram of the normalised second-order work for different stress ratios, $\eta = q\ /\ p'$, and effective confining stresses, σ'_3, for the densest and loosest virtual specimen, respectively. It can be seen that, in both cases, d^2W_{norm} attains negative values along some incremental stress directions included in the south-west quadrant of the circular diagrams (i.e. along stress directions with $d\sigma'1 < 0$ and $\sqrt{2}\ d\sigma'_3 < 0$) when η increases above a certain value; the threshold value of η, at a given σ'_3, is lower when the granular material is looser. However, the opening of the instability cone, as well as the stress directions included inside the cone, depend on the density of the granular material. For example, the instability cones of looser material are broader than those of denser material and the direction of isotropic stress unloading ($d\sigma'_1 = d\sigma'_2 = d\sigma'_3 < 0$), which corresponds to the effective stress path with constant q and decreasing p', is included in the former but not in the latter for $\sigma'_3 = 100$ kPa (Fig. 4.74a). This is better illustrated in Fig. 4.75, which shows the instability cones at various stress states in the Rendulic stress plane, determined in the DEM simulations by Sibille et al. (2008).

The results of the numerical directional analyses presented here are in good agreement with the results of physical axisymmetric loading tests of Chu et al. (2003), shown in Fig. 4.76. Chu et al. (2003) imposed the condition of $dq = 0$ and $d\varepsilon_{vol} = 0$ to loose sand specimens that were previously subjected to drained triaxial compression, and checked whether the undrained stress state could be sustained or not. It was observed that, when the conditions were switched to undrained and the deviatoric stress was kept constant, the loose specimen underwent a runaway deformation (i.e. the equilibrium stress state became unsustainable and instability was triggered) in the case that the stress ratio was sufficiently high. This indicates that undrained flow instability of loose sand is triggered only if the stress ratio is above a certain threshold. Figure 4.76 shows that the unstable direction of isotropic stress unloading is excited as the pore-water pressure increases and the mean effective stress decreases under constant q.

Chu et al. (2003) also reported instabilities of loose and dense sand specimens subjected to isotropic stress unloading under drained axisymmetric conditions. In these tests, the deviatoric stress is kept constant and the mean effective stress is lowered, while the volume of the specimen is free to change (see also the studies by Sassitharan et al. 1993, Anderson and Riemer 1995). Instability cannot occur in these tests as far as the pore-water pressure is under control yet it is indicated by the rapid generation of strains. Figure 4.77 shows the results of two constant-q drained tests performed on dense specimens. Specifically, Fig. 4.77 shows the effective stress paths in the q - p' space and the evolution of the effective confining stress and strains with time. It can be seen that instability is triggered in both tests at points B and B' since a sharp increase in the strain rate is observed, thus, dense sand may undergo instability under drained conditions.

It is noted that there exists a duality in the procedure of directional analysis: one can impose strain probes (instead of stress probes) along different directions in the strain space (stress space), monitor the response in the stress space (strain space) and compute the second-order work, in order to detect bifurcation points and instabilities. For example, Chu et al. (1993) subjected medium-loose and dense specimens to drained triaxial compression up to different effective stress ratios, σ'_1 / σ'_3, and for different effective confining stresses, σ'_3, and then imposed strain probes along different directions in the triaxial strain space. Proper control parameters were chosen in order to expose the flow instability, if it was to occur. Chu et al. (1993) investigated, in this way, the influence of the void ratio, effective stress ratio, effective confining stress and strain-increment direction on the triggering of flow instability. The term *flow instability* describes, according to Chu et al. (1993), the runaway non-localised deformation of sand, characterised by the sharp increase (or jump) in strains and excess pore-water pressure and the decrease of strength. Chu et al. (1993) generalised the notion of flow instability for both loose and dense sand, in both undrained and drained conditions, since they applied a general axisymmetric loading programme by means of strain-path testing.

Figure 4.78 shows the results of axisymmetric strain-probe tests performed by Chu et al. (1993) on two dense sand specimens (Z01 and Z02) at different levels of stress ratio σ'_1 / σ'_3 (3.5 and 3.0, respectively), the same level of effective confining stress σ'_3 (150 kPa) and along the same strain-probe direction dε_v / dε_1 = -0.67. Figure 4.78a shows the effective stress paths of both tests in the Rendulic plane after the initiation of the strain-probe instability check, while Fig. 4.78b shows the evolution of the major principal strain, ε_1, and pore-water pressure, u, with time in test Z01. Both specimens underwent a runaway collapse, with a rapid increase in the rate of accumulation of strain and excess pore-water pressure. Interestingly, when the dilation rate was set constant to dε_v / dε_1 = -0.67 the pore-water pressure increased and the effective stress path followed the direction of isotropic stress unloading towards the failure envelope. This may be the result of the control imposing the condition of dq = 0 and dσ_3 = 0 during the instability check (Chu and Leong 2001), though Chu et al. (1993) reported that the deviatoric stress, q, ran out of control and decreased when the stress path reached the failure surface. These results show that flow instability can be induced along the direction of isotropic stress unloading even in the case of dense dilating sand.

Chu et al. (1992) performed axisymmetric strain-path tests along different directions in the strain space, determined by the ratio $d\varepsilon_v / d\varepsilon_1$. The dense specimens tested were loaded from the isotropic consolidation state towards failure, imposing a constant dilatancy ratio $d\varepsilon_v / d\varepsilon_1$. The set of control parameters was such that instability was not allowed to occur, thus, the stress unloading behaviour (decrease in p' and q) could be observed efficiently. Figure 4.79a shows the effective stress paths (ESPs) in the q - p' plane for two tests on dense sand specimens consolidated to different mean effective stress and loaded along the same incremental-strain direction $d\varepsilon_v / d\varepsilon_1 = -0.67$. It can be seen that q reaches a peak value and then decreases, as the pore-water pressure increases and the mean effective stress decreases, while the sand dilates. The ESPs reach the failure envelope determined in conventional triaxial compression tests (drained) at the minimum-q state and remain stationary at this condition. It is important to notice that the characteristics of flow deformation are observed in these drained tests, which were conducted on dense dilating sand specimens. On the other hand, Fig. 4.79b shows the ESPs of tests on dense sand specimens consolidated to different mean effective stress and loaded along the same incremental-strain direction $d\varepsilon_v / d\varepsilon_1 = -0.11$. It can be seen that the deviatoric stress increases steadily, as the pore-water pressure decreases and the mean effective stress increases, while the sand dilates, and a failure envelope different than the one determined in the conventional triaxial compression test is reached ultimately. The conditions in tests ζ1 and ζ3 were identical except for the different values of $d\varepsilon_v / d\varepsilon_1$, thus, the different responses should be due to this factor.

Darve et al. (1995a) performed numerical simulations of axisymmetric strain-path tests using the incrementally non-linear constitutive model. The virtual material was loaded from the isotropic consolidation state under constant $R = -d\varepsilon_3 / d\varepsilon_1$, which is equivalent to imposing a constant ratio $d\varepsilon_v / d\varepsilon_1$. The results of the analyses are shown in Fig. 4.80. Dilation of the virtual material occurs when the ratio R is higher than 0.5, contraction when the ratio is lower than 0.5 and no-volume change when the ratio is 0.5. It can be seen that the behaviour under isochoric conditions is of the flow type, exhibiting stress unloading after a state of peak q, due to the increase in pore-water pressure. In the case that the material dilates the behaviour is, similarly, of the flow type but showing more severe stress unloading as the ratio R increases. In the case that the material contracts the behaviour is of the flow type when the ratio R is 0.450 or 0.425, while non-flow behaviour with a continuous increase in q is observed when $R = 0.400$.

The results of the numerical analyses performed by Darve et al. (1995a), shown in Fig. 4.80, agree well with the results of the physical experiments performed by Chu et al. (1992), shown in Fig. 4.79: the response of sand may turn from stable, exhibiting a continuous increase in q, to potentially unstable, exhibiting stress unloading after a peak-q state, when the ratio $d\varepsilon_v$ / $d\varepsilon_1$ decreases. Both loose and dense sand may undergo flow instability, under undrained or drained conditions. Moreover, it can be inferred that the instability line, introduced by Lade (Lade et al. 1988 and 1992) as "the line connecting the tops of a series of effective stress paths from undrained tests on loose soils" (Fig. 4.69), lacks intrinsic value since it corresponds to a particular type of triaxial loading, i.e. to undrained (isochoric) triaxial loading. Chu, Darve and their colleagues showed that different "instability lines" can be determined when the ratio $d\varepsilon_v$ / $d\varepsilon_1$ is varied in strain-path testing, while instability may be triggered at a stress ratio lower than the one corresponding to Lade's instability line, proving that the latter is not the lower boundary of the region of potential instability.

Prunier et al. (2009) used the incrementally piecewise-linear (octolinear) and incrementally non-linear constitutive models of Darve and performed three-dimensional bifurcation analyses in the principal stress space, simulating the response of Hostun Sand. Prunier et al. (2009) verified under 3D stress conditions the findings of the numerical analyses performed previously by Darve et al. (2004) under axisymmetric conditions. A large bifurcation domain was detected in the principal stress space, as shown in Fig. 4.81. The lower boundary of the bifurcation domain comprises the stress states at which the determinant of the symmetric part of the constitutive matrix vanishes along one unique first unstable stress direction. The shape of this bifurcation surface is approximately conical having the apex at the origin of the stress space, yet, a dependence on the mean effective stress can be inferred. Darve et al. (2004) have reported a further dependence of the shape of this surface on the relative density of sand (Fig. 4.72). The upper limit of the bifurcation domain is the failure surface (the Mohr-Coulomb envelope). It is noted that the generalisation of Lade's instability line in the principal stress space is a conical surface intermediate between the two boundaries of the bifurcation domain (Daouadji et al. 2011).

Prunier et al. (2009) also verified the existence of 3D instability cones in the principal stress space. They performed radial loading tests in the deviatoric plane until different 3D stress states inside the bifurcation domain were reached. Thereafter, they conducted a directional analysis by probing along different incremental-stress directions in the 3D space. Consequently, both the stress probes and the origin stress states of the probes were purely 3D. Figures 4.82 shows the cones of unstable stress directions determined using the octolinear and non-linear constitutive models of Darve. The instability cones presented are the first opened beyond the bifurcation surface. All the instability cones are directed towards the origin of the stress space, irrespective of the model used or the value of the Lode angle at the origin stress state of the instability cones. This means that some incremental-stress directions corresponding to $d\sigma'_1 < 0$, $d\sigma'_2 < 0$, $d\sigma'_3 < 0$ are *intrinsically* unstable, because they are associated with the first unique unstable stress direction along the bifurcation surface. It is noted that when the effective stress ratio increases beyond this bifurcation limit, the direction of isotropic stress unloading is soon included in the instability cones, especially in the case of loose sand.

4.6 INVESTIGATION OF THE FLOW BEHAVIOUR OF SANDS WITHIN THE FRAMEWORK OF ANISOTROPIC CRITICAL STATE THEORY

The Critical State Theory (CST) (Roscoe et al. 1958, Schofield and Wroth 1968) is a framework within which soil liquefaction has been traditionally investigated (Castro 1969, Poulos et al. 1985, Sladen et al. 1985, Been et al. 1991, Jefferies and Been 2006). One of the key aspects of the CST is the reference to the ultimate material state (critical state) by means of a state parameter (Wroth and Basset 1965) for describing and modelling the mechanical behaviour of soils. Whether sand is susceptible to flow liquefaction or not depends on its state. Been and Jefferies (1985) proposed the state parameter $\psi = e - e_c(p')$ for sands which is the difference between the current void ratio, e, and the void ratio at critical state at the current mean effective stress, $e_c(p')$. The susceptibility of sands to flow liquefaction increases when ψ increases. A characteristic example of state dependence is that sand of a given void ratio may dilate at low effective consolidation stress, while it may contract and liquefy at high effective consolidation stress.

On the other hand, Li and Dafalias (2012) introduced the Anisotropic Critical State Theory which takes into consideration the effects of fabric anisotropy on the mechanical behaviour of sand, and especially on dilatancy, by means of the *dilatancy state parameter* $\zeta = e - e_d(p')$, which is a function of the fabric anisotropy variable A, described in Chapter 3. The dilatancy state parameter, ζ, is the difference between the current void ratio, e, of sand and the void ratio at the image point located on the moving *dilatancy state line* at the current mean effective stress, $e_d(p')$. The susceptibility of sands to flow liquefaction increases when ζ increases. A characteristic example of dependence on the dilatancy state parameter ζ is that sand of a given void ratio, consolidated to a given mean effective stress, may dilate when loaded with the σ_1-axis being normal to the bedding plane, while it may contract and liquefy when loaded with the σ_1-axis being parallel to the bedding plane.

The dependence of dilatancy on the state of sand was modelled by Manzari and Dafalias (1997) and Li and Dafalias (2000). On the other hand, Dafalias and Manzari (2004) took into consideration the effects of the evolution of fabric anisotropy on dilatancy and modelled successfully the behaviour of sand upon reversing the loading direction beyond the phase-transformation point (Ishihara et al. 1975). Microscopic studies have shown that drastic changes in fabric anisotropy occur past the phase-transformation point (Nemat-Nasser 1980, Nemat-Nasser and Tobita 1982, Oda et al. 1985, Rothenburg and Bathurst 1989, Yimsiri and Soga 2010). By considering these fabric changes the liquefaction behaviour of sands under cyclic undrained loading, manifested as repetitive excursions of the effective stress path through the origin of the q - p' plane (i.e. the *initial liquefaction* described by Seed and Lee, 1966), can be modelled successfully. The repetition of the mechanism of loss and regain of strength under undrained (isochoric) conditions, associated with cyclic stresses and strains, is the behaviour of medium-dense to dense sand termed *cyclic mobility* (Kramer 1996; Figure 4.38). Dafalias and Manzari (2004) suggested that “a fabric is generated, demised, and regenerated in each cycle” of this loading process, while this periodic destruction and regeneration of microstructure has been verified in microscopic studies (Huang et al. 2018).

Figure 4.83 shows the results of the undrained triaxial compression tests on Toyoura Sand, performed by Verdugo and Ishihara (1996), together with the results of the simulations of these tests, performed by Dafalias and Manzari (2004). Two fundamental aspects of the liquefaction behaviour of sand are successfully reproduced in the simulations. First, the behaviour of sand with void ratio e = 0.833 is found to change gradually from highly dilative to highly contractive, when the initial mean effective stress, p'_i, changes from 100 kPa to 3000 kPa. Thus, flow deformation may or may not occur depending on the initial state of sand. The simulative ability of the constitutive model, which uses a unique set of model parameters, is spectacular since the agreement with the experimental data is very satisfactory over the wide range of p'_i. This ability is attributed to the incorporation of a state-dependent dilatancy function into the critical-state compatible constitutive model. The second characteristic of the liquefaction behaviour that is reproduced successfully in the simulations concerns the response of sand to the reversal of the loading direction beyond the phase transformation point, which corresponds to an immediate switch from plastic dilation to plastic contraction. From a Plasticity Theory standpoint, loading is imposed due to kinematic hardening even though the deviatoric stress and stress ratio decrease. Figure 4.83 shows that the simulations of the undrained response of sand to reverse loading reproduce well the experimental results. Dafalias and Manzari (2004) suggested that the simulation of the sand’s response to reverse loading is the key to the successful simulation of the sand’s response to cyclic loading and highlighted the importance of the evolving fabric anisotropy in the modelling of such behaviour.

Figure 4.84 shows the results of cyclic undrained triaxial tests on Toyoura Sand, performed by Ishihara et al. (1975), together with the results of the simulations of these tests, performed by Dafalias and Manzari (2004). The well-known excursions of the effective stress path through the origin of the stress space, and the associated “butterfly stress-path orbits” that are characteristic of cyclic mobility, are shown to occur in the simulations when the deviatoric stress is unloaded, while the sand is undergoing plastic dilation, and reloaded in the opposite direction. However, the agreement with the experimental data is not as satisfactory as in the case of monotonic loading. Dafalias and Manzari (2004) suggested that this may be due to the fact that the cyclic loading tests were performed 20 years before the monotonic, using different experimental techniques and instrumentation.

Najma and Latifi (2017) used the constitutive model of Dafalias and Manzari (2004) in order to derive an analytical flow-liquefaction criterion for fully contractive sands. They expressed the stress ratio at the onset of flow as a function of the model parameters, state parameter and void ratio, and introduced the flow liquefaction line and flow liquefaction surface in the q - p' and q - p' - e space, respectively. These loci comprise the analytically predicted extremum (peak) points of the effective stress path, satisfying the condition dq / dp' = 0. Figure 4.85 shows the results of monotonic undrained triaxial compression tests on Toyoura Sand, performed by Ishihara (1993), together with the results of the simulations of these tests, performed by Najma and Latifi (2017). The flow liquefaction line is also shown. It can be seen that the simulation curves fit well the experimental data, with the states at which flow deformation is triggered being predicted accurately. Moreover, it is shown that the flow liquefaction line curves when the mean effective stress increases considerably and does not go through the point indicating the contractive steady state (as suggested by Sladen et al. 1985, Lade 1992) or through the origin of the stress space (as suggested by Vaid and Chern 1983 and Lade 1993).

Najma and Latifi (2017) also investigated whether the flow liquefaction line can be used to predict the onset of flow observed in drained constant-q tests on saturated and dry sands, performed by Sassitharan et al. (1993) and Skopek et al. (1994), respectively. They found that the structural collapse of very loose sand was predicted successfully since the experimental point of collapse triggering is located on the analytically-derived flow liquefaction line. Najma and Latifi (2017) performed, additionally, simulations of cyclic undrained triaxial tests on Toyoura Sand and found that the stress states at the onset of flow (i.e. the states at which the strength suddenly decreases towards the steady state residual level) are located on the analytically-derived flow liquefaction line. Figure 4.86 shows the results of a drained constant-q test on saturated Ottawa Sand together with the results of the simulation of this test, while Fig. 4.87 shows the simulation results of cyclic undrained triaxial tests on Toyoura Sand. Apparently, the Dafalias and Manzari (2004) model can predict the states at which the mechanism of flow deformation is triggered, for a variety of loading conditions, even though the model was not developed for this particular purpose.

Andrade et al. (2013) derived "a general liquefaction flow instability criterion for elastoplastic soils based on the concept of loss of uniqueness". They highlighted that the triggering of flow instability is a function of the state of soil and not a material property. In their approach, the loss of uniqueness of the incremental constitutive response flags the onset of flow liquefaction instability; the proposed criterion is closely related to the concepts of vanishing of the second-order work (Hill 1958, Vardoulakis and Sulem 1995, Darve et al. 1995a) and of loss of controllability (Nova 1994). Andrade et al. (2013) showed that when their criterion was adapted to the model of Dafalias and Manzari (2004), a critical value of the hardening modulus that is associated with the loss of uniqueness could be determined in a closed analytical form. This means that when the hardening modulus H, which evolves as the state of soil changes, becomes equal to the critical hardening modulus H_L, which is also an evolving parameter, then the uniqueness is lost, and instability occurs in the form of flow liquefaction.

Figure 4.88a shows the results of undrained triaxial compression tests on Toyoura Sand with e = 0.833, performed by Verdugo and Ishihara (1996), at effective consolidation stress varying from 100 kPa to 3000 kPa. The star symbols mark the states of peak strength at which flow instability is triggered in properly controlled tests. The line passing through these states is the experimentally defined instability line. Figure 4.88b shows the simulations of Verdugo-Ishihara tests, performed by Andrade et al. (2013) using the model of Dafalias and Manzari (2004). The points of flow-liquefaction triggering, and the corresponding instability line, were determined in the simulations by monitoring the evolution of the difference of the hardening modulus from the critical hardening modulus: when the difference H - H_L vanishes, flow liquefaction is deemed to occur. Figure 4.89 shows the evolution of the difference H - H_L during the simulations and the predicted points of flow-liquefaction triggering. It can be seen that both the model of Dafalias and Manzari (2004) and the flow-liquefaction criterion of Andrade et al. (2013) can predict the onset of flow and make the distinction between the response of sand denser and looser than critical: flow liquefaction is triggered only when the initial mean effective stress is equal to or higher than 2000 kPa when the void ratio of Toyoura Sand is e = 0.833.

It has been shown so far that the critical-state compatible constitutive models proposed by Dafalias and his colleagues can simulate successfully both the monotonic and cyclic undrained behaviour of sands, for a wide range of initial combinations of void ratio and mean effective stress, using a unique set of model constants. The models can simulate both the behaviour of contractive and dilative sands and predict whether flow instability is triggered or not (in a properly controlled loading programme), depending on the value of the state parameter. Li and Dafalias (2004) developed a constitutive framework for simulating the response of inherently anisotropic sands to *non-proportional loading* and predicted successfully the onset of flow liquefaction in such cases. It is noted that the multiaxial loading, in which the deviatoric stress components change proportionally and the stress principal axes remain fixed with respect to the fabric principal axes, is termed *proportional loading*; otherwise, the loading is termed *non-proportional*. The proportional loading paths are radial in both deviatoric planes, i.e. in the octahedral plane and the Y_s - X_s plane (where $Y_s = 2\tau_{z\theta}$ and $X_s = \sigma_{zz} - \sigma_{\theta\theta}$), though in the latter case the value of b should be also kept constant. Two interesting cases of non-proportional loading are associated with the circular stress paths centred at the origin of these planes (Miura et al. 1986, Lanier 1988, Wang et al. 1990).

Lanier (1988) performed loading tests on dry sand in the true triaxial apparatus along circular stress paths in the octahedral plane. In these tests the mean effective stress, p', and deviatoric stress, q, were kept constant, while the direction of shearing changed continuously. From a theoretical point of view, the first invariant of the stress tensor, I_1, and the second invariant of the deviatoric stress tensor, J_2, were kept constant, while the Lode angle changed continuously; note that the Lode angle is a function of the second, J_2, and third, J_3, invariant of the deviatoric stress tensor. Lanier (1988) reported that dense sand contracts on the failure surface when the stress state moves on a circular stress path with sufficiently large radius, centred at the origin of the octahedral plane, and highlighted the risk of liquefaction for dense sands subjected to complex loading. On the other hand, Miura et al. (1986) subjected dense sand specimens to drained rotation of the stress principal axes at constant stress principal values in the hollow cylinder apparatus. In these tests the stress state remains stationary in both the q - p' space and principal stress space (since the quantities q, p', I_1, J_2 and J_3 are kept constant). Plastic contraction was accumulated gradually even after the completion of seven cycles of principal stress rotation, despite the high value of the relative density of sand and the condition of constant q and η. These results indicate that sand may liquefy under constant q if the stress principal axes rotate under undrained conditions. The experimental results presented by Nakata et al. (1998) and Yang et al. (2007) verified this suggestion.

Li and Dafalias (2004) simulated the response of sand to undrained rotation of the stress principal axes at constant q observed in the tests of Nakata et al. (1998). In their critical-state compatible model the dilatancy is considered to depend both on state and inherent fabric anisotropy and three different plastic loading mechanisms are taken into account. The first mechanism is associated with plastic strains induced by the increase in stress ratio, $\eta = q / p'$, while the second mechanism is associated with plastic strains induced by the increase in q and p' under constant η. The third mechanism, termed the *rotational shear mechanism* (Wang et al. 1990), is introduced to account for the plastic deformation induced by non-proportional loading. Nevertheless, in the tests of Nakata et al. (1998), the stress ratio η increases during principal stress rotation, as a result of the induced plastic contraction, thus the effects of the first and third loading mechanisms are, in fact, coupled. Figure 4.90 shows the results of the tests of Nakata et al. (1998) and of the simulations of Li and Dafalias (2004). It can be seen that the model simulates successfully the accumulation of plastic contraction and the onset of flow liquefaction (see also Figs 4.55 to 4.59).

Li and Dafalias (2012) introduced the Anisotropic Critical State Theory (ACST), as a revision of the classical Critical State Theory (CST) of Roscoe et al. (1958) and Schofield and Wroth (1968) in order to account for the fabric anisotropy effects on the dilatancy and critical state of soils. The basic principles of the ACST have been discussed in Chapter 3. Here, the results of the simulations of Li and Dafalias (2012) are presented, using a model that was developed within the framework of ACST. The monotonic undrained loading tests performed by Yoshimine et al. (1998) were simulated using this model. The results of the physical tests and simulations of these tests are shown in Figs 4.90 and 4.91. The model simulates successfully the differences in the dilatancy behaviour of sand when the principal stress direction angle, α, and intermediate principal stress parameter, b, change, while the potentially unstable flow deformation is reproduced numerically whenever observed in the physical tests. Moreover, new models developed recently within the framework of ACST address the issue of sand's response to stress reversal and principal stress rotation, accounting for the effects of fabric anisotropy evolution and non-coaxiality on the dilatancy and other mechanical characteristics (Papadimitriou et al. 2019, Petalas et al. 2019).

4.7 SUMMARY

Flow deformation of loose sands is a liquefaction phenomenon exhibited as a strength drop accompanied by accumulation of unidirectional shear strain. The strength decreases to a minimum level after a transient-peak state as a result of the buildup of excess pore-water pressure. The mobilised minimum undrained strength is lower than the initial static equilibrium stress and depends on the void ratio, initial mean effective stress and mode of loading, as well as on the direction of the stress principal axes with respect to the fabric principal axes. Flow deformation can be triggered under monotonic, cyclic or even constant-q undrained loading, yet, the development of shear strain is unidirectional and the stress ratio increases monotonically, rendering this behaviour different than the so-called undrained cyclic mobility (liquefaction) of dense sands. Interestingly, dense dilating sands subjected to monotonic drained loading may also undergo flow deformation, if the loading is imposed along certain incremental strain directions in the strain space.

It has been suggested in the literature that flow deformation of sands is triggered under cyclic undrained loading or undrained loading involving rotation of the stress principal axes when the effective stress path crosses a fixed surface in the stress space, which is determined by means of monotonic undrained loading tests. Various flow surfaces have been proposed by different researchers such as the line connecting the origin of the q - p' plane with the state of transient-peak strength, or the post-peak regime of the effective stress path of the monotonic undrained loading test. Some researchers suggest that the stress ratio at the triggering of flow is practically unique for loose sand, irrespective of the consolidation and undrained loading history, and depends only on the principal stress direction angle, α, and the intermediate principal stress parameter, b, at the onset of flow. Other researchers suggest that the stress ratio at the triggering of flow depends also on the consolidation stress ratio, the static shear stress with respect to the cyclic shear stress and the void ratio variation of loose sand.

Flow deformation of sands is a potentially unstable behaviour since the strength drops to a level lower than that required for static equilibrium, thus, the response becomes dynamic under load-controlled conditions. For this reason flow instability has been investigated within the framework of Stability and Bifurcation Theory. Recent studies show that due to the non-associative characteristics of sands flow instability and other diffuse instabilities may occur inside the failure surface. Specifically, there exists a large domain in the stress space, called the bifurcation domain, which is bounded by the failure surface at the upper limit and the bifurcation surface at the lower limit and contains all the potentially unstable stress states. A given stress - strain state reached after a given stress - strain history is reputed to be potentially unstable if the second-order work, d^2W, becomes non-positive at this state along one or more incremental stress directions; however, the exposure of instability requires additionally that the control parameters are proper.

Given the fact that d^2W is a directional scalar quantity that depends on the previous stress - strain history, while the non-positive sign of this quantity is the necessary condition for instability, it is obvious that, from a theoretical standpoint, the flow instability criterion should take into consideration the stress - strain history and the incremental stress direction. The present study sets these theoretical considerations as a starting point for challenging the established belief that the crossing of a fixed surface in the stress space, determined by means of monotonic undrained loading tests, flags the triggering of flow of sand subjected to undrained loading, irrespective of the previous stress - strain history.

The liquefaction behaviour of sands has been traditionally investigated within the framework of Critical State Theory (CST) introduced by Roscoe et al. (1958) and Schofield and Wroth (1968). One of the key aspects of the CST is the reference to the ultimate material state (critical state) by means of a state parameter for describing and modelling the mechanical behaviour of soils. Whether sand is susceptible to flow liquefaction or not depends on its state. Been and Jefferies (1985) proposed the state parameter $\psi = e - e_c(p')$ for sands which is the difference between the current void ratio, e, and the void ratio at critical state at the current mean effective stress, $e_c(p')$. The susceptibility of sands to flow liquefaction increases when ψ increases. A characteristic example of state dependence is that sand of a given void ratio may dilate at low effective consolidation stress, while it may contract and liquefy at high effective consolidation stress.

On the other hand, Li and Dafalias (2012) introduced the Anisotropic Critical State Theory (ACST) which takes into consideration the effects of fabric anisotropy on the mechanical behaviour of sand, and especially on dilatancy, by means of the dilatancy state parameter $\zeta = e - e_d(p')$, which is a function of the fabric anisotropy variable A. The dilatancy state parameter, ζ, is the difference between the current void ratio, e, of sand and the void ratio at the image point located on the moving dilatancy state line at the current mean effective stress, $e_d(p')$. The susceptibility of sands to flow liquefaction increases when ζ increases. A characteristic example of dependence on the dilatancy state parameter ζ is that sand of a given void ratio, consolidated to a given mean effective stress, may dilate when loaded with the σ_1-axis being normal to the bedding plane, while it may contract and liquefy when loaded with the σ_1-axis being parallel to the bedding plane. The constitutive models developed recently within the framework of ACST describe efficiently the flow liquefaction behaviour of sands, capturing both the effects of state and fabric anisotropy, as well as the effects of stress reversal and principal stress rotation.

4.8 BIBLIOGRAPHY

Alarcon-Guzman A, Leonards GA, Chameau JL (1988) Undrained monotonic and cyclic strength of sands. Journal of Geotechnical Engineering, Vol. 114, No.10, pp. 1089-1109

Anderson SA, Riemer MF (1995) Collapse of saturated soil due to reduction in confinement. Journal of Geotechnical Engineering, Vol. 121, No.2, 216-220

Andrade JE, Ramos AM, Lizcano A (2013) Criterion for flow liquefaction instability. Acta Geotechnica (2013) 8: 525-535

Arthur JRF, Chua KS, Dunstan T (1979) Dense sand weakened by continuous principal stress direction rotation. Géotechnique 29 (1), 91-96

Arthur JRF, Chua KS, Dunstan T, Rodriquez del C JI (1980) Principal stress rotation: a missing parameter. Proc. ASCE, Vol. 106, GT4, pp. 419-433

Arthur JRF, Bekenstein S, Germaine JT, Ladd CC (1981) Stress path tests with controlled rotation of principal stress directions. Laboratory Shear Strength of Soil, ASTM, STP 740, pp. 516-540

Been K, Jefferies MG (1985) A state parameter for sands. Géotechnique 35 (2), 99–112

Been K, Jefferies MG, Hachey J (1991) The critical state of sands. Géotechnique 41 (3), 365–381

Bigoni D (2000) Bifurcation and instability of non-associative elastoplastic solids. Material Instabilities in Elastic and Plastic Solids, H. Petryk (Ed.), CISM Courses and Lectures No. 414, pp. 1-52, 2000 Springer-Verlag, Wien New York, ISBN 3-211-83328-5

Bigoni D (2012) Nonlinear solid mechanics. Bifurcation theory and material instability. Cambridge University Press (2012)

Bishop AW (1971) Shear strength parameters for undisturbed and remolded soil specimens. Roscoe Memorial Symp., 3-58

Bjerrum L (1973) Problems of soil mechanics and construction on soft clays and structurally unstable soils (collapsible, expansive and others): state-of-the-art report. Proc. 8th Int. Conf. Soil Mech. Found. Engng, Moscow 3, 109-159

Broms BB, Casbarian AO (1965) Effects of rotation of the principal stress axes and of the intermediate principal stresses on the shear strength. Proc. 6th International Conference on Soil Mechanics and Foundation Engineering, Vol. 1, pp. 18-23

Casagrande A (1936) Characteristics of cohesionless soils affecting the stability of slopes and earthfills. Journal of the Boston Society of Civil Engineering, January, 13-32

Casagrande A, Watson JD (1938) Compaction tests and critical density investigations of cohesionless materials for Franklin Falls Dam, Merrimack Valley flood control. Corps of Engineers, U.S. Army Engineering Office, p. BII-7

Casagrande A (1975) Liquefaction and cyclic deformation of sands: a critical review. Fifth Panamerican Conference on Soil Mechanics and Foundation Engineering, Buenos Aires, Argentina, November 1975

Castro G (1969) Liquefaction of sands. Harvard Soil Mechanics Series No. 81, Harvard University, Cambridge, Mass

Chu J, Lo S-CR, Lee IK (1992) Strain-softening behavior of granular soil in strain-path testing. Journal of Geotechnical Engineering, Vo. 118, No. 2, pp. 191-208

Chu J, Lo S-CR, Lee IK (1993) Instability of granular soils under strain path testing. Journal of Geotechnical Engineering, Vo. 119, No. 5, pp. 874-892

Chu J, Leong WK (2001) Pre-failure strain softening and pre-failure instability of sand: a comparative study. Géotechnique 51 (4), 311–321

Chu J, Leroueil S, Leong WK (2003) Unstable behaviour of sand and its implication for slope instability. Canadian Geotechnical Journal, 40: 873-885

Cornforth DH (1964) Some experiments on the influence of strain conditions on the strength of sand. Géotechnique 14, 143–167

Dafalias YF, Manzari MT (2004) A simple plasticity sand model accounting for fabric change effects. J. Eng. Mech., 130(6), 622-634

Daouadji A, Darve F, Al Gali H, Hicher PY, Laouafa F, Lignon S, Nicot F, Nova R, Pinheiro M, Prunier F, Sibille L, Wan R (2011) Diffuse failure in geomaterials: Experiments, theory and modelling. Int. J. Numer. Anal. Meth. Geomech. (2011), 35(16), 1731-1773

Darve F, Flavigny M, Meghachou M (1995a) Constitutive modelling and instabilities of soil behaviour. Computers and Geotechnics 17 (1995), 203-224

Darve F, Flavigny M, Meghachou M (1995b) Yield surfaces and principal of superposition: revisit through incrementally non-linear constitutive relations. International Journal of Plasticity, Vol. 11, No. 8, pp. 927-948, 1995

Darve F, Laouafa F (2000): Instabilities in granular materials and application to landslides. Mech. Cohes-Frict. Mater., 2000; 5:627-652

Darve F, Servant G, Laouafa F, Khoa HDV (2004) Failure in geomaterials: continuous and discrete analysis. Comput. Methods Appl. Mech. Engrg. 193 (2004), 3057-3085

Desrues J, Lanier J, Stutz P (1985) Localization of the deformation in tests on sand sample. Engineering Fracture Mechanics, Vol. 21, No. 4, pp. 909-921

Desrues J, Chambon R, Mokni M, Mazerolle F (1996) Void ratio inside shear bands in triaxial sand specimens studied by computed tomography. Géotechnique 46 (3), 529-546

Desrues J, Georgopoulos I-O (2006) An investigation of diffuse failure modes in undrained triaxial tests on loose sand. Soils and Foundations, Vol.46, No.5, 585-594

Desrues J, Viggiani G (2004) Strain localization in sand: an overview of the experimental results obtained in Grenoble using stereophotogrammetry. International Journal for Numerical and Analytical Methods in Geomechanics, 2004, 28: 279-321

Drescher A, Vardoulakis I (1982) Geometric softening in triaxial tests on granular materials. Géotechnique 32 (4), 291-303

Duncan JM (1996) State of the art: limit equilibrium and finite element analysis of slopes. Journal of Geotechnical Engineering 1996; 122 (7): 577-596

Eckersley D (1990) Instrumented laboratory flowslides. Géotechnique 40 (3), 489–502

Finno RJ, Harris WW, Mooney MA, Viggiani G (1996) Strain localization and undrained steady state of sand. J. Geotech. Engrg., ASCE, 122(6), 462-473

Fu P, Dafalias YF (2011) Fabric evolution within shear bands of granular materials and its relation to critical state theory. International Journal for Numerical and Analytical Methods in Geomechanics, 2011, 35: 1918-1948

Gens A (1985) A state boundary surface for soils not obeying Rendulic's principle. Proc. of 11th Int. Conf. on SMFE, San Francisco, 2, 473-476

Georgiannou VN, Hight DW, Burland JB (1991) Behaviour of clayey sands under undrained cyclic triaxial loading. Géotechnique 41 (3), 383–393

Georgiannou VN, Tsomokos A, Stavrou K (2008) Monotonic and cyclic behaviour of sand under torsional loading. Géotechnique 58 (2), 113–124

Georgiannou VN (2011) Behavioural patterns of fine sands. Geotech. Eng. J. SEAGS AGSSEA 42 (4), 25–41

Georgiannou VN, Konstadinou M (2014) Torsional shear behavior of anisotropically consolidated sands. J. Geotech. Geoenviron. Eng., ASCE 140 (2), ISSN: 1090-0241/04013017(14)

Georgiannou VN, Konstadinou M, Triantafyllos PK (2018) Sand behavior under stress states involving principal stress rotation. Journal of Geotechnical and Geoenvironmental Engineering, 2018, 144(6): 04018028

Goldscheider M (1975) Dilatanzverhalten von sand bei geknickten verformungswegen. Mech. Res. Com., 2, 143-188

Gudehus G (1979) A comparison for some constitutive laws for soils under radially symmetric loading and unloading. Third Int. Conf. on Num. Meth. In Geomechanics, Ed. Wittke, Balkema Publ. (1979) 1309-1323

Gutierrez M, Ishihara K, Towhata I (1991) Flow theory for sand during rotation of principal stress direction. Soils and Foundations, Vol.31, No.4, pp. 121-132

Gutierrez M, Ishihara K, Towhata I (1993) Model for the deformation of sand during rotation of principal stress directions. Soils and Foundations, Vol.33, No.3, pp. 105-117

Gutierrez M, Vardoulakis I (2007) Energy dissipation and post-bifurcation behaviour of granular soils. International Journal for Numerical and Analytical Methods in Geomechanics, 31:435-455

Hanzawa H (1980) Undrained strength and stability analysis for a quick sand. Soils and Foundations, Vol.20, No.2, 17-29

Hettler A, Vardoulakis I (1984) Behaviour of dry sand tested in a large triaxial apparatus. Géotechnique 34 (2), 183-198

Hight DW (1983) Laboratory investigations of sea-bed clays, PhD Thesis, University of London (Imperial College of Science and Technology)

Hight DW, Gens A, Symes MJ (1983) The development of a new hollow cylinder apparatus for investigating the effects of principal stress rotation in soils. Géotechnique 33, No. 4, 355-383

Hill R (1958) A general theory of uniqueness and stability in elastic-plastic solids. Journal of the Mechanics and Physics of Solids (1958); 6:239-249

Huang X, Kwok CY, Hanley KJ, Zhang Z (2018?) DEM analysis of the onset of flow deformation of sands: linking monotonic and cyclic undrained behaviours. Acta Geotechnica ?

Hyodo M, Tanimizu H, Yasufuku N, Murata H (1994) Undrained cyclic and monotonic triaxial behaviour of saturated loose sand. Soils and Foundations, Vol.34, No.1, 19-32

Ikeda K, Yamakawa Y, Desrues J, Murota K (2008) Bifurcations to diversify geometrical patterns of shear bands on granular materials. Physical Review Letters 2008, 100:198001

Ishihara K, Li S-I (1972) Liquefaction of saturated sand in triaxial torsion shear test. Soils and Foundations, Vol.12, No.2, 19-39

Ishihara K, Tatsuoka F, Yasuda S (1975) Undrained deformation and liquefaction of sand under cyclic stresses. Soils and Foundations, Vol.15, No.1, 29-44

Ishihara K (1983) Soil response in cyclic loading induced by earthquakes, traffic and waves. Proc. 7th Asian Regional Conf. on Soil Mechanics and Foundation Engineering, Vol. 2, pp. 42-66

Ishihara K, Towhata I (1983) Sand response to cyclic rotation of principal stress directions as induced by wave loads. Soils and Foundations, Vol.23, No.4, 11-26

Ishihara K, Verdugo R, Acacio AA (1991) Characterization of cyclic behavior of sand and post-seismic stability analysis. In: The Asian regional conference on soil mechanics and foundation engineering, Bangkok, Thailand

Ishihara K (1993) Liquefaction and flow failure during earthquake. Géotechnique, Vol. 43, No. 3, pp.351-415

Jefferies M, Been K (2006) Soil liquefaction. A critical state approach. CRC Press, Taylor and Francis Group, 1st Edition

Kato S, Ishihara K, Towhata I (2001) Undrained shear characteristics of saturated sand under anisotropic consolidation. Soils and Foundations, Vol.41, No.1, pp. 1-11

Konrad J-M (1990a) Minimum undrained strengths of two sands. Journal of Geotechnical Engineering, Vol. 116, No. 6, 932-947

Konrad J-M (1990b) Minimum undrained strength versus steady-state strength of sands. Journal of Geotechnical Engineering, Vol. 116, No. 6, 948-963

Konrad J-M (1993) Undrained response of loosely compacted sands during monotonic and cyclic compression tests. Géotechnique 43, No. 1, 69-89

Konstantinou M, Georgiannou VN (2013) Cyclic behaviour of loose anisotropically consolidated Ottawa sand under undrained torsional loading. Géotechnique 63, No. 13, 1144-1158

Konstantinou M, Georgiannou VN (2014) Prediction of pore water pressure generation leading to liquefaction under torsional cyclic loading. Soils and Foundations, Vol.54, No.5, 993-1005

Kramer SL (1996) Geotechnical Earthquake Engineering. Prentice Hall, New Jersey

Lade PV, Nelson RB, Ito YM (1987) Nonassociated flow and stability of granular materials. Journal of Engineering Mechanics, Vol. 113, No. 9, 1302-1318

Lade PV, Nelson RB, Ito YM (1988) Instability of granular materials with nonassociated flow. Journal of Engineering Mechanics, Vol. 114, No. 12, 2173-2191

Lade PV (1989) Experimental observations of stability, instability, and shear planes in granular materials. Ingenieur-Archiv 59 (1989), 114-123

Lade PV, Pradel D (1990a) Instability and plastic flow of soils. I: Experimental observations. Journal of Engineering Mechanics, Vol. 116, No. 11, pp. 2532-2550

Lade PV, Pradel D (1990b) Instability and plastic flow of soils. II: Analytical investigation. Journal of Engineering Mechanics, Vol. 116, No. 11, pp. 2551-2566

Lade PV (1992) Static instability and liquefaction of loose fine sandy slopes. Journal of Geotechnical Engineering, Vol.118, No.1, 51-71

Lade PV (1993) Initiation of static instability in the submarine Nerlerk berm. Canadian Geotechnical Journal 30: 895-904

Lade PV (1994) Creep effects on static and cyclic instability of granular soils. Journal of Geotechnical and Engineering, Vol.120, No.2, 404-419

Lade PV, Rodriguez NM, Van Dyck EJ (2014) Effects of principal stress directions on 3D failure conditions in cross-anisotropic sand. Journal of Geotechnical and Geoenvironmental Engineering, 2014, 140(2): 04013001

Lanier J (1988) Special stress paths along the limit surface of a sand specimen with a use of a true triaxial apparatus. Advanced Triaxial Testing of Soil and Rock, ASTM STP 977, R. T. Donaghe, R. C. Chaney, and M. L. Silver (Eds.), American Society for Testing and Materials, Philadelphia, 1988, pp. 859-869

Laouafa F, Darve F (2002) Modelling of slope failure by a material instability mechanism. Computers and Geotechnics 29 (2002) 301-325

Leong WK, Chu J (2002) Effect of undrained creep on instability behaviour of loose sand. Canadian Geotechnical Journal, 39: 1399-1405

Li XS (1997) Modeling of dilative shear failure. J. Geotech. Geoenviron. Eng., 123(7), 609-616

Li XS, Dafalias YF, Wang Z-L (1999) State-dependent dilatancy in critical constitutive modelling of sand. Can. Geotech. J. 36, 599-611

Li XS, Dafalias YF (2000) Dilatancy for cohesionless soils. Géotechnique 50, No. 4, 449-460

Li XS, Dafalias YF (2004) A constitutive framework for anisotropic sand including non-proportional loading. Géotechnique 54, No. 1, 41-55

Li XS, Dafalias YF (2012) Anisotropic critical state theory: role of fabric. Journal of Engineering Mechanics, Vol. 138, No. 3, 263-275

Lü X, Huang M, Qian J (2018) Influences of loading direction and intermediate principal stress ratio on the initiation of strain localization in cross-anisotropic sand. Acta Geotech., 13: 619-633, 2018

Lyapunov, AM (1907) Problème général de la stabilité des mouvements. Annales de la Faculté des Sciences de Toulouse 1907; 9:203–274.

Manzari MT, Dafalias YF (1997) A critical state two-surface plasticity model for sands. Géotechnique 47, No. 2, 255-272

Matsuoka H (1974) Stress-strain relationship of sands based on the mobilized plane. Soils and Foundations, Vol.14, No.2, pp. 47-61

Matsuoka H, Ishizaki H (1981) Deformation and strength of anisotropic soil. Proc., 10th ICSMFE, Stockholm, Vol. 1, pp. 699-702

Miura S, Toki S (1982) A sample preparation method and its effect on static and cyclic deformation-strength properties of sand. Soils and Foundations, Vol.22, No.1, 61-77

Miura K, Miura S, Toki S (1986) Deformation behavior of anisotropic dense sand under principal stress axes rotation. Soils and Foundations, Vol.26, No.1, 36-52

Mooney MA, Finno RJ, Viggiani GM (1998) A unique critical state for sand? J. Geotech. Geoenviron. Eng. 1998.124:1100-1108

Najma A, Latifi M (2017) Predicting flow liquefaction, a constitutive model approach. Acta Geotech. (2017), 12(4): 793-808

Nakata Y, Hyodo M, Murata H, Yasufuku N (1998) Flow deformation of sands subjected to principal stress rotation. Soils and Foundations, Vol.38, No.2, 115-128

Nemat-Nasser S (1980) On behavior of granular material in simple shear. Soils and Foundations, Vol.20, No.3, 59-73

Nemat-Nasser S, Tobita Y (1982) Influence of fabric on liquefaction and densification potential of cohesionless sand. Mechanics of Materials, 1, 43-62

Nicot F, Darve F, Dat Vu Khoa H (2007) Bifurcation and second-order work in geomaterials. Int. J. Numer. Anal. Meth. Geomech., 2007; 31:1007-1032

Nicot F, Darve F (2011) Diffuse and localized failure modes: Two competing mechanisms. International Journal for Numerical and Analytical Methods in Geomechanics, Vol. 35, 586-601

Nicot F, Challamel N, Lerbet J, Prunier F, Darve F (2011) Bifurcation and generalized mixed loading conditions in geomaterials. International Journal for Numerical and Analytical Methods in Geomechanics, Vol. 35, 1409-1431

Nicot F, Darve F (2015) Describing failure in geomaterials using the second-order work approach. Water Science and Engineering 2015, 8(2): 89-95

Nova R (1989) Liquefaction, stability, bifurcations of soil via strain-hardening plasticity. In Numerical Methods for the Localisation and Bifurcation of granular bodies; Proceedings of the International Workshops, Gdansk, Dembicki E., Gudehus G., Sikora Z. (eds). 1989; 117-132

Nova R (1994) Controllability of the incremental response of soil specimens subjected to arbitrary loading programmes. Journal of the Mechanical Behavior of Materials, 5(2):193-201

Oda M, Koishikawa I, Higuchi T (1978) Experimental study of anisotropic shear strength of sand by plane strain test. Soils and Foundations, Vol.18, No.1, 25-38

Oda M, Nemat-Nasser S, Konishi J (1985) Stress-induced anisotropy in granular masses. Soils and Foundations, Vol.25, No.3, 85-97

O'Sullivan C, Wadee MA, Hanley KJ, Barreto D (2013) Use of DEM and elastic stability analysis to explain the influence of the intermediate principal stress on shear strength. Géotechnique 63, No. 15, 1298-1309

Papadimitriou AG, Chaloulos YK, Dafalias YF (2019) A fabric-based sand plasticity model with reversal surfaces within anisotropic critical state theory. Acta Geotech., 14: 253-277, 2019

Petalas AL, Dafalias YF, Papadimitriou AG (2019) SANISAND-FN: An evolving fabric-based sand model accounting for stress principal axes rotation. Int. J. Numer. Anal. Methods Geomech., 2019; 43:97-123

Peacock WH, Seed HB (1968) Sand liquefaction under cyclic loading simple shear conditions. Journal of the Soil Mechanics and Foundations Division, 1968, Vol. 94, Issue 3, Pg. 689-708

Poulos SJ (1981) The steady state of deformation. Journal of the Geotechnical Engineering Division, ASCE, Vol. 107, pp. 553-562

Poulos SJ, Castro G, France JW (1985) Liquefaction evaluation procedure. Journal of Geotechnical Engineering, ASCE, Vol.111, No.6, pp. 772-792

Poulos SJ, Castro G, France JW (1988) Closure to discussion: Liquefaction evaluation procedure. Journal of Geotechnical Engineering, ASCE, Vol.114, No.2, pp. 251-259

Prunier F, Nicot F, Darve F, Laouafa F, Lignon S (2009) Three-dimensional multiscale bifurcation analysis of granular media. Journal of Engineering Mechanics, Vol. 135, No. 6, 493-509

Riemer MF, Seed RB (1997) Factors affecting apparent position of steady state line. Journal of Geotechnical and Geoenvironmental Engineering, Vol. 123 (3), pp. 281-288

Roscoe KH, Schofield AN, Wroth CP (1958) On the yielding of soils. Géotechnique 8 (1), 22–53

Roscoe KH, Burland JB (1968) On the generalized stress-strain behaviour of “wet” clay. In Engineering plasticity. Edited by J. Heyman and F.A. Leckie. Cambridge University Press, London, UK. pp.535-609

Rothenburg L, Bathurst RJ (1989) Analytical study of induced anisotropy in idealized granular materials. Géotechnique 39, No. 4, 601-614

Salvatore E, Mondoni G, Ando E, Albano M, Viggiani G (2017) Determination of the critical state of granular materials with triaxial tests. Soils Found. (2017), https://doi.org/10.1016/j.sandf.2017.08.005

Sasitharan S, Robertson PK, Sego DC, Morgenstern NR (1993) Collapse behavior of sand. Can. Geotech. J. 30, 569-577

Schofield AN, Wroth CP (1968) Critical state soil mechanics. McGraw-Hill, London

Seed HB, Lee KL (1966) Liquefaction of saturated sands during cyclic loading. J. Soil Mech. and Found. Div., ASCE, 92(6), 105-134

Shibuya S, Hight DW (1987) A bounding surface of granular materials. Soils and Foundations, Vol.27, No.4, 123-136

Shibuya S, Hight DW, Jardine RJ (2003a) Four-dimensional local boundary surfaces of an isotropically consolidated loose sand. Soils and Foundations, Vol.43, No.2, 89-103

Shibuya S, Hight DW, Jardine RJ (2003b) Local boundary surfaces of a loose sand dependent on consolidation path. Soils and Foundations, Vol.43, No.3, 85-93

Sibille L, Nicot F, Donzé FV, Darve F (2007) Material instability in granular assemblies from fundamentally different models. Int. J. Numer. Anal. Meth. Geomech., 2007; 31:457–481

Sibille L, Donzé F-V, Nicot F, Chareyre B, Darve F (2008) From bifurcation to failure in a granular material: a DEM analysis. Acta Geotechnica, 3:15-24

Sivathayalan S, Vaid YP (2002) Influence of generalized initial state and principal stress rotation on the undrained response of sands. Canadian Geotechnical Journal, 39 (1): 63 – 76

Sivathayalan S, Da Ha (2011) Effect of static shear stress on the cyclic resistance of sands in simple shear loading. Canadian Geotechnical Journal, 48: 1471 – 1484

Skopek P, Morgenstern NR, Robertson PK, Sego DC (1994) Collapse of dry sand. Can. Geotech. J., 31, 1008-1014 (1994)

Sladen JA, D'Hollander RD, Krahn J (1985) The liquefaction of sands, a collapse surface approach. Canadian Geotechnical Journal 22: 564-578

Symes MJ, Gens A, Hight DW (1984) Undrained anisotropy and principal stress rotation in saturated sand. Géotechnique 34, No. 1, 11-27

Symes MJ, Shibuya S, Hight DW, Gens A (1985) Liquefaction with principal stress rotation. Proc., 11th ICSMFE, Int. Conf. on Soil Mech. and Found. Engrg. (ICSMFE), San Francisco, Calif., Vol. 4

Tatsuoka F (1972) Fundamental study of deformation characteristics of sands using triaxial apparatus, Deng Thesis, University of Tokyo (in Japanese)

Tatsuoka F, Ishihara K (1973) Stress path and dilatancy performance of a sand. Proc. of 8th Int. Conf. on SMFE, Vol. 1, No. 2, pp. 419-424

Tatsuoka F, Sakamoto M, Kawamura T, Fukushima S (1986) Strength and deformation characteristics of sand in plane strain compression at extremely low pressures. Soils and Foundations, Vol.26, No.1, pp. 65-85

Tavenas F, Trak B, Leroueil S (1980) Remarks on the validity of stability analysis. Can. Geotech. J. 1980; 17: 61-73

Terzaghi K, Peck RB (1948) Soil mechanics in engineering practice. 2nd edn. Chichester: Wiley

Theocharis AI, Vairaktaris E, Dafalias YF, Papadimitriou AG (2017) Proof of incompleteness of Critical State Theory in granular mechanics and its remedy. Journal of Engineering Mechanics, Vol. 143 (2), 1-12

Theocharis AI, Vairaktaris E, Dafalias YF, Papadimitriou AG (2019) Necessary and sufficient conditions for reaching and maintaining critical state. International Journal for Numerical and Analytical Methods in Geomechanics, 43: 2041-2045

Tong Z, Zhang J, Yu Y, Ga Zhang (2010) Drained deformation behavior of anisotropic sands during cyclic rotation of principal stress axes. Journal of Geotechnical and Geoenvironmental Engineering, Vol. 136, No.11, pp. 1509-1518

Tong Z, Fu P, Dafalias YF, Yao Y (2014) Discrete element method analysis of non-coaxial flow under rotational shear. International Journal for Numerical and Analytical Methods in Geomechanics

Towhata I, Ishihara K (1985) Undrained strength of sand undergoing cyclic rotation of principal stress axes. Soils and Foundations, Vol.25, No.2, pp. 135-147

Uthayakumar M, Vaid YP (1998) Static liquefaction of sands under multiaxial loading. Canadian Geotechnical Journal 35, pp. 273-283

Vaid YP, Chern JC (1983) Effect of static shear on resistance to liquefaction. Soils and Foundations, Vol.23, No.1, pp. 47-60

Vaid YP, Chern JC (1985) Cyclic and monotonic undrained response of saturated sands. *In* Advances in the Art of Testing Soils Under Cyclic Loading Conditions, Proceedings of the ASCE Convention, Detroit, pp. 171–176

Vaid YP, Chung EKF, Kuebris RH (1990) Stress path and steady state. Canadian Geotechnical Journal 27, pp. 1-7

Vardoulakis I (1980) Shear band inclination and shear modulus of sand in biaxial tests. International Journal for Numerical and Analytical Methods in Geomechanics, 4: 103-119 (1980)

Vardoulakis I, Graf B (1982) Imperfection sensitivity of the biaxial test on dry sand. Proc. IUTAM Conf. Deformation and failure of granular materials, Delft, pp. 485-491, Rotterdam, Balkema

Vardoulakis I, Graf B (1985) Calibrations of constitutive models for granular materials using data from biaxial experiments. Géotechnique 35, No. 3, 299-317

Vardoulakis I (1986) Dynamic stability analysis of undrained simple shear on water-saturated granular soils. Int. J. Numer. Anal. Methods Geomech. 10 (1986) 177-190

Vardoulakis I, Sulem J (1995) Bifurcation analysis in geomechanics. Chapman and Hall, 1995

Vardoulakis I, Georgopoulos I-O (2005) The "stress-dilatancy" hypothesis revisited: shear-banding related instabilities. Soils and Foundations, Vol.45, No.2, pp. 61-76

Verdugo R, Ishihara K (1996) The steady state of sandy soils. Soils and Foundations, Vol.36, No.2, pp. 81-91

Wang Z-L, Dafalias YF, Shen C-K (1990) Bounding surface hypoplasticity model for sand. Journal of Engineering Mechanics, Vol. 116, No. 5, 983-10

Wroth CP, Basset RH (1965) A stress-strain relationship for the shearing behaviour of a sand. Géotechnique 15, No. 1, 32-56

Yang ZX, Li XS, Yang J (2007) Undrained anisotropy and rotational shear in granular soil. Géotechnique 57, No. 4, 371-384

Yamamuro JA, Lade P (1993) Effects of strain rate on instability of granular soils. Geotechnical Testing Journal, Vol.16, No.3, pp. 304-313

Yamamuro JA, Lade P (1998) Steady state concepts and static liquefaction of silty sands. Journal of Geotechnical and Geoenvironmental Engineering, Vol. 124 (9), pp. 868-877

Yamamuro JA, Covert KM (2001) Monotonic and cyclic liquefaction of very loose sands with high silt content. Journal of Geotechnical and Geoenvironmental Engineering, Vol. 127 (4), pp. 314-324

Yimsiri S, Soga K (2010) DEM analysis of soil fabric effects on behaviour of sand. Géotechnique 60, No. 6, 483-495

Yoshimine M, Ishihara K, Vargas W (1998) Effects of principal stress direction and intermediate principal stress on undrained shear behavior of sand. Soils and Foundations, Vol. 38, No. 3, 179-188

Yoshimine M, Ishihara K (1998) Flow potential of sand during liquefaction. Soils and Foundations, Vol. 38, No. 3, 189-198

Yoshimine M, Özay R, Sezen A, Ansal A (1999) Undrained plane strain shear tests on saturated sand using a hollow cylinder torsional shear apparatus. Soils and Foundations, Vol. 39, No. 2, 131-136

Zdravković L, Jardine RJ (2000) Undrained anisotropy of Ko-consolidated silt. Canadian Geotechnical Journal 37: 178-200

Zdravković L, Jardine RJ (2001) The effect on anisotropy of rotating the principal stress axes during consolidation. Géotechnique 51, No. 1, 69-83

Zdravković L, Potts DM, Hight DW (2002) The effect of strength anisotropy on the behaviour of embankments on soft ground. Géotechnique 52, No. 6, 447-457

Zhao J, Guo N (2013) Unique critical state characteristics in granular media considering fabric anisotropy. Géotechnique 63, No. 8, 695-704

Zhou W, Liu J, Ma G, Chang X (2017) Three-dimensional DEM investigation of critical state and dilatancy behaviors of granular materials. Acta Geotechnica (2017) 12:527-540

4.9 FIGURES

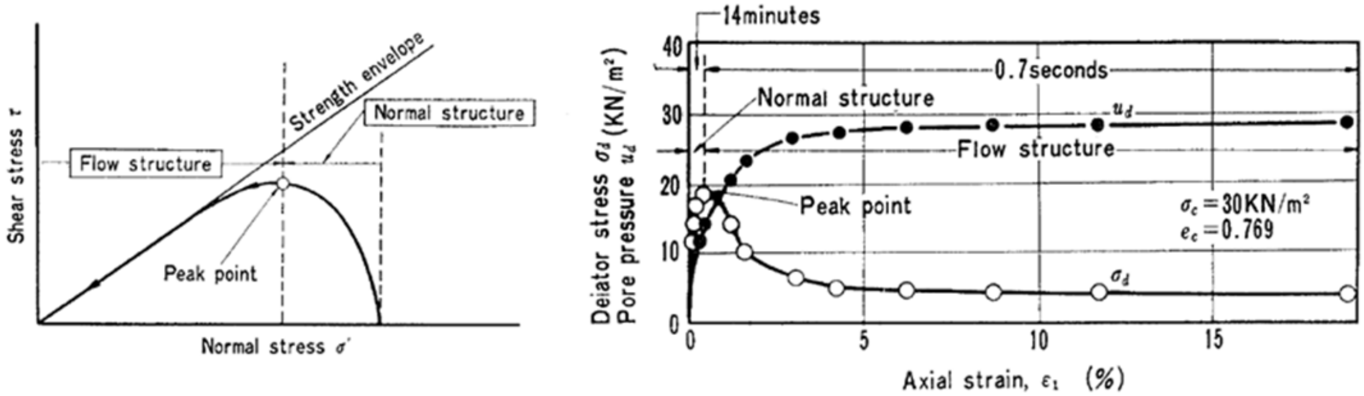

Fig. 4.1 Flow deformation of loose saturated sand subjected to monotonic stress-controlled undrained loading (data after Castro 1969; figure after Hanzawa 1980)

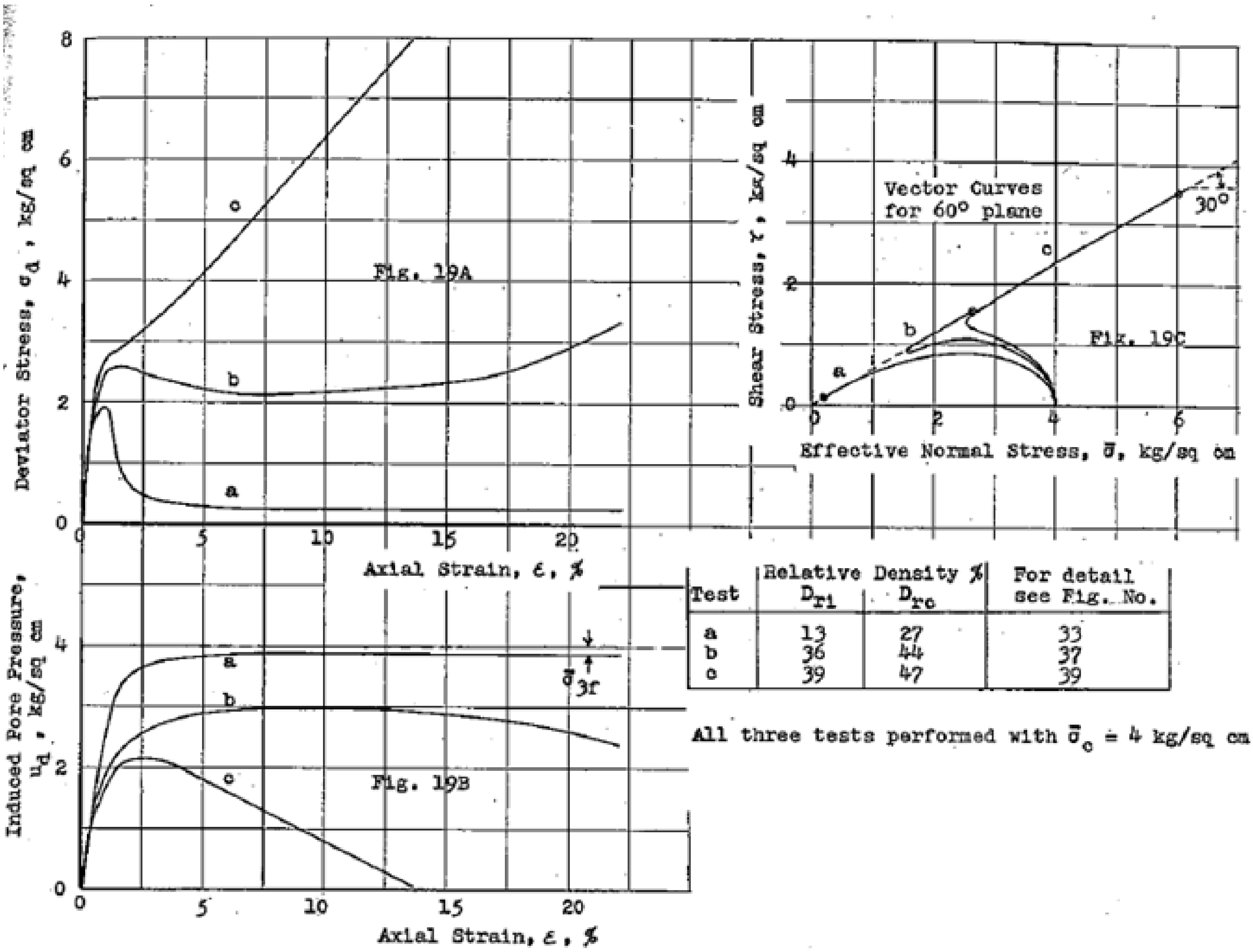

Test	Relative Density % D_{ri}	D_{rc}	For detail see Fig. No.
a	13	27	33
b	36	44	37
c	39	47	39

Fig. 4.2 Characteristic monotonic undrained behaviours of sand specimens consolidated isotropically to the same effective confining stress but having different relative density (after Castro 1969)

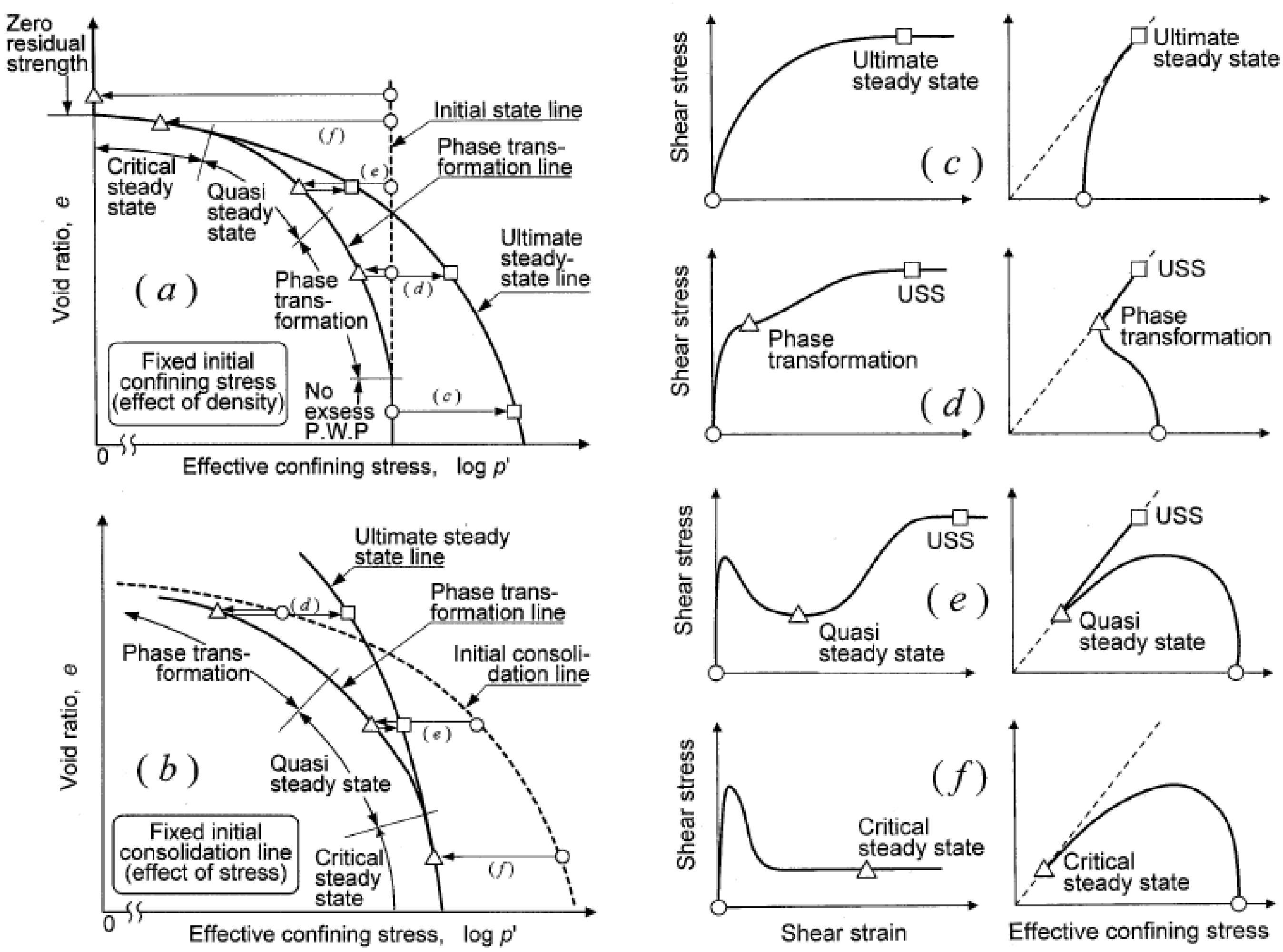

Fig. 4.3 Characteristic monotonic undrained behaviours of sand subjected to large deformation (after Yoshimine and Ishihara 1998)

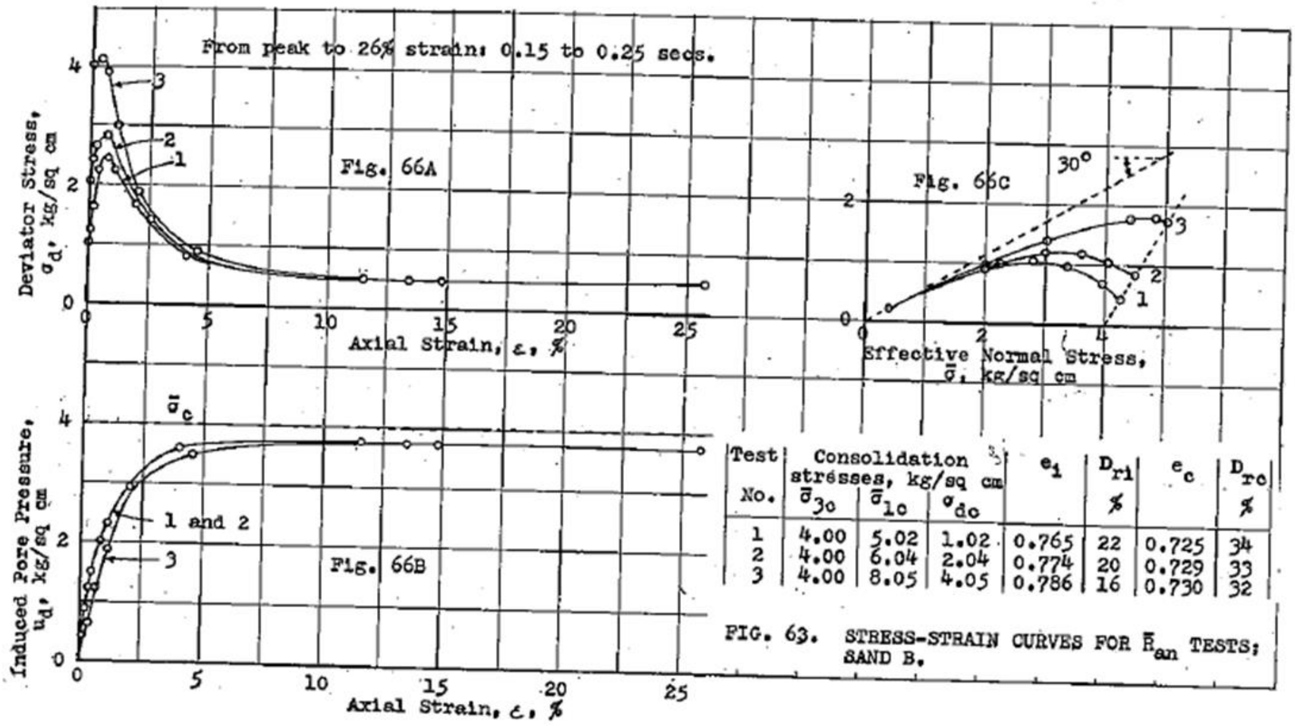

Test No.	Consolidation stresses, kg/sq cm $\bar{\sigma}_{3c}$	$\bar{\sigma}_{1c}$	σ_{dc}	e_i	D_{ri} %	e_c	D_{rc} %
1	4.00	5.02	1.02	0.765	22	0.725	34
2	4.00	6.04	2.04	0.774	20	0.729	33
3	4.00	8.05	4.05	0.786	16	0.730	32

Fig. 4.4 Flow deformation of anisotropically consolidated sand subjected to monotonic undrained loading (after Castro 1969)

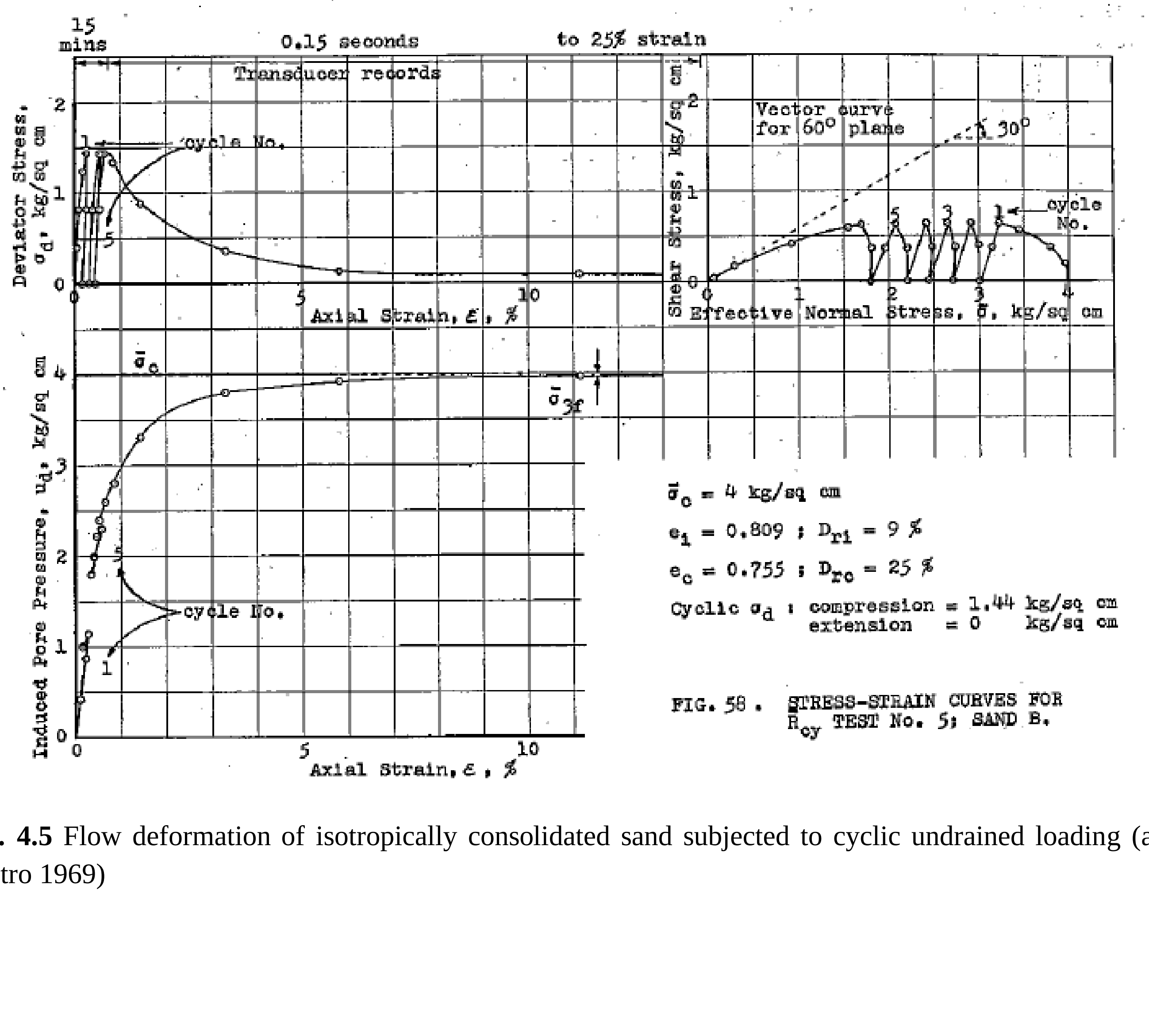

Fig. 4.5 Flow deformation of isotropically consolidated sand subjected to cyclic undrained loading (after Castro 1969)

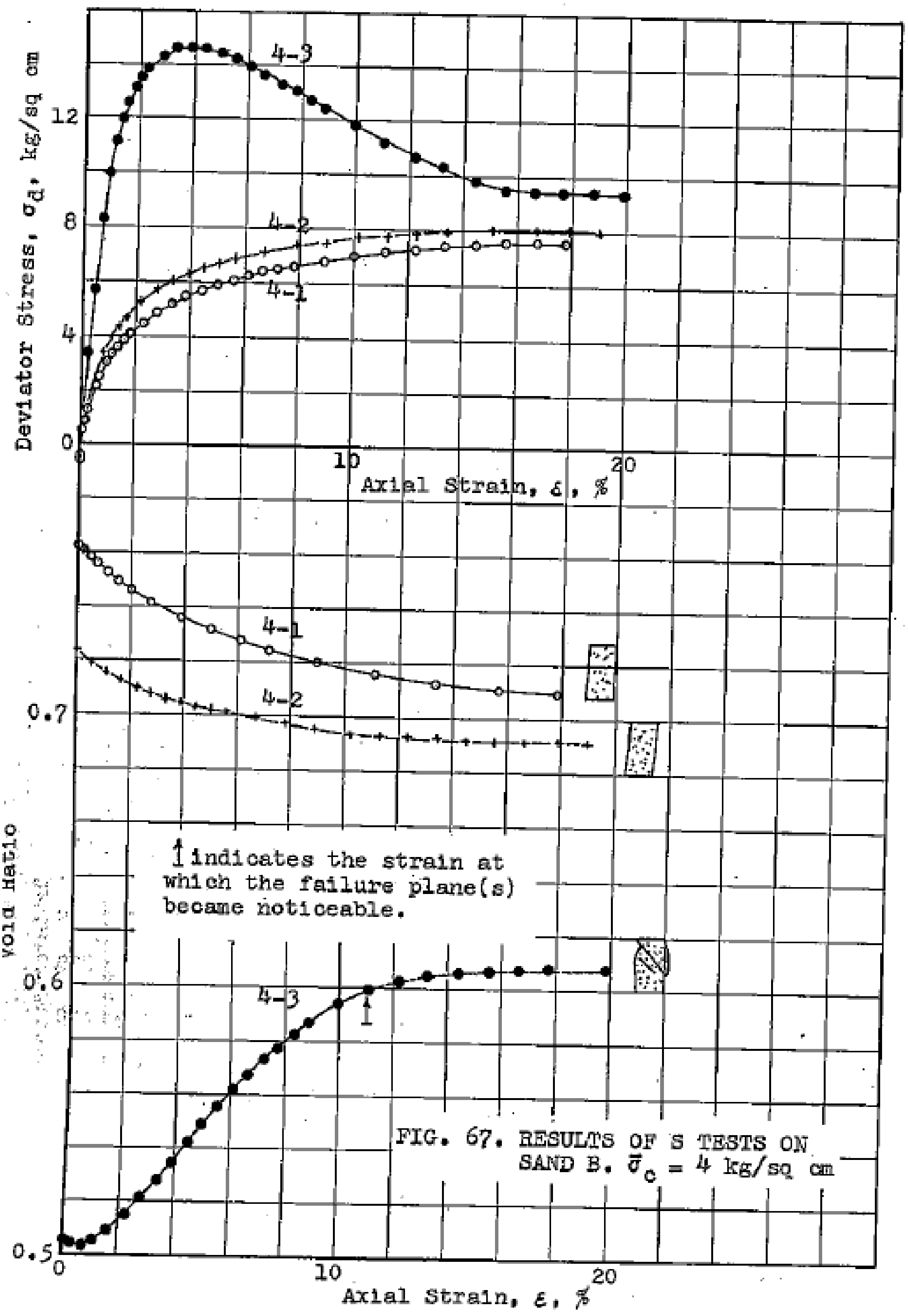

Fig. 4.6 Behaviour of isotropically consolidated sand subjected to monotonic drained loading under control of strain (after Castro 1969)

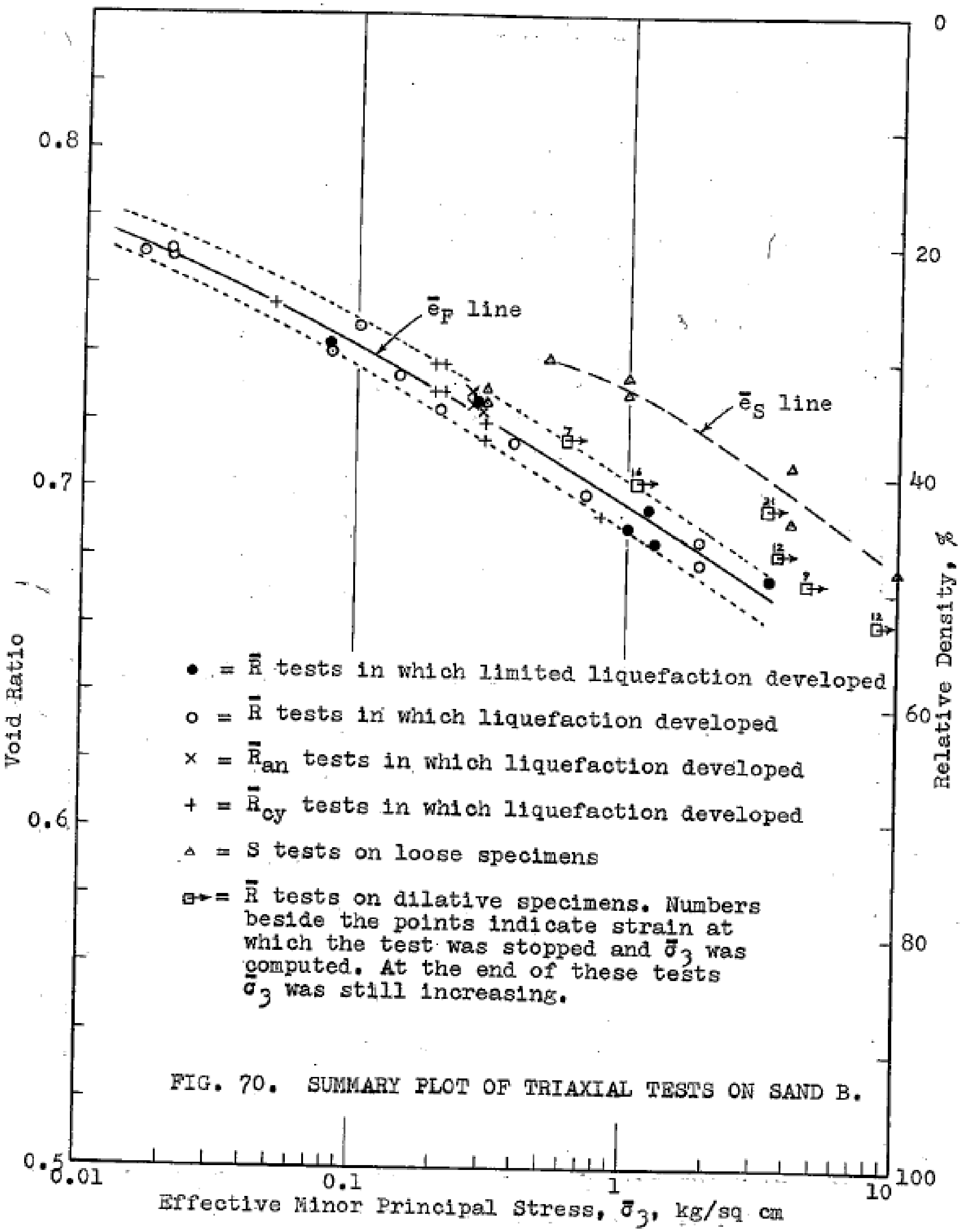

Fig. 4.7 Two different Critical Void Ratio lines determined by Castro for the same sand. Symbols: R-bar for monotonic undrained tests on isotropically consolidated (IC) specimens, Ran-bar for monotonic undrained tests on anisotropically consolidated (AC) specimens, Rcy-bar for cyclic undrained tests on IC specimens and S for monotonic drained tests on IC specimens (after Castro 1969)

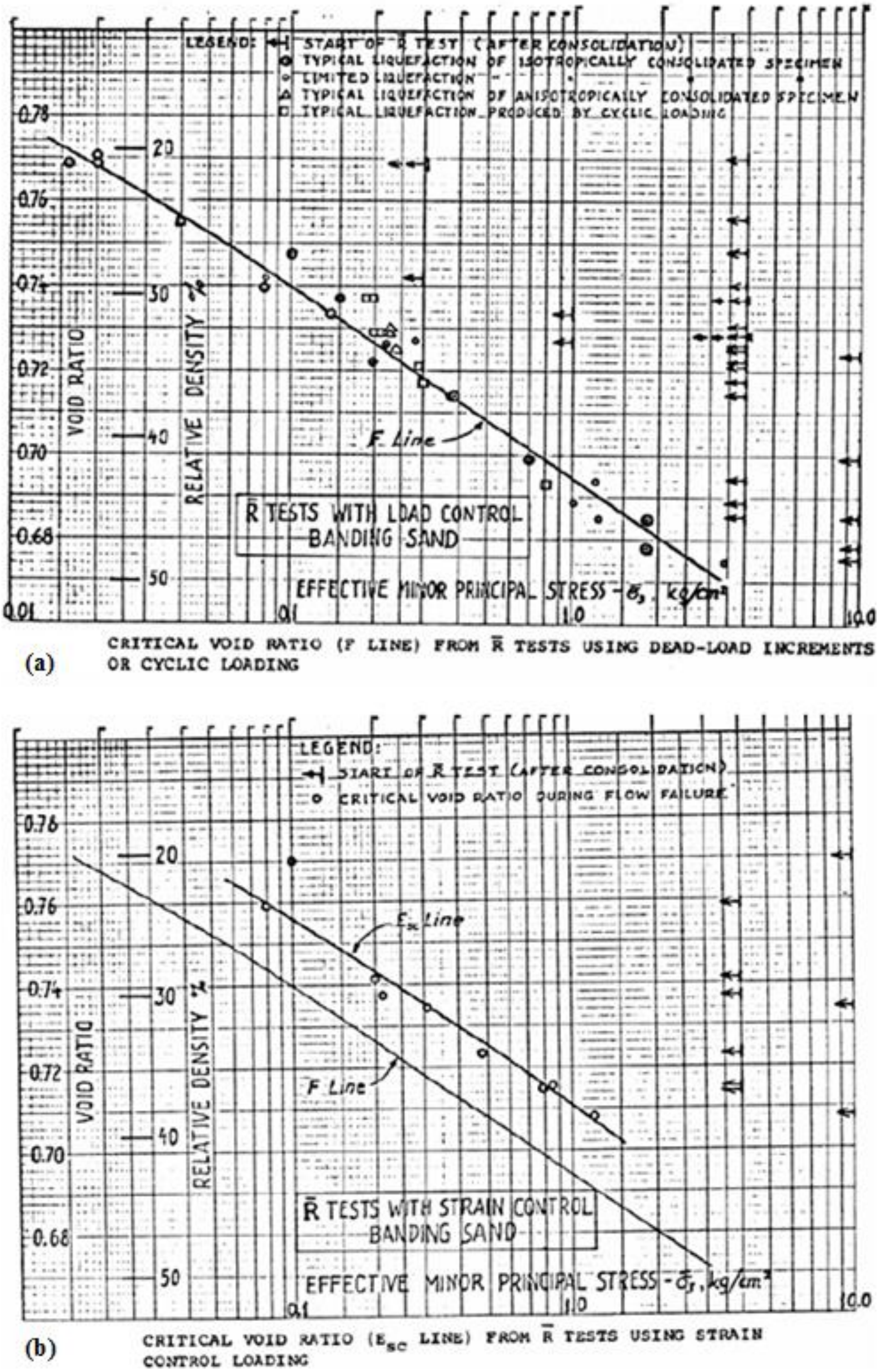

Fig. 4.8 Two different Critical Void Ratio lines determined by Castro for the same sand: **a** the F-Line determined by means of load-controlled undrained tests on loose sand and **b** the E_{sc}-Line determined by means of strain-controlled undrained tests on loose sand (data after Castro 1969; figure after Casagrande 1975)

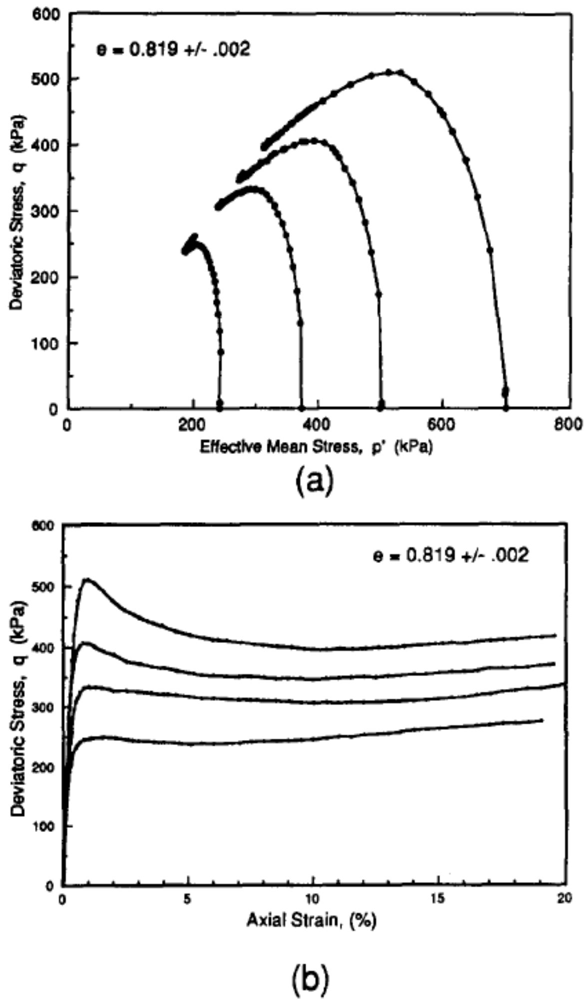

Fig. 4.9 a Effective stress paths and **b** stress - strain curves of monotonic undrained compression tests on specimens having the same void ratio but subjected to different effective confining stress after isotropic consolidation (after Riemer and Seed 1997)

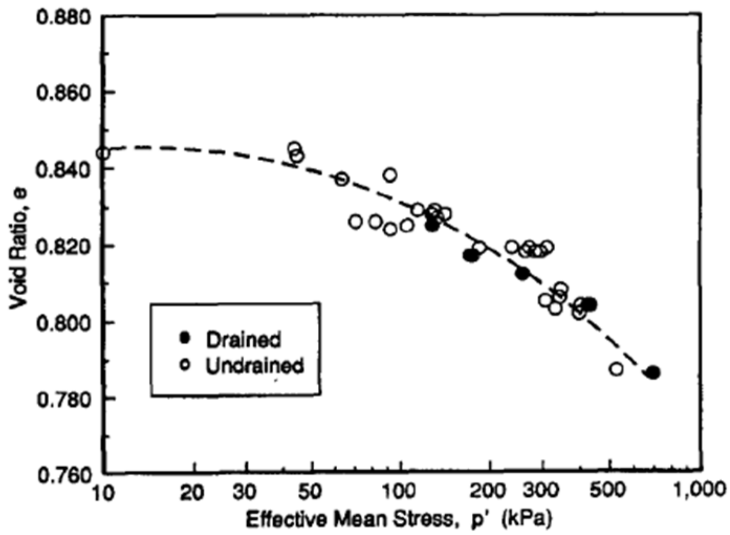

Fig. 4.10 Steady state line determined as the locus of the quasi-steady states observed in undrained compression tests and ultimate steady states observed in drained compression tests on loose specimens (after Riemer and Seed 1997)

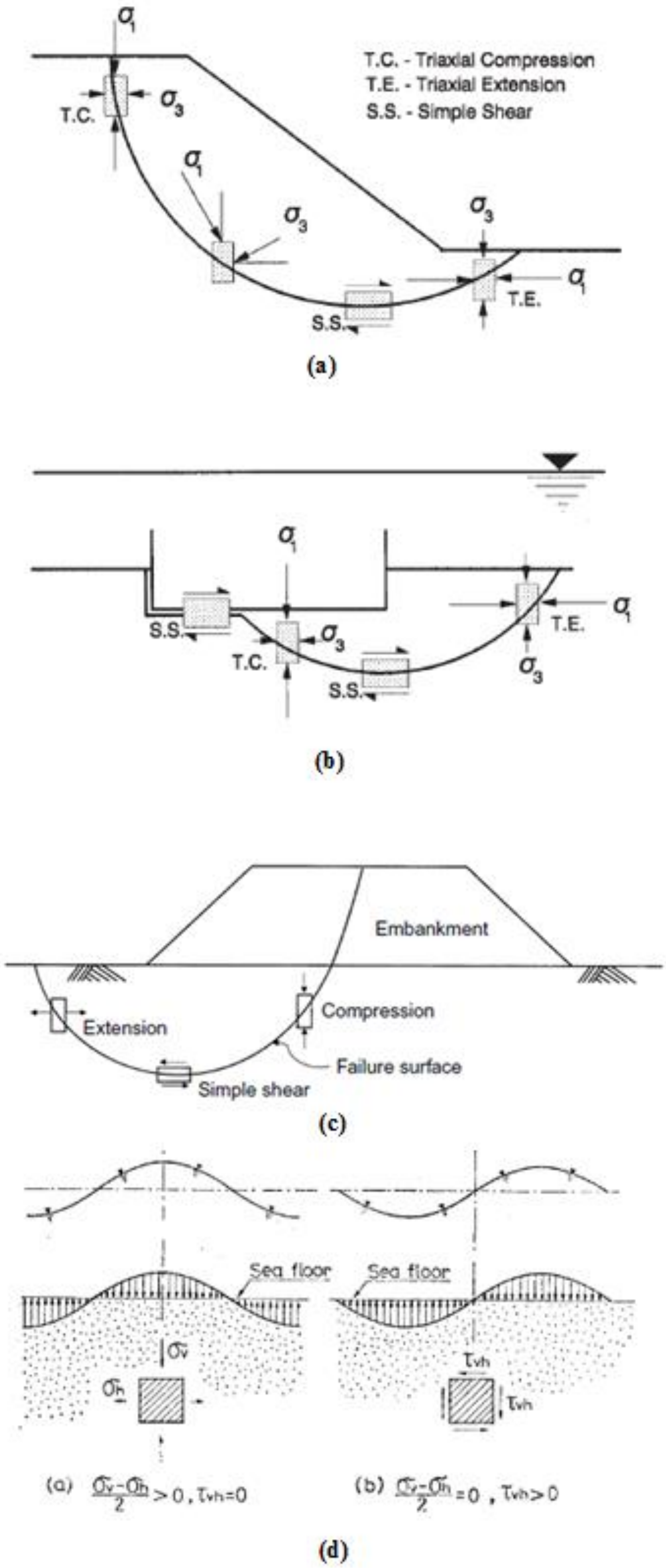

Fig. 4.11 Direction of the stress principal axes along a potential failure surface: **a** in sloping ground, **b** under the foundation of a structure and **c** under an embankment; **d** rotation of the stress principal axes in the soil elements of the seabed due to wave propagation (**a** and **b**: after Uthayakumar and Vaid 1998, **c**: after Bjerrum 1973 and Zdravkovic et al. 2002, **d**: after Ishihara and Towhata 1983)

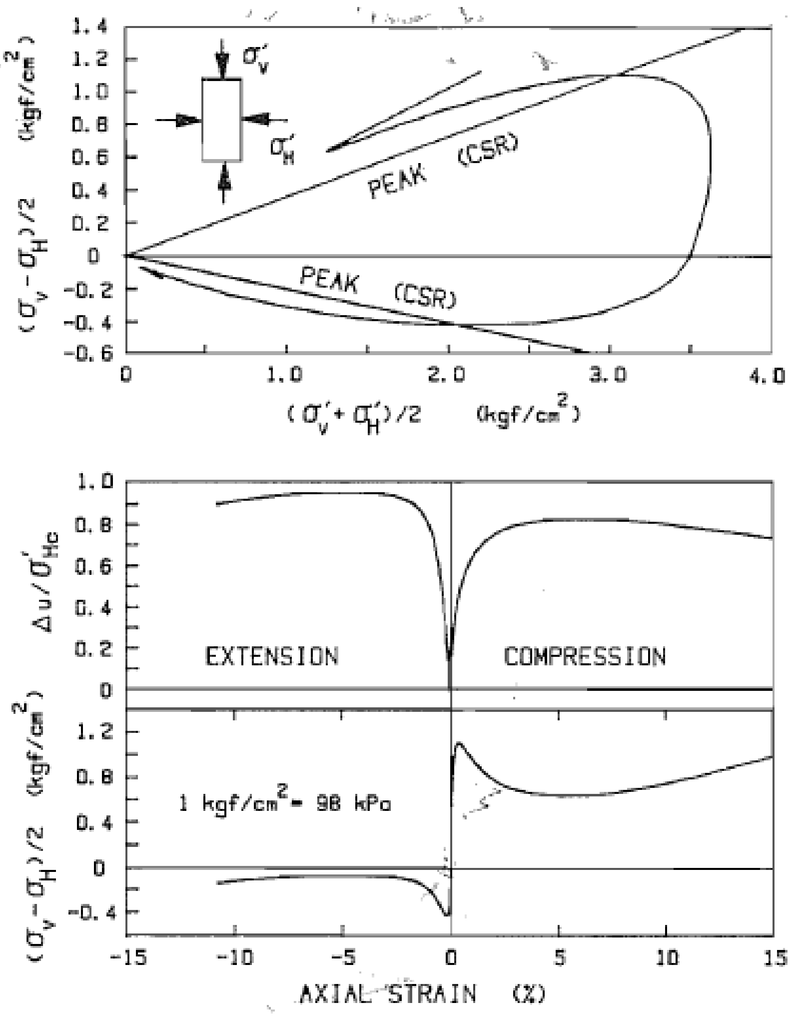

Fig. 4.12 Effective stress paths and evolution curves of shear stress and pore-water pressure with axial strain during triaxial compression and extension tests on specimens with identical initial states (after Vaid et al. 1990)

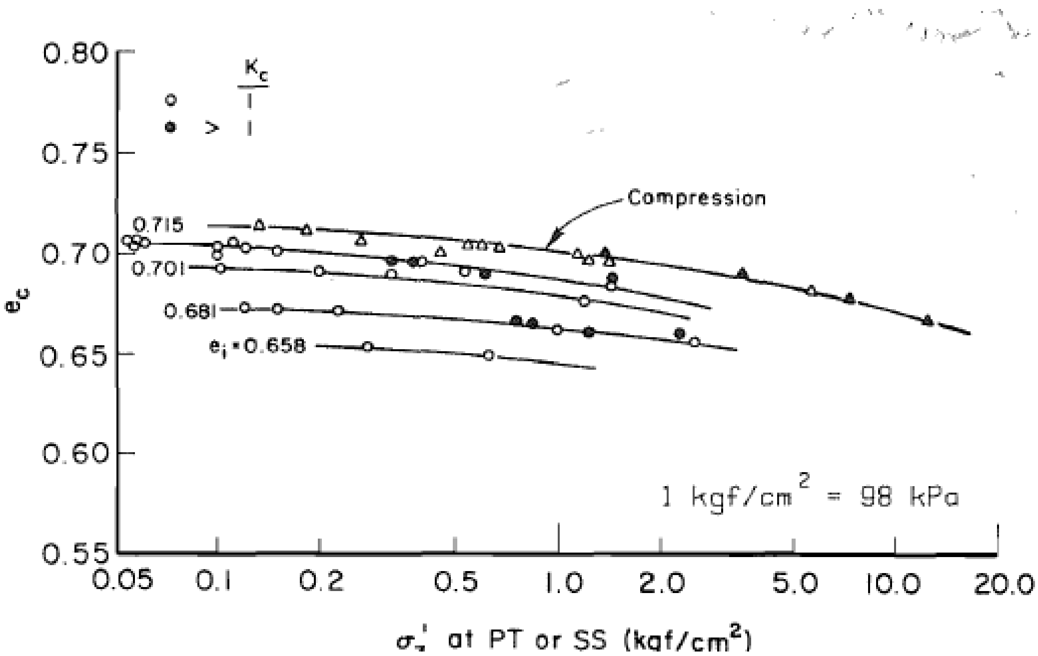

Fig. 4.13 Steady state lines of sand in triaxial compression and extension (after Vaid et al. 1990)

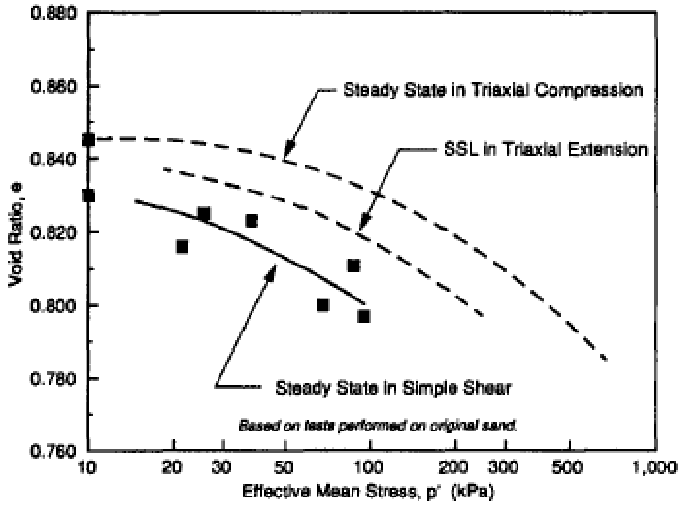

Fig. 4.14 Steady state lines of sand in triaxial compression, extension and simple shear (after Riemer and Seed 1997)

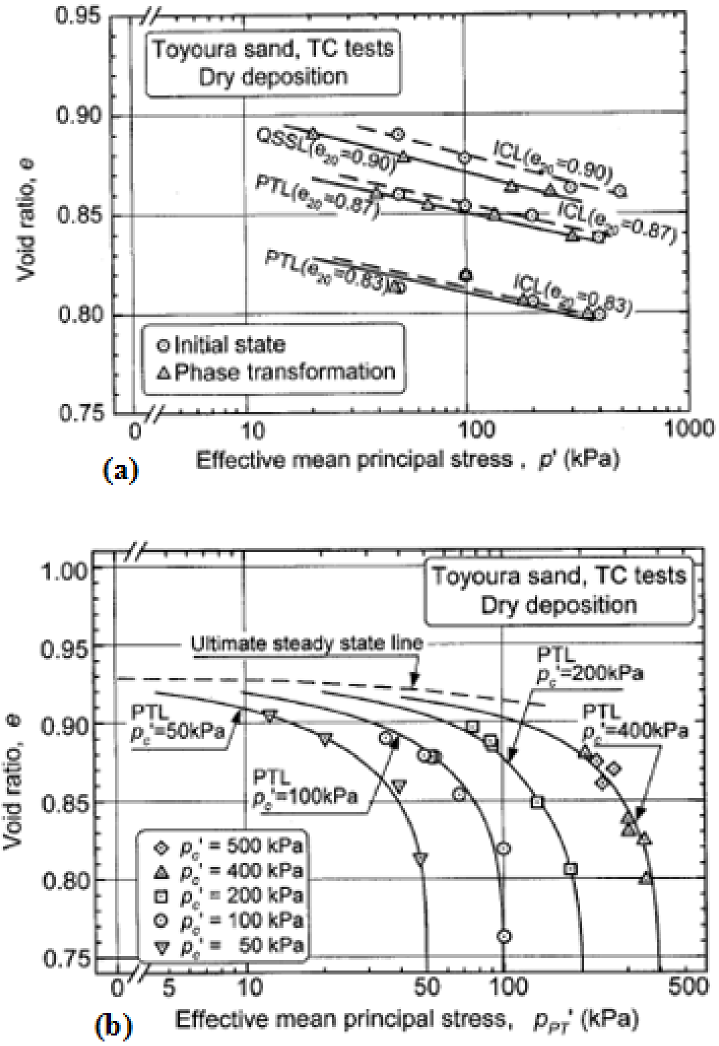

Fig. 4.15 Phase transformation lines and ultimate steady state line of sand in undrained triaxial compression. **a** Isotropic consolidation lines and phase transformation lines corresponding to different deposition void ratios e_{20}. **b** Phase transformation lines corresponding to different consolidation stresses p'_c and ultimate steady state line (after Yoshimine and Ishihara 1998)

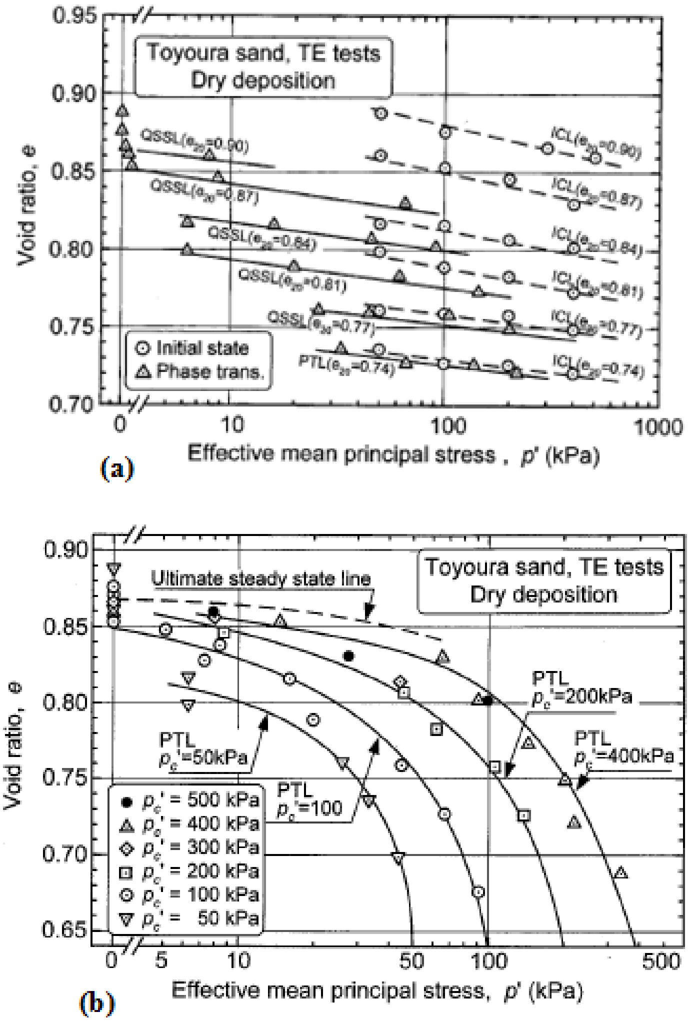

Fig. 4.16 Phase transformation lines and ultimate steady state line of sand in undrained triaxial extension. **a** Isotropic consolidation lines and phase transformation lines corresponding to different deposition void ratios e_{20}. **b** Phase transformation lines corresponding to different consolidation stresses p'_c and the assumed location of the ultimate steady state line (after Yoshimine and Ishihara 1998)

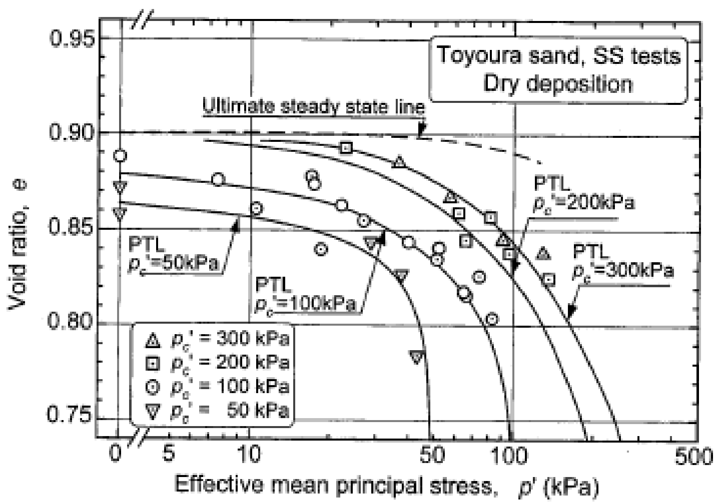

Fig. 4.17 Phase transformation lines and the assumed location of the ultimate steady state line of sand in undrained simple shear (after Yoshimine and Ishihara 1998)

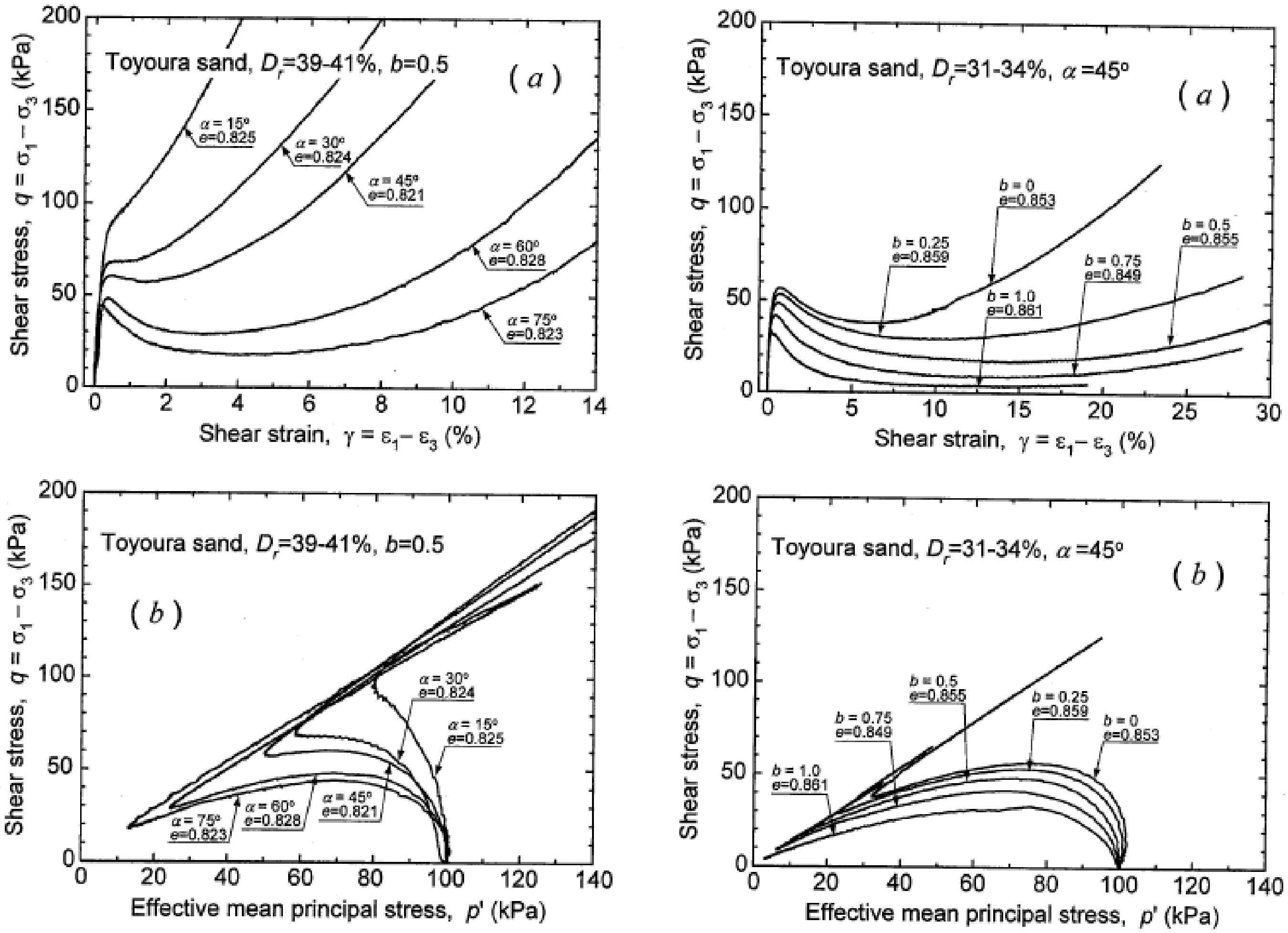

Fig. 4.18 Undrained behaviour of sand subjected to monotonic loading with constant values of α and b. Loading under the condition of b = 0.5 and different constant values of α: **a** stress - strain curves and **b** effective stress paths. Loading under the condition of α = 45° and different constant values of b: **a** stress - strain curves and **b** effective stress paths (after Yoshimine et al. 1998)

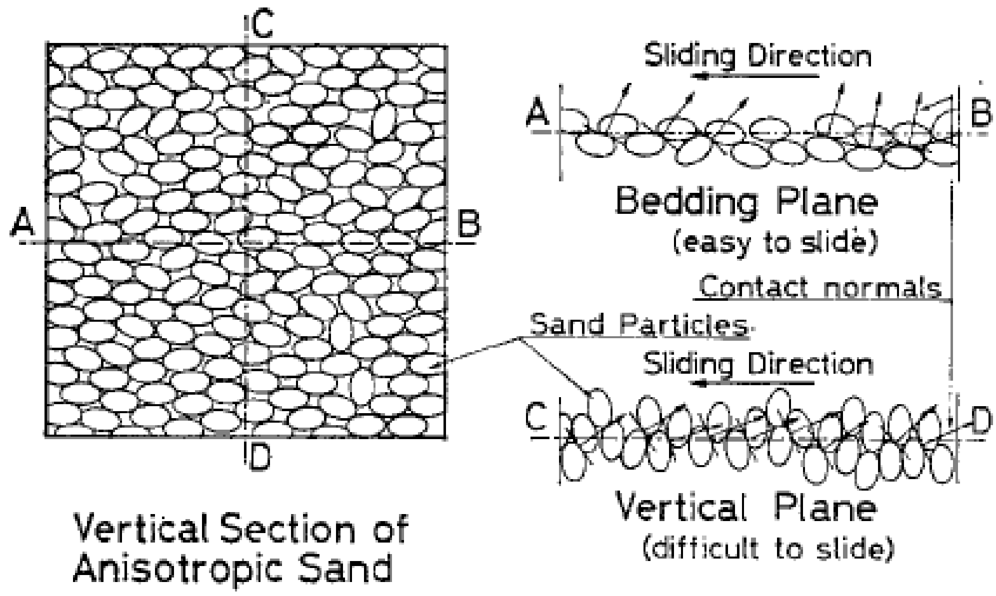

Fig. 4.19 Deformation mechanism of sliding on the horizontal bedding planes (after Miura et al. 1986)

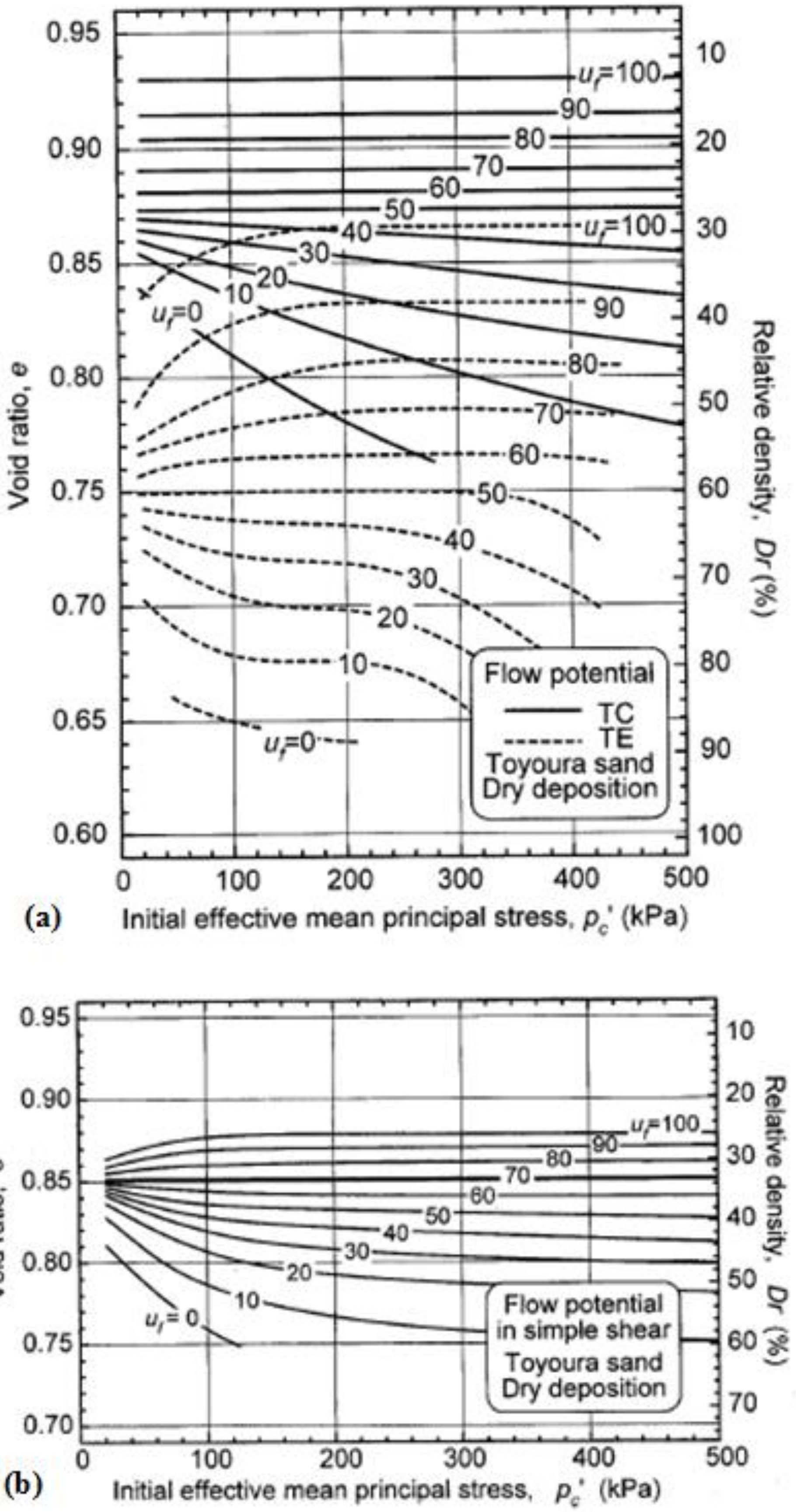

Fig. 4.20 Flow potential lines of dry deposited Toyoura sand in the state diagram: **a** in triaxial compression and extension and **b** in simple shear (after Yoshimine and Ishihara 1998)

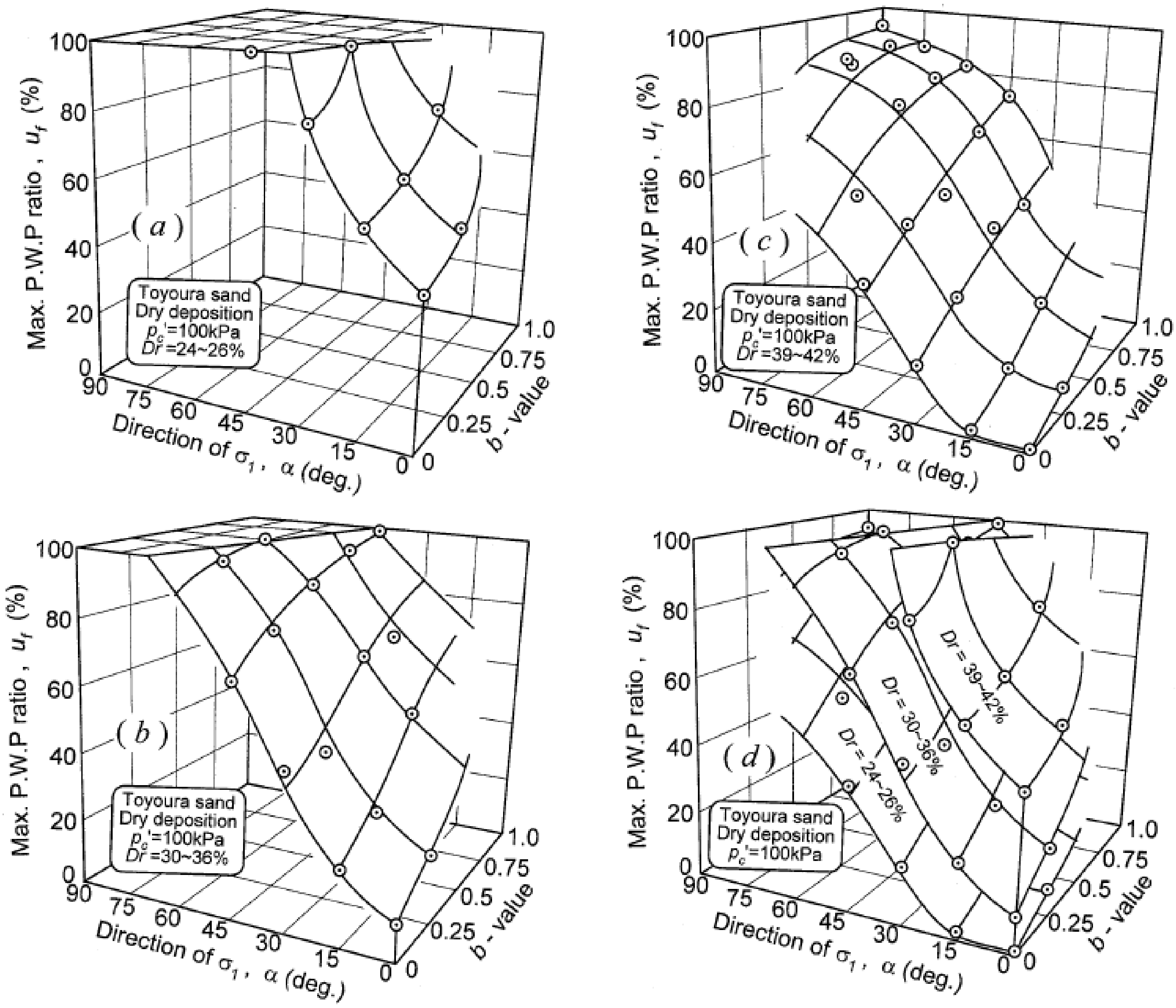

Fig. 4.21 Flow potential surfaces in the α - b - u_f space of dry deposited Toyoura sand at different initial states. It is noted that the relative density ranges in the bottom right figure are displayed by error in reverse order on the flow potential surfaces (after Yoshimine and Ishihara 1998)

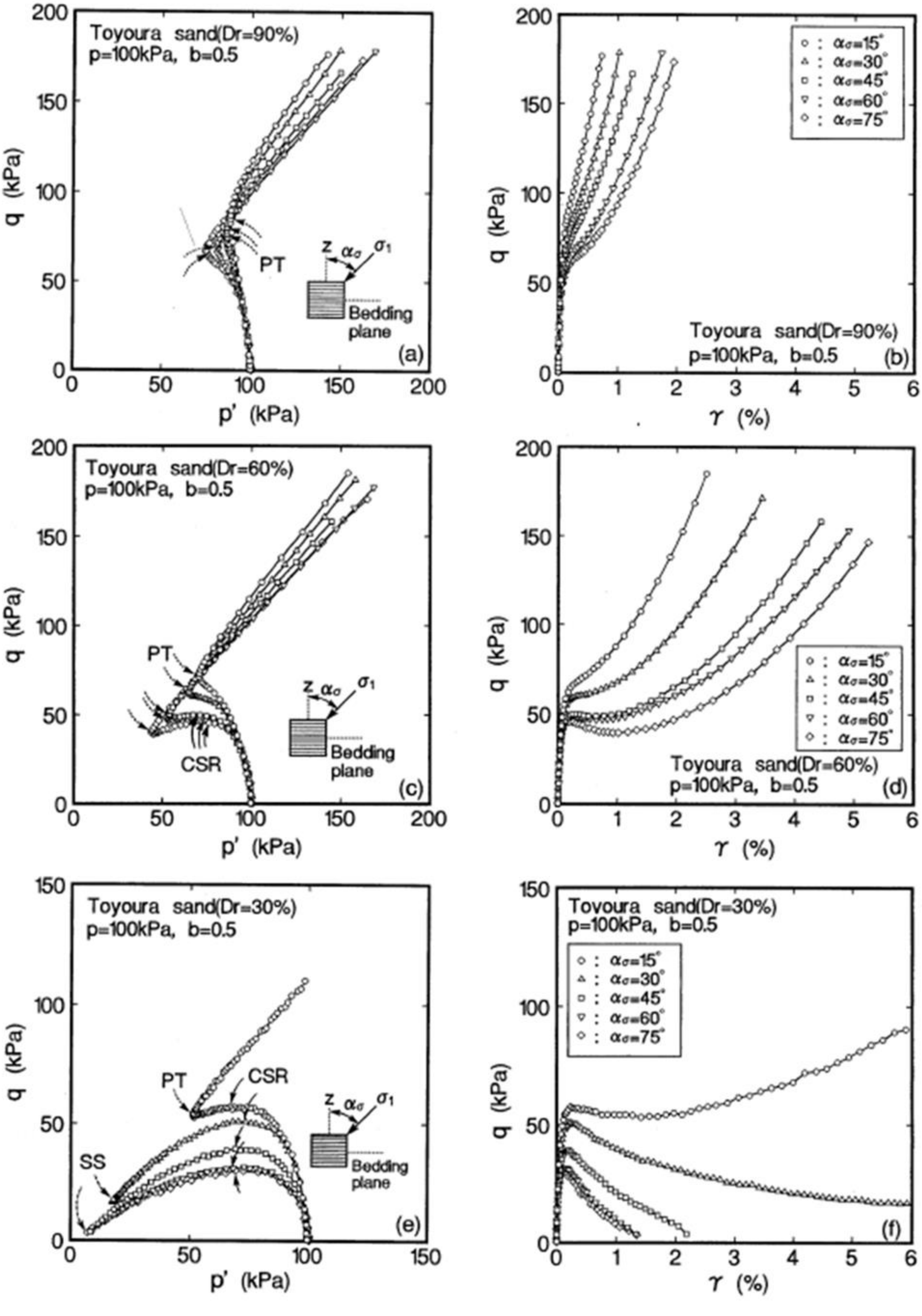

Fig. 4.22 Effect of the principal stress direction on the monotonic undrained behaviour of sand at different relative densities. Effective stress paths and stress - strain curves at D_r = 90% (**a** and **b**), 60% (**c** and **d**) and 30% (**e** and **f**) (after Nakata et al. 1998)

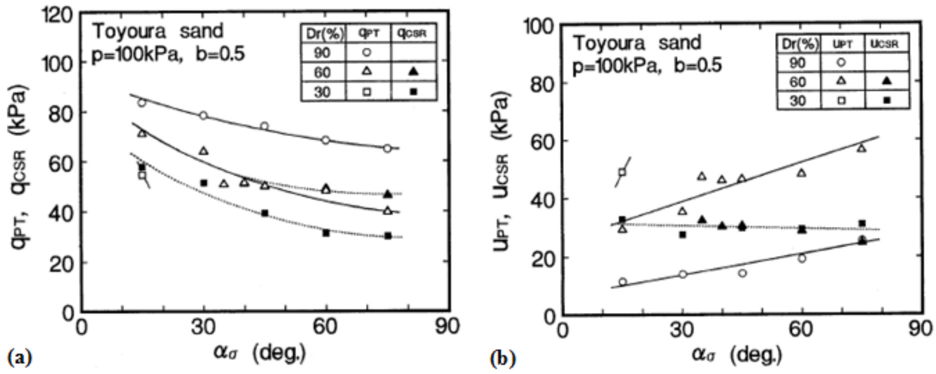

Fig. 4.23 Effect of the principal stress direction on the **a** deviatoric stress and **b** excess pore-water pressure at the phase transformation (PT) and transient peak (CSR) point (after Nakata et al. 1998)

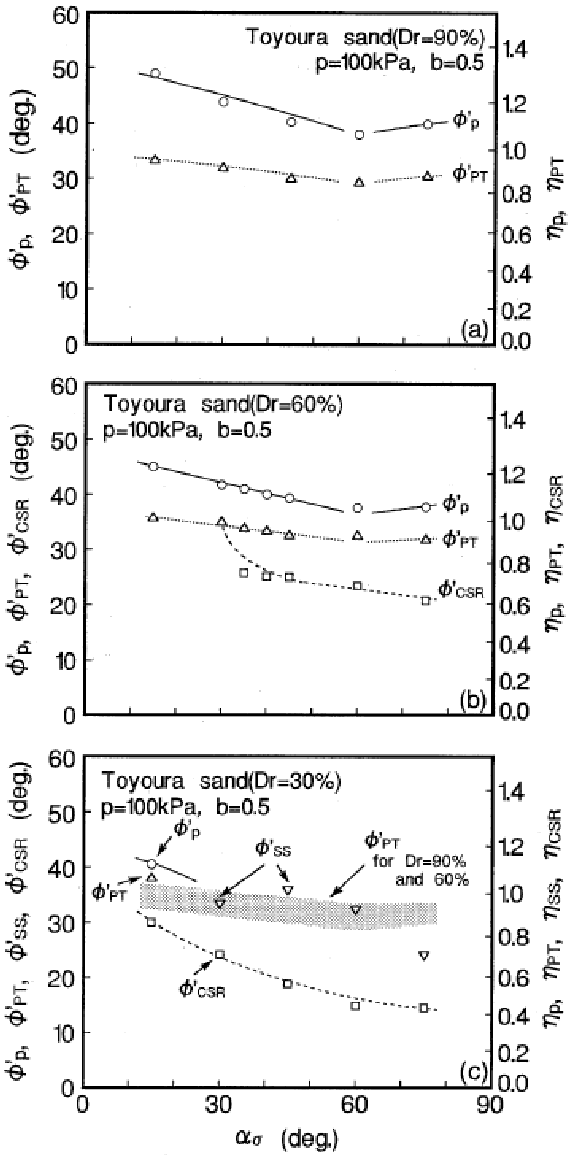

Fig. 4.24 Effect of the principal stress direction on the mobilised friction angle at the characteristic states of sand with: **a** D_r = 90%, **b** D_r = 60% and **c** D_r = 30%. "CSR" stands for critical stress ratio, "PT" for phase transformation, "SS" for contractive steady states and "P" for peak failure states. The grey-shaded area in **c** shows the range of φ'_{PT} for *Dr* = 90% and 60% (after Nakata et al. 1998)

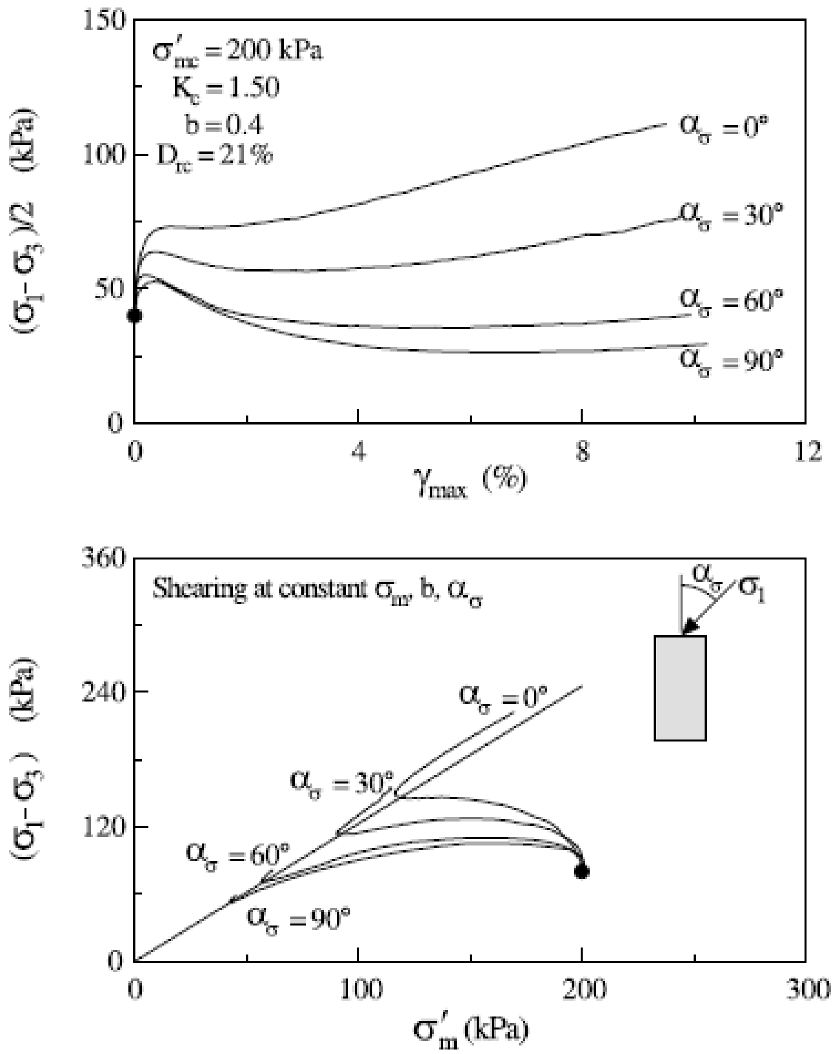

Fig. 4.25 Influence of the principal stress direction angle, α, on the undrained behaviour of loose sand with a generalised initial stress state. **a** Stress - strain curves and **b** effective stress paths (after Sivathayalan and Vaid 2002)

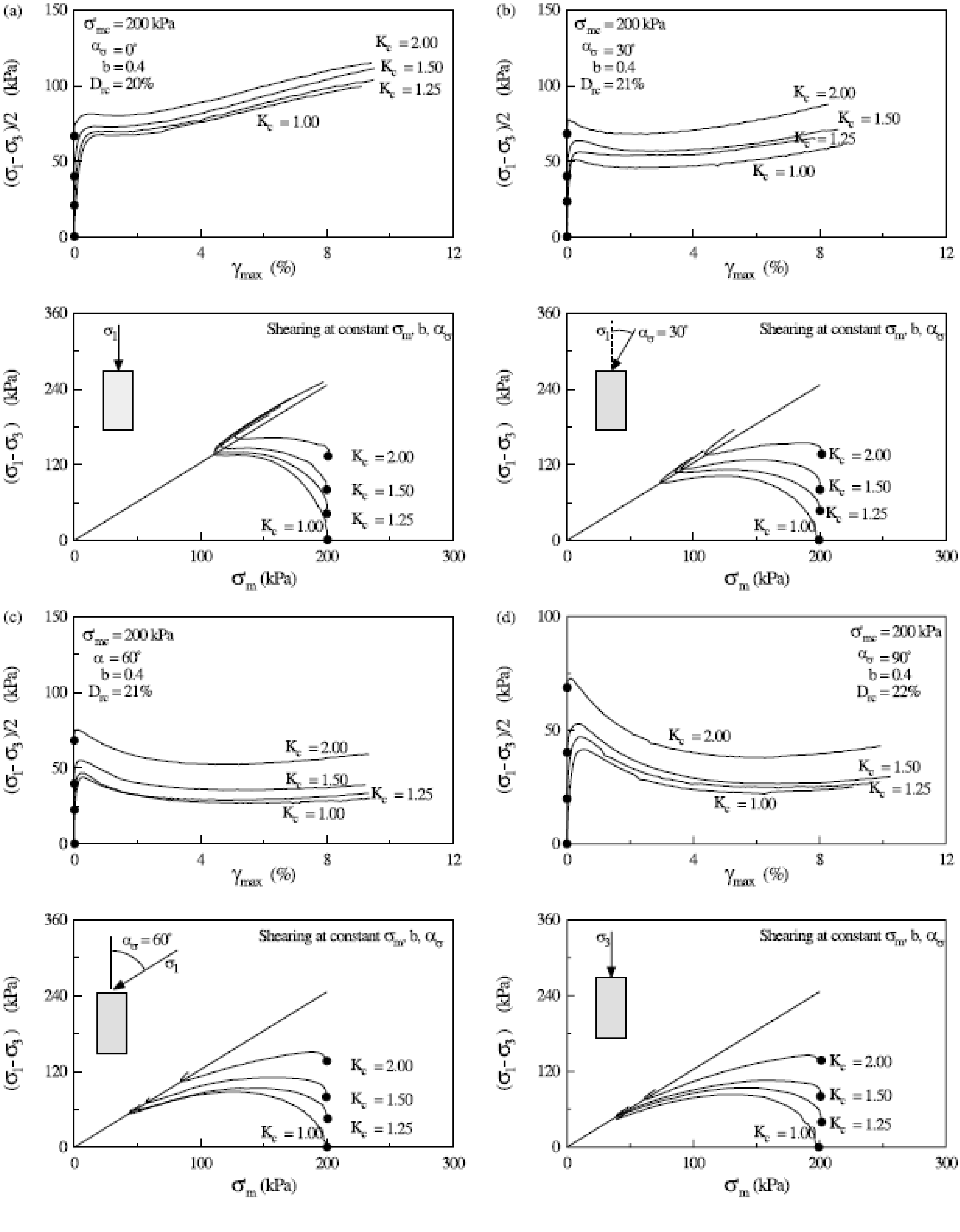

Fig. 4.26 Influence of the consolidation stress ratio K_c (= σ'_{1c} / σ'_{3c}) on the undrained behaviour of loose sand with a generalised initial stress state: **a** α = 0°, **b** α = 30°, **c** α = 60° and **d** α = 90° (after Sivathayalan and Vaid 2002)

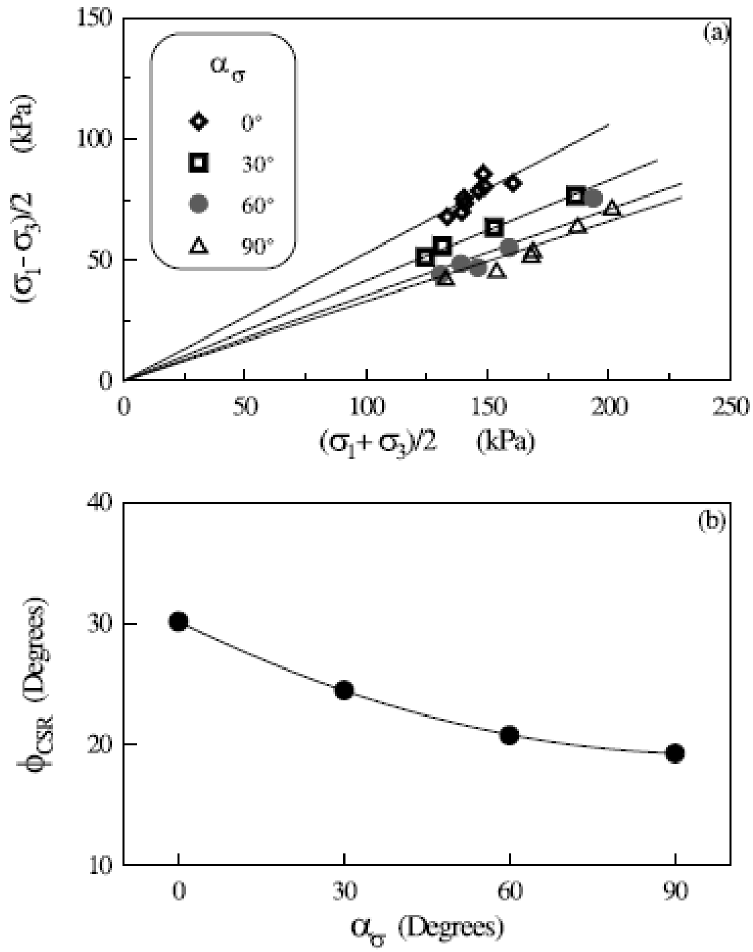

Fig. 4.27 Effective stress state (**a**) and mobilised friction angle (**b**) at the onset of flow for different values of the principal stress direction angle, α (after Sivathayalan and Vaid 2002)

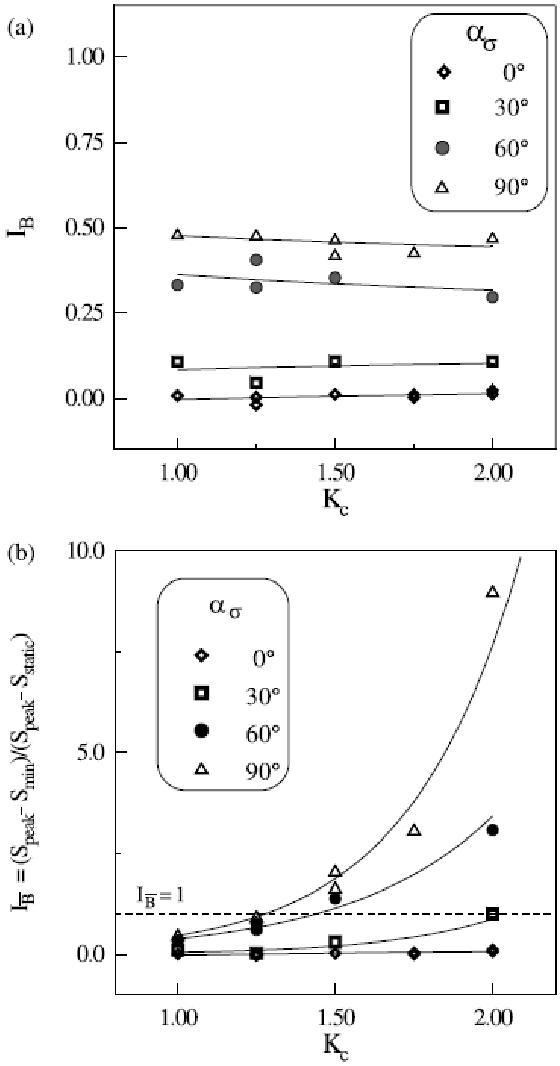

Fig. 4.28 Dependence of the brittleness index (**a**) and modified brittleness index (**b**) on α and K_c (after Sivathayalan and Vaid 2002)

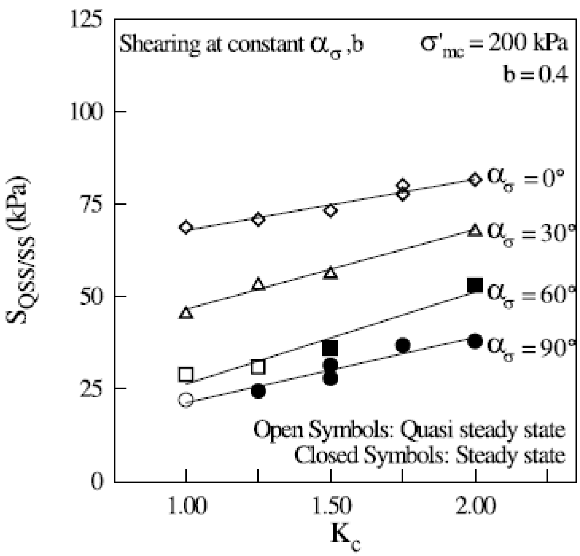

Fig. 4.29 Dependence of the minimum undrained strength mobilised at quasi-steady state or steady state on K_c and α (after Sivathayalan and Vaid 2002)

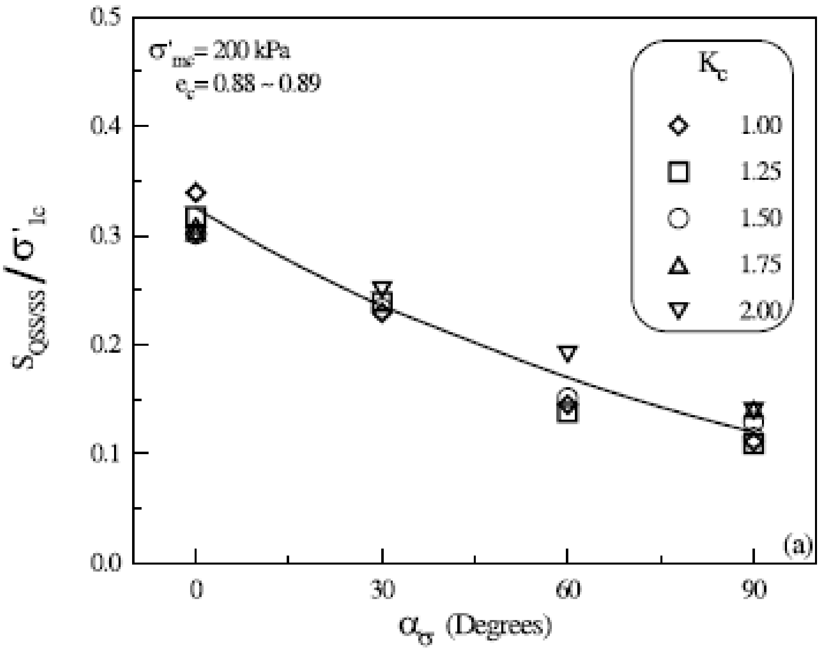

Fig. 4.30 Dependence of the normalised minimum undrained strength on α (after Sivathayalan and Vaid 2002)

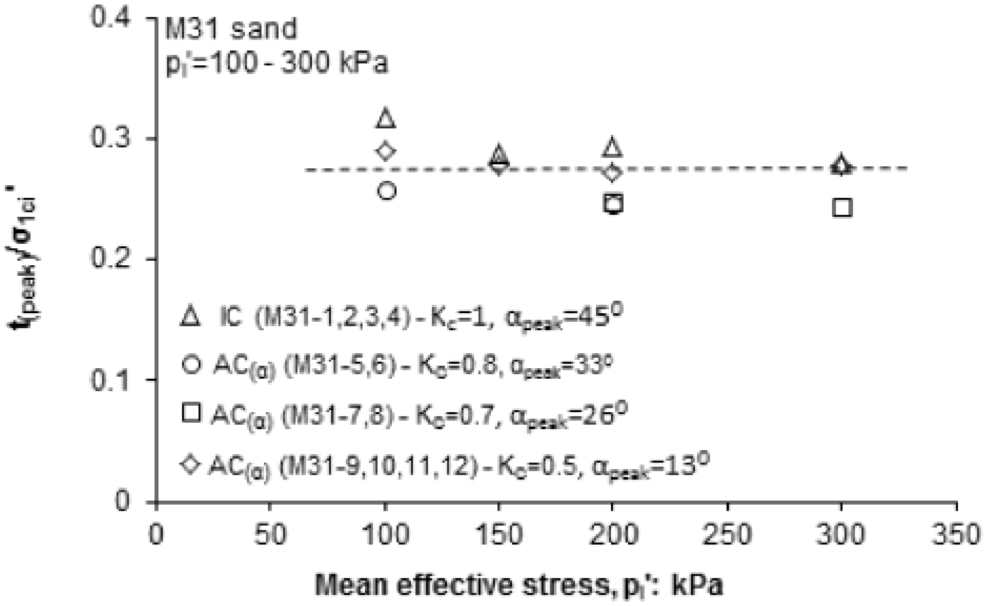

Fig. 4.31 Normalised transient-peak strength of M31 sand (after Georgiannou et al. 2018)

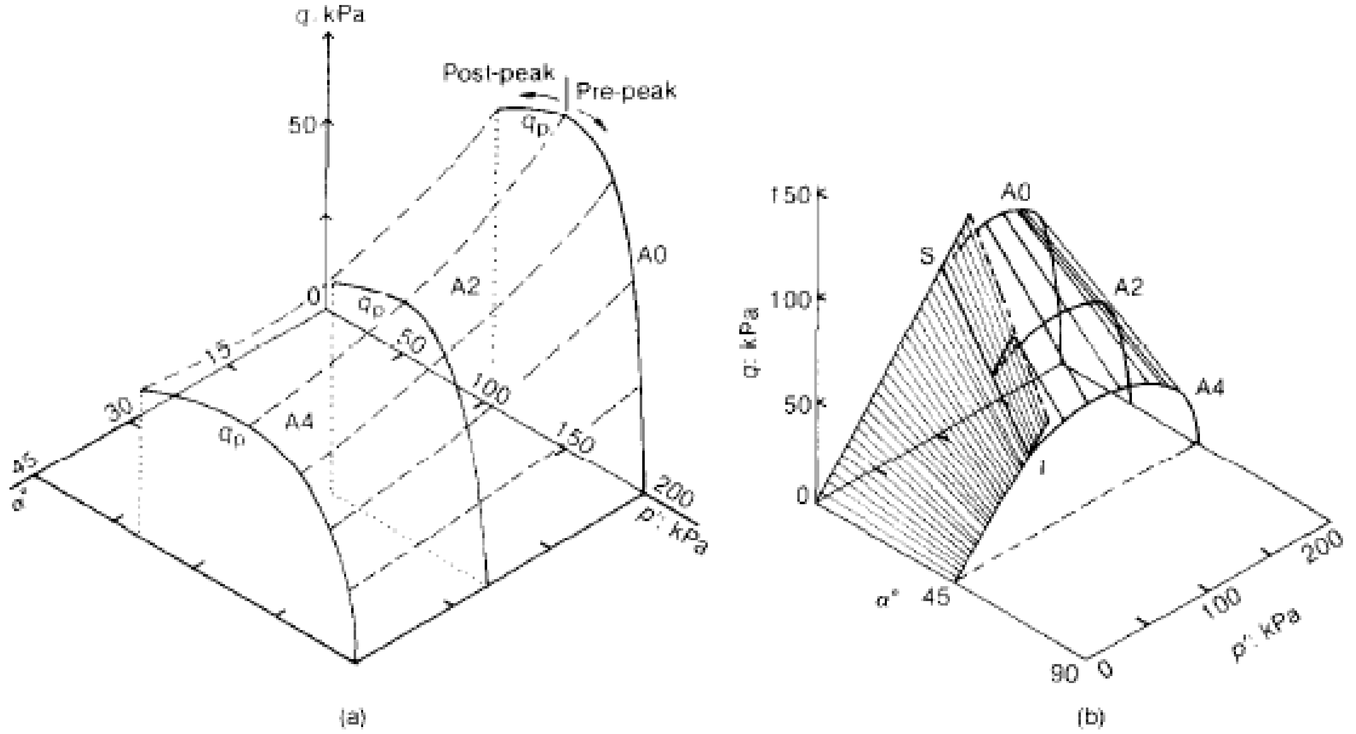

Fig. 4.32 a The contractant region of the Local Boundary Surface (LBS). **b** The set of failure lines closing the LBS in the dilatant region (after Symes et al. 1984)

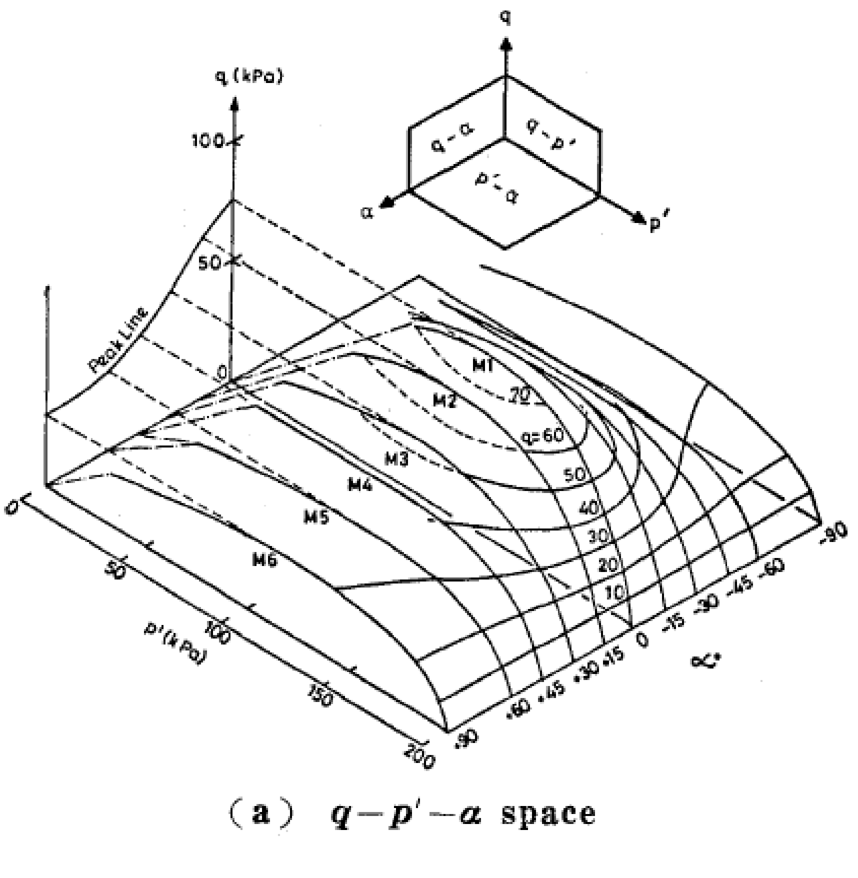

Fig. 4.33 a The set of undrained effective stress paths for loose sand that forms the Local Boundary Surface in the q - p' - α space (b = 0.5). Continued in the next page (after Shibuya and Hight 1987)

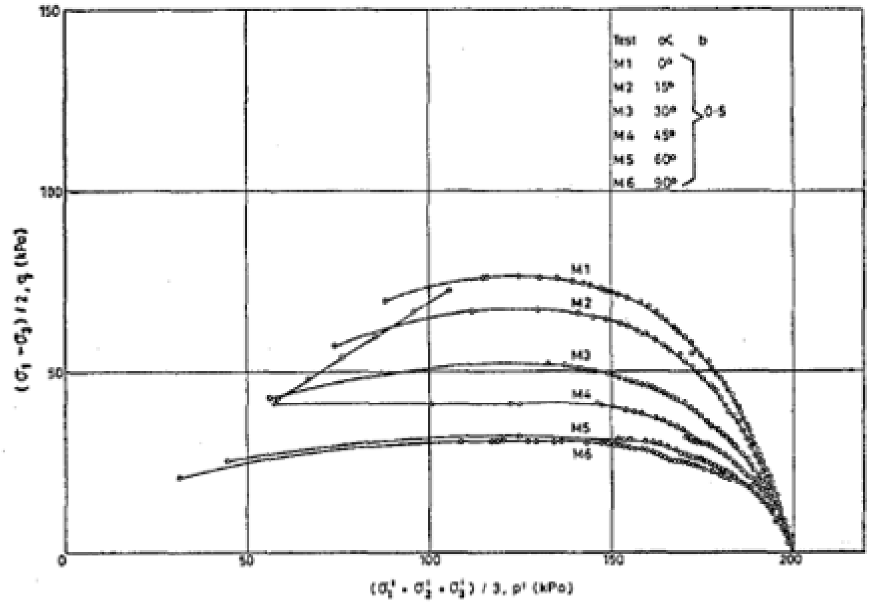

(b) Projection on to $q-p'$ plane

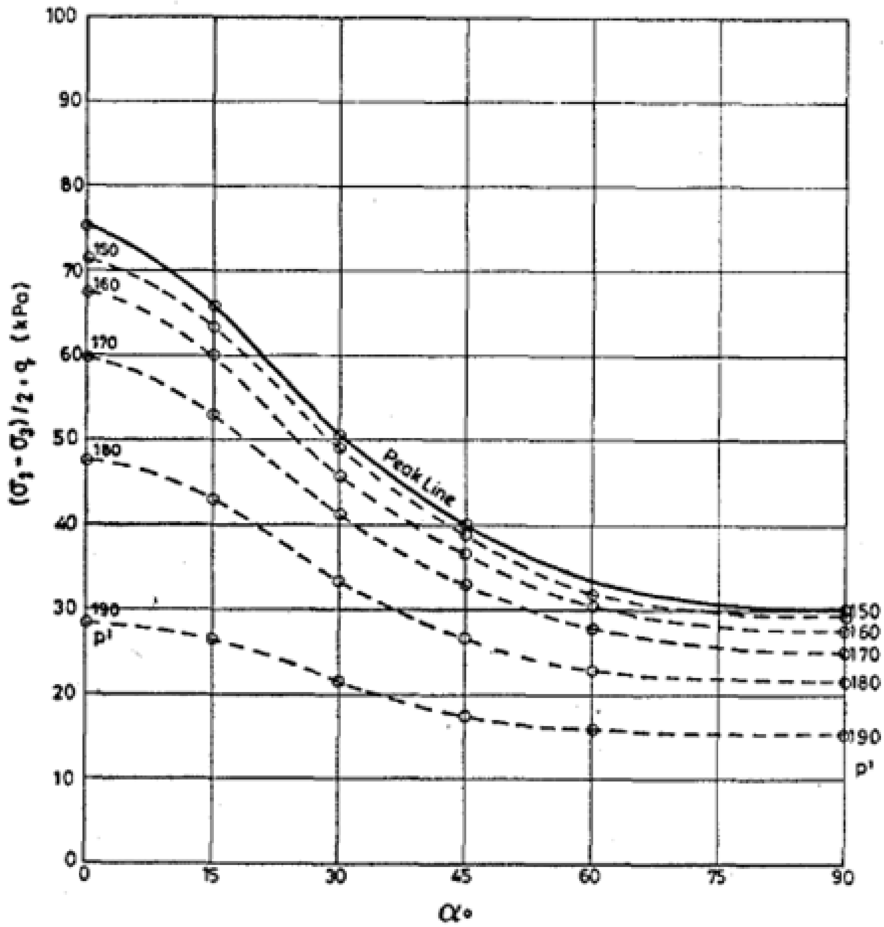

(c) Projection on to $q-\alpha$ plane

Fig. 4.33 b Projection of the LBS on the *q* - *p'* plane in the form of constant-α curves (effective stress paths). **c** Projection of the pre-peak region of the LBS on the *q* - α plane in the form of constant-*p'* contours (after Shibuya and Hight 1987)

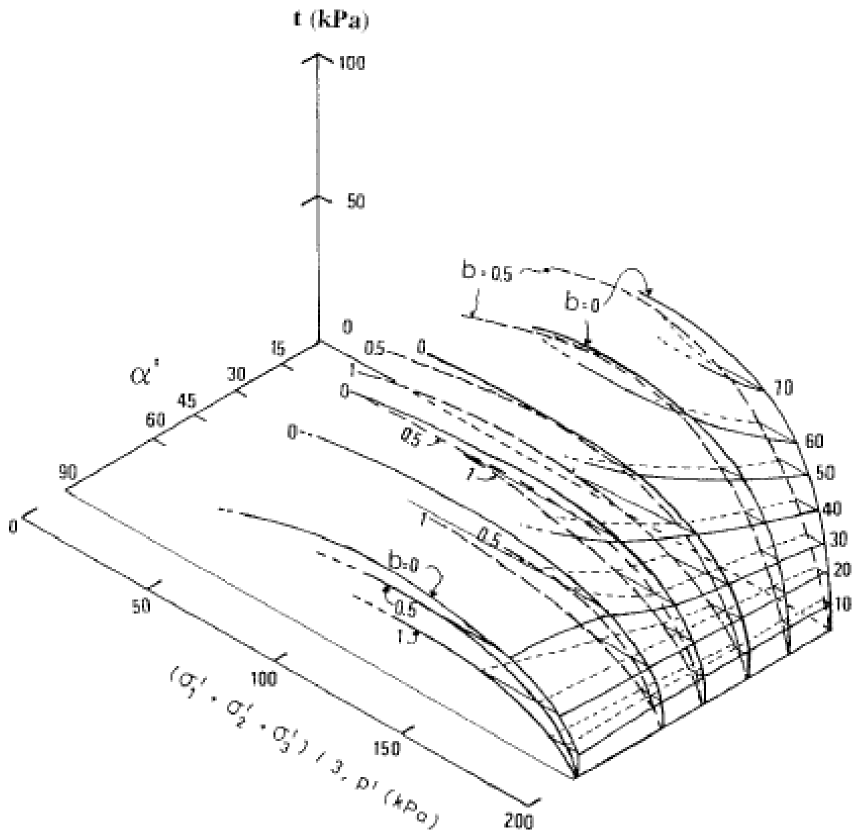

Fig. 4.34 The four-dimensional Local Boundary Surface of isotropically consolidated loose sand (after Shibuya et al. 2003a)

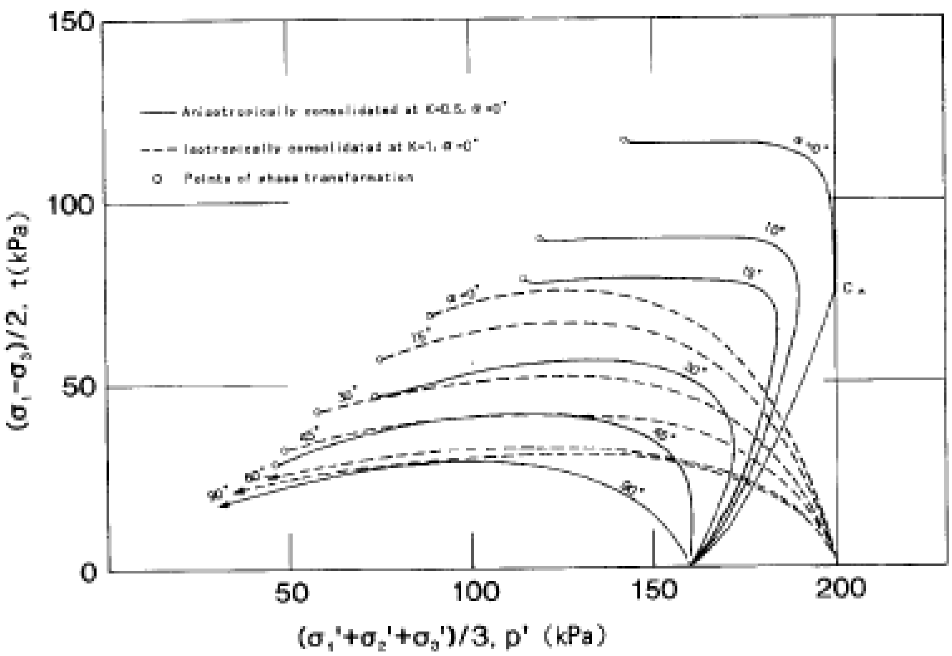

Fig. 4.35 a Undrained effective stress paths for loose IC (broken lines) and AC (solid lines) sand for different α and b = 0.3. Note that C_A is the stress state at the end of anisotropic consolidation (after Shibuya et al. 2003b)

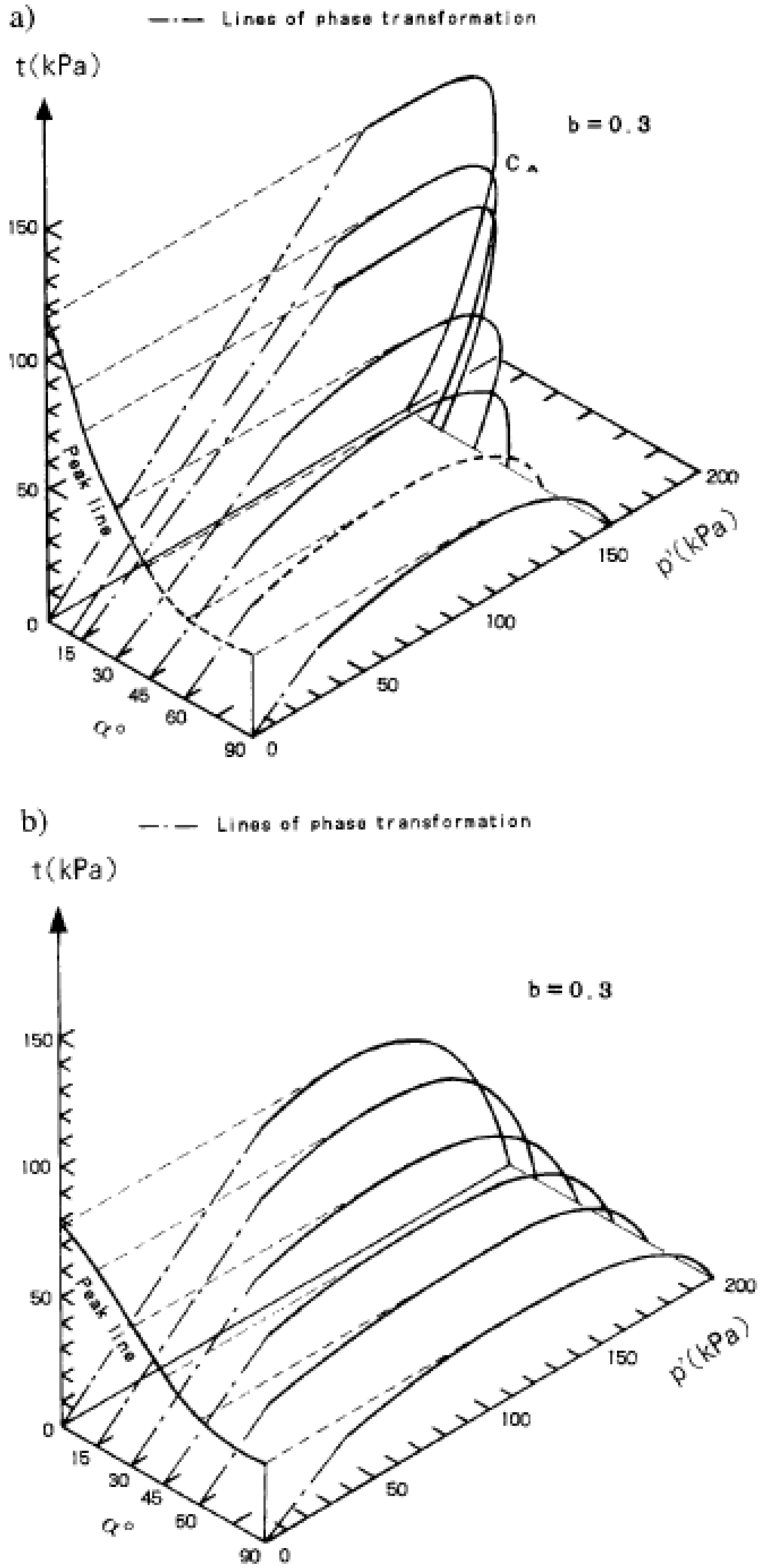

Fig. 4.36 The Local Boundary Surface in the *q* - *p'* - *α* space (*b* = 0.3) for **a** anisotropically consolidated and **b** isotropically consolidated sand. Note that C_A is the stress state at the end of anisotropic consolidation (after Shibuya et al. 2003b)

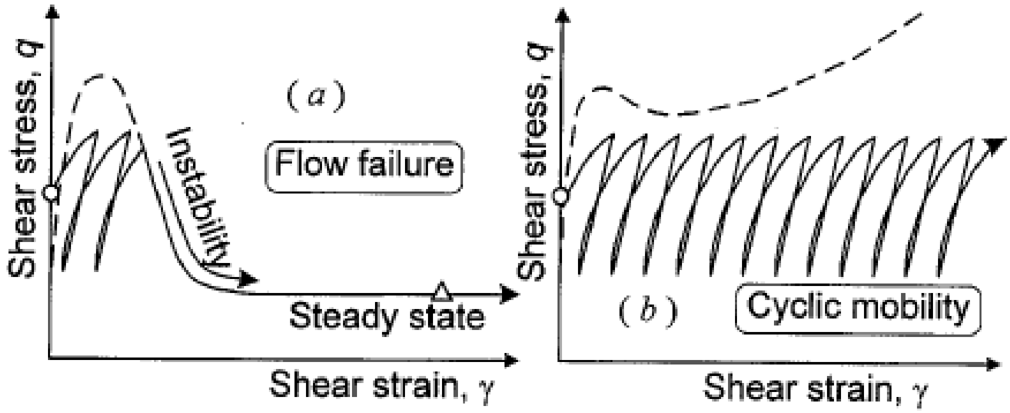

Fig. 4.37 a Flow deformation and **b** cyclic mobility triggered under cyclic loading (after Yoshimine and Ishihara 1998)

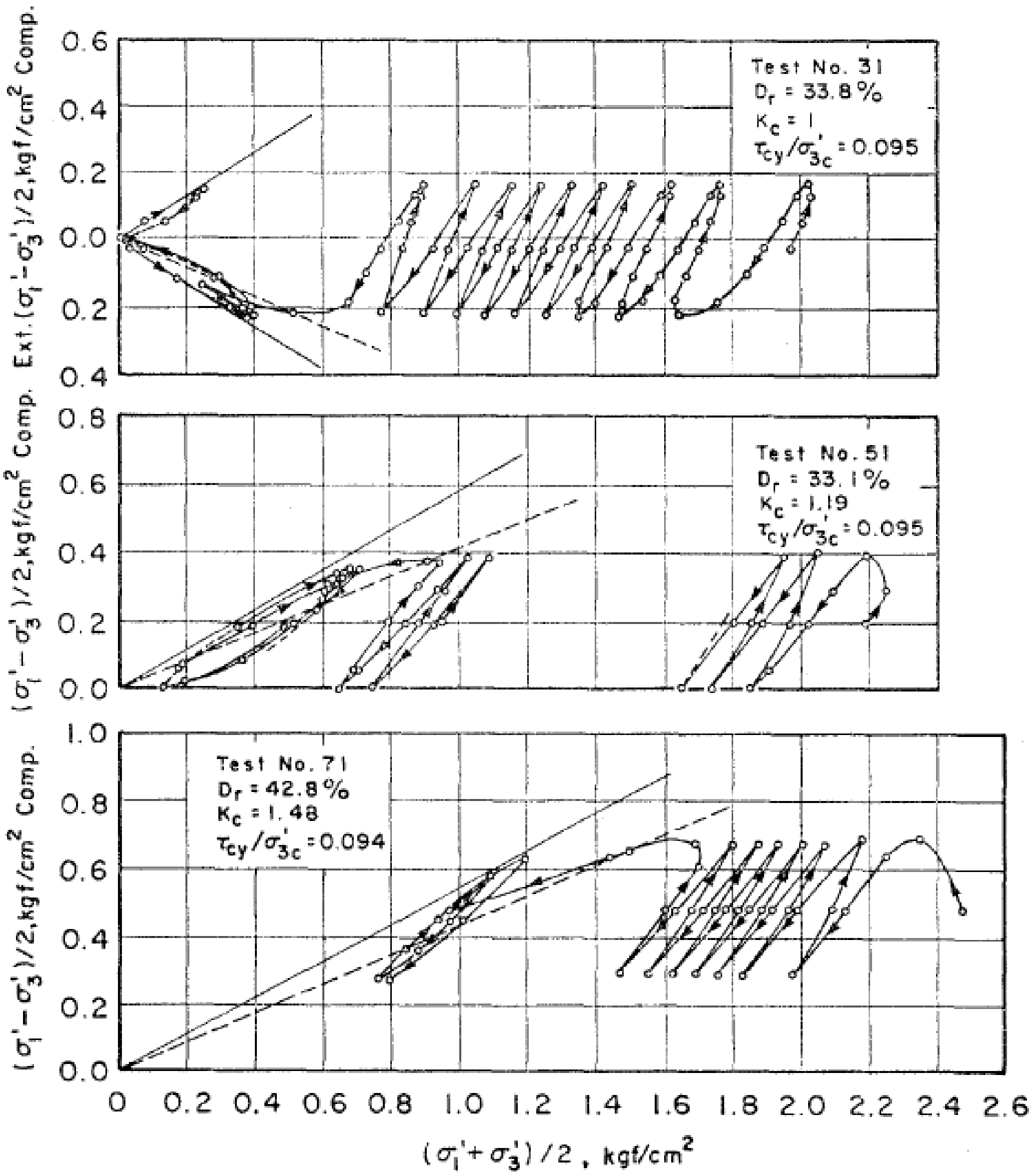

Fig. 4.38 Effective stress paths of cyclic undrained triaxial loading tests on loose IC and AC sand. The solid lines represent the failure envelopes, while the broken ones are the CSR-lines (after Vaid and Chern 1983)

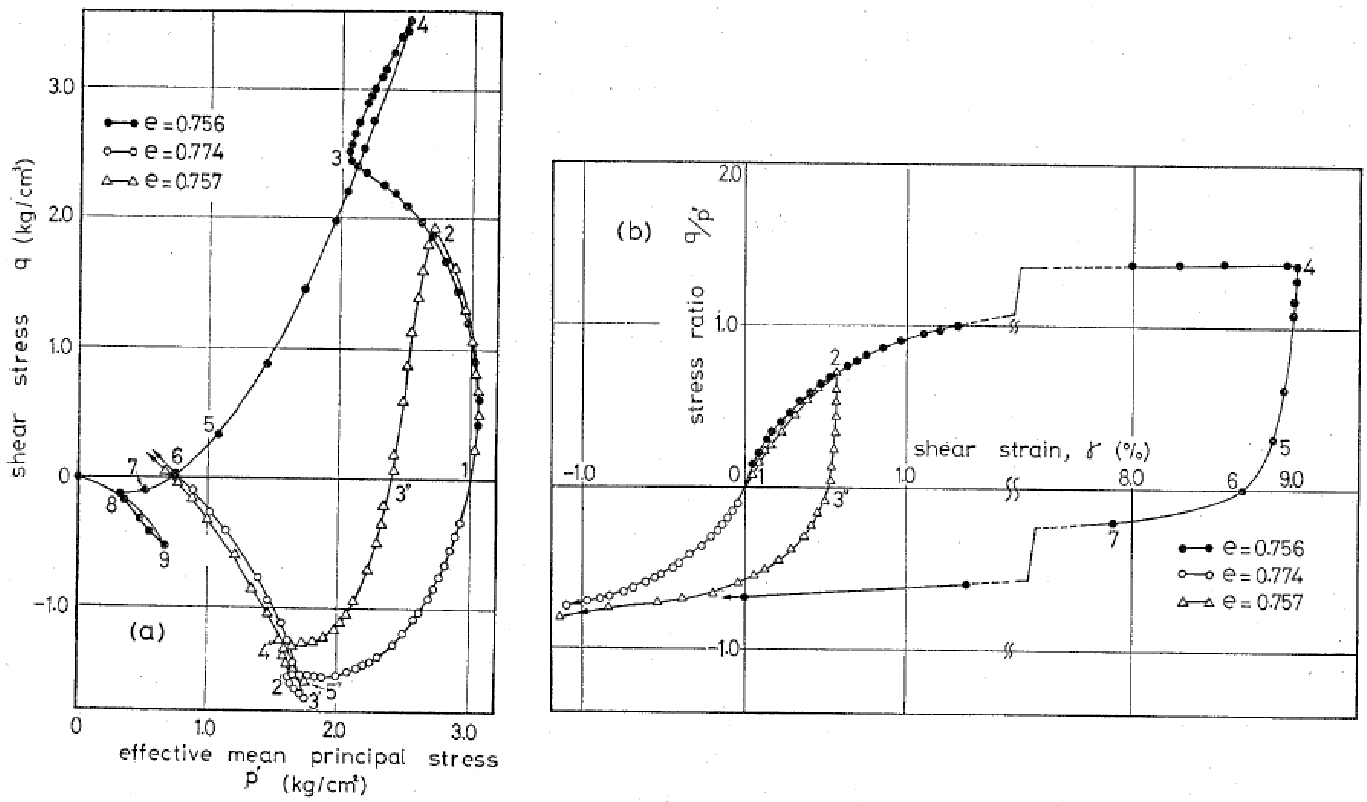

Fig. 4.39 Triggering of instability and liquefaction upon reversing the loading direction beyond the phase transformation point (after Ishihara et al. 1975)

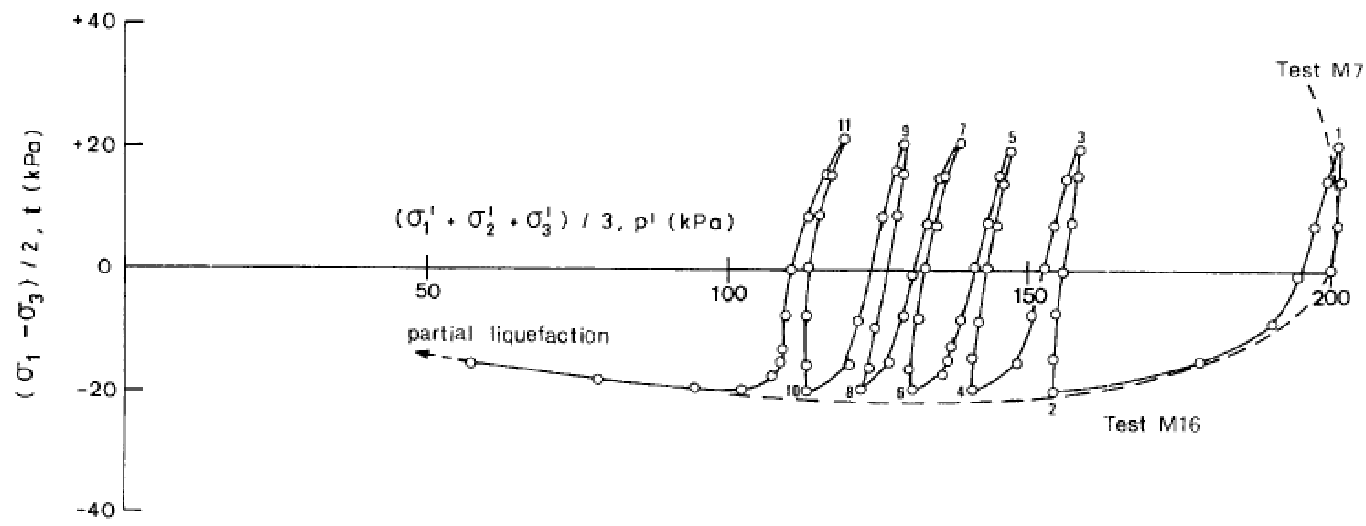

Fig. 4.40 Undrained effective stress path of cyclic triaxial compression - extension test. The broken lines M7 and M16 represent the undrained ESPs of monotonic compression and extension test, respectively (after Shibuya et al. 2003a)

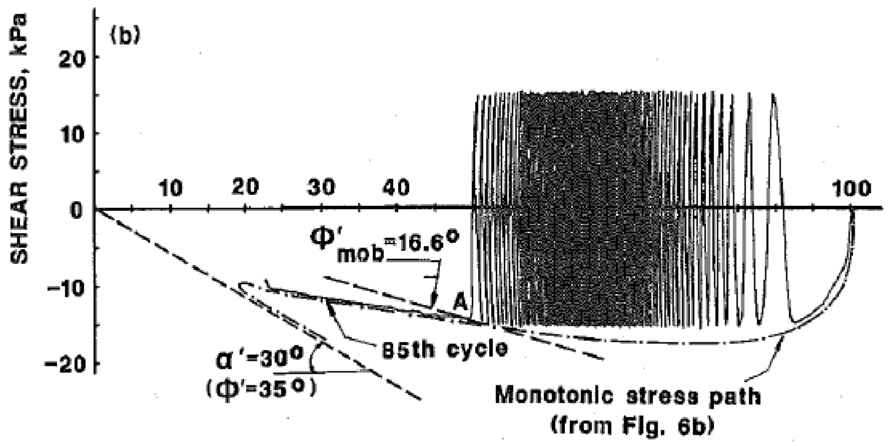

Fig. 4.41 Undrained effective stress path of cyclic torsional shear test on IC sand (after Alarcon-Guzman et al. 1988)

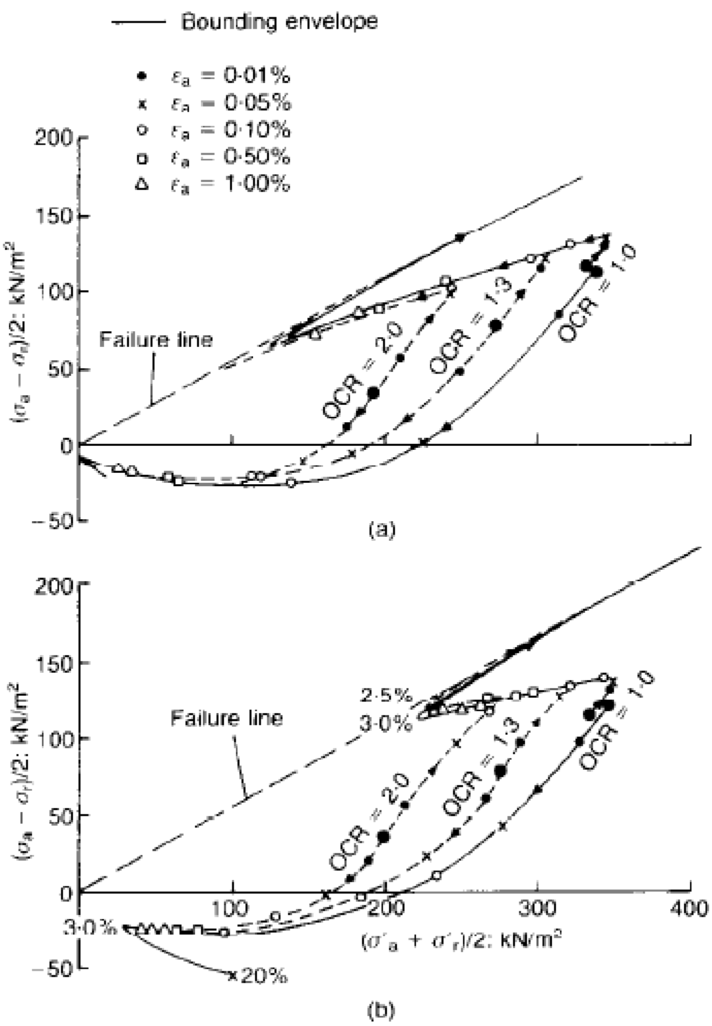

Fig. 4.42 Undrained effective stress paths for two clayey sands subjected to monotonic triaxial compression or extension at different overconsolidation ratios OCR: **a** Ham river sand / kaolin and **b** Gullfaks clayey sand (after Georgiannou et al. 1991)

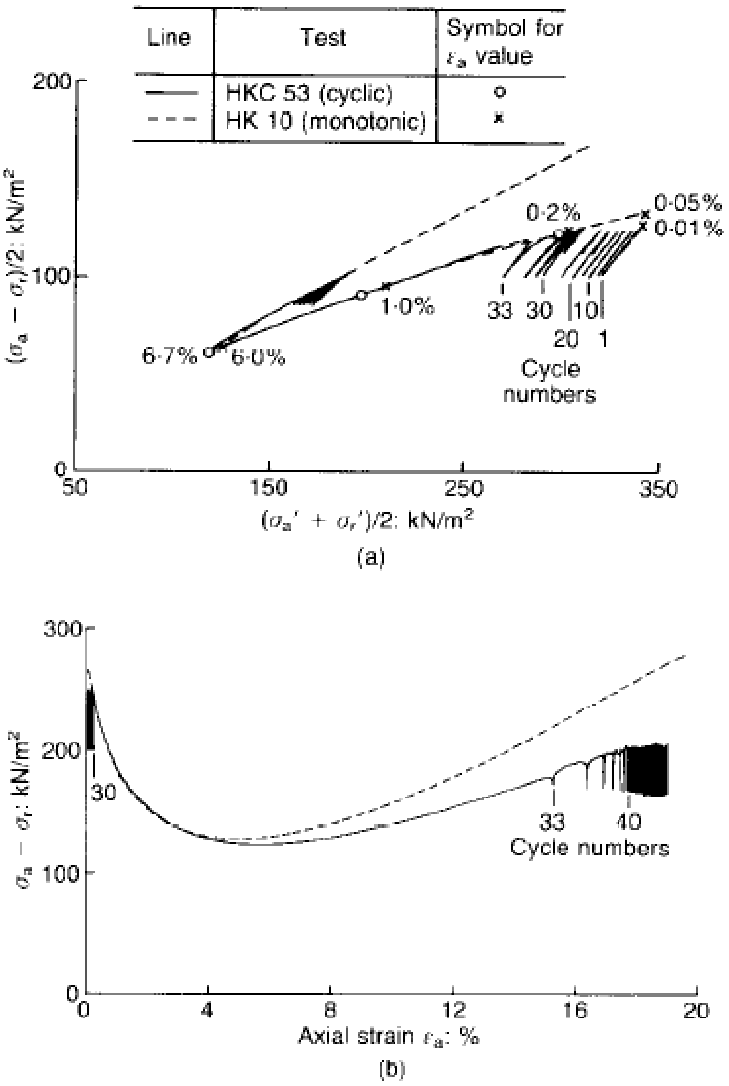

Fig. 4.43 Undrained cyclic and monotonic triaxial compression tests on normally consolidated (OCR = 1) Ham river sand / kaolin specimens: **a** effective stress paths and **b** stress - strain curves (after Georgiannou et al. 1991)

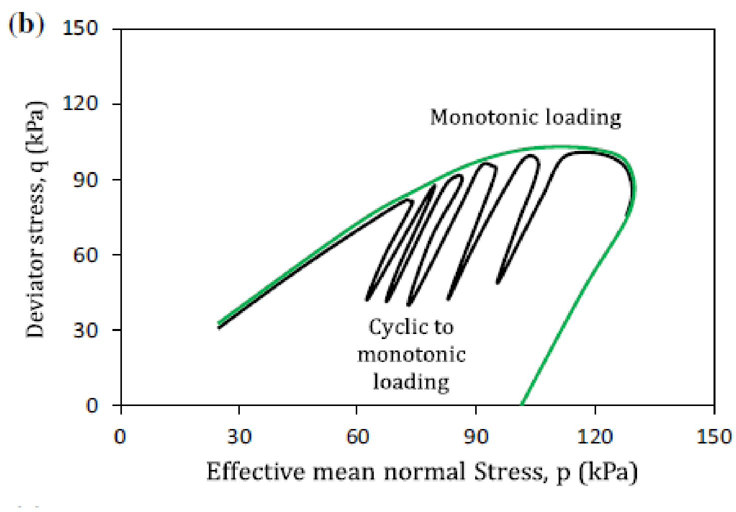

Fig. 4.44 Monotonic undrained effective stress path as a bounding envelope to the cyclic undrained effective stress path in triaxial loading tests on sand (after Ishihara et al. 1991)

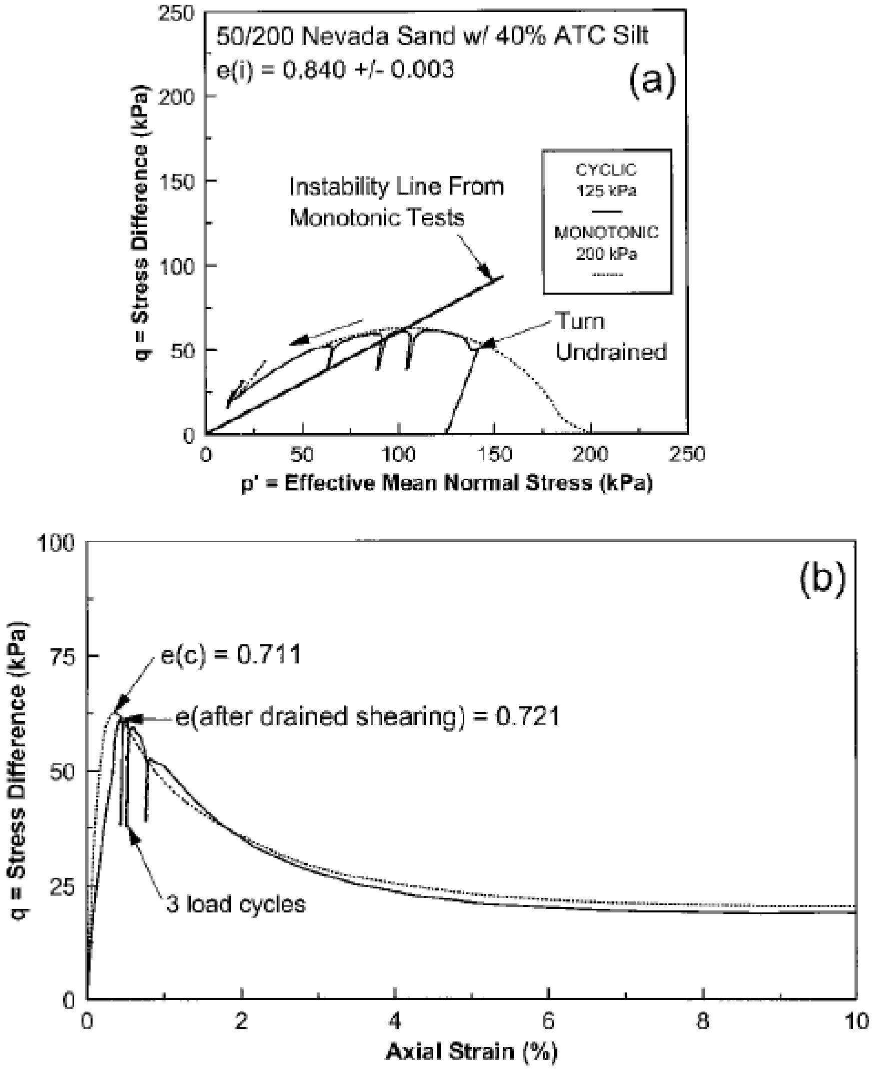

Fig. 4.45 Monotonic undrained effective stress path as a bounding envelope to the cyclic undrained effective stress path in triaxial loading tests on silty sand: **a** effective stress paths and **b** stress - strain curves (after Yamamuro and Covert 2001)

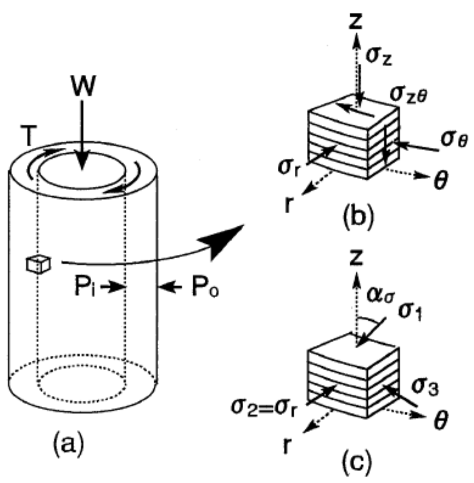

Fig. 4.46 a Boundary loads in a hollow cylinder specimen and generated average stresses on **b** the vertical and horizontal planes and **c** the principal stress planes (after Nakata et al. 1998)

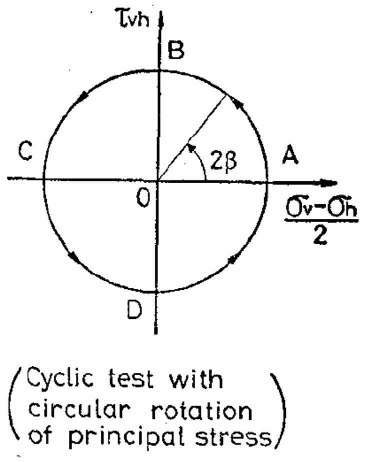

Fig. 4.47 Continuous, monotonic rotation of the stress principal axes with constant *t*: stress path in the $\tau_{z\theta}$ – $(\sigma_{zz} - \sigma_{\theta\theta})$ / 2 deviatoric plane (after Ishihara and Towhata 1983)

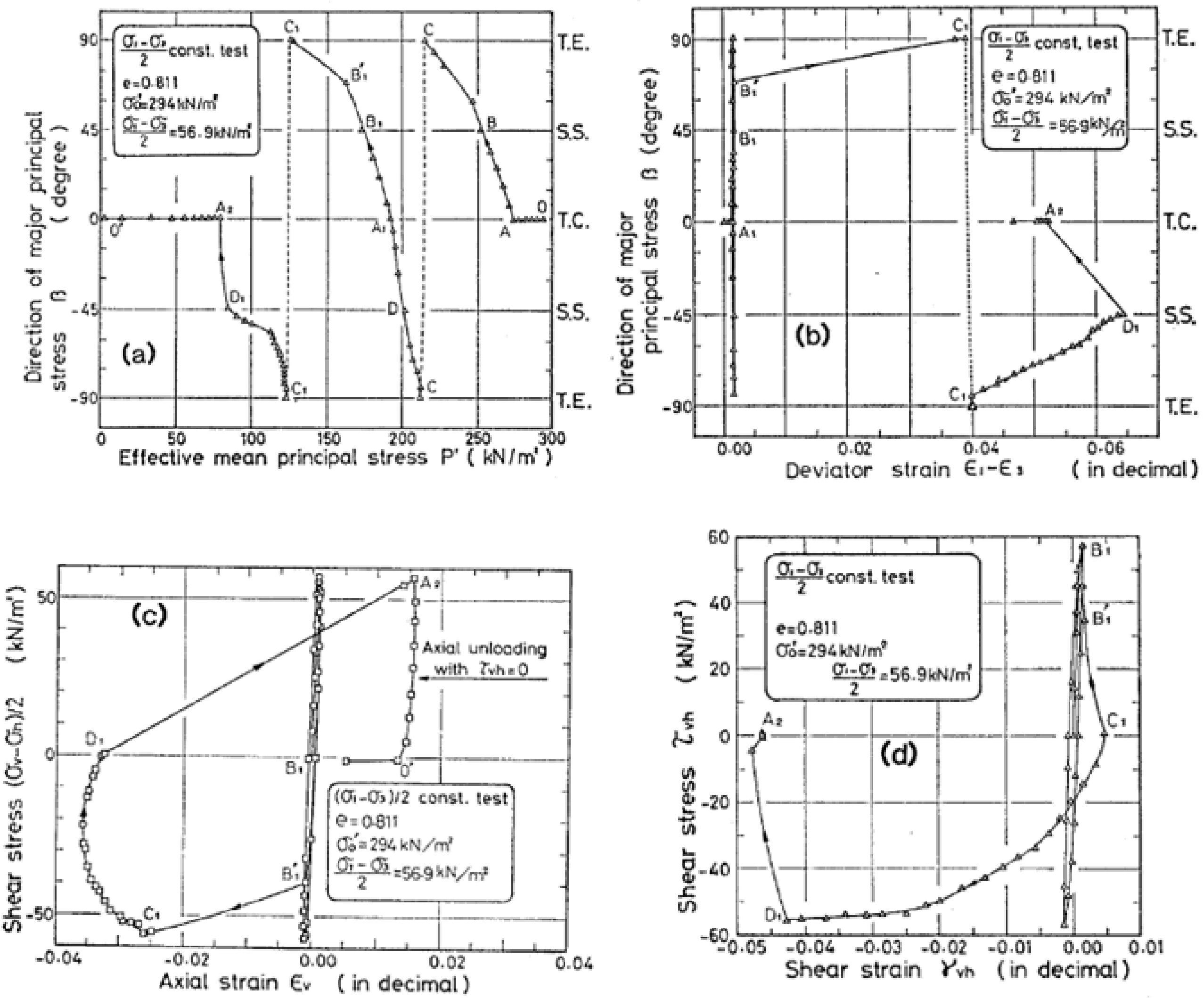

Fig. 4.48 a Evolution of the mean effective stress during the monotonic rotation of the stress principal axes. **b** Evolution of the strain difference ε_1 - ε_3 during the monotonic rotation of the stress principal axes. **c** Stress - strain curve in the triaxial mode. **d** Stress - strain curve in the torsional-shear mode (after Ishihara and Towhata 1983)

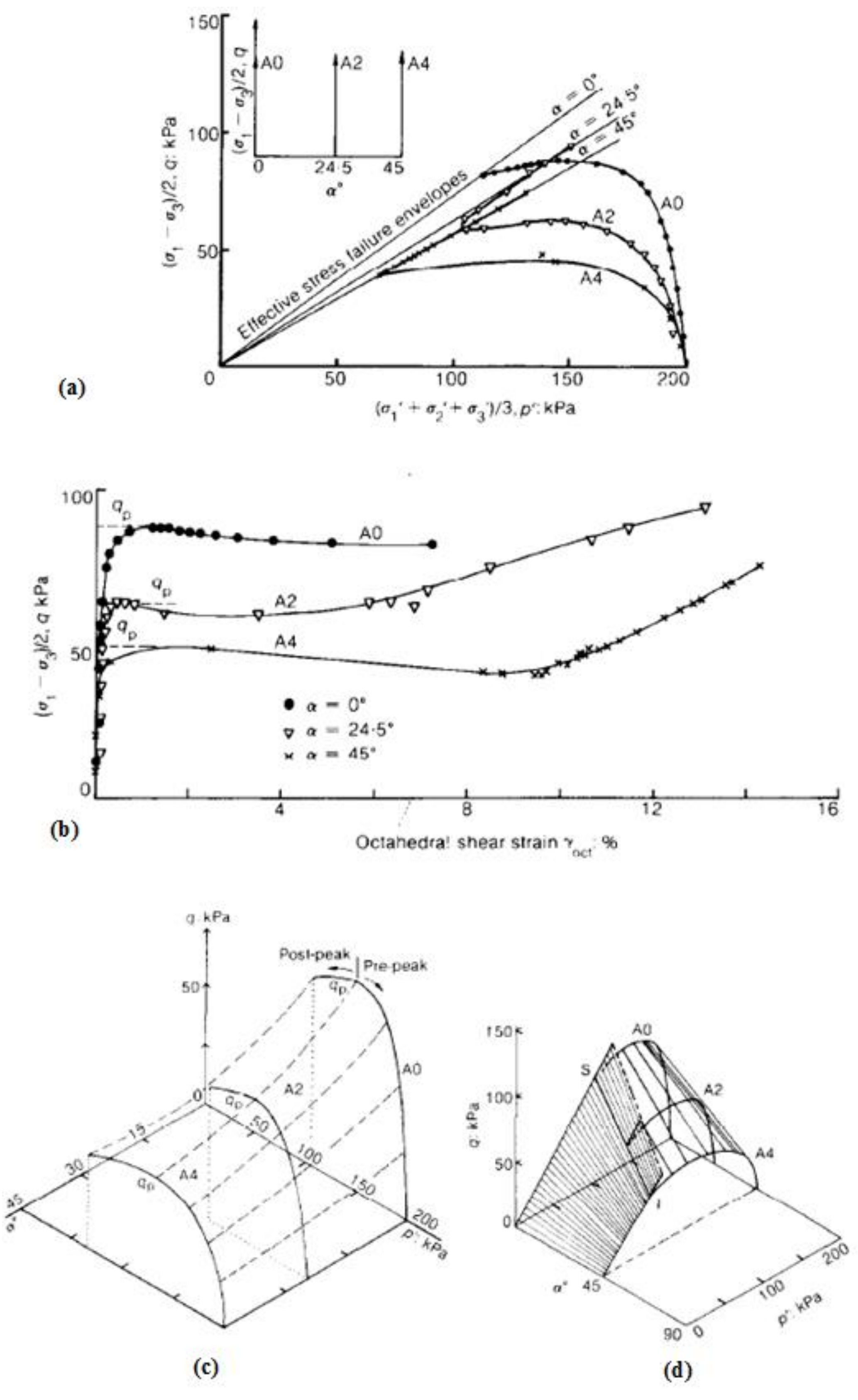

Fig. 4.49 a Undrained effective stress paths in the *t* - *p'* space of tests with constant *α* and *b* (= 0.5) forming the Local Boundary Surface (LBS). **b** Stress - strain curves. **c** The contractant region of the LBS. **d** The set of failure lines closing the LBS in the dilatant region (after Symes et al. 1984)

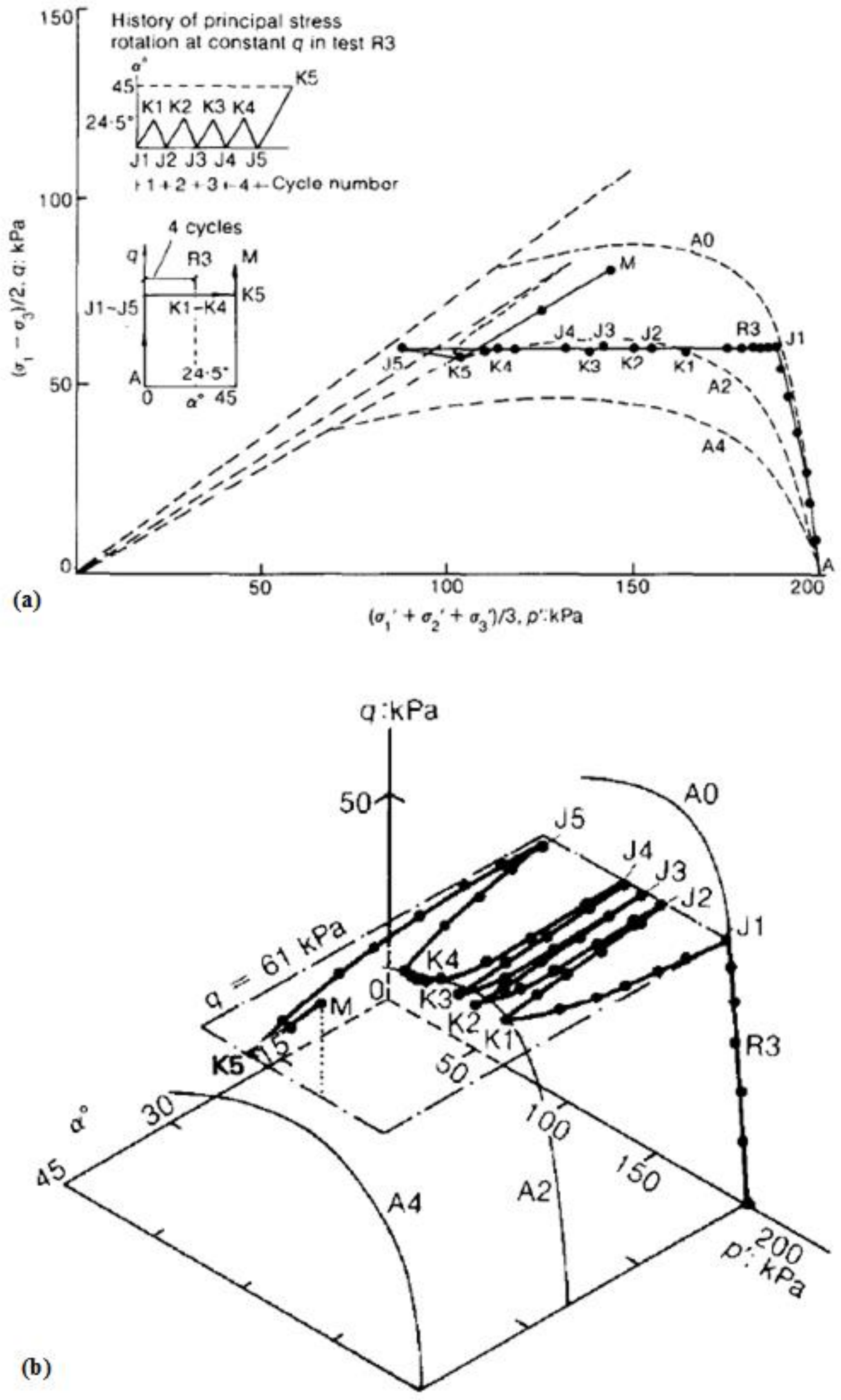

Fig. 4.50 Undrained effective stress path **a** in the t - p' space and **b** in the t - p' - α space of a test imposing cyclic rotation of the stress principal axes at constant t and b (= 0.5) (after Symes et al. 1984)

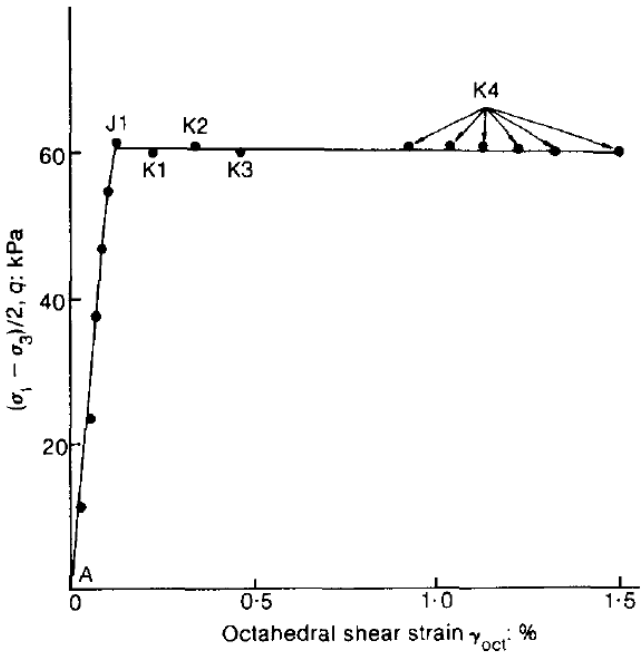

Fig. 4.51 Evolution of shear strain γ_{oct} during cyclic rotation of the stress principal axes at constant t = 61 kPa in test R3 (after Symes et al. 1984)

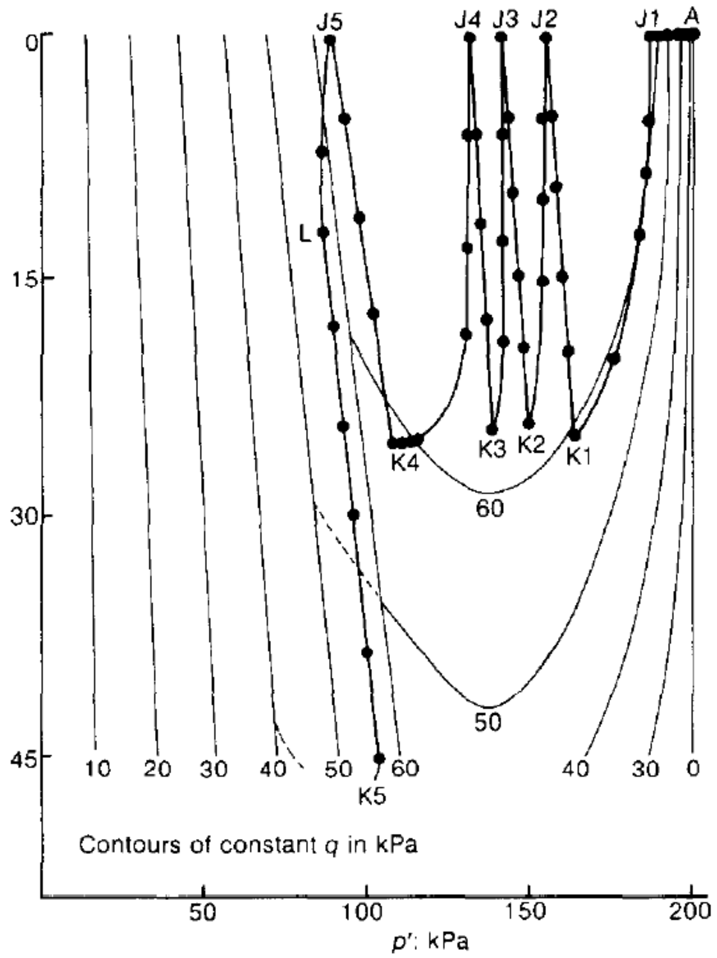

Fig. 4.52 Projection of the effective stress path R3 and Local Boundary Surface on the α - p' plane. The LBS is projected as a set of contours of constant t (= (σ_1 - σ_3) / 2) (after Symes et al. 1984)

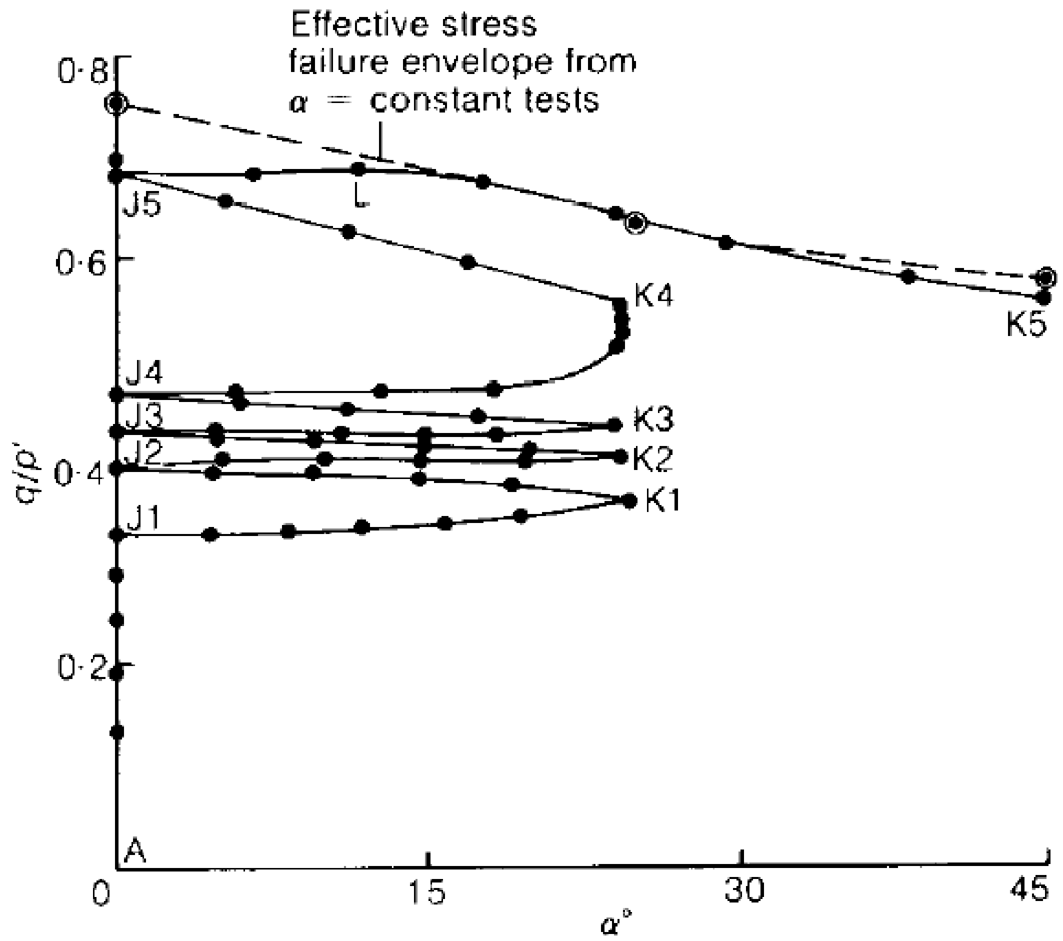

Fig. 4.53 Effective stress path R3 and failure surface in the t / p' - α plane (after Symes et al. 1984)

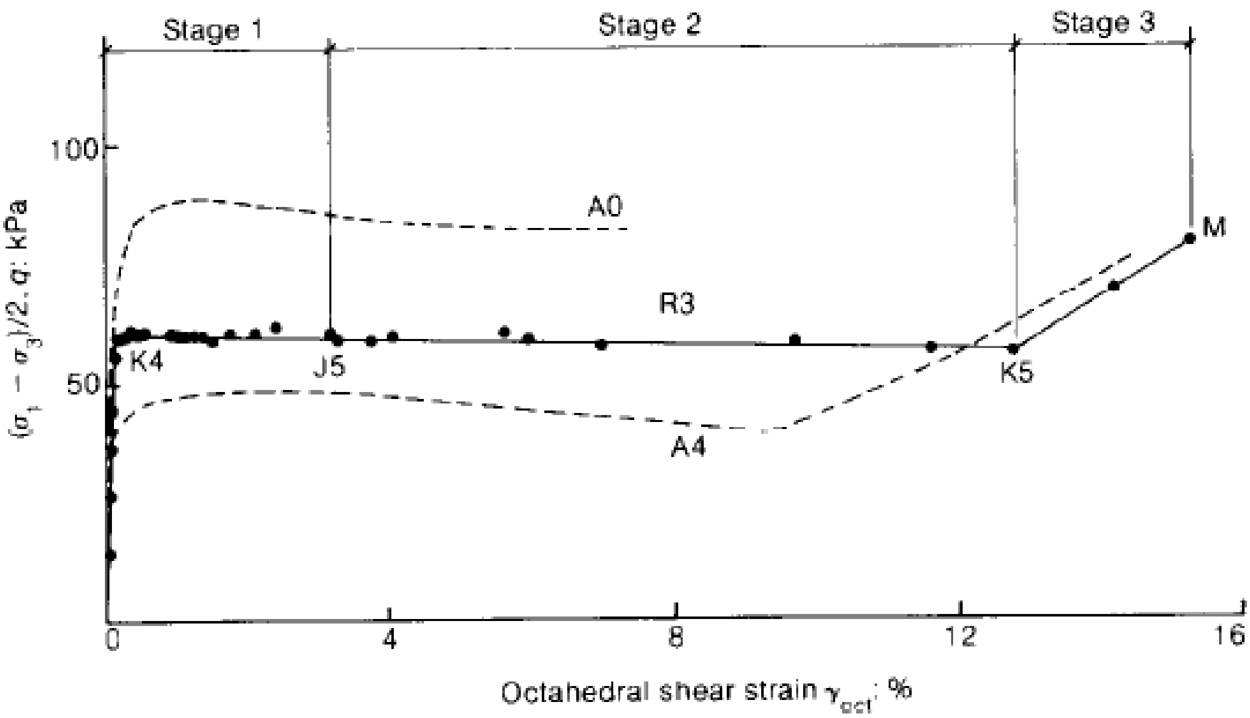

Fig. 4.54 Stress - strain behaviour during the three stages of test R3 (after Symes et al. 1984)

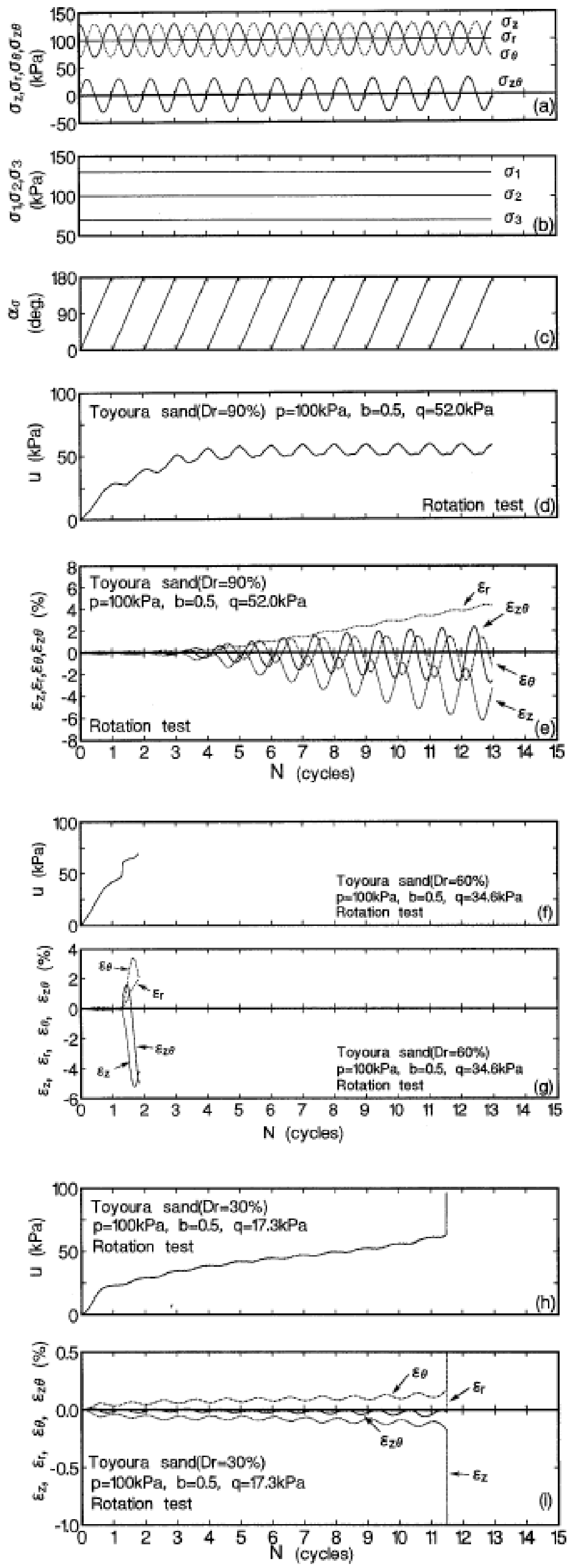

Fig. 4.55 Cyclic change of the total stresses and evolution of excess pore-water pressure and strains during the monotonic rotation of the stress principal axes: **a** to **e** D_r = 90% (test D30), **f** and **g** D_r = 60% (test M20), **h** and **i** D_r = 30% (test L10) (after Nakata et al. 1998)

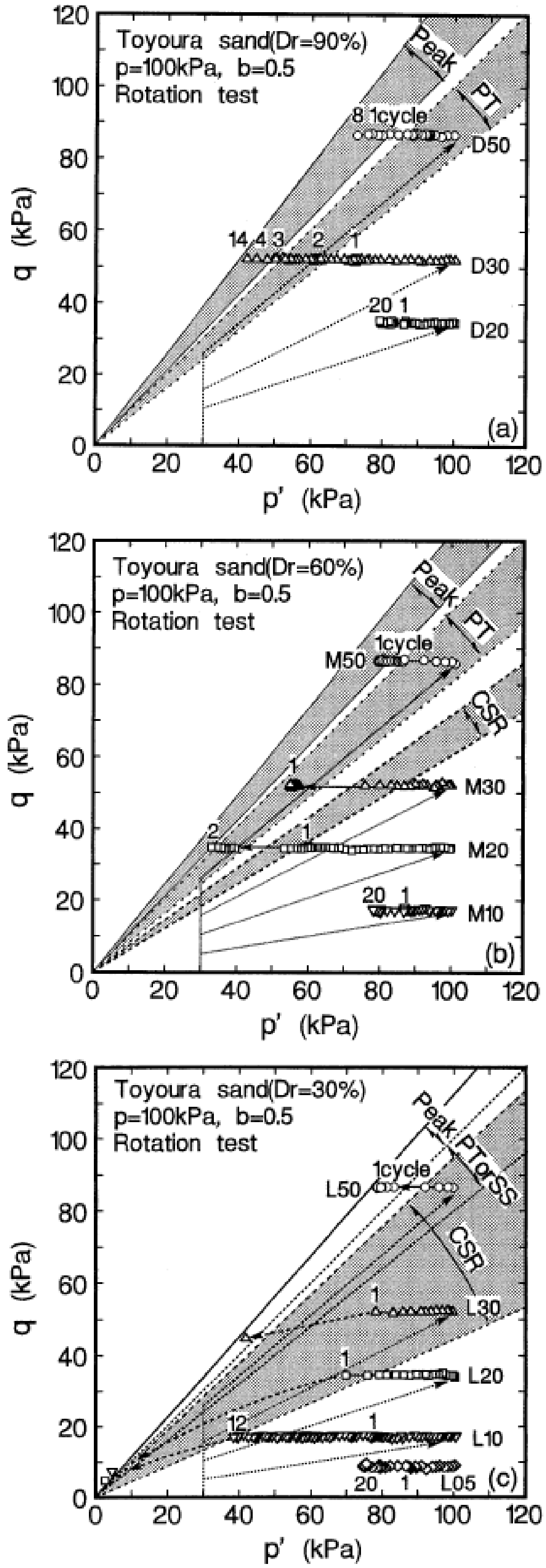

Fig. 4.56 Undrained effective stress paths in the q - p' plane of tests imposing monotonic undrained rotation of the stress principal axes at constant q: **a** D_r = 90%, **b** D_r = 60% and **c** D_r = 30%. It is noted that the PT-zone is wrongly displayed in Fig. 4.56a (after Nakata et al. 1998)

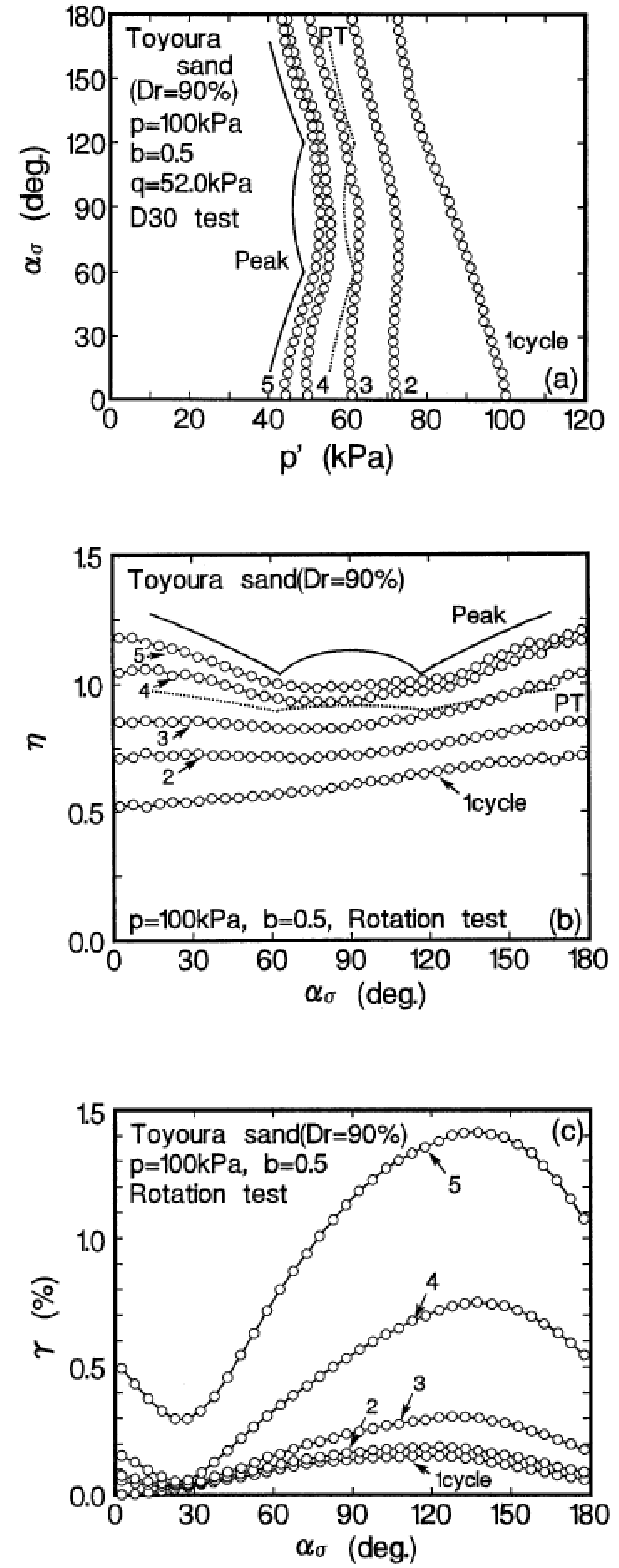

Fig. 4.57 Undrained principal stress rotation test on the dense specimen D30: **a** α - p' plot, **b** η - α plot and **c** γ - α plot (after Nakata et al. 1998)

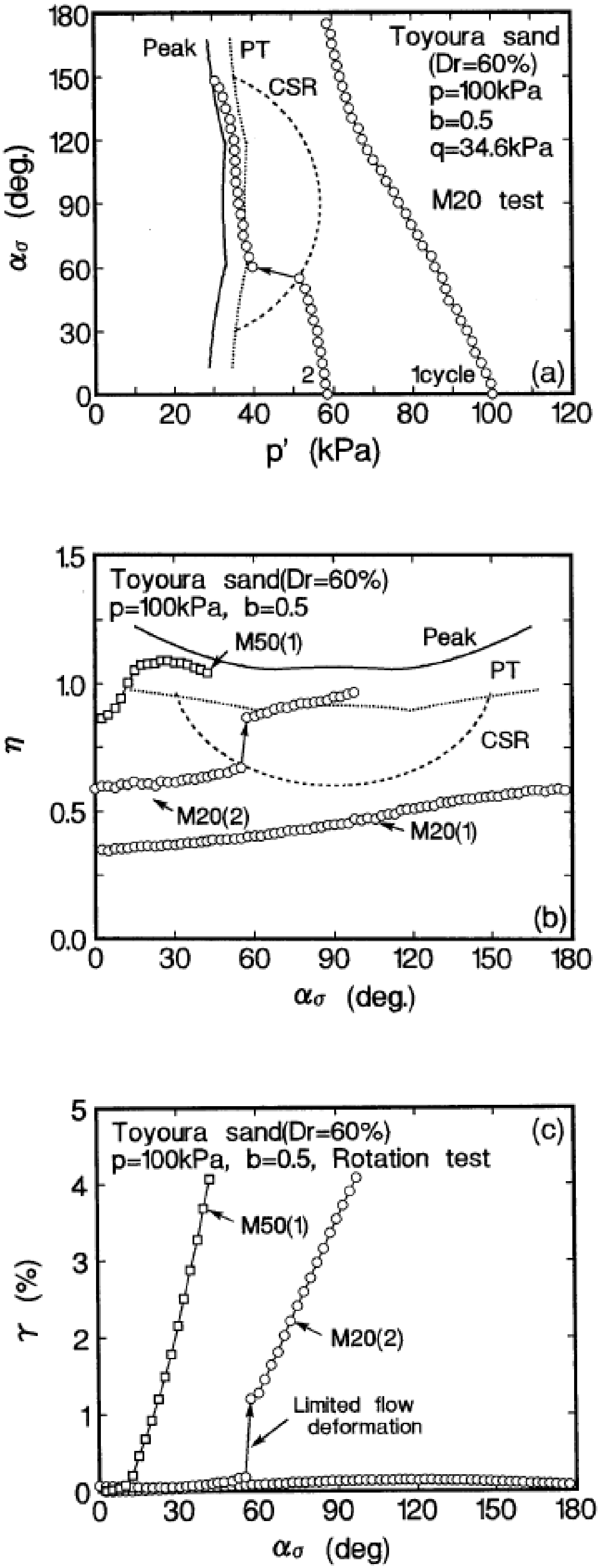

Fig. 4.58 Undrained principal stress rotation tests on the medium-dense specimens M20 and M50: **a** α - p' plot, **b** η - α plot and **c** γ - α plot (after Nakata et al. 1998)

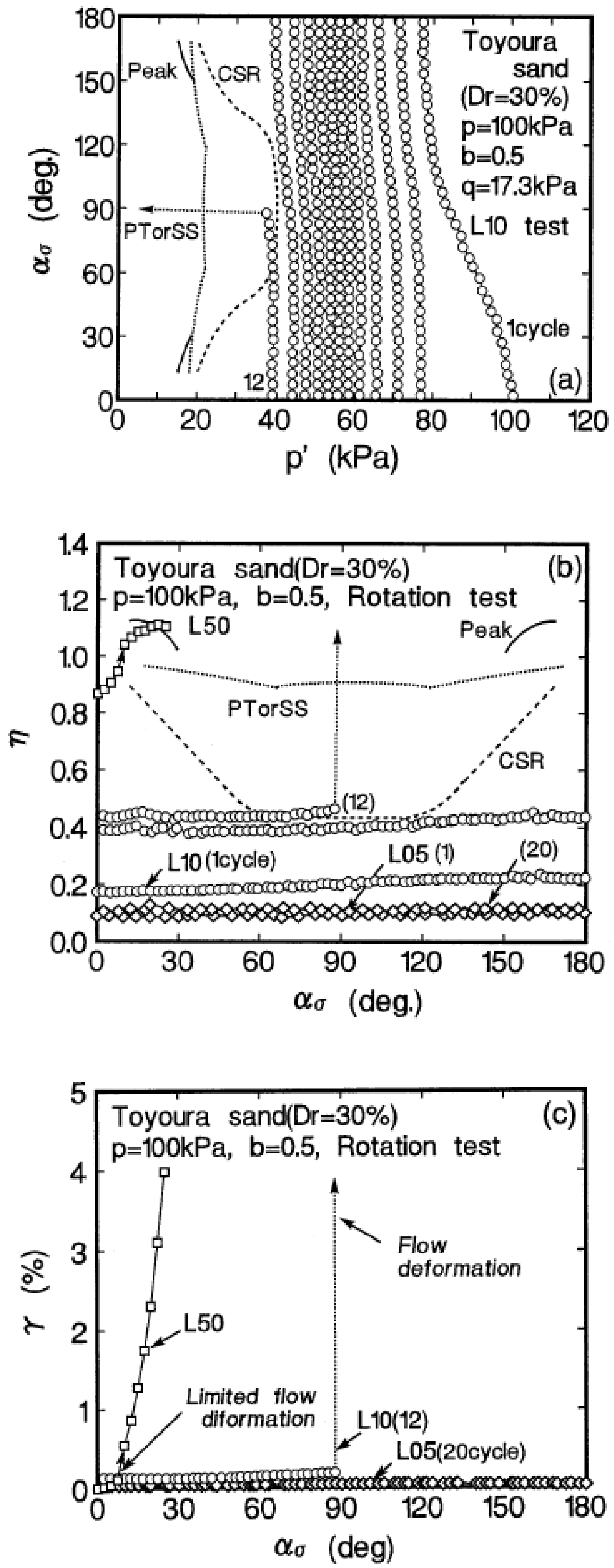

Fig. 4.59 Undrained principal stress rotation tests on the loose specimens L05, L10 and L50: **a** α - p' plot, **b** η - α plot and **c** γ - α plot (after Nakata et al. 1998)

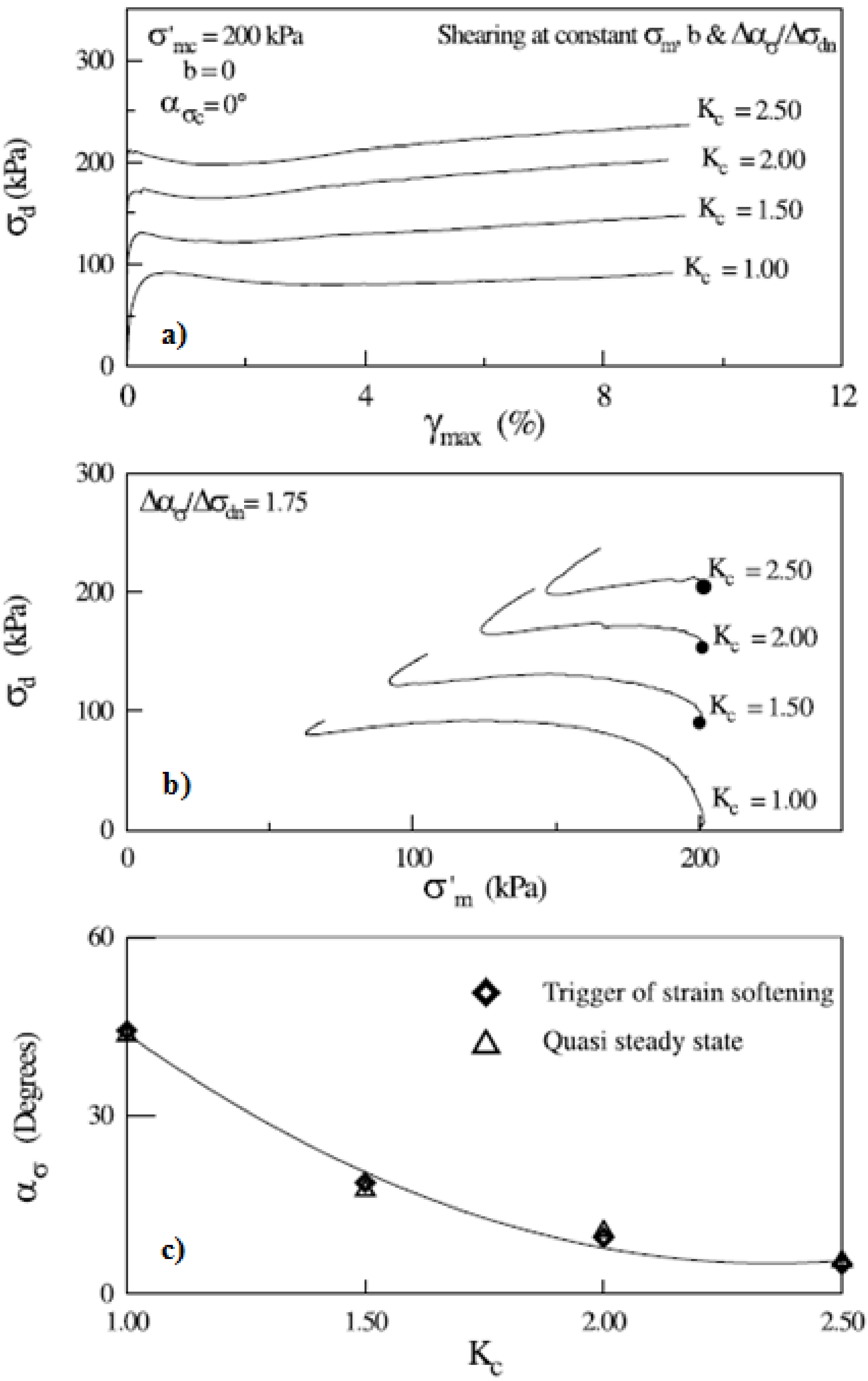

Fig. 4.60 Influence of the initial shear stress on the undrained behaviour of loose sand under loading involving principal stress rotation: **a** stress - strain curves, **b** effective stress paths and **c** value of α at the transient-peak state and quasi-steady state against K_c (after Sivathayalan and Vaid 2002)

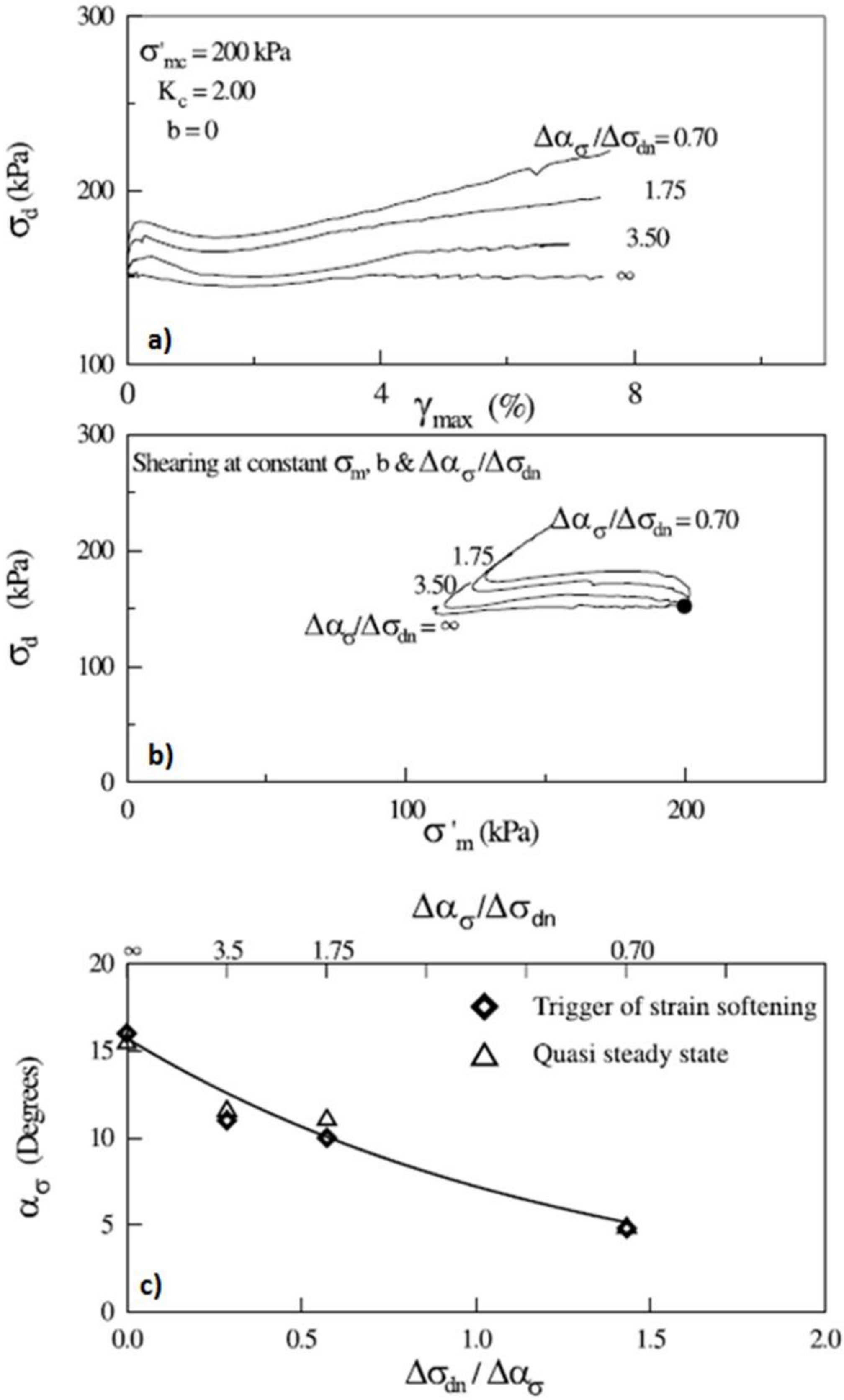

Fig. 4.61 Influence of the degree of principal stress rotation on the undrained behaviour of sand consolidated to an anisotropic, axisymmetric stress state (K_c = 2, b = 0 and α = 0°): **a** stress - strain curves, **b** effective stress paths and **c** value of α at the transient-peak state and quasi-steady state against $\Delta\alpha$ / $\Delta\sigma_{dn}$ (after Sivathayalan and Vaid 2002)

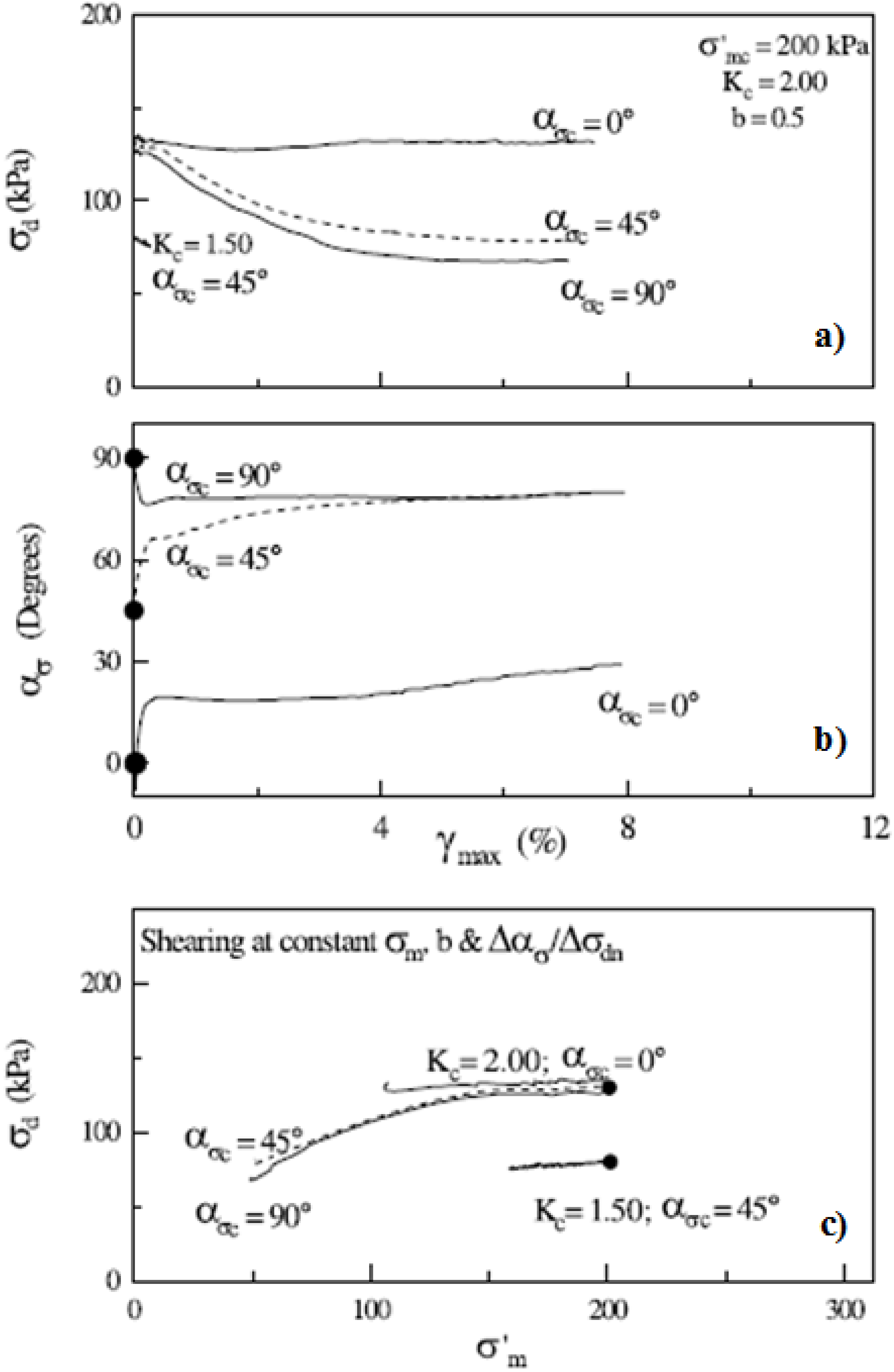

Fig. 4.62 Influence of the static shear stress and initial direction of the σ_1-axis on the undrained behaviour of sand under principal stress rotation with $\Delta\alpha$ / $\Delta\sigma_{dn} = \infty$: **a** stress - strain curves, **b** α - γ plot and **c** effective stress paths (after Sivathayalan and Vaid 2002)

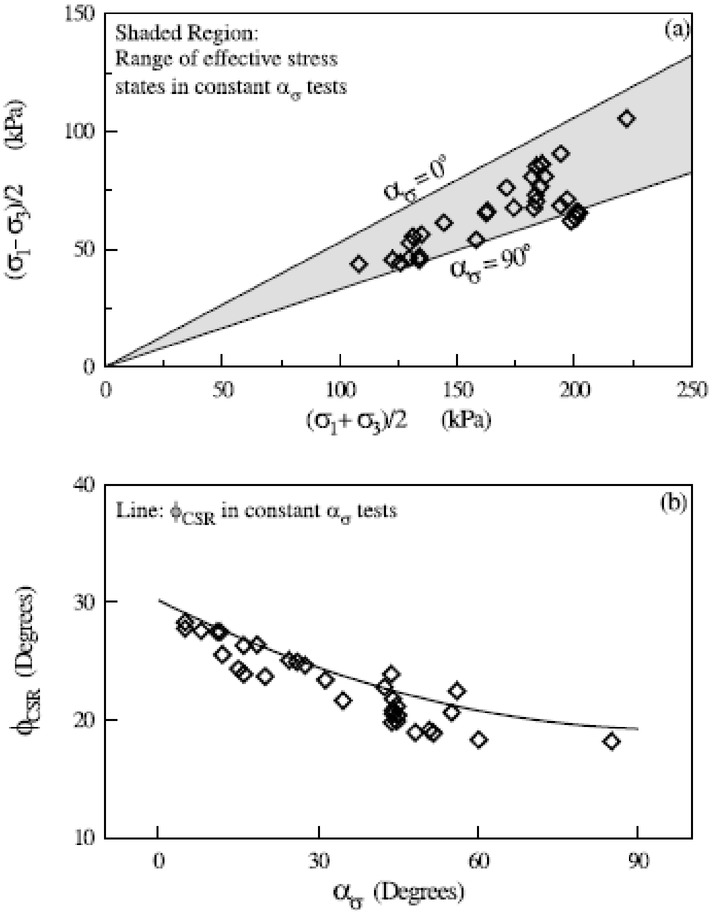

Fig. 4.63 Stress characteristics at the onset of stress unloading and flow: **a** effective stress states, **b** φ_{CSR} - α plot (after Sivathayalan and Vaid 2002)

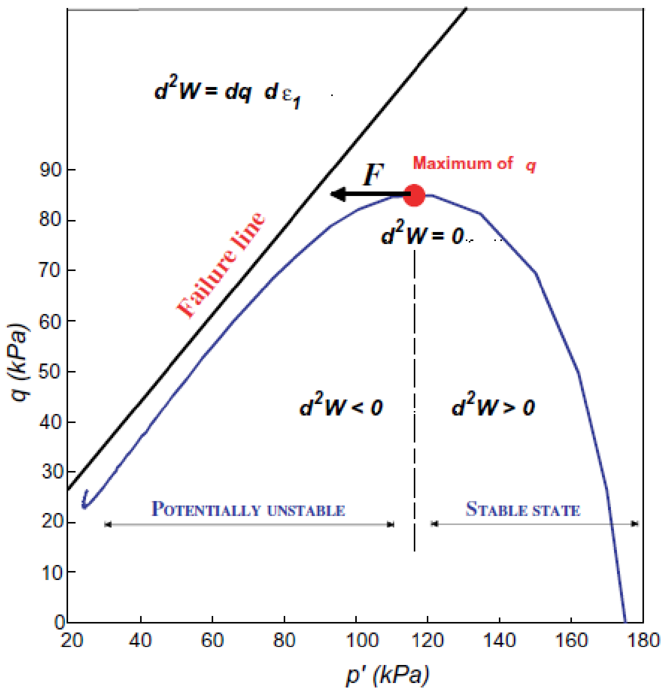

Fig. 4.64 Vanishing of the second-order work in an undrained triaxial compression test on loose saturated sand (after Darve et al. 2004)

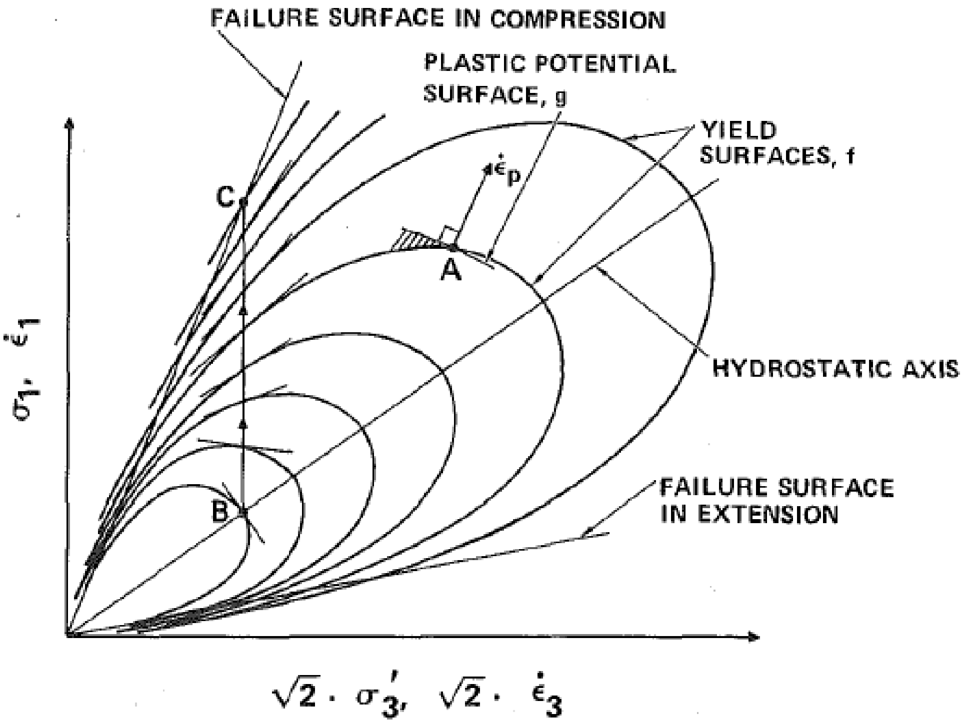

Fig. 4.65 Yield surfaces of an isotropic granular material in the Rendulic plane. BC is the stress path of a drained triaxial compression test (after Lade et al. 1988)

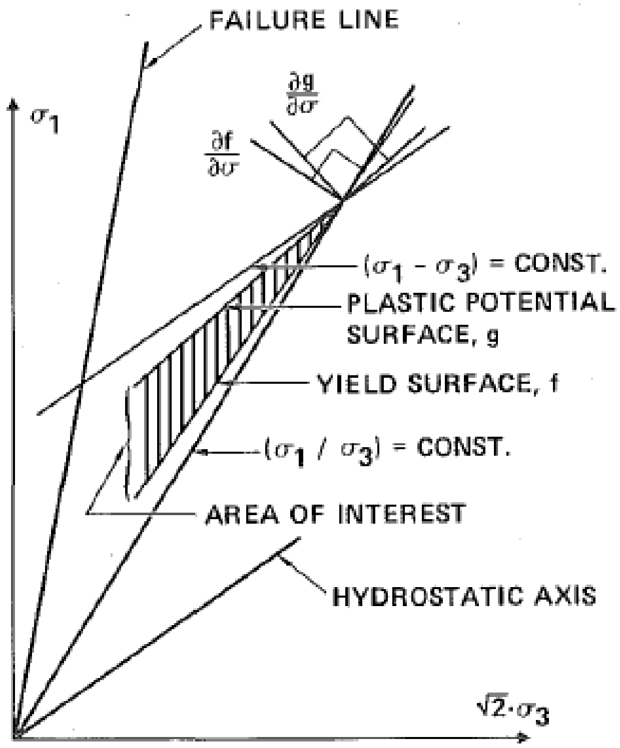

Fig. 4.66 The wedge formed between the yield surface and plastic potential surface of a granular material with non-associative flow characteristics. Stress paths with decreasing effective stresses move through this particular wedge (after Lade et al. 1988)

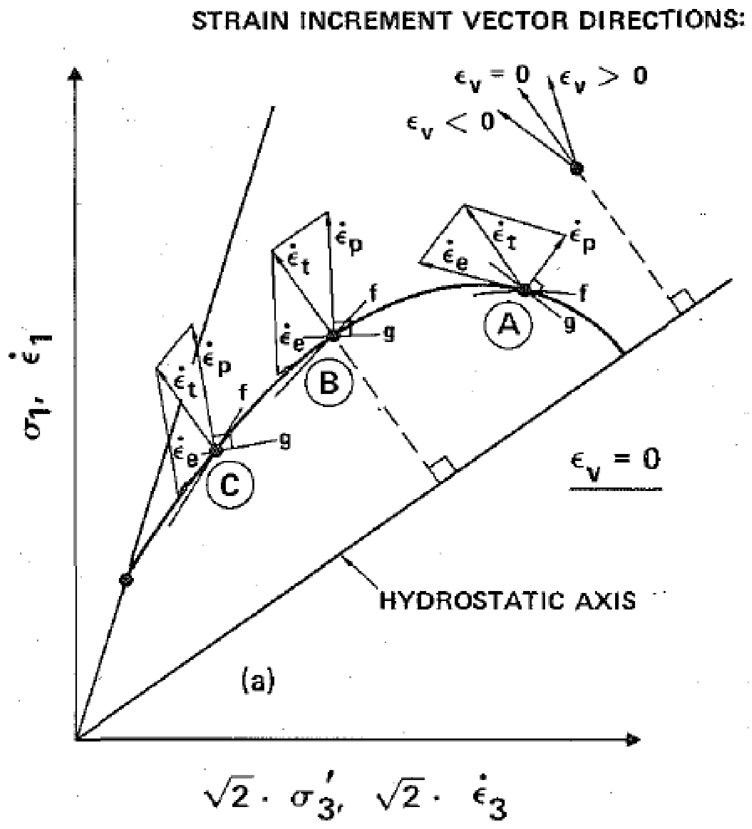

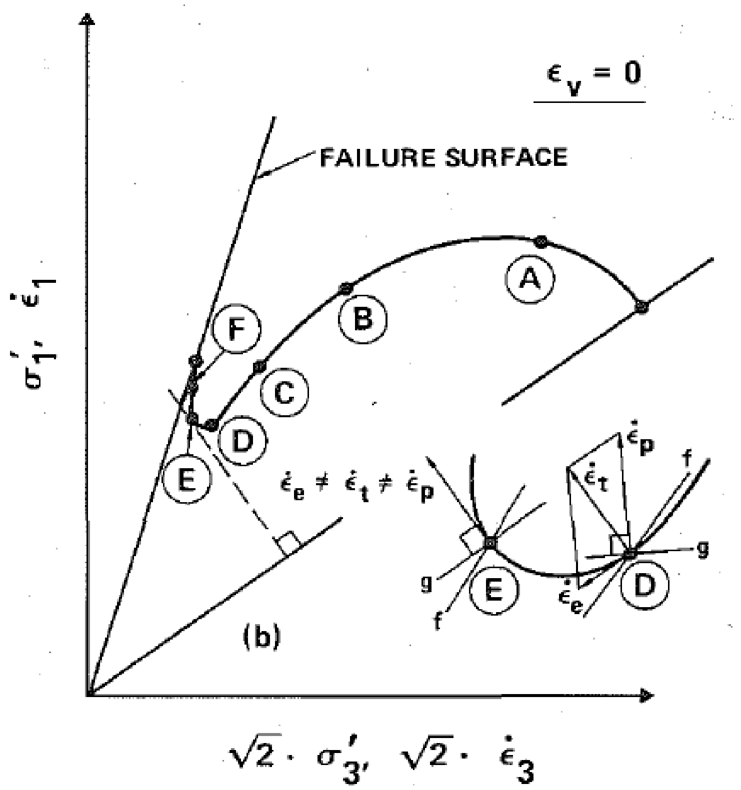

Fig. 4.67 Typical response of sand to undrained triaxial compression: **a** unstable response, **b** temporarily unstable response (after Lade et al. 1988) (to be continued in the next page)

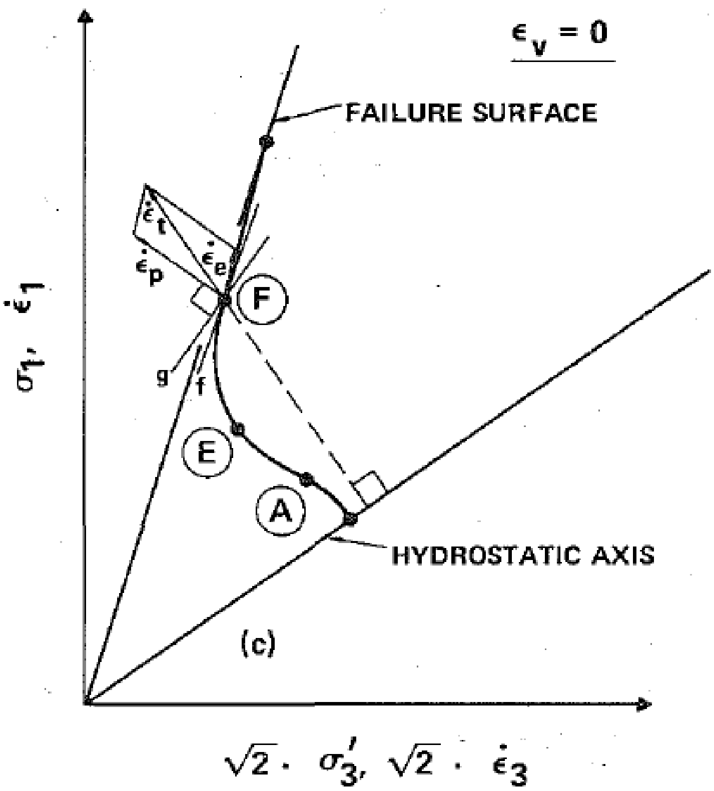

Fig. 4.67 Typical response of sand to undrained triaxial compression: **c** stable response (after Lade et al. 1988) (**a** and **b** in the previous page)

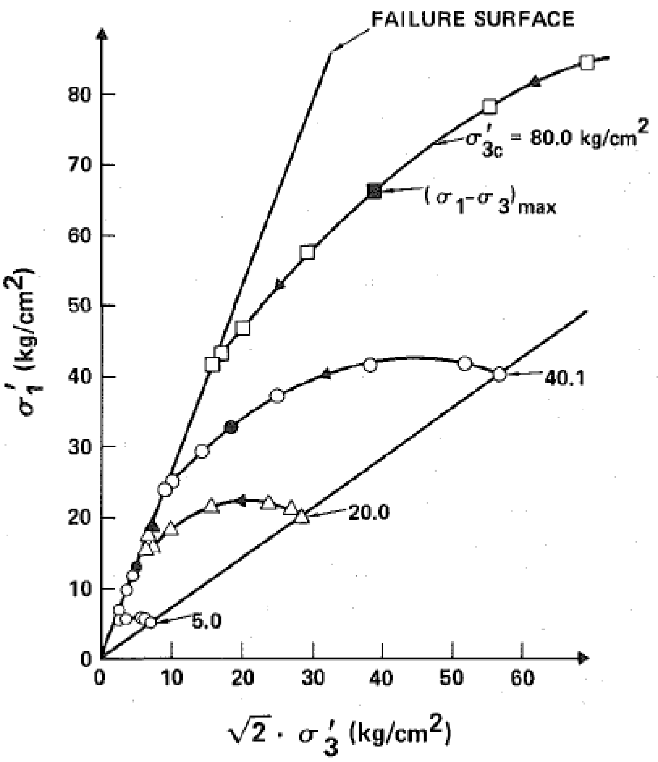

Fig. 4.68 States of maximum stress difference $(\sigma_1 - \sigma_3)_{max}$ in the Rendulic plane (after Lade et al. 1988)

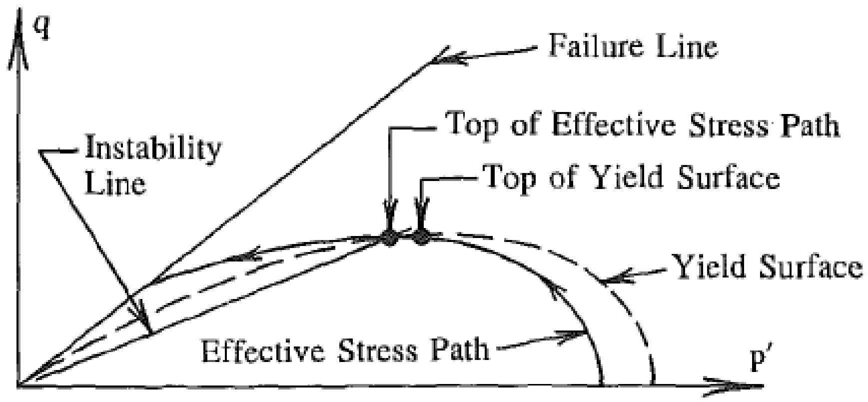

Fig. 4.69 Definition of Lade's Instability Line in the *q* - *p'* plane (after Lade et al. 1992)

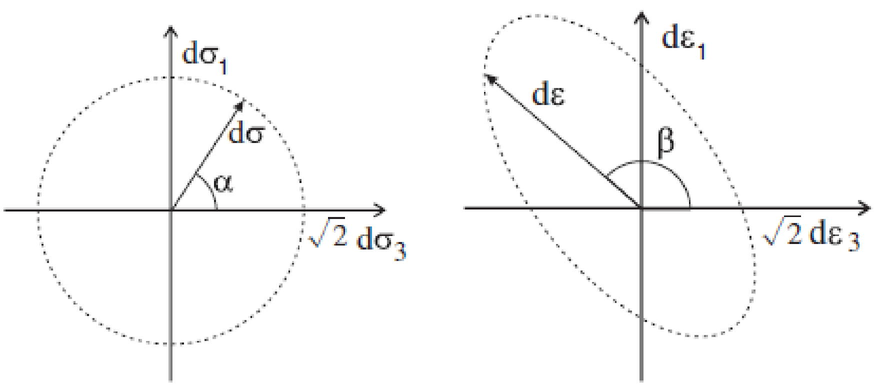

Fig. 4.70 Gudehus' directional analysis in the Rendulic plane (after Sibille et al. 2007)

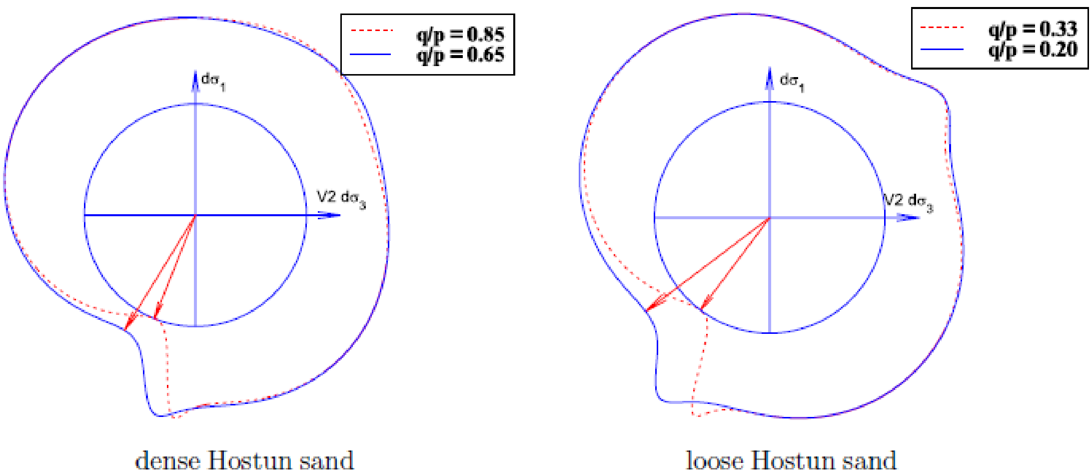

Fig. 4.71 Circular presentation of the normalised second-order work, for dense and loose Hostun Sand, determined by means of axisymmetric stress probing at different stress ratios $\eta = q / p'$ using the incrementally non-linear constitutive model of Darve (data after Darve and Laouafa 2000; Figure after Sibille et al. 2007)

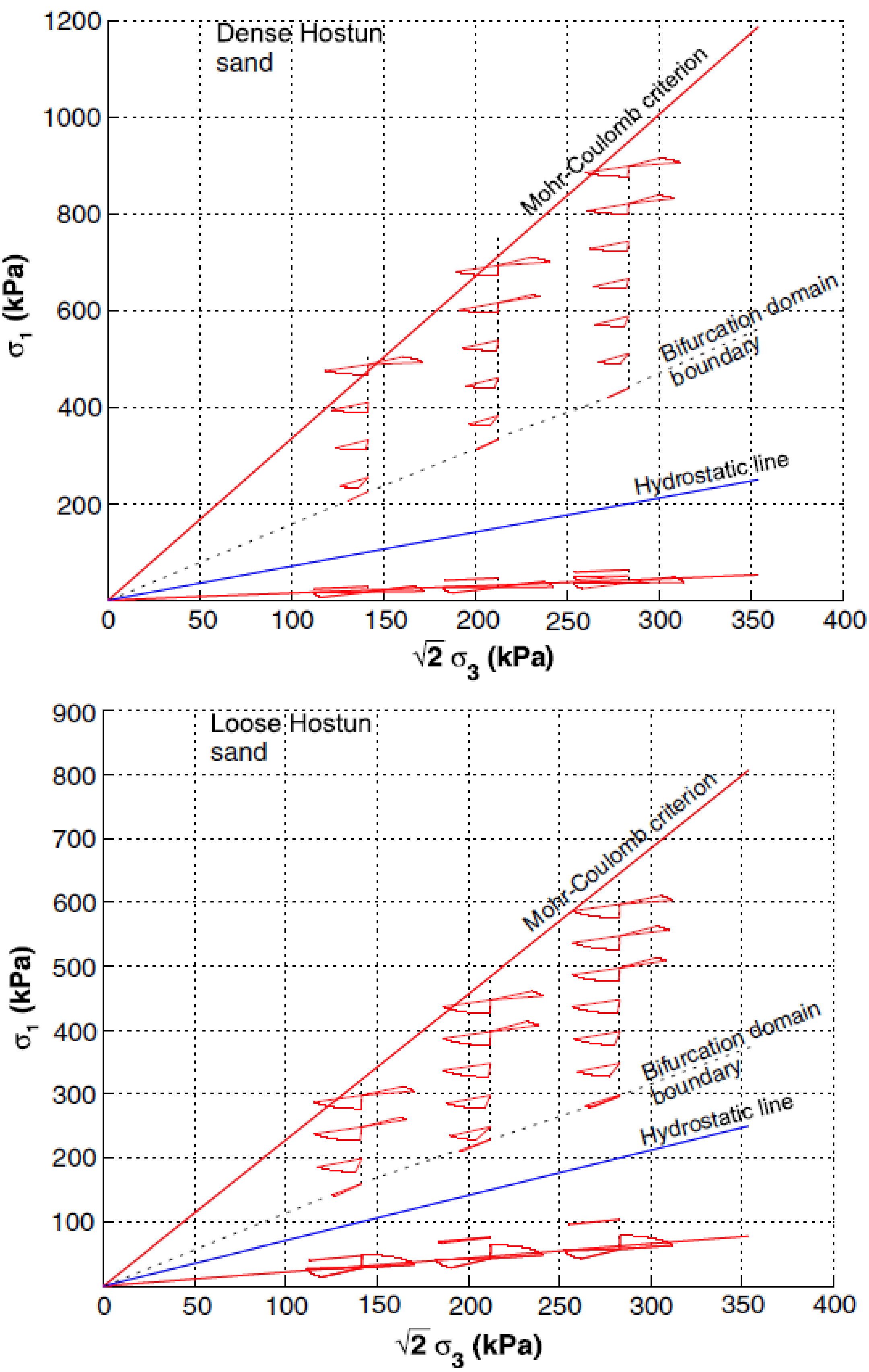

Fig. 4.72 Cones of unstable stress directions and boundaries of the bifurcation domain in the Rendulic stress plane, determined using the incrementally non-linear constitutive model of Darve (data after Darve et al. 2004; Figure after Sibille et al. 2007)

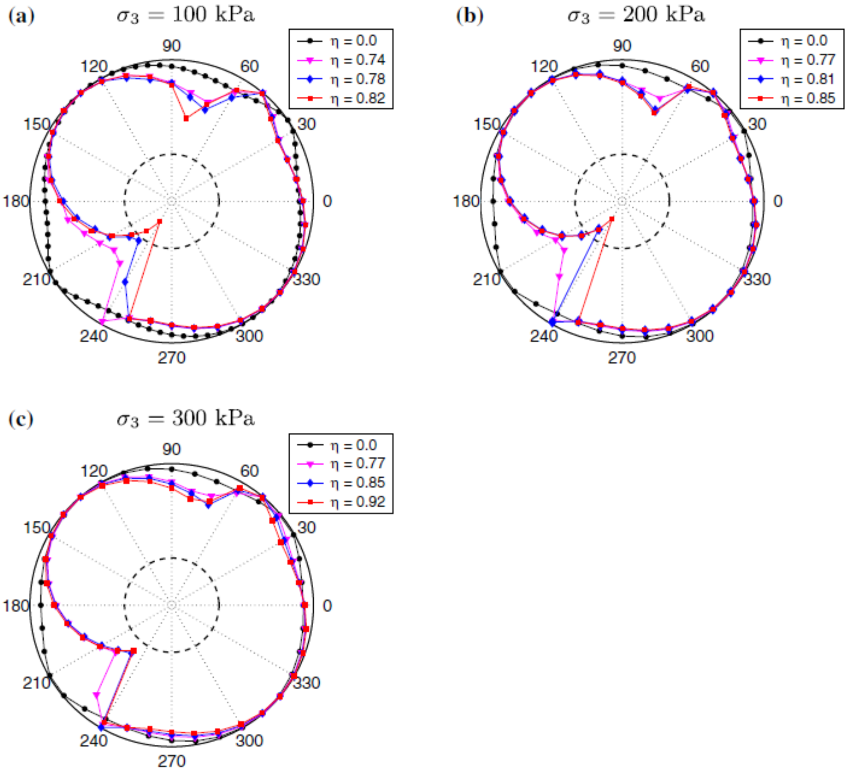

Fig. 4.73 Circular presentation of the normalised second-order work, for the densest virtual specimen, determined by means of axisymmetric stress probing at different stress ratios, $\eta = q / p'$, and confining stresses, σ'_3, using the discrete element method (after Sibille et al. 2008)

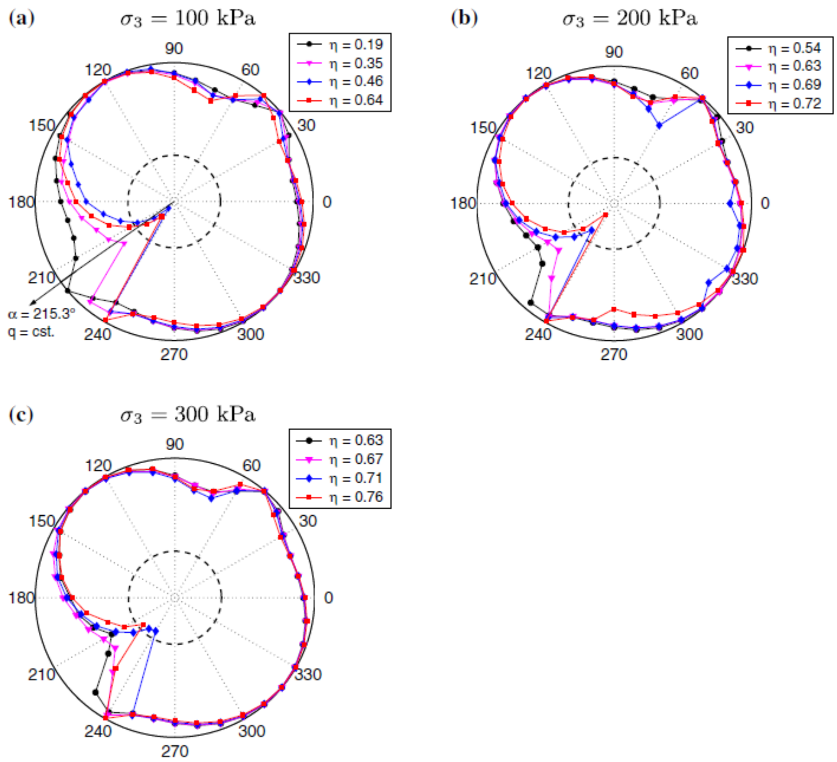

Fig. 4.74 Circular presentation of the normalised second-order work, for the loosest virtual specimen, determined by means of axisymmetric stress probing at different stress ratios, $\eta = q / p'$, and confining stresses, σ'_3, using the discrete element method (after Sibille et al. 2008)

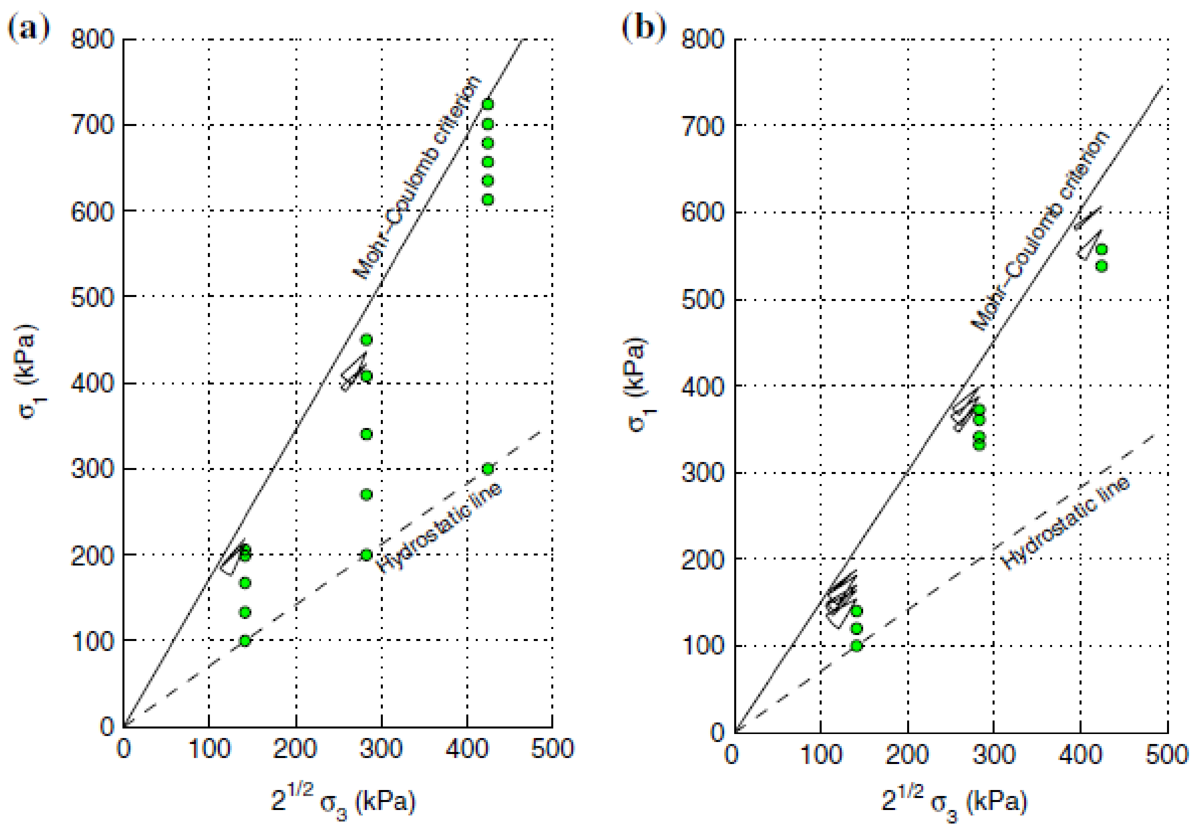

Fig. 4.75 Cones of unstable stress directions, at various stress states in the Rendulic plane, determined in the DEM simulations of the response of a granular material (densest in **a** and loosest in **b**) to stress probing. The solid circles correspond to stress states at which the value of the normalised second-order work remained positive for the stress probes imposed (after Sibille et al. 2008)

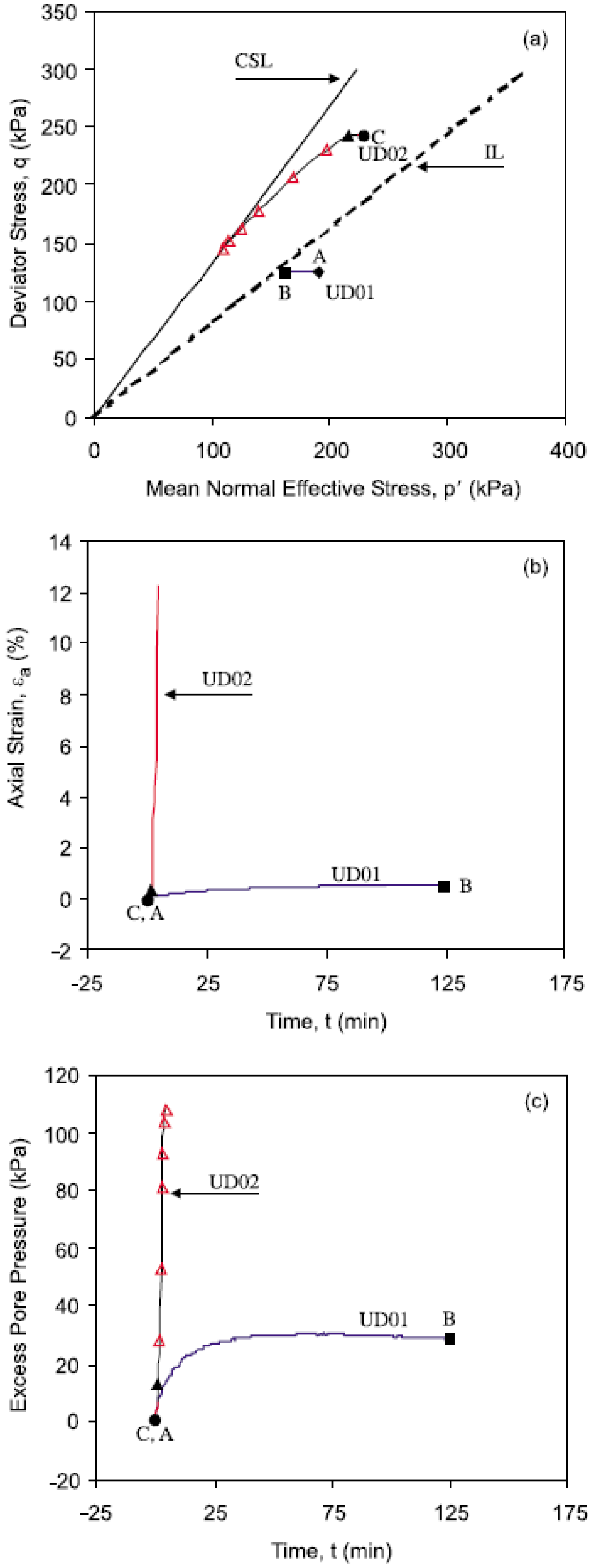

Fig. 4.76 Sustainability of the undrained axisymmetric stress state of two loose sand specimens under the stationary condition of dq = 0 and dε_{vol} = 0. The specimens were previously subjected to drained triaxial compression up to different levels of stress ratio (after Chu et al. 2003)

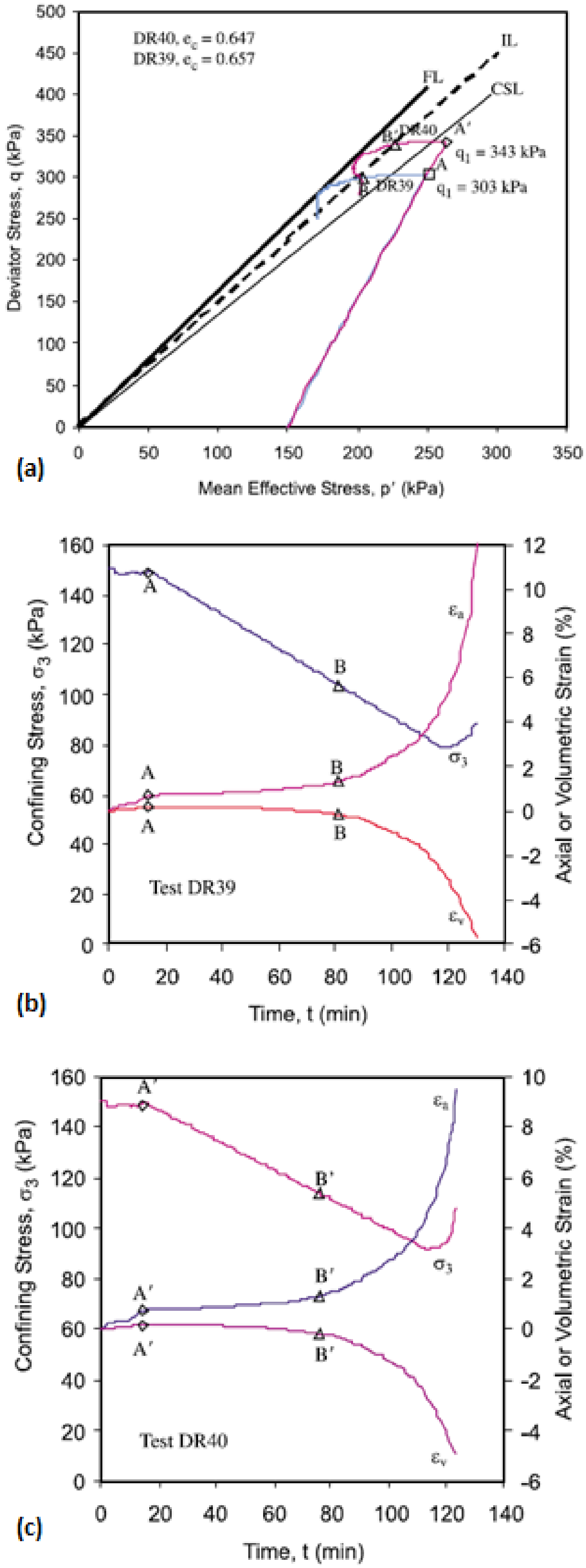

Fig. 4.77 Drained axisymmetric constant-q loading tests performed on two dense sand specimens. **a** Effective stress paths in the q - p' space. **b** Evolution of effective confining stress and strains in time, during test DR39. **c** Evolution of effective confining stress and strains in time, during test DR40 (after Chu et al. 2003)

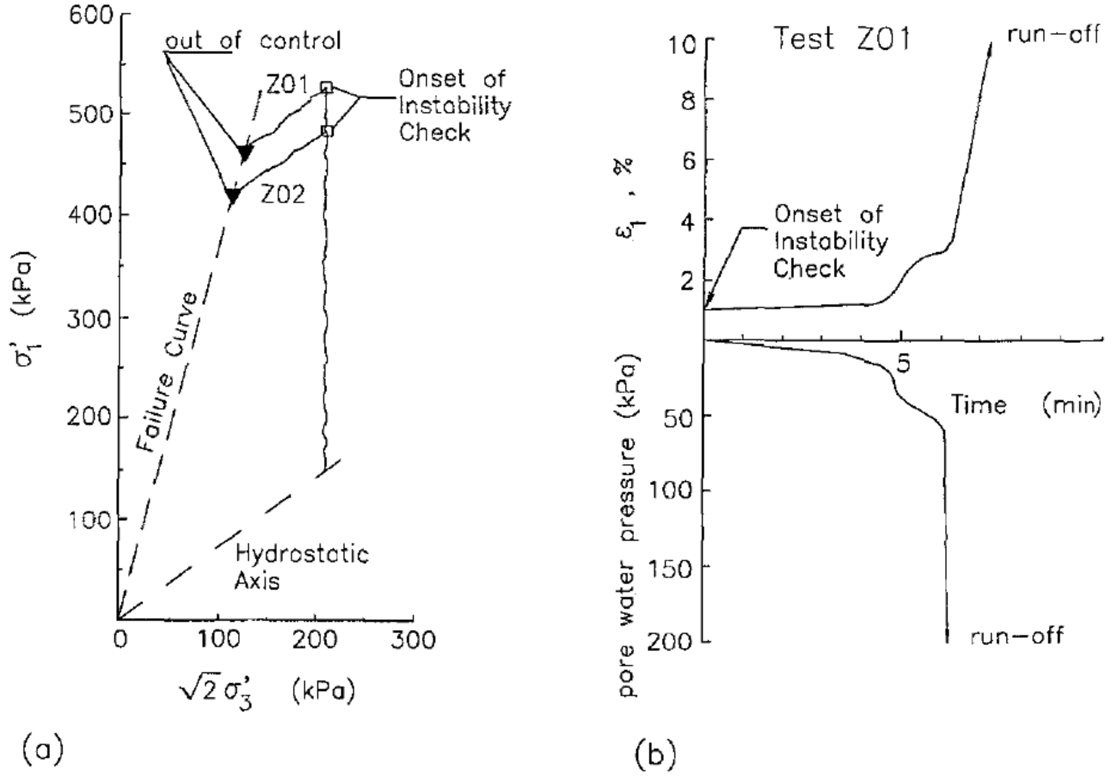

Fig. 4.78 Axisymmetric strain probing along the direction $d\varepsilon_v / d\varepsilon_1 = -0.67$ performed in tests on two dense sand specimens. **a** Effective stress paths in the Rendulic plane. **b** Evolution of principal strain ε_1 and pore-water pressure u in time, during test Z01 (after Chu et al. 1993)

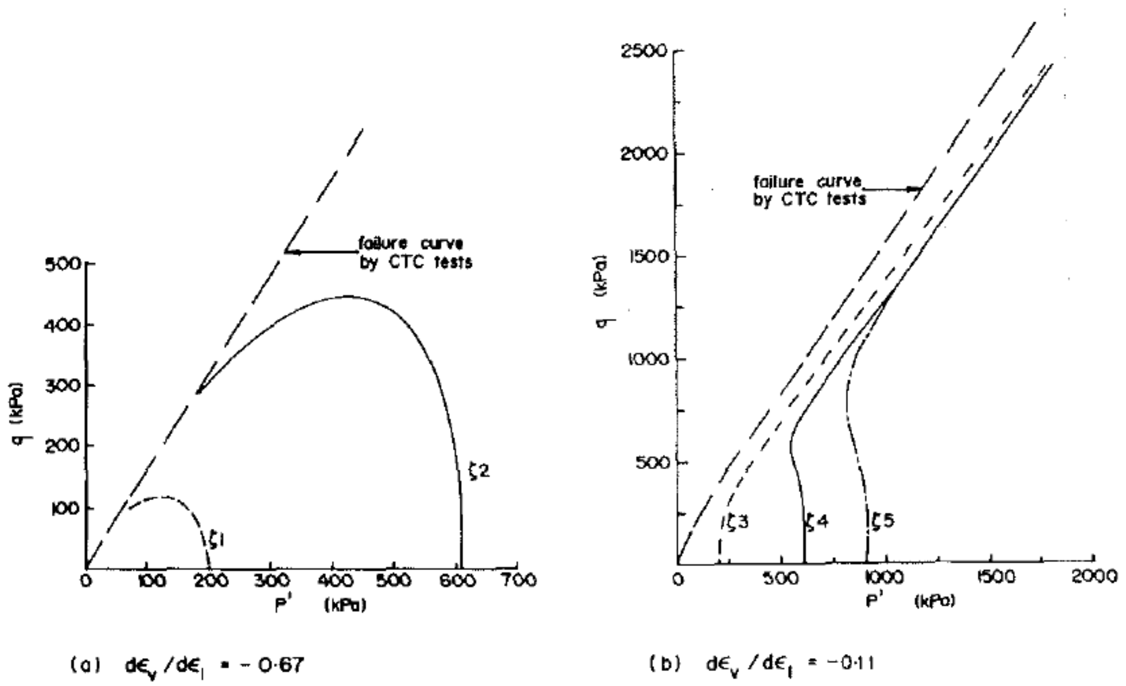

Fig. 4.79 Effective stress paths in the q - p' plane of axisymmetric strain-path tests on dense sand specimens along different incremental strain directions, $d\varepsilon_v / d\varepsilon_1$, and at different initial mean effective stresses. **a** Tests with $d\varepsilon_v / d\varepsilon_1 = -0.67$. **b** Tests with $d\varepsilon_v / d\varepsilon_1 = -0.11$. CTC stands for conventional triaxial compression (after Chu et al. 1992)

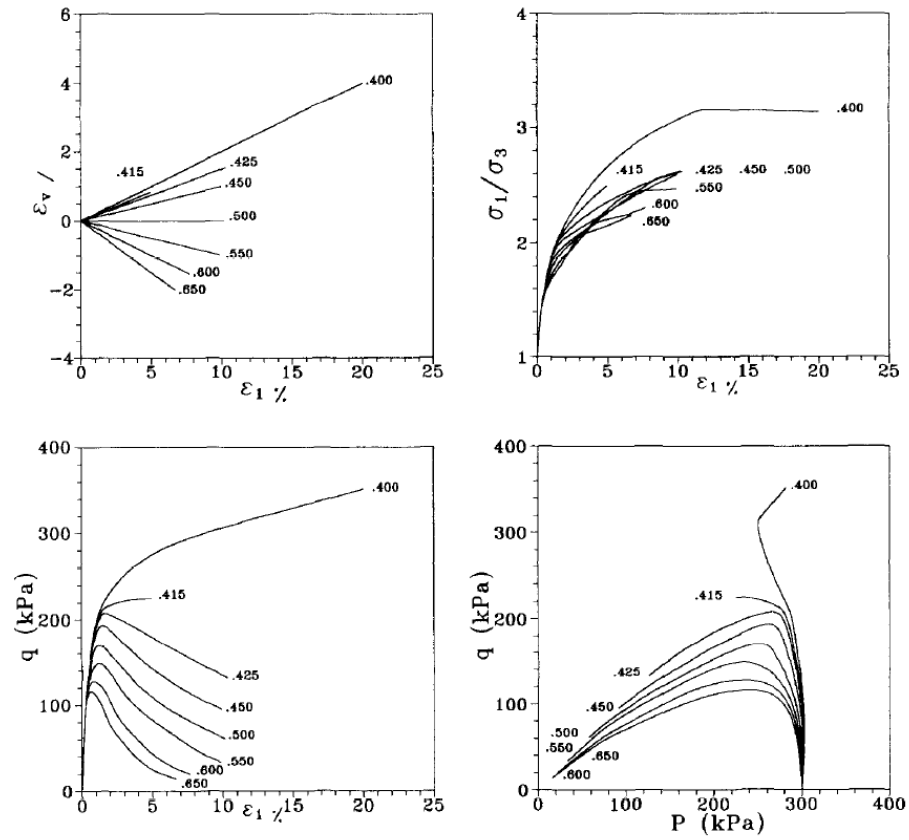

Fig. 4.80 Results of the numerical strain-path tests using the incrementally non-linear constitutive model of Darve. The labels on the curves indicate the value of the ratio $R = -d\varepsilon_3 / d\varepsilon_1$ (after Darve et al. 1995)

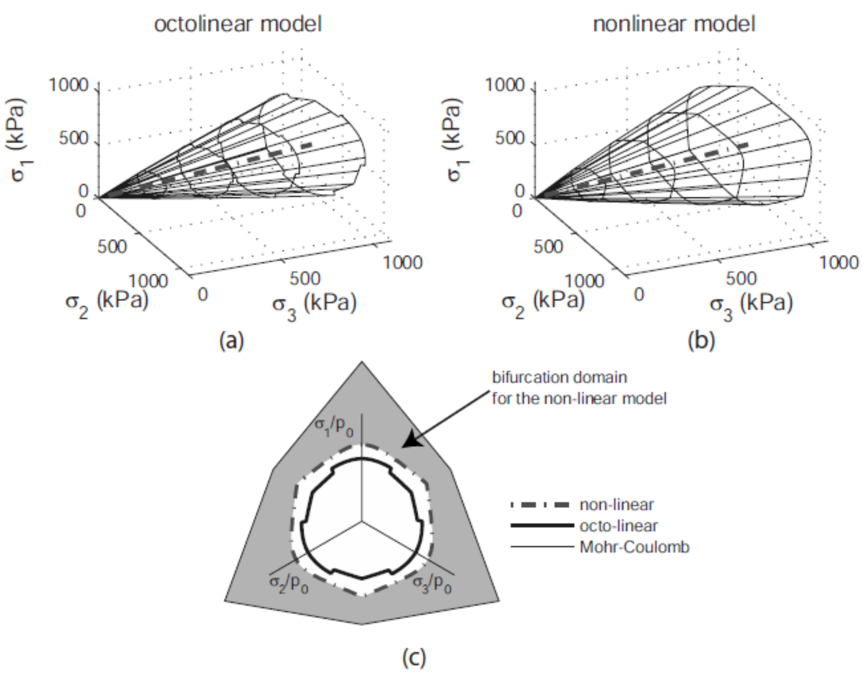

Fig. 4.81 Bifurcation domain in the principal stress space, determined using the octolinear (**a**) and nonlinear (**b**) model of Darve, calibrated to simulate the response of dense Hostun Sand (after Prunier et al. 2009)

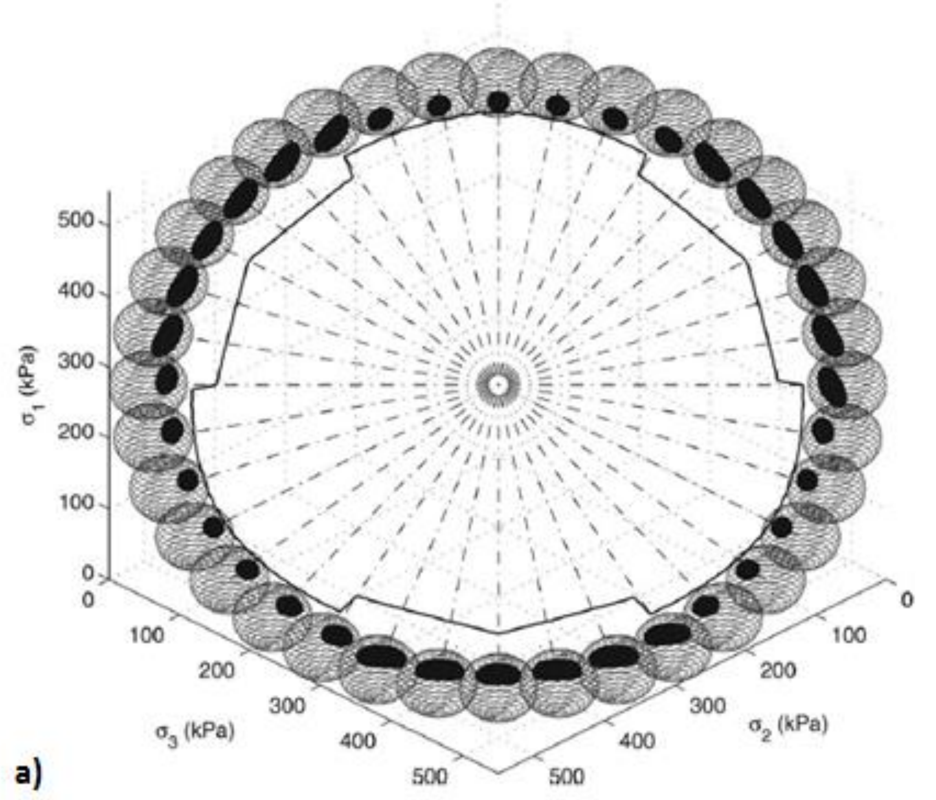

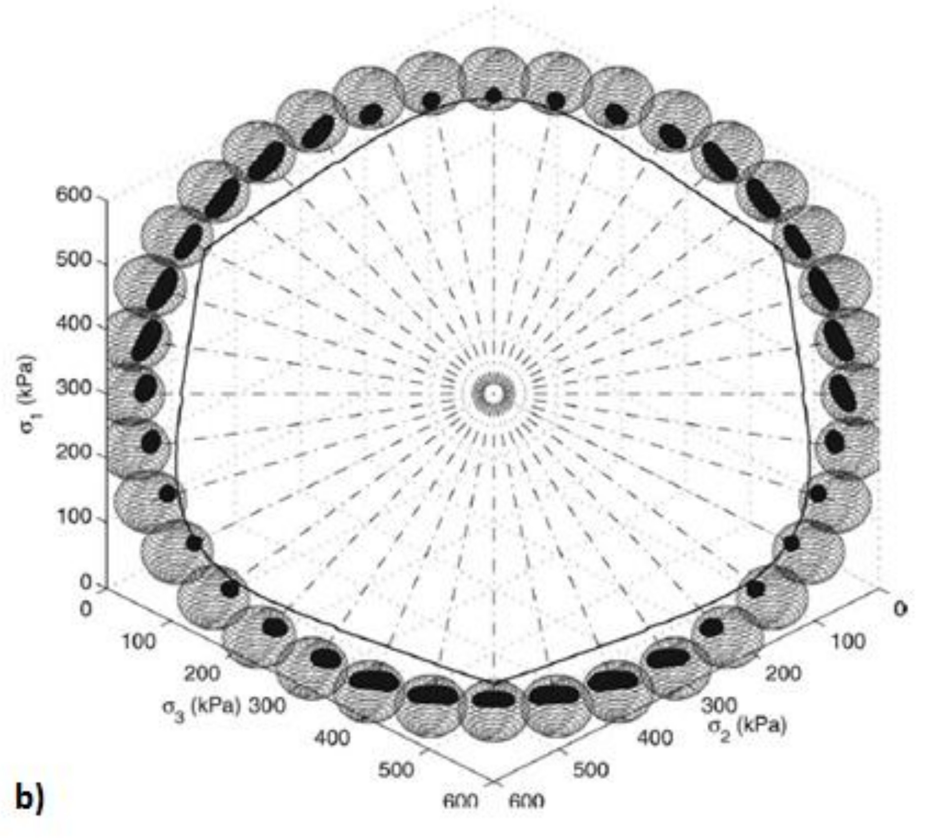

Fig. 4.82 3D cones of unstable stress directions determined after radial loading in the deviatoric plane using the octolinear (**a**) and nonlinear (**b**) model of Darve (after Prunier et al. 2009)

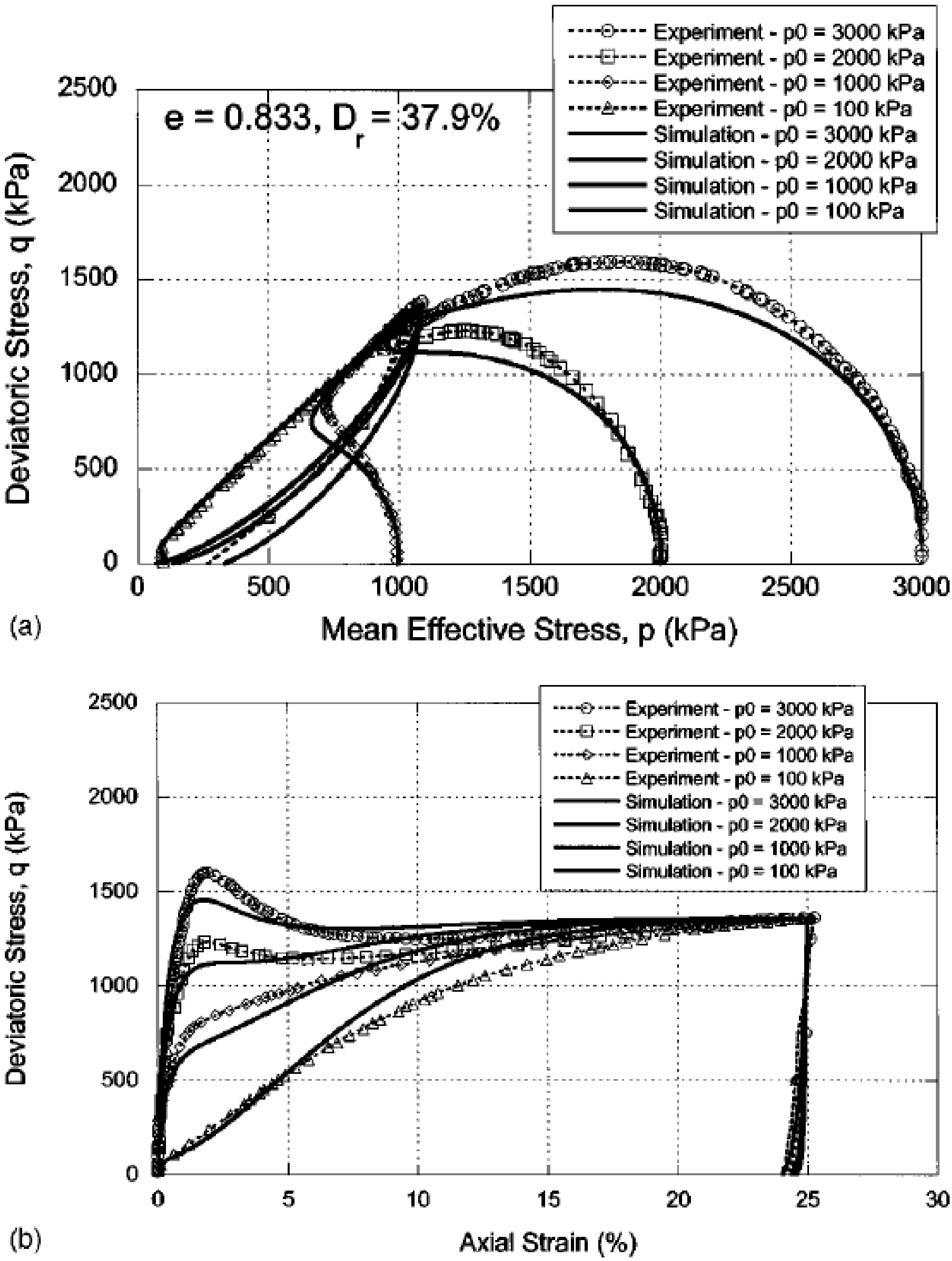

Fig. 4.83 Simulations of the undrained triaxial compression tests on Toyoura Sand. **a** Effective stress paths in the q - p' space. **b** Stress - strain curves. The physical experiments were performed by Verdugo and Ishihara (1996), while the simulations of these tests were performed by Dafalias and Manzari (2004) (figure after Dafalias and Manzari 2004; experimental data after Verdugo and Ishihara 1996)

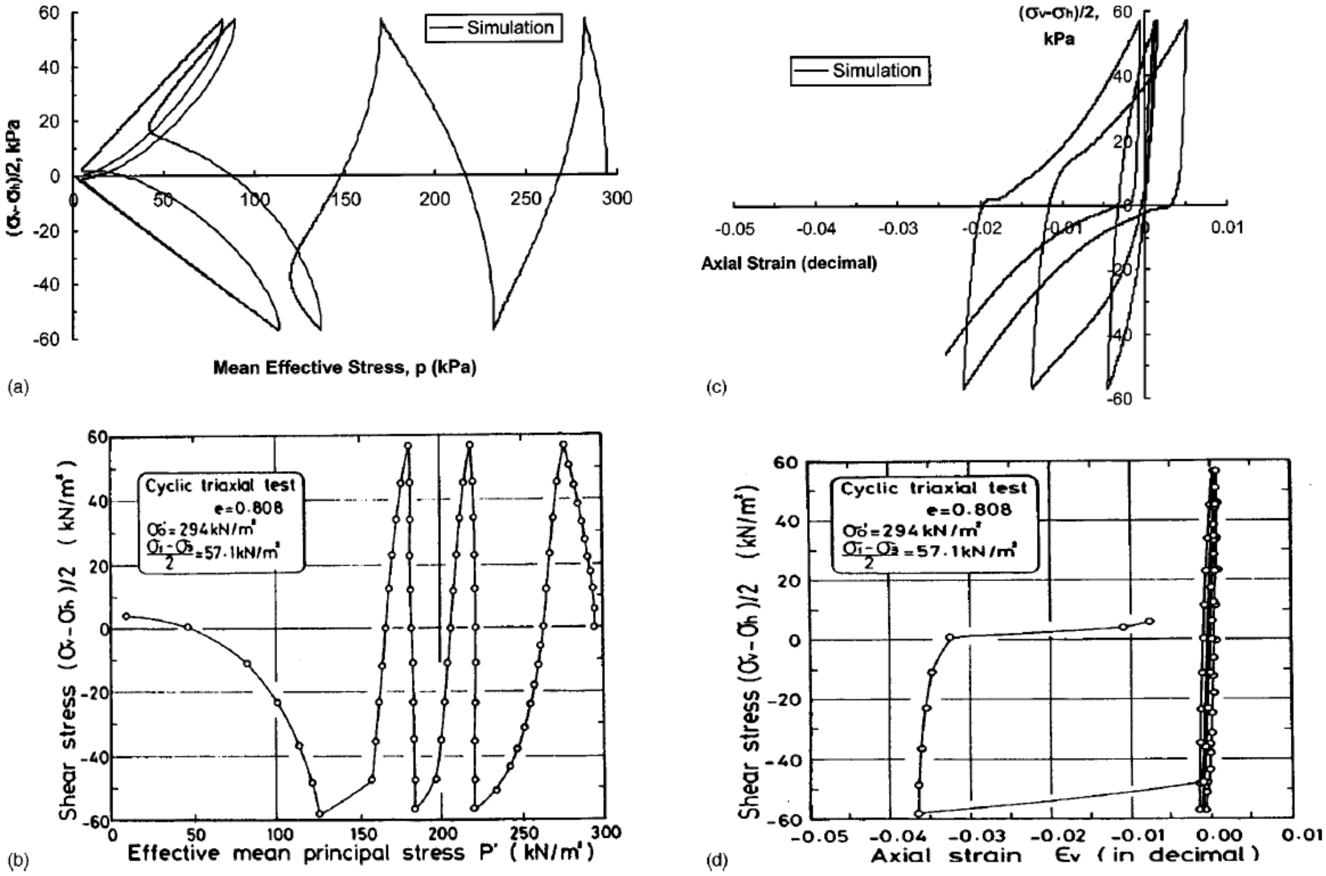

Fig. 4.84 Simulations of the cyclic undrained triaxial tests on Toyoura Sand. **a** and **b** Effective stress paths in the *t* - *p'* space. **c** and **d** Stress - strain curves. The physical experiments were performed by Ishihara et al. (1975), while the simulations of these tests were performed by Dafalias and Manzari (2004) (figure after Dafalias and Manzari 2004; experimental data after Ishihara et al. 1975)

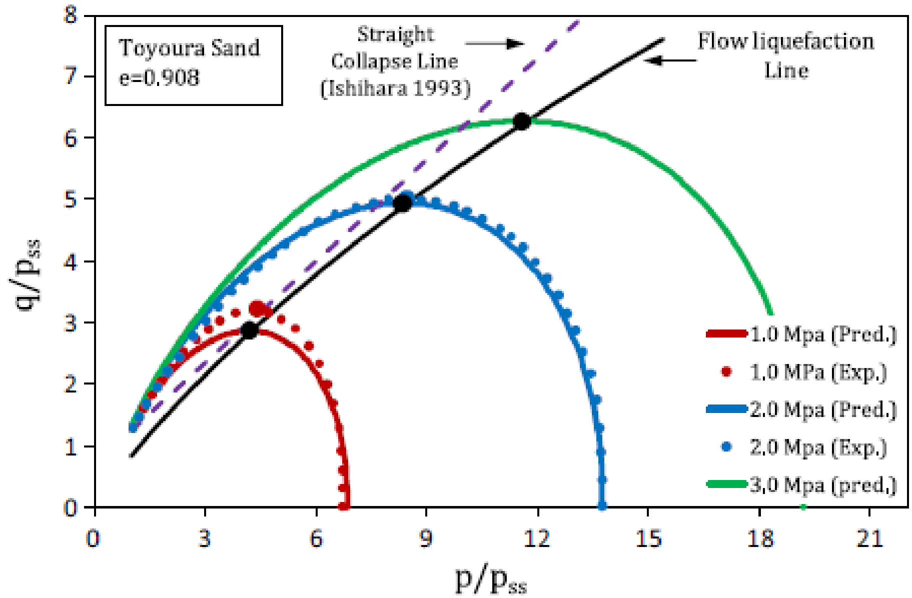

Fig. 4.85 Physical undrained triaxial compression tests on Toyoura Sand and simulations (figure after Najma and Latifi 2017; experimental data after Ishihara 1993)

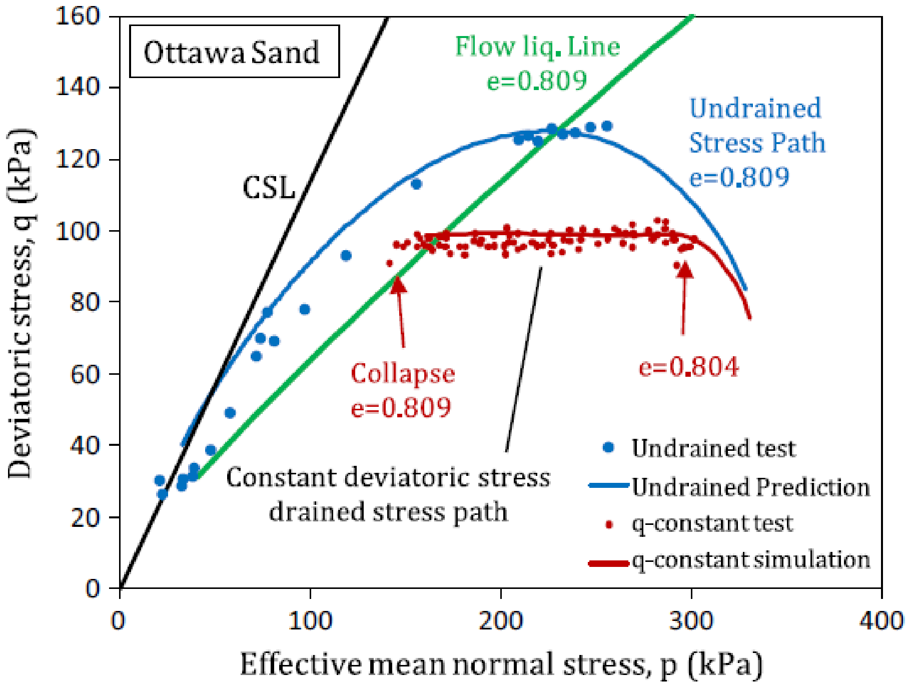

Fig. 4.86 Physical drained constant-*q* loading test on saturated Ottawa Sand and simulation of this test (figure after Najma and Latifi 2017; experimental data after Sassitharan et al. 1993)

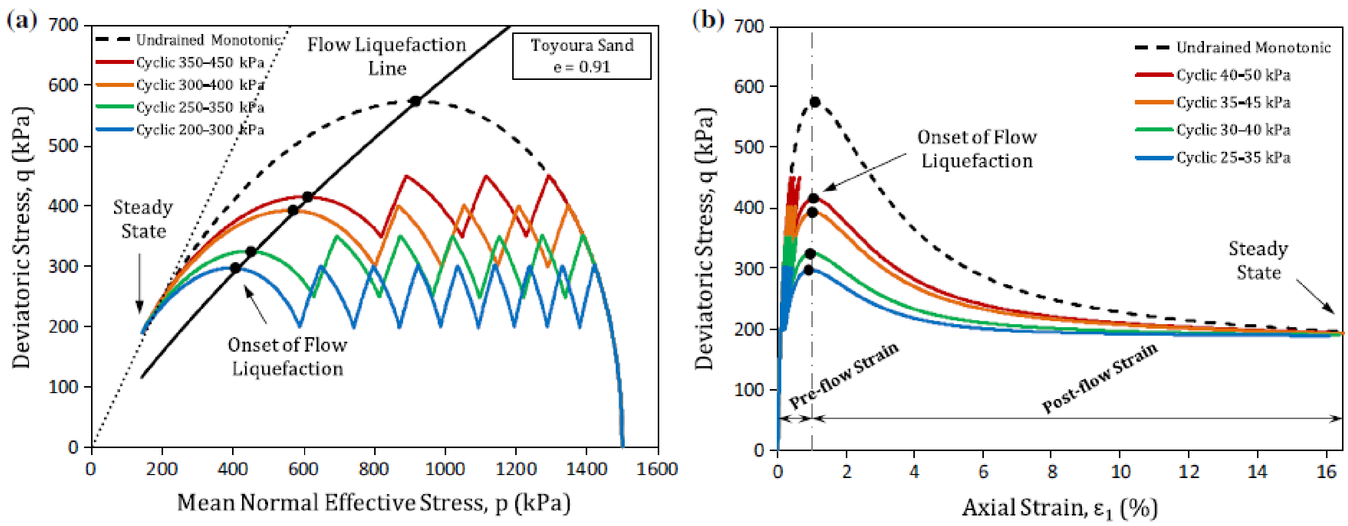

Fig. 4.87 Simulations of cyclic undrained triaxial tests on Toyoura Sand (after Najma and Latifi 2017)

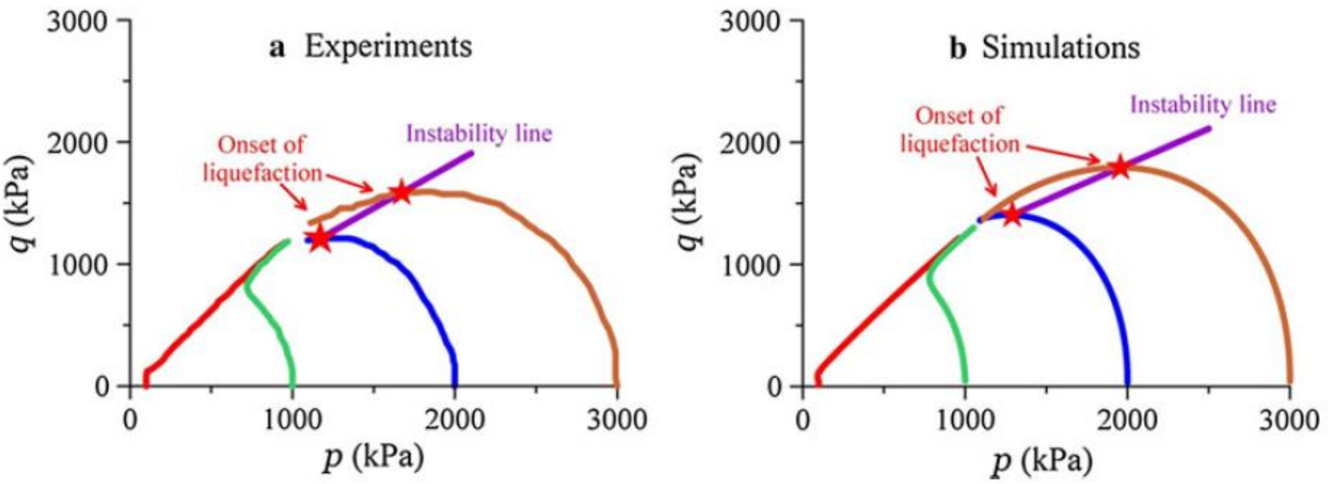

Fig. 4.88 a Undrained triaxial compression tests on Toyoura Sand with e = 0.833, performed by Verdugo and Ishihara (1996). **b** Simulations of Verdugo-Ishihara's tests performed by Andrade et al. (2013) using the model of Dafalias and Manzari (2004) (figure after Andrade et al. 2013; experimental data after Verdugo and Ishihara 1996)

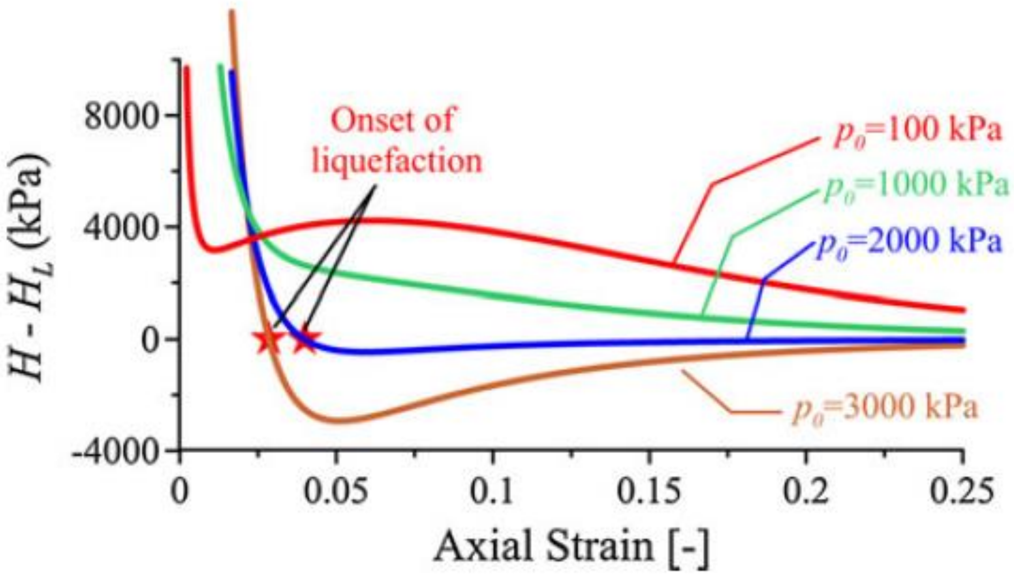

Fig. 4.89 Evolution of the difference of the hardening modulus from the critical hardening modulus in the simulations of Verdugo-Ishihara's undrained triaxial compression tests (after Andrade et al. 2013)

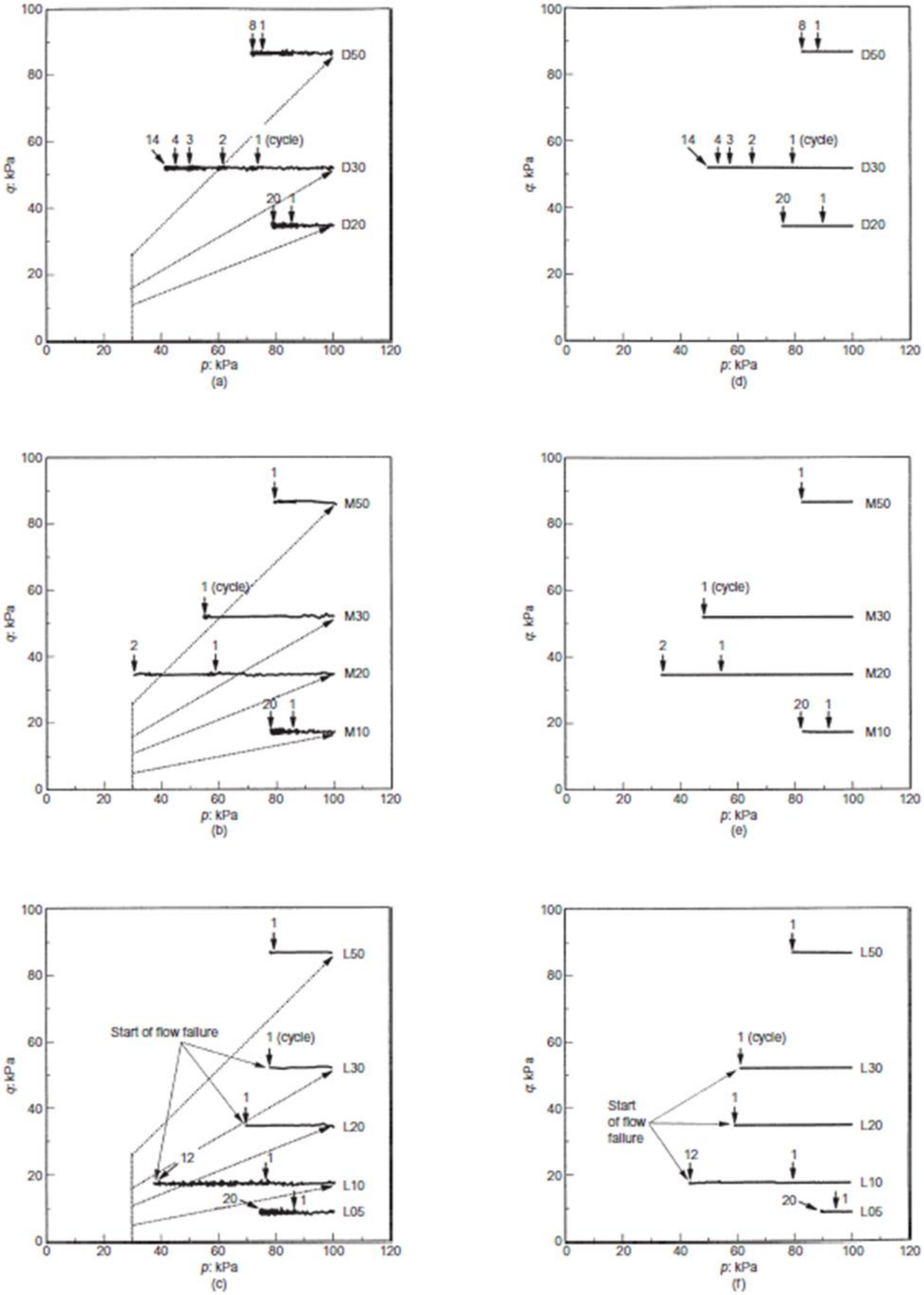

Fig. 4.89 Effective stress paths in the *q* - *p'* plane of the undrained loading tests imposing rotation of the stress principal axes at constant *q* and *b* = 0.5, performed by Nakata et al. (1998) (**a** to **c**) and simulations of these tests performed by Li and Dafalias (2004) (**d** to **f**). **a** and **d** D_r = 90%; **b** and **e** D_r = 60; **c** and **f** D_r = 30% (figure after Li and Dafalias 2004; data after Nakata et al. 1998)

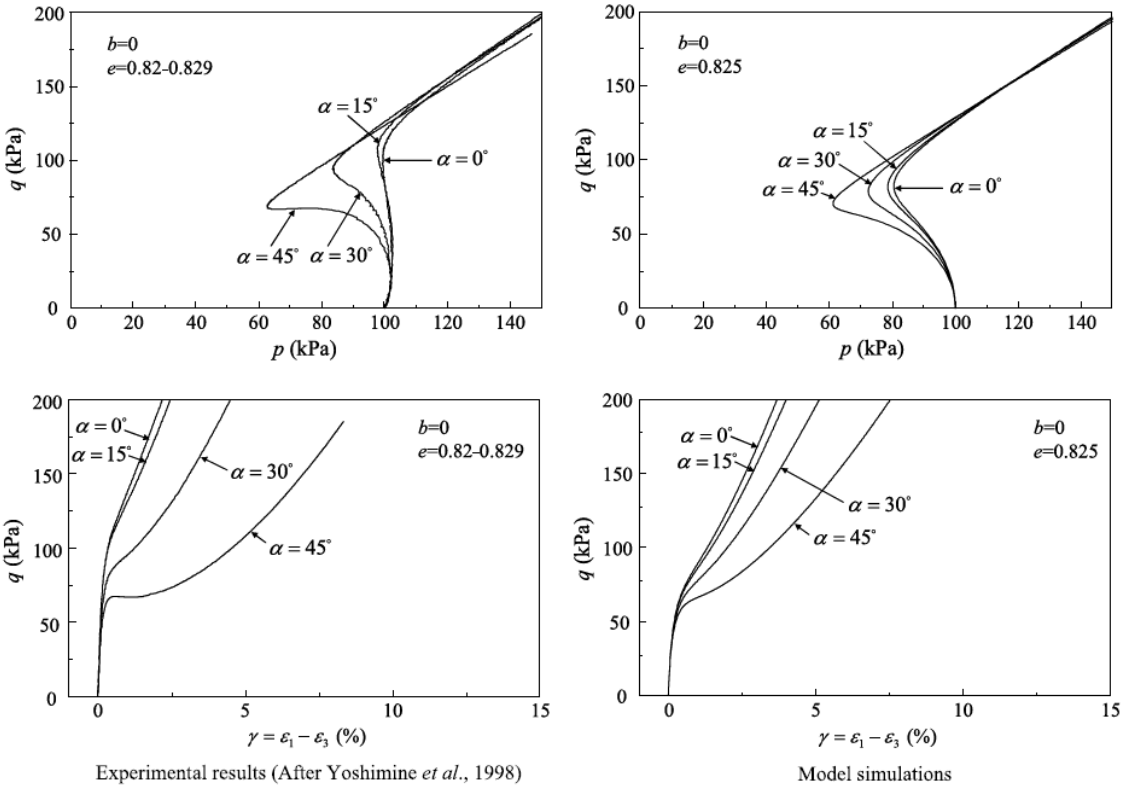

Fig. 4.90 Results of undrained loading tests on anisotropic sand at b = 0 and different values of α and simulations of these tests (figure after Li and Dafalias 2012; data after Yoshimine et al. 1998)

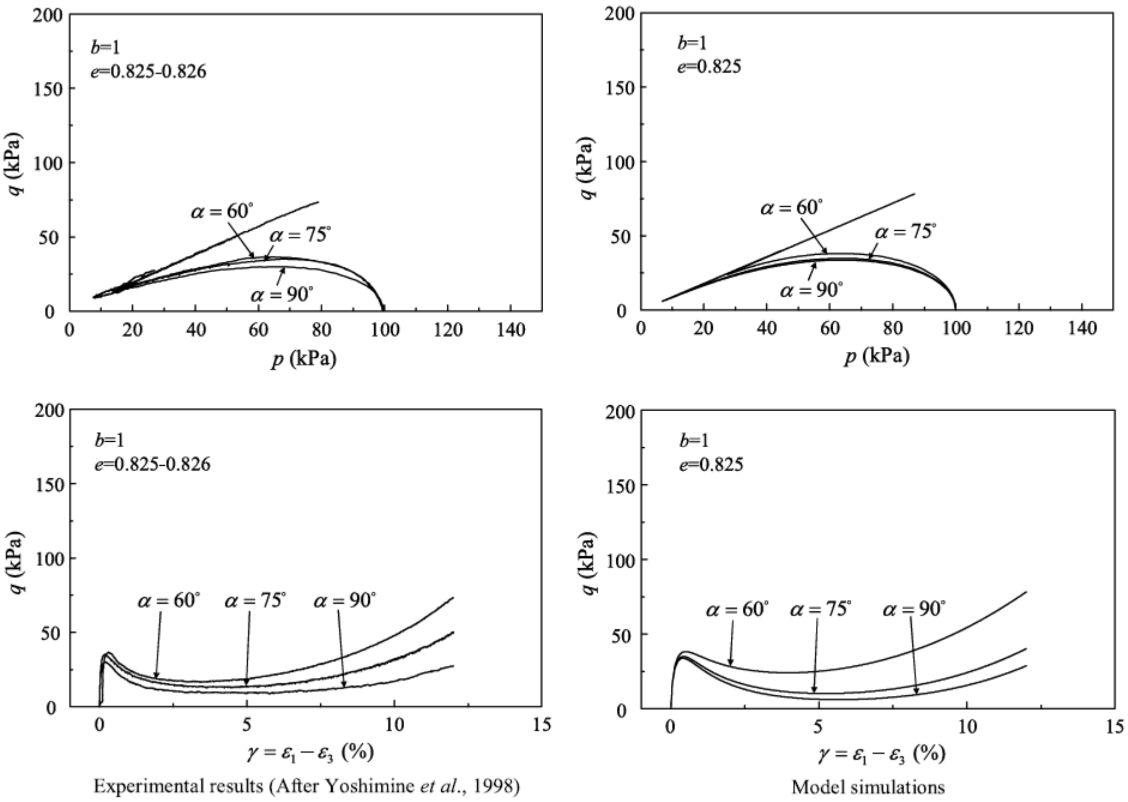

Fig. 4.91 Results of undrained loading tests on anisotropic sand at b = 1 and different values of α and simulations of these tests (figure after Li and Dafalias 2012; data after Yoshimine et al. 1998)

CHAPTER 5: APPARATUS, MATERIALS AND TESTING TECHNIQUES

5.1 INTRODUCTION

The hollow cylinder torsional shear apparatus (HCA) is presented and its capabilities are discussed. The independent control of the axial load and torque and the pressure inside and outside the cylinder offers the capability to control independently the magnitude of the three principal stresses and the direction of the two principal axes (PA) of stress in the wall of the hollow cylindrical specimen. The relationships used to calculate the average stresses and strains in torsional-shear testing are derived and the limitations that the inevitable non-uniformities of stress and strain impose are discussed. The HCA was upgraded to allow the independent control of the pressure inside and outside the cylinder, the measurement instrumentation was recalibrated, while new on-sample instrumentation was installed, calibrated and used in preliminary tests. This Chapter also presents the characteristics of the material tested (M31 Sand) and describes the specimen preparation method.

5.2 THE CONCEPT OF TORSIONAL SHEAR LOADING OF A HOLLOW CYLINDRICAL SPECIMEN

Figure 5.1a shows a hollow cylindrical specimen with a vertical axis subjected to axial load, F, torque about the central vertical axis, T, inner pressure, p_i, and outer pressure, p_o. The height of the cylinder is H, the inner radius is r_i and the outer radius is r_o. As described by Hight et al. (1983), the torque, T, induces shear stresses, $\tau_{z\theta}$ and $\tau_{\theta z}$, in horizontal and vertical planes, respectively, the axial load, F, contributes to the development of the vertical normal stress, σ_{zz}, while the outer pressure, p_o, and the inner pressure, p_i, contribute to the development of the vertical normal stress, σ_{zz}, and induce the horizontal normal stresses along the circumferential direction, $\sigma_{\theta\theta}$, and the radial direction, σ_{rr}. The flexibility of the membranes and the stationarity of the water inside the triaxial cell prevent the development of shear stresses on the periphery of the specimen (τ_{rz} , $\tau_{r\theta}$) thus σ_{rr} is always a principal stress (not necessarily the intermediate principal stress, σ_2). The stresses $\tau_{z\theta}$, $\tau_{\theta z}$, σ_{zz} and $\sigma_{\theta\theta}$ acting on the soil element are shown in Fig. 5.1b, while the deformed soil element after the development of the strains $\varepsilon_{z\theta}$, $\varepsilon_{\theta z}$, ε_{zz} and $\varepsilon_{\theta\theta}$ is shown in Fig. 5.1c. Figure 5.1b shows that the direction of the major and minor principal stress, σ'_1 and σ'_3 respectively, rotates under torsional-shear loading in a vertical plane perpendicular to the direction of the intermediate principal stress, σ'_2. The inclination of the σ'_1-axis to the vertical is indicated by the angle α (or $\alpha_{\sigma'1}$). It is noted that the stresses and strains vary along the radial direction due to the curvature of the specimen and the difference between the inner and outer pressure, while the restraint at the specimen's end loading platens induces further non-uniformities.

Hight et al. (1983) showed that the effects of stress non-uniformities can be minimised by selecting proper specimen geometry and using internal instrumentation placed in the central part of the specimen, as well as by limiting the difference between the inner and outer pressure. Under these conditions the HCA has some remarkable advantages compared with other testing apparatuses. For example, compared with the simple-shear apparatus (Roscoe 1953, Roscoe et al. 1967) the HCA can impose monotonic loading involving rotation of the stress PA on specimens either isotropically or anisotropically consolidated, with or without a constraint on the lateral deformation, thus imposing no restriction on the zero-extension direction. In contrast to the simple-shear apparatus, the rotation of the stress PA in the HCA can be imposed either at constant or varying value of the intermediate principal stress parameter, $b = (\sigma'_2 - \sigma'_3) / (\sigma'_1 - \sigma'_3)$ (Bishop 1971), and it can continue beyond the peak-failure state, while the complementary shear stresses, $\tau_{\theta z}$, develop automatically.

The HCA can also impose monotonic loading at different angles α with a fixed and controlled value of b and p making the direction of the σ'_1-axis inclined at different angles with respect to the normal to the bedding plane formed due to gravity deposition (see Chapter 2). Figures 5.2a and b show the total stress path (TSP) in the q - p' plane and the stress path in the Y_s - X_s plane ($Y_s = \sigma'_{zz} - \sigma'_{\theta\theta}$, $X_s = 2\tau_{z\theta}$) of a test at constant α, p and b. It is noted that the angle between the radial vector connecting the current stress state with the origin of the Y_s - X_s plane and the X_s-axis is equal to 2α (see Eq. 5.22d in the following) and thus the stress path shown in Fig. 5.2b progresses along the radial direction in this stress plane because α is constant. This type of loading, described with the term *radial loading*, is not feasible in the triaxial, plane-strain or true-triaxial apparatus without using tilted specimens, a technique that causes the development of parasitic stresses or strains. Moreover, the value of b in triaxial tests is either 0 (triaxial compression) or 1 (triaxial extension), while in plane-strain tests b cannot be controlled. Consequently, in the HCA the effect of α on the mechanical behaviour of soils can be investigated separately from the effect of b. Thus, the HCA has the prerequisite capabilities for investigating the effects of the inherent anisotropy on strength, dilatancy and deformability.

Cyclic torsional-shear tests are also advantageous compared with cyclic triaxial tests. In the case that cyclic torsional-shear loading is imposed on isotropically consolidated sand the mean total stress, p, and the intermediate principal stress parameter, b, are kept constant while the angle α changes from $+45^o$ to -45^o, and vice versa, whenever the shear stress, $\tau_{z\theta}$, becomes zero and reverses direction. Consequently, the pore-water pressure build up in cyclic undrained torsional-shear tests is not related to a change in p or b while the σ'_1-axis is symmetrically oriented with respect to the bedding plane in each half of a loading cycle. On the other hand, in cyclic triaxial tests on isotropically consolidated sand the angle α alternates between 0^o and 90^o, the parameter b alternates between 0 and 1 and the mean total stress, p, changes according to the relationship Δq / Δp = ±3 / 1. It is obvious that the pore-water pressure build up in cyclic undrained triaxial tests is affected by the change in p and b as well as by the change in α and q. Figure 5.3a shows the total stress paths in the q - p' plane of cyclic tests on isotropically consolidated specimens in triaxial and torsional-shear loading mode, while Fig. 5.3b shows the corresponding stress paths in the Y_s - X_s plane; note that that the stress $–q$ corresponds to triaxial extension in this figure thus the slope Δ(-q) / Δp is 3 / 1. It can be inferred that the capabilities of the HCA are valuable for evaluating the undrained behaviour of soils under cyclic loading, especially when the effects of the shear stress, $\tau_{z\theta}$, on the horizontal planes in situ are to be investigated in the laboratory.

Rotation of the stress PA can be performed in the HCA at fixed effective stress principal values (PV). In this case the mean effective stress, p', the deviatoric stress, q, and the intermediate principal stress parameter, b, are kept constant while the axes of the minor and major principal stress rotate continuously. It has been reported that loose and dense sands deform plastically in shear and contract under this type of principal stress rotation (Miura et al. 1986, Tong et al. 2010), described with the term *rotational shear* (Wang et al. 1990) The investigation of the behaviour of sands under rotational shear, which cannot be explained within the framework of classical Plasticity Theory, is of paramount importance because the tendency to contract under undrained conditions induces pore-water pressure build up and puts sands at risk of liquefaction. For example, Ishihara and Towhata (1983) showed that this type of shearing is imposed on the seabed soil deposits due to travelling waves. Figures 5.4a and b show the effective stress path in the q - p' plane and the stress path in the Y_s - X_s plane from a rotational-shear test. It was one of the aims of the present study to upgrade the HCA in order to perform this type of tests.

5.3 DERIVATION OF THE RELATIONSHIPS FOR THE AVERAGE STRESSES AND STRAINS IN THE HOLLOW CYLINDRICAL SPECIMEN

Figure 5.5a shows a cross section of a hollow cylindrical specimen having an outer radius, r_o, an inner radius, r_i, and being subjected to outer pressure, p_o, and inner pressure, p_i. In the case that the bedding planes of the granular specimen formed by gravity deposition are horizontal and no torque or end-restraint forces are applied the stress and strain conditions are axisymmetric, i.e. there exists a dependence only on the variable r, which indicates the distance of the soil element *abcd* from the centre of the cylinder. The soil element *abcd* is an infinitesimal segment of a ring located at radius r and defined by the circumferential increment dθ and the radial increment dr.

Figure 5.5b shows the stresses applied on the soil element and its displacement from the position *abcd* to the new position *a'b'c'd'*. The force equilibrium for a soil element with dz = 1 along the radial direction yields:

$\Sigma F_r = 0 \Rightarrow$

$\sigma_r \, r \, \mathrm{d}\theta + 2\sigma_\theta \sin(\mathrm{d}\theta / 2) \, \mathrm{d}r - [\sigma_r + (\partial\sigma_r / \partial r) \, \mathrm{d}r] \, (r + \mathrm{d}r) \, \mathrm{d}\theta = 0 \Rightarrow$

$$\sigma_r(r) - \sigma_\theta(r) = r \, \mathrm{d}\sigma_r / \mathrm{d}r \qquad (5.1)$$

because two acute angles with normal sides one by one are equal, $\sin(\mathrm{d}\theta / 2) \approx \mathrm{d}\theta$, the second order increments and the body forces are negligible and there exists only a dependence of stresses on r; note that $\mathrm{d}\theta$ is expressed in radians. Equation 5.1 indicates that whenever the inner and outer pressure are not equal ($p_i \neq p_o$) a gradient of radial stress, $\sigma_{rr}(r)$ (or $\sigma_r(r)$), is established and the average radial stress, σ_{rr}, is not equal to the average circumferential stress, $\sigma_{\theta\theta}$. On the other hand, whenever $p_i = p_o = p$ the relationship $\sigma_{rr} = \sigma_{\theta\theta} = p$ holds for the average values yet there may exist a variation in $\sigma_{rr}(r)$ and $\sigma_{\theta\theta}(r)$ across the cylinder wall, for example, due to a variation in $\tau_{z\theta}(r)$ (Hight et al. 1983). This means that, in general, the actual distribution of σ_{zz}, $\sigma_{\theta\theta}$ and $\tau_{z\theta}$ depends on the elastoplastic characteristics of sand (material's constitutive law).

The radial displacement of the points on the line *ab* in Fig. 5.5b is u while that of the points on the line *cd* is $u + (\partial u / \partial r) \, \mathrm{d}r$ since $u = u(r)$. Consequently, the radial strain, $\varepsilon_{rr}(r)$, is given by the normalised elongation of the line *ac*:

$$\varepsilon_{rr}(r) = -(a'c' - ac) / ac = -(u + (\partial u / \partial r) \, \mathrm{d}r - u) / \mathrm{d}r = -\mathrm{d}u / \mathrm{d}r \qquad (5.2)$$

taking into account that extensive strain is conventionally negative and that the radial strain depends only on the variable r. Equation 5.2 indicates that the determination of the radial strain at any point requires the knowledge of the gradient of the displacement at that point and not just the knowledge of the displacement at the inner and outer surface, $u_i = \Delta r_i$ and $u_o = \Delta r_o$, respectively. Similarly, the line *ab* is stretched to its new position *a'b'* thus the circumferential strain, $\varepsilon_{\theta\theta}(r)$, is:

$$\varepsilon_{\theta\theta}(r) = -(a'b' - ab) / ab = -[(r + u) \, \mathrm{d}\theta - r \, \mathrm{d}\theta] / (r \, \mathrm{d}\theta) = -u / r \qquad (5.3)$$

Equation 5.3 indicates that the determination of the circumferential strain at any point requires the knowledge of the displacement at that point and not just the knowledge of the displacement at the inner and outer surface, $u_i = \Delta r_i$ and $u_o = \Delta r_o$, respectively.

For the determination of the average radial strain, ε_{rr}, and circumferential strain, $\varepsilon_{\theta\theta}$, it is assumed that the radial displacement, u, varies linearly across the cylinder wall (Hight et al. 1983):

$$u(r) = [(\Delta r_o - \Delta r_i) / (r_o - r_i)] \, (r - r_i) + \Delta r_i \qquad (5.4)$$

since $u(r_o) = u_o = \Delta r_o$ and $u(r_i) = u_i = \Delta ri$; note that Eq. 5.4 does not coincide with the function $u(r) = C_1 r + C_2 / r$ (C_1 and C_2 are constants) derived for an isotropic linear elastic hollow cylinder subjected to pressures p_i and p_o while it satisfies the axisymmetric condition $u(r = 0) = 0$ if and only if $r_o / r_i = \Delta r_o / \Delta r_i$. From Eqs 5.2, 5.3 and 5.4 the average strains can be derived:

$$\varepsilon_{rr} = -\left[\frac{\int_{r_i}^{r_o} \frac{du}{dr} rdr}{\int_{r_i}^{r_o} rdr}\right] = -\frac{\Delta r_o - \Delta r_i}{r_o - r_i} \tag{5.5a}$$

$$\varepsilon_{\theta\theta} = -\left[\frac{\int_{r_i}^{r_o} \frac{u}{r} rdr}{\int_{r_i}^{r_o} rdr}\right] = -\frac{\Delta r_o + \Delta r_i}{r_o + r_i}$$

(5.5b)

Hight et al. (1983) also assumed a linear elastic stress distribution for $\sigma_{rr}(r)$ to derive the relationship for the average radial stress, σ_{rr}:

$$\sigma_{rr}(r) = \frac{p_o r_o^2 - p_i r_i^2}{r_o^2 - r_i^2} + \frac{(p_i - p_o) r_o^2 r_i^2}{(r_o^2 - r_i^2) r^2} \text{ (Lamé's equation)} \tag{5.6a}$$

$$\sigma_{rr} = \frac{\int_{r_i}^{r_o} \sigma_{rr}(r) dr}{\int_{r_i}^{r_o} dr} = \frac{p_o r_o + p_i r_i}{r_o + r_i} \tag{5.6b}$$

It is noted that Lamé's equation (Eq. 5.6a) is derived by using the radial displacement function $u(r) = C_1 r + C_2 / r$ (C_1 and C_2 are constants).

The relationships for the averages of normal stresses σ_{zz} and $\sigma_{\theta\theta}$ are derived by considering the force equilibrium only. The average circumferential stress, $\sigma_{\theta\theta}$, is determined from the force equilibrium along the horizontal direction x for the one half of the hollow cylindrical specimen cut by means of a vertical plane containing the cylinder axis and being normal to x as shown in Fig. 5.6a:

$\Sigma F_x = 0 \Rightarrow$

$2\sigma_{\theta\theta} (r_o - r_i) H + p_i 2r_i H - p_o 2r_o H = 0 \Rightarrow$

$$\sigma_{\theta\theta} = (p_o r_o - p_i r_i) / (r_o - r_i) \tag{5.7}$$

However, the same result can be obtained by integrating the function $\sigma_{\theta\theta}(r) = (p_o r_o^2 - p_i r_i^2) / (r_o^2 - r_i^2) + (p_o - p_i) r_o^2 r_i^2 / [(r_o^2 - r_i^2) r^2]$ given by Lamé's equation in the same way as in Eq. 5.6b. The average axial stress, σ_{zz}, is determined from the force equilibrium along the vertical direction z for the top loading platen, stressed by the loading rod, supported by the hollow cylindrical specimen and being in contact with the fluids in the outer and inner cell environment as shown in Fig. 5.6b:

$\Sigma F_z = 0 \Rightarrow$

$\sigma_{zz} [\pi (r_o^2 - r_i^2)] + p_i (\pi r_i^2) - p_o (\pi r_o^2) - F = 0 \Rightarrow$

$$\sigma_{zz} = F / [\pi (r_o^2 - r_i^2)] + (p_o r_o^2 - p_i r_i^2) / (r_o^2 - r_i^2) \tag{5.8}$$

where F is the contact force that is applied on the top loading platen from the loading rod (see Fig. 5.1a). It should be noted that in the upgraded HCA the servo-control mechanism imposes at any time the target contact force, F, while neutralising the buoyancy force that acts on the rod and depends on the current value of the pressure p_o. In the case that the servo-control mechanism is de-activated and the pressure p_o is increased then the load cell will record a decrease in the contact force, F, due to the buoyancy effect; the buoyancy term is not included in Eq. 5.8. An alternative configuration allows the control of F while the buoyancy force is neutralised by coupling the valves of the outer cell pressure and vertical pressure (see Section 5.6.3). Note that if $p_o = p_i$ then the average axial stress is $\sigma_{zz} = F / [\pi (r_o^2 - r_i^2)] + p_o$.

The relationships for the averages of strains ε_{zz} and $\gamma_{z\theta} = 2\varepsilon_{z\theta}$ are derived based on geometric considerations. The relationship for the average axial strain, ε_{zz}, is derived by assuming a linear variation of the axial displacement with z:

$$v(z) = (v_H / H)\, z \tag{5.9a}$$

$$\varepsilon_{zz}(z) = -dv / dz = -v_H / H = \varepsilon_{zz} \tag{5.9b}$$

where the variable z is zero at the base of the specimen, H is the height of the specimen, $v(z = H) = v_H$ is the displacement at the top of the specimen, $v(z = 0) = 0$ is the displacement at the base of the specimen and $\varepsilon_{zz}(z) = -dv / dz$ is the axial strain because the extensive strain corresponds to $dv > 0$ and is negative according to the convention used here (see Fig. 5.1). It is noted that the axial strain, $\varepsilon_{zz}(z)$, may become non-uniform along the height of the cylindrical specimen due to the end-restraint effects but this problem can be solved by using on-sample instrumentation or by applying the digital image correlation (DIC) technique or photogrammetry (see Chapter 2) in order to measure the displacement, v, in the central part of the cylindrical specimen. On the other hand, the shear strain $\gamma_{z\theta} = 2\varepsilon_{z\theta}$ is inevitably non-uniform across the cylinder wall since it is a linear function of the radius r, though the level of non-uniformity can be minimised by selecting a specimen geometry with a small ratio $(r_o - r_i) / r_i$. In the case that the top of the cylindrical specimen ($z = H$) rotates by an amount of $\Delta\theta$ radians in regard to the base ($z = 0$) and the specimen remains a right hollow cylinder after deformation (see Fig. 5.1) the boundary conditions in a horizontal cross section are $\gamma_{z\theta}(r = r_i) = \Delta\theta\, r_i / h$ and $\gamma_{z\theta}(r = r_o) = \Delta\theta\, r_o / h$, while $\gamma_{z\theta}(r = 0) = 0$, and thus the shear strain, $\gamma_{z\theta}(r)$, is:

$$\gamma_{z\theta}(r) = \Delta\theta\, r / h \tag{5.10}$$

The average shear strain, $\gamma_{z\theta}$, across the cylinder wall is determined by solving the integral:

$$\gamma_{z\theta} = \frac{\int_A \gamma_{z\theta} dA}{\int_A dA} = \frac{\int_0^{2\pi}\int_{r_i}^{r_o} \Delta\theta \cdot (r / H) \cdot r \cdot dr \cdot d\theta}{\left[\pi(r_o^2 - r_i^2)\right]} = \frac{2\Delta\theta}{3H} \cdot \frac{\left(r_o^3 - r_i^3\right)}{(r_o^2 - r_i^2)} \tag{5.11}$$

where dA = [r dθ + (r + dr) dθ] / 2 dr = r dr dθ, as can be seen in Fig. 5.5b.

For the determination of the average shear stress, $\tau_{z\theta}$, an assumption should be made for the constitutive relationship between $\tau_{z\theta}$ and $\varepsilon_{z\theta}$ and then this relationship can be applied for the different level of shear strain $\varepsilon_{z\theta}$ or stress $\tau_{z\theta}$ at the points along the cylinder wall. For example, if the hyperbolic stress - strain relationship indicated by the solid curve in Fig. 5.7a is used then the distribution of $\tau_{z\theta}(r)$ along the cylinder wall is similar to the stress - strain relationship, as shown in Fig. 5.7b (i), since the specimen remains a right hollow cylinder after deformation and the shear strain $\gamma_{z\theta}(r)$ is a linear function of the radius r. However, the stress - strain relationship is frequently approximated by a bi-linear relationship, as shown with the dashed line in Fig. 5.7a, indicating that the soil response is linear elastic for $\gamma < \gamma_y$ (or $\tau < \tau_y$; the subscript y stands for yield) and perfectly plastic otherwise. The variation of the shear stress $\tau_{z\theta}$ with r in the case that all the soil elements across the cylinder wall deform elastically, as shown in Fig. 5.7b (ii), is given by the relationship:

$$\tau_{z\theta,el}(r) = \tau_{max}\, r / r_o \tag{5.12}$$

where the constant $\tau_{max} \leq \tau_y$ expresses the maximum elastic shear stress at $r = r_o$ and can be determined from the boundary conditions. Specifically, the torque T imposed on the upper boundary of the specimen (Fig. 5.1a) having a surface A is the surface integral of the infinitesimal torque dT = $r\, \tau_{z\theta}$ dA = $r^2\, \tau_{z\theta}$ dr dθ acting on a soil element at radius r as the one shown in Fig. 5.5b:

$$T = \int_A r \cdot \tau_{z\theta} \cdot dA = \int_0^{2\pi}\int_{r_i}^{r_o} r^2 \cdot \tau_{z\theta} \cdot dr \cdot d\theta \tag{5.13}$$

Substituting $\tau_{z\theta}$ from Eq. 5.12 into Eq. 5.13 and solving for τ_{max} one may get:

$$T = \pi / 2\; \tau_{max} / r_o\, (r_o^4 - r_i^4) \Rightarrow$$

$$\tau_{max} = 2\, r_o\, T / [\pi\, (r_o^4 - r_i^4)] \leq \tau_y \tag{5.14}$$

Substituting τ_{max} from Eq. 5.14 into Eq. 5.12 one may get:

$$\tau_{z\theta,el}(r) = 2\, r\, T / [\pi\, (r_o^4 - r_i^4)] \tag{5.15}$$

The average elastic shear stress, $\tau_{z\theta,el}$, across the cylinder wall can be now determined by solving the integral:

$$\tau_{z\theta,el} = \frac{\int_A \tau_{z\theta} dA}{\int_A dA} = \frac{\int_0^{2\pi}\int_{r_i}^{r_o} 2\cdot T / \left[\pi(r_o^4 - r_i^4)\right]\cdot r^2 \cdot dr \cdot d\theta}{\left[\pi(r_o^2 - r_i^2)\right]} = \frac{4T}{3\pi}\cdot\frac{(r_o^3 - r_i^3)}{(r_o^2 - r_i^2)(r_o^4 - r_i^4)} \tag{5.16}$$

Similarly, the variation of the shear stress $\tau_{z\theta}$ with r in the case that all the soil elements across the cylinder wall deform plastically, as shown in Fig. 5.7b (iii), is given by the relationship:

$$\tau_{z\theta,pl}(r) = \tau_{max} = \tau_y \tag{5.17}$$

indicating that $\tau_{z\theta}$ is constant across the cylinder wall and equal to the yield stress, τ_y. Obviously, the average plastic shear stress, $\tau_{z\theta,pl}$, across the cylinder wall is also equal to $\tau_{max} = \tau_y$ and can be determined by solving Eq. 5.13 for $\tau_{z\theta,pl} = \tau_{max}$:

$T = 2\,\pi\,\tau_{max} / 3\,(r_o^3 - r_i^3) =>$

$$\tau_{z\theta,pl} = \tau_{max} = 3\,T / [2\,\pi\,(r_o^{\,3} - r_i^3)] \tag{5.18}$$

The ratio of the average plastic shear stress over the average elastic shear stress, $\tau_{z\theta,pl} / \tau_{z\theta,el}$, is:

$$\frac{\tau_{z\theta,pl}}{\tau_{z\theta,el}} = \frac{9}{8}\cdot\frac{(r_o^2 - r_i^2)(r_o^4 - r_i^4)}{(r_o^3 - r_i^3)^2} = 1.023 \tag{5.19}$$

since $r_o = 35$ mm and $r_i = 20$mm in this study. Equation 5.18 is used in this study to compute the average shear stress as a function of the imposed torque, T, and the geometry.

Summarising, the relationships for the average stresses in the hollow cylindrical specimen are:

$$\sigma_{zz} = \frac{F}{\pi\left(r_o^2 - r_i^2\right)} + \frac{p_o r_o^2 - p_i r_i^2}{r_o^2 - r_i^2} \tag{5.20a}$$

$$\sigma_{rr} = \frac{p_o r_o + p_i r_i}{r_o + r_i} \tag{5.20b}$$

$$\sigma_{\theta\theta} = \frac{p_o r_o - p_i r_i}{r_o - r_i} \tag{5.20c}$$

$$\tau_{z\theta} = \frac{3T}{2\pi(r_o^3 - r_i^3)} \tag{5.20d}$$

while the relationships for the average strains are:

$$\varepsilon_{zz} = -\frac{v_H}{H} \tag{5.21a}$$

$$\varepsilon_{rr} = -\frac{\Delta r_o - \Delta r_i}{r_o - r_i} \tag{5.21b}$$

$$\varepsilon_{\theta\theta} = -\frac{\Delta r_o + \Delta r_i}{r_o + r_i} \tag{5.21c}$$

$$\gamma_{z\theta} = 2\varepsilon_{z\theta} = \frac{2\Delta\theta}{3H} \cdot \frac{\left(r_o^3 - r_i^3\right)}{\left(r_o^2 - r_i^2\right)} \tag{5.21d}$$

The symbols used in Eqs 5.20 and 5.21 are described in Fig. 5.1 as discussed previously. It is noted that the complementary shear stresses are equal in magnitude, $\tau_{z\theta} = \tau_{\theta z}$. It is also noted that the definitions in Eqs 5.20 and 5.21 ensure that $\Sigma\sigma\varepsilon$ equals the work per unit volume done by the external forces (Hight et al. 1983).

5.4 DERIVATION OF THE RELATIONSHIPS FOR THE PRINCIPAL VALUES AND DIRECTIONS OF STRESS AND STRAIN IN THE HOLLOW CYLINDRICAL SPECIMEN

The relationships for the principal values and directions of stress in the hollow cylindrical specimen can be derived by using the Mohr circle representation of stress shown in Fig. 5.8. In the stress system depicted in Fig. 5.8 the intermediate principal stress, σ_2, coincides with the radial stress, σ_{rr}, while the axes of the major, σ_1, and minor, σ_3, principal stress belong in a vertical plane normal to the radial direction. The σ_1 - σ_3 Mohr circle can be determined if the stresses acting on two orthogonal planes with normals belonging in the aforementioned vertical plane are known. In the case of the hollow cylindrical specimen the stresses σ_{zz} and $\tau_{z\theta}$ act on the horizontal plane, while the stresses $\sigma_{\theta\theta}$ and $\tau_{\theta z}$ act on the vertical plane normal to the circumferential direction (recall that $\tau_{z\theta} = \tau_{\theta z}$). Consequently, the points (σ_{zz} , $\tau_{z\theta}$) and ($\sigma_{\theta\theta}$, -$\tau_{\theta z}$) belong to the σ_1 - σ_3 Mohr circle and are diametrically opposite thus the centre of the circle is the point $C((\sigma_{zz} + \sigma_{\theta\theta}) / 2 , 0)$ and the radius of the circle is $R = [(\sigma_{zz} - \sigma_{\theta\theta})^2 / 4 + \tau_{z\theta}^2]^{1/2}$.

The σ_1 - σ_3 Mohr circle is drawn with centre C and radius R. Then, a horizontal line is drawn from point $H(\sigma_{zz} , \tau_{z\theta})$ and the point at which this line intersects the σ_1 - σ_3 Mohr circle is the Pole of the circle and specifically the origin of the planes. The plane on which σ_1 acts upon can be found by connecting the Pole with the point $M(\sigma_1 , 0)$. This plane makes an angle α with the horizontal plane, as shown in Fig. 5.8, thus the σ_1-axis makes an angle α with the vertical (see also Fig. 5.1b). The angle between the line connecting the pole with the centre C and the σ-axis (i.e. the horizontal axis of the stress space) is 2α. The magnitude of the three principal stresses and the inclination angle of the σ_1-axis with respect to the vertical can be determined from the geometric features shown in Fig. 5.8:

$$\sigma_1 = \frac{(\sigma_{zz} + \sigma_{\theta\theta})}{2} + \sqrt{(\frac{\sigma_{zz} - \sigma_{\theta\theta}}{2})^2 + \tau_{z\theta}{}^2} \tag{5.22a}$$

$$\sigma_2 = \sigma_{rr} \tag{5.22b}$$

$$\sigma_3 = \frac{(\sigma_{zz} + \sigma_{\theta\theta})}{2} - \sqrt{(\frac{\sigma_{zz} - \sigma_{\theta\theta}}{2})^2 + \tau_{z\theta}{}^2} \tag{5.22c}$$

$$tan\,2\alpha = \frac{2\tau_{z\theta}}{(\sigma_{zz} - \sigma_{\theta\theta})} \tag{5.22d}$$

The relationships for the principal strains and the inclination angle of the ε_1-axis with respect to the vertical are derived in a similar way:

$$\varepsilon_1 = \frac{(\varepsilon_{zz} + \varepsilon_{\theta\theta})}{2} + \sqrt{(\frac{\varepsilon_{zz} - \varepsilon_{\theta\theta}}{2})^2 + \varepsilon_{z\theta}{}^2} \tag{5.23a}$$

$$\varepsilon_2 = \varepsilon_{rr} \tag{5.23b}$$

$$\varepsilon_3 = \frac{(\varepsilon_{zz} + \varepsilon_{\theta\theta})}{2} - \sqrt{(\frac{\varepsilon_{zz} - \varepsilon_{\theta\theta}}{2})^2 + \varepsilon_{z\theta}{}^2} \tag{5.23c}$$

$$tan\,2\alpha_{\varepsilon 1} = \frac{2\varepsilon_{z\theta}}{(\varepsilon_{zz} - \varepsilon_{\theta\theta})} \tag{5.23d}$$

Finally, it is noted that the Eqs 5.22d and 5.23d can be used in terms of incremental stresses and strains, respectively, in order to determine the inclination angle of the dσ_1-axis and dε_1-axis with respect to the vertical:

$$tan\,2\alpha_{d\sigma 1} = \frac{2d\tau_{z\theta}}{(d\sigma_{zz} - d\sigma_{\theta\theta})} \tag{5.24}$$

$$tan\,2\alpha_{d\varepsilon 1} = \frac{2d\varepsilon_{z\theta}}{(d\varepsilon_{zz} - d\varepsilon_{\theta\theta})} \tag{5.25}$$

It is noted that in the case of equal pressures inside and outside the hollow cylinder, p_i = p_o, the relationship between the intermediate principal stress parameter, *b*, and the principal stress direction angle, α, is $b = \sin^2 \alpha$ (Hight et al. 1983).

5.5 NON-UNIFORMITIES OF STRESSES AND STRAINS IN THE HOLLOW CYLINDRICAL SPECIMEN

It has been shown that the independent control of the four stresses σ_{zz}, $\tau_{z\theta}$, p_o and p_i applied on the boundaries of the hollow cylindrical specimen allows the independent control of the magnitude of the three principal stresses, σ_1, σ_2 and σ_3, and the direction of the two principal stresses in the $z\theta$-plane. However, stresses and strains may vary across the wall of the hollow cylindrical specimen due to the curvature of the specimen and difference in the outer and inner pressures and this variation may occur even in the theoretical case that the boundary stresses are uniform and no end restraint is imposed. Specifically, non-uniform shear strain, $\gamma_{z\theta}$, develops due to the curvature of the specimen, while non-uniform radial stress, σ_{rr}, and circumferential stress, $\sigma_{\theta\theta}$, develop due to the different outer and inner pressures, p_o and p_i, respectively. In the case that the distribution of shear stress, $\tau_{z\theta}$, is not perfectly plastic its variation across the wall may cause non-uniformities in σ_{zz}, σ_{rr} and $\sigma_{\theta\theta}$, even under the condition $p_o = p_i$ (Hight et al. 1983). The end restraint due to rigid and rough loading platens imposes further stress - strain non-uniformities. Generally, the stress - strain distributions across the specimen wall depend on the material's constitutive law.

Hight et al. (1983) suggested that bounds should be set, first, to the difference between the calculated and real averages of stresses and strains, and second, to the magnitude of deviation of stresses and strains from the real averages, i.e. the level of non-uniformity. Hight et al. (1983) characterised the magnitude of the difference between the calculated stress (strain) average, σ_{av} (ε_{av}), and the real stress (strain) average, σ^*_{av} (ε^*_{av}), by using the following normalised parameter:

$$\beta_1 = \frac{\left|\sigma^*_{av} - \sigma_{av}\right|}{\sigma_L} \text{ (in terms of stresses)} \tag{5.26a}$$

$$\beta_1 = \frac{\left|\varepsilon^*_{av} - \varepsilon_{av}\right|}{\varepsilon_L} \text{ (in terms of strains)} \tag{5.26b}$$

where σ_L (ε_L) is a measure of the stress (strain) level defined for each particular case. The calculated stress or strain average is obtained from Eq. 5.20 or 5.21, respectively, for the imposed boundary pressures and loads and the measured boundary displacements and rotations. Note that the normalised parameter, β_1, is inversely proportional to accuracy. In order to quantify the level of stress or strain non-uniformity Hight et al. (1983) introduced the following parameter:

$$\beta_3 = \frac{\int_{r_i}^{r_o} \left|\sigma(r) - \sigma^*_{av}\right| dr}{(r_o - r_i)\sigma_L} \qquad \text{(in terms of stresses)}$$

(5.27a)

$$\beta_3 = \frac{\int_{r_i}^{r_o} \left| \varepsilon(r) - \varepsilon^*_{av} \right| dr}{(r_o - r_i)\varepsilon_L} \quad \text{(in terms of strains)} \tag{5.27b}$$

where $\sigma(r)$ ($\varepsilon(r)$) is the function describing the distribution of the particular stress (strain) under consideration across the wall of the hollow cylindrical specimen. As can be seen in Fig. 5.9 the parameter β_3 gives a measure "of the average of the absolute values of the differences between the stress distribution and the real average" (Hight et al. 1983).

The value of the parameters β_1 and β_3 depends on the specimen geometry, the value of p_o / p_i or $\sigma_{r,av} / \sigma_{\theta,av}$ (stress-path dependence) and the material's constitutive law. Hight et al. (1983) investigated the influence of the specimen geometry, in terms of the ratio r_i / r_o, and of the stress path, in terms of the ratio $\sigma_{r,av} / \sigma_{\theta,av}$, on the non-uniformities of stress and strain for an isotropic linear elastic specimen with free ends. Figure 5.10 shows the variation of the parameter β_3 for the stresses $\sigma_{\theta\theta}$ and σ_{rr} with the ratios r_i / r_o (a / b in the figure) and $\sigma_{r,av} / \sigma_{\theta,av}$; the parameter indicating the stress level is σ_L = ($|\sigma_{\theta,av}|$ + $|\sigma_{z,av}|$) / 2 and free specimen's ends were assumed. The corresponding value of the parameter β_1 is zero since the average circumferential stress, $\sigma_{\theta,av}$, and radial stress, $\sigma_{r,av}$, are computed by integrating the distributions of isotropic linear elastic analysis (Lamé's equations). Figure 5.10 shows that the stress non-uniformities increase, i.e. β_3 increases, when r_i / r_o decreases and when $\sigma_{r,av} / \sigma_{\theta,av}$ decreases, while there exists a limiting curve for β_3 when $-1 < \sigma_{r,av} / \sigma_{\theta,av} < 0$. Figure 5.11 shows the variation of the parameters β_1 and β_3 for the stress $\tau_{z\theta}$ with the ratio r_i / r_o (a / b in the figure); the parameter indicating the stress level is $\tau_L = \tau_{z\theta,av}$ and the isotropic linear elastic analysis is run for a hollow cylindrical specimen with free ends. Both parameters β_1 and β_3 are non-zero since the average shear stress, $\tau_{z\theta,av}$, is equal to the yield stress which is constant across the specimen wall according to the assumption of perfectly plastic behaviour while the elastic stress distribution corresponds to a linear variation across the specimen wall (see Fig. 5.7b). It can be seen that β_1 and β_3 increase when the ratio r_i / r_o decrease. In the case that a plastic analysis is run and the material has yielded at every point of the specimen wall then, obviously, $\beta_1 = \beta_3 = 0$.

Figure 5.12 shows the variation of the parameter β_3 for the strains $\varepsilon_{\theta\theta}$ and ε_{rr} with the ratios r_i / r_o (a / b in the figure) and $\sigma_{r,av} / \sigma_{\theta,av}$; the parameter indicating the strain level is ε_L = ($|\varepsilon_{\theta,av}|$ + $|\varepsilon_{z,av}|$) / 2 and the isotropic linear elastic analysis is run for three values of the Poisson's ratio, v, assuming free specimen's ends. It can be seen that β_3 increases when r_i / r_o decreases, when $\sigma_{r,av} / \sigma_{\theta,av}$ decreases and when v increases, while there exists a limiting curve for β_3 which is common for the incompressible material (v = 0.50) and the material with v = 0.30 or 0.15 when $-1 < \sigma_{r,av} / \sigma_{\theta,av} < 0.14$. Figure 5.13 shows the variation of the parameter β_1 for the strains $\varepsilon_{\theta\theta}$ and ε_{rr} with the ratios r_i / r_o (a / b in the figure) and $\sigma_{r,av} / \sigma_{\theta,av}$; the parameter indicating the strain level is ε_L = ($|\varepsilon_{\theta,av}|$ + $|\varepsilon_{z,av}|$) / 2 and the isotropic linear elastic analysis is run for three values of the Poisson's ratio, v, assuming free specimen's ends. The parameter β_1 is non-zero because the assumed variation of the radial displacement, $u(r)$, across the specimen wall (see Eq. 5.4) does not coincide with that obtained from the isotropic linear elastic analysis. It can be seen that β_1 increases when r_i / r_o decreases, when $\sigma_{r,av} / \sigma_{\theta,av}$ decreases and when v increases, while there exists a limiting curve for β_1 which is common for the incompressible material (v = 0.50) and the material with v = 0.30 or 0.15 when $-1 < \sigma_{r,av} / \sigma_{\theta,av} < 0.14$.

On the base of the results presented in Figs 5.10, 5.11 and 5.13 it is apparent that the stress and strain non-uniformities decrease when r_i / r_o increases. Hight et al. (1983) designed a new hollow cylinder apparatus for testing specimens with inner diameter $d_i = 2\ r_i$ = 203 mm, outer diameter $d_o = 2\ r_o$ = 254 mm and height H = 254 mm thus with r_i / r_o = 0.80. Apart from the requisite for a sufficiently high ratio r_i / r_o in order to minimise the stress and strain non-uniformities the selection of the specimen geometry was also based on other design requisites discussed by Hight et al. (1983). The hollow cylinder apparatus used in this study has been made in Japan and has a ratio of inner to outer radius r_i / r_o = 20 / 35 mm / mm = 0.57. The analysis by Hight et al. (1983) presented in the following was run for the particular dimensions of their hollow cylinder apparatus thus it is not directly related to the hollow cylinder apparatus used in this study. However, the results of this analysis are valuable in the sense that they offer information about the effect of the material's constitutive law and end restraint on the stress and strain non-uniformities in a hollow cylindrical specimen with r_i / r_o = 0.80 and offer insight into the factors affecting the stress - strain non-uniformities for the case of r_i / r_o = 0.57.

Figure 5.14 shows the variation of the parameter β_3 for the stresses $\sigma_{\theta\theta}$, σ_{rr} and σ_{zz} with the ratio t / t_f in a loading test with $\alpha = 0^o$ and b = 0.5, where $t = (\sigma_1 - \sigma_3) / 2$ and t_f is the value of t at failure (q is used instead of t in the figure); the parameter indicating the stress level is $\sigma_L = (|\sigma_{r,av}|+|\sigma_{\theta,av}|+|\sigma_{z,av}|) / 3$. A finite element analysis was run by assuming that the hollow cylindrical specimen has free ends and its constitutive behaviour can be described by the modified Cam-clay form of strain-hardening plasticity. Figure 5.14 also shows the corresponding values of β_3 obtained from an isotropic linear elastic analysis of the hollow cylindrical specimen with free ends. The results of the elastoplastic analysis indicate that the axial stress, σ_{zz}, is non-uniformly distributed across the specimen wall and the level of non-uniformity, as expressed by the parameter β_3, is of the same order of magnitude as that of the stresses $\sigma_{\theta\theta}$ and σ_{rr}. The non-uniformity of σ_{zz} is not induced by the non-uniformity of the other two normal stresses via the Poisson's effect (Saada 1988) since there exist not any rigid ends to impose a reaction along the z-direction. The results also indicate that the differences in β_3 in the elastic and elastoplastic analyses are small and Hight et al. (1983) reported that the same holds true for other cases investigated by these authors. Figure 5.15 shows the variation of σ_{zz}, $\sigma_{\theta\theta}$ and σ_{rr} across the specimen wall at $t = 2 / 3\ t_f$ based on the elastoplastic and elastic analyses. It can be seen that the stresses $\sigma_{\theta\theta}$ and σ_{rr} exhibit similar non-uniformities yet σ_{zz} is non-uniform only in the elastoplastic analysis presumably due to the plastic interaction between the strength components.

Apart from the non-uniformities arising from the curvature of the specimen wall and the difference between the inner and outer pressures additional non-uniformities in stress and strain result from the frictional restraint and stiffness of the loading platens. The radial displacement is impeded at the specimen's ends (top and bottom) thus the shear stress, τ_{rz}, develops together with the complementary shear stress, τ_{zr}, but decays with the distance from the specimen's boundaries. Hight et al. (1983) reported that "these shear stresses result predominantly in additional circumferential stress, in bending moments which affect the distribution of vertical stress and in rotations of principal stress out of the plane of the cylinder wall". They also stated that the specimen geometry, the material's constitutive law and the applied pressure and load combinations influence the stress disturbance due to end restraint. Figure 5.16 shows the stress distributions in a hollow cylindrical specimen with fixed ends based on the linear elastic analyses with v = 0.499 (Poisson's ratio) and different specimen heights H. The inner diameter of the specimen is d_i = 200 mm, the outer diameter of the specimen is d_o = 250 mm, the inner pressure is p_i = 350 kPa, the outer pressure is p_o = 400 kPa, the vertical stress is σ_{zz} = 400 kPa and the shear stress $\tau_{z\theta}$ = 0 kPa; the addition of a torque is not expected to alter the displayed stress non-uniformities of σ_{rr}, $\sigma_{\theta\theta}$ and σ_{zz} on the base of linear elastic analysis. The contours shown in Fig. 5.16 are expressed as percentage of the stress predicted for a linear elastic element without end restraint to show the effect of end restraint on the development of non-uniformities.

Figure 5.16 shows that the distribution of $\sigma_{\theta\theta}$ and σ_{zz} changes when the boundary conditions change in regard to the fixity of the ends. The effects of end restraint on stresses are important in a large portion of the specimen when the height is small (e.g. when H = 100 mm or 150 mm). On the other hand, in the case that H is large (e.g. when H = 250 mm for the particular specimen which has an outer diameter of d_o = 250 mm) there exists a part at the centre of the specimen that remains practically unaffected by the end-restraint effects. The effects of end restraint on the radial stress σ_{rr} appear to be limited only in the vicinity of the boundaries irrespective of the value of H. Hight et al. (1983) reported that the stress disturbance in σ_{rr} due to end restraint is local for all load / pressure combinations, not only for the one displayed in Fig. 5.16. On the contrary, the stress disturbance in $\sigma_{\theta\theta}$ and σ_{zz} is sensitive to the specimen geometry (especially to the specimen height), to the load / pressure combinations (especially to p_o - p_i), and to Poisson's ratio, v; Hight et al. (1983) stated that the level of non-uniformities is higher under drained conditions with v < 0.49.

Hight et al. (1983) performed also elastoplastic analyses of hollow cylindrical specimens (d_i = 200 mm, d_o = 250 mm and H = 250 mm) with fixed ends assuming that the material behaviour can be described by the modified Cam-clay form of strain-hardening plasticity. The results of the elastoplastic analyses are shown together with those of the linear elastic analyses (with v = 0.3) in Fig. 5.17. The imposed stress path in terms of average stresses in these analyses was the same as that shown in Fig. 5.14, i.e. $\alpha = 0^{o}$ and b = 0.50. Figure 5.17 shows the value of the ratios ($\sigma_{\theta\theta}$ - $\sigma_{\theta\theta,av}$) / σ_L and (σ_{zz} - $\sigma_{zz,av}$) / σ_L (σ_L = ($\sigma_{zz,av}$ + $\sigma_{\theta\theta,av}$ + $\sigma_{rr,av}$) / 3) inside the specimen wall indicating the stress non-uniformities in a specimen with fixed ends at two different levels of the average shear stress, $t = 2 / 3\ t_f$ and $t = t_f$ (t_f is the value of $t = (\sigma_1 - \sigma_3) / 2$ at failure); the plot of the ratio $(\sigma_{rr} - \sigma_{rr,av}) / \sigma_L$ was not presented by Hight et al. (1983) because the elastoplastic analyses showed that the distribution of σ_{rr} is not altered much due to end restraint, as was also shown in the elastic analyses (see Fig. 5.16). The results shown in Fig. 5.17 indicate that the stress distributions and thus the stress non-uniformities are similar for linear elastic and elastoplastic materials and that the level of non-uniformities increases as the specimen is sheared to failure.

Hight et al. (1983) set bounds for the ratio p_o / p_i in order to keep the stress (and strain) non-uniformities arising from the specimen curvature alone within admissible limits. Figure 5.18 shows the loci of stress states in the π-plane associated with admissible non-uniformities for p_o / p_i varying in the range [0.9 , 1.2] and for $\alpha = 0^o$, 90^o or 45^o; note that the ratios $p_o / p_i = 0.9$ and 1.2 are associated with similar levels of stress non-uniformities. It can be seen that the curvature induced stress non-uniformities depend on the value of α being much less when $\alpha = 45^o$ than when $\alpha = 0^o$. The hollow cylinder apparatus used in this study accommodates a specimen with $d_i = 40$ mm, $d_o = 70$ mm and $H = 140$ mm ($r_i / r_o = 0.57$) thus the limitations shown in Fig. 5.18 cannot be directly applied. In this study the ratio p_i / p_o generally varies in the range [0.75 , 1.30], i.e. it varies within the bounds set by Gutierrez (1989) who performed the analysis proposed by Hight et al. (1983) for the case of a hollow cylindrical specimen with $d_i = 60$ mm, $d_o = 100$ mm and $H = 200$ mm ($r_i / r_o = 0.60$). This is discussed in detail in Section 7.7.4.

5.6 THE HOLLOW CYLINDER APPARATUS OF THE NATIONAL TECHNICAL UNIVERSITY OF ATHENS BEFORE UPGRADING

The hollow cylinder apparatus (HCA) of the National Technical University of Athens (NTUA) is described in the state before the upgrade accomplished for the needs of the present study. A detailed description can be also found in the work by Tsomokos (2005). The HCA has been manufactured to particular specifications for NTUA by the Japanese company SEIKEN, INC., and accommodates a hollow cylindrical specimen with inner diameter $d_i = 40$ mm, outer diameter $d_o = 70$ mm and height $H = 140$ mm thus the ratio of the inner to outer radius is $r_i / r_o = 0.57$. The apparatus has the capability to accommodate a solid cylindrical specimen with diameter $d_o = 70$ mm and height $H = 140$ mm as well. The HCA can impose generalised monotonic or cyclic loading under stress-controlled or strain-control conditions. The loading is imposed by means of pneumatic pistons and flexible air - water interfaces located away from the submerged membranes. The manufacturers provided quality function generators for dynamic torsional and triaxial loading, as well as slope generators for static loading. However, new control and data acquisition hardware and software systems were developed at NTUA for the needs of the study by Konstadinou (2013) and the present study.

Figure 5.19 shows the drawing of the constitutive units and parts of the HCA (after SEIKEN, INC.) including, from left to right, the water unit, the loading system and the triaxial cell mounted on a steel plate welded on a steel frame, the air unit and the electric measurement and control unit; all dimensions are in millimetres. Figures 5.20 to 5.24 show the description and specifications of the parts included in Fig. 5.19, with each part identified by a unique number within the unit that it belongs; the name of each part, given by the manufacturer, has been preserved throughout the text for the sake of consistency. Figure 5.25 shows the drawing of the triaxial cell, Fig. 5.26 shows the piping system diagram, Fig. 5.27 shows the electric block diagram and Fig. 5.28 shows the drawing of the triaxial cell including optional parts. Figure 5.29 shows the photo of the water unit, the loading system, the triaxial cell and the base frame, Fig. 5.31 shows the photo of the valves mounted on the base plate of the triaxial cell while Fig. 5.33 shows the drawing of the valves mounted on the panel of the base box of the water unit and on the base plate of the triaxial cell. Figure 5.35 shows the photo of the HCA (all units and parts) before the upgrade accomplished for the needs of this study.

5.6.1 BASE, TRIAXIAL CELL AND LOADING SYSTEM

The triaxial cell and loading system are mounted on a steel plate welded on a frame with dimensions 700 x 600 x 105 (in mm) which is supported by four columns, as shown in the photo in Fig. 5.29. When set in position for testing the triaxial cell is fixed in place with a clamp mechanism (No 12 in Fig. 5.19; see also Fig. 5.31) and connected to the loading system by means of a gain cushion (No 6 in Fig. 5.19; see also Fig. 5.29). The triaxial cell can be disconnected from the loading system and its base plate can slide on the steel plate (see Fig. 5.25) by means of pressurised air flow that reduces friction. The pressurised air flow is supplied from the air slide system in the air unit (No 5 in Fig. 5.19; see also Fig. 5.26) when the valve mounted on the triaxial cell's base plate is open (first valve on the right, in the back row, in Figs 5.29, 5.31 and 5.33b). Consequently, the triaxial cell can be moved easily in order to prepare the specimen before testing or dismount the specimen after testing. For example, Fig. 5.32 shows a sand specimen under partial vacuum in the moved triaxial cell before shear testing. The vacuum pump shown in Fig. 5.29 provides the vacuum which can be regulated (to become less negative) from the vacuum system panel of the air unit (No 7 in Fig. 5.19; see also Fig. 5.26).

A specimen pedestal is screwed on the cell lower plate (not to be confused with the steel plate or the base plate of the triaxial cell; see Fig. 5.25). The pedestal is equipped with an annular porous stone with embedded vanes preventing the occurrence of slippage at the interface with the specimen; the porous stone is shown in Fig. 5.30. A low-weight aluminium cap equipped with a similar porous stone is placed on top of the specimen, as shown in Fig. 5.32. Two hydraulic lines are connected to the pedestal, one leading to the pore-water pressure transducer mounted on the base plate of the triaxial cell and from there to the base box (No 5 in Fig. 5.19) and back-pressure tank (No 3 in Fig. 5.19) of the water unit, and the other leading to the base box of the water unit and from there to the burette measuring the volume changes (Fig. 5.26). One hydraulic line is connected to the specimen cap leading to the base box of the water unit and from there to the vacuum tank or the de-aired water tank of the water unit.

The first hydraulic line connected to the specimen pedestal and the one connected to the specimen cap allow the water to circulate through the specimen from the de-aired water tank towards the vacuum tank during the process of saturation (see Fig. 5.26). Figure 5.33 shows the drawing of the valves mounted on the panel of the base box of the water unit and on the base plate of the triaxial cell indicating the open / closed state during the water circulation process. It is noted that the first (unlabeled) valve on the right in the front row of the base plate of the triaxial cell in Fig. 5.33b should be partially open in order to induce a small pressure gradient along the height of the specimen which sustains a very slow flow of water. It is also noted that carbon dioxide (CO_2) can be circulated prior to water if the specimen is formed using the air-pluviation method. The second hydraulic line connected to the specimen pedestal allows the water to move from the specimen to the base box of the water unit and from there to the volume-change measuring burette and vice versa during the phase of consolidation or drained shearing (see Fig. 5.26). Figure 5.31 shows the set of valves mounted on the base plate of the triaxial cell. The combination of open / closed states of three of these valves (labelled as “specimen low” in the front row, “specimen low” in the back row and “specimen high”; see also Fig. 5.33b) allows the conditions to be switched from drained to undrained. For example, the photo in Fig. 5.31 shows a combination of open / closed states corresponding to undrained loading in which the pore-water pressure is applied through the open “specimen low” valve (in the back row) to the hydraulic line leading to the pore-water pressure transducer mounted on the base plate of the triaxial cell, thus it can be measured, but all hydraulic lines leading to the base box of the water unit are sealed.

The triaxial cell (Figs 5.25, 5.28 and 5.29) has a total height of 920 mm (including the length of the piston rod, coupling, gain cushion and mid-joint plate above the cylindrical shell described next) and a diameter at base equal to 200 mm. The transparent plastic cylindrical shell, which is made of polymethyl methacrylate (lucite) and has a nominal strength of 10 kgf / cm^2 (≈ 1 MPa) against pressure and a height of 450 mm, is mounted on the cell lower plate (not to be confused with the base plate of the triaxial cell or the steel plate; see Fig. 5.25) and sealed with an O-ring. The cell upper plate is mounted on three cell tie rods which are screwed on the cell lower plate, having three small O-rings at the connections. A chromium plated piston rod can move inside a cylindrical guide which is a part of the cell upper plate by means of two oiled stroke ball bearings and an air type bushing. In this configuration the corrosion of the rod is prevented while the friction and pressure losses from the cell environment are minimised. The piston rod is connected to the loading system outside the cylindrical cell by means of a torque coupler just above the gain cushion and the mid-joint plate, while it is also connected to the vertical load and torque transducer by means of another torque coupling inside the cylindrical cell (Fig. 5.25). A low-weight aluminium torque head (blue in colour; see Fig. 5.29) is attached to the vertical load and torque transducer and bears a collar with an anti-slip surface. The aluminium torque head is carefully screwed to the specimen cap compressing the O-ring attached to the cap and imposing an extension force on the specimen which should be neutralised by loosening the piston clamp until the initial unstressed state is restored. This process is repeated until a torque-bearing and sealed connection between the torque head and specimen cap is achieved, while it is ensured that the axis of the specimen is vertical and the ends of the specimen are horizontal and parallel to each other.

Figure 5.25 shows that the torsional angle transducer (potentiometer) is placed inside the cylindrical cell and bears a balance weight with a pulley mechanism and a pressure wheel. The pressure wheel is pressed against the collar with the anti-slip surface (pressure wheel touch ring) by means of a rod penetrating the cell upper plate and having an accessible knob and a lock nut mounted on it outside the cylindrical shell; when the wheel is put in place the lock nut under the knob is fastened while a bent metal blade provides the normal force on the contact surface (while the outer pressure is zero) via its elasticity. A non-sliding contact between the wheel and the anti-slip surface is thus established and the rotation of the specimen cap induces a rotation of the wheel amplified by the ratio of the collar diameter to the wheel diameter. Two types of wheels are available with the one used in this study having an amplification ratio of two over one. Figures 5.19 and 5.25 show that the vertical displacement transducer (dial gauge; see No 7 in Fig. 5.19) is placed outside the cylindrical shell and functions by means of a metal lever which is hinged at its centre (centre point touch lever) while it touches at one end the coupling under the gain cushion and at the other end the metal cylinder that intrudes into the dial gauge. It is noted that the HCA can accommodate gap sensors for measuring small strains associated with torsional or vertical displacements (see for example Fig. 5.28).

Figure 5.19 shows that the volume-change measuring burette (No 8) is mounted on the supporting column (No 9) on the left side of the cylindrical shell. The burette has a nominal strength of 10 kgf / cm^2($\approx$ 1 MPa) against pressure and is equipped with a differential pressure transducer at its base. The top of the burette is connected to a pneumatic line imposing the same pressure as that imposed inside the rubber bladder of the back-pressure tank (No 3 in the water unit in Fig. 5.19; see also Fig. 5.26); it also has an exhaust to the atmosphere. The bottom of the burette is connected to a hydraulic line that leads to the base box of the water unit and from there to the "specimen low" valve mounted on the base plate (front row) of the triaxial cell (see Figs 5.26, 5.31 and 5.33b). Consequently, whenever the hydraulic line connecting the specimen pedestal with the bottom of the burette is open the volume changes of the specimen can be measured and the back pressure can be simultaneously transmitted from the burette to the pore water without using the back-pressure tank of the water unit. This situation corresponds to consolidation or drained loading.

Figure 5.19 shows the parts of the loading system (loading apparatus). Four aluminium-made supporting columns (No 9) are screwed to two parallel metal plates. The lower plate is mounted on the base frame (No 13) while the upper plate supports the torque loading system (No 4), the torque loading air actuator (No 5) and a two-column piston-fixing frame (No 2) that guides the vertical piston and restrains its movement with two lock nuts on one hand and supports the vertical loading air actuator (No 1) on the other; a photo of the loading system is shown in Fig. 5.29. The electro-pneumatic (EP) valve head system (No 10) that supplies the pressurised air to the torque loading air actuator and the light-steel relief tank (No 14) are mounted on the pair of supporting columns on the right side of the cylindrical cell; the relief tank has a nominal strength of 10 kgf / cm^2 (≈ 1 MPa) against pressure. Figure 5.26 shows that the vertical loading air actuator has two chambers with different cross sectional areas (45.4 cm^2 and 27.7 cm^2) and different air pressures imposed by the vertical pressure and counter pressure system of the air unit (No 3 in Figs 5.19 and 5.26) thus both compression and extension loading can be achieved. Similarly, the torque loading air actuator has two chambers with different cross sectional areas (27.3 cm^2 and 16.3 cm^2) and different air pressures imposed by the EP valve head system thus torque can be imposed on the specimen both in the clockwise and counterclockwise direction.

Figure 5.34 shows the electro-pneumatic valve head system in detail, with Fig. 5.34a showing the pneumatic lines behind the panel and Fig. 5.34b showing the front panel. The primary air pressure is applied from the air unit (Fig. 5.26) to the three-way valve on the bottom left side of the panel (primary air pressure valve) and to the air regulator of the relief tank. The second three-way valve (actuator drive valve) on the top right of the panel is always set to the position Bal. P. (balance pressure). The air regulator is set to supply air under a pressure of around 4 kgf / cm^2(≈ 400 kPa) to the relief tank and from there to the left chamber of the torque loading air actuator, i.e. a pressure equal to one half of that supplied by the air compressor to the air unit. During testing the primary air pressure valve is set to the EP transducer position opposite to the exhaust position. After the test is over and the torque piston is disconnected from the torque loading system (No 4 in Fig. 5.19) the primary air pressure valve is set to the exhaust position impeding the flow of pressurised air towards the EP valve and from there towards the right chamber of the torque actuator thus the torque piston moves to the right. It is noted that at the beginning of the test the torque piston does not necessarily move immediately when the primary air pressure valve is set to the EP transducer position because the EP valve is controlled from the EP servo controller of the electric measuring and control unit (No 2 in Fig. 5.19) thus it can be moved slowly (with almost zero velocity) by rotating a knob in order to be connected to the torque loading system; the knob has the label *zero* and it belongs to the *valve out section* of the EP servo controller, while the switch *dither* should be set *on* before the turning of the knob in order to minimise the effects of static friction on the servo valve movement by means of applying a minute vibration, as will be discussed in Section 5.6.4.

5.6.2 WATER UNIT

Figure 5.19 shows the parts of the water unit. The de-aired water tank (No 1) is made of a transparent plastic material (lucite, which is the same material as Perspex or Plexiglass) and has a capacity of 1.5 *l* and a nominal strength of -1 kgf / cm^2(≈ -100 kPa) against negative pressure (i.e. pressure below the atmospheric level). A regulated vacuum is applied to the top of the de-aired water tank from the vacuum system panel of the air unit (No 7). The water inside the tank boils under vacuum and the dissolved air forms bubbles which are removed gradually as the time passes. Once the vacuum is neutralised the de-aired water can be circulated under gravity or higher pressure through the hydraulic lines belonging to the left side of the base box of the water unit (No 5), flushing the air out of the lines. Consequently, de-aired water can reach the volume-change measuring burette and the specimen pedestal. The vacuum tank (No 2) is identical to the de-aired water tank and can also receive a regulated vacuum from the air unit, while this partial vacuum can be delivered to the specimen cap via the specimen-high valve (see Figs 5.31 and 5.33). In this way de-aired water can be circulated through the specimen as described in Section 5.6.1.

The back-pressure tank (No 3 in Fig. 5.19) is made of lucite and has a capacity of 2.0 *l* and a nominal strength of 10 kgf / cm^2 (≈ 1 MPa) against pressure, while it is equipped with a rubber bladder inside the plastic cell. The level of back pressure is regulated in the lateral and back-pressure system of the air unit (No 2 in Fig. 5.19) and the pressurised air is supplied in the rubber bladder, as well as on top of the volume-change burette (see also Fig. 5.26). It is noted that during drained testing the back pressure is applied to the specimen pedestal using the burette and not the back-pressure tank. The confining (lateral) pressure tank (No 4 in Fig. 5.19) is identical to the back-pressure tank. The level of lateral pressure is regulated in the lateral and back-pressure system of the air unit (No 2 in Fig. 5.19) and the pressurised air is supplied in the rubber bladder, as well as on top of the triaxial cell (see also Fig. 5.26). It is noted that during triaxial testing the lateral pressure, which is equal to the pressure inside and outside the hollow cylindrical specimen, is applied to the triaxial cell by supplying pressurised air directly from the lateral and back-pressure system, and not by using the lateral-pressure tank. The lateral-pressure tank was used after the upgrade of the HCA, when the inner pressure, p_i, was differentiated from the outer pressure, p_o.

5.6.3 AIR UNIT

Figure 5.19 shows the air unit comprising the lateral and back-pressure system (No 2), the vertical pressure and counter pressure system (No 3), the electric-pneumatic (EP) regulating system (No 4), the pressure-ratio relay and air-slide system (No 5), the primary pressure system and master gauge panel (No 6) and the vacuum system panel. The air unit is also shown in the photo in Fig. 5.35, while the drawing of the network of the unit's pneumatic lines is shown in Fig. 5.26. It can be seen that the air compressor supplies pressurised air to the primary pressure system and from there the pressurised air is distributed to the other systems of the air unit as well as to the EP valve head system of the torque loading unit. The pressure of the air supplied by the compressor is around 8 kgf / cm^2 (≈ 800 kPa).

Fig. 5.36 shows the lateral pressure (LP) and back pressure (BP) system in detail, with Figs 5.36a and b showing the pneumatic lines behind the panel and the front view of the panel, respectively. This system supplies pressurised air first to the back pressure tank and volume change burette and second to the lateral pressure tank and triaxial cell (see also Fig. 5.26). The level of the two different pressures can be read on the pressure gauge by setting the meter switch either to the BP position or to the LP position. The BP regulator is used to adjust manually the level of back pressure while the lower-left three-way valve should be set to the BP position in order to allow the air to flow towards the BP tank and burette otherwise the pneumatic lines beyond the air unit are exhausted to atmosphere. It is noted that after the upgrade of the HCA the BP regulator was disabled and an individual servo valve was activated which was moved by a servo controller (which was later substituted for a drive) in order to change the back pressure under the same rate and simultaneously with the lateral pressure; by these means the saturation process was performed at constant difference between the lateral pressure and backpressure in an automatic and continuous manner. This was also feasible before the upgrade by setting the valve bias to the functional position during saturation and supplying a second input of pressurised air to the LP servo valve in the EP regulating system of the air unit (No 4 in Fig. 5.26) but this capability provided by the pneumatic positive relay mechanism of the valve was never used, thus, the backpressure was controlled only manually.

The upper-right three-way valve in the LP and BP system shown in Fig. 5.36 should be set to the LP position in order to allow the air to flow towards the LP tank and triaxial cell otherwise the pneumatic lines beyond the air unit are exhausted to atmosphere. However, the level of lateral pressure is not adjusted by this system. Figure 5.26 shows that the right servo valve in the EP regulating system of the air unit (No 4) can be moved either manually or by a clutched motor (equipped with a tacho-generator) in order to supply pressurised air to the lower-right three-way valve in the LP and BP system (No2). It is noted that the motor receives electric signal (voltage change) from a servo controller in the electric measurement and control unit (see Fig. 5.19) in order to move the EP valve. By default the rate of voltage change is adjusted manually using knobs on the panel of the servo controller yet automatic control of the lateral pressure (common inside and outside the hollow cylindrical specimen) was applied through a LabVIEW software developed at NTUA for the needs of the study by Konstadinou (2013). The apparatus was further upgraded and a new LabVIEW software was developed for the needs of the present study to achieve the independent automatic control of the inner and outer pressure. Figure 5.37 shows a servo valve in a metal body that is equipped with a clutch mechanism, a direct-current (DC) motor and a tacho generator. Two metal bodies of this type are mounted on the chassis in the EP regulating system of the air unit (No 4).

Fig. 5.38 shows the vertical pressure system in detail, with Figs 5.38a and b showing the pneumatic lines behind the panel and the front view of the panel, respectively. This system supplies pressurised air first to the upper chamber of the vertical loading actuator and second to the lower chamber of the vertical loading actuator (see also Fig. 5.26); the pressure applied to the upper chamber is called the vertical pressure (VP) while the one applied to the lower chamber is called the balance pressure (BP). The level of the two different pressures can be read on the pressure gauge by setting the meter switch either to the VP position or to the BP position. The BP regulator is used to adjust manually the level of balance pressure while the lower-left three-way valve should be set to the actuator position in order to allow the air to flow towards the actuator's lower chamber otherwise the pneumatic lines beyond the air unit are exhausted to atmosphere. Similarly, the lower-right three-way valve should be set to the actuator position in order to allow the air to flow towards the actuator's upper chamber.

The level of vertical pressure is not adjusted by the VP system instead it is adjusted by means of the left servo valve in the EP regulating system of the air unit (No 4 in Fig. 5.26) which can be moved either manually or by a clutched motor equipped with a tacho-generator. It should be noted that this servo valve has two inputs of pressurised air, one from the primary pressure system (No 6 in Fig. 5.26) and another from the pressure-ratio relay system (No 5 in Fig. 5.26). Since the valve has a pneumatic positive relay mechanism the output pressure of the valve is the sum of the signal pressure and the set bias pressure. The bias pressure is related to the lateral pressure by a factor that has to do with the cross-sectional area of the vertical piston that intrudes the pressurised triaxial cell and the cross-sectional area of the vertical load actuator inside the upper chamber. Since a buoyancy force, which is proportional to the outer pressure, p_o, in the triaxial cell and to the piston's cross-sectional area, acts on the vertical piston the vertical load acting on the specimen decreases whenever p_o increases. The bias pressure is the amount of pressure added to the signal pressure to get the vertical pressure that should be applied on the upper chamber of the vertical loading actuator in order to impose the target vertical load on the specimen under the simultaneous action of the buoyancy force. This function was deactivated after the upgrade of the HCA because the servo controller can neutralise the buoyancy force and apply the target vertical load at any time by means of a closed-loop control operation programmed in LabVIEW.

Figure 5.39 shows the electric-pneumatic (EP) regulating system in detail, with Figs 5.39a and b showing the pneumatic lines and electric parts behind the panel and the front view of the panel, respectively. The system consists of two metal bodies equipped with a servo valve, a clutch mechanism, a direct-current (DC) motor and a tacho generator, as shown in the photo in Fig. 5.37. The servo valves have a pneumatic positive relay mechanism and can be moved either manually, when the clutch mechanism is rotated counterclockwise and set to the "out position", or by the motor, when the clutch mechanism is rotated clockwise and set to the "in position".

The valves receive pressurised air from the primary pressure system in the air unit (No 6 in Fig. 5.26) and, optionally, from a second source (system 2 or 5 in the air unit in Fig. 5.26) if the bias pressure is input, as discussed previously. The tacho generator and the motor receive electrical signal (voltage change) from a servo controller in the electric measurement and control unit (see Fig. 5.19) in order to move the EP valve. By default the rate of voltage change is adjusted manually using knobs on the panel of the servo controller yet automatic control of the lateral pressure (common inside and outside the hollow cylindrical specimen) and vertical pressure was applied through a LabVIEW software developed at NTUA for the needs of the study by Konstadinou (2013). The apparatus was further upgraded and a new LabVIEW software was developed for the needs of the present study to achieve the independent automatic control of the inner pressure, outer pressure and vertical pressure.

Fig. 5.40 shows the pressure-ratio relay and air-slide system in detail, with Figs 5.40a and b showing the pneumatic lines behind the panel and the front view of the panel, respectively. The air slide regulator adjusts the pressure of the air supplied to the base plate of the triaxial cell in order to reduce the friction during sliding. The triaxial cell valve is set to the position cell slide in order to supply the pressurised air to the valve mounted on the base plate of the triaxial cell (see Fig. 5.31). The pressure ratio regulator modifies the input lateral pressure (by means of a valve equipped with a pneumatic positive relay mechanism) to produce the bias pressure that should be applied additively to the upper chamber of the vertical load actuator in order to counterbalance the buoyancy force acting on the rod intruding into the pressurised triaxial cell. The bias pressure is applied to the (vertical pressure) servo valve in the electric-pneumatic regulating system (No 4 in Fig. 5.26) and from there to the upper chamber of the vertical actuator chamber. However, the supply of the pressurised air is impeded if the vertical pressure valve on the right side of the panel shown in Fig. 5.40b is set to the exhaust position. The pressure of the air slide system or the bias pressure can be measured using the pressure gauge depending on the position of the meter switch.

Fig. 5.41 shows the primary pressure system and master gauge panel in detail, with Figs 5.41a and b showing the pneumatic lines behind the panel and the front view of the panel, respectively. The compressor air regulator adjusts the pressure that is supplied from the compressor before it is distributed to the other systems of the air unit. The adjusted pressure has a value of around 8 kgf / cm^2 (≈ 800 kPa). The master gauge panel can be used to measure the pressure in the systems of vertical pressure, balance pressure, back pressure and lateral pressure depending on the position of the four-way valve. In the case that the three-way valve is not in the exhaust position the pressurised air that is measured in the master gauge can be also directed towards the quick coupler.

Fig. 5.42 shows the vacuum system in detail, with Figs 5.42a and b showing the pneumatic lines behind the panel and the front view of the panel, respectively. This system is connected to a vacuum pump. The vacuum regulator adjusts the vacuum delivered from the vacuum pump. The vacuum or partial vacuum can be measured in the vacuum gauge and distributed to the vacuum tank, when the vacuum tank valve is not set in the exhaust position, and to the de-aired water tank, when the D.A.W. tank valve is not set in the exhaust position. A nylon tube can be connected to the quick coupler on the panel in order to deliver the partial vacuum inside the specimen mould and keep the membrane pushed against the internal surface of the mould during the preparation of the specimen.

5.6.4 ELECTRIC MEASUREMENT AND CONTROL UNIT

The electric measurement and control unit shown in Fig. 5.19 consists of the EP servo controller EO-290U (No 2), the electric amplifiers EA-400 (No3), the pressure controller (No 4), which includes a slope DC generator EO-340DU and the EM servo controllers EO-470U, and the cabinet (No 6) with a built-in power transformer for converting 220 V to 100 V (AC). The description of the electric parts that follows is based on the operation manual by SEIKEN, INC.

Electric amplifiers EA-400 series

The electric amplifiers receive and amplify the electrical signal from the transducers measuring the pressures and loads, display the voltage or the mechanical quantity corresponding to the signal and transmit the signal to the Analog to Digital Converter (ADC). Figure 5.43 shows the front and rear view of a typical electric amplifier unit (EA-400 series). The function of the switches and variable regulators of the front panel are described next:

A1. R-BAL (10 revolutions variable regulator VR):

This VR is used for balancing the initial resistance output of the transducer and bridge circuit so that the output voltage is set to zero when the transducer is under zero load / pressure.

A2. C-BAL (1 revolution variable regulator VR):

This VR is used for balancing the capacitance output of the bridge circuit of the transducer.

A3. DV-SEL (snap switch):

This switch is used for changing the function of the DV indication on the display. When set to the GAIN position, DV functions as a digital volt meter showing the original output voltage (rated voltage 5 V). When set to the DV position, DV displays the value of the engineering quantity corresponding to the output voltage via the calibration relationship of the amplifier. To calibrate the amplifier the output voltage is set to zero when the transducer is under zero load / pressure (see the A1 item of this list) while the DV display is set to the desired value when the transducer is under full load. For example, if the rated capacity of the transducer is 200 kgf then the DV is set to 200.0 by turning DV variable regulator (see the A6 item below) while the output voltage attains its maximum value (rated voltage 5V); the maximum DV is 1999. When the DV-SEL switch is set to C position the DV is used for adjusting the capacitance output using the C-BAL variable regulator (see the A1 item) during calibration. It is noted that the two-point calibration of the amplifier is followed by multiple-point calibration of the transducers in order to check the linearity of the latter. The DV-SEL switch is set to DV position during testing.

A4. ATT switch:

This switch is used for changing the sensitivity of the amplifier. When set to the ½ position the sensitivity becomes two times higher though the maximum value of the physical (engineering) quantity that can be measured falls to one half (reverse attenuator).

A5. GAIN (10 revolutions variable regulator VR):

This variable regulator is used for changing continuously the sensitivity of the amplifier from zero to maximum by adjusting the output voltage of the amplifier.

A6. DV (10 revolutions variable regulator VR):

This VR is used for adjusting the DV until the calibration number of the transducer corresponding to full load conditions is displayed (see the A3 item above).

A7. CAL switch:

This switch is used for calibrating the sensitivity of the amplifier. Calibration in two steps corresponding to 1 and ½ setting of sensitivity can be performed using this switch, which should be set to the OFF position during testing.

A8. AL (1 revolution variable regulator VR):

This is a spare VR which is not used at the time of writing this documentation.

A9. POWER switch:

This is the ON/OFF switch of the power supply.

The following list describes the functions of the terminals on the back panel of the electric amplifier units (EA-400 series):

B1. AC 100 V CORD:

This is the power supply cord.

B2. INPUT CONNECTOR:

This is the connector for the input signal from the transducer.

B3. OUT TERMINALS:

These are output terminals for connecting recorders or controllers with high impedance. The output from these terminals is max. ±5 V / 5 kΩ resistance.

B4. E (GND) TERMINALS:

These are ground terminals.

B5. INT E EXT TERMINALS:

In the case that multiple amplifiers are used it is necessary to synchronise the carrier frequencies of the amplifiers to avoid mutual interference. One amplifier is chosen to be the "parent" and the INT-EXT switch is set to INT position. The INT-EXT switches of the other amplifiers are set to EXT position. The INT-E terminal of the parent amplifier is connected to the EXT-E terminal of the remaining amplifiers with attached cords. In the case that only one amplifier is used the INT-EXT switch is set to the INT position and the connection to the other amplifiers is not needed.

B6. CAL ADJ variable regulators (VRS) on the side panel:

These VRS are used for adjusting the calibration value to the rated output strain of the transducer. Usually, VR marking 1 is the adjustment for around 2000 μst and another marking ½ is the adjustment for around 1000 μst.

Operation and calibration of the electric amplifiers EA-400 series

The procedure to make the electric amplifiers EA-400 series operate is as follows:

1. The power switch of the amplifier is set to "on" and the amplifier is left for about 15 minutes to warm up.

2. Remove any load from the transducer.

3. Set the ATT switch to "1" (up) position.

4. Set the CAL switch to "off" (neutral) position.

5. Set DV-SEL switch to "c" position.

6. Turn slightly the C-BAL VR to attain a digital indication as close as possible to 000 (0.00 or 00.0). Continue to the next step even if the digital indication is not exactly zero, e.g. if it is 00.5 or 0.05.

7. Turn the DV-SEL switch to GAIN position.

8. Turn the R-BAL VR until the digital indication is exactly zero (000 or 00.0 or 0.00). In the case that the digital indication cannot be set to exactly zero then turn the DV-SEL switch to "c" position and set the digital indication as close as possible to zero by

turning the C-BAL VR. By these means the digital indication can be set to exactly zero by repeating this process and turning R-BAL and C-BAL VRS consecutively.

9. Turn the DV-SEL to GAIN position and set the digital indication to 0.00 or 00.0 by turning the R-BAL VR.

10. Set the CAL switch to “up” position.

11. Set the digital indication to 500 (or 50.0 or 5.00) by turning the GAIN VR; this digital indication corresponds to an output voltage of 5 V.

12. Set the DV-SEL switch to DV position.

13. Set the digital indication to the value corresponding to the rated capacity of the physical (engineer) quantity of the transducer by turning the DV VR. For example, if a load cell with a rated capacity of 200 kgf is used then the digital indication is set to 199.9 (see the A3 item above) and this indication corresponds to an output voltage of 5V. Recall that no load acts upon the transducer.

14. Turn the CAL switch to “off” position.

15. Measurements can be now taken.

Whenever measurements are taken the position of each switch should be as described next: the ATT switch is set either to “1” or to”1/2” position; the CAL switch is set to “off” position; the DV SEL switch is set either to GAIN or to DV position in order to show the output voltage or the value of the physical (engineer) quantity, respectively, with the digital indication of 500 (or 5.00 or 50.0) corresponding to an output voltage of 5 V in the former case.

Operation remark

1. Once the adjustment of the C-BAL VR is done the procedure need not to be repeated each time the amplifier is used. The R-BAL VR can be used instead to set the digital indication to zero. In the case that the extension cable is changed the C-BAL VR should be adjusted once again.

2. If the ATT switch is set to “1/2” position the one half of the rated capacity of the transducer can be made to correspond to an output voltage of 5 V thus the sensitivity of the amplifier becomes two times higher than that corresponding to “1” position. In order to do so the ATT switch is set to “1/2” position and the CAL switch is set to “down” position to adjust the digital indication by turning the GAIN VR. The digital indication should be set to ½ of the capacity of the transducer while the DV-SEL switch is set to the DV position.

The (re-)calibration procedure of the electric amplifiers EA-400 series is as follows:

1. A transducer (load cell, pressure transducer, differential pressure transducer, displacement transducer etc.) is connected to the electric amplifier.

2. The operation method described above is followed in order to take zero balance and GAIN adjustment.

3. The DV-SEL switch is set to GAIN position and the ATT switch is set to "1" position. In the case that no physical load is applied on the transducer the C-BAL and R-BAL VRS are set to zero. After the completion of this process the CAL switch is set to "up" position that corresponds to the rated capacity of the transducer. In the case that the capacity of the transducer is, for example, 200 kgf then the GAIN VR is turned so that the digital indication shows 500 (or 50.0 or 5.00). Afterwards, the CAL switch is turned to "off" position and the digital indication returns to zero.

4. The maximum amount of the physical quantity (load, displacement, pressure) is applied on the transducer precisely. For example, the pressure corresponding to 200 kgf can be applied on the load cell with a capacity of 200 kgf using a DH Budenberg hydraulic dead-weight tester. If in that case the digital indicator shows, for example, 51.0 then the GAIN VR is turned until the indication becomes 50.0. The indication should show 0 after the removal of the physical load.

5. The body of the amplifier is pulled out of the chassis and two small VRS are exposed on the right side having the stamps CALIB 1 and CALIB 2. The CAL switch is set to the "up" (1) position corresponding to the rated capacity of the transducer. Let the digital indication be 50.5 then the CALIB 1 VR situated at the right side is turned until the indication becomes 50.0. Afterwards, the CAL switch is set to the "down" (1/2) position corresponding to one half of the rated capacity of the transducer and the CALIB 2 VR is turned until the indication becomes 25.0. The CAL switch is reset to "off" position and a physical load, let it be 200 kgf at ATT 1, is applied on the transducer. If the digital indication is 50.0 then the (re-)calibration process has been accomplished; if not the same procedure is repeated from the beginning.

End of description of the electric amplifiers EA-400 series

EP servo controller EO-290 (U)

The front view of the EP servo controller EO-290 (U) is shown in Fig. 5.44, while the rear view is shown in Fig. 5.45. This servo controller can perform closed-loop control of dynamic or static loads imposed on soil specimens by means of pneumatic servo valves and pistons. The apparatus may function with hydraulic servo valves as well. The EP servo controller EO-290 (U) consists of the following parts:

- Dynamic Function Generator which produces the dynamic reference signal.
- Static Function Generator which produces the static DC slope reference signal.
- Mixture Amplifier of FB (feedback) and reference signal.

- Two Control Systems available by means of an alternating switch.
- Servo Amplifier.
- Limit and Auto Stop Circuits for safety control.

This controller can alternatively perform automatic control by means of a personal computer (PC).

Functions of the EP servo controller EO-290 (U)

1. POWER BUTTON:

This is the ON/OFF button of the power supply. The lamp is turned on when the button is ON.

2. OP-SELECT BUTTON:

This button is used for selecting [MANU] or [CPU] operation. [MANU] is manual operation. [CPU] is the operation partly supported by a PC. In the case that this button is capped the controller is exclusively in the manual operation mode.

3. EMERGENCY BUTTON:

This is the button for emergency stop. When this button is pushed the lamp is turned on and the button becomes locked. To unlock the button the knob should be turned clockwise. The lamp will shed light even when the external emergency stop signal has been activated.

(Regarding the input terminals of external emergency stop signal please refer to the description that follows concerning the IN/OUT TERMINALS on the back panel).

4. LED LAMPS, SWITCHES UNDER EMERGENCY BUTTON:

Whenever a LED lamp is turned on a limit signal has been activated. The limit signal may or may not stop the control depending on the position of the ON/OFF switch. If the limit signal has been activated and the control has stopped this situation remains until the cause of the activation is removed and the RESET button is pushed. Whenever the switch under the lamp is turned on the controller stops under the following limit conditions:

[ACT]: The circuit that monitors the output to the servo valve has reached its limit and thus the lamp is turned on and the control stops.

[EXT]: An over stroke limit device (micro switch) that functions mechanically reaches its limit. The input terminals are marked as (1-2) on the back panel.

[AUX]: This is a spare limit circuit with the input terminals marked as (3-4) on the back panel.

5. The OP-SELECT button can be pushed in order to activate the optional operation of PC support.

6. DYNAMIC FUNCTION GENERATOR:

This part produces dynamic target signal for performing dynamic loading tests. Alternatively, an external source can be used for producing the dynamic target signal.

6-1. MULTI RANGE (frequency range):

This switch has distinct positions and is used in combination with the FREQUENCY DIAL, described next, to change the frequency of the target signal and, thus, control the loading frequency.

6-2. FREQUENCY DIAL (frequency fine control dial; Hz):

This dial can be rotated continuously in order to adjust the oscillation frequency of the target signal in combination with the MULTI RANGE SWITCH (10 - 100%) as shown next.

MULTI RANGE SWITCH	FREQUENCY (Hz)
x 0.01	0.01 - 0.1
x 0.1	0.1 - 1
x 1	1 - 10
x 10	10 - 100

6-3. WAVE (oscillation wave selection switch):

This switch is used to select the waveform among sine, triangle and square waves.

6-4. POL (oscillation starting polarity switch):

This switch is used to change the initial polarity of the waveform, being either positive or negative.

6-5. START (start switch for oscillations):

The oscillations start/stop manually if the switch is set to MANU position otherwise the oscillations start/stop in accordance with the commands taken from the external source (CPU support operation by means of a PC) when the switch is set to the AUTO position. In order to start or stop the oscillations manually the buttons START or STOP on the right side of the panel should be pushed, respectively.

6-6. PRESET COUNTER:

This part is used for counting the number of oscillations while an auto-stop module is available to stop the oscillations when the preset number of oscillations is completed. The electro COUNTER shows six digits. The counting mode is set to ADDING COUNT from zero. When the oscillations number reaches the preset number the module gives a COUNT UP signal for AUTO STOP (the default mode upon delivery is UPF).

6-7. COUNT:

This switch is used for selecting the counting range as shown next.

COUNT SWITCH	COUNTING RANGE
x 1	x 1 (counting number=actual oscillations number)
x 10	x 1/10 (CN=1/10 AON)
x 100	x 1/100 (CN=1/100 AON)

The counting number is changed in accordance with the COUNT switch. The PRESET COUNTER should be set accordingly.

6-8. CONT ON/OFF:

This switch is used for selecting AUTO STOP or NON STOP when the module sends the COUNT UP signal. If the switch is set to ON then the AUTO STOP is activated otherwise the AUTO STOP is de-activated.

6-9. PRESET AND RESET MODES OF THE COUNTER:

The following drawing and instructions explain how to preset and reset the counter.

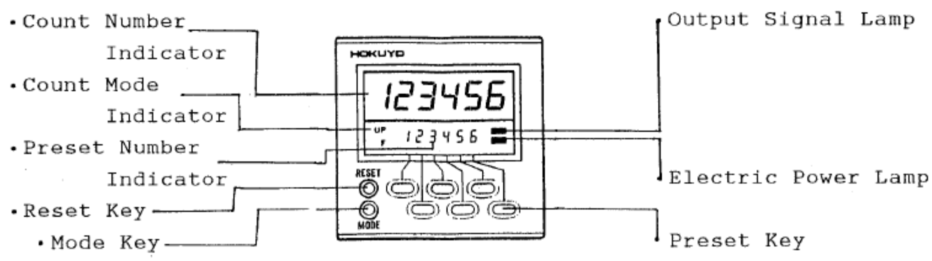

PRESET MODE:

a) This mode is available irrespective of whether the electric power is on or off.

b) The MODE KEY is pushed to activate the PRESET MODE. The PRESET NUMBER INDICATOR flickers. Every time the PRESET KEY is pushed the given digit will increase by one unit. In this way each digit may be preset to the desired value.

c) When the PRESET is completed the MODE KEY is pushed and the COUNT UP mode is activated.

d) In order to change the PRESET NUMBER during the counting process the PRESET MODE should be first activated (by pushing the MODE KEY) and the PRESET NUMBER can be then changed as described previously (in the b item). Finally, the MODE KEY should be pushed. In the case that the PRESET NUMBER is lower than the current number of oscillations the COUNT UP signal is shown immediately.

RESET MODE:

a) RESET is activated by pushing the RESET KEY more than 0.2 seconds. The COUNT NUMBER becomes zero and the output changes from ON to OFF.

b) The electric power lamp is turned on when the electric power is on.

c) The output signal lamp is turned on when the COUNT NUMBER reaches the PRESET NUMBER and the output signal appears.

6-10. MONITOR JACK:

This is an output terminal for monitoring the output voltage using an external measuring instrument. The measuring instrument must have an impedance more than 100 kΩ. The original waveform and voltage level has a rated level of 10 V peak to peak that is not adjusted through the DYNAMIC LEVEL SETTING DIAL (DY PEAK DIAL described next).

6-11. Additional information concerning the 6-5 item: When the START switch is set to MANU the oscillations start. The output can be checked using the MONITOR JACK. COUNTER does not function during this oscillation. If the switch is then changed to AUTO the oscillations stop. When the START button (on the right side of the panel) is pushed while the oscillations occur in MANU mode the oscillating signal enters this time in the reference signal circuit through the DY DIAL, which adjusts the amplitude of the reference signal, and COUNTER begins to work concurrently. If the START switch is set to AUTO from MANU in this state the oscillations continue to occur as previously.

7. SLOPE GENERATOR:

This function generator produces as an output a Slope DC Voltage that is the command signal for the servo controller. The DC Voltage increases or decreases in a preset constant rate.

After the upgrading of the HCA the rate of the voltage corresponding to the target rate of torsional-shear stress, $\tau_{z\theta}$, can be easily produced externally using the LabVIEW software in a closed-loop control system. Consequently, the operation of the SLOPE GENERATOR is not described further herein; the description can be found in the operation manual by SEIKEN, INC. or in the work by Tsomokos (2005).

8. TEST FORM PLACER AND SERVO AMPLIFIER SECTION:

This unit consists of feedback (FB) Mode Selection, BIAS reference setting, Static and Dynamic Signal Input, Mixture Amplifier of FB and Reference signals and Servo Amplifier.

8-1. Outline of this section: As shown in Fig. 5.44 this section can be divided into two main control systems. The first control system is PRIM (A) which is used mainly for the consolidation process while the second control system is SEC (B) which is used for the shearing process. The two control systems have approximately the same functions which are the FB Mode Selection, BIAS reference setting, Mixture Amplifier and servo gain controller. Accordingly, the servo control can be switched from PRIM (A) to SEC (B) system and vice versa. In order to perform the switch the difference in the voltage level of both systems can be monitored and the servo valve can be controlled by either system. The functions used for zero adjusting of the servo valve are built in. (It is noted that in this study both consolidation and shearing are performed under stress-controlled conditions using pneumatic servo valves and the same LabVIEW program thus no switch is needed).

This controller can be connected to three different kinds of servo valves. The one kind is hydraulic servo valve while the other two kinds are pneumatic servo valves.

8-2. PRIM (A) SYSTEM (used mainly for consolidation):

8-2-1. FB SELECTION:

This switch is used for selecting the FB mode. Four types of modes are available which are L (load), D_1 (large displacement), D_2 (small displacement) and AUX (auxiliary).

8-2-2. BIAS +/-:

This is the manual dial for setting the BIAS reference voltage before applying static or dynamic load. It can be set to 0 - ±5 V with the polarity being adjusted by the polarity switch on the left of the dial.

8-2-3. GAIN:

This is the dial for setting the amplification level of the differential signal between REF and FB from PRIM (A) to provide the input for the servo amplifier. The maximum amplification level is about 25 times.

8-3. COMMON SECTION:

This section is used for inputting the slope DC reference signal etc. to both the PRIM (A) and SEC (B) systems.

8-3-1. REF 1:

This switch is used for selecting a static reference signal among three types, SLOPE (SLOPE DC GENERATOR), EXT (SIGNAL FROM EXTERNAL SOURCE) and OFF (NO SIGNAL).

8-3-2. REF 2:

This switch has the same function as the REF 1 switch. It is used for selecting a reference signal among two types, AUX (AUXILIARY OF EXTERNAL SIGNAL) and OFF (NO SIGNAL). In the case that this switch is not used it is set to the OFF position.

8-3-3. SELECT:

This push button is used for switching the control from the PRIM (A) to the SEC (B) system and vice versa. The difference in the voltage of the two systems should be set to zero at the instant of switching using the A/B AND SENSE TRIMMER, as explained in a subsequent chapter.

8-4. SEC (B) SYSTEM (used mainly for shearing):

8-4-1. FB SEL:

This switch is used for selecting the FB mode among five types, LL, LD_1, LD_2, DD and AUX.

LL (static load, dynamic load with no high-pass filter)

LD_1 (static load, dynamic large displacement differentiated by 0.2 Hz high-pass filter)

LD_2 (static load, dynamic small displacement differentiated by 0.2 Hz high-pass filter)

8-4-2. BIAS +/-:

This is the manual dial for setting the BIAS reference voltage before applying static or dynamic load. It can be set to 0 - ±5 V with the polarity being adjusted by the polarity switch on the left of the dial.

8-4-3. GAIN:

This is the dial for setting the amplification level of the differential signal between REF and FB from SEC (B) system to provide the input for the servo amplifier. The maximum amplification level is about 25 times.

8-4-4. REF 1, REF 2:

This switch is used for selecting the reference signal as described previously in the 8-3-1 and 8-3-2 items. When these switches are set to the ON position the signal is put in the SEC (B) system.

8-4-5. DY-PEAK:

This dial is used for setting the dynamic amplitude level. It can be set to 0 - ±5 V that is 0 – 10 V peak-to-peak by turning the dial 0 - 10 times.

8-4-6. DY-INT/EXT SWITCH:

This switch can be used for selecting the dynamic reference signal either from the internal (function generator) or the external source. When the dynamic reference signal is put in from an external source the voltage level, frequency, waveform etc. should be considered carefully.

8-4-7. START/STOP BUTTON:

This button is used for starting or stopping manually the oscillations of the Dynamic Function Generator. In the case that auto-stop signal is activated the oscillations stop automatically.

8-4-8. SELECT PRIM/SEC PUSH BUTTON, LAMP:

This button is used for switching from PRIM (A) to SEC (B) control system and vice versa. At the instant of switching the voltage difference in the two systems is set to zero and the lamp turns on.

8-4-9. MONITOR DV (DIGITAL INDICATOR):

This digital indicator is used for monitoring the levels of FB, servo amplification and voltage difference between the two servo control systems. The MONITOR SEL switch to the right of the digital indicator is used for selecting the display.

8-4-10. MONITOR SEL SWITCH:

A. L, D_1, D_2, AUX: The feedback input level is monitored at this points. The trimmer can be turned carefully in the clockwise direction for about 20 revolutions (without a stopper) until the maximum voltage level (i.e. rated 5 V) is displayed. If the trimmer is then turned in the counterclockwise direction a smaller voltage can be displayed in the monitor. The trimmers should be turned with caution.

B. VALVE OUT: When the switch is set to this position the voltage applied to the servo valve is displayed. The voltage level is adjusted by the ZERO DIAL in the VALVE OUT section to the right of the MONITOR SEL section. The type of the servo valve is selected by the VALVE SEL switch in the VALVE OUT section.

C. A/B and SENSE (TRIMMER): These points are used for controlling the voltage difference between PRIM (A) and SEC (B) described in the 8-4-8 item. If the voltage difference is large the outmost left digit in the monitor becomes “1”. In this case the monitoring sensitivity is too high and should be decreased by turning the sensitivity trimmer counterclockwise. When a number less than “1999” is displayed this number can be decreased by turning the GAIN DIAL in the SEC (B) section. If the displayed number becomes small the monitoring sensitivity can be increased by turning the sensitivity trimmer clockwise to make the number near “0”. When the number becomes approximately “0” the servo control system can be switched from PRIM (A) to SEC (B).

D. DITHER ON/OFF AND ADJ TRIMMER: A minute vibration is imposed to the servo valve in order to reduce the static friction. The signal causing the vibration is activated or de-activated by setting the switch to the ON or OFF position, respectively. The ADJ trimmer adjusts the signal level.

8-4-11. ZERO DIAL:

This dial is use for adjusting the voltage level (zero point) of the servo valve.

8-4-12. VALVE SEL SWITCH:

This switch is used for selecting the servo valve type.

SV: Hydraulic servo valve (Tokyo Seimitsu Sokki Co. Ltd. 400 Ω ± 15 mA).

EP-1: Pneumatic servo valve (Fujikura Rubber Co. Ltd. RT-8-2, 0-10 V).

EP-2: Pneumatic servo valve (FEST MPYE 0-10 V).

Note: SV & EP-1 with neutral shift, EP-2 with DC 24 V excitation.

8-4-13. MONITOR SEL, MONITOR JACK at the centre below:

This output terminal can be used for checking the internal state externally, using a measuring instrument with impedance more than 1 MΩ.

9. ARRANGEMENT AND FUNCTION OF THE REAR SIDE CONNECTOR

CONNECTOR NUMBER:

AC 100 V: Input of electric power source (AC 100 V, ±10%, 50-60 Hz).

GND: Grounded terminal.

1: It is used for inputting the dynamic reference signal from an external source (DY=> EXT INPUT).

2: Input connector for L (P) and loading feedback signal.

3: Input connector for D1 (DL) and Displacement-1 (large displacement) feedback signal.

4: Input connector for D2 (DS) and Displacement-2 (small displacement) feedback signal.

5: Input connector for Auxiliary (AUX) feedback signal (rated ±5 V).

6. Signal input connector from slope generator to COMMON-REF-1.

7. External input connector for COMMON-REF-1.

8. Auxiliary input connector for COMMON-REF-2.

9. Output connector for hydraulic servo valve (SV).

10. Output connector for pneumatic valve (EP-1) (Fujikura Rubber Co. Ltd.).

11. Output connector for pneumatic valve (EP-2) (FEST) - with 24 V excitation.

12, 13 & 14. These connectors are used if a PC is used for control.

End of description of the EP servo controller EO-290 (U)

EM servo controller EO-470 (U)

1. GENERAL:

The front and rear view of the EM servo controller EO-470 (U) are shown in Fig. 5.46. This apparatus is used to drive the DC servo motor for applying the vertical load or confining pressure under open or closed-loop conditions for soil testing. It consists of the functions of driving and controlling the DC servo motor and the circuit for setting reference signal and selecting FB according to the desired type of test.

Main parts:

A1. Test type section: The role of this section is to select and set the reference signal, select the feedback input, make calculations concerning the combination of the two signals and amplify the voltage difference of the two signals.

A2. Amplification section: This section is used for amplifying the power of DC servo motor.

A3. Electric circuit section: This section is used for controlling and driving an electromagnetic clutch.

Available control:

B1. Open-loop control of speed (Tacho generator control).

B2. Closed-loop control of load and displacement.

Optional functions:

C1. PID Control Circuit Unit for performing closed-loop control.

C2. Timer Control Unit for controlling the power (ON/OFF) of the motor.

C3. Thermal Relay Unit, incorporated in the rear panel, for safety stop of the DC motor when detecting excess current.

C4. The apparatus with the suffix “U” in the model type includes I/F circuit in order to control a reference, a feedback signal, ON/OFF control of motor and clutch from a PC.

2. DESCRIPTION OF THE REGULATORS AND SWITCHES ON THE FRONT AND REAR PANELS

Note: When using the model with the suffix “U” it should be confirmed before changing MANUAL control to PC or conversely that the corresponding switch for motor and clutch is put off.

This controller is used in combination with other controllers, measuring instruments and the main parts of the testing apparatus. The interaction between the different parts should be considered carefully for safety reasons. This section describes only the functions of this single controller.

2-1 FUNCTIONS OF REGULATORS AND SWITCHES

2-1-1. [A] REF SWITCH 1, 2, OFF:

This switch is for selecting the reference signal. The positions 1, 2 and OFF are available. Input connection is made to REF 1-E, 2-E terminals on the rear side. The rated input level is ±5.00 V. Input impedance is 50 kΩ. Input frequency is limited from static (DC) to very low frequency in consideration of the response of the motor speed.

2-1-2. [A] FB SWITCH 1, 2, OFF:

This switch is for selecting a feedback signal from the sensor amplifier etc. The positions 1, 2 and OFF are available. Input connection is made to FB 1-E, 2-E terminals on the rear side. The input characteristics are the same as those of the REF input connection.

2-1-3. [A] BIAS, [B] RATE DIAL (0-100%, 1000 uniform divisions): L, UL SWITCH (LOAD +, UNLOAD -)

This dial is used for setting a static reference level. When the dial is used in combination with the polarity selection switch L (+), UL (-) the setting range becomes 0 to +5 V or -5 V. In the case of open-loop control (B: TG-FB) the dial works as the loading speed controller (B: RATE) the full span of which corresponds to the motors maximum revolution.

2-1-4. ZERO REGULATOR:

This regulator is located to the upper right of the RATE DIAL. Even when the REF, FB and BIAS are zero (GAIN is adjusted to some degree) the motor may turn slightly due to the zero drift of the complete circuit system.

2-1-5. SELECTOR - SWITCH RELATION:

A1. CLUTCH <INT> <EXT> <ON> <OFF>

ON/OFF SWITCH is used for activating/de-activating an electromagnetic clutch.

The following operation settings are needed for switching ON/OFF:

In the case of INT position the manual operation is selected and the ON/OFF switch controls the clutch. If the ON position is selected a lamp will be lighted.

In the case of EXT position the ON/OFF SWITCH is available when the rear (EXT-CONT) terminals are connected. Therefore, when the SWITCH is set to the ON position the external terminals can control the clutch.

Optional: If the CPU control function is activated and the ON/OFF SWITCH is set to ON and the OPERATION SWITCH is set to CPU then the CPU can change the clutch ON/OFF through I/F connector.

The clutch model is MZ-2.5D (OGURA). The rated electric power is DC 24 V, 0.6 A. The cables from the clutch are connected to the rear side terminals “+” and “-”, in accordance with the following drawing:

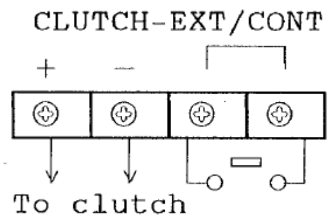

External control of the clutch can be achieved by shortening EXT/CONT rear terminals with an electric relay contact etc.

A2. MOTOR <ON> <OFF>

This switch is used for driving the motor. The lamp will be lighted when the switch is set to the ON position, while when the switch is set to the OFF position the lamp will turn off and the motor will stop.

In the case that the MOTOR STOP terminals on the rear side are shortened by the external relay connection the motor will stop.

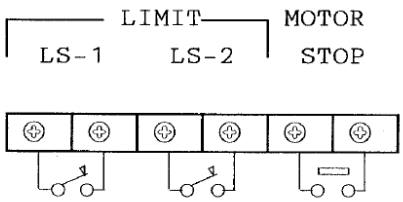

Optional: If the CPU control is used and the OP SEL SWITCH is set to the CPU position the CPU signal can set the motor ON/OFF.

A3. OP-SEL <MANU> <CPU>

This switch is used for selecting the operation type. The one type is MANUAL operation while the other is CPU operation. Computer (CPU) control includes the ON/OFF function of the clutch and motor, and REF and FB signals.

A4. CONT-SELECT <A: NOR> <B: TG-FB>

This switch is used for selecting between the closed-loop function (STD FB- sensor servo loop) and the open-loop function ([B] TG-FB, tacho generator feedback).

In the case of STD FB (closed-loop control) the reference signal can be set: (i) [A] BIAS dial setting value, (ii) INPUT from REF-1 or REF-2. (In the case of CPU/OP it is feasible to input REF from (i) and CPU-REF). Regarding the feedback value, the feedback signal from (i) FB-1, FB-2 is feasible. (In the case of CPU/OP the CPU FB is active).

In the case of TG-FB (open-loop control) the reference signal can be set: (i) [B] RATE dial setting value and (ii) INPUT from REF-1 or REF-2. (In the case of CPU/OP it is feasible to input REF from (i) and CPU-REF).

2-1-6. MS (RESET) BUTTON:

(LS-1) and (LS-2) of LIMIT SWITCH on the rear terminal panel are input terminals for contact signal which can stop the motor. When the motor functions a loading jack moves. If the loading jack reaches the upper or lower limit the limit switch closes and the motor stops. If either of the limit switches is closed the MS lamp on the front panel is lighted. The motor should be moved on the opposite direction to open the switch and the MS lamp will turn off by pushing then the MS button.

2-1-7. MONITOR (DV DISPLAY):

This monitor shows the I/O level. It is used in combination with the selection switch on its right side and the sensitivity switch DV-HI/LO.

2-1-8. DISPLAY SELECTION, DV-HI/LO SWITCH:

The DV-HI/LO switch changes the sensitivity of the display by a ratio of 10 to 1.

The positions of the SELECTION SWITCH are:

[A] REF: The display shows the reference level which is selected by the REF SWITCH 1 and 2. The rated voltage is 5 V. In the LO position the display shows 500 at 5 V maximum. In the HI position the display shows 199.9 at 2 V maximum. It is recommended to generally monitor at LO.

[A] FB: The display shows the feedback level which is selected by FB SWITCH 1 and 2. The rated voltage is 5 V. In the LO position the display shows 500 at 5 V maximum. In the HI position the display shows 199.9 at 2 V maximum. It is recommended to generally monitor at LO.

[A] BIAS: The display shows the BIAS voltage. The rated voltage is 5 V (at full RATE). In the LO position the display shows 500 at 5 V maximum. In the HI position the display shows 199.9 at 2 V maximum. It is recommended to generally monitor at LO.

MOTOR: The display shows the voltage of TACHO GENERATOR. Depending on the type of the motor the generated voltage is 3 V / krpm or 7 V / krpm. For motor rated revolution rate 3 krpm the generated voltage is 9 V or 21 V and the display is 900 or 210 at LO; the HI sensitivity may be preferable when the motor is functioning at low revolution rate. The polarity (sign) of the displayed value depends on the movement direction.

[B] RATE: The display shows the loading speed.

2-1-9. GAIN DIAL:

CONT-SEL A: STD-FB (closed-loop control)

This dial adjusts the amplification of the voltage difference between reference and feedback. In the outmost left position the amplification is zero and as the dial is turned to the right the GAIN increases. When the maximum value “1000” is displayed the amplification is 500 times by default. (It is feasible to adjust the GAIN to 1000 times amplification using the internal regulator).

CONT-SEL B: TG-FB (open-loop control)

When sending a speed order signal from RATE DIAL to SERVO MODULE this part serves as an amplifying regulator which raises the rated output voltage from 5 V to 10 V. Consequently, zero division corresponds to zero voltage while 1000 division corresponds to 10 V.

2-1-10. MONITOR OUTPUT JACK SELECTOR:

This output jack can be used for monitoring the I/O signals of various internal circuits of the controller by means of digital volt meter, oscilloscope etc. The signals that can be checked are:

1. REF voltage from CPU.

2. Selected voltage from REF-1 or REF-2.

3. Adjusted voltage from A-BIAS.

4. Adjusted voltage from B-RATE.

5. Input voltage of SERVO MODULE (SMD-IN).

6. Output voltage of TACHO GENERATOR.

7. Spare.

2-1-11. POWER:

This is the ON/OFF electric power button.

2-1-12 MOTOR MOVEMENT DIRECTION SELECTOR SWITCH ON THE REAR PANEL (M REV-CCW/CW):

The position of this switch in combination with the connection of the cables to the terminals on the rear panel make the motor move clockwise or counter clockwise.

2-1-13. TIMER TERMINALS:

These terminals on the rear panel can be connected with an external optional controller (Timer Unit) and make the motor stop under pre-defined conditions.

2-1-14. AC 100 V, GND TERMINAL ON THE REAR PANEL:

The first terminal is connected to electric power source AC 100 V, 50-60 Hz while the second terminal is used for grounding.

2-1-15. PID INPUT/OUTPUT TERMINAL AND CPU I/O CONNECTOR:

The terminal and connector are used in the case of external control by means of a PC.

2-1-16. REGULATORS <I, G, Φ, V, O> IN SVA ADJ BLOCK:

These regulators are semi fixed VRS of the power module of the Servo Motor adjusted by the manufacturer and should not be modified.

End of description of the EM servo controller EO-470 (U)

5.7 THE HOLLOW CYLINDER APPARATUS OF THE NATIONAL TECHNICAL UNIVERSITY OF ATHENS AFTER UPGRADING

The hollow cylinder apparatus (HCA) of the National Technical University of Athens (NTUA) was upgraded for the needs of the present study. The aim was to control independently the magnitude of the three principal stresses and the direction of the minor and major principal stresses with respect to the vertical. By these means the stress paths shown in Figs 5.2 and 5.4 can be performed and the effects of inherent anisotropy, mode of loading and principal stress rotation on the mechanical behaviour of soils can be investigated. Note that in earlier studies performed at the NTUA (Tsomokos 2005, Kontsadinou 2013) the pressure inside and outside the hollow cylindrical specimen was the same thus the principal stress direction angle, $\alpha_{\sigma'1}$, and the intermediate principal stress parameter, b, could not be controlled independently since b = $\sin^2 \alpha_{\sigma'1}$. This means that the influence of $\alpha_{\sigma'1}$ on soil's mechanical behaviour cannot be investigated without altering b, and vice versa. Moreover, the effect of principal stress rotation on soil's mechanical behaviour cannot be investigated without altering the Lode angle, and vice versa. In order to remedy this deficiency a fourth servo valve was added to the existing three (the third servo valve and servo controller were also installed for the needs of the present study), as well as a new drive, in order to control independently the inner and outer cell pressures, p_i and p_o, respectively, and the pore-water pressure, u. The upgrade process involved important modifications of the metal chassis, electric-cable connections, hydraulic lines and pneumatic lines. New software was developed in LabVIEW programming environment that allows the closed-loop control of stresses using a PC. The measurement instrumentation was recalibrated, while new on-sample instrumentation was installed, calibrated and used and its performance was assessed.

The independent control of the magnitude and direction of the principal stresses (Fig. 5.1b) is achieved by controlling the boundary loads and pressures acting on the hollow cylindrical specimen shown in Fig. 5.1a. The vertical load, F, is imposed by the vertical pneumatic actuator shown in Fig. 5.26 and described in Section 5.6.1. A pneumatic servo valve in the Air Unit (see Figs 5.26 and 5.37, and Section 5.6.3) supplies the pressurised air to the actuator, while a servo controller EO-470 (U) in the electric and measurement unit (see Figs 5.19 and 5.46, and Section 5.6.4) controls the motor that moves the servo valve. The electric signal from the load cell is amplified in the electric amplifiers (EA-400 series; see Fig. 5.43 and Section 5.64) and gives the feedback which is compared at any instant with the reference signal produced by the LabVIEW program. The difference between the reference and feedback signal is amplified in the servo controller's circuits (GAIN function; see Section 5.6.4) and the closed-loop control adjusts the speed of the motor that moves the servo valve in order to impose the target voltage that changes under constant or alternating rate. It is noted that the target voltage corresponds to the target load, F, via the calibration relationship of the load cell. The actual stress acting on the specimen depends also on the cross-sectional area of the specimen and the membrane stress though this dependence is not considered in the closed-loop control in order to avoid the potential destabilisation of the loading system.

The principles of closed-loop stress control described for the vertical load, F, are also applied in the case of the inner pressure, p_i, outer pressure, p_o, and torque, T. The control of p_i and p_o is achieved using two servo controllers EO-470 (U), one of which was newly installed. The control of T is achieved using the existing servo controller EO-290 (U), shown in Fig. 5.44 and described in Section 5.6.4, which interacts with the servo valve in the loading system, shown in Figs 5.19, 5.16 and 5.34 and described in Section 5.6.1. The pore-water pressure, u, is controlled using a newly installed drive (accessed from the back of the chassis / cabinet) that moves the servo valve by generating voltage changes under constant rate (slope generator), adjusted by the LabVIEW software. By these means the saturation of the specimen is achieved by increasing simultaneously the confining pressure and backpressure with the same rate and thus keeping their difference constant. Two servo valves equipped with two DC servo motors were installed in the chassis for adjusting automatically the backpressure and the inner cell pressure. An electric amplifier was installed for conditioning the signal from the inner cell pressure transducer, while another electric amplifier was installed for conditioning the signal from the differential pressure transducer used for measuring the volume changes in the inner cell environment; the second amplifier was installed for future usage, awaiting the addition of a second burette. Figure 5.47 shows the Air Unit and the Electric Measurement and Control Unit after the upgrade of the HCA for the needs of the present study.

Figure 5.48 shows the LabVIEW program developed for producing the reference electric signal input to the servo controllers and recording the data; the program was developed by Dr. Georgopoulos while the author provided the necessary feedback as the user of the apparatus. The vertical piston stress, $\sigma_p = F / [\pi (r_o^2 - r_i^2)]$, the torsional-shear stress, $\tau_{z\theta}$, the outer cell pressure, p_o, and the inner cell pressure, p_i, can be changed under a constant rate (positive or negative) until the target (final) value is attained. The servo-motor moves the servo valve in order to keep the feedback electric signal as close as possible to the reference electric signal that corresponds to the constant-rate change of the mechanical quantity in a closed-loop control process. The program makes the difference between the reference and the feedback voltage zero before the activation of the servo controller in the Electric Measurement and Control Unit in order to avoid unintended movements of the servo valve. The servo motor stops moving when the target (final) value of the mechanical quantity is attained while the limit switches deactivate the servo motor automatically in the case of over stroke; however, the servo motor moves again if needed in order to sustain the target value. In the case of the drive that moves the servo valve that adjusts the back pressure a relay is used to automatically stop the drive when the target value is attained; caution is needed when using this drive because it does not automatically stop in the case of over stroke. The dimensions of the specimen and the data recording frequency are set as input values to the program with the latter being as high as 5 Hz.

The program displays the current values of the voltage and mechanical quantities, and plots some basic diagrams.

The transducers used to measure the vertical load, F, torque, T, outer cell pressure, p_o, inner cell pressure, p_i, pore-water pressure, u, vertical displacement, v, and torsional angle, θ, were recalibrated after the upgrade of the apparatus was completed. The calibration of the transducers followed the calibration of the amplifiers described in Section 5.6.4. A portable digital manometer was used for calibrating the pressure transducers at positive pressures while the pore-water pressure transducer was also calibrated against negative pressures (partial vacuum). A hydraulic deadweight tester (Budenberg) and a torque calibrator were used for calibrating the torque / load cell against force and torque, respectively. A Mitutoyo micrometer head and mounting system were used for calibrating the dial gauge, which measures v, and the potentiometer, which measures θ. Figure 5.49 shows the calibration data for the amplifier unit and potentiometer used for measuring the torsional angle provided by the manufacturing company of the HCA. Figure 5.50 compares the calibration data obtained in this study with those provided by the manufacturing company for the case that the sensitivity is set to the default value in the amplifier unit (ATT 1; see Section 5.6.4); the figure plots the torsional angle of the potentiometer's wheel, which is twice the torsional angle of the specimen's cap, against the output voltage. The two sets of calibration points yield similar values of the calibration coefficient while the linearity of the transducer is verified. The rest of the transducers were recalibrated and checked in the same way.

On-sample instrumentation (Hall Effect transducers) was installed, calibrated and used in preliminary tests. Figure 5.51 shows the calibration relationship between the relative displacement of the two magnets, LR, and the output voltage, V. The calibration curve has the typical shape reported in literature (Clayton and Khatrush 1986) consisting of a linear central part and two extreme non-linear parts. However, the output voltage has a limited range (< 1 V DC) possibly because the excitation (supply) voltage is low; the excitation voltage was set to 5 V DC lacking a source capable of supplying a higher voltage. After the calibration procedure was completed the Hall Effect transducer was placed on a specimen, as shown in Fig. 5.52. Figure 5.53 shows the displacement of the transducer, ΔLR, against the measured voltage during undrained loading of the specimen. The analysis of the results showed that the increase in the outer diameter of the specimen computed based on the measured displacement of the transducer (i.e. $\Delta d_o = 1/2\ \Delta LR$) was unrealistically high, as can be seen in Fig. 5.54 which plots ΔLR against the axial displacement, Δh, of the specimen subjected to undrained loading. This malfunction is presumably attributed to the DC source that may not have sustained the excitation voltage during operation.

Further development, e.g. the addition of a source supplying a higher (10 V DC) and sustainable voltage, is needed for acquiring reliable data with the Hall Effect transducers though this development was not performed in this study. It is noted that in order to compute the average horizontal normal strains, ε_{rr} and $\varepsilon_{\theta\theta}$, the displacements at the inner and outer surface of the cylinder ($u_i = \Delta r_i$ and $u_o = \Delta r_o$) should be measured (see Section 5.3). Thus, both a belt measuring the displacement Δr_o and a second burette measuring the volume changes inside the inner cell environment are needed. Since a second burette was not available the computation of ε_{rr} and $\varepsilon_{\theta\theta}$ for the tests of this study was based on the assumption of $\varepsilon_{rr} = \varepsilon_{\theta\theta}$ (see Table 5.1), while in some cases the assumption of $\varepsilon_{rr} = 0$ was made to check whether the results change qualitatively in regards to the assumption made (see Chapters 6 and 7).

Moving parts were also designed and manufactured in the machinery shop for the needs of the present study. The new pedestal and mould shown in Fig. 5.55 were manufactured for testing squat hollow cylindrical sand specimens while the pedestal shown in Fig. 5.56 was manufactured for preparing and testing hollow cylindrical stabilised-sand specimens. The moulds shown in Fig. 5.57 were designed and manufactured for preparing triaxial stabilised-sand specimens. The specimen's cap shown in Fig. 5.58 was designed and manufactured for achieving the connection between the cap and the load cell needed for extension testing in the high-pressure triaxial apparatus; extension testing was performed using this cap while the deviatoric stress was controlled during saturation and consolidation. The spacer disk (access ring) placed in the conventional triaxial apparatus was modified and on-sample transducers (Linear Variable Differential Transformers) were installed for measuring the local axial strain, as shown in Fig. 5.59. Moreover, new metal parts were designed and manufactured for extending the stroke of the loading ram and imposing boundary conditions that impede the occurrence of certain bifurcation modes. The high-pressure triaxial apparatus was also used in order to perform tests at mean effective stress as high as 6 MPa. Some valves and tube connections that were improper for high-pressure testing were refitted in the triaxial cell and new specimen's caps were manufactured, while a new independent unit for water de-airing was added.

Generalised loading tests with constant α, b and p (with the value of α being independent of the value of b) were performed successfully after the upgrade of the HCA in order to investigate the effect of the inherent anisotropy on the mechanical behaviour of sand. Figures 5.60a and b show the stress paths in the q_d - p' and Y - X planes, respectively, of undrained tests with constant α, b and p. Sand was also subjected to shearing by rotating the stress principal axes while keeping the effective stress principal values constant in order to investigate the effect of principal stress rotation on the dilatancy of sand. Figure 5.61a shows the stress path from a rotational-shear test in the Y_s - X_s plane, while Fig. 5.61b shows the evolution of the volumetric strain, ε_{vol}, and effective stress principal values, σ'_1, σ'_2 and σ'_3, with the principal stress rotation angle, $\alpha^*_{\sigma'1}$. Triaxial compression tests at elevated stresses were performed successfully after the modification of the HPTA. Figures 5.62a and b shows the effective stress paths in the q_d - p' plane and the evolution of Δu / p'_{in} with ε_q in undrained compression tests with p'_{in} = 1000 - 6000 kPa.

5.8 MATERIALS AND SPECIMEN PREPARATION METHOD

The sand used in this study is the uniform, medium-fine, quartz M31 Sand with the grading shown in Fig. 5.63 (ASTM D422); the microscope image of the sand's grains is also shown in Fig. 5.63. The specific gravity of the grains is G_s = 2.66 (ASTM D854), while the minimum and maximum void ratio measured in this study are e_{min} = 0.50 and e_{max} = 0.80, respectively (ASTM D4253 and D4254). It is noted that vibrations were applied when needed (sieve analysis, determination of e_{min}) without using a vibrating machine. Table 5.2 summarises the physical characteristics of M31 Sand determined in this study, while Altuhafi et al. (2016) reported the shape properties (aspect ratio, sphericity and convexity) and the roughness and angularity indices for this sand.

The sand specimens were formed by depositing dry (uniform) sand through de-aired water filling the mould using a funnel with an attached tube. Very loose fabric is formed using this methodology and densification is achieved by placing a weight on top of the specimen (e.g. the specimen's cap) and gently tapping the mould. By these means both the lower and the upper parts of the specimen are densified and the void ratio becomes more homogeneous. It is noted that the penetration of the vanes of the porous stone (see Fig. 5.30) may disturb locally the void ratio of sand when the cap is placed on top of the specimen. The sand quantity deposited inside the mould is measured before and after testing by collecting the excess sand material during deposition.

The two membranes are placed around the specimen's cap and sealed with O-rings; the inner membrane can be used to support the weight of the cap if very loose specimens are to be formed. A partial vacuum of around 40 kPa is imposed while the cap and the membranes are left free to move vertically and radially, respectively. The valve supplying the vacuum is closed for a short period to check for potential vacuum losses due to membrane puncture. The valve is opened again and de-aired water is circulated through the specimen as described in Sections 5.6.1 and 5.6.2 and shown in Fig. 5.33. Afterwards the loading rod is connected to the specimen's cap, the triaxial cell is assembled and a mean effective stress of 40 kPa is imposed by means of different cell pressure and backpressure, as described in Section 5.6.1. The cell pressure and backpressure are then increased under the same rate keeping their difference constant, while the servo-controller keeps the piston stress, $F / [\pi (r_o^2 - r_i^2)]$, zero by counterbalancing the gravity and buoyancy forces that act upon the loading rod.

The specimen is left for 90 - 120 min under high backpressure and the degree of saturation is checked at u = 300 kPa; the value of the coefficient B (Skempton 1954) should be higher than 0.96 to proceed to the consolidation process. Stress-controlled isotropic or anisotropic consolidation and generalised preshearing, lasting for 90 - 120 min, can be easily performed using the four servo-controllers described in Section 5.7. It is noted that the apparatus should not be left unattended for long periods of time under stress-controlled conditions thus long rest periods were avoided in this study. After the consolidation is completed stress-controlled drained or undrained generalised loading can be easily imposed by using the four servo-controllers described in Section 5.7; the results of shearing tests are presented in Sections 6 and 7.

5.9 CONCLUSIONS

The concept of subjecting a hollow cylindrical soil specimen to a vertical load and torque and different pressures inside and outside the hollow cylinder was discussed. The magnitude of the three principal stresses and the direction of the major and minor principal axis of stress in regards to the vertical can be controlled under this type of loading. The usage of the Hollow Cylinder Apparatus (HCA) offers the capability to investigate the effects of the inherent anisotropy, intermediate principal stress parameter and principal stress rotation on the mechanical behaviour of soils. However, due to the different pressures inside and outside the hollow cylinder and the curvature of the cylinder wall non-uniformities of stress and strain arise; further stress-strain non-uniformities arise due to the end restraint.

The relationships yielding the average values of stresses and strains as functions of the boundary loads, pressures and displacements were derived and the methodology proposed by Hight et al. (1983) for the analytical determination of the level of non-uniformity was presented. The level of non-uniformities depends, among the other factors, on the ratio of the inner over the outer cell pressure, p_i / p_o, as well as on the geometry of the specimen. Gutierrez (1989) performed the analysis proposed by Hight et al. (1983) for the case of a hollow cylindrical specimen with geometry similar to that of the specimens used in this study thus the bounds for the ratio p_i / p_o proposed by Gutierrez (1989) were also adopted in this study.

The HCA of the National Technical University of Athens was described before the upgrade carried out for the needs of this study. The pressures inside and outside the hollow cylinder were obligingly equal at this state thus any change in the principal stress direction angle, α, was accompanied by a change in the intermediate principal stress parameter, b. In order to control independently the pressures p_i and p_o a new servo controller, servo valve and electric amplifier unit were installed and a LabVIEW program was developed. Radial loading tests with constant and independent α, b and p (p is the mean total stress) and rotational-shear tests in which the stress principal axes were rotated at constant σ'_1, σ'_2 and σ'_3 were performed successfully after the upgrade of the apparatus. On-sample transducers for measuring the local strains were installed, calibrated and used though the excitation of the instruments was insufficient yielding unreliable results; a higher and stable voltage supply may remedy this problem.

5.10 BIBLIOGRAPHY

Altuhafi FN, Coop MR, Georgiannou VN (2016) Effect of particle shape on the mechanical behavior of natural sands. Journal of Geotechnical and Geoenvironmental Engineering, 142(12): 0401671

ASTM D422-63(2007)e2, Standard Test Method for Particle-Size Analysis of Soils (Withdrawn 2016), ASTM International, West Conshohocken, PA, 2007, www.astm.org

ASTM D854-14, Standard Test Methods for Specific Gravity of Soil Solids by Water Pycnometer, ASTM International, West Conshohocken, PA, 2014, www.astm.org

ASTM D4253-16e1, Standard Test Methods for Maximum Index Density and Unit Weight of Soils Using a Vibratory Table, ASTM International, West Conshohocken, PA, 2016, www.astm.org

ASTM D4254-16, Standard Test Methods for Minimum Index Density and Unit Weight of Soils and Calculation of Relative Density, ASTM International, West Conshohocken, PA, 2016, www.astm.org

Bishop AW (1971) Shear strength parameters for undisturbed and remolded soil specimens. Roscoe Memorial Symp., 3-58

Clayton CRI, Khatrush SA (1986) A new device for measuring local axial strains on triaxial specimens. Géotechnique 36 (4), 593-597

Gutierrez M (1989) Behavior of sand during rotation of principal stress directions. D. Eng. Thesis, Tokyo University

Hight DW, Gens A, Symes MJ (1983) The development of a new hollow cylinder apparatus for investigating the effects of principal stress rotation in soils. Géotechnique 33, No. 4, 355-383

Ishihara K, Towhata I (1983) Sand response to cyclic rotation of principal stress directions as induced by wave loads. Soils and Foundations, Vol.23, No.4, 11-26

Konstadinou M (2013) Experimental study of the anisotropic behaviour of cohesionless soils under torsional shear. PhD Thesis, Geotechnical Division, National Technical University of Athens

Miura K, Miura S, Toki S (1986) Deformation behavior of anisotropic dense sand under principal stress axes rotation. Soils and Foundations, Vol.26, No.1, 36-52

Roscoe KH (1953) An apparatus for the application of simple shear to soil samples. Proc. 3rd Int. Conf. Soil Mech., 1: 186-191

Roscoe KH, Basset RH, Cole ERL (1967) Principal axes observed during simple shear of a sand. Proc. Geotech. Conf., Oslo, pp. 231-237

Saada AS (1988) State of the art paper: Hollow cylinder torsional devices: their advantages and limitations. Advanced triaxial testing of soil and rock, ASTM STP 977, 766-795

SEIKEN, INC (1997) Constitutional parts and drawings of ASK torsional triaxial test apparatus, desk top EP servo universal model DTC-452

SEIKEN, INC (1998) Technical documentation of ASK torsional dynamic triaxial apparatus, desk top model EO servo universal type model No. DTC-452

Skempton AW (1954) The pore-pressure coefficients *A* and *B*. Géotechnique 4, No. 4, 143-147

Tong Z, Zhang J, Yu Y, Ga Zhang (2010) Drained deformation behavior of anisotropic sands during cyclic rotation of principal stress axes. Journal of Geotechnical and Geoenvironmental Engineering, Vol. 136, No.11, pp. 1509-1518

Triantafyllos PK, Georgiannou VN, Dafalias YF, Georgopoulos I-O (2019) New findings on the evolution of the instability surface of loose sand. Acta Geotechnica, https://doi.org/10.1007/s11440-019-00887-7

Tsomokos A (2005) Experimental study of the behaviour of a soil element under monotonic and cyclic torsional shear. PhD Thesis, National Technical University of Athens

Wang Z-L, Dafalias YF, Shen C-K (1990) Bounding surface hypoplasticity model for sand. Journal of Engineering Mechanics, Vol. 116, No. 5, 983-1001

5.11 TABLES

Table 5.1 List of symbols and equations used to calculate the average stresses, strains and other parameters

Direction HC	**Stress**	**Strain**
Vertical	$\sigma_{zz} = \frac{F}{\pi\left(r_o^2 - r_i^2\right)} + \frac{p_o r_o^2 - p_i r_i^2}{r_o^2 - r_i^2}$	$\varepsilon_{zz} = -\frac{v_H}{H}$
Circumferential	$\sigma_{\theta\theta} = \frac{p_o r_o - p_i r_i}{r_o - r_i}$	$\varepsilon_{\theta\theta} = \frac{(\varepsilon_{vol} - \varepsilon_{zz})}{2}$ **or** $\varepsilon_{\theta\theta} = \varepsilon_{vol} - \varepsilon_{zz}$
Radial	$\sigma_{rr} = \frac{p_o r_o + p_i r_i}{r_o + r_i}$	$\varepsilon_{rr} = \frac{(\varepsilon_{vol} - \varepsilon_{zz})}{2}$ **or** $\varepsilon_{rr} = 0$

Rotational	$\tau_{z\theta} = \dfrac{3T}{2\pi(r_o^3 - r_i^3)}$	$\gamma_{z\theta} = 2\varepsilon_{z\theta} = \dfrac{2\theta\left(r_o^3 - r_i^3\right)}{3H(r_o^2 - r_i^2)}$
Principal	**Stress**	**Strain**
Major	$\sigma_1 = \dfrac{\sigma_{zz} + \sigma_{\theta\theta}}{2} +$ $+\sqrt{\left(\dfrac{\sigma_{zz} - \sigma_{\theta\theta}}{2}\right)^2 + \tau_{z\theta}^2}$	$\varepsilon_1 = \dfrac{\varepsilon_{zz} + \varepsilon_{\theta\theta}}{2} +$ $+\sqrt{\left(\dfrac{\varepsilon_{zz} - \varepsilon_{\theta\theta}}{2}\right)^2 + \varepsilon_{z\theta}^2}$
Intermediate	$\sigma_2 = \sigma_{rr}$	$\varepsilon_2 = \varepsilon_{rr}$
Minor	$\sigma_3 = \dfrac{\sigma_{zz} + \sigma_{\theta\theta}}{2} -$ $-\sqrt{\left(\dfrac{\sigma_{zz} - \sigma_{\theta\theta}}{2}\right)^2 + \tau_{z\theta}^2}$	$\varepsilon_3 = \dfrac{\varepsilon_{zz} + \varepsilon_{\theta\theta}}{2} -$ $-\sqrt{\left(\dfrac{\varepsilon_{zz} - \varepsilon_{\theta\theta}}{2}\right)^2 + \varepsilon_{z\theta}^2}$
Invariant	**Stress**	**Strain**
	$q = (\dfrac{1}{2}\{(\sigma_1 - \sigma_2)^2 +$ $+(\sigma_2 - \sigma_3)^2 + (\sigma_3 - \sigma_1)^2\})^{1/2}$	$\gamma = (\dfrac{2}{9}\{(\varepsilon_1 - \varepsilon_2)^2 +$ $+(\varepsilon_2 - \varepsilon_3)^2 + (\varepsilon_3 - \varepsilon_1)^2\})^{1/2}$
	$p' = \dfrac{\sigma_1^{'} + \sigma_2^{'} + \sigma_3^{'}}{3} =$ $= \dfrac{\sigma_1 + \sigma_2 + \sigma_3}{3} - u$	$\varepsilon_{vol} = \varepsilon_1 + \varepsilon_2 + \varepsilon_3 \ (= \dfrac{-\Delta V}{V})$
	$\tau_{oct} = \dfrac{1}{3}(\{(\sigma_1 - \sigma_2)^2 +$ $+(\sigma_2 - \sigma_3)^2 + (\sigma_3 - \sigma_1)^2\})^{1/2}$	$\gamma_{oct} = \dfrac{2}{3}(\{(\varepsilon_1 - \varepsilon_2)^2 +$ $+(\varepsilon_2 - \varepsilon_3)^2 + (\varepsilon_3 - \varepsilon_1)^2\})^{1/2}$
Parameters	**Stress**	**Strain**
Difference	$q_d = \sigma_1 - \sigma_3$	
	$X = \dfrac{\sigma_{zz}^{'} - \sigma_{\theta\theta}^{'}}{\sigma_{zz}^{'} + \sigma_{\theta\theta}^{'}}$, $X_s = \sigma_{zz}^{'} - \sigma_{\theta\theta}^{'}$	$X_\varepsilon = \dfrac{\varepsilon_{zz} - \varepsilon_{\theta\theta}}{2}$

	$Y = \frac{2\tau_{z\theta}}{\sigma'_{zz} + \sigma'_{\theta\theta}}$, $Y_s = 2\tau_{z\theta}$	$Y_\varepsilon = \varepsilon_{z\theta}$
Principal direction of stress/strain	$\alpha \equiv \alpha_{\sigma'1} = 0.5 \cdot \tan^{-1}\frac{Y}{X} =$ $= 0.5 \cdot \tan^{-1}\frac{Y_s}{X_s}$	$\alpha_{\varepsilon 1} = 0.5 \cdot \tan^{-1}\frac{Y_\varepsilon}{X_\varepsilon}$
Principal direction of incremental stress/strain	$\alpha_{d\sigma'1} = 0.5 \cdot \tan^{-1}\frac{dY_s}{dX_s}$	$\alpha_{d\varepsilon 1} = 0.5 \cdot \tan^{-1}\frac{dY_\varepsilon}{dX_\varepsilon}$
Ratio	$b = \frac{\sigma'_2 - \sigma'_3}{\sigma'_1 - \sigma'_3}$	
Ratio	$\sin\varphi = \frac{\sigma'_1 - \sigma'_3}{\sigma'_1 + \sigma'_3}$	
Ratio	$\eta = \frac{q}{p'}$	
Ratio	$K_c = \frac{\sigma'_{3c}}{\sigma'_{1c}}$	
Second-order work	$d^2W = (d\sigma_{zz} - d\sigma_{\theta\theta})(\frac{d\varepsilon_{zz} - d\varepsilon_{\theta\theta}}{2}) + 2d\tau_{z\theta}d\varepsilon_{z\theta}$, for isochoric conditions under b=0.5	
Angle between the σ'₁-axis and the planes of max(τ/σₙ')	$\theta_{1,2} = \pm\left(45^\circ - \varphi_{mob}/2\right)$	

Table 5.2 Physical characteristics of M31 Sand

Specific gravity, G_s (-):	**2.66**
Minimum void ratio, e_{min} (-):	**0.50**
Maximum void ratio, e_{max} (-):	**0.80**
Grain size D_{10} (mm):	**0.214**
Grain size D_{30} (mm):	**0.258**
Grain size D_{50} (mm):	**0.310**
Grain size D_{60} (mm):	**0.339**
Coefficient of uniformity, C_u (-):	**1.58**
Coefficient of curvature, C_h (-):	**0.92**

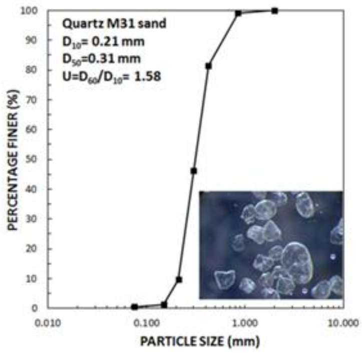

D_p is the grain size (diameter) corresponding to p% finer in the grain size distribution curve. The coefficient of uniformity is $C_u = D_{60}/D_{10}$ while the coefficient of curvature is $C_h = (D_{30})^2 / (D_{60}*D_{10})$

5.12 FIGURES

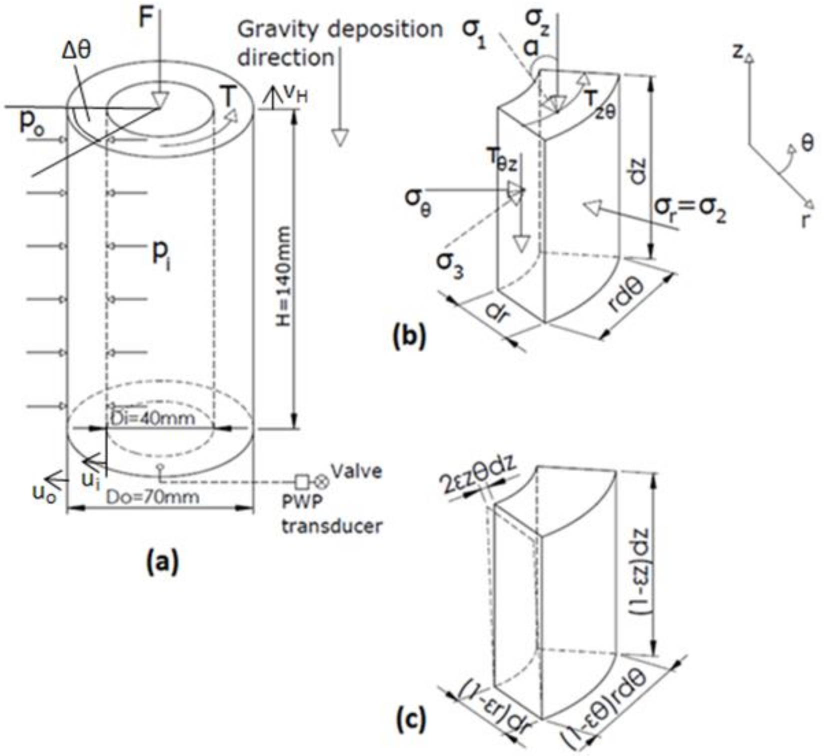

Fig. 5.1 **a** Hollow cylindrical specimen and applied boundary loads. **b** Stress components on the undeformed soil element. **c** Strain components associated with the combined multiaxial and torsional deformation

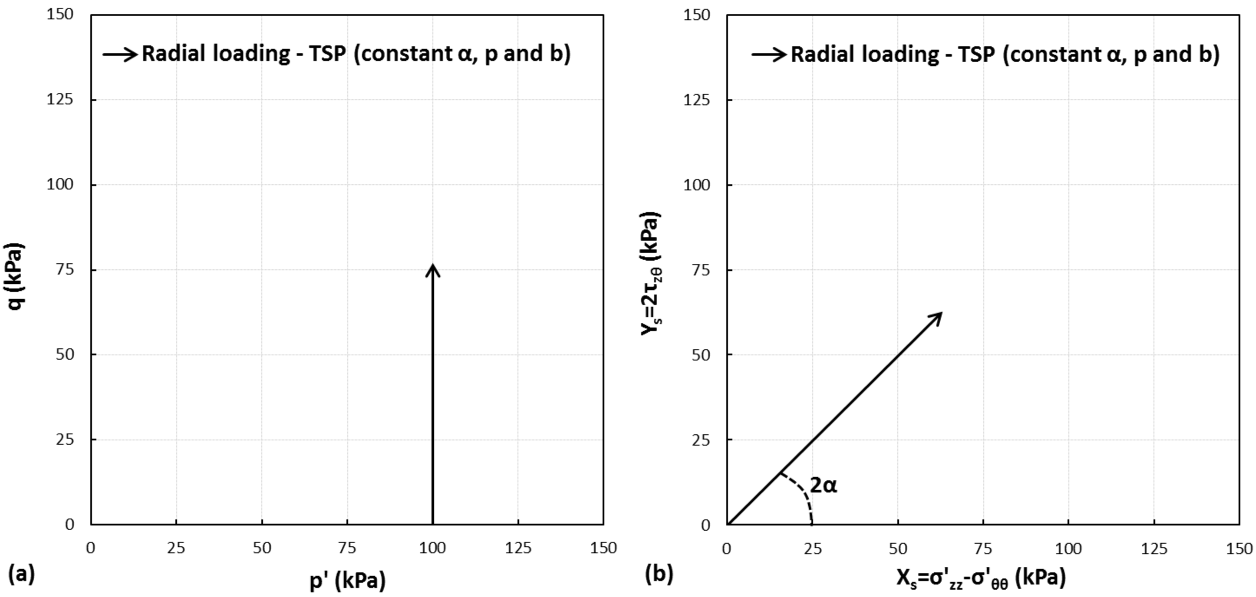

Fig. 5.2 Radial loading on isotropically consolidated soil. **a** Total stress path in the q - p' plane. **b** Stress path in the Y_s - X_s plane

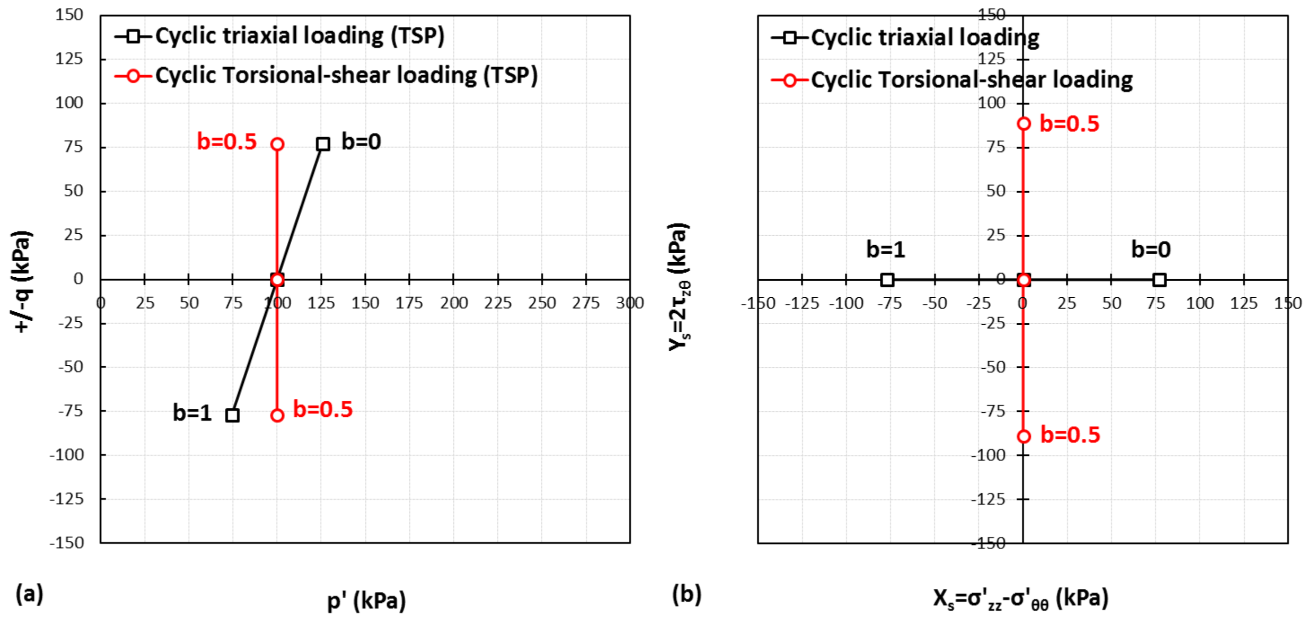

Fig. 5.3 Cyclic loading in triaxial and torsional-shear mode on isotropically consolidated soil. **a** Total stress paths in the *q* - *p'* plane. **b** Stress paths in the Y_s - X_s plane

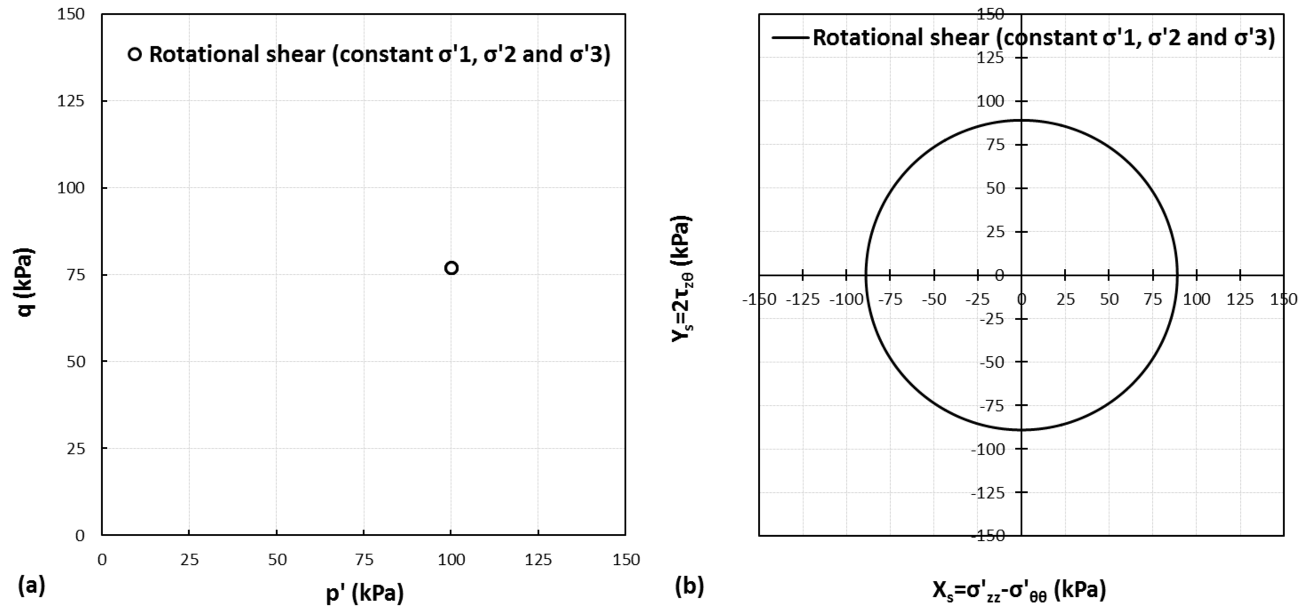

Fig. 5.4 Rotation of the stress principal axes at constant effective stress principal values. **a** Total stress paths in the *q* - *p'* plane. **b** Stress paths in the Y_s - X_s plane

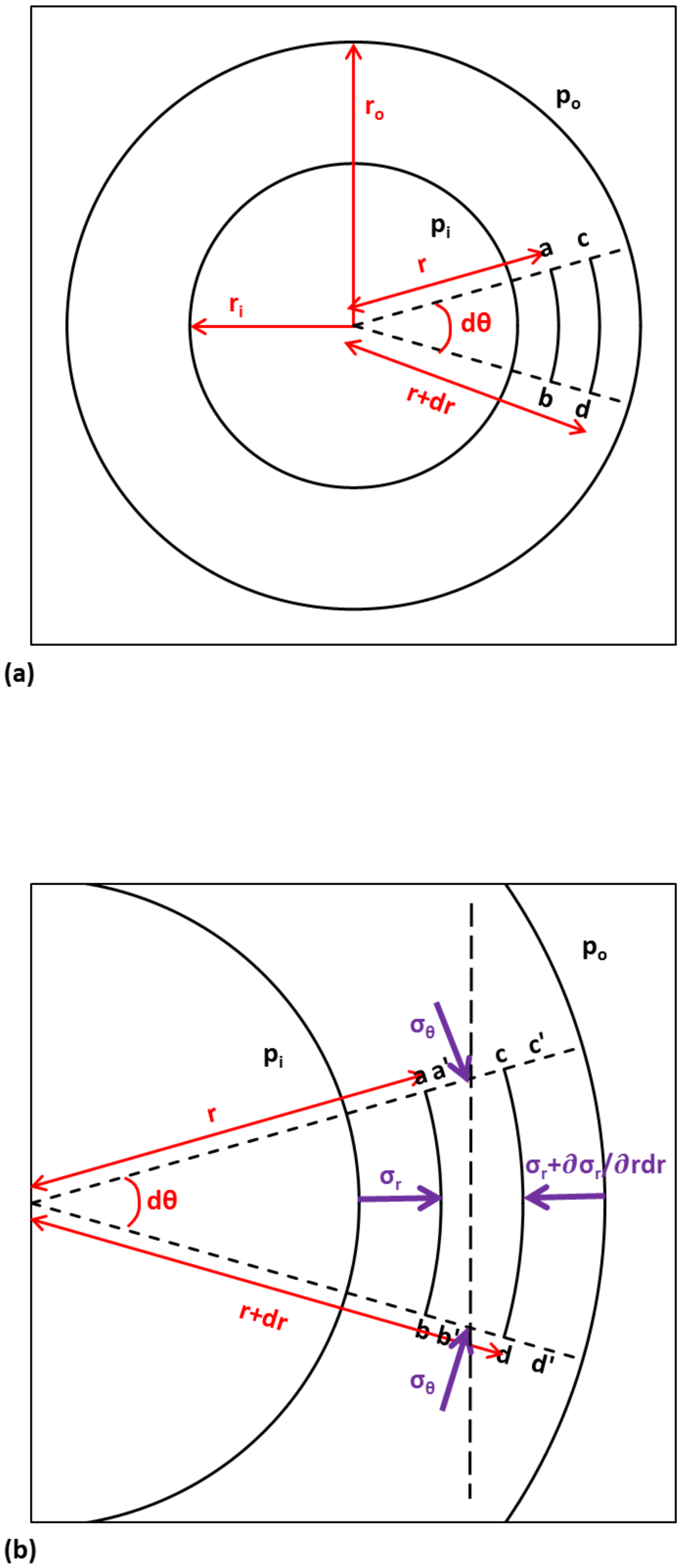

Fig. 5.5 Displacements and force equilibrium along the radial direction for a soil element. **a** Definition of a soil element in the hollow cylindrical specimen. **b** Stresses applied on the soil element and corresponding displacements

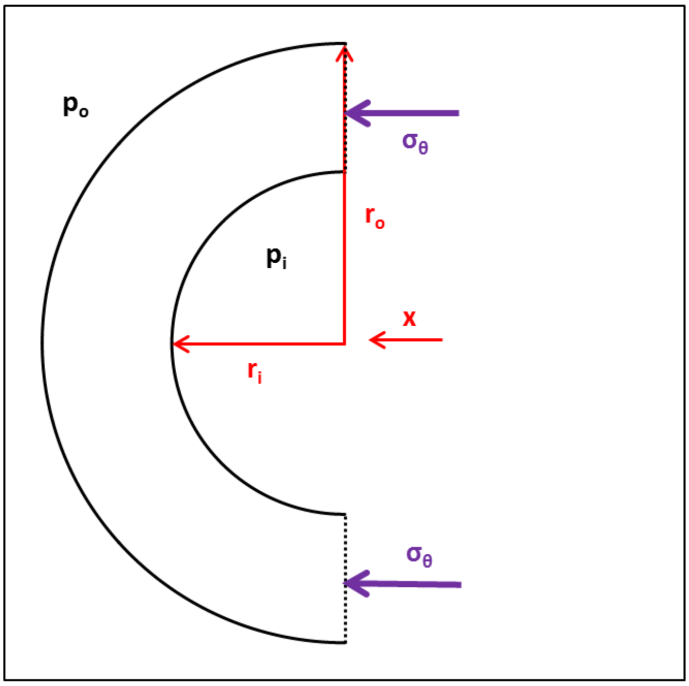

(a)

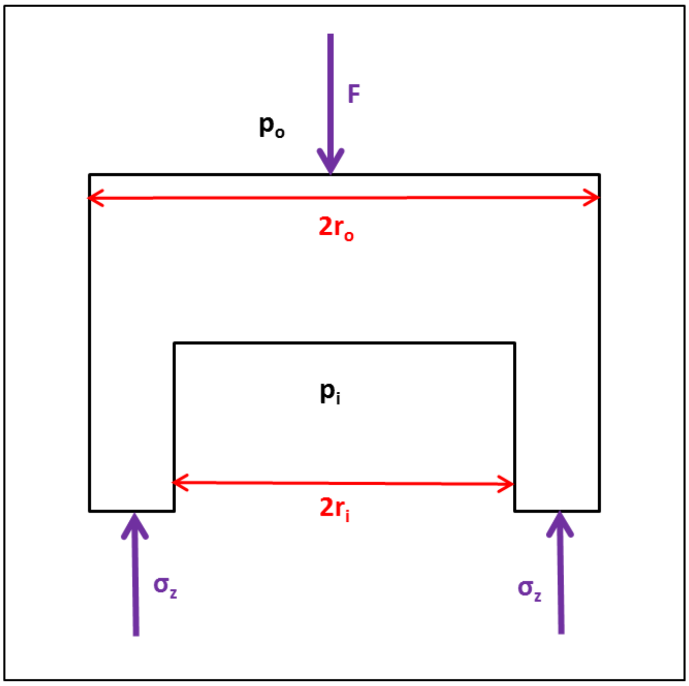

(b)

Fig. 5.6 Force equilibrium along the horizontal direction *x* for the half part of the hollow cylindrical specimen (**a**) and force equilibrium along the vertical direction for the top loading platen supported by the hollow cylindrical specimen (**b**)

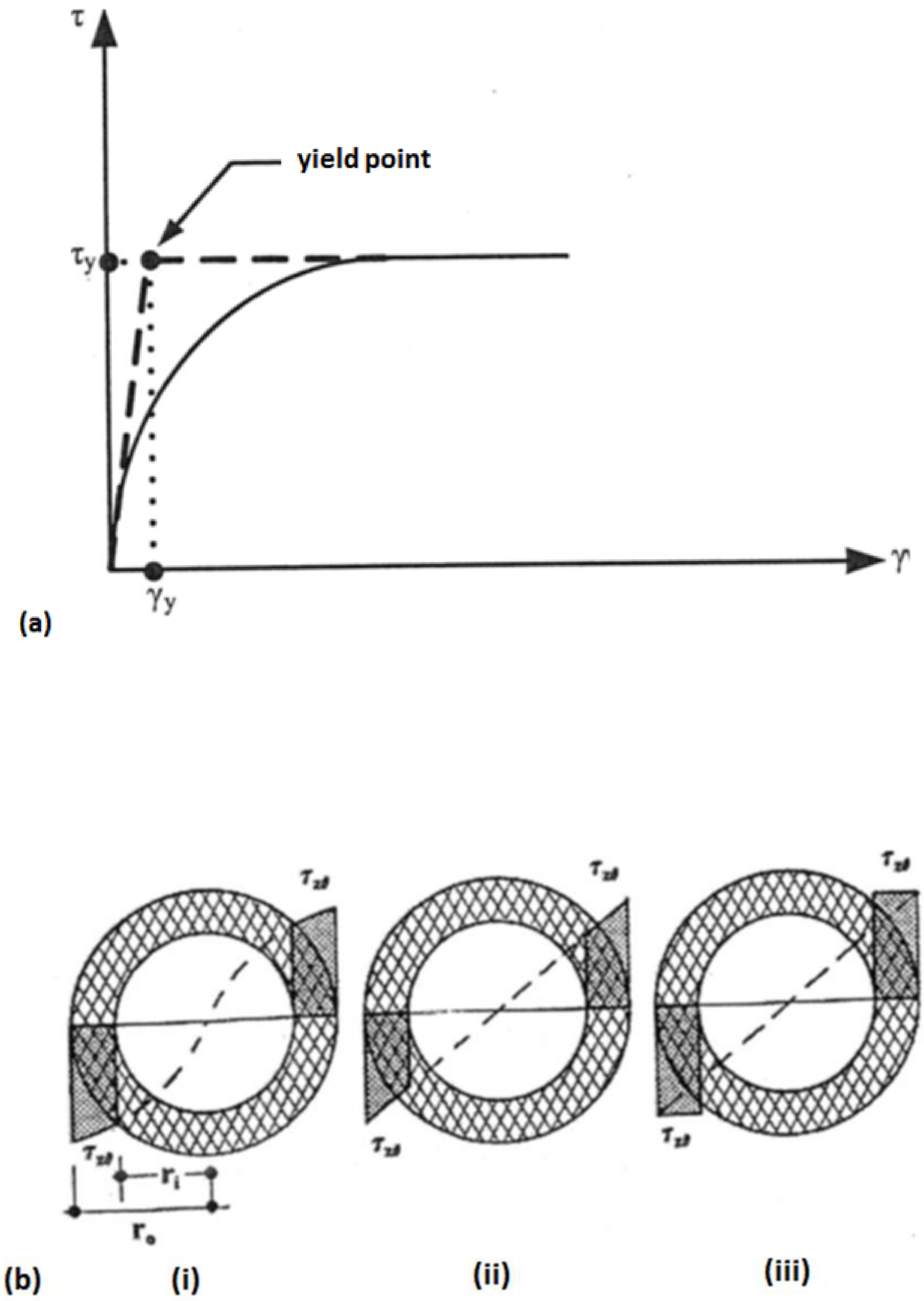

Fig. 5.7 Constitutive relationship between $\tau_{z\theta}$ and $\varepsilon_{z\theta}$ (**a**) and distribution of the shear stress, $\tau_{z\theta}$, along the cylinder wall (**b**). The real distribution is shown in (i), the elastic distribution is shown in (ii) and the perfectly plastic distribution is shown in (iii) (after Tsomokos 2005)

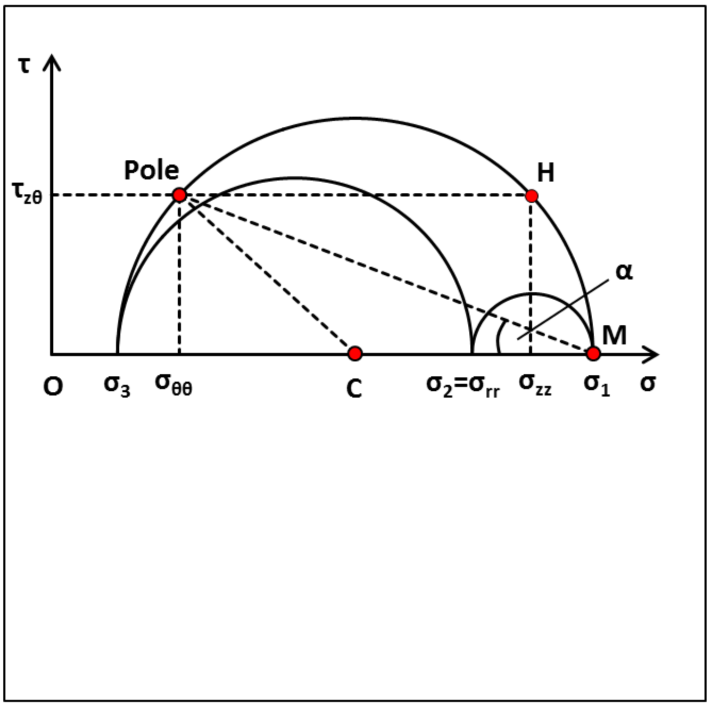

Fig. 5.8 Mohr circle representation of the stress in the wall of the hollow cylindrical specimen

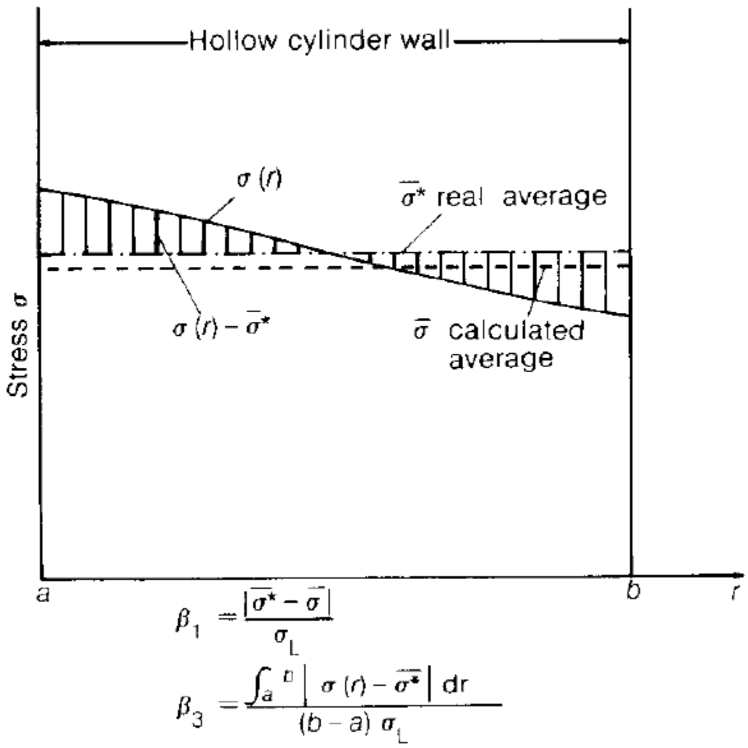

Fig. 5.9 Parameters used by Hight et al. (1983) to quantify stress non-uniformities and accuracy. Note that *a* is the inner radius (r_i) and *b* is the outer radius (r_o) (after Hight et al. 1983)

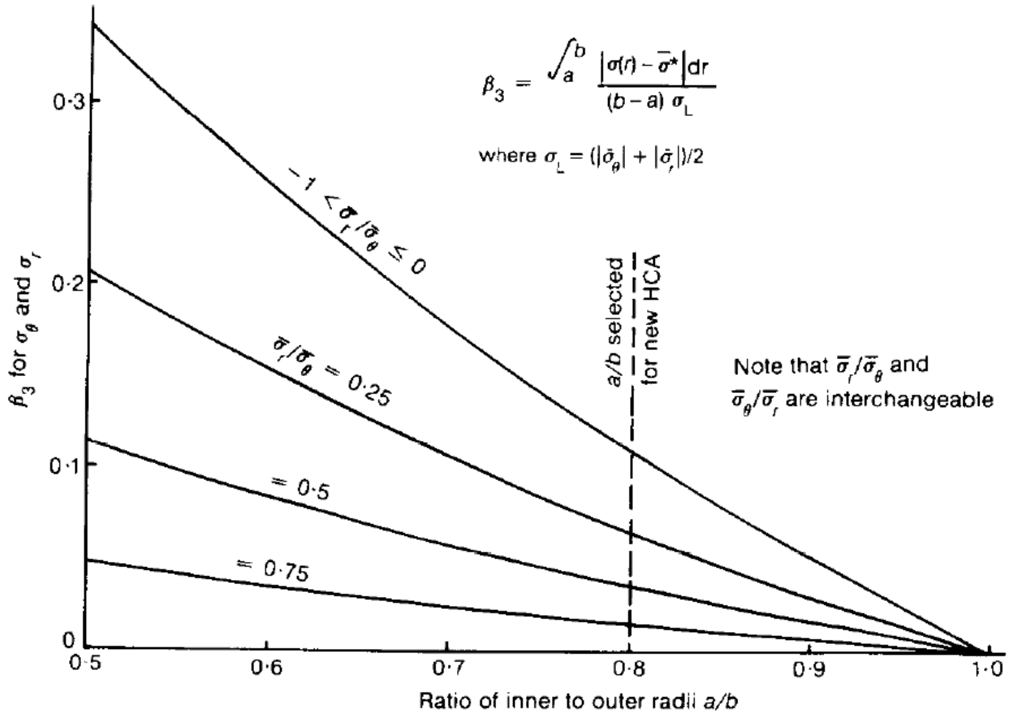

Fig. 5.10 Variation of the parameter β_3 for the stresses $\sigma_{\theta\theta}$ and σ_{rr} with the ratios r_i / r_o and $\sigma_{r,av} / \sigma_{\theta,av}$ for an isotropic linear elastic specimen with free ends. Note that a is the inner radius (r_i), b is the outer radius (r_o) and the bar above the symbol for stress indicates the average value (after Hight et al. 1983)

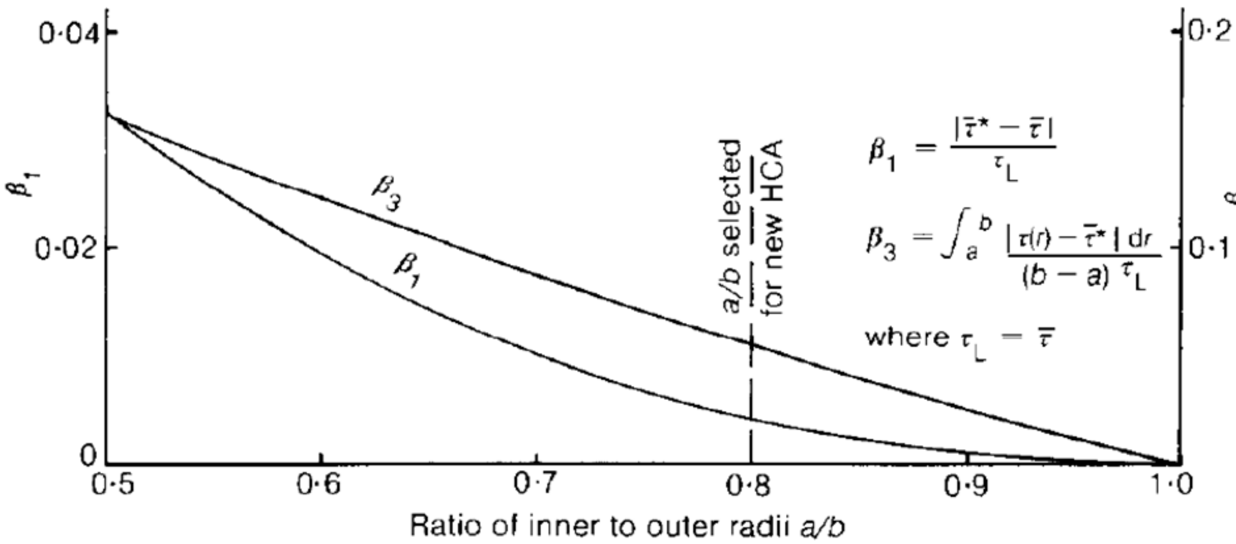

Fig. 5.11 Variation of the parameters β_1 and β_3 for the stress $\tau_{z\theta}$ with the ratio r_i / r_o for an isotropic linear elastic specimen with free ends. Note that a is the inner radius (r_i), b is the outer radius (r_o) and the bar above the symbol for stress indicates the average value (after Hight et al. 1983)

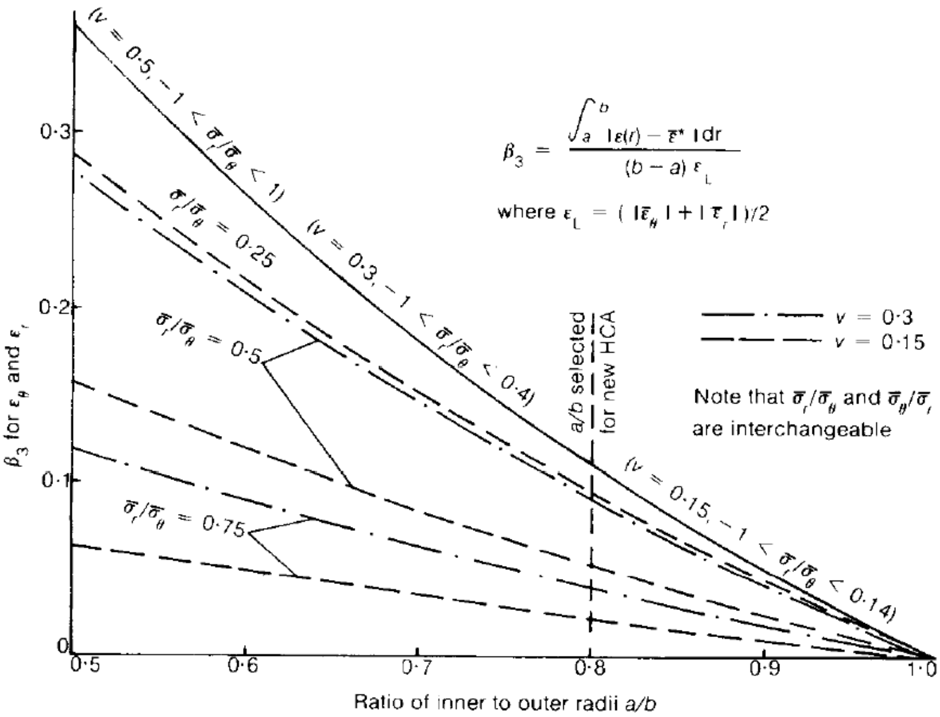

Fig. 5.12 Variation of the parameter β_3 for the strains $\varepsilon_{\theta\theta}$ and ε_{rr} with the ratios r_i / r_o and $\sigma_{r,av} / \sigma_{\theta,av}$ for an isotropic linear elastic specimen with free ends. Note that *a* is the inner radius (r_i), *b* is the outer radius (r_o) and the bar above the symbol for stress or strain indicates the average value (after Hight et al. 1983)

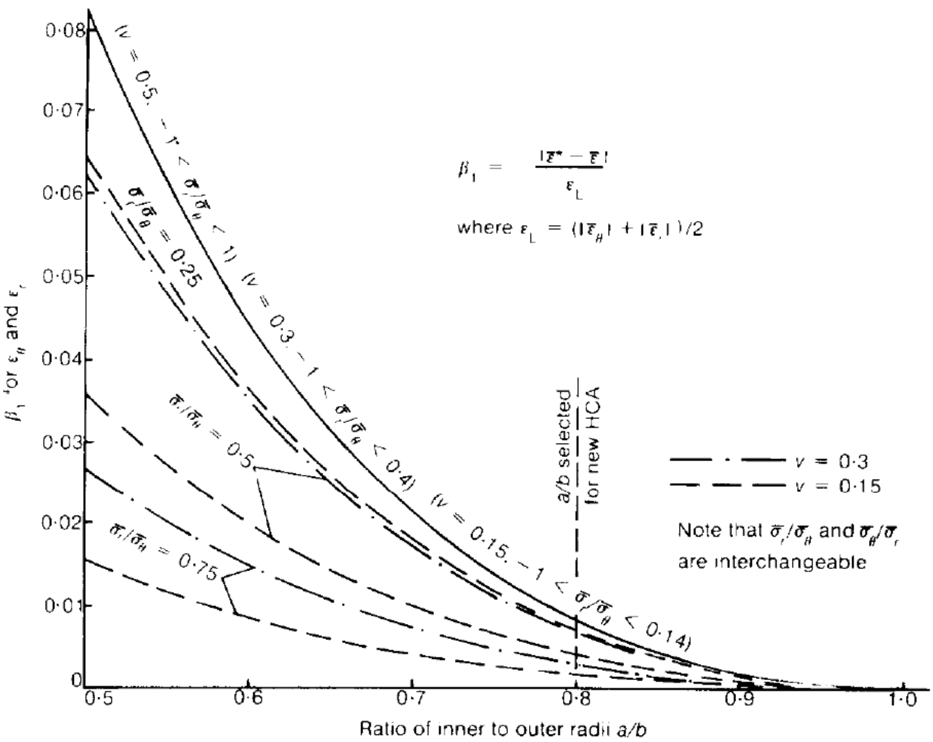

Fig. 5.13 Variation of the parameter β_1 for the strains $\varepsilon_{\theta\theta}$ and ε_{rr} with the ratios r_i / r_o and $\sigma_{r,av} / \sigma_{\theta,av}$ for an isotropic linear elastic specimen with free ends. Note that *a* is the inner radius (r_i), *b* is the outer radius (r_o) and the bar above the symbol for stress or strain indicates the average value (after Hight et al. 1983)

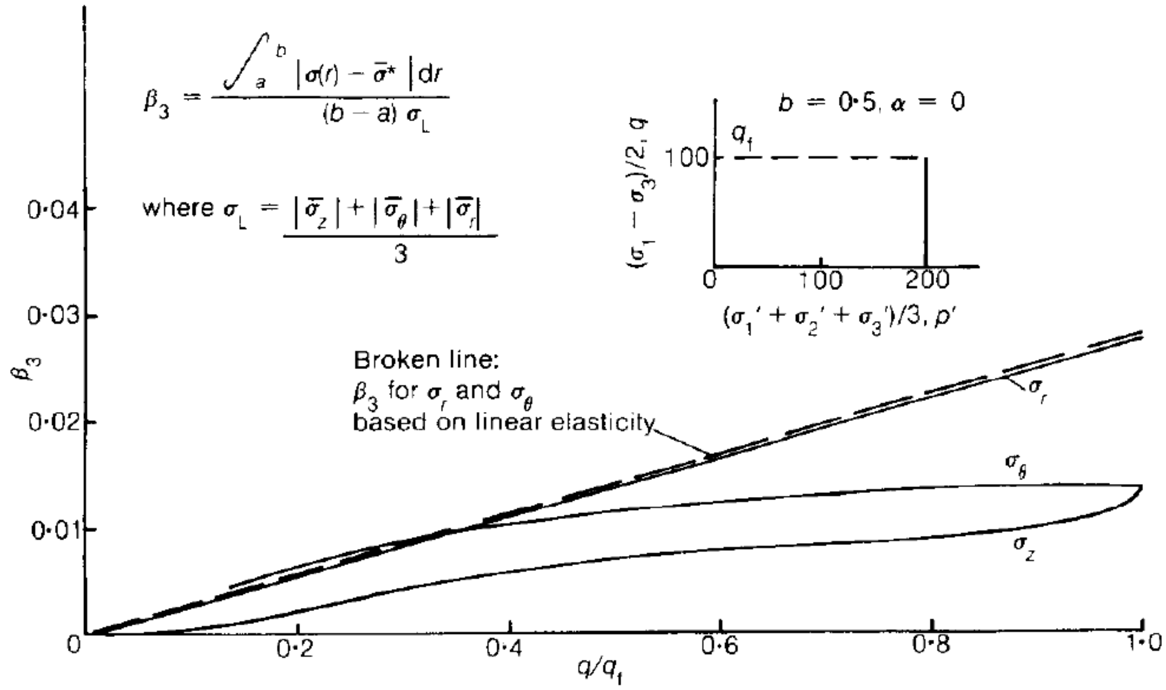

Fig. 5.14 Variation of the parameter β_3 for the stresses $\sigma_{\theta\theta}$, σ_{rr} and σ_{zz} with the ratio t / t_f (q / q_f in the figure) during a loading test with $\alpha_{\sigma'1} = 0°$ and $b = 0.5$. The hollow cylindrical specimen has free ends and a ratio of inner to outer radius r_i / $r_o = 0.8$. The results are from either an elastoplastic finite element analysis or an isotropic linear elastic analysis (after Hight et al. 1983)

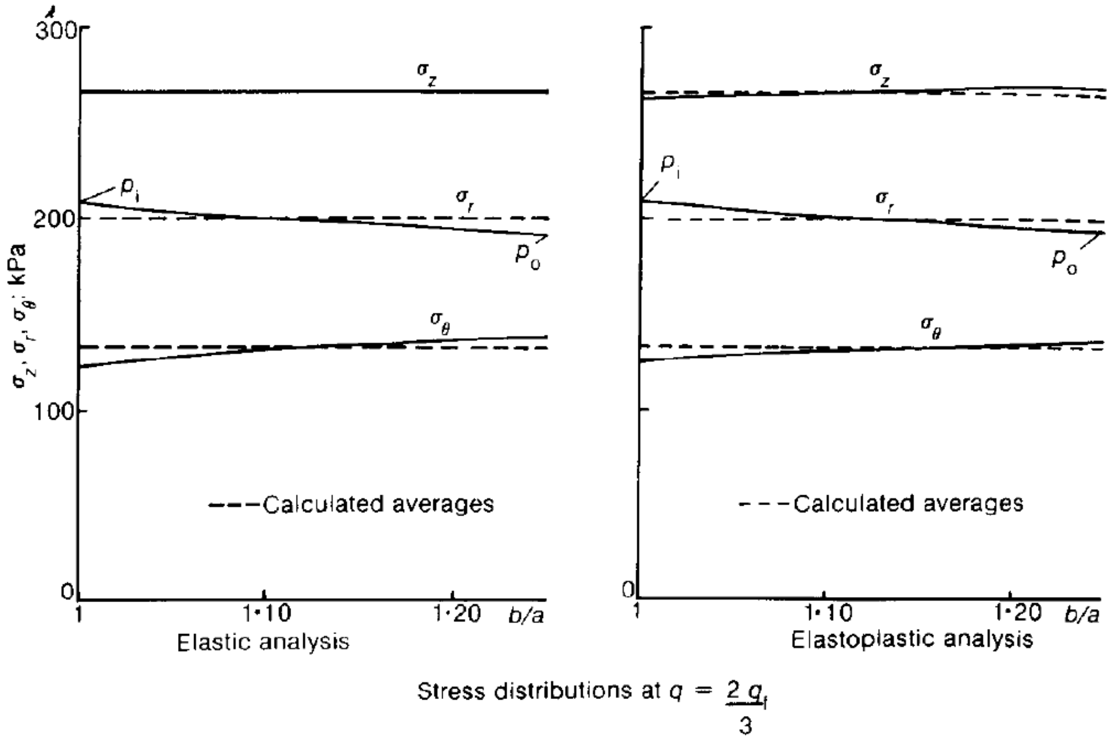

Fig. 5.15 Variation of the stresses $\sigma_{\theta\theta}$, σ_{rr} and σ_{zz} across the specimen wall at $t = 2 / 3\ t_f$ in a loading test with $\alpha_{\sigma'1} = 0°$ and $b = 0.5$. The hollow cylindrical specimen has free ends and a ratio of inner to outer radius r_i / r_o = 0.8. The results are from either an elastoplastic finite element analysis or an isotropic linear elastic analysis. The horizontal axis is r / a (not b / a) and q is used instead of t in the figure (after Hight et al. 1983)

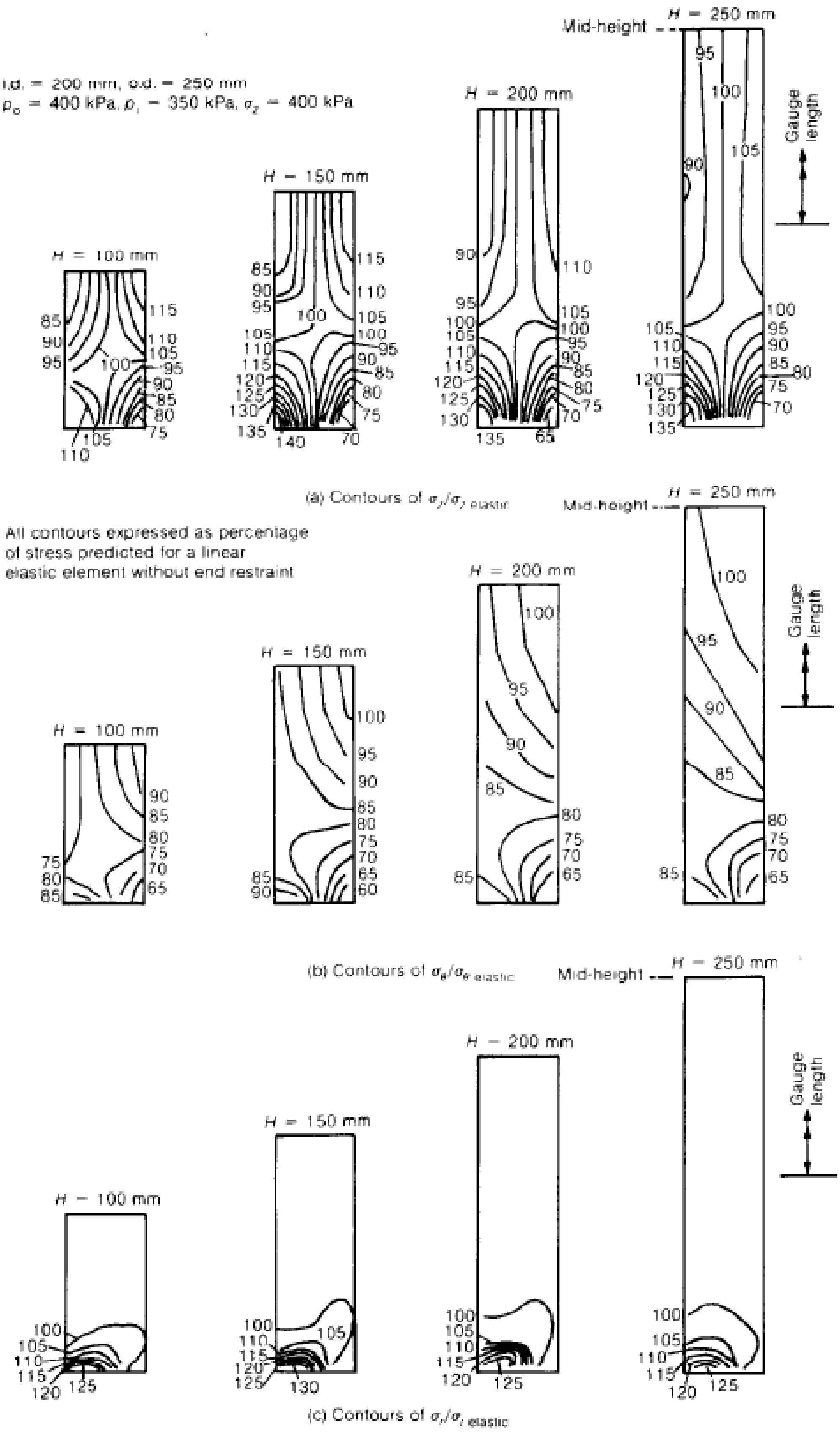

Fig. 5.16 Stress distributions in a hollow cylindrical specimen with fixed ends based on the linear elastic analyses with ν = 0.499 and different specimen heights, *H* (after Hight et al. 1983)

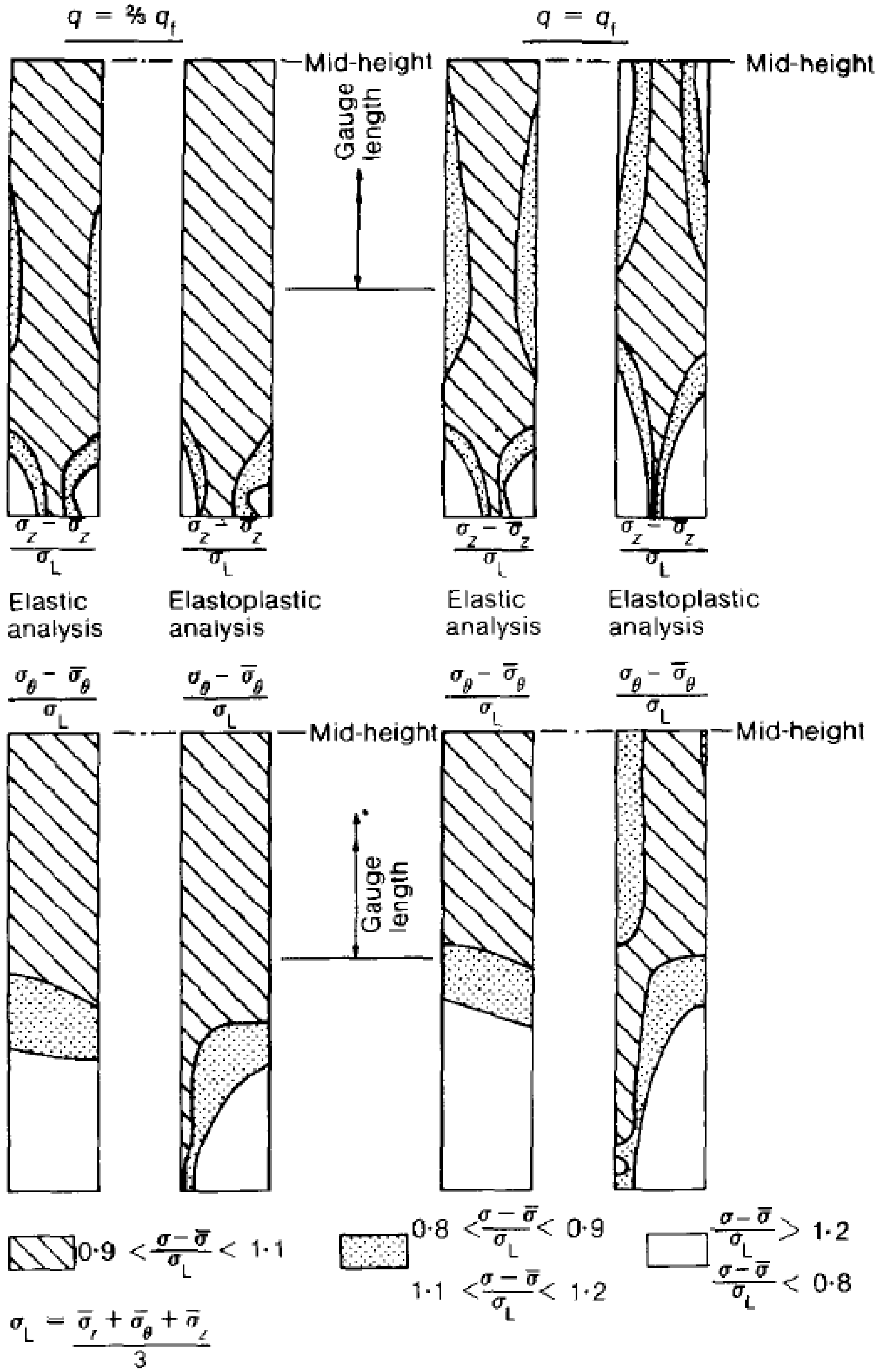

Fig. 5.17 Stress non-uniformities in a hollow cylindrical specimen with fixed ends (d_i = 200 mm, d_o = 250 mm and H = 250 mm) based on elastic and elastoplastic analyses (after Hight et al. 1983)

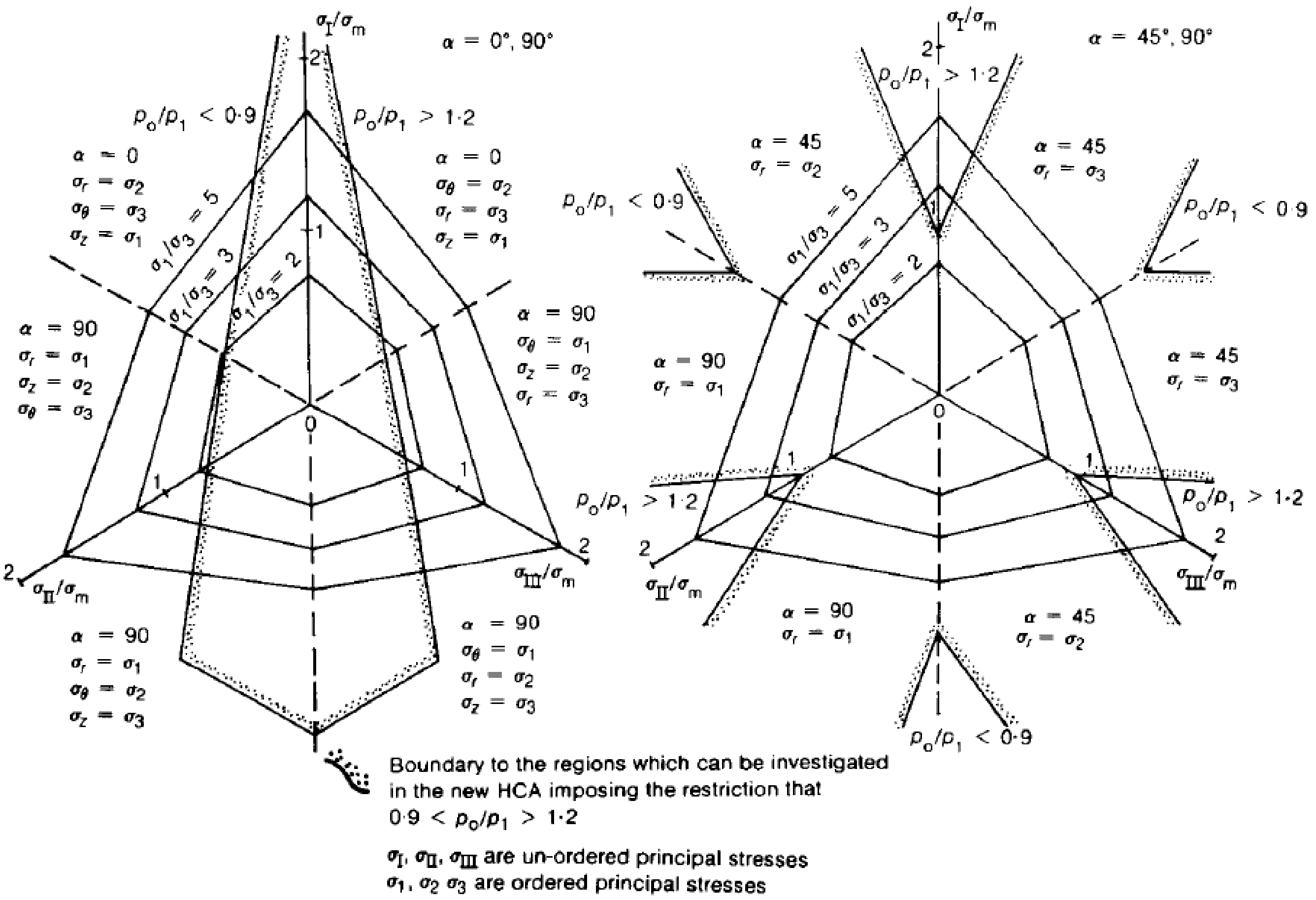

Fig. 5.18 Stress states associated with admissible level of stress non-uniformities due to specimen curvature alone in a hollow cylindrical specimen with d_i = 200 mm, d_o = 250 mm and H = 250 mm when p_o / p_i varies in the range [0.9 , 1.2] (after Hight et al. 1983)

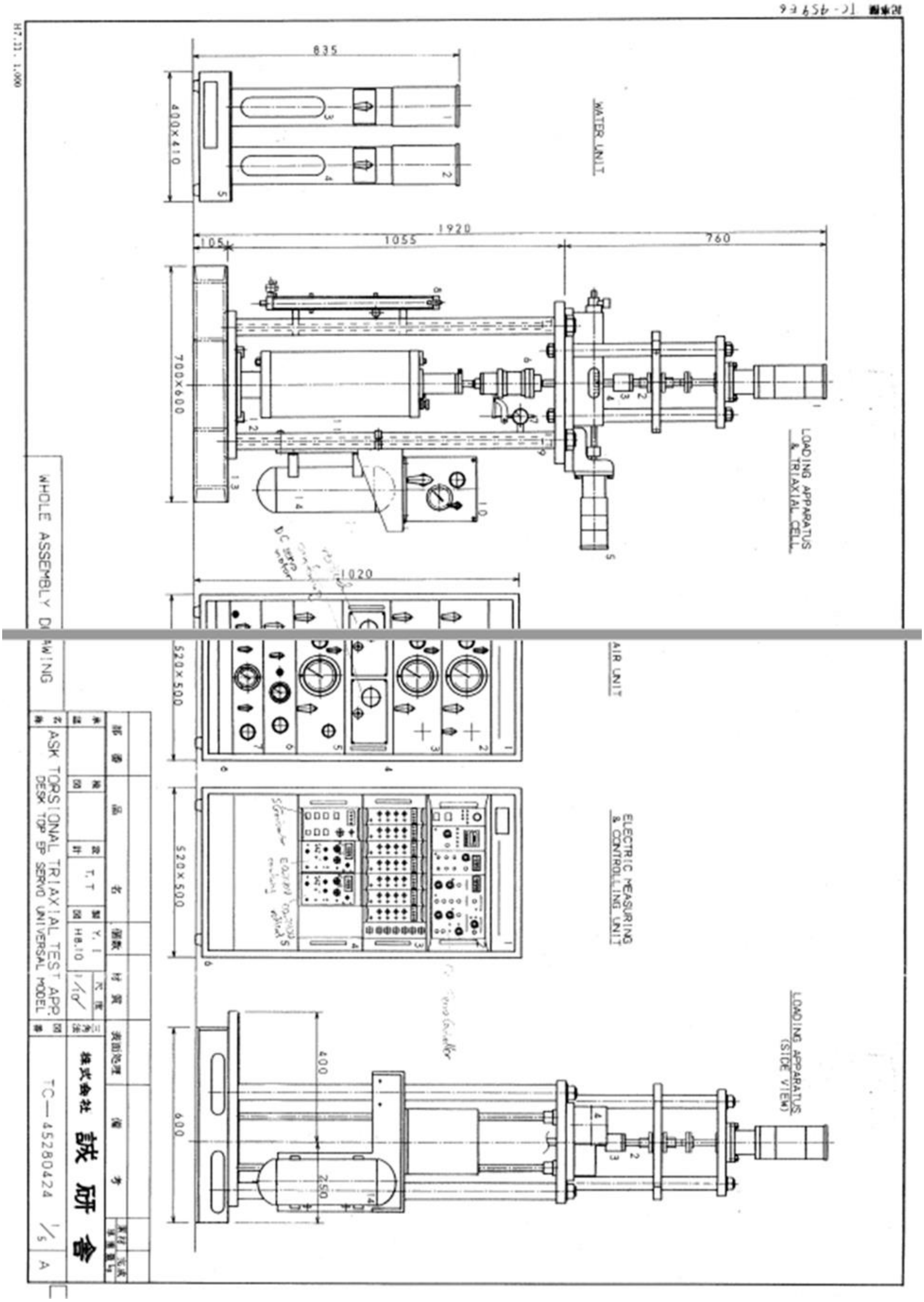

Figure 5.19 Whole assembly drawing of the hollow cylinder apparatus (Drawing No TC-45280424 1/5). All dimensions are in millimetres (after SEIKEN, INC.)

CONSTITUTIONAL PARTS SHOWN ON DRAWING		MARCH• 1997	1/5
NAME OF EQUIPMENT	DRAWING NO.	45280424	1/5

ASK TORSIONAL TRIAXIAL APPARATUS
DESK TOP EP SERVO UNIVERSAL MODEL NO. DTC-452

NO.	PARTS NAME	Q'TY	SPECIFICATIONS
	WATER UNIT		
1	De-aired Water Tank	1	Capacity 1.5ℓ Lucite Acrylic Resin Resist. Vacuum $-1kgf/cm^2$
2	Vacuum Tank	1	Capacity 1.5ℓ Lucite Acrylic Resin Resist. Vacuum $-1kgf/cm^2$
3	Back Pressure Tank	1	Capacity 2ℓ, balloon type Resist. Pressure $10kgf/cm^2$
4	Confining Pressure Tank	1	Capacity 2ℓ Resist. Pressure $10kgf/cm^2$
5	Base Box		Alminum Made, painted Whitey valve• copper pipe manifold connection
	LOADING APPARATUS		
1	Vertical Loading Air Actuator	1	Type II Cross sectional area: Comp. $45.4cm^2$, tens. $27.7cm^2$
2	Piston Fixing Frame	1	Lock nut fixing type
3	Rolling Motion Cutting Joint	1	Ball bearing type
4	Torque Loading System	1	Wire pulley• ball spline type

NOTE

SEIKEN, INC.

Figure 5.20 Description and specifications of the parts shown in Drawing No TC-45280424 1/5 (part 1/5) (after SEIKEN, INC.)

CONSTITUTIONAL PARTS SHOWN ON DRAWING			MARCH• 1997	2/5
NAME OF EQUIPMENT		DRAWING NO.	45280424 1/5	
ASK TORSIONAL TRIAXIAL APPARATUS DESK TOP MODEL, EP SERVO UNIVERSAL TYPE MODEL NO. DTC-452				
NO.	PARTS NAME	Q'TY	SPECIFICATIONS	
5	Torque Loading Air Actuator	1	Type 1 Cross sectional area: Comp. 27.3cm², tens. 16.3cm²	
6	Gain Cushion	2	Urethane core type Two kinds for torsional and standard vertical test Details shown in the drawing of Triaxial Cell	
7	Vertical Displacement Transducer	1	DG type Capacity 20mm With a center point touch lever	
8	Volume Change	1	Capacity 50mℓ Pressurized burette type Resist. pressure 10kgf/cm² With diff. pres. transducer	
9	Supporing Column	4	Aluminum made, alumited treating	
10	EP Valve Head	1	Electro Pneumatic Servo Valve Type With air regulator for counter pressure	
11	Triaxial Cell	1	Details are shown in the attached drawing of Triaxial Cell. Available both for torsional & Vertical triaxial test	
NOTE				
SEIKEN, INC.				

Figure 5.21 Description and specifications of the parts shown in Drawing No TC-45280424 1/5 (part 2/5) (after SEIKEN, INC.)

CONSTITUTIONAL PARTS SHOWN ON DRAWING		MARCH• 1997	3/5
NAME OF EQUIPMENT	DRAWING NO.	45280424	1/5

ASK TORSIONAL TRIAXIAL APPARATUS
DESK TOP EP SERVO UNIVERSAL MODEL NO. DTC-452

NO.	PARTS NAME	Q'TY	SPECIFICATIONS
12	Fixing Clamp	2	For fixing triaxial cell
13	Base Frame	1	Frame & plate steel welding construction,
14	Relief Tank	1	Light steel tank, paint treating Capacity 5ℓ, Resist. pressure $10 kgf/cm^2$
	AIR UNIT		
1	Name Panel	1	Apparatus name mark printed
2	Confining & Back Pressure System Panel	1	Pressure gage ϕ 100mm With a back pressure air regulator $0\sim 10 kgf/cm^2$
3	Vertical Pressure & Counter Pressure System	1	Pressure gage ϕ 100mm With a counter pressure air regulator $0\sim 10 kgf/cm^2$
4	Electric Air Regulating Unit	2	Two range type for vertical and confining pressure Automatic type by DC servo motor drive Manual operation is also available
5	Ratio Relay Pressure System Panel	1	Pressure gage ϕ 100mm Two air regulators $0\sim 10 kgf/cm^2$

NOTE

SEIKEN, INC.

Figure 5.22 Description and specifications of the parts shown in Drawing No TC-45280424 1/5 (part 3/5) (after SEIKEN, INC.)

CONSTITUTIONAL PARTS SHOWN ON DRAWING			MARCH. 1997	4/5
NAME OF EQUIPMENT		DRAWING NO.	45280424	1/5
ASK TORSIONAL TRIAXIAL APPARATUS DESK TOP EP SERVO UNIVERSAL MODEL NO. DTC-452				

NO.	PARTS NAME	Q'TY	SPECIFICATIONS
6	Primary Pressure & Master Gage Panel	1	Primary pressure gage ϕ 60mm Air regulator 0~ 15kgf/cm², Non bleed type Four point switching to the master gage
7	Vacuum System Panel	1	Vacuum gage ϕ 60mm Vacuum control regulator 0~ -1kgf/cm²
8	Cabinet	1	Desk top type, aluminum made With fan & blank panel
	ELECTRIC MEASURING AND CONTROLLING UNIT		
1	Name Panel	1	With electric power switch
2	EP Servo Controller	1	Model EO-290U Closed loop servo controlling type for static & dynamic test Built-in static & dynamic function generators
3	Electric Amplifiers	7	EA-400 series, 7ch. With output connector panel for 7 points

NOTE

SEIKEN, INC.

Figure 5.23 Description and specifications of the parts shown in Drawing No TC-45280424 1/5 (part 4/5) (after SEIKEN, INC.)

CONSTITUTIONAL PARTS SHOWN ON DRAWING		MARCH· 1997	5/5
NAME OF EQUIPMENT	DRAWING NO.	45280424	1/5
ASK TORSIONAL TRIAXIAL APPARATUS DESK TOP EP SERVO UNIVERSAL MODEL NO. DTC-452			

NO.	PARTS NAME	Q'TY	SPECIFICATIONS
4	Pressure Controller		For controlling vertical and confining pressure
-1)	Loading Speed Set	1	EO-340DU, Slope DC generator Setting speed range 0.01~ 100% FB FS/MIN.
-2)	Elec· Mecha Servo Controller	2	EO-470U For controlling vertical & confining pressure electric air regulating unit Available for closed and open loop control
5	Blank Panel	2	
6	Cabinet	1	Desk top type, Aluminum made Built-in power transformer for converting 220v to 100v

NOTE

SEIKEN, INC.

Figure 5.24 Description and specifications of the parts shown in Drawing No TC-45280424 1/5 (part 5/5) (after SEIKEN, INC.)

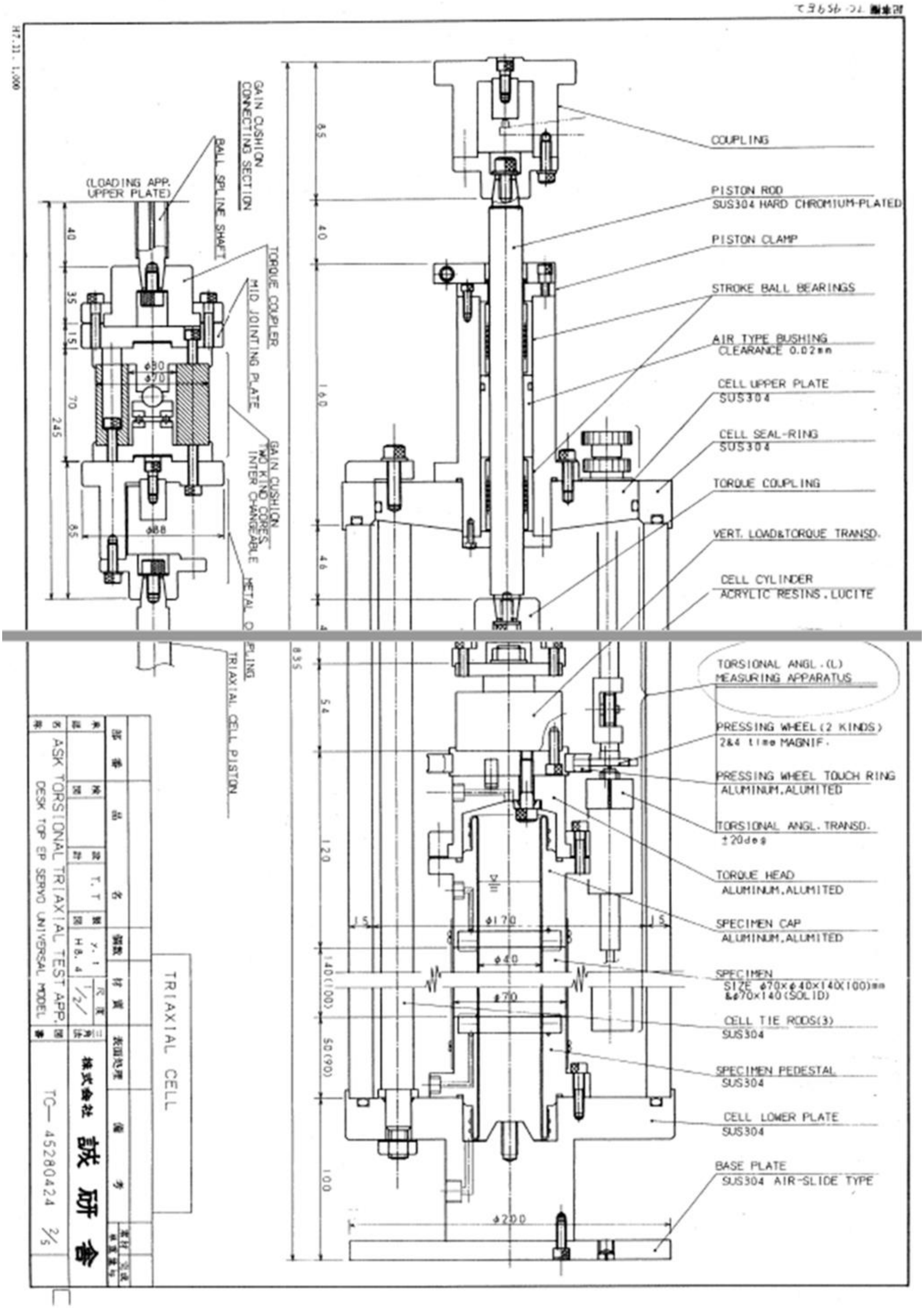

Figure 5.25 Drawing of the triaxial cell of the hollow cylinder apparatus (Drawing No TC-45280424 2/5). All dimensions are in millimetres (after SEIKEN, INC.)

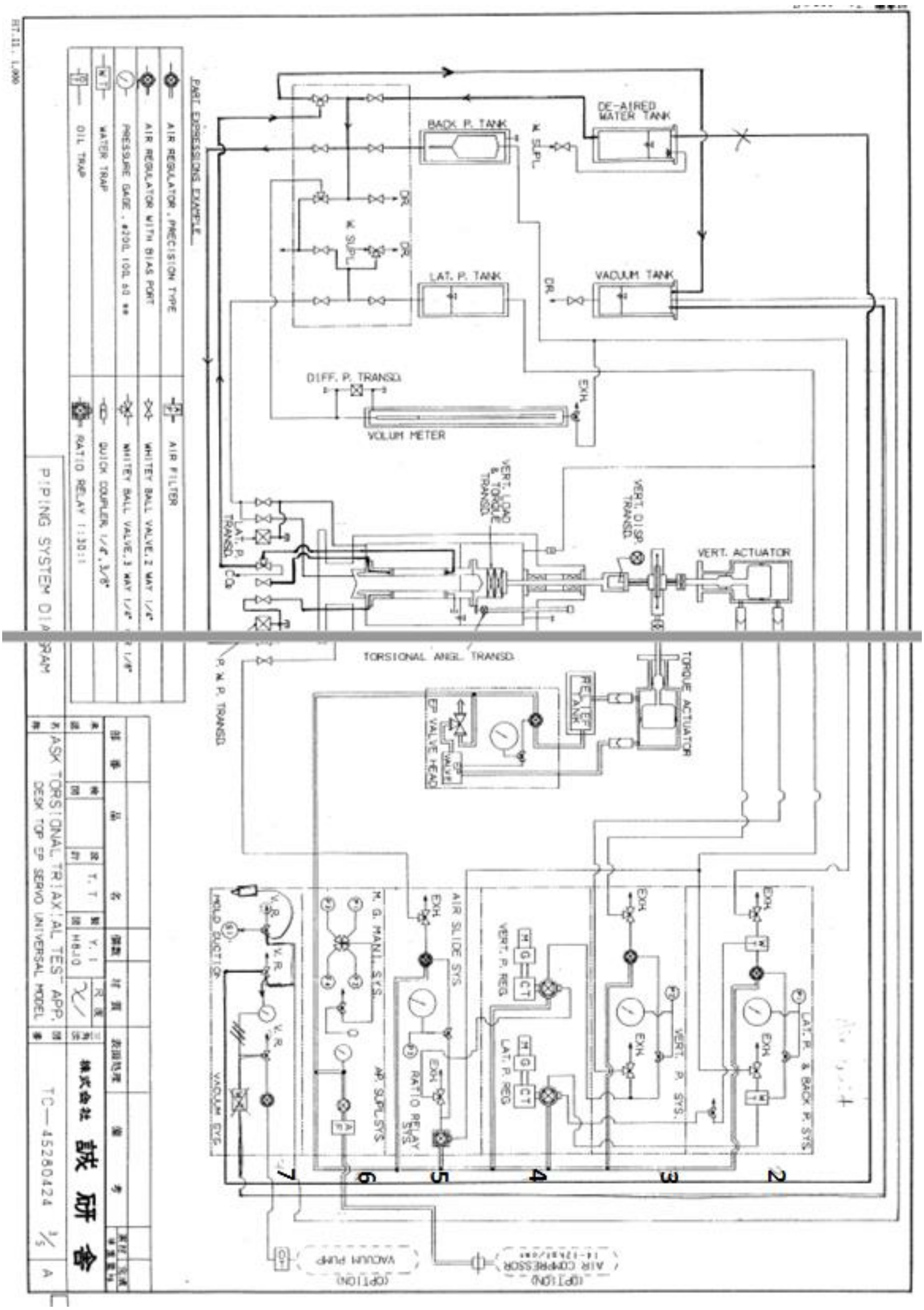

Figure 5.26 Piping system diagram of the hollow cylinder apparatus (Drawing No TC-45280424 3/5) (after SEIKEN, INC.)

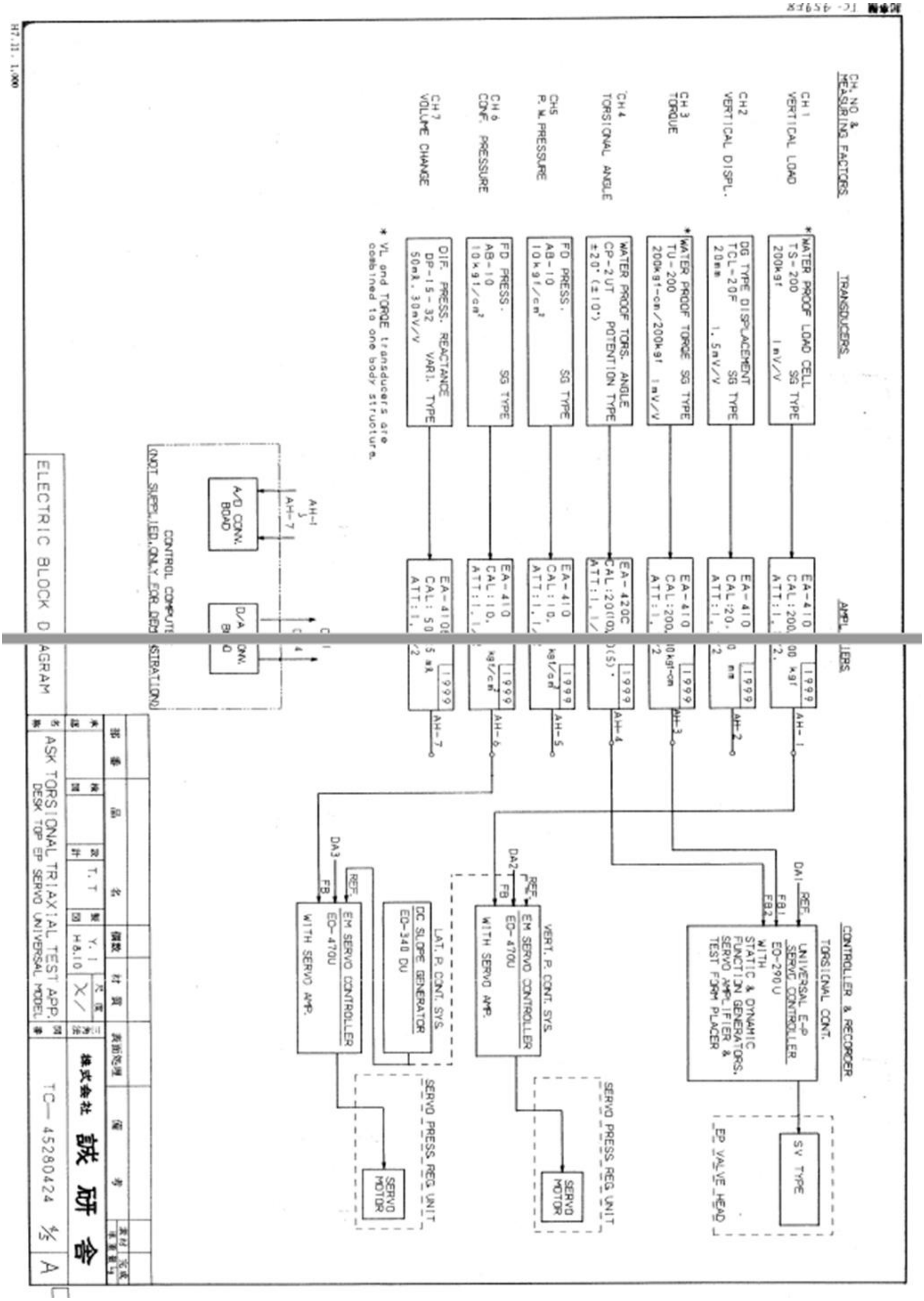

Figure 5.27 Electric block diagram of the hollow cylinder apparatus (Drawing No TC-45280424 4/5) (after SEIKEN, INC.)

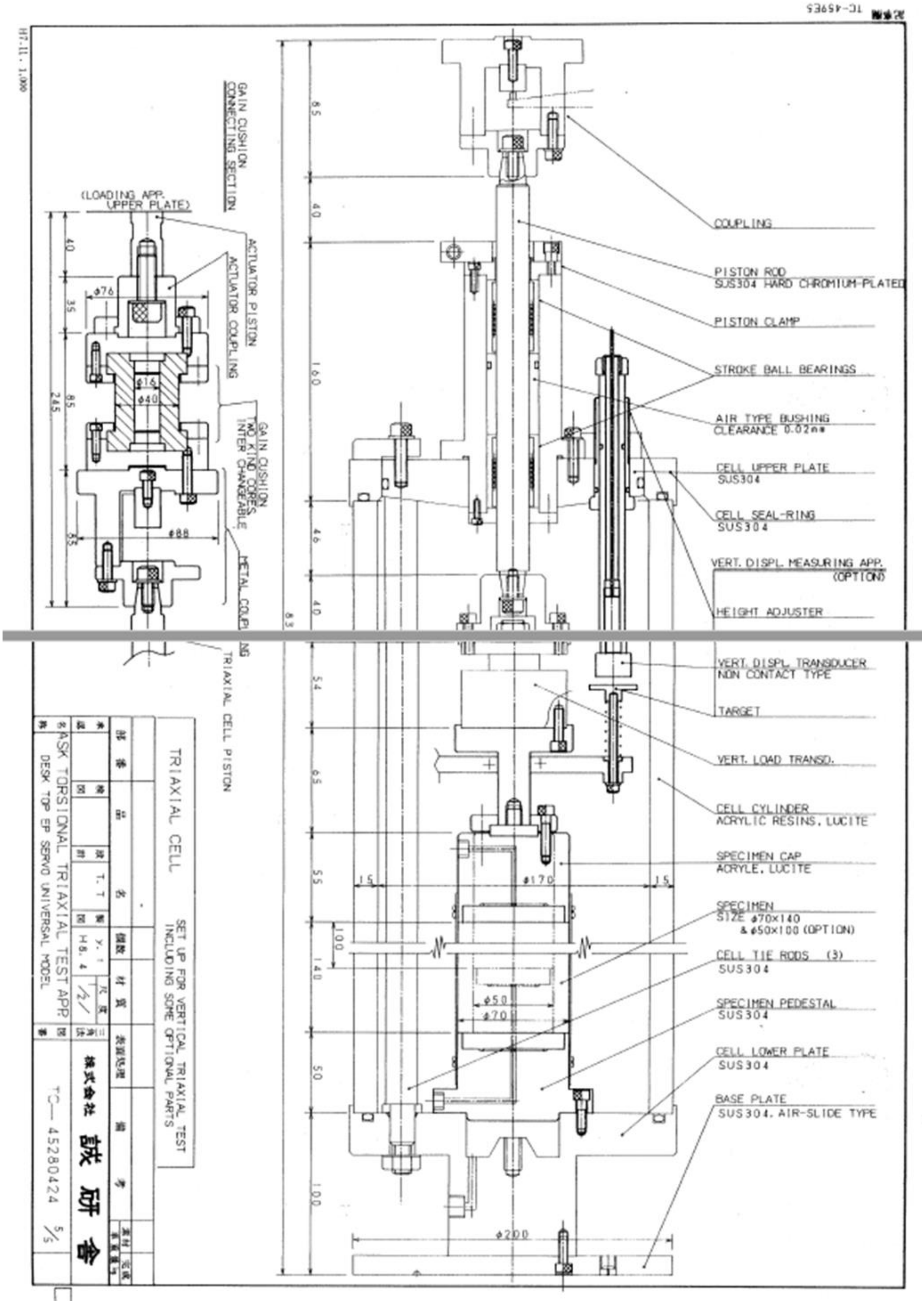

Figure 5.28 Drawing of the triaxial cell of the hollow cylinder apparatus including optional parts for vertical triaxial test (Drawing No TC-45280424 5/5). All dimensions are in millimetres (after SEIKEN, INC.)

Figure 5.29 Photo of the triaxial cell and loading system mounted on the steel plate and frame. The plastic cylindrical shell and the seal ring of the triaxial cell are not included in the photo. The water unit is shown on the left

Figure 5.30 Photo of a porous stone with embedded vanes

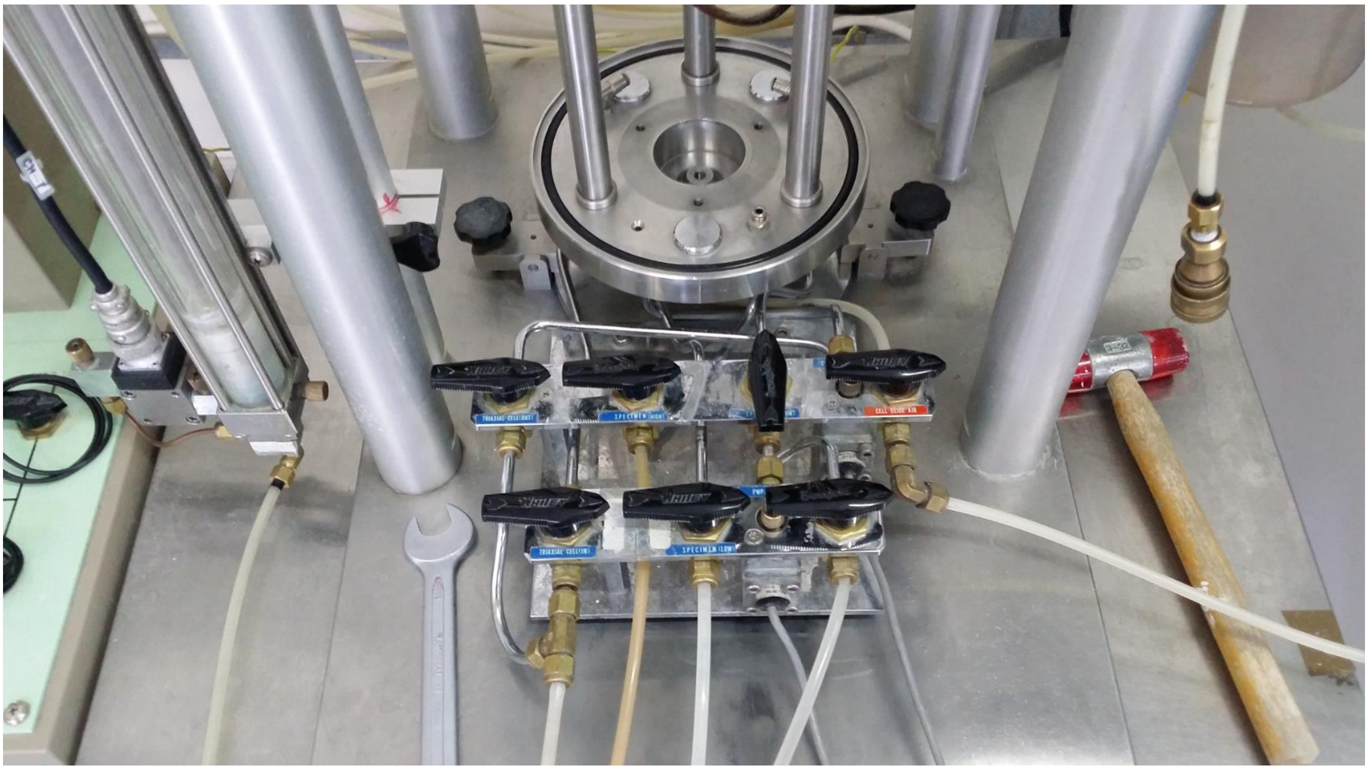

Figure 5.31 Photo of the valves mounted on the base plate of the triaxial cell

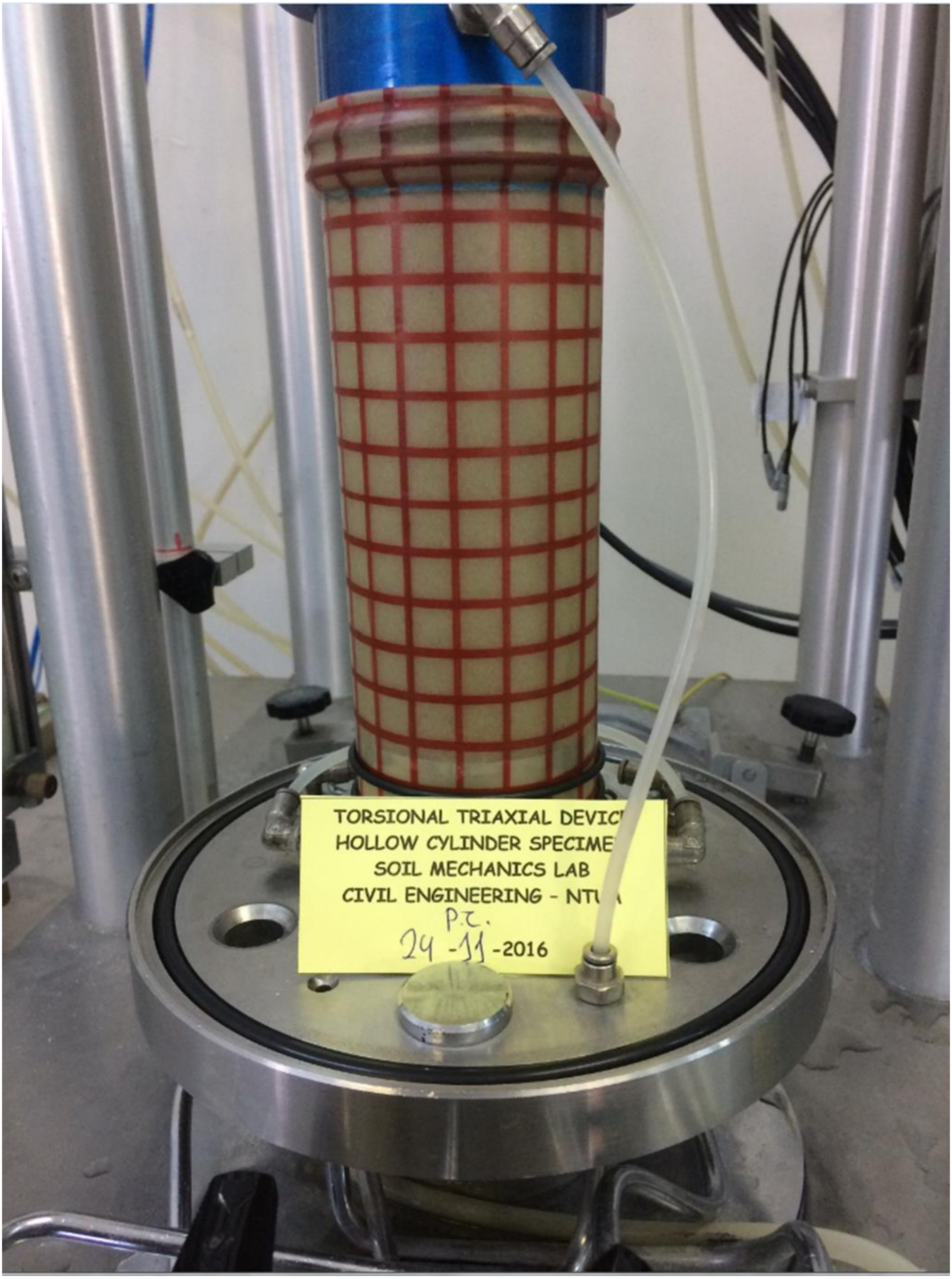

Figure 5.32 Photo of a sand specimen under suction before shear testing

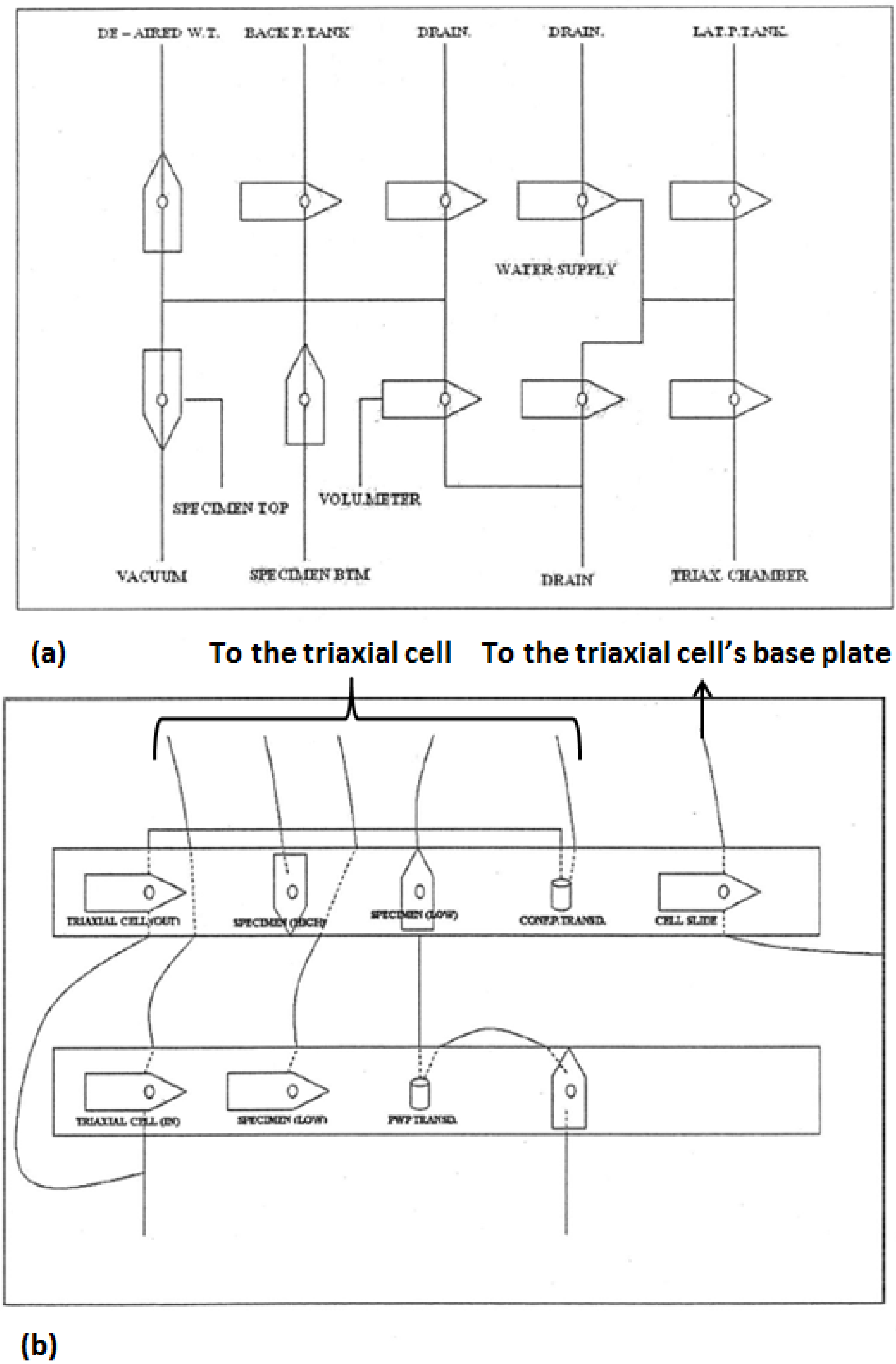

Figure 5.33 Circulation of de-aired water through the specimen during the saturation process. **a** Open / closed state of the valves mounted on the panel of the base box of the water unit. **b** Open / closed state of the valves mounted on the base plate of the triaxial cell (after Tsomokos 2005)

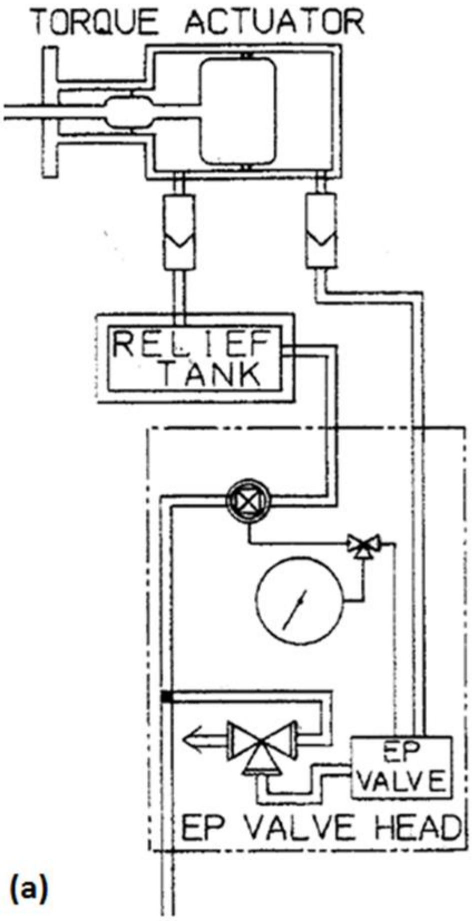

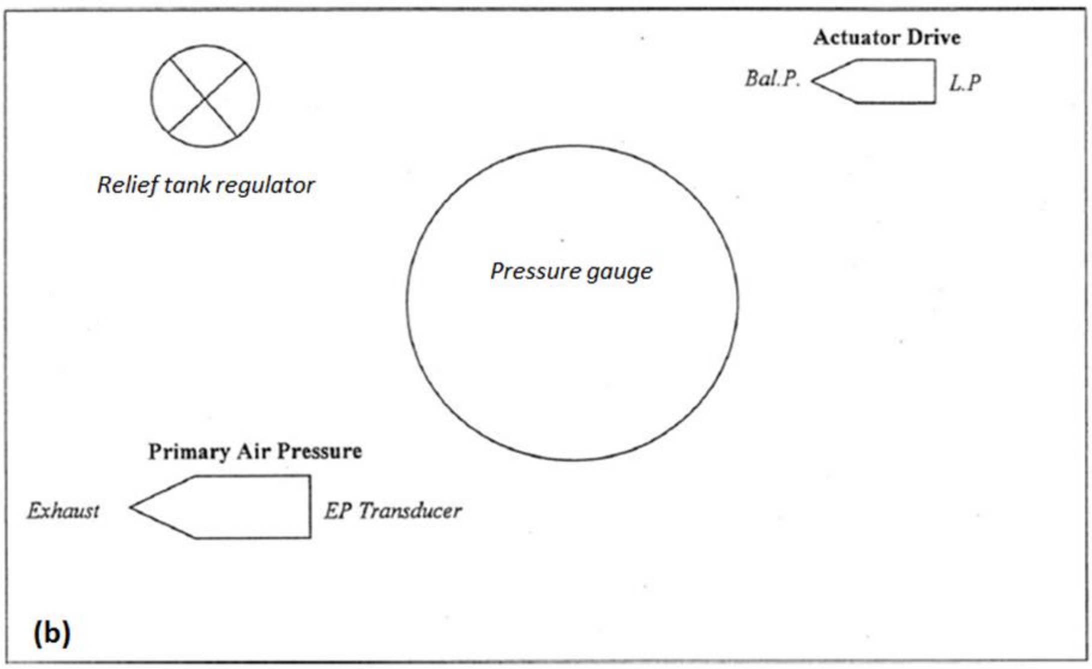

Figure 5.34 Electro-pneumatic valve head system for torque loading. **a** Drawing of the pneumatic lines behind the panel. **b** Drawing of the front panel (**a** after SEIKEN, INC. and **b** after Tsomokos 2005)

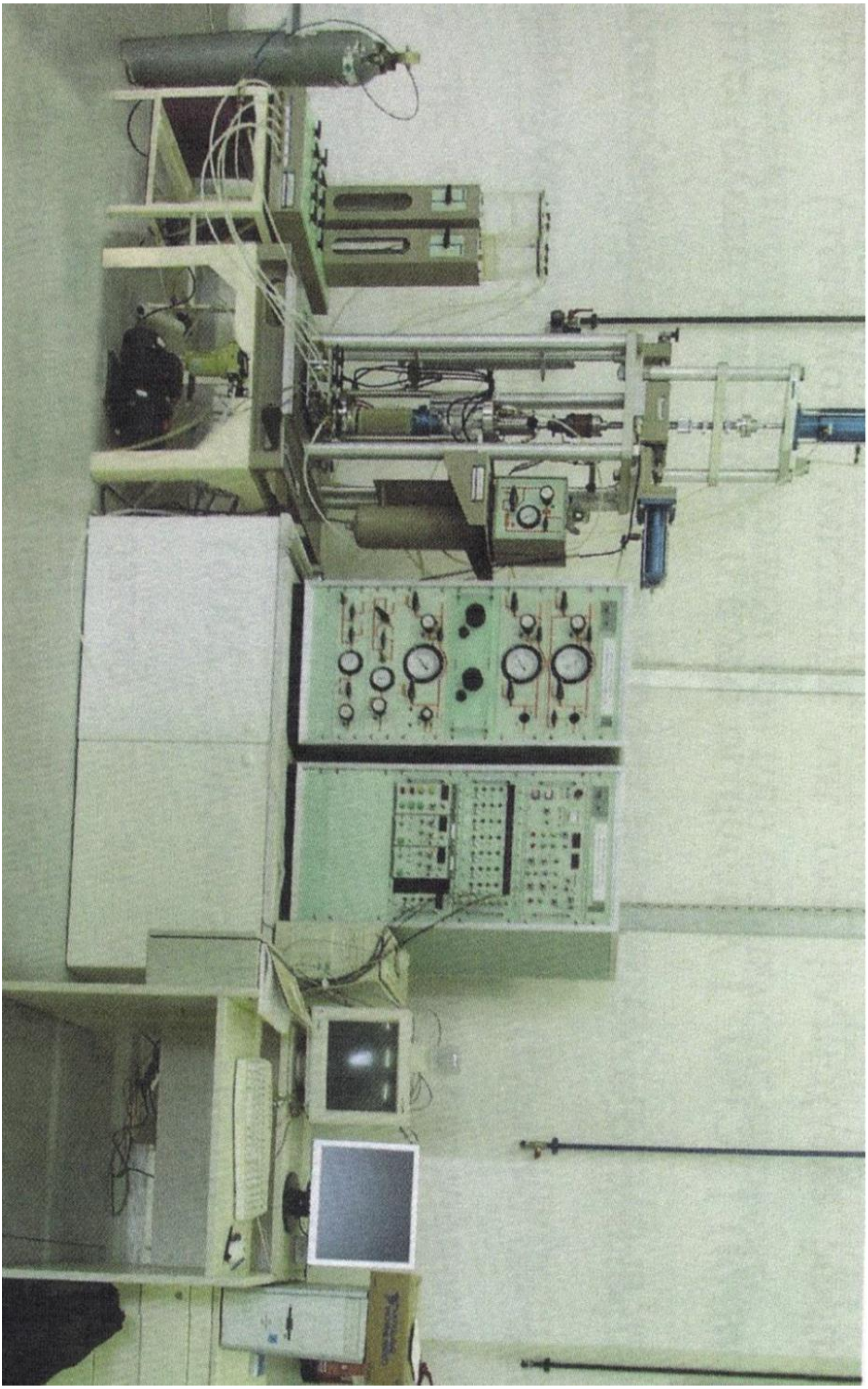

Figure 5.35 Photo of the hollow cylinder apparatus before the upgrade accomplished for the needs of this study (after Konstadinou 2013)

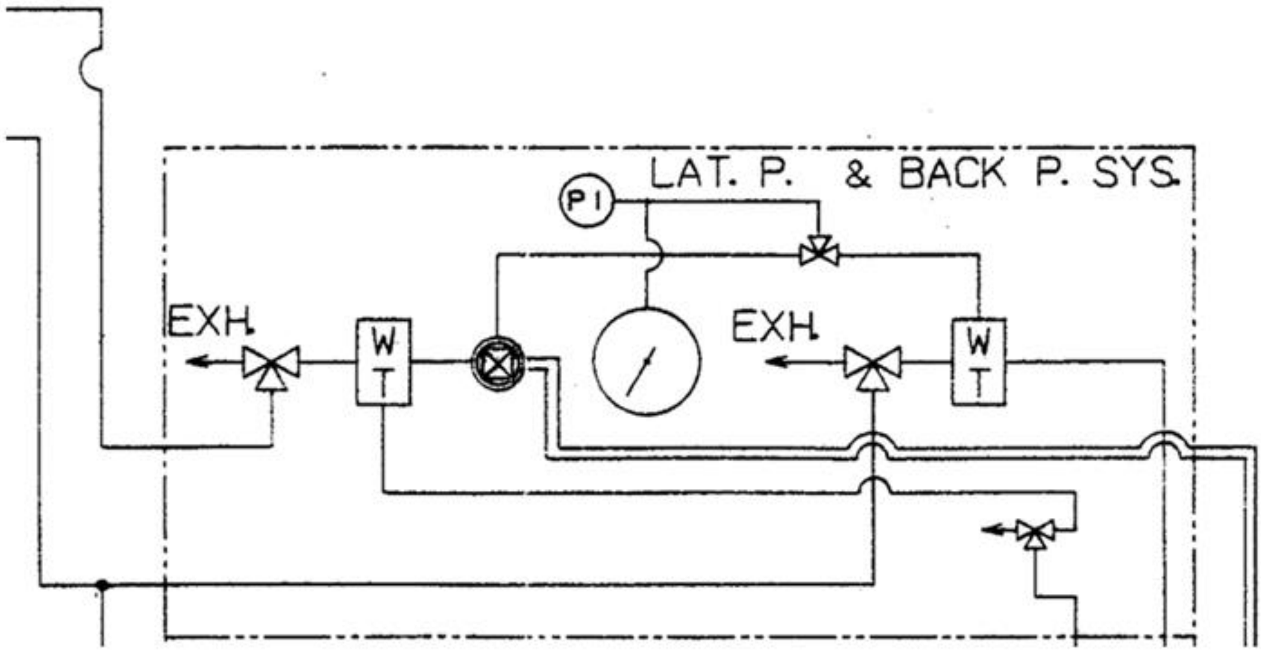

(a)

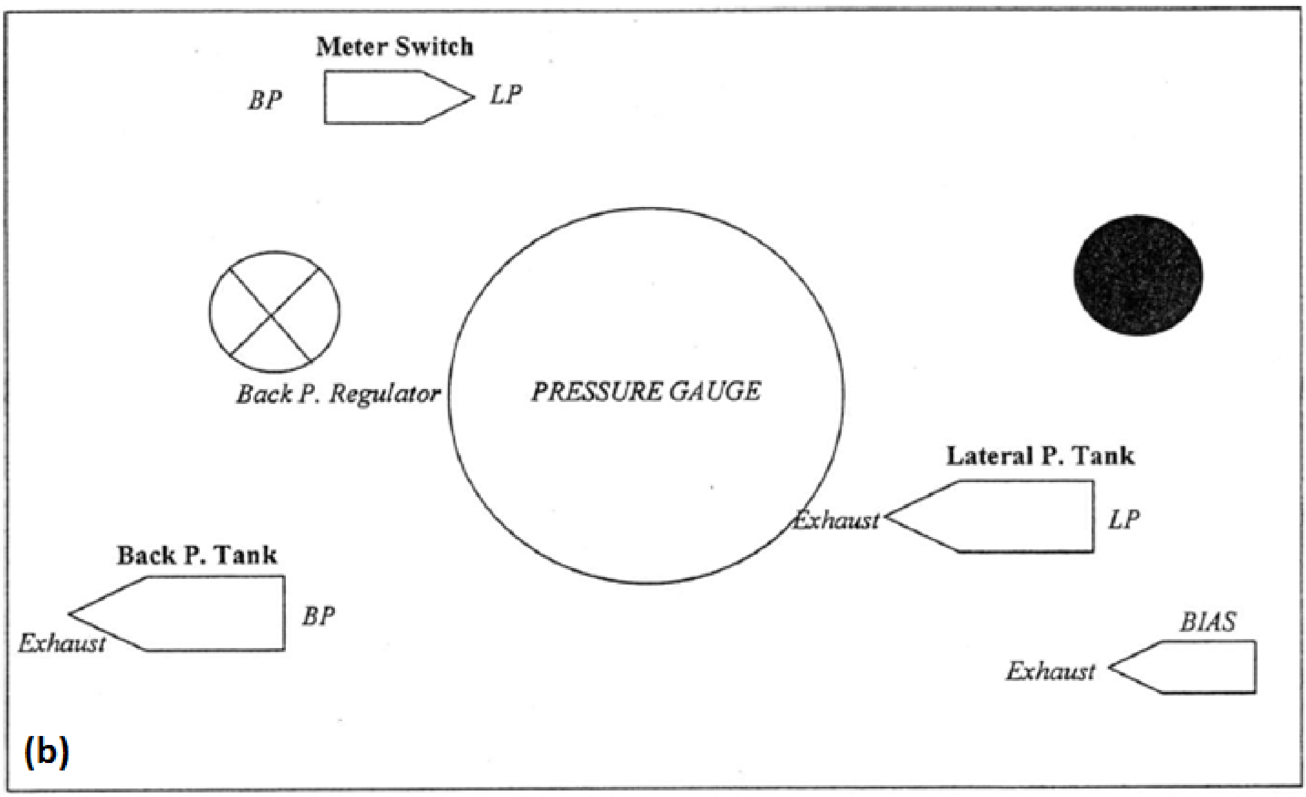

(b)

Figure 5.36 Lateral and back pressure system of the air unit. **a** Drawing of the pneumatic lines behind the panel. **b** Drawing of the front panel (**a** after SEIKEN, INC. and **b** after Tsomokos 2005)

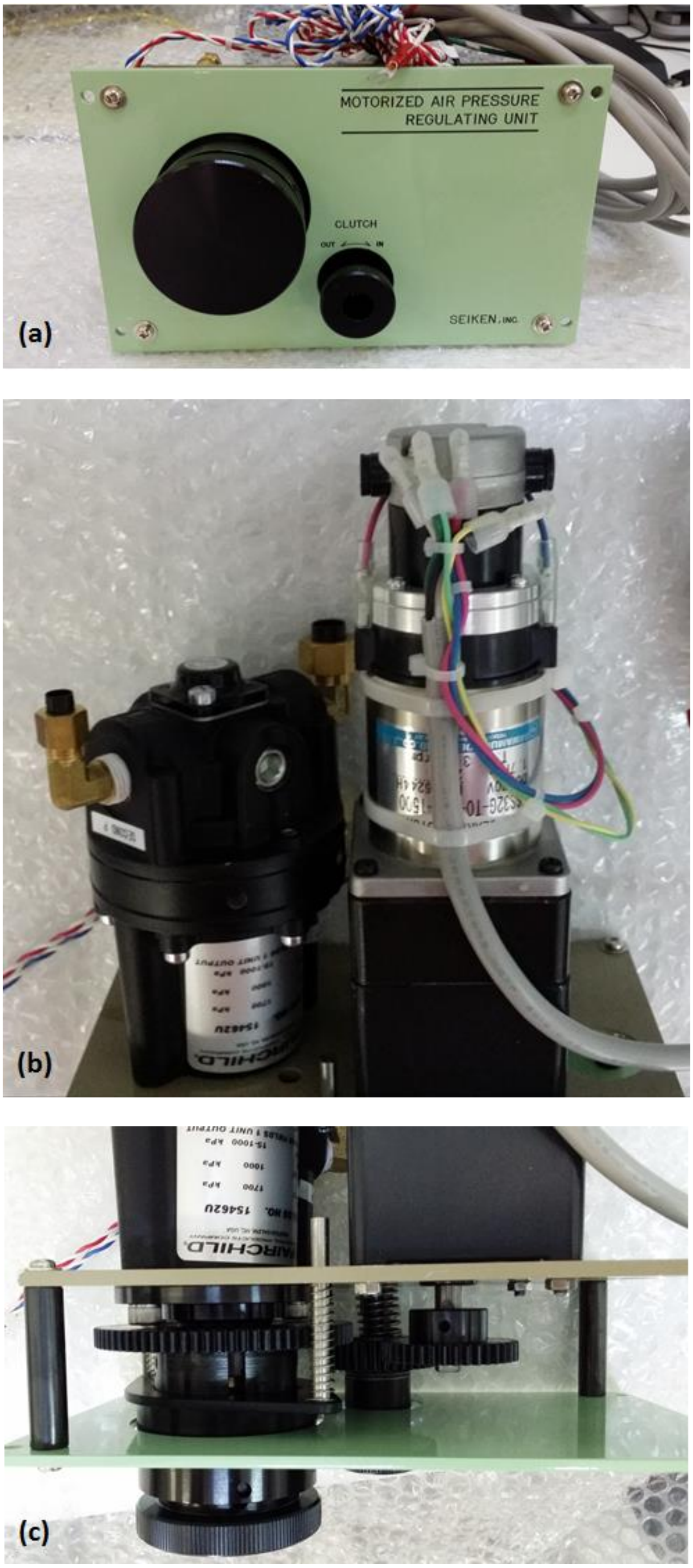

Figure 5.37 Metal body equipped with a servo valve, a tacho generator, a motor and a clutch mechanism. **a** Front view of the metal body. **b** Upper view of the servo valve, tacho generator and motor **c** Upper view of the clutch mechanism

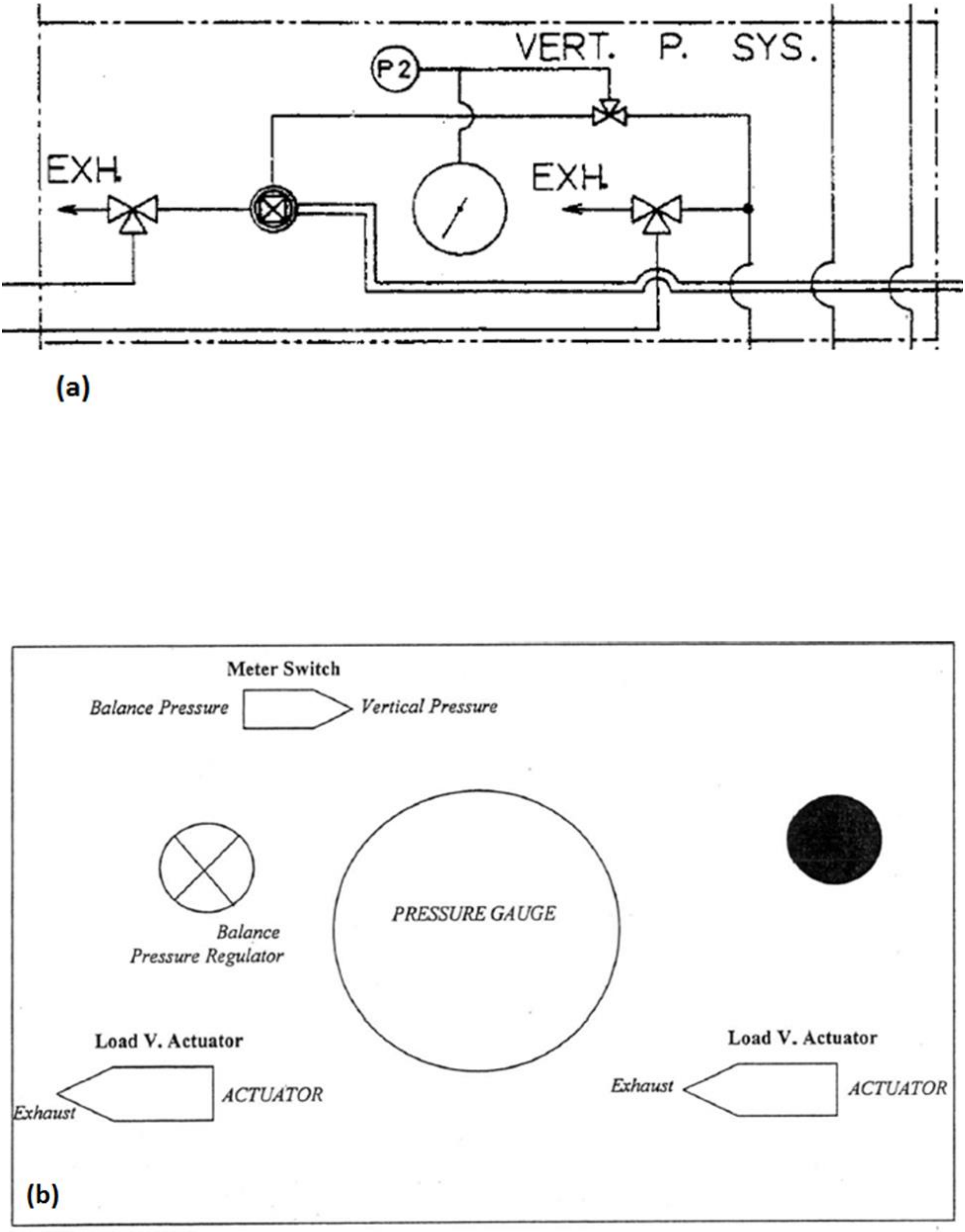

Figure 5.38 Vertical pressure system of the air unit. **a** Drawing of the pneumatic lines behind the panel. **b** Drawing of the front panel (**a** after SEIKEN, INC. and **b** after Tsomokos 2005)

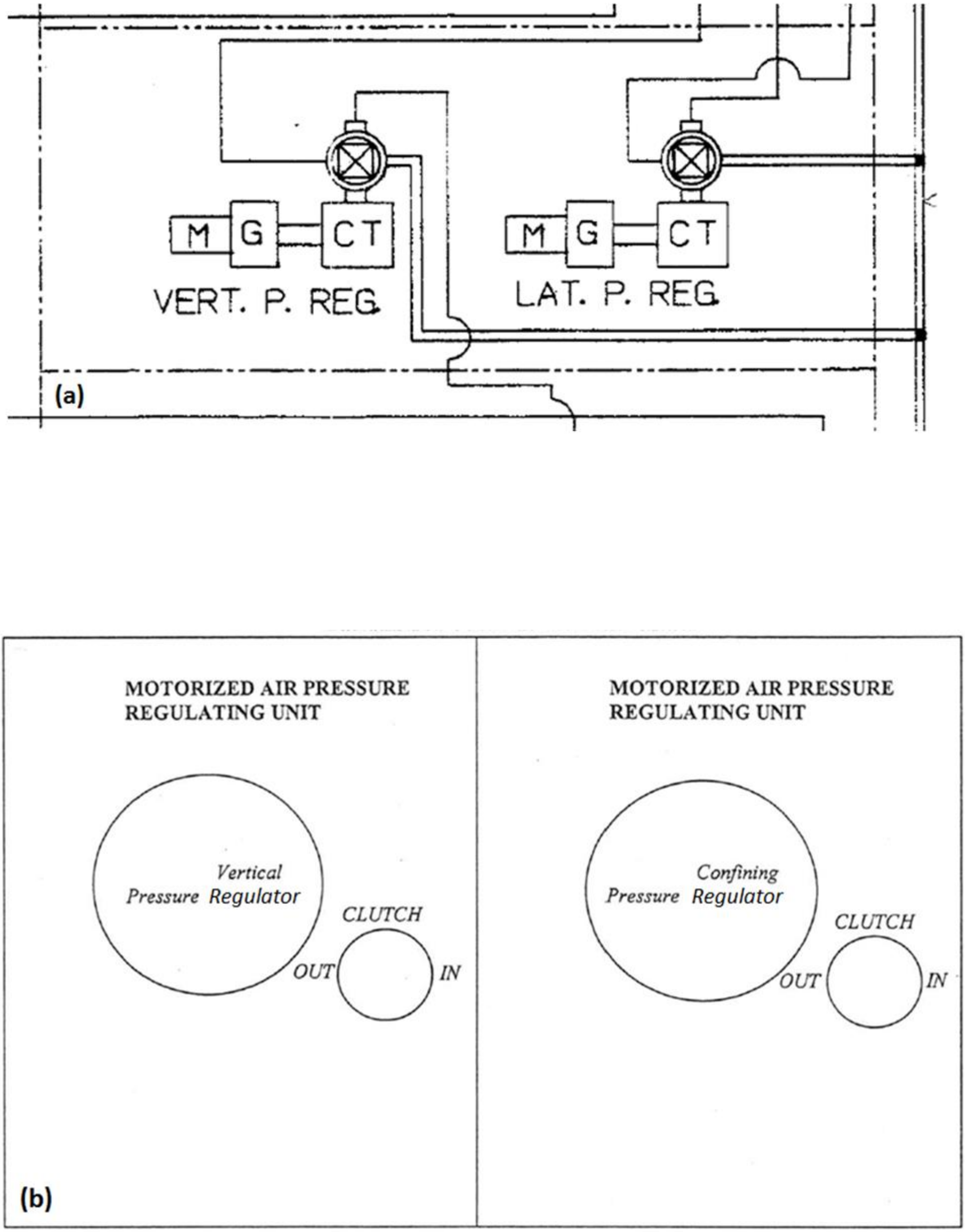

Figure 5.39 Electric-pneumatic regulating system of the air unit. **a** Drawing of the pneumatic lines and electrical parts behind the panel. **b** Drawing of the front panel (**a** after SEIKEN, INC. and **b** after Tsomokos 2005)

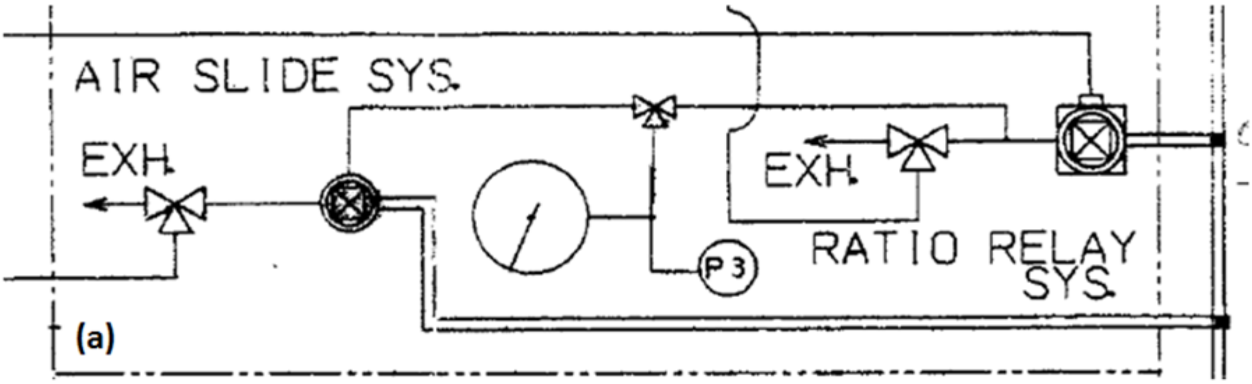

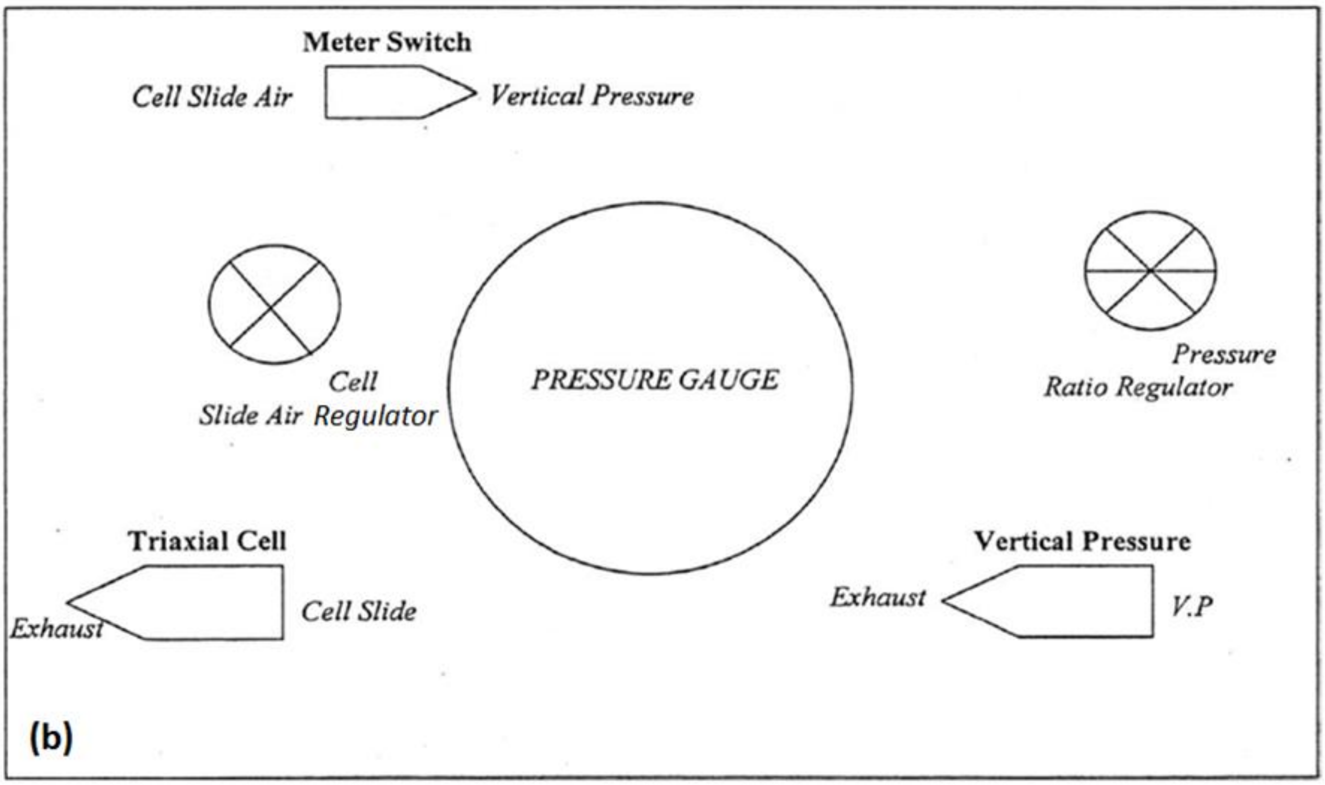

Figure 5.40 Pressure ratio relay and air slide system of the air unit. **a** Drawing of the pneumatic lines behind the panel. **b** Drawing of the front panel (**a** after SEIKEN, INC. and **b** after Tsomokos 2005)

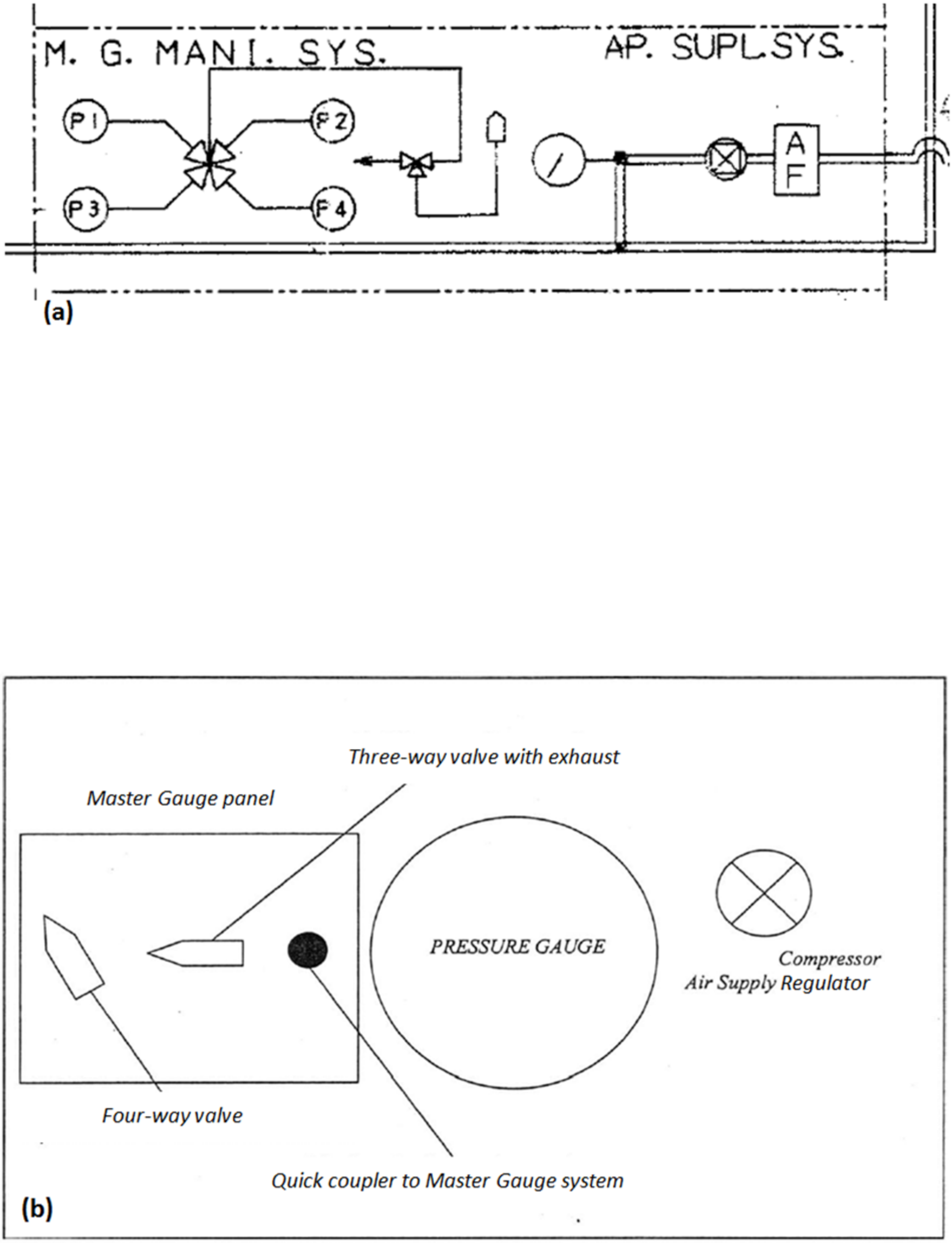

Figure 5.41 Primary pressure system and master gauge panel. **a** Drawing of the pneumatic lines behind the panel. **b** Drawing of the front panel (**a** after SEIKEN, INC. and **b** after Tsomokos 2005)

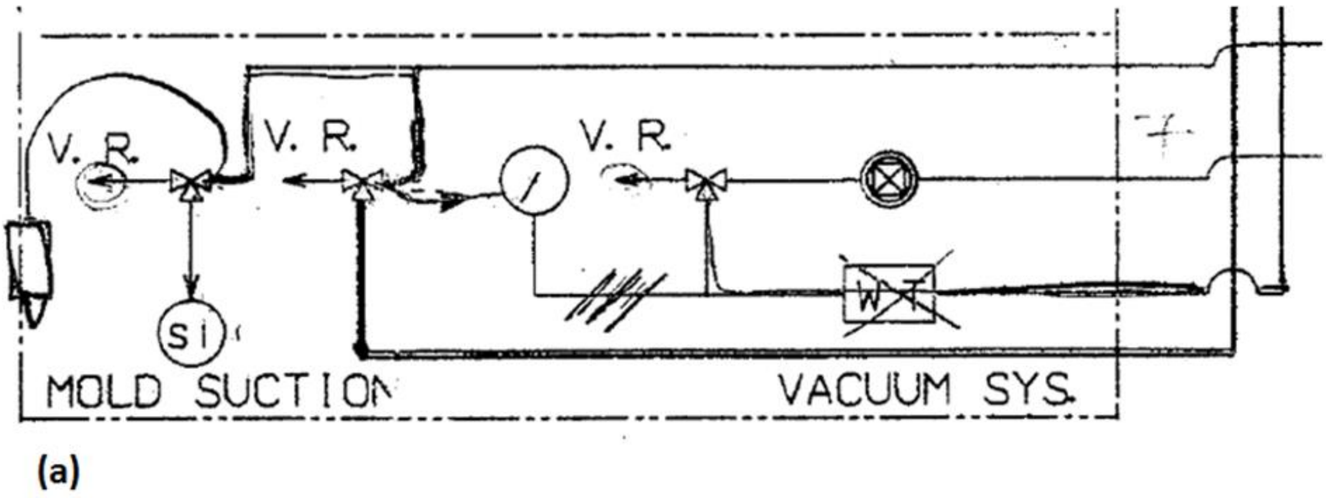

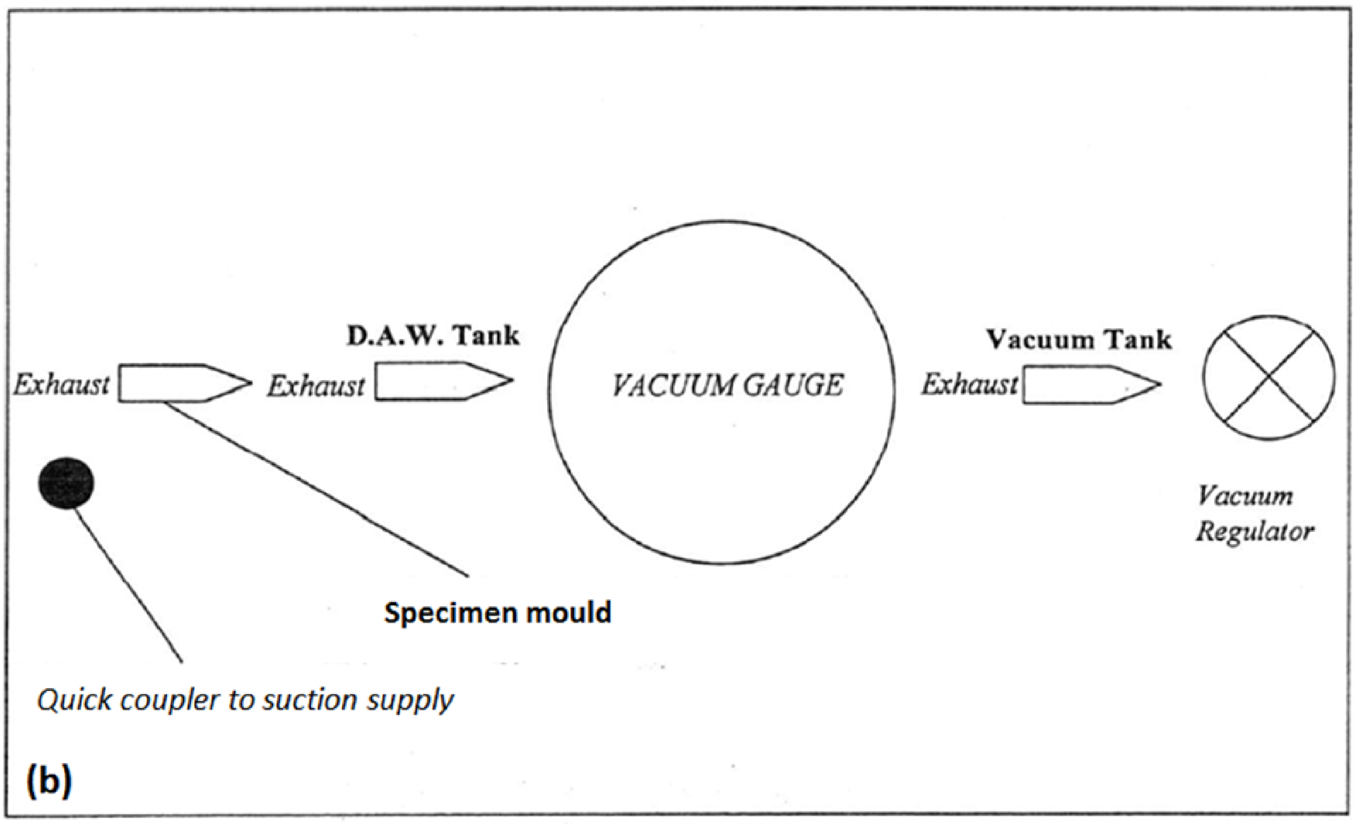

Figure 5.42 Vacuum system. **a** Drawing of the pneumatic lines behind the panel. **b** Drawing of the front panel (**a** after SEIKEN, INC. and **b** after Tsomokos 2005)

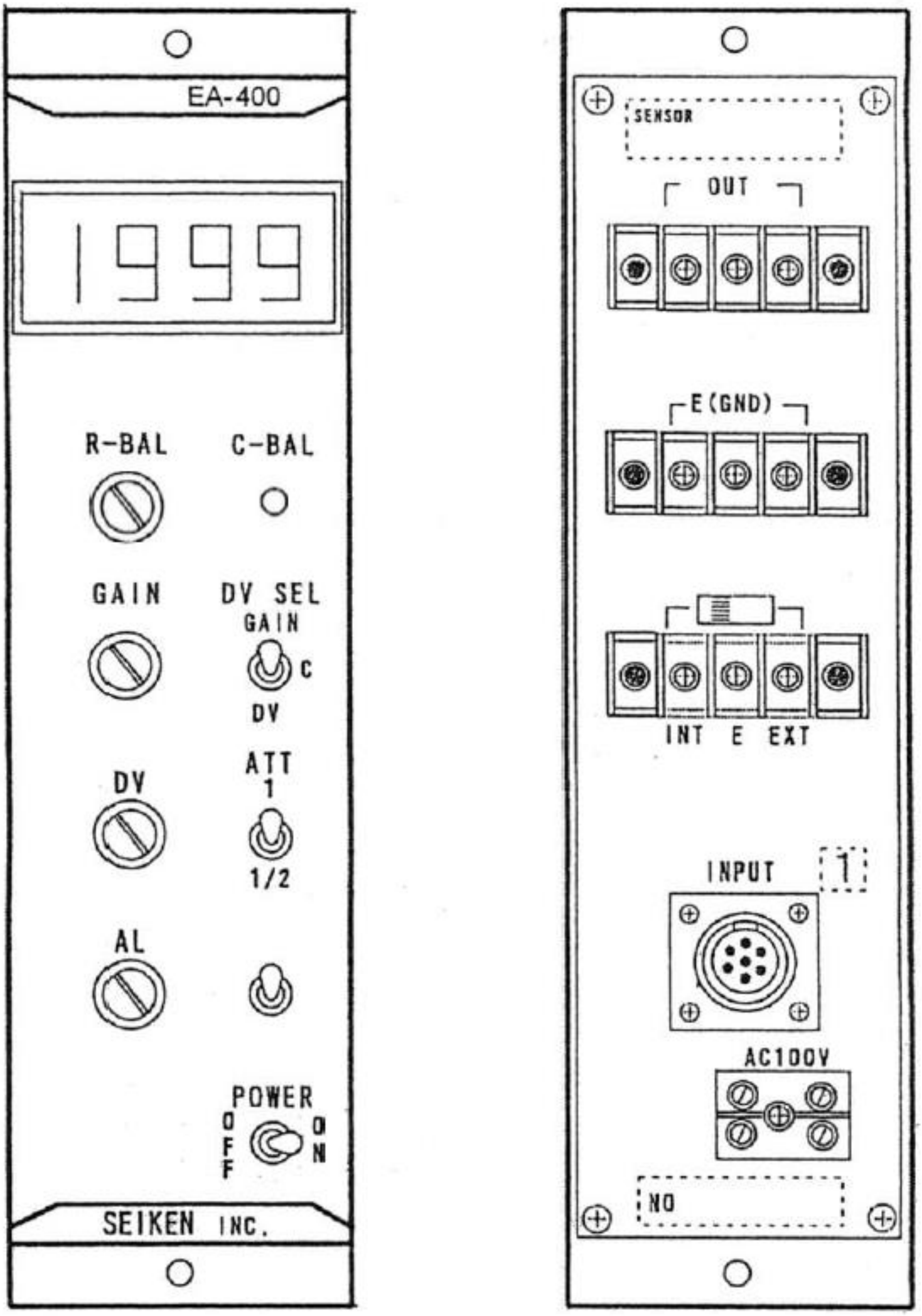

Figure 5.43 Amplifier unit (front and rear view): Model EA400 Series (after SEIKEN, INC.)

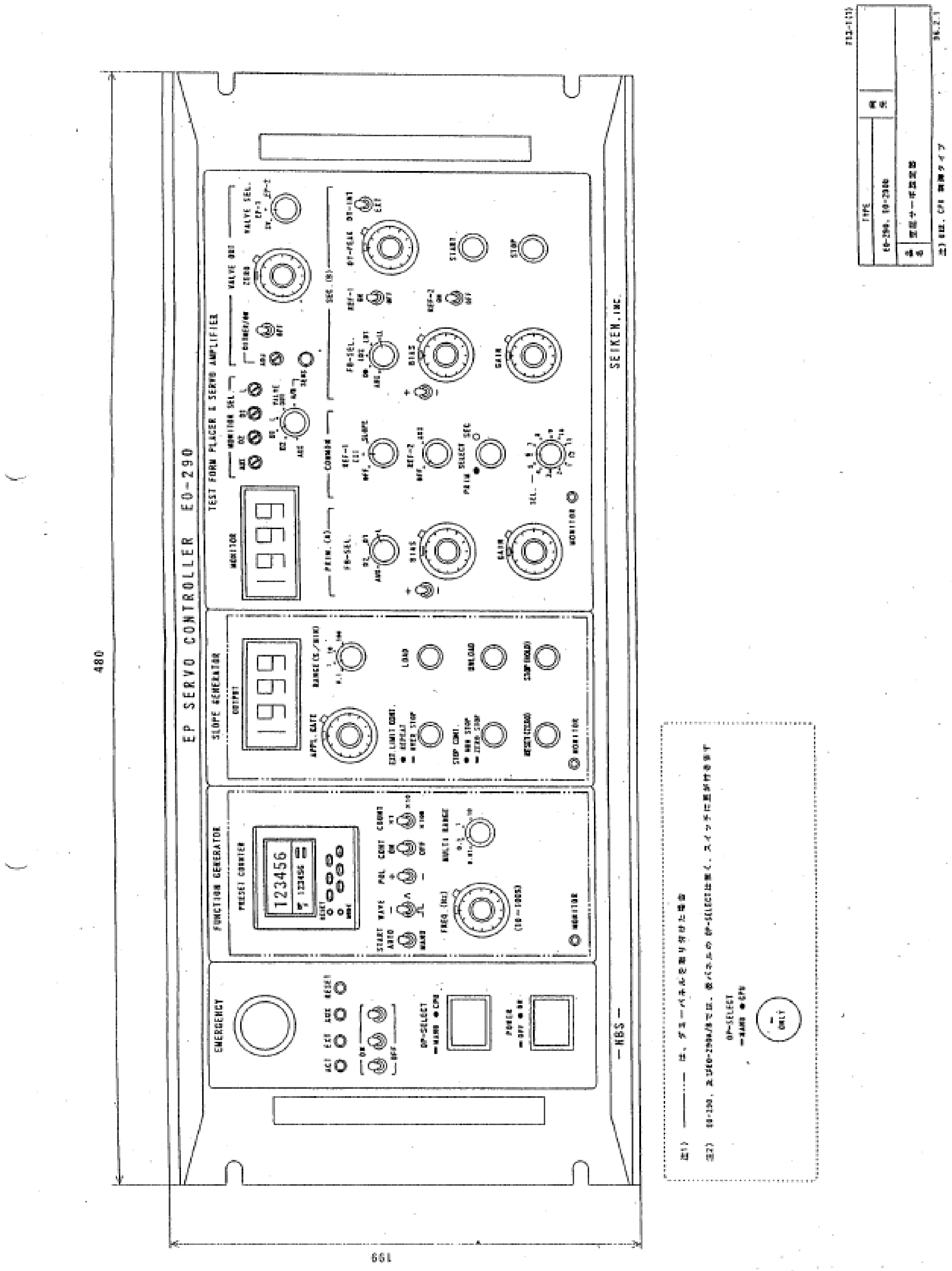

Figure 5.44 Front view of the servo controller EO-290 (U) (after SEIKEN, INC.)

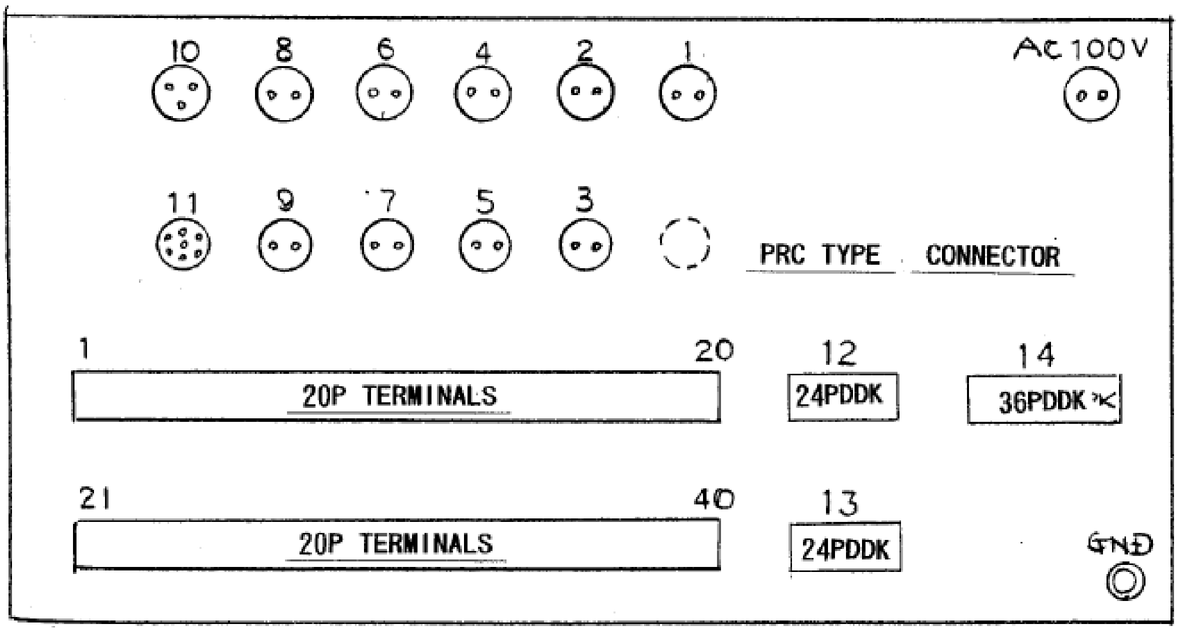

Figure 5.45 Rear view of the servo controller EO-290 (U) (after SEIKEN, INC.)

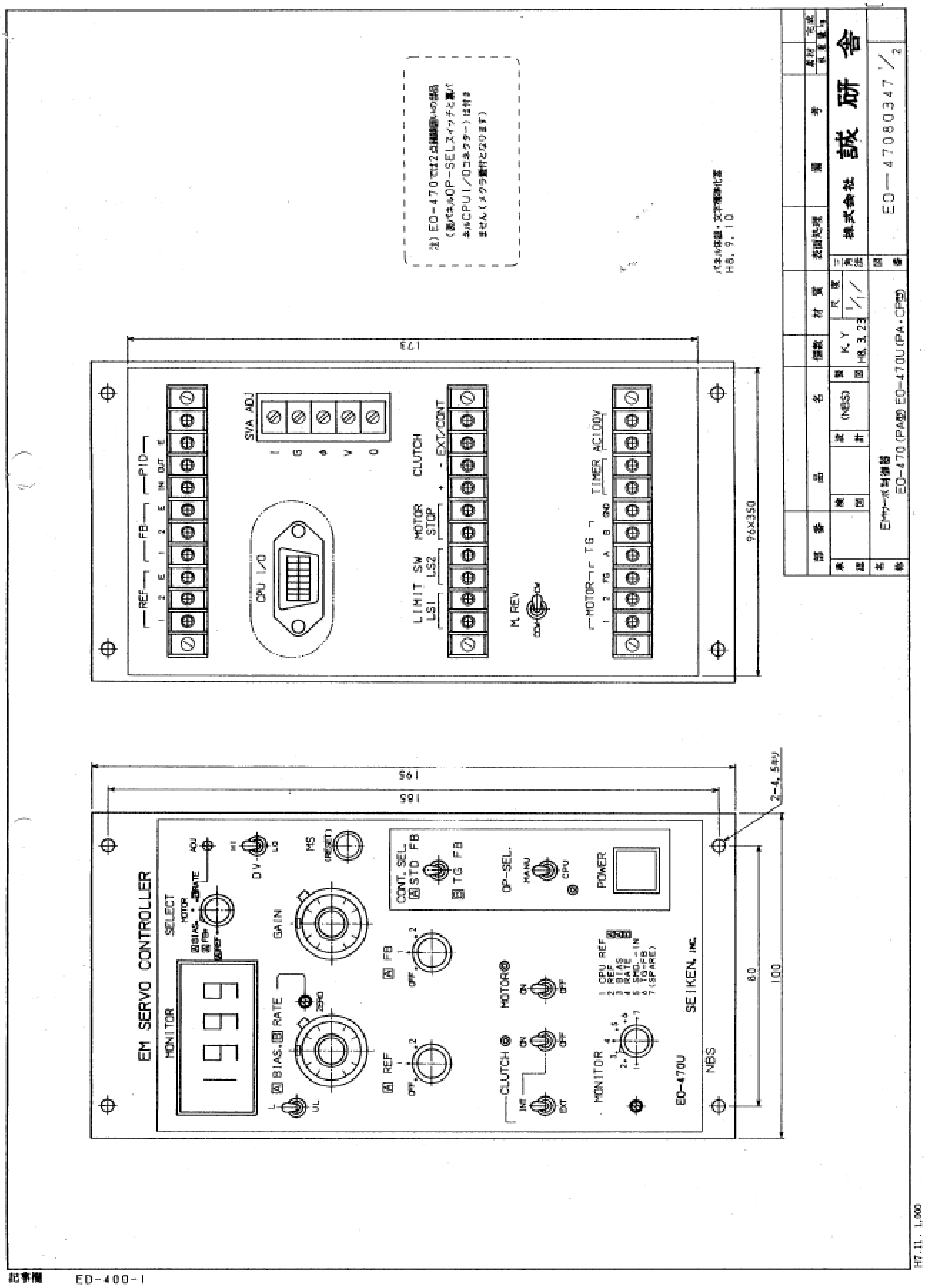

Figure 5.46 Front and rear view of the servo controller EO-470 (U) (after SEIKEN, INC.)

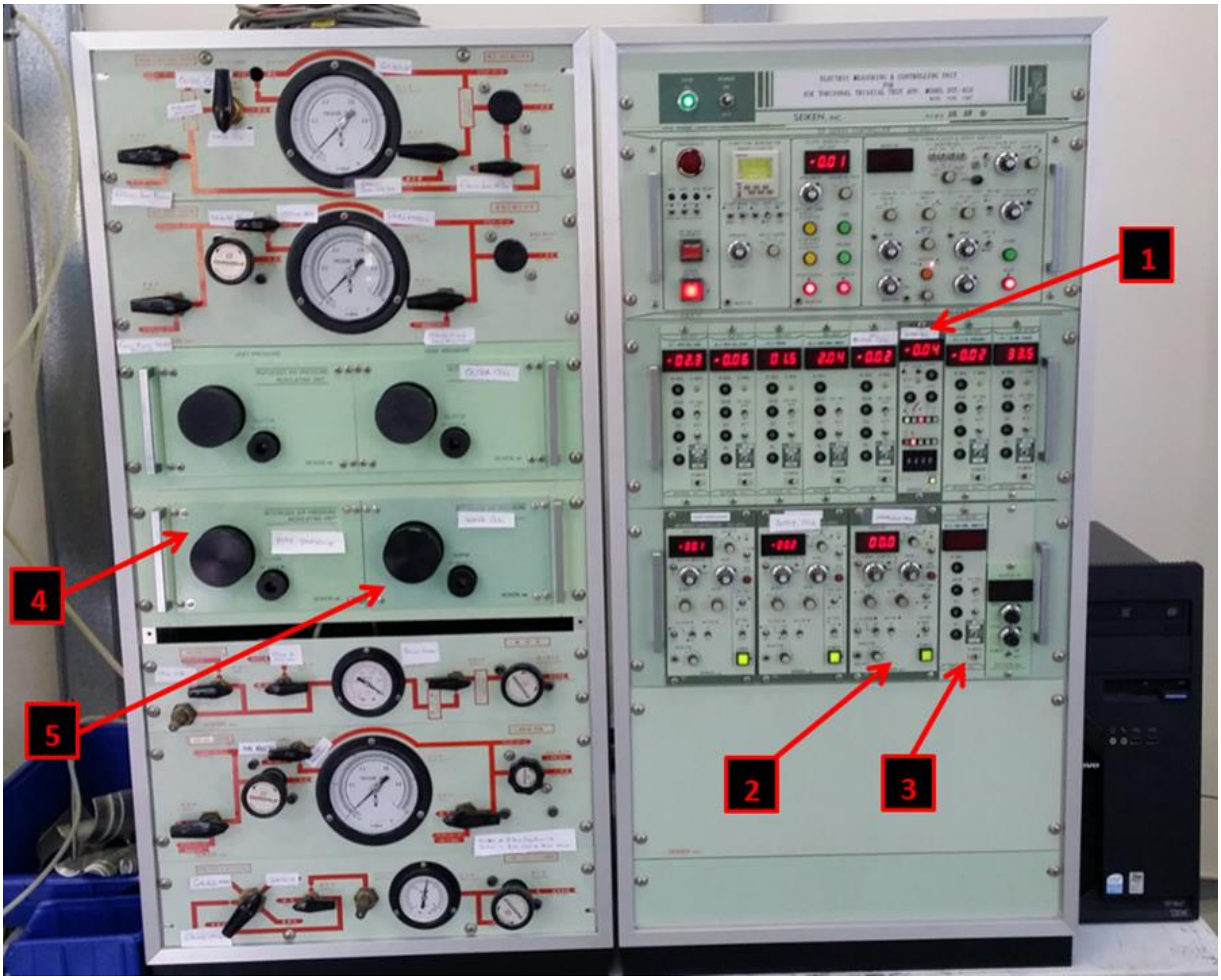

Figure 5.47 Photo of the hollow cylinder apparatus (Air Unit and Electric Measurement and Control Unit) after the upgrade accomplished for the needs of this study. **1.** Newly installed amplifier for conditioning the signal from the inner cell pressure transducer. **2.** Newly installed servo controller that drives the DC servo motor connected to the servo valve adjusting the inner cell pressure. **3.** Newly installed amplifier for conditioning the signal from the differential pressure transducer used for measuring the volume changes in the inner cell environment (this amplifier was installed for future usage, waiting the addition of a second burette). **4.** Newly installed servo valve equipped with DC servo motor used for adjusting the backpressure. **5.** Newly installed servo valve equipped with DC servo motor used for adjusting the inner cell pressure

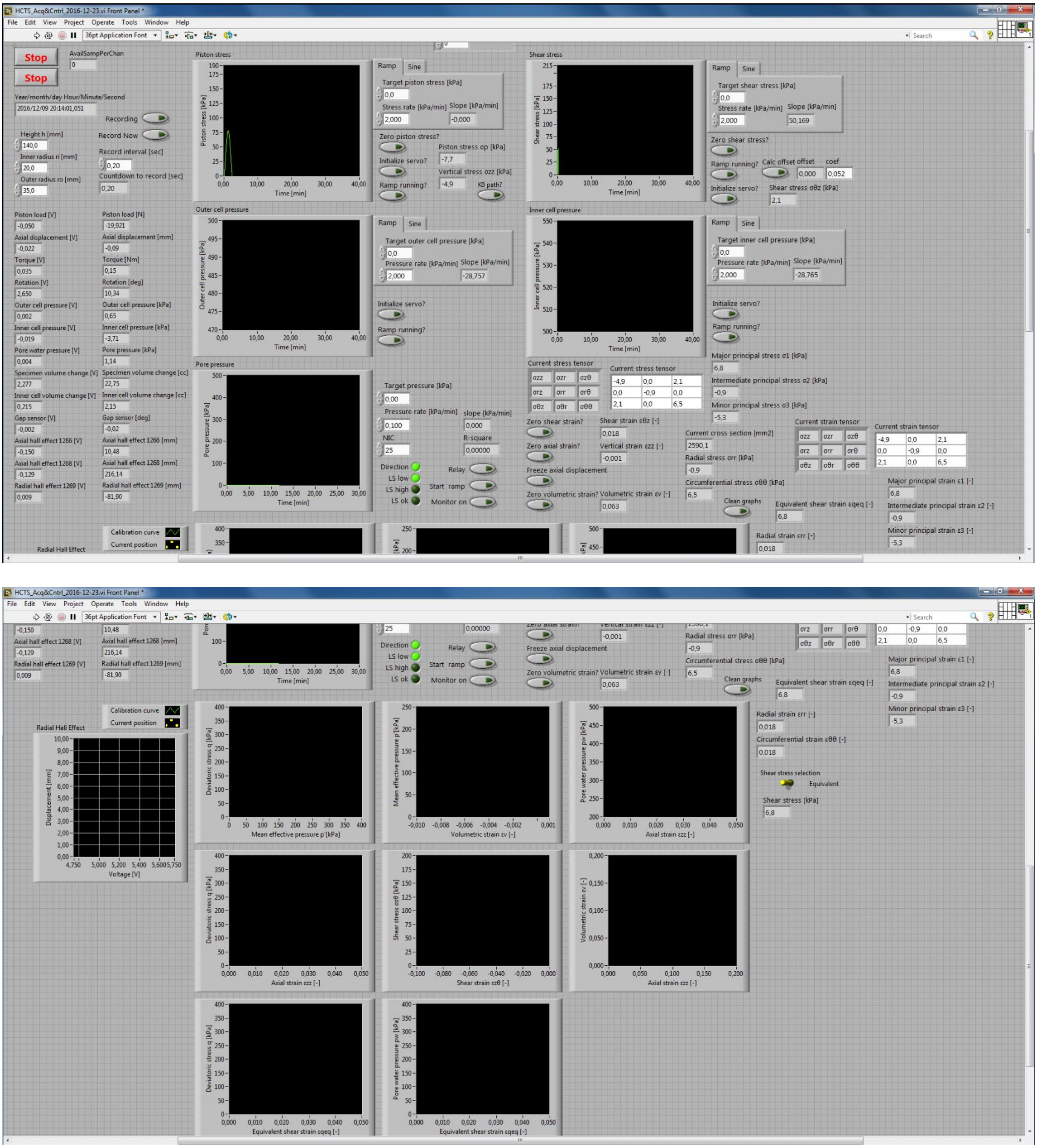

Figure 5.48 LabVIEW program developed for producing the reference electric signal input to the servo controllers and recording the data

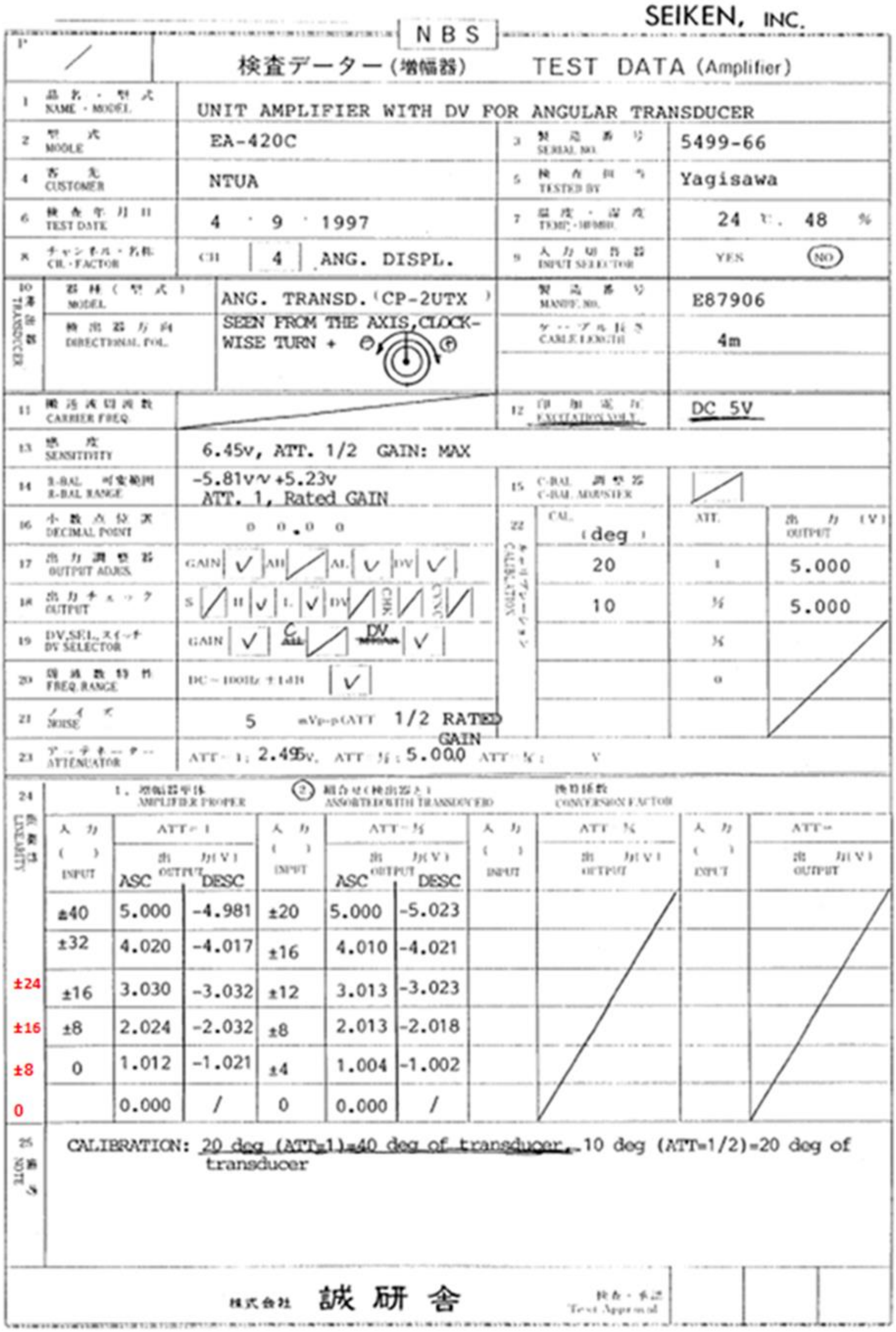

SEIKEN, INC.

NBS

検査データー (増幅器) TEST DATA (Amplifier)

1 NAME · MODEL	UNIT AMPLIFIER WITH DV FOR ANGULAR TRANSDUCER		
2 MODEL	EA-420C	3 SERIAL NO.	5499-66
4 CUSTOMER	NTUA	5 TESTED BY	Yagisawa
6 TEST DATE	4 · 9 · 1997	7 TEMP. · HUMID.	24 ℃. 48 %
8 CH. · FACTOR	CH 4 ANG. DISPL.	9 INPUT SELECTOR	YES NO
10 TRANSDUCER MODEL	ANG. TRANSD. (CP-2UTX)	MANUF. NO.	E87906
DIRECTIONAL POL.	SEEN FROM THE AXIS, CLOCK-WISE TURN + ⊖ ⊕	CABLE LENGTH	4m
11 CARRIER FREQ.		12 EXCITATION VOLT.	DC 5V
13 SENSITIVITY	6.45v, ATT. 1/2 GAIN: MAX		
14 R-BAL RANGE	-5.81v~+5.23v ATT. 1, Rated GAIN	15 C-BAL ADJUSTER	
16 DECIMAL POINT	0 0 . 0 0		
17 OUTPUT ADJUS.	GAIN ✓ AH AL ✓ DV ✓		
18 OUTPUT	S H ✓ L ✓ DV CHK SYNC		
19 DV SELECTOR	GAIN ✓ CAL DV ✓		
20 FREQ. RANGE	DC ~ 100Hz ±1dB ✓		
21 NOISE	5 mVp-p (ATT 1/2 RATED GAIN)		
22 ATTENUATOR	ATT 1: 2.495v, ATT 1/2: 5.000 ATT 1/4: V		

22 CALIBRATION

CAL. (deg)	ATT.	OUTPUT (V)
20	1	5.000
10	1/2	5.000
	1/4	
	0	

24 LINEARITY — 1. AMPLIFIER PROPER; ② ASSORTED WITH TRANSDUCER; CONVERSION FACTOR

	INPUT ( )	ATT = 1 OUTPUT (V) ASC	DESC	INPUT ( )	ATT = 1/2 OUTPUT (V) ASC	DESC	INPUT ( )	ATT 1/4 OUTPUT (V)	INPUT ( )	ATT = OUTPUT (V)
	±40	5.000	-4.981	±20	5.000	-5.023				
	±32	4.020	-4.017	±16	4.010	-4.021				
±24	±16	3.030	-3.032	±12	3.013	-3.023				
±16	±8	2.024	-2.032	±8	2.013	-2.018				
±8	0	1.012	-1.021	±4	1.004	-1.002				
0		0.000	/	0	0.000	/				

25 NOTE: CALIBRATION: 20 deg (ATT=1)=40 deg of transducer, 10 deg (ATT=1/2)=20 deg of transducer

株式会社 誠研舎 — Test Approval

Figure 5.49 Calibration of the amplifier unit and potentiometer used for measuring the torsional angle (after SEIKEN, INC.)

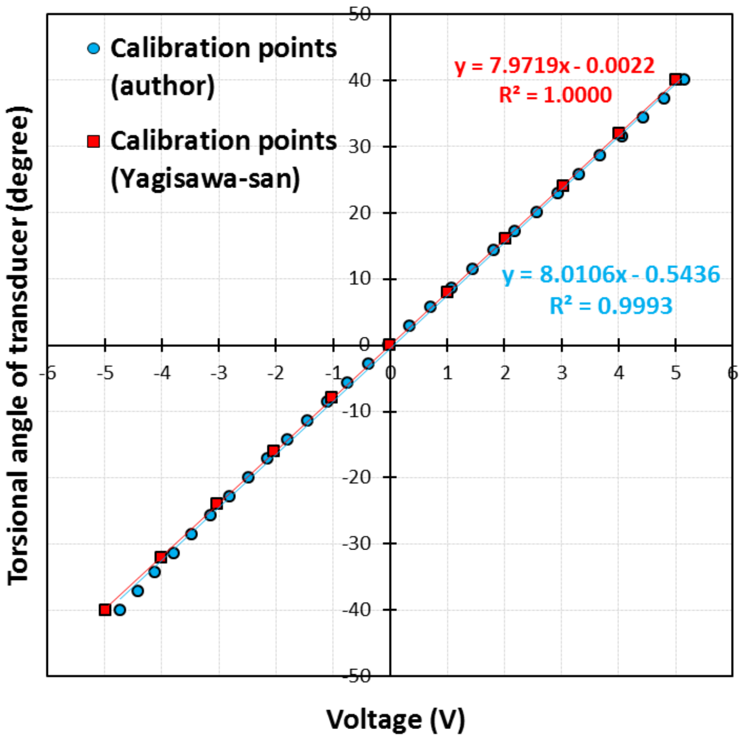

Figure 5.50 Calibration of the potentiometer used for measuring the torsional angle by the author and Yagisawa-san. Note that the torsional angle of the potentiometer's wheel is twice the torsional angle of the specimen's cap and that the sensitivity is set to the default value in the amplifier unit (ATT 1)

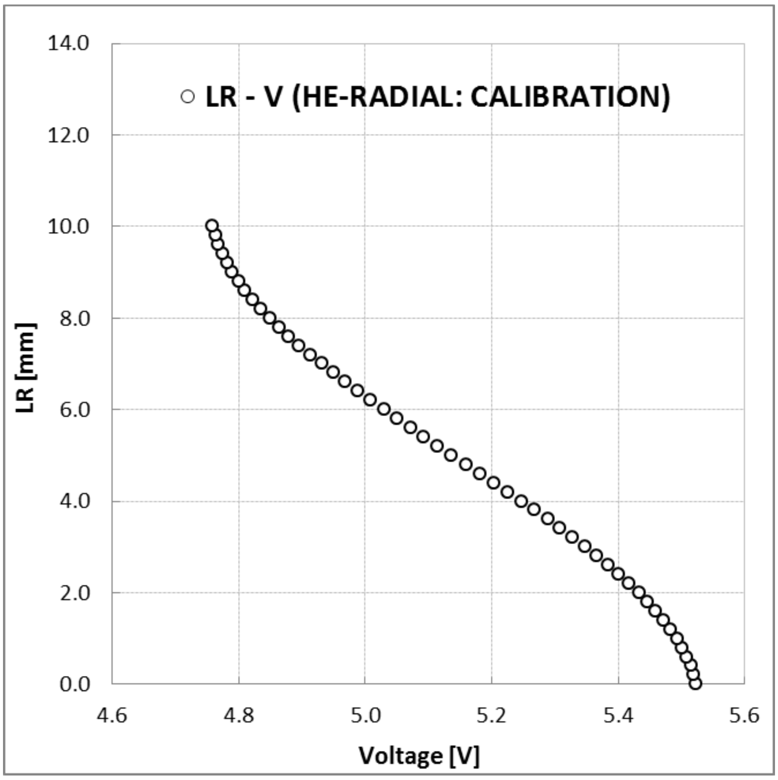

Figure 5.51 Calibration of the Hall Effect transducer used for measuring the radial displacement. The output voltage has a limited range presumably due to insufficient excitation

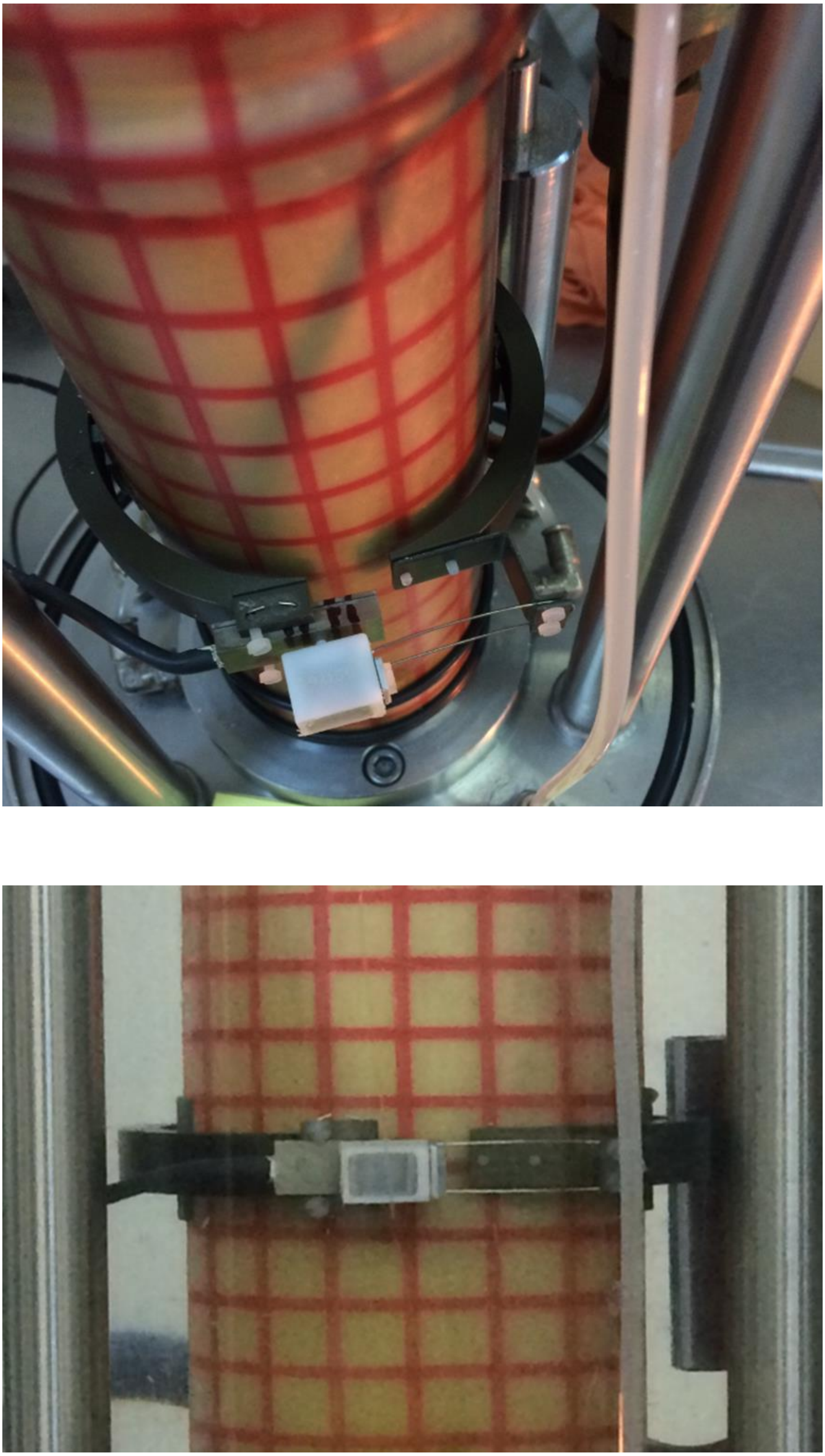

Figure 5.52 On sample set up of the Hall Effect transducer used for measuring the radial displacement

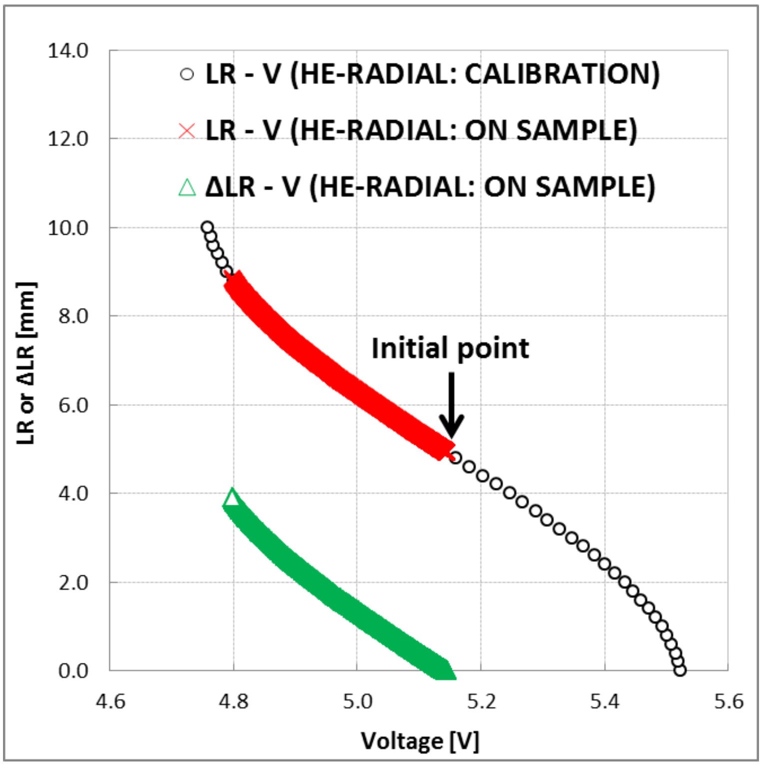

Figure 5.53 Measurement of the radial displacement at the outer boundary of the hollow cylindrical specimen using the Hall Effect transducer

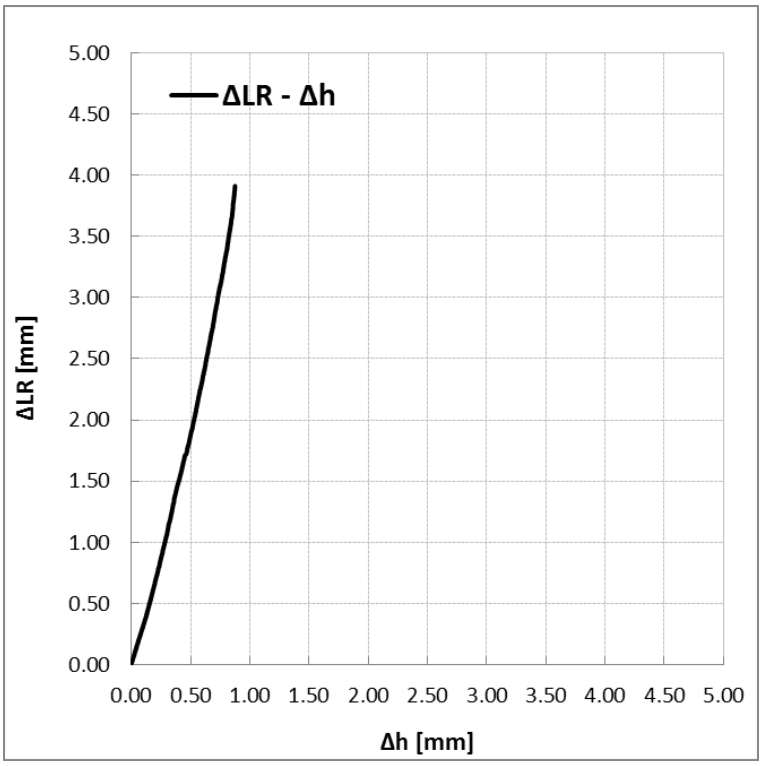

Figure 5.54 Displacement of the Hall Effect magnets against axial displacement of the specimen subjected to undrained loading

Figure 5.55 New pedestal and mould manufactured for preparing and testing squat HC specimens

Figure 5.56 New pedestal manufactured for preparing and testing HC stabilised-sand specimens

Figure 5.57 New moulds designed and manufactured for preparing triaxial stabilised-sand specimens

Figure 5.58 New specimen's cap designed and manufactured for achieving the connection between the cap and load cell needed for extension testing in the high-pressure triaxial apparatus

Figure 5.59 Modification of the spacer disk (access ring) placed in the conventional triaxial apparatus and installation of on-sample transducers (LVDTs) for measuring local axial strain. New metal parts were designed and manufactured to extend the stroke of the loading ram and impose boundary conditions that impede the occurrence of certain bifurcation modes

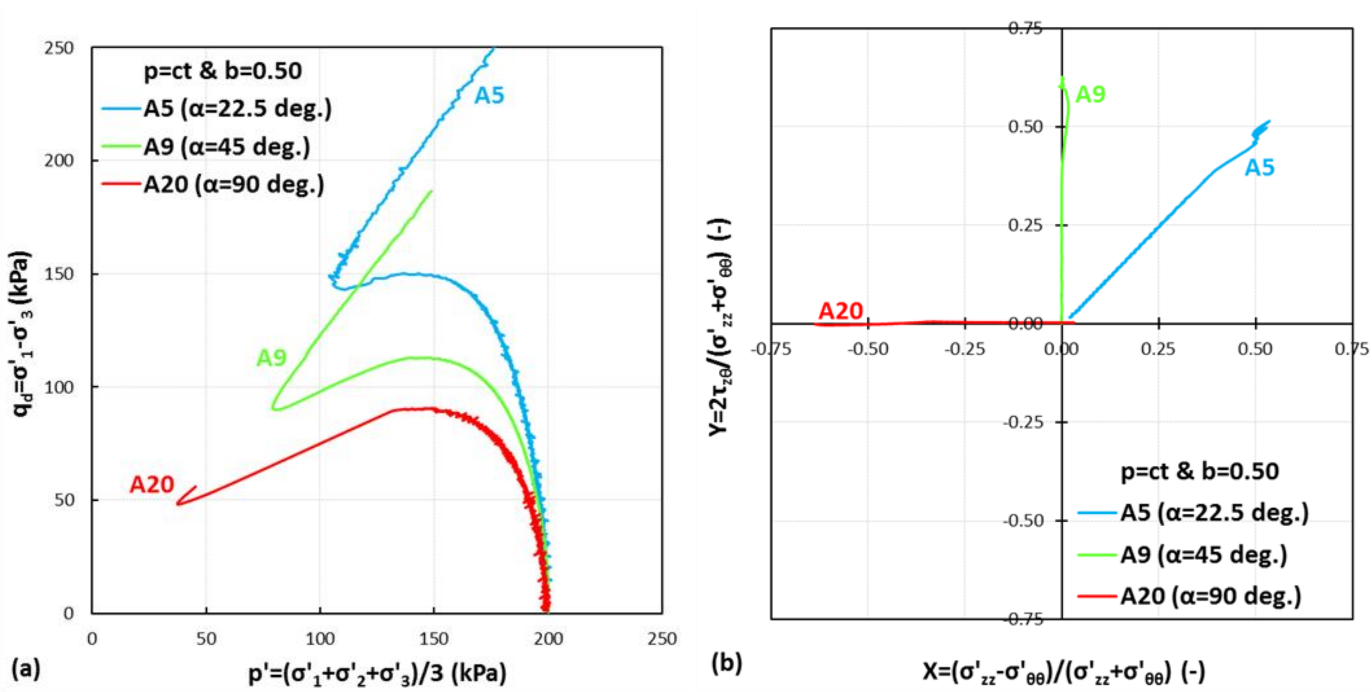

Figure 5.60 Undrained loading of sand at constant and independent α, b and p. **a** Effective stress path in the q_d - p' plane. **b** Stress path in the Y - X plane

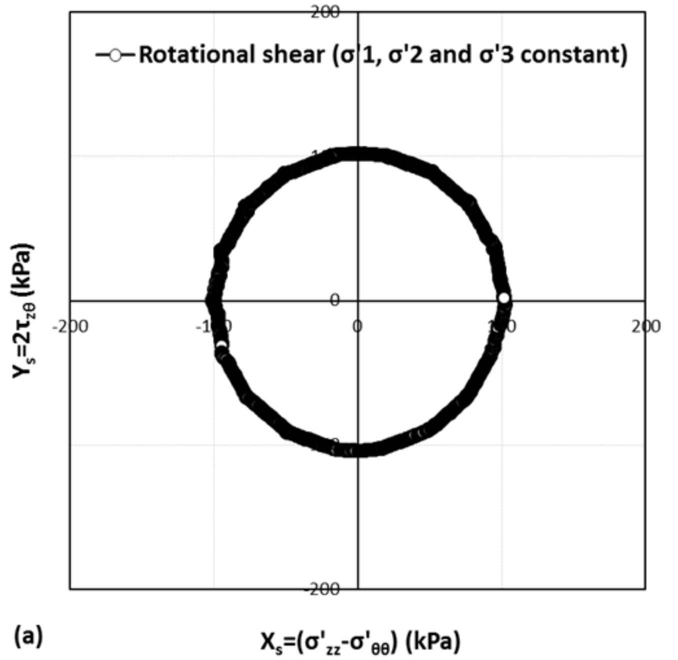

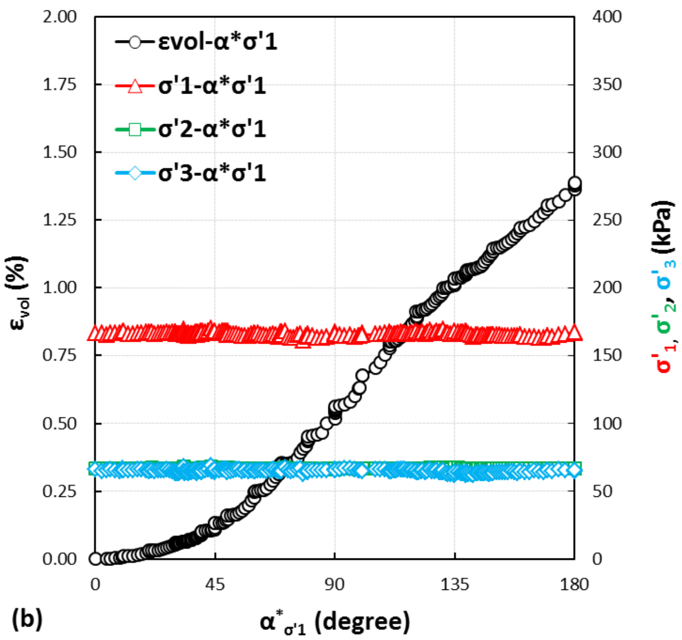

Figure 5.61 Rotation of the stress principal axes at constant effective stress principal values (rotational shear). **a** Stress path in the Y_s - X_s plane. **b** Effective stress principal values and volumetric strain against the principal stress direction angle

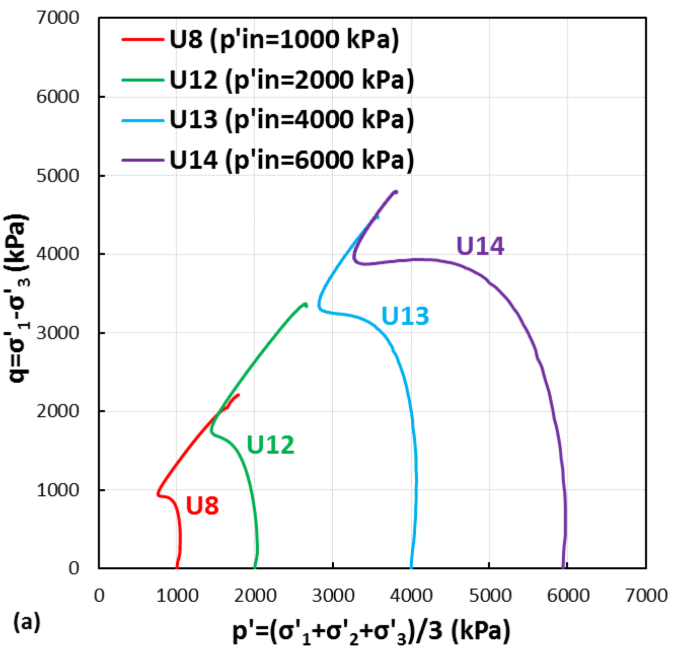

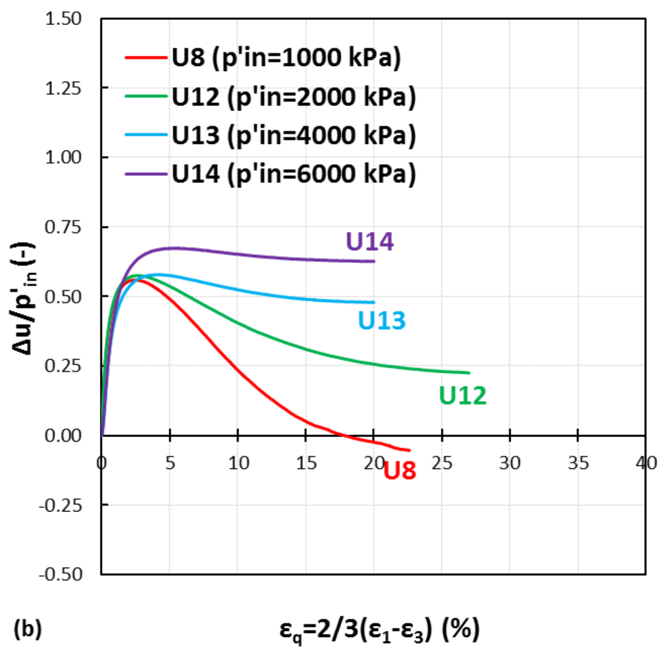

Figure 5.62 Triaxial compression tests at elevated mean effective stresses. **a** Stress paths in the q_d - p' plane. **b** Evolution of normalised excess pore-water pressure with shear strain

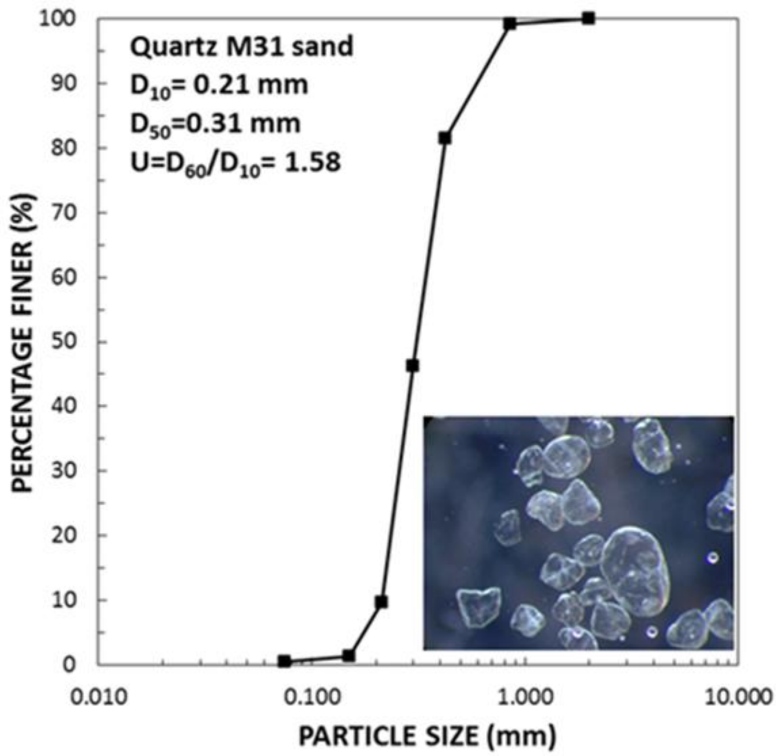

Figure 5.63 Grading curve of M31 Sand and microscope image of grains

CHAPTER 6: ANISOTROPIC CRITICAL STATE OF M31 SAND

6.1 INTRODUCTION

The behaviour of M31 Sand under drained and undrained triaxial compression is investigated at effective stresses ranging from 100 kPa to 6000 kPa. The sand is tested in the high-pressure triaxial apparatus (HPTA), the conventional triaxial apparatus (CTA) and the hollow cylinder apparatus (HCA), under strain- and stress-controlled loading conditions, using different instrumentation and applying a variety of boundary conditions and loading rates. The test results, which are consistent and repeatable before the occurrence of bifurcations, are interpreted within the framework of Critical State Soil Mechanics (CSSM). The critical state strength envelope in the q - p' plane and the critical state line (CSL) in the e - p' plane are determined for M31 Sand. The dependence of dilatancy and strength of M31 Sand on the state parameter ψ proposed by Been and Jefferies (1985) is investigated. Using the hollow-cylinder apparatus, an attempt is made to rotate the stress principal axes at critical state while keeping the effective stress principal values constant. Finally, the dilatancy and non-coaxiality of M31 Sand is investigated under both radial loading and rotational shearing in the hollow cylinder apparatus.

6.2 APPARATUSES, MATERIALS AND TESTING TECHNIQUES

Details concerning the tested materials, the specimen preparation method and the apparatuses (triaxial and hollow cylinder) used for the loading tests are given in Chapter 5 and in the articles by Triantafyllos et al. (2020a and b) presented in the Appendix. It is noted that the loading tests in the triaxial apparatuses (high pressure and conventional) were performed in a strain-controlled loading mode at a constant rate of axial displacement. On the other hand, the loading tests in the hollow cylinder apparatus (HCA) were performed in a stress-controlled loading mode at a constant rate of stress, using pneumatic pistons, flexible air-water interfaces and electric servo controllers to apply the pressures and loads. The control of stresses achieved in the HCA allows a variety of unstable bifurcations of deformation to occur, as described in the article by Triantafyllos et al. (2020a). Details concerning the experimental and theoretical investigation of bifurcations in geomaterials are given in the literature review presented in Sections 2.9 and 4.5, while a comprehensive treatise on this subject is given by Vardoulakis and Sulem (1995). The high-pressure triaxial apparatus was modified in order to perform tests at effective stresses as high as 6 MPa, while the conventional triaxial apparatus was modified to accommodate on-sample strain-measuring instrumentation (Linear Variable Differential Transformers, LVDTs). The hollow cylinder apparatus was upgraded in order to achieve the independent control of the three effective stress principal values and of the direction of the major and minor stress principal axes.

6.3 BEHAVIOUR OF M31 SAND UNDER DRAINED TRIAXIAL COMPRESSION

This section reports the results of drained triaxial compression tests on M31 Sand specimens.

6.3.1 THE EFFECT OF THE VOID RATIO ON THE DRAINED BEHAVIOUR OF M31 SAND

Figure 6.1 shows the results of the drained triaxial compression tests in the q - p' (a), q - ε_q (b), ε_{vol} - ε_q (c) and η - ε_q (d) planes. $q = [1 / 2 \{(\sigma'_1 - \sigma'_2)^2 + (\sigma'_2 - \sigma'_3)^2 + (\sigma'_3 - \sigma'_1)^2\}]^{1/2}$ is the deviatoric stress which degenerates to $q = \sigma'_1 - \sigma'_3$ under axisymmetric loading conditions, $\varepsilon_q = 2^{1/2} / 3\ [(\varepsilon_1 - \varepsilon_2)^2 + (\varepsilon_2 - \varepsilon_3)^2 + (\varepsilon_3 - \varepsilon_1)^2]^{1/2}$ is the deviatoric strain which degenerates to $\varepsilon_q = 2 / 3\ (\varepsilon_1 - \varepsilon_3)$ under axisymmetric conditions, $p' = (\sigma'_1 + \sigma'_2 + \sigma'_3) / 3$ is the mean effective stress, $\varepsilon_{vol} = \varepsilon_1 + \varepsilon_2 + \varepsilon_3$ is the volumetric strain, and $\eta = q / p'$ is the stress ratio. The symbols in Fig.6.1 used to distinguish each test from another also indicate the states at phase transformation (Ishihara et al. 1975), at peak failure and at the end of testing, in the order of appearance; peak failure occurs when the stress ratio η attains the maximum value in the course of shearing. The loading tests were performed on water-pluviated and saturated sand specimens, which had different initial void ratios, e_i, albeit being consolidated to the same effective stress, p'_{in} = 100 kPa (the subscript "in" stands for initial conditions, i.e. after consolidation and before shearing). Table 6.1 gives the details concerning the apparatus used in each test, the applied loading rate and boundary conditions (free or fixed top-platen tilting, solid or hollow cylindrical specimen), as well as the void ratio e of the specimens; the state parameter ψ proposed by Been and Jefferies (1985) is also reported for each specimen as computed after the determination of the critical state line (CSL) of M31 Sand.

Figure 6.1b shows the stress - strain behaviour of M31 Sand in the q - ε_q plane. The peak strength q_p (the subscript "p" stands for peak) increases with decreasing e_i, while the higher values of q_p are generally mobilised at lower values of ε_q; it is noted that the peak strength had not been mobilised at the moment that test D7 was aborted, thus, only two characteristics states are denoted on the corresponding curve. The secant elastoplastic modulus at a given ε_q in the pre-peak regime increases when the void ratio decreases. Past the peak state the deviatoric stress q decreases and a practically unique ultimate strength q_{ult} is mobilised at large deviatoric strains (ε_q > 30%). Specimens with similar initial void ratio exhibit similar stress - strain behaviour (e.g. the specimens in tests D2 and D3) indicating the repeatability of the test results.

Figure 6.1c shows the volume-change (dilatancy) behaviour of M31 Sand in the ε_{vol} - ε_q plane; contraction is positive according to the convention of Soil Mechanics. The sand initially shows contraction followed by dilation. The behaviour changes from contractive to dilative at the phase-transformation point (PTP), which is identified as the first point of zero-slope tangent of the ε_{vol} - ε_q curve. Phase transformation occurs generally at lower values of ε_q when the void ratio decreases. The volumetric strain at PTP is relatively small (ε_{vol} < 0.50%) and increases with void ratio. Past the PTP the slope of the ε_{vol} - ε_q curve becomes gradually steeper until the peak-failure state is reached, and becomes less steep beyond peak. These results indicate that the dilatancy ratio $D = d\varepsilon^p{}_{vol} / d\varepsilon^p{}_q$ (the superscript "p" stands for plastic) increases in magnitude (i.e. becomes more negative), attains a peak concurrently with the peak stress ratio at the failure state and subsequently decreases towards a nearly zero value at large ε_q. The peak value of D and the ultimate dilation (expressed by the accumulated volumetric strain at large ε_q) become more negative when the initial void ratio decreases. The volume-change behaviour of specimens D2 and D3, which have a similar void ratio, is identical indicating the repeatability of the test results.

Figure 6.1d shows the hardening behaviour of M31 Sand in the η - ε_q plane. The peak value of the stress ratio, η_p, is mobilised concurrently with the peak value of the deviatoric stress, q_p, and the two quantities evolve similarly in the course of shearing. The peak stress ratio is mobilised generally at a lower deviatoric strain and has a higher value when the void ratio decreases. A softening behaviour is observed post-peak in the sense that the stress ratio decreases and attains a practically unique value of around 1.25 at large ε_q. It is noted that a persistent softening is observed at large ε_q, even in the case that the dilatancy ratio has become almost zero (e.g. in test D5), possibly due to the inhomogeneous deformation of the sand specimen loaded by means of rough end platens.

Figure 6.2 shows the results of the drained triaxial compression tests in the q - p' (a), q - ε_q (b), ε_{vol} - ε_q (c) and η - ε_q (d) planes for sand specimens consolidated to a mean effective stress p'_{in} = 200 kPa. The stress - strain, dilatancy and hardening characteristics of the sand exhibit the same dependence on void ratio as the one described previously. It can be inferred that the response of different sand specimens is similar when the void ratio is similar (e.g. specimens D9, D10 and D11). However, the response of specimens D10 and D11 becomes unpredictable post-peak and diverges from a unique pattern like the one exhibited pre-peak. This is a typical case of bifurcation of the deformation mode that results in a non-unique response depending on the perturbations and imperfections in the system (specimen - apparatus) (Triantafyllos et al. 2020a).

Specimen D11, which was tested in the HCA, collapsed just after the peak state because the stress-controlled loading programme imposed a continuous increase in the deviatoric stress q while the material exhibited a softening behaviour. Consequently, the controllability of the loading programme was lost and a diffuse bifurcation occurred as the specimen suddenly bulged; Figure 6.3a shows the photo of the deformed specimen at the end of testing, taken under the effect of light refraction. On the other hand, specimen D10 was loaded in a displacement-controlled mode in the HPTA (which has a non-transparent triaxial cell) and the controllability of the loading programme was maintained post-peak. In this case, bifurcation occurred first in a diffuse barrelling and then in a localised mode (shear-banding) (Triantafyllos et al. 2020a and b) while the top platen tilted. Figure 6.3b shows the photo of the deformed specimen at an axial displacement that is 1.63 times higher than the one corresponding to the end point marked on the curves of test D10 in Fig. 6.2. It is noted that the bifurcations are detected by means of visual inspection as well as by interpretation of the test data. For example, a sudden decrease in q and η is observed in tests D10 and D11, while a perturbation of the shape of the volumetric strain curve is observed in test D11.

6.3.2 THE EFFECT OF THE MEAN EFFECTIVE STRESS ON THE DRAINED BEHAVIOUR OF M31 SAND

Figure 6.4 shows the results of the drained triaxial compression tests on sand specimens consolidated to different mean effective stresses p' ranging from 100 kPa to 1000 kPa; the results are plotted in the q - p' (a), q - ε_q (b), ε_{vol} - ε_q (c) and η - ε_q (d) planes. The stress - strain curves shown in Fig. 6.4b indicate that sand of a given void ratio mobilises a higher strength q at the peak and ultimate states when the initial mean effective stress increases. It is noted that specimens D1, D8 and D13 have initial void ratio in the range 0.710 - 0.717, while specimens D15, D16 and D17 have initial void ratio in the range 0.674 - 0.691. The peak failure occurs at higher deviatoric strain ε_q when the initial mean effective stress increases.

Figure 6.4c shows the volume-change behaviour of M31 Sand in the ε_{vol} - ε_q plane. It can be seen that the sand initially contracts and then dilates irrespective of the value of the initial mean effective stress in the range 100 - 1000 kPa. Phase transformation occurs generally at higher deviatoric strain ε_q when the initial mean effective stress increases, while the contractive volumetric strain at the PTP increases with p'. The peak dilatancy ratio, which is mobilised concurrently with the peak stress ratio, is lower in magnitude (less negative) when p' increases; the mobilisation of the peak D occurs at higher ε_q when p' increases. The rate of dilation at large ε_q is nearly zero when the initial mean effective stress is high (e.g. in test D17). The ultimate dilation becomes less negative as the initial mean effective stress increases, while it can be inferred that at very large effective stress (e.g. higher than 1000 kPa) the sand may undergo a net contraction for the given values of void ratio.

Figure 6.4d shows the hardening behaviour of M31 Sand in the η - ε_q plane. The evolution of stress ratio is more or less the same for all specimens but specimen D17, which was consolidated to the highest mean effective stress, p' = 1000 kPa. The mobilised stress ratio increases, attains a peak and then decreases towards a common value of around 1.25 at large deviatoric strains. The softening is less significant for p' = 1000 kPa. The comparison of the results shown in Figs 6.4c and d indicates that the hardening characteristics are less sensitive to variations in p' and e compared to the dilatancy characteristics.

6.4 BEHAVIOUR OF M31 SAND UNDER UNDRAINED TRIAXIAL COMPRESSION

This section reports the results of undrained triaxial compression tests on M31 Sand specimens.

6.4.1 THE EFFECT OF THE VOID RATIO ON THE UNDRAINED BEHAVIOUR OF M31 SAND

Figure 6.5 shows the results of the undrained triaxial compression tests in the q - p' (a), q - ε_q (b), Δu / p'_{in} - ε_q (c) and η - ε_q (d) planes; u is the pore-water pressure in excess of the value of the atmospheric pressure p_a, Δu is the excess pore-water pressure and Δu / p'_{in} is the excess pore-water pressure divided by the initial mean effective stress to yield the normalised excess pore-water pressure. Since the specimens are water-saturated, an increase in u indicates that plastic contraction occurs, accompanied by a concurrent elastic expansion of equal magnitude, while the overall volume remains constant because both the water and solid phases are practically incompressible. The specimens tested have different void ratios and are consolidated to a mean effective stress p'_{in} = 300 kPa.

Figure 6.5a shows the effective stress paths (ESPs) of the undrained tests in the q - p' plane; Figure 6.6a shows the initial part of the ESPs in detail. In the case of loose specimen U6, the mean effective stress initially decreases, due to the buildup of pore-water pressure, and thereafter increases, due to the decrease in the pore-water pressure (and increase in the major principal stress, σ'_1). The deviatoric stress initially increases and reaches a transient peak, whereupon it decreases to a minimum level and increases again. The decrease in q is due to the pore-water pressure buildup and occurs stably, before and after the transient peak state, in this displacement-controlled test. Phase transformation occurs at the “elbow” point of the ESP, at minimum p'. Past the PTP the effective stress path reaches the failure envelope, which is the line of maximum mobilised η, and the stress state moves along this line since the increase in p' mobilises a larger amount of q. The slope of the failure line decreases gently as the stress p' increases to 1000 kPa in test U6, while at higher stresses it decreases abruptly. This behaviour is possibly due to the usage of rough end platens. The deformation at moderate strains is of the diffuse-barrelling mode, however, concealed zones of localised strain may exist and become apparent after growing at larger strains, as realised in Fig. 6.7. The photo in Fig. 6.7 shows the deformed specimen at an axial displacement that is 1.13 times higher than the one corresponding to the end point marked on the curves of test U6 in Fig. 6.5, while the deformed shape might have changed during the unloading of the specimen and dismantling of the triaxial cell.

On the other hand, the ESP of test U5 on dense sand moves vertically in the initial phase of shearing as the deviatoric stress q increases under a constant value of p'; see Fig. 6.6a. Thereafter, the ESP curves gently as the mean effective stress increases past the PTP, and the effective stress state moves along the failure line which shows a steeper slope than the one corresponding to the loose specimen U6. The slope of the failure line does not exhibit an abrupt decrease because shearing was aborted at ε_q = 12% due to the drop of the absolute pore-water pressure below the level of atmospheric pressure. Figure 6.6b shows the evolution of pore-water pressure u during shearing in tests U4, U5 and U6. It can be seen that u falls below zero (i.e. it falls below the atmospheric pressure in absolute terms) in test U6 albeit the initial value of u being as high as 1675 kPa. Shearing under globally measured $u < 0$ may result in stationary stresses even before the water's theoretical cavitation limit of -97 kPa (at 25 ℃) is realised though this situation is not relevant to a true ultimate undrained state. The ESP of test U4 on medium-loose sand lies between the ESPs corresponding to loose (U6) and dense (U5) sand exhibiting a failure line with intermediate slope. Figure 6.6b shows that u drops below zero also in test U4 though this occurs at a higher value of ε_q than that in test U5.

Figure 6.5b shows the stress - strain curves of the undrained compression tests U4, U5 and U6 in the q - ε_q plane. In the case of loose specimen U6, stress unloading (strength drop) is exhibited past the transient-peak state as a result of pore-water pressure build up; it is noted that the stress ratio η increases while q decreases, thus, the material undergoes hardening during this phase of spontaneous stress unloading. A plateau of minimum undrained strength is observed in the vicinity of the PTP. Past the PTP, the sand regains strength as the mean effective stress increases. The deviatoric stress increases initially with an increasing rate and afterwards with a decreasing rate until the plateau of the ultimate undrained strength is reached, where q remains constant with further shearing.

The dense sand specimen U5 exhibits a very stiff behaviour with continuously increasing q, as shown in Fig. 6.5b. The deviatoric stress at the end of testing is much higher for the dense specimen U5 compared to the loose specimen U6; however, the true ultimate strength was not mobilised in test U5 due to the development of negative u. The stress - strain curve of the test on medium-loose specimen U4 lies between the two curves of tests U5 and U6; in test U4, q reaches a plateau at moderate strains (ε_q = 20%) which, however, is not relevant to the true ultimate undrained strength because the pore-water pressure u has become negative. It can be seen that failure occurs at a lower ε_q when the void ratio is lower.

Figure 6.5c shows the curves Δu / p'_{in} - ε_q of tests U4, U5 and U6; the increase in Δu / p'_{in} corresponds to plastic contraction, while the decrease in Δu / p'_{in} corresponds to plastic dilation. It can be seen that the sand initially contracts and then dilates irrespective of the void ratio. Phase transformation occurs at a lower ε_q and Δu / p'_{in} when e is lower. The slope of the Δu / p'_{in} - ε_q curve attains the most negative value in the course of shearing at peak failure, being more negative for specimens with lower e. The rate of dilation of loose specimen U6 becomes almost zero at large ε_q indicating that the ultimate undrained state has been practically reached. On the other hand, the dense specimen U5 dilates strongly at the end of testing. The Δu / p'_{in} - ε_q curve for the medium-loose specimen U4 exhibits a clear plateau at moderate strains (ε_q = 20%) as a result of the development of negative pore-water pressure u.

6.4.2 THE EFFECT OF THE MEAN EFFECTIVE STRESS ON THE UNDRAINED BEHAVIOUR OF M31 SAND

Figure 6.8 shows the results of two undrained triaxial compression tests on medium-loose sand specimens (with a relative density D_r = 40 - 42%) consolidated to mean effective stresses p' = 300 and 1000 kPa; the results are plotted in the q - p' (a), q - ε_q (b), Δu / p'_{in} - ε_q (c) and η - ε_q (d) planes. Figure 6.8a shows that the effective stress state of specimen U4, which was consolidated to a mean effective stress p' = 300 kPa, moves vertically in the q - p' plane at the initial phase of shearing until the phase-transformation point is reached where it turns gently towards higher mean effective stresses p'. Thereafter, the effective stress state moves along the failure line while the stresses p' and q increase as a result of the decreasing pore-water pressure and imposed total stress path.

On the other hand, Fig. 6.8a shows that the ESP in the q - p' plane of test U8, performed on a specimen consolidated to a mean effective stress p' = 1000 kPa, exhibits a more contractive trend in the initial phase of shearing as it turns towards lower stresses p' due to the pore-water pressure buildup. Nevertheless, past the PTP the effective stress state in test U8 moves along the same failure line as that in test U4, with the two ESPs diverging only at large p' possibly due to the occurrence of bifurcation. The effective stress states attained at the end of testing are very close for the two specimens though the potential increase in p' and q has not been realised in test U4 because the absolute pore-water pressure decreased below the level of atmospheric pressure and the tests was aborted.

Figure 6.8b shows that the stress - strain behaviour of specimen U8 is initially stiffer compared to specimen U4 in terms of tangent modulus though this trend is reversed in the vicinity of the PTP where specimen U8 exhibits a yielding plateau; Figure 6.9a shows the initial part of the stress - strain curves of the two tests in detail. However, it is noted that phase transformation occurs at a lower ε_q in test U4 compared to test U8 thus the tangent modulus decreases, before phase transformation, and increases, after phase transformation, accordingly. These results indicate that the mean effective stress influences both the frictional and dilatancy mechanisms of sand though in the opposite trend, i.e. the increase in p' results in the mobilisation of a higher deviatoric stress q yet it suppresses dilatancy. Figure 6.8b also shows that the stress - strain curves converge at higher strains and the peak and ultimate failure is realised at the same stress - strain states for the two specimens; however, the true ultimate undrained strength was not mobilised for specimen U4, as discussed previously.

Figure 6.8c shows that both specimens U4 and U8 tend initially to contract and then dilate since the normalised excess pore-water pressure, Δu / $p'_{in,}$ initially increases and then decreases. However, the increase in consolidation stress p'_{in} makes the sand more contractive since the value of Δu / p'_{in} at the PTP is higher while the absolute value of the slope of the Δu / p'_{in} - ε_q curve at peak is lower and the absolute value of Δu / p'_{in} at the end of testing is also lower for specimen U8, which was consolidated to a mean effective stress p' = 1000 kPa, compared to specimen U4, which was consolidated to p' = 300 kPa. Both specimens reach an ultimate state of continued shearing under constant ratio Δu / p'_{in} though this is a true ultimate undrained state only for the case of specimen U8.

Figure 6.8d shows the hardening behaviour of specimens U4 and U8 in the η - ε_q plane. It can be seen that the evolution of η with ε_q is more or less the same for the two specimens, with the tangent modulus (plastic modulus) being somewhat higher for specimen U4 compared to specimen U8 in the initial phase of shearing; this is illustrated in detail in Fig. 6.9b. The same stress ratio is mobilised at the same deviatoric strain for both specimens at peak and ultimate failure (ultimately, there is some difference in the values of η as the stress - strain curve in test U8 became perturbed); however, the two specimens mobilise a different stress ratio at phase transformation, while the deviatoric strain is also different.

Figure 6.10 shows the results of the undrained triaxial compression tests on medium-dense sand specimens (with a relative density D_r = 56 - 57%) consolidated to mean effective stresses p' = 325 and 6000 kPa; 6the results are plotted in the q - p' (a), q - ε_q (b), Δu / p'_{in} - ε_q (c) and η - ε_q (d) planes. The undrained behaviour of specimen U5, which was consolidated to a mean effective stress p' = 325 kPa, is more dilative than that of specimen U14, which was consolidated to p' = 6000 kPa, as indicated by the characteristics of the ESPs shown in Fig. 6.10a. The ESP U5 moves vertically during the initial phase of shearing and then along the failure line, without showing any decrease in q or p'. On the other hand, the ESP U14 shows a state of transient-peak strength followed by stress unloading as a result of the pore-water pressure buildup; strength begins to increase just before the PTP as the states of minimum q and minimum p' do not coincide in this test. The effective stress states reached at the end of testing are approximately the same for the two specimens though the increase in p' and q was halted in test U5 due to the development of negative pore-water pressure.

Figure 6.10b shows the stress - strain behaviour of the specimens U5 and U14, while Fig. 6.11a shows the initial part of the stress - strain curves in detail. The stress - strain behaviour of specimen U14 is initially stiffer compared to specimen U5 in terms of tangent modulus though this trend is reversed in the vicinity of the PTP where specimen U14 exhibits a yielding plateau. However, it is noted that phase transformation occurs at a lower ε_q in test U5 compared to test U14 thus the tangent modulus decreases, before phase transformation, and increases, after phase transformation, accordingly. The stress - strain curves appear to converge at around ε_q = 10% albeit showing extreme differences before that point; however, the ultimate undrained strength was not mobilised in test U5 due to the development of negative pore-water pressure.

Figure 6.10c shows the dilatancy behaviour of specimens U5 and U14 in terms of evolution of the normalised excess pore-water pressure. It can be seen that the undrained behaviour of medium-dense sand (D_r = 56 - 57%) turns from highly dilative at mean consolidation stress p' = 325 kPa to highly contractive (but not fully contractive) at stress p' = 6000 kPa. Phase transformation occurs at strain ε_q = 0.29%, with an excess pore-water pressure ratio of Δu / p'_{in} = 0.33, in test U5, and at strain ε_q = 4.63%, with an excess pore-water pressure ratio of Δu / p'_{in} = 0.67, in test U14. The slope of the Δu / p'_{in} - ε_q curve in test U5 has a very negative value at peak failure indicating a strong tendency for dilation. On the other hand, the slope of the Δu / p'_{in} - ε_q curve in test U14 has a slightly negative value at peak failure indicating a very weak tendency for dilation. Specimen U14 underwent a net plastic contraction, as indicated by the ultimate value of Δu / p'_{in} being equal to 0.63, albeit dilating for a while at large strains.

Figure 6.10d shows the hardening behaviour of the specimens U5 and U14 in the η - ε_q plane, while Fig. 6.11b shows the initial part of the η - ε_q curves in detail. Specimen U5 exhibits a brittle behaviour since the stress ratio attains a distinct peak at low deviatoric strain followed by significant softening. On the other hand, specimen U14 exhibits a ductile behaviour with only faint softening since the stress ratio increases up to the peak value at moderate strain and then decreases slightly towards the ultimate value; it is noted that the deviatoric stress decreases due to the pore-water pressure buildup while the stress ratio increases, i.e. the material hardens during this phase of spontaneous stress unloading. Had the pore-water pressure had the capacity to decrease further, specimen U5 would have mobilised ultimately the same stress ratio as the one mobilised by specimen U14. The stress ratio at peak is considerably higher for specimen U5 compared to specimen U14, while the stress ratio at phase transformation exhibits the opposite trend.

Figure 6.12 shows a photo of the deformed specimen U14 at an axial displacement that is 1.27 times higher than the one corresponding to the end point marked on the curves of test U14 in Fig. 6.10. The deformed shape is expected to have change slightly during unloading of the specimen and dismantling of the triaxial cell. The deformation of the specimen is of the diffuse-barrelling mode at moderate strains though concealed zones of localised strain may exist and become apparent after growing at larger strains, as realised in Fig. 6.12. It can be seen that the medium-dense specimen reached a state of continued shearing under constant stresses q and p'

and constant pore-water pressure u in a diffuse heterogeneous mode of deformation because a contractive response is induced and the development of shear zones is delayed under high-pressure loading. It is noted that the high-pressure triaxial apparatus was modified in order to perform tests at this level of effective stress.

Figure 6.13 shows the results of the undrained triaxial compression tests on loose sand specimens (with a relative density D_r = 30 - 35%) consolidated to mean effective stresses p' =200 and 300 kPa; the results are plotted in the q - p' (a), q - ε_q (b), Δu / p'_{in} - ε_q (c) and η - ε_q (d) planes. Specimen U3 was loaded in a stress-controlled mode in the HCA, while specimen U6 was loaded in a displacement-controlled mode in the HPTA. The results indicate that both specimens underwent stress unloading after the state of transient-peak strength as a result of pore-water pressure buildup. This behaviour, termed limited flow deformation since phase transformation occurs and strength is regained, is exhibited either stably or unstably, depending on the set of the chosen control parameters. For example, the loading programme is controllable during flow when the rate of axial displacement is imposed, while the controllability is lost when the rate of axial stress is imposed, resulting in a dynamic bifurcated response. The unstable behaviour of specimen U3 presented here cannot be described confidently by the data collected under low data-acquisition frequency in this test, for example the PTP was not recorded. The unstable flow deformation of M31 Sand is investigated extensively in Chapter 7 and in the article by Triantafyllos et al. (2020a).

6.5 RELIABILITY ANALYSIS OF THE TEST RESULTS

The analysis and evaluation of the experimental data presented indicate that the test results are consistent and repeatable. For example, drained triaxial loading of similar specimens in the same apparatus and under the same testing conditions (e.g. specimens D2 and D3 tested in the HPTA or specimens D6 and D7 tested in the HCA) results in a similar behaviour of sand in terms of stress - strain, dilatancy and hardening characteristics, as shown in Fig. 6.1. Moreover, drained triaxial loading of similar specimens under the same testing conditions but in different apparatuses (e.g. specimens D3 and D5 tested in the HPTA and CTA, respectively, or specimens D1 and D6 tested in the HPTA and HCA, respectively, or specimens D9 and D11 tested in the HPTA and HCA, respectively) results in a similar behaviour of sand in terms of stress - strain, dilatancy and hardening characteristics, as shown in Figs 6.1 and 6.2. The same suggestions can be made in the case of undrained triaxial loading. For example, the specimens U3 and U6 had similar void ratios and were loaded in the HCA and HPTA, respectively, at an initial mean effective stress of 200 and 300 kPa, respectively. The results shown in Fig. 6.13 in the q - p' (a), q - ε_q (b), Δu / p'_{in} - ε_q (c) and η - ε_q (d) planes appear to be in good agreement for both tests, if one takes into account the differences in the consolidation stress and primarily in the control parameters (i.e. load versus strain control).

The analysis and evaluation of the experimental data presented here also indicate that the behaviour of M31 Sand under both drained and undrained triaxial compression is similar to the behaviour of other sands and granular materials reported in literature (see Chapters 2, 3 and 4). For example, Fig. 6.1 shows that at a given consolidation stress p' the sand becomes more dilative in drained mode of loading as the void ratio decreases, exhibiting a higher strength, stress ratio and dilatancy ratio at peak failure and a practically unique strength and stress ratio at ultimate failure when the dilation ceases. Additionally, Fig. 6.4 shows that sand of a given void ratio becomes more dilative in drained mode of loading as the consolidation stress p' decreases, exhibiting a higher stress ratio and dilatancy ratio at peak failure and a higher ultimate dilation. However, the stress ratio mobilised ultimately is practically unique irrespective of the initial stress and void ratio.

Similarly, the undrained behaviour of M31 Sand in triaxial compression is reminiscent of the undrained behaviour of other sands and granular materials. For example, Fig. 6.5 shows that at a given consolidation stress p' the sand shows a stronger tendency for dilation in undrained mode of loading as the void ratio decreases, exhibiting a higher stress ratio and dilatancy ratio (expressed indirectly by the slope of the curve Δu / p'_{in}) at peak failure and a practically unique stress ratio at ultimate failure when the tendency for dilation ceases; however, the value of strength at peak and ultimate failure depends on the value of the current mean effective stress. Moreover, Fig. 6.10 shows that sand of a given relative density (e.g. D_r = 56 - 57%) may exhibit either a dilative or a contractive response depending on the value of mean effective stress. As the mean effective stress increases the stress ratio and dilatancy ratio decrease (the latter decreases in magnitude), while the ultimate stress ratio and strength appear to be practically unique.

Consequently, it can be suggested that the experimental results presented in this study are reliable and proper to be used in the constitutive modelling of the mechanical behaviour of M31 Sand. In the next section the critical state behaviour of M31 Sand is investigated and the critical state parameters are determined. These parameters can be used in the calibrating process of constitutive models within the framework of Critical State Soil Mechanics (CSSM).

6.6 CRITICAL STATE OF M31 SAND

The critical state characteristics of M31 Sand are investigated next. The state at the end of testing is characterised as a critical state only if certain conditions are met; Table 6.1 reports the tests in which a critical state has been attained. The first condition to be met is that the deformation of the specimen should be mainly of the diffuse-barrelling mode, as characterised at the end of testing by means of visual inspection, lacking any signs or exhibiting only faint signs of strain localisation in shear zones. Moreover, the sand should undergo continued shear deformation under (practically) constant stresses q and p', showing (practically) no tendency to change in volume. However, due to the usage of rough end platens the loading tests are occasionally terminated while the global measurements indicate the occurrence of softening and plastic dilation. In the case of undrained loading tests the pore-water pressure u at the end of testing should be non-negative (with zero u corresponding to atmospheric pressure). In the case of high-pressure loading the tests are terminated as soon as the aforementioned conditions are first attained, to avoid the continued grain crushing and alteration of the critical state characteristics. Under these conditions the states determined at the end of testing using the data obtained by global measurements can be considered representative of the true ultimate material states (critical states) for normalisation purposes albeit the deformation being inhomogeneous (Triantafyllos et al. 2020b).

Figure 6.14 shows the ultimate states in the q - p' plane for drained and undrained triaxial compression tests on sand specimens; the ultimate conditions discussed previously were attained in these tests. It can be seen that a unique straight line passing through the origin in the q - p' plane captures all the ultimate stress states, irrespective of the loading path (drained or undrained), initial mean effective stress, initial void ratio, ultimate mean effective stress and ultimate void ratio. The line has a slope of M = 1.24, corresponding to an angle of shearing resistance φ_c = 30.9°. The ultimate shearing resistance results from the frictional and constant-volume remoulding mechanisms. This behaviour is typical for sands at critical state.

Figure 6.15 shows the initial and ultimate states in the e - p' plane (the horizontal axis shows the values of p' in logarithmic scale) for drained and undrained triaxial compression tests on sand specimens; with the exception of test U5, the ultimate conditions discussed previously were attained in all other tests. The initial states are marked as small solid circles, the critical states are marked as large hollow circles and the state at the end of test U5 is marked as a large hollow square; it is noted that the test U5 was terminated before the mobilisation of the ultimate undrained strength due to the development of negative pore-water pressure u (see Fig. 6.10). The paths of the evolving states (p' , e) are also shown as dashed horizontal straight lines, in the case of undrained tests, or as dashed curved lines, in the case of drained tests. The meaning of the labels A1, A2, A3, B1, B2, C1 and C2 will be explained next.

Figure 6.15 shows that a unique curved line captures all the ultimate states in the e - p' plane, irrespective of the loading path (drained or undrained), initial mean effective stress, initial void ratio, ultimate mean effective stress and ultimate void ratio. This will be called the critical state line (CSL) of M31 Sand in the e - p' plane or simply the CSL, hereinafter; however, it is recognised that the 3D CSL actually exists in the three-dimensional p' - e' - q space and that Figs 6.14 and 6.15 show the projections of the 3-D CSL line on the q - p' and e - p' planes, respectively. The equation proposed by Li and Wang (1998) is used to describe the CSL:

$$e_c(p') = e_\Gamma - \lambda(p'/p_a)^\alpha \quad (6.1)$$

where $e_c(p')$ is the critical void ratio e_c at mean effective stress p', p_a is the atmospheric pressure at the level of sea (101 kPa), while e_Γ, λ and α are material constants with values given in Table 6.2. Equation 6.1 is used to calculate the state parameter $\psi = e - e_c(p')$, proposed by Been and Jefferies (1985), hereinafter.

Figure 6.15 shows some representative critical state characteristics of sands. For example, sand specimens subjected to drained triaxial compression at a given initial mean effective stress p'_i reach practically the same ultimate state (p' , e_c), irrespective of the initial void ratio e_i. This situation is indicated by the labels A1, A2 and A3 showing the ultimate states from drained tests at initial stresses 100 kPa, 200 kPa and 300 kPa, respectively. Moreover, sand specimens having similar void ratios e_i reach practically the same ultimate state (p' , e_c) under undrained triaxial compression, irrespective of the initial mean effective stress p'_i. This situation is indicated by the labels B1 and B2 showing the ultimate states for undrained tests on specimens with void ratios of around 0.660 and 0.630, respectively. As noted previously, the state (p' , e) at the end of test U5, marked as a hollow square in Fig. 6.15, is not an ultimate undrained state. Nevertheless, the results of test U5 are included in the figure and compared with the results of test U14 to highlight that these two specimens, which have similar void ratios e_i (of around 0.630), appear to reach approximately the same undrained critical state, within experimental error, albeit the consolidation stress in test U14 being 18.3 times higher than that in test U5. Finally, it is shown that different specimens which reach a critical state at the same stress p' develop a similar fabric in terms of void ratio e_c, irrespective of the loading history (drained or undrained) and irrespective of the initial values of mean effective stress p'_i and void ratio e_i; this situation is indicated by the labels C1 and C2.

Figure 6.16 shows the stress - dilatancy relationship (η - D) and the relationship between the evolving state parameter and dilatancy (ψ - D) for M31 Sand subjected to drained loading at various initial conditions; the values of η are plotted on the left vertical axis and the data (D , η) are indicated by black symbols, while the values of ψ are plotted on the right vertical axis and the data (D , ψ) are indicated by red symbols. It is noted that the total incremental strains are used to calculate the dilatancy ratio D at stress ratios η higher than 0.50 assuming that the elastic incremental strains are negligible compared to the plastic incremental strains (i.e. $D = d\varepsilon^p_{vol} / d\varepsilon^p_q \approx d\varepsilon_{vol} / d\varepsilon_q$). Specimen D1 is sheared at $p'_i = 100$ kPa, with $e_i = 0.715$ and $\psi_i = -0.042$ (Fig. 6.16a), specimen D16 is sheared at $p'_i = 700$ kPa, with $e_i = 0.676$ and $\psi_i = -0.049$ (Fig. 6.16b), specimen D2 is sheared at $p'_i = 100$ kPa, with $e_i = 0.671$ and $\psi_i = -0.086$ (Fig. 6.16c) and specimen D5 is sheared at $p'_i = 100$ kPa, with $e_i = 0.665$ and $\psi_i = -0.092$ (Fig. 6.16d).

Figures 6.16a and b show that the stress - dilatancy relationship is similar for the sand specimens D1 and D16 albeit having different initial void ratios and being consolidated to different mean effective stresses (Table 6.1) because the evolution of the state parameter is similar. Specifically, the initial value of ψ is around -0.040 for both specimens and changes only slightly up to the phase-transformation point that corresponds to the transient state of zero dilatancy (D = 0); for example, ψ at PT is equal to -0.042 for specimen D1 and to -0.039 for specimen D16. Past the PTP the state parameter becomes rapidly less negative and tends towards zero, ψ = 0, at the ultimate steady state of zero dilatancy, D = 0 (critical state). Failure of specimen D1 is realised at ψ = -0.029 with mobilised values of η = 1.31 and D = -0.107, while failure of specimen D16 is realised at ψ = -0.023 with mobilised values of η = 1.32 and D = -0.109; the maximum values of η and D (D attains a negative maximum) are mobilised concurrently at failure in each test. The stress - dilatancy relationship can be described by a practically unique straight line pre- and post-peak (peak here means peak failure) that intercepts the D = 0 axis at around $\eta = M$. A more careful analysis of the results shows that phase transformation occurs at η = 1.19 for both specimens, while critical states are attained at η = 1.21 and 1.18 for specimens D1 and D16, respectively. The low value of the ultimate stress ratio in test D16 is possibly due to the nonhomogeneous deformation of the sand specimen loaded by means of rough end platens.

Figures 6.16c and d show that the stress - dilatancy relationship and the evolution of the state parameter are similar for the sand specimens D2 and D5 indicating the repeatability of the results of tests on specimens consolidated to the same stress and at similar void ratios. However, the stress - dilatancy behaviour is different for specimens D2 and D5 compared to specimens D1 and D16 because the former are denser than the latter in terms of ψ. Specifically, the stress - dilatancy relationship for dense sand cannot be described by a unique line pre- and post-peak (peak here means peak failure) and the plot of η against D becomes hook-shaped. Specimen D2 undergoes phase transformation at η = 1.12, with ψ = -0.083, and failure at η = 1.40, with ψ = -0.062, while specimen D5 undergoes phase transformation at η = 1.12, with ψ = -0.091, and failure at η = 1.43, with ψ = -0.070; the dilatancy ratio D attains the negative maximum value at failure being equal to -0.240 and to -0.348 for specimens D2 and D5, respectively. Specimen D5 reached a critical state at η = 1.21, while specimen D2 did not reach a critical state because the test was aborted early. Figure 6.17 shows the η - D and ψ - D plots for tests on both loose (D1 and D16) and dense (D2 and D5) sand specimens to ease the comparison of the different behaviours. The yellow lines indicate the diversion from linearity of the stress - dilatancy relationship pre- and post-peak in the case of dense sand (specimen D5). This stress - dilatancy behaviour is verified by Discrete Element Method (DEM) analyses and other micromechanical studies, while it is attributed to state dependence (Wan et al. 2010, Zhou et al. 2017).

Figure 6.18 shows the stress ratio η (solid lines with reference to the left vertical axis) and state parameter ψ (dashed lines with reference to the right vertical axis) against the deviatoric strain ε_q for M31 Sand subjected to drained loading; three symbols are illustrated along each curve to indicate the phase-transformation, peak-failure and ultimate state in ascending order of strain. It can be inferred that the sand exhibits clearly a state-dependent behaviour. For example, specimens D1 and D16 exhibit similar hardening characteristics albeit having different initial void ratios and being consolidated to different mean effective stresses (Table 6.1) because the evolution of the state parameter is similar; moreover, Fig. 6.4c shows that the dilatancy characteristics are also similar for these two specimens. Phase transformation, indicated by the first symbol along each curve, occurs at higher η when ψ is less negative, while peak-failure occurs at lower η when ψ is less negative. Despite the differences in the values of η observed at low strains when the state parameter differs, all specimens exhibit ultimately a practically unique value of η as the state parameter tends towards zero at critical state.

Figure 6.19 shows the stress ratio η against the state parameter ψ at phase transformation from drained and undrained loading tests on M31 Sand; different sets of data points (ψ_{pt} , η_{pt}), along with the corresponding trend lines, are shown in Fig. 6.19a for drained or undrained loading tests, while one set of data points (ψ_{pt} , η_{pt}), along with the corresponding trend line, is shown in Fig. 6.19b for drained and undrained loading tests. It can be seen that, irrespective of the loading mode (drained or undrained), the stress ratio η_{pt} increases linearly with ψ_{pt} (ψ increases when it becomes less negative) and attains a value of around M when $\psi_{pt} = 0$; it is noted that the trend line in Fig. 6.19b was determined without fixing the intercept value at M and that the correlation shown corresponds to data collected from tests in three different apparatuses, using different instrumentation and applying a variety of boundary conditions and loading rates. The test results indicate that the stress ratio at phase transformation lacks intrinsic value, as suggested previously by Darve et al. (1995). Manzari and Dafalias (1997) and Li and Dafalias (2000) proposed a model that can simulate this state-dependent behaviour of sand at phase transformation.

Figure 6.20 shows the stress ratio η and dilatancy ratio D against the state parameter ψ at peak failure from drained and undrained loading tests on M31 Sand; the dilatancy ratio is plotted only for drained tests. Different sets of data points (ψ_p , η_p), along with the corresponding trend lines, are shown in Fig. 6.20a for drained or undrained loading tests, while one set of data points (ψ_p , η_p), along with the corresponding trend line, is shown in Fig. 6.20b for drained and undrained loading tests. It can be seen that the stress ratio η_p decreases linearly with ψ_p in both loading modes though its value is somewhat higher at a given ψ_p in drained than in undrained mode because the contribution of dilation to shearing resistance is higher than that of dilative constant-volume remoulding (Triantafyllos et al. 2020b). Nevertheless, the common trend line shown in Fig. 6.20b describes well both the drained and undrained behaviour of sand and intercepts spontaneously the $\psi_p = 0$ axis at around M. The dilatancy ratio D_p shows a trend to decrease linearly in magnitude with ψ_p (i.e. D_p becomes less negative when ψ_p becomes less negative) and the trend line intercepts spontaneously the $\psi_p = 0$ axis at around zero. These state-dependent peak characteristics of sand were modelled by Wood et al. (1994), Manzari and Dafalias (1997) and Li and Dafalias (2000) and have been also observed in DEM studies (Huang et al. 2014).

The test results presented confirm the state dependence of the dilatancy and strength of M31 Sand and indicate that the critical states can be used as reference states in order to normalise and describe the mechanical behaviour of sand. The determined critical state parameters of M31 Sand can be used in the calibrating process of constitutive models within the framework of Critical State Soil Mechanics (CSSM).

6.7 ROTATION OF THE STRESS PRINCIPAL AXES AT CRITICAL STATE OF M31 SAND

This section reports the results of the tests performed in accordance with the thought experiment described by Dafalias (2016).

6.7.1 STATEMENT OF THE PROBLEM

In this section an attempt is made, using the hollow cylinder apparatus (HCA), to rotate the stress principal axes (PA) at critical state of sand, while keeping the effective stress principal values (PV), σ'_1, σ'_2 and σ'_3, constant. In the light of the recently developed Anisotropic Critical State Theory (ACST) by Li and Dafalias (2012), Dafalias (2016) conceived this loading process as a though experiment to check whether the classical Critical State Theory (CST) by Roscoe et al. (1958) and Schofield and Wroth (1968) is complete or not, as discussed next.

According to the CST, the phenomenon during which a granular material keeps deforming in continuing shearing, under constant volume and stress, is termed the critical state (CS) and the analytical conditions stated to be necessary and sufficient for reaching and maintaining CS are given by:

$$\eta = q / p' = \eta_c = M \tag{6.2a}$$

$$e = e_c = e_c(p') \tag{6.2b}$$

where $\eta_c = M$ is the value of the deviatoric stress ratio at CS, which is a material constant, and $e_c = e_c(p')$ is the value of the void ratio at CS, which is a unique function of p'. It is noted that one of the premises of the CST is that the fabric of the granular material at CS is isotropic, supposedly due to the intense remoulding needed to reach such a state, thus no fabric-related quantities are included in Eqs 6.2. Contrarily, the results of recent studies indicate the existence of a strongly anisotropic fabric at critical state, coaxial in direction with the stress (Thornton 2000, Zhang and Thornton 2007, Li and Li 2009, Fu and Dafalias 2011).

Li and Dafalias (2012) introduced the Anisotropic Critical State Theory (ACST) which takes into account the role of the anisotropic fabric of granular materials at CS. Li and Dafalias (2012) stated that "an appropriate measure of fabric anisotropy" should reach its critical value, together with the stress ratio and void ratio, in order to reach and maintain critical state. They defined the Fabric Anisotropy Variable (FAV) A as (see Section 3.3):

$$A = \mathbf{F} : \mathbf{n} = F\, \mathbf{n_F} : \mathbf{n} = F\, N \tag{6.3}$$

where **F** is a deviatoric second-order fabric tensor associated with anisotropy, $\mathbf{n_F}$ is the unit-norm deviatoric tensor-valued direction of **F**, F is the norm of **F**, **n** is the unit-norm deviatoric tensor-valued loading direction, and $N = \mathbf{n_F} : \mathbf{n}$ is a scalar-valued measure of the relative orientation of **F** and **n**. In the course of shearing the fabric tensor evolves towards a critical value norm-wise and direction-wise, i.e. both F and N tend towards 1 thus A tends also towards 1; note that the norm F is normalised in such a way that it becomes $F_c = 1$ at CS. Consequently, the necessary and sufficient conditions for reaching and maintaining critical state, according to the ACST, are:

$$\eta = q / p' = \eta_c = M \tag{6.4a}$$

$$e = e_c = e_c(p') \tag{6.4b}$$

$$A = A_c = 1 \tag{6.4c}$$

Dafalias (2016) stated that if a sand is brought to a critical state by means of monotonic loading with fixed stress PA in regard to the specimen axes and afterwards the stress PA are rotated at constant effective stress PV then, according to the CST, the sand should not undergo plastic volumetric changes but should remain at CS instead, since the analytically expressed requirements of critical values for the stress and void ratio are not violated. If plastic volumetric changes indeed occur then the analytical conditions of CST are necessary but not sufficient for reaching and maintaining CS, unless tacitly assumed that the "fixity of stress and strain rate directions in regard to the sample is considered at CS". Theocharis et al. (2017 and 2019) realised this thought experiment by means of Discrete Element Method (DEM) simulations of this loading process and confirmed numerically the one of the two outcomes hypothesized by Dafalias (2016), namely that the granular material contracted immediately upon initiating the rotation of the stress PA at CS. The authors showed that the use of the fabric anisotropy variable A can explain the observed dilatancy patterns. An effort is made in this study to perform the thought experiment described by Dafalias (2016) in the hollow cylinder apparatus; the test results are presented next.

6.7.2 STRESSES AND STRAINS IN A HOLLOW CYLINDRICAL SPECIMEN SUBJECTED TO GENERALISED LOADING

In order to perform the stress PA rotation experiment described previously one has to control independently the three effective stress PV, σ'_1, σ'_2 and σ'_3, and the orientation of the major and minor stress PA with respect to the vertical; this was achieved by upgrading the hollow cylinder apparatus of the National Technical University of Athens, as described in detail in Chapter 5.

Figure 6.21 shows the boundary loads applied on the hollow cylindrical specimen (a), the stress components on the undeformed soil element (b) and the strain components associated with the combined multiaxial and torsional deformation (c). The equations used to calculate the average stresses σ_{zz}, $\sigma_{\theta\theta}$, σ_{rr}, $\tau_{z\theta}$, σ_1, σ_2, and σ_3 and the associated strains ε_{zz}, $\varepsilon_{\theta\theta}$, ε_{rr}, $\varepsilon_{z\theta}$, ε_1, ε_2, and ε_3 are presented in Chapter 5 and in the article by Triantafyllos et al. (2020a). The angle between the axis of the major principal stress σ'_1 and the vertical (z-axis) is termed the principal stress direction angle and is symbolised with α or $\alpha_{\sigma'1}$, while the angle of the axis of the rate (or increment) $d\sigma'_1$ to the vertical is symbolised with $\alpha_{d\sigma'1}$; it is noted that the direction of gravity is along the vertical and the bedding plane of the specimen is expected to be horizontal. The relationships $\tan 2\alpha_{\sigma'1} = 2\tau_{z\theta} / (\sigma'_{zz} - \sigma'_{\theta\theta})$ and $\tan 2\alpha_{d\sigma'1} = 2d\tau_{z\theta} / (d\sigma'_{zz} - d\sigma'_{\theta\theta})$ are used to compute analytically the angles $\alpha_{\sigma'1}$ and $\alpha_{d\sigma'1}$, respectively. Similarly, the direction angles of the major principal strain and strain rate, $\alpha_{\varepsilon 1}$ and $\alpha_{d\varepsilon 1}$, are computed analytically by the relationships $\tan 2\alpha_{\varepsilon 1} = 2\varepsilon_{z\theta} / (\varepsilon_{zz} - \varepsilon_{\theta\theta})$ and $\tan 2\alpha_{d\varepsilon 1} = 2d\varepsilon_{z\theta} / (d\varepsilon_{zz} - d\varepsilon_{\theta\theta})$, respectively. It is noted that given the stress-controlled conditions and the inelastic behaviour of sand the stress and strain increments are defined manually in each incremental step. The intermediate principal stress parameter is $b = (\sigma'_2 - \sigma'_3) / (\sigma'_1 - \sigma'_3)$. The deviatoric stress and strain under generalised loading conditions are given by the equations $q = 1 / 2^{1/2} [(\sigma'_1 - \sigma'_2)^2 + (\sigma'_2 - \sigma'_3)^2 + (\sigma'_3 - \sigma'_1)^2]^{1/2} = 1 / 2^{1/2} [\Sigma(\sigma'_i - \sigma'_j)^2]^{1/2}$ and $\varepsilon_q = 2^{1/2} / 3 [(\varepsilon_1 - \varepsilon_2)^2 + (\varepsilon_2 - \varepsilon_3)^2 + (\varepsilon_3 - \varepsilon_1)^2]^{1/2} = 2^{1/2} / 3 [\Sigma(\varepsilon_i - \varepsilon_j)^2]^{1/2}$, respectively.

Figure 6.22a shows the Y_s - X_s deviatoric stress plane, where the stress $Y_s = 2\tau_{z\theta}$ is associated with the torsional-shear mode of loading and the stress $X_s = \sigma'_{zz} - \sigma'_{\theta\theta}$ is associated with the triaxial mode of loading. The black solid line in the figure shows a part of the stress path corresponding to drained rotation of the stress PA axes while keeping the effective stress PV constant. Specifically, the σ'_1- and σ'_3-axis rotate around the horizontal σ'_2-axis while σ'_1, σ'_2 and σ'_3 are kept constant (Fig. 6.21b); the rotation is performed counterclockwise in the stress plane. The black radial vector that joins the origin of the Y_s - X_s plane to the current stress state makes an angle of $2\alpha_{\sigma'1}$ with the horizontal axis, indicating the current direction of the principal stress σ'_1, and has a length equal to the current stress difference $q_d = \sigma'_1 - \sigma'_3$.

Some characteristic directions of stress and rate of stress and strain are indicated with unit vectors in the Y_s - X_s plane in Fig. 6.22a. The green unit vector $\boldsymbol{\sigma}$ that has its origin at the stress state and points along the radial direction makes an angle of $2\alpha_{\sigma'1}$ with the horizontal axis, indicating the direction of the principal stress, σ'_1. Accordingly, the blue unit vector $d\boldsymbol{\sigma}$ that has its origin at the stress state and points along the tangential to the stress path direction makes an angle of $2\alpha_{d\sigma'1}$ with the horizontal axis, indicating the direction of the rate of principal stress, $d\sigma'_1$. In the same way the unit vector that points along the direction of the principal strain rate, $d\varepsilon_1$, is defined in the Y_ε - X_ε plane (not shown here), where $Y_\varepsilon = \varepsilon_{z\theta}$ and $X_\varepsilon = (\varepsilon_{zz} - \varepsilon_{\theta\theta}) / 2$, and is superimposed on the stress state in the Y_s - X_s plane; this is the red unit vector $d\boldsymbol{\varepsilon}$ shown in the figure that makes an angle of $2\alpha_{d\varepsilon 1}$ with the horizontal axis. The results of this study are also plotted in the Y - X plane shown in Fig. 6.22b, where $Y = 2\tau_{z\theta} / (\sigma'_{zz} + \sigma'_{\theta\theta})$ and $X = (\sigma'_{zz} - \sigma'_{\theta\theta}) / (\sigma'_{zz} + \sigma'_{\theta\theta})$ are the normalised "shear" stresses. The black radial vector that joins the origin of the Y - X plane to the current stress state makes an angle of $2\alpha_{\sigma'1}$ with the horizontal axis, indicating the current direction of the principal stress, σ'_1, and has a length equal to sin $\varphi = (\sigma'_1 - \sigma'_3) / (\sigma'_1 + \sigma'_3)$. However, the blue unit vector, d$\boldsymbol{s}$, which is tangential to the stress path at the current stress state, points along the current direction of the rate dσ'_1 only if the stress sum $(\sigma'_{zz} + \sigma'_{\theta\theta})$ is kept constant. The red unit vector d$\boldsymbol{\varepsilon}$ is superimposed on the stress state and makes an angle of $2\alpha_{d\varepsilon1}$ with the horizontal axis, indicating the direction of the rate of principal strain, dε_1.

The convention used for the value and sign of the principal stress direction angle $\alpha_{\sigma'1}$ is discussed next. $\alpha_{\sigma'1}$ is positive and changes from 0° to 45° when $X_s \geq 0$ and $Y_s \geq 0$, while this angle is negative and changes from 0° to -45° when $X_s \geq 0$ and $Y_s \leq 0$; both cases refer to compression-like loading and the only difference between them is the direction of the imposed shear stress $\tau_{z\theta}$. Accordingly, $\alpha_{\sigma'1}$ is positive and changes from 45° to 90° when $X_s \leq 0$ and $Y_s \geq 0$, while this angle is negative and changes from -90° to -45° when $X_s \leq 0$ and $Y_s \leq 0$; both cases refer to extension-like loading and the only difference between them is the direction of the imposed shear stress $\tau_{z\theta}$. Figure 6.23a shows the value of the principal stress direction angle $\alpha_{\sigma'1}$ at various stress states in the Y_s - X_s plane; the value and sign of the direction angle $\alpha_{d\sigma'1}$ follows the same convention using the dY_s - dX_s reference frame. The same convention is also used to describe the value and sign of the principal strain direction angle $\alpha_{\varepsilon1}$ at strain states in the Y_ε - X_ε plane, while the dX_ε and dY_ε axes are superimposed on a given stress state in the Y_s - X_s plane to offer the reference frame for determining the direction angle $\alpha_{d\varepsilon1}$ using again the same convention. Figure 6.23b shows the value of the principal stress direction angle $\alpha^*_{\sigma'1}$ at various stress states in the Y_s - X_s plane according to the alternative, and convenient for plotting diagrams, convention that $\alpha^*_{\sigma'1}$ increases continuously from 0° to 180° during a full cycle of rotation of the stress PA.

A radial stress path in the Y_s - X_s (or Y - X) plane corresponds to loading at fixed principal stress direction $\alpha_{\sigma'1}$. For example, the conventional triaxial compression test corresponds to loading with $X_s > 0$ and $Y_s \equiv 0$ ($\alpha_{\sigma'1} = 0°$), under the condition of $b = 0$, the conventional triaxial extension test corresponds to loading with $X_s < 0$ and $Y_s \equiv 0$ ($\alpha_{\sigma'1} = 90°$ or, identically, -90°), under the condition of $b = 1$, while the torsional shear test on isotropically consolidated specimen corresponds to loading with $Y_s > 0$ or <0 and $X_s \equiv 0$ ($\alpha_{\sigma'1}$ = +45° or -45°, respectively), under the condition of $b = 0.5$. It is noted that the plots of stress paths in the Y_s - X_s (or Y - X) deviatoric plane offer no information about the value of b. A circular stress path in the Y_s - X_s plane, with the centre of the circle located at the origin, corresponds to loading during which the axes of the principal stresses σ'_1 and σ'_3 are rotated in the vertical plane while the value of the stress difference $q_d = \sigma'_1 - \sigma'_3$ is kept constant. Thus, this type of stress path also corresponds to rotation of the stress PA while keeping the effective stress PV, σ'_1, σ'_2

and σ'_3, constant. A circular stress path in the Y - X plane, with the centre of the circle located at the origin, corresponds to stress PA rotation under a constant value of sin φ = (σ'_1 - σ'_3) / (σ'_1 + σ'_3). Thus, this type of stress path also corresponds to rotation of the stress PA while keeping the effective stress PV, σ'_1, σ'_2 and σ'_3, constant.

6.7.3 RESPONSE OF M31 SAND TO ROTATION OF THE STRESS PRINCIPAL AXES AT CONSTANT VALUES OF σ'1, σ'2 AND σ'3

In the experiment given the code name PAR1, a sand specimen, with the characteristics reported in Table 6.3, was first subjected to anisotropic consolidation by increasing the mean effective stress from p' = 40 kPa to 100 kPa along the stress path, in the q - p' plane, corresponding to constant $\eta = q / p' = 1.00$ and afterwards it was subjected to drained stress PA rotation while keeping the effective stress PV, σ'_1, σ'_2 and σ'_3, constant. One full cycle of stress PA rotation was performed at η = 1.00 and p' = 100 kPa, with b = 0.0, changing the direction of the σ'_1-axis from $\alpha^*_{\sigma'1} = 0^o$ to 90^o to 180^o.

Figure 6.24a shows the effective stress path (ESP) in the q - p' plane followed during anisotropic consolidation and stress principal axes rotation. A constant-p' vertical path is initially followed in the stress space at p' = 40 kPa from the isotropic state to the state that lies on the line with slope η = 1.00, and this line is followed subsequently as the p' and q increase under constant η until the state with p' = 100 kPa is reached. During the consolidation phase the stress parameter, b, is kept constant at 0 (i.e. $\sigma'_2 \equiv \sigma'_3$) and the stress direction angle, $\alpha^*_{\sigma'1}$, is kept fixed at 0^o (i.e. the σ'_1-axis is vertical). During the subsequent stress rotation phase the stresses p' and q are stationary thus the corresponding ESP is a point in the mathematical sense, though, some fluctuation in stresses actually occurs and a cluster of neighbouring points describes the ESP followed during stress rotation. Nevertheless, the changes in both stresses p' and q are rather small and cannot justify the behaviour discussed next, which is attributed to the rotation of the stress PA.

Figure 6.24b shows the volumetric strain, ε_{vol}, plotted against the mean effective stress, p', during the consolidation and stress PA rotation phases; ε_{vol} is set to zero at the beginning of the stress PA rotation phase in order to ease the comparison of the volume changes developed during the two phases. The increase in stress ratio, η, from 0 to 1.00 under a constant value of p', induced an overall contractive volumetric strain, ε_{vol}, of 0.07%. Interestingly, a slight dilation of around -0.02% was first observed and then contraction occurred while the stress ratio was increasing. The subsequent increase in p' and q under constant η resulted in a rise of ε_{vol} to 0.36%, while a further increase to 0.38% was observed during the creep period, lasting 35 minutes, at 100 kPa. On the other hand, one full cycle of rotation of the stress PA induced a much higher contraction, namely ε_{vol} = 1.39%, albeit keeping the magnitude of the effective principal stresses σ'_1, σ'_2 and σ'_3, and thus of p' and η, constant.

Figure 6.24c shows the evolution of the volumetric strain, ε_{vol}, and of the magnitude of the effective principal stresses, σ'_1, σ'_2 and σ'_3, as the stress direction angle, $\alpha^*_{\sigma'1}$, increases from 0° to 90° to 180° during a full cycle of rotation of the stress PA; the figure also shows the evolution of ε_{vol} during consolidation at $\alpha^*_{\sigma'1}$=0°. It can be seen that the magnitude of the three effective principal stresses is kept practically constant during the rotation of the stress PA yet the volumetric strain increases continuously. The slope of the ε_{vol} - $\alpha^*_{\sigma'1}$ curve initially increases, reaches its maximum value, indicated by the tangent dashed purple line, at around $\alpha^*_{\sigma'1}$ = 114° (corresponding to $\alpha_{\sigma'1}$ = -66°) and then decreases; it is noted that the rate $d\varepsilon_{vol}$ / $d\alpha^*_{\sigma'1}$ becomes maximum when the direction of the rate of principal strain is around $\alpha^*_{d\varepsilon1}$ = 135° (corresponding to $\alpha_{d\varepsilon1}$ = -45°) that is when the specimen deforms in quasi simple-shear mode ($d\varepsilon_{zz} = 0$, $d\varepsilon_{\theta\theta} = d\varepsilon_{rr} \rightarrow 0^+$, $d\varepsilon_{z\theta} \neq 0$), possibly because sliding occurs more easily along the horizontal bedding plane (Miura et al. 1986, Triantafyllos et al. 2020a). The value of ε_{vol} is around 0.50% at $\alpha^*_{\sigma'1}$ = 90° and increases to 1.39% at $\alpha^*_{\sigma'1}$ = 180°. These results indicate that the profound effect of stress PA rotation is to induce plastic contraction of sand even though the effective stress PV are kept constant. It should be noted that this type of plastic behaviour cannot be justified within the framework of classical Plasticity Theory because p', q and b are stationary. This situation is one of the cases of rotational shear as described by Wang et al. (1990).

Figure 6.25 shows the strain path in the Y_ε - X_ε deviatoric strain plane of test PAR1, during the phase of stress rotation. The anisotropic characteristics of sand's deformability are apparent since the positive maximum triaxial strain X_ε (compressive) is around 0.08% while the negative maximum triaxial strain X_ε (extensive) is around -1.06%, being developed well beyond the state with $\alpha_{\sigma'1}$ = 90° (see also Triantafyllos et al. 2020a). The torsional-shear strain Y_ε exhibits a positive maximum of around 0.93% and a negative maximum of around -1.14%. The strain trajectory has an open elliptical shape with the residual deformation at the end of the stress rotation cycle being of the torsional-shear mode. This may be the result of the predominant sliding occurring along the bedding plane, manifested macroscopically as a persistent and strong deformation along the directions $\alpha_{d\varepsilon1} = \pm45°$ (Miura et al. 1986, Triantafyllos et al. 2020a). It is noted that the deformation of the specimen remained homogeneous until the end of the stress rotation cycle, without showing any zones of strain localisation or barrelling.

Figure 6.26 shows the stress path in the Y_s - X_s deviatoric stress plane of the stress rotation phase in test PAR1. The unit vectors superimposed on the various stress states indicate the direction, $\alpha_{\sigma'1}$, of the principal stress (green vectors $\boldsymbol{\sigma}$), the direction, $\alpha_{d\sigma'1}$, of the rate of principal stress (blue vectors $d\boldsymbol{\sigma}$) and the direction, $\alpha_{d\varepsilon1}$, of the rate of principal strain (red vectors $d\boldsymbol{\varepsilon}$). It is noted that the rate of principal total strain is used here, without separating the plastic from the elastic part, and that the assumption of equal horizontal normal strains is made, i.e. $\varepsilon_{rr} \equiv \varepsilon_{\theta\theta}$ (Tatsuoka et al. 1986). As expected, the direction of vector $d\boldsymbol{\sigma}$ is normal to the direction of vector $\boldsymbol{\sigma}$, while the direction of vector d**ε** is intermediate between the directions of the two other vectors, indicating the non-coaxial behaviour of sand during the rotation of the stress PA.

Figure 6.26 shows that the angle $\alpha^*_{d\varepsilon 1}$ ($\alpha_{d\varepsilon 1}$) becomes equal to 45º (+45º) or 135º (-45º), indicating that the specimen deforms in quasi simple-shear mode, when $\alpha^*_{\sigma' 1}$ ($\alpha_{\sigma' 1}$) is equal to 33º (+33º) or 114º (-66º), respectively; the unit vectors d**ε** become then parallel to the vertical axis. The relationship between the direction angles of principal stress, stress rate and strain rate is also illustrated in Fig. 6.27 which shows the plot of $\alpha^*_{d\sigma' 1}$ and $\alpha^*_{d\varepsilon 1}$ against $\alpha^*_{\sigma' 1}$; the relationships depicted are periodical with a period of 180º and the horizontal axis plots the quantity $N \cdot 180 + \alpha^*_{\sigma' 1}$, where N is the number of the completed cycles of rotation of the stress PA, i.e. $N = 0$ during the first cycle in the case investigated here. Coaxiality of principal stress and principal strain rate occurs whenever a red circle point touches the dashed bisector line. The non-coaxiality angle $\alpha^*_{d\varepsilon 1} - \alpha^*_{\sigma' 1}$, which shows how much the direction of principal strain rate deviates from that of principal stress, is realised in Fig. 6.27 as the vertical distance of the red circle points from the dashed bisector line. It can be seen that the non-coaxiality angle does not remain constant during the first cycle of rotation of the stress PA. Instead it becomes minimum at around $\alpha^*_{\sigma' 1} = 45$º, when the specimen is subjected to torsional-shear stress, while it becomes maximum at around $\alpha^*_{\sigma' 1} = 114$º and $\alpha^*_{d\varepsilon 1} = 135$º, when the specimen deforms in quasi simple-shear mode, which means that the non-coaxiality angle becomes maximum concurrently with the rate $d\varepsilon_{vol} / d\alpha^*_{\sigma' 1}$ (see also Fig. 6.24c).

In the experiment given the code name PAR2, a sand specimen, with the characteristics reported in Table 6.3, was consolidated isotropically to a mean effective stress $p' = 200$ kPa and subjected to undrained loading along the principal stress direction $\alpha_{\sigma' 1} = 15$º, under $b = 0.5$ and constant p. The stress path in the Y_s - X_s plane is a straight line that goes through the origin and makes an angle of $2\alpha_{\sigma' 1} = 30$º with the horizontal axis, thus, this type of loading will be termed undrained (U) radial loading, hereinafter. However, if the sand is loose enough to undergo the so-called flow deformation then stability is lost (for the chosen set of control parameters in hollow-cylinder testing) and the bifurcated response becomes non-unique, meaning that the stress path follows an unpredictable route that may diverge from the radial direction. Since the loading programme dictates a proportional increase in the Y_s and X_s "shear" stress components while the strength of the specimen decreases during flow due to pore-water pressure buildup it is apparent that the controllability of the loading programme is lost when stability is lost (Triantafyllos et al. 2020a). Strength, stability and controllability are regained past the phase-transformation point (PTP) whereupon the sand is sheared to failure in a dilative mode. The aim is to stop the radial loading as close as possible to a critical state, switch to drained conditions without disturbing the effective stress state, and perform a drained rotation of the stress PA while keeping the magnitude of the three principal stresses, σ'_1, σ'_2 and σ'_3, constant.

Figure 6.28 shows the volume change behaviour of sand during isotropic consolidation and stress rotation in terms of evolution of the volumetric strain, ε_{vol}, a) with mean effective stress, p', and b) with stress direction angle, $\alpha_{\sigma'1}$. As can be seen in Fig. 6.28a, the isotropic consolidation to a mean effective stress p' = 200 kPa induced a volumetric strain of ε_{vol} = 0.58%; thereafter, the volumetric strain increased to ε_{vol} = 0.63% during a rest period lasting 70 minutes. Following the rest period the stress ratio, η, and the stress parameter, b, were increased from zero to 0.14 and 0.53, respectively, resulting in a minor increase in volumetric strain to ε_{vol} = 0.64%. Afterwards, the direction of the σ'_1-axis was rotated from $\alpha_{\sigma'1}$ = 0^o to $\alpha_{\sigma'1}$ = 14.5^o without inducing any further contraction due to the low value of the stress ratio (see Fig. 6.28b), and the sand was again left to rest for only 10 minutes because the volumetric strain was stationary at ε_{vol} = 0.64%.

The specimen was then subjected to undrained radial loading, exhibiting a contractive response that turned into dilative at the PTP. Drained conditions were imposed at a post-peak failure state at stress p' = 507 kPa and stress ratio η = 1.02, while the sand was still dilating, and the direction of the σ'_1-axis was rotated from $\alpha_{\sigma'1}$ = 14.3^o to $\alpha_{\sigma'1}$ = 29.3^o, keeping the magnitude of the three effective principal stresses, σ'_1, σ'_2 and σ'_3, constant. However, as can be seen in Fig. 6.28b, in the last phase of stress rotation the magnitude of the principal effective stress σ'_1 was increased while its direction was rotated from $\alpha_{\sigma'1}$ = 29.3^o to $\alpha_{\sigma'1}$ = 26.3^o. Figures 6.28a and b show that a contractive plastic volumetric strain of around ε_{vol} = 0.23% was induced by the rotation of the stress PA, under constant p' and q, from $\alpha_{\sigma'1}$ = 14.3^o to $\alpha_{\sigma'1}$ = 29.3^o. Contraction from ε_{vol} = 0.23% to 0.28% was also observed during the rotation of the stress PA from $\alpha_{\sigma'1}$ = 29.3^o to $\alpha_{\sigma'1}$ = 26.3^o though the stress ratio, η, increased from 1.00 τo 1.03 and the stress parameter, b, decreased from 0.53 to 0.46 during this phase. It is noted that the volumetric strain was reset to zero at the beginning of stress rotation to ease the comparison with the volumetric strain developed during consolidation and that Fig. 6.28 gives no information about the phase of undrained radial loading expect that it ended at p' = 507 kPa.

Figure 6.29 shows the results of the test PAR2 in terms of effective stress path in the q - p' plane (a), stress - strain curve in the q - ε_q plane (b) and evolution curves of stress ratio, η, normalised excess pore-water pressure, Δu / p'_{in}, and volumetric strain, ε_{vol}, with deviatoric strain ε_q (c). As shown in Fig. 6.29a, the specimen exhibits a strength drop after a transient-peak state, resulting in flow deformation, yet phase transformation occurs and the strength increases again. The effective stress state reaches and progresses along the failure line which shows a progressively decreasing slope. Afterwards, the loading conditions are switched from undrained to drained without disturbing the effective stress state and the stress principal axes are rotated while keeping the effective stress principal values constant. However, it can be seen that the stresses p' and q are not kept constant all along the stress rotation, as discussed previously. The characteristics of the stress - strain curve shown in Fig. 6.29b indicate the drop and regaining of strength, as well as the existence of two "kink" points, the first being related to the deceleration of the system as the specimen regains strength and the second being rather related to strain localisation. In the last phase of loading, q increases because σ'_1 increases, as discussed previously.

Figure 6.29c shows that the stress ratio, η, increases and attains the maximum value past the PTP, which is realised here as the point of maximum Δu / p'_{in}. Afterwards, η decreases, initially at a high rate and later at a low rate, showing a trend to stabilise at large strains. The excess pore-water pressure ratio initially increases, attains the maximum value at the PTP, and then decreases as the sand dilates towards peak failure and beyond; the rate of plastic dilation, as indicated by the slope of the Δu / p'_{in} - ε_q curve, decreases in magnitude at large strains. The conditions were switched to drained at around ε_q = 12.5%, without changing neither the effective stress state (p' = 507 kPa, η= 1.02, b = 0.55; $\alpha_{\sigma'1}$ = 14.3^{o}) nor the void ratio (e = 0.726), and rotation of the stress PA was initiated before a critical state is reached because the deformation of the specimen was becoming increasingly inhomogeneous. It is noted that the volumetric strain, ε_{vol}, remained constant (at zero value) during the undrained radial loading, while the excess pore-water ratio, Δu / p'_{in}, remained practically constant during the drained stress rotation. It can be seen that plastic contraction was induced at the instant at which the direction of the stress PA began to change (see also Fig. 6.28b) despite the fact that the sand was previously dilating plastically on the failure surface.

Figure 6.30 shows the stress path of test PAR2 in the X - Y deviatoric stress plane (a) and the corresponding strain path in the X_ε - Y_ε deviatoric strain plane (b). In the course of undrained loading the stress path diverges from the radial direction of $\alpha_{\sigma'1}$ = 15^{o} during the unstable flow deformation, moving towards the X-axis, i.e. the stress direction angle decreases spontaneously. Afterwards, the stress path moves back to stress states with $\alpha_{\sigma'1}$ = 15^{o} as the control of the loading programme is regained past the PTP. The stress path shows that the mobilised stress ratio, sin φ, indicated by the distance of the current state from the origin, increases during flow deformation and decreases past the peak-failure state. The radial loading is terminated in the softening regime, the conditions are switched to drained, and stress rotation is then performed, first along the counterclockwise direction and then along the clockwise direction. Concerning the strain path, it can be seen that it initially progresses along a more or less fixed radial direction but later it gently turns towards the X_ε-axis. Thereafter, the strain path turns suddenly along the direction of the Y_ε-axis as soon as the stress rotation is initiated.

Figure 6.31 shows the initial part of the stress path of test PAR2 in the X_s - Y_s deviatoric stress plane corresponding to the response up to the PTP, including the phase of flow deformation. The unit vectors $\boldsymbol{\sigma}$, d$\boldsymbol{\sigma}$ and d$\boldsymbol{\varepsilon}$ that indicate the direction of principal stress, stress rate and strain rate, respectively, are superimposed at three different stress states. Figure 6.31a shows the unit vectors $\boldsymbol{\sigma}$, d$\boldsymbol{\sigma}$ and d$\boldsymbol{\varepsilon}$ at a stress state just before the onset of flow deformation; it can be seen that the direction of the rate of principal stress coincides with that of principal stress ($\alpha_{d\sigma'1}$ = $\alpha_{\sigma'1}$ = 15^{o}) yet the direction of the rate of principal strain diverges from that of principal stress ($\alpha_{d\varepsilon 1}$ = 20^o), being biased towards the vertical axis, dY_ε. This pattern of non-coaxiality may be due to the depositional anisotropy of sand because sliding occurs more easily along the horizontal bedding plane (Miura et al. 1986, Triantafyllos et al. 2020a).

Flow instability in test PAR2 is triggered near the transient-peak state and is manifested as a fast accumulation of shear strain with a concurrent drop of strength induced by the sudden pore-water pressure buildup. Figure 6.31b shows the unit vectors **σ**, d**σ** and d**ε** at the transient-peak state indicating that the unstable bifurcated route followed post-peak corresponds to a predominant unloading of the torsional-shear stress $\tau_{z\theta}$, i.e. the stress direction angle, $\alpha_{\sigma'1}$, decreases during flow deformation. Triantafyllos et al. (2020a) suggested that this behaviour indicates a predisposition to torsional-shear stress unloading due to the horizontal bedding plane of sand. Figure 6.31c shows that in the course of flow deformation the vector indicating the direction of the rate of principal stress becomes nearly opposite to the vector indicating the direction of the rate of principal strain, while their common axis is parallel to the line defined by the radial stress path pre-peak.

In the experiment given the code name PAR3 the specimen was consolidated isotropically to a mean effective stress p' = 100 kPa and sheared undrained along the principal stress direction $\alpha_{\sigma'1}$ = 15^o, under b = 0.5 and constant p. The radial loading was terminated while the specimen was still dilating on the failure surface, the conditions were switched to drained without changing the stress state or the void ratio, and rotation of the stress PA was performed while keeping the magnitude of the three effective principal stresses, σ'_1, σ'_2 and σ'_3, constant. The experiments PAR3 and PAR2 are similar yet the consolidation stress is lower and the specimen void ratio is higher in the former test (Table 6.3). Moreover, the specimen in test PAR3 was in good shape concerning the deformation non-homogeneity at the time stress PA rotation was initiated and the magnitude of the effective principal stresses, σ'_1, σ'_2 and σ'_3, was kept practically constant all along the stress rotation.

Figure 6.32 shows the volume change behaviour of sand during isotropic consolidation and stress rotation in terms of evolution of the volumetric strain, ε_{vol}, a) with mean effective stress, p', and b) with stress direction angle, $\alpha_{\sigma'1}$. Figure 6.32a shows that consolidating the sand specimen to a mean effective stress p' = 100 kPa induced a volumetric strain of ε_{vol} = 0.26% that only increased to ε_{vol} = 0.27% after a 35 minute rest period. Afterwards, the stress ratio, η, and the intermediate principal stress parameter, b, were increased from zero to 0.14 and 0.50, respectively, and the direction of the σ'_1-axis was rotated to $\alpha_{\sigma'1}$ = 15^o resulting in an indiscernible volume change, while a 60 minute rest period resulted in a minor increase in volumetric strain to ε_{vol} = 0.28%. On the other hand, Figs 6.32a and b show that the rotation of the stress PA at constant mean effective stress p' = 343.2 kPa and stress ratio η = 1.05 from $\alpha_{\sigma'1}$ = 15.0^o to $\alpha_{\sigma'1}$ = 42.3^o induced a contractive volumetric strain of ε_{vol} = 0.61%, i.e. more than two times higher than that induced during isotropic consolidation.

Figure 6.33 shows the results of test PAR3 in terms of effective stress path in the q - p' plane (a), stress - strain curve in the q - ε_q plane (b) and evolution curves of stress ratio, η, normalised excess pore-water pressure, Δu / p'_{in}, and volumetric strain, ε_{vol}, with deviatoric strain ε_q (c). The effective stress path shown in Fig. 6.33a and the stress - strain curve shown in Fig. 6.33b indicate a stable contractive response during the undrained radial loading that turned into dilative at the PTP. Thereafter, the sand specimen failed in a dilative mode and the stresses q and p' kept increasing as a result of the decreasing, due to plastic dilation, pore-water pressure and imposed total stress path. Figure 6.33c shows that the stress ratio, η, increased during the undrained radial loading, attained the maximum value at peak failure, and then decreased during the phase of plastic dilation and strain softening. The excess pore-water pressure ratio, Δu / p'_{in}, increased during the undrained contractive response, attained the maximum value at the PTP, and then decreased during the phase of plastic dilation. The conditions were switched to drained at around ε_q = 7.6%, without changing the effective stress state (p' = 343.2 kPa, η = 1.05, b = 0.52; $\alpha_{\sigma'1}$ = 15.0^o) or the void ratio (e = 0.744), and rotation of the stress PA was initiated before a critical state is reached, while the specimen was in good shape concerning the deformation non-homogeneity. Sand immediately contracted plastically when the direction of the stress PA changed albeit being previously dilating on the failure surface. Interestingly, the ratio dε_{vol} / dε_q attained a constant value of 0.47 all along the stress rotation, changing only in the latest phase.

Figure 6.34a shows the stress path of test PAR3 in the Y_s - X_s deviatoric stress plane, while Fig. 6.34b shows the corresponding strain path in the Y_ε - X_ε deviatoric strain plane. The stress path remained radial in the course of undrained loading, indicating that stability was sustained in this test, while it became circular during the drained stress rotation. The circular stress path progressed counterclockwise since the σ'_1-axis was rotated from $\alpha_{\sigma'1}$ = 15.0^o to $\alpha_{\sigma'1}$ = 42.3^o. The strain path progressed initially along a more or less fixed radial direction but later it gently turned towards the X_ε-axis. Thereafter, the strain path turned suddenly along the direction of the Y_ε-axis as soon as the stress rotation was initiated and curved counterclockwise as the stress rotation continued.

Figure 6.35 shows the stress path of test PAR3 in the Y_s - X_s deviatoric stress plane along with the unit vectors indicating the direction of principal stress, rate of principal stress and rate of principal (total) strain superimposed on various stress states. M31 Sand exhibits non-coaxial behaviour under undrained radial loading since the direction of the rate of principal strain diverges from that of principal stress, being biased towards the vertical axis, dY_ε, though, as the mobilised stress ratio increases and sand is sheared well-beyond the peak-failure state the two directions become coincident. It is noted that peak failure occurs at strain ε_q = 3.5% and stress ratio η = 1.15, while the direction of the rate of principal strain at ε_q = 1.0% and η = 1.08 is $\alpha_{d\varepsilon 1}$ = 23.0^o and progressively evolves to $\alpha_{d\varepsilon 1}$ = 19.7^o, at ε_q = 4.4% and η = 1.14, and to $\alpha_{d\varepsilon 1}$ = 15.6^o, at ε_q = 6.1% and η = 1.09. Strong non-coaxiality is exhibited at the instant at which the stress PA are rotated away from the orientation of $\alpha_{\sigma'1} = 15^o$ since the direction of the rate of principal strain changes from $\alpha_{d\varepsilon 1} = 15^o$ to $\alpha_{d\varepsilon 1} \approx 40^o$. Thereafter, the behaviour of sand remains strongly non-coaxial in the course of stress PA rotation from $\alpha_{\sigma'1} = 15.0^o$ to $\alpha_{\sigma'1} = 42.3^o$ since the direction of the rate of principal strain is always intermediate between the directions of the rate of principal stress and of principal stress, lagging behind the former.

Figure 6.36 shows the relationship between the direction angles of principal stress, rate of principal stress and rate of principal strain observed in test PAR3. The black arrows indicate the movement of data points in the course of undrained radial loading (vertical arrow) and drained stress rotation (inclined arrows); coaxiality of principal stress and principal strain rate occurs whenever a red point, circle or square, touches the dashed bisector line. It can be seen that, during the undrained radial loading, the axis of principal strain rate changes its orientation from $\alpha_{d\varepsilon 1} = 23.0^o$ to $\alpha_{d\varepsilon 1} = 15.0^o$, thus, becoming collinear with the axis of principal stress and of principal stress rate. It may be suggested that this is the macroscopic manifestation of the evolution of fabric that is rearranged in order to become more anisotropic and align, in terms of principal directions of the tensor describing its characteristics, with the principal directions of the stress tensor. However, at the instant at which the direction of loading changes, because stress rotation is initiated, the coaxiality of strain rate and stress ceases as can be seen from the jump in the value of $\alpha_{d\varepsilon 1}$ from 15.0^o to around 40^o; as discussed previously, at this very instant the plastic dilation turns into plastic contraction. In the course of stress rotation the direction of the principal strain rate remains intermediate between the directions of the principal stress rate and principal stress, lagging behind the former.

6.7.4 EVALUATION OF THE RESULTS OF TESTS IMPOSING ROTATION OF THE STRESS PRINCIPAL AXES AT CONSTANT VALUES OF σ'_1, σ'_2 AND σ'_3

It has been shown that sand undergoes considerable plastic contraction when the stress principal axes are rotated while the effective stress principal values, σ'_1, σ'_2 and σ'_3, are kept constant. This behaviour is exhibited irrespective of whether the sand is previously contracting, during anisotropic consolidation, or dilating at post-peak failure states, during undrained radial loading, while the aim was to perform rotation of the stress PA at critical state. However, it is almost impossible to reach a critical state in the hollow cylinder apparatus without triggering instabilities, such as diffuse bulging, barrelling and shear banding, and thus violating the homogeneity of deformation. Testing of very loose specimens, e.g. those prepared by moist tamping, is a means to delay strain localisation though the collapse associated with undrained loading of such specimens (see Desrues and Georgopoulos 2006) render the performance of stress PA rotation at critical state impossible, while the same holds true in the case of drained loading under control of stress because the condition of constant stress cannot be sustained without excessive straining that brings the loading systems to their limits, even before the stress PA rotation is initiated.

Figure 6.3a shows the bulged deformation of a loose specimen subjected to drained triaxial compression in the HCA. Stability was lost in the vicinity of the peak-failure state and the specimen suddenly collapsed rendering any further loading impossible. Figure 6.37 shows a squat loose specimen, with a height to outer diameter ratio of 1:1, which bulged under drained triaxial compression in the HCA. A new pedestal was designed and manufactured in the machinery shop in order to achieve larger strains in hollow-cylinder testing and bring the sand as close as possible to critical state. Nevertheless, instability occurred in the vicinity of the peak-failure state thus this attempt also failed. It is noted that the instability occurring at peak state in drained triaxial compression is physically justified for the set of control parameters corresponding to hollow-cylinder testing since the loading programme dictates an increase in stress q while the sand undergoes strain softening (or, ideally, steady plastic flow under constant deviatoric stress, q); the attempt to control the axial strain also resulted in instabilities due to the usage of pneumatic loading pistons. Moreover, the instability is theoretically predicted by the Bifurcation Theory, which states that the second-order work must necessarily vanish to trigger instability, since at states near peak failure the direction of stress unloading is included inside the instability cone, determined by the incrementally non-linear model of Darve, as discussed in Chapter 4.

A solution to overcome this problem was proposed by professor Papadimitriou who suggested to load the sand specimens first in undrained triaxial compression and then switch the conditions to drained as close as possible to critical state and perform stress PA rotation at constant effective stress PV. In the case that sand is loose and exhibits limited flow deformation (arrested at phase transformation) stability is regained past the phase-transformation point because strength is regained. This is theoretically predicted by the Bifurcation Theory since the effective stress path progresses past the PTP along incremental stress directions that are not included inside the instability cones, as far as the deformation remains non-localised (see Chapter 4). Triantafyllos et al. (2020a) showed that in the course of undrained radial loading in the HCA the second-order work becomes non-positive past the transient-peak state (i.e. the state at which q, but not η, becomes temporarily maximum) though it again becomes positive past the PTP. Thus, it was decided to perform undrained radial loading tests in order to reach as close as possible to critical state before the stress PA are rotated under drained conditions while keeping the effective stress PV constant. The direction of the σ'_1-axis was kept fixed at an orientation nearly normal to the bedding plane (i.e. at $\alpha_{\sigma'1}$ = 15.0°) to ensure the shortest route to a critical state though the stress parameter b was kept constant at 0.5.

The undrained radial loading in test PAR2 was terminated while the sand was still dilating on the failure surface (in a coaxial deformation mode) and the stress PA were rotated under drained conditions while keeping the effective stress PV constant. The sand contracted plastically (and showed strong non-coaxiality) from the very beginning of stress rotation. At the time when the stress rotation was initiated the specimen had been deformed in a barrelling mode and zones of strain localisation had been formed, as can be seen in the photos of the specimen presented in Fig. 6.38. In test PAR3 the sand specimen was still dilating in a coaxial deformation mode when the stress PA rotation was initiated. The sand contracted plastically and showed strong non-coaxiality from the very beginning of stress rotation, while the specimen was in good shape concerning the deformation non-homogeneity, as can be seen the photos of the specimen presented in Fig. 6.39.

A critical state was not attained in either test (PAR2 or PAR3) though by assuming a unique CSL in the e - p' plane irrespective of the loading mode (Salvatore et al. 2017) and considering the effects of the loading mode on the critical stress ratio (Papadimitriou et al. 2019) it appears that the sand was close to critical state when the stress rotation was initiated. Figure 6.40a shows the evolution of the stress ratio, η, in tests PAR2 and PAR3, while Figure 6.40b shows the evolution of the state (p' , e) in relation to the critical state line of M31 Sand determined under triaxial compression loading. More results and a detailed analysis are presented in the unpublished article by the author under the title "Novel findings on the dilatancy and non-coaxiality of sand under generalised loading", presented in the Appendix.

6.8 CONCLUSIONS

The behaviour of M31 Sand under drained and undrained triaxial compression was investigated at effective stresses ranging from 100 kPa to 6000 kPa. The test results obtained using two triaxial apparatuses and the hollow-cylinder apparatus are consistent and repeatable before the occurrence of bifurcations, being in good agreement with the results of similar tests reported in the literature. The critical state characteristics of M31 Sand were investigated; a unique critical stress ratio $\eta = q / p' = \eta_c = M$ and a unique critical state line (CSL) in the e - p' plane were found. By referring to the CSL the state parameter ψ proposed by Been and Jefferies (1985) was determined and its evolution throughout loading was monitored. A state-dependent behaviour was confirmed for M31 Sand since the dilatancy and strength parameters at phase transformation and peak failure can be normalised with respect to ψ.

An attempt was made to reach a critical state under undrained radial loading in the hollow-cylinder apparatus and then switch the conditions to drained and rotate the stress principal axes while keeping the effective stress principal values, σ'_1, σ'_2 and σ'_3, constant. It was found that the behaviour of sand under undrained radial loading is non-coaxial since the direction of the rate of principal strain diverges from the direction of principal stress. However, in the course of loading the direction of the rate of principal strain approaches progressively the direction of principal stress until the two directions become coincident at large strains past the peak-failure state. The radial loading was terminated while the sand was still dilating on the failure surface, in a coaxial deformation mode, and the stress PA were rotated while keeping the effective stress PV constant. At the instant at which stress rotation was initiated the sand contracted and the response became strongly non-coaxial. A significant amount of plastic contraction was accumulated in the course of stress rotation, while the response remained non-coaxial.

Although a critical state had not been attained when the rotation of the stress PA was initiated in the tests performed in this study the results presented support the claim that the Anisotropic Critical State Theory by Li and Dafalias (2012) constitutes a necessary revision of the classical Critical State Theory by Roscoe et al. (1958) and Schofield and Wroth (1968). A more detailed discussion on this topic is presented in the unpublished article by the author under the title “Novel findings on the dilatancy and non-coaxiality of sand under generalised loading”, presented in the Appendix.

6.9 BIBLIOGRAPHY

Been K, Jefferies MG (1985) A state parameter for sands. Géotechnique 35 (2), 99–112

Dafalias YF (2016) Must critical state theory be revisited to include fabric effects? Acta Geotechnica (2016) 11:479, DOI 10.1007/s11440-016-0441-0

Darve F, Flavigny M, Meghachou M (1995) Constitutive modelling and instabilities of soil behaviour. Computers and Geotechnics 17 (1995), 203-224

Desrues J, Georgopoulos I-O (2006) An investigation of diffuse failure modes in undrained triaxial tests on loose sand. Soils and Foundations, Vol.46, No.5, 585-594

Fu P, Dafalias YF (2011) Fabric evolution within shear bands of granular materials and its relation to critical state theory. International Journal for Numerical and Analytical Methods in Geomechanics, 2011, 35: 1918-1948

Huang X, O’Sullivan C, Hanley KJ, Kwok CY (2014) Discrete-element method analysis of the state parameter. Géotechnique 64, No. 12, 954-965

Ishihara K, Tatsuoka F, Yasuda S (1975) Undrained deformation and liquefaction of sand under cyclic stresses. Soils and Foundations, Vol.15, No.1, 29-44

Li XS, Wang Y (1998) Linear representation of steady-state line for sand. J. Geotech. Geoenviron. Eng., 124(12), 1215-1217

Li XS, Dafalias YF (2000) Dilatancy for cohesionless soils. Géotechnique 50, No. 4, 449-460

Li X, Li XS (2009) Micro-macro quantification of the internal structure of granular materials. J. Eng. Mech., 135(7), 641-656

Li XS, Dafalias YF (2012) Anisotropic critical state theory: role of fabric. Journal of Engineering Mechanics, Vol. 138, No. 3, 263-275

Manzari MT, Dafalias YF (1997) A critical state two-surface plasticity model for sands. Géotechnique 47, No. 2, 255-272

Miura K, Miura S, Toki S (1986) Deformation behavior of anisotropic dense sand under principal stress axes rotation. Soils and Foundations, Vol.26, No.1, 36-52

Papadimitriou AG, Chaloulos YK, Dafalias YF (2019) A fabric-based sand plasticity model with reversal surfaces within anisotropic critical state theory. Acta Geotech., 14: 253-277, 2019

Roscoe KH, Schofield AN, Wroth CP (1958) On the yielding of soils. Géotechnique 8 (1), 22–53

Salvatore E, Mondoni G, Ando E, Albano M, Viggiani G (2017) Determination of the critical state of granular materials with triaxial tests. Soils Found. (2017), https://doi.org/10.1016/j.sandf.2017.08.005

Schofield AN, Wroth CP (1968) Critical state soil mechanics. McGraw-Hill, London

Tatsuoka F, Sonoda S, Hara K, Fukushima S, Pradhan TBS (1986) Failure and deformation of sand in torsional shear. Soils and Foundations, Vol.26, No.4, pp. 79-97

Theocharis AI, Vairaktaris E, Dafalias YF, Papadimitriou AG (2017) Proof of incompleteness of Critical State Theory in granular mechanics and its remedy. Journal of Engineering Mechanics, Vol. 143 (2), 1-12

Theocharis AI, Vairaktaris E, Dafalias YF, Papadimitriou AG (2019) Necessary and sufficient conditions for reaching and maintaining critical state. International Journal for Numerical and Analytical Methods in Geomechanics, 43: 2041-2045

Thornton C (2000) Numerical simulations of deviatoric shear deformation of granular media. Géotechnique 50, No. 1, 43-53

Triantafyllos PK, Georgiannou VN, Dafalias YF, Georgopoulos I-O (2020a) New findings on the evolution of the instability surface of loose sand. Acta Geotech. 15, 197-221, https://doi.org/10.1007/s11440-019-00887-7

Triantafyllos PK, Georgiannou VN, Pavlopoulou E-M, Dafalias YF (2020b) Strength and dilatancy of sand before and after stabilisation with colloidal-silica gel. Géotechnique (under review)

Vardoulakis I, Sulem J (1995) Bifurcation analysis in geomechanics. Chapman and Hall, 1995

Wan R, Nicot F, Darve F (2010) Micromechanical formulation of stress-dilatancy as a flow rule in plasticity of granular materials. Journal of Engineering Mechanics, 136, 589-598

Wang Z-L, Dafalias YF, Shen C-K (1990) Bounding surface hypoplasticity model for sand. Journal of Engineering Mechanics, Vol. 116, No. 5, 983-1001

Wood DM, Belkheier K, Liu DF (1994) Strain softening and state parameter for sand modelling. Géotechnique 44, No. 2, 335-339

Zhang L, Thornton C (2007) A numerical examination of the direct shear test. Géotechnique 57, No. 4, 343-354

Zhou W, Liu J, Ma G, Chang X (2017) Three-dimensional DEM investigation of critical state and dilatancy behaviors of granular materials. Acta Geotechnica (2017) 12:527-540

6.10 TABLES

Table 6.1 Details of triaxial compression tests

Code	Apparatus	Top-platen tilting	Loading rate (mm/min or kPa/min)	Initial conditions			Final conditions			
				e (-)	*p'* (kPa)	ψ (-)	*e* (-)	*p'* (kPa)	ψ (-)	Critical state?
D1	HPTA	FREE	0.300	0.715	100.6	-0.042	0.749	167.0	-0.003	YES
D2	HPTA	FREE	0.300	0.671	101.1	-0.086	0.733	178.9	-0.019	NO
D3	HPTA	FREE	0.300	0.676	100.9	-0.081	0.747	170.0	-0.005	YES
D4	HPTA	FREE	0.300	0.650	100.8	-0.107	0.743	170.0	-0.009	NO
D5	CTA	FREE	0.005	0.665	101.5	-0.092	0.744	168.0	-0.008	YES
D6	HCA	FIXED	15	0.727	100.1	-0.030	0.734	177.7	-0.017	NO
D7	HCA	FIXED	50	0.697	97.9	-0.060	0.697	173.6	-0.055	NO
D8	HPTA	FREE	0.300	0.710	200.6	-0.040	0.746	334.6	0.004	YES
D9	HPTA	FREE	0.300	0.695	200.2	-0.055	0.748	341.4	0.006	YES
D10	HPTA	FREE	0.300	0.680	203.1	-0.070	0.735	339.6	-0.007	NO
D11	HCA	FIXED	15	0.694	200.7	-0.056	0.719	320.5	-0.024	NO
D12	HPTA	FREE	0.600	0.678	301.1	-0.066	0.739	505.8	0.005	YES
D13	HPTA	FREE	0.300	0.717	299.3	-0.027	0.743	499.2	0.009	YES
D14	HPTA	FREE	0.300	0.709	302.7	-0.035	0.722	531.7	-0.011	NO
D15	HPTA	FIXED	0.300	0.691	501.1	-0.043	0.717	834.0	-0.002	YES
D16	HPTA	FIXED	0.300	0.676	701.4	-0.049	0.707	1156.4	0.001	YES
D17	HPTA	FIXED	0.300	0.674	1001.3	-0.038	0.682	1663.3	-0.006	YES
U1	HPTA	FIXED	0.300	0.722	100.2	-0.035	0.722	809.1	0.002	YES
U2	HPTA	FREE	0.300	0.697	98.5	-0.060	0.697	1390.5	-0.001	NO
U3	HCA	FIXED	7.5	0.709	199.5	-0.041	0.709	505.5	-0.025	NO
U4	HPTA	FREE	0.300	0.674	297.8	-0.070	0.674	1789.8	-0.010	NO
U5	HPTA	FREE	0.300	0.631	324.6	-0.112	0.631	3629.0	0.000	NO
U6	HPTA	FREE	0.300	0.695	300.5	-0.050	0.695	1446.4	-0.001	YES
U7	HPTA	FREE	0.300	0.670	499.3	-0.064	0.670	2096.0	-0.005	NO
U8	HPTA	FREE	0.100	0.681	999.5	-0.032	0.681	1791.2	-0.004	YES
U9	HPTA	FIXED	0.300	0.678	999.5	-0.034	0.678	1938.4	-0.002	YES
U10	HPTA	FREE	0.100	0.698	1452.1	0.002	0.698	941.9	-0.017	NO
U11	HPTA	FREE	0.100	0.669*	1505.2	-0.025	0.669	2096.3	-0.005	YES

U12	HPTA	FREE	0.100	0.662*	1999.9	-0.016	0.662	2659.9	0.004	YES
U13	HPTA	FREE	0.300	0.660	4000.7	0.039	0.660	3574.5	0.028	YES
U14	HPTA	FREE	0.300	0.628	5942.8	0.054	0.628	3789.1	0.002	YES

*The measurement of the initial dimensions of the specimen contains gross and systematic errors; the reported value of *e* is an estimated value based on a different test which yielded similar results, in accordance with the following figures:

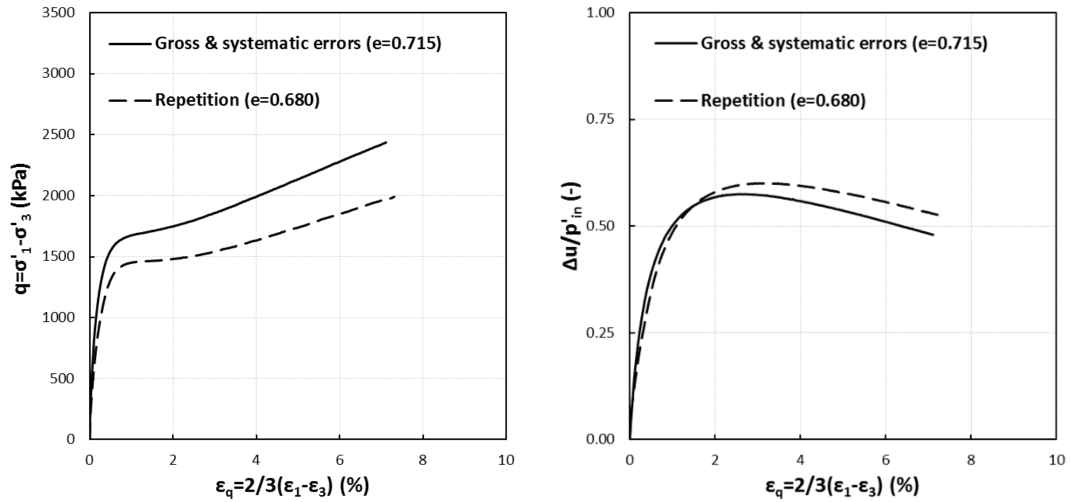

Table 6.2 Critical state parameters for M31 Sand

	$e_c(p') = e_\Gamma - \lambda(p'/p_a)^\alpha$, $p_a = 101$ kPa			$\eta_c = (q\,/\,p')_c = M$
	e_Γ	λ	α	M
M31 Sand	0.7682	0.0112	0.70	1.24

Table 6.3 Details of stress rotation tests

Code	Apparatus	Top-platen tilting	Conditions at the beginning of undrained radial loading						Conditions at the beginning of drained stress rotation						
			e (-)	*p'* (kPa)	ψ (-)	η (-)	*b* (-)	$\alpha_{\sigma'1}$ (°)	*e* (-)	*p'* (kPa)	ψ (-)	η (-)	*b* (-)	$\alpha_{\sigma'1}$ (°)	Critical state?
PAR1	HCA	FIXED	-	-	-	-	-	-	0.693	99.9	-0.064	1.01	0.01	0.00	NO
PAR2	HCA	FIXED	0.726	197.4	-0.024	0.14	0.53	14.5	0.726	507.0	-0.008	1.02	0.55	14.3	NO
PAR3	HCA	FIXED	0.744	99.6	-0.013	0.14	0.50	15.0	0.744	343.2	0.003	1.05	0.52	15.0	NO

6.11 FIGURES

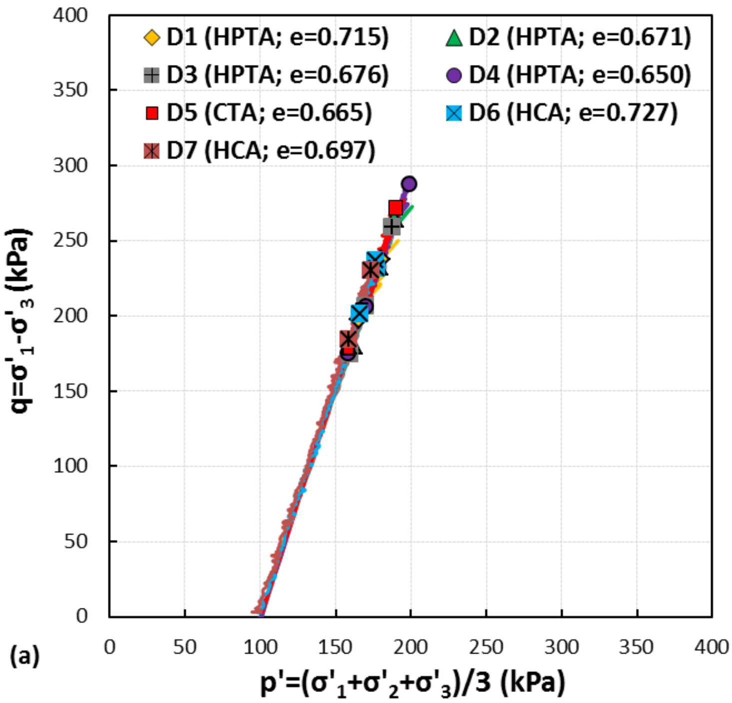

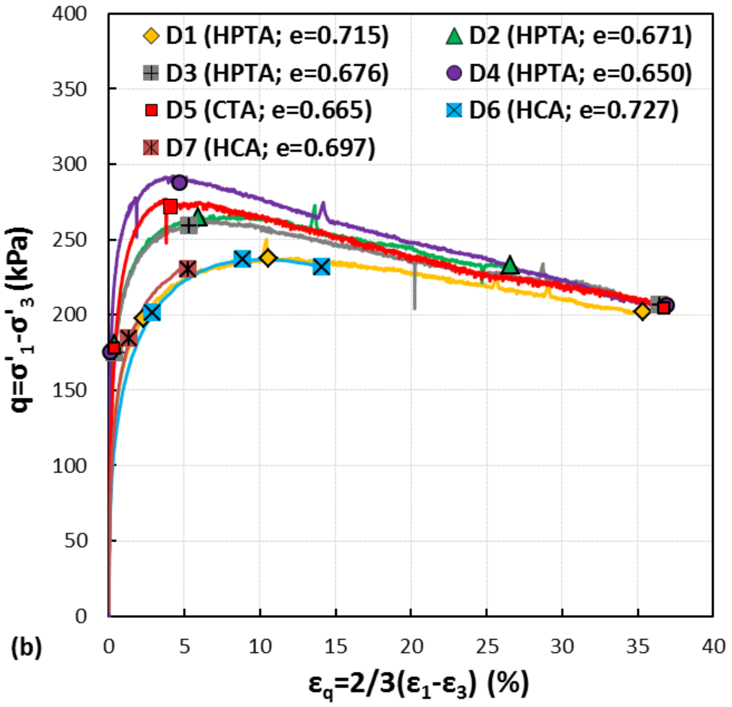

Fig. 6.1 Response of M31 Sand to drained triaxial compression at initial mean effective stress p' = 100 kPa. **a** Effective stress paths. **b** Stress - strain curves (**c** and **d** on next page)

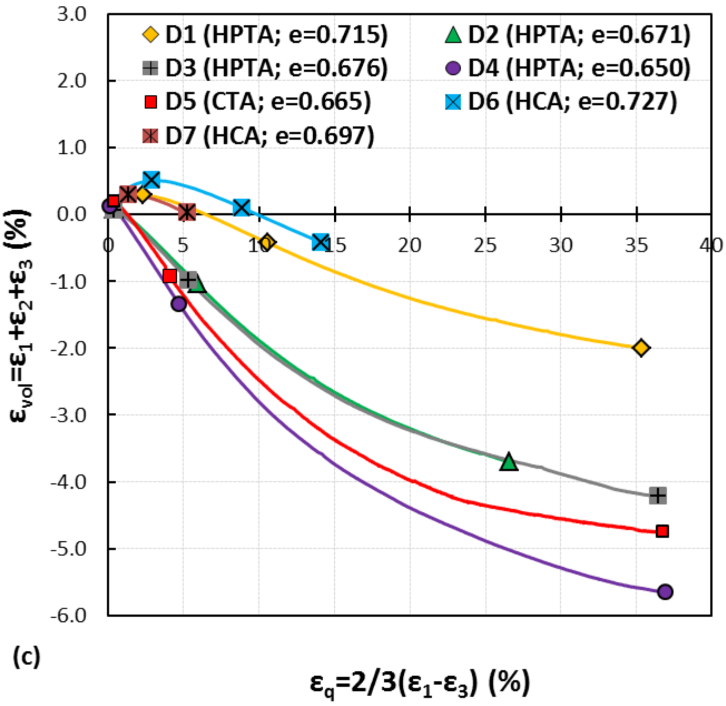

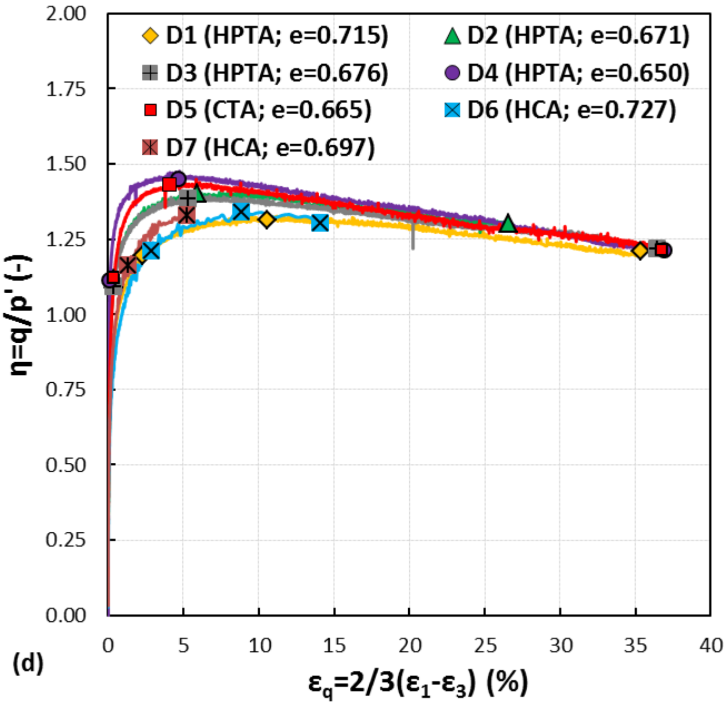

Fig. 6.1 Response of M31 Sand to drained triaxial compression at initial mean effective stress *p'* = 100 kPa. **c** Evolution of volumetric strain. **d** Evolution of stress ratio

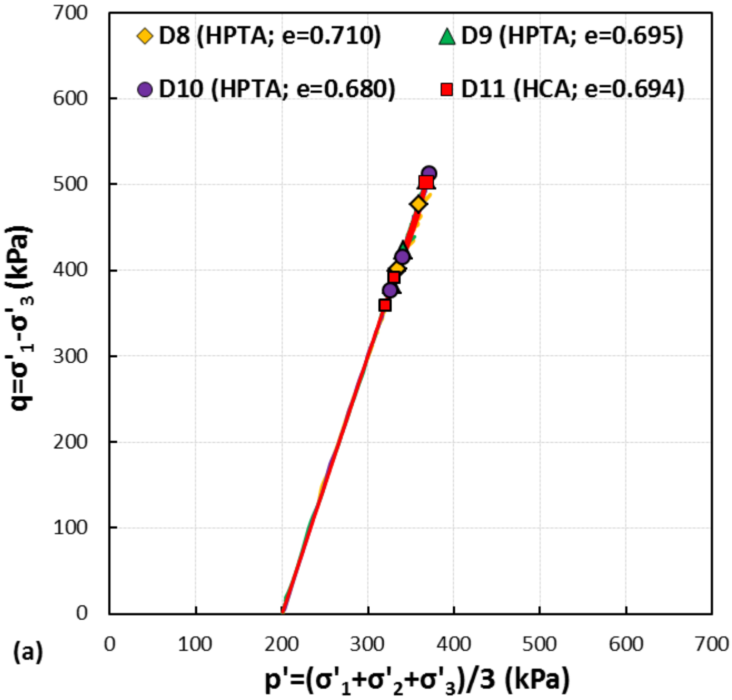

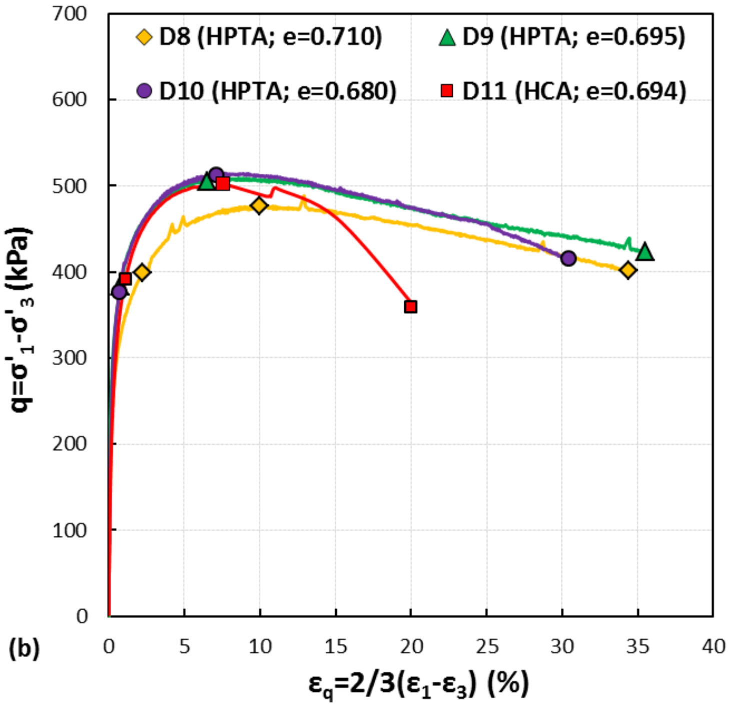

Fig. 6.2 Response of M31 Sand to drained triaxial compression at initial mean effective stress p' = 200 kPa. **a** Effective stress paths. **b** Stress-strain curves (**c** and **d** on next page)

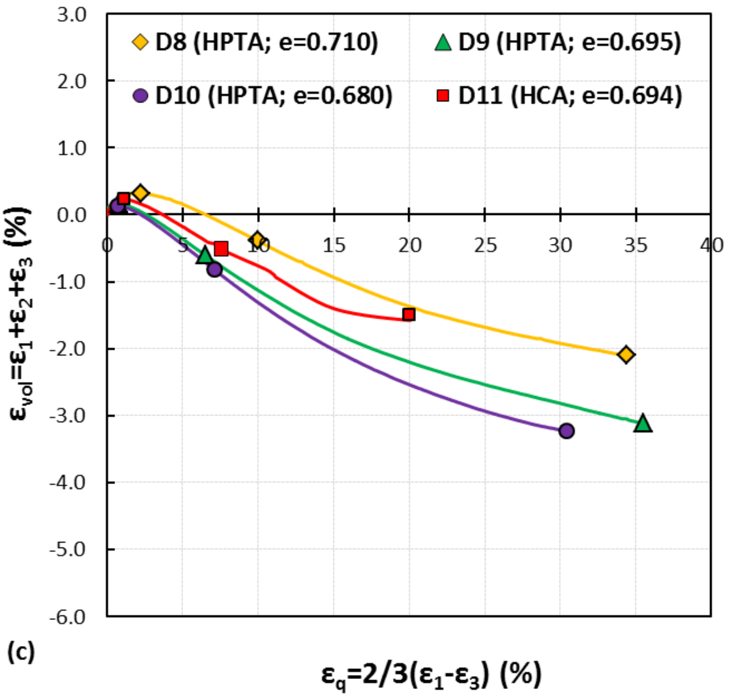

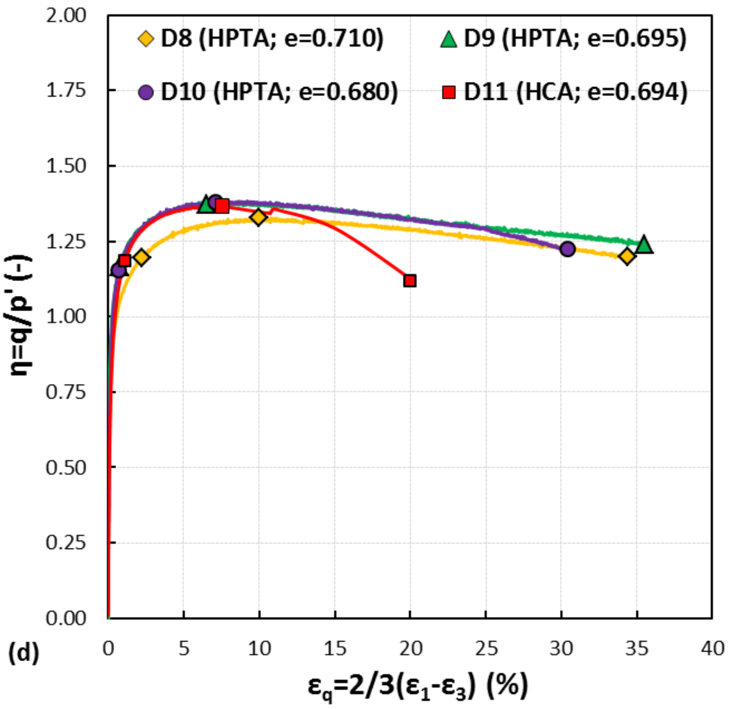

Fig. 6.2 Response of M31 Sand to drained triaxial compression at initial mean effective stress *p'* = 200 kPa. **c** Evolution of volumetric strain. **d** Evolution of stress ratio

Fig. 6.3 Bifurcation modes of deformation in drained triaxial compression. **a** Diffuse bulging. **b** Diffuse barrelling followed by shear banding and tilting of the top platen. The deformed specimen in photo b is shown at an axial displacement that is 1.63 times higher than the one corresponding to the end point marked on the curves of test D10 in Fig. 6.2

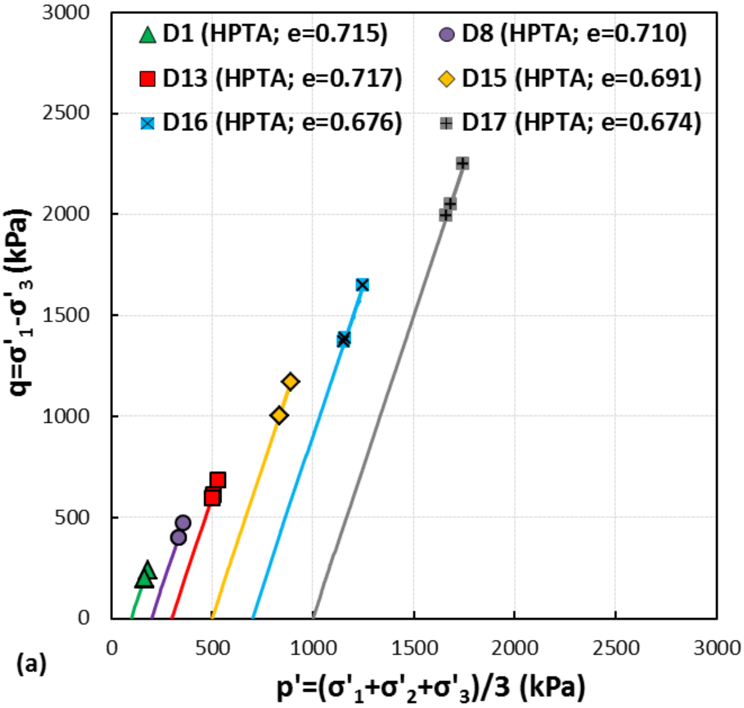

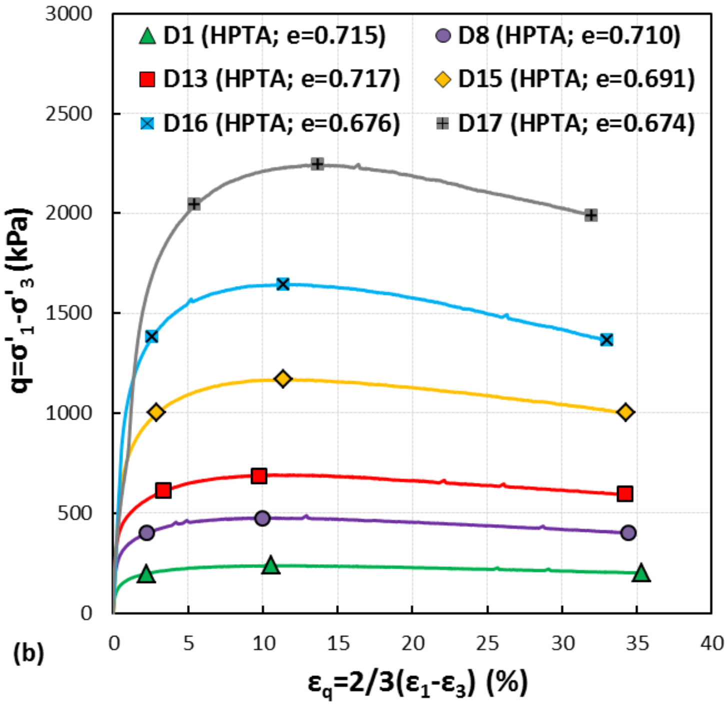

Fig. 6.4 Response of M31 Sand to drained triaxial compression at different initial mean effective stresses p' = 100 - 1000 kPa. **a** Effective stress paths. **b** Stress - strain curves (**c** and **d** on next page)

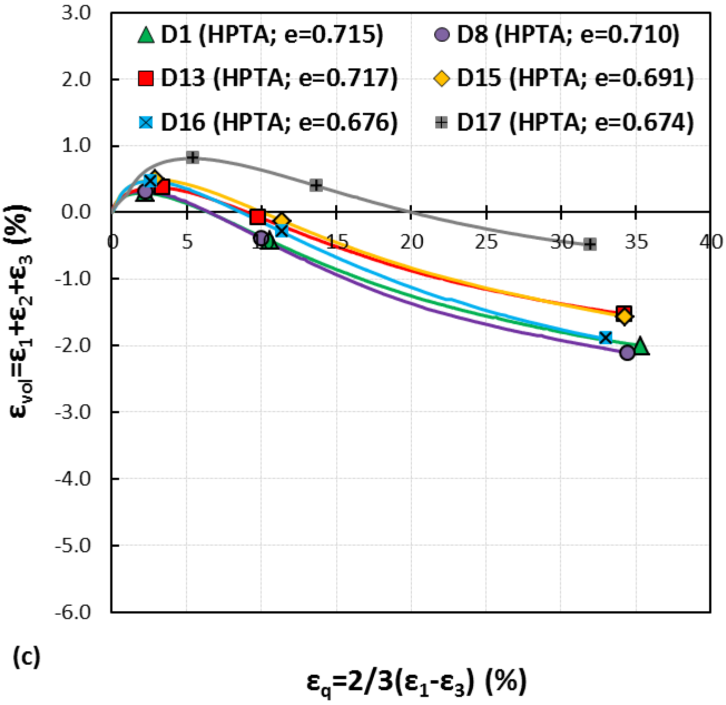

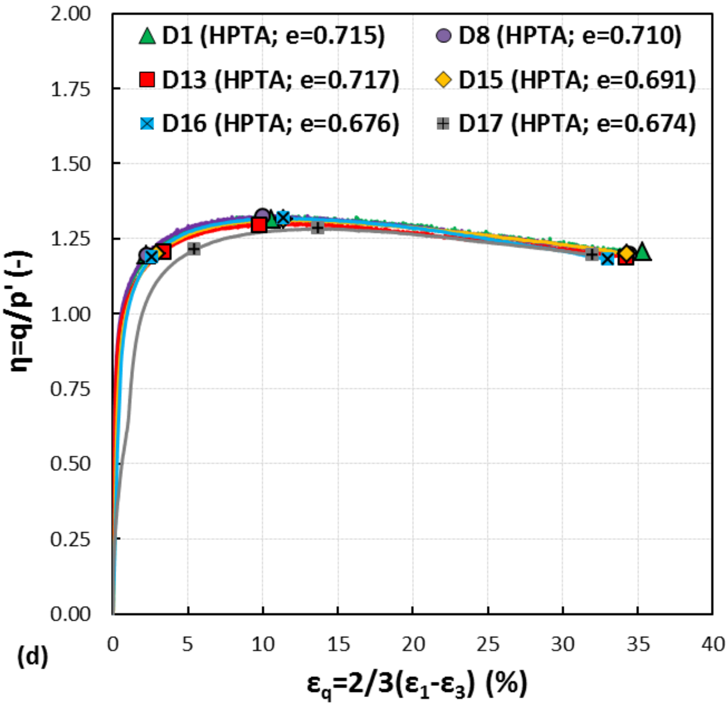

Fig. 6.4 Response of M31 Sand to drained triaxial compression at different initial mean effective stresses *p'* = 100 - 1000 kPa. **c** Evolution of volumetric strain. **d** Evolution of stress ratio

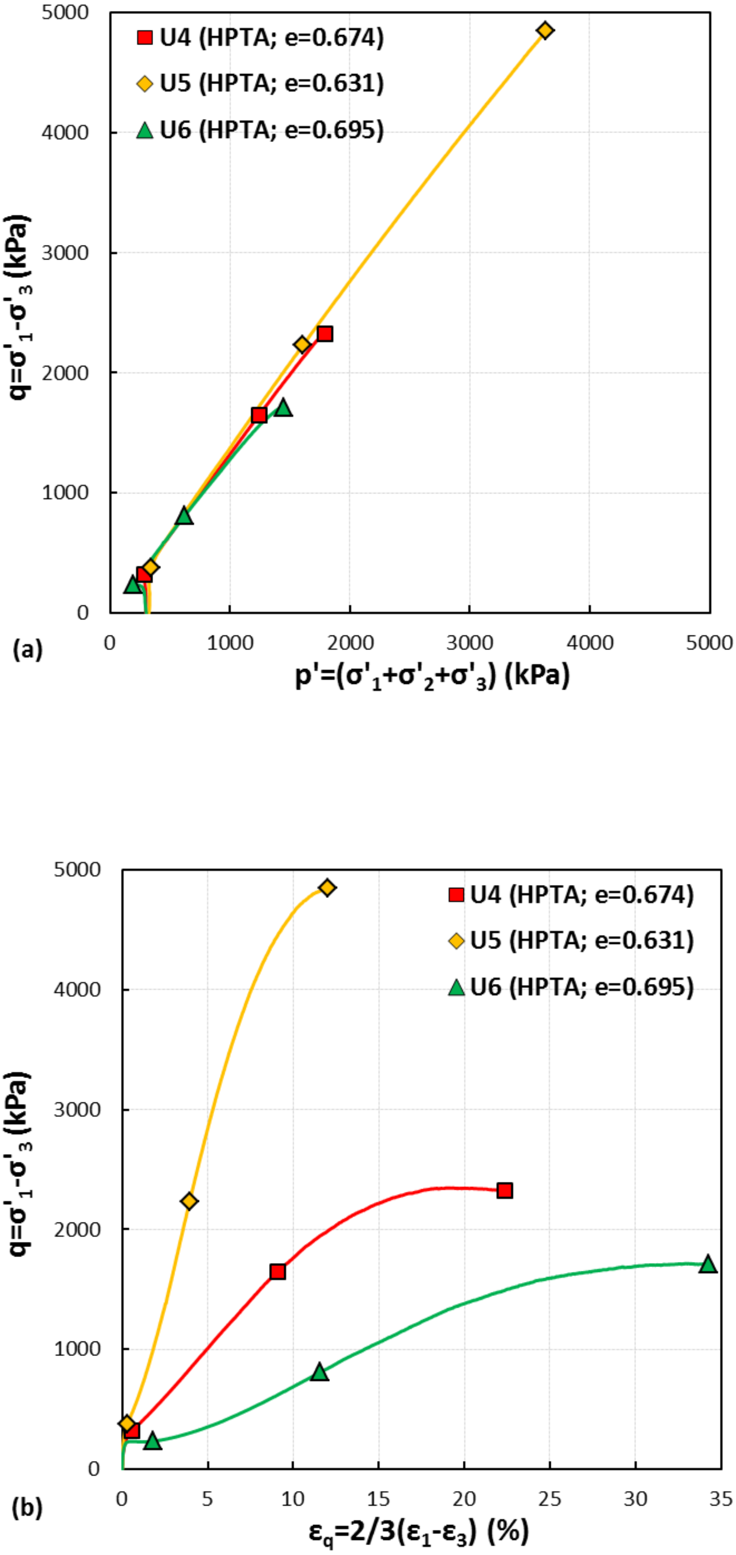

Fig. 6.5 Response of M31 Sand to undrained triaxial compression at initial mean effective stress p' = 300 kPa. **a** Effective stress paths. **b** Stress - strain curves (**c** and **d** on next page)

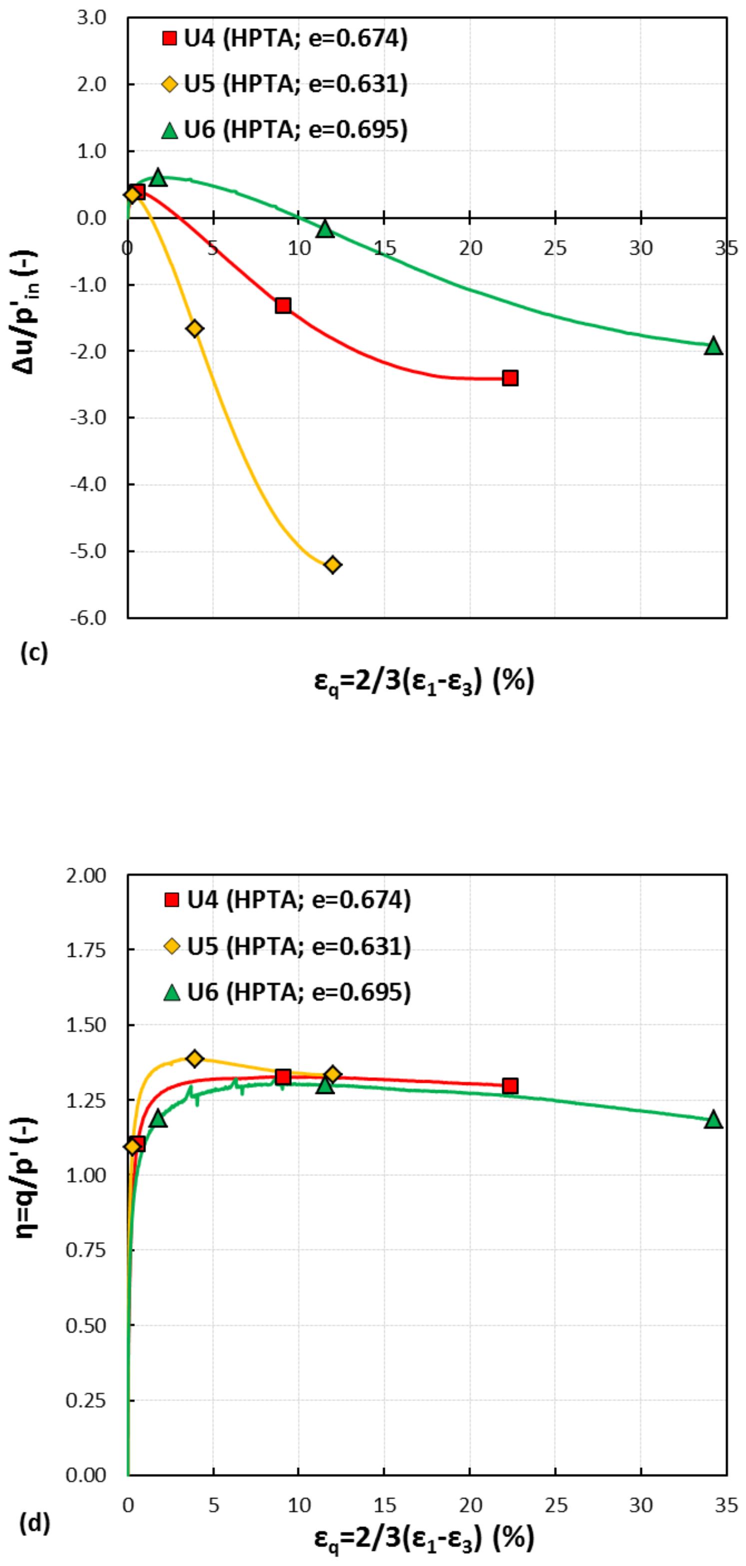

Fig. 6.5 Response of M31 Sand to undrained triaxial compression at initial mean effective stress p' = 300 kPa. **c** Evolution of normalised excess pore-water pressure. **d** Evolution of stress ratio

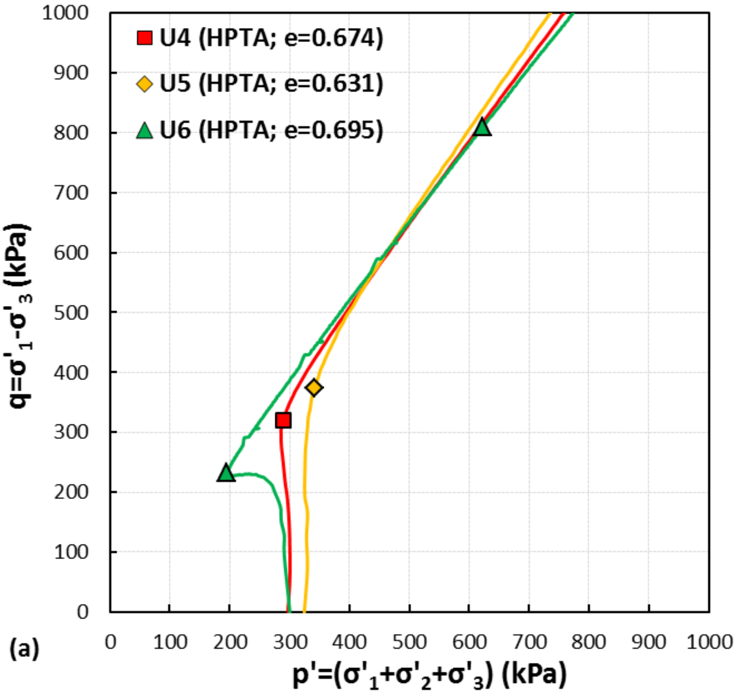

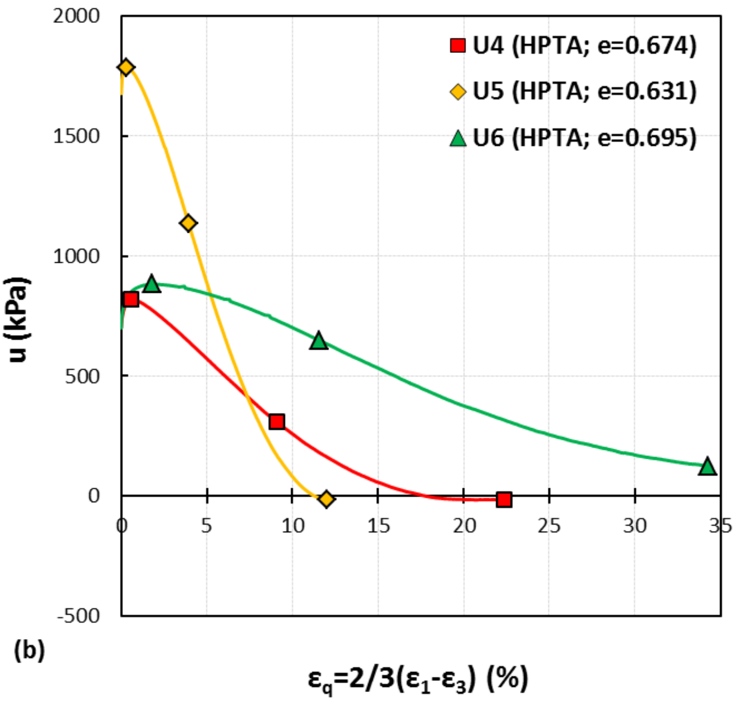

Fig. 6.6 Response of M31 Sand to undrained triaxial compression at initial mean effective stress p' = 300 kPa. **a** The initial part of the effective stress paths in detail. **b** Evolution of pore-water pressure

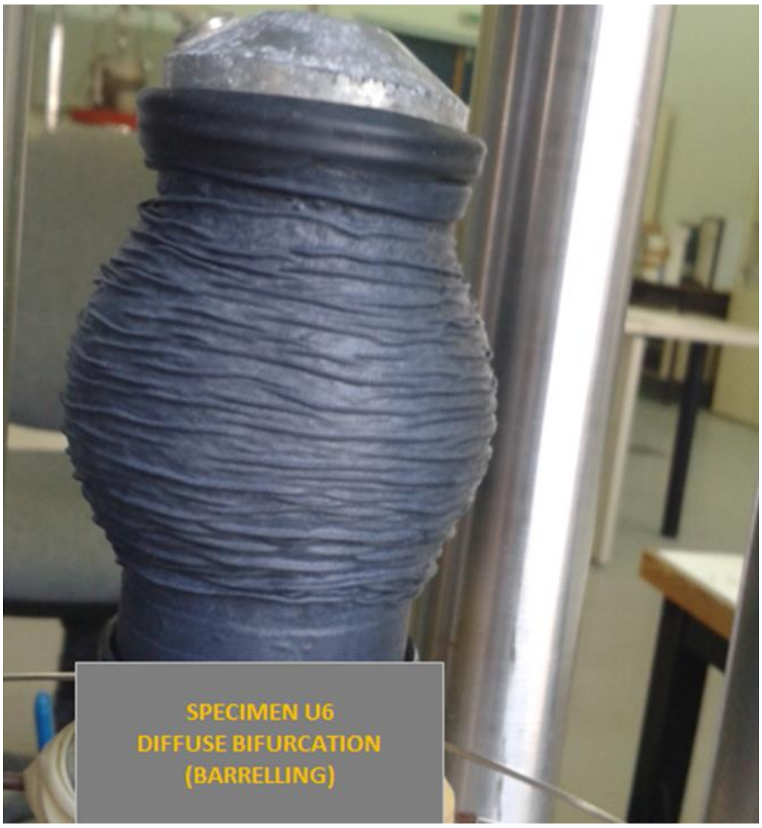

Fig. 6.7 Diffuse-barrelling deformation preceding the formation of shear zones in undrained triaxial compression. The deformed specimen is shown at an axial displacement that is 1.13 times higher than the one corresponding to the end point marked on the curves of test U6 in Fig. 6.5

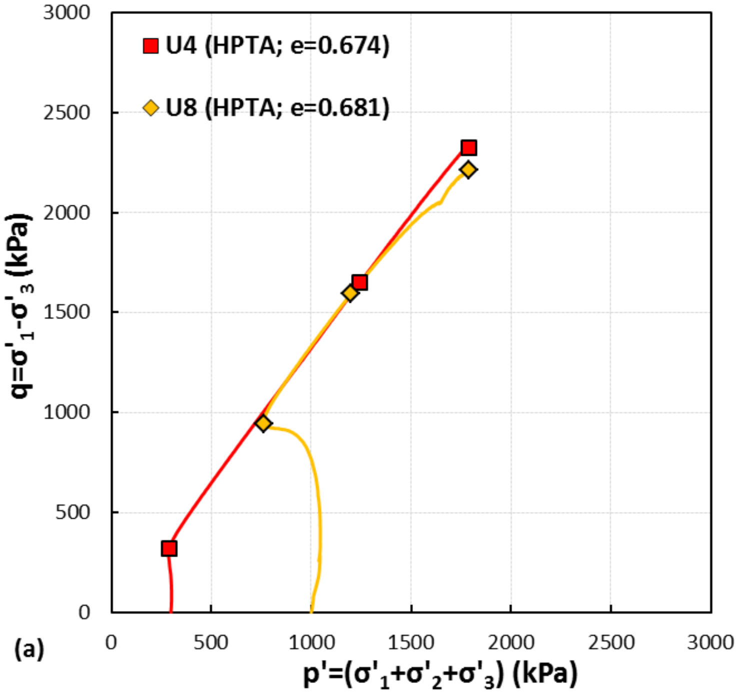

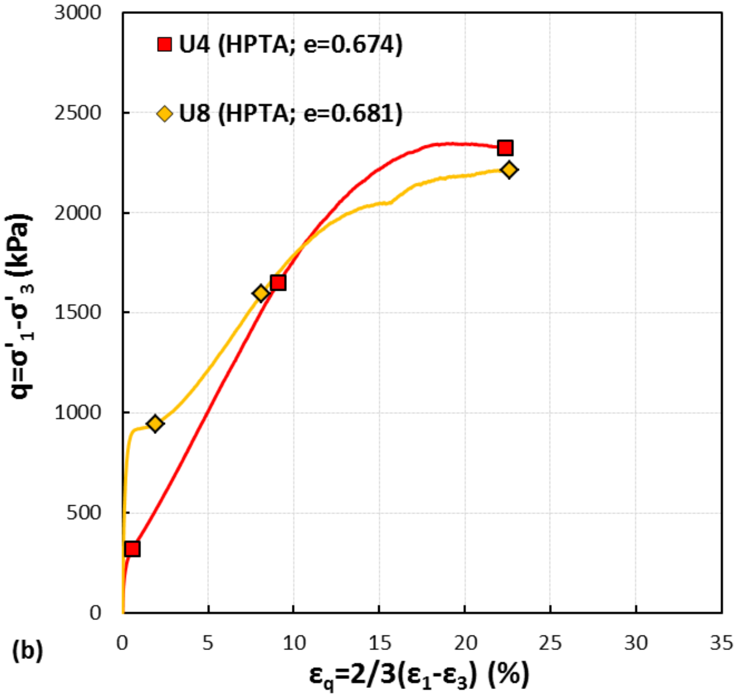

Fig. 6.8 Response of medium-loose M31 Sand to undrained triaxial compression at initial mean effective stresses *p'* = 300 and 1000 kPa. **a** Effective stress paths. **b** Stress - strain curves (**c** and **d** on next page)

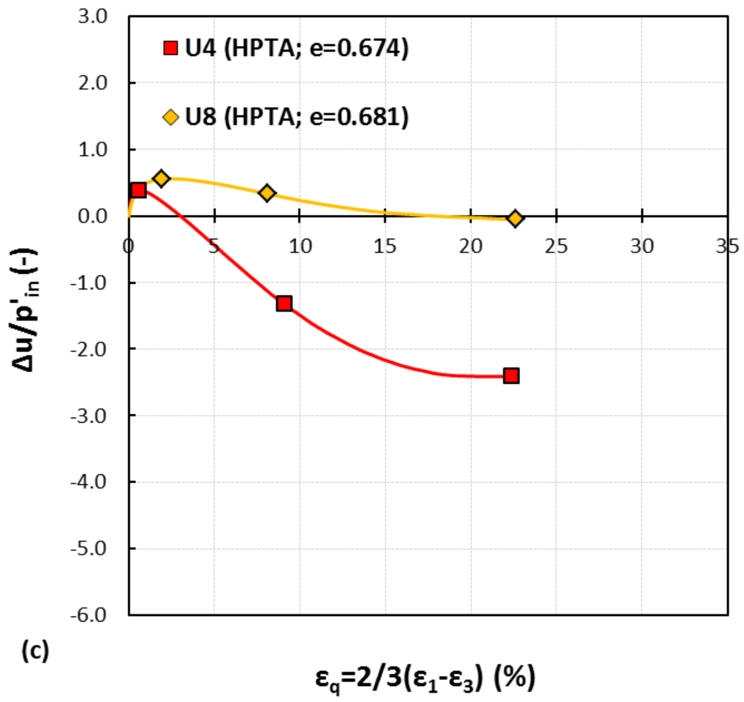

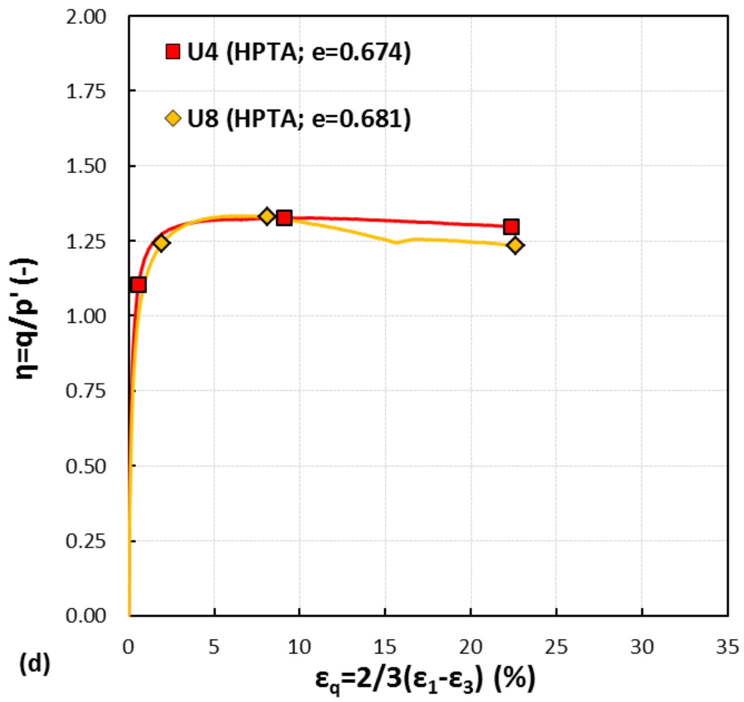

Fig. 6.8 Response of medium-loose M31 Sand to undrained triaxial compression at initial mean effective stresses *p'* = 300 and 1000 kPa. **c** Evolution of normalised excess pore-water pressure. **d** Evolution of stress ratio

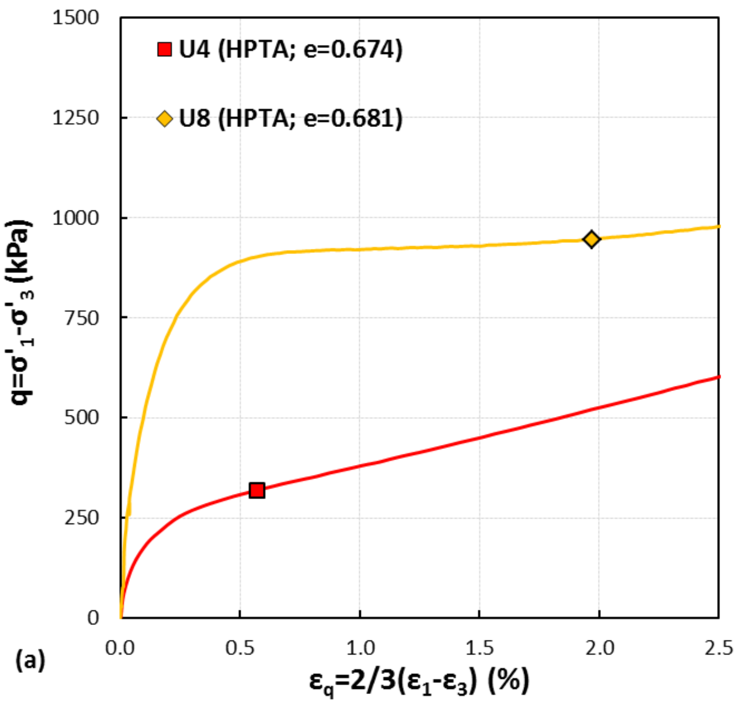

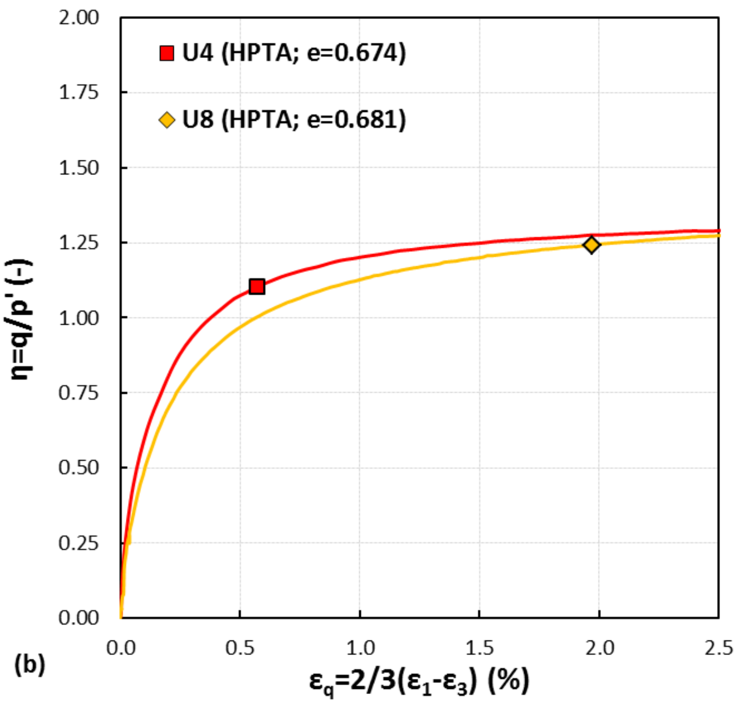

Fig. 6.9 Response of medium-loose M31 Sand to undrained triaxial compression at initial mean effective stresses p' = 300 and 1000 kPa. **a** The initial part of the q - ε_q curves in detail. **b** The initial part of the η - ε_q curves in detail

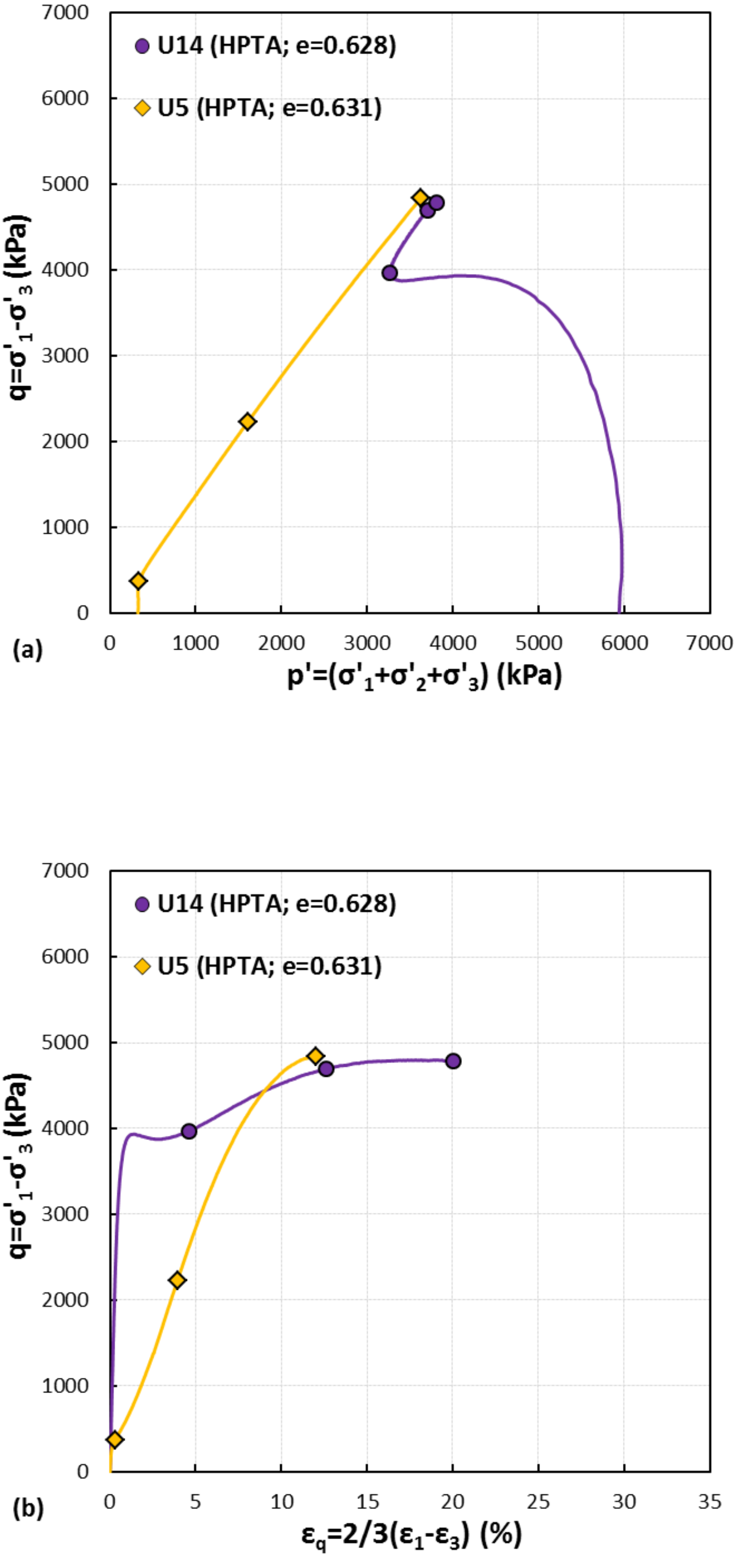

Fig. 6.10 Response of medium-dense M31 Sand to undrained triaxial compression at initial mean effective stresses p' = 325 and 6000 kPa. **a** Effective stress paths. **b** Stress - strain curves (**c** and **d** on next page)

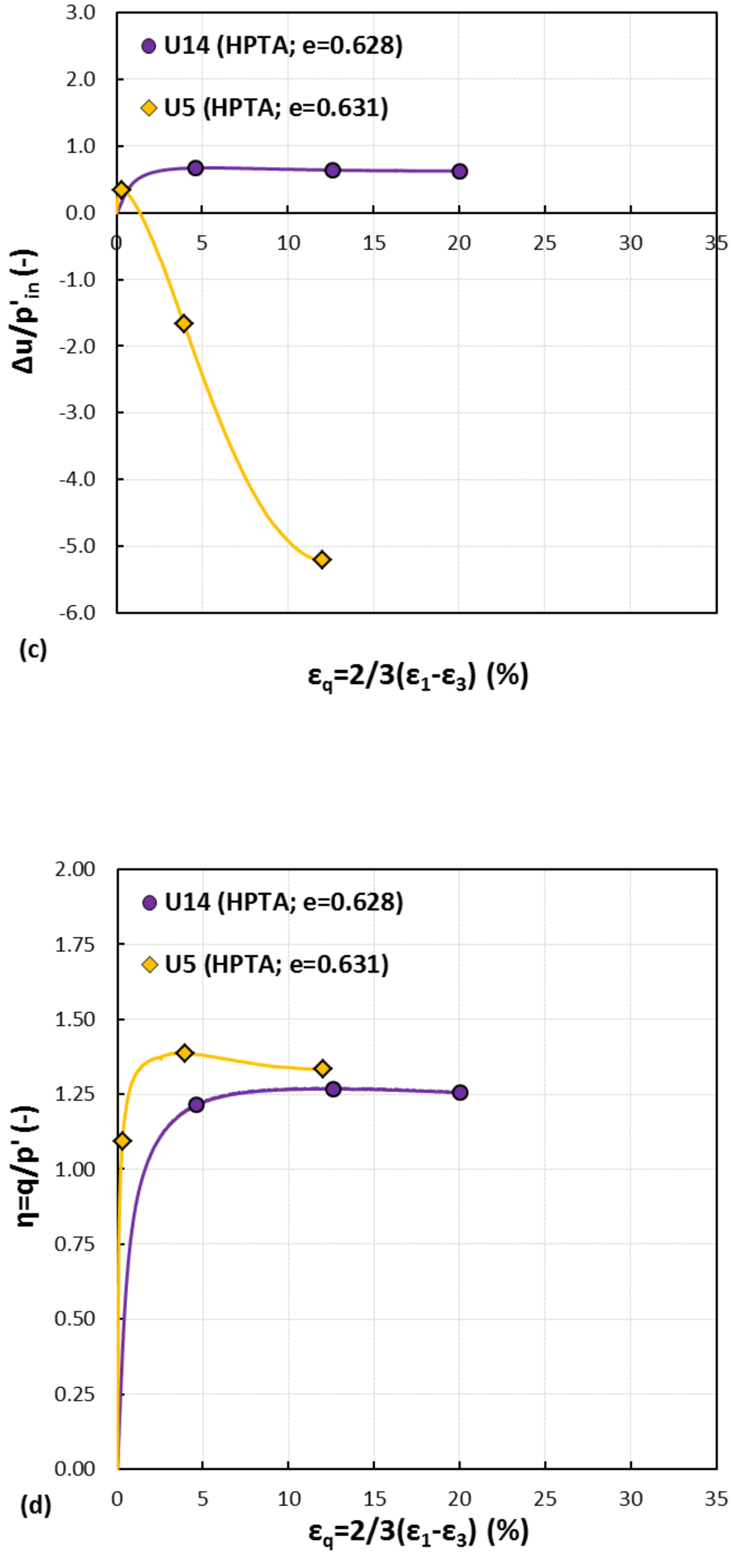

Fig. 6.10 Response of medium-dense M31 Sand to undrained triaxial compression at initial mean effective stresses *p'* = 325 and 6000 kPa. **c** Evolution of normalised excess pore-water pressure. **d** Evolution of stress ratio

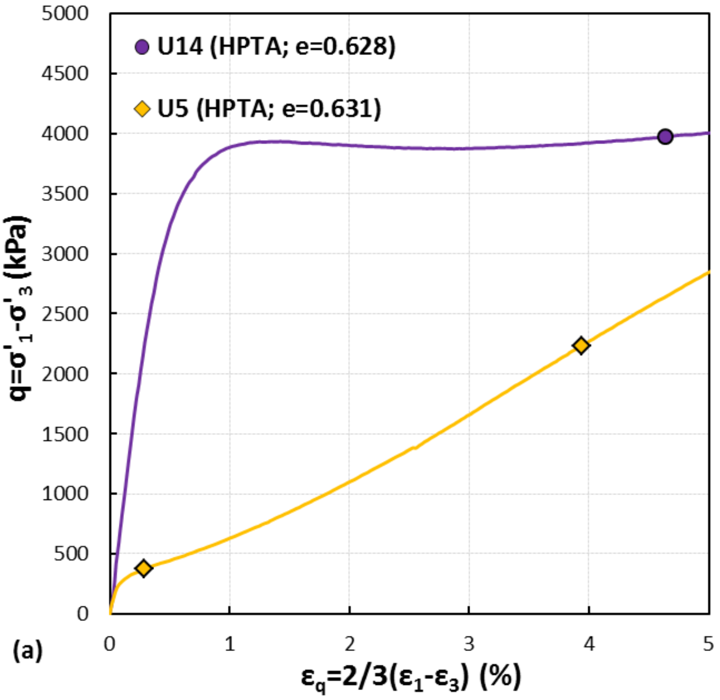

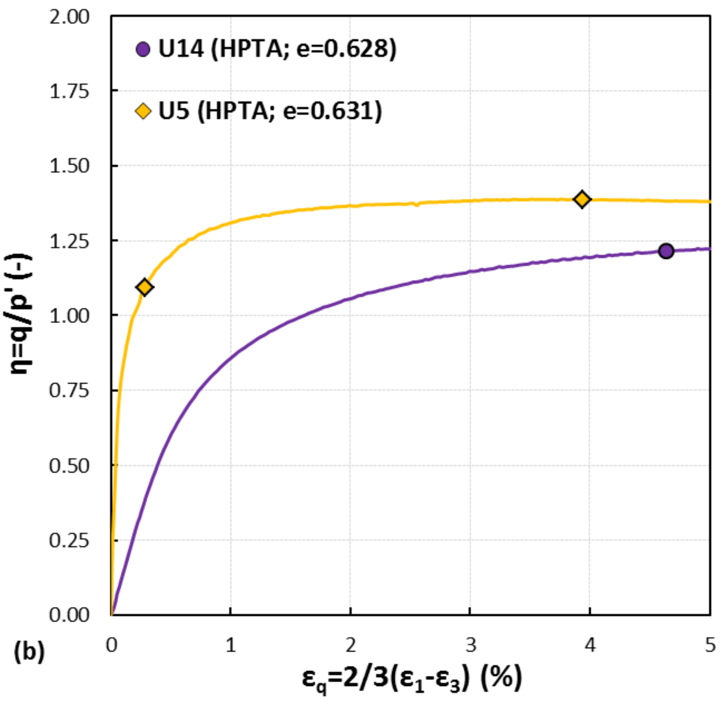

Fig. 6.11 Response of medium-dense M31 Sand to undrained triaxial compression at initial mean effective stresses p' = 325 and 6000 kPa. **a** The initial part of the q - ε_q curves in detail. **b** The initial part of the η - ε_q curves in detail

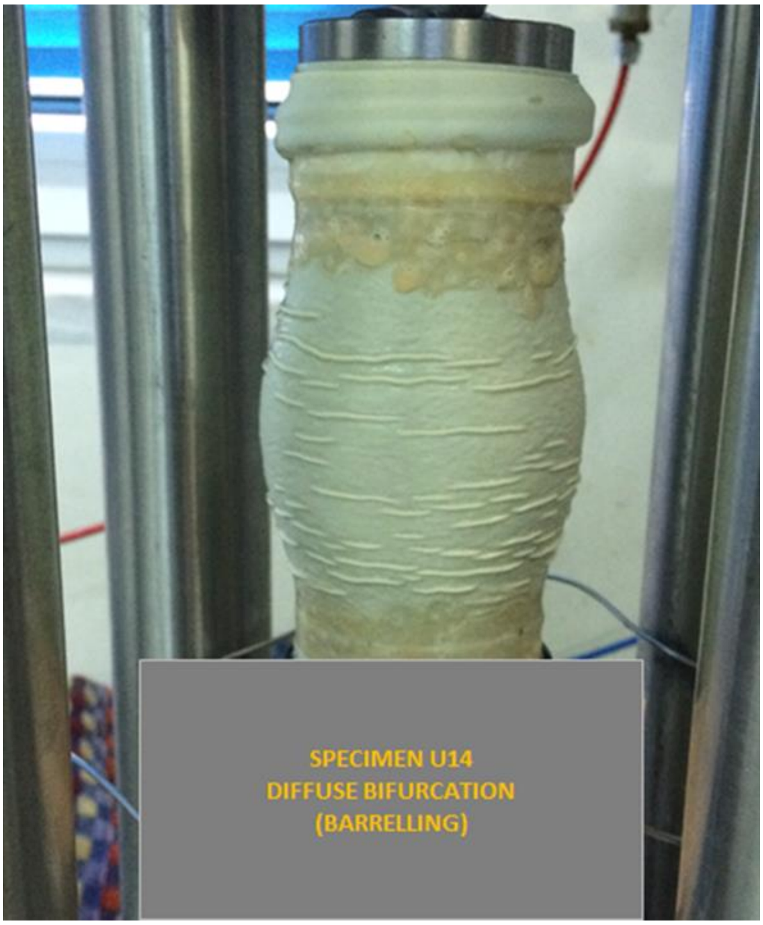

Fig. 6.12 Diffuse-barrelling deformation preceding the formation of shear zones in undrained triaxial compression. The photo shows the deformed specimen at an axial displacement that is 1.27 times higher than the one corresponding to the end point marked on the curves of test U14 in Fig. 6.10

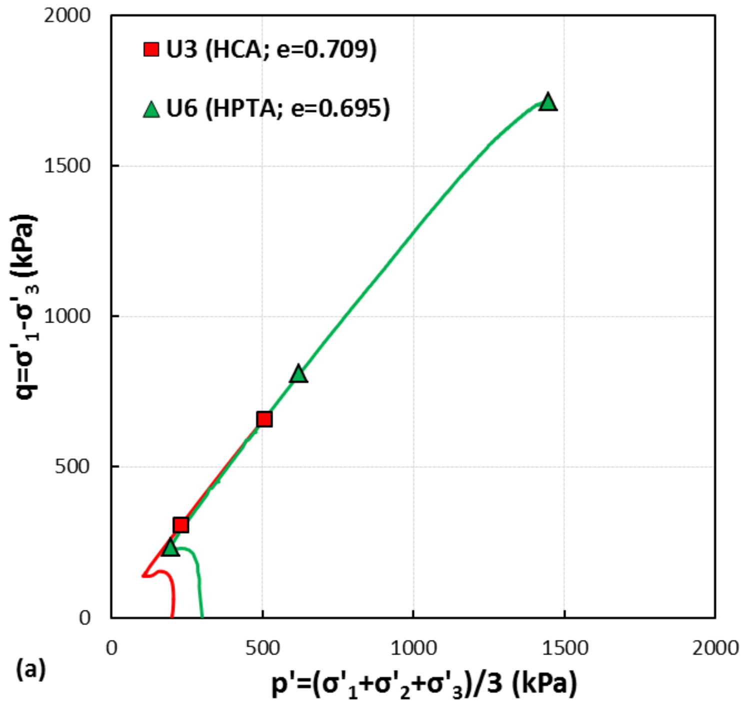

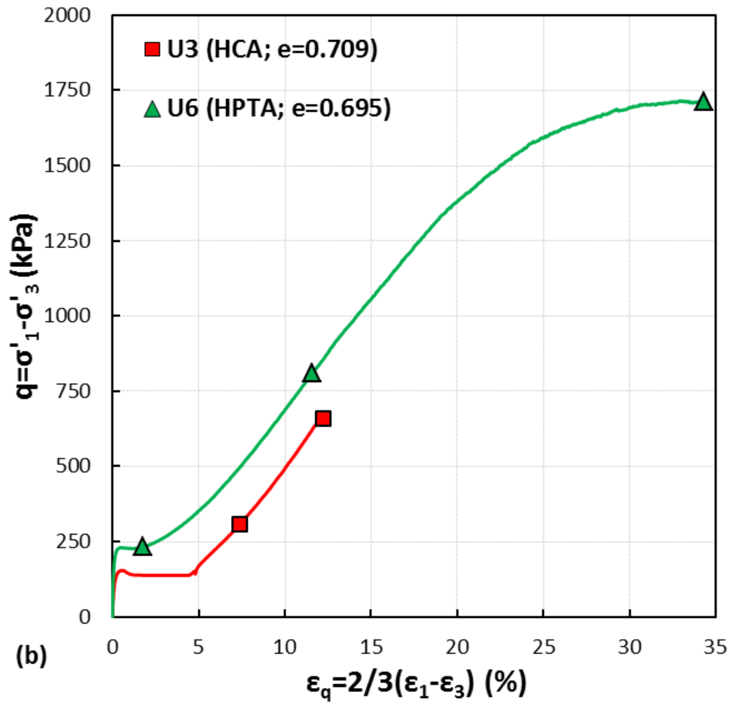

Fig. 6.13 Response of loose M31 Sand to undrained triaxial compression at initial mean effective stresses *p'* = 200 and 300 kPa. **a** Effective stress paths. **b** Stress - strain curves (**c** and **d** on next page)

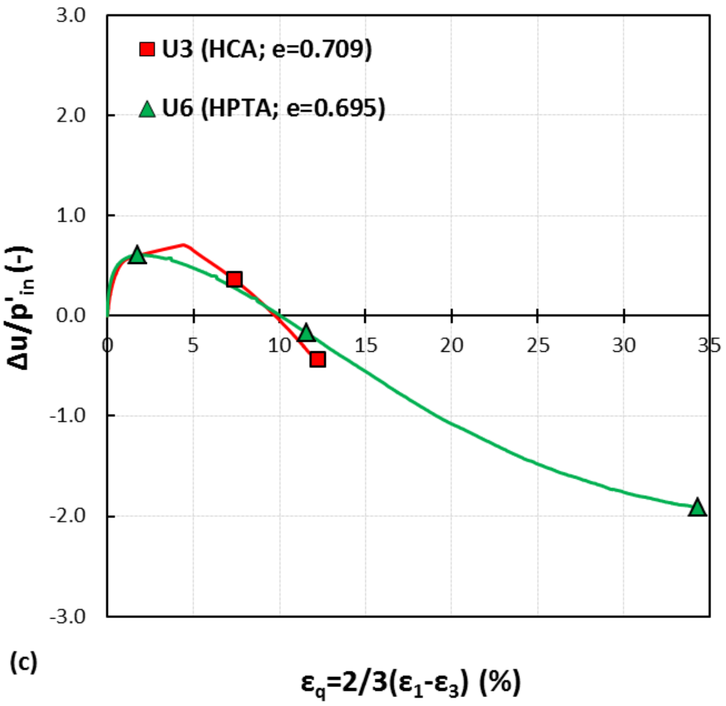

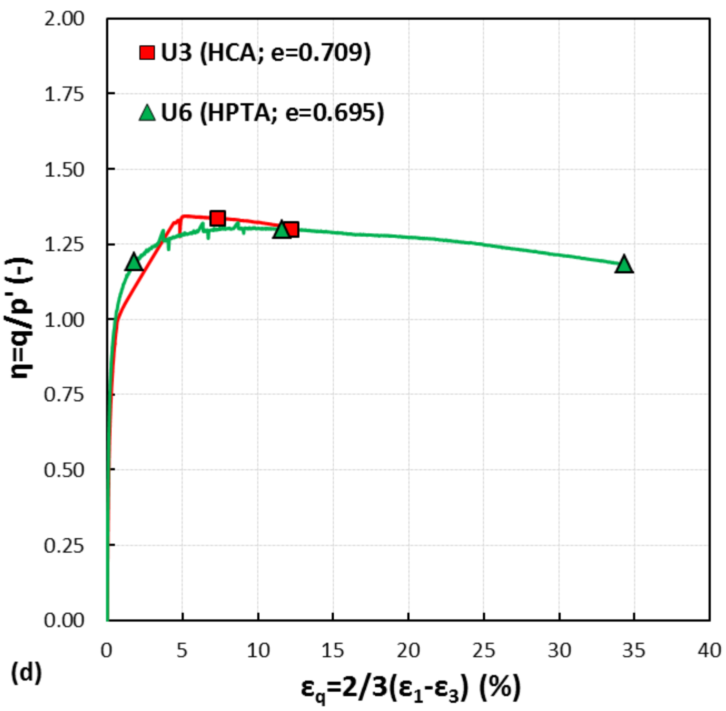

Fig. 6.13 Response of loose M31 Sand to undrained triaxial compression at initial mean effective stresses *p'* = 200 and 300 kPa. **c** Evolution of normalised excess pore-water pressure. **d** Evolution of stress ratio

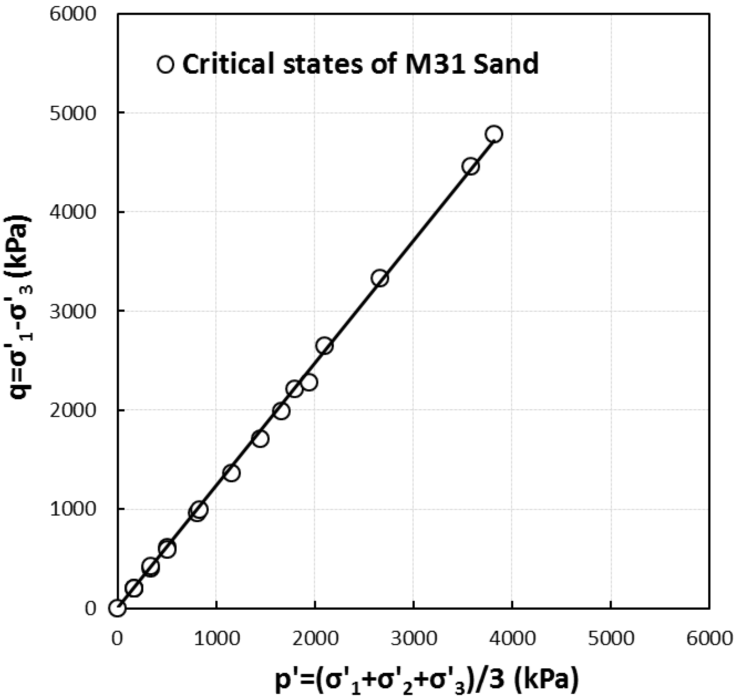

Fig. 6.14 Critical states of M31 Sand in the *q* - *p'* plane

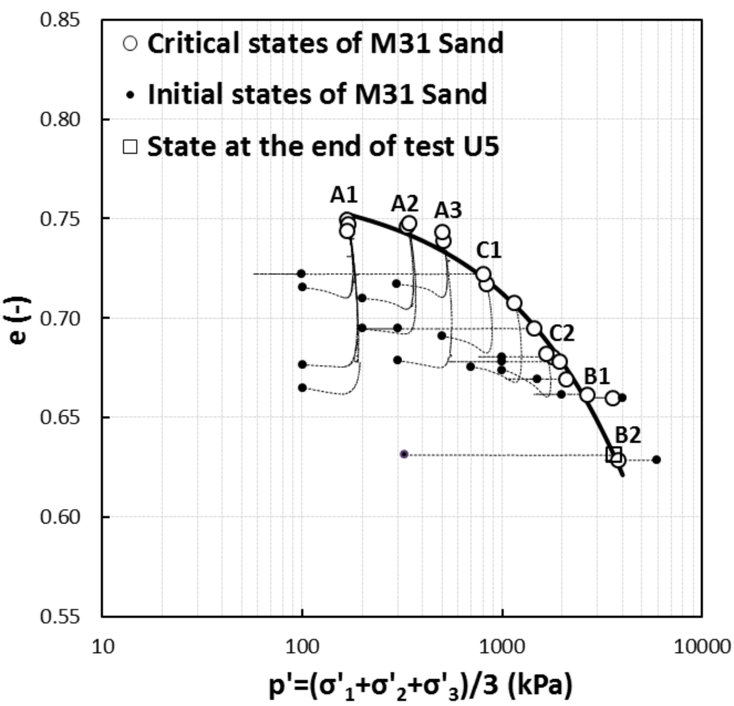

Fig. 6.15 Critical states of M31 Sand in the *e* - *p'* plane

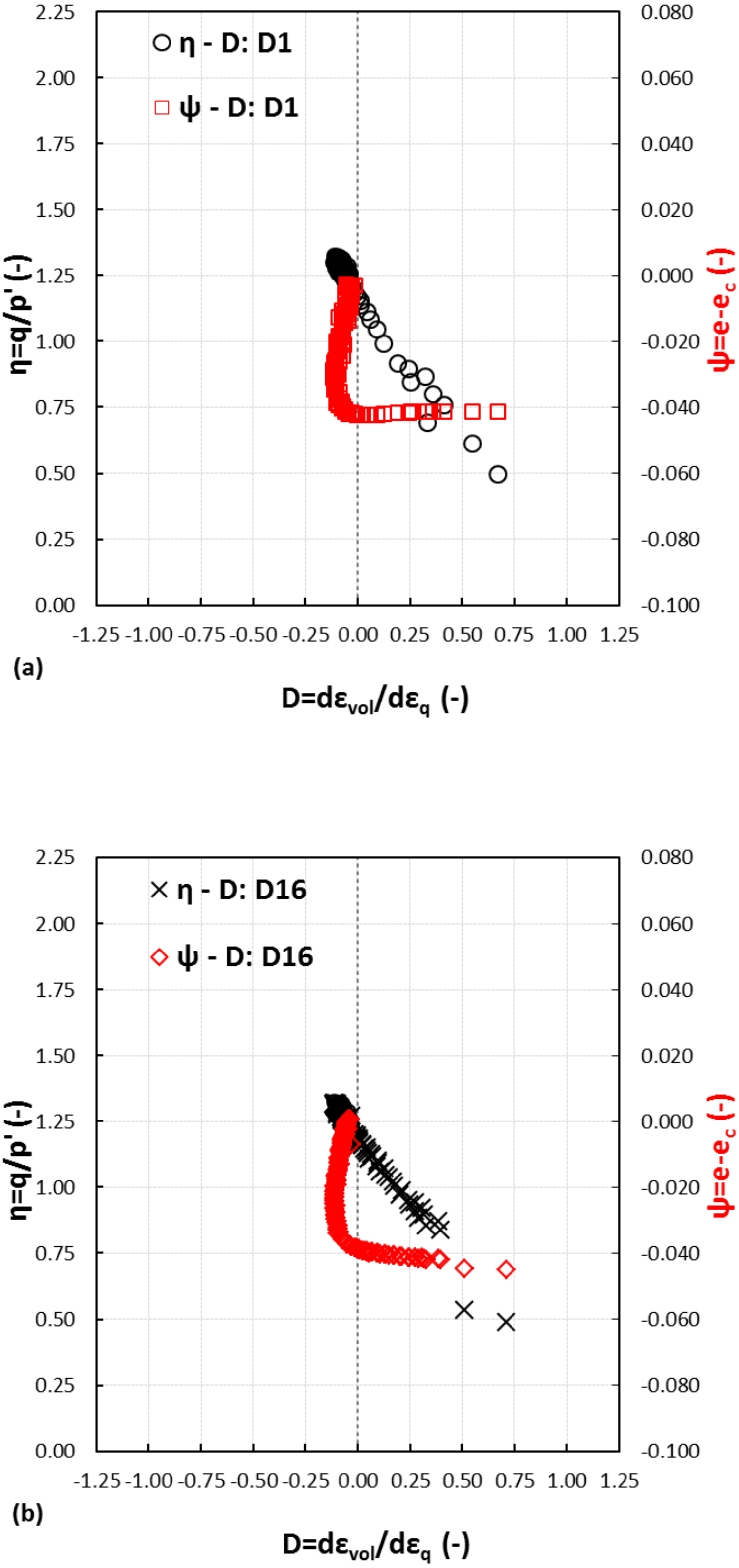

Fig. 6.16 Stress - dilatancy relationship (η - D) and evolution of the state parameter (ψ - D) for M31 Sand subjected to drained loading at various initial conditions. **a** Specimen D1 with $e_i = 0.715$, $p'_i = 100$ kPa and $\psi_i = -0.042$. **b** Specimen D16 with $e_i = 0.676$, $p'_i = 700$ kPa and $\psi_i = -0.049$ (**c** and **d** on next page)

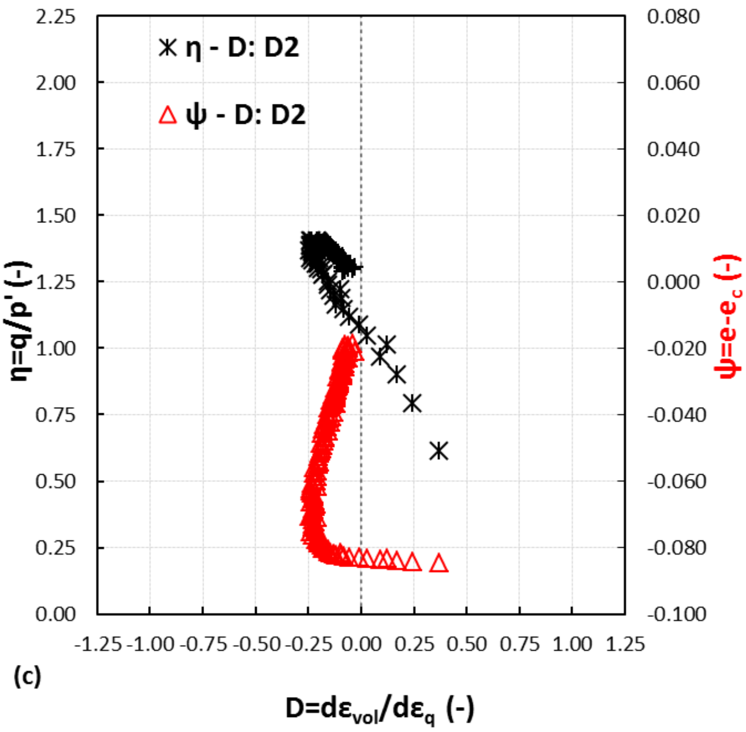

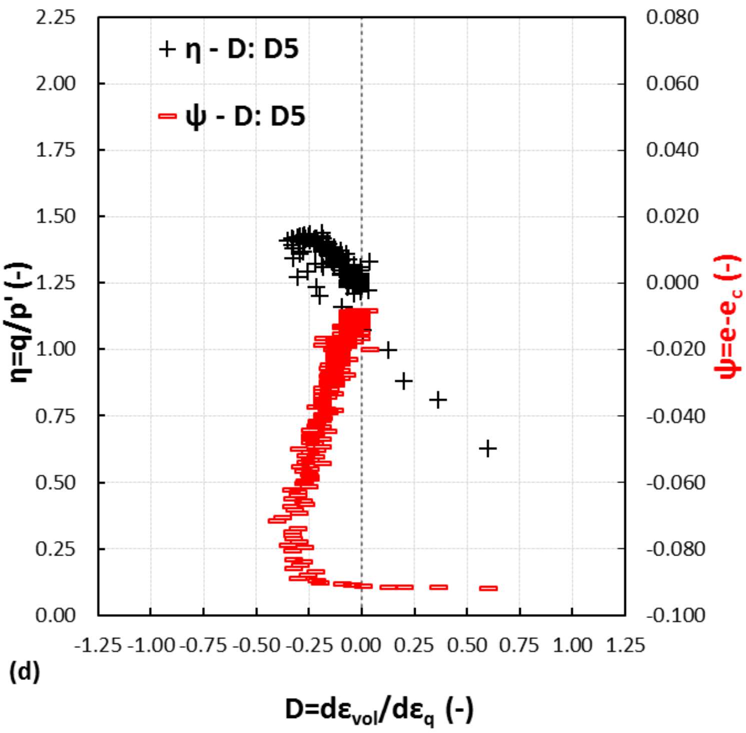

Fig. 6.16 Stress - dilatancy relationship (η - D) and evolution of the state parameter (ψ - D) for M31 Sand subjected to drained loading at various initial conditions. **c** Specimen D2 with $e_i = 0.671$, $p'_i = 100$ kPa and $\psi_i = -0.086$. **c** Specimen D5 with $e_i = 0.665$, $p'_i = 100$ kPa and $\psi_i = -0.092$

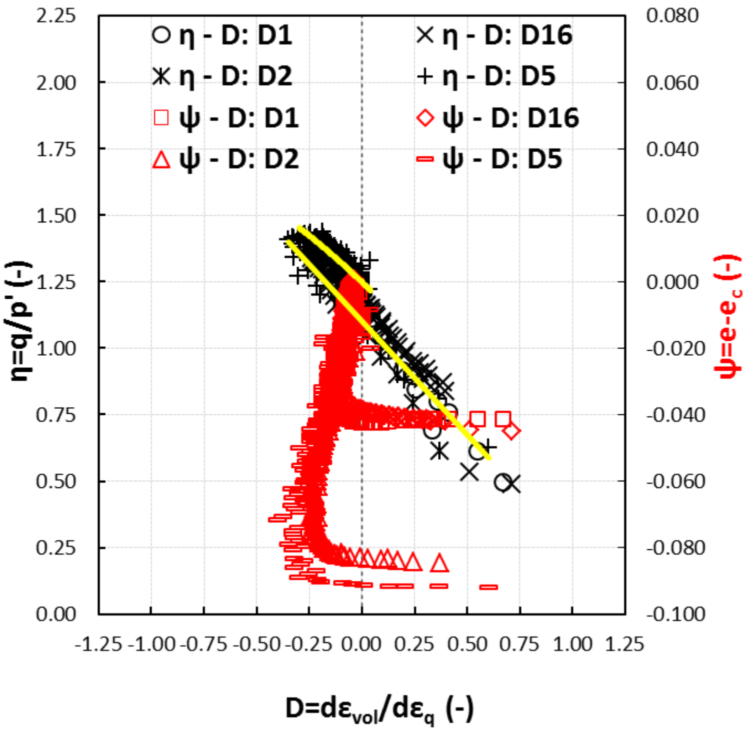

Fig. 6.17 Stress - dilatancy relationship (η - D) and evolution of the state parameter (ψ - D) for loose and dense M31 Sand subjected to drained loading. The yellow lines indicate the diversion from linearity of the stress - dilatancy relationship pre- and post-peak in the case of dense sand

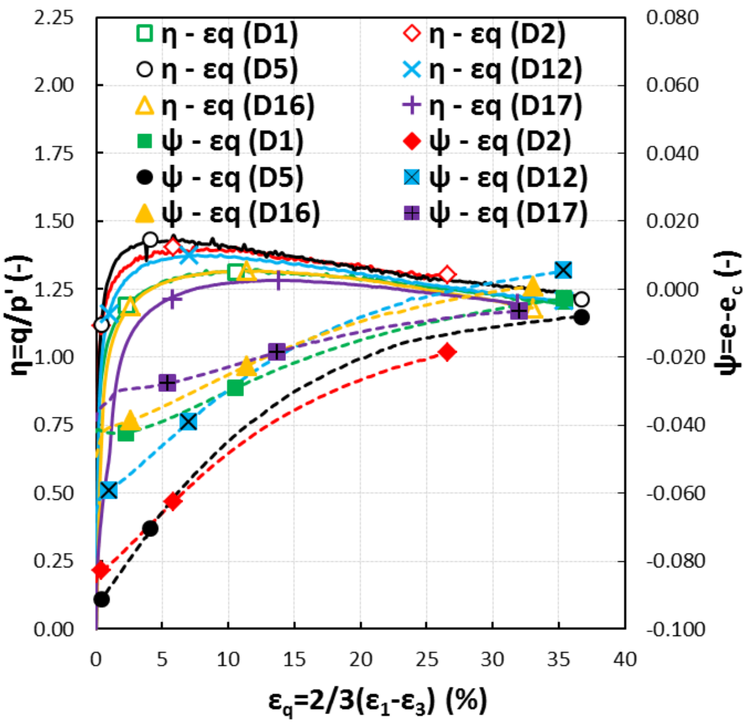

Fig. 6.18 Evolution of η and ψ with ε_q for M31 Sand subjected to drained loading

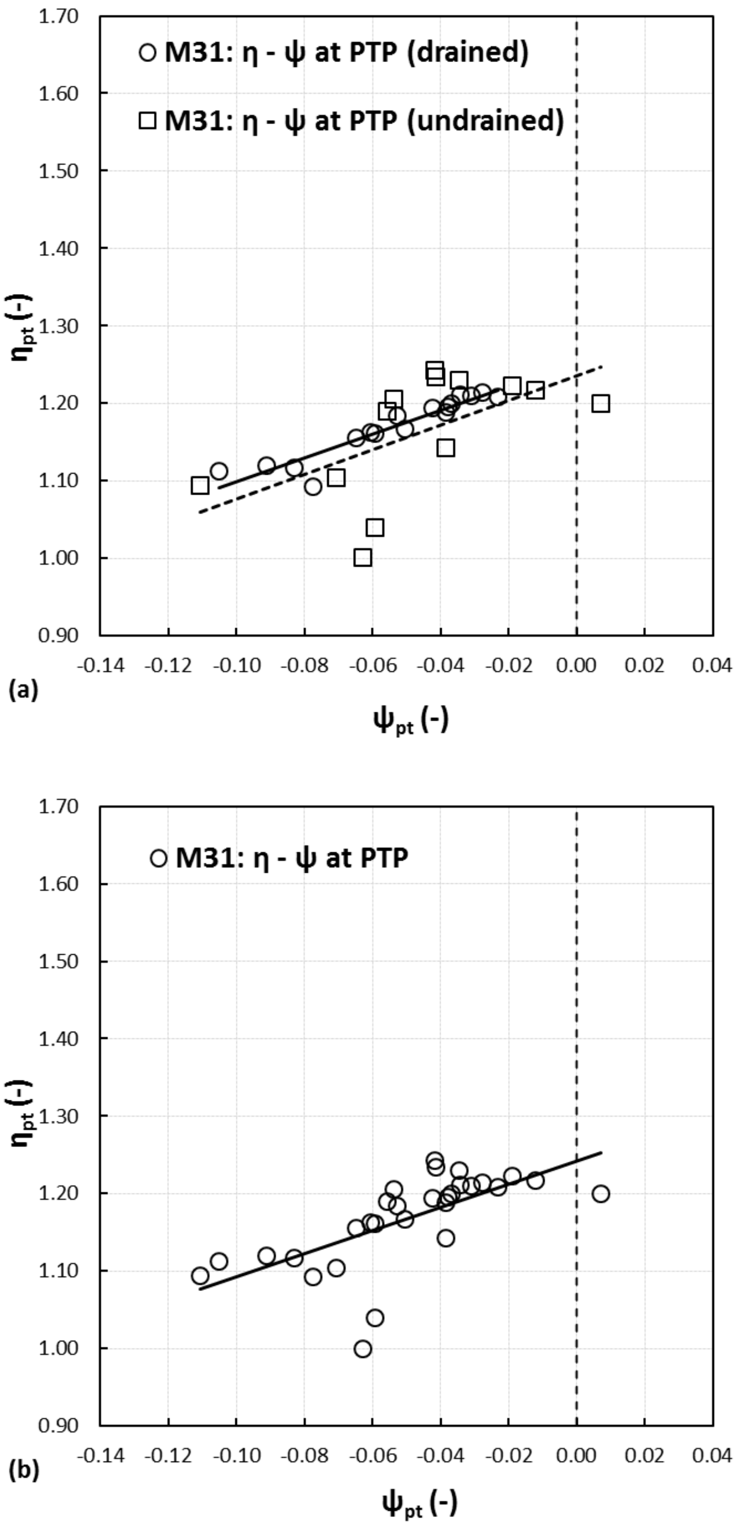

Fig. 6.19 Stress ratio η against the state parameter ψ at phase transformation for M31 Sand subjected to drained and undrained loading. **a** Different sets of data points in drained or undrained loading mode and corresponding trend lines. **b** One set of data points in drained and undrained loading mode and corresponding trend line

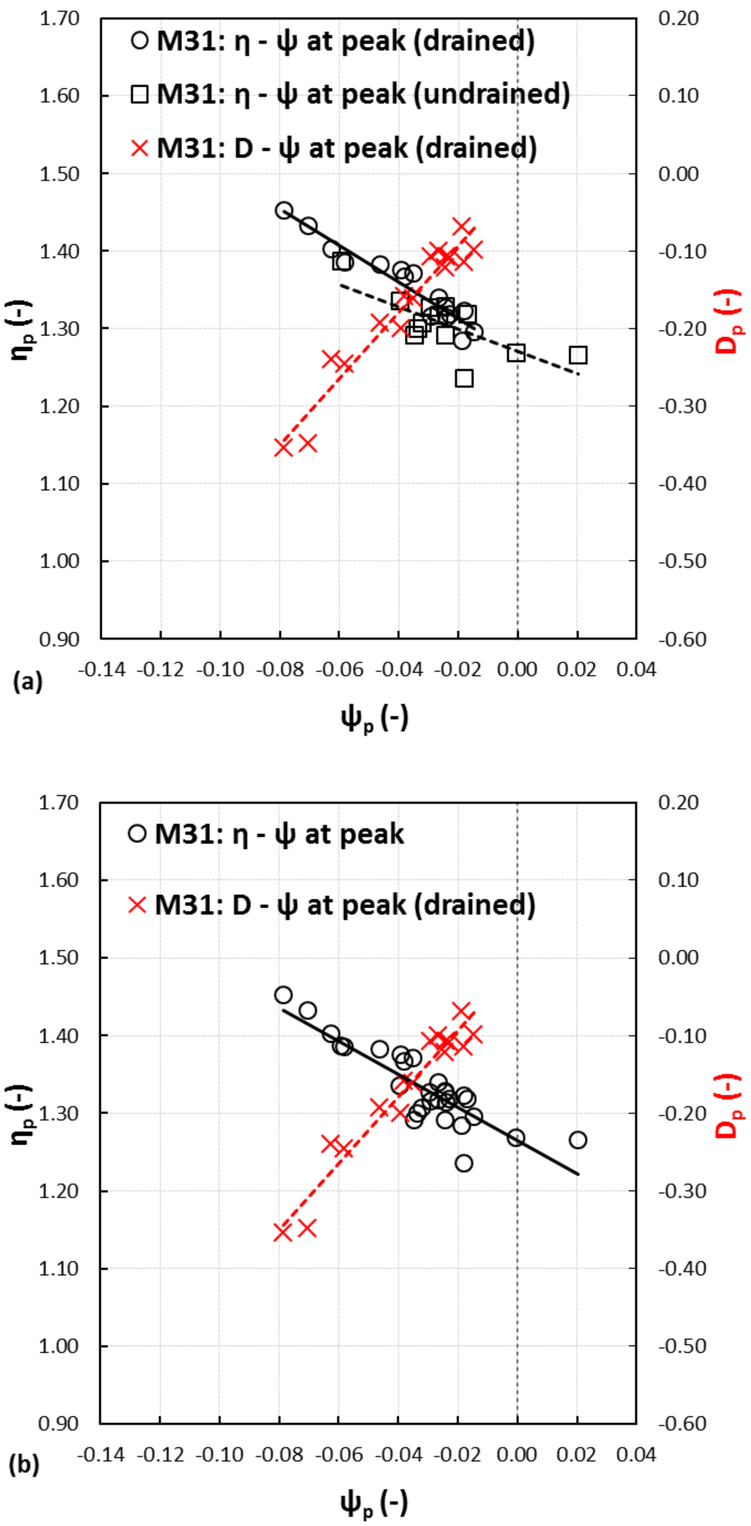

Fig. 6.20 Stress ratio η and dilatancy ratio D against the state parameter ψ at peak failure for M31 Sand subjected to drained and undrained loading. **a** Different sets of data points in drained or undrained loading mode and corresponding trend lines. **b** One set of data points in drained and undrained loading mode and corresponding trend line

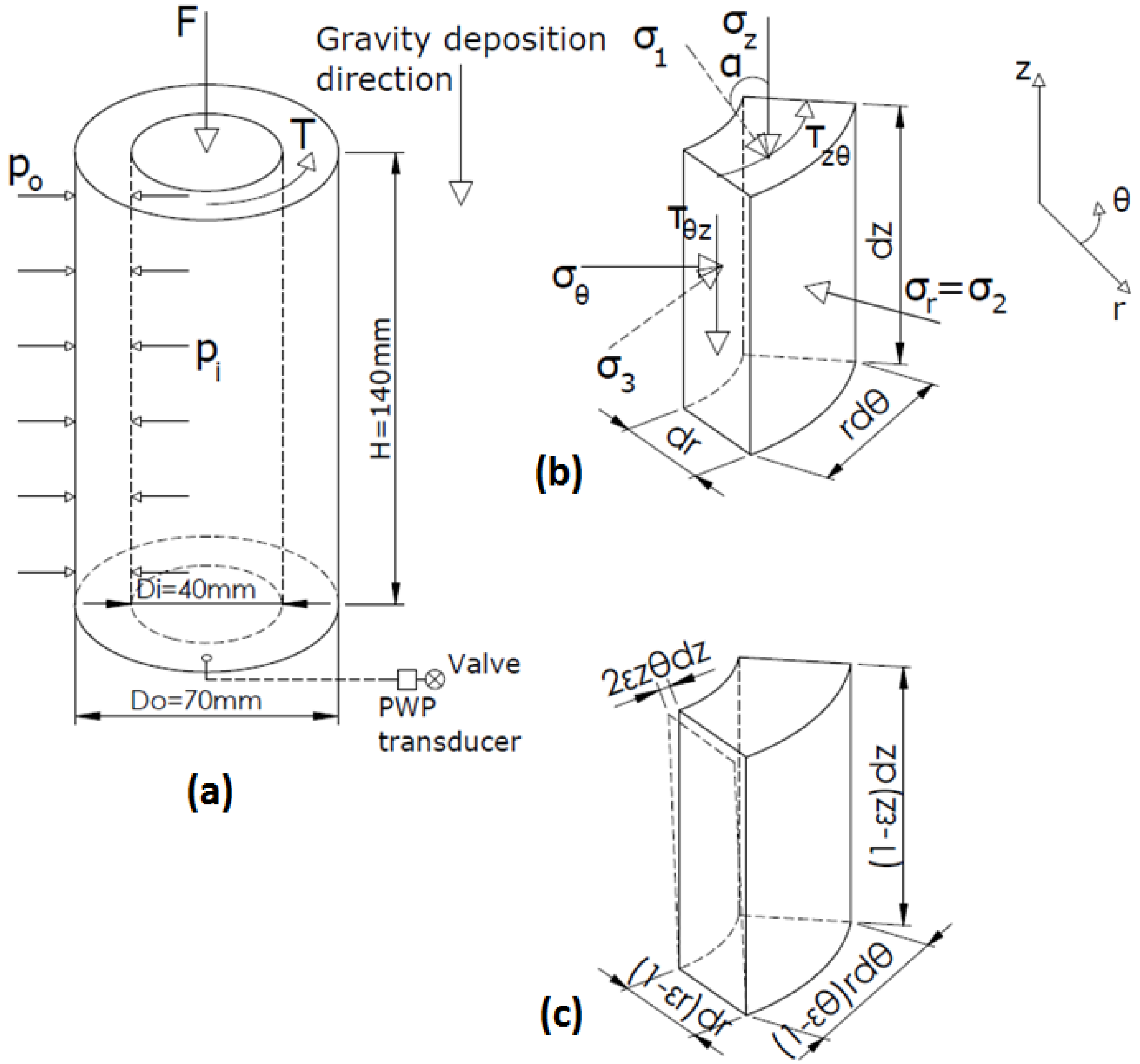

Fig. 6.21 a Hollow cylindrical specimen and applied boundary loads. **b** Stress components on the undeformed soil element. **c** Strain components associated with the combined multiaxial and torsional deformation

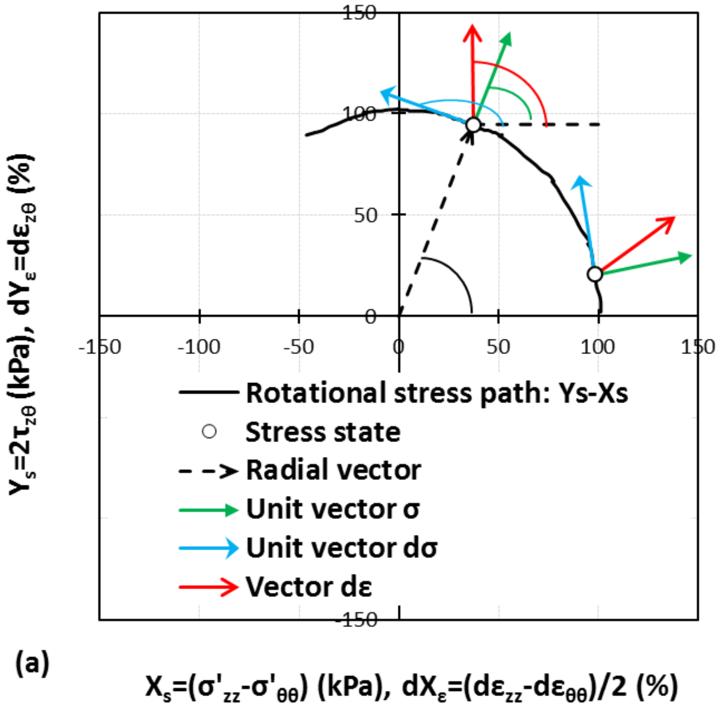

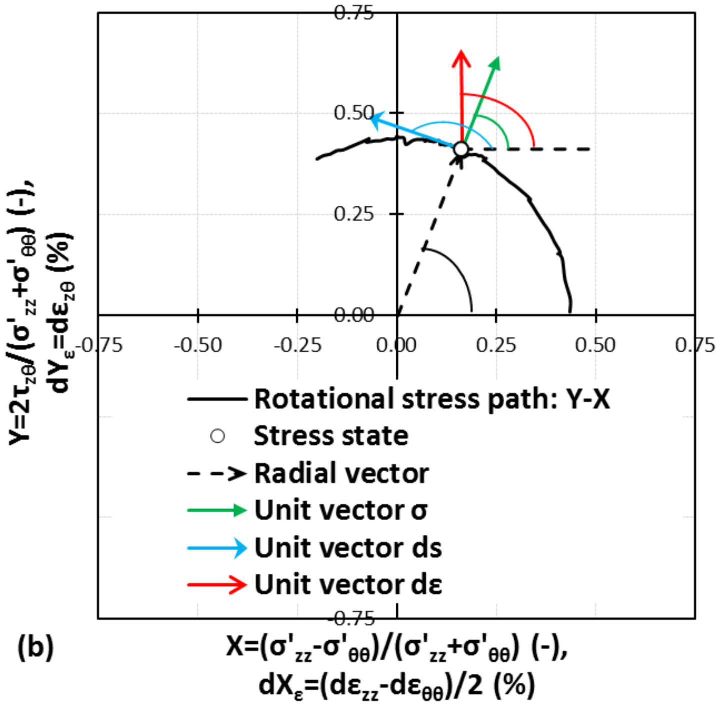

Fig. 6.22 Stress path and directions of principal stress, stress rate and strain rate: **a** in the Y_s - X_s deviatoric plane and **b** in the Y - X deviatoric plane. The axes dX_ε and dY_ε are superimposed on a given stress state to offer the reference frame for determining the direction angle $\alpha_{d\varepsilon 1}$ of the axis of the rate of principal strain dε_1

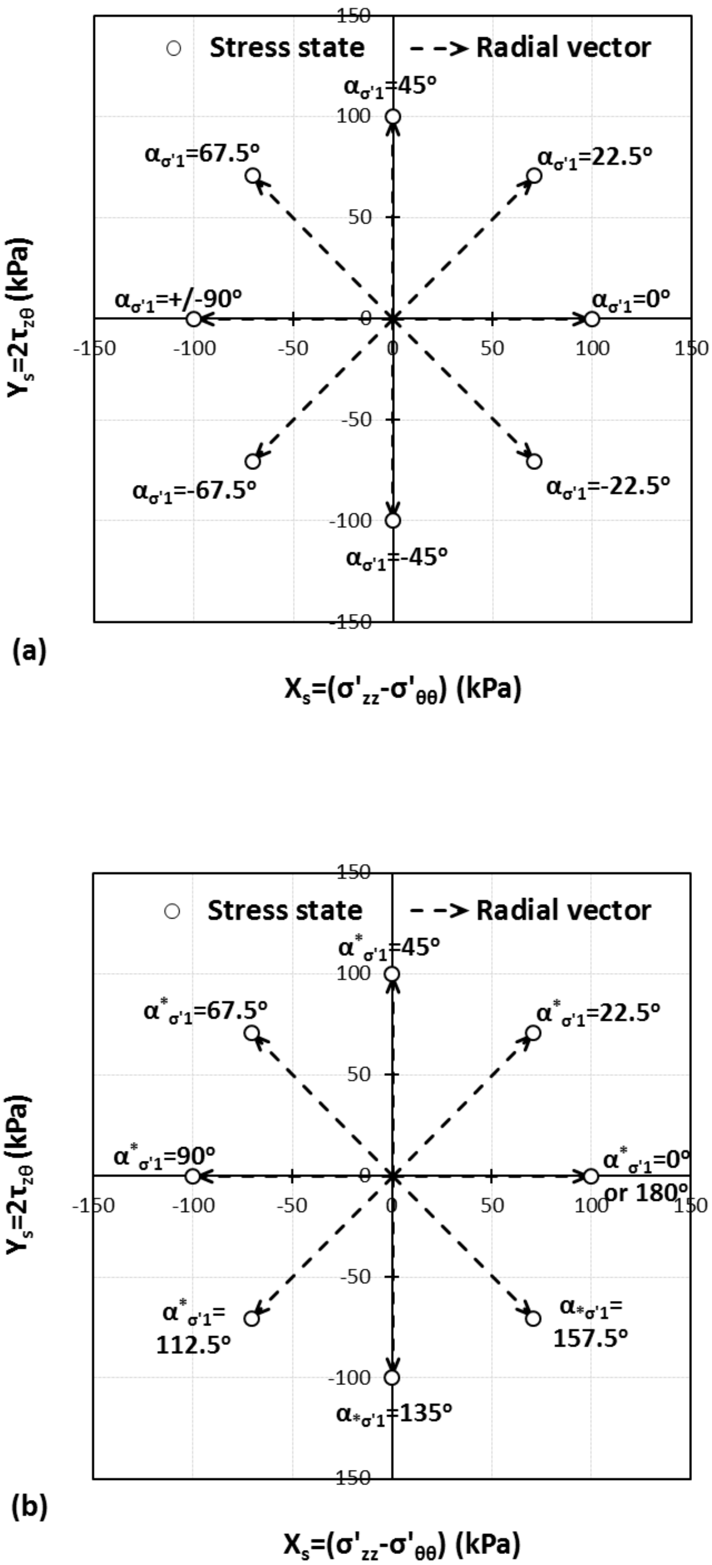

Fig. 6.23 Value and sign of the stress direction angles $\alpha_{\sigma'1}$ and $\alpha^*_{\sigma'1}$ in the Y_s - X_s deviatoric plane

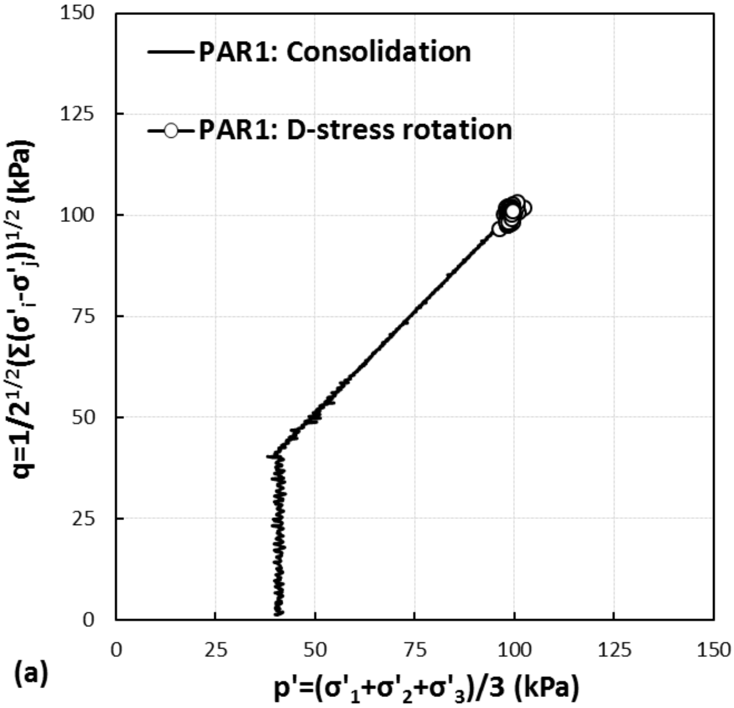

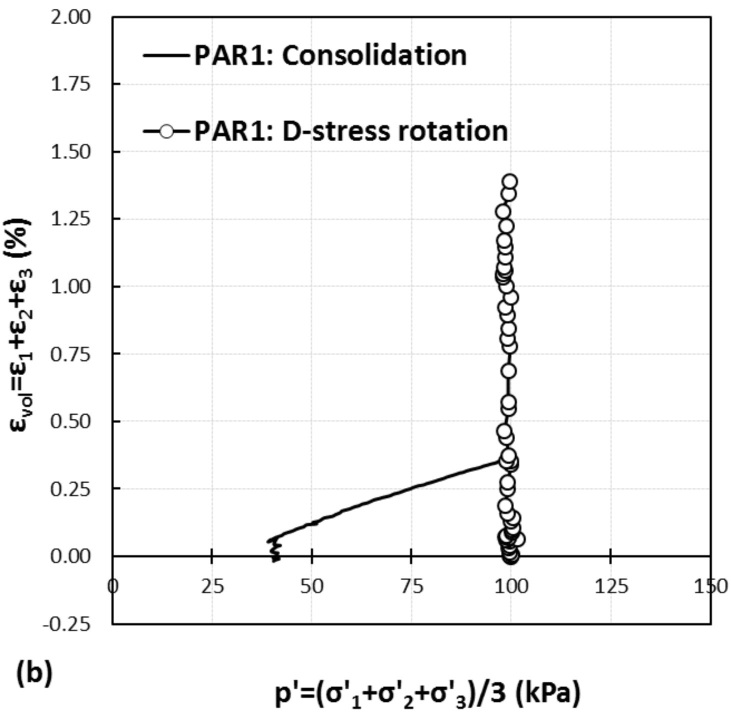

Fig. 6.24 M31 Sand subjected to anisotropic consolidation and stress principal axes rotation at η = 1.00. **a** Effective stress path in the q - p' plane. **b** Volumetric strain, ε_{vol}, against mean effective stress, p' (**c** on next page)

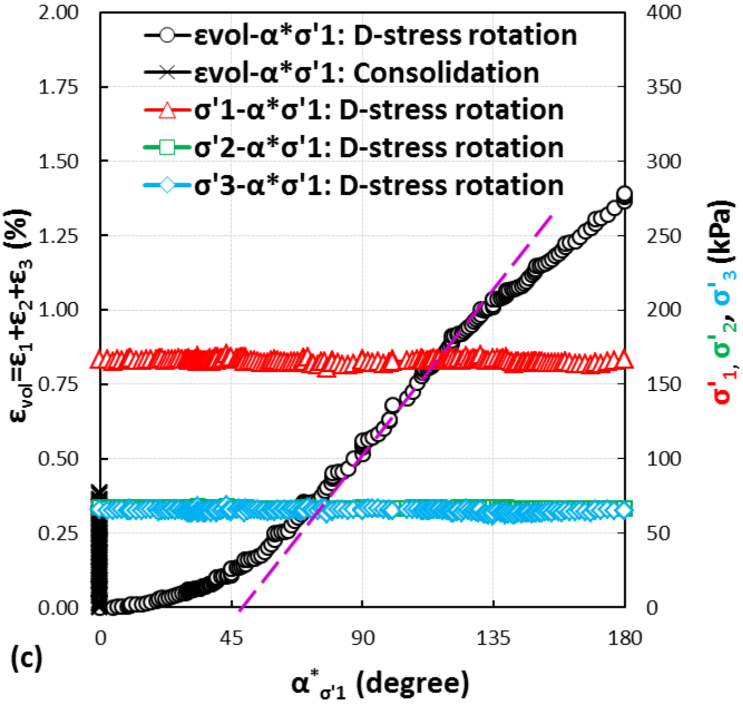

Fig. 6.24 M31 Sand subjected to anisotropic consolidation and stress principal axes rotation at η = 1.00. **c** Volumetric strain, ε_{vol}, and magnitude of effective principal stresses, σ'_1, σ'_2 and σ'_3, against principal stress direction angle, $\alpha^*_{\sigma'1}$

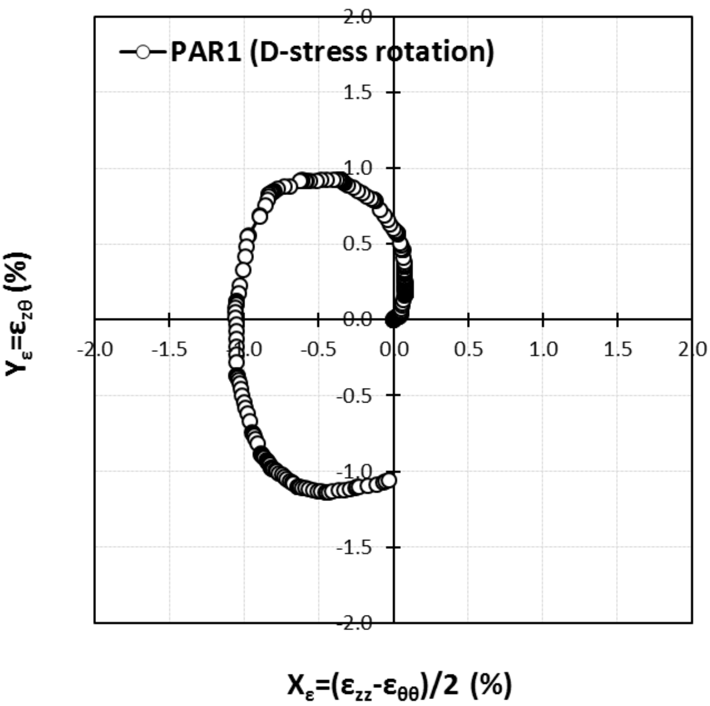

Fig. 6.25 Strain path in the deviatoric strain plane from stress rotation test on M31 Sand

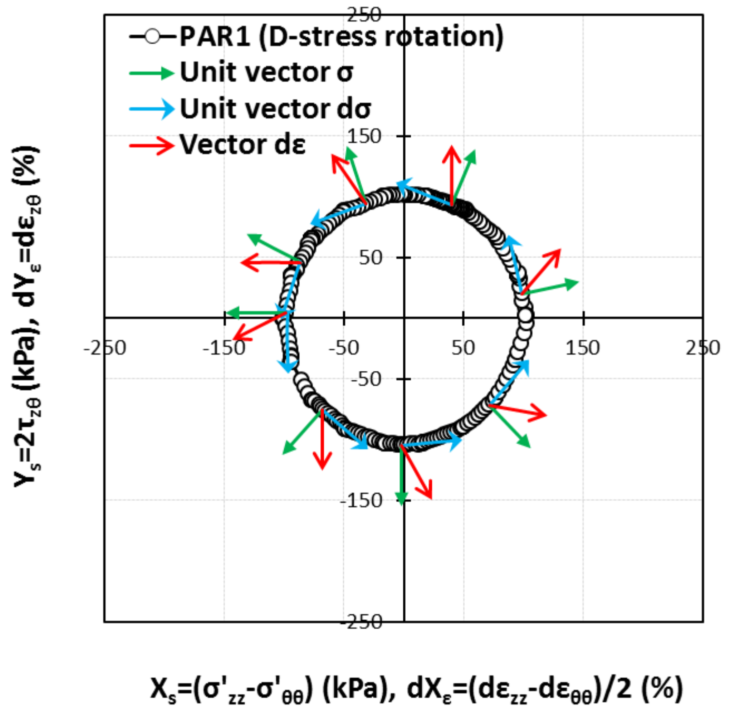

Fig. 6.26 Stress path in the deviatoric stress plane from stress rotation test on M31 Sand. The unit vectors indicate the directions of principal stress, rate of principal stress and rate of principal strain at various stress states

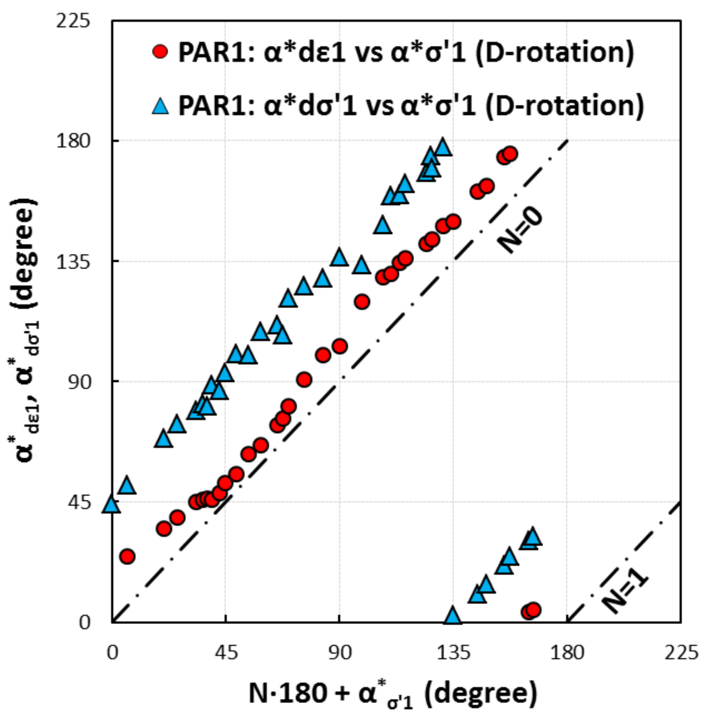

Fig. 6.27 Relationship between the direction angles of principal stress, rate of principal stress and rate of principal strain during the first cycle of rotation of the stress principal axes (N = 0)

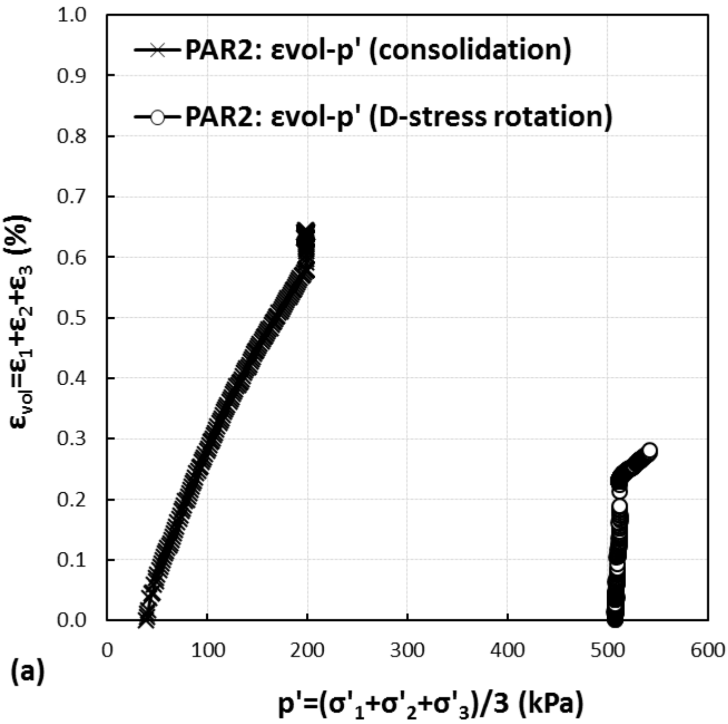

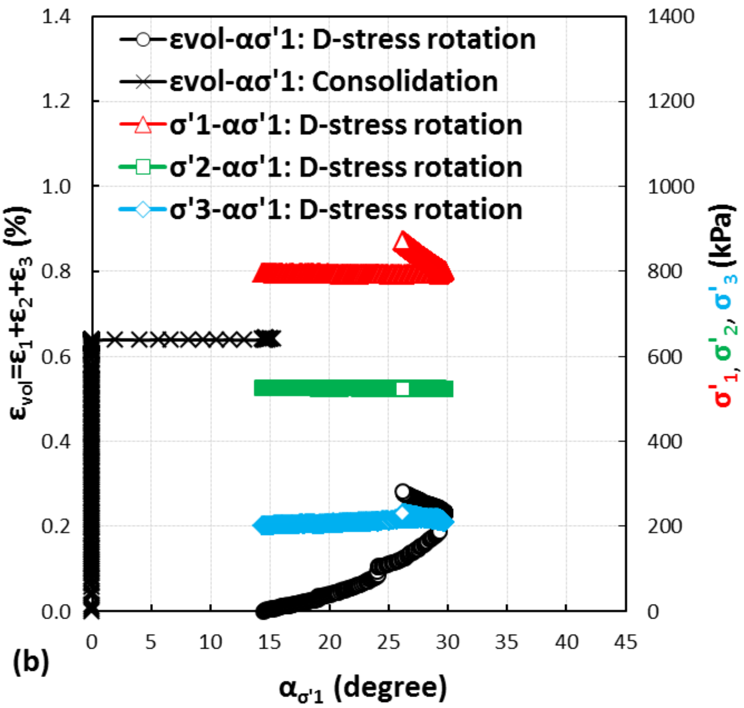

Fig. 6.28 Volume change behaviour of M31 Sand during isotropic consolidation and stress rotation. **a** Volumetric strain against mean effective stress. **b** Volumetric strain and magnitude of the effective principal stresses against principal stress direction angle

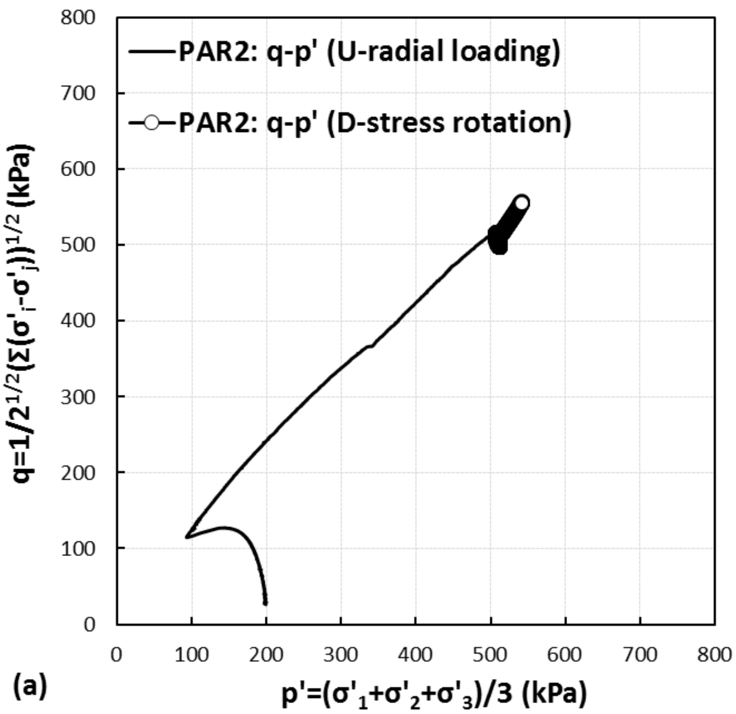

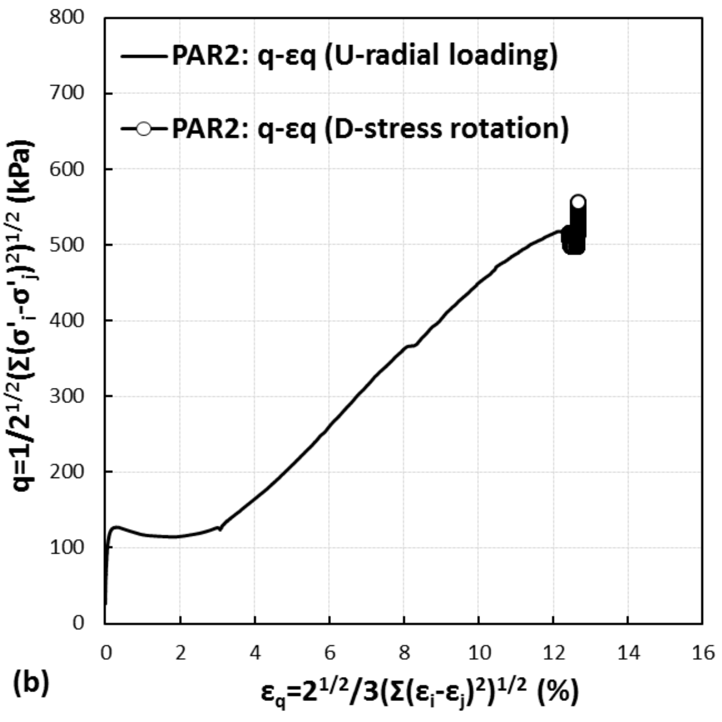

Fig. 6.29 M31 Sand subjected to undrained radial loading followed by drained stress rotation. **a** Effective stress path in the q - p' plane. **b** Stress - strain curve in the q - ε_q plane (**c** on next page)

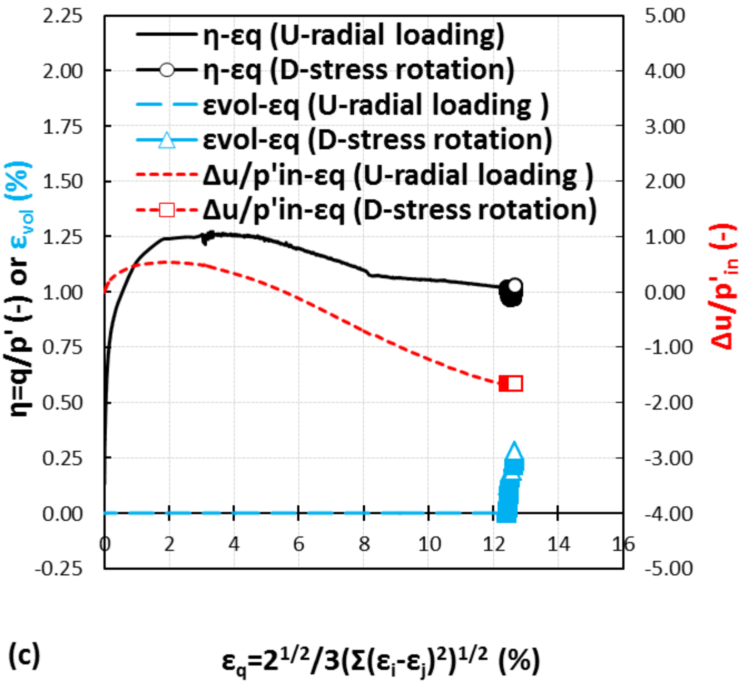

Fig. 6.29 M31 Sand subjected to undrained radial loading followed by drained stress rotation. **c** Evolution of stress ratio, η, normalised excess pore-water pressure, $\Delta u\ /\ p'_{in}$, and volumetric strain, ε_{vol}, with deviatoric strain, ε_q

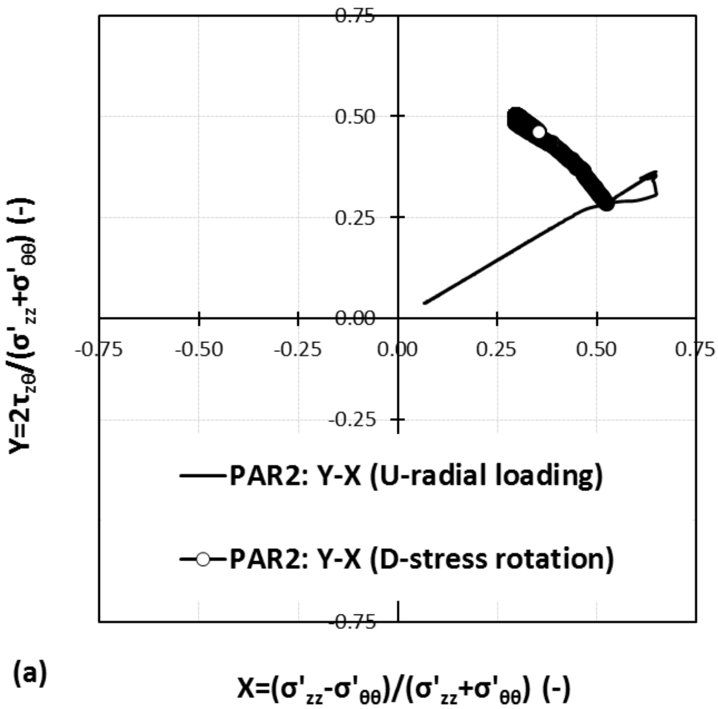

Fig. 6.30 M31 Sand subjected to undrained radial loading followed by drained stress rotation. **a** Stress path in the deviatoric stress plane (**b** on next page)

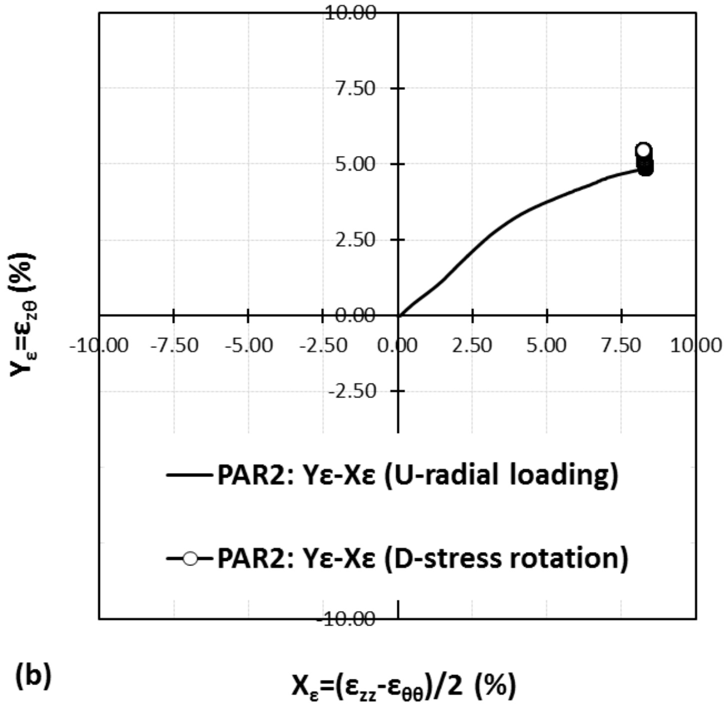

Fig. 6.30 M31 Sand subjected to undrained radial loading followed by drained stress rotation. **b** Strain path in the deviatoric strain plane

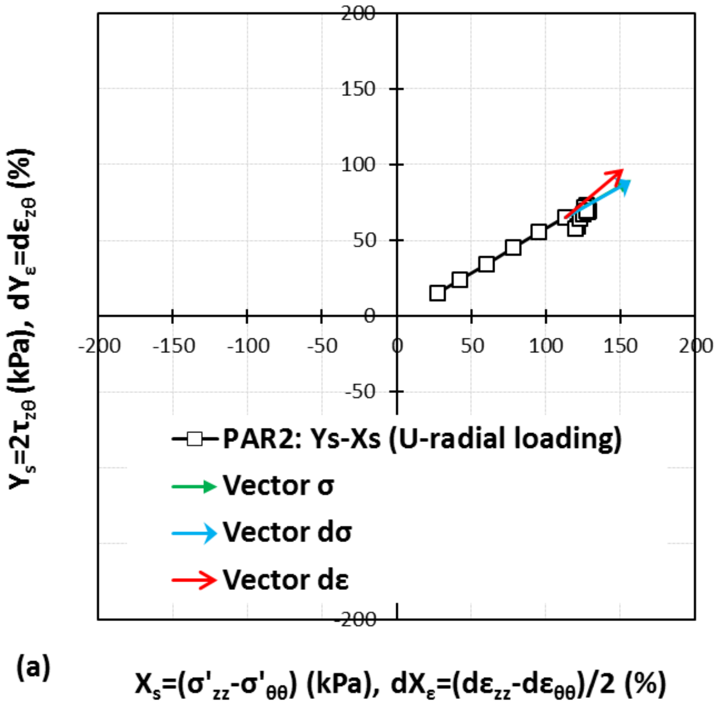

Fig. 6.31 Flow deformation of M31 Sand subjected to undrained radial loading. **a** Direction of principal stress, stress rate and strain rate at a stress state just before the onset of flow (**b** and **c** on next page)

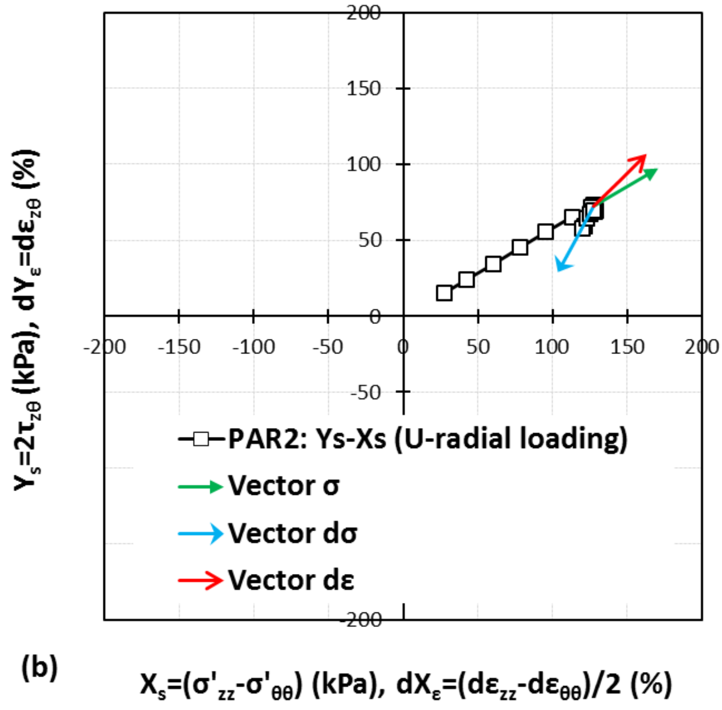

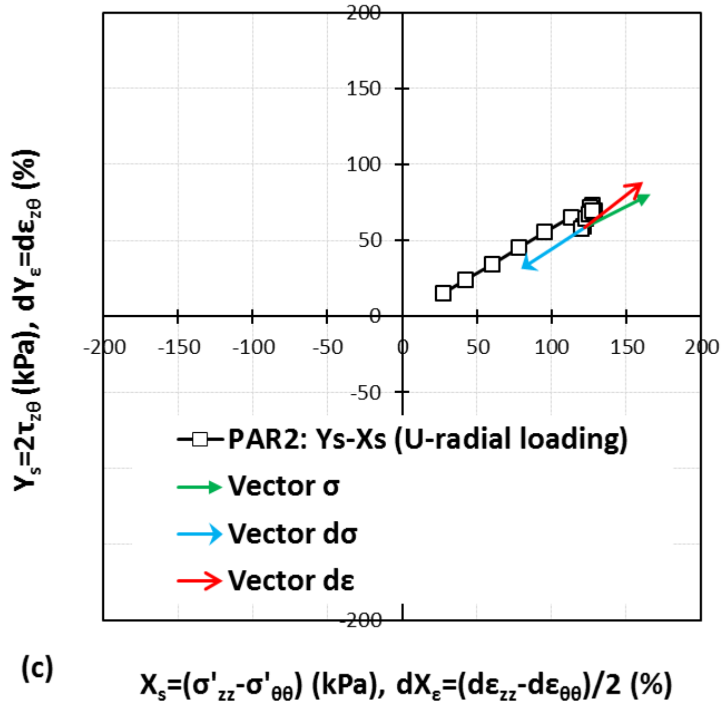

Fig. 6.31 Flow deformation of M31 Sand subjected to undrained radial loading. **b** Direction of principal stress, stress rate and strain rate at the onset of flow deformation. **c** Direction of principal stress, stress rate and strain rate during flow deformation

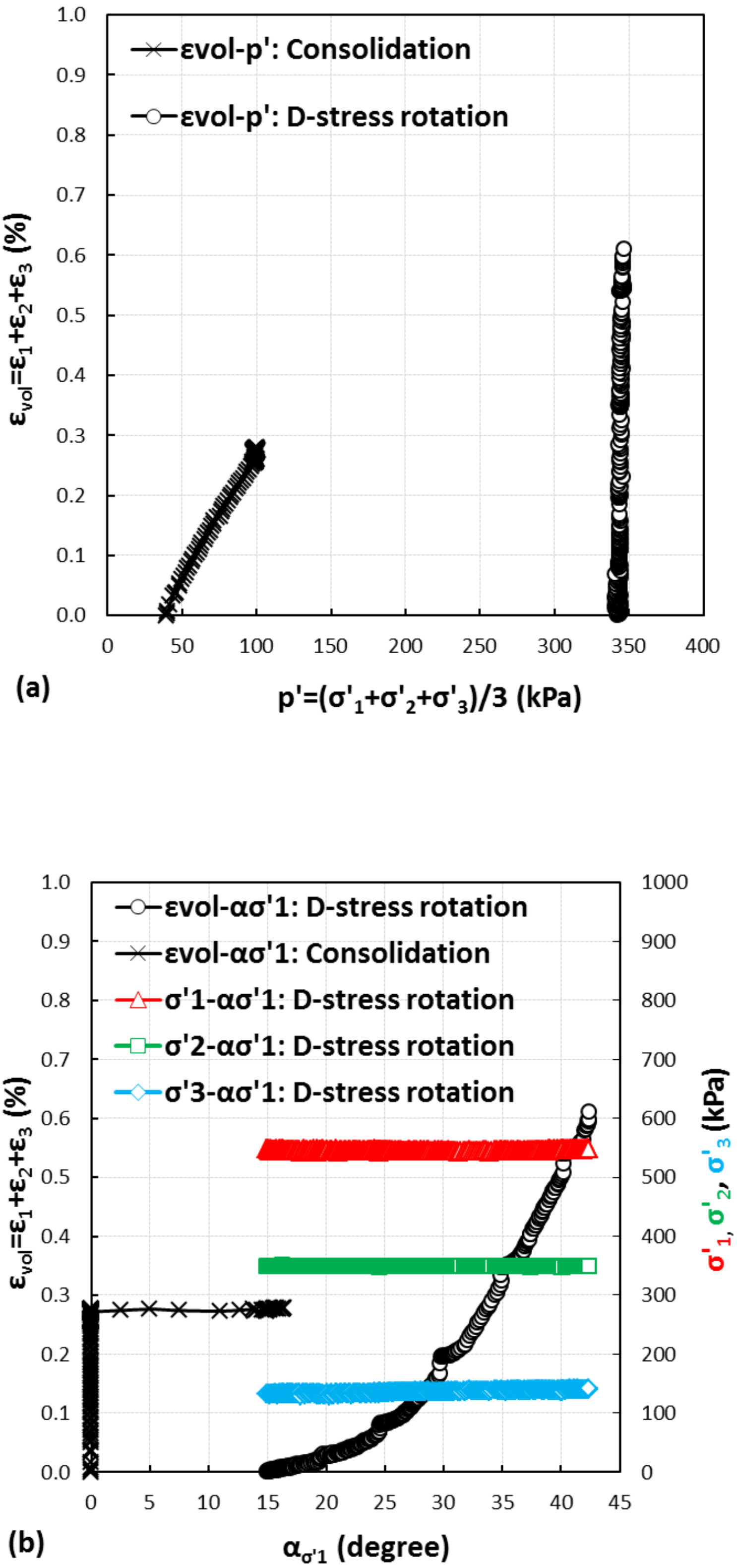

Fig. 6.32 Volume change behaviour of M31 Sand during isotropic consolidation and stress rotation. **a** Volumetric strain against mean effective stress. **b** Volumetric strain and magnitude of effective principal stresses against principal stress direction angle

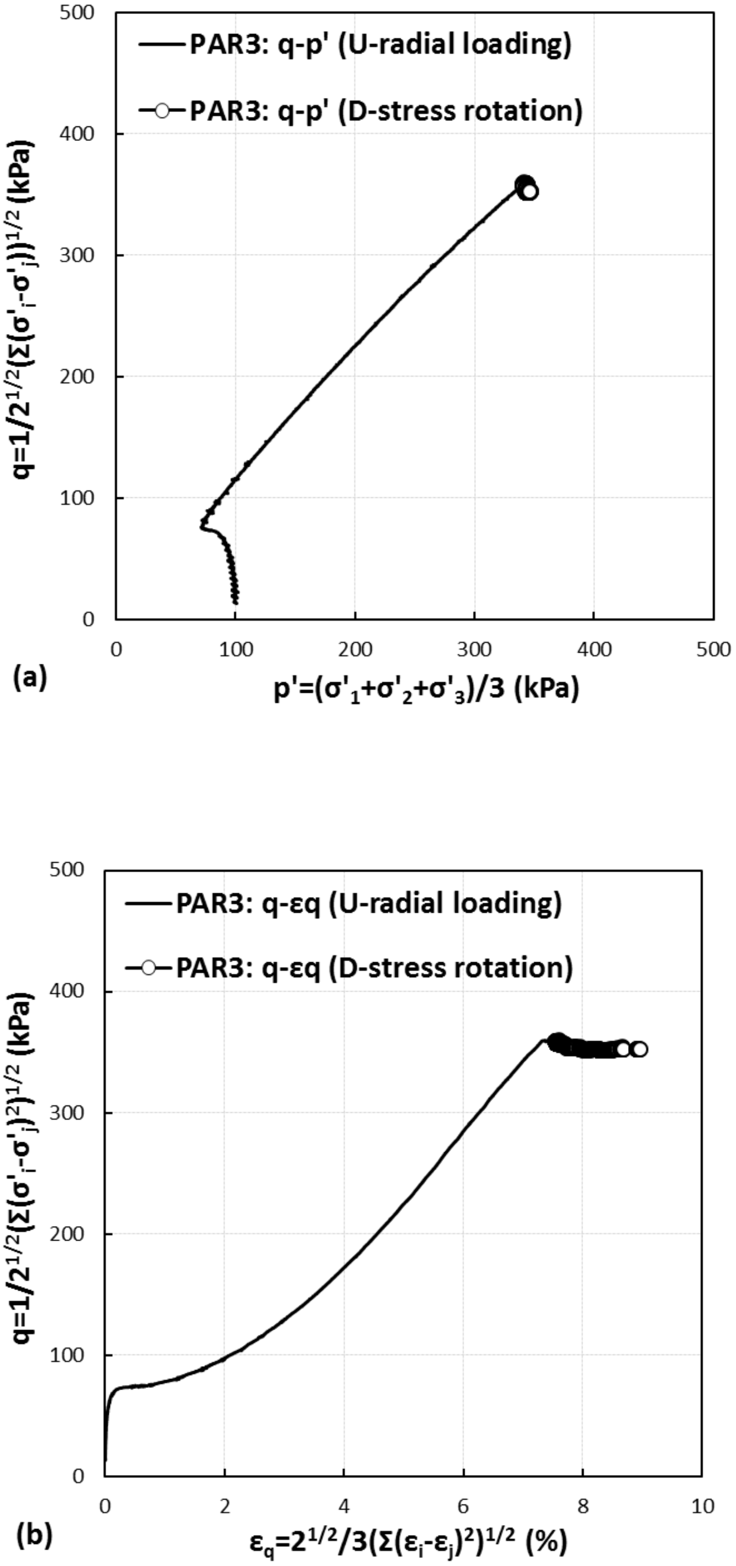

Fig. 6.33 M31 Sand subjected to undrained radial loading followed by drained stress rotation. **a** Effective stress path in the q - p' plane. **b** Stress - strain curve in the q - ε_q plane (**c** on next page)

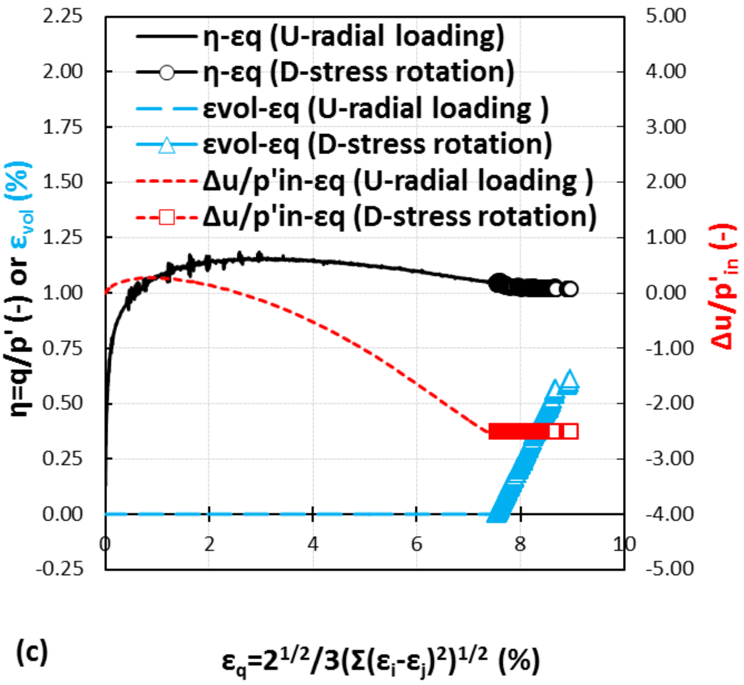

Fig. 6.33 M31 Sand subjected to undrained radial loading followed by drained stress rotation. **c** Evolution of stress ratio, η, normalised excess pore-water pressure, $\Delta u\ /\ p'_{in}$, and volumetric strain, ε_{vol}, with deviatoric strain, ε_q

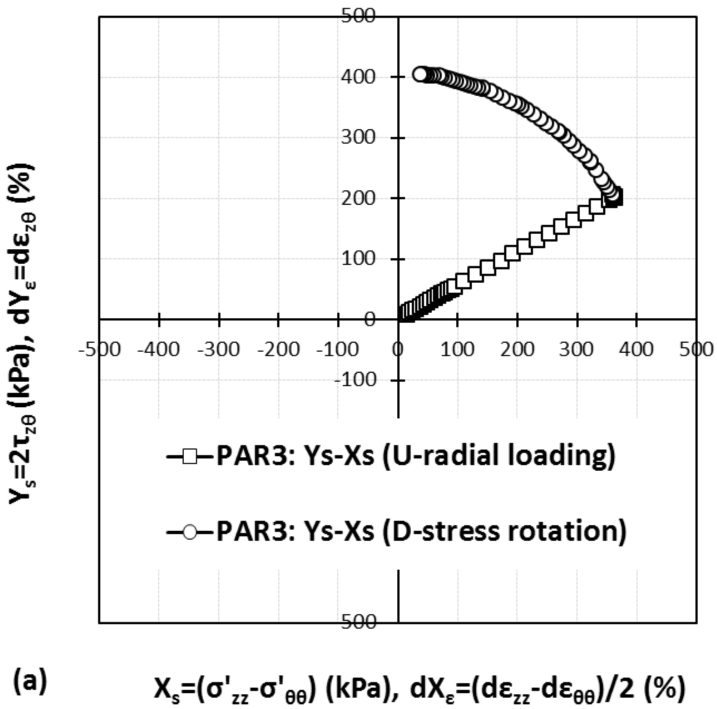

Fig. 6.34 M31 Sand subjected to undrained radial loading followed by drained stress rotation. **a** Stress path in the deviatoric stress plane (**b** on next page)

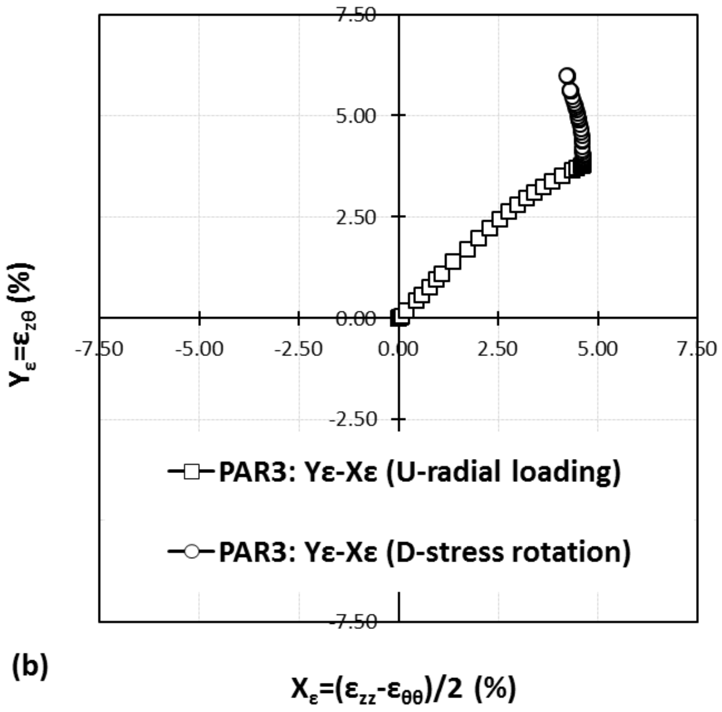

Fig. 6.34 M31 Sand subjected to undrained radial loading followed by drained stress rotation. **b** Strain path in the deviatoric strain plane

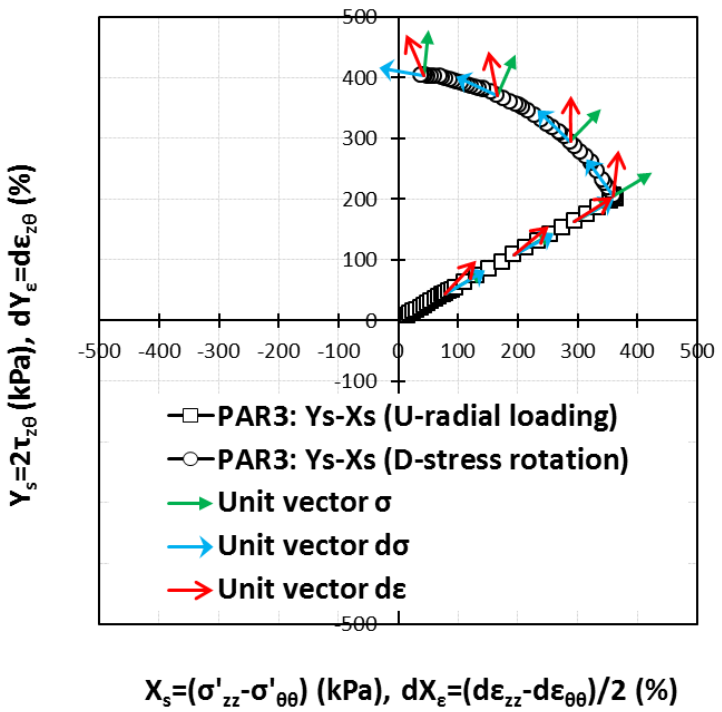

Fig. 6.35 Non-coaxiality of M31 Sand subjected to undrained radial followed by drained stress rotation. The unit vectors superimposed on various stress states in the deviatoric stress plane indicate the direction of principal stress, rate of principal stress and rate of principal strain

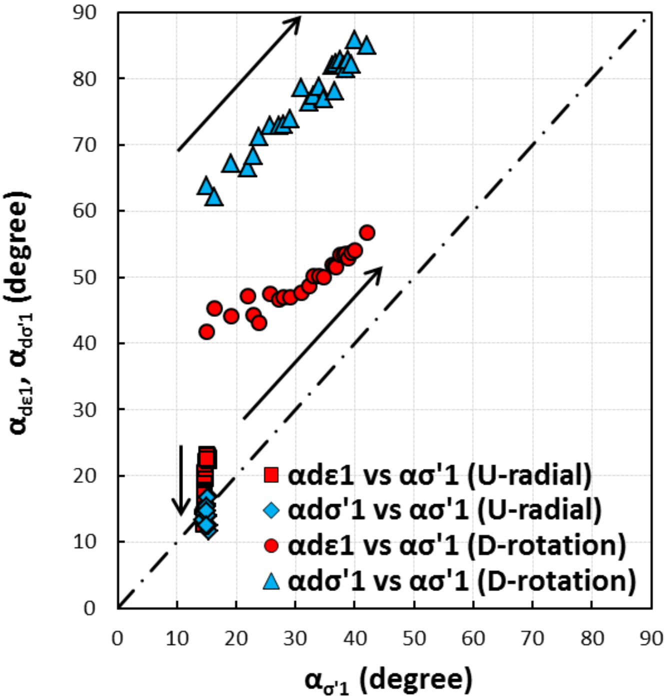

Fig. 6.36 Non-coaxiality of M31 Sand subjected to undrained radial followed by drained stress rotation: relationship between the direction angles of principal stress, rate of principal stress and rate of principal strain

Fig. 6.37 Squat specimen with a height to outer diameter ratio of 1:1 bulged under drained triaxial compression

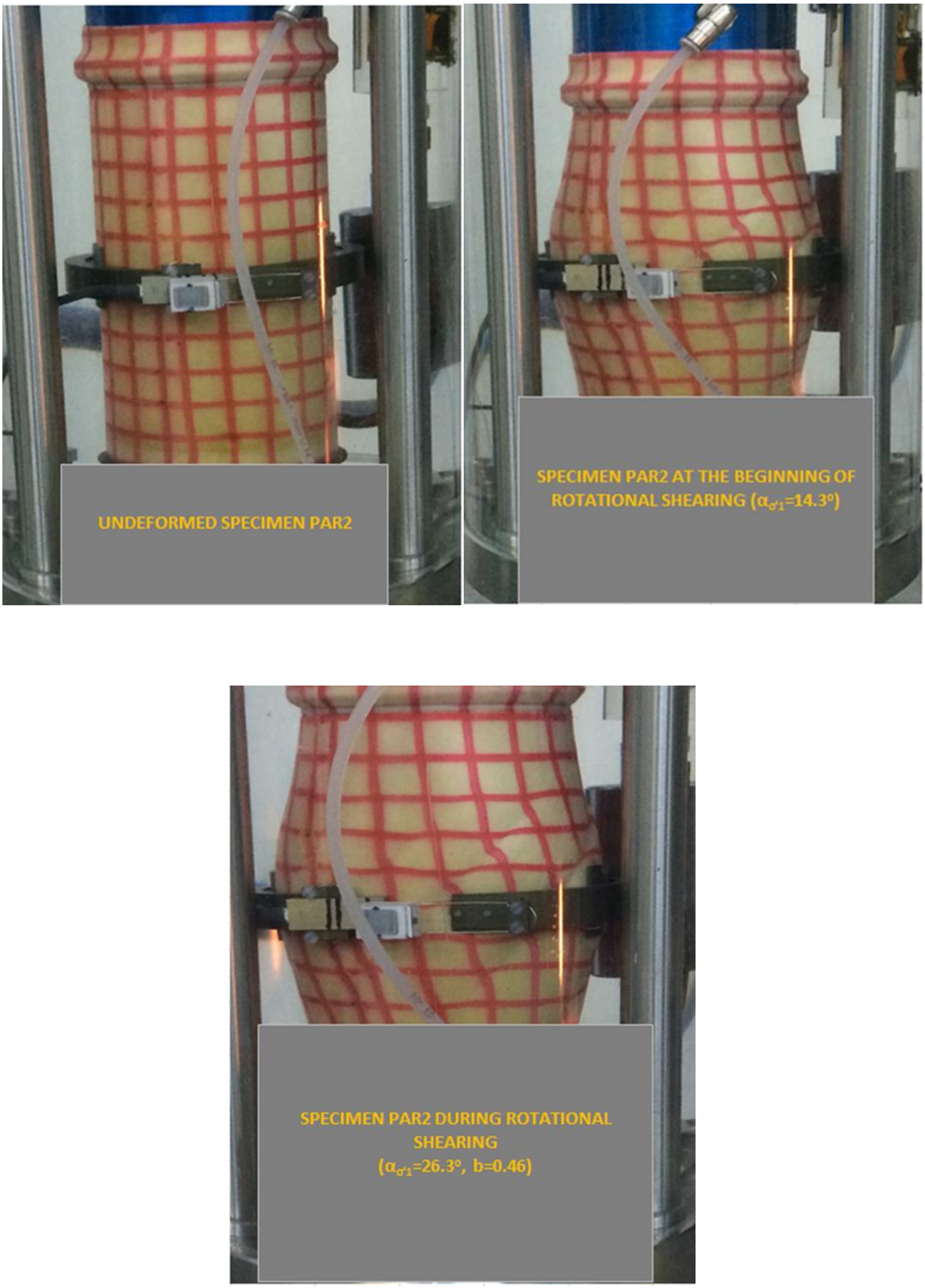

Fig. 6.38 Deformation of specimen PAR2 at the beginning and at the end of stress principal axes rotation. The photos were taken under the refraction induced by the crossing of light through the water-perspex-air interfaces

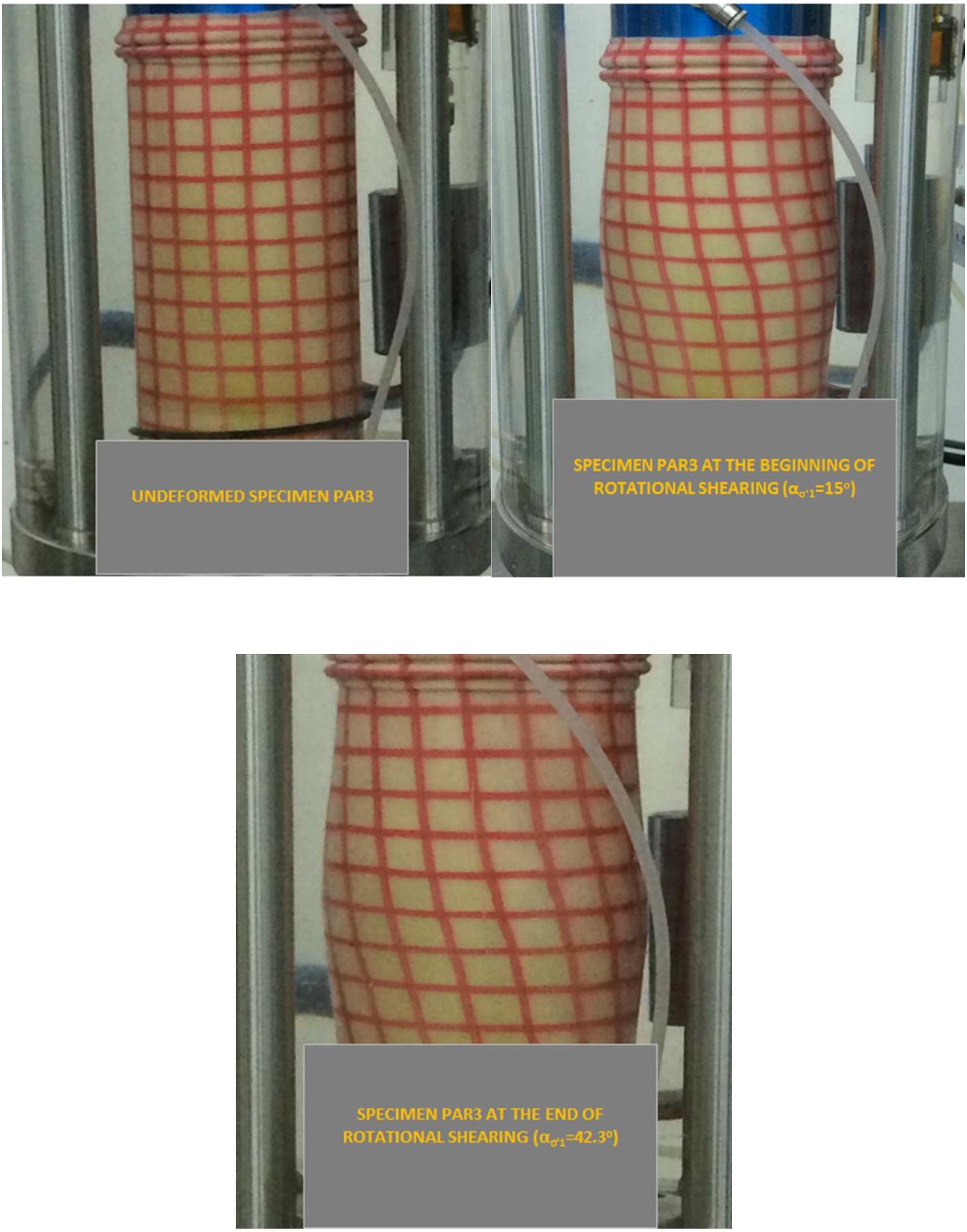

Fig. 6.39 Deformation of specimen PAR3 at the beginning and at the end of stress principal axes rotation. The photos were taken under the refraction induced by the crossing of light through the water-perspex-air interfaces

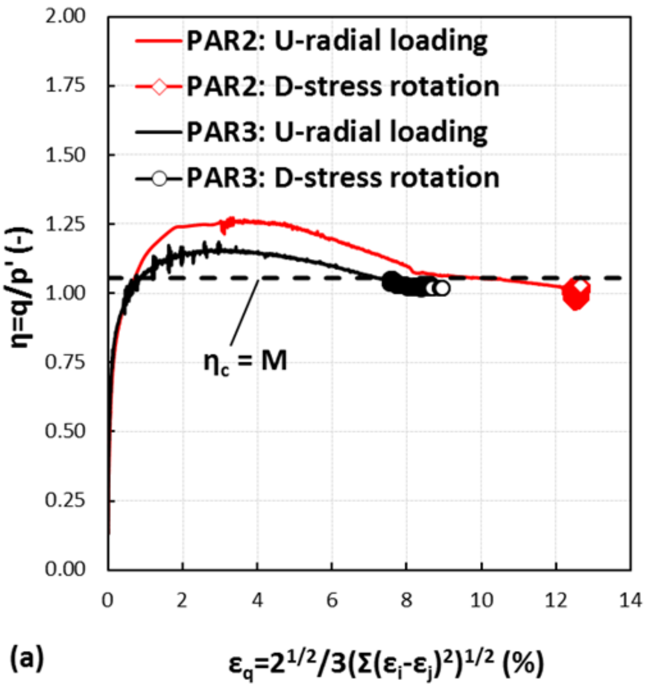

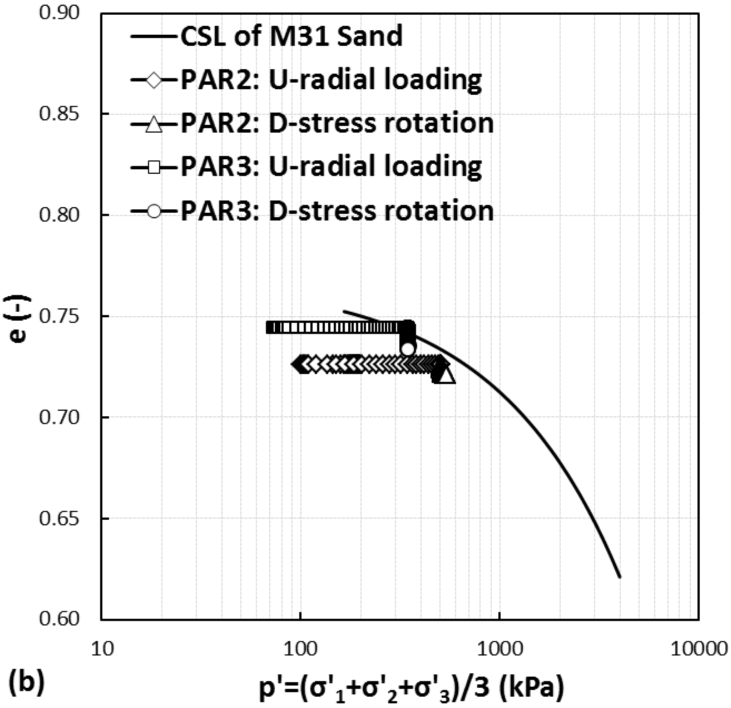

Fig. 6.40 Undrained radial loading followed by drained stress rotation in tests PAR2 and PAR3. **a** Evolution of stress ratio. **b** Evolution of state in relation to the critical state line of M31 Sand determined in triaxial compression mode

CHAPTER 7: ANISOTROPIC FLOW DEFORMATION OF M31 SAND

7.1 INTRODUCTION

The anisotropic behaviour of M31 Sand under generalised undrained loading is investigated in the hollow cylinder apparatus. The testing programme includes radial loading along different fixed directions of the stress principal axes, corresponding to both compressive and extensive directions with respect to the horizontal bedding plane, as well as loading that imposes rotation of the stress principal axes. The mean total stress, *p*, and the intermediate principal stress parameter, *b*, are kept constant in each test, with the latter parameter having a common value in all tests. The deviatoric stress is either increased monotonically, kept fixed or changed periodically during the rotation of the stress principal axes. The dependence of the conditions that trigger the unstable flow deformation of sand on the inherent anisotropy and stress - strain history is investigated. The experimental results of this macroscopic study are interpreted using the core principles of the Bifurcation Theory and an effort is made to shed light on the effects of the inherent anisotropy on the diffuse and localised unstable bifurcations under various stress - strain histories.

7.2 APPARATUS, MATERIALS AND TESTING TECHNIQUES

Details concerning the tested materials, the specimen preparation method and the apparatus used in the loading tests are given in Chapter 5 and in the article by Triantafyllos et al. (2020) presented in the Appendix. It is noted that the loading tests were performed on water-pluviated and saturated sand specimens in the hollow cylinder apparatus (HCA), in a stress-controlled loading mode at a constant rate of stress, using pneumatic pistons, flexible air-water interfaces and electric servo controllers to apply the pressures and loads. The control of stresses achieved in the HCA allows a variety of unstable bifurcations of deformation to occur, as described in the article by Triantafyllos et al. (2020). Details concerning the experimental and theoretical investigation of bifurcations in geomaterials are given in the literature review presented in Sections 2.9 and 4.5, while a comprehensive treatise on this subject is given by Vardoulakis and Sulem (1995). The hollow cylinder apparatus was upgraded in order to achieve the independent control of the three effective stress principal values (PV) and of the direction of the major and minor stress principal axes (PA).

7.3 BOUNDARY LOADS, STRESSES AND STRAINS IN A HOLLOW CYLINDRICAL SPECIMEN SUBJECTED TO GENERALISED LOADING

The model hollow cylindrical specimen shown in Fig. 7.1a has a height of H = 140 mm, an inner radius of R_i = 20 mm and an outer radius of R_o = 35 mm, occupying a volume of V = 363 cc; the small letters h, r_i and r_o symbolise the current value of the respective length dimension during consolidation, pre-shearing or shearing. p_i is the cell pressure applied inside the hollow cylinder, p_o is the cell pressure applied outside the hollow cylinder, while F and T are the vertical load and torque, respectively, applied on the upper horizontal surface of the hollow cylinder by means of a vertical loading ram, which may move vertically and rotate. u is the pore-water pressure, v is the vertical displacement of the vertical loading ram, θ is the torsional angle (or the angular displacement) of the moving platen placed on top of the specimen with respect to the fixed pedestal and ΔV is the volume change of the specimen. The boundary stresses are imposed by means of pneumatic pistons and flexible air-water interfaces located away from the membranes of the submerged specimen under the isochoric constraint, due to undrained conditions, allowing the occurrence of unrestrained flow deformation.

The vertical load, F, and torque, T, are measured inside the triaxial cell using a toque - load cell while the buoyancy and gravity forces that act upon the vertical loading ram are automatically counterbalanced at all times by the servo-controller that moves the servo-valves to adjust the applied pressures. The pore-water pressure, u, is measured using a pressure transducer placed in the hydraulic line connected to the bottom platen (pedestal) of the specimen, as shown in Fig. 7.1a, while the outer cell pressure, p_o, and the inner cell pressure, p_i, are measured using two other pressure transducers. The torsional angle, θ, is measured inside the triaxial cell using a potentiometer placed in contact with the rigid connector between the top platen of the specimen and the loading ram. The vertical displacement, v, is measured outside the triaxial cell using a dial gauge placed in contact with the rigid loading ram. The volume change, ΔV, is measured using a burette and a differential pressure transducer. The data are recorded with a frequency, f, as high as 5 Hz in order to capture the high-velocity response whenever flow deformation occurs.

Figure 7.1 shows the boundary loads applied on the hollow cylindrical specimen (a), the stress components on the undeformed soil element (b) and the strain components associated with the combined multiaxial and torsional deformation (c). The equations used to calculate the average stresses σ_{zz}, $\sigma_{\theta\theta}$, σ_{rr}, $\tau_{z\theta}$, σ_1, σ_2, and σ_3 and the associated strains ε_{zz}, $\varepsilon_{\theta\theta}$, ε_{rr}, $\varepsilon_{z\theta}$, ε_1, ε_2, and ε_3 are presented in Table 7.1 and the derivation of these equations is discussed in detail in Chapter 5. The assumption of equal horizontal normal strains, $\varepsilon_{\theta\theta} = \varepsilon_{rr}$, is made (Tatsuoka et al. 1986), while in some cases, explicitly mentioned in the text, the radial strain is assumed to be equal to zero, $\varepsilon_{rr} = 0$ (plane-strain deformation). The current area of the cross section of the specimen is used to calculate the average stresses, while the stresses induced due to the elastic stretching of the membranes are taken into account during the data processing using the methodology proposed by Tatsuoka et al. (1986). However, the Labview software that interacts with the servo-controllers and the servo-valves in order to impose the target stresses does not account for either the membrane stresses or the change in the current area of the specimen's cross section that affects the value of the imposed stresses. This type of stress control becomes less accurate as the strains become larger, because the imposed stresses differ compared to the target stresses, yet the loading system is protected from catastrophic instabilities.

The angle between the axis of the major principal stress σ'_1 and the vertical (z-axis), shown in Fig. 7.1b, is termed the principal stress direction angle and is symbolised with α or $\alpha_{\sigma'1}$, while the angle of the axis of the rate (or increment) $d\sigma'_1$ to the vertical is symbolised with $\alpha_{d\sigma'1}$; it is noted that the direction of gravity is along the vertical and the bedding plane of the specimen is expected to be horizontal. The relationships $\tan 2\alpha_{\sigma'1} = 2\tau_{z\theta} / (\sigma'_{zz} - \sigma'_{\theta\theta})$ and $\tan 2\alpha_{d\sigma'1} = 2d\tau_{z\theta} / (d\sigma'_{zz} - d\sigma'_{\theta\theta})$ are used to compute analytically the angles $\alpha_{\sigma'1}$ and $\alpha_{d\sigma'1}$. Similarly, the direction angles of the major principal strain and strain rate, $\alpha_{\varepsilon1}$ and $\alpha_{d\varepsilon1}$, are computed analytically by the relationships $\tan 2\alpha_{\varepsilon1} = 2\varepsilon_{z\theta} / (\varepsilon_{zz} - \varepsilon_{\theta\theta})$ and $\tan 2\alpha_{d\varepsilon1} = 2d\varepsilon_{z\theta} / (d\varepsilon_{zz} - d\varepsilon_{\theta\theta})$, respectively. The intermediate principal stress parameter is $b = (\sigma'_2 - \sigma'_3) / (\sigma'_1 - \sigma'_3)$. The deviatoric stress and strain under generalised loading conditions are given by the equations $q = 1 / 2^{1/2} [(\sigma'_1 - \sigma'_2)^2 + (\sigma'_2 - \sigma'_3)^2 + (\sigma'_3 - \sigma'_1)^2]^{1/2} = 1 / 2^{1/2} [\Sigma(\sigma'_i - \sigma'_j)^2]^{1/2}$ and $\varepsilon_q = 2^{1/2} / 3 [(\varepsilon_1 - \varepsilon_2)^2 + (\varepsilon_2 - \varepsilon_3)^2 + (\varepsilon_3 - \varepsilon_1)^2]^{1/2} = 2^{1/2} / 3 [\Sigma(\varepsilon_i - \varepsilon_j)^2]^{1/2}$, respectively. The octahedral shear stress and strain under generalised loading conditions are given by the equations $\tau_{oct} = 1 / 3 [(\sigma'_1 - \sigma'_2)^2 + (\sigma'_2 - \sigma'_3)^2 + (\sigma'_3 - \sigma'_1)^2]^{1/2} = 1 / 3 [\Sigma(\sigma'_i - \sigma'_j)^2]^{1/2}$ and $\gamma_{oct} = 2 / 3 [(\varepsilon_1 - \varepsilon_2)^2 + (\varepsilon_2 - \varepsilon_3)^2 + (\varepsilon_3 - \varepsilon_1)^2]^{1/2} = 2 / 3 [\Sigma(\varepsilon_i - \varepsilon_j)^2]^{1/2}$, respectively. The mean effective stress and the volumetric strain are given by the equations $p' = (\sigma'_1 + \sigma'_2 + \sigma'_3) / 3$ and $\varepsilon_{vol} = \varepsilon_1 + \varepsilon_2 + \varepsilon_3$, respectively. The relationships presented here are also reported in Table 7.1.

Figure 7.2a shows the Y_s - X_s deviatoric stress plane, where the stress $Y_s = 2\tau_{z\theta}$ is associated with the torsional-shear mode of loading and the stress $X_s = \sigma'_{zz} - \sigma'_{\theta\theta}$ is associated with the triaxial mode of loading. The black solid line in the figure shows a part of a drained stress path that corresponds to rotation of the axes of the principal stresses σ'_1 and σ'_3 while keeping the magnitude of the principal effective stresses σ'_1, σ'_2 and σ'_3 constant and the orientation of the σ'_2-axis fixed along the horizontal (radial) direction (Fig. 7.1b); the rotation is performed counterclockwise. The black radial vector that joins the origin of the Y_s - X_s plane to the current stress state makes an angle of $2\alpha_{\sigma'1}$ with the horizontal axis, indicating the current direction of the principal stress σ'_1, and has a length equal to the current stress difference $q_d = \sigma'_1 - \sigma'_3$.

Some characteristic directions of stress and rate of stress and strain are indicated with unit vectors in the Y_s - X_s plane in Fig. 7.2a. The green unit vector $\boldsymbol{\sigma}$ that has its origin at the stress state and points along the radial direction makes an angle of $2\alpha_{\sigma'1}$ with the horizontal axis, indicating the direction of the principal stress, σ'_1. Correspondingly, the blue unit vector d$\boldsymbol{\sigma}$ that has its origin at the stress state and points along the tangential to the stress path direction makes an angle of $2\alpha_{d\sigma'1}$ with the horizontal axis, indicating the direction of the rate of principal stress, dσ'_1. In the same way the unit vector that points along the direction of the principal strain rate, dε_1, is defined in the Y_ε - X_ε plane (not shown here), where $Y_\varepsilon = \varepsilon_{z\theta}$ and $X_\varepsilon = (\varepsilon_{zz} - \varepsilon_{\theta\theta}) / 2$, and is superimposed on the stress state in the Y_s - X_s plane; this is the red unit vector d$\boldsymbol{\varepsilon}$ shown in the figure that makes an angle of $2\alpha_{d\varepsilon1}$ with the horizontal axis. The Y - X plane, shown in Fig. 7.2b, is also used in this study, where $Y = 2\tau_{z\theta} / (\sigma'_{zz} + \sigma'_{\theta\theta})$ and $X = (\sigma'_{zz} - \sigma'_{\theta\theta}) / (\sigma'_{zz} + \sigma'_{\theta\theta})$ are the normalised "shear" stresses. The black radial vector that joins the origin of the Y - X plane to the current stress state makes an angle of $2\alpha_{\sigma'1}$ with the horizontal axis, indicating the current direction of the principal stress, σ'_1, and has a length equal to $\sin\varphi = (\sigma'_1 - \sigma'_3) / (\sigma'_1 + \sigma'_3)$. However, the blue unit vector, d**s**, which is tangential to the stress path at the current stress state, points along the current direction of the rate dσ'_1 only if the stress sum $(\sigma'_{zz} + \sigma'_{\theta\theta})$ is kept constant. The red unit vector d$\boldsymbol{\varepsilon}$ is superimposed on the stress state and makes an angle of $2\alpha_{d\varepsilon1}$ with the horizontal axis, indicating the direction of the rate of principal strain, dε_1.

The convention used to determine the value and sign of the stress direction angle $\alpha_{\sigma'1}$ is discussed next. $\alpha_{\sigma'1}$ is positive and changes from 0° to 45° when $X_s \geq 0$ and $Y_s \geq 0$, while this angle is negative and changes from 0° to -45° when $X_s \geq 0$ and $Y_s \leq 0$; both cases refer to compression-like loading and the only difference between them is the direction of the imposed shear stress $\tau_{z\theta}$. Correspondingly, $\alpha_{\sigma'1}$ is positive and changes from 45° to 90° when $X_s \leq 0$ and $Y_s \geq 0$, while this angle is negative and changes from -90° to -45° when $X_s \leq 0$ and $Y_s \leq 0$; both cases refer to extension-like loading and the only difference between them is the direction of the imposed shear stress $\tau_{z\theta}$. Figure 7.3a shows the value of the stress direction angle $\alpha_{\sigma'1}$ at various stress states in the Y_s - X_s plane; the value and sign of the direction angle $\alpha_{d\sigma'1}$ follows the same convention using the dY_s - dX_s reference frame. The same convention is also used to determine the value and sign of the strain direction angle $\alpha_{\varepsilon1}$ at strain states in the Y_ε - X_ε plane, while the axes dX_ε and dY_ε are superimposed on a given stress state in the Y_s - X_s plane to offer the reference frame for determining the direction angle $\alpha_{d\varepsilon1}$ using again the same convention. Figure 7.3b shows the value of the stress direction angle $\alpha^*_{\sigma'1}$ at various stress states in the Y_s - X_s plane according to the alternative, and convenient for plotting diagrams, convention that $\alpha^*_{\sigma'1}$ increases continuously from 0° to 180° during a full cycle of rotation of the stress PA.

It is noted that a radial stress path in the Y_s - X_s (or in the Y - X) plane corresponds to loading at fixed principal stress direction $\alpha_{\sigma'1}$. For example, the conventional triaxial compression test corresponds to loading with $X_s > 0$ and $Y_s \equiv 0$ ($\alpha_{\sigma'1}$ = 0°), under the condition of $b = 0$, the conventional triaxial extension test corresponds to loading with

$X_s < 0$ and $Y_s \equiv 0$ ($\alpha_{\sigma'1} = 90^o$ or, identically, -90^o), under the condition of $b = 1$, while the torsional shear test on isotropically consolidated specimen corresponds to loading with $Y_s > 0$ or < 0 and $X_s \equiv 0$ ($\alpha_{\sigma'1} = +45^o$ or -45^o, respectively), under the condition of $b = 0.5$; it is noted that the plots of stress paths in the Y_s - X_s (or Y - X) deviatoric plane offer no information about the value of b. A circular stress path in the Y_s - X_s plane, with the centre of the circle located at the origin, corresponds to loading during which the axes of the principal stresses σ'_1 and σ'_3 are rotated in the vertical plane while the value of the stress difference, $q_d = \sigma'_1 - \sigma'_3$, is kept constant. Thus, this type of stress path also corresponds to rotation of the stress PA while keeping the effective stress PV, σ'_1, σ'_2 and σ'_3, constant. A circular stress path in the Y - X plane, with the centre of the circle located at the origin, corresponds to stress PA rotation under a constant value of $\sin \varphi = (\sigma'_1 - \sigma'_3) / (\sigma'_1 + \sigma'_3)$. Thus, this type of stress path also corresponds to rotation of the stress PA while keeping the effective stress PV, σ'_1, σ'_2 and σ'_3, constant.

7.4 CONSOLIDATION AND LOADING PATHS

This section describes the consolidation and loading paths of the hollow-cylinder tests on M31 Sand specimens.

7.4.1 CONSOLIDATION PATHS

Following the saturation process described in Chapter 5, ensuing a value of the coefficient $B = du / dp > 0.96$ at $u = 300$ kPa, the sand specimens are consolidated either isotropically, in the case of A-series loading tests (with some exceptions discussed next), or anisotropically, in the case of B- and C-series loading tests. The consolidation stress ratio, $K_c = \sigma'_{3c} / \sigma'_{1c}$, in each test is reported in Table 7.2.

The isotropic consolidation (IC) lasts between 90 and 120 minutes during which the mean effective stress, p', increases from 40 kPa to the value of p'_c and then the sand specimen is left to rest at stress p'_c. The consolidation stress, p'_c, is in general equal to 200 kPa though in tests A24, A25 and A26 the stress p'_c is equal to 100 kPa. The specimen in test A23 is anisotropically consolidated at $K_c = 0.50$, while the specimens in tests A1, A3, A4 and A6 are consolidated isotropically and then subjected to drained pre-shearing by increasing the deviatoric stress, q, under constant $p' = p'_c$ and $b = 0.5$, until the stress ratios $\eta = q / p'$ and $K_c = \sigma'_{3c} / \sigma'_{1c}$ reach the values 0.13 and 0.86, respectively; the value of K_c is reported in Table 7.2 as 1.00 / 0.86 in these tests. Thereafter, the axis of the major principal stress, σ'_1, is rotated from the vertical to the inclined orientation α (which is actually the orientation of principal stress kept fixed during the subsequent radial loading, as discussed in Section 7.4.2) while keeping the magnitude of the three effective principal stresses, σ'_1, σ'_2 and σ'_3, constant. The volumetric strain accumulated during pre-shearing is negligible (< 0.02%) due to the low value of the stress ratio, η. The sand specimen is again left to rest at stress p'_c.

The results of test A6 are presented next to ease the comprehension of the described process.

Figure 7.4 shows the behaviour of M31 Sand in test A6 during the phases of isotropic consolidation and drained pre-shearing in terms of q - p' (a), Y_s - X_s (b), ε_{vol} - p' (c) and ε_{zz} - ε_{vol} (d) curves. Figure 7.4a shows that the sand specimen is consolidated isotropically to a mean effective stress of $p' = p'_c = 200$ kPa and then the deviatoric stress, q, increases under constant p' (and $b = 0.50$) until the stress ratio, η, reaches the value 0.13. Thereafter, stress PA rotation is performed at constant stresses q and p'. Figure 7.4b shows that both the "shear" stresses $Y_s = 2\tau_{z\theta}$ and $X_s = \sigma'_{zz} - \sigma'_{\theta\theta}$ are zero during isotropic consolidation, then the stress X_s increases to 30 kPa, because the stress σ'_{zz} increases while the stress $\sigma'_{\theta\theta}$ decreases to induce shearing along the principal stress direction $\alpha = 0^o$ with $b = 0.50$, and finally the stress X_s decreases while the stress Y_s increases to induce a stress PA rotation from $\alpha = 0^o$ to $\alpha = 30^o$ at approximately constant principal stress values. It is noted that the stress PA rotation is performed stepwise and the part of the circular stress path is approximated by a part of a polygon.

Figure 7.4c shows that the increase in stress p' from 40 kPa to 200 kPa during isotropic consolidation in test A6 induces a volumetric strain, ε_{vol}, of 0.56%, which increases to 0.57% after a rest period of 5 minutes and to 0.58% during the phase at which the stress ratio, η, increases at constant p'. The volumetric strain increases further to 0.59% during the phase of stress PA rotation and to 0.60% after a 60 minute rest period. Figure 7.4d shows the plot of the axial strain, ε_{zz}, against the volumetric strain, ε_{vol}; the red dashed line in the figure indicates the relationship $\varepsilon_{zz} = 1 / 3\ \varepsilon_{vol}$ that corresponds to isotropic deformation of the sand specimen. It can be seen that the deformation of the sand specimen under isotropic loading is strongly anisotropic since the axial (vertical) strain is considerably lower than the one third of the volumetric strain, with the ratio $\varepsilon_{zz} / \varepsilon_{vol}$ being equal to 0.116 (i.e. lower than 1 / 8) at the end of isotropic consolidation; it is noted that ε_{zz} is measured outside the triaxial cell using a dial gauge thus the value of the axial strain free from the error induced by the compliance of the loading system may be even lower. These results indicate that a strongly anisotropic fabric with a horizontal bedding plane is formed when the sand is pluviated through water under the action of gravity, as described in Chapter 5.

Results of the tests performed in the triaxial apparatuses (see Chapters 5 and 6) using on-sample instrumentation for measuring the local axial strain also indicate the anisotropic deformability of M31 Sand during isotropic consolidation. Figure 7.5a shows the evolution of axial strain, ε_{zz}, with volumetric strain, ε_{vol}, during isotropic consolidation of two different sand specimens, one of which is consolidated to a mean effective stress of $p'_c = 101$ kPa in the conventional triaxial apparatus (CTA) using Linear Variable Differential Transformers (LVDTs) for measuring the local axial strain, while the other is consolidated to a mean effective stress of $p'_c = 1452$ kPa in the high-pressure triaxial apparatus (HPTA) using inclinometers for measuring the local axial strain. Figure 7.5a shows that the ratio $\varepsilon_{zz} / \varepsilon_{vol}$ is lower than 1 / 3 being equal to 0.126 at the end of consolidation in the case of low-pressure consolidation and to 0.147 in the case of high-pressure consolidation. Figure 7.5b shows the initial part of the ε_{zz} - ε_{vol} curve of the high-pressure test, the complete ε_{zz} - ε_{vol} curve of the low-pressure test and the initial part of the ε_{zz} - ε_{vol} curve of test A6 performed in the HCA using a dial gauge for measuring the global axial strain. It can be seen that the relationship between ε_{zz} and ε_{vol} at small strains is similar for the three specimens tested in the HPTA, CTA and HCA, having a depositional void ratio of 0.734, 0.670 and 0.728, respectively.

The anisotropic consolidation (AC) in B- and C-series tests is performed in two phases, each followed by a rest period; the whole process lasts around 120 minutes. During the first phase the deviatoric stress, q, increases at constant p' = 40 kPa until the stress ratio, η, and the consolidation ratio, K_c, attain the target values. The value of K_c is 0.80, 0.50 or 0.40 in B-series tests, while in C-series tests the value of K_c is varied in the range between 0.48 and 0.75, as reported in Table 7.2. Thereafter, the sand specimen is consolidated along the constant-η stress path in the q - p' plane as the mean effective stress increases from 40 kPa to the target consolidation stress, p'_c, and then the sand specimen is left to rest at stress p'_c. The consolidation stress, p'_c, is in general equal to 200 kPa though in tests B6 and B7 the stress p'_c is equal to 100 kPa. During the second phase of consolidation the major and minor principal stresses, σ'_{1c} and σ'_{3c}, are kept constant while the intermediate principal stress, σ'_{2c}, increases until the stress parameter b reaches the value of 0.50. The mean effective stress also increases, in this phase, from the value of p'_c to the value of p'_i reported in Table 7.2 though the deviatoric stress, q, and the stress ratio, η, decrease. Thereafter, the sand specimen is left to rest at stress p'_i. The results of test B1 are presented next to ease the comprehension of the described process.

Figure 7.6 shows the behaviour of M31 Sand in test B1 during the two phases of anisotropic consolidation in terms of q - p' (a), Y_s - X_s (b), ε_{vol} - p' (c) and ε_{zz} - ε_{vol} (d) curves. Figure 7.6a shows that the deviatoric stress, q, increases at constant stress p' = 40 kPa until the stress ratio, η, reaches the value of 0.23 (corresponding to K_c = 0.80). Thereafter, the sand specimen is consolidated along the constant-η stress path, until the mean effective stress, p', increases to 200 kPa, and left to rest at 200 kPa. In the second phase of consolidation the mean effective stress, p', increases from 200 kPa to 207 kPa, the deviatoric stress, q, decreases from 46 kPa to 41 kPa and the stress ratio, η, decreases from 0.23 to 0.20.

Figure 7.6b shows the plot of the mean effective stress, p', and the deviatoric stress, q, against the volumetric strain, ε_{vol}, during anisotropic consolidation in test B1; black symbols are used to indicate the data points (ε_{vol}, p'), with the values of p' plotted on the left vertical axis, while red symbols are used to indicate the data points (ε_{vol}, q), with the values of q plotted on the right vertical axis. It can be seen that the increase in q (and η) under constant p' did not induce a discernible volumetric strain, indicating an elastic response. The volumetric strain accumulated during the subsequent constant-η consolidation is ε_{vol} = 0.57%, while after a 42 minute rest period ε_{vol} increases to 0.60%. Thereafter, the increase in mean effective stress, p', from 200 kPa to 207 kPa resulted in a rise of ε_{vol} to 0.64%, while after a 34 minute rest period ε_{vol} increased to 0.66%.

It is noted that the volumetric strain induced during the rest period in test B1 over the volumetric strain induced during the preceding consolidation process gives a percentage of 6.3% in the first phase and of 51.4% in the second phase. Moreover, the rate dp' / dε_{vol} at 200 kPa is lower in the second consolidation phase compared to the first consolidation phase (the ratio of the rates is 0.43), as indicated by the slope of the purple dotted tangent lines shown in Fig. 7.6b. These results indicate the existence of a strongly anisotropic fabric of sand since in the second consolidation phase the radial direction is compressed as the intermediate principal stress, σ'_2, increases (while the other two principal stresses remain constant), thus the high compressibility and relatively intense creep may be related to the orientation of the stress rate dσ'_2 in relation to the horizontal bedding plane; however, the effects of changing the b-parameter should not be overlooked. On the other hand, in the first consolidation phase the three principal stresses increase with the ratios of their values kept constant while the rate of the major principal stress acts normal to the bedding plane. Figure 7.6c shows the p' - ε_{vol} curve of test B1 focusing in the part around the stress p' = 200 kPa to highlight the differences in the compressibility rates dp' / dε_{vol} and in the amount of creep induced volumetric strain.

Figure 7.6d shows the plot of the axial strain, ε_{zz}, against the volumetric strain, ε_{vol}, during anisotropic consolidation in test B1; the red dashed line indicates the relationship $\varepsilon_{zz} = \varepsilon_{vol}$ that corresponds to K_o-consolidation. The relationship between the axial strain, ε_{zz}, and the volumetric strain, ε_{vol}, during the phase of constant-η consolidation is practically linear with a slope of dε_{zz} / dε_{vol} = 0.20 indicating that lateral strains develop when M31 Sand is consolidated anisotropically at K_c = 0.80. Moreover, these results indicate that the sand specimen is less compressible along the vertical direction than it is along the horizontal directions albeit the major principal stress and the rate of the major principal stress acting along the vertical direction. It can be seen that the axial strain, ε_{zz}, remains practically constant at 0.13% during the second phase of consolidation and rest period, despite the fact that the volumetric strain, ε_{vol}, increases from 0.60% to 0.64%, when the mean effective stress increases from 200 kPa to 207 kPa, and it further increases to 0.66% during the second rest period.

Figure 7.7 shows the evolution of axial strain, ε_{zz}, with volumetric strain, ε_{vol}, during anisotropic consolidation of sand specimens at different values of K_c in B-series tests; the red dashed line indicates the relationship $\varepsilon_{zz} = \varepsilon_{vol}$ that corresponds to K_o-consolidation. The results shown correspond only to the constant-η consolidation phase in tests B1, B2 and B3 (see Table 7.2), while the phases of constant-p' loading, creep and second consolidation are omitted; the strains are reset to zero at the beginning of the constant-η consolidation to ease the comparison of the results of different tests. It can be seen that the relationship between the axial strain, ε_{zz}, and the volumetric strain, ε_{vol}, is practically linear with a slope $d\varepsilon_{zz} / d\varepsilon_{vol}$ that increases when the consolidation stress ratio, K_c, decreases. The specimen consolidated at $K_c = 0.40$ deformed practically in a K_o-mode exhibiting only a slight expansion along the horizontal directions, which corresponds to normal strains $\varepsilon_{\theta\theta} = \varepsilon_{rr} \approx -\varepsilon_{zz} / 10$ at the end of consolidation.

7.4.2 LOADING PATHS

Three different series of undrained loading tests are performed each corresponding to a different loading path. The conditions of constant intermediate principal stress parameter $b = 0.50$ and constant mean total stress $p = p_i$ are imposed in all tests; the value of the initial mean effective stress p'_i is reported in Table 7.2 for each test, where the initial pore-water pressure, u_i, is in general equal to 300 kPa thus the initial mean total stress can be calculated as $p_i = p'_i + u_i$. In A-series tests the isotropically consolidated sand specimens are subjected to undrained loading along a fixed principal stress direction, $\alpha_{\sigma'1}$. The loading programme dictates a monotonic increase in the deviatoric stress, q, which is achieved by changing the stresses σ_{zz} and $\sigma_{\theta\theta}$ in opposite trends so that the stress difference $\sigma_{zz} - \sigma_{\theta\theta}$ increases and the stress half-sum $(\sigma_{zz} + \sigma_{\theta\theta}) / 2$ remains constant and equal to σ_{rr}, while the torsional shear stress $\tau_{z\theta}$ increases proportionally to the stress difference $\sigma_{zz} - \sigma_{\theta\theta}$ in order to maintain the ratio $2\tau_{z\theta} / (\sigma_{zz} - \sigma_{\theta\theta})$ constant and equal to tan $2\alpha_{\sigma'1}$. The stress path in the Y_s - X_s deviatoric plane is a straight line that goes through the origin and makes an angle of $2\alpha_{\sigma'1}$ with the horizontal axis, thus, this type of loading will be termed undrained (U) radial loading, hereinafter; the stress path in the Y - X deviatoric plane is similarly radial.

However, if the sand loaded in A-series tests is loose enough to undergo the so-called flow deformation then stability is lost (for the chosen set of control parameters) and the bifurcated response becomes non-unique, meaning that the stress path follows an unpredictable route that may diverge from the radial direction. Since the loading programme dictates a proportional increase in the deviatoric stress components Y_s and X_s while the strength of the specimen decreases during flow, due to the pore-water pressure buildup, it is apparent that the controllability of the loading programme is lost when stability is lost (Triantafyllos et al. 2020). Strength, stability and controllability are regained past the phase transformation point (PTP) whereupon the sand is sheared to failure in a dilative mode. It is noted that the Y and X stress ratios depend on the pore-water pressure generation and, thus, they are uncontrollable even when the response of the specimen is stable.

The results obtained during shearing in test A4 are presented next to ease the comprehension of the loading process in A-series tests and to show how the specimen - apparatus system responds in the case that stability is lost. Figure 7.8a shows the stress path of test A4 in the Y_s - X_s plane, while Fig. 7.8b shows the corresponding stress path in the Y - X plane; the specimen in this test was subjected to pre-shearing after isotropic consolidation thus a small shear stress (or a mobilised stress ratio, depending on the stress plane) is apparent at the beginning of shearing. It can be seen that the unstable bifurcated part of the stress path diverges from the radial direction and moves towards the X_s-axis (i.e. the principal stress direction angle, $\alpha_{\sigma'1}$, decreases) following a steeply inclined straight line because the spontaneous unloading of the torsional shear stress, Y_s, is more severe than that of the triaxial stress, X_s. Stability is regained past the PTP and the stress path progresses again along the initial radial direction as the stresses Y_s and X_s increase again proportionally.

In B-series tests the anisotropically consolidated sand specimens are subjected to undrained loading by means of increasing the deviatoric stress, q, and simultaneously rotating the σ'_1-axis from the direction of $\alpha_{\sigma'1} = 0^o$ towards the direction of $\alpha_{\sigma'1} = 45^o$. These loading conditions are achieved when the torsional shear stress, $\tau_{z\theta}$, increases monotonically, while all the other stresses are kept constant. The stress path before the triggering of instability is a vertical line in the Y_s - X_s deviatoric plane that begins from the consolidation point $(\sigma'_{zz} - \sigma'_{\theta\theta})_c$ on the X_s-axis, which indicates the static shear stress developed during anisotropic consolidation and kept constant during shearing, and moves parallel to the Y_s-axis. The stress path in the Y - X deviatoric stress plane before the triggering of instability begins from the consolidation point $[(\sigma'_{zz} - \sigma'_{\theta\theta}) / (\sigma'_{zz} + \sigma'_{\theta\theta})]_c$ on the X-axis, which indicates the stress ratio $\sin \varphi = [(\sigma'_1 - \sigma'_3) / (\sigma'_1 + \sigma'_3)]_c$ mobilised during anisotropic consolidation, and moves initially parallel to the Y_s-axis but afterwards it curves gently and moves away from the Y_s-axis. The stress path in both deviatoric planes follows an unpredictable route in the course of unstable flow deformation.

The results obtained during shearing in test B1 are presented next to ease the comprehension of the loading process in B-series tests and to show how the sand specimen responds in the case that stability is lost. Figure 7.9a shows the stress path of test B1 in the Y_s - X_s plane, while Fig. 7.9b shows the corresponding stress path in the Y - X plane; the specimen in this test was subjected to anisotropic consolidation at $K_c = 0.80$. As far as the response of the sand specimen remains stable the torsional shear stress, Y_s, increases while the triaxial stress, X_s, remains constant and the stress path in the Y_s - X_s plane moves parallel to the Y_s-axis, while the stress direction angle, $\alpha_{\sigma'1}$, increases. During the phase of unstable flow deformation both the torsional shear stress, Y_s, and the triaxial stress, X_s, are spontaneously unloaded hence the stress path in the Y_s - X_s plane moves back along a different route than that followed before the triggering of instability, while the principal stress direction angle, $\alpha_{\sigma'1}$, decreases; it can be seen that the unloading of the Y_s stress component is more severe than that of the X_s stress component. Stability is regained past the PTP and the stress path moves again vertically as the value of Y_s increases under constant X_s.

The stable part of the stress path of test B1 in the Y - X plane, shown in Fig. 7.9b, moves initially vertically and then curves gently and moves away from the Y-axis as the principal stress direction angle, $\alpha_{\sigma'1}$, increases, while the unstable bifurcated part of the stress path moves rapidly away from the Y-axis and, concurrently, the principal stress direction angle, $\alpha_{\sigma'1}$, decreases. Once stability has been regained the stress path moves back towards the Y-axis along a more or less circular route, while the principal stress direction angle, $\alpha_{\sigma'1}$, increases.

In C-series tests the anisotropically consolidated specimens are subjected to undrained loading by means of rotating the stress PA while keeping the magnitude of the three total principal stresses, σ_1, σ_2 and σ_3, constant. In order to impose this type of loading the stresses σ_{zz}, $\sigma_{\theta\theta}$ and $\tau_{z\theta}$ should be changed sinusoidally with a proper phase difference while the stress σ_{rr} should be kept constant. However, the stresses are actually changed in small successive linear increments that approximate the sinusoidal functions. The rotation of the stress PA is performed monotonically and stepwise, while the undrained creep behaviour is observed during the short-time (≈ 2 min) pause periods between the successive steps.

The rotation of the stress PA in C-series tests induces an increase in the stress ratio, $\eta = q / p'$, while the deviatoric stress, q, is kept constant because the pore-water pressure, u, increases as the sand contracts plastically and the mean effective stress, p', decreases. These conditions, which can actually lead to effective failure of the sand specimen, correspond to isotropic stress unloading in the σ'_1 - σ'_2 - σ'_3 space (i.e. $d\sigma'_1 = d\sigma'_2 = d\sigma'_3 = -du$). The stress path before the triggering of instability is circular in the Y_s - X_s deviatoric plane with the circle's centre located at the origin, as the principal stress direction angle, $\alpha_{*\sigma'1}$ ($\alpha_{\sigma'1}$), changes from 0° (0°) to 45° (+45°) to 90° (±90°) to 135° (-45°) to 180° / 0° (0°) during a full cycle of rotation of the stress PA. The stress path before the triggering of instability is spiral in the Y - X deviatoric plane with the spiral's centre point located at the origin. The stress path follows an unpredictable route in both deviatoric planes when the deformation bifurcates during flow.

The results obtained during shearing in test C1 are presented next to ease the comprehension of the loading process in C-series tests and to show how the sand specimen responds in the case that stability is lost. Figure 7.10a shows the stress path of test C1 in the Y_s - X_s plane, while Fig. 7.10b shows the corresponding stress path in the Y - X plane; the specimen in this test was subjected to anisotropic consolidation at $K_c = 0.48$. The stress path in the Y_s - X_s plane follows a polygonal route that approximates well the circular stress path corresponding to constant stress, q_d, at the value developed during anisotropic consolidation, as far as the response of the specimen - apparatus system remains stable. However, in the course of unstable flow deformation the torsional shear stress, Y_s, and the triaxial stress, X_s, are spontaneously unloaded thus the stress path moves towards the interior of the circle corresponding to the initial stress, q_d. It can be seen that the unloading of the Y_s stress component is predominant compared to that of the X_s stress component hence the stress path moves along a very steep, almost vertical, straight line. The stress path becomes again circular once stability has been regained though the new circle has a smaller radius compared to that of the initial circle.

The stress path of test C1 in the Y - X plane, shown in Fig. 7.10b, moves smoothly away from the origin in a spiral route as the stress ratio, $\sin\varphi$, and the principal stress direction angle, $\alpha_{\sigma'1}$, increase simultaneously during the phase of stable response. After the triggering of flow deformation the stress path bifurcates and moves rapidly away from the origin, while the principal stress direction angle, $\alpha_{\sigma'1}$, decreases. In the final phase of loading, past the PTP, the stress path moves along a more or less circular route while the principal stress direction angle, $\alpha_{\sigma'1}$, increases.

Some issues concerning the unstable bifurcated behaviour of the specimen - apparatus system should be addressed here. First it is noted that the instability of loose specimens subjected to undrained loading occurs because the imposed loading programme, which uses as control parameters the stresses Y_s, X_s and σ_{rr}, does not comply with the spontaneous decrease in strength induced by the buildup of pore-water pressure, u, which is an uncontrollable parameter indicating the material plastic volume-change response. Consequently, the behaviour of the specimens becomes unstable and dynamic when the increase in u induces a decrease in q (which is a function of Y_s, X_s and b) and the specific set of control parameters is chosen, while if a different set of control parameters was chosen the response would remain absolutely stable and quasi-static. It should be also noted that the bifurcated behaviour of sand specimens during flow deformation depends on the imperfections and perturbations in the specimen - apparatus system. For example, if a loading system imposing mixed conditions of strain and stress control was used the stress path during flow deformation would move along the radial direction in both deviatoric planes in all types of loading tests, i.e. the principal stress direction angle, $\alpha_{\sigma'1}$, would not change. However, there is strong evidence, which will be presented next, that the horizontal bedding plane is an influential characteristic of the system, affecting the spontaneous event of stress PA rotation occurring during the bifurcated response.

7.5 USEFUL CONCEPTS FOR THE INTERPRETATION OF THE EXPERIMENTAL RESULTS

This section presents some useful concepts for the interpretation of the experimental results of this study.

7.5.1 THE LOCAL BOUNDARY SURFACE CONCEPT

Symes et al. (1984) and Shibuya et al. (1987, 2003a, 2003b) introduced the concept of the Local Boundary Surface (LBS) to interpret the anisotropic behaviour of loose sand specimens subjected to undrained loading in the hollow cylinder apparatus (HCA), under a variety of loading conditions, either monotonic or cyclic, which included rotation of the stress PA. The LBS is visualised in the q_d - p' - $\alpha_{\sigma'1}$ - b space using a set of effective stress paths (ESPs) of monotonic loading tests with fixed values of the principal stress direction angle, $\alpha_{\sigma'1}$, and intermediate principal stress parameter, b, at constant mean total stress, p. It was shown that the ESPs of monotonic or cyclic undrained tests, with fixed or changing values of $\alpha_{\sigma'1}$ and b, can progress, in the phase of plastic contraction, only within the domain bounded by the LBS. Moreover, it was shown that instability and flow deformation of loose sand specimens is triggered in stress-controlled tests whenever the ESP reaches the post-peak regime of the LBS (i.e. the regime past the transient-peak state) with an outwards incremental stress direction. In this case the spontaneous generation of pore-water pressure is such that the ESP follows obligingly the LBS instead of crossing it. Similar results were reported by other researchers (Alarcon-Guzman et al. 1988, Georgiannou et al. 1991).

Symes et al. (1984) and Shibuya et al. (1987, 2003a, 2003b) showed that the shape of the LBS depends on the void ratio and consolidation stress history, while as far as the shear strain developed during shearing is small (e.g. $\gamma_{oct} << 1.0\%$) this shape expresses phenomenologically the initial anisotropy of sand due to the gravity deposition and consolidation stress history. However, the anisotropic characteristics of fabric, which are the cause of the anisotropic macroscopic behaviour of sand, are altered gradually as the sand is sheared to failure and beyond (Oda et al. 1985) and the effects of induced anisotropy cannot be observed separately when the LBS is determined.

The ESPs of the A-series loading tests on sand specimens having a similar void ratio are used in this study to map the LBS of loose M31 Sand in the q_d - p' - $\alpha_{\sigma'1}$ space, under the condition of b = 0.50. An example is given in Fig. 7.11a which shows the projection of the LBS of isotropically consolidated (IC) sand on the q_d - p' plane mapped by means of the ESPs of tests A5 ($\alpha_{\sigma'1} = 22.5^{o}$), A9 ($\alpha_{\sigma'1} = 45^{o}$) and A20 ($\alpha_{\sigma'1} = 90^{o}$). The LBS is used to interpret the undrained behaviour of anisotropically consolidated (AC) M31 Sand under loading imposing rotation of the stress PA (in B- and C-series tests), while it is checked whether or not the LBS can be used to predict the triggering of flow instability.

7.5.2 THE INSTABILITY LINE AND INSTABILITY SURFACE CONCEPTS

Lade (1993) defined a straight line that goes through the origin in the q_d - p' plane and connects the (transient) peak-q_d points of a series of ESPs of monotonic undrained tests, performed on loose sand specimens consolidated isotropically to different mean effective stresses. Lade (1993) stated that this Instability Line (IL) is the lower boundary of the region of potential instability though many researchers opposed his suggestion and showed that instabilities may be triggered below this line under loading associated with general drainage conditions and controlled dilatancy rates (e.g. Chu et al. 1992 and 1993, Darve et al. 1995, Daouadji et al. 2011; see Section 4.5).

In the case that loading is imposed under undrained conditions many experimental studies report that instabilities are triggered under monotonic or cyclic loading when the effective stress state crosses the IL (Vaid and Chern 1983, Konrad 1993, Yamamuro and Covert 2001, Georgiannou et al. 2008) though the dependence of the position of the IL on the consolidation stress ratio, K_c, and pre-shearing indicates the non-uniqueness of the IL (Doanh et al 1997, Kato et al. 2001). Other experimental studies report that either the IL or the post-peak regime of the ESP of monotonic undrained test forms a boundary to a stable response under cyclic (stress-controlled) loading depending on the value of the static shear stress (Hyodo et al. 1994).

Nakata et al. (1998) performed monotonic undrained loading tests in the HCA along different radial directions in the Y_s - X_s deviatoric stress plane under the condition of b = 0.50. It was found that for a given void ratio of sand (in loose state) and initial mean effective stress the slope of the IL decreases when the principal stress direction angle, $\alpha_{\sigma'1}$, increases due to the initial anisotropy of gravity deposited sand characterised by a horizontal bedding plane. Moreover, it was found that flow deformation may occur when loose sand is subjected to undrained stress PA rotation under constant deviatoric stress, q, in the same way as it occurs under cyclically imposed q. Nakata et al. (1998) stated that "flow deformation occurs when the effective stress state of the sample attains the critical stress ratio" (i.e. the stress ratio corresponding to the slope of the IL at the current value of $\alpha_{\sigma'1}$), irrespective of whether IC sand is subjected to loading at fixed principal stress direction, $\alpha_{\sigma'1}$, or AC sand is subjected to stress PA rotation at constant q; in the latter case it was shown that the level of q does not affect the flow-triggering condition. Sivathayalan and Vaid (2002) reported similar results of undrained tests with fixed or rotating stress PA indicating that the mobilised friction angle, φ, at the onset of flow decreases when the principal stress direction angle, $\alpha_{\sigma'1}$, increases, irrespective of the stress history preceding the onset of flow, while the relationship between the two angles was found to be more or less unique (for a given value of b).

The ESPs of the A-series loading tests on sand specimens having a similar void ratio are used in this study to determine the ILs in the q_d - p' space corresponding to different values of $\alpha_{\sigma'1}$ and b = 0.50. An example is given in Fig. 7.11a which shows the ILs determined in tests A5 ($\alpha_{\sigma'1}$ = 22.5°), A9 ($\alpha_{\sigma'1}$ = 45°) and A20 ($\alpha_{\sigma'1}$ = 90°). The solid circles shown in Fig. 7.11a indicate the instability points (IPs), while the dashed lines connecting the IPs to the origin are the ILs. Instability is triggered at, or just after, the state of transient-peak strength because the specimen cannot sustain the applied stresses as the strength decreases and a runaway deformation occurs. At the instability point the rate of deviatoric stress becomes momentarily zero, dq = 0, while the rates of shear strain, dγ_{oct}, and pore-water pressure, du, increase (for a given time step) thus the deformation of the specimen becomes dynamic and the controllability of the loading programme is lost (Nova 1994). Strength, stability and controllability are regained past the phase-transformation point (PTP) (Triantafyllos et al 2020).

The Instability Surface (IS) is introduced in this study as the locus of the IPs in the Y - X deviatoric plane observed in the A-series tests performed on loose sand specimens having a similar void ratio; for example, the IS that goes through the IPs observed in tests A5 ($\alpha_{\sigma'1}$ = 22.5°), A9 ($\alpha_{\sigma'1}$ = 45°) and A20 ($\alpha_{\sigma'1}$ = 90°) is shown in Fig. 7.11b with a dashed line. The IS is actually the generalisation of Lade's concept since it indicates the polar coordinate combinations (sin φ_{ip} , 2$\alpha_{\sigma'1}$) at the triggering of instability, while the mobilised stress ratio, sin φ_{ip}, is related to the slope of Lade's IL at the given principal stress direction angle, $\alpha_{\sigma'1}$. This study queries whether the triggering of flow instability under principal stress rotation (i.e. in the B- and C-series tests) can be correlated to the crossing of the IS (determined in the A-series tests) or not.

7.5.3 IMPLICATIONS OF THE SECOND-ORDER WORK CRITERION

Daouadji et al. (2011) presented a comprehensive work highlighting the role of the second-order work criterion (Hill 1958) in predicting the occurrence of diffuse bifurcations in geomaterials that lead to catastrophic failure-like events before the classical Mohr - Coulomb failure criterion is satisfied; the second-order work, d^2W, is a scalar yet directional quantity the value and the sign of which depend on the current state, the previous stress - strain history and the direction of the incremental stress. Daouadji et al. (2011) stated that three necessary and sufficient conditions must be met in order to trigger instability: (i) the stress state must be located inside the bifurcation domain, (ii) the incremental stress direction must be included inside the instability cone and (iii) the control parameters must be proper in the sense that they allow the manifestation of instability. The first condition ensures that at the current stress state, attained after a given stress - strain history, there exist incremental stress directions along which the second-order work, d^2W, becomes non-positive, while the second condition states that the direction of the imposed incremental stress actually coincides with one of these directions. The third condition ensures that the behaviour of the system can spontaneously change from (quasi)static to dynamic.

This study investigates the undrained flow deformation of loose sand using proper control parameters that allow the spontaneous occurrence of instabilities. The triggering of flow instability typically occurs before the Mohr - Coulomb criterion is satisfied, i.e. in the hardening regime, while the sand specimen undergoes a diffuse deformation during flow. Consequently, the second-order work criterion can be used to predict the triggering of flow. The second-order work criterion indicates that the flow-triggering condition cannot depend solely on the current state, as suggested by Nakata et al. (1998) and Sivathayalan and Vaid (2002). On the contrary, it should also depend on the stress - strain history that precedes the mobilisation of the current state and on the current direction of the incremental stress. This study investigates the dependence of the flow-triggering condition on the stress - strain history and incremental stress direction.

7.5.4 THE MECHANISMS OF SHEARING AND SLIDING ALONG THE BEDDING PLANE

Miura et al. (1986) performed monotonic drained loading tests in the HCA along different radial directions in the Y_s - X_s deviatoric stress plane under the condition of b = 0.50, as well as loading tests during which the direction of the stress PA was rotated while keeping the effective stress PV constant. It was shown that dense sand exhibited the weakest response, showing the minimum strength and maximum deformability, when two distinct kinematical mechanisms were mobilised. These mechanisms correspond to shearing and sliding along the bedding plane, as discussed next. It is recalled that a horizontal bedding plane is formed when sand is deposited under the action of gravity meaning that the preferred orientation of the long axes of non-spherical grains is horizontal.

Figure 7.12 shows a soil element in the vertical $z\theta$-plane subjected to loading along the principal stress direction $\alpha_{\sigma'1} = 45^o$ in the case that the mobilised angle of shearing resistance is $\varphi = 20^o$ (Fig. 7.12a) or $\varphi = 35^o$ (Fig. 7.12b). The dashed lines indicate the horizontal bedding plane formed under gravity deposition, while the solid inclined lines indicate the following three characteristic planes: *mm*' is the plane on which the major principal stress, σ'_1, acts, $\alpha\alpha$' is the plane of maximum stress obliquity nearer to the bedding plane, while $\beta\beta$' is the plane of maximum stress obliquity further to the bedding plane. It is recalled that the planes of maximum stress obliquity inside a stressed soil element are those along which the maximum ratio of shear stress over effective normal stress, τ / σ', is mobilised and these planes are oriented at an angle of $\pm(45^o - \varphi / 2)$ to the σ'_1-axis, where φ is the mobilised angle of shearing resistance.

The acute angle by which the horizontal bedding plane should be conceptually rotated in order to coincide with the maximum stress obliquity plane is termed ω; ω ranges between -90^o and +90^o, being positive when the rotation should occur counterclockwise, as shown in Fig. 7.12. It is noted that ω evolves during shearing in accordance with the changes in φ and $\alpha_{\sigma'1}$. In the case that $\omega = 0^o$ one of the maximum stress obliquity planes coincides with the horizontal bedding plane. Miura et al. (1986) observed that the mobilised angle of shearing resistance, φ, at peak failure in radial tests becomes minimum when loading is imposed along the fixed principal stress direction, $\alpha_{\sigma'1}$, corresponding to $\omega = 0^o$, while the deformability of sand at a given φ is the highest when the value of $\alpha_{\sigma'1}$ is such that $\omega = 0^o$. It was suggested that the resistance against shearing is minimum along the bedding plane presumably because sliding occurs more easily along this plane, due to the less restrictive kinematic conditions associated with the interlocking of the horizontally aligned (in the statistical sense) non-spherical grains.

Miura et al. (1986) also showed that the deformability of dense sand subjected to stress PA rotation is the highest when the direction of incremental principal strain, $\alpha_{d\varepsilon1}$, becomes equal to $\pm45^o$ and the soil elements deform momentarily in simple-shear mode corresponding to $d\varepsilon_{zz} = d\varepsilon_{\theta\theta} = d\varepsilon_{rr} \approx 0$ and $d\varepsilon_{z\theta} \neq 0$. This pattern of behaviour was observed twice in each cycle of stress PA rotation at $\alpha_{\sigma'1} = 30^o$ and -75^o, irrespective of the value of mobilised φ and of the number of previous cycles of stress PA rotation, while the value of mobilised φ was such that neither of the planes of maximum stress obliquity was aligned with the horizontal bedding plane. Nevertheless, the right $z\theta$-angles undergo the maximum shear distortion when $\alpha_{d\varepsilon1} = \pm45^o$ thus the high deformability of sand in simple-shear mode is presumably due to the predominant sliding occurring on the bedding plane, as a result of the less restrictive kinematic conditions. This situation is illustrated in Fig. 7.13 which shows a deformed soil element with horizontal bedding plane when $\alpha_{d\varepsilon 1}$ = +45° and dε_{zz} = d$\varepsilon_{\theta\theta}$ = 0 (= dε_{rr}); the thin dashed lines indicate the horizontal bedding plane, while the thick dashed line indicates the undeformed soil element.

The present study investigates the effects of the (kinematically-induced) mechanisms of shearing and sliding along the bedding plane on the undrained strength and deformability of sand subjected to loading both at fixed and rotating directions of the stress PA. The loading system and the control parameters used allow the spontaneous occurrence of instabilities, while the specimens tested exhibit strongly anisotropic characteristics, verified by the test results. Taking advantage of these conditions special care is taken to highlight the role of the two fabric-related mechanisms in the triggering of unstable bifurcations in both diffuse and localised modes.

7.6 UNDRAINED BEHAVIOUR OF ISOTROPICALLY CONSOLIDATED M31 SAND UNDER LOADING WITH FIXED STRESS PRINCIPAL AXES

Figure 7.14 shows the results of the A-series tests in the q_d - p' (a), Y - X (b), τ_{oct} - γ_{oct} (c) and Δu / p'_i - γ_{oct} (d) planes. Loose sand specimens are subjected to undrained loading with fixed stress PA inclined at various orientations, $\alpha_{\sigma'1}$, with respect to the vertical, under the condition of b = 0.50 and constant p. The specimens are isotropically consolidated (IC) to a mean effective stress of p'_c = 200 kPa (= p'_i), having an initial void ratio e_i between 0.707 and 0.719, except from the specimen in test A3 which has e_i = 0.726. Instability is triggered and flow deformation occurs in all tests, irrespective of the value of $\alpha_{\sigma'1}$. Flow deformation is initiated at the instability point (IP), indicating the onset of stress unloading and runaway behaviour, and terminated at the phase-transformation point (PTP), being the point of minimum p' and maximum Δu; the IPs are marked with solid circles in Figs 7.14a and b. The state of transient-peak strength is very close to the IP, while the state of minimum undrained strength practically coincides with the PTP in this study. Diffuse deformation is observed before the PTP, while localised deformation is observed at large strains in the phase of dilative failure. The specimens in extension-like tests with $\alpha_{\sigma'1} \geq 60°$ are particularly prone to necking at shear strain $\gamma_{oct} \geq 8\%$ thus Fig. 7.14 presents the results up to a strain value of around γ_{oct} = 8%.

The effective stress paths of the A-series tests in the q_d - p' plane shown in Fig. 7.14a indicate that the undrained behaviour of loose IC M31 Sand (formed by means of pluviation through water under the action of gravity) is strongly anisotropic, becoming, in general, more contractive and less stiff when the principal stress direction angle, $\alpha_{\sigma'1}$, increases. Specifically, the mobilised strength, q_d, at the transient-peak state and at the phase-transformation point decrease with $\alpha_{\sigma'1}$, as also does the mobilised stress ratio, q_d / p', at the instability point. However, the weakest response and the lowest strengths are observed in the tests with $\alpha_{\sigma'1}$ = 67.5° (A14) and

75º (A16) and not in the test with $\alpha_{\sigma'1}$ = 90º (A20) possibly because one of the planes of maximum stress obliquity is closer to the horizontal bedding plane in the former tests that it is in the latter test, as shown next. It is noted that the minimum undrained strength mobilised at the PTP is possibly influenced by the spontaneous rotation of the stress PA occurring when stability and controllability are lost (as described in Section 7.4.2) thus the effects of anisotropy can be evaluated with confidence before the triggering of instability, while the deformation of the specimen remains fairly homogeneous.

Figure 7.14b shows the stress paths of the A-series tests in the *Y* - *X* deviatoric plane. It can be seen that past the IP the stress paths in tests A3, A4, A14 and A16 diverge from the radial direction moving towards the *X*-axis because the unloading of the torsional shear stress, Y_s, is more severe than that of the triaxial stress, X_s, as described in Section 7.4.2. The principal stress direction angle, $\alpha_{\sigma'1}$, may decrease or increase depending on whether the loading is compression-like or extension-like regarding the orientation of the σ'_1-axis with respect to the bedding plane. The decrease in $\alpha_{\sigma'1}$ is insignificant, yet discernible, in the compression-like tests A3 and A4; for example, $\alpha_{\sigma'1}$ changes from 22.3º to 19.2º in test A4. On the other hand, in the extension-like tests A14 and A16 $\alpha_{\sigma'1}$ drops to around 85º indicating an almost complete unloading of the torsional shear stress, Y_s. It is noted that the value of the intermediate principal stress parameter, *b*, remains fixed at around 0.50 in the compression-like tests though it drops to around 0.30 in the extension-like tests when controllability is lost. Moreover, it is noted that stability and controllability is regained past the PTP though the results of the extension-like tests presented here do not show the re-establishment of the initial stress conditions because the analysis of the data stops before the deformation of the specimen becomes inhomogeneous.

The stress - strain curves of the A-series tests shown in Fig. 7.14c indicate that the shear strain, γ_{oct}, at the IPs is very small ($\gamma_{oct} \leq 0.50\%$) and that the shear strain accumulated during flow deformation increases when the principal stress direction angle, $\alpha_{\sigma'1}$, increases. The specimens in the compression-like tests begin to regain strength at a shear strain of 2 - 3%, while the specimens in the extension-like tests hardly regain strength and only at a shear strain larger than 6%. The strength increases above the value corresponding to the triggering of flow in the compression-like tests, as a result of plastic dilation occurring past the PTP, while it remains below that value in the extension-like tests because the tendency for dilation is very weak even at a shear strain as high as 8%. It can be seen that the weakest response, either stable or unstable, is exhibited in the tests with $\alpha_{\sigma'1}$ = 67.5º (A14) and 75º (A16) and not in the test with $\alpha_{\sigma'1}$ = 90º (A20). Similarly, Fig. 7.14d shows that the shear strain, γ_{oct}, and the value of the normalised excess pore-water pressure, $\Delta u / p'_i$, at the PTP increases, in general, when the principal stress direction angle, $\alpha_{\sigma'1}$, increases. However, the maximum ratio $\Delta u / p'_i$, with a value of around 0.90, is developed in the tests with $\alpha_{\sigma'1}$ = 67.5º (A14) and 75º (A16) and not in the test with $\alpha_{\sigma'1}$ = 90º (A20).

Figure 7.15 shows the relationship between the mobilised angle of shearing resistance, φ, the principal stress direction angle, $\alpha \equiv \alpha_{\sigma'1}$, and the angle between the plane of maximum stress obliquity and the bedding plane, ω_1 (Fig. 7.15a) or ω_2 (Fig. 7.15b); it is recalled that the angle ω_1 corresponds to the plane of maximum stress obliquity nearer to the bedding plane, i.e. abs(ω_1) < abs(ω_2) ("abs" stands for the absolute value). The plane of maximum stress obliquity nearer to the bedding plane will be termed the ω_1-plane, hereinafter, while the plane of maximum stress obliquity further to the bedding plane will be termed the ω_2-plane. The horizontal axis shows the φ-values, the vertical axis shows the ω-values, while the dashed lines in the figure indicate the loci of equal α. The data points from tests A4, A14, A16 and A20 are plotted to show how the values of φ, ω, and α evolve during shearing and especially in the course of unstable flow response.

Figure 7.15 shows that the principal stress direction angle, $\alpha \equiv \alpha_{\sigma'1}$, remains fixed at 90^o during flow in test A20 (the data points corresponding to the phase of flow are sparsely populated). On the other hand, the angle α decreases slightly in test A4, while it increases considerably in tests A14 and A16. A common pattern of ω-evolution is observed during flow irrespective of whether α increases or decreases: the ω_1-plane moves away from the bedding plane when stability and controllability is lost, while the ω_2-plane approaches the bedding plane. It is noted that the ω_1-plane is approaching the bedding plane before the triggering of instability in tests A14 and A16 but the response bifurcates and a different route is followed in the ω - φ - α space past the instability point. Moreover, it can be seen that the ω_1-plane is closer to the bedding plane, before and after the triggering of instability, in tests A14 and A16 compared to test A20; for example, the angle ω_1 at the IP is -14.5^o, -19.8^o and -34.7^o in tests A14, A16 and A20, respectively.

The results presented in Fig. 7.15 justify why the weakest response of sand is exhibited in tests A14 and A16, with α = 67.5^o and 75^o respectively, and not in test A20, with α = 90^o (see Fig. 7.14); it is noted that the behaviour of the specimens loaded at α = 60^o in tests A12 and A13 is similar to that of the specimens loaded at α = 67.5^o and 75^o, since past the IP the strength decreases significantly, the principal stress direction angle, α, increases and the ω_1-plane moves away from the bedding plane though the strength of the former specimens at the IP is somewhat higher. It can be suggested that the proximity of the plane of maximum stress obliquity to the bedding plane affects the strength and deformability of sand, while the horizontal bedding plane is a characteristic of the specimen - apparatus system that also affects the patterns of diffuse bifurcation. However, the effects of stress PA rotation, as well as of the change in the value of b, on the strength and deformability of sand should not be overlooked.

Figure 7.16 shows the IPs in the Y - X deviatoric plane of all A-series loading tests on loose M31 Sand consolidated to a mean effective stress of p'_c = 200 kPa (the results of the tests at p'_c = 100 kPa are given in Table 7.2). The IPs and their reflections in the negative-Y regime are indicated with solid circles in the case of loose sand and with hollow circles in the case of very loose sand. Curve fitting to the IPs (solid circles) yields the Instability Surface (IS) of loose IC M31 Sand shown with a solid line. The shape of the IS is elliptic with the major axis coinciding with the *X*-axis and the minor axis being located in the positive-*X* regime, parallel to the *Y*-axis. The IS is open at one end (i.e. the ellipse is cut at one end) because the response of loose sand is stable at $\alpha < 10^{o}$.

The IPs shown in Fig. 7.16 are not equidistant from the origin of the *Y* - *X* plane because flow instability is triggered, in general, at a lower stress ratio, sin φ, when the principal stress direction angle, α, increases. Consequently, the shape of the IS indicates the effects of the anisotropy of sand on the flow-instability condition. Since flow instability is triggered in the A-series tests at very low shear strain, γ_{oct}, and relatively low stress ratio, q / p', the initial anisotropy of fabric due to the preferred orientation of the long axes of grains and due to the packing of grains formed under gravity deposition is not expected to have been altered significantly at the IPs; this suggestion is supported by the results of microscopic studies that quantify the fabric anisotropy and show that considerable fabric changes occur past the phase-transformation point or the peak-failure state (Oda et al. 1985, Yimsiri and Soga 2010). It is, thus, suggested that the shape of the Instability Surface expresses phenomenologically the initial anisotropy of sand and for this reason it will be termed the initial Instability Surface, hereinafter.

Figure 7.16 shows the contours of equal shear strain γ_{oct} (0.25%, 0.50% and 1.00%) and of equal normalised excess pore-water pressure Δu / p'_i (0.15, 0.30, 0.45 and 0.60) together with the IS in the *Y* - *X* deviatoric plane. The γ_{oct}-contours are indicated with dotted lines while the Δu / p'_i-contours are indicated with dashed lines; both sets of contours correspond to the contractive phase of response of loose sand specimens in the A-series tests. The shape of the contours is elliptic with the major axis coinciding with the *X*-axis and the minor axis being located in the positive-*X* regime, parallel to the *Y*-axis. The contour corresponding to Δu / $p'_i = 0.60$ is open at one end (i.e. the ellipse is cut at one end) because the normalised excess pore-water pressure accumulated at the PTP at $\alpha < 20^{o}$ is lower than 0.60. The stress states on a given contour are not equidistant from the origin of the *Y* - *X* plane which means that the same amount of shear strain or plastic volumetric strain is induced at a different mobilised stress ratio, sin φ, depending on the value of α. Specifically, the value of sin φ corresponding to a given value of γ_{oct} or Δu / p'_i decreases when α increases. The value of γ_{oct} at the IP is around 0.50% in the compression-like loading regime and shifts gradually to 0.25% in the extension-like loading regime, while a practically constant value of Δu / $p'_i = 0.30$ is exhibited at the IP irrespective of the value of α and e (see Table 7.2). These results indicate that the deformability of loose sand is strongly anisotropic.

Figure 7.17a shows the unit vectors d$\boldsymbol{\varepsilon}$ that indicate the direction of the principal strain rate, $\alpha_{d\varepsilon 1}$, at the onset of instability superimposed on the IPs in the *Y* - *X* deviatoric plane (see also Section 7.3 for the definition of the unit vectors d$\boldsymbol{\varepsilon}$); the direction $\alpha_{d\varepsilon 1}$ is computed using the incremental relationship tan $2\alpha_{d\varepsilon 1} = 2d\varepsilon_{z\theta} / (d\varepsilon_{zz} - d\varepsilon_{\theta\theta})$ in terms of total strains and under the assumption of $\varepsilon_{\theta\theta} = \varepsilon_{rr}$, while the direction of the corresponding principal stress rate is still radial (i.e. $\alpha_{d\sigma'1} = \alpha_{\sigma'1}$). It can be seen that the direction of the principal strain rate, $\alpha_{d\varepsilon 1}$, does not generally coincide with that of the principal stress, $\alpha_{\sigma'1}$, since the unit vectors $d\boldsymbol{\varepsilon}$ deviate from the radial direction towards the dY_ε-direction (notice that the axes $dY_\varepsilon = d\varepsilon_{z\theta}$, $dX_\varepsilon = d(\varepsilon_{zz} - \varepsilon_{\theta\theta}) / 2$ are superimposed on a given stress state in the Y - X plane to offer the reference frame for determining the direction angle $\alpha_{d\varepsilon 1}$). As expected, the direction of the principal strain rate coincides with that of the principal stress when $\alpha_{\sigma'1} = 0^o$ or 90^o.

Figure 7.17b shows the variation of the difference between the angles $\alpha^*_{d\varepsilon 1}$ and $\alpha^*_{\sigma'1}$ at the IPs with respect to $\alpha^*_{\sigma'1}$. It is recalled that the angles $\alpha^*_{d\varepsilon 1}$ and $\alpha^*_{\sigma'1}$ vary between 0^o and 180^o, and increase monotonically in the counterclockwise direction in the Y - X plane, according to the alternative convention presented in Section 7.3, thus, a positive angle difference, $\alpha^*_{d\varepsilon 1} - \alpha^*_{\sigma'1}$, means that the axis of principal stress lags behind the axis of principal strain rate and vice versa. Figure 7.17b shows that using the assumption of $\varepsilon_{\theta\theta} = \varepsilon_{rr}$ the angle difference $\alpha^*_{d\varepsilon 1} - \alpha^*_{\sigma'1}$ is positive when $\alpha^*_{\sigma'1} < 50^o$ and negative when $\alpha^*_{\sigma'1} \geq 50^o$. The positive maximum of $\alpha^*_{d\varepsilon 1} - \alpha^*_{\sigma'1}$ is observed at $\alpha^*_{\sigma'1} = 22.5^o$ while the negative maximum is observed at $\alpha^*_{\sigma'1} = 75^o$. Using the assumption of $\varepsilon_{rr} = 0$ (plane-strain deformation) the angle difference, $\alpha^*_{d\varepsilon 1} - \alpha^*_{\sigma'1}$, becomes lower than the one corresponding to the assumption of $\varepsilon_{\theta\theta} = \varepsilon_{rr}$ when $\alpha^*_{\sigma'1} < 45^o$, being again maximum at $\alpha^*_{\sigma'1} = 22.5^o$, while it becomes negligible when $\alpha^*_{\sigma'1} \geq 60^o$; however, the assumption of plane-strain deformation is rather inappropriate for extension-like tests since the ultimate mode of specimen deformation is necking associated with shortening of the radial dimension.

Taking into account that a large portion of the total shear strain at the IPs is plastic (for example, if a specimen is unloaded just before the triggering of instability the residual shear strain is large) the results presented in Fig. 7.17 indicate that the plastic deformation of sand is non-coaxial under loading with fixed stress PA. The fact that the unit vectors $d\boldsymbol{\varepsilon}$ deviate from the radial direction towards the dY_ε-direction, which corresponds to $\alpha_{d\varepsilon 1} = 45^o$, may be attributed to the initial fabric anisotropy of sand since the torsional-shear mode of deformation, $dY_\varepsilon = d\varepsilon_{z\theta}$, dominates over the triaxial mode of deformation, $dX_\varepsilon = d(\varepsilon_{zz} - \varepsilon_{\theta\theta}) / 2$, because sliding occurs more easily along the horizontal bedding plane (Miura et al. 1986). The non-coaxiality angle, $\alpha^*_{d\varepsilon 1} - \alpha^*_{\sigma'1}$, attains a maximum value between 5.2^o and 11.5^o at $\alpha^*_{\sigma'1} = 22.5^o$ (irrespective of the assumption used for the calculation of $\varepsilon_{\theta\theta}$ and ε_{rr}) thus the direction angle of the principal strain rate, $\alpha^*_{d\varepsilon 1}$, ranges between 27.7^o and 34^o, indicating that the mechanism of sliding along the bedding plane is partially mobilised. The mobilisation of this mechanism may then justify the unstable bifurcated behaviour of the specimen in test A4 presented in Figs 7.14b and 7.15a, i.e. the non-proportional unloading of the torsional-shear stress compared to the triaxial stress, resulting in a spontaneous rotation of the stress PA and divergence between the plane of maximum stress obliquity nearer to the bedding plane and the bedding plane.

7.7 UNDRAINED BEHAVIOUR OF ANISOTROPICALLY CONSOLIDATED M31 SAND UNDER LOADING WITH ROTATING STRESS PRINCIPAL AXES

This section resports the results of loading tests on anisotropically consolidated M31 Sand specimens in which the stress principal axes are rotated.

7.7.1 UNDRAINED BEHAVIOUR OF AC M31 SAND UNDER LOADING WITH ROTATING STRESS PA: FLOW INSTABILITY TRIGGERED ON THE INITIAL INSTABILITY SURFACE

The results of the B-series tests (B1 - B7) and selected C*-series tests (C1 and C2) are presented here. Loose sand specimens are subjected to monotonic rotation of the stress PA under increasing or constant deviatoric stress, q, in B- or C*-series tests, respectively, and flow instability is triggered during the first half of the first cycle of stress PA rotation; the latter feature differentiates the tests C1 and C2 from the other C-series tests the results of which are presented in Section 7.7.2. The specimens in tests B1 (and B4), B2 (and B5) and B3 are consolidated at K_c = 0.80, 0.50 and 0.40, respectively, to a mean effective stress of p'_c = 200 kPa, while the specimens in tests B6 and B7 are consolidated at K_c = 0.50 and 0.40, respectively, to a mean effective stress of p'_c = 100 kPa. The specimens in tests C1 and C2 are consolidated at K_c = 0.48 and 0.66, respectively, to a mean effective stress of p'_c = 200 kPa. The mean effective stress at the beginning of shearing is $p'_i > p'_c$ due to the pre-shearing process (Table 7.2). In this Section, the combined effects of the consolidation and loading history on the undrained behaviour of AC sand under stress PA rotation are investigated. Emphasis is put on investigating whether the initial Instability Surface, determined based on the results of the loading tests on IC sand at fixed stress PA, forms a boundary to a stable response when AC sand is subjected to stress PA rotation or not.

Figure 7.18 shows the results of the tests B1, B2, B3, C1 and C2 in the q_d - p' (a) and in the Y - X (b) planes. The labels attached to the hollow circles in the q_d - p' plane (Fig. 7.18a) indicate the value of the principal stress direction angle, $\alpha_{\sigma'1}$, at the marked stress states, while the red solid circles indicate the instability points (IPs) and the corresponding red labels indicate the value of $\alpha_{\sigma'1}$ at the triggering of instability. The acceleration of the development of shear strain and pore-water pressure and the loss of strength signal the triggering of flow instability in the same way as in the case of the A-series tests. The dashed and dotted straight lines that go through the origin of the q_d - p' plane represent the instability lines (ILs) at different values of $\alpha_{\sigma'1}$ determined in the A-series tests. The ILs are included in Fig. 7.18a to check whether instability in the B- and C*-series tests is triggered at the same combination of the mobilised stress ratio, q_d / p', and principal stress direction angle, $\alpha_{\sigma'1}$, as in the case of the A-series tests or not, with the comparison being made for sand specimens having a similar void ratio, e. The IPs determined in the B- and C*-series tests are shown in the

Y - X plane (Fig. 7.18b) with red solid circles while the initial Instability Surface determined in the A-series tests is shown a with red solid line to check whether instability in the B- and C*-series tests is triggered at the same combination of the mobilised stress ratio, sinφ, and principal stress direction angle, $\alpha_{\sigma'1}$, as in the case of the A-series tests or not.

It is noted that the PTP was not recorded in test C2 due to low-frequency (f = 0.5 Hz) data acquisition. In order to avoid the false interpretation of the test results shown in Fig. 7.18a, as a consequence of plotting sparsely recorded data points, the location of the PTP in the q_d - p' plane is estimated in test C2, based on the data collected with confidence in the tests A17 (K_c = 1.00) and C6 (K_c = 0.64) in which phase transformation occurred at $\alpha_{\sigma'1}$ = 86.2° and 76.2°, respectively. The unloading branch of the ESP of test C2 is assumed to coincide with that of test A17, ending at the same PTP, as shown with the grey broken line (the effective stress paths of tests C2 and A17 are shown together in Fig. 7.23b). The value of $\alpha_{\sigma'1}$ at the IP in tests C2 and A17 is 79.6° and 79.1°, respectively, and the incremental stress direction (in the Y - X plane) just before the triggering of instability is radial in both tests, while the stress state and the incremental stress direction in the q_d - p' plane at the IP is similar in both tests (see Fig. 7.23b). Consequently, the evolution of the stress state during the unstable flow is expected to be practically the same in tests C2 and A17. This is also justified by the findings of Shibuya et al. (2003b) indicating that the Local Boundary Surface (LBS) of AC sand coincides in the post-peak regime with that of IC sand when $\alpha_{\sigma'1} \geq 45°$ while the anisotropic consolidation is performed at $\alpha_{\sigma'1}$ = 0° and K_c = 0.50. It is recalled that the LBS describes the undrained behaviour of sand at small strains under both fixed and rotating directions of the stress PA.

Figure 7.18a shows that the IP determined in the B-series tests is located very close to the IL determined in the A-series tests when the value of the principal stress direction angle, $\alpha_{\sigma'1}$, indicated on the label of the IP is close to that characterising the IL. For example, instability was triggered at $\alpha_{\sigma'1}$ = 12.6° in test B1 with K_c = 0.40 and the IP determined in this test is located in the q_d - p' plane very close to the IL corresponding to $\alpha_{\sigma'1}$ = 10° (9.8°) determined in test A2 with K_c = 1.00 (see also Table 7.2). The comparison between the ESPs of the B-series tests shows that a lower increase in q_d and $\alpha_{\sigma'1}$ triggers flow instability when K_c decreases. These results indicate that the flow potential of sand becomes higher when the static shear stress increases and that the K_o-consolidated sand is vulnerable against flow triggered by small disturbances in the stress conditions. It is recalled that approximately K_o-conditions are achieved when the sand specimens are consolidated at K_c = 0.40 (see Fig. 7.7). On the other hand, sand consolidated at higher values of K_c suffers differently since it mobilises a lower transient-peak and minimum undrained strength due to a higher value of $\alpha_{\sigma'1}$ at the IP and PTP, respectively, and due to a lesser degree of expansion of the Local Boundary Surface (LBS) induced by anisotropic consolidation (Zdravkovic and Jardine 2001, Shibuya et al. 2003b; Sivathayalan and Vaid 2002). It is noted that the

ESPs of the B-series tests correspond to traces along different LBSs depending on the value of K_c.

Figure 7.18a shows that the IP determined in tests C1 and C2 is located in the q_d - p' plane very close to the IL determined in the A-series tests when the value of the principal stress direction angle, $\alpha_{\sigma'1}$, indicated on the label of the IP is close to that characterising the IL. In the C*-series tests a lower increase in $\alpha_{\sigma'1}$ precedes the triggering of flow instability when K_c decreases. It is recalled that the rotation of the stress PA under constant stress difference, q_d, induces plastic contraction of sand and thus the pore-water pressure, u, and the effective stress ratio, q_d / p', increase. The comparison between the ESPs in the q_d - p' plane of the C*- and B-series tests on specimens consolidated at the same K_c (i.e. of tests C1 and B2) shows that the value of $\alpha_{\sigma'1}$ and Δu / p'_i at the IP is lower in the case that q_d increases compared to the case that q_d is kept constant. It is noted that the value of Δu / p'_i at the IP is indicated by the horizontal distance between the consolidation state and the instability point. The difference in the rotational capacity and normalised excess pore-water pressure at the IP may be justified if the position of the ESP in relation to the LBS is taken into consideration: in test C1 the ESP moves, before the triggering of instability, below the LBS while in test B2 the ESP moves along the LBS.

Figure 7.18b shows that the IPs determined in the B- and C*-series tests are located in the Y - X plane very close to the initial Instability Surface determined in the A-series tests. The stress paths of tests B1, B2, B3 and C1 move momentarily along the radial direction in the Y - X plane in the vicinity of the IP, while in the course of unstable flow the stress paths curve gently towards the X-axis; this occurs because the unloading of the torsional shear stress, Y_s, is more severe than that of the triaxial stress, X_s, as described in Section 7.4.2. After the regain of strength past the PTP the stress paths of tests B1, B2, B3 and C1 move along a more or less circular route on the failure surface while the principal stress direction angle, $\alpha_{\sigma'1}$, increases. It is noted that instability was triggered in test C2 during the pause period between the steps of stress PA rotation because the pore-water pressure increased due to creep. Consequently, the mechanical state of the system was not sustained during the pause period even though the control parameters did not change and equilibrium was lost as the system developed spontaneously kinetic energy; Nicot et al. (2007) showed that this situation corresponds to a proper bifurcation point.

Figure 7.18b shows the unit vectors d$\boldsymbol{\varepsilon}$ in the Y - X plane that indicate the direction of the rate of principal strain, $\alpha^*_{d\varepsilon 1}$, at the IPs in the tests B1, B2, B3, C1 and C2. It can be inferred that the non-coaxiality angle, $\alpha^*_{d\varepsilon 1}$ - $\alpha^*_{\sigma'1}$, at the IP is positive in all but C2 tests indicating that the axis of the principal stress lags behind the axis of the rate of principal strain, considering that both angles increase in the counterclockwise direction in the Y - X plane (the asterisk indicates that the alternative convention for the sign and value of the direction angles is used; see Section 7.3). However, in test C2 the plastic deformation of sand is coaxial at the IP because instability is actually triggered under radial loading, as discussed previously. It is interesting to observe that the vectors d**ε** in tests B1 and C1 are almost parallel to the positive d$Y_ε$-axis indicating that the mechanism of sliding along the bedding plane is almost fully mobilised since this situation corresponds to $\alpha^*_{d\varepsilon 1}$ = 45° (or 135°) while the value of $\alpha^*_{d\varepsilon 1}$ at the IP in tests B1 and C1 is 42.7° and 40.6°, respectively. Consequently, the sliding mechanism along the bedding plane may be related to the non-proportional unloading of the torsional shear stress, Y_s, compared to the triaxial stress, X_s, which is more profound in tests B1 and C1 compared to the other tests (see also the labels indicating the value of $\alpha_{\sigma'1}$ during flow in Fig. 7.18a).

Figures 7.19a shows the rotational capacity, $\Delta\alpha_{\sigma'1}$, at two different levels of shear strain (γ_{oct} = 0.01% and 0.10%) and at the IP as a function of K_c, while Fig. 7.19b shows the normalised excess pore-water pressure, Δu / p'_i, at the IP as a function of K_c; $\Delta\alpha_{\sigma'1}$ shows the monotonic increase of the angle of rotation of the stress PA from 0° to 180°, in the first cycle of rotation, from 180° to 360° in the second cycle of rotation etc. It can be seen that the rotational capacity at each shear strain level and at the IP increases when K_c increases, irrespective of the loading history, while the rotational capacity at a given K_c is always higher in the C*-series tests, in which the stress difference, q_d, is kept constant, compared to the B-series tests, in which q_d increases simultaneously with $\alpha_{\sigma'1}$. Similarly, the normalised excess pore-water pressure, Δu / p'_i, at the IP increases when K_c increases, irrespective of the loading history, while the value of Δu / p'_i at a given K_c is always higher in the C*-series tests compared to the B-series tests. These results corroborate the idea that the amount of rotation of the stress PA and the plastic contraction that can be sustained by the sand before the triggering of flow instability decreases when the static shear stress increases and when the ESP moves closer to the LBS. Consequently, the consolidation and loading history influences the undrained behaviour of sand under stress PA rotation.

Figure 7.20a shows the mobilised angle of shearing resistance, φ, against the principal stress direction angle, $\alpha_{\sigma'1}$, at the IP in the A-, B- and C*-series tests. The test results shown correspond to loading under b = 0.50 and constant p, with fixed or rotating stress PA, and all specimens are consolidated to a mean effective stress of p'_c = 200 kPa at K_c values varying between 0.40 and 1.00. It can be seen that the mobilised φ at the IP decreases, in general, when $\alpha_{\sigma'1}$ increases and that there exists a more or less unique relationship between φ and $\alpha_{\sigma'1}$, irrespective of the consolidation and loading history; the solid line shown expresses this relationship, being actually the transformation of the Instability Surface (IS) from the Y - X plane to the φ - $\alpha_{\sigma'1}$ plane. These results agree well with the findings of the studies by Nakata et al. (1998) and Sivathayalan and Vaid (2002). Figure 7.20b shows the IPs and the stress paths in the Y - X plane of the A-, B- and C*-series tests; the IPs shown in Fig. 7.20a are also shown in Fig. 7.20b. It can be seen that the IPs determined in the B- and C*-series tests are located very close to the IS determined in the A-series tests indicating that the IS forms a boundary to a stable response of sand to undrained loading, irrespective of the consolidation and loading history. However, the lack of dependence of the flow-instability condition on the previous stress - strain history does not comply with the theoretical considerations discussed in Section 7.5.3, while this notion will be falsified in the following under the light shed by the results of the C-series tests.

The stress paths in Fig. 7.20b exhibit some common characteristics in the course of unstable flow in all series of tests despite the fact that the bifurcated response is unpredictable and non-unique since it depends on the imperfections and perturbations in the system. For example, the unloading of the torsional shear stress, Y_s, is predominant in all series of tests, both under compression-like and extension-like loading conditions, as can be realised by the curving of the stress paths past the IP. This behaviour is noticeable when the value of the principal stress direction angle, $\alpha_{\sigma'1}$, at the IP ranges between 22.5^o and 35^o or between 60^o and 75^o; it has been shown that the first case corresponds to sliding along the bedding plane while the second case corresponds to shearing along the bedding plane. Moreover, the stress paths in tests A4, A6, C1 and B1 are similarly curved during the unstable flow in a pattern typically attributed to moving along a boundary surface in the Roscoe sense (Roscoe et al. 1958, Symes et al. 1984), while this pattern is repeatable when the same loading conditions are imposed on two similar specimens, as in the case of tests B1 and B4 (the stress path B4 is shown with a dashed line).

The results presented here indicate that the horizontal bedding plane is a characteristic that influences the bifurcated behaviour of the specimen - apparatus system. However, an extended discussion on the various non-material characteristics that may affect the unstable bifurcated response of the specimen - apparatus system is presented in the end of this chapter and in the article by Triantafyllos et al. (2020), presented in the Appendix.

7.7.2 UNDRAINED BEHAVIOUR OF AC M31 SAND UNDER LOADING WITH ROTATING STRESS PA: FLOW INSTABILITY TRIGGERED BEYOND THE INITIAL INSTABILITY SURFACE

In this section it is shown that the initial Instability Surface (IS) established previously can be crossed stably when loose anisotropically consolidated (AC) M31 Sand is subjected to undrained rotation of the stress principal axes (PA) while keeping the magnitude of the three total principal stresses, σ_1, σ_2 and σ_3, constant. The specimens in the C-series tests, the results of which are presented here, have an initial void ratio, e_i, ranging between 0.704 and 0.721 after being consolidated to a mean effective stress of p'_c = 200 kPa (and then pre-sheared to a mean effective stress $p'_i > p'_c$), at values of K_c ranging between 0.64 and 0.75 (Table 7.2). The combinations of e and K_c are such that the static shear stress, q_d, sustained during the rotation of the stress PA (before the triggering of instability) is higher than the minimum undrained strength mobilised in the A-series tests at $\alpha_{\sigma'1} \geq 45^o$, with the comparison being made between specimens having a similar void ratio. Moreover, under these combinations of K_c and e at least one full cycle of stress PA rotation is performed before the triggering of instability.

Figure 7.21 shows the results of the tests C3, C4, C5 and C6 in the q_d - p' (a) and in the Y - X (b) planes. The labels attached to the hollow circles in the q_d - p' plane (Fig. 7.21a) indicate the value of the principal stress direction angle, $\alpha_{\sigma'1}$, at the marked stress states, while the red solid rhombuses mark the instability points (IPs) and the corresponding red labels indicate the value of $\alpha_{\sigma'1}$ at these points. The acceleration of the development of shear strain and pore-water pressure and the loss of strength signal the triggering of flow instability in the same way as in the case of the A-series tests. However, the red rhombus marks the state at which the controllability of the loading programme is lost in test C6 (Nova 1994, Nicot et al. 2011) at peak failure because the static shear stress, q_d, cannot be further sustained, while flow-instability is triggered at another failure state (reached upon further stress rotation) marked with a square symbol that has an x at its centre. The dashed and dotted straight lines that go through the origin of the q_d - p' plane represent the instability lines (ILs) at different values of $\alpha_{\sigma'1}$ determined in the A-series tests. The IPs determined in the C-series tests in the Y - X plane (Fig. 7.21b) are shown with red solid rhombuses and one red solid square. The initial Instability Surface determined in the A-series tests is shown with a red solid line, while the Instability Surface determined in the C-series tests, i.e. the one that goes through the rhombuses, is shown with a red dashed line.

Figure 7.21a shows that the IP determined in the tests C3, C4, C5 and C6, characterised by the value of $\alpha_{\sigma'1}$ on the attached label, is located in the q_d - p' plane to the left of and away from the IL determined in the A-series tests, characterised by a similar value of $\alpha_{\sigma'1}$. This means that the stress ratio, q_d / p', at the triggering of flow instability is not uniquely related to the principal stress direction angle, $\alpha_{\sigma'1}$, but it depends on the consolidation and loading history instead. Recalling that $\alpha_{\sigma'1}$ changes from 0° to 90° to -45° and to 0° again during a full cycle of rotation of the stress PA it can be inferred that the monotonic rotation angle, $\Delta\alpha_{\sigma'1}$, at the IP increases when K_c increases. For example, flow instability is triggered during the fourth cycle of stress PA rotation at $\Delta\alpha_{\sigma'1} = 597.4°$ ($\alpha_{\sigma'1} = 57.4°$) in test C3 with $K_c = 0.75$, and during the second cycle of stress PA rotation at $\Delta\alpha_{\sigma'1} = 244.4°$ ($\alpha_{\sigma'1} = 64.4°$) in test C6 with $K_c = 0.64$. On the other hand, the value of the normalised excess pore-water pressure, Δu / p'_i, at the IP, indicated by the horizontal distance between the consolidation state and the instability point, does not change monotonically with K_c, presumably because it is also strongly dependent on the value of the void ratio, e. It is noted that flow instability is triggered past the peak-failure state in test C6 and that the state of minimum undrained strength was not recorded in test C5 but it was estimated in the same way as in test C2 instead (see Section 7.7.1).

Figure 7.21b shows that the IPs determined in the tests C3, C4, C5 and C6 are located in the Y - X plane beyond the Instability Surface determined in the A-series tests indicating that the stress ratio, sinφ, at the triggering of flow instability is not uniquely related to the principal stress direction angle, $\alpha_{\sigma'1}$, but it depends on the consolidation and loading history instead. An interesting observation is that stability is sustained if the angle between the stress path and the IS at the intersection point is small, i.e. if the stress path moves almost tangentially to the IS. For example, the results of the tests C6 and C3 corroborate the notion that the instability condition depends on the incremental stress direction. It is noted that instability was triggered in the tests C4 and C5 during the pause period between the steps of stress PA rotation because the pore-water pressure increased due to creep. Consequently, the stress path in these tests probes the IS along the radial direction yet stability is sustained presumably due to the effects of the consolidation and loading history. The results of test C6 also indicate that the triggering of flow instability may occur after the stress PA are rotated on the failure surface.

The instability points in the *Y* - *X* plane (Fig. 7.21b) from the C-series tests (marked with rhombuses) determine a new Instability Surface that is located between the initial Instability Surface and the failure surface. The shape of the new IS corresponds to a part of an ellipse similar to that representing the initial IS though it is more expanded. Recalling that the anisotropy of sand evolves in the course of loading (Oda et al. 1985, Yimsiri and Soga 2010) it may be speculated that the new IS corresponds to a different state of anisotropy compared to that indicated by the initial IS hence it will be called the evolved IS, hereinafter. It should be noted, though, that there exist an infinite number of such surfaces, each determined by the states at which instability is triggered under a specific stress - strain history in a set of similar loading tests, and that these surfaces lack intrinsic value. Nevertheless, the utility of the concept of the initial and evolved instability surfaces is to show that the triggering of instability depends on the stress - strain history, while the subsequent pattern of unstable flow depends on the proximity of the IP to the failure surface, as will be shown in the following.

Figure 7.22 shows the mobilised angle of shearing resistance, φ, against the principal stress direction angle, $\alpha_{\sigma'1}$, at characteristic stress states. The states at which flow instability is triggered are indicated with: 1) solid and hollow circles in the case of the A-series tests on loose and very loose IC sand specimens, respectively, 2) solid squares in the case of the B- and C*-series tests on loose AC sand specimens that flow during the first half of the first cycle of stress PA rotation, 3) solid rhombuses in the case of the C-series tests on loose AC sand specimens that exhibited flow past the first cycle of stress PA rotation (one rhombus indicates the state at which the controllability of the loading programme was lost at the peak-failure state) and 4) a solid square with an x at its centre in the case of the specimen in test C6 that exhibited flow instability at a failure state, while the stress PA were rotated on the failure surface. The peak-failure states are indicated with x-symbols. The initial IS is shown with a thin red solid line, the evolved IS is shown with a red dashed line and the failure surface is shown with a thick red solid line. The evolution of φ and $\alpha_{\sigma'1}$ during the test C6 is indicated with a black solid line.

Figure 7.22 shows that the mobilised angle of shearing resistance, φ, at the triggering of flow instability is not uniquely related to the principal stress direction angle, $\alpha_{\sigma'1}$, as suggested by Nakata et al. (1998) and Sivathayalan and Vaid (2002), but it depends on the consolidation and loading history instead. For example, flow instability is triggered at around $\alpha_{\sigma'1} = 60^o$ and at $\varphi = 20.0^o$, 25.6^o or 39.1^o in tests A13, C3 and C6, respectively (Table 7.2). These results prove that the stress ratio at the triggering of diffuse flow instability lacks intrinsic value, as it was also shown in the study by Darve et al. (1995); however, in the present study the experimental evidence is obtained without relaxing the isochoric (due to undrained conditions) constraint. The results of test C6 indicate that the monotonic loading may continue in a stable mode beyond the initial IS and until reaching the failure surface. Thereupon, softening occurs obligingly as the stress state moves on the anisotropic failure surface (Symes et al. 1984).

The failure surface shown in Fig. 7.22 is the curve fitted to the peak-failure states determined in the A-, B- and C-series tests with $p'_c = 200$ kPa and $b = 0.5$, including the tests C1, C2 and D1. The octahedral shear strain, γ_{oct}, at failure is generally less than 8% thus the deformation of the specimen is fairly homogeneous. In the case that the response of sand is very contractive and ductile the value of γ_{oct} at failure is marginally higher than 8% yet the deformation of the specimen is still homogeneous. In extension-like tests the deformation of the specimen shows signs of necking at high strains thus the failure states are defined, whenever possible, before the triggering of this type of bifurcation. In some extension-like tests the value of b at failure varies between 0.30 and 0.50 but the effect of this variation on the strength characteristics when shearing is imposed along the bedding plane is rather small (Lam and Tatsuoka 1988). It is noted that the anisotropic failure surface shows a minimum of φ in the range of $\alpha_{\sigma'1}$ from 60^o to 75^o indicating that some characteristics of the initial fabric, for example the horizontal bedding plane, may endure even after the sand is sheared to peak failure. Similar results were reported in the Discrete Element Method (DEM) simulations of loading tests on homogeneously deforming specimens by Jiang et al. (2017), while Chen and Huang (2019) incorporated this type of non-monotonic variation of peak stress ratio with $\alpha_{\sigma'1}$ in their model.

The results presented in Figs 7.20, 7.21 and 7.22 indicate that instability may or may not be triggered when the stress state reaches the initial IS depending on the direction of the incremental stress. It is noted that the direction of the incremental (normalised) stress in the Y - X plane is uncontrollable, because it depends on the rate of the pore-water pressure, du, and does not generally coincide with the direction of the incremental principal stress, $d\sigma'_1$ (see Section 7.3), which is controllable as far as the response of sand is stable. Stability is sustained if the angle between the stress path and the initial IS is small. For example, stability is sustained in the case that the stress path of test C6 moves tangentially to the initial IS (Fig. 7.21b) though stability is lost in the case that the stress path of test C2 probes the initial IS perpendicularly (Fig. 7.20b). However, the value of the stress difference, q_d, should be also taken into consideration when investigating the effect of the incremental stress direction on the triggering of instability at two stress states with identical values of $\alpha_{\sigma'1}$ and φ.

Figure 7.23 shows the stress paths of the tests C2, C6, A2 and A17 in the q_d - p' (a) and in the Y - X (b) planes; the symbols used are the same as in Figs 7.21 and 7.22. It can be seen that the stress paths of the tests C2 and C6 reach the initial IS at $\alpha_{\sigma'1}$ = 80^o and -80^o, while the value of q_d is 87 kPa and 94 kPa, and the value of p' is 128 kPa and 149 kPa, respectively (note that the value of φ is similar in both tests when the stress paths reach the IS). The specimens in these two tests have a similar void ratio, e, and are consolidated practically to the same stress p'_i and at the same stress ratio K_c. Consequently, the only factor that differs considerably when the initial IS is probed, and may justify why instability is triggered in test C2 but not in test C6, is the direction of the incremental stress (in the Y - X plane), which depends on the evolution of the excess pore-water pressure and is, thus, affected by the small differences in e and K_c.

On the other hand, the stress paths of the tests C6 and A2 reach the initial IS at $\alpha_{\sigma'1}$ = 10^o and probe it along different directions of incremental stress yet the value of the stress difference, q_d, is also different, being equal to 97 kPa and 163 kPa, respectively (see Figs 7.23a and b). Consequently, the fact that instability is triggered in test A2 but not in test C6 may be related to the different direction of incremental stress (in the Y - X plane) as well as to the different level of deviatoric stress. It is noted that Prunier et al. (2009) investigated numerically and analytically the influence of the level of deviatoric stress on the instability criterion under general 3D stress conditions yet the direction and rotation of the stress PA with respect to the depositional fabric axes were not taken into consideration. Lastly, the stress paths of the tests C2 and A17 reach the IS at $\alpha_{\sigma'1}$ = 80^o and probe it along the radial direction, while the stress state and the incremental stress direction in the q_d - p' plane is also the same in both tests thus instability is triggered when the initial IS is probed in these tests.

Figure 7.24 shows the normalised excess pore-water pressure, Δu / p'_i, against the principal stress direction angle, $\alpha_{\sigma'1}$, at phase transformation (pt) and at the instability point (ip) for the A- and C-series (C3 to C6) tests. The data of the A-series tests are indicated with hollow symbols while the data of the C-series tests are indicated with similar but solid symbols. In this figure it is considered that the principal stress direction angle at phase transformation has the same value as at the IP, in order to visualise clearly the data points and ease the interpretation of the results. Moreover, the value of Δu / p'_i at the PTP in test C5 is estimated in the same way as in test C2 since the data corresponding to the response of sand at phase transformation were not recorded due to low-frequency data acquisition.

A new flow parameter, $U_I = (u_{pt} - u_{ip}) / p'_i$, is introduced, and plotted against $\alpha_{\sigma'1}$ in Fig. 7.24 for both series of tests, in order to distinguish the plastic contraction occurring unstably during flow from that occurring stably before the triggering of flow (Borja 2006) and quantify indirectly the former. Discrete Element Method (DEM) simulations have shown that the unloading of the stresses p' and q occurring during the isochoric flow of granular materials is related to a loss of intergranular contacts and weakening of the force-bearing grain structures (Gong et al. 2012, Guo and Zhao

2013). Considering that the spontaneous (and conditionally unstable) unloading of stresses occurring during the undrained flow deformation of saturated sands is the result of the pore-water pressure build up the flow parameter U_I may express macroscopically the type of destructuration described in the DEM studies, which is stress - strain history dependent as shown next.

Figure 7.24 shows that in the case of the A-series tests the normalised excess pore-water pressure at the IP, $(\Delta u\ /\ p'_i)_{ip}$, is around 0.30, irrespective of the value of $\alpha_{\sigma'1}$, while the normalised excess pore-water pressure at the PTP, $(\Delta u\ /\ p'_i)_{pt}$, is equal to 0.44 at $\alpha_{\sigma'1} = 10^o$, attains a maximum value of 0.90 - 0.91 at $\alpha_{\sigma'1} = 60^o$-75^o and then decreases slightly to 0.83 at $\alpha_{\sigma'1} = 90^o$. Consequently, the flow parameter, U_I, in the A-series tests increases from 0.16 to 0.61 and then decreases to 0.51 when $\alpha_{\sigma'1}$ increases from 10^o to 60^o and then to 90^o. On the other hand, the ratio $(\Delta u\ /\ p'_i)_{ip}$ in the C-series tests (C3 to C6) is 0.68 - 0.69 when $\alpha_{\sigma'1}$ ranges between 57.4^o and 64.4^o and decreases to 0.55 when $\alpha_{\sigma'1}$ ranges between 79.6^o and 90.0^o, while the ratio $(\Delta u\ /\ p'_i)_{pt}$ is around 0.85 when $\alpha_{\sigma'1}$ ranges between 57.4^o and 90.0^o. Consequently, the flow parameter, U_I, in the C-series tests increases from 0 to around 0.30 when $\alpha_{\sigma'1}$ increases from 30^o to 90^o.

The results presented in Fig. 7.24 indicate that the normalised excess pore-water pressure at the IP, $(\Delta u\ /\ p'_i)_{ip}$, depends strongly on the stress history while the normalised excess pore-water pressure at the PTP, $(\Delta u\ /\ p'_i)_{pt}$, is practically unaffected by the stress history and depends only the value of $\alpha_{\sigma'1}$ at phase transformation. For example, the ratio $(\Delta u\ /\ p'_i)_{pt}$ is only slightly lower in the C-series tests (C3 to C6) compared to the A-series tests when the comparison is made at the same $\alpha_{\sigma'1}$ ranging between 57.4^o and 79.6^o. Similar findings indicating the dependence of $(\Delta u\ /\ p'_i)_{pt}$ on $\alpha_{\sigma'1}$, which is likely the result of the depositional fabric anisotropy, were reported by Yoshimine et al. (1998) and Yoshimine and Ishihara (1998). Moreover, the plastic contraction induced during the phase of unstable flow, indicated by the parameter U_I, is strongly dependent on the stress history, being considerably lower at a given $\alpha_{\sigma'1}$ in the C-series tests compared to the A-series tests. It is noted that a lower value of U_I in the C-series tests corresponds to a higher value of sinφ at the IP indicating that the pattern of flow becomes less contractive at a given $\alpha_{\sigma'1}$ when flow is triggered nearer to the failure surface, possibly due to the induced-anisotropy effects.

Figures 7.25a and b show the stress path of test C3 in the q_d - p' (a) and in the Y - X (b) planes, and the strain path in the Y_ε - X_ε plane (c); the symbols used are the same as in Figs 7.21a and b with the only difference being that the large hollow circles and the attached labels in Figs 7.25b and c mark some characteristic states described in the following, while the unit vectors superimposed on various stress states in Fig. 7.25b indicate the direction of the incremental principal strain, $\alpha_{d\varepsilon1}$. The effective stress paths (ESPs) of the tests A8 and A13, which were conducted on specimens having a similar void ratio to that of the specimen in test C3, are also included in Fig. 7.25a in order to visualise the Local Boundary Surface (LBS) of loose isotropically consolidated M31 Sand at $\alpha_{\sigma'1}$ = 45° and 60°, respectively. The test results in this study indicate that the LBS of AC sand, consolidated at $\alpha_{\sigma'1}$ = 0° and $K_c \geq 0.60$, coincides in the post-peak regime with that of IC sand when $\alpha_{\sigma'1} \geq 45°$; similar results have been reported by Shibuya et al. (2003b). It is recalled that the LBS describes the undrained behaviour of sand at small strains under both fixed and rotating directions of the stress PA.

Figure 7.25a shows that the stress path of test C3 in the q_d - p' plane crosses the instability line (IL) determined in test A8 ($\alpha_{\sigma'1}$ = 45°) at point 1 marking a stress state with $\alpha_{\sigma'1}$ = 45°. This means that the initial IS in the Y - X plane, shown with a red solid line in Fig. 7.25b, is probed at point 1 yet stability is sustained. It is noted that the initial IS is probed during the fifth cycle of rotation of the stress PA and that the angle between the stress path and the initial IS at the intersection point is small. These results indicate that the direction of the incremental stress (in the Y - X plane) is a factor that determines whether instability is triggered when the initial IS is probed or not. Instability is actually triggered when the ESP in the q_d - p' plane probes the post-peak regime of the LBS with an outwards direction at point 2 with $\alpha_{\sigma'1}$ = 57.4° and φ = 25.6°, during the fifth cycle of rotation of the stress PA. It is noted that the less steep of the planes of maximum stress obliquity makes an angle of 11° with the horizontal bedding plane at point 1 while it coincides with it at point 2. These results corroborate the notion that the triggering of diffuse flow instability during the undrained rotation of the stress PA occurs preferably at stress states that correspond to unfavourable deformation kinematics, i.e. to shearing and sliding along the bedding plane.

Figure 7.25b shows that the stress path of test C3 in the Y - X plane moves along the radial direction during the phase of unstable flow, indicating that the torsional-shear and triaxial stresses are unloaded proportionally in this test. The strength, stability and controllability are regained past the PTP and the rotation of the stress PA continues on the failure surface, at the stress difference, q_d, corresponding approximately to the initial conditions (Fig. 7.25a). The point H in Figs 7.25b and c indicates the dilative state at which the homogeneity of deformation is lost; the octahedral shear strain, γ_{oct}, at point H is 8.2%. However, the strain localisation observed with the naked eye (photos of the deformed specimen are shown next, in Fig. 7.28) is weak, having no detectable effect on the global measurements. On the other hand, the pairs of points 3 - 4 and 5 - 6 indicate the initiation and termination of two strong localisation events at a nominal shear strain γ_{oct} of around 16% and 18%, respectively.

The strong localisation events at points 3 - 4 and 5 - 6 are detected by naked-eye inspection (see Fig. 7.28) and interpretation of the stresses and strains. For example, the direction of the incremental strain, $\alpha_{d\varepsilon 1}$, at point 3 ($\alpha_{\sigma'1}$ = -72.5°) and 5 ($\alpha_{\sigma'1}$ = -62.5°) is -49.4° and -45.1°, respectively, indicating that strong non-coaxiality and sliding along the bedding plane are exhibited concurrently at the triggering of these localised instabilities. However, in the course of localised straining the plastic deformation becomes gradually coaxial, as indicated by the red unit vectors in Fig. 7.25b, the development of strains is accelerated and the strain path kinks (Fig. 7.25c).

The results obtained from the global measurements indicate that the less steep of the planes of maximum stress obliquity makes an angle of 11° with the horizontal bedding plane at points 3 and 4 while it coincides with it at points 5 and 6. Consequently, the triggering of localised instabilities during the undrained rotation of the stress PA appears to occur preferably at stress states that correspond to unfavourable deformation kinematics, in the same way as the triggering of diffuse instabilities does, with the only difference being that the latter are triggered first in the course of the monotonic loading (Desrues and Viggiani 2004, Nicot and Darve 2011, Lü et al. 2018). However, due to the lack of deformation homogeneity the results obtained from the global measurements should be treated with caution.

Figure 7.26 shows the relationship between the direction angles of principal stress, $\alpha^*_{\sigma'1}$, rate of principal stress, $\alpha^*_{d\sigma'1}$, and rate of principal strain, $\alpha^*_{d\varepsilon1}$ during the third, fourth and fifth cycle of rotation of the stress PA in test C3; the asterisk (*) indicates that the alternative convention described in Section 7.3 is used, thus, the direction angle of principal stress, $\alpha^*_{\sigma'1}$, increases from 0° to 90° to 180° during a full cycle of rotation of the stress PA. The direction angles $\alpha^*_{d\varepsilon1}$ and $\alpha^*_{d\sigma'1}$ are plotted against $\alpha^*_{\sigma'1}$ and the inclined dashed lines indicate the condition of coaxiality of the plastic deformation, $\alpha^*_{d\varepsilon1} = \alpha^*_{\sigma'1}$. The depicted relationships are periodical with a period of 180° and the horizontal axis plots the quantity N·180 + $\alpha^*_{\sigma'1}$, where N is the number of the completed cycles of rotation of the stress PA, i.e. N = 2, 3 or 4 during the third, fourth or fifth cycle, respectively, in the case investigated here. The data plotted in Fig. 7.26 correspond to the states on which a unit vector is superimposed in Fig. 7.25b. The plastic deformation of sand during the rotation of the stress PA is non-coaxial, as far as stability is sustained, since the direction of the rate of principal strain is intermediate between the directions of the rate of principal stress and of the principal stress, lagging before the former. The non-coaxiality angle, $\alpha^*_{d\varepsilon1} - \alpha^*_{\sigma'1}$, indicated by the vertical distance of the red circles (or squares) from the inclined dashed lines, decreases, in general, during the rotation of the stress PA, as far as stability is sustained, as a result of the loading process.

The degree of non-coaxiality changes abruptly when instabilities are triggered at points 2, 3 and 5; it is recalled that diffuse instability (flow) is triggered at point 2, while localised instabilities are triggered at points 3 and 5. The response of sand becomes suddenly coaxial when flow is triggered at point 2 (IP), while the deformation of the specimen is homogeneous, because the direction of the incremental stress, $\alpha^*_{d\sigma'1}$, in the Y_s - X_s plane changes due to the unloading of the stresses Y_s and X_s, the vector d$\boldsymbol{\sigma}$ becomes approximately opposite to the vectors $\boldsymbol{\sigma}$ and d$\boldsymbol{\varepsilon}$ and the direction of the principal stress, $\alpha^*_{\sigma'1}$, remains practically constant during flow. This can be realised from the fact that the value of the differences $\alpha^*_{d\sigma'1} - \alpha^*_{\sigma'1}$ and $\alpha^*_{d\varepsilon1} - \alpha^*_{\sigma'1}$ is around 90° and 0°, respectively, at point 2 (IP) (Fig. 7.26), while the stress path moves along the radial direction in the Y - X plane past the point 2 (Fig. 7.25b). On the other hand, a sudden transition to simple-shear deformation along the direction $\alpha^*_{d\varepsilon1} \approx 135°$ (or $\alpha_{d\varepsilon1} \approx -45°$) is observed at points 3 and 5 when the strong localisation events are triggered, resulting in a high degree of non-coaxiality. However, the response becomes coaxial as the localised straining continues. It is noted that the stresses and strains computed based on the global measurements after the localisation of strain are nominal and the true material response is actually unknown. It is worth mentioning though that Vardoulakis showed that the behaviour of sand becomes strongly non-coaxial at the onset of shear banding due to the rotation of the directions of stress and strain rate as the sand begins to deform in simple shear (Vardoulakis et al. 1978, Vardoulakis and Georgopoulos 2005, Gutierrez and Vardoulakis 2007).

Figure 7.27 shows the evolution of the normalised excess pore-water pressure, Δu / p'_i, and of the octahedral shear strain, γ_{oct}, with the monotonic rotation angle, $\Delta\alpha_{\sigma'1}$, in test C3; it is recalled that the angle $\Delta\alpha_{\sigma'1}$ increases monotonically from 0° to 180° during the first cycle of rotation of the stress PA, then from 180° to 360° during the second cycle of rotation etc. The hollow circles without label indicate here the points with $\alpha_{\sigma'1}$ = 90° while the hollow circles with the numbers 1 - 6 and the letter H on the label indicate the points discussed in the previous paragraphs. The value of the slope d(Δu / p'_i) / d($\Delta\alpha_{\sigma'1}$) at point 1 with $\alpha_{\sigma'1}$ = 45° during the fifth cycle of rotation of the stress PA is similar to that at the point with $\alpha_{\sigma'1}$ = 90° during the first cycle of rotation, being higher compared with the value exhibited at $\alpha_{\sigma'1}$ = 90° during the intermediate cycles of rotation; it is recalled that the initial IS is probed at point 1. The local tangent lines are shown at the points under investigation to highlight this interesting effect of strain-history memory which is rather related to the bedding plane since at point 1 the less steep of the planes of maximum stress obliquity makes an angle of only 11° with the bedding plane. The local maximum of γ_{oct} in each cycle of rotation of the stress PA (under stable conditions) occurs well beyond the state with $\alpha_{\sigma'1}$ = 90°. Analysis of the data shows that the same holds true for the extreme value of the normal strains ε_{zz} and $\varepsilon_{\theta\theta}$ indicating the induced-anisotropy effect (Tian and Yao 2018).

In an effort to investigate the utility of the flow parameter, U_I, as a means to describe the dependence of the flow behaviour on the stress - strain history and quantify macroscopically the damage induced to the sand's structure during flow (see Fig. 7.24), a comparison is made between the results of the tests C3 and A11. The value of (Δu / $p'_i)_{pt}$ (the subscript "pt" means "at phase-transformation") is 0.86 and 0.70 in test C3 and A11, respectively, while the value of U_I is 0.18 and 0.39 in test C3 and A11, respectively. These results indicate that the looser specimen in test C3 (e = 0.721), which became unstable at $\alpha_{\sigma'1}$ = 57.4°, is less contractive during flow than the denser specimen in test A11 (e = 0.699), which became unstable at $\alpha_{\sigma'1}$ = 49.5°, because the value of U_I is lower in test C3, albeit the value of (Δu / $p'_i)_{pt}$ being higher in test A11. This conclusion is also supported by the comparison between the values of the accumulated shear strain, γ_{oct}, at the PTP which are 3.93%, in test C3, and 3.54% in test A11. Apparently, the stress - strain history that precedes the triggering of flow influences the subsequent flow behaviour. The flow parameter, U_I, describes efficiently this stress - strain history dependence while the ratio (Δu / $p'_i)_{pt}$, used by

Yoshimine et al. (1998) and Yoshimine and Ishihara (1998) as a parameter indicating the *flow potential* of sand, depends only on the value of $\alpha_{\sigma'1}$ at the PTP and on the void ratio, e, (for fixed values of the effective consolidation stress, p'_c, and stress parameter, b) thus it cannot describe this type of dependence.

The post-flow dilatancy behaviour of the specimen in test C3 is investigated next. The normalised excess pore-water pressure, $\Delta u \,/\, p'_i$, decreases from 0.86, at the PTP, to 0.77, at point H, as the shear strain, γ_{oct}, increases from 3.9% to 8.2% (Fig. 7.27). Thereafter, the stress PA are rotated from $\alpha_{\sigma'1} = 59.1^o$, at point H, to $\alpha_{\sigma'1} = -72.5^o$, at point 3, under practically constant $\eta = q \,/\, p' = 1.00$ (or $q_d \,/\, p' = 1.16$) and $\Delta u \,/\, p'_i = 0.77$, while the shear strain increases to $\gamma_{oct} = 15.8\%$ (Figs 7.25 and 7.27). The sand deforms in an undrained steady state similar to that observed in the DEM simulations of drained principal stress rotation tests performed by Li and Yu (2010), Tong et al. (2014) and Theocharis et al. (2017), showing no tendency for plastic volume change and having a void ratio lower than the critical at the current mean effective stress, $e < e_c(p')$, while the non-coaxiality angle remains practically constant. Two strong localisation events are triggered at points 3 and 5 and the pore-water pressure measured at the base of the specimen decreases (Fig. 7.27) possibly because the sand inside the shear zones shows a tendency to dilate (or dilates in some degree) in order to attain a true critical state (Desrues et al. 1996, Vardoulakis and Georgopoulos 2005).

Figure 7.28 shows the photos of the specimen in test C3 at different levels of the shear strain, γ_{oct}. The photo in Fig. 7.28b is taken at point H, at shear strain $\gamma_{oct} = 8.2\%$. Some faint signs of strain localisation are observed since the grid lines on the membrane become wavy at some places and the specimen shows a slight neck at its lower part. Figure 7.28c shows the specimen at point 3, at shear strain $\gamma_{oct} = 15.8\%$, just before the triggering of the first strong localisation event. The grid lines at point 3 are wavier compared to the grid lines at point H but show the same inclination angle along the height of the specimen, while a discernible neck is observed at the lower part of the specimen. However, the results obtained from the global measurements as the state changes from point H to point 3 have still physical relevance since the non-coaxial plastic behaviour shown in Fig. 7.26 is typical for sand subjected to rotation of the stress PA under homogeneous deformation (see, for example, Fig. 7.33). The specimen undergoes strong simple-shear deformation with $\alpha^*_{d\varepsilon 1} \approx 135^o$ in the initial phase of the two strain localisation events (just after points 3 and 5) and this is depicted in the residual deformation pattern shown in Fig. 7.28d: the upper part of the specimen has been deformed in an extensional mode while the lower part has been deformed in an extensional - torsional mode indicating that the simple-shear deformation was localised in the lower part.

Figures 7.29a and b show the stress path of test C5 in the q_d - p' (a) and in the Y - X (b) planes; the symbols used are the same as in Figs 7.21a and b with the only difference being that the large hollow circles and the attached labels in Fig. 7.29b mark some characteristic states described in the following, while the unit vectors superimposed on various stress states in Fig. 7.29b indicate the direction of the incremental principal strain, $\alpha_{d\varepsilon 1}$. The state of minimum undrained strength was not recorded in test C5 but it was estimated in the same way as in test C2 instead (see Section 7.7.1). The ESPs of the tests A14 and A17, which were conducted on specimens having a similar void ratio to that of the specimen in test C5, are also included in Fig. 7.29a in order to visualise the LBS of loose isotropically consolidated M31 Sand at $\alpha_{\sigma' 1} = 67.5^o$ and 80^o, respectively.

Figure 7.29b shows that the stress path of test C5 in the Y - X plane probes the initial IS at point 2, with $\alpha_{\sigma' 1} = 79.2^o$, yet stability is sustained. It is noted that the initial IS is probed during the second cycle of rotation of the stress PA and that the angle between the stress path and the initial IS at the intersection point is small. However, the stress path becomes suddenly radial at point 2 because the pore-water pressure increases during the pause period between the steps of rotation of the stress PA due to creep and instability is triggered at point 3, with $\alpha_{\sigma' 1} = 79.6^o$. The stress state in the q_d - p' plane at point 2, with $\alpha_{\sigma' 1} = 79.2^o$, is located in the interior of the LBS, visualised by means of the ESP from test A17 performed at $\alpha_{\sigma' 1} = 80^o$. On the other hand, the stress state at point 3, with $\alpha_{\sigma' 1} = 79.6^o$, is located close to the LBS, visualised by means of the ESP from test A14 performed at $\alpha_{\sigma' 1} = 67.5^o$. It is noted that the principal stress direction angle, $\alpha_{\sigma' 1}$, is actually equal to 72.1^o (and not 67.5^o) at the state in the post-peak regime of the ESP of test A14 which is closer to point 3. Consequently, these results indicate that flow instability is not necessarily triggered when the initial IS is probed, because the incremental stress direction and the stress - strain history influence the instability condition, but it is triggered when the LBS is probed in the post-peak regime with an outwards direction instead.

It can be argued though that instability is actually triggered in test C5 at point 2 since the mechanical state of the system becomes unsustainable without changing the control parameters (Nicot et al. 2007). If this instability condition is adopted the new initial IS will be less expanded in the extension-like regime ($\alpha_{\sigma' 1} > 45^o$) compared to the old initial IS since the sustainability of the mechanical state is also lost in the A-series tests before the requirements of the instability criterion adopted in this study are satisfied (see Fig 7.14a). In this case instability in test C5 will again be triggered beyond the alternative initial IS, determined using the alternative instability criterion, i.e. the loss of sustainability of the mechanical state. Consequently, the statement that the stress - strain history and the incremental stress direction influence the triggering of flow instability of loose sand will again be verified. It is recalled that the triggering of flow instability is considered to occur in this study when the development of shear strain and excess pore-water pressure is accelerated and the deviatoric stress begins to decrease, indicating the loss of strength due to the uncontrollable generation of excess pore-water pressure.

Figure 7.30 shows the relationship between the direction angles of principal stress, $\alpha^*_{\sigma' 1}$, rate of principal stress, $\alpha^*_{d\sigma' 1}$, and rate of principal strain, $\alpha^*_{d\varepsilon 1}$ during the first and second cycle of rotation of the stress PA in test C5; the asterisk (*) indicates that the alternative convention described in Section 7.3 is used, thus, the direction angle of principal stress, $\alpha^*_{\sigma'1}$, increases from 0° to 90° to 180° during a full cycle of rotation of the stress PA. The direction angles $\alpha^*_{d\varepsilon1}$ and $\alpha^*_{d\sigma'1}$ are plotted against $\alpha^*_{\sigma'1}$ and the inclined dashed lines indicate the condition of coaxiality of the plastic deformation, $\alpha^*_{d\varepsilon1} = \alpha^*_{\sigma'1}$. The depicted relationships are periodical with a period of 180° thus the horizontal axis plots the quantity N·180 + $\alpha^*_{\sigma'1}$, where N is the number of the completed cycles of rotation of the stress PA, i.e. N = 0 or 1 during the first or second cycle, respectively, in the case investigated here. The data plotted in Fig. 7.30 correspond to the states on which a unit vector is superimposed in Fig. 7.29b.

Figure 7.30 shows that the plastic deformation of sand during the rotation of the stress PA is non-coaxial since the direction of the rate of principal strain is intermediate between the directions of the rate of principal stress and of the principal stress, lagging before the former. The non-coaxiality angle, $\alpha^*_{d\varepsilon1}$ - $\alpha^*_{\sigma'1}$, indicated by the vertical distance of the red circles from the inclined dashed line decreases, in general, in the course of the monotonic loading but remains non-zero as far as stability is sustained. On the other hand, coaxiality of the principal stress and rate of principal strain is observed at the IP (point 3) because the stress path is moving along the radial direction from point 2 to point 3. The direction of the incremental principal stress in the Y_s - X_s plane at point 3 is opposite to that of the principal stress, as indicated by the value of the difference $\alpha^*_{d\sigma'1}$ - $\alpha^*_{\sigma'1}$ which is around 90°, because the stresses Y_s and X_s are suddenly unloaded past the IP.

Figure 7.31 shows the evolution of the normalised excess pore-water pressure, Δu / p'_i, and of the octahedral shear strain, γ_{oct}, with the monotonic rotation angle, $\Delta\alpha_{\sigma'1}$, in test C5; it is recalled that the angle $\Delta\alpha_{\sigma'1}$ increases monotonically from 0° to 180° during the first cycle of rotation of the stress PA, then from 180° to 360° during the second cycle of rotation etc. The hollow circle without label marks here the state with $\alpha_{\sigma'1}$ = 90° while the hollow circles with the numbers 1 - 3 on the label mark the states discussed previously (point 1 is discussed next). The value of the slope d(Δu / p'_i) / d($\Delta\alpha_{\sigma'1}$) at point 1 with $\alpha_{\sigma'1}$ = 67.6° (and at point 2 with $\alpha_{\sigma'1}$ = 79.2°) during the second cycle of stress rotation is similar to that at the point with $\alpha_{\sigma'1}$ = 90° during the first cycle of stress rotation; it is recalled that the initial IS is probed at point 2. The local tangent lines are shown at the points under investigation to highlight this interesting effect of strain - history memory which is rather related to the bedding plane since at point 1 the less steep of the planes of maximum stress obliquity makes an angle of only 13.8° with the bedding plane. The local maximum of γ_{oct} during the first cycle of rotation of the stress PA occurs well beyond the state with $\alpha_{\sigma'1}$ = 90°.

Figures 7.32a and b show the stress path of test C6 in the q_d - p' (a) and in the Y - X (b) planes; the symbols used are the same as in Figs 7.21a and b with the only difference being that the large hollow circles and the attached labels in Fig. 7.32b mark some characteristic states described in the following, while the unit vectors superimposed on various stress states in Fig. 7.32b indicate the direction of the incremental principal strain, $\alpha_{d\varepsilon1}$. The effective stress paths (ESPs) of the tests A5, A9, A11, A13 and A17, which were conducted on specimens having a similar void ratio to that of the specimen in test C6, are also included in Fig. 7.32a in order to visualise the Local Boundary Surface (LBS) of loose isotropically consolidated M31 Sand at $\alpha_{\sigma'1} = 22.5^o$, 45^o, 50^o, 60^o and 80^o, respectively. The test results in this study indicate that the LBS of AC sand, consolidated at $\alpha_{\sigma'1} = 0^o$ and $K_c \geq 0.60$, coincides in the post-peak regime with that of IC sand when $\alpha_{\sigma'1} \geq 45^o$; similar results have been reported by Shibuya et al. (2003b). It is recalled that the LBS describes the undrained behaviour of sand at small strains under both fixed and rotating directions of the stress PA.

Figure 7.32a shows that the stress path of test C6 in the q_d - p' plane crosses the instability lines (IL) determined in the tests A17 ($\alpha_{\sigma'1} = 80^o$) and A9 ($\alpha_{\sigma'1} = 45^o$) at the stress states with $\alpha_{\sigma'1} = -80^o$ (point 2) and -45^o, respectively, yet stability is sustained. The ESP continues to move parallel to the horizontal axis, as the mean effective stress, p', decreases due to the buildup of pore-water pressure while the stress difference, q_d, remains constant, until it reaches the failure line at point 3 with $\alpha_{\sigma'1} = 30.2^o$. Flow instability is not triggered as the stress state moves from point 1 (consolidation state) to point 3 (failure state) because the ESP does not cross the post-peak regime of the Local Boundary Surface (LBS). Instead, the ESP moves beneath the rising LBS as the stress p' decreases and the angle $\alpha_{\sigma'1}$ changes from -45^o to 30.2^o. It is noted that the evolution of the stress state from point 1 to point 3 corresponds to isotropic stress unloading since $d\sigma'_1 = d\sigma'_2 = d\sigma'_3 = -du$.

Rotation of the stress PA is performed on the anisotropic failure surface from point 3, with $\alpha_{\sigma'1} = 30.2^o$ and $\varphi = 46.0^o$, to point 4, with $\alpha_{\sigma'1} = 64.4^o$ and $\varphi = 39.1^o$. The softening occurring at failure is due to the shape of the anisotropic failure surface (Symes et al. 1984, Triantafyllos et al. 2020) (see also Fig. 7.22). At point 3 the plastic contraction of sand turns into mild plastic dilation and the pore-water pressure, u, begins to decrease (see also Fig. 7.34) while the specimen deformation is still homogeneous ($\gamma_{oct} = 1.7\%$). From point 3 to point 4 the stress difference, q_d, decreases partly due to the membrane stretching and partly due to the material response indicating that the controllability of the loading programme is lost as the stress PA are rotated on the failure surface. Flow instability is triggered on the failure surface at point 4 with $\alpha_{\sigma'1} = 64.4^o$, $\varphi = 39.1^o$ and $\gamma_{oct} \approx 6.6\%$ thus the effects of the induced-anisotropy on the subsequent flow behaviour are expected to be pronounced (Yamada and Ishihara 1981, Oda et al. 1985, Yimsiri and Soga 2010, Li and Yu 2010); it is noted that the actual value of γ_{oct} at point 4 is not known because the potentiometer used to measure the torsional angle went out of range just before point 4. Three zero-dilatancy states are observed in test C6 since the mild plastic dilation initiated at point 3 turns into plastic contraction just before point 4 (IP) and the plastic contraction changes into strong plastic dilation at point 5 (PTP) (see also Fig. 7.34).

Figure 7.32b shows that the stress path of test C6 in the Y - X plane becomes tangential to the initial IS (shown with a red solid line) at point 2 with $\alpha_{\sigma'1} = -80^o$ and thereafter it moves on it and beyond it in a parallel trajectory. The stress path retreats inside the initial IS at around $\alpha_{\sigma'1} = -35^o$ and crosses again the initial IS, moving beyond it, at the stress state with $\alpha_{\sigma'1} = 10^o$. The angle between the stress path and the initial IS at $\alpha_{\sigma'1} = 10^o$ is small while the current stress difference, q_d, is lower than the minimum undrained strength corresponding to $\alpha_{\sigma'1} = 10^o$ since the stress state is located in the interior of the Local Boundary Surface (LBS) (see also Fig. 7.23b). Thereafter, the stress path moves outside the initial IS until it reaches the failure surface at point 3 with $\alpha_{\sigma'1} = 30.2^o$. The current stress difference, q_d, is lower than the minimum undrained strength corresponding to $\alpha_{\sigma'1} = 30.2^o$ and thus flow instability is not triggered at point 3. However, as the principal stress direction angle, $\alpha_{\sigma'1}$, changes from 30.2^o to 64.4^o the LBS is lowered and the current stress difference, q_d, becomes unsustainable because it is higher than the minimum undrained strength corresponding to $\alpha_{\sigma'1} = 64.4^o$ (see also Fig. 7.32a) thus flow instability is triggered at point 4. The less steep of the planes of maximum stress obliquity coincides with the horizontal bedding plane at point 4.

The results of test C6 indicate that the stress - strain history and the incremental stress direction (in the Y - X plane) affect the triggering of flow instability, which appears to occur preferably at stress states corresponding to unfavourable deformation kinematics, i.e. to shearing and sliding along the bedding plane, when the stress PA rotate under undrained conditions. Moreover, it is proved experimentally that the stress state of loose sand subjected to undrained stress-controlled loading may move along the direction of isotropic stress unloading (in the σ'_1 - σ'_2 - σ'_3 space), from the consolidation state, at low stress ratio, to the failure state, at high stress ratio, without triggering a diffuse flow instability. This novel finding is of great importance both from an experimental and a theoretical point of view for the reasons discussed next.

It has been shown in Chapter 4 that diffuse flow instability may be triggered before failure in physical triaxial tests on loose or dense sands, under undrained or fully-drained (at the flow triggering point) conditions, when the direction of incremental stress coincides with the direction of isotropic stress unloading (Lade et al. 1988, Chu et al. 1993 and 2003, Sasitharan et al. 1993, Chu and Leong 2001). Moreover, it has been shown that loose sands may undergo flow instability inside the failure surface when subjected to undrained rotation of the stress PA while keeping the total stress PV constant (in multiaxial mode) and this situation also corresponds to isotropic stress unloading (Symes et al. 1984, Shibuya et al. 1987, 2003a and 2003b, Nakata et al. 1998, Sivathayalan and Vaid 2002). Laouafa and Darve (2002) showed numerically that the first unstable direction of incremental stress under axisymmetric conditions is unique and corresponds to $d\sigma'_1 < 0$, $d\sigma'_2 = d\sigma'_3 < 0$ and that plenty of new unstable directions appear as the stress ratio increases, while the same result was obtained under general 3D conditions by Prunier et al. (2009). Darve et al. (2004), Sibille et al. (2008) and Prunier et al. (2009) performed continuous, discrete and multiscale numerical analyses and showed that the direction of isotropic stress unloading is included inside the instability cones which have their origin at stress states inside the failure surface, at least in the case of loose sand. Consequently, it appears to be rather impossible to move in the stress space along the direction of isotropic stress unloading from the consolidation state, at low stress ratio, to the failure state, at high stress ratio, without triggering a diffuse instability. However, the results of test C6 reported here prove the feasibility of this situation.

Another novel finding of this study concerns the proof of the feasibility of triggering a diffuse instability at high stress ratio along an incremental stress direction corresponding to increasing stresses dσ'_1, dσ'_2, d$\sigma'_3 \geq 0$ and decreasing stress ratio, $\eta = q / p'$. This situation has been predicted by numerical directional analyses using the models of Darve (Darve and Laouafa 2000, Darve et al. 2004, Sibille et al. 2007, Prunier et al. 2009) yet the loading programme leading to an instability of this type has been unknown so far. It can be observed in Fig. 7.32 that when the sand fails at point 3 with $\alpha_{\sigma'1} = 30.2^o$ the effective stress path turns towards states with higher mean effective stress, p', and lower stress difference, q_d (or q), thus the stress ratio, q_d / p' (or q / p'), decreases as the stress state remains obligingly on the anisotropic failure surface (see also Fig. 7.22). Actually, the sand undergoes a mild plastic dilation (see also Fig. 7.34) and spontaneous unloading of the deviatoric stress (loss of strength) thus the controllability of the loading programme is lost without triggering flow. Since the loss of controllability indicates the triggering of instability (Nova 1994, Nicot et al. 2011, Daouadji et al. 2011) a peculiar diffuse instability is triggered at point 3 along the direction of incremental stress (in the σ'_1 - σ'_2 - σ'_3 space) corresponding to dσ'_1, dσ'_2, d$\sigma'_3 \geq 0$ and d$\eta < 0$, proving experimentally the predictions of the numerical analyses by Darve. It is noted that the unloading of the deviatoric stress is partly due to the membrane stretching and partly due to the material response thus the results do not change if the elastic membrane stretches are not taken into account in the analysis of the data.

Figure 7.33 shows the relationship between the direction angles of principal stress, $\alpha^*_{\sigma'1}$, rate of principal stress, $\alpha^*_{d\sigma'1}$, and rate of principal strain, $\alpha^*_{d\varepsilon1}$ during the first and second cycle of rotation of the stress PA in test C6; the asterisk (*) indicates that the alternative convention described in Section 7.3 is used, thus, the direction angle of principal stress, $\alpha^*_{\sigma'1}$, increases from 0° to 90° to 180° during a full cycle of rotation of the stress PA. The direction angles $\alpha^*_{d\varepsilon1}$ and $\alpha^*_{d\sigma'1}$ are plotted against $\alpha^*_{\sigma'1}$ and the inclined dashed lines indicate the condition of coaxiality of the plastic deformation, $\alpha^*_{d\varepsilon1} = \alpha^*_{\sigma'1}$. The depicted relationships are periodical with a period of 180° thus the horizontal axis plots the quantity $N \cdot 180 + \alpha^*_{\sigma'1}$, where N is the number of the completed cycles of rotation of the stress PA, i.e. N = 0 or 1 during the first or second cycle, respectively, in the case investigated here. The data plotted in Fig. 7.33 correspond to the states on which a unit vector is superimposed in Fig. 7.32b, while at these states the torsional angle is measured accurately. Figure 7.33 shows that the plastic deformation of sand during the rotation of the stress PA is non-coaxial since the direction of the rate of principal strain is intermediate between the directions of the rate of principal stress and of the principal stress, lagging before the former. The non-coaxiality angle, $\alpha^*_{d\varepsilon1} - \alpha^*_{\sigma'1}$, indicated by the vertical distance of the red circles from the inclined dashed line decreases, in general, in the course of the monotonic hardening (increase in η) and post-failure softening (decrease in η) but remains non-zero.

Figure 7.34 shows the evolution of the normalised excess pore-water pressure, Δu / p'_i, the octahedral shear strain, γ_{oct}, the torsional shear strain, $\gamma_{z\theta}$, and the triaxial shear strain, ε_{zz} - $\varepsilon_{\theta\theta}$, with the monotonic rotation angle, $\Delta\alpha_{\sigma'1}$, in test C6; it is recalled that the angle $\Delta\alpha_{\sigma'1}$ increases monotonically from 0^o to 180^o during the first cycle of rotation of the stress PA, then from 180^o to 360^o during the second cycle of rotation etc. The hollow circles with the numbers 1 - 3 and 5 on the label and the red solid circle with the number 4 on the label mark the states discussed previously. The value of the slope d(Δu / p'_i) / d($\Delta\alpha_{\sigma'1}$) at point 2 with $\alpha_{\sigma'1}$ = -80^o during the first cycle of stress rotation is the highest before the triggering of flow instability; it is recalled that the initial IS is probed at point 2 yet flow instability is triggered at point 4. It can be seen that the normalised excess pore-water pressure ratio, Δu / p'_i, begins to decrease at point 3 (failure point) indicating that the sand begins to dilate plastically. The mild plastic dilation turns suddenly into plastic contraction just before point 4 (IP) since the ratio Δu / p'_i begins to increase again. The triggering of flow at point 4 is indicated by the abrupt rise in Δu / p'_i and the termination of flow at point 5 (PTP) is indicated by the maximum value of Δu / p'_i, while the subsequent decrease in Δu / p'_i shows that the sand undergoes strong plastic dilation and regains strength. It is noted that three zero-dilatancy states are observed in this test. The local extremum of γ_{oct} and ε_{zz} - $\varepsilon_{\theta\theta}$ during the first cycle of rotation of the stress PA occurs well beyond the state with $\alpha_{\sigma'1}$ = 90^o due to the induced-anisotropy effects (Tian and Yao 2018).

The results of the tests C3 to C6 show clearly that the incremental stress direction in different stress spaces, namely in the Y - X (and Y_s - X_s) deviatoric plane and in the σ'_1 - σ'_2 - σ'_3 principal stress space influence the triggering of instability. In test C3 flow instability is triggered at $\alpha_{\sigma'1}$ = 57.4^o because the pore-water pressure, u, and the stress ratio, η, increase while the LBS is lowered and the minimum undrained strength decreases as the stress PA rotate under constant b. The incremental stress direction at the IP is parallel to the hydrostatic axis in the σ'_1 - σ'_2 - σ'_3 space and almost radial in the Y - X plane; potential destabilisation of sand under similar stress conditions has been reported by Sivathayalan and Vaid (2002). In tests C4 and C5 the pore-water pressure increased due to creep during the pause period between the steps of rotation of the stress PA and thus the stress ratio increased too, resulting in the triggering of flow instability. The incremental stress direction at the IP is similar in both stress spaces to that observed in test C3, but the value of $\alpha_{\sigma'1}$ differs; similar results have been reported by Lade (1992) and Leong and Chu (2002).

On the other hand, in test C6 the stress state reaches the failure surface at $\alpha_{\sigma'1}$ = 30.2^o and the sand begins to dilate plastically while the current stress difference, q_d, is lower than the minimum undrained strength corresponding to $\alpha_{\sigma'1}$ = 30.2^o thus flow is not triggered (Symes et al. 1984, Poulos et al. 1985). However, diffuse instability (not of the flow type) is triggered, with dσ'_1, dσ'_2, dσ'_3 $\geq$ 0 and dη < 0, because the controllability of the loading programme is lost (Nova 1994), while the incremental stress direction in the Y - X plane is tangential to the failure surface. Afterwards, the incremental stress direction changes in the σ'_1 - σ'_2 - σ'_3 space as the plastic dilation turns into plastic contraction, the LBS is lowered (rendering the current stress difference higher than the minimum undrained strength) and flow instability is triggered with $d\sigma'_1$, $d\sigma'_2$, $d\sigma'_3$, $d\eta < 0$, while the incremental stress direction in the Y - X plane is tangential to the failure surface. This is a novel finding to the author's best knowledge.

7.7.3 UNDRAINED BEHAVIOUR OF AC M31 SAND UNDER LOADING WITH ROTATING STRESS PA AND PERIODICALLY CHANGING DEVIATORIC STRESS

In the previous section it was shown that stability may be sustained under undrained rotation of the stress principal axes (PA) at constant total stress principal values (PV) when the stress path in the Y - X plane probes the initial Instability Surface (IS) at small angles or tangentially. The direction along which the initial IS is probed is uncontrollable since it depends on the spontaneous rate of generation of the excess pore-water pressure. However, some combinations of the consolidation stress ratio, K_c, and void ratio, e, ensure that at least one full cycle of rotation of the stress PA is performed stably and in that case the rate of generation of the excess pore-water pressure decreases in the subsequent cycles (Ishihara and Towhata 1983, Nakata et al. 1998, Yang et al. 2007) rendering feasible the probing of the initial IS at small angles. In an effort to investigate further this behaviour of sand the stress path D1 with the loading characteristics shown in Fig. 7.35 was designed. In test D1 the monotonic rotation of the stress PA is performed continuously, under a very low frequency (f = 10^{-3} Hz) that ensures the homogenisation of the pore-water pressure inside the specimen, while the deviatoric stress, q, changes periodically in a way that is associated with unloading in the extension-like regime, when $\alpha_{\sigma'1}$ changes from 45^o to 90^o. The mean total stress, p, is held essentially constant, while the intermediate principal stress parameter, b, oscillates between 0.40, at $\alpha_{\sigma'1} = \pm 90^o$, and 0.52, at $\alpha_{\sigma'1} = 0^o$.

Figures 7.36a and b show the stress path of test D1 in the q_d - p' (a) and in the Y - X (b) planes; the symbols used are the same as in Figs 7.21a and b with the only difference being that the large hollow circles and the attached labels in Fig 7.36b mark some characteristic states described in the following, while the unit vectors superimposed on various stress states in Fig. 7.36b indicate the direction of the incremental principal strain, $\alpha_{d\varepsilon 1}$. The effective stress paths (ESPs) of the tests A10, and A17, which were conducted on specimens having a similar void ratio to that of the specimen in test D1, are also included in Fig. 7.36a in order to visualise the Local Boundary Surface (LBS) of loose isotropically consolidated M31 Sand at $\alpha_{\sigma'1} = 45^o$ and 80^o, respectively. It is noted that the Local Boundary Surface (LBS) of loose sand is not expected to be altered significantly due to the small changes in the value of b in test D1, especially in the extension-like regime (Lam and Tatsuoka 1988, Shibuya et al. 2003a). Moreover, the test results in this study indicate that the LBS of AC sand, consolidated at $\alpha_{\sigma'1} = 0^o$ and $K_c \geq 0.60$, coincides in the post-peak regime with that of IC sand when $\alpha_{\sigma'1} \geq 45^o$, while the LBS describes the undrained behaviour of sand at small strains under both fixed and rotating directions of the stress PA, at constant or cyclically changing values of q; similar results have been reported by Shibuya et al. (2003a and b).

Figures 7.36a and b show that the stress path of test D1 probes almost concurrently the initial IS and the LBS at point 1, with $\alpha_{\sigma'1}$ = 40°, and at the neighbouring state with $\alpha_{\sigma'1}$ = 45°, respectively. However, flow is not triggered because the stress path in the Y - X plane probes the initial IS tangentially, while the stress path in the q_d - p' plane probes the LBS inwards. The unloading of the stress difference, q_d, beyond point 1 counterbalances the tendency for the stress path in the Y - X plane to move away from the origin, as a result of the pore-water pressure build up, and ensures a stress trajectory tangential to the initial IS; in the meanwhile, the stress path in the q_d - p' plane continues to move below the LBS which is also moving downwards. However, the stress difference, q_d, begins to increase at $\alpha_{\sigma'1}$ = 90° and the rate of generation of excess pore-water pressure is accelerated thus the stress path in the q_d - p' plane moves along the direction of isotropic stress unloading and probes the LBS outwards, while the stress path in the Y - X plane moves beyond the initial IS and probes the evolved IS radially, triggering flow instability at point 2. It is noted that the IP (point 2) belongs to the evolved IS determined previously using the results of the tests C3 to C6.

It is interesting to compare the results of test D1 (Figs 7.36a and b) with those of test C3 (Fig. 7.25a and b) since in both cases the stress path in the Y - X plane probes the initial IS at approximately the same point (having the label "point 1"), while instability is triggered at close states in the q_d - p' plane (having the label "point 2"). Instability in test C3 is triggered at point 2 shortly after the initial IS is probed at point 1, while in test D1 point 2 is far beyond point 1 as a result of the stress history associated with the unloading of the deviatoric stress. Apparently, the partial control of the incremental stress direction in both stress spaces postpones the triggering of flow instability in test D1. In these two tests the IPs are close to each other in the σ'_1 - σ'_2 - σ'_3 space but the values of $\alpha_{\sigma'1}$ at the IPs are different. In both tests instability is triggered along the direction of isotropic stress unloading in the q_d - p' plane and along the radial direction in the Y - X plane. The comparison of the results of the tests D1 and A17 is also interesting: the value of $(\Delta u / p'_i)_{pt}$, U_I and $\gamma_{oct,pt}$ (the subscript "pt" means at phase transformation) is 0.90, 0.23 and 3.26% and 0.91, 0.59 and 4.53%, respectively, indicating that the looser specimen in test D1, with e = 0.738 and α_{ip} = -85.5° (the subscript "ip" means at the instability point), is less contractive after the onset of flow than the denser specimen in test A17, with e = 0.727 and α_{ip} = 79.1°, due to the stress - strain history effects.

Figure 7.37 shows the relationship between the direction angles of principal stress, $\alpha^*_{\sigma'1}$, rate of principal stress, $\alpha^*_{d\sigma'1}$, and rate of principal strain, $\alpha^*_{d\varepsilon1}$ during the first, second and third cycle of rotation of the stress PA in test D1; the asterisk (*) indicates that the alternative convention described in Section 7.3 is used, thus, the direction angle of principal stress, $\alpha^*_{\sigma'1}$, increases from 0° to 90° to 180° during a full cycle of rotation of the stress PA. The direction angles $\alpha^*_{d\varepsilon 1}$ and $\alpha^*_{d\sigma'1}$ are plotted against $\alpha^*_{\sigma'1}$ and the inclined dashed lines indicate the condition of coaxiality of the plastic deformation, $\alpha^*_{d\varepsilon 1} = \alpha^*_{\sigma'1}$. The depicted relationships are periodical with a period of 180^o thus the horizontal axis plots the quantity N·180 + $\alpha^*_{\sigma'1}$, where N is the number of the completed cycles of rotation of the stress PA, i.e. N = 0, 1 or 2 during the first, second or third cycle, respectively, in the case investigated here. The data plotted in Fig. 7.37 correspond to the states on which a unit vector is superimposed in Fig. 7.36b.

Figure 7.37 shows that the plastic deformation of sand during the combined rotation of the stress PA and periodic change of the stress difference, q_d, is non-coaxial since the direction of the rate of principal strain is intermediate between the directions of the rate of principal stress and of the principal stress, lagging before the former. The non-coaxiality angle, $\alpha^*_{d\varepsilon 1}$ - $\alpha^*_{\sigma'1}$, indicated by the vertical distance of the red circles from the inclined dashed line varies in the course of rotation of the stress PA due to the complex stress - strain history. The plastic deformation becomes suddenly coaxial at point 2 (IP) because the direction of the rate of principal stress becomes opposite to the direction of the principal stress in the Y_s - X_s plane and the stress path moves along the radial direction in the Y - X plane during flow, as the stresses Y_s and X_s are unloaded proportionally in this test; this can be realised by the fact that the difference $\alpha^*_{d\sigma'1}$ - $\alpha^*_{\sigma'1}$ is around -90^o at point 2. On the other hand, the plastic deformation is unexpectedly coaxial at point 1 because the sand entered the mode of simple-shear deformation along the direction $\alpha^*_{d\varepsilon 1}$ = 45^o before point 1 and this mode cannot be easily changed due to the sliding occurring on the bedding plane.

Figure 7.38 shows the evolution of the normalised excess pore-water pressure, Δu / p'_i, the octahedral shear strain, γ_{oct}, the torsional shear strain, $\gamma_{z\theta}$, and the triaxial shear strain, ε_{zz} - $\varepsilon_{\theta\theta}$, with the monotonic rotation angle, $\Delta\alpha_{\sigma'1}$, in test D1; it is recalled that the angle $\Delta\alpha_{\sigma'1}$ increases monotonically from 0^o to 180^o during the first cycle of rotation of the stress PA, then from 180^o to 360^o during the second cycle of rotation etc. The hollow circles without label mark here the states with $\alpha_{\sigma'1}$ = 90^o while the hollow circles with the numbers 1 and 2 on the label mark the states discussed in the previous paragraphs. The value of the slope d(Δu / p'_i) / d($\Delta\alpha_{\sigma'1}$) at point 1 with $\alpha_{\sigma'1}$ = 40^o during the third cycle of stress rotation is similar to that at the state with $\alpha_{\sigma'1}$ = 90^o during the first cycle of stress rotation; it is recalled that the initial IS is probed at point 1 yet flow instability is triggered at point 2. This common slope is rather related to the initial anisotropy of sand while the steepest slope exhibited at the states with $\alpha_{\sigma'1}$ between 90^o and -45^o is related to the increase in q_d (Fig. 7.35a). Figure 7.38d shows that the strain increment d(ε_{zz} - $\varepsilon_{\theta\theta}$) is inert at point 1 (irrespective of the assumption used for calculating $\varepsilon_{\theta\theta}$) and only the strain increment d$\gamma_{z\theta}$ contributes to shear deformation. This means that the sand deforms homogeneously in simple-shear mode along the incremental strain direction $\alpha_{d\varepsilon 1}$ = 45^o, with the maximum shear distortion, dγ, occurring to $z\theta$-angles. The simple-shear deformation lasts from $\alpha_{\sigma'1}$ = 20^o to 40^o thus the response of sand turns from remarkably non-coaxial to unexpectedly coaxial.

7.8 DISCUSSION ON THE BIFURCATION OF THE BEHAVIOUR OF THE SPECIMEN – APPARATUS SYSTEM

In the present study a variety of bifurcations of the specimen - apparatus system was captured using the pneumatic loading system of the Hollow Cylinder Apparatus (HCA) of the National Technical University of Athens (NTUA). The response of the system becomes dynamic with a burst of kinetic energy when flow-instability is triggered. The stress paths of the radial tests in the deviatoric plane follow unpredictable routes past the instability point (IP) associated with a predominant unloading of the torsional-shear stress when the stress state at the triggering of instability corresponds to shearing and sliding along the horizontal bedding plane. The mechanical state in the vicinity of Lade’s instability line (IL) becomes unsustainable without varying the control parameters. Sudden transitions to strong simple-shear deformation are captured in both diffuse and localised modes. The triggering of both diffuse and localised instabilities occurs preferably at stress states corresponding to unfavourable deformation kinematics, i.e. to shearing and sliding along the horizontal bedding plane, when the stress principal axes (PA) are rotated under undrained conditions, as if the bedding plane acts like an imperfection. On the other hand, the observed behaviour of the system may be attributed to the stress - strain non-uniformities, deformation inhomogeneities and inertial phenomena due to the boundary conditions imposed in hollow cylinder testing. The effects of the boundary conditions on the response of the system are discussed next.

The bifurcated behaviour of the system in the radial test A4 ($\alpha_{\sigma'1}$ = 22.5° and b = 0.50) is investigated next. The boundary loads p_o, p_i, F and T (Fig. 7.1) are controlled in this test under isochoric saturated conditions to yield:

$$\mathrm{d}\tau_{z\theta} = c \text{ (} c \text{ is a positive constant)} \tag{7.1a}$$

$$\mathrm{d}\sigma_{zz} = c \tag{7.1b}$$

$$\mathrm{d}\sigma_{\theta\theta} = -c \tag{7.1c}$$

$$\mathrm{d}\sigma_{rr} = 0 \tag{7.1d}$$

$$\mathrm{d}\varepsilon_{zz} + \mathrm{d}\varepsilon_{\theta\theta} + \mathrm{d}\varepsilon_{rr} = 0 \tag{7.1e}$$

The total normal stresses, shear stresses and normal strains (elastoplastic) appearing in Eq. 1 are given in Table 7.1 and shown in Fig. 7.1; it is noted that the effective normal stresses are uncontrollable.

The second-order work, d^2W, is computed in terms of the average stresses and strains given in Eq. 1. Owing to the lack of coaxiality of the principal axes of stress and plastic strain rate the second-order work, d^2W, in cylindrical coordinates is given by the following relationship:

$$\mathrm{d}^2W = \mathrm{d}\sigma_{ij}\,\mathrm{d}\varepsilon_{ij} = \mathrm{d}\sigma'_{zz}\,\mathrm{d}\varepsilon_{zz} + \mathrm{d}\sigma_{z\theta}\,\mathrm{d}\varepsilon_{z\theta} + \mathrm{d}\sigma_{zr}\,\mathrm{d}\varepsilon_{zr} +$$

$$+ \mathrm{d}\sigma_{\theta z}\,\mathrm{d}\varepsilon_{\theta z} + \mathrm{d}\sigma'_{\theta\theta}\,\mathrm{d}\varepsilon_{\theta\theta} + \mathrm{d}\sigma_{\theta r}\,\mathrm{d}\varepsilon_{\theta r} + \tag{7.2}$$

$$+ \mathrm{d}\sigma_{rz}\,\mathrm{d}\varepsilon_{rz} + \mathrm{d}\sigma_{r\theta}\,\mathrm{d}\varepsilon_{r\theta} + \mathrm{d}\sigma'_{rr}\,\mathrm{d}\varepsilon_{rr}$$

In hollow-cylinder testing the following relationships hold:

$$\mathrm{d}\sigma_{zr}\,\mathrm{d}\varepsilon_{zr} = \mathrm{d}\sigma_{\theta r}\,\mathrm{d}\varepsilon_{\theta r} = \mathrm{d}\sigma_{rz}\,\mathrm{d}\varepsilon_{rz} = \mathrm{d}\sigma_{r\theta}\,\mathrm{d}\varepsilon_{r\theta} = 0 \tag{7.3a}$$

$$\sigma_{\theta z} = \sigma_{z\theta} \text{ and } \sigma_{\theta z} \equiv \tau_{\theta z},\ \sigma_{z\theta} \equiv \tau_{z\theta} \tag{7.3b}$$

$$\varepsilon_{\theta z} = \varepsilon_{z\theta} \text{ (tensorial component)} \tag{7.3c}$$

Thus, Eq. 7.2 can be re-written:

$$\mathrm{d}^2W = \mathrm{d}\sigma'_{zz}\,\mathrm{d}\varepsilon_{zz} + \mathrm{d}\sigma'_{\theta\theta}\,\mathrm{d}\varepsilon_{\theta\theta} + \mathrm{d}\sigma'_{rr}\,\mathrm{d}\varepsilon_{rr} + 2\mathrm{d}\tau_{z\theta}\,\mathrm{d}\varepsilon_{z\theta} =$$

$$= 1/2\ \mathrm{d}\sigma'_{zz}\,\mathrm{d}\varepsilon_{zz} + 1/2\ \mathrm{d}\sigma'_{zz}\,\mathrm{d}\varepsilon_{zz} + 1/2\ \mathrm{d}\sigma'_{\theta\theta}\,\mathrm{d}\varepsilon_{\theta\theta} + 1/2\ \mathrm{d}\sigma'_{\theta\theta}\,\mathrm{d}\varepsilon_{\theta\theta} +$$

$$+ 1/2\ \mathrm{d}\sigma'_{zz}\,\mathrm{d}\varepsilon_{\theta\theta} - 1/2\ \mathrm{d}\sigma'_{zz}\,\mathrm{d}\varepsilon_{\theta\theta} + 1/2\ \mathrm{d}\sigma'_{\theta\theta}\,\mathrm{d}\varepsilon_{zz} - 1/2\ \mathrm{d}\sigma'_{\theta\theta}\,\mathrm{d}\varepsilon_{zz} +$$

$$+ \mathrm{d}\sigma'_{rr}\,\mathrm{d}\varepsilon_{rr} + 2\ \mathrm{d}\tau_{z\theta}\,\mathrm{d}\varepsilon_{z\theta} =$$

$$= \mathrm{d}\sigma'_{zz}\,(\mathrm{d}\varepsilon_{zz} - \mathrm{d}\varepsilon_{\theta\theta}) / 2 - \mathrm{d}\sigma'_{\theta\theta}\,(\mathrm{d}\varepsilon_{zz} - \mathrm{d}\varepsilon_{\theta\theta}) / 2 + \mathrm{d}\sigma'_{zz} / 2\ (\mathrm{d}\varepsilon_{zz} + \mathrm{d}\varepsilon_{\theta\theta}) + \tag{7.4}$$

$$+ \mathrm{d}\sigma'_{\theta\theta} / 2\ (\mathrm{d}\varepsilon_{zz} + \mathrm{d}\varepsilon_{\theta\theta}) + \mathrm{d}\sigma'_{rr}\,\mathrm{d}\varepsilon_{rr} + 2\ \mathrm{d}\tau_{z\theta}\,\mathrm{d}\varepsilon_{z\theta} =$$

$$= (\mathrm{d}\sigma'_{zz} - d\sigma'_{\theta\theta})\ (\mathrm{d}\varepsilon_{zz} - \mathrm{d}\varepsilon_{\theta\theta}) / 2 + 2\ \mathrm{d}\tau_{z\theta}\,\mathrm{d}\varepsilon_{z\theta} + \mathrm{d}\sigma'_{rr}\,\mathrm{d}\varepsilon_{rr} +$$

$$+ (\mathrm{d}\sigma'_{zz} + \mathrm{d}\sigma'_{\theta\theta}) / 2\ (\mathrm{d}\varepsilon_{zz} + \mathrm{d}\varepsilon_{\theta\theta})$$

The following conditions hold:

$$\varepsilon_{zz} + \varepsilon_{\theta\theta} + \varepsilon_{rr} = 0 \Rightarrow \mathrm{d}\varepsilon_{zz} + \mathrm{d}\varepsilon_{\theta\theta} + \mathrm{d}\varepsilon_{rr} = 0 \text{ (isochoric condition)} \tag{7.5a}$$

$$b = 0.5 \Rightarrow (\sigma'_{zz} + \sigma'_{\theta\theta}) / 2 = \sigma'_{rr} \Rightarrow (\mathrm{d}\sigma'_{zz} + \mathrm{d}\sigma'_{\theta\theta}) / 2 = \mathrm{d}\sigma'_{rr} \tag{7.5b}$$

Equation 7.4 can be re-written using Eqs 7.5:

$$\mathrm{d}^2W = (\mathrm{d}\sigma'_{zz} - \mathrm{d}\sigma'_{\theta\theta})\ (\mathrm{d}\varepsilon_{zz} - \mathrm{d}\varepsilon_{\theta\theta}) / 2 + 2\ \mathrm{d}\tau_{z\theta}\,\mathrm{d}\varepsilon_{z\theta} \tag{7.6}$$

Equation 7.6 indicates that the proper energy-conjugate pairs of stress and strain are:

$$X_s = \sigma'_{zz} - \sigma'_{\theta\theta} \text{ conjugated to } X_\varepsilon = (\varepsilon_{zz} - \varepsilon_{\theta\theta}) / 2 \tag{7.7a}$$

$$Y_s = 2\tau_{z\theta} \text{ conjugated to } Y_\varepsilon = \varepsilon_{z\theta} \tag{7.7b}$$

The control parameters of the generalised undrained loading programme are the X_s and Y_s “shear” stresses while the response parameters are the X_ε and Y_ε “shear” strains, respectively. The second order work can be also expressed in the following normalised form (varying between -1 and 1):

$$\mathrm{d}^2W_{norm} = \mathrm{d}^2W / \{[(\mathrm{d}(\sigma'_{zz} - \sigma'_{\theta\theta}))^2 + (2\mathrm{d}\tau_{z\theta})^2]^{1/2}\ [(\mathrm{d}(\varepsilon_{zz} - \varepsilon_{\theta\theta}) / 2)^2 + (\mathrm{d}\varepsilon_{z\theta})^2]^{1/2}\} \tag{7.8}$$

Equations 7.1a to 7.1e correspond to the loading programme A4 while Eqs 7.6 to 7.8 are valid for any undrained loading programme with b = 0.5 performed in this study.

Equation 7.8 is now used to determine the normalised second-order work, d^2W_{norm}, in test A4 and monitor its evolution. Figure 7.39a shows the evolution of the effective principal stresses, σ'_1, σ'_2 and σ'_3, and of the "shear" stresses X_s / 2 and Y_s / 2 ($X_s = \sigma_{zz} - \sigma_{\theta\theta}$ and $Y_s = 2\tau_{z\theta}$) with mean effective stress, p', in test A4, while Fig. 7.39b shows the evolution of the normalised second-order work, d^2W_{norm}, and of the "shear" stresses X_s / 2 and Y_s / 2 with mean effective stress, p', in test A4. The data plotted in Fig. 7.39b correspond to the response of sand until the phase-transformation point (PTP). The hollow circles mark the transient-peak point on the curves, while the solid circles mark the instability point (IP), with the latter being located just beyond the former. The non-coincidence of the transient-peak and instability points is the result of the increasing area of the specimen's cross section, membrane stretching and requirement for accelerated strain rates at the IP. The vertical dashed lines in Fig. 7.39a divide the post-peak response into three phases, each of which lasts for one second; it is noted that the pre-peak response lasted 456 seconds.

Figures 7.39a and b show that the stresses X_s and Y_s begin to decrease at the IP, the development of strains is accelerated and the normalised second-order work, d^2W_{norm}, becomes negative indicating the loss of strength, stability and controllability. It is noted that the loading programme in test A4 dictates a monotonic increase in the Y_s and X_s "shear" stresses under a unit ratio of increments. Strength, stability and controllability are regained past the PTP where d^2W_{norm} becomes positive again. The bifurcation of the response of the system is easily conceived since the curves indicating the evolution of Y_s and X_s diverge in the vicinity of the IP because the unloading of the torsional-shear stress, Y_s, is predominant when controllability is lost. The question is now straightforward: which is the governing imperfection in the system that induces the observed bifurcated behaviour?

Inertial response of the loading system: since the development of strains is accelerated past the IP it may be argued that the observed behaviour is due to the inertial interaction between the specimen and the loading system. Figure 7.40 shows the vertical displacement of the loading ram, v, against time, t, past the transient-peak state in test A4; it is noted that t = 0 at the transient-peak state. The main graph plots the data up to the PTP while the inset graph plots the data up to a state beyond the PTP. Analysis of the data shows that during the first and third phase of the post-peak response the vertical velocity is practically constant (~ 10^{-2} mm/s and 10^{0} mm/s, respectively) while during the second phase the vertical acceleration is practically constant and of the order of magnitude $10^{-4}\,g$ (g = 9.81 m/s^2 is the acceleration of gravity). Similarly, the angular acceleration during the second phase of the post-peak response divided by the average radius of the annular specimen is of the order of magnitude $10^{-4}\,g$. Moreover, the increase in the vertical displacement, v, and torsional angle, θ, from the transient-peak state to the phase-transformation point is only 1.8 mm and 7.4°, respectively, thus the pneumatic actuators are expected to function without problems, while no dynamic pressure changes are observed inside the cell environment. These data indicate that the observed bifurcation pattern is not the result of inertial phenomena.

Stress-strain non-uniformities: It is well known that the stresses and strains across the wall of the hollow-cylinder specimen are non-uniform, due to the torque-induced shear stress and strain on the curved wall and due to the difference between the inner and outer cell pressure, p_i and p_o, respectively, while the non-smooth, rigid ends induce another type of non-uniformities (Hight et al. 1983, Sayao and Vaid 1991). Generally, the non-uniformities increase with the stress ratio, η or sin φ, and with the pressure ratio, p_i / p_o, or pressure difference, $p_i - p_o$. Ultimate limits to the value of p_i / p_o are physically imposed, via implosion or explosion of the specimen, while more strict limits ensure an acceptable level of non-uniformities for a given specimen geometry and stress path. For example, Nakata et al. (1998) suggested that the level of non-uniformities is acceptable when $0.75 < p_i / p_o < 1.30$ in loading tests on hollow cylindrical specimens with dimensions $H / D_o / D_i$ = 200 / 100 / 60 (in mm) (see also Gutierrez 1989).

Figure 7.41 shows the evolution of the pressure ratio, p_i / p_o, with octahedral shear strain, γ_{oct}, in test A4 and other A-series tests. The pressure ratio, p_i / p_o, increases in the course of shearing but remains practically constant or decreases during flow while it remains inside the permissible limits when the shear strain is $\gamma_{oct} \leq 8\%$. Testing at $\alpha_{\sigma'1} = 0^o$ and $b = 0.50$ suffers from high values of p_i / p_o at low strains and excessive specimen bulging at high strains thus the interpretation of the results of such tests past the IP is avoided (see, for example, Fig. 7.22). The value of γ_{oct}, $\gamma_{z\theta}$, p_i / p_o and φ at the IP in test A4 is 0.50%, 0.49%, 1.06 and 29.9^o, respectively, while the direction angle of principal stress, $\alpha_{\sigma'1}$, and strain rate, $\alpha_{d\varepsilon1}$, are 22.3^o and 31.1^o, respectively. These results corroborate the notion that the bifurcation in test A4, associated with a predominant unloading of the torsional-shear stress, Y_s, as compared to the unloading of the triaxial stress, X_s, is rather related to the depositional anisotropy of sand (i.e. to the existence of a horizontal bedding plane) and not to the stress - strain non-uniformities at the IP.

Strain localisation: The development of zones of localised strain inside the volume of the specimen is the main factor that impedes the investigation of the true behaviour of the soil element in laboratory testing. In the present study strain localisation was not observed with the naked eye before the occurrence of phase transformation and before the accumulation of octahedral shear strain, γ_{oct}, at least equal to 8%; however, the studies of Desrues et al. (1996) and Desrues and Viggiani (2004) definitely show that there exist complex mechanisms of strain localisation, even in the case of loose sand, that cannot be detected by naked-eye inspection. Figures 7.42 and 7.43 show the photos of the deformed specimens in different A-series tests taken at the PTP (Figs 7.42a) or at the end of testing (Figs 7.42b, c and d and Figs 7.43a and b).

The very loose specimen (e = 0.745) in test A10 which was loaded at $\alpha_{\sigma'1}$ = 45^o with b = 0.5 (Fig. 7.42b) deformed homogeneously even at a shear strain as high as γ_{oct} = 11.8%, while phase-transformation, followed by weak plastic dilation, occurred at γ_{oct} = 6.5%. On the other hand, the loose specimens in the extension-like tests A19 and A20 (Fig. 7.42c and d, respectively) which were loaded at $\alpha_{\sigma'1}$ = 90^o with b = 0.5 showed signs of necking at the lower part when γ_{oct} increased beyond 8% due to the end restraint and stress-path effects. Nevertheless, the necking under the condition of $\alpha_{\sigma'1}$ = 90^o and b = 0.5 is well distributed compared to that under the condition of $\alpha_{\sigma'1}$ = 90^o and b = 1.0, as can be seen in the photos shown in Figs 7.43a and b. Figure 7.43a shows the necking pattern of the specimen in test A23, under the condition of $\alpha_{\sigma'1}$ = 90^o and b = 1, while Fig. 7.43b shows the necking pattern of the specimen in test A20, under the condition of $\alpha_{\sigma'1}$ = 90^o and b = 0.5. In any case, necking does not occur in the vicinity of the IP in any test thus the bifurcated behaviour of the specimen in test A4 (Fig. 7.39) is not attributed to strain localisation. Moreover, most of the failure states were determined before the occurrence of this type of bifurcation thus the shape of the failure surface shown in Fig. 7.22 is rather attributed to the depositional anisotropy of sand.

Effects of flexible versus stiff boundaries, buckling instabilities and failure in the σ_2-direction: The results presented so far indicate that the stress - strain non-uniformities at the IP in test A4 are rather minor, while the deformation of the specimen is still homogeneous. However, small perturbations in the stress - strain field in combination with minute spatial void ratio variations may trigger either diffuse or localised bifurcations and induce inhomogeneities that develop progressively (Vardoulakis and Sulem 1995, Desrues and Viggiani 2004, Andrade et al. 2008). Lade and Rodriguez (2014) captured a variety of instabilities in hollow-cylinder tests on dense sand with $\alpha_{\sigma'1}$ = 90^o and extreme values of b, namely buckling instabilities and failure in the σ'_2-direction, and suggested that “the flexible membranes allow the development of non-uniform strains, shear bands and necking”; they also suggested that the usage of stiff boundaries in testing of sand specimens yields higher values of strength and stiffness compared to that obtained using flexible boundaries under identical stress conditions and homogeneous deformation. None of the severe instabilities reported by Lade and Rodriguez (2014) was observed in test A4 before the triggering or after the termination of the bifurcated flow response. Moreover, the stresses $\tau_{z\theta}$ and F / [π (r_o^2 - r_i^2)] applied by the same stiff boundary were unloaded in a different way, with the unloading of the torsional-shear stress being predominant, as can be seen in Fig. 7.44.

On the other hand, slight necking was observed in the extension-like tests A14, A16 and A20 at large strains, $\gamma_{oct} \geq$ 8%. The fact that necking occurred in all these tests, while the direction of the σ'_1-axis with respect to the stiff and flexible boundaries is more or less the same (and the σ'_2-axis is common), indicates that the effects of depositional anisotropy may explain better why the response of the specimens in the tests A14 and A16 is weaker compared to that of the specimen in test A20 (see Fig.

7.14c), even at very low shear strain, and why a predisposition to unloading of the torsional-shear stress is exhibited during flow in the former tests (see Fig. 7.14b).

7.9 CONCLUSIONS

The undrained behaviour of loose M31 Sand was investigated under generalised loading with fixed or rotating stress principal axes (PA). An effort was made to figure out the conditions under which the unstable flow deformation is triggered. The results of radial tests, with fixed $\alpha_{\sigma'1}$ and b = 0.5, on isotropically consolidated (IC) sand show that flow instability is triggered near the transient-peak state beyond which the strength decreases as a result of the pore-water pressure build up. The controllability of the loading programme is lost when stability is lost, while the second-order work, d^2W, vanishes. Strength, stability and controllability are regained past the phase-transformation point (PTP) when the second-order work becomes positive again. It was also found that the inherent anisotropy affects the strength and deformability of sand at the instability point (IP), PTP and peak-failure state. Specifically, the undrained response of IC sand becomes less stiff and more contractive as the σ'_1-axis tends to align with the horizontal bedding plane, yet, the weakest response is observed for $\alpha_{\sigma'1}$ between 60° and 75° when one of the planes of maximum stress obliquity tends to become horizontal. An Instability Surface (IS) was defined in the deviatoric plane (Y - X plane) as a generalisation of Lade's instability line (IL) indicating the dependence of the instability stress ratio, sin φ, on $\alpha_{\sigma'1}$ resulting from the inherent anisotropy of sand. The non-coaxial deformation characteristics of sand at the IPs also indicate that the sliding along the horizontal bedding plane is a predominant deformation mechanism.

The results of the tests on anisotropically consolidated (AC) sand involving rotation of the stress PA showed that the stress - strain history has a profound effect on the undrained behaviour of loose sand and flow-instability condition. AC sand becomes especially prone to liquefaction when the static shear stress increases in the sense that a small stress disturbance involving an increase in the deviatoric stress and rotation of the stress PA triggers flow. In conditions of stress rotation at constant deviatoric stress excess pore-water pressure is continuously accumulated and the stress ratio increases inducing flow instability and failure of sand; this situation corresponds to isotropic stress unloading in the principal stress space. The deformation of sand is non-coaxial during stress rotation with the degree of non-coaxiality decreasing, but not vanishing, as the stress ratio increases. It was shown that the flow-triggering condition depends on the stress - strain history, including the effect of $K_c = \sigma'_{3c} / \sigma'_{1c}$ and direction of incremental stress, since stability is sustained whenever the stress path crosses the previously established IS at a small angle, while stability is lost when the stress path crosses the post-peak regime of the Local Boundary Surface (LBS) with an outwards direction. Accordingly, the pattern of flow deformation depends on how close to the failure surface the flow instability is triggered; a new flow parameter indicates this dependence which may be related to the stress-induced anisotropy. The results presented here also show that the triggering of both diffuse and localised instabilities occurs preferably at stress states corresponding to unfavourable deformation kinematics though the effects of the boundary conditions in hollow-cylinder testing need further investigation and should not be overlooked.

This study reports novel findings: the effective stress state of loose sand subjected to rotation of the stress PA at constant total stress principal values (PV) may move from the consolidation state up to the peak-failure state along the direction of isotropic stress unloading without triggering flow instability. Afterwards, a quasi-static diffuse instability may be triggered on the failure surface under increasing stresses and decreasing stress ratio, followed by a dynamic diffuse instability (flow) under decreasing stresses and stress ratio.

7.10 BIBLIOGRAPHY

Alarcon-Guzman A, Leonards GA, Chameau JL (1988) Undrained monotonic and cyclic strength of sands. Journal of Geotechnical Engineering, Vol. 114, No.10, pp. 1089-1109

Andrade JE, Baker JW, Ellison KC (2008) Random porosity fields and their influence and their influence on the stability of granular media. Int. J. Numer. Anal. Meth. Geomech. (2008), 32, 1147-1172

Borja RI (2006) Condition for liquefaction instability in fluid-saturated granular soils. Acta Geotechnica 2006; 1:211-224

Chen Z, Huang M (2019) Non-coaxial behavior modeling of sands subjected to principal stress rotation. Acta Geotech. (2019). https://doi.org/10.1007/s11440-018-0760-4

Chu J, Lo S-CR, Lee IK (1992) Strain-softening behavior of granular soil in strain-path testing. Journal of Geotechnical Engineering, Vo. 118, No. 2, pp. 191-208

Chu J, Lo S-CR, Lee IK (1993) Instability of granular soils under strain path testing. Journal of Geotechnical Engineering, Vo. 119, No. 5, pp. 874-892

Chu J, Leong WK (2001) Pre-failure strain softening and pre-failure instability of sand: a comparative study. Géotechnique 51 (4), 311–321

Chu J, Leroueil S, Leong WK (2003) Unstable behaviour of sand and its implication for slope instability. Canadian Geotechnical Journal, 40: 873-885

Daouadji A, Darve F, Al Gali H, Hicher PY, Laouafa F, Lignon S, Nicot F, Nova R, Pinheiro M, Prunier F, Sibille L, Wan R (2011) Diffuse failure in geomaterials:

Experiments, theory and modelling. Int. J. Numer. Anal. Meth. Geomech. (2011), 35(16), 1731-1773

Darve F, Flavigny M, Meghachou M (1995) Constitutive modelling and instabilities of soil behaviour. Computers and Geotechnics 17 (1995), 203-224

Darve F, Laouafa F (2000): Instabilities in granular materials and application to landslides. Mech. Cohes-Frict. Mater., 2000; 5:627-652

Darve F, Servant G, Laouafa F, Khoa HDV (2004) Failure in geomaterials: continuous and discrete analysis. Comput. Methods Appl. Mech. Engrg. 193 (2004), 3057-3085

Desrues J, Chambon R, Mokni M, Mazerolle F (1996) Void ratio inside shear bands in triaxial sand specimens studied by computed tomography. Géotechnique 46 (3), 529-546

Desrues J, Viggiani G (2004) Strain localization in sand: an overview of the experimental results obtained in Grenoble using stereophotogrammetry. International Journal for Numerical and Analytical Methods in Geomechanics, 2004, 28: 279-321

Doanh T, Ibraim E, Mattioti R (1997) Undrained instability of very loose Hostun sand in triaxial compression and extension. Part 1: experimental observations. Mechanics of Cohesive-Frictional Materials, Vol. 2, 47-70 (1997)

Georgiannou VN, Hight DW, Burland JB (1991) Behaviour of clayey sands under undrained cyclic triaxial loading. Géotechnique 41 (3), 383–393

Georgiannou VN, Tsomokos A, Stavrou K (2008) Monotonic and cyclic behaviour of sand under torsional loading. Géotechnique 58 (2), 113–124

Gong G, Thornton C, Chan AHC (2012) DEM simulations of undrained triaxial behavior of granular material. Journal of Engineering Mechanics, Vol. 138, No 6, 560-566

Guo N, Zhao J (2013) The signature of shear-induced anisotropy in granular media. Computers and Geotechnics, 47, 1-15

Gutierrez M (1989) Behavior of sand during rotation of principal stress directions. D. Eng. Thesis, Tokyo University

Gutierrez M, Vardoulakis I (2007) Energy dissipation and post-bifurcation behaviour of granular soils. International Journal for Numerical and Analytical Methods in Geomechanics, 31:435-455

Hight DW, Gens A, Symes MJ (1983) The development of a new hollow cylinder apparatus for investigating the effects of principal stress rotation in soils. Géotechnique 33, No. 4, 355-383

Hill R (1958) A general theory of uniqueness and stability in elastic-plastic solids. Journal of the Mechanics and Physics of Solids (1958); 6:239-249

Hyodo M, Tanimizu H, Yasufuku N, Murata H (1994) Undrained cyclic and monotonic triaxial behaviour of saturated loose sand. Soils and Foundations, Vol.34, No.1, 19-32

Ishihara K, Towhata I (1983) Sand response to cyclic rotation of principal stress directions as induced by wave loads. Soils and Foundations, Vol.23, No.4, 11-26

Jiang M, Zhang A, Fu C (2017) 3D DEM simulations of drained triaxial tests on inherently anisotropic granulates. European Journal of Environmental and Civil Engineering, DOI: 10.1080/19648189.2017.1385541

Kato S, Ishihara K, Towhata I (2001) Undrained shear characteristics of saturated sand under anisotropic consolidation. Soils and Foundations, Vol.41, No.1, pp. 1-11

Konrad J-M (1993) Undrained response of loosely compacted sands during monotonic and cyclic compression tests. Géotechnique 43, No. 1, 69-89

Lade PV, Nelson RB, Ito YM (1988) Instability of granular materials with nonassociated flow. Journal of Engineering Mechanics, Vol. 114, No. 12, 2173-2191

Lade PV (1992) Static instability and liquefaction of loose fine sandy slopes. Journal of Geotechnical Engineering, Vol.118, No.1, 51-71

Lade PV (1993) Initiation of static instability in the submarine Nerlerk berm. Canadian Geotechnical Journal 30: 895-904

Lade PV, Rodriguez NM (2014) Comparison of true triaxial and hollow cylinder tests on cross-anisotropic sand specimens. Geotechnical Testing Journal, Vol. 37, No. 4, 585-596

Lam WK, Tatsuoka F (1988) Effects of initial anisotropic fabric and σ_2 on strength and deformation characteristics of sand. Soils and Foundations, Vol.28, No.1, pp. 89-106

Laouafa F, Darve F (2002) Modelling of slope failure by a material instability mechanism. Computers and Geotechnics 29 (2002) 301-325

Leong WK, Chu J (2002) Effect of undrained creep on instability behaviour of loose sand. Canadian Geotechnical Journal, 39: 1399-1405

Li X, Yu H-S (2010) Numerical investigation of granular material behaviour under rotational shear. Géotechnique 60, No. 5, 381-394

Lü X, Huang M, Qian J (2018) Influences of loading direction and intermediate principal stress ratio on the initiation of strain localization in cross-anisotropic sand. Acta Geotech., 13: 619-633, 2018

Miura K, Miura S, Toki S (1986) Deformation behavior of anisotropic dense sand under principal stress axes rotation. Soils and Foundations, Vol.26, No.1, 36-52

Nakata Y, Hyodo M, Murata H, Yasufuku N (1998) Flow deformation of sands subjected to principal stress rotation. Soils and Foundations, Vol.38, No.2, 115-128

Nicot F, Darve F, Dat Vu Khoa H (2007) Bifurcation and second-order work in geomaterials. Int. J. Numer. Anal. Meth. Geomech., 2007; 31:1007-1032

Nicot F, Darve F (2011) Diffuse and localized failure modes: Two competing mechanisms. Int. J. Numer. Anal. Meth. Geomech., 2011; 35: 586-601

Nicot F, Challamel N, Lerbet J, Prunier F, Darve F (2011) Bifurcation and generalized mixed loading conditions in geomaterials. International Journal for Numerical and Analytical Methods in Geomechanics, Vol. 35, 1409-1431

Nova R (1994) Controllability of the incremental response of soil specimens subjected to arbitrary loading programmes. Journal of the Mechanical Behavior of Materials, 5(2):193-201

Oda M, Nemat-Nasser S, Konishi J (1985) Stress-induced anisotropy in granular masses. Soils and Foundations, Vol.25, No.3, 85-97

Poulos SJ, Castro G, France JW (1985) Liquefaction evaluation procedure. Journal of Geotechnical Engineering, ASCE, Vol.111, No.6, pp. 772-792

Prunier F, Nicot F, Darve F, Laouafa F, Lignon S (2009) Three-dimensional multiscale bifurcation analysis of granular media. Journal of Engineering Mechanics, Vol. 135, No. 6, 493-509

Roscoe KH, Schofield AN, Wroth CP (1958) On the yielding of soils. Géotechnique 8 (1), 22–53

Sasitharan S, Robertson PK, Sego DC, Morgenstern NR (1993) Collapse behavior of sand. Can. Geotech. J. 30, 569-577

Sayao A, Vaid YP (1991) A critical assessment of stress nonuniformities in hollow cylinder test specimens. Soils and Foundations, Vol.31, No.1, 60-72

Shibuya S, Hight DW (1987) A bounding surface of granular materials. Soils and Foundations, Vol.27, No.4, 123-136

Shibuya S, Hight DW, Jardine RJ (2003a) Four-dimensional local boundary surfaces of an isotropically consolidated loose sand. Soils and Foundations, Vol.43, No.2, 89-103

Shibuya S, Hight DW, Jardine RJ (2003b) Local boundary surfaces of a loose sand dependent on consolidation path. Soils and Foundations, Vol.43, No.3, 85-93

Sibille L, Nicot F, Donzé FV, Darve F (2007) Material instability in granular assemblies from fundamentally different models. Int. J. Numer. Anal. Meth. Geomech., 2007; 31:457–481

Sibille L, Donzé F-V, Nicot F, Chareyre B, Darve F (2008) From bifurcation to failure in a granular material: a DEM analysis. Acta Geotechnica, 3:15-24

Sivathayalan S, Vaid YP (2002) Influence of generalized initial state and principal stress rotation on the undrained response of sands. Canadian Geotechnical Journal, 39 (1): 63 – 76

Symes MJ, Gens A, Hight DW (1984) Undrained anisotropy and principal stress rotation in saturated sand. Géotechnique 34, No. 1, 11-27

Tatsuoka F, Sonoda S, Hara K, Fukushima S, Pradhan TBS (1986) Failure and deformation of sand in torsional shear. Soils and Foundations, Vol.26, No.4, pp. 79-97

Theocharis AI, Vairaktaris E, Dafalias YF, Papadimitriou AG (2017) Proof of incompleteness of Critical State Theory in granular mechanics and its remedy. Journal of Engineering Mechanics, Vol. 143 (2), 1-12

Tian Y, Yao Y-P (2018) Constitutive modeling of principal stress rotation by considering inherent and induced anisotropy of soils. Acta Geotech., 13: 1299-1311, 2018

Tong Z, Fu P, Dafalias YF, Yao Y (2014) Discrete element method analysis of non-coaxial flow under rotational shear. International Journal for Numerical and Analytical Methods in Geomechanics, 38: 1519-1540

Triantafyllos PK, Georgiannou VN, Dafalias YF, Georgopoulos I-O (2020) New findings on the evolution of the instability surface of loose sand. Acta Geotech. 15, 197-221, https://doi.org/10.1007/s11440-019-00887-7

Vaid YP, Chern JC (1983) Effect of static shear on resistance to liquefaction. Soils and Foundations, Vol.23, No.1, pp. 47-60

Vardoulakis I, Goldscheider M, Gudehus G (1978) Formation of shear bands in sand bodies as a bifurcation problem. International Journal for Numerical and Analytical Methods in Geomechanics, 1978, 2: 99-128

Vardoulakis I, Sulem J (1995) Bifurcation analysis in geomechanics. Chapman and Hall, 1995

Vardoulakis I, Georgopoulos I-O (2005) The “stress-dilatancy” hypothesis revisited: shear-banding related instabilities. Soils and Foundations, Vol.45, No.2, pp. 61-76

Yamada Y, Ishihara K (1981) Undrained deformation characteristics of loose sand under three-dimensional stress conditions. Soils and Foundations, Vol. 21, No. 1, 97-107

Yamamuro JA, Covert KM (2001) Monotonic and cyclic liquefaction of very loose sands with high silt content. Journal of Geotechnical and Geoenvironmental Engineering, Vol. 127 (4), pp. 314-324

Yang ZX, Li XS, Yang J (2007) Undrained anisotropy and rotational shear in granular soil. Géotechnique 57, No. 4, 371-384

Yimsiri S, Soga K (2010) DEM analysis of soil fabric effects on behaviour of sand. Géotechnique 60, No. 6, 483-495

Yoshimine M, Ishihara K, Vargas W (1998) Effects of principal stress direction and intermediate principal stress on undrained shear behavior of sand. Soils and Foundations, Vol. 38, No. 3, 179-188

Yoshimine M, Ishihara K (1998) Flow potential of sand during liquefaction. Soils and Foundations, Vol. 38, No. 3, 189-198

Zdravković L, Jardine RJ (2001) The effect on anisotropy of rotating the principal stress axes during consolidation. Géotechnique 51, No. 1, 69-83

7.11 TABLES

Table 7.1 List of the symbols and equations used to calculate the average stresses, strains and other parameters

Direction HC	Stress	Strain
Vertical	$\sigma_{zz} = \dfrac{F}{\pi\left(r_o^2 - r_i^2\right)} + \dfrac{p_o r_o^2 - p_i r_i^2}{r_o^2 - r_i^2}$	$\varepsilon_{zz} = \dfrac{v}{H}$
Circumferential	$\sigma_{\theta\theta} = \dfrac{p_o r_o - p_i r_i}{r_o - r_i}$	$\varepsilon_{\theta\theta} = \dfrac{(\varepsilon_{vol} - \varepsilon_{zz})}{2}$ **or** $\varepsilon_{\theta\theta} = \varepsilon_{vol} - \varepsilon_{zz}$
Radial	$\sigma_{rr} = \dfrac{p_o r_o + p_i r_i}{r_o + r_i}$	$\varepsilon_{rr} = \dfrac{(\varepsilon_{vol} - \varepsilon_{zz})}{2}$ **or** $\varepsilon_{rr} = 0$
Rotational	$\tau_{z\theta} = \dfrac{3T}{2\pi(r_o^3 - r_i^3)}$	$\gamma_{z\theta} = 2\varepsilon_{z\theta} = \dfrac{2\theta\left(r_o^3 - r_i^3\right)}{3H(r_o^2 - r_i^2)}$
Principal	**Stress**	**Strain**
Major	$\sigma_1 = \dfrac{\sigma_{zz} + \sigma_{\theta\theta}}{2} + \sqrt{\left(\dfrac{\sigma_{zz} - \sigma_{\theta\theta}}{2}\right)^2 + \tau_{z\theta}^2}$	$\varepsilon_1 = \dfrac{\varepsilon_{zz} + \varepsilon_{\theta\theta}}{2} + \sqrt{\left(\dfrac{\varepsilon_{zz} - \varepsilon_{\theta\theta}}{2}\right)^2 + \varepsilon_{z\theta}^2}$
Intermediate	$\sigma_2 = \sigma_{rr}$	$\varepsilon_2 = \varepsilon_{rr}$
Minor	$\sigma_3 = \dfrac{\sigma_{zz} + \sigma_{\theta\theta}}{2} - \sqrt{\left(\dfrac{\sigma_{zz} - \sigma_{\theta\theta}}{2}\right)^2 + \tau_{z\theta}^2}$	$\varepsilon_3 = \dfrac{\varepsilon_{zz} + \varepsilon_{\theta\theta}}{2} - \sqrt{\left(\dfrac{\varepsilon_{zz} - \varepsilon_{\theta\theta}}{2}\right)^2 + \varepsilon_{z\theta}^2}$
Invariant	**Stress**	**Strain**
	$q = (\dfrac{1}{2}\{(\sigma_1 - \sigma_2)^2 + (\sigma_2 - \sigma_3)^2 + (\sigma_3 - \sigma_1)^2\})^{1/2}$	$\gamma = (\dfrac{2}{9}\{(\varepsilon_1 - \varepsilon_2)^2 + (\varepsilon_2 - \varepsilon_3)^2 + (\varepsilon_3 - \varepsilon_1)^2\})^{1/2}$
	$p' = \dfrac{\sigma_1' + \sigma_2' + \sigma_3'}{3} = \dfrac{\sigma_1 + \sigma_2 + \sigma_3}{3} - u$	$\varepsilon_{vol} = \varepsilon_1 + \varepsilon_2 + \varepsilon_3 \; (= \dfrac{-\Delta V}{V})$

	$\tau_{oct} = \frac{1}{3}(\{(\sigma_1 - \sigma_2)^2 + (\sigma_2 - \sigma_3)^2 + (\sigma_3 - \sigma_1)^2\})^{1/2}$	$\gamma_{oct} = \frac{2}{3}(\{(\varepsilon_1 - \varepsilon_2)^2 + (\varepsilon_2 - \varepsilon_3)^2 + (\varepsilon_3 - \varepsilon_1)^2\})^{1/2}$
Parameters	**Stress**	**Strain**
Difference	$q_d = \sigma_1 - \sigma_3$	
	$X = \frac{\sigma'_{zz} - \sigma'_{\theta\theta}}{\sigma'_{zz} + \sigma'_{\theta\theta}}$, $X_s = \sigma'_{zz} - \sigma'_{\theta\theta}$	$X_\varepsilon = \frac{\varepsilon_{zz} - \varepsilon_{\theta\theta}}{2}$
	$Y = \frac{2\tau_{z\theta}}{\sigma'_{zz} + \sigma'_{\theta\theta}}$, $Y_s = 2\tau_{z\theta}$	$Y_\varepsilon = \varepsilon_{z\theta}$
Direction of major principal stress/strain	$\alpha \equiv \alpha_{\sigma'1} = 0.5 \cdot \tan^{-1}\frac{Y}{X} = 0.5 \cdot \tan^{-1}\frac{Y_s}{X_s}$	$\alpha_{\varepsilon 1} = 0.5 \cdot \tan^{-1}\frac{Y_\varepsilon}{X_\varepsilon}$
Direction of major principal incremental stress/strain	$\alpha_{d\sigma'1} = 0.5 \cdot \tan^{-1}\frac{dY_s}{dX_s}$	$\alpha_{d\varepsilon 1} = 0.5 \cdot \tan^{-1}\frac{dY_\varepsilon}{dX_\varepsilon}$
Ratio	$b = \frac{\sigma'_2 - \sigma'_3}{\sigma'_1 - \sigma'_3}$	
Ratio	$\sin\varphi = \frac{\sigma'_1 - \sigma'_3}{\sigma'_1 + \sigma'_3}$	
Ratio	$\eta = \frac{q}{p'}$	
Ratio	$K_c = \frac{\sigma'_{3c}}{\sigma'_{1c}}$	
Second-order work	$d^2W = (d\sigma_{zz} - d\sigma_{\theta\theta})(\frac{d\varepsilon_{zz} - d\varepsilon_{\theta\theta}}{2}) + 2d\tau_{z\theta}d\varepsilon_{z\theta}$, for isochoric conditions under b=0.5	
Angle between the σ'1-axis and the planes of max(τ/σn')	$\theta_{1,2} = \pm(45^\circ - \varphi_{mob}/2)$	

Table 7.2 Details of the loading tests

Test	α (°)	b (-)	e_i (-)	p'_i (kPa)	K_c (-)	α_{ip} (°)	b_{ip} (-)	φ_{ip} (°)	$\gamma_{oct,ip}$ (%)	$\tau_{oct,ip}$ (kPa)	Δu_{ip} / p'_i (-)
A1	0	0.5	0.737	199	1.00 /0.86	0.0	0.51	31.2	0.43	58.4	0.30
A2	10	0.5	0.716	199	1.00	9.8	0.52	35.9	0.49	66.5	0.29
A3	15	0.5	0.726	200	1.00 /0.86	15.0	0.50	31.7	0.47	59.9	0.30
A4	22.5	0.5	0.719	199	1.00 /0.86	22.3	0.51	29.9	0.50	55.6	0.31
A5	22.5	0.5	0.706	200	1.00	22.3	0.50	31.9	0.48	61.1	0.29
A6	30	0.5	0.717	199	1.00 /0.86	29.9	0.51	28.0	0.49	53.1	0.30
A7	40	0.5	0.721	199	1.00	39.7	0.50	24.1	0.44	45.8	0.31
A8	45	0.5	0.727	199	1.00	44.7	0.50	22.3	0.38	44.0	0.29
A9	45	0.5	0.707	200	1.00	44.9	0.49	23.8	0.36	46.1	0.30
A10	45	0.5	0.745	199	1.00	44.9	0.50	19.7	0.32	38.7	0.29
A11	50	0.5	0.699	199	1.00	49.5	0.50	23.5	0.37	45.1	0.31
A12	60	0.5	0.719	199	1.00	59.3	0.51	20.5	0.23	39.7	0.30
A13	60	0.5	0.719	200	1.00	59.3	0.51	20.0	0.24	34.8	0.37
A14	67.5	0.5	0.712	199	1.00	68.9	0.51	18.8	0.27	34.7	0.33
A15	75	0.5	0.706	199	1.00	74.2	0.51	20.6	0.20	42.4	0.25
A16	75	0.5	0.717	199	1.00	74.0	0.51	18.4	0.24	33.7	0.34
A17	80	0.5	0.727	198	1.00	79.1	0.50	17.8	0.27	32.8	0.34
A18	67.5*	0.5	0.714	199	1.00	62.5	0.50	20.0	0.30	39.0	0.31
A19	90	0.5	0.727	199	1.00	89.8	0.51	19.1	0.31	34.1	0.35
A20	90	0.5	0.714	200	1.00	89.6	0.52	19.7	0.31	36.7	0.32
A21	0	0	0.709	200	1.00	0.0	0.00	25.0	0.89	72.5	0.47
A22	90	1	0.697	200	1.00	90.0	1.00	16.3	0.16	33.7	0.18
A23	90	1	0.718	200	0.50	90.0	1.00	15.7	0.42	23.1	0.17
A24	30	0.5	0.726	99	1.00	29.4	0.51	27.4	0.31	26.5	0.28
A25	45	0.5	0.734	99	1.00	44.0	0.52	20.8	0.31	20.0	0.30
A26	80	0.5	0.717	100	1.00	79.3	0.52	17.7	0.22	16.3	0.34
B1	R0+	0.5	0.727	207	0.80	34.1	0.50	24.0	0.39	50.6	0.26
B2	R0+	0.5	0.711	223	0.50	19.1	0.50	32.7	0.40	78.3	0.20
B3	R0+	0.5	0.728	232	0.40	12.6	0.50	34.0	0.16	89.6	0.15
B4	R0+	0.5	0.711	206	0.80	34.4	0.51	24.9	0.33	54.4	0.23
B5	R0+	0.5	0.696	224	0.50	18.5	0.50	32.1	0.45	78.4	0.19
B6	R0+	0.5	0.701	111	0.50	20.7	0.51	33.1	0.40	41.0	0.17
B7	R0+	0.5	0.727	115	0.40	14.0	0.50	35.2	0.17	46.0	0.15
C1	R0+	0.5	0.730	225	0.48	26.3	0.51	29.3	0.40	64.7	0.28
C2	R0+	0.5	0.721	214	0.66	79.6	0.51	19.8	0.42	35.3	0.40
C3	R0+	0.5	0.721	209	0.75	57.4	0.51	25.6	0.45	23.7	0.68
C4	R0+	0.5	0.716	210	0.72	90.0	0.51	20.3	0.40	27.1	0.55
C5	R0+	0.5	0.713	212	0.70	79.6	0.51	23.4	0.50	30.9	0.55

C6	R0+	0.5	0.704	216	0.64	64.4	0.50	39.1	6.57	34.5	0.69
D1	R0+	.4-.5	0.738	211	0.70	-85.5	0.40	21.9	0.33	23.2	0.67

*Loading at the fixed stress direction $\alpha_{\sigma'1}$ = 67.5° was followed by loading at the fixed incremental stress direction $\alpha_{d\sigma'1}$ = 45°. Index "i", for "initial, "c", for consolidation and "ip", for instability point

7.12 FIGURES

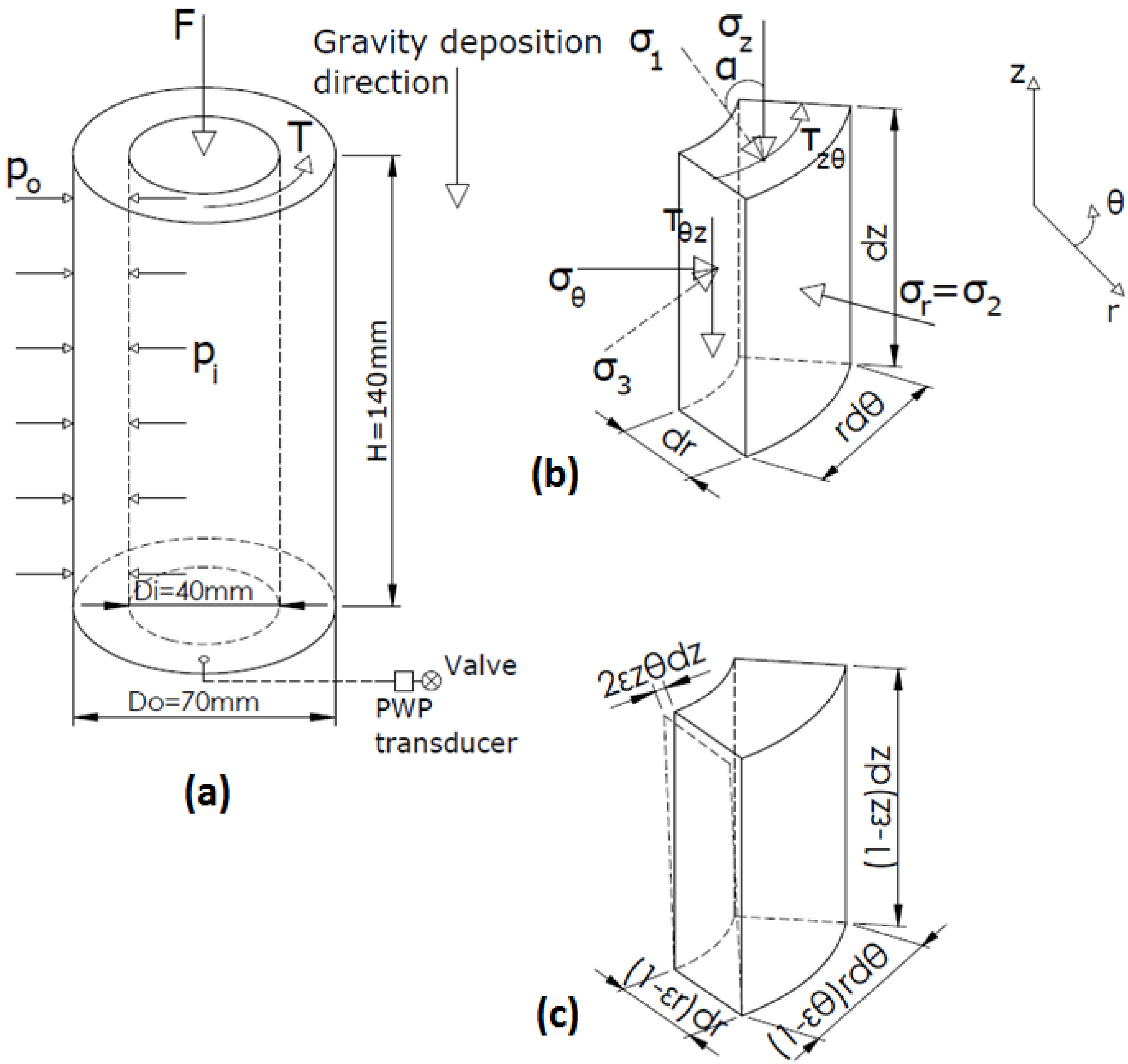

Fig. 7.1 **a** Hollow cylindrical specimen and applied boundary loads. **b** Stress components on the undeformed soil element. **c** Strain components associated with the combined multiaxial and torsional deformation

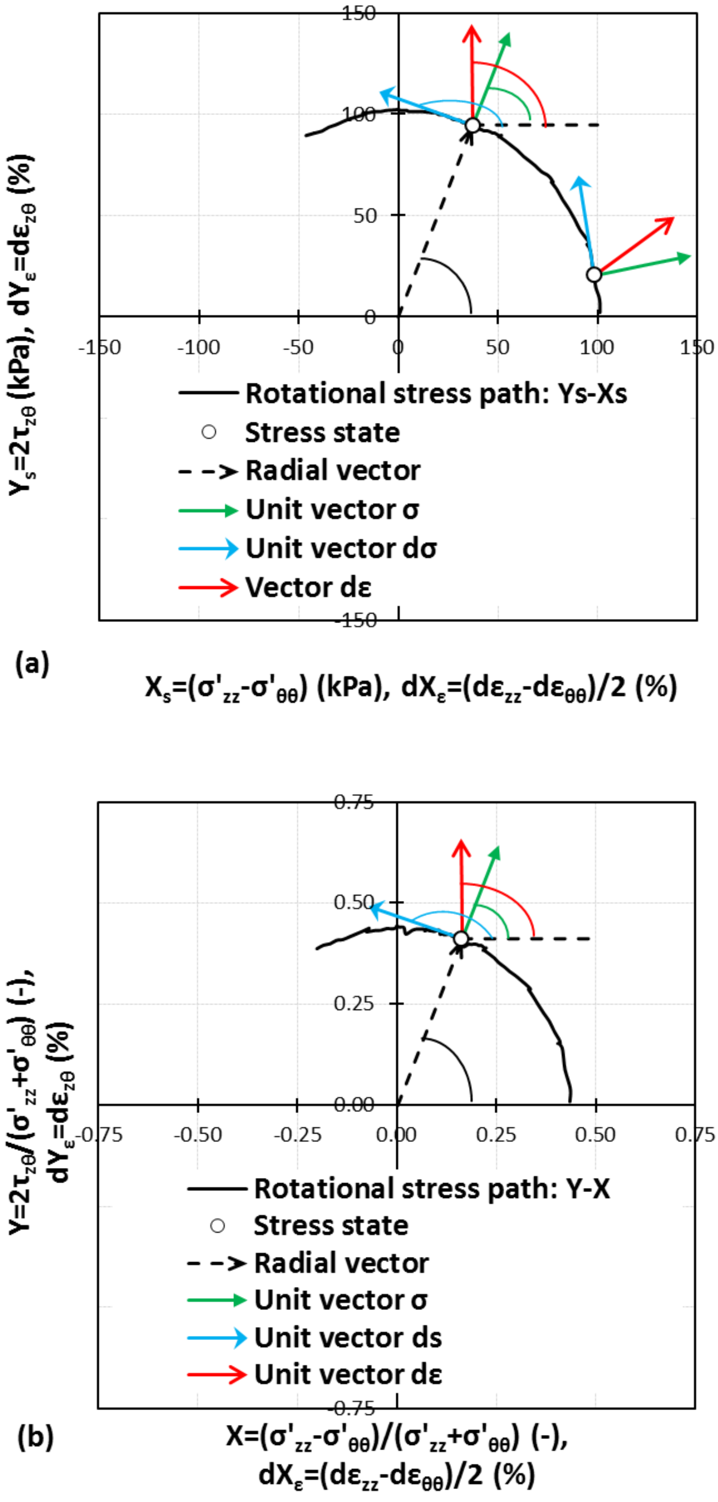

Fig. 7.2 Stress path and directions of principal stress, stress rate and strain rate: **a** in the Y_s - X_s deviatoric plane and **b** in the Y - X deviatoric stress plane. The axes dX_ε and dY_ε are superimposed on a given stress state to offer the reference frame for determining the direction angle $\alpha_{d\varepsilon 1}$ of the axis of the rate of principal strain $d\varepsilon_1$

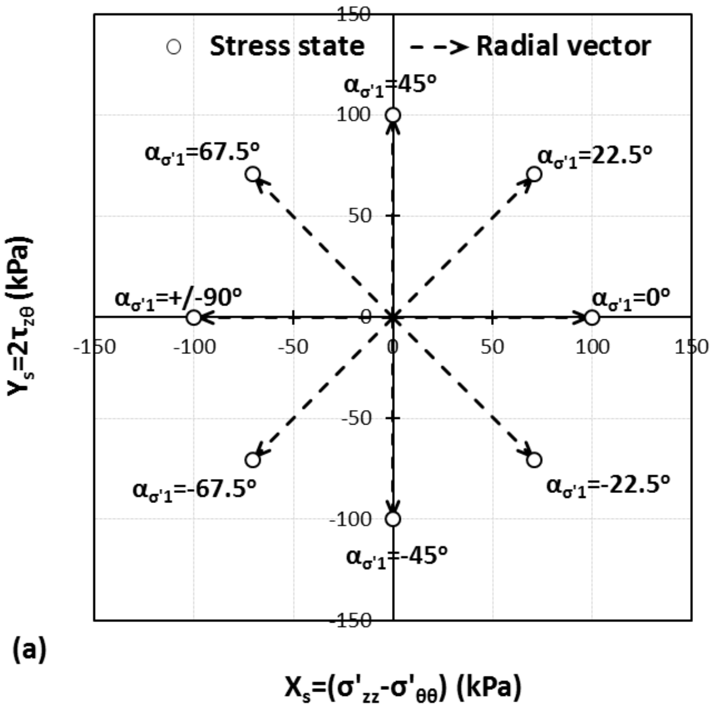

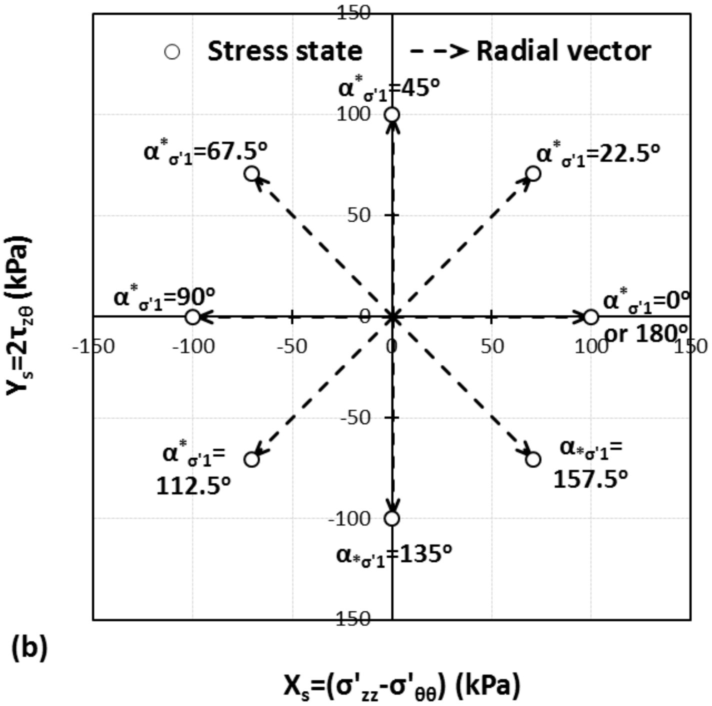

Fig. 7.3 Value and sign of the stress direction angles $\alpha_{\sigma'1}$ and $\alpha^{*}_{\sigma'1}$ in the Y_s - X_s deviatoric plane

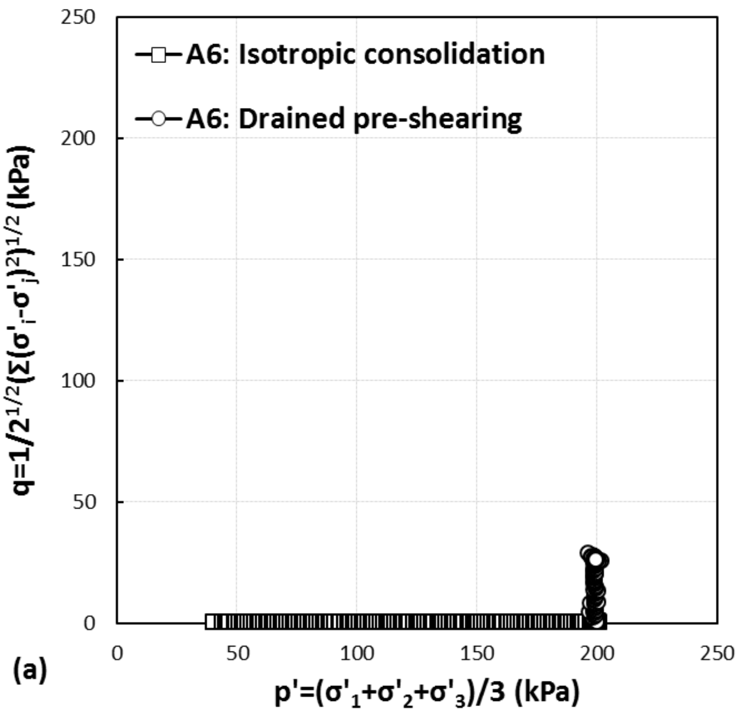

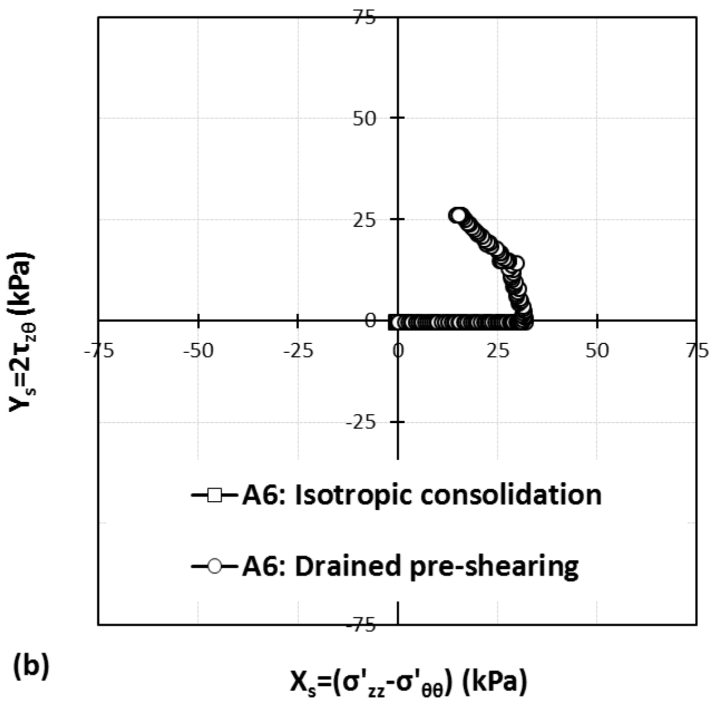

Fig. 7.4 Isotropic consolidation and drained pre-shearing of the sand specimen in test A6. **a** Effective stress path in the q - p’ plane. **b** Stress path in the Y_s - X_s deviatoric stress plane (**c** and **d** on next page)

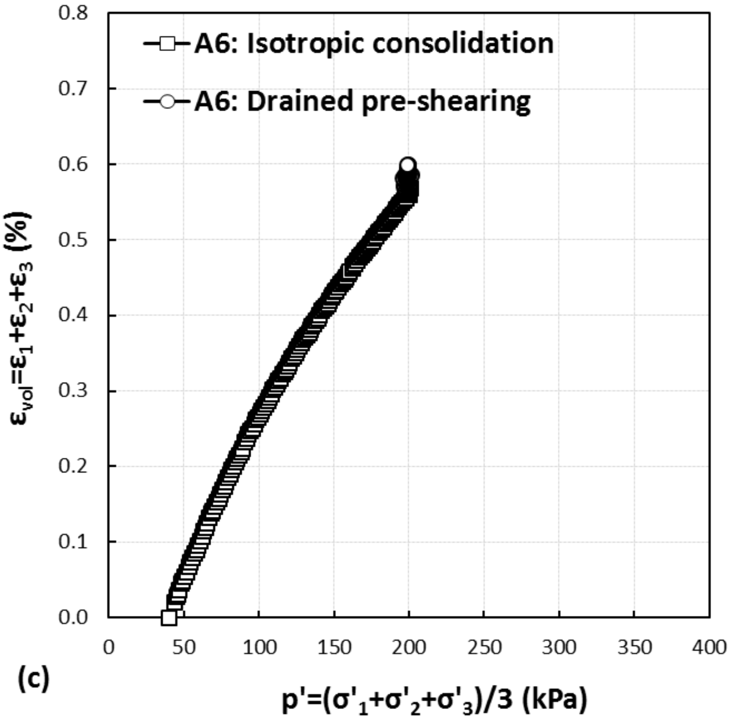

(c)

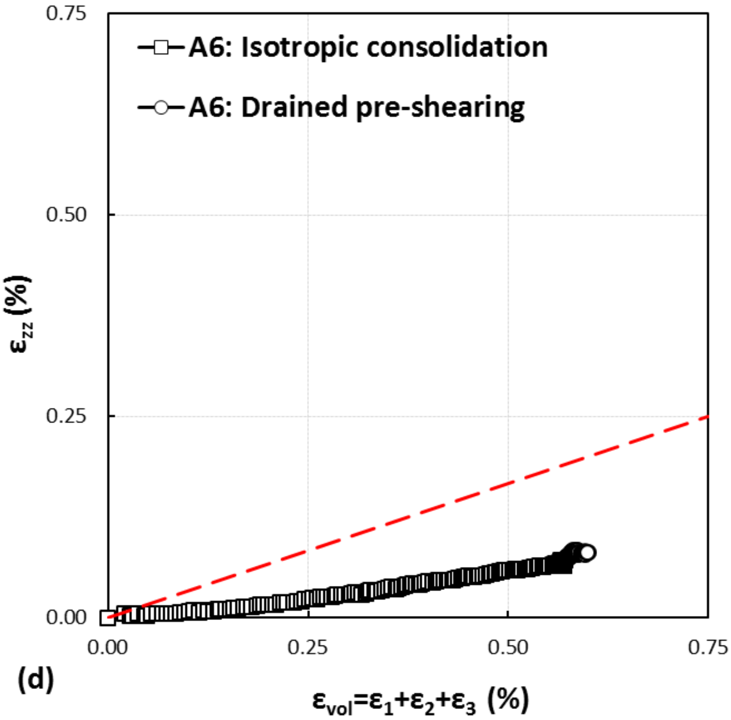

(d)

Fig. 7.4 Isotropic consolidation and drained pre-shearing of the sand specimen in test A6. **c** Volumetric strain against mean effective stress. **d** Axial strain against volumetric strain

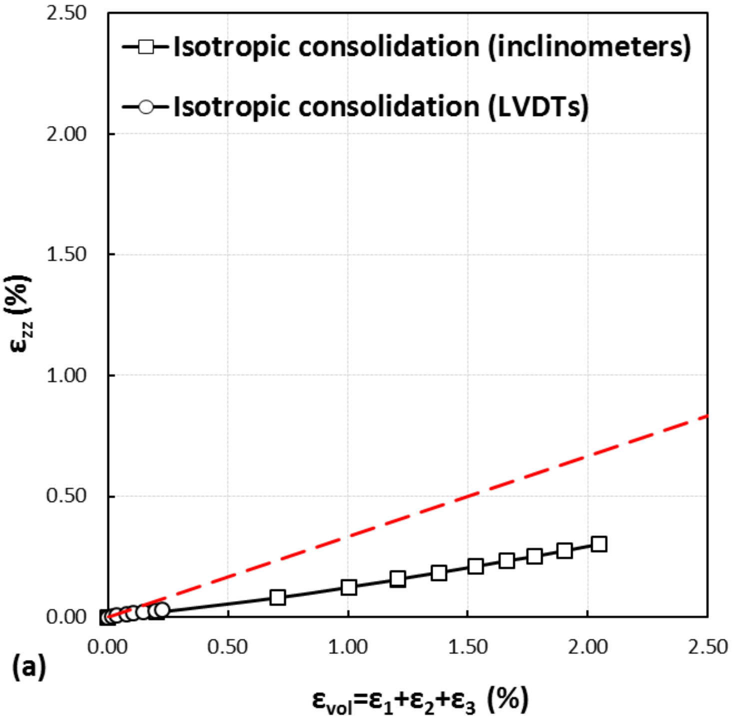

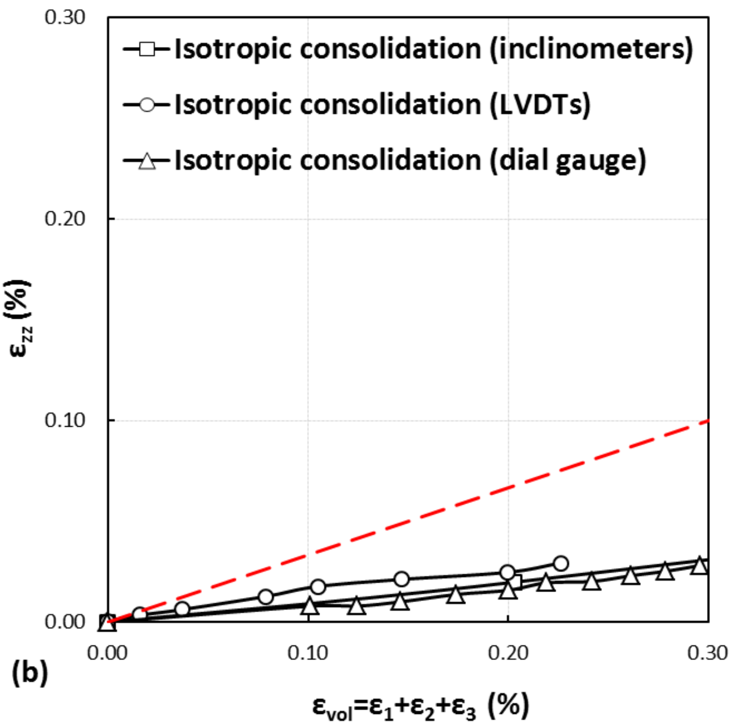

Fig. 7.5 Axial and volumetric strain developed during isotropic consolidation of sand specimens. **a** Local axial strain against volumetric strain. **b** Axial strain (local or global) against volumetric strain

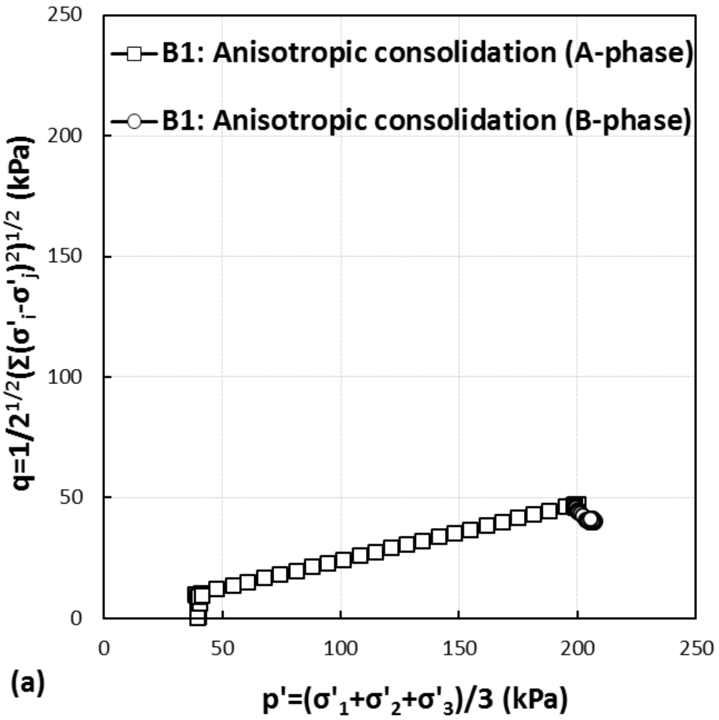

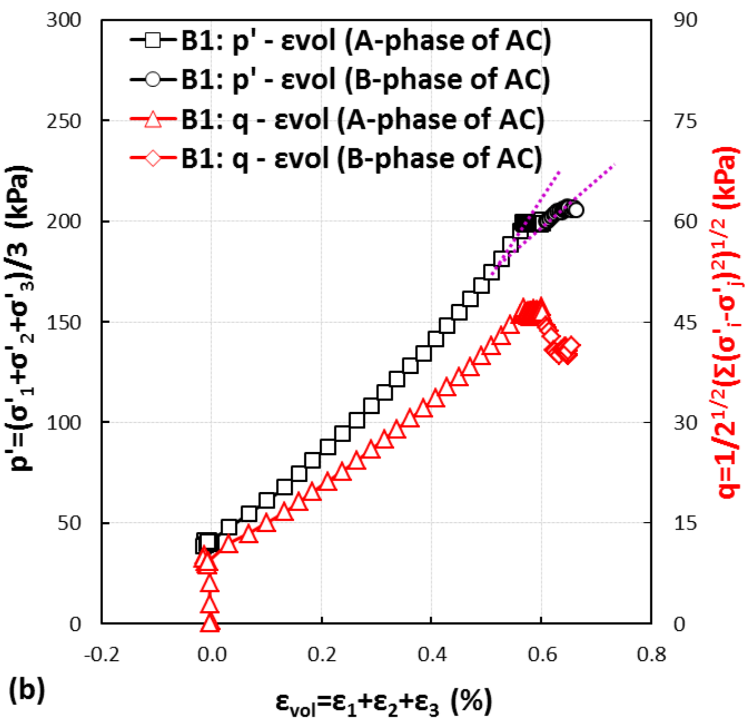

Fig. 7.6 Anisotropic consolidation of the sand specimen in test B1. **a** Effective stress path in the *q* - *p*' plane. **b** Mean effective stress and deviatoric stress against volumetric strain (**c** and **d** on next page)

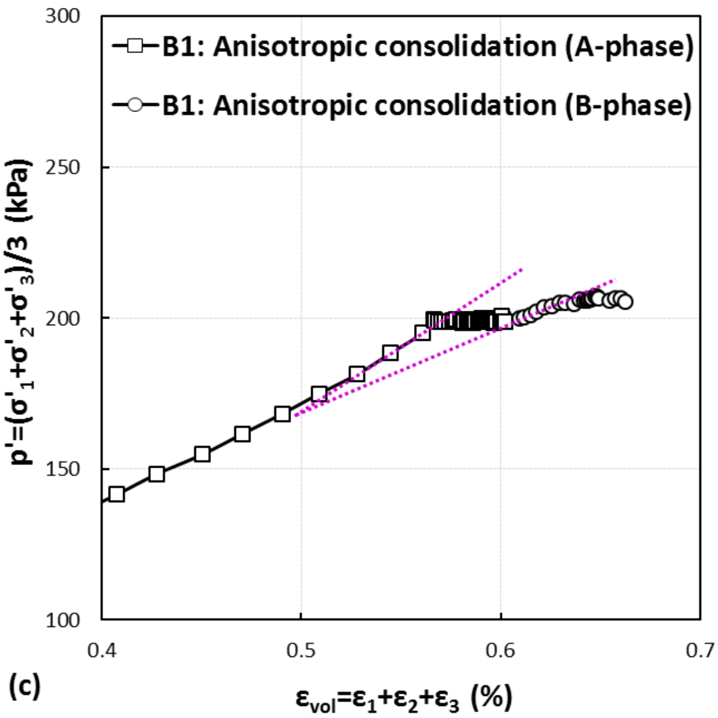

(c)

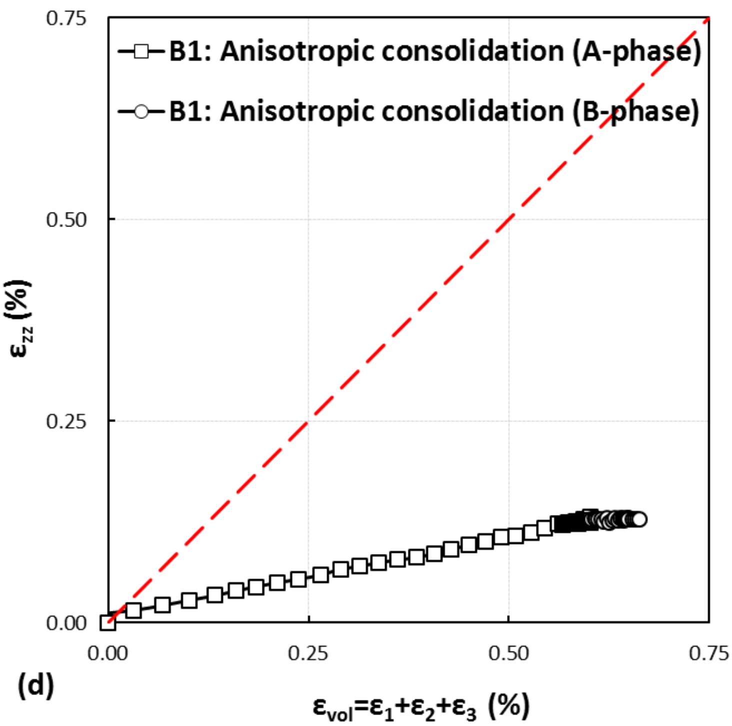

(d)

Fig. 7.6 Anisotropic consolidation of the sand specimen in test B1. **c** Mean effective stress against volumetric strain. **d** Axial strain against volumetric strain

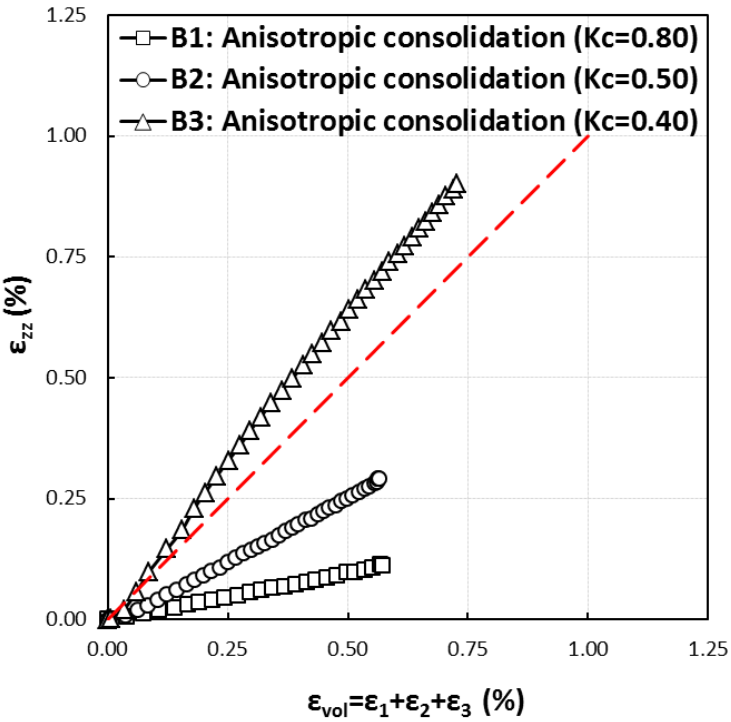

Fig. 7.7 Evolution of axial and volumetric strain during anisotropic consolidation of M31 Sand at different consolidation stress ratios $K_c = \sigma'_3 / \sigma'_1$

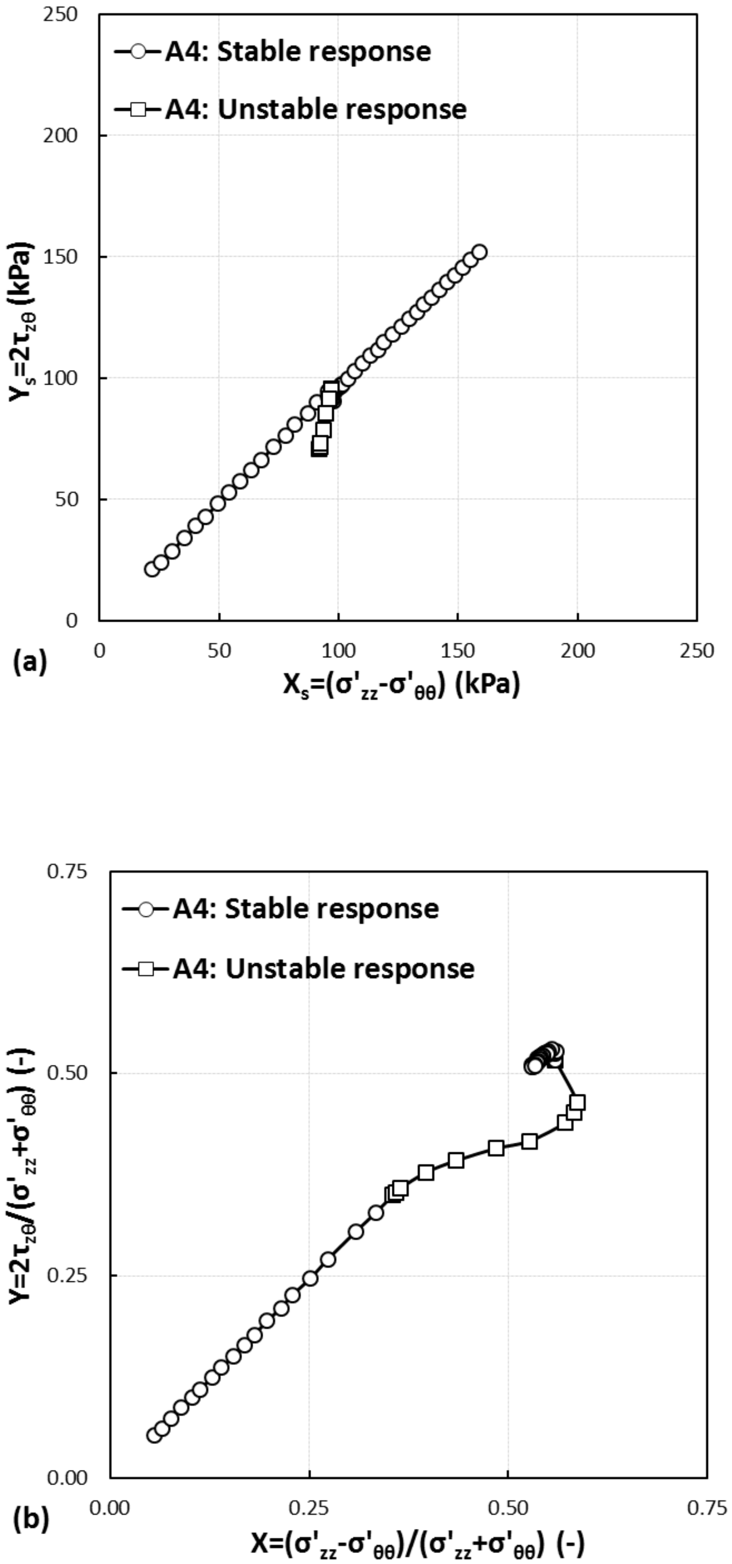

Fig. 7.8 Stable and unstable response of sand specimen subjected to undrained loading in test A4. **a** Stress path in the Y_s - X_s plane. **b** Stress path in the Y - X plane

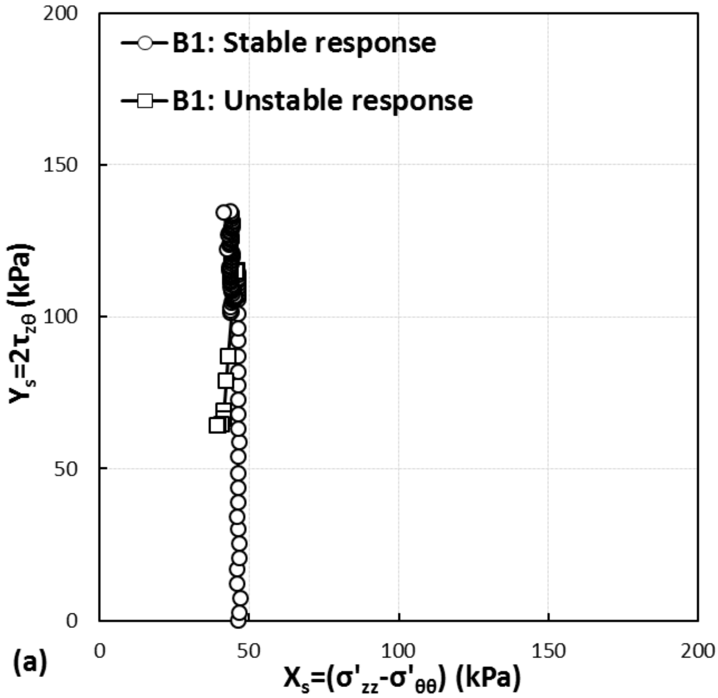

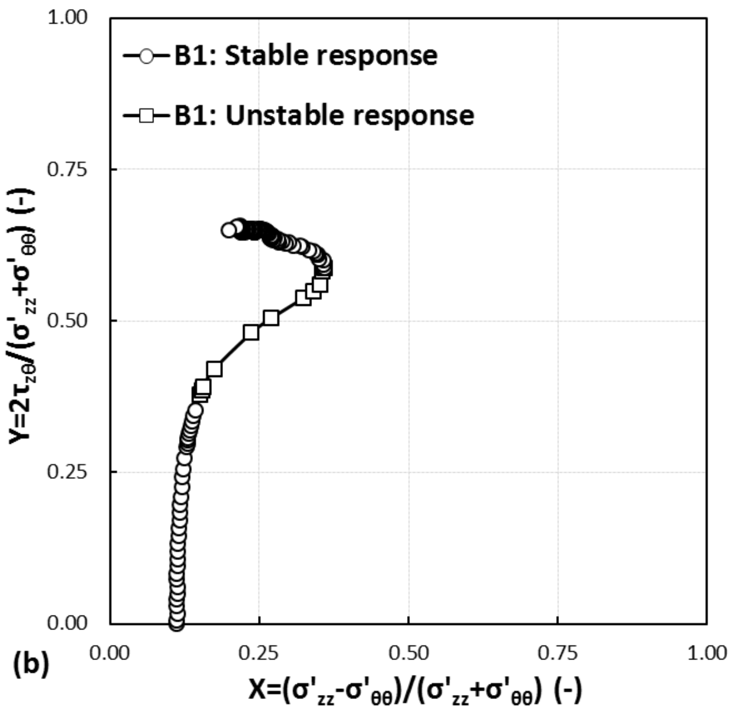

Fig. 7.9 Stable and unstable response of sand specimen subjected to undrained loading in test B1. **a** Stress path in the Y_s - X_s plane. **b** Stress path in the Y - X plane

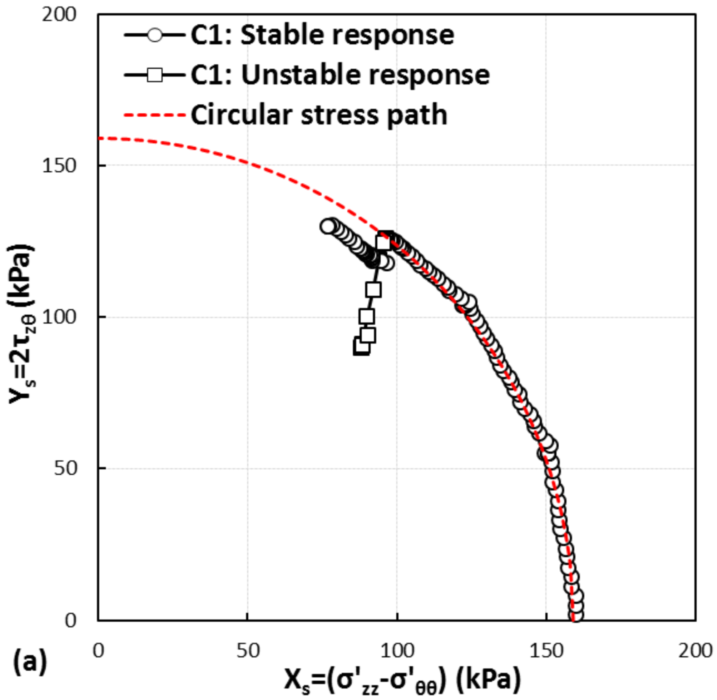

(a)

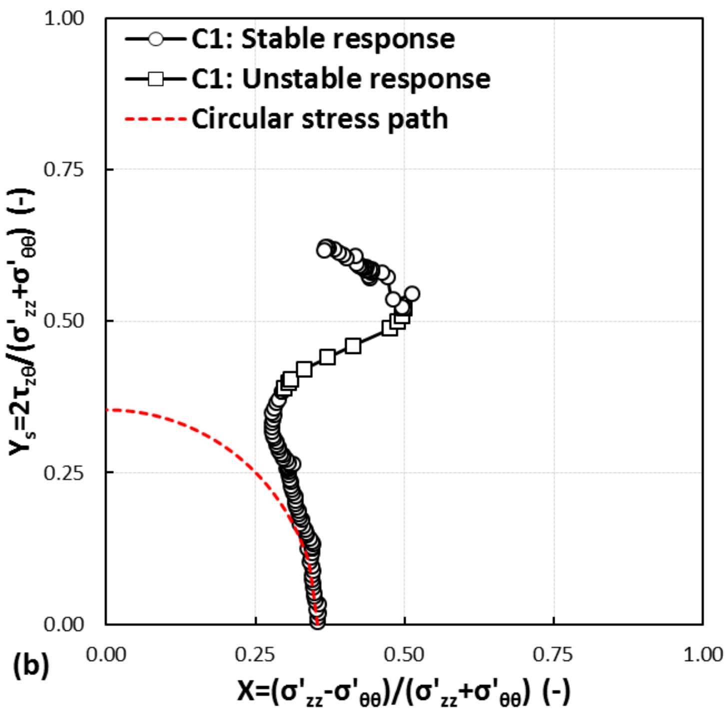

(b)

Fig. 7.10 Stable and unstable response of sand specimen subjected to undrained loading in test C1. **a** Stress path in the Y_s - X_s plane. **b** Stress path in the Y - X plane

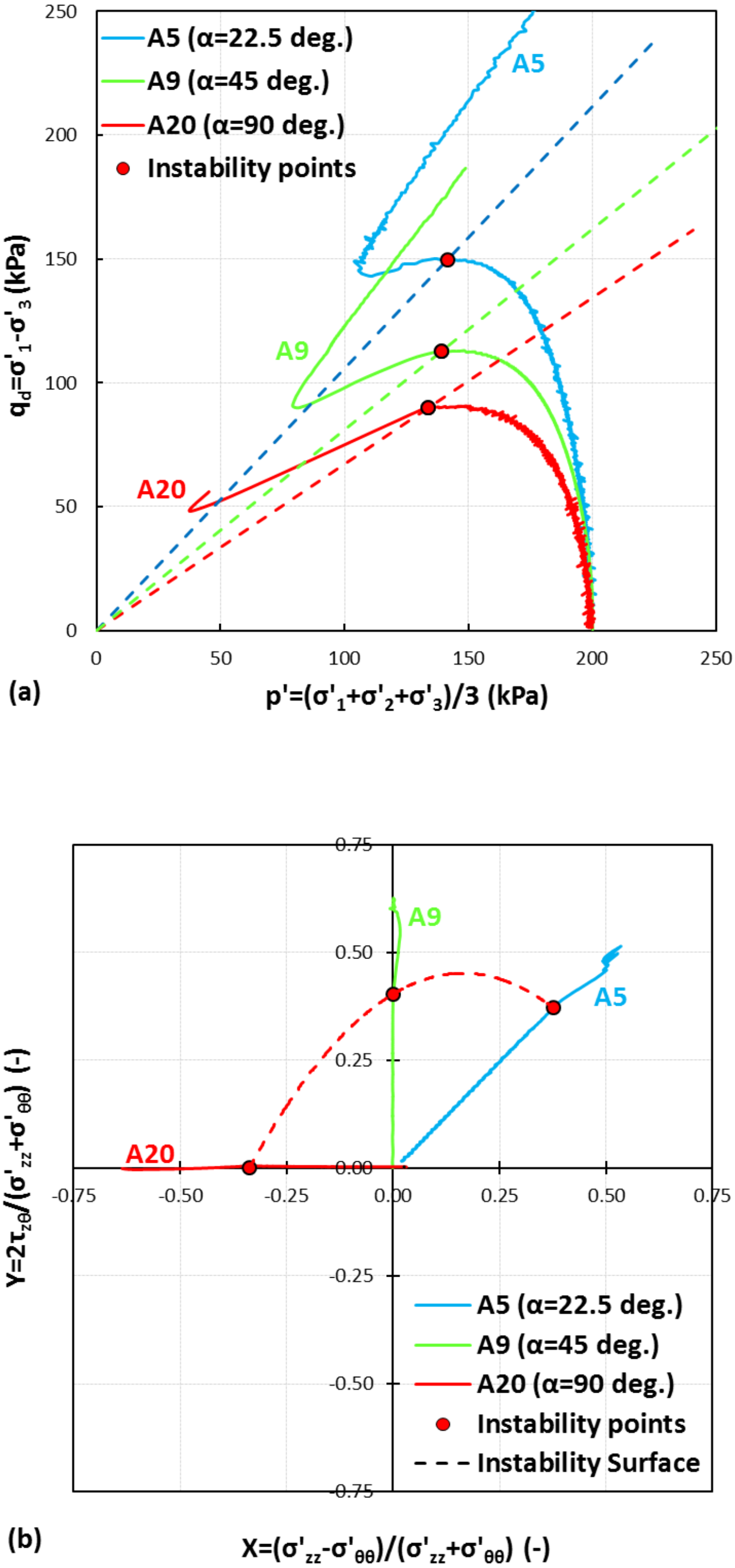

Fig. 7.11 Definition of the Local Boundary Surface, Instability Line and Instability Surface of loose sand using the stress paths of the A-series loading tests **a** in the q_d - p' plane and **b** in the Y - X plane

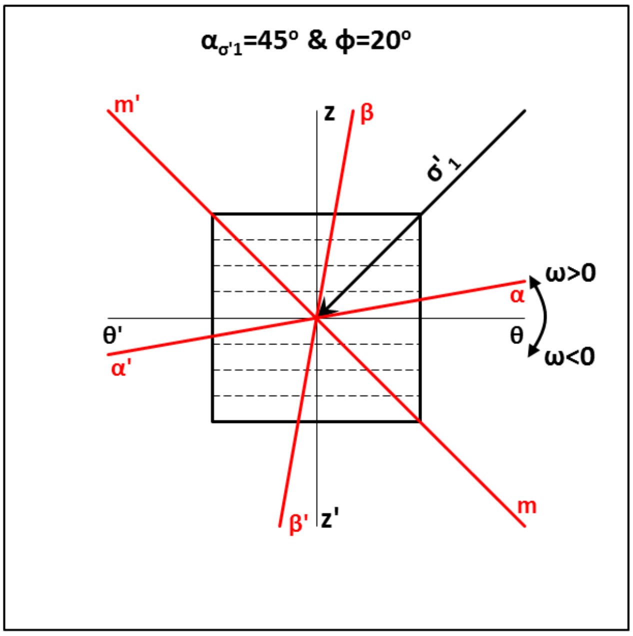

(a)

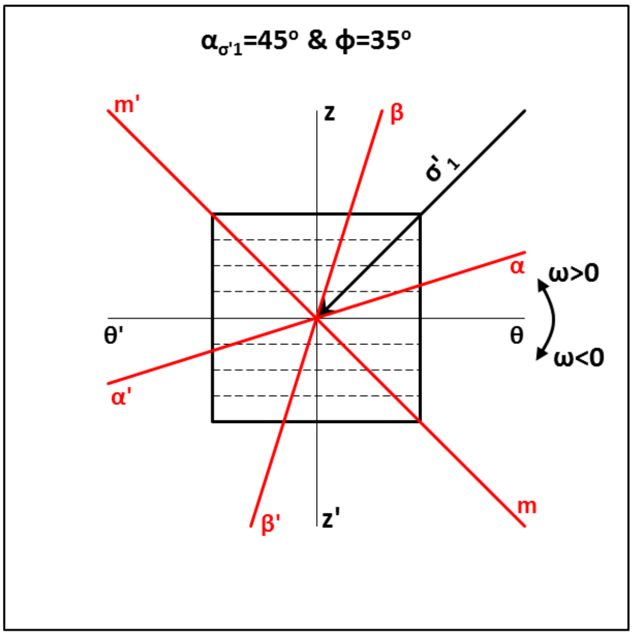

(b)

Fig. 7.12 Relative orientation of the planes of maximum stress obliquity and horizontal bedding plane in a soil element subjected to loading at $\alpha_{\sigma'1}$ = 45° when **a** φ = 20° and **b** φ = 35°

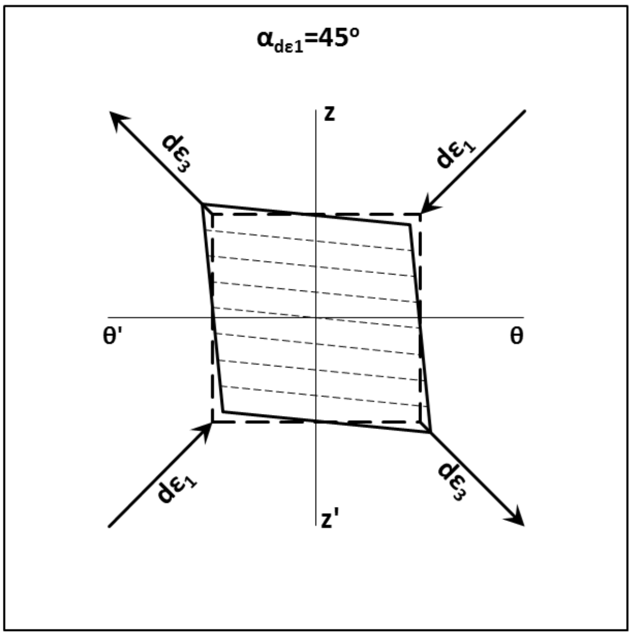

Fig. 7.13 Deformation of a soil element with horizontal bedding plane in transient simple-shear mode, $d\varepsilon_{zz} = d\varepsilon_{\theta\theta} = d\varepsilon_{rr} = 0$, along the direction of incremental strain $\alpha_{d\varepsilon 1}$ = 45°

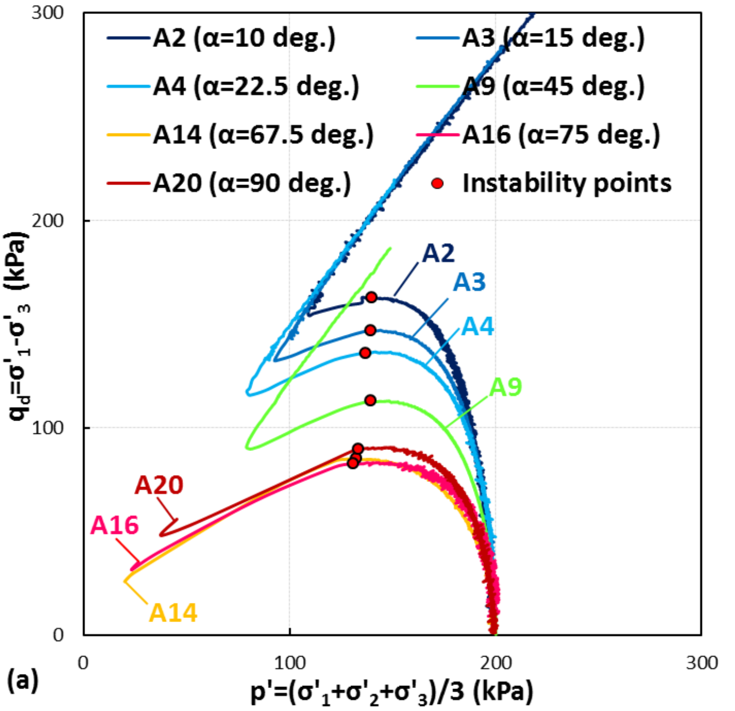

(a)

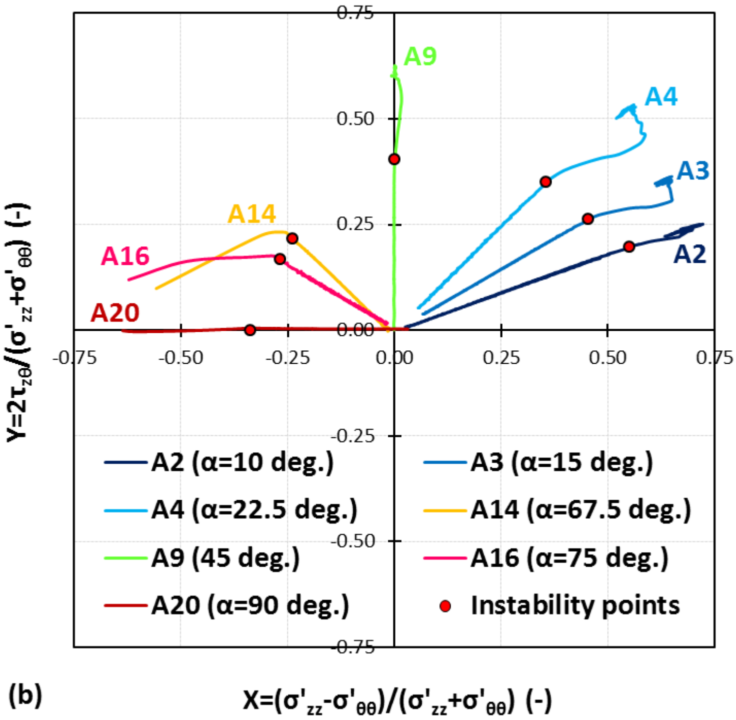

(b)

Fig. 7.14 Response of loose isotropically consolidated M31 Sand to undrained loading with fixed stress principal axes. **a** Effective stress paths in the q_d - p' plane. **b** Stress paths in the Y - X deviatoric plane (**c** and **d** on next page)

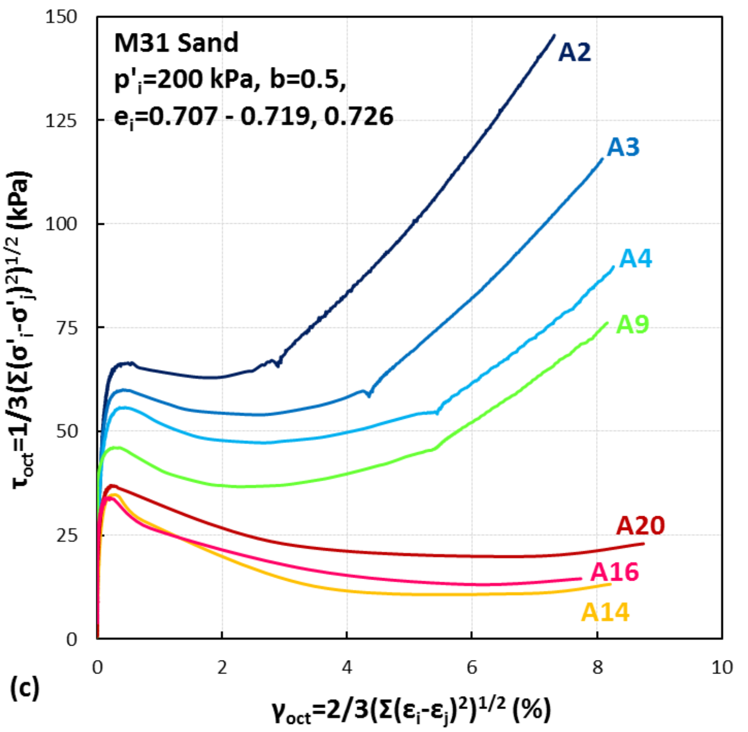

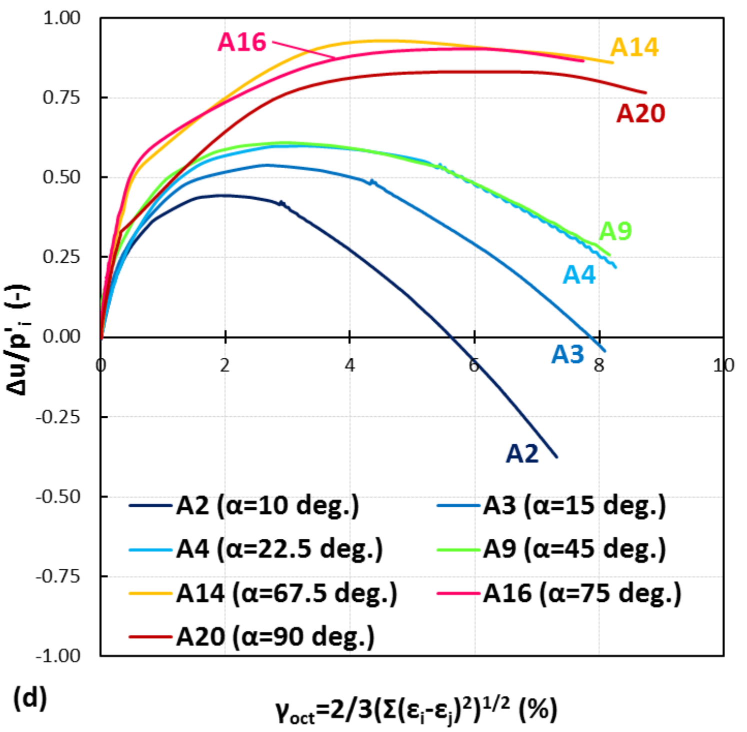

Fig. 7.14 Response of loose isotropically consolidated M31 Sand to undrained loading with fixed stress principal axes. **c** Stress - strain curves. **d** Evolution of normalised excess pore-water pressure

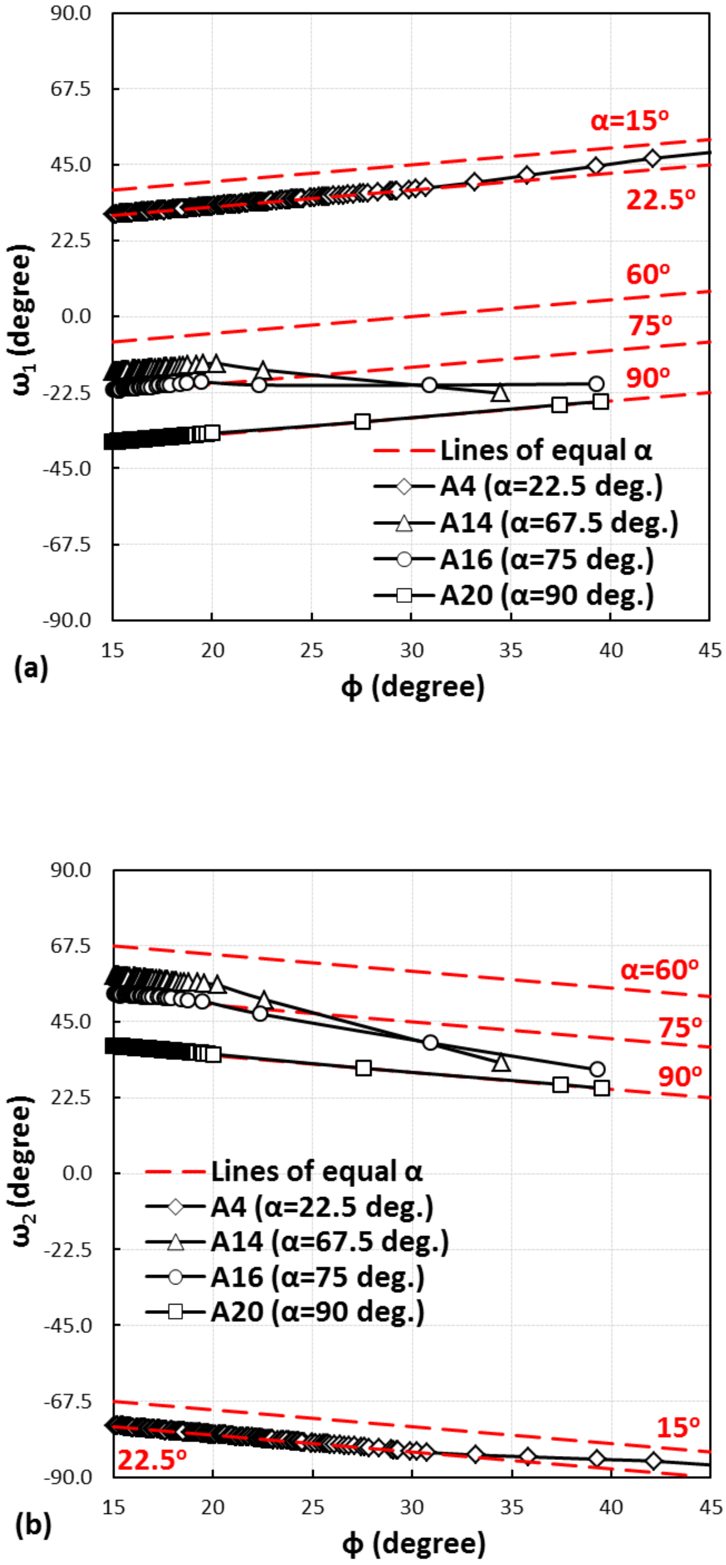

Fig. 7.15 Relationship between φ, ω and α for the plane of maximum stress obliquity **a** nearer to the bedding plane and **b** further to the bedding plane

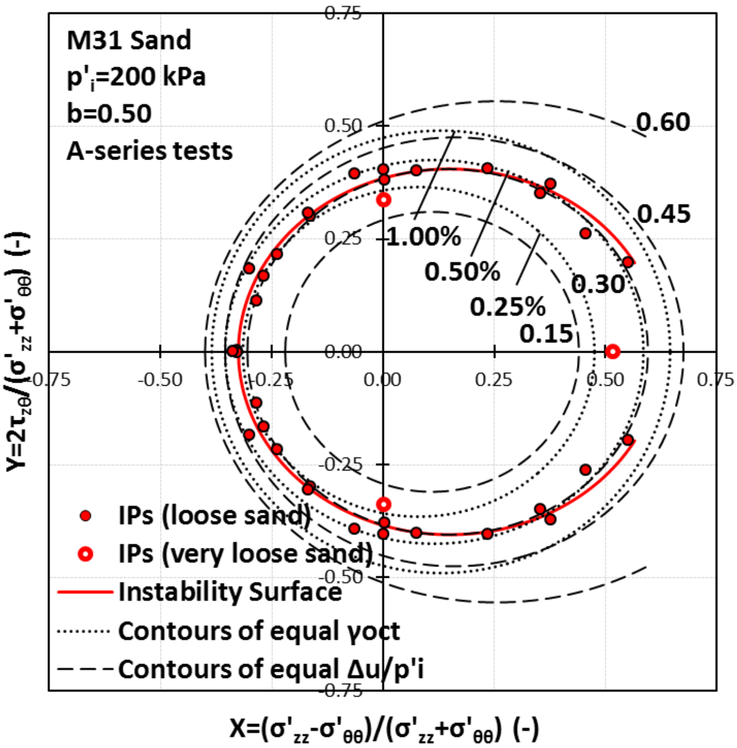

Fig. 7.16 Instability Surface of loose isotropically consolidated M31 Sand and contours of equal γ_{oct} and Δu / p'_i in the Y - X deviatoric plane

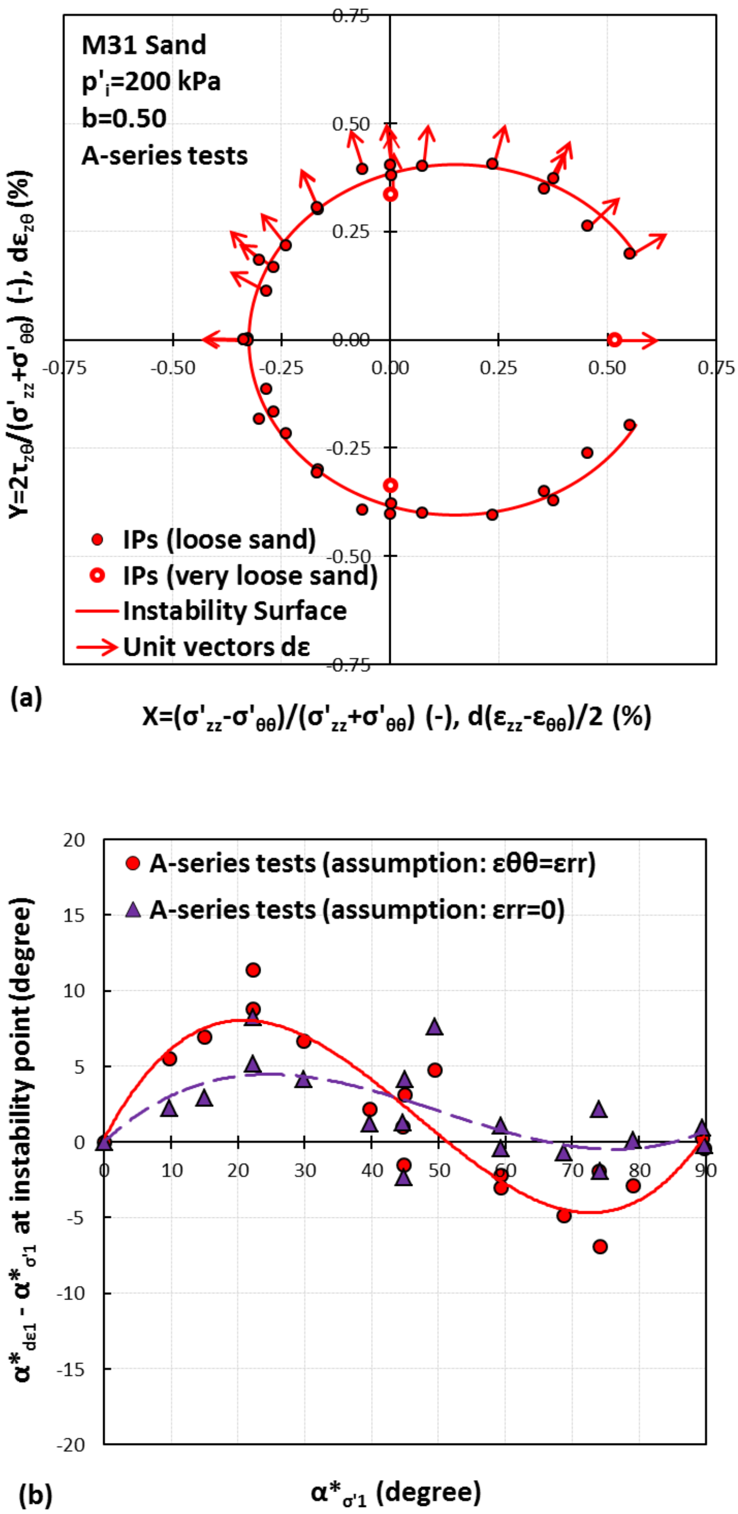

Fig. 7.17 Non-coaxial plastic deformation of loose M31 Sand at the onset of instability. **a** Direction of principal strain rate, $\alpha_{d\varepsilon 1}$, at the onset of instability indicated with the unit vectors, d**ε**, superimposed on the instability points in the *Y* - *X* deviatoric plane. **b** Non-coaxiality angle, $\alpha^*_{d\varepsilon 1}$ - $\alpha^*_{\sigma' 1}$, against the principal stress direction angle, $\alpha^*_{\sigma' 1}$, at the instability point

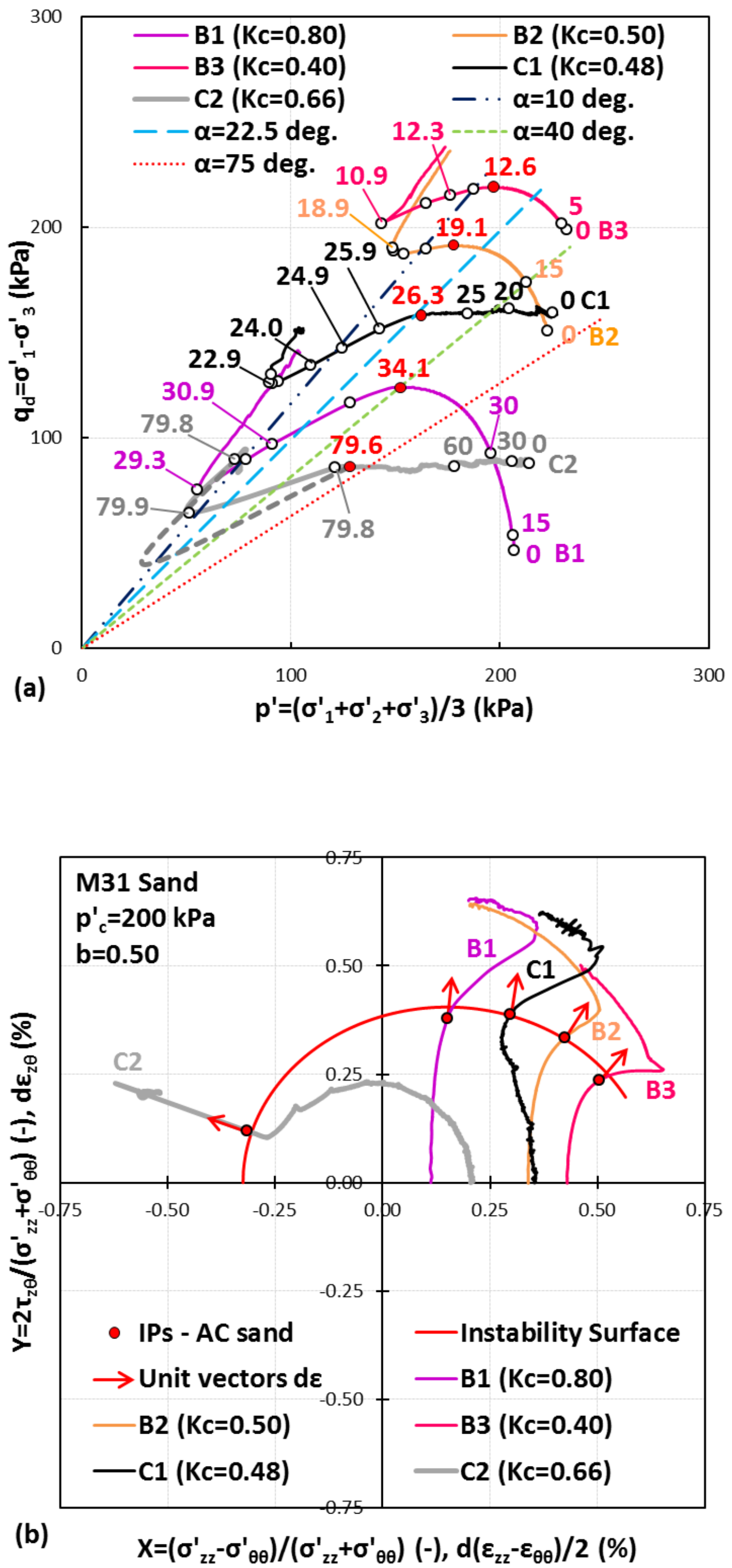

Fig. 7.18 Response of loose anisotropically consolidated M31 Sand to undrained loading with rotating stress principal axes. **a** Effective stress paths in the q_d - p' plane. **b** Stress paths in the Y - X deviatoric plane

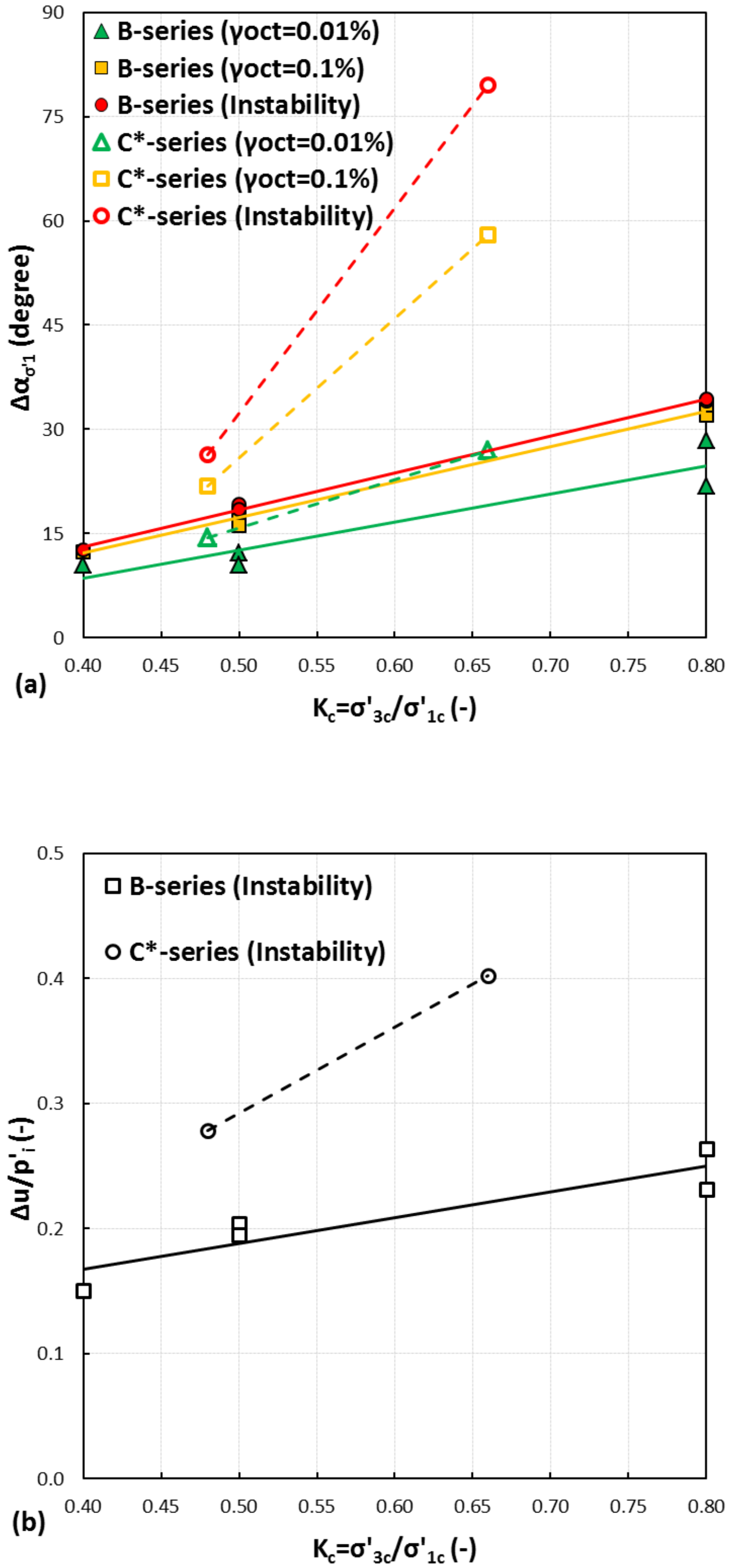

Fig. 7.19 Response of loose anisotropically consolidated M31 Sand to undrained loading with rotating stress principal axes. **a** Rotational capacity at two different shear strain levels and at the instability point. **b** Normalised excess pore-water pressure at the instability point

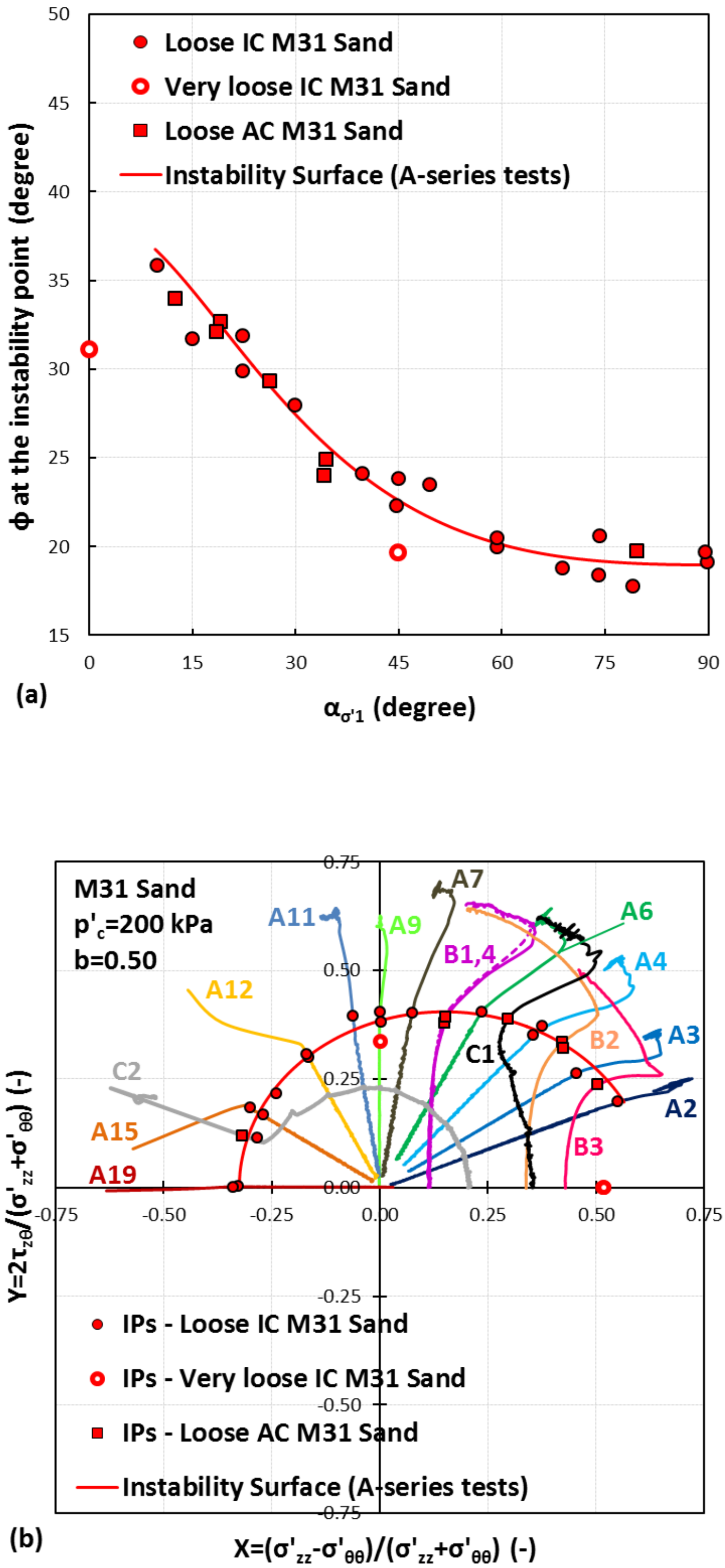

Fig. 7.20 Flow instability of loose M31 Sand under undrained loading with fixed or rotating stress principal axes. **a** Mobilised angle of shearing resistance, φ, against the principal stress direction angle, $\alpha_{\sigma'1}$, at the instability point. **b** Instability points and stress paths in the Y - X deviatoric plane

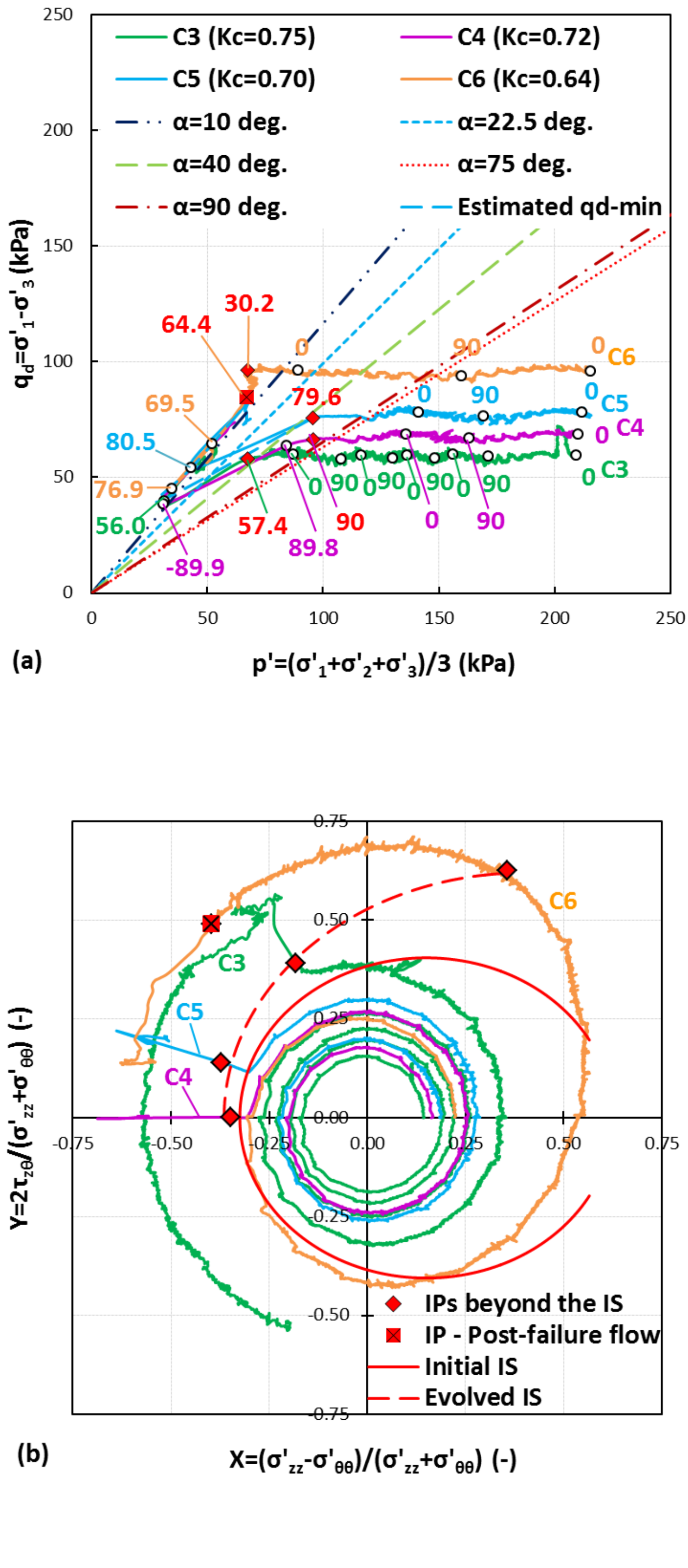

Fig. 7.21 Response of loose anisotropically consolidated M31 Sand to undrained loading with rotating stress principal axes. **a** Effective stress paths in the q_d - p' plane. **b** Stress paths in the Y - X deviatoric plane

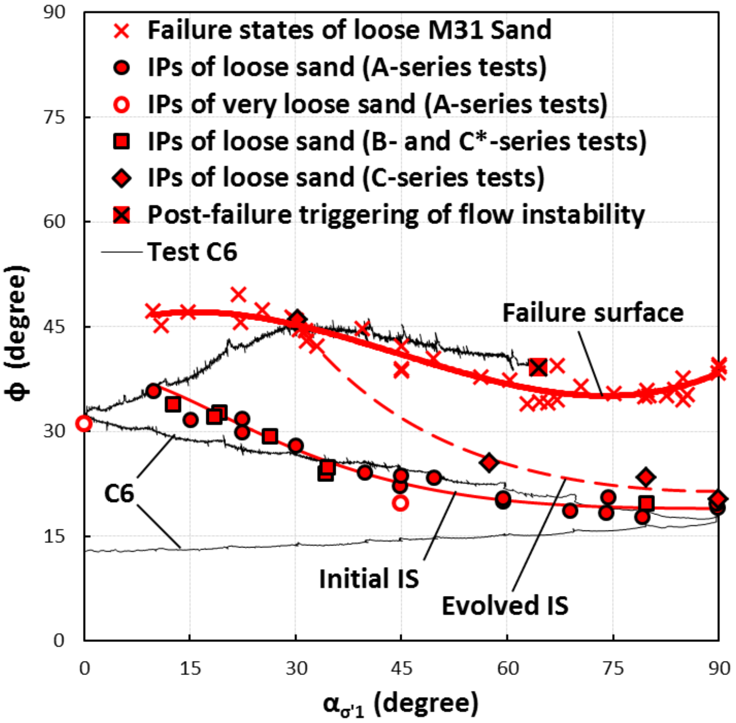

Fig. 7.22 Stress-history effects on the flow-instability condition of loose M31 Sand: Mobilised angle of shearing resistance, φ, against the principal stress direction angle, $\alpha_{\sigma'1}$, at characteristic stress states

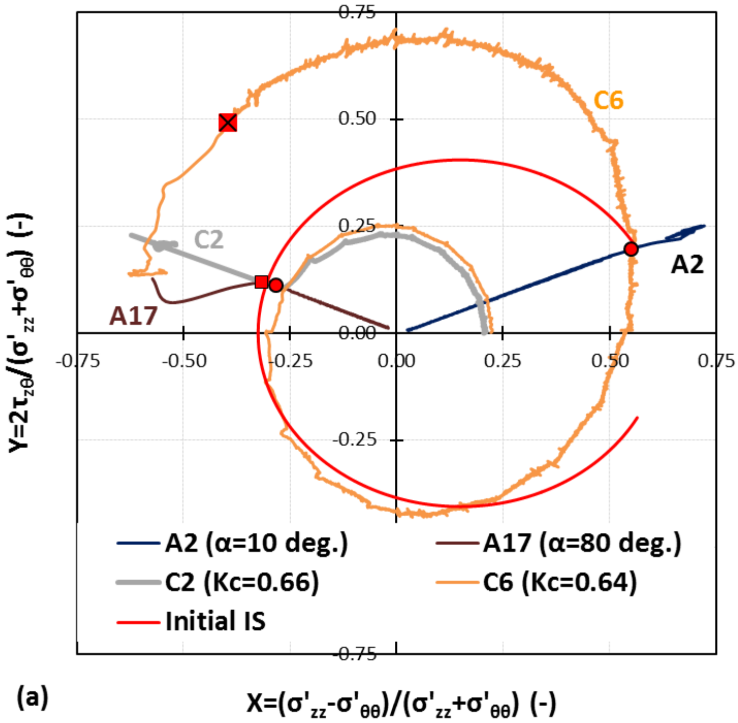

(a)

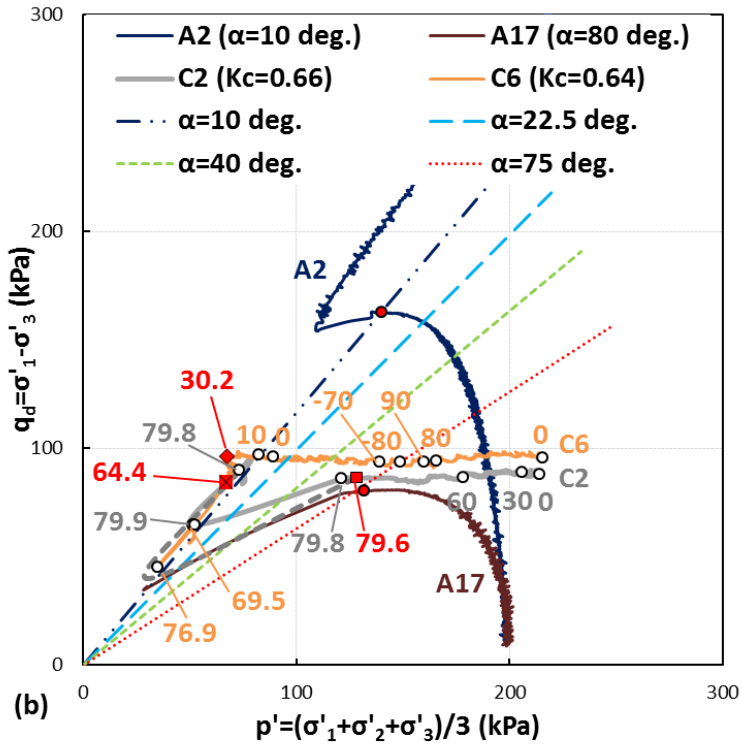

(b)

Fig. 7.23 Influence of the incremental stress direction on the flow-instability condition of loose M31 Sand. **a** Effective stress paths in the q_d - p' plane. **b** Stress paths in the Y - X deviatoric plane

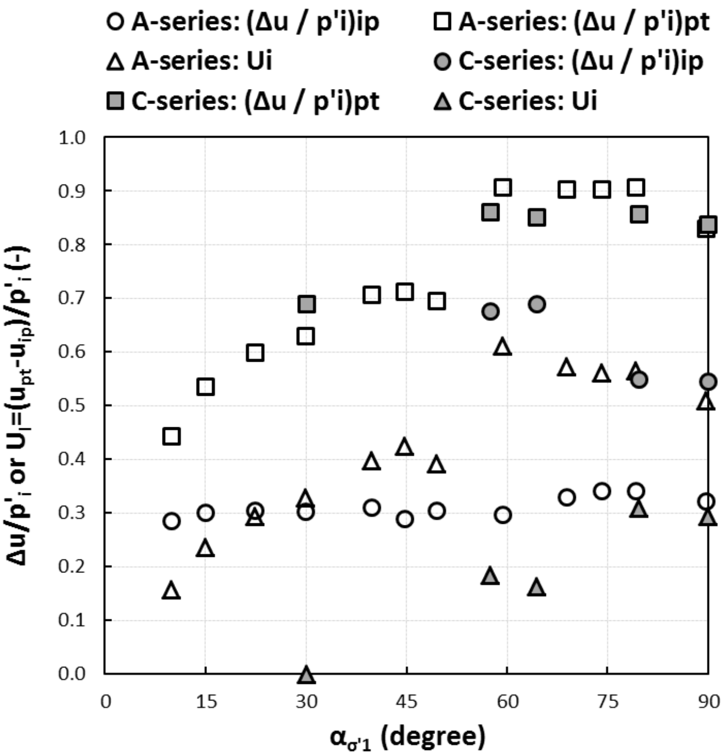

Fig. 7.24 Strain-history effects on the triggering condition and deformation pattern of flow of loose M31 Sand: Normalised excess pore-water pressure, Δu / p'_i, against the principal stress direction angle, $\alpha_{\sigma'1}$, at characteristic stress states, and the flow parameter, U_I, against the principal stress direction angle, $\alpha_{\sigma'1}$

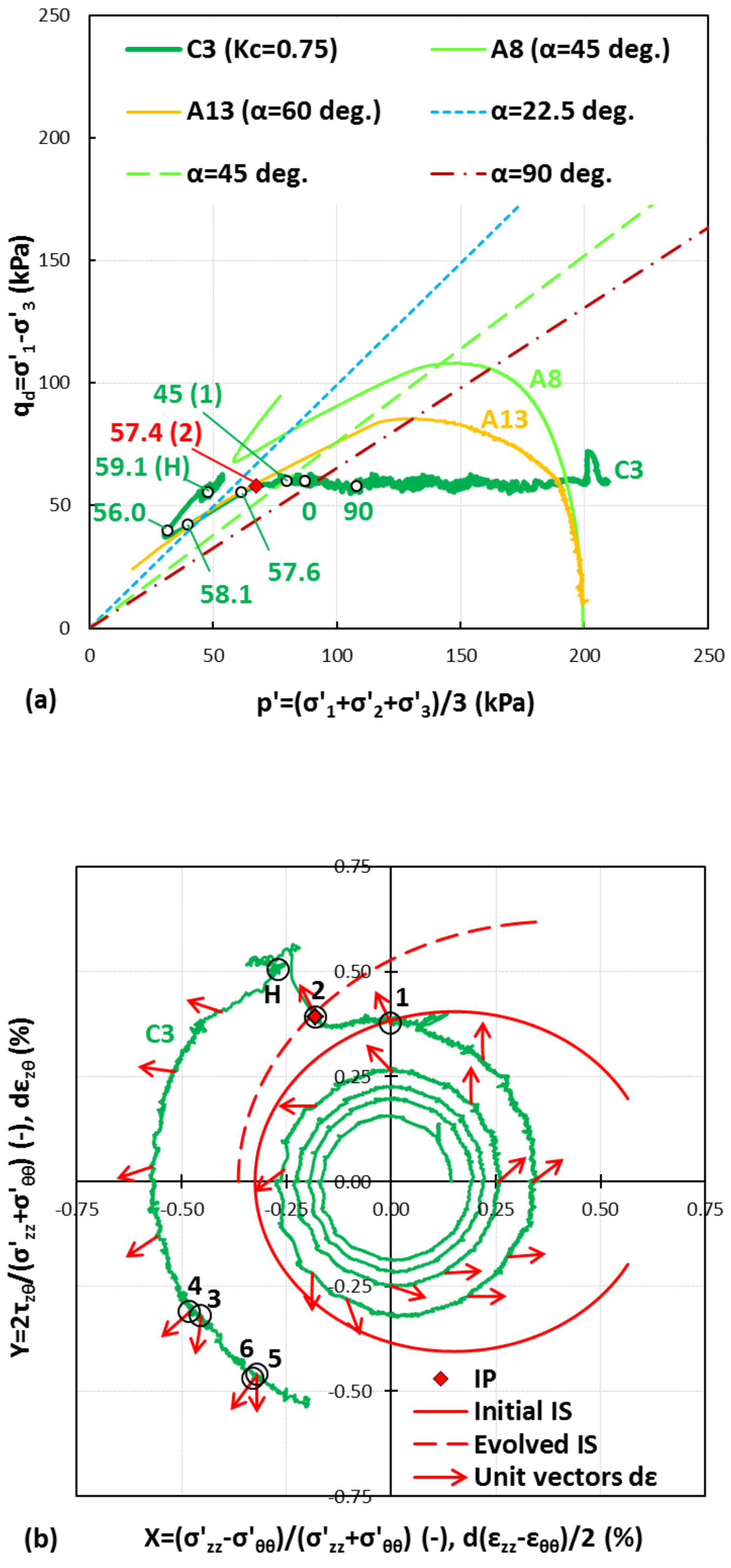

Fig. 7.25 Response of loose anisotropically consolidated M31 Sand to undrained loading with rotating stress principal axes. **a** Effective stress path of test C3 in the q_d - p' plane. **b** Stress path of test C3 in the Y - X deviatoric plane (**c** on next page)

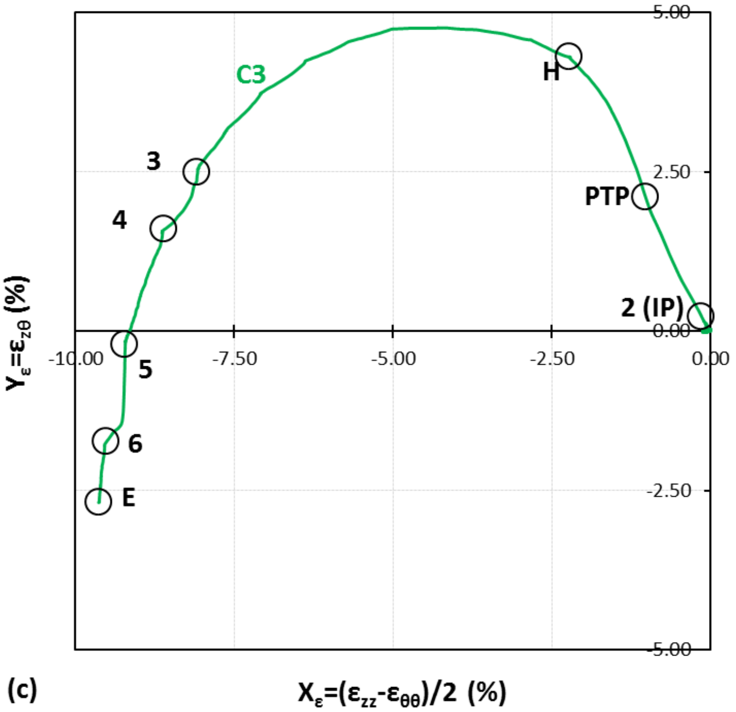

Fig. 7.25 Response of loose anisotropically consolidated M31 Sand to undrained loading with rotating stress principal axes. **c** Strain path of test C3 in the Y_ε - X_ε deviatoric plane

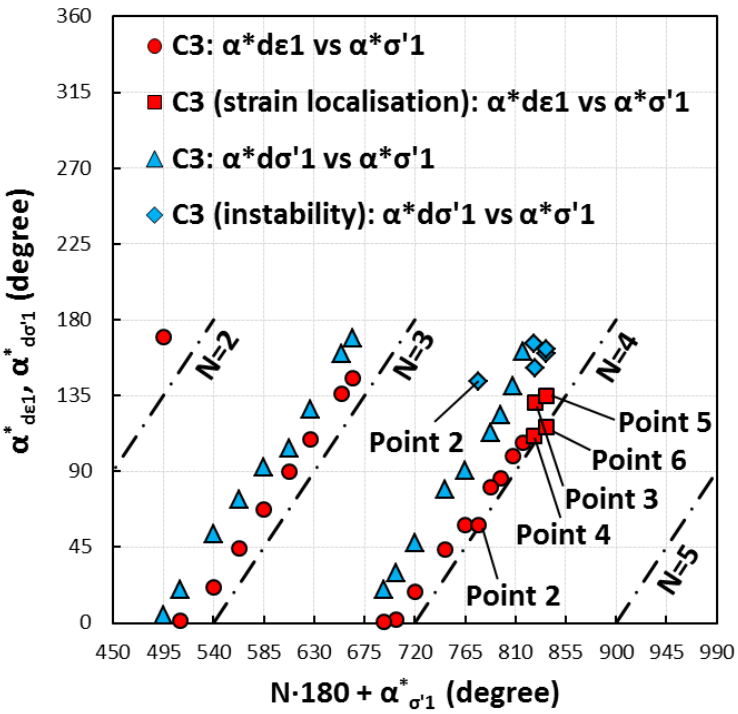

Fig. 7.26 Relationship between the direction angles of principal stress, rate of principal stress and rate of principal strain during the third, fourth and fifth cycle of rotation of the stress principal axes in test C3 (N = 2, 3 and 4)

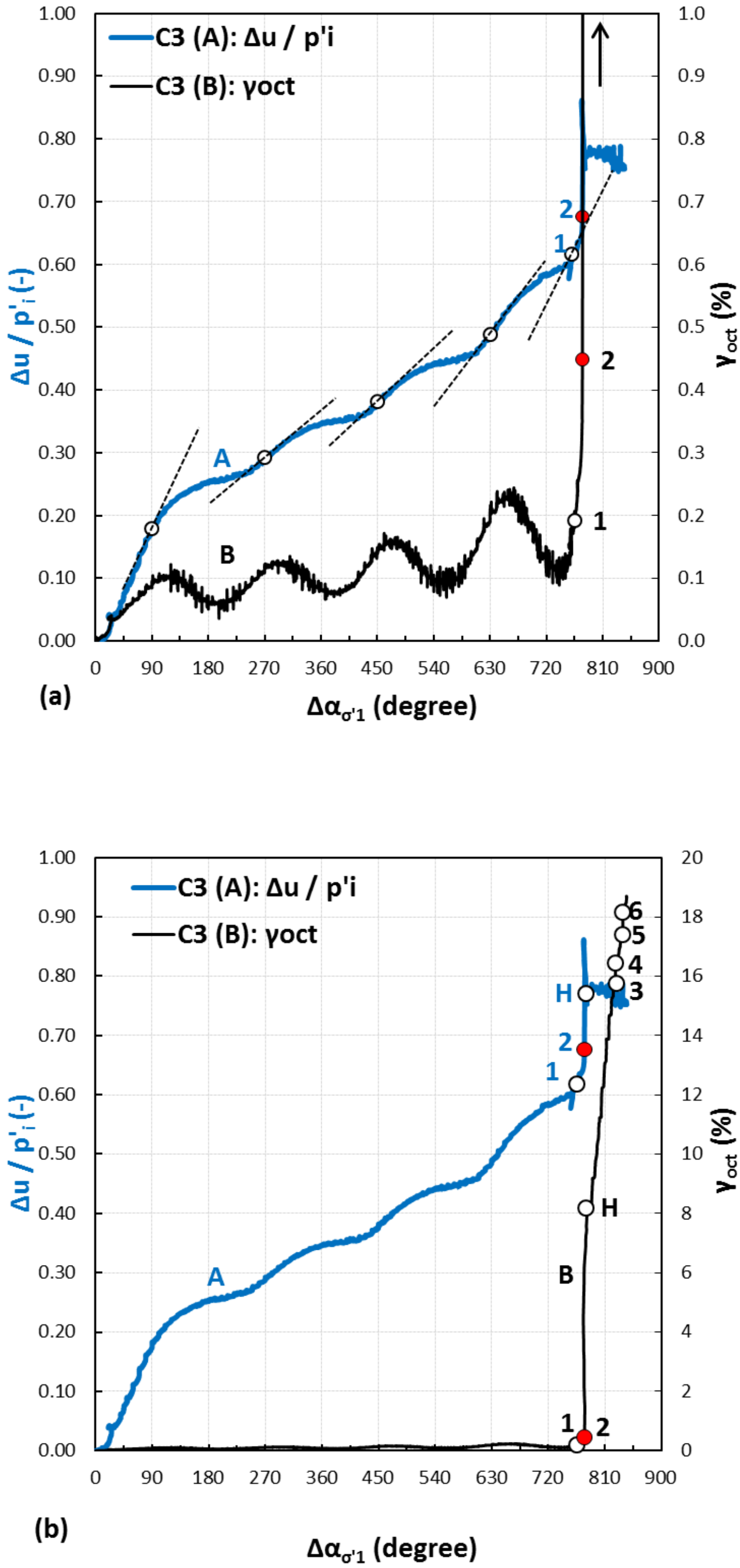

Fig. 7.27 Normalised excess pore-water pressure and octahedral shear strain against the monotonic rotation angle in test C3 (the curve showing the evolution of the shear strain γ_{oct} is zoomed in **a**)

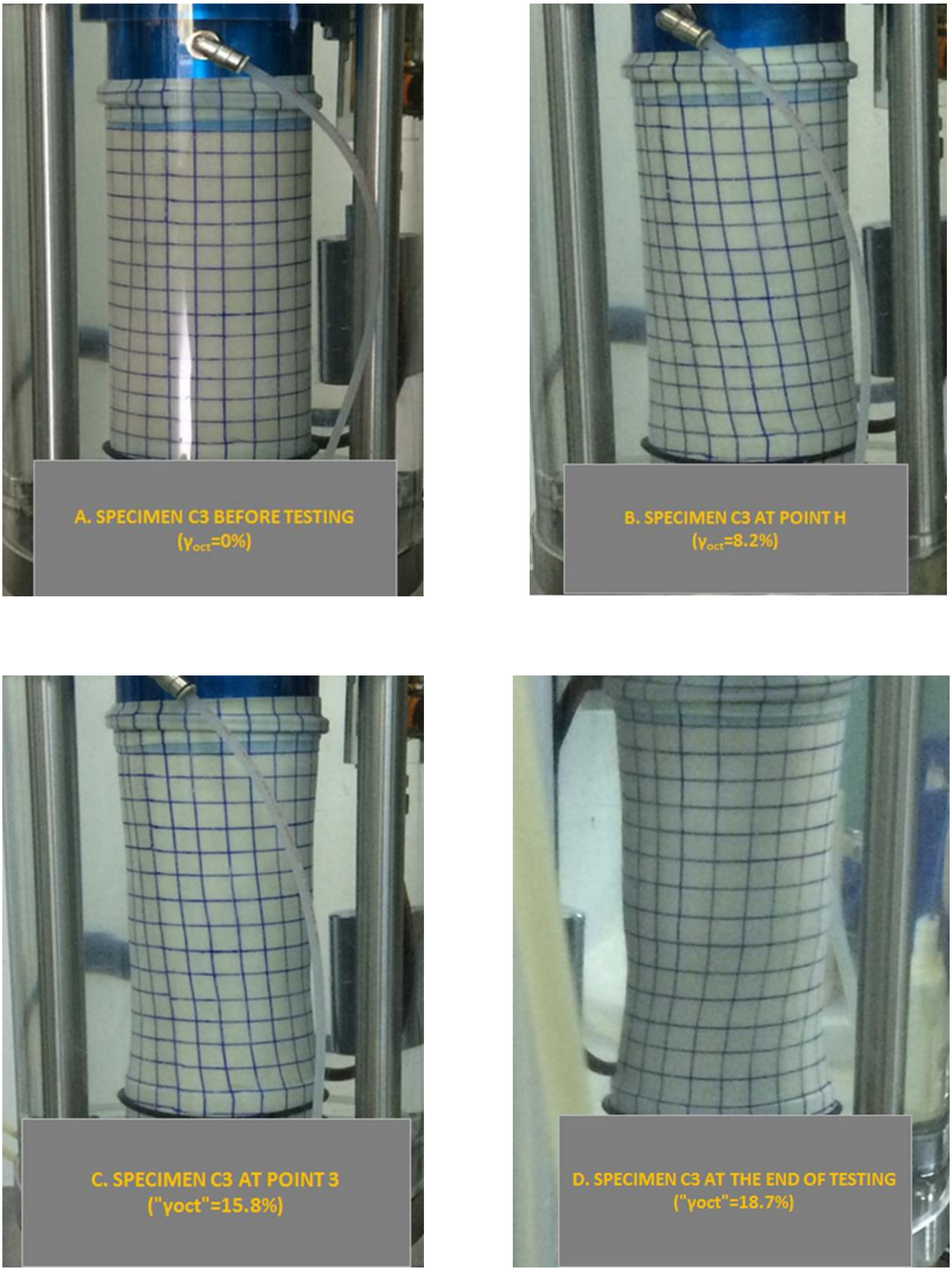

Fig. 7.28 Photos of the specimen in test C3 at different levels of shear strain. **a** Specimen before testing. **b** Specimen at point H. **c** Specimen at point 3. **d.** Specimen at the end of testing. The photos were taken under the refraction induced by the crossing of light through the water-perspex-air interfaces

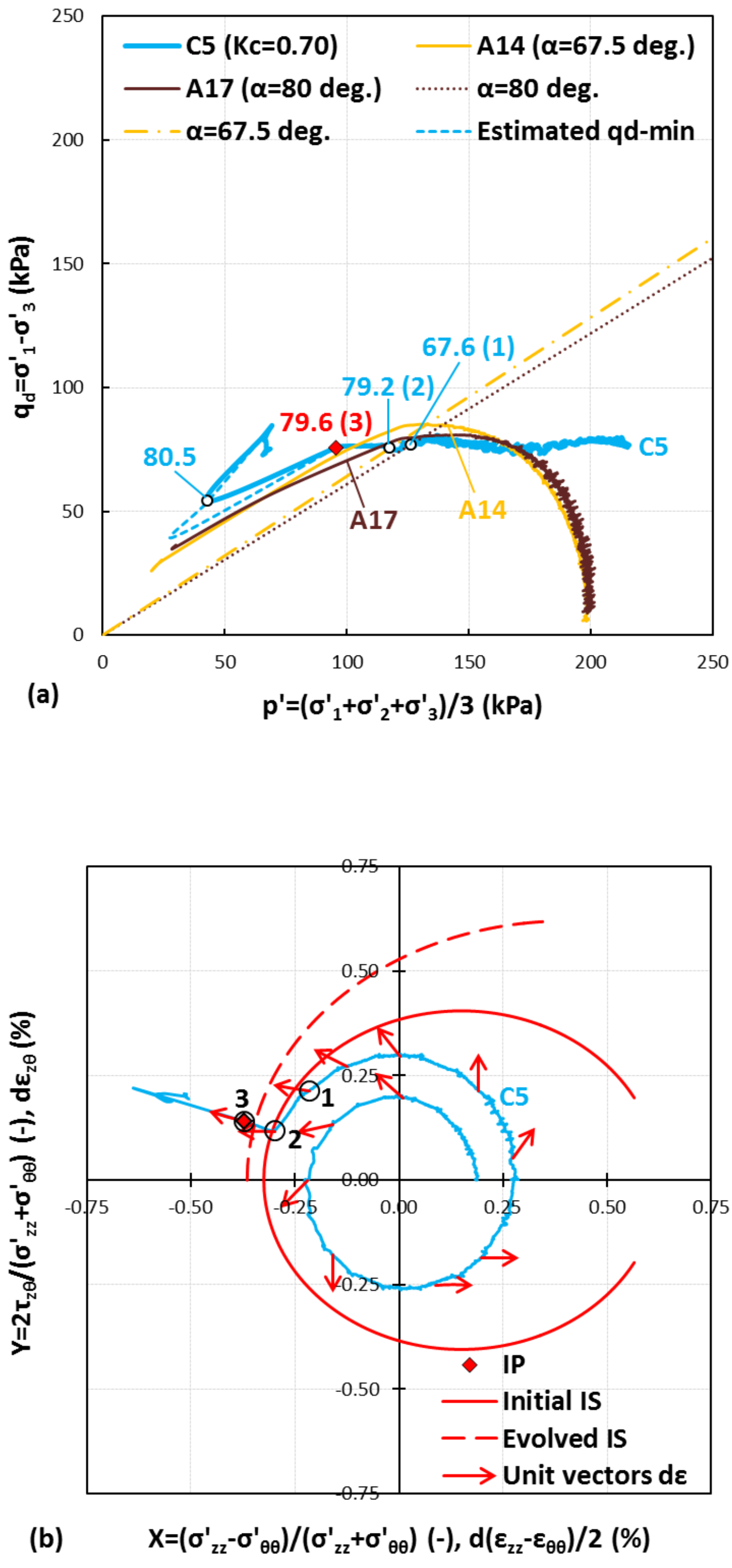

Fig. 7.29 Response of loose anisotropically consolidated M31 Sand to undrained loading with rotating stress principal axes. **a** Effective stress path of test C5 in the q_d - p' plane. **b** Stress path of test C5 in the *Y* - *X* deviatoric plane

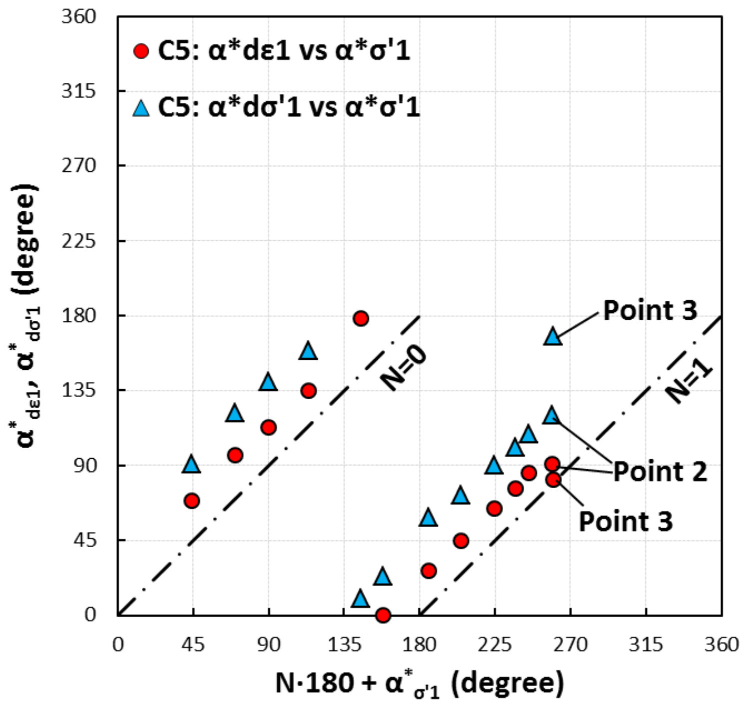

Fig. 7.30 Relationship between the direction angles of principal stress, rate of principal stress and rate of principal strain during the first and second cycle of rotation of the stress principal axes in test C5 (N = 0 and 1)

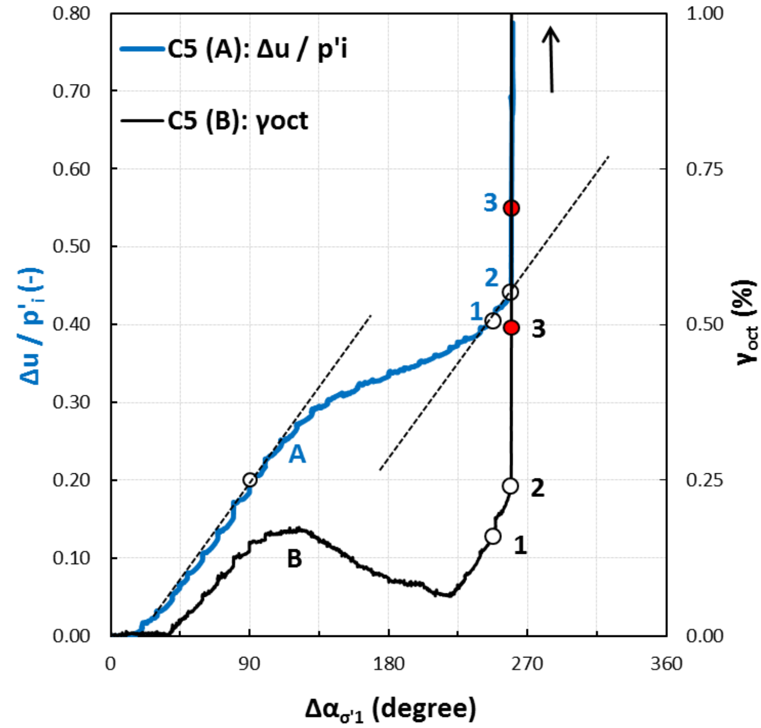

Fig. 7.31 Normalised excess pore-water pressure and octahedral shear strain against the monotonic rotation angle in test C5

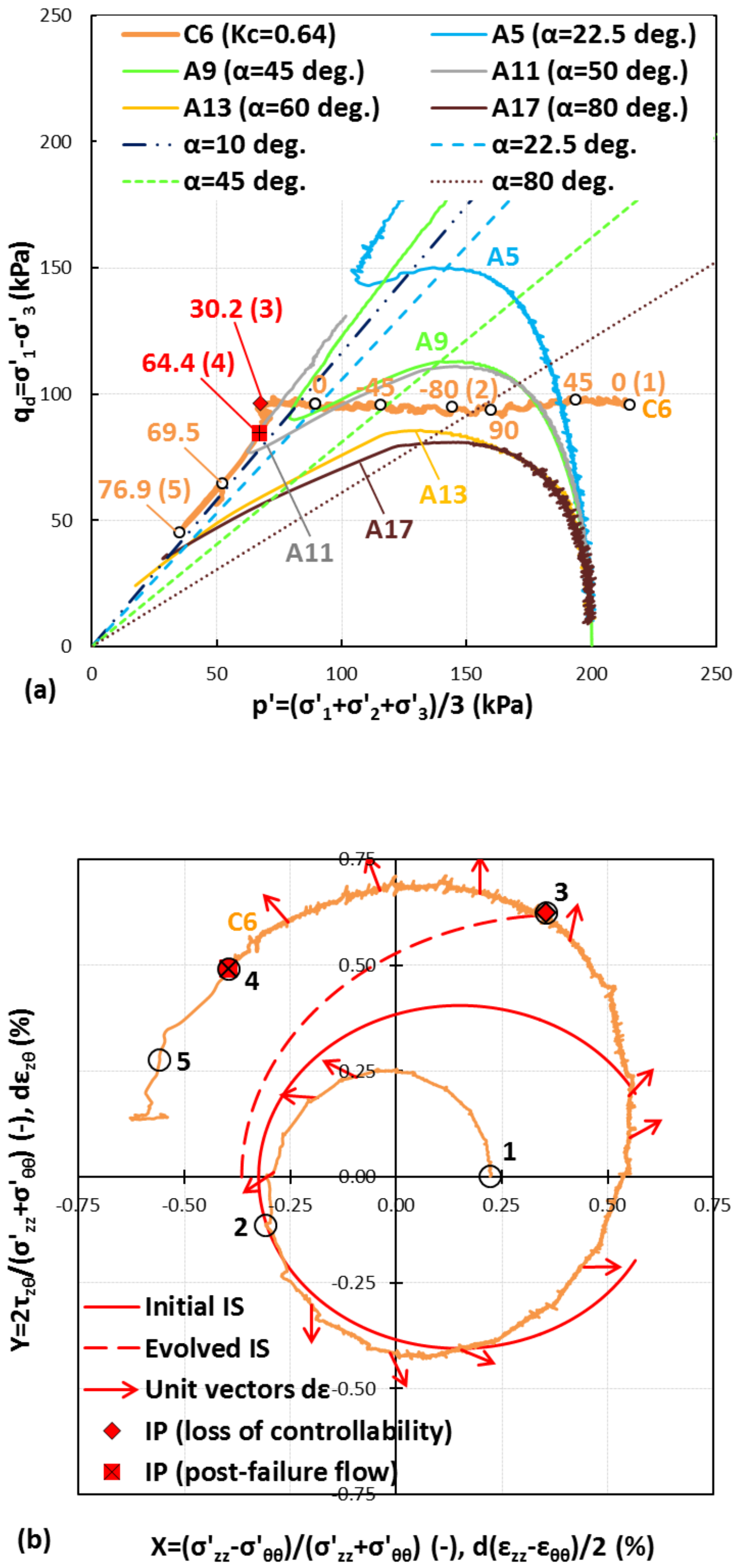

Fig. 7.32 Response of loose anisotropically consolidated M31 Sand to undrained loading with rotating stress principal axes. **a** Effective stress path of test C6 in the q_d - p' plane. **b** Stress path of test C6 in the Y - X deviatoric plane

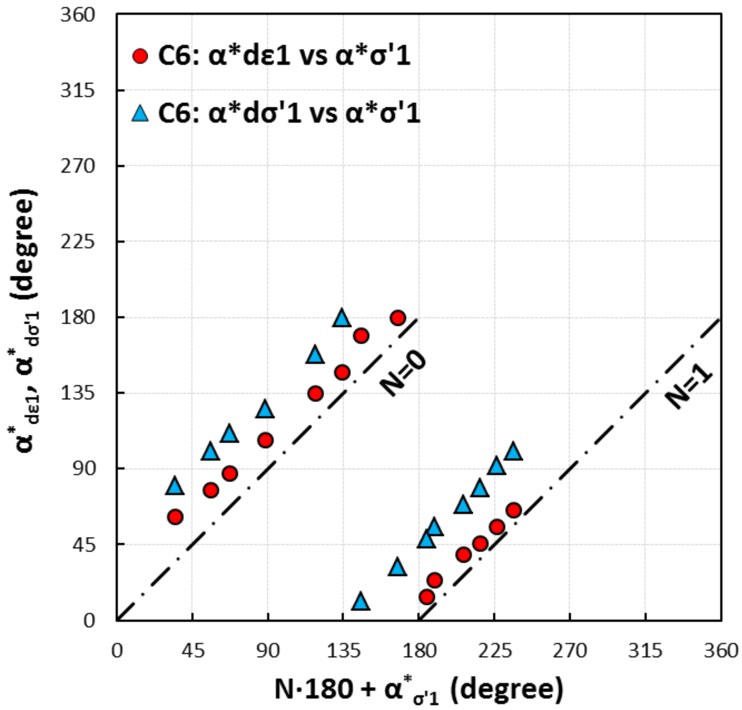

Fig. 7.33 Relationship between the direction angles of principal stress, rate of principal stress and rate of principal strain during the first and second cycle of rotation of the stress principal axes in test C6 (N=0 and 1)

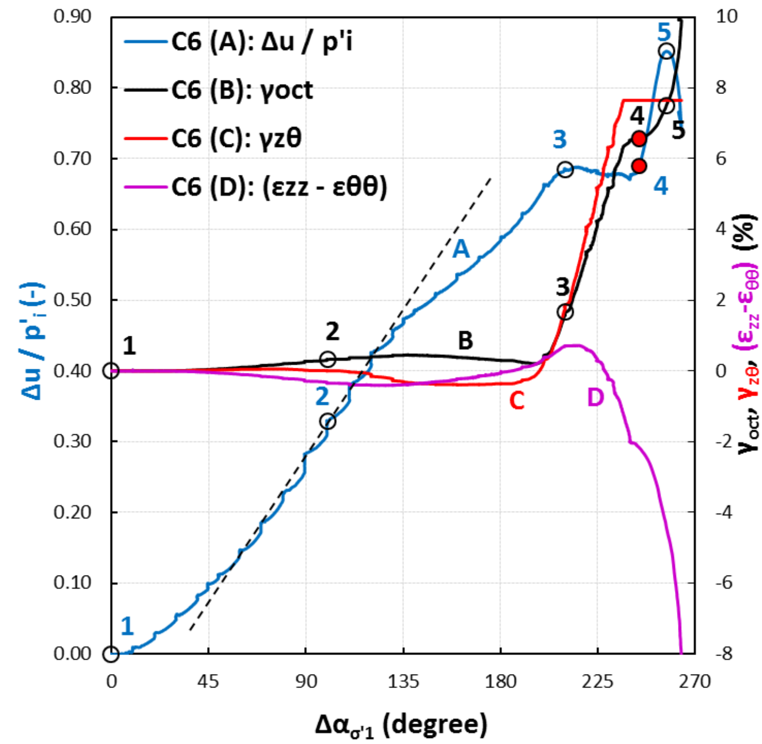

Fig. 7.34 Normalised excess pore-water pressure, octahedral shear strain, torsional shear strain and triaxial shear strain against the monotonic rotation angle in test C6

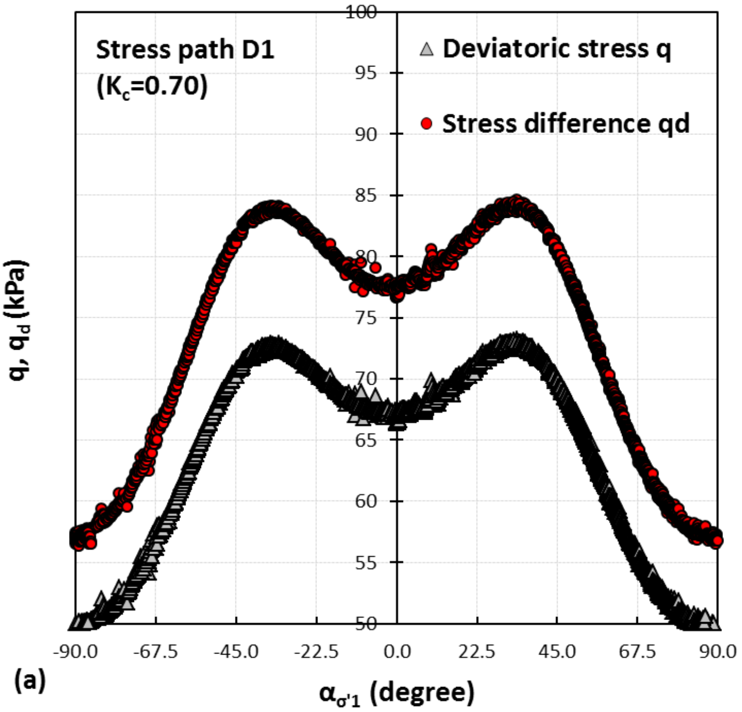

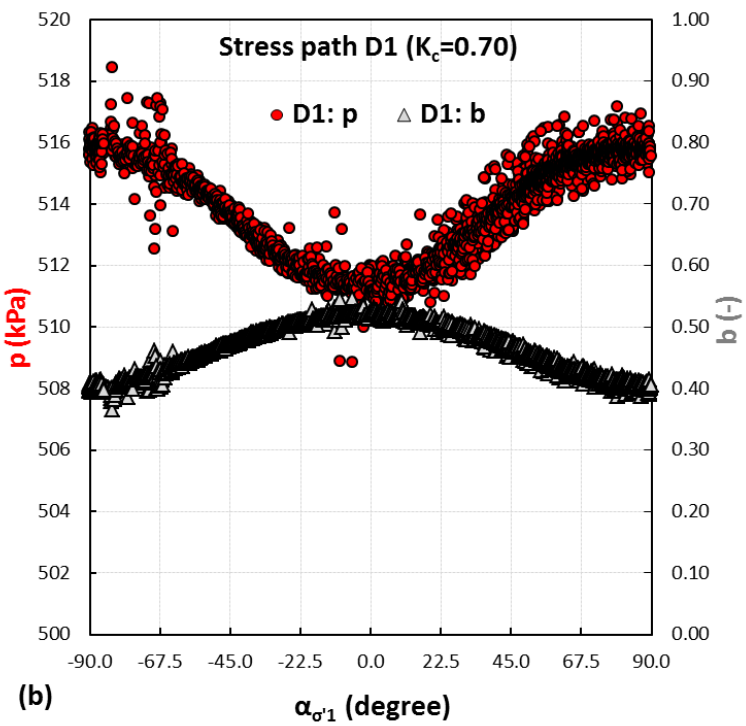

Fig. 7.35 Loading characteristics of test D1. **a** Deviatoric stress and stress difference against the principal stress direction angle. **b** Mean total stress and intermediate principal stress parameter against the principal stress direction angle

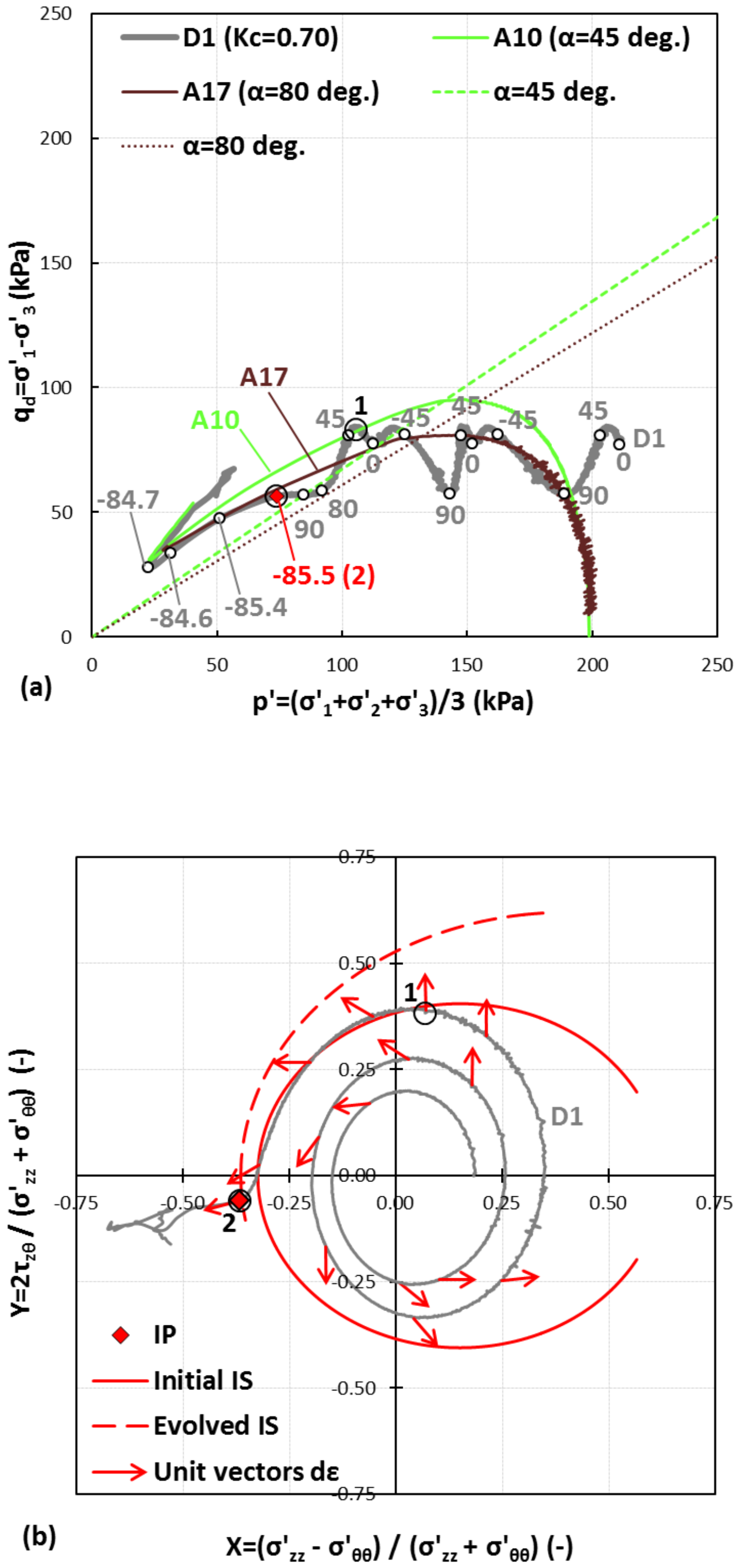

Fig. 7.36 Response of loose anisotropically consolidated M31 Sand to undrained loading with rotating stress principal axes and periodically changing deviatoric stress. **a** Effective stress path of test D1 in the q_d - p' plane. **b** Stress path of test D1 in the Y - X deviatoric plane

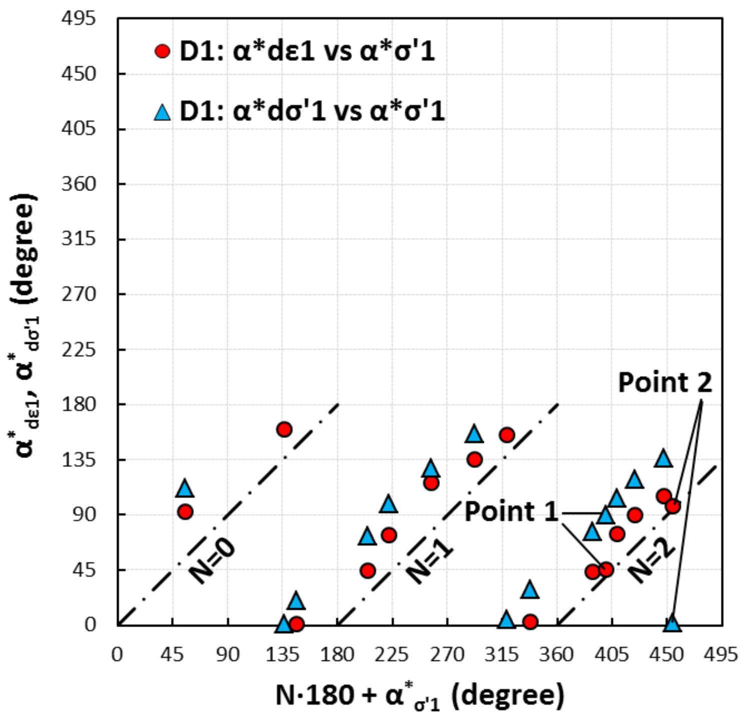

Fig. 7.37 Relationship between the direction angles of principal stress, rate of principal stress and rate of principal strain during the first, second and third cycle of rotation of the stress principal axes in test D1 (N = 0, 1 and 2)

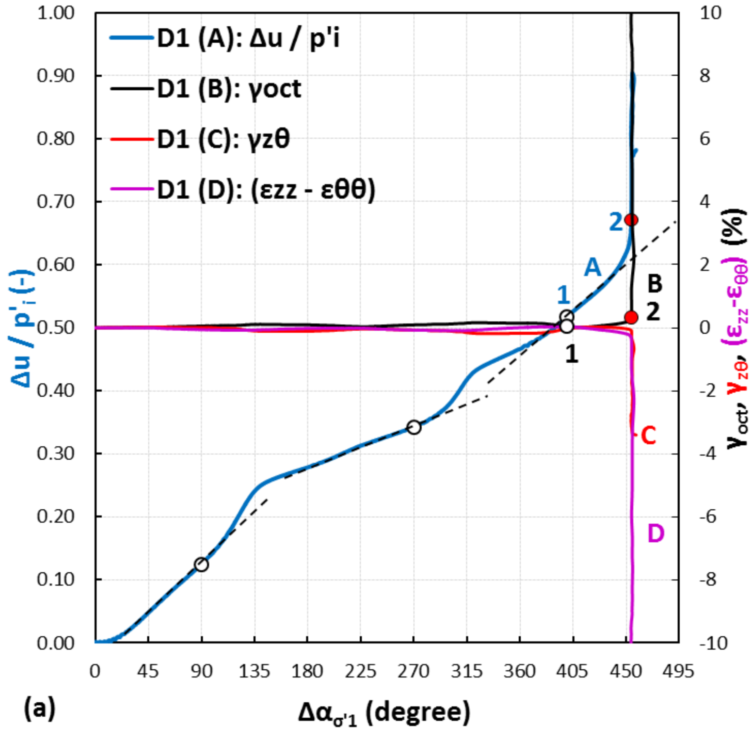

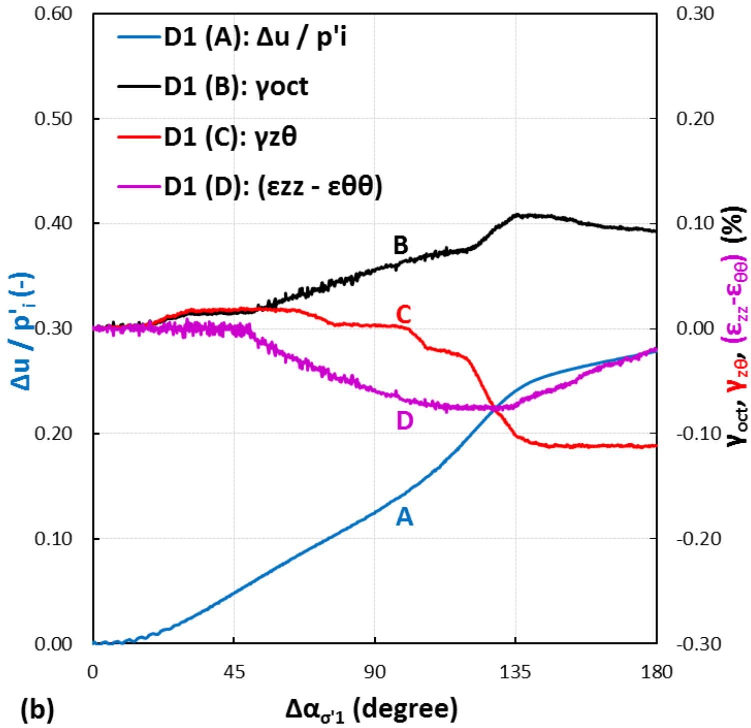

Fig. 7.38 Normalised excess pore-water pressure, octahedral shear strain, torsional shear strain and triaxial shear strain against the monotonic rotation angle in test D1. **a** Complete principal stress rotation history. **b** First cycle of rotation of the stress principal axes (**c** and **d** on next page)

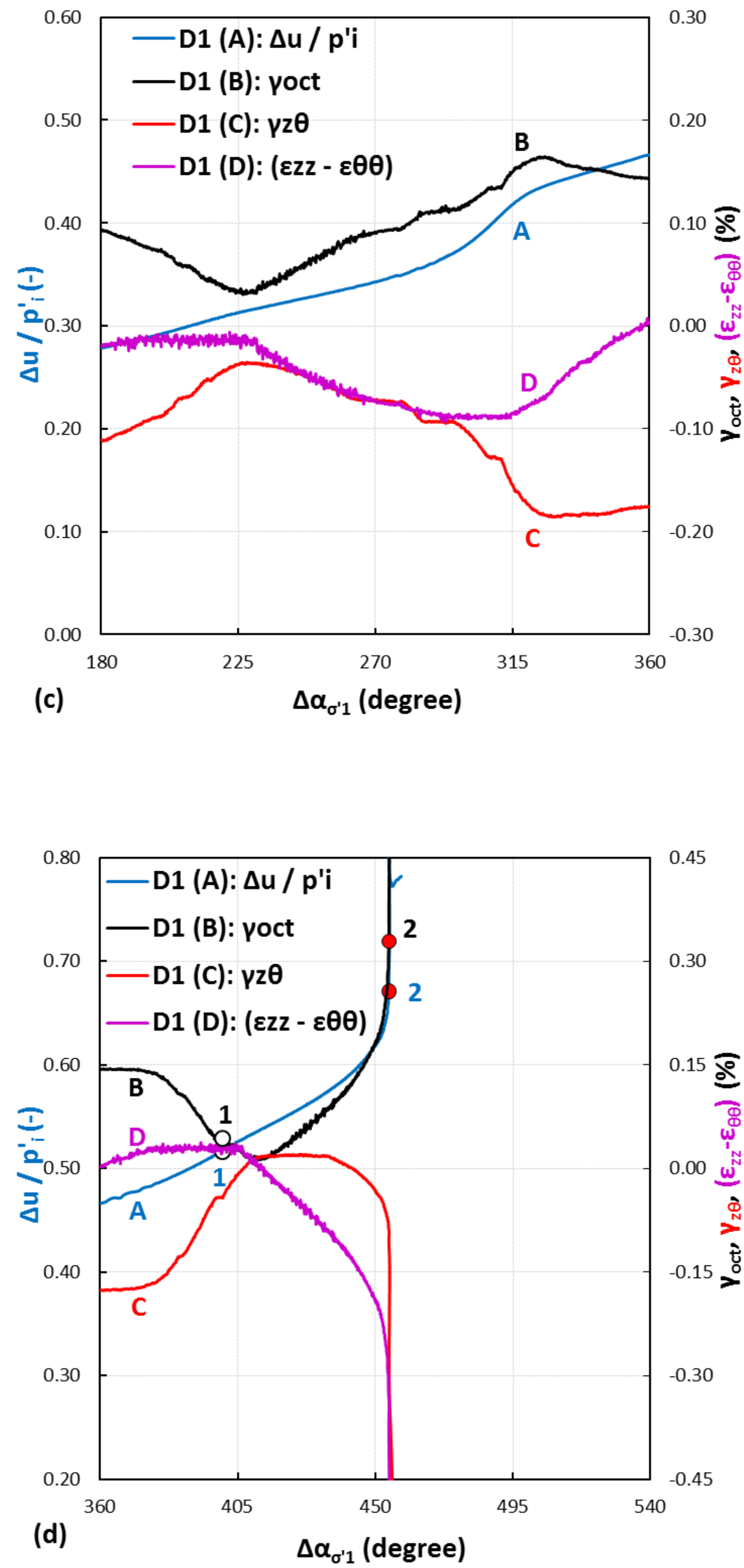

Fig. 7.38 Normalised excess pore-water pressure, octahedral shear strain, torsional shear strain and triaxial shear strain against the monotonic rotation angle in test D1. **c** Second cycle of rotation of the stress principal axes. **d** Third cycle of rotation of the stress principal axes

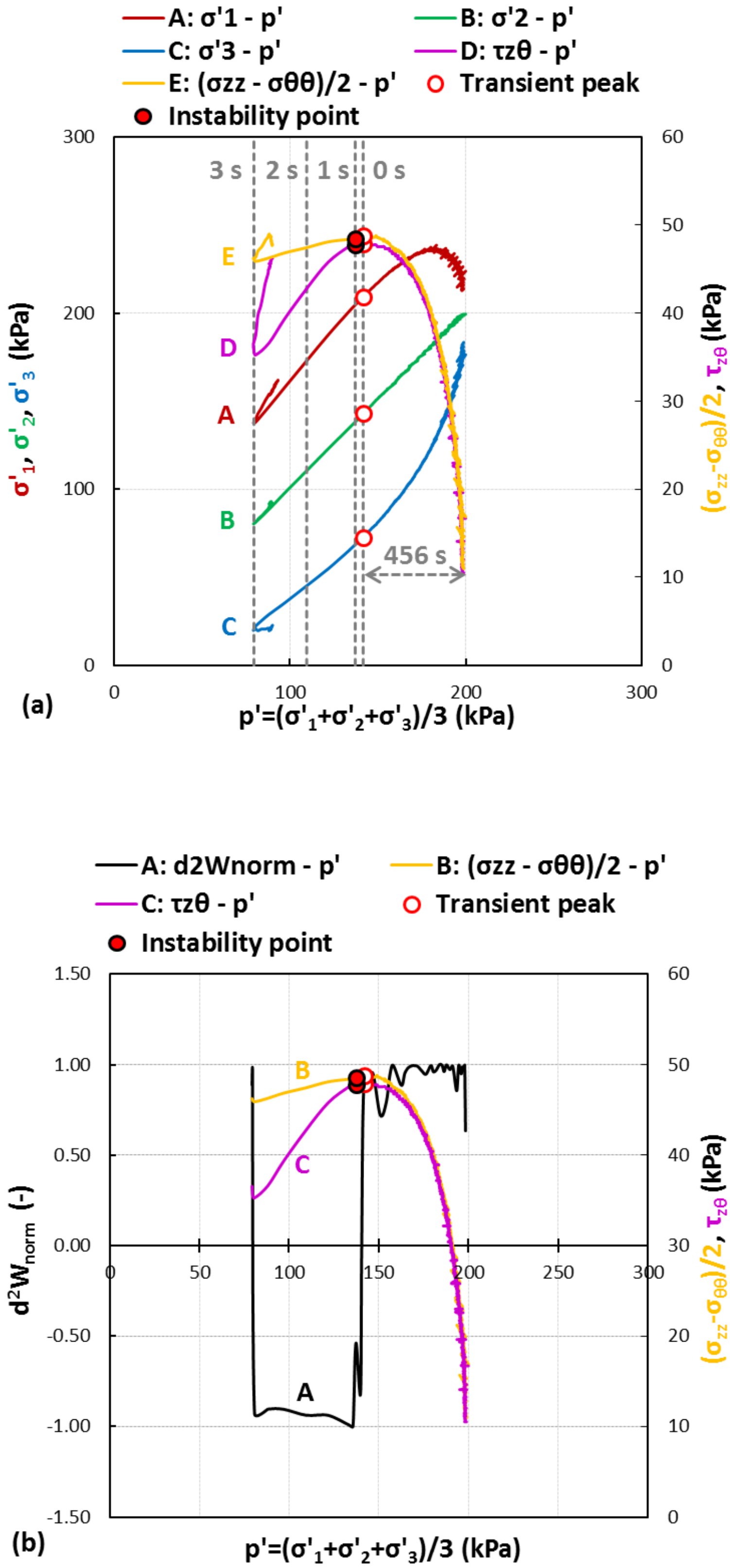

Fig. 7.39 Instability and bifurcation of the behaviour of the specimen - apparatus system in test A4. **a** Evolution of the effective principal stresses and shear stresses with mean effective stress. **b** Evolution of the normalised second-order work and shear stresses with mean effective stress

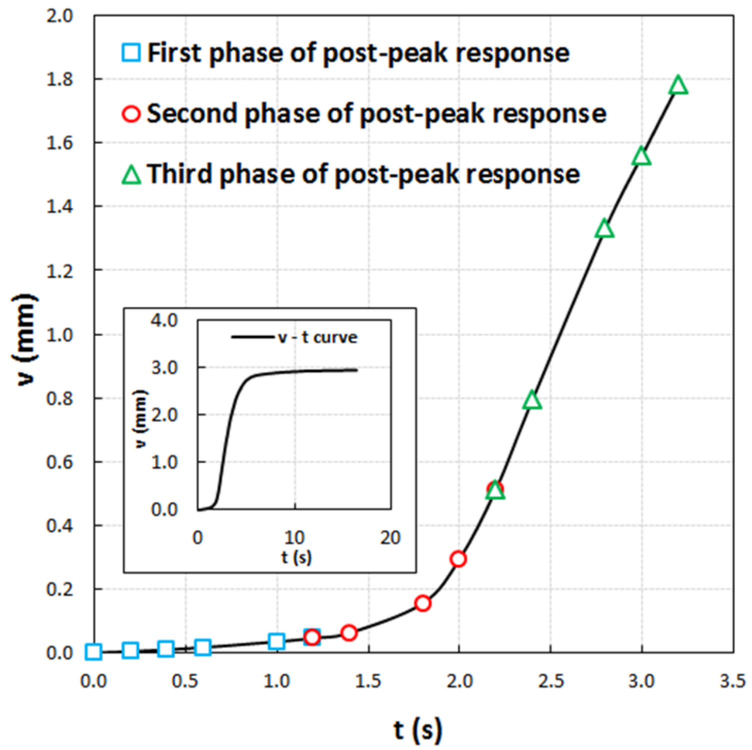

Fig. 7.40 Vertical displacement of the loading ram against time past the transient-peak state in test A4

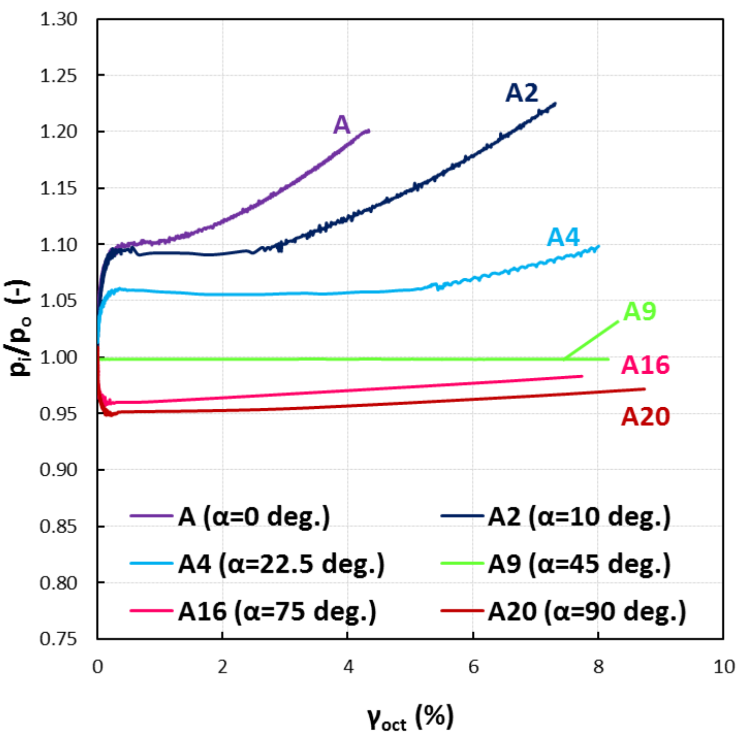

Fig. 7.41 Evolution of the pressure ratio with octahedral shear strain in test A4 and other A-series tests

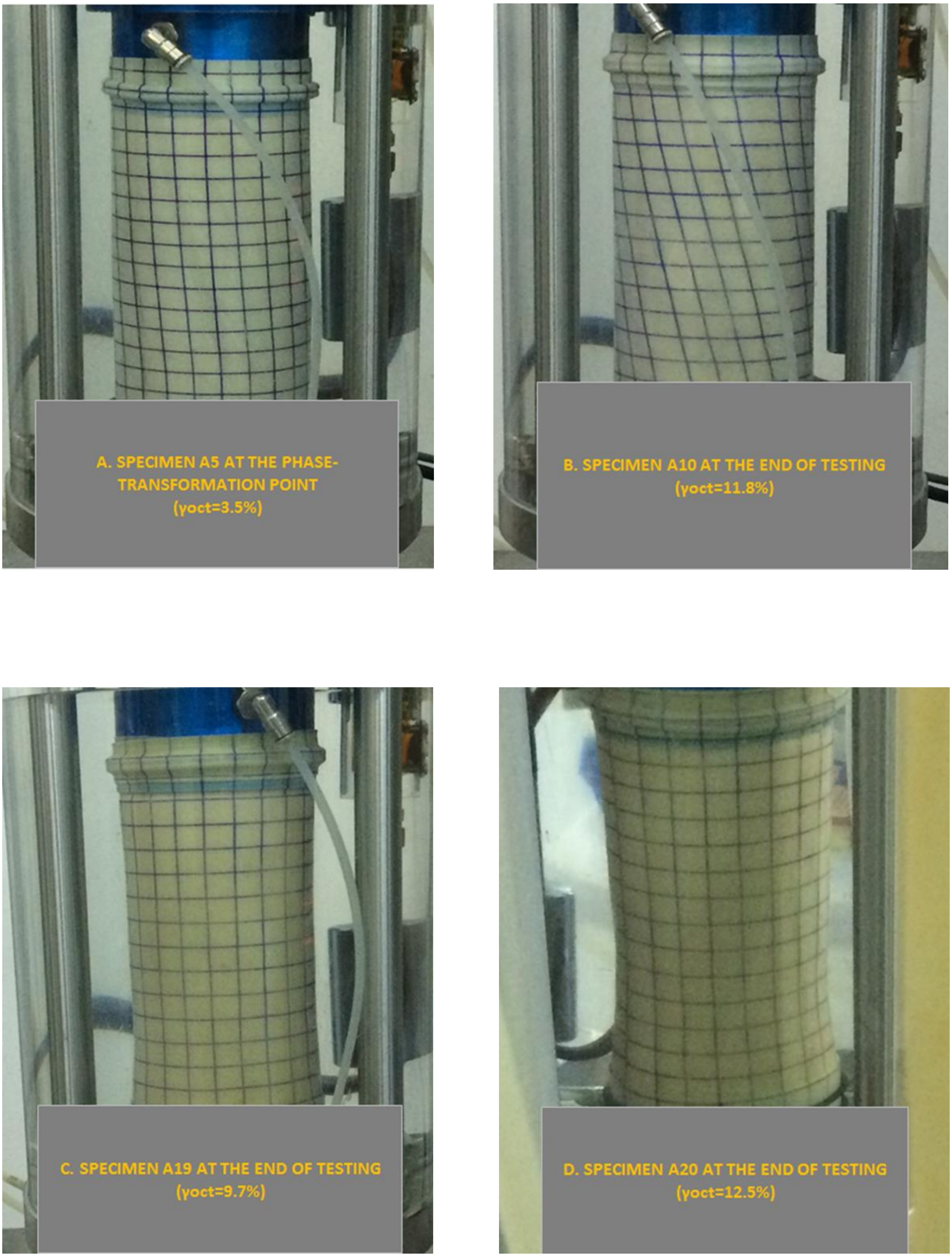

Fig. 7.42 Deformation of the specimens at the phase-transformation point or at the end of testing in the A-series tests. **a** Specimen in test A5 ($\alpha_{\sigma'1}$ = 22.5°, b = 0.5) at γ_{oct} = 3.5%. **b** Specimen in test A10 ($\alpha_{\sigma'1}$ = 45°, b = 0.5) at γ_{oct} = 11.8%. **c** Specimen in test A19 ($\alpha_{\sigma'1}$ = 90°, b = 0.5) at γ_{oct} = 9.7%. **d** Specimen in test A20 ($\alpha_{\sigma'1}$ = 90°, b = 0.5) at γ_{oct} = 12.5%. The photos were taken under the refraction induced by the crossing of light through the water-perspex-air interfaces

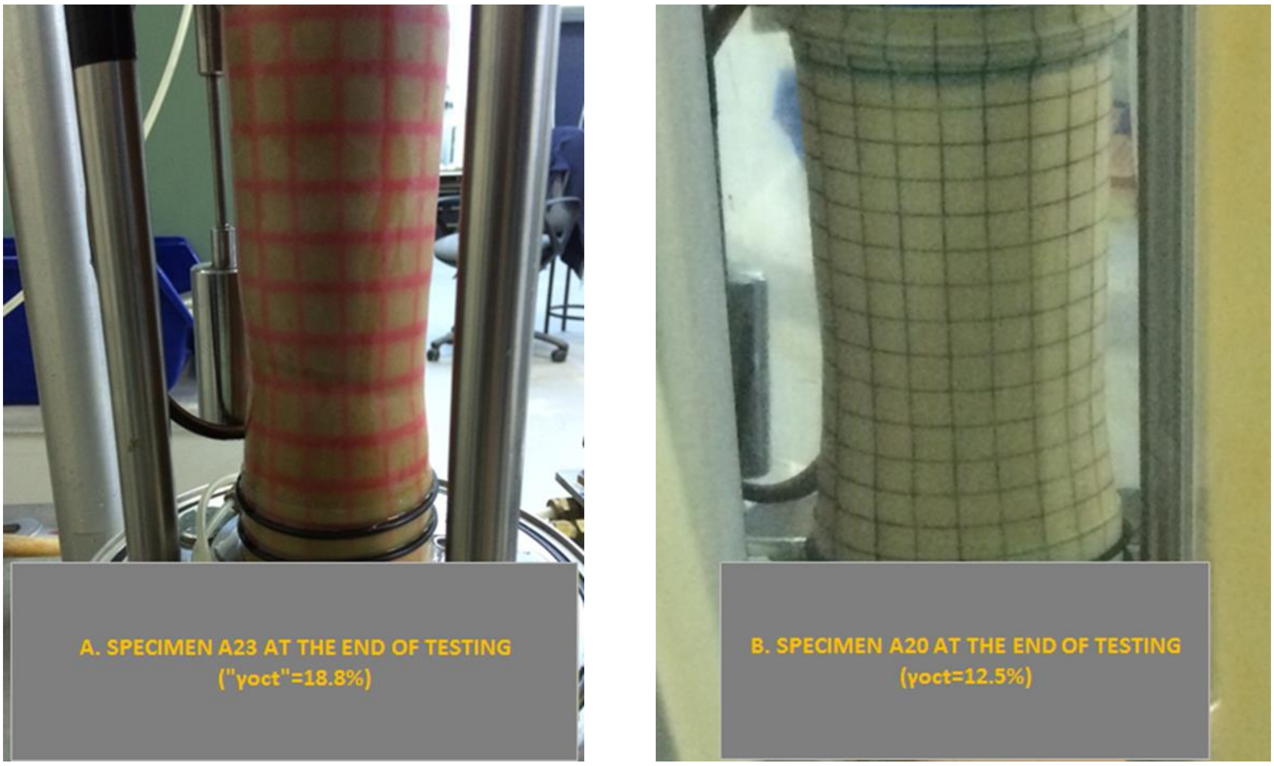

Fig. 7.43 Deformation of the specimens at the end of testing in the A-series tests. **a** Specimen in test A23 ($\alpha_{\sigma'1}$ = 90°, b = 1.0) at "γ_{oct}" = 18.8%. **b** Specimen in test A20 ($\alpha_{\sigma'1}$ = 90°, b = 0.5) at γ_{oct} = 12.5%. The right photo was taken under the refraction induced by the crossing of light through the water-perspex-air interfaces

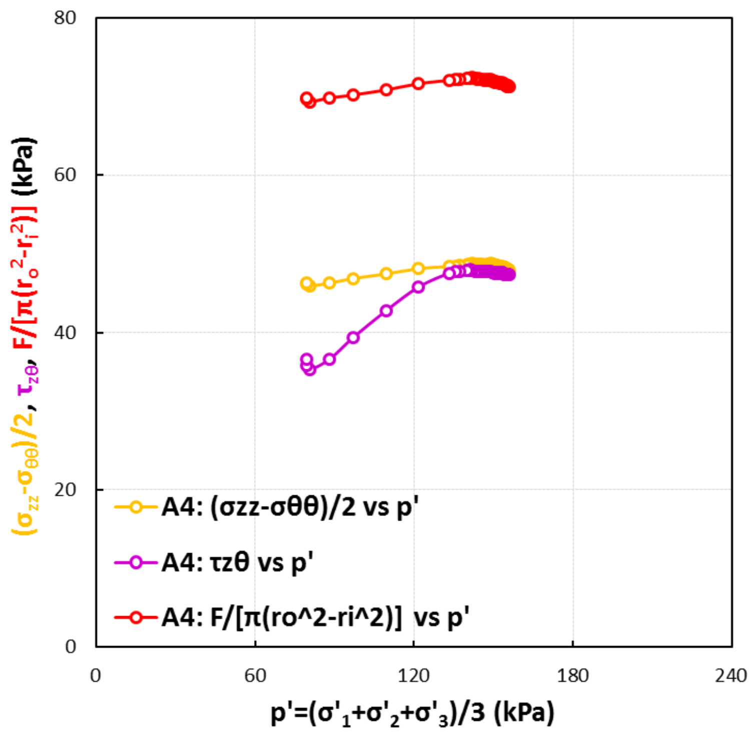

Fig. 7.44 Unloading of the different stresses imposed by the same stiff boundary in test A4

CHAPTER: 8 SUMMARY AND CONCLUSIONS

This thesis investigates experimentally the mechanical behaviour of sand under triaxial and generalised loading. The anisotropic flow deformation and critical state of M31 Sand were investigated using the hollow cylinder apparatus and two triaxial apparatuses of the National Technical University of Athens, all of which were either updated or modified for the needs of the present study. Monotonic and cyclic loading was imposed on water pluviated sand specimens under a broad range of consolidation effective stresses, $p'_c = (\sigma'_{1c} + \sigma'_{2c} + \sigma'_{3c}) / 3$, and stress ratios, $K_c = \sigma'_{3c} / \sigma'_{1c}$, with fixed or rotating stress principal axes (PA) and with two different values of the intermediate principal stress parameter, $b = (\sigma'_2 - \sigma'_3) / (\sigma'_1 - \sigma'_3)$.

The results of monotonic triaxial compression tests indicate the existence of a unique critical state line in the $p' - e - q$ space for M31 Sand, irrespective of the initial value of void ratio and mean effective stress and drainage conditions. The state parameter, ψ, proposed by Been and Jefferies (1985) normalises the strength and dilatancy characteristics of sand while the stress – dilatancy relationship depends on state. The results of monotonic undrained loading tests at different fixed directions of the σ'_1-axis with respect to the vertical, measured by angle $\alpha_{\sigma'1}$, and with constant p and b = 0.5 showed that the inherent anisotropy affects the strength and deformability of isotropically consolidated sand at the instability point, phase transformation point and peak-failure state. The response of sand becomes, in general, more contractive and less stiff when the angle $\alpha_{\sigma'1}$ increases yet the weakest response is observed when one of the maximum stress obliquity planes tends to align at failure with the horizontal bedding plane. The same amount of shear strain, γ_{oct}, or normalised excess pore-water pressure, $\Delta u / p'_i$, is accumulated in the contractive phase of response at a lower deviatoric stress ratio, $\eta = q / p'$, when $\alpha_{\sigma'1}$ is higher. Moreover, flow instability is triggered at a lower deviatoric stress ratio when $\alpha_{\sigma'1}$ is higher. Despite the fixity of the stress PA the deformation of sand is (weakly) non-coaxial up to the peak-failure state, becoming coaxial only after intense dilative straining post-peak, while the principal direction of incremental stain is biased towards $\alpha_{d\varepsilon 1} = +45^{\circ}$, possibly because sliding occurs more easily along the horizontal bedding plane.

Undrained loading tests were conducted on anisotropically consolidated sand with monotonically rotating stress PA at constant p and b = 0.5 and with either monotonically increasing, constant or cyclically changing deviatoric stress, q, in order to investigate the effects of consolidation and loading history on the mechanical behaviour of sand. It was found that the combinations of $\varphi = \sin^{-1} [(\sigma'_1 - \sigma'_3) / (\sigma'_1 +$

σ'_3)] and $\alpha_{\sigma'1}$ at the triggering of flow instability are not unique, albeit being stated differently in previous studies (Nakata et al. 1998, Sivathayalan and Vaid 2002). On the contrary, the triggering condition and deformation pattern of flow depend on the stress - strain history, including the effect of K_c and incremental stress direction; a new flow parameter indicates this dependence. It was also shown that a small stress disturbance involving rotation of the stress PA can trigger flow when the sand is consolidated at low K_c. For higher values of K_c the rotation of the stress PA at constant q may still induce plastic contraction, flow instability and failure of sand. Apart from the effects of stress - strain history on bifurcation the inherent anisotropy also plays an important role since the triggering of both diffuse and localised instabilities occurs preferably at stress states corresponding to unfavourable deformation kinematics, i.e. to shearing and sliding along the horizontal bedding plane.

The rotation of the stress PA is associated with strong non-coaxiality that persists past the state of peak failure. Distinct non-coaxiality patterns and elastic-plastic coupling, associated with the unloading of the non-diagonal component of the stress tensor, were observed during the first cycles of undrained stress rotation, at low deviatoric stress ratio, when the deviatoric stress was kept constant. The non-coaxiality angle, ξ, decreases with the deviatoric stress ratio in both non-coaxiality patterns, though, the sand ultimately deforms in a steady state corresponding to a stabilised angle of non-coaxiality, mean effective stress and deviatoric stress ratio, only to be arrested by the triggering of diffuse or localised instabilities. These non-coaxiality patterns are, in general, independent of the value of K_c and the number of the previous stress rotation cycles and are also observed in the case that the deviatoric stress changes periodically. On the other hand, distinct non-coaxiality patterns are observed before peak failure depending on the value of K_c when the rate of undrained stress rotation decreases as the deviatoric stress increases, though, the differences become less pronounced past the peak-failure state. Interestingly, stronger non-coaxiality corresponds to a lower K_c and the effect of pre-shearing on non-coaxiality appears to be more important than the effect of the rate of stress rotation, which has been previously pointed out by Gutierrez et al. (1991).

Among the novel findings of this study are those indicating that the stress state of loose sand subjected to undrained principal stress rotation at constant deviatoric stress may move along the direction of isotropic stress unloading from the consolidation state, at low deviatoric stress ratio, to the failure state without triggering flow. This behaviour is a contrast to the predictions of recent models developed within the framework of Bifurcation Theory which indicate that the direction of isotropic unloading belongs to the set of unstable directions of loose sand even at low deviatoric stress ratio, away from the peak failure state (Darve and Laouafa 2000, Darve et al. 2004, Sibille at al. 2007, Prunier et al. 2009). Once the failure surface has been reached it was shown that a quasi-static diffuse instability can be triggered under increasing effective stresses and decreasing stress ratio, followed by a dynamic diffuse instability under decreasing stresses and stress ratio. Consequently, the experimental results verify for the first time the predictions of the numerical analyses by Darve that instability may occur under increasing effective stresses and decreasing stress ratio (Darve and Laouafa 2000, Darve et al. 2004, Sibille at al. 2007, Prunier et al. 2009).

This study shows that sand exhibits strong non-coaxiality and contracts whenever the loading with fixed stress PA is interrupted by a continuous rotation of the stress PA. The degree of non-coaxiality and associated contractancy becomes higher when the previous shearing becomes more intense in terms of shear strain accumulation. The novel findings reported herein indicate that the influence of pre-shearing on sand's behaviour is more important than the influence of the degree of stress rotation and the level of η, p', e and b, reported in previous studies (Miura et al. 1986, Gutierrez et al. 1991, Li and Yu 2010, Tong et al. 2010 and 2014), but diminishes gradually as the stress rotation continues. Specifically, it is shown that sand exhibits strong non-coaxiality and contracts immediately upon initiating the rotation of the stress PA at constant effective stress principal values (PV) very close to critical state albeit it was previously dilating on the failure surface in a coaxial deformation mode, under radial loading; the phenomenon becomes increasingly intense as critical state is approached. Dafalias's (2016) thought experiment is the limiting case of the sequence of experiments performed herein thus the presented experimental evidence is supporting the claim that the Anisotropic Critical State Theory by Li and Dafalias (2012) constitutes a necessary revision of the classical Critical State Theory.

Accordingly, the effect of pre-shearing on the non-coaxiality and contractancy of highly-stressed sand is also apparent when undrained loading is imposed after anisotropic consolidation. In this case, a small stress disturbance involving rotation of the stress PA induces strong non-coaxiality and the associated plastic contraction triggers flow instability. This situation is the diffuse analogue of the mechanism in the incipient shear band described by Vardoulakis (Vardoulakis et al. 1978, Vardoulakis and Graf 1985, Vardoulakis and Georgopoulos 2005) and may explain the vulnerability of sands to spontaneous liquefaction, in stress-rotation conditions, when the static shear stress is high.

The results of this thesis offer new knowledge and contribute towards the deeper understanding of the effects of anisotropy and loading history on the mechanical behaviour of sand. The deposition process and loading history influence the formation and evolution of fabric and this microscopic process controls the macroscopic mechanical behaviour of sand at every state, including the critical one. Consequently, the necessity is highlighted to develop models that can simulate the effects of fabric on the mechanical behaviour of sand under generalised and complex loading conditions, similar to those imposed in the current study. The future research will be directed towards the application of techniques for measuring the fabric tensor of granular media by means of physical properties like the electrical conductivity and the mechanical wave velocity. Likewise, the investigation of the mechanical behaviour of sand under true triaxial loading conditions is an attractive subject for future research.

BIBLIOGRAPHY

Been K, Jefferies MG (1985) A state parameter for sands. Géotechnique 35 (2), 99–112

Dafalias YF (2016) Must critical state theory be revisited to include fabric effects? Acta Geotechnica (2016) 11:479, DOI 10.1007/s11440-016-0441-0

Darve F, Laouafa F (2000): Instabilities in granular materials and application to landslides. Mech. Cohes-Frict. Mater., 2000; 5:627-652

Darve F, Servant G, Laouafa F, Khoa HDV (2004) Failure in geomaterials: continuous and discrete analysis. Comput. Methods Appl. Mech. Engrg. 193 (2004), 3057-3085

Gutierrez M, Ishihara K, Towhata I (1991) Flow theory for sand during rotation of principal stress direction. Soils and Foundations, Vol.31, No.4, pp. 121-132

Li X, Yu H-S (2010) Numerical investigation of granular material behaviour under rotational shear. Géotechnique 60, No. 5, 381-394

Li XS, Dafalias YF (2012) Anisotropic critical state theory: role of fabric. Journal of Engineering Mechanics, Vol. 138, No. 3, 263-275

Miura K, Miura S, Toki S (1986) Deformation behavior of anisotropic dense sand under principal stress axes rotation. Soils and Foundations, Vol.26, No.1, 36-52

Nakata Y, Hyodo M, Murata H, Yasufuku N (1998) Flow deformation of sands subjected to principal stress rotation. Soils and Foundations, Vol.38, No.2, 115-128

Prunier F, Nicot F, Darve F, Laouafa F, Lignon S (2009) Three-dimensional multiscale bifurcation analysis of granular media. Journal of Engineering Mechanics, Vol. 135, No. 6, 493-509

Sibille L, Nicot F, Donzé FV, Darve F (2007) Material instability in granular assemblies from fundamentally different models. Int. J. Numer. Anal. Meth. Geomech., 2007; 31:457–481

Sivathayalan S, Vaid YP (2002) Influence of generalized initial state and principal stress rotation on the undrained response of sands. Canadian Geotechnical Journal, 39 (1): 63 – 76

Tong Z, Zhang J, Yu Y, Ga Zhang (2010) Drained deformation behavior of anisotropic sands during cyclic rotation of principal stress axes. Journal of Geotechnical and Geoenvironmental Engineering, Vol. 136, No.11, pp. 1509-1518

Tong Z, Fu P, Dafalias YF, Yao Y (2014) Discrete element method analysis of non-coaxial flow under rotational shear. Int. J. Numer. Anal. Meth. Geomech., 2014; 38:1519–1540

Vardoulakis I, Goldscheider M, Gudehus G (1978) Formation of shear bands in sand bodies as a bifurcation problem. International Journal for Numerical and Analytical Methods in Geomechanics, 1978, 2: 99-128

Vardoulakis I, Graf B (1985) Calibrations of constitutive models for granular materials using data from biaxial experiments. Géotechnique 35, No. 3, 299-317

Vardoulakis I, Georgopoulos I-O (2005) The “stress-dilatancy” hypothesis revisited: shear-banding related instabilities. Soils and Foundations, Vol.45, No.2, pp. 61-76

APPENDIX

The following articles have been either published or submitted for publication to international Journals:

ARTICLE: Georgiannou VN, Konstadinou M, Triantafyllos PK (2018) Sand behavior under stress states involving principal stress rotation. Journal of Geotechnical and Geoenvironmental Engineering, 2018, 144(6): 04018028

DOI: 10.1061/(ASCE)GT.1943-5606.0001878

ABSTRACT: The behavior of sands exhibiting both unstable and stable response, in their loose deposited state, under axial - torsional shearing involving continuous principal stress rotation is investigated using the hollow cylinder apparatus. This paper examines the parameters affecting the major principal stress direction attained at instability and / or phase transformation during torsional shearing following anisotropic consolidation. It is shown that constant stress ratio (t / p') lines, including the instability and phase transformation lines, are associated with the same major principal stress rotation with respect to the vertical within a wide range of initial mean effective stresses along the same consolidation stress ratio, K_c. In sands exhibiting instability, smaller principal stress rotations are required for the mobilization of the effective stress ratio at the onset of instability as the initial shear stress level increases (K_c decreases). In sands exhibiting stable response, principal stress rotation at phase transformation increases with increasing dilatancy tendencies. The dependence of the angle of shearing resistance, φ', mobilized at instability (IL), phase transformation (PTL), and failure (FL) lines on principal stress rotation and the intermediate stress parameter, b, is examined to verify whether the mobilized angle of shearing resistance can be considered as a material property. In continuous rotation tests, contrary to fixed principal stress direction and b tests, the angle of shearing resistance at IL can be considered as material property. However, the angle of shearing resistance at PTL depends on b and the direction of the principal stress. Moreover, phase transformation takes place at lower stress ratios as density increases.

ARTICLE: Triantafyllos PK, Georgiannou VN, Dafalias YF, Georgopoulos I-O (2020) New findings on the evolution of the instability surface of loose sand. Acta Geotechnica, 2020, 15(1): 197-221

DOI: 10.1007/s11440-019-00887-7

ABSTRACT: The conditions that trigger the unrestrained flow deformation of loose anisotropic sand are investigated. An Instability Surface (IS) is defined in the deviatoric plane. It comprises the transient-peak states at which flow instability is triggered when isotropically consolidated sand is subjected to monotonic undrained loading at various fixed directions of principal stress, α, under constant mean total stress, p, and fixed stress parameter, $b = (\sigma'_2 - \sigma'_3) / (\sigma'_1 - \sigma'_3) = 0.5$. Generalised undrained loading including rotation of the σ'_1-axis is also imposed on anisotropically consolidated sand. The mobilisation of the instability stress ratio, $\sin \varphi_{ip} = (\sigma'_1 - \sigma'_3) / (\sigma'_1 + \sigma'_3)$, that corresponds to stress direction α via the IS-locus, generally, triggers flow under loading with both fixed and rotating σ'_1-axis. Novel results are also presented: loose sand is subjected to undrained principal stress rotation at constant deviatoric stress, yet, the previously established IS is crossed stably and flow is triggered after stress rotation is imposed on the failure surface, while a non-flow diffuse instability is triggered on the failure surface under increasing stresses and decreasing stress ratio. The experimental results indicate that the triggering of flow instability depends on the stress - strain history as well as on the incremental stress direction. It is also shown that both diffuse and localised instabilities occur preferably at stress states corresponding to unfavourable deformation kinematics.

ARTICLE: Triantafyllos PK, Georgiannou VN, Pavlopoulou EM, Dafalias YF (2020) Strength and dilatancy of sand before and after stabilisation with colloidal-silica gel. Géotechnique (under review)

DOI:

ABSTRACT: To evaluate the effect of stabilisation, with a colloidal-silica aqueous gel, on subsequent sand behaviour the dilatancy and peak and ultimate strength characteristics of M31 Sand have been investigated before and after stabilisation. Triaxial compression tests were performed in drained and undrained mode, at effective stresses ranging from 100 to 6000 kPa. Important changes in the sand's mechanical behaviour were observed after stabilisation, including a significant increase in stress ratio and dilatancy rate at peak and a relocation of the treated sand's critical state line in the *e - p'* plane, substantially above this manifested by the untreated sand; however, the two lines converge at high stresses. The results confirmed a state dependent behaviour for the sand not applicable to the treated sand which exhibits predominantly stress dependent behaviour. A modified state parameter was used to normalise the treated sand's behaviour at peak failure.

ARTICLE: Triantafyllos PK, Georgiannou VN, Dafalias YF, Georgopoulos I-O (2020) Novel findings on the dilatancy and non-coaxiality of sand under generalised loading. Acta Geotechnica (accepted for publication)

DOI:

ABSTRACT: The dilatancy and non-coaxiality of sand are investigated under generalised loading including rotation of the stress principal axes (PA), in drained and undrained conditions. Weak non-coaxiality is exhibited under radial loading being dependent on the stress direction relative to the deposition direction, as well as on state, and gradually diminishing beyond peak failure. On the contrary, non-coaxiality is stronger and persists in the post-peak regime when sand is subjected to rotation of the stress PA. In conditions involving undrained rotation of the stress PA at constant total stress principal values (PV) distinct non-coaxiality patterns and elastic - plastic coupling are observed under increasing stress ratio, while a steady state is ultimately attained. This study shows that sand exhibits strong non-coaxiality and contracts immediately upon initiating the rotation of the stress PA at constant effective stress PV very close to critical state (CS) while it was previously dilating on the failure surface in a coaxial-deformation mode, under radial loading; the phenomenon becomes increasingly intense as CS is approached. The degree of non-coaxiality and associated contractancy becomes higher when the previous shearing becomes more persistent, in terms of shear strain accumulation, while the influence of pre-shearing is stronger than that of the degree of stress rotation and the level of $\eta = q / p'$, p', e and $b = (\sigma'_2 - \sigma'_3) / (\sigma'_1 - \sigma'_3)$, but diminishes gradually during stress rotation.